RTO-EN-8
AC/323(AVT)TP/23

RTO-EN-8

**NORTH ATLANTIC TREATY ORGANIZATION**

**RESEARCH AND TECHNOLOGY ORGANIZATION**

BP 25, 7 RUE ANCELLE, F-92201 NEUILLY-SUR-SEINE CEDEX, FRANCE

© RTO/NATO 2000

Single copies of this publication or of a part of it may be made for individual use only. The approval of the RTA Information Policy Executive is required for more than one copy to be made or an extract included in another publication. Requests to do so should be sent to the address above.

**RTO EDUCATIONAL NOTES 8**

# Measurement Techniques for High Enthalpy and Plasma Flows

(Techniques de mesure pour les écoulements de plasma et les écoulements à haute enthalpie)

*This report is a compilation of the edited proceedings of the "Measurement Techniques for High Enthalpy and Plasma Flows" course held at the von Kármán Institute for Fluid Dynamics (VKI) in Rhode-Saint-Genèse, Belgium, 25-29 October 1999.*

Published April 2000

*Distribution and Availability on Back Cover*

RTO-EN-8
AC/323(AVT)TP/23

**NORTH ATLANTIC TREATY ORGANIZATION**

**RESEARCH AND TECHNOLOGY ORGANIZATION**

BP 25, 7 RUE ANCELLE, F-92201 NEUILLY-SUR-SEINE CEDEX, FRANCE

**RTO EDUCATIONAL NOTES 8**

# Measurement Techniques for High Enthalpy and Plasma Flows

(Techniques de mesure pour les écoulements de plasma et les écoulements à haute enthalpie)

*This report is a compilation of the edited proceedings of the "Measurement Techniques for High Enthalpy and Plasma Flows" course held at the von Kármán Institute for Fluid Dynamics (VKI) in Rhode-Saint-Genèse, Belgium, 25-29 October 1999.*

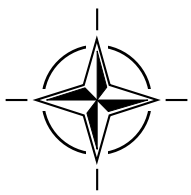

# The Research and Technology Organization (RTO) of NATO

RTO is the single focus in NATO for Defence Research and Technology activities. Its mission is to conduct and promote cooperative research and information exchange. The objective is to support the development and effective use of national defence research and technology and to meet the military needs of the Alliance, to maintain a technological lead, and to provide advice to NATO and national decision makers. The RTO performs its mission with the support of an extensive network of national experts. It also ensures effective coordination with other NATO bodies involved in R&T activities.

RTO reports both to the Military Committee of NATO and to the Conference of National Armament Directors. It comprises a Research and Technology Board (RTB) as the highest level of national representation and the Research and Technology Agency (RTA), a dedicated staff with its headquarters in Neuilly, near Paris, France. In order to facilitate contacts with the military users and other NATO activities, a small part of the RTA staff is located in NATO Headquarters in Brussels. The Brussels staff also coordinates RTO's cooperation with nations in Middle and Eastern Europe, to which RTO attaches particular importance especially as working together in the field of research is one of the more promising areas of initial cooperation.

The total spectrum of R&T activities is covered by 7 Panels, dealing with:

- SAS Studies, Analysis and Simulation
- SCI Systems Concepts and Integration
- SET Sensors and Electronics Technology
- IST Information Systems Technology
- AVT Applied Vehicle Technology
- HFM Human Factors and Medicine
- MSG Modelling and Simulation

These Panels are made up of national representatives as well as generally recognised 'world class' scientists. The Panels also provide a communication link to military users and other NATO bodies. RTO's scientific and technological work is carried out by Technical Teams, created for specific activities and with a specific duration. Such Technical Teams can organise workshops, symposia, field trials, lecture series and training courses. An important function of these Technical Teams is to ensure the continuity of the expert networks.

RTO builds upon earlier cooperation in defence research and technology as set-up under the Advisory Group for Aerospace Research and Development (AGARD) and the Defence Research Group (DRG). AGARD and the DRG share common roots in that they were both established at the initiative of Dr Theodore von Kármán, a leading aerospace scientist, who early on recognised the importance of scientific support for the Allied Armed Forces. RTO is capitalising on these common roots in order to provide the Alliance and the NATO nations with a strong scientific and technological basis that will guarantee a solid base for the future.

The content of this publication has been reproduced
directly from material supplied by RTO or the authors.

Published April 2000

Copyright © RTO/NATO 2000
All Rights Reserved

ISBN 92-837-1030-4

*Printed by Canada Communication Group Inc.*
*(A St. Joseph Corporation Company)*
*45 Sacré-Cœur Blvd., Hull (Québec), Canada K1A 0S7*

# Measurement Techniques for High Enthalpy and Plasma Flows

## (RTO EN-8)

# Executive Summary

The RTO AVT/VKI Special Course on "Measurement Techniques for High Enthalpy and Plasma Flows" gathered specialists in this area from Europe, USA and Russia who combined their efforts to produce this comprehensive set of notes. The following topics were covered: a review of various high enthalpy and plasma flow facilities, intrusive and non intrusive measurement techniques for the characterization of flows generated in these facilities and the utilization of plasma facilities for the evaluation of material catalysis properties.

Most of the facility types presently used to generate high enthalpy flows were reviewed. The first class of facilities currently used in the USA and in Europe are the arc jet type where the test gas is heated through an electric discharge between electrodes. In this case, high levels of enthalpy can be achieved for moderate levels of stagnation pressures (typically up to 100 bars). With respect to shock tube facility, arc-jet facilities provide a longer run time. In order to increase the Reynolds number while maintaining a level of enthalpy relevant for flight conditions, the combination of a free piston gun tunnel and a shock tube was developed. The facility produces a high Reynolds number and high enthalpy flow field over a very short time (typical of a shock tube level). In most of the previously discussed facilities, some particulate matter or residual electrode materials are present in the flow and may affect the determination of material catalysis. The approach taken by Russian scientists for this particular issue is to use an inductively coupled plasma generator which produces very clean plasma. However, since the flow conditions are subsonic and correspond to a low Reynolds value, a methodology of extrapolation of the plasmatron facility to flight conditions was presented.

In all the facilities presented, there is a considerable need for assessment of flow field properties to support numerical modeling of high enthalpy flows in its transposition to flight conditions. Accessing the details of the flow field (composition, state of the species, velocity, temperatures ...) requires an important investment in measurement techniques. The adaptation of intrusive measurement techniques to high enthalpy flow facilities which provide macroscopic information (pitot pressure and stagnation heat flux) were presented. These techniques provide a good initial screening for the determination of flow properties which require further development using non-intrusive measurement techniques. Techniques starting with pyrometry for the measurement of material sample temperature, to more sophisticated techniques based on spectroscopy (emission, absorption, laser induced emission) were discussed in their application to arc jet, free piston shock tunnel and inductively couple plasma facilities.

As illustrated by the requirements in terms of flow physics modeling at the beginning of the course, non-intrusive measurement techniques are essential for the qualification of numerical modeling. It was illustrated that the assessment of flow properties is not only important for validation of numerical modeling but also in the analysis of material catalysis. Consequently, a continuous effort should be devoted to the improvement and application of those techniques in high enthalpy and plasma flow facilities. In particular, problems associated with flow thermal and chemical non-equilibrium require more detailed information on the state of the species, the vibrational / chemical coupling, which require even more refined information on the flow.

The material assembled in this report was prepared under the combined sponsorship of the RTO AVT Panel, the Consultant and Exchange and the Partnership for Peace Programmes of RTO and the von Kármán Institute (VKI) for Fluid Dynamics. We wish to thank all the lecturers for their outstanding work, as well as the organizers of RTO and VKI.

# Techniques de mesure pour les écoulements de plasma et les écoulements à haute enthalpie

## (RTO EN-8)

# Synthèse

Le cours spécial RTO/AVT « Techniques de mesure pour les écoulements à haute enthalpie et les plasmas » a réuni des spécialistes européens, américains et russes dans ce domaine qui ont mis leurs efforts en commun pour produire ces notes détaillées. Les sujets suivants ont été traités: revue des souffleries à haute enthalpie et à plasma, des techniques de mesures intrusives et non intrusives utilisées pour la caractérisation de ces écoulements et utilisation des souffleries à plasma pour l'étude des propriétés catalytiques des matériaux.

La plupart des types d'installations utilisées pour générer des écoulements à haute enthalpie ont été passées en revue. Une première classe d'installations utilisées fréquemment aux USA et en Europe est du type soufflerie à arc dans laquelle le gaz est chauffé grâce à un arc électrique entre deux électrodes. Dans ce cas, des niveaux importants d'enthalpie peuvent être atteints pour des niveaux de pression d'arrêt modestes (de l'ordre de 100 bars). Par rapport aux tubes à choc, les souffleries à arc offrent un temps d'essai plus long. De manière à accroître le nombre de Reynolds tout en gardant un niveau d'enthalpie significatif par rapport aux conditions de vol, la combinaison d'une soufflerie à piston libre et d'un tube à choc a été développée. Cette installation génère un écoulement à haute enthalpie avec un nombre de Reynolds élevé mais avec une durée d'essai très courte (typique d'un tube à choc). Dans la plupart des installations décrites jusqu'ici, des particules ou des résidus de matière provenant des électrodes sont présents dans l'écoulement et peuvent affecter la détermination des propriétés catalytiques des matériaux testés. De ce point de vue, l'approche des scientifiques russes est d'utiliser des générateurs de plasma de type inductifs qui produisent un plasma très pur. Néanmoins, comme l'écoulement de plasma ainsi créé est subsonique et correspond à un bas nombre de Reynolds, une méthodologie d'extrapolation des conditions du plasmatron vers le vol a été présentée.

Dans toutes les installations présentées, il y a un important besoin de connaissance des propriétés de l'écoulement pour supporter la modélisation numérique dans sa transposition aux conditions de vol. Accéder aux détails de l'écoulement (composition chimique, état des espèces, vitesse, températures ...) nécessite un investissement important dans les techniques de mesure. L'adaptation des techniques de mesure intrusives aux souffleries à haute enthalpie et à plasma qui fournissent des informations macroscopiques (pression pitot et flux de chaleur au point d'arrêt) a été présentée. Ces techniques permettent une bonne première approche décrivant les conditions d'écoulement qui cependant nécessite un approfondissement en utilisant des techniques de mesure non intrusives. Ces techniques, en commençant par la pyrométrie pour la mesure de température de surface d'échantillon de matériau puis les techniques plus sophistiquées basées sur la spectroscopie (émission, absorption, émission induite par laser) ont été discutées dans leur application aux souffleries à arc, aux tubes à choc à compression par piston et aux générateurs à plasma par induction.

Comme mis en évidence par les besoins en termes de modélisation physique au début du cours, les techniques de mesure non-intrusives sont essentielles dans le processus de qualification des modèles numériques. Comme illustré dans ce cours, une meilleure connaissance des écoulements à haute enthalpie n'est pas uniquement nécessaire pour la validation numérique mais aussi dans le processus d'analyse des propriétés catalytiques des matériaux. En conséquence, un effort continu et soutenu est nécessaire pour le développement et l'application de ces techniques dans les souffleries à haute enthalpie et à plasma.

Les notes assemblées dans ce rapport ont été préparées grâce au concours du panel RTO/AVT des programmes RTO des Consultants et des échanges et du Partenariat pour la Paix, et de l'Institut von Kármán (IVK) de dynamique des fluides. Nous voulons remercier tous les conférenciers pour l'excellent travail qu'ils ont accompli ainsi que les organisateurs du RTO et de l'IVK.

Click inside the blue boxes or on the titles to view the corresponding section

# Contents


| | Page |
|---|---|
| **Executive Summary** | **iii** |
| **Synthèse** | **iv** |
| **Publications of the RTO Applied Vehicle Technology Panel** | **vii** |
| **Special Course Staff** | **ix** |

| | Reference |
|---|---|
| **Overview of Characteristics and Experiments in IPM Plasmatrons**<br>by A.N. Gordeev | **1A** |
| **Methodology, Technical Approach and Measurement Techniques for Testing of TPM Thermal Protection Materials in IPM Plasmatrons**<br>by A.N. Gordeev | **1B** |
| **Overview of IRS Plasma Wind Tunnel Facilities**<br>by M. Auweter-Kurtz and T. Wegmann | **2A** |
| **Diagnostic Tools for Plasma Wind Tunnels and Reentry Vehicles at the IRS**<br>by M. Auweter-Kurtz, M. Feigl and M. Winter | **2B** |
| **Measurement Requirements for Improved Modeling of Arcjet Facility Flows**<br>by D.G. Fletcher | **3A** |
| **Nonintrusive Diagnostic Strategies for Arcjet Stream Characterization**<br>by D.G. Fletcher | **3B** |
| **Overview of Measurement Techniques at CORIA**<br>by L. Robin, P. Boubert, A. Bourdon, A. Bultel, B. van Ootegem and P. Vervisch | **4A** |
| **Laser Induced Fluorescence in High Enthalpy Facilities in the Tsniimach Center (Moscow – Russia)**<br>by L. Robin | **4B** |
| **Molecular Diagnostics for the Study of Hypersonic Flows**<br>by F. Grisch | **5** |
| **The VKI Plasmatron Characteristics and Performance**<br>by B. Bottin, O. Chazot, M. Carbonaro, V. Van Der Haegen and S. Paris | **6** |
| **Spectroscopic Techniques for Measurement of Velocity and Temperature in the DLR High Enthalpy Shock Tunnel HEG**<br>by W.H. Beck | **7A** |
| **Rotational and Vibrational Temperature Measurements in the DLR High Enthalpy Shock Tunnel HEG Using LIF and Flash Lamp Absorption**<br>by W.H. Beck | **7B** |

**Combined Measurements and Computations of High Enthalpy and Plasma Flows for Determination of TPM Surface Catalycity** 8A
by A.F. Kolesnikov

**Extrapolation from High Enthalpy Tests to Flight Based on the Concept of Local Heat Transfer Simulation** 8B
by A.F. Kolesnikov

**Heat Flux Measurements in High Enthalpy Flows** 9A
by A. Gülhan

**Application of Pyrometry and IR-Thermography to High Surface Temperature Measurements** 9B
by A. Gülhan

# Publications of the RTO Applied Vehicle Technology Panel

MEETING PROCEEDINGS (MP)

**Design for Low Cost Operation and Support**
MP-37, Spring 2000

**Structural Aspects of Flexible Aircraft Control**
MP-36, Spring 2000

**Aerodynamic Design and Optimization of Flight Vehicles in a Concurrent Multi-Disciplinary Environment**
MP-35, Spring 2000

**Gas Turbine Operation and Technology for Land, Sea and Air Propulsion and Power Systems (Unclassified)**
MP-34, Spring 2000

**New Metallic Materials for the Structure of Aging Aircraft**
MP-25, April 2000

**Small Rocket Motors and Gas Generators for Land, Sea and Air Launched Weapons Systems**
MP-23, April 2000

**Application of Damage Tolerance Principles for Improved Airworthiness of Rotorcraft**
MP-24, January 2000

**Gas Turbine Engine Combustion, Emissions and Alternative Fuels**
MP-14, June 1999

**Fatigue in the Presence of Corrosion**
MP-18, March 1999

**Qualification of Life Extension Schemes for Engine Components**
MP-17, March 1999

**Fluid Dynamics Problems of Vehicles Operation Near or in the Air-Sea Interface**
MP-15, February 1999

**Design Principles and Methods for Aircraft Gas Turbine Engines**
MP-8, February 1999

**Airframe Inspection Reliability under Field/Depot Conditions**
MP-10, November 1998

**Intelligent Processing of High Performance Materials**
MP-9, November 1998

**Exploitation of Structural Loads/Health Data for Reduced Cycle Costs**
MP-7, November 1998

**Missile Aerodynamics**
MP-5, November 1998

EDUCATIONAL NOTES

**Measurement Techniques for High Enthalpy and Plasma Flows**
EN-8, April 2000

**Development and Operation of UAVs for Military and Civil Applications**
EN-9, April 2000

**Planar Optical Measurements Methods for Gas Turbine Engine Life**
EN-6, September 1999

**High Order Methods for Computational Physics (published jointly with Springer-Verlag, Germany)**
EN-5, March 1999

**Fluid Dynamics Research on Supersonic Aircraft**
EN-4, November 1998

**Integrated Multidisciplinary Design of High Pressure Multistage Compressor Systems**
EN-1, September 1998

**TECHNICAL REPORTS**

**Recommended Practices for Monitoring Gas Turbine Engine Life Consumption**
TR-28, April 2000

**Verification and Validation Data for Computational Unsteady Aerodynamics**
TR-26, Spring 2000

**A Feasibility Study of Collaborative Multi-facility Windtunnel Testing for CFD Validation**
TR-27, December 1999

# Special Course Staff

### COURSE DIRECTOR and LOCAL COORDINATOR

Professeur J-M. CHARBONNIER
Associate Professor Aeronautics/Aerospace Department
von Kármán Institute for Fluid Dynamics
Chaussée de Waterloo, 72
B-1640 Rhode-Saint-Genèse – Belgium

### LECTURERS

Prof. M. CARBONARO
Director, von Kármán Institute for Fluid Dynamics
Chaussée de Waterloo, 72
B-1640 Rhode-Saint-Genèse - Belgium

Mr. F. GRISCH
ONERA/Dept Mesures Physiques
29, Avenue de la Division Leclerc
92320 Châtillon Cedex - France

Dr. L. ROBIN
Université de Rouen
CORIA/CNRS UMR 6614
Place Emile Blondel
76821 Mont Saint Aignan Cedex - France

Prof. Monika AUWETER-KURTZ
IRS, University of Stuttgart
Pfaffenwaldring 31
D-70569 Stuttgart - Germany

Dr. W. BECK
High Enthalpy Shock Tunnel HEG
Aerothermodynamics Department
Institute for Fluid Mechanics, DLR
Bunsenstrasse, 10
D-37073 Göttingen - Germany

Dr. Ing. Ali GÜLHAN
DLR Section Köln-Porz
Wind Tunnel Division
Porz-Wahnheide
Linder Höhe
D-51147 Köln - Germany

Dr. KOLESNIKOV
Institute for Problems in Mechanics (IPM)
Russian Academy of Sciences
Prospect Vernadskogo, 101-1
117526 Moscow - Russia

Dr. GORDEEV
Institute for Problems in Mechanics (IPM)
Russian Academy of Sciences/Plasma Laboratory
Prospect Vernadskogo, 101-1
117526 Moscow - Russia

Dr. D.G. FLETCHER
NASA Ames Research Center
Reacting Flow Environments Branch
MS 230-2
Moffett Field, CA 94035-1000

### PANEL EXECUTIVE

Dr. P. Tonn

**Mail from Europe:**
RTA/OTAN
BP 25 - 7, rue Ancelle
92201 Neuilly-sur-Seine Cedex
France

**Mail from USA and Canada:**
RTA/NATO
Unit PSC 116
APO AE 09777

**☎ 33 (1) 55 61 22 85**
**Fax: 33 (1) 55 61 22 98**

# OVERVIEW OF CHARACTERISTICS AND EXPERIMENTS IN IPM PLASMATRONS

**A. N. Gordeev**

*Institute for Problems in Mechanics of Russian Academy of Sciences, 101-1 prospect Vernadskogo, 117526 Moscow, Russia.*
*Tel.: +7 095 434 36 74, Fax: +7 095 938 20 48, E-mail: gordeev@ipmnet.ru*

ABSTRACT

Characteristics of IPG series plasmatrons as well as there application for reentry simulation and testing of thermal protection materials are discussed in the presented paper on the basis of 35-years experience of Plasma Laboratory of IPM RAS. Successful application of plasmatrons for simulation of reentry conditions and testing of thermal protection materials is based on using of plasmatron's advantages such as purity of plasma flow, its high stability, excellent reproducibility as well as wide ranges of realized pressure and heat flux. Using of subsonic regimes together with plasmatron's ability for independent smooth regulation of regime parameters such as pressure and power injected in plasma make a plasmatron the most flexible and powerful instrument for simulation of thermochemical action of shock layer on the surface of descent space vehicle, especially when it is necessary to solve problems concerned radiative & convective heating and/or non-equilibrium heat transfer. To the present day long-term aging tests (up to 100 15-minutes testing cycles for one sample) in dissociated gas flow were fulfilled only using plasmatrons. Also there are discussed tests of ablative thermal protection materials, studies of thermo-chemical interaction between dissociated flows and reusable thermal protection materials as well as some «non-space» applications of plasmatrons as deposition of diamond films and testing of industrial materials on heat shock.

## 1. INTRODUCTION: ADVANTAGES OF INDUCTION PLASMATRONS

In world practice gas heating by electric energy, enjoy wide application for the simulation of re-entry conditions to test reusable thermal protection materials. However traditional methods like ohmic heating and electric arc heating don't give needed performance characteristics. Ohmic heaters do not allow to reach high temperatures and electric arc heaters pollute gas flow by products of electrodes erosion. On the contrary induction method of gas heating most completely fits the requirements of simulation of physical parameters of hypersonic vehicles aerodynamic heating.

Discharge device of a plasmatron includes two main elements – quartz tube, that is used as discharge channel and induction coil (inductor), on which runs high-frequency current, that induces circular currents in discharge. In such device there are no electrodes, which are the main source of flow contamination and disturbancies in arc-jet facilities. Discharge in subsonic flow of air, discharge channel and inductor of the powerful plasmatron IPG-3 are presented in Fig.1.

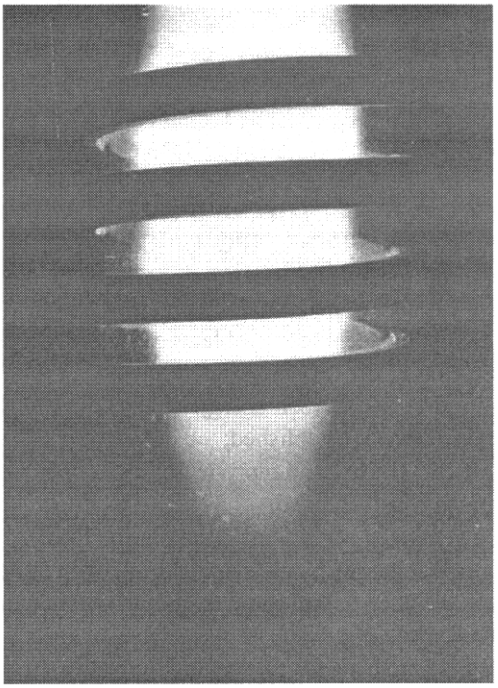

***Figure 1.*** *Inductively coupled plasma in the IPG-3 plasmatron (discharge channel diameter – 200 mm).*

In the plasmatrons of IPG series hot gas does not contact with discharge channel wall due to flow vortex in discharge channel and that ensures high purity of plasma flow. Also flow vortex makes discharge very stable in wide range of pressure and discharge existence is not limited in time.

Induction plasma generators have a high ability to simulate aerodynamic heating of hypersonic vehicles. Due to using contactless heating of gas flow by induction current, these facilities create exceptionally pure plasma flow of any gases also they show high stability and excellent reproducibility of regimes. Last but not least advantage of a plasmatron is the feasibility to make long-term aging tests in real time. Taken together, these advantages make induction plasma generators best suited to fulfill aging tests of reusable thermal protection materials. Besides, using of pure subsonic plasma jets allows to simulate most precisely thermochemical action of shock layer plasma on thermal protection materials of descent space vehicles. In particular, plasmatrons give an opportunity to

*Paper presented at the RTO AVT Course on "Measurement Techniques for High Enthalpy and Plasma Flows", held in Rhode-Saint-Genèse, Belgium, 25-29 October 1999, and published in RTO EN-8.*

simulate flight conditions such as total enthalpy and pressure, temperature and concentrations profiles within boundary layer and hence heat flux and surface temperature.

## 2. PLAMATRONS OF THE IPG SERIES: STEP BY STEP

During the last 35 years four induction plasma generators of IPG-series have been created in IPM under the supervision of Dr. M. Yakushin. Electrodeless high frequency discharge in gas flow was used in these facilities for generation of subsonic and supersonic high enthalpy jets of air and other gases. The progress of the IPG plasmatrons followed the directions of the increase of power, discharge channel diameter, total pressure range, making it possible to use different gases. Table 1 shows main characteristics of IPG facilities, which were in use previously (IPG-1, IPG-2) and which are in operation now (IPG-3, IPG-4). Compared to first generation, existing plasmatrons increase 15 times in power, 3 orders of magnitude in pressure range.
The following technical problems were solved during the creation of the IPG facilities:

- a compromise between energy and gas dynamics parameters was established;
- excellent stability and reproducibility of operation regimes were achieved;
- tube generator was agreed upon plasma load;
- quartz discharge channels and gas injection system were designed to withstand operation without any forced cooling;
- effective methods for plasma ignition were developed.

One of the main aims of IPG series development was to ensure high working ability and high reliability in operation for all parts and elements of facilities due to using of reliable approaches which are as simple as possible as well as schemes and principles verified by experience. Vertical orientation of discharge channel with plasma flow directed upward has been applied for all four facilities and it allowed to avoid problems concerned operation at high pressures where Archimedean forces disturb discharge oriented horizontally but gasdynamic stabilization is not so effective as at low pressures. The problems were solved successfully to make a choice of optimal conceptual sketches, materials for manufacturing and commercial equipment of general use. Units and elements of facilities have been designed to keep high reliability under heavy duty operation conditions including joint action of high temperature, chemically active gases, low pressure, significant radiative & convective heat fluxes, high-frequency electromagnetic fields, which are attended by phenomena caused by skin-effect.

To secure the safe working conditions for maintenance personnel reliable means of protection have been designed in the facilities of IPG series.

Particular attention has been given to IPG facilities universality, which allows among other things quick going from subsonic to supersonic operation mode and vice versa. The time of this conversion is about a few minutes. So samples and models could be changed quickly between testing cycles during aging tests of thermal protection materials and full-scale design elements.

The IPG-1 facility vas used for the simulation of convective & radiative heat transfer from chemically equilibrium boundary layer to the surface at atmospheric pressure. Ablative materials for reentry vehicles «Voskhod», «Soyuz», «Zond-4», «Luna-16» were investigated at the intensive blowing of vapor into initial air plasma flow [1-8]. Also the first into initial air plasma flow [1-8]. Also the first

***Table 1.*** *Main parameters of the IPG plasmatrons*

| Parameters | IPG-1 (1963 – 1977) | IPG-2 (1977 – 1989) | IPG-3 (1984 – ....) | IPG-4 (1989 – ....) |
|---|---|---|---|---|
| Electric power supplied to plasmatron, kW | 60 | 90 | 1000 | 100 |
| Generator anode power supply, kW | 30 | 60 | 750 | 80 |
| Frequency, MHz | 11 | 17 | 0.44 | 1.76 |
| Discharge channel, mm | 60 | 60 | 150–200 | 80 |
| Snagnation pressure, atm | 1,0 | 0,05–1,0 | 0,01–0,3 | 0,01–1,0 |
| Gas mass flows rate, g/s | 1,2 | 2–3 | 8–11 | 2–5 |
| Working gases | Ar, Air, $CO_2$ | Air, $N_2$, $O_2$, | Air, $N_2$ | Air, $N_2$, $O_2$, $CO_2$, Ar, $CO_2$+$N_2$+Ar, Ar+organic gases |

experiments with planet atmospheres as working gases were carried out using this facility. The outward appearance of the IPG-1 is shown in Fig.2.

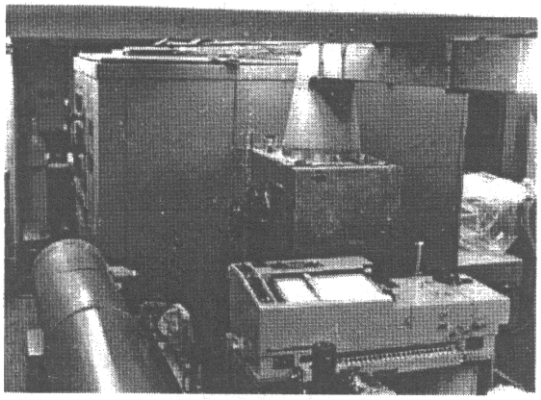

***Figure 2.*** *The outward appearance of the IPG-1 plasmatron (1963-1977).*

Expanded programme of testing was realized in the IPG-2 during Buran programme and samples (30 mm diameter) of black ceramic tile [9-11] and different types of carbon-carbon materials with antioxidative coatings were subjected aging tests with duration up to 100 cycles. 5 coatings for ceramic tile and about 50 coatings for carbon-carbon materials were put through the IPG-2 facility. Non-equilibrium convective heat transfer from dissociated air, oxygen and nitrogen flows to thermal protection materials was studied using the IPG-2 at pressures P = 0.05-1.0 atm and main results on catalycity of Buran's thermal protection materials were obtained using this facility [9, 12-16]. The outward appearance of the IPG-2 is shown in Fig.3.

The main problem solved using the IPG-3 facility is laboratory testing of full-scale ceramic tile and other full-scale design elements under conditions corresponding to the peak heating part of "Buran's" re-entry trajectory [9-11, 17].

The IPG-3 plasmatron of 1 MW class is the most powerful facility of the IPG series. Its outward appearance is shown by Fig.4.

The creation of the IPG-4 facility introduces radical alteration in the plasmatron technology of IPM. The IPG-4 facility fully corresponds to modern requirements in performances and potentialities, and permits to solve wide spectrum of problems in experimental high temperature gas dynamics. The fundamental difference of IPG-4 from preceding facilities of the IPG series is that the opportunity was realized for the first time to obtain stable high- enthalpy jets in the pressure range P = 0.01-1.0 atm at constant gas enthalpy. Pressure and enthalpy (H = 10-40 MJ/kg) can be regulated smoothly. It allows to

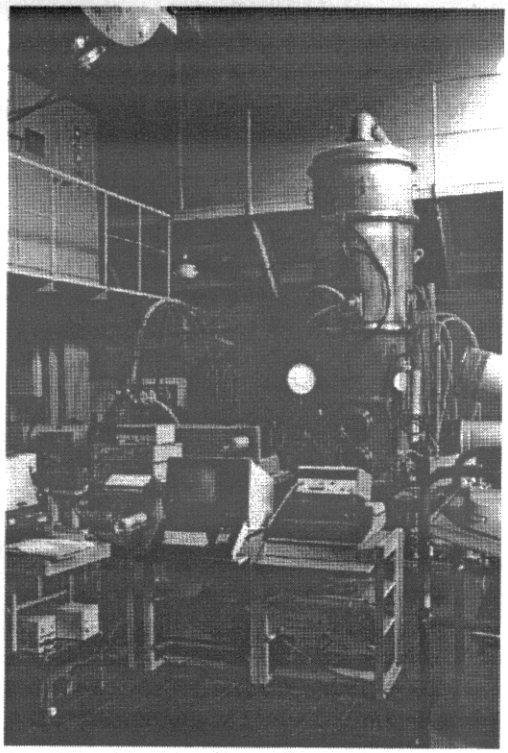

***Figure 3.*** *The outward appearance of the IPG-2 plasmatron (1977-1989).*

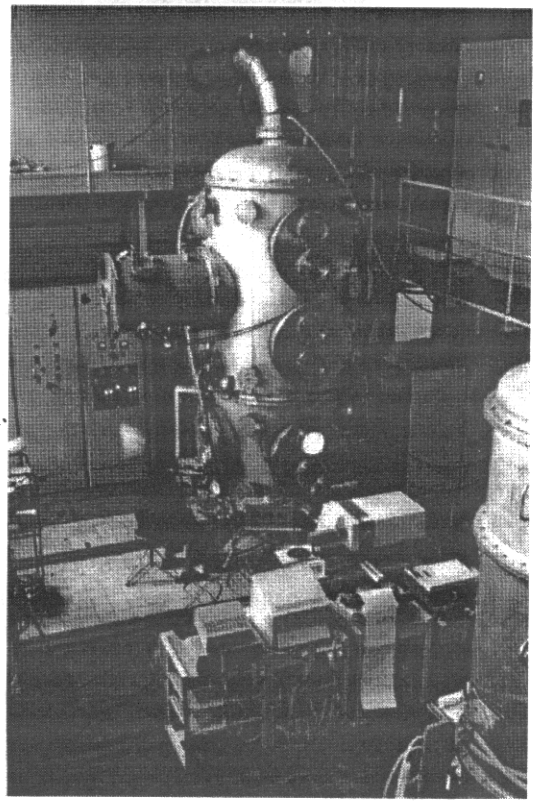

***Figure 4.*** *The outward appearance of the IPG-3 plasmatron (1983-....).*

vary the degree of the disequilibrium of dissociated boundary layer on the model from frozen to equilibrium. It makes it possible to extend the area of

trajectory parameters simulation for the hypersonic vehicles in existence and under consideration.

Up to now the IPG-4 plasmatron is «working horse» of Plasma Lab. Due to its universality and low cost of exploitation the IPG-4 is in operation practically every day. It was used to make test campaigns for ESTEC/ESA, Aerospatiale, SEP and many others as well as to study surface catalycity and non-equilibrium heat transfer in different dissociated gases [18-25]. The outward appearance of the IPG-4 is given in Fig.5.

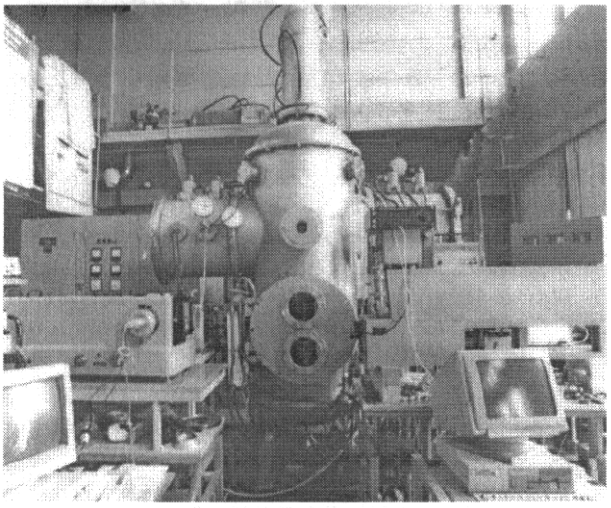

***Figure 5.*** *The outward appearance of the IPG-4 plasmatron (1989-....).*

## 3. MODERN PLASMATRONS OF THE IPG SERIES

The IPG-3 and the IPG-4 plasmatrons meet modern requirements to facilities for the testing of hypersonic vehicle thermal protection. These requirements are derived from the necessity to work on the following problems:

- the investigation of the thermochemical stability of thermal projection materials under conditions modeling aerodynamic heating;
- the determination of the catalytic properties of surfaces at high temperatures;
- the study of ablative materials including intensive radiative & convective heating at high pressures (up to 1 atm and higher)
- the experimental and numerical studies of plasma flow in
  - * discharge channels of induction plasma generators;
  - * sub- and supersonic non-equilibrium high enthalpy jets;
  - * dissociated boundary layers over models;
- synthesis of new coatings in high enthalpy jets of carbon-hydrate- containing gases by using chemical vapor deposition (CVD).

The IPG-3 and the IPG-4 plasmatrons, which are in operation now, differ in their technical potentialities and it leads to different application.

The IPG-3 facility is used to solve problems of practical character, i.e. testing of working capacity of large-scale samples of thermal protection materials and full-scale (150-500 mm) elements of thermal protection system of «Bor», «Buran» and advanced hypersonic vehicles as follows. High-enthalpy air flows were used for testing of full-scale ceramic tile with its real fastening to skin imitator (100 testing cycles of 10-minutes duration of each cycle at T = 1250°C), ceramic tile in simulated non-standard situations, full-scale part of man-hole cover with window, light-weight structures of carbon-carbon with antioxidative coating (200 x 200 mm, 2 mm thickness) as well as large samples of thermal protection materials (diameter ~100 mm).

The IPG-4 application is directed to research works, for example, non-equilibrium heat exchange between high-enthalpy dissociated flows and different surfaces such as metals, quartz, ceramics, carbon-carbon materials with antioxidative coatings. Database was created on catalytic properties of thermal protection materials. Also thermochemical stability of thermal protection materials have been studied including determination of maximum working temperatures of TPM, making aging tests, studies of surface degradation together with changes of surface emissivity and catalycity as the functions of temperature and time. Comparative study was made on Buran's materials behavior in different dissociated gas environments.

Consider the design of the IPG-4 facility. Schematic diagram of test chamber in Fig.6 (see next page) and. schematic diagram of IPG-4 facility with its infrastructure and scientific equippment are shown in Fig.7.

**Test chamber** consists of low pressure test chamber shell, inductor chamber, induction heater, fast positioning device, instrument positioning device, water-cooled shields.

*Test chamber shell* is designed to produce and to maintain specified pressure under the effect of high temperature and chemically active gas environment, as well as to protect maintenance personnel. The shell of cylindrical form is made one-sectional. It is equipped with elliptic bottoms, man-holes with corresponding covers, mating units, optical windows and lead-in for high frequency feeder.

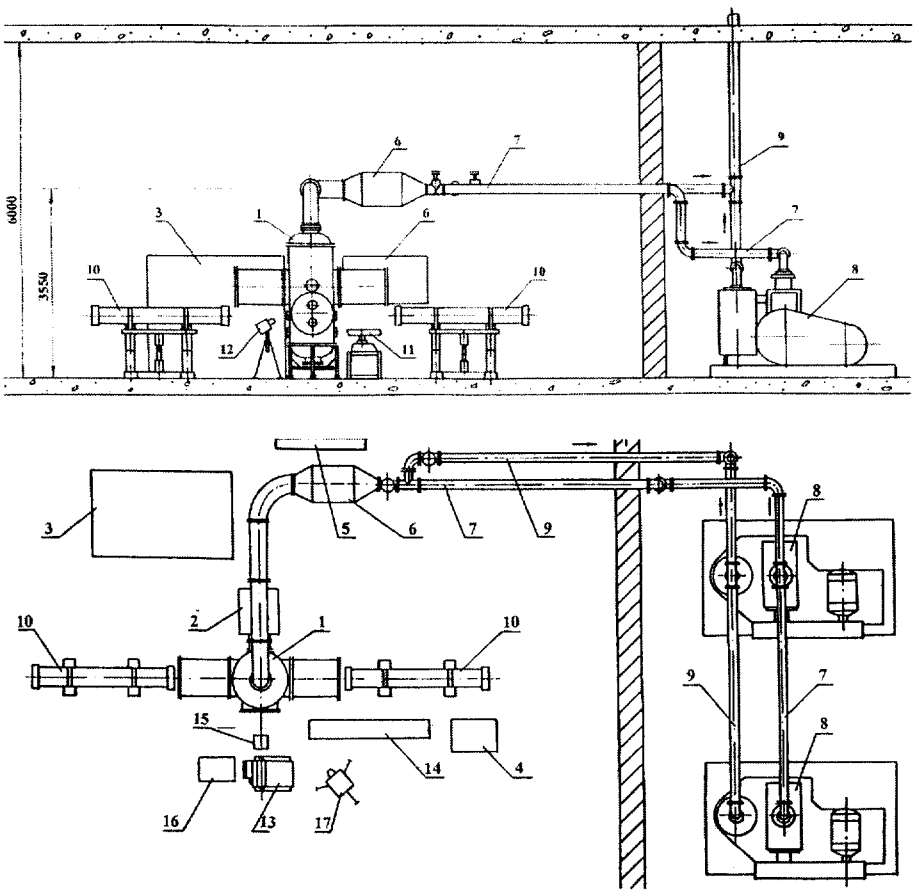


***Figure 6.*** *Conceptual sketch of the IPG-4 facility. 1 - test chamber, 2 - load matching unit of RF-generator, 3 - RF-generator unit, 4 - main control panel, 5 - control panel of cooling system, 6 - plasma-water heat exchanger, 7 - vacuum line, 8 - vacuum pump, 9 - exhaust line, 10 - shadow instrument "IAB-458", 11 - pyrometer, I2 - AGA-780 infrared thermovision system, I3 - monachromator, 14 - grating spectrograph, I5 - Fabry-Perot scanning interferometer, I6 - data logging system ORION-3530, I7 - videocamera.*

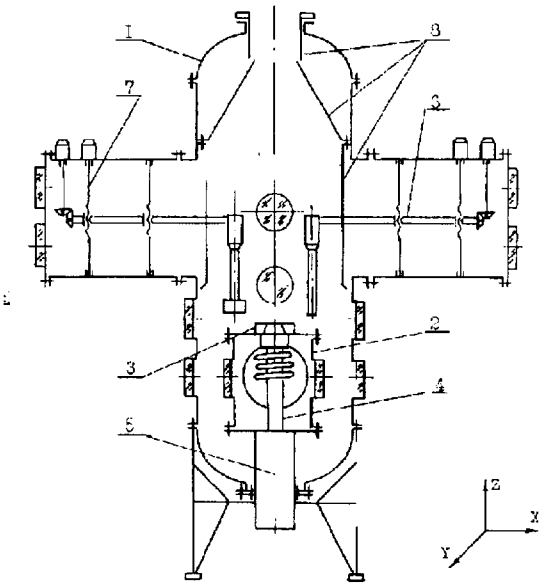


***Figure 7.*** *Conceptual sketch of the test chamber of the IPG-4 facility. 1- low pressure test chamber wall, 2 - inductor chamber, 3 - nozzle unit, 4 - discharge channel, 5 - ignition device, 6,7 - positioning devices, 8 - cooled shields.*

*Inductor chamber* contains 5-turns inductor and discharge channel. That is designed to provide atmospheric pressure around an inductor. In addition, water-cooled walls of inductor chamber is a shield from powerful electromagnetic field, which is generated by inductor.

**Induction heater** includes discharge channel, gas feed unit, top and bottom interfaces and nozzle unit (if it is necessary).

*Discharge channel* and gas feed unit are designed for making optimal gas flow, which guarantees the maintenance of stable steady state discharge in gas flow.

*Nozzle unit* is designed for forming and accelerating of plasma jet up to supersonic or high subsonic velocities. Conical supersonic nozzles do not used in the IPG-4 facility, since jet diameter (at available capacity of vacuum system) is too small for testing of typical samples of 15-30 mm diameters. However application of sonic nozzles with critical section diameters 15-40 mm allow to make such tests. Also it should be

emphasized, that when developing nozzle unit for the IPG-2 facility it was observed experimentally instability of discharge under operation with supersonic nozzle. To eliminate this effect gas injection system and discharge channel of the IPG-2 were renovated to obtain stable discharge. This experience was used in the design of the IPG-4 facility and instability was not observed in this on.

*Criterion of discharge stability for operation in supersonic regime was found at simple and rough assumptions: (i) discharge is vortex stabilized (not by water-cooled walls of discharge channel) (ii) plasma volume is more lesser than volume of discharge channel including gas supply pipe up to inlet valve, and (iii) pressure drop between inlet section of nozzle and valve is to be more lesser than pressure drop on valve. This criterion, which was used to obtain stable discharge, is presented by formula:*

$$\frac{\partial G_{out}}{\partial P} - \frac{\partial G_{in}}{\partial P} > \frac{\tau_1}{\tau_2} \cdot \alpha$$

*where $G_{out}$ – mass flow through sonic section of supersonic nozzle, $G_{in}$ – mass flow through inlet valve, P – pressure in discharge channel, $\tau_1$ – V/v (V – volume between inlet valve and critical section of nozzle, v – volume flow of gas through discharge channel in stable regime), $\tau_2$ – time of discharge expansion from channel axis to its wall in motionless gas, $\alpha$ – value depending on design of inductor, discharge channel and on way gas injection into discharge channel, etc. One can easily obtain from presented criterion that $\tau_1/\tau_2 \sim V/G$ and to increase stability of discharge one has to decrease V, to increase mass flow rate of gas and as well as to use inlet valve operating in subsonic regime, etc.*

*Top and bottom interfaces* are intended for fastening of discharge channel and gas feed unit to test chamber and inductor chamber.

*Positioning devices* are designed to insert models and gauges into plasma jet, to withdraw these ones after measurements or tests, as well as to move them smoothly along and across a jet during measurements. Two-direction positioning device allows to move the holder with gauges along X, Y, directions. Express positioning device allows to move a model or a sample into specified position in the jet and to withdraw them. Introducing and withdrawing times of express positioning device are about 1 s. Both devices allow to move sample/probe along jet axis during experiment.

*Water-cooled shields* were designed to protect test chamber wall from hot gas and they are mounted along walls inside the shell

**Gas supply system** of IPG-4 facility allows to use different gases. This system includes control section and gas flow control panel. The panel is placed so that to guarantee convenient observation and control.

**Evacuation and exhaustion system** is designed for (i) the producing of specified pressure in the test chamber, (ii) the cooling of hot gases, which were heated in discharge, before evacuation, (iii) the exhaustion of cool evacuated gases into atmosphere. The conceptual sketch of this system includes the following units: gas cooler, water-cooled vacuum pipeline, vacuum pipeline, control and stop valves, exhausting fan.

*Plasma-water heat exchanger* is designed for the cooling of hot gas flowing out from test chamber. The cooler represents water-gas heat exchanger which is made of corrosion-resistant materials. It is equipped with gauges to measure and to control gas and water temperatures.

*Water-cooled vacuum pipeline* is placed between test chamber and gas cooler. Vacuum pipeline has anti-vibration inserts, which are placed near vacuum pumps to protect vacuum pipeline, gas cooler and test chamber from the adverse action of pumps vibrations. All above-mentioned units are made of corrosion-resistant material.

*Plunger vacuum pump* has got capacity of 0.3 $m^3/s$ at P = 0.01 atm. There is an opportunity to connect vacuum systems of the IPG-4 and IPG-3 facilities and to use all three pumps with total capacity 1.3 $m^3/s$

*Control and stop valves* are made of corrosion-resistant materials. They have remotely operated drive.

*The exhausting fan* of corrosion-resistant design is placed external to room in exit part of exhaust line.

**Cooling system** is used for water cooling of different elements of other systems such as inductor chamber, nozzle unit, heat exchanger, vacuum pipelines, tube of RF-generator etc. Each cooled element has got individual cooling surcuit that is equipped with rotameters and thermometers. Thermometers are mounted in inlet and outlet cooling water pipelines to measure water temperature and mass flow. Such simple, cheap and reliable system allows to make complete calorymetry of the facility. Electronic flowmeters and thermocouples are used to measure inlet and outlet parameters of cooling waterfor in precise scientific measurements (heat flux, enthalpy) together with computer data logging system.

**Tube generator** is used as power supply system. The automatically operated switch connects the tube generator to the commercial power supply line (380 V, 50 Hz, 3 phases). Commercial tube generator is based on the powerful generator triode «ГУ-66А», which is of 100 kW power at 10 kV voltage across an anode. Combined air-water cooling is used for this tube. Tube generator includes electric circuits, which transform the voltage of commercial power supply line (50 Hz) into high frequency voltage (1.76 MHz). Among these are voltage controller, anode transformer, high voltage rectifier, anode circuit. Anode voltage controller allows

to vary rectified and stabilized anode voltage between 0 and 9.5 kV. High voltage transformer (380/8400 V) is of 100 kW power. The variation of tube generator power is realized by fine controlled linkage between anode circuit and load circuit. Load circuit includes the bank of capacitors and 5-turns water-cooled induction coil (so-called inductor), which is made of copper tube. Load circuit is tuned to the frequency 1.76 MHz under operation conditions.

Subsonic and supersonic flows created by the IPG-4 plasmatron are shown in Fig.8.

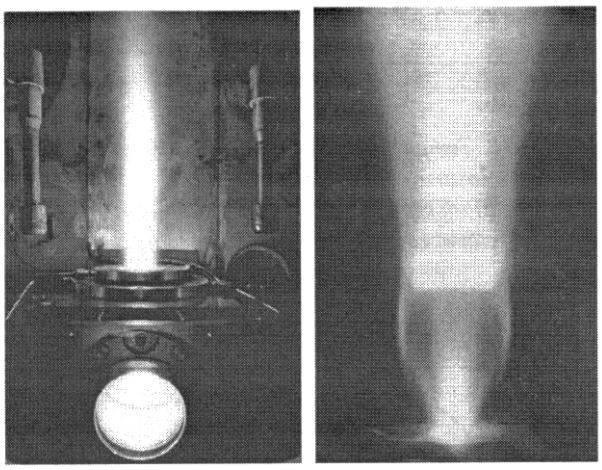

*a)* *b)*

***Figure 8.*** *Subsonic(a) and supersonic(b) air plasma jets of the IPG-4 facility.*

Conceptual schcetch of the IPG-3 facility is similar in general to that one of the IPG-4. One of the most significant distinctions between the two facilities is conceptual sketch of test chamber. To ensure atmospheric pressure around inductor small inductor chamber is used in the IPG-4 (test chamber diameter 800 mm), but in the IPG-3 test chamber of 1200 mm diameter is divided into two chambers of law and atmospheric pressure by thick flange.

Complex diagnostics of physical parameters of high-enthalpy dissociated gas flows in plasmatrons of the IPG series includes experimental and numerical techniques as follows:

- measurements of heat fluxes to model surface using stationary water-cooled calorimeters;
- total enthalpy measurements using enthalpymeter with gas sampling;
- measurements of total pressure profiles using water-cooled Pitot tubes;
- spectrometric temperature measurements in discharge and in high-temperature core of subsonic flows;
- pyrometric measurements of surface temperature of samples surfaces in the range $T_w$ = 300-2200 K using optical pyrometers ($\lambda$ = 0.55-0.65μm) and infrared thermovision systems ($\lambda$ = 3.5-10.8 μm);
- numerical calculations of free subsonic flow and flow over models of viscous dissociated reacting gas using Navier-Stokes equations at M << 1 as well as numerical calculations of non-equilibrium boundary layer on a surface of the models under conditions of experiments in plasmatrons.

Data of subsonic high-enthalpy dissociated flow diagnostics are considered carefully in cited literature. A summary Table 2 shows parameters of subsonic high enthalpy air jets, which have been realized in the facilities of the IPG series which are in operation now. These subsonic jets most closely correspond to the requirements of hypersonic heat transfer simulation at blunt body tip-nose radius R ~ 1 m.

***Table 2.*** *P*arameters of subsonic high enthalpy air jets

| **Parameters** | **IPG-3** | **IPG-4** |
|---|---|---|
| Generator anode power supply, kW | 60–750 | 15–80 |
| Total enthalpy, MJ/kg | 10–40 | 10 – 40 |
| Total pressure, atm | 0,01–0,3 | 0,01 –1,0 |
| Gas temperature near exit section of discharge channel, K | 7000–11000 | 4500–10500 |
| Velocity, m/s | 500–1100 | 20 – 950 |
| Radius of test model, cm | 1,5–17,5 | 0,5-4,0 |
| Heat flux, W/cm$^2$ | 10–1000 | 15 – 600 |
| Reynolds number | 50–150 | 50 – 200 |
| Mach number | 0,2–0,5 | 0,02 – 0,5 |
| Efficiency, % | 55 | 40 – 64 |

## 4. TESTS OF ABLATIVE MATERIALS UNDER RADIATIVE & CONVECTIVE HEATING

The first experiments with real heat protection materials, which have been made 35 years ago, were tests of ablative materials under radiative & convective heating. These works established metodology, technical approach and main specific features of tests in IPM.

First of all, from the very beginning there were no attempts to obtain maximally possible Mach and Reynolds numbers, but it was realized simulation of thermochemical action of shock layer plasma on material near stagnation point using subsonic plasma flows at M<<1. Enthalpy, pressure and velocity gradient in stagnation point were chosen as close as possible to those in real flight. To obtain radiative heat flux close to that in flight the length of discharge and jet was chosen close to typical thickness of shock layer. Complete simulation theory for non-equilibrium convective heat transfer in stagnation point was developed significantly later in 80's years and later [26-28].

Experiments were carried out at atmospheric pressure and condition at the axis of equilibrium air plasma flow were as follows: H = 40 MJ/kg (T = 8500 K), V = 30 m/s. Total heat flux to stagnation point of hemispherical water-cooled model of 30 mm diameter was 400 W/cm$^2$ with radiative heat flux ~30% of this value. Maximum surface temperature of tested samples achieved ~3000 K. Main directions of work were investigations of spectra of pure air plasma, spectra of boundary layer, temperature and species concentration profiles across boundary layer, determination of spectral absorption coefficients of pure air plasma and destruction products of ablative materials injected in boundary layer.

Of coarse, effective enthalpy determination together with other measurements, which are conventional for ablative materials, have been applied to many different candidate materials and materials used in real flights.

Sample of ablative material tested in high-enthalpy air flow of the IPG-1 facility is shown in Fig.9. Profiles of temperature and species concentrations across boundary layer on ablative material used in real flights are given in Figure 10 and Figure 11 respectively.

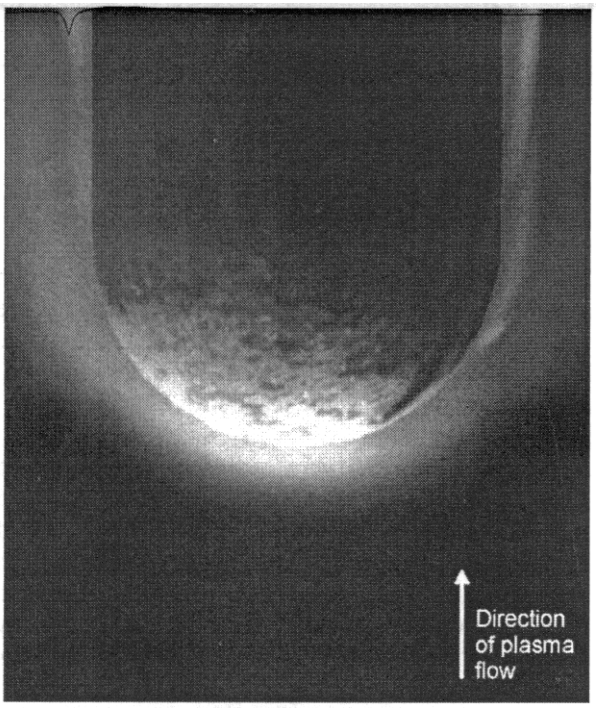


***Figure 9.*** *Ablative material in air plasma flow of the IPG-2 facility (note, that plasma flow at atmospheric pressure and temperature 8500 K is not seen near very bright boundary layer!).*

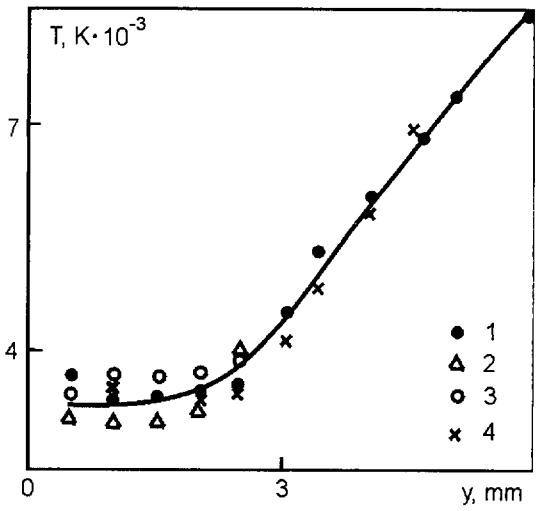


***Figure 10.*** *Temperature distributions across the boundary layer on ablative material.*
*1-3 – rotational temperatures determined by $N_2$ and $N_2^+$, 4 – vibrational temperature determined by CN molecule.*

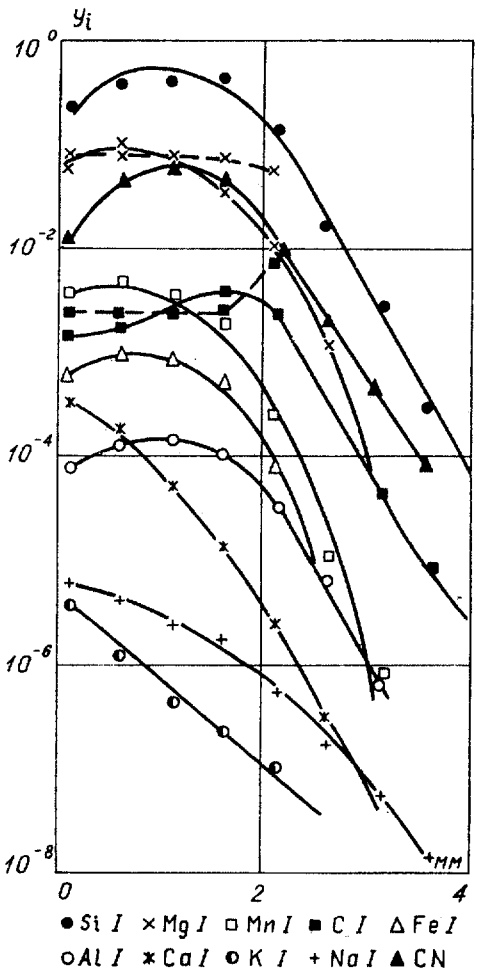


***Figure 11.*** *Relative concentration of species across the boundary layer on ablative material.*

## 5. TESTING OF REUSABLE THERMAL PROTECTION MATERIALS AND FULL-SCALE ELEMENTS OF THERMAL PROTECTION SYSTEMS

### 5.1.Aging tests of carbon-carbon materials with antioxidative coatings

Aging tests of carbon-carbon materials with antioxidative coatings were carried out using the IPG-2, the IPG-3 and the IPG-4 facilities. Main parameters of those were presented above. The IPG-2 facility was main test instrument for testing of small samples during Buran program to obtain temperature, pressure and time dependencies of mass loss rate. The IPG-3 facility was used to test large samples or full-scale structures. The IPG-4 facility is used now instead of disassembled IPG-2.

All experiments were carried out using stagnation point configuration at constant anode power of generator. Used models was cylindrical with flat ends and samples were about half model diameter. It guaranteed the uniformity of heat flux to heated surface of sample. The difference between maximum and minimum temperatures over front sample surface did not exceed 20°C even for large samples. The samples were of disk form of 2-10 mm thickness. The designed holders and models allowed samples to be removed from model between the cycles of testing for visual and microscopic inspection, photographing and weighing. Duration of each testing cycle varied from 10 to 30 minutes in different test programmes and corresponded to specified time of peak heating part of the reentry trajectory.

First aging tests of carbon-carbon material with different SiC based antioxidative coatings were made in 1980 and two samples withstood 100 testing cycles of 15 minutes duration at P = 0.06 atm and initial surface temperature 1500°C in the IPG-2 facility. Time dependencies of sample mass and surface temperature for the best sample of the lot in question are presented in Fig.12.

One can see from Fig.12, that surface temperature of sample decreases with number of cycles. Special study showed that this effect is caused by decrease of surface surface catalicyty due to silica layer formation on front surface of the sample as a result of plasma-flow interaction but not change of surface emissivity. The samples with other coatings of the same branch showed that thin cracks of coating results in increase of mass loss rate, but the other coatings demonstrated effect of self-healing even when hole of 0.5 mm diameter was made in the coating by powerful $CO_2$-laser.

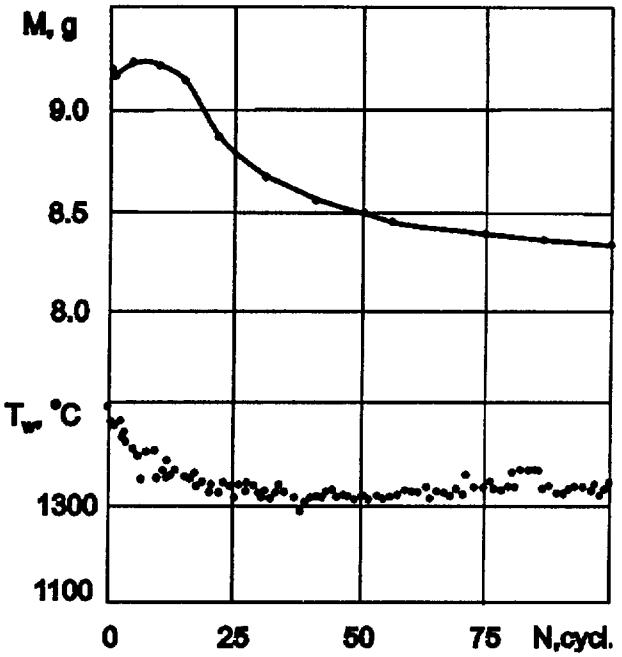


*Figure 12. Mass loss in 15-minutes testing cycle of carbon-carbon sample with antioxidative SiC-based coating.*

Carbon-carbon material with glass-silicide antioxidative coating which was used for manufacturing of nose-cap and leading edges of Buran and of coarse it was subjected systematic study. The antioxidative glass-silicide coating, which is based on high-melting borosilicate glass doped with $MoSi_2$, was developed by NIIGrafit for deposition on siliconized C-C materials [29].

30-cycles aging tests were carried out using the IPG-2 and the IPG-3 facilities. In the IPG-2 facility tests were made at constant surface temperature 1480°C and pressure 100 hPa. In the IPG-3 facility tests were made at constant pressure 16 hPa anode power of HF-generator 325 kW. It corresponded to surface temperature 1500°C in the beginning of the first testing cycle. Time dependencies of mass loss rate during 30-cycles aging tests are shown in Fig.13 (see next page). One of the curves corresponds to test of samples of 30 mm diameter in the IPG-2 facility and the other one shows data obtained in the IPG-3 facility at average temperature $T_w$= 1477°C, which was found over all test cycles. Taking into account pressure dependence of mass loss rate and influence of scale factor two presented curves are in acceptable agreement.

The result of thermochemical action of dissociated air is seen in Fig.14 which shows the coating surface on front and back sides of the sample. Note, that back side of the sample had practically the same surface

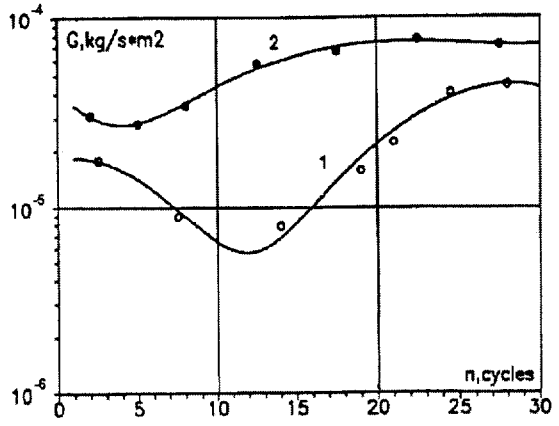


*Figure 13. Mass loss rate of siliconized carbon-carbon material with glass-silicide coating as a function vs the number of 10-minutes test cycles.*
*1- the IPG-2 facility, sample of 30 mm diameter $T_w$= 1480°C, P = 0.1 atm, 2- the IPG-3 facility, sample of 84 mm diameter $T_w$~ 1480, P = 0.016 atm*

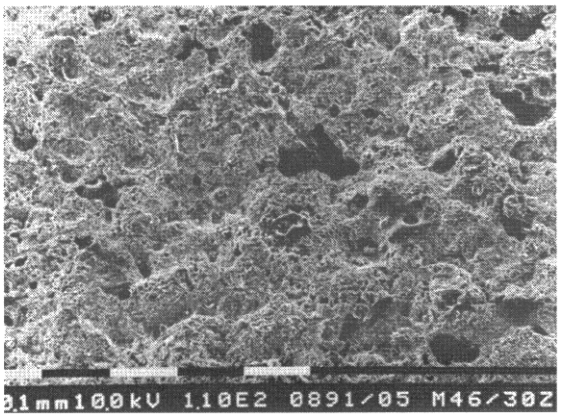


*a)*

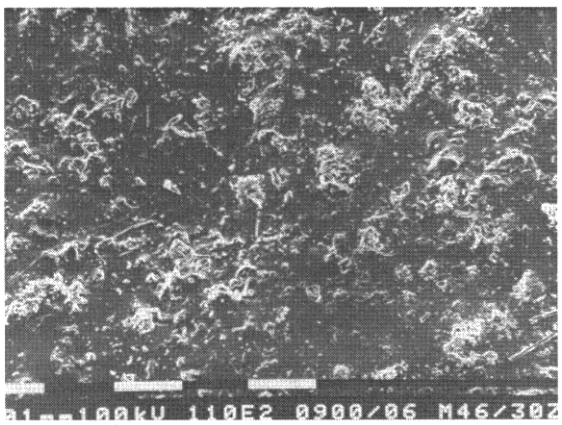

*b)*

*Figure 14. Surface of antioxidative glass-silicide coating for Buran's nose cap after 30 10-minutes testing cycles at $T_w$= 1450°C (SEM photo). a - front surface of the sample exposed to dissociated air, b - rear surface of the same sample after testing.*

temperature as front surface but it was exposed to stagnant non-dissociated air since fibrous material was used for back side thermal insulation. As a result back side surface is practically identical to initial surface state before test.

### 5.2. Testing of material of thermal protection tile

Careful study of properties of tile material described in [30] were carried out using the IPG-2 facility including 100-cycles test of one sample, studies of coating degradation in for different surface temperatures and in different gas environments. However the most important results was obtained very simply. Comparison of tile surface morphology after one testing cycle and after one real flight of Bor-4 vehicle showed identical changes (see Fig.15a,b). And plasmatron was the only test facility that demonstrated this effect!

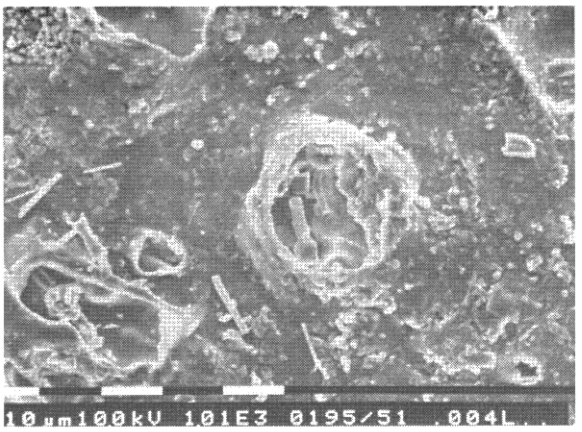


*a)*

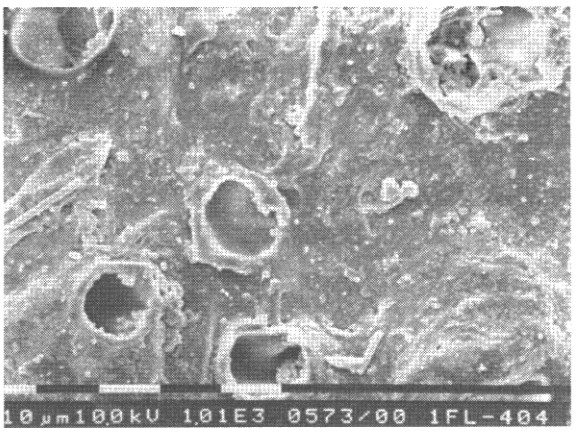


*b)*

*Figure 15. Tile coating surface after one-cycle test in plasmatron (a) and after real flight of «Bor-4» (b).*

### 5.3 Tests of full-scale thermal protection tile

Testing of full-scale black ceramic tile was carried out in the IPG-3 facility. Experiments were performed,

using air, at pressure 0.026 atm, total flow enthalpy 17.3 MJ/kg, and surface temperature at the center of front surface of tile 1250°C.

The surface temperature distribution was derived from infrared thermovision system data. Tiles were mounted into the cylindrical sample holder of the same material so that the tile surface was perpendicular to the axis of symmetry of the subsonic jet. The model was configured to simulate all designated features of the tile heat protection. Up to 100 cycles of tile testing were conducted, with each cycle being 10 minutes long. The front surface of the tile, which was initially black, became grey after testing as a result of repeated exposure to the dissociated air flow. This "surface greying effect", which results in decreasing the total hemispherical emissivity $\varepsilon_{th}$, was studied later and its thermochemical nature was found. Surface degradation was caused by interaction of the tile coating material with atoms of oxygen. Tile before testing together with tiles after 1 and 100 testing cycles are shown in Fig.16. Note, that tile after 100 cycles is grey but not black, however its total hemispherical emissivity at 1250°C decreased non-significantly.

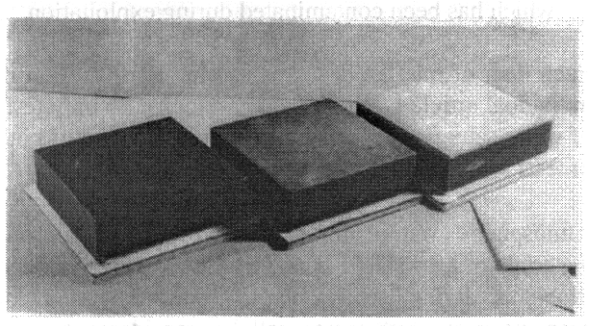

***Figure 16.*** *Full-scale Buran's ceramic tiles with black glassy coating: a – before testing, b – after 1 testing cycle, c – after 100 testing cycles.*

Tile surface study performed with a scanning electron microscope (SEM) showed that the near surface layer of the tile coating changes with the increasing of testing time. Open pores were generated in the near surface layer after the only cycle of testing. The development of the near surface porous layer, as the number of testing cycles increases, is illustrated by the SEM photographs in Fig.17. Test conditions were $T_w$= 1250°C and P = 0.026 atm.

The maximum and average thickness of the near surface porous layer depends on the number of testing cycles, as shown in Fig.18 (one can see all experimental points are in good agreement with square root dependence besides 100-cycle point of maximum thickness). In spite of these changes in near surface layer, the tile did not acquire any fissures or shape changes, even after 1000 minutes of exposure to the high temperature dissociated air. The results demonstrate the important requirement that the surface catalytic activity, with respect to heterogeneous recombination of nitrogen and oxygen atoms, remain constant after the 100-cycle exposure testing.

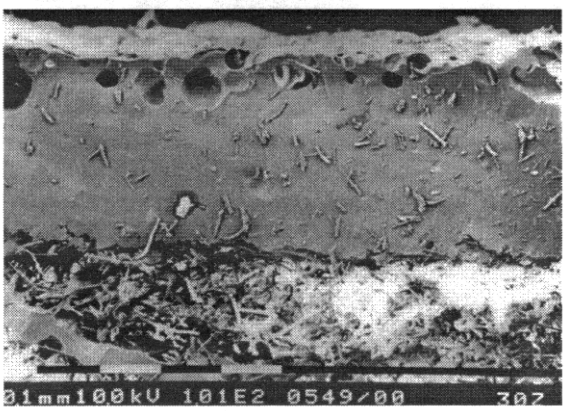


***Figure 17.*** *Section of black tile coating after 30 testing cycles at $T_w$ = 1250°C, $\tau_{cycle}$ = 600 s.*

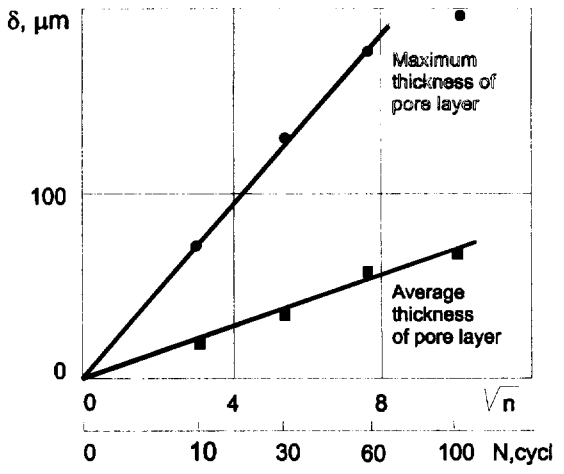


***Figure 18.*** *Maximum and average pore layer thickness as a functions of testing cycle number (P = 100 mbar, $T_w$ = 1250°C, $\tau_{cycle}$ = 600 s).*

**Full-scale elements of thermal protection systems**

The greatest model (Ø525 mm) ever tested in the IPG-3 plasmatron is full-scale window of Buran's manhole cover with its fastening and nearest tiles. Window includes three glasses with heat reflecting coatings on rear sides. Photo of this model before test is shown in Fig.19 (see next page).

Because manhole cover is located on the side of vehicle, heat fluxes to this element are not high and model axis was arranged at angle ~70° to flow axis. The choice of regime was made by heat flux using thin black heat protection tile which covered glass of window. Surface temperature was measured by infrared thermovision system and heat flux was determined by stationary surface temperature. In experiments

maximum temperature of front surface of quartz glass achieved 800°C.

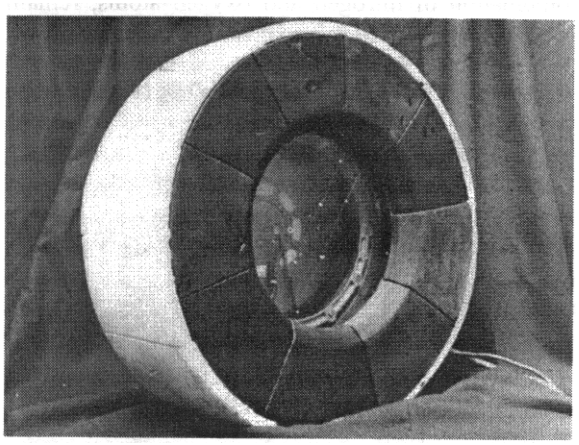

*Figure 19. The greatest model (∅525 mm) tested in the IPG-3 plasmatron – full-scale window of Buran's manhole cover before testing.*

Since flow around model and flow around window in flight differ significantly and therefore temperature fields differ significantly, too, main aim of experiment was to verify method of calculation of window, but not to simulate real heating curve. That's why tests were fulfilled in regimes with constant pressure and power at specified constant heat flux. Surface temperature of quartz glass were measure by thermovisor and temperatures of inner surfaces – by thermocouples. It was found that measured and calculated curves are in good agreement.

The greatest full-scale carbon-carbon light-weight structures tested in the IPG-3 plasmatron have got dimension 220x220 mm. These elements were tested in cylyndrical mask of 350 mm diameter and tests were made in stagnation point configuration.

### 5.4. Simulation of non-standard situations

The non-standard situations, which are possible during the exploitation of reusable thermal protection materials, are sufficiently different and, moreover, the most dangerous situations are different for various types of materials. The simulation of non-standard situations using plasma-jet facilities requires much more ingenuity than the routine tests, and individual approach is necessary for each situation. As a rule, the careful analysis of a wide range of fine physical and chemical effects is required for the correct design of experiment. Sometimes the experiment in plasmatron is the last step in the long sequence of investigations, which include complicated computer calculations and hypersonic wind tunnel experiments. It should be emphasized, that neither numerical modeling nor wind tunnel experiment are not able to give the total solution of the problem.

Non-standard situations for heat protection materials of "Buran" have been simulated in the IPG-3 facility, because it gives the opportunity to test full-scale tiles. However, advance thermal protection elements can have considerably larger dimensions, than existing tiles. In this case it is impossible to test real-scale thermal protection elements and the IPG-4 facility can be acceptable choice when simulation can be realized using models lesser than 100 mm in diameter.

The non-standard situations, that have been studied in the IPG-3 plasmatron, can be subdivided by the following manner:

- reentry along a trajectory with over-design heating, up to the emergency reentry, when a reusable vehicle, after saving the payload, loses it's serviceability (totally or partly);
- damages of thermal protection element coating, such as a loss of a part of coating, cracking, coming off a substrate;
- total or partial loss of a thermal protection element;
- water saturation of porous or fibrous thermal protection materials;
- overequilibrium heating of noncatalytic coating, which has been contaminated during exploitation.

Each item of this list deserves careful consideration in individual article but hereinafter we consider only tests of water saturated tiles as typical representative of kind of tests in question.

Atmospheric water influence on porous or fibrous materials of heat shield is one of the most complicated problems during vehicle exploitation. Saturation of such materials with water will be considered for the example of ceramic tiles. The technique of hydrophobization was developed and tested in exploitation for ceramic tiles of "Space Shuttle". However, it turns out, that sometimes the tiles have contained water. In this case it is necessary to determine the amount and the location of water in tiles (it is the subject of a separate investigation) and to predict correctly the behavior of tile, basing on laboratory experiment data. Since saturation of tiles with water can lead not only to coating coming off and to the loss of coating, but also to the appearance of inner damages, the residual strength of material after tests is important criterion.

Obviously, water contained in tiles freezes at putting a vehicle into orbit and becomes ice. The difference between thermal expansion coefficients of tile material and ice can lead to the rupture of material fibers during further cooling and heating, which cause the decrease of material strength.
The essential aspect should be emphasized: ice can be produced in tiles not only during putting into orbit, but also at a launch position. In this case mechanical properties of ice, and, possibly, predicted behavior of

tiles considerably differs from the those in previous case.

The use of literature data on mechanical properties of ice can lead to the great mistakes in prediction, since even under the nature conditions there are more than 20 kinds of ice with different characteristics. Structure and properties of ice essentially depend on a large number of parameters, such as temperature gradient, rate of water cooling, gas and salt content of water, etc. It is obvious that the very specific kind of ice - friable ice, which consists of long needle-shaped crystals and is formed by vacuum pumping of water vapors - this ice differs essentially from routine kinds of ice by it's structure and properties. Therefore, during tests of water-saturated tiles careful simulation of pressure decrease rate is important as well as the rate and conditions of cooling, corresponding to possible situations at launch position.

One more important aspect, which can be easily overlooked at cursory analysis of the problem, is chemical composition of water. The fact is that alkaline metals, contained in water as salts, and primarily K and Na, are deposited on fibers surface at the vaporization of water during reentry. These metals have extremely high diffusion coefficients in silicate glasses, which leads to their quick propagation over the whole volume of fibers at high temperature. The increase of K and Na content in silica leads to the decrease of its softening temperature and to the material shrinkage, especially in case of tiles, repeatedly saturated with water. Therefore, water with the chemical composition, corresponding to the composition of rainfall at the location of launch position, should be used in the experiments with tiles, multiply saturated with water. The mentioned examples demonstrate clearly the main problems associated with testing of water-saturated tiles. Besides, there are some technical problems, which have been resolved. For example, practically all vacuum pumps "don't like" water vapors, etc.

Tiles saturated with 30, 100, 300 and 500 g of water were tested under different conditions of freezing but in the same regime: $T_w$= 1250°C (for «dry» tyle), P=0.026 atm, $\tau_{cycle}$ = 10 min. It was found that only in one experiment at 500 g of water was observed additional coating damage due to ice vaporization. In all other test coating was not damaged and residual tension strength of tiles was found the same as before tests. Temperature field was measured by infrared thermovision system and time dependencies of maximum, average, and minimum surface temperatures for tile containing 30 g of water are presented in Fig.20. Note, that maximum surface temperature at water vapor blowing from tile surface is higher than without blowing.

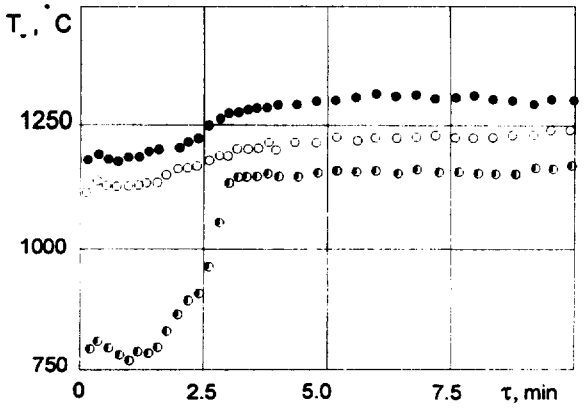


*Figure 20 Time dependencies of maximum, average, and minimum surface temperatures for tile containing 30 g of water.*

## 6. STUDY OF THERMOCHEMICAL PLASMA-SURFACE INTERACTION

Optical spectral analysis is one of the most promising methods for the study of plasma action on reusable/non-ablative thermal protection materials (TPM). Although optical spectra of destruction products of reusable thermal protection materials are "poor" (in contrast to "rich" spectra of destruction products of ablative materials), they give reasonably good possibilities to study physiochemistry of plasma-material interaction. Application of spectral analysis makes it possible to observe *in situ* degradation of antioxidative coatings during aging tests of any duration and analysis of boundary layer spectrum permits to find, what kinds of species are at a loss from substrate/coating during test, to see time dependencies of those losses *etc.*

Many essential features of thermochemical action on thermal protection material by dissociated air flow may be found using optical spectra analysis in combination with making tests in different plasma environments such as air, nitrogen, oxygen and argon. As a rule mass loss of carbon-carbon materials with antyoxidation coating is generally resulted from the oxidation but atomic oxygen is essentially more active than molecular. Comparative study of optical spectra of boundary layer allows to understand what components are arisen in boundary layer due to thermal vaporization and what components are arisen in boundary layer due to thermochemical action of the initial flow. Obviously, above mentioned approach is to be combined with data on temperature, pressure and time dependencies of mass loss rate, as well as photos of surface obtained using SEM etc.

Consider two examples of spectral analysis application for study of plasma-material interaction. Emission optical spectra were obtained during tests of C-C

material with glass-silicide coating in dissociated air and nitrogen flows. All experiments were carried out at constant pressure P = 100 hPa using the IPG-4 facility.

More than 20 rather intensive spectral lines of molybdenum were found when sample was exposed to dissociated air flow. Also sensitive lines of BI, SiI, MnI, KI, NaI were observed in boundary layer overflowed by dissociated air flow. Note, that simple qualitative chemical analysis gives two interesting results. Specially made plasma jet tests showed that there are no even weak sensitive lines of molybdenum while sample is exposed to dissociated nitrogen flow but lines NaI, KI, BI, SiI were found in these spectra. These result suggest that molibdenum atoms arising is caused by the thermochemical action of oxygen but the other components arise in boundary layer due to thermal evaporation. The band of wavelength 377-394 nm, containing sensitive lines of molybdenum MoI379.83 nm, MoI386.41 nm and MoI390.30 nm, is shown in Fig.21 for dissociated air flow (a) and dissociated nitrogen flow (b).

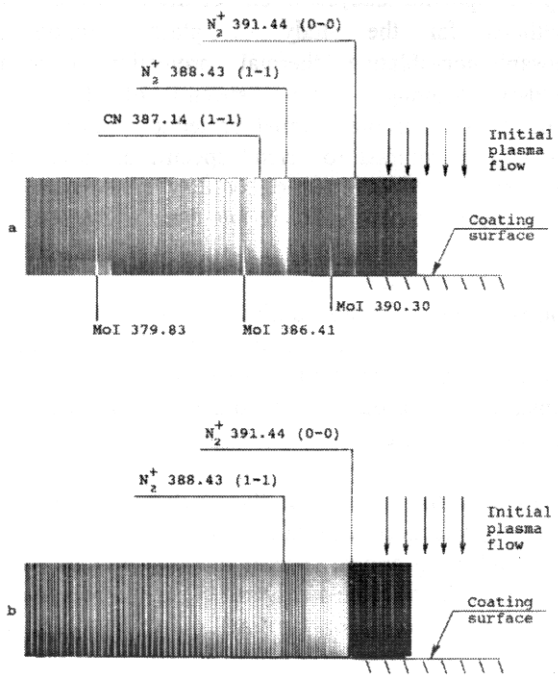


***Figure 21.*** *Spectra of boundary layer over surface of glass-silicide coating (λλ = 337-394 nm).*
*a - dissociated air flow, b - dissociated nitrogen flow.*

So, one can make conclusion that it is atomic oxygen that causes such damages to coating. The most effective way of molybdenum loss is associated with the oxidation of $MoSi_2$ followed by evaporation of exceptionally volatile molybdenum oxides and it is one of the leading mass loss processes.

It was found later, that intensities of molybdenum lines in boundary layer become unstable before the beginning of catastrophic destruction of the C-C material with glass-silicide coating, but at the same time intensities of other lines of main components of the coating such as silicon and boron don't demonstrate such behaviour as it is seen from Fig.22.

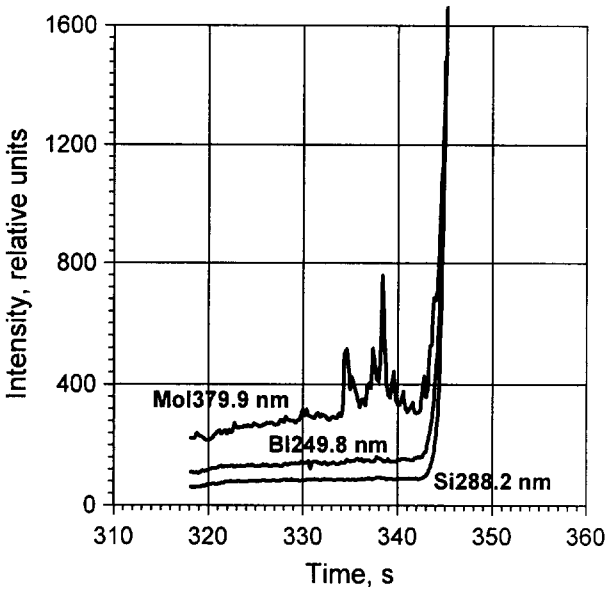


***Figure 22.*** *Time dependencies of sensitive lines intensities of different atoms which appeared in boundary layer due to coating degradation.*

As it is seen from Figure 22, intensities of lines of silicon and boron before the beginning catastrophic destruction are enough stable and those begin to increase only with the increase of surface temperature. At the same time intensity of molybdenum line begin to pulse ~10 s before the beginning of catastrophic destruction. Peak intensities can be 2-3 times higher than its quasi-stationary level. There is no such peaks at usual operating temperatures, they appear only before destruction. This result shows that destruction is caused by intensive oxidation of $MoSi_2$ particles, containing in the coating, by atomic oxygen from oncoming flow.

At the same time observable peaks shows, that before boiling heavy oxidation is blocked time by time with formation of protective film of oxides, and finally it becomes so strong, that the formation of film does not realized. So, study of specific features in behavior of boundary layer over tested sample before catastrophic destruction allowed to obtain new information on mechanism of destruction even for well-known material & coating. Of coarse, this approach is mostly fruitful for new TPM/coatings.

Thus, it was found, that before catastrophic destruction one can find few peaks of molybdenum lines intensity. There is no any peaks at usual operating temperatures. 100% repeatability in appearance of those peaks allows to consider them as «spectral precursors» of catastrophic destruction.

Study of spectral precursors of catastrophic destruction can be easily made practically in each laboratory, working on TPM testing in plasma jets. First of all, it can give important information about physico-chemical processes, that initiate catastrophic destruction of tested reusable TPM. Of coarse, that information can be used to improve tested material.

## 7. STUDY OF NON-EQUILIBRIUM HEAT TRANSFER

One of most important fields of activity in Plasma Lab of IPM is a study of non-equilibrium heat transfer. This works were initiated by programs of development of space planes «Space Shuttle» and «Buran», since peak reentry heating of these vehicles depend significantly on surface catalycity of thermal protection materials. Really, heat flux to full-catalytic surface near stagnation point is greater by several fold than heat flux to non-catalytic surface. It required to renovate old and to develop new methods of catalycity determination.

Experimental & theoretical method of surface catalicity determination developed in IPM is based on comparison of measured heat fluxes to tested material with results of numerical heat flux calculation where effective probability of heterogeneous recombination is varying parameter. Main specific features of used approach were as follows. Fist, catalytic tests were carried out under simulated reentry conditions which are as close as possible to flight conditions. Second, codes for numerical calculations were specially developed for treatment of experimental results obtained in subsonic jets of plasmatrons.

Method of catalycity determination is described in individual article of Dr.Kolesnikov in the present Lecture Series.

## 8. TESTS IN PLANETARY ATMOSPHERES

First reusable light-weight thermal protection materials for spaceplanes were developed in the frames of Shuttle' and Buran' programmes. Ultralight-weight fibrous heat-insulative and carbon-carbon materials became available and now they are not too expensive. Successful exploitation showed their high reliability. Joint influence of all these circumstances allowed to formulate a question about possible application of new materials in advanced planetary probes instead of conventional ablative materials. However, in the absence of blowing one has to consider possible influence of heterogeneous recombination on heat flux. Taking into account, that Martian atmosphere is rarefied, such influence is very possible. Actually, calculations presented in [ ] showed, that heat flux distributions over front surface of entry vehicle depends significantly on surface catalycity in relation to reactions $CO+O \rightarrow CO_2$ and $O+O \rightarrow O_2$.

Since 1996 to 1999 Plasma Lab of IPM together with TsAGI, TsNIIMASH and IM MSU have participated in Project 036 of International Scientific and Technology Center intended for development of heat protection system for interplanetary flight and IPM team was responsible for determination of surface catalycity under conditions of entry into Martian atmosphere.

That is why first of all it is necessary to obtain of stable, steady-state jets of $CO_2$-plasma and to expand operating envelope of the facility as far as possible. That first step is one of the key points in work on catalycity determination, because without highly developed, stable, steady-state regimes of facility it is very difficult (or impossible) to obtain reliable experimental data on heat transfer.

When developing plasmatron operation with new working gas, the main aim in fist stage is to clarify basic possibilities of facility, i.e. to obtain operating envelope in coordinates «pressure - power». Operating envelope in these coordinates is one of the main characteristics of plasma jet facility (arc-jets and plasmatrons), because that one is determined by basic properties of used generator and pumping system, but together with test chamber they are just these parts of facility which are the most conservative and difficult for renovation. For example, operating envelopes in coordinates «pressure - heat flux to catalytic/non-catalytic wall» can be easily changed by changing of model's form and dimension, by change of model's position in a jet and, finally, by using of new design decision of discharge device as a last measure.

Practically, the most difficult task is to obtain at least one stable, steady-state regime. If that one is available, success of step-by-step procedure of operating envelope expansion is generally a matter of time. Pressure 100 hPa and moderate anode power ~40 kW were selected as start point for work on determination of operation envelope in $CO_2$, because existing geometry of discharge channel was developed to be optimal for operation in air at 100 hPa, and moderate power allows to have enough power to support discharge existence on one hand and to avoid quick overheating of discharge channel on other.

Mass flow rate of carbon dioxide G =2.8 g/s was used in first experiments, because excellent results were obtained with that value in air. Later, G =1.8 g/s was found as optimal value. Criteria of mass flow rate optimization were the following: (1) good quality of plasma jet, (2) absence of discharge channel overheating and (3) ranges of parameters (P, $N_{a.p.}$), where foregoing conditions are fulfilled, are to be as wide as possible. To clarify first point, it should be

noted, that visible length of jet was used to estimate plasma jet quality in first experiments, because it is known that quick destruction of jet does not allow to have high heat flux to a model. As to third criterion, it is very important to have a feasibility to obtain pressure and power dependencies of heat flux, dynamic pressure etc. instead of individual points, since it allows to avoid rough mistakes and to ensure clear, understandable presentation of results. Mass flow optimization allowed to realize stable discharge without limitation in operation time in wide range of pressure and power.

Operating envelope in coordinates «pressure - anode power» is shown in Fig.23 for subsonic regimes of the IPG-4 facility operation in $CO_2$ atmosphere.

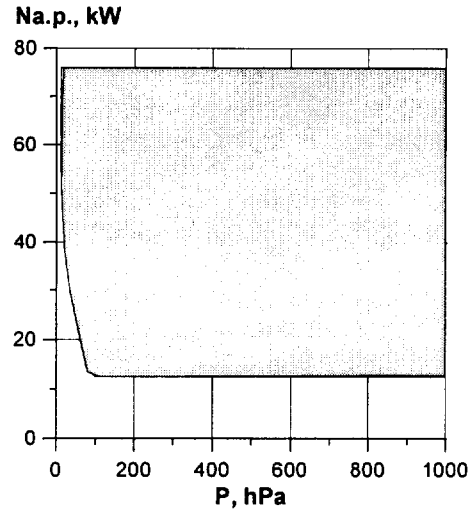


*Figure 23. Operating envelope in coordinates «pressure - anode power» for subsonic regimes of the IPG-4 facility operation in $CO_2$ atmosphere.*

Presented data have been obtained at mass flow of carbon dioxide 1.8 g/s. This value is optimum for the IPG-4 facility operation with $CO_2$ flow at $P < 200$ hPa. As it is seen from Fig.1, total range of power regulation provided by HF-generator can be realized at high pressures. At low pressures and low currents (i.e. low power) simultaneous influence of several factors appears and the border of discharge existence area results a curve, however in pressure range 10-100 hPa, i.e. in the range of significant curvature of the border, heat conductivity is kept as basic physical mechanism of discharge propagation. The main result that can be found from Fig.1 is that operating envelope (in coordinates «anode power - pressure») is limited for $CO_2$-environment mainly by capacity of exhaust system and regulation range of HF-generator (11-1000 hPa, 12-76 kW. So pressure range covers two orders of magnitude and ratio between maximum and minimum available levels of power is about four.

To determine catalycity it is necessary to have available regimes where catalycity influence on heat flux is significant, therefore to find such regimes is necessary to make heat flux measurements with catalytic and non-catalytic calorimeters. However, there was no experimental data on surface catalycity in dissociated $CO_2$, so it was necessary to find high-catalytic and low-catalytic reference materials. In the first stage. In the first stage of work copper was found as material with the highest catalycity [ ] and flow enthalpy and velocity were numerically calculated by measured heat flux, dynamic and static pressure.

Measured and calculated parameters for three regimes of the IPG-4 facility are given in Table 3.

*Table 3. Parameters of regimes of the IPG-4 plasmatron operating with $CO_2$ as working gas*

| Parameters | Regimes | | |
|---|---|---|---|
| | I | II | III |
| $N_{a.p.}$, kW | 29 | 37 | 44 |
| $q_w^{Cu}$, W/cm$^2$ | 40 | 64 | 89 |
| $P_{stat}$, hPa | 100 | 100 | 100 |
| $P_{dyn}$, Pa | 10.5 | 17.5 | 24.5 |
| H, MJ/kg | 11.4 | 15.3 | 18.5 |
| $T_e$, K | 3180 | 3630 | 5030 |
| V, m/s | 45 | 67 | 96 |

Two reusable TPM were studied with both materials were used in real reentry to Earth atmosphere. First one is Buran's ceramic thermal protection tile with glassy coating based on $SiO_2$-$B_2O_3$-$SiB_4$ system [30] and Buran's siliconized carbon-carbon material with glass-silicide antoxidative coating for carbon-carbon nose-cap and leading edges. Obtained effective probabilities are shown in Figure 24.

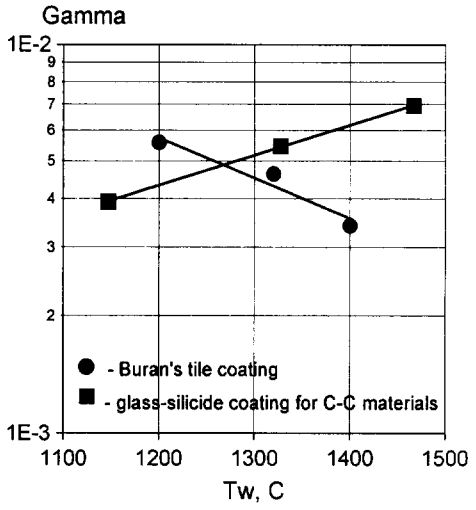


*Figure 24. Temperature dependencies of effective recombination probabilities for tested materials.*

Mars atmosphere in comparison with heat flux to full catalytic surface.

## 9. ALTERNATIVE WAYS

Not only problems concerned reentry problem were investigated in Plasma Lab of IPM. Flexibility of using and good control of regimes allowed to use plasmatrons for heat tests of industrial ceramic thermal protection materials and full-scale elements of industrial heat exchangers which must withstand heat shocks and extremal heat loading.

The other challenging direction of work was deposition of diamond and diamond-like films using IPG-4 plasmatron. Films were deposited even in air plasma flow and their catalycity was determined [31], but unfortunately these efforts did not find financial support.

## 10. CONCLUSION: LESSONS LEARNED FROM 35-YEARS HISTORY OF IPM PLASMA LAB

1. Experimentalists working with large facilities intended for test support of challenging space projects must be good forecasters, because facility is to be ready in general before decision on project realization.
2. To obtain good scientific results in modern high-temperature gas-dynamics it is necessary to unite experimentalists and theorists in one team under common supervision.
3. To present reliable test results, test laboratory is to be independent on material developers and vehicle designers.

## REFERENCES


1. Yu.A.Buyevich, O.K.Egorov, M.I.Yakushin. On Destruction Mechanism of Semi-Transparent Polymers. – Prikladnaya Mekhanika i Tekhnicheskaya Fizika, 4, 1968, pp.72-79 (in Russian).
2. E.B.Georg, Yu.K.Rulev, G.F.Sipachev, M.I.Yakushin. Experimental Investigation of the Boundary Layer on Ablating Specimens in the Joint Presence of Convective and Radiant Heat Fluxes.- Fluid Dynamics, March 1974, pp.212-216.
3. E.B.Georg, Yu.K.Rulev, M.I.Yakushin. Investigation of Heat Flux at the Forward Critical Point of Bodies Placed in a High-Temperature Subsonic Stream.- Fluid Dynamics, Narch 1975, pp.792-798.
4. E.B.Georg, M.I.Yakushin. Thermal Boundary Layer on Models Disintegrating in a High-Enthalphy Gas Stream.- Fluid Dynamics, Jan. 1977, pp.21-27.
5. E.B.Georg, M.I.Yakushin. The Structure of Concentration Boundary Layer on Models Disintegrating in High-Enthalphy Air Stream. - Inzhenerno Fizicheskii Zhurnal, 32(4), 1977, pp.581-587 (In Russian).
6. E.B.Georg, M.I.Yakushin. On Structure of Multi-Component Boundary Layer of Ablating Models.- Prikladnaya Mekhanika i Tekhnicheskaya Fizika, 1, 1977, pp.76-80, (In Russian).
7. E.B.Georg, M.I.Yakushin. Radiational Properties of the Decomposition Products at a Nodel Around Which Flows a Subsonic High-Temperature Plasma Stream.- Fluid Dynamics, May 1979, pp.854-857.
8. E.B.Georg, M.I.Yakushin. Temperature of Nitrogen Plasma Jet at Reduced Pressures.- Fluid Dynamics, Sept.1986, pp.335-337.
9. A.N.Gordeev, A.F.Kolesnikov, M.I.Yakushin. An Induction Plasma Application to "Buran's" Heat Protection Tiles Ground Tests.- SAMPE Journal, 28(3), May/June 1992, pp.29-33
10. Gordeev A N, Yakushin M I - .The thermochemical stability of carbon-carbon using an atioxidation coating for Buran - Part II.- SAMPE Journal, 29(2), March/April 1993, pp.27-31.
11. Gordeev A N, Yakushin M I, Kravetskii G A. et.al., Antioxidation Glass-Silicide Coating for Carbon-Carbon Materials and its Aging in Air Plasma Flow. - Proceedings of the 2nd European Workshop on Thermal Protection Systems & 3rd European Workshop on High Temperature Materials, Stuttgart, 23-27 October 1995, pp.217-224.
12. A.N.Gordeev, A.F.Kolesnikov, M.I.Yakushin. Investigation of Heat Transfer on Models in Subsonic Jets of an Induction Plasmotron.- Fluid Dynamics, May 1984, pp.942-948.
13. A.N.Gordeev, A.F.Kolesnikov, M.I.Yakushin. Effect of Surface Catalytic Activity on Nonequilibrium Heat Transfer in a Subsonic Jet of Dissociated Nitrogen.- Fluid Dynamics, November 1985, pp.478-484.
14. Vasil'evskii S.A., Kolesnikov A.F., Yakushin M.I. Determination of the Effective Probabilities of the Heterogeneous Recombination of Atoms When Heat Flow is Influenced by Gas-Phase Reactions. High Temperature, Vol. 29, No. 3, 1991, pp. 411-419.
15. S.A.Vasil'evskii, A.F.Kolesnikov, M.I.Yakushin. Increased Heat Transfer to a Titanium Surface with Oxygen Injection into the Nonequilibrium Boundary Layer. - Fluid Dynamics, Jan.1992, pp.598-604.
16. S.A.Vasil'evskii, A.F.Kolesnikov, M.I.Yakushin. Determination of the Effective Probabilities of the Heterogeneous Recombination of Atoms When Heat Flow is Influenced by Gas-Phase Reactions.- High Temperature, Nov.1991, pp.411-419.
17. Baronets P. N., Kolesnikov A. F., Kubarev S. N., Pershin I. S., Trukhanov A. S., Yakushin M. I. Overequilibrium Heating of the Surface of a Heat-

Shield Tile in a Subsonic Jet of Dissociated Air. - Fluid Dynamics, Vol. 26, No. 3, 1991, pp. 437-442.

18. V.Labaste, A.Kolesnikov, L.Ferenbach, H.Guegan, P.Guigue-Joguet Influence of Aging Upon Catalycity of C/C Material Protected Against Oxydation. Proc. of the Intern. Symposium on Advanced Materials for Lightweight Structures '94, ESA-ESTEC, Noordwijk, The Netherlands, 22-25 March 1994, ESA WPP-070, pp. 273-280.
19. Gülhan A., Vennemann D., Yakushin M.I., Zhestkov B.E. Comparative Oxidation Tests on Reference Material in Two Induction Heated Facilities. 46th International Astronautical Congress, October, 1995 Oslo, Norway, 9 p.
20. Vennemann D., Yakushin M.I. Oxidation Tests on SiC Reference Material in an Induction Heated Facility under Sub- and Supersonic Flow Conditions. AIAA 96-4566, 1996. 7th International Spaceplanes Conference, 18-21 November 1996, Norfolk, USA, 8 p.
21. Yakushin M.I., Gordeev A.N., Vennemann D., Novelli A. Mass Loss of SiC Sample Surfaces Under Different Flow Conditions. AIAA Paper 98-2605. 20th AIAA Advanced Measurement and Ground Testing Technology Conference, June 15-18, 1998, Albuquerque, NM, ESA-ESTEC.
22. Gordeev A.N., Yakushin M.I., Bykova N.G. Spectral Precursors of Catastrophic Destruction: Detection, Study and Possible Application for Plasma-Jet Tests. 3rd European Workshop on Thermal Protection Systems, ESTEC, 25-27 March 1998, Netherlands, Noordwijk, p. 329-333.
23. Bykova N.G., Vasil'evskii S.A., Gordeev A.N., Kolesnikov A.F., Pershin I.S., Yakushin M.I. Determination of the Effective Probabilities of Catalytic Reactions on the Surfaces of Heat Shield Materials in Dissociated Carbon Dioxide Flows. Fluid Dynamics, Vol. 32, No. 6, 1997, pp. 876-886.
24. Kolesnikov A.F., Pershin I. S., Vasil'evskii S. A., Yakushin M. I. Study of Quartz Surface Catalycity in Dissociated Carbon Dioxide Subsonic Flows, AIAA Paper 98-2847, 1998.
25. Kolesnikov A.F., Yakushin M. I., Vasil'evskii S.A., Pershin I. S., Gordeev A. N. Catalysis Heat Effects on Quartz Surface in High-Enthalpy Oxygen and Carbon Dioxide Flows. The Third European Symposium on Aerothermodynamics for Space Vehicles, November 24-26, 1998, ESTEC, Noordwijk, The Netherlands, SP-426.
26. A.F.Kolesnikov, M.I.Yakushin. Modeling Convective Nonequilibrium Heat Transfer of Bodies with Hypersonic Flows at Induction Plasmatrons. - High Temperature, Jan.1989, pp.569-577.
27. A.F.Kolesnikov Conditions of Simulation of Stagnation Point Heat Transfer from a High-Enthalpy Flow. Fluid Dynamics, Vol. 28, No. 1, 1993, pp. 131-137.
28. A.F.Kolesnikov, V.S.Shchelin Numerical Analysis of Simulation Accuracy for Hypersonic Heat Transfer in Subsonic Jets of Dissociated Nitrogen. Fluid Dynamics, Vol. 25, No. 2, 1990, pp.278-286.
29. Kostikov V I et.al 1995 Heat-Resistant Antioxidative Protective Coating for C-C, C-SiC and Graphite Materials. - Proceedings 1-st International Conference "Perspectives of Mastering Outer Space", Moscow.
30. G.E.Lozino-Lozinsky. "Buran's" First Flight.- In: Gagarin Scientific Readings on Astronautics and Aeroinatics 1989, Nauka, Moscow, 1990, pp.22-40 (In Russian).
31. A.F.Kolesnikov, I.S.Pershin et al Determination of the Catalytic Efficiency of Diamond Films in the Stream of Disoociated Air. 4-th European Congress on Diamond, Diamond-Like and Relative Materials, September 1993, Portugal, p.115.

# METHODOLOGY, TECHNICAL APPROACH AND MEASUREMENT TECHNIQUES FOR TESTING OF TPM THERMAL PROTECTION MATERIALS IN IPM PLASMATRONS

**A. N. Gordeev**

*Institute for Problems in Mechanics of Russian Academy of Sciences, 101-1 prospect Vernadskogo, 117526 Moscow, Russia.*
*Tel.: +7 095 434 36 74, Fax: +7 095 938 20 48, E-mail: gordeev@ipmnet.ru*

## ABSTRACT

*An induction plasmatron application for testing of thermal protection materials is discussed in presented paper on the basis of 35-years experience of Plasma Laboratory of IPM RAS. Metodology of testing of thermal protection materials in plasmatrons was based on simulation of hypersonic reentry heating near stagnation point using subsonic plasma jets, possibility to regulate pressure and flow enthalpy smoothly and independently of one another and the using of plasmatron's advantages such as purity of plasma flow, its high stability and reproducibility as well as wide ranges of realized pressure and heat flux. Purity of plasma flow allows to fulfill long-term aging tests (up to 100 15-minutes testing cycles for one sample) at excellent stability and reproducibility flow parameters. Conventional techniques of measurements and analysis such as pyrometry, SEM etc. are discussed together with developed approach to study of thermochemical stability of materials using complex application of optical spectral analysis, tests in different gases and methods of post test analysis.*

## 1. INTRODUCTION: METODOLOGY AND TECHNICAL APPROACH

Induction plasma generators are the mostly suited to simulate aerodynamic heating of hypersonic vehicles when purity and stability of plasma flow are necessary to solve a problem in question. Owing to using contactless heating of gas flow by induction current, these facilities create exceptionally pure plasma flow of any gases as well as show high stability and excellent reproducibility of regimes. Last but not least advantage is a feasibility to make long-term aging tests in real time. Taken together, these advantages make induction plasma generators best suited to make aging tests of reusable thermal protection materials as it was shown in [1-3]. Besides, using of pure subsonic plasma jets make it feasible to simulate precisely such flight conditions as total enthalpy and pressure, a chemical composition and species distributions within boundary layer, heat flux, surface temperature, nonequilibrium gas-phase and surface reactions, i.e. thermochemical action of shock layer plasma on thermal protection materials near stagnation point.

Methodology and technical approach for testing of materials developed in IPM RAS includes the following items:

- testing of sample and full-scale elements of thermal protection system in stagnation point configuration, but if it is necessary to obtain very low heat flux or to test very large model one can use model arrangement at an angle of attack;
- development of test models to make fastening and heat insulation of rear side of sample as close to real vehicle as possible and to assure easy assembling/disassembling of model;
- choice of test regimes and making of preliminary tests using step-by-step heating;
- application of different test procedure (constant pressure and power, constant pressure and surface temperature or specified heating curve) for differently directed test campaigns;
- using of optical methods for surface temperature measurements;
- application of optical spectral analysis together with tests in different gases for investigation of thermochemical stability of reusable thermal protection materials.

Consider briefly above presented parts of technical approach, that was described in [4-6].

## 2. TEST CONFIGURATIONS

Two main test configurations are presented in Fig.1a,b (see next page). The first one is classical stagnation point configuration. Typical model diameters for 80 mm diameter of jet generated by plasmatron are in the range 45-60 mm. Stagnation point configuration is used both for aging tests and catalycity determination since it is convenient for numerical flow analysis. The second one is configuration with model arrangement at an angle of attack, that is used to test very large sample and/or to obtain very low heat flux to test model. To determine catalycity in this configuration one has to use rough models or to solve fulfill 3D Navier-Stokes problem. The greatest model ever tested in IPM using this configuration was of 525 mm diameter at 200 mm diameter of inlet section of discharge channel.

*Paper presented at the RTO AVT Course on "Measurement Techniques for High Enthalpy and Plasma Flows", held in Rhode-Saint-Genèse, Belgium, 25-29 October 1999, and published in RTO EN-8.*

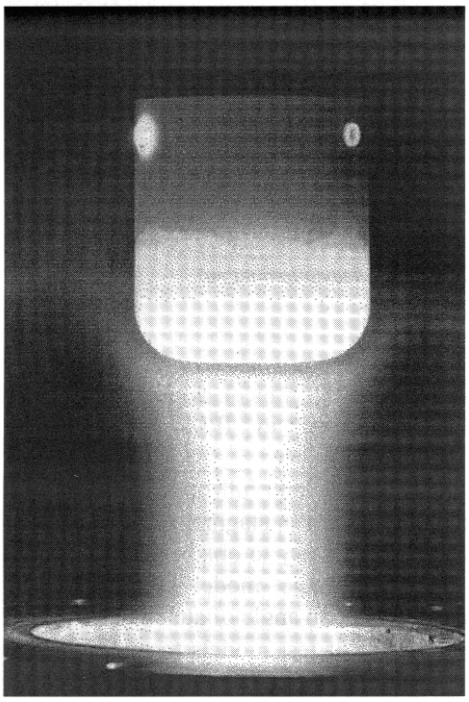

*a)*

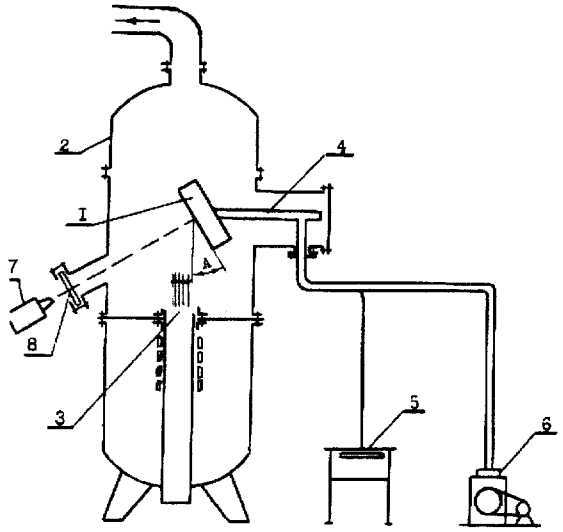


*b)*

***Figure 1.*** *Test configurations: a – photo of test using stagnation point configuration, b – configuration of model arrangement at an angle of attack (1 - test model, 2 - test chamber, 3 - dissociated air flow, 4 - water-cooled holder, 5 - data loging system, 6 - vacuum pumps, infrared thermovision system, 8 - infrared window).*

## 3. SAMPLES AND MODELS

Conceptual sketch of test model used for sample testing since 1992 is shown on Fig.2. This model represents flat faced cylinder of 50 mm diameter with edge rounded with 11.5 mm radius.

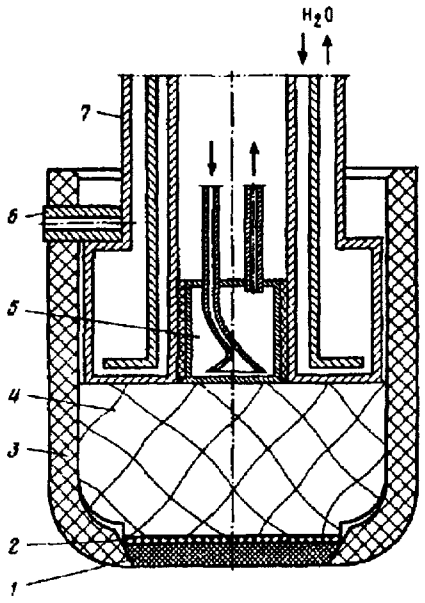


***Figure 2.*** *Test model for aging and catalytic tests in stagnation point configuration. Test model for tests in stagnation point configuration. 1 - sample, 2 - spacer, 3 - mask, 4 - heat insulator, 5 - stationary water-cooled calorimeter, 6 - pin, 7 - water-cooled holder.*

Water-cooled stationary calorimeter is used for measurement of heat loss from rear side of sample to water-cooled holder and it allows to use heat balance to determine heat flux to hot surface that is necessary for catalycity determination.

Development of the models for testing of full-scale elements is individual complicated problem, since such model must meet very many requirements. Model is to be easy for manufacturing and as cheap as possible, simple in exploitation, easy for assembling/ disassembling. The only recommendation is to make design of heat insulation of rear side of a sample as close as possible to that one, which is used in real vehicle.

## 4. STEP-BY-STEP HEATING AS THE FIRST TEST OF NEW THERMAL PROTECTION MATERIAL

Method of step-by-step heating was used in experiments on a study of boundary layer spectrum before boiling of glass-silicide coating. This simple experiment is usually carried out in the very beginning of test program for a new material, since it allows to solve simultaneously a set of problems (calibration of used pyrometers, estimation of maximum operation temperature, quick comparison with previously tested

materials, etc.) in one 20-minute experiment. Essence of experiment is step-by-step change of power and as a result step-by-step heating of a sample up to its catastrophic destruction at constant pressure and mass flow of air. It is possible, since power, mass flow of gas and stagnation pressure are not linked among themselves in subsonic operation regimes of plasmatron and one can vary them independently of one another.

It is necessary to discuss this technique more carefully, because it plays special role in methodology of testing, used in IPM. First, such approach allows to create a database on dependencies of surface temperature against anode power for different coatings/materials tested under the same conditions of non-equilibrium heat transfer. As a rule, experiments are carried out at the same pressure 100 hPa and the same set of power levels is used and constant surface temperature is to be achieved on each "step". So, one can quickly compare obtained results with numerous data on previously tested materials and make conclusions concerned joint influence of surface catalycity and emissivity on sample temperature without any special individual careful studies of total emissivity and effective probability of a heterogeneous recombination as functions of temperature. Note, that these characteristic are known for some materials of database and such knowledge can be used for comparative study of new material.

Second, approximate temperature of the beginning of destruction allows to see potentialities of new material for high-temperature application, since maximum operation temperature depends in the main on used chemical system, but lifetime in the main depends on quality of technology of coating application

Third, character of kinetics of heating makes it possible to make conclusions about a possible direction of catalycity change during experiment. Typical kinetics of step by step heating is presented on Fig.3. Data were obtained using test stagnation point configuration. Temperature peak at constant power corresponds to catastrophic destrucion of sample. It is seen from Fig.3, that surface temperature decrease is observed during first steps at rather low temperatures of a sample on each "step". It can be caused by catalycity decrease or increase of coating emissivity, however, according available experience the first reason is significantly more probable, than second one.

The second relation, concerned step-by-step heating, is derived from power dependency of surface temperature and an example is given in Fig.4. It is interesting, that the long-term statistics accumulated in tests of ~100 various combinations "reusable C-C material/ antioxidative coating", that before the beginning of

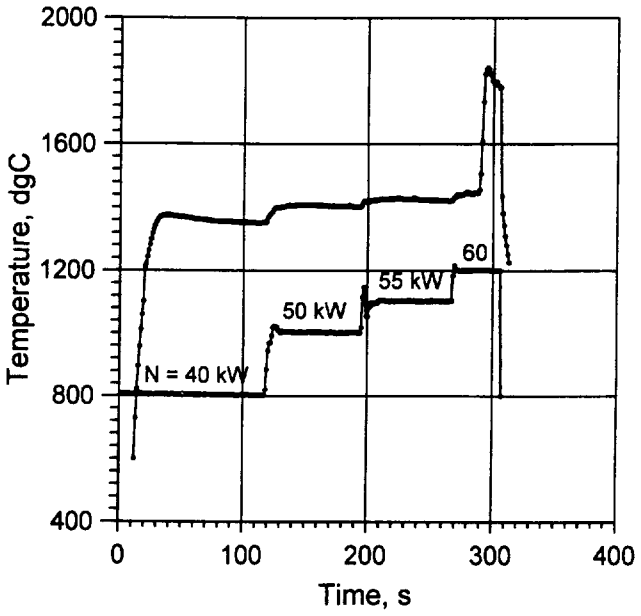


*Figure 3. Time dependencies of surface temperature of gllass-silicide coating and anode power of generator.*

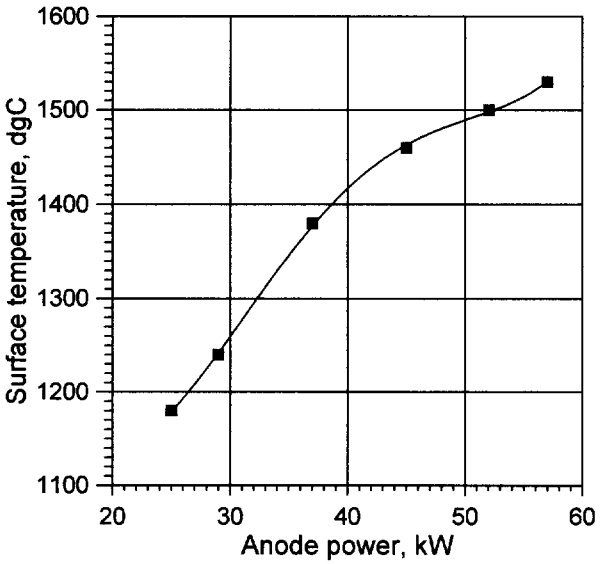


**Figure 4.** *Surface temperature of tested sample with glass-silicide coating vs anode power of HF-generator.*

catastrophic destruction the relation T(N) passes through a point of inflection. One of candidate reasons of the effect is heat effect of substrate oxidation, that is negligible at "low" temperatures, increases and becomes significant before the beginning of catastrophic destruction. Although exact explanation of discussed effect is not found yet, it has prognostic power and can be used in experimental practice to avoid catastrophic destruction, if it is necessary.

Step-by-step heating of sample was used in presented experiments together with recording of kinetics of boundary layer spectra on each «step».

## 5. MEASUREMENT TECHNIQUES

### Mass loss of sample

This technique seems very simple and primitive. Really, accuracy of laboratory weighing is excellent. However, it makes it possible to observe water adsorption in porous materials etc. Practically, accuracy ~0.1-0.01 mg is enough. Real problem is to avoid sticking of sample and heat insulator (especially in cyclic tests). Very often spacer helps to solve this problem.

Commonly used samples for selective tests and research works are of disk form of 26.5 mm diameter with conical side surface as it is seen from Fig.2. However it is possible to use separable samples shown in Fig.5.

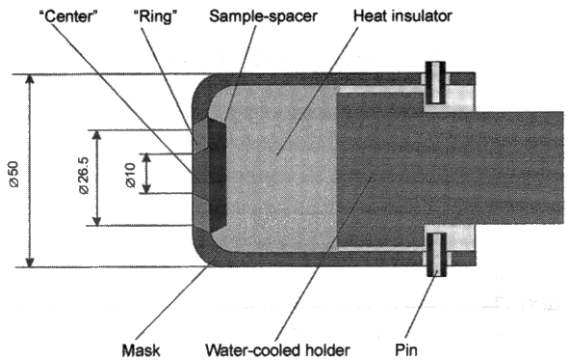


***Figure 5.*** *Sketch of test model with eparable sample.*

A "separable" sample consists of two parts: a "center" with 10 mm diameter of front surface and 30° half angle of conical side surface is inserted into a "ring", so that the assembled "separable" sample has the same form and dimensions as the standard sample (thickness - 2.9 mm, diameter of front surface - 26.5 mm and half angle of conical side surface - 30°) and it can be mounted and tested in the same sample holder. Using "separable" samples made it possible to weigh individually the "center" and the "ring" between test cycles. Thus one can determine the mass loss rates in the central and peripheral parts of the sample. Note, that the ratio of the front surface areas of the "center" and the "ring" is about 1/6. It should be emphasized here that "separable" samples were proposed for experiments under conditions with significant mass loss because that allows to neglect mass loss/gain on the side and back surfaces of sample (or part of sample). That is why the mass loss rate was defined as the ratio of mass loss and front surface area of the sample. Before the main test program standard and "separated" samples were comparatively tested in order to verify a possible influence of the sample's separation on its total mass loss and no significant difference was found.
Separable samples were used to show that mass loss rate is uniform over sample surface in subsonic tests, but it can be significantly non-uniform in supersonic tests and ratio edge/center can change about order of magnitude [6]

### Surface temperature

Measurements of front surface temperatures of the samples, heated in induction plasma jet, were carried out using pyrometers. This choice is determined not only by problems of sensing element mounting into investigated samples, but by high-frequency interference from electromagnetic field of inductor as well as the problems in many times repeated assembling/disassembling of the model during aging tests. The first advantage of pyrometers is that pyrometry is contactless method of measurement. The second one is their universality, i.e. the opportunity to work with any kinds of materials, including highly specific materials like ceramic tiles and fibrous materials exposed to plasma flow. Generally recognized advantages of pyrometry are remained: pyrometry is contactless method and (if it is necessary) freedom from time-transit effects. However if it is necessary, thermocouples can be used (and they have been used) for measurement of temperature of rear side of a sample, temperature of some parts of test model, etc.

*Optical pyrometer* with disappearing filament POV-80 was used as the reference instrument for surface temperature measurements. This pyrometer, using standard wavelength $\lambda$ = 0.65 μm, is characterized by high accuracy of brightness temperature measurement, simplicity of design and using.. Due to the optical system of $20^x$ magnification, pyrometer allows to observe the small details of sample surface, including sites of origins for thermochemical destruction of carbon-carbon materials with antioxidation coatings. The size of minimally small measured object is ~1 mm at the distance between object and pyrometer ~1 m.

The disadvantages of this device are impossibilities of continuous registration of temperature and of measurement of quickly changed temperatures as well as the necessity of the correction for spectral emissivity of an object and for spectral transmittance of optical window of vacuum chamber. The correction for the transmittance of vacuum chamber optical window and for sample spectral emissivity must be made using conventional formula. Spectral transmittance of optical window of test chamber was calculated using data on optical properties of used type of quartz and it was found $\tau$ = 0.935 so this correction may be calculated

precisely. However the main error is of systematic nature. Its source is the error of emissivity, used in calculation of true temperature from brightness temperature. The accuracy of used optical pyrometer is so high (0,2% over 1400-2000°C temperature range and 0.15% over 800-1400°C), that error of brightness temperature measurements practically does not influence on the accuracy of true temperature determination.

The simplest way to estimate spectral emissivity of developed materials and coatings is to measure spectral reflection coefficient of a sample at room temperature and at wavelength used by pyrometer. It allows to find spectral emissivity from Kirchhoff law for nontransparent bodies: $\varepsilon_\lambda = 1 - R_\lambda$. Taking into account that at absence of chemical and phase changes $d\varepsilon_\lambda/dT$ is rarely more than 10K, it is acceptable to use values obtained using above mentioned way. Actually, optical pyrometer is not sensitive to spectral emissivity error. $\varepsilon_\lambda = 0.85$ was accepted for studied coating and for true surface temperature T = 1300°C spectral emissivity error $\Delta\varepsilon_\lambda \sim 0.10$ leads to temperature error $\Delta T = 12°C$ and at T = 1500°C - $\Delta T = 16°C$.

*Partial radiation pyrometers* with photoelectric sensors have been used in these tests when it was necessary to record data into computer memory. Used devices is equipped with silicon and germanium photodiode sensors. For these devices bands of sensitivity 0.5-1.1 μm and 0.7-1.6 μm respectively, temperature ranges: 600-1300°C and 1000-2000°C, accuracy: 1.5% and 1% (for exploitation at environment temperature -40...+40°C, but when measuring in laboratory room at constant environment temperature it is to be better). The two devices with analog output 0-100 mV were used with multichannel digital recorder OPION–3500 and computer Pentium Pro 180. Response time of such system is determined by analog electronic circuit of pyrometer and its value is about 0.5-1 s.

Respectively large dimension of observed area (about 5 mm at 1 m distance between object and pyrometer) is of advantage or of disadvantage in accordance with situation. Insensitivity to plasma radiation is an advantage of these pyrometers in any case. The last fact is explained both by the increase of sample radiation at infrared range and by the decrease of plasma radiation at this range. Wide band of spectral sensitivity brings some additional difficulties into introducing the correction for object emissivity. Therefore corrections were made in real time during tests to make measured temperature equal to data of precision optical pyrometer corrected for spectral emissivity and transmittance of optical window. To establish necessary corrections calibrations of electronic pyrometers using optical pyrometer were made in individual experiments with step by step heating of tested samples. Obtained corrections were constant during all test program.

*Infrared thermovision system* is another type of non-intrusive optical system for temperature measurements that was used for sample surface temperature.

The type of pyrometer is to be chosen as applied to the material under investigation. Sometimes this choice requires large work on "the agreement" of a pyrometer with an object. It should be taken into consideration not only temperature range, accuracy, minimal angle size of measured object, speed of response, i.e. technical performance data, which can be found in the specification, but the agreement of pyrometer spectral sensitivity with spectral emissivity of investigated materials and with spectrum of plasma radiation as well.

In many cases it is expedient to use pyrometers with spectral range, which agrees with the most intensive emission band of an object and does not agree with of intensive plasma radiation bands. The most simply, one can find emission bands by measuring spectral reflection coefficient p over wavelength range 1-15 μm, since for nontransparent materials Kirchhoff law can be written as $\varepsilon_\lambda = 1 - R_\lambda$

Unlikely, when the surface temperatures of plasma jet heated samples are measured, pyrometer spectral emissivity band has not to coincide with bands of intensive plasma jet radiation.

When testing ceramic heat protection tiles, thermovision system AGA-780 was in considerable use. This system is especially effective with the measurements of temperature of quartz as well as glasses and ceramics, based on silicon dioxide. It takes place because narrow-band filter, which is used in this device for measurements of high temperatures, has $\lambda_{eff} = 5\,\mu m$, that corresponds with intensive absorption (and emission) band of above-mentioned materials. It is exceptionally important, that spectral emissivities of guartz and quartz-based ceramics on $\lambda_{eff} = 5\,\mu m$ are closed to 1, they are well known and practically nondependent on temperature (it is correct both for "black" and for "white" thermal protection tiles).

Since investigation of a ceramic tile was extensive, careful and prolonged, spectral emissivities of tile coatings have been measured carefully using special-purpose facilities (the Institute for High Temperatures of Russian Academy of Sciences et.al.). It allowed to make measurements of true surface temperature with high accuracy both in routine cyclic tests and in

experiments on non-standard heating. One of the most interesting works of the last type was the investigation of water-saturated tile behavior. It should be emphasized, that thermovisor gave the only opportunity to make this work, because highly nonuniform temperature distribution over investigated surface (600 < T<1300°C) varied with time quite guickly.

Simple evaluation shows, that extremely low reflection coefficient of quartz and of tile coatings at the wavelength 5 μm ($R_{\lambda=5\mu m}$ = 0.02) makes negligibly small the radiation reflected from surface and detected by thermovisor. It is true both for plasma space radiation and for radiation of heated up to few hundred degrees quartz discharge channel. Brightness temperature of plasma jet at $\lambda_{eff}$ = 5 μm low and really it does not exceed 200°C, therefore direct plasma radiation along the optical axis of thermovisor also is very small and does not influence on the results of tile surface temperature measurements.

The correction for transmittance of vacuum chamber optical window is not small at thermovision measurement. However, using of BaF monocristalline optical window allows to calculate required value precisely, since optical characteristics of this material are known with high accuracy. It has been this material, which was chosen for it's moisture-resistance and transparence at visible band.

The calibration of thermovision system over temperature range 200-1500°C has been made in our laboratory by means of two specially designed absolutely° black body models. The first one was used at 800-1500°C (it was heated by 1 MW generator of the IPG-3 facility!) and the second one - at 200-1100°C. Optical pyrometer with disappearing filament POV-80 (T > 800°C ), infrared pyrometer POI (400 < T 900°C) and specially calibrated Chromel-alumel thermocouple (200 < T < 1100°C) were used as reference devices. Results obtained by using of these two models showed excellent agreement. The error° of calibration is about 15°C.

In closing, it should be noted, that, when measuring other materials, for example, based on $Al_2O_3$, the employment of this thermovision system is not so far effective as in the case of ceramic tiles with silicate or borosilicate coatings. It lakes place, because emissivity of $Al_2O_3$ at used wavelength 5 μm is known with poor accuracy, but results of true temperature calculation are sensitive to emissivity errors. For instance, at measured brightness temperature T = 1200°C, the error in emissivity ~0.05 leads to error ~40°C. The accuracy, as poor as above-mentioned, is sufficient usually and very often this disadvantage is not balanced out by opportunity to measure the time-dependence of temperature field over whole front surface of a sample.

**Surface morphology**

Surface morphology is very informative and photography of sample one can find in any report or article. Additionally, scanning electron microscopy (SEM) is excellent method for using after test campaign. Note, that to get pictures of samples with bad electrical conductivity one has to deposit thin gold film on studied surface. It is useful to obtained not only usual photos but photos of sections and two SEM photos of the same coating of ceramic tile.

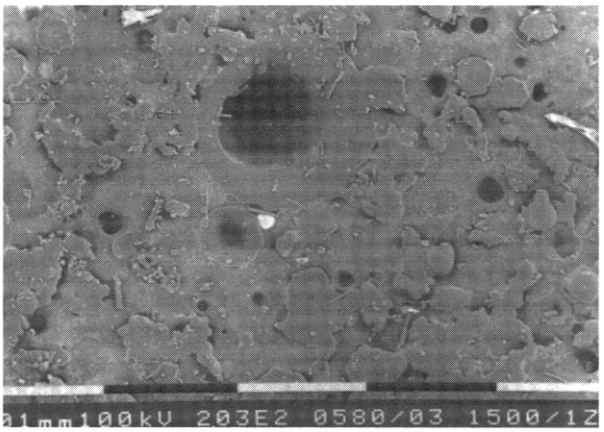


*a)*

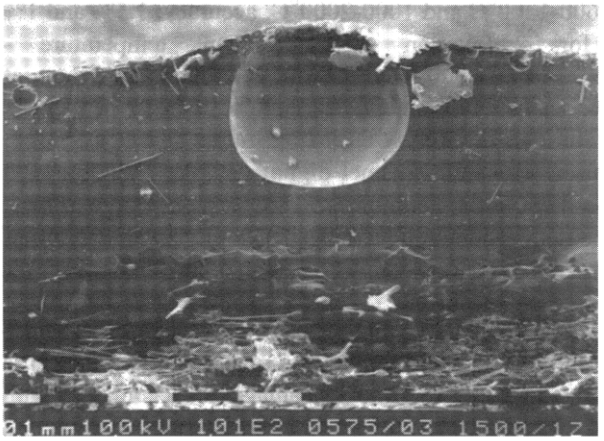


*b)*

***Figure 6.*** *SEM photos of thermal protection tile coating; a – surface, b - section.*

One can see that section gives more informative picture.

**Residual strength**

Residual strength has been used for study of carbon-carbon and tile materials after testing. Fig.7 shows results of residual bending strength measurements for carbon-carbon samples of 84 mm diameter, which withstood 1, 3, 10, 30 cycles at 1480°C in the IPG-3 facility.

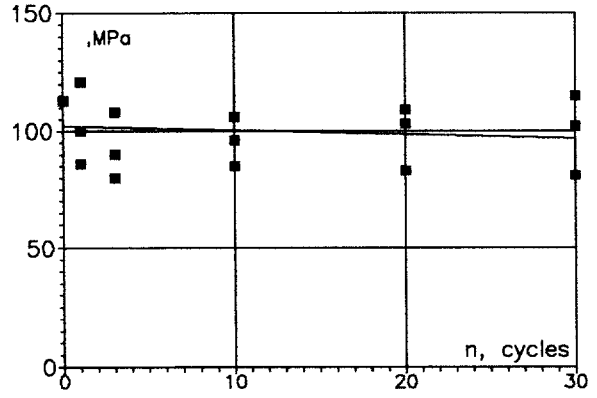


***Figure 7.*** *Residual bending strength of siliconized C-C material with glass-silicide coating after 3 10, 20, 30 testing cycles at 1480°C.*

Otherwise, tile material is tested for tension residual strength, since this type of loading is the most dangerous for tile material.

## 6. TEST PROCEDURE

Test procedure described below is typical and it was used in real study of SiC reference material oxidation which was made for ESTEC/ESA [4-6].

*Preparation to test.*

1. Checking of coincidence of masks and samples.
2. Weighting of the samples.
3. Photographing of front and back side of each samples.
4. Visual inspection of surface of each sample using microscope. Description of observed details.
5. Classifying of the samples into two groups: (i) for pretests and calibration and (ii) for main test program.
6. Measuring of spectral reflection coefficient of each sample in the range 0.3-2.5 mm at room temperature.
7. Measuring of total emissivity of each sample at room temperature.
8. Measuring of temperature dependence of reflection coefficient $\lambda = 0.6328$ μm for SiC and graphite materials at room temperature.

*Calibration and test conditions measurements in the IPG-4 plasmatron of IPM.*

1. At constant air mass flow through discharge channel and at constant pressure in test chamber, which is equal to specified total pressure, dependence of steady-state sample temperature versus RF-generator power is to be measured during step by step heating of a sample. Power levels, which are necessary to achieve specified temperatures are determined by interpolation. Also these series of experiments are used to calibrate using recording pyrometer by reference optical pyrometer with $\lambda = 0.65$ mm. Obtained corrections as well as correction for spectral emissivity (based on data of point 1.6) are taken into account by computer system during test cycles.
2. Taking into consideration (i) very weak pressure dependence of sample temperature and (ii) the fact that dynamic pressure is significantly less than total pressure, test chamber pressure which is corresponded to specified total pressure is determined in individual experiments with Pitot tube. Also these experiments are used to measure dynamic pressure and hence to determine flow velocity.
3. Checking of regimes validity is made by measuring sample temperature at established test chamber pressure and generator power. Measurements of heat fluxes and plasma flow parameters for all regimes are made after calibration and before tests. Required number of samples is equal to the number of used regimes + four samples for calibration, pre-tests and reserve.
4. The following parameters are to be measured for each selected regime:

- heat flux to water-cooled flux-meter of the form identical with that one of tested model,
- enthalpy (is computed using heat flux measurements to high catalytic cold wall),
- dynamic pressure,
- pressure in test chamber.

*Tests cycle.*

The following parameters are recorded during each cycle:

- temperature of front surface of a sample (with correction for spectral emissivity),
- pressure in test chamber, - heat flux from back side of a sample,
- temperature dependency of reflection coefficient of a sample at $\lambda = 0.6328$ mm during heating.
- power in anode circuit of RF-generator.
- repressuration of the test chamber at sample surface is to be made after temperature below 400 C.

After each cycle the following measurements and actions are to be made:
disassembling of test model and visual inspection of all details and sample; damaged details are replaced, measuring of mass loss per cycle,

measuring of spectral reflection coefficient of front side in the range 0.3-2.5 μm at room temperature,
measuring of total emissivity of front side at room temperature,
photographing of front and back side of a sample (Polaroid, two copies),
assembling of the model for next cycle.

## 7. STUDIES OF THERMOCHEMICAL INTERACTION BETWEEN PLASMA AND MATERIAL

### Pressure and temperature dependencies of mass loss rate

Temperature and pressure dependencies of mass loss rate were obtained using the IPG-2 facility. Pressure dependence of mass loss rate averaged over four 10-minutes cycles at $T_w$= 1480°C is given in Fig.8. The dependence found is linear in lgP - lgG coordinates, so $G(P) = A \cdot P^B$. Least square method gives $G(P) \sim P^{-0.19}$, that suggests the coating is gas-tight, since Medford established that $m(P) \sim P^{0.8}$ [7,8] when free molecular diffusion of oxygen through pores and fissues is the main mechanism, defining mass loss rate. It should be emphasized that two facilities, – the IPG-2 and IPG-3, – were used to obtain pressure dependence but since 1989 such experiment may be realized using only IPG-4 facility which allows operation in uniquely wide pressure range.

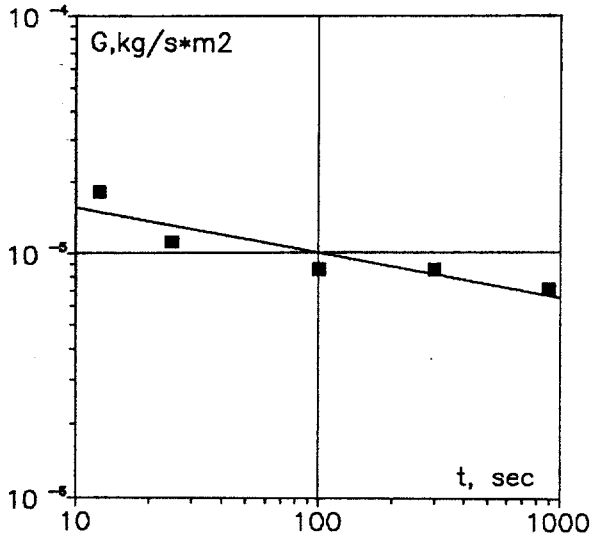


***Figure 8.*** *Pressure dependency of mass loss rate of carbon-carbon material with antioxidative glass-silicide coating.*

Mass loss rate versus inverse absolute temperature is shown in Fig.9. Data on mass loss rate at pressure P = 100 hPa were averaged over six 10-minutes testing cycles. Mass loss rate for carbon-carbon material without any antioxidation protection are presented in Fig.12 to make visible the effect of antioxidation coating deposition. Sharp increase of temperature is caused by the effect of "boiling" of the coating.

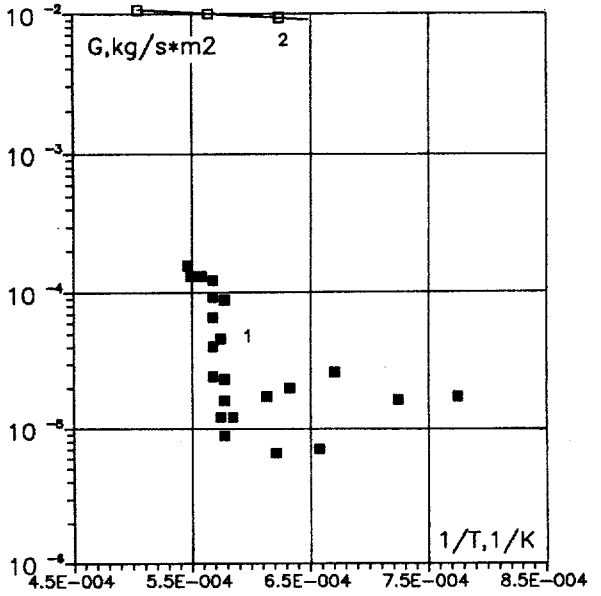


***Figure 9.*** *Temperature dependency of mass loss rate of carbon-carbon material with antioxidative glass-silicide coating. 1 - tested material, 2 carbon carbon material without any antioxidation protection.*
*spectra*

### Thermochemical stability of reusable TPM

*Thermochemical stability of reusable material* is its important characteristics. It is ability of material to withstand concurrent influence of high temperature and chemically active components of initial flow (primarily atomic oxygen). In practice a thermochemical stability is estimated by number of test cycles (or total time) without impermissible degradation of strength, emissivity, catalycity of material under simulated reentry conditions in real time scale.

Carbon-carbon materials are in considerable use in aerospace vehicles due to their unique characteristics. High strength, low specific weight, stability of thin-walled structures of large size under thermal shock and the opportunity to make design elements with beforehand specified properties with maximum strength along direction of maximum load make carbon-carbon using highly attractive for designers. Carbon-carbon materials have high friction properties and they are also biologically inert.

When using carbon-carbon materials as reusable thermal protection materials, it is of great importance that, unlike metals and alloys, the strength of carbon-

carbon materials increases with temperature in gradual manner so that the value at T ~ 2200°C is nearly twice as large as this one at room temperature. Therefore at the preset time maximum exploitation temperature and life time of materials on hand under reentry conditions are limited by the quality of antioxidation coating, which is to prevent carbon-carbon substrate from oxygen access. Concurrently a coating is to the multi-purpose and to meet a number of requirements on emissivity, catalycity, hydrophoby, gas-permeability, coefficient of thermal expansion.

An analysis showed, that the following parameters are to be measured during tests or after them: mass loss and morphology of sample surface, after each cycle of testing, residual flexural strength and gas-permeability coefficient after tests. Surface catalycity and emissivity are also of importance for reusable thermal protection materials used on hypersonic vehicles.

Of special importance for carbon-carbon materials with antioxidation coating but without any oxidation protection in material volume is the formation of destruction zones, since their formation often is the beginning of catastrophic destruction of a sample, or at best is the forerunner of this process. Therefore if tested material may come to catastrophic destruction it is important to find the forerunners of the formation of destruction zones and the reasons of their formation.

General criteria of thermochemical stability estimation are in our opinion as follows:

- decrease of residual strength below specified value;
- occurrence of destruction zones of hazard dimensions.

General parameters, which are to be monitored during or after tests are:

- sample temperature as a function of time at constant parameters of initial plasma flow;
- morphology of sample surface;
- mass loss as a function of the number of test cycles.

Acceptable values of flexural strength decrease, of closely related with it mass loss and of dimensions of destruction zones are to be determined individually for each specific material and specific exploitation conditions.

When testing extensively thermal protection material or hypersonic vehicle, it is also appropriate to make:

- chemical analysis of a sample before and after test using one of recent contactless methods;
- measurements of gas-permeability coefficient of samples coating in initial state and after test.

In conclusion it should be emphasized, that nowadays there is no universal method to estimate a thermochemical stability of carbon-carbon materials with antioxidation coating. It is caused by the fact that tolerable changes of material characteristics essentially depend on used combination coating/substrate. Moreover, these tolerable changes may be different for the same material under different exploitation conditions.

For example, consider carbon-carbon material with he coating based on SiC and without additional oxidative protection in material volume. At temperatures 1600-1700°C, which are maximally permissible for such coating, the formation of destruction zone with following catastrophic destruction is the most dangerous. Unlikely, at respectively low temperatures ~1200-1400°C the decrease of strength as a result of carbon-carbon substrate oxidation is of greatest hazard to the same material. One may find even total oxidation of substrate as it has been obtained in one of 100-cycle test in our laboratory.

*Optical spectral analysis* is one of the most promising methods for the study of plasma action on reusable/non-ablative thermal protection materials (TPM). Its application makes it possible to observe *in situ* degradation of antioxidation coatings during aging tests in plasmatron, since analysis of boundary layer spectrum permits to find, what kinds of species are at a loss from substrate/coating during test, to see time dependencies of those losses *etc.*

For some other combinations of C-C materials and antioxidative coatings it was found, that after catastrophic destruction during oxidation tests one can find only strongly damaged pieces instead of sample. Note, that when coating contains large mass percent of oxididazable species, increase of surface temperature will cause heavy oxidation sooner or later and large amount of produced heat will result very quick transition from quasi-stationary regime to intense burning, i.e. catastrophic destruction. So, to avoid quick catastrophic destruction is important not only in real flight, but in ground tests, too. Really, very often thermochemical stability of large samples or full-scaled elements is lower, than it was found in testing of small samples, but it is very desirable to save expensive and deficit samples for post-test analysis.
Optical spectra analysis is one of the most promising techniques for investigation of physiochemical action of high enthalpy flow on thermal protection materials.

In experimental reentry simulation optical spectra analysis was used not only for plasma diagnostics of high enthalpy jets but for study of plasma-material interaction. The following problems were solved using this method in the investigations of ablative materials:

- qualitative analysis of chemical composition of thermal destruction products;
- quantitative analysis of chemical composition of thermal destruction products including concentration distribution of different atoms, molecules and ions;
- measurements of temperature distribution across the boundary layer including analysis of local thermal equilibrium in the boundary layer using measurements of translation, rotation and vibration temperatures as well as the measurements of atomic lines exitation temperature;
- determination of absorption coefficients and emissivity of destruction products.

These investigation were carried out under large blowing parameter $B = \rho_w v_w / \rho_\infty v_\infty > 0.5$ when mass flow rate of destruction products is compared with mass flow rate in initial plasma jet. In that case vapor concentrations are great and the radiation intensity of destruction products is orders of magnitude greater than that of pure plasma of initial flow.

When testing reusable thermal protection materials the situation became exactly opposite. All observed spectrum of destruction products may consist of a few atomic lines . As a rule they are sensitive lines of different atoms. Two exceptions are possible. 10, 20 or more lines may be observed when atoms of heavy metals such as molibdenum, tungsten, zirconium etc. come to boundary layer from the surface or when those are generated by disoociation of molecules . The other possibility is realized when far great mass loss rate occurs for materials under extreme, nonstandard conditions and for bad materials. It should be emphasized that it is rather difficult to find molecular bands in spectra of destruction products even if the presence of some molecules in boundary layer is obvious (for example, SiO molecules near $SiO_2$ surface heated to 1100°C).

Although optical spectra of destruction products of reusable thermal protection materials are "poor" ( in contrast to "rich" spectra of destruction products of ablative materals), they give reasonably good possibilities to study physiochemistry of plasma-material interaction. Although there is no need to study absorption coefficients of destruction products and it is impossible to measure temperature distribution near the surface since temperature gradient near surface is far too large, there is sufficient number of useful feasibilities. For example it is possible to determine ratio of component concentrations in boundary layer using coincidences of exitaion energy of spectral lines of different atoms. For example, it is feasible in practically important case of silicon and boron atoms (Ref.10). The other attractive feasibility is connected with small mass loss rate of reusable materials. This is small mass rate that leads to diffusion of gaseous products of oxidation and vapor components across boundary layer instead of blowing of destruction products for ablative materials. It may be shown that under some assumptions mass loss rate of the component is directly proportional to total intensity of its spectral lines over boundary layer. It makes the especially attractive to study time dependencies of atomic lines intensities. Of coarse, qualitative chemical analysis of boundary layer composition is kept of importance. In any case optical spectra analysis is the only simple and inexpensive technique that allows to study thermochemical behavior of reusable thermal protection materials *in situ* over cyclic aging tests of arbitrary duration without any special preparation of samples.

It is evident that applications of optical spectra analysis for the study of thermochemical action on reusable thermal protection materials by dissociated air jets merit essentially more detailed consideration but here it is sufficient to emphasize that all above mentioned feasibilities may be made more powerful in combination with making tests in different plasma environments such as air, nitrogen, oxygen and argon.

*The scheme of experimental setup [9]*, used for a study of emission spectra of boundary layer on tested samples, is presented in the Fig.10.

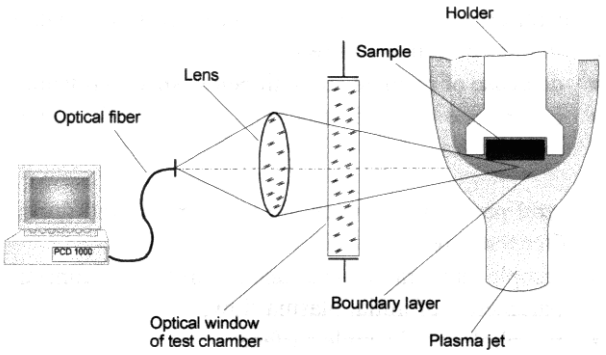


***Figure 10.*** *Conceptual sketch of experimental setup for spectral study of boundary layer on tested samples.*

The main element of the setup is the plug-in computer dual spectrometer PCD 1000, that works in spectral range 200 - 950 nm. The one of the spectrometers works in the range 200 - 450 nm, has 25 μm input slit and its resolution is about 1 nm, the other works in the range 450 -950 nm with resolution ~3 nm, a fiber output cross section serves as its input slit. The optical fibers of 50 μm diameter are used to direct the emission to the spectrometers. The quartz lens of 120 mm focus, used in the setup, creates on the fiber input the 4 times reduced image of the central section of plasma jet. It means, that in the range 200 - 450 nm the emission is taken from the plasma jet area of 0.1x0.2 $mm^2$, but in

the range 450 -950 nm - from the area of 0.2x0.2 $mm^2$. Note, that only intensive doublets of atomic sodium and potassium were found in long wave band but the most interesting lines are grouped in short wave band, so only short wave spectrometer was used practically in all experiments.
Since 1963 spectrometers with difractional gratings and focal length 3 m and 1 m were used for spectra registration using photo plates and photomultipliers. Now CCD-camera with 1024x1024 matrix can be used for careful experiments with high spectral resolution and spatial resolution across boundary layer.

**Spectral precursors of catastrophic destruction**

Spectral precursors of catastrophic destruction were observed in tests of C-C material with glass-silicide antioxidative coating. The most interesting zone of spectrum of boundary layer over glass-silicide coating is shown in Figure 11. The most important atomic lines, which are appeared in emission spectrum of boundary layer due to coating degradation, are sensitive (last) lines of atomic molybdenum, silicon and boron and those are shown in the Figure 11. Also there is some number of relatively weak lines of atomic molybdenum as well as lines of manganese, sodium and potassium, which present in the coating in small concentrations. However,

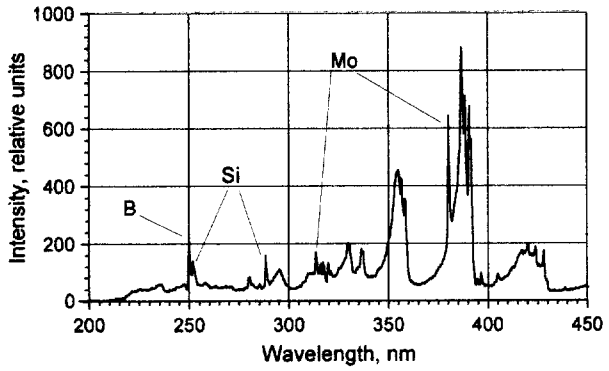


*Figure 11. Spectrum of boundary layer over glass-silicide coating.*

lines,because, as one can see from Figure 11, radiation of hot flow over a model is recorded by spectrometer, too, although it is less intensive, than spectrum of free jet, but it is more intensive, than it is possible to expect for boundary layer.

It was found, that intensities of molybdenum lines become unstable before the beginning of catastrophic destruction, but at the same time intensities of other lines of main components of the coating such as silicon and boron don't demonstrate such behavior. Typical variation of molybdenum lines intensities is shown in Figure 12 with time between the two recordings is 0.4 s, but to have more precise picture it is necessary to see kinetics of changing of basic parameters.

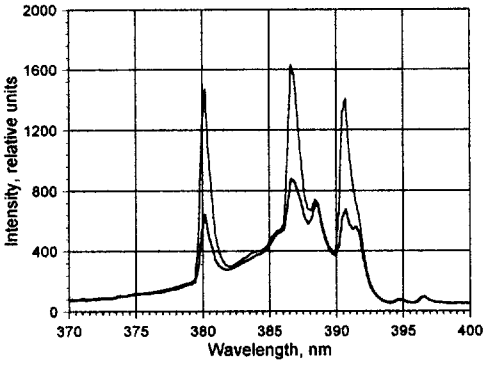


*Figure 12. Fragments of two spectra of boundary layer on glass-silicide coating recorded with delay 0.4 s.*

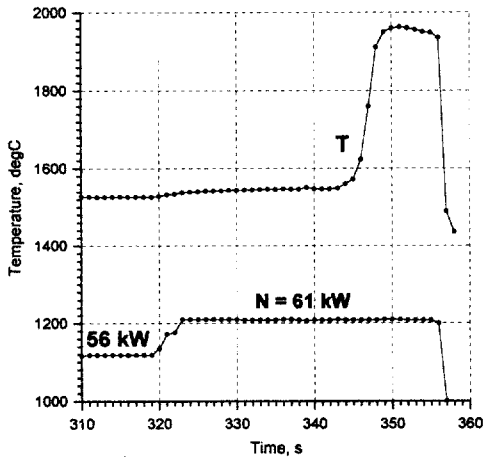


*Figure 13. Time dependencies of sample's surface temperature and generator's anode power before catastrophic destruction («boiling»).*

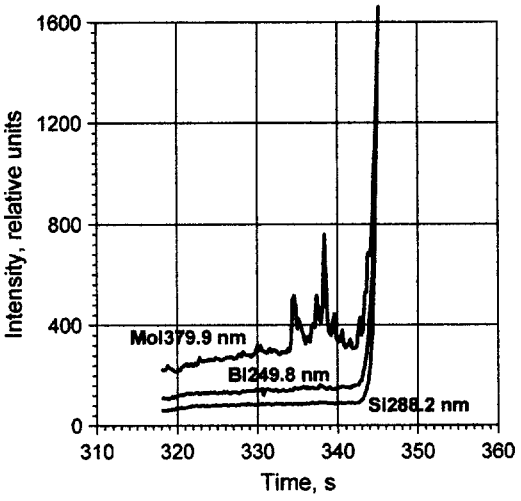


*Figure 14. Time dependencies of sensitive lines intensities of different atoms which appeared in boundary layer due to coating degradation.*

Time dependency of surface temperature of glass-silicide coating is shown on Figure 13 together with anode power of HF-generator before the beginning of boiling, and time-dependencies of intensities of sensitive lines of a molybdenum, boron and silicon are submitted on Figure 14 for the same test. As it is seen from Figures 13, 14, intensities of lines of silicon and boron before the beginning of boiling are enough stable and those begin to increase only with the increase of surface temperature. At the same time intensity of molybdenum line begin to pulse ~10 s before the beginning of «boiling». Peak intensities can be 2-3 times higher than its quasi-stationary level. There is no such peaks at usual operating temperatures, they appear only before «boiling». This result is in a good agreement with previous data on physico-chemical mechanism of «boiling»: it is caused by intensive oxidation of $MoSi_2$ particles, containing in the coating, by atomic oxygen from oncoming flow [2,3]. At the same time observable peaks shows, that before boiling heavy oxidation is blocked time by time with formation of protective film of oxides, and only then it becomes such strong, that the formation of film does not realized. So, study of specific features in behaviour of boundary layer over tested sample before catastrophic destruction allowed to obtain new information on mechanism of destruction even for well-known material & coating. Of coarse, such study can be more fruitful for new TPM and/or coatings.

Thus, it was found, that before boiling one can find few peaks of molybdenum lines intensity. There is no such peaks at usual operating temperatures. Repeatability in appearance of those peaks before «boiling» allows to consider them as «spectral precursors» of catastrophic destruction.
It is obviously, that boiling of glass-silicide coating is only one of many possible kinds of catastrophic destruction. However, it is more possible to find precursors when oxidizable components is exposed to dissociated air before the beginning of catastrophic destruction. Such situation can be found with multilayer and multiphase coatings, containing components, which can be oxidized with production of large amount of heat.

Other types of antioxidation coatings applied on C-C materials were preliminary tested to find spectral precursor of catastrophic destruction. The first results showed, that tested coating is not the only coating with spectral precursors of catastrophic destruction and there are different types of spectrum behavior before destruction. At the same time first attempts to find spectral precursors were not successful with the carbon-carbon samples with SiC-based coating. However, it means only, that searches are to be continued.

Study of spectral precursors of catastrophic destruction can be easily made practically in each laboratory, working on TPM testing in plasma jets. First of all, it can give important information about physico-chemical processes, that initiate catastrophic destruction of tested reusable TPM. Of coarse, that information can be used to refine chemical composition and technology of coating and, hence, to remove the beginning of catastrophic destruction to higher temperatures.

Besides, it is well known, that scale factor is very important for thermochemical stability of samples and full-scale elements of carbon-carbon materials with antioxidation coatings, which are used for oxidation tests, because usually it is difficult to realize on full-scale elements the same level of thermochemical stability, that has been demonstrated in tests of small samples. Knowledge about spectral precursors of catastrophic destruction can be used fruitfully to save expensive large samples and/or full scale elements from catastrophic destruction in plasma jet tests and to have an opportunity to make after-test analysis of substrate and coating exposed to extreme thermochemical loading. Actually, if one knows what kind of spectral precursor type takes place on material/coating on hand, it is not too difficult to develop special code to produce signal for test interruption (or for decrease of power put in plasma), when precursors appears in spectrum.

**Tests in different gases**

Many essential features of thermochemical action on thermal protection material by dissociated air flow may be found using optical spectra analysis in combination with making tests in different plasma environments such as air, nitrogen, oxygen and argon. As a rule mass loss of carbon-carbon materials with antyoxidation coating is generally resulted from the oxidation but atomic oxygen is essentially more active than molecular. Comparative study of optical spectra of boundary layer allows to understand what components is arised in boundary layer due to thermal vaporization and what components is arised in boundary layer due to thermochemical action of the initial flow. Obviously, above mentioned approach is to be combined with data on temperature, pressure and time dependencies of mass loss rate, as well as photos of surface obtained using SEM etc.

Emission optical spectra were obtained during tests in dissociated air and nitrogen flows. All experiments were carried out at constant pressure **P** = 100 hPa using the IPG-4 facility. More than 20 rather intensive spectral lines of molybdenum were found when sample was exposed to dissociated air flow. Also sensitive lines of BI, SiI, MnI, KI, NaI were observed in

boundary layer overflowed by dissociated air flow. Note, that simple qualitative chemical analysis gives two interesting results. The observation of molybdenum lines alone is the result of great importance for the understanding of thermochemical action of dissociated air on the glass-silicide coating.

Specially made plasma jet tests showed that there are no even weak sensitive lines of molybdenum while dissociated nitrogen overflowed the sample but lines NaI, KI, BI, SiI were found in these spectra. These result suggest that molibdenum atoms arising is caused by the thermochemical action of oxygen but the other components arise in boundary layer due to thermal evaporation. Taking into account that back side of tested sample which was exposed to non-dissociated air practically at the same pressure and temperature (since tests were made in subsonic flow and back side was heat insulated), one can make conclusion that it is atomic oxygen that causes such damages to coating. The most effective way of molybdenum loss is associated with the oxidation of $MoSi_2$ followed by evaporation of exceptionally volatile molybdenum oxides and it is one of the leading mass loss processes.

## CONCLUSION

Effective test methods were developed for reusable thermal protection materials on the basis of plasmatron advantages and subsonic modeling of hypersonic heating. Complex approach, which includes tests in maximally wide pressure and temperature ranges together with tests in different gases and optical spectral analysis application, showed its efficiency for a study of thermochemical stability of reusable materials and physico-chemical mechanisms of plasma-material interaction.

## REFERENCES


1. A.N.Gordeev, A.F.Kolesnikov, M.I.Yakushin. An Induction Plasma Application to "Buran's" Heat Protection Tiles Ground Tests.- SAMPE Journal, 28(3), May/June 1992, pp.29-33
2. A.N.Gordeev, M.I.Yakushin - .The thermo-chemical stability of carbon-carbon using an atioxidation coating for Buran - Part II.- SAMPE Journal, 29(2), March/April 1993, pp.27-31.
3. A.N.Gordeev, M.I.Yakushin, G.A.Kravetskii et.al., Antioxidation Glass-Silicide Coating for Carbon-Carbon Materials and its Aging in Air Plasma Flow. - Proceedings of the 2nd European Workshop on Thermal Protection Systems & 3rd European Workshop on High Temperature Materials, Stuttgart, 23-27 October 1995, pp.217-224.
4. A.Gülhan, D.Vennemann, M.I.Yakushin, B.E.Zhestkov Comparative Oxidation Tests on Reference Material in Two Induction Heated Facilities. 46th International Astronautical Congress, October, 1995 Oslo, Norway, 9 p.
5. D.Vennemann, M.I.Yakushin Oxidation Tests on SiC Reference Material in an Induction Heated Facility under Sub- and Supersonic Flow Conditions. AIAA 96-4566, 1996. 7th International Spaceplanes Conference, 18-21 November 1996, Norfolk, USA, 8 p.
6. M.I.Yakushin, A.N.Gordeev, D.Vennemann, A.Novelli Mass Loss of SiC Sample Surfaces Under Different Flow Conditions. AIAA Paper 98-2605. 20th AIAA Advanced Measurement and Ground Testing Technology Conference, June 15-18, 1998, Albuquerque, NM, ESA-ESTEC.
7. J.E.Medford. Prediction of Oxidation Performance of Reinforced Carbon-Carbon Material for Space Shuttle Leading Edges. - *AIAA Paper* No.75-730, 1975, pp.1-14.
8. J.E.Medford. Multi-Cycle Plasma Arc Evaluation of Oxidation Inhibited Carbon-Carbon Material for Shuttle Leading Edges. - ASME Paper No.72-ENAV-26, August, 1972.
9. A.N.Gordeev, M.I.Yakushin, N.G.Bykova Spectral Precursors of Catastrophic Destruction: Detection, Study and Possible Application for Plasma-Jet Tests. 3rd European Workshop on Thermal Protection Systems, ESTEC, 25-27 March 1998, Netherlands, Noordwijk, p. 329-333.

# Overview of IRS Plasma Wind Tunnel Facilities

Monika Auweter-Kurtz,
Thomas Wegmann
Universität Stuttgart
Institut für Raumfahrtsysteme
Pfaffenwaldring 31
70550 Stuttgart
Germany

## Introduction

Upon entering the atmosphere of celestial bodies, spacecrafts encounter gases at velocities of more than ten km/s, thereby being subjected to great heat loads. Figure 1.1 shows artist's concept of X-38 reentering Earth's atmosphere [1]. The X-38 is a technology demonstrator for the proposed Crew Return Vehicle (CRV), which will be designed for an emergency return from the International Space Station.

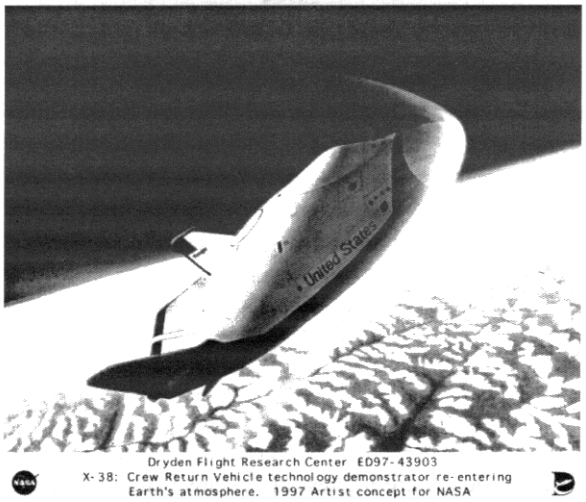


**Fig. 1.1: X-38 re-entering Earth's atmosphere [1]**

The task of a thermal protection system (TPS) is to protect the substructure of the vehicle against local and global overheating.

A heatshield material should have:

- a low mass,
- a smooth surface to avoid an early flow change from laminar to turbulent,
- the necessary strength to withstand aerodynamic, aeroelastic, chemical and heat loads,
- material catalycity be as low as possible, that is it should not encourage the recombination of oxygen and nitrogen or nitrogen oxide formation,
- an emissivity as high as possible, at least 0.8, in order to reject a large portion of the heat input at the lowest possible temperature.

For the qualification of heatshield materials regarding these requirements a lot of different ground testing facilities are necessary which cannot all be discussed during this lecture. This lecture concentrates on the plasma wind tunnel facilities (PWK) which have been in use at the IRS (Institut für Raumfahrtsysteme of Stuttgart University) for more than a decade [2, 3]. Firstly, they are used for the qualification of heatshield materials in regard to chemical and high enthalpy loads occurring during reentry into the earth's atmosphere and entry into other planetary atmospheres [4 - 8]. Secondly, they are tools for the development of reentry measurement techniques [9 - 12]. In addition, these facilities can be used for the validation of numerical codes [13 - 16].

In ground test facilities the simulation of the real gas composition as it is set up near the surface of the spacecrafts and probes is only possible for a few ms with free ballistic ranges. Resulting measurement times are of only a few µs. So-called hot shot tunnels [17] or piston shock tunnels [18] offer measurement times of a few ms, but due to the high gas temperature of the oncoming flow predissociation cannot be avoided. The duration of test runs within these facilities is far too short for the development and testing of heat protection materials since the surface largely remains cold and therefore hardly interacts with the hot gas.

For the development of heat protection materials for entry bodies one, therefore, depends on plasma wind tunnels, which do not offer a complete simulation of entry conditions. Because of a restriction of the arc chamber pressure and the strong nonequilibrium phenomena in the arc tunnels it is in principle impossible to correctly simulate the flight environment, which means characteristic Reynolds number and Mach number, for the first phase of reentry (Fig. 1.2).

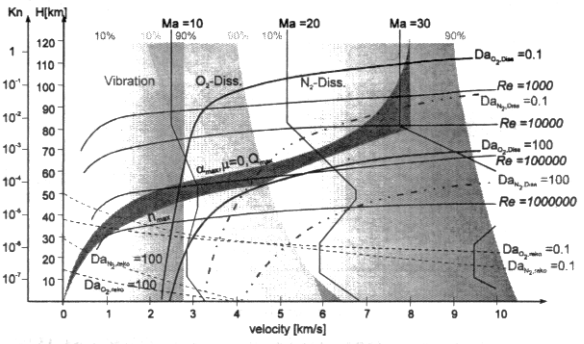


**Fig. 1.2: Reentry flight zones [19]**

*Paper presented at the RTO AVT Course on "Measurement Techniques for High Enthalpy and Plasma Flows", held in Rhode-Saint-Genèse, Belgium, 25-29 October 1999, and published in RTO EN-8.*

With the exception of tunnels operating at high ambient pressure and able to simulate the flight conditions of the last phase of reentry, a plasma wind tunnel has to be seen as a tool for the simulation of the flow near the material surface. Therefore, the goal has to be the duplication of the conditions near the surface of a vehicle which have to be determined first by calculation or by a flight experiment (Fig. 1.3). Such wind tunnels are then suitable for the development of TPS materials.

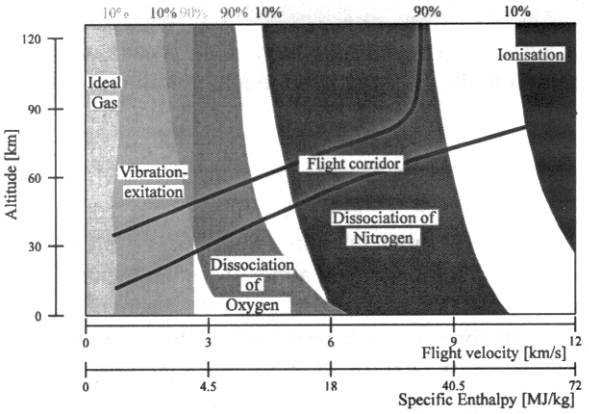


**Fig. 1.3: Reentry flight conditions**

With plasma wind tunnels a continuous stream of plasma of high specific enthalpy and velocity is produced with the help of thermal or magnetoplasmadynamic generators (TPG or MPG). Our plasma wind tunnels PWK 4 and PWK 5, equipped with thermal arc generators (TAG), are suitable for the studies of aerodynamic loads of high enthalpy flows. High impact pressures and fairly high Mach numbers and specific enthalpies can be generated. However, the exhaust velocity is limited to several km/s and low impact pressures cannot be achieved. The erosion rate of heat protection material with an oxidation protection coating (defined as mass loss per exposed area and time) is especially high at low pressure levels and, therefore, in regions of high velocities [20 - 22]. These conditions can be simulated with the help of MPGs in PWK 1 and PWK 2.

The inductively heated PWK 3 is used for basic research on TPS materials, especially regarding their catalytic behavior, because no plasma impurities occur from electrode erosion. In addition, tests in a pure oxygen or in a mainly $CO_2$ atmosphere, for example for entry into Mars' or Venus' atmosphere, can be performed [23, 24].

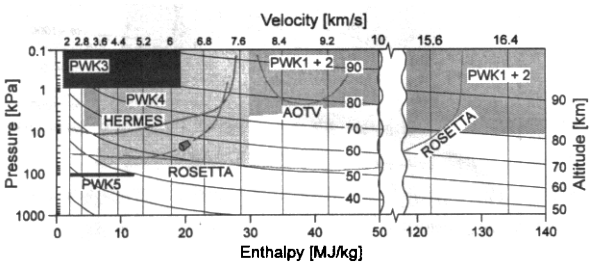


**Fig. 1.4: Simulation regimes of the PWKs at IRS**

The simulation regimes of the PWKs at IRS can be seen in Figure 1.4 together with some typical reentry trajectories.

A PWK must be able to be used for the following:

- qualification of TPS materials,
- basic research on TPS materials,
- verification of numerical codes,
- development and qualification of diagnostics methods,
- development and qualification of flight experiments.

It is of the utmost importance that the impurity level in the plasma is as low as possible and especially materials of high catalycity, as for example copper, have to be avoided as this would lead to a falsification of the results.

# 2. Simulation Requirements for Reentry Vehicles

For the development of thermal protection systems for reentry bodies especially the oxidation behavior of TPS materials has to be studied, in particular if the vehicle has to be designed as a reusable one. For this purpose facilities are needed to simulate in steady state conditions the required surface temperature on the material, pressure, specific enthalpy and mass flow rate.

First the simulation requirements for a small winged reentry vehicle will be shown and discussed. For re-usable winged space vehicles like HERMES, HOPE or CRV the heat loads and therefore also the chemical loads are highest at the nose cap and at the leading edges. For HERMES, which was studied in Europe during the 80s, most data are available and is therefore used here as an example. Based on the tra-

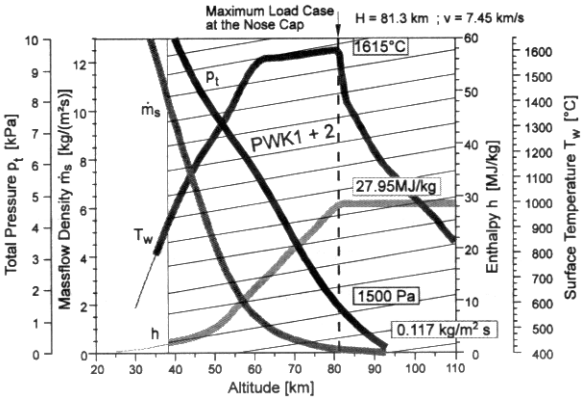


**Fig. 2.1: Surface temperature, pressure and specific enthalpy at the nose cap of HERMES during reentry for landing in Istres and the required mass flow within the PWK. (Thick lines: simulation region with PWK 1 or PWK 2, hatched zone: simultaneous simulation with PWK 1 or PWK 2)**

jectory of HERMES the pressure, density and the specific enthalpy of these surface elements was calculated [5]. The surface temperature, pressure and specific enthalpy are shown as a function of altitude in Fig. 2.1 for the nose cap and in Fig. 2.2 for the leading edge.

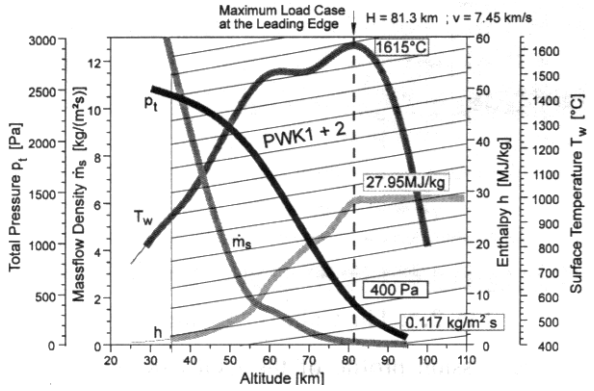


**Fig. 2.2: Surface temperature, pressure and specific enthalpy at the leading edge of HERMES during reentry for landing in Cayenne and the required mass flow within the PWK. (Thick lines: simulation region with PWK 1 or PWK 2, hatched zone: simultaneous simulation with PWK 1 or PWK 2)**

Candidate TPS materials of modern reusable vehicles are of carbon fiber with carbon or SiC matrixes and an oxidation protection coating on top which in most cases again consists of SiC. The erosion of these materials is most severe at high temperature and low pressure levels due to active oxidation [20 - 22]. These conditions can be duplicated with the help of an MPG as used in the plasma wind tunnels PWK 1 and PWK 2. The surface temperature, pressure and specific enthalpy regions of the trajectory which are achievable with these facilities are marked in Figs. 2.1 and 2.2 by a thick line. The density and velocity profile together with the cross section of the plasma beam of PWK 1 and PWK 2 of ca. 0.031 $m^2$ lead to the required mass flow for these tunnels, which is included in Figs. 2.1 and 2.2. The hatched zone marks the region where surface temperature, specific enthalpy, pressure and mass flow rate can be duplicated simultaneously. In the case of the leading edge, this region is limited by the maximum possible mass flow whereas in the case of the nosecap the maximum achievable stagnation pressure is the limiting factor. But for both cases the low pressure and high temperature phase of the reentry can be simulated including the maximum temperature point.

If the gas were in thermodynamic and chemical equilibrium near the material surface during reentry and within the test facility, this simulation with the help of a magnetoplasmadynamic wind tunnel would be perfect. In both situations this is not the case and for both situations the exact gas composition is still unknown today. But a lot of research programs are under way so that in the future more knowledge will be gained in this area. With the help of computer programs in which non-equilibrium chemistry is included, the reentry situation as well as the MPG wind tunnel situation is being simulated [14, 25]. At the same time, measurement techniques are being developed for the analysis of the high enthalpy gas during the material tests in ground based facilities [26, 27] as well as during the vehicle reentry [9-12].

Compared to the trajectory of a winged spacecraft like HERMES, the reentry of a ballistic or semiballistic space capsule from a low earth orbit is marked by essentially higher heat loads due to the steeper ascent. Figure 2.3 shows the heat flow on the wall, the pressure at the stagnation point, the mass flow and the specific enthalpy all dependent on the altitude. Because the reuse of a space capsule has not been demanded yet, ablation materials are normally used for the thermal protection shield. On the German-Japanese EXPRESS mission, launched in 1995, a first experiment was conducted to determine whether ceramic thermal protection materials can be used in order to enlarge the possibility of reentry measurement techniques. A C/C-SiC tile for the stagnation point region, manufactured by the DLR Stuttgart, was qualified during the flight [28].

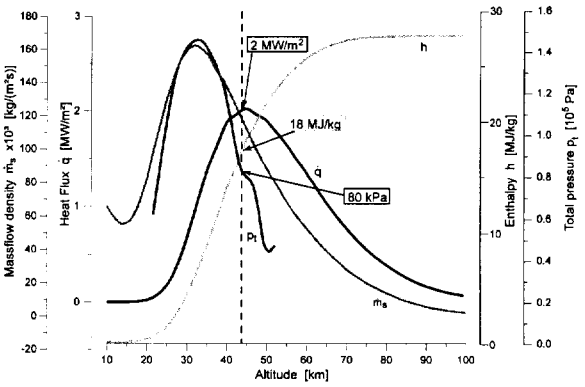


**Fig. 2.3: Stagnation pressure, specific enthalpy, heat flux and mass flow density for the nose cone of EXPRESS as a funtion of the altitude**

The EXPRESS capsule is a typical example of a ballistic, reentry capsule protected by an ablator. The hot reentry phase, which can be simulated in a ground facility like a plasma wind tunnel, begins at a nominal height of 100 km at a speed of approximately 7.4 km/s. The heating during the capsule's descent was calculated according to the results from earlier flights performed by the manufacturers from the Russian company Khrunichev. The maximum was expected at a heat load of 2 $MW/m^2$ after 235 s at a height of 45 km. At this point in time the stagnation point pressure should be about 75 kPa. The maximum stagnation pressure of 15 MPa should be reached after approximately 275 s. The capsule would at this point be at a nominal height of 32 km. The maximum stagnation pressure cannot be reached in the IRS PWKs equipped with MPGs. However, the heat flow

profile is fully feasible. Figure 2.4 shows the course of the heat flow during reentry as well as the course of the heat flow as simulated in the PWK. Because ceramic thermal protection was used at the tip of EXPRESS, maximum erosion at low pressure and high temperature was to be expected just as with HERMES. Therefore, using the MPG tunnel the worst case was examined.

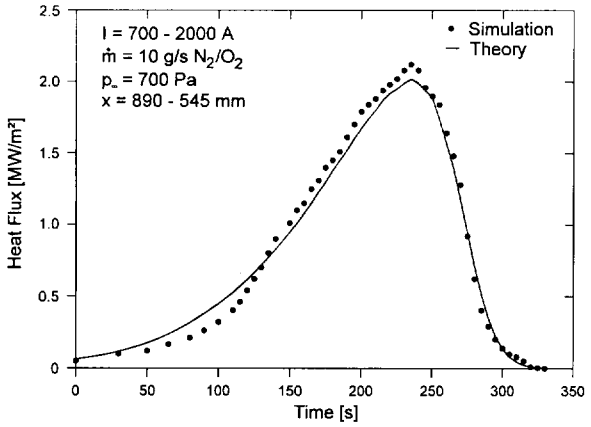


**Fig. 2.4: Heat flux profile of the EXPRESS mission**

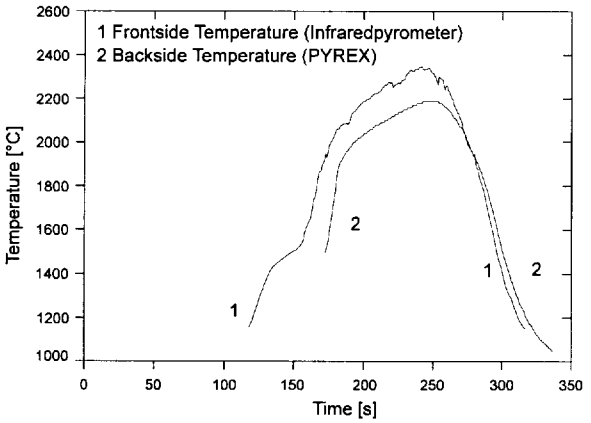


**Fig. 2.5: Surface temperature of the ceramic heat shield of the EXPRESS capsule in the PWK**

During the flight qualification of the EXPRESS experiments, maximum surface temperatures of approximately 2300°C (see Fig. 2.5) resulted from a duplication of the heat flow profile in the MPG-tunnel at the IRS. The front and rear temperatures of the ceramic tile were measured pyrometrically. The rear temperature was to be determined by an EXPRESS experiment - the miniature pyrometer PYREX from the IRS [9].

At the IRS a semi-ballistic capsule COLIBRI (Concept of a Lifting Body for Reentry Investigations) was designed as a testbed to perform autonomously scientific and technology experiments during the reentry flight [29] with three primary goals:

- to investigate aerothermodynamic phenomena encountered during hypersonic flight,
- to test advanced materials and concepts for thermal protection systems, and
- to perform both flight dynamics and navigation as well as guidance, and control experiments during a controlled atmospheric flight.

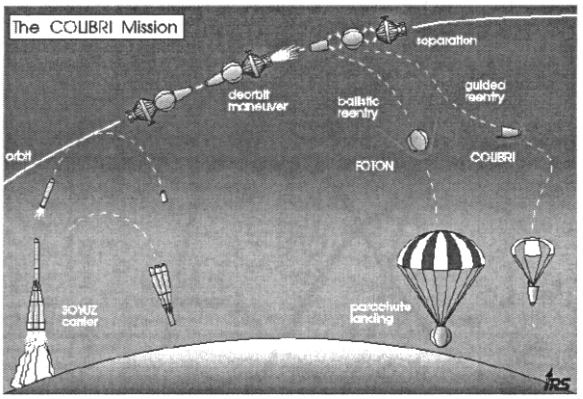


**Fig. 2.6: The Colibri Mission [29]**

The mission profile of the COLIBRI capsule is illustrated in Fig. 2.6. A "piggy-back"-flight opportunity on a Russian FOTON carrier-capsule was considered for this study that would be launched into a low Earth orbit by a Soyuz rocket. The drawback associated with this low-coast approach is that entry conditions are defined by the ballistic FOTON capsule to be recovered in southern Russia and can not be selected independently. Thus, the recovery area of FOTON is at the lower end of the attainable landing area of the semi-ballistic COLIBRI vehicle as illustrated in Fig. 2.7. Though FOTON enters the atmosphere following a ballistic path, the reentry flight of COLIBRI will be autonomous and controlled. In order to ease the recovery of the vehicle, a landing accuracy of 5 km is regarded as sufficient.

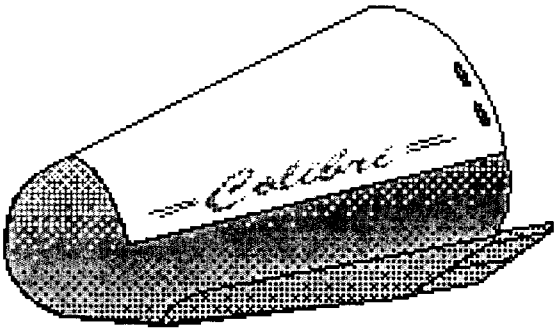

**Fig. 2.7: The COLIBRI capsule [29]**

An example of the calculated conditions for the semiballistic Colibri capsule project is shown in Fig. 2.8. The maximum heat flux of ~ 2.2 MW/m$^2$ is expected at a stagnation pressure of 20 kPa and a corresponding specific enthalpy of 26 MJ/kg. These conditions are well within the simulation region of the plasma wind tunnel PWK 4, equipped with the thermal plasma generator RB3.

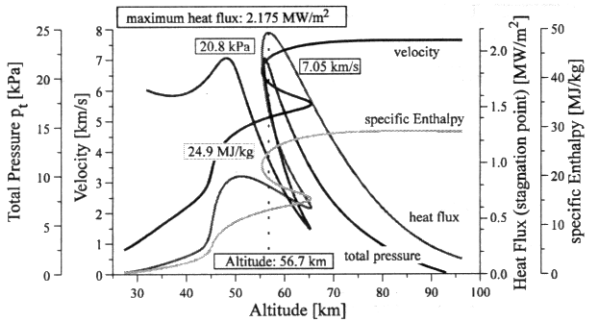


**Fig. 2.8: Total pressure, velocity, heat flux and specific enthalpy vs. altitude for the COLIBRI reentry mission [29]**

Huygens is an European probe which will be used to investigate the atmosphere of the Saturnian moon Titan. It is being carried to the Saturn system with the Cassini spacecraft, which was designed, built and launched by NASA [30]. During the entry into Titan's atmosphere, the probe has to be decelerated aerodynamically from about 6.1 km/s to 400 m/s within three minutes. This will be done by a heat shield with a diameter of 2.7 m. In Fig. 2.9 the heat flux, specific enthalpy and dynamic pressure of a typical probe trajectory are plotted versus the altitude.

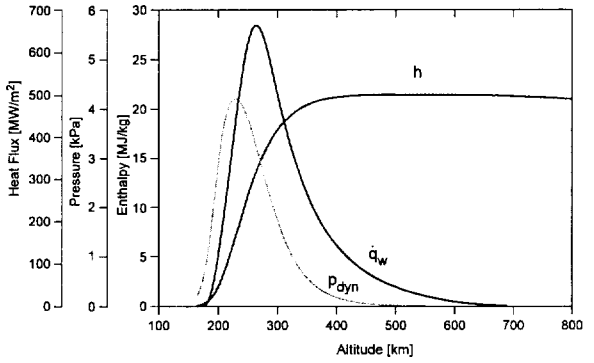


**Fig. 2.9: Heat flux, pressure and specific enthalpy profiles for the entry of Huygens into the atmosphere of Titan [7]**

These conditions can be completely simulated in a PWK equipped with an MPG at the IRS [7, 8]. For this mission the composition of Titan's atmosphere presented a special challenge for the test facilities. The atmosphere consists of approximately 80 - 90 % nitrogen, 3 - 10 % methane and presumably about 10 % argon. Carbon based gases are very difficult to handle in plasma generators because the carbon settles on the electrodes especially when they are water-cooled. The erosion caused by carbon is large if it is in contact with hot glowing cathodes. Therefore, special measures were necessary to avoid any contact of the glowing tungsten cathode with carbon, to assure the anode attachment and to avoid short cuttings of isolated generator segments due to a carbon layer formation. In the IRS MPG facility continuous operation with methane components up to 10%, as required, could be reached for several hours.

The capability of the IRS plasma wind tunnels to produce plasma flows of an enthalpy level of more than one hundred MJ/kg can be used to duplicate the stagnation point flow field of very fast space vehicles as expected for the reentry flight of a comet sample return probe like ROSETTA (see Fig. 2.10) or of a Mars or Venus sample return probe [31]. In case of a comet sample return mission the earth entry velocity of the probe is in the range of about 15 km/s. This yields a specific enthalpy of about 130 MJ/kg and a maximum heat flux to the probe of more than 20 MW/m$^2$. During the aerobraking maneuver of a sprint-type manned Mars mission similar values of the quantities mentioned above are expected (see Fig. 2.11)

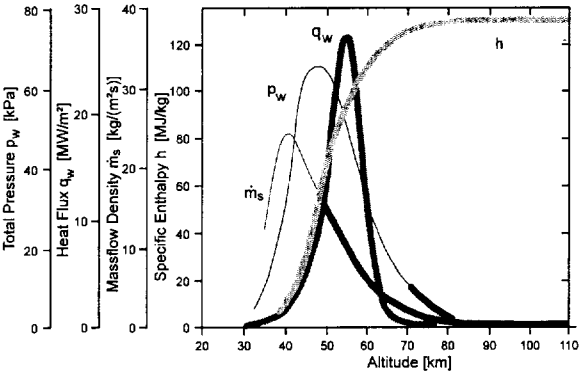


**Fig. 2.10: Heat flux, pressure, specific enthalpy profiles and mass flow rate for the reentry of ROSETTA [31]**
**(Thick lines: simulation region with PWK)**

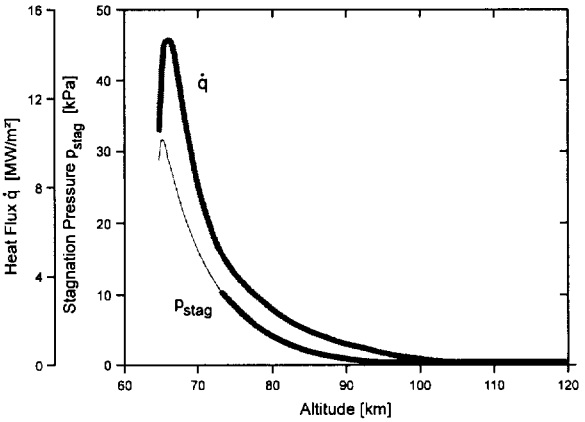


**Fig. 2.11: Heat flux and stagnation pressure profiles during aerobraking flight of a sprint type Mars mission in the Earth's atmosphere [31]**
**(Thick lines: simulation region with PWK)**

# 3. Plasma Wind Tunnels

The term plasma wind tunnel is to be understood as a stationary test facility in which a high enthalpy flow is produced with the help of a plasma generator. The operating times range typically from several minutes to several hours. Arc-driven high enthalpy shock tube tunnels, such as the ONERA High En-

thalpy Wind Tunnel F4 [32], which like other shock tube tunnels have operating times of a few milliseconds, are actually plasma wind tunnels too. But today they are put in a class with the shock tube tunnels. There are various types of plasma wind tunnels, depending on the kind of plasma generator used.

As already pointed out it is basically impossible to create a complete simulation of all gas parameters with plasma generators. The combustion chamber pressures necessary for this would be around 10 GPa. It is not primarily the mechanical loads which makes this impossible. With continually operated arcjet accelerators the pressure is principally limited to 1 MPa up to approximately 10 MPa. At such a pressure level already a nitrogen arc with a diameter of 1 cm and a temperature of 20 kK is optically thick [33]. This means that the arc changes into a radiation source which according to the Stefan-Boltzmann Law radiates proportionately $T^4$ almost like a black body radiator. When, however, the radiation losses are so extremely high, the device can, on the one hand, not be cooled and on the other hand every increase of the arc energy leads to a drastic increase of the radiation losses and, in contrast to this, only to a small increase of plasma flow enthalpy which is emitted from the device. Thus for material development for the thermal protection of entry bodies one is dependent on plasma wind tunnels that do not offer a complete simulation of entry conditions. Therefore, one equips varied tunnels so that the influence of individual aspects which are important for material investigations can be estimated. These tunnels can be operated for minutes or for hours on end, whereby the specific enthalpy, the pressure, the heat flux, the wall temperature and the concentrations of the most important plasma components can be reproduced near the surface.

A plasma wind tunnel consists of the following components:

- a vacuum tank at IRS equipped with a moveable platform for positioning of the TPS sample,
- a vacuum pump system for creating the low ambient pressure necessary for the simulation,
- a plasma generator to create the high enthalpy plasma flow,
- a suitable power supply system, usually a rectifier plant, or a high frequency generator,
- the auxiliary components such as a gas and cooling water supply at different pressures, emission purifier etc.,
- and the measurement equipment and data processing system.

As an example for the facilities at IRS the scheme of the PWK 1 facility can be seen in Fig. 3.1. Figure 3.2 shows a photograph of PWK 1.

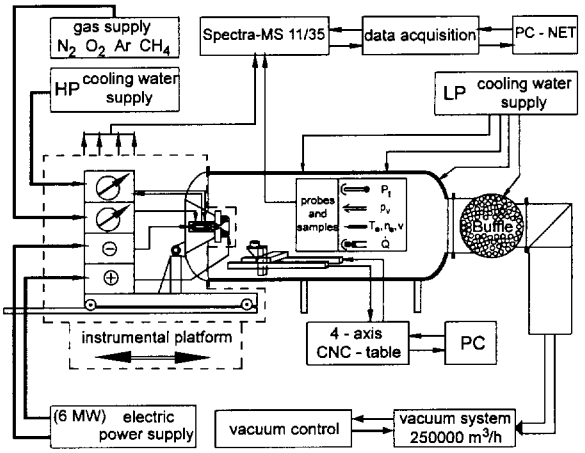


**Fig. 3.1: Scheme of plasma wind tunnel PWK 1**

The vacuum tank used for the plasma wind tunnel PWK 1 is a 5 m long steel tank with a diameter of 2 m, divided into three cylindrical segments all of which have a double-wall cooling. The connection between the last two segments is protected against heat by a water-cooled copper shield.

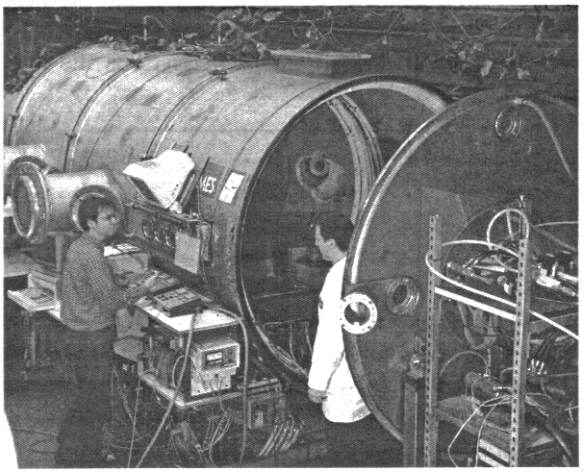

**Fig. 3.2: The plasma wind tunnel PWK 1**

The tank is closed with a hemispherical part which is connected to the vacuum system (see section 3.2) and protected against heat by water-cooled copper shields. On the other side the vacuum chamber can be opened by moving the plane cover plate on a guide rail. The plasma source is not located in the vacuum tank, but flanged on a conical part of the plate. The cone-shaped element of the end plate enables the plasma source to be fixed at that point. The whole plasma jet range is accessible by optical methods.

The tank is equipped with a 4-axis positioning system on which the different probes and the specimen support system can be mounted. This allows the simulation of parts of the reentry trajectories by moving the specimen in the plasma flow.

Windows with optical glass allow pyrometric temperature measurements on the front side of the specimen at distances from the plasma source between about 50 mm and 1000 mm. Moreover, spec-

troscopic measurements perpendicular to the plasma jet axis are possible through three movable flanges of three optical glasses each, which are located on both sides of the tank opposite each other and on the top (see Fig. 3.2).

An additional vacuum tank of identical size and with the same equipment is available in a second laboratory of IRS (Fig. 3.3). However, this vacuum tank consists only of one segment, made of stainless steel, to prevent corrosion caused by atomic oxygen.

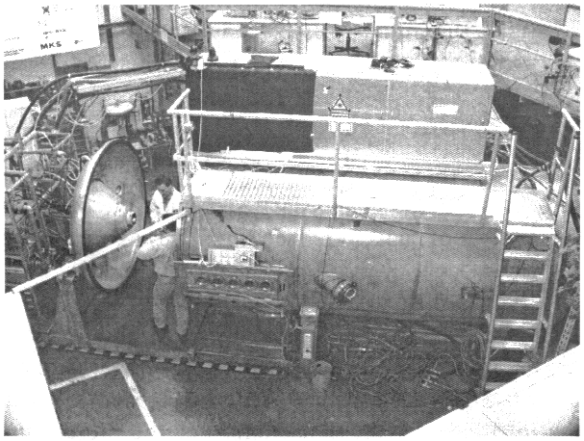

**Fig. 3.3: The plasma wind tunnel PWK 2**

As long as the above described vacuum tanks are equipped with magnetoplasmadynamic generators (section 4.2), these plasma wind tunnels are called PWK 1 or PWK 2, respectively. If, instead, a thermal plasma generator (section 4.1) is used, they are called PWK 4.

The whole experimental setup of PWK 3, shown in Fig. 3.4, consists of the inductively heated plasma source IPG3 (section 4.3) and the vacuum chamber. The size of this vacuum chamber is about 2 m in length and 1.6 m in diameter. Material support systems and mechanical probes can be installed onto a moveable platform inside the tank. Optical accesses to the vacuum chamber are provided in order to observe the plasma flow and to perform optical diagnostics. As can be seen in Fig. 3.5, the plain lid of PWK 3 is to carry the plasma generator and the external resonant circuit, which contains the capacitors with the connection to the plasma generator.

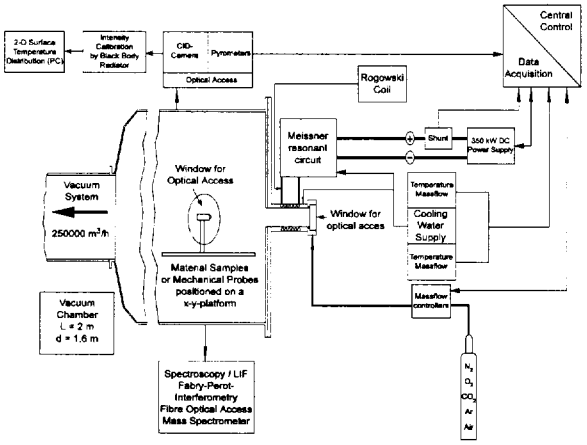


**Fig. 3.4: Scheme of plasma wind tunnel PWK 3**

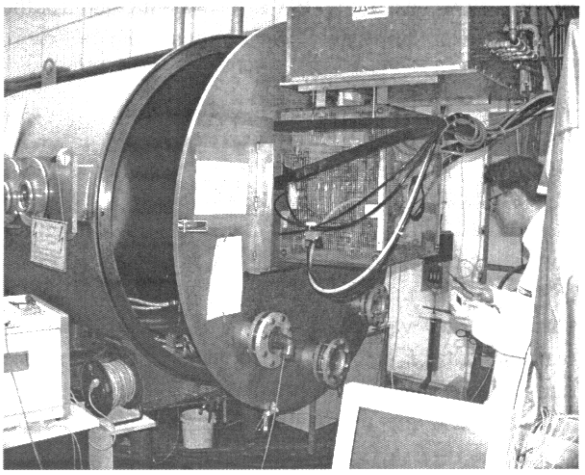

**Fig. 3.5: The plasma wind tunnel PWK 3**

All the plasma wind tunnels PWK 1 - 4 are connected to the central vacuum (section 3.2), the central power (section 3.1) and the central gas supply system.

The plasma wind tunnel PWK 5, also equipped with a thermal plasma generator (section 4.1), is not connected to a vacuum system. Thus, this test facility is suitable for testing TPS materials at pressure levels higher than $10^5$ Pa. The scheme of PWK 5 can be seen in Fig. 3.6.

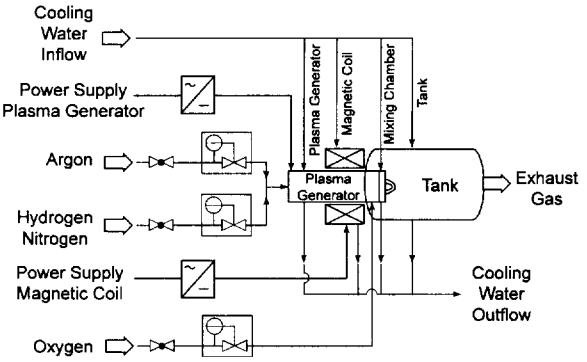


**Fig. 3.6: Scheme of plasma wind tunnel PWK 5**

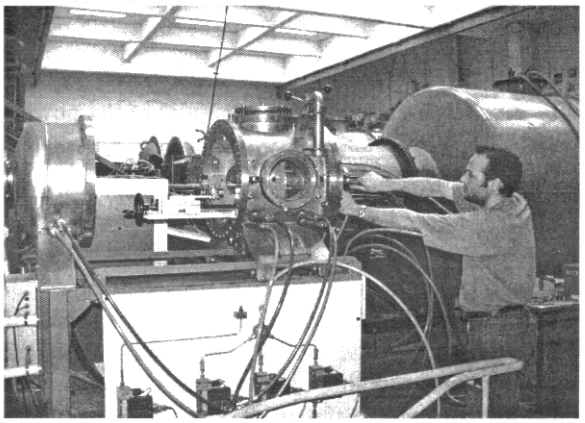

**Fig. 3.7: The plasma wind tunnel PWK 5**

The tank of PWK 5 (Fig. 3.7) is a 0.7 m long steel chamber with a diameter of 0.5 m, equipped with

double-wall cooling. It is equipped with a specimen support system which is moveable manually along the plasma flow. Also the PWK 5 is connected to the central power supply and gas supply system.

## 3.1 Power supplies

The electric power for the arc plasma generators is supplied by a current-regulated thyristor rectifier consisting of six identical units supplying 1 MW each (Figs. 3.8 - 3.9). These may be connected in series or parallel, thus varying the desired output level of current, voltage, and power. The current ripple is less than 0.5 %. The maximum current is 48 kA supplied at 125 V and the maximum voltage is 6000 V at a current of 1000 A.

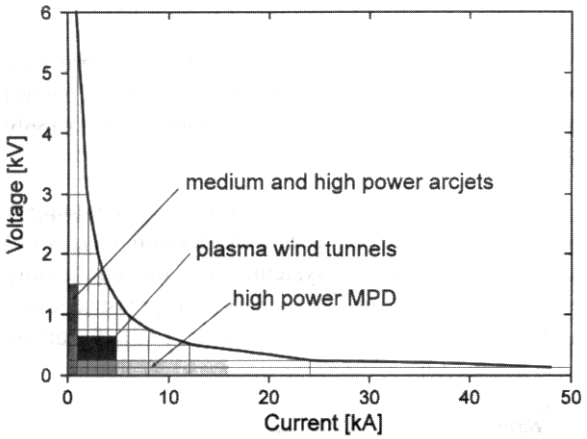


**Fig. 3.8: Voltage vs. power characteristic of the power supply system**

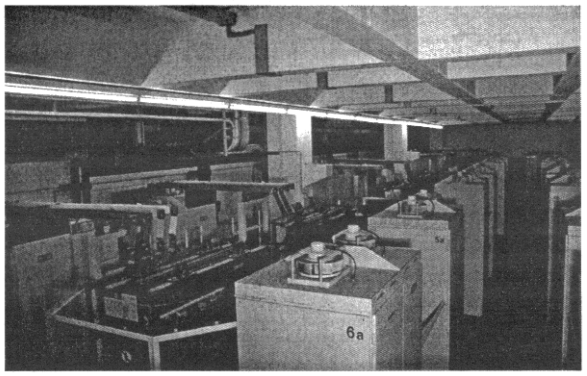

**Fig. 3.9: High voltage thyristor units of the power supply system**

For the inductively heated plasma wind tunnel PWK 3 a radio frequency generator with a primary power of 400 kW is used. This device allows the operation of an induction coupled plasma generator with a coil power of 150 kW at a nominal frequency of 650 kHz. An external resonance circuit is designed for an optimal coupling into the plasma over a wide pressure range with different gases.

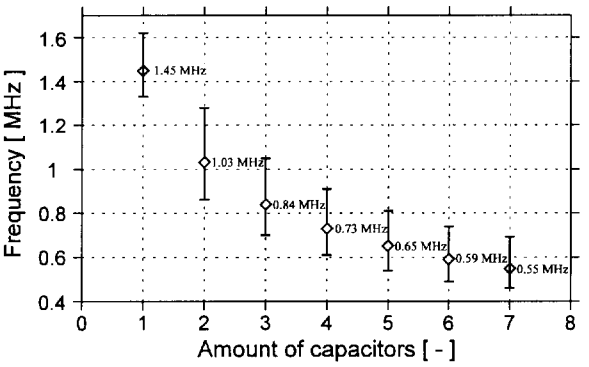


**Fig. 3.10: Nominal operating frequencies for different capacitor switchings**

The resonant circuit is built in Meissner type switching [34] using a metal-ceramic triode with an oscillator efficiency of about 75 % [35]. Its nominal frequency can be changed by switching the order or the number of capacitors (see Fig. 3.10) as well as by the use of coils with different inductivities. A maximum of 7 capacitors with a capacity of 6000 pF ± 20% each can be connected. The external resonant circuit is cooled by a high pressure water cooling circuit. The error bars in Fig. 3.10 take into account the tolerances of the capacitors. For the present investigations it is tuned to a nominal frequency of 0,55 MHz using a water-cooled 5-turn coil with a length of about 120 mm. The incoming anode power can be adjusted by the control of the anode voltage.

## 3.2 Vacuum System

A vacuum pump system is used to simulate pressures at altitudes up to 90 km. This pumping system consists of four stages: the first two stages consist of roots blowers, the third stage is a multiple slide valve type pump, and the last stage (pumping up to atmospheric pressure) is a rotary vane type pump (Figs. 3.11 - 3.12). The total suction power of the pumps amounts to 6000 $m^3/h$ at atmospheric pressure and reaches about 250000 $m^3/h$ at 10 Pa measured at the intake pipe of the system, which has a diameter of

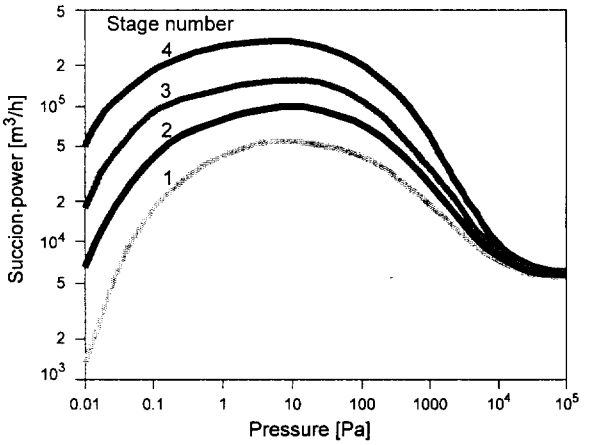


**Fig. 3.11: Suction power of the vacuum system**

1 m. The base pressure of the system is 0.5 Pa. The

desired tank pressure can be adjusted between the best achievable vacuum and 100 kPa by removing one or more pumps from the circuit and/or mixing additional air into the system close to the pumps.

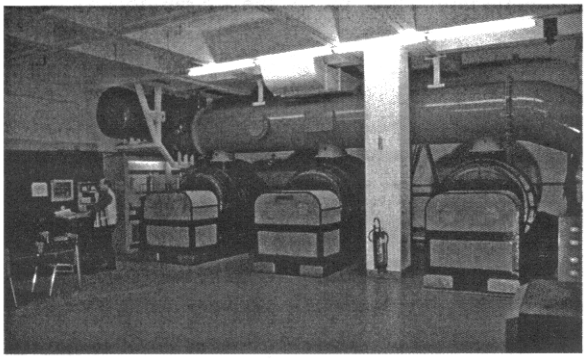

**Fig. 3.12: Roots pump stage (4th stage) of the vacuum system**

# 4. Plasma Generators

Two plasma generator concepts, the thermal and the magnetoplasmadynamic generator (TPG and MPG), are in use in the arc heated plasma wind tunnels; they mainly differ in the acceleration concept.

In thermal arc generators (TAG) the test gas is heated by means of an electric arc and usually accelerated through a Laval nozzle. Regarding magnetoplasmadynamic generators (MPG), additional electromagnetic forces are used to accelerate the test gas. The inductive plasma generator (IPG) also belongs to the group of TPGs. With this electrodeless design the plasma is produced by inductive heating using a radio frequency generator. With the TPG, where the gas is first constricted into a kind of chamber, the hypothetic chamber conditions $p_0$, $h_0$ and $T_0$ may be used as reference parameters. This does not make sense with an MPG, where magnetic acceleration occurs in the nozzle.

## 4.1 Thermal arc generators (TAG)

Thermal arc generators for wind tunnel applications are run at high pressures, high mass flows and an electric power of up to 100 MW [36]. In order to keep the electrode losses and especially the erosion of the cathode to a minimum, the current intensity of the TAG should be kept as low as possible. As a result the voltage is high. The electrodes of those apparatus that are used for the simulation of reentry into the earth's atmosphere are mostly water-cooled and usually made of copper. During the simulation of atmospheres without oxygen components, hot, glowing cathodes made of thoriated tungsten may be employed, their advantage being an extremely low rate of erosion.

The erosion of the cold cathodes is relatively high and influences the quality of the plasma flow. Especially copper particles are unwanted in the plasma since they may be deposited on the material that still has to be examined and they possibly influence the catalycity of the samples. In addition, in the case of water-cooled cathodes, a locally settled arc attachment spot on the cathode leads to its destruction. Therefore, with most TAGs the electric arc attachment at the cathode is rotated by means of a magnetic field.

The anode attachment of the arc at these high pressures is actually unstable because it is not possible to create enough charge carriers in the anode layer. So one or several moving arc attachment spots are formed which would destroy the water-cooled anodes of the TAG. One can try to prevent this by "stabilizing" the anode attachment with the help of an axial magnetic field and/or a gas turbulence. This process is called stabilization, but it is actually more like a destabilization because the arc attachment is caused to move rapidly over the electrode.

In principle there are three different concepts, the hollow electrode arc heaters used for example at the DLR in Cologne [37] and at SIMOUN by Aerospatiale [38], the constricted arc plasma generators, used for example at NASA Ames [36] and the glowing rod-shaped cathode device as for example developed at the IRS and described below.

The attainable exit speed $c_e$ of the plasma with all these TPGs is essentially dependent on two values: the mean effective molecular weight $\overline{M}_{eff}$ of the gas which corresponds to a temperature and a pressure which lies between the values in the combustion chamber and those at the nozzle end, and the attainable arc chamber temperature $T_0$.

In a first approximation, the exit velocity is given by:

$$c_e \cong \sqrt{\frac{2\,\kappa_{eff}}{\kappa_{eff}-1}\,\frac{R\,T_0}{\overline{M}_{eff}}} \quad , \qquad (4.1)$$

since the temperature at the nozzle exit can be considered as very low compared to the arc chamber temperature $T_0$. The dependence on the effective adiabatic coefficient $\kappa_{eff}$ is low.

The gas used in PWK facilities is determined by the composition of the atmosphere to be simulated. The effective mean molecular weight is hereby mainly dependent on the pressure in the accelerator and the temperature by means of the dissociation and the ionization degree. It decreases as the temperature rises and the pressure falls. In order to reach high flow velocities, the temperature in the arc chamber must be as high as possible. The maximum arc chamber temperature is limited by the maximum possible cooling rate at the chamber wall.

TAGs are operated at high pressures (from several $10^5$ Pa to approx. 10 MPa), high weight rates of flow (up to several kg/s) and electric power of up to a maximum of 100 MW. In order to keep the erosion of the electrodes and the electrode fall losses to an absolute minimum, the working point of a TAG is at the lowest possible current intensity because both losses are proportional to the current intensity. Therefore the necessary power for accelerating the gas is coupled in at the highest possible voltage level, usually at several kV. However, undesired discharges must be prevented which in turn limits the voltage. Thus, voltages higher than 30 kV are difficult to obtain and current intensities of several kA in larger facilities are unavoidable. This leads to a proportionately high erosion of both electrodes and consequently to a high impurity level and low electrode life times.

In order to simulate high enthalpy air flows at pressure levels above 5 kPa, which is the limit of MPGs (see section 4.2) and in heat flux ranges between 100 kW/m$^2$ and about 3 MW/m$^2$ in stagnation point configuration, a coaxial thermal plasma generator (TPG) called RB3 (Fig. 4.1) has been developed for the PWK 4. In Fig. 4.2 the nozzle part of the RB3 generator installed in PWK 4 can be seen. Figure 4.3 shows the generator in operation during a material test.

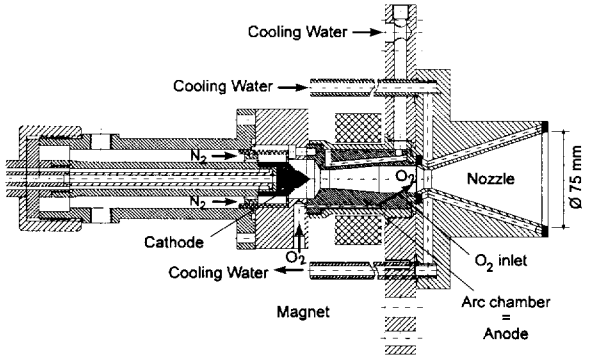


**Fig. 4.1: Plasma source RB3**

The test gas is heated in the discharge chamber by an electric arc and accelerated in a nozzle. In the present version a 2 % thoriated tungsten cathode is used. The anode is a water-cooled copper cylinder, whereas the nozzle is electrically insulated. Since contact between the oxygenic part of the test gas and the cathode has to be avoided, the air used for re-entry simulation is divided into two parts. As main part the nitrogen is passed along the cathode into the plenum chamber. The oxygen is injected at the downstream end of the anode towards the nozzle throat. To ensure a good mixing of the nitrogen and the oxygen, the injection point is positioned in the subsonic part of the TAG so that a backflow of oxygen into the cathode region cannot be ruled out completely. However, tests have shown that the cathode erosion rate due to the bi-throat design for RB3 is as low as observed in the MPGs operated in PWK 1 and PWK 2 and in the order of the sublimation rate [39]. To avoid anode erosion due to spotty arc attachment, a coil is used to generate an axial magnetic field which moves the arc rapidly around.

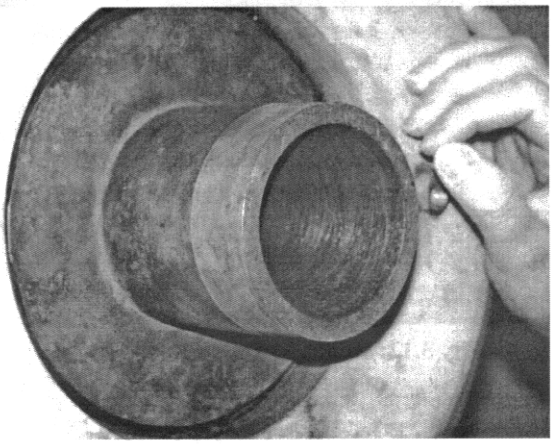

**Fig. 4.2: RB3 installed in PWK 4**

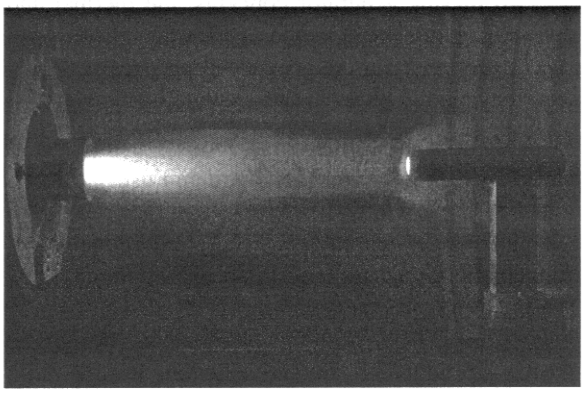

**Fig. 4.3: RB3 in operation**

The adjustable parameters in PWK 4 equipped with RB3 are the arc current, the mass flow rate, the ambient pressure and the distance to the exit of the plasma source. The arc voltage is decreasing with rising arc current and is in the order of 120 - 160 V, increasing with mass flow (Fig. 4.12). The thermal efficiency, defined as

$$\eta_{th} = \frac{P_{el} - \dot{Q}_{tot}}{P_{el}} \quad , \qquad (4.2)$$

with the total electrical input power $P_{el}$ and the total heat losses inside the plasma source $\dot{Q}_{tot}$, is about 72 % with a mass flow rate of 5 g/s $N_2/O_2$ and about 82 % with 10 g/s $N_2/O_2$ (Fig. 4.14). It decreases slightly with increasing current due to the increase of pressure in the arc chamber, whereas the averaged specific enthalpy at the nozzle exit

$$\bar{h} = \frac{P_{el} - \dot{Q}_{tot}}{\dot{m}} \qquad (4.3)$$

increases (see Fig. 4.13). The arc chamber pressure, which determines the maximum expansion ratio, is in the order of 40 to 90 kPa, increasing with mass flow and arc current (Fig. 4.15).

The conditions in the measurement section of PWK 4, namely the stagnation pressure, the heat flux measured with a cold copper probe and the corresponding local specific enthalpy calculated with Pope's theory [40], are plotted as functions of the ambient pressure in Figs. 4.4 and 4.5 for two different mass flow rates. With 5 g/s (Fig. 4.4) at an ambient pressure of 450 Pa the maximum heat load situation of the Japanese space plane Hope can be simulated. By increasing the mass flow rate to 10 g/s (Fig. 4.5) and slightly increasing the ambient pressure, the stagnation pressure reaches ca. 10 kPa at a heat flux level of ~ 2.2 MW/m$^2$ and a specific enthalpy of 24 MJ/kg. In order to meet the requirements of Colibri, the stagnation pressure has to be increased again by a factor of two, which can easily be done by further increasing the mass flow rate, the power and the ambient pressure.

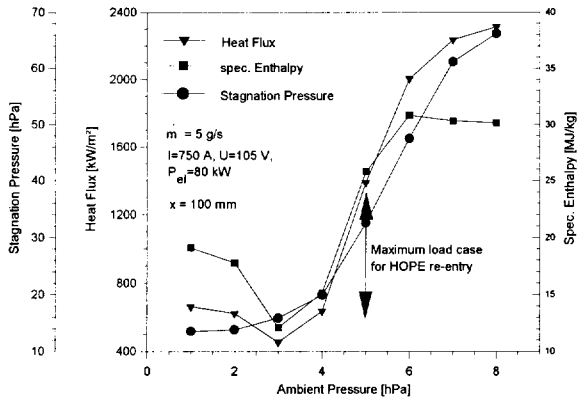


**Fig. 4.4: Local specific enthalpy, heat flux and stagnation pressure as a function of the ambient pressure for a mass flow rate of 5 g/s air [2]**

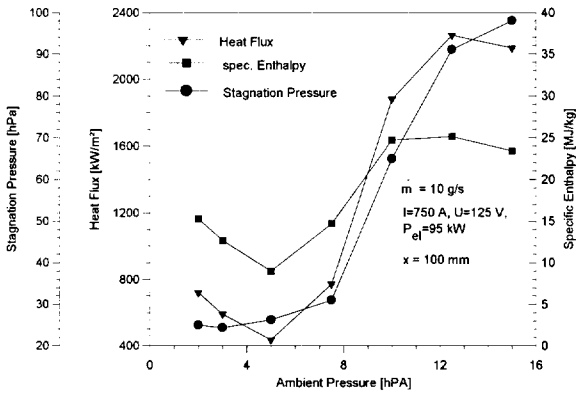


**Fig. 4.5: Local specific enthalpy, heat flux and stagnation pressure as a function of the ambient pressure for a mass flow rate of 10 g/s air [2]**

For the plasma generation in PWK 5 a TAG is also used. The high enthalpy flow is created by the atmospheric plasma generator APG1 [41], shown in Fig. 4.6. The design is based on an arc heater developed by Wilhelmi [42]. It consists of a water-cooled copper anode and mixing chamber and a tungsten cathode. Because of the hot cathode, only inert gases can be fed along the cathode. The ignition of the arc is performed by a Paschen breakdown as for the other TAGs and MPGs. Due to the higher chamber pressure in this device, argon is used as propellant during the ignition. The argon is then gradually replaced by the test gas. The oxygen is injected into the mixing chamber downstream behind the anode.

Two anodes with diameters of 8 mm and 10 mm are available. The current-voltage and current-power characteristic is shown in Fig. 4.7. The maximum electric power is about 46 kW. The optimal operation range with respect to the erosion of the electrodes is between 200 - 500 A. In this range averaged specific enthalpies $\bar{h}$ at the nozzle end of 6 MJ/kg up to 11 MJ/kg are generated with a total mass flow of 1.1 g/s $N_2/O_2$. The maximum thermal efficiency at these conditions is about 40 % [43].

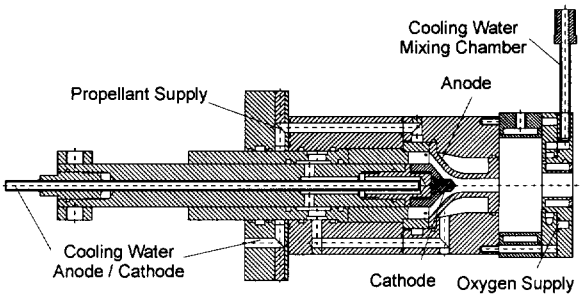


**Fig. 4.6: The atmospheric plasma generator APG1 [43]**

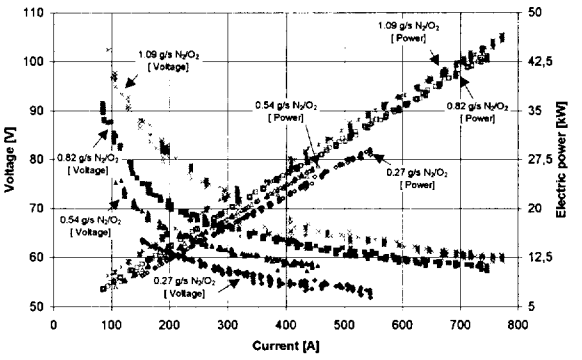


**Fig. 4.7: Current-voltage and current-power characteristic, 10 mm anode, distance of the electrodes: 3 mm [43]**

## 4.2 Magnetoplasmadynamic generators (MPG)

In the 60s and early 70s first investigations were performed to determine to what extent MPGs, being developed as plasma thrusters, were suitable for the simulation of entry conditions. Applied field as well as self-field accelerators were tested at that time [44, 45].

The acceleration principle of a self-field MPG is shown schematically in Fig. 4.8. An arc is produced between the cathode and anode of these devices. The gas is heated up, dissociated and partly ionized by the

arc within the heating chamber. The self-induced magnetic field due to the high arc current creates a Lorentz force which accelerates the plasma in the supersonic part of the nozzle in addition to the thermal acceleration through the Laval nozzle. Therefore, the attainable exit velocities are much higher compared to those with the TAG. The magnetoplasmadynamic acceleration can be shown to be proportional to the square of the current [46]. Therefore, to achieve high gas velocities, it is essential to operate at a high current level (kA).

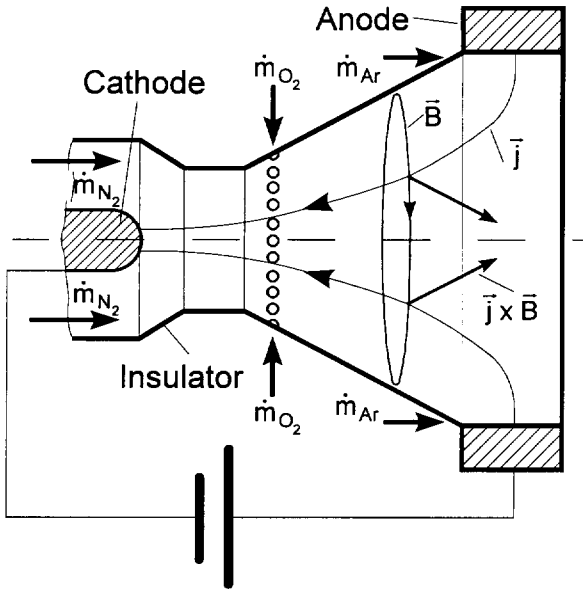


**Fig. 4.8: Scheme of a self-field MPG**

With the applied field MPG, an applied magnetic field is used to accelerate the plasma instead of the self-induced field in the case of a self-field MPG. Since the required densities for plasma wind tunnels are relatively high, extremely high magnetic fields of 10 - 90 T have to be generated when using an applied field MPG. At AVCO in the US, a prototype apparatus for dynamic pressures reaching nearly 1 MPa and mass flows up to 0.6 kg/s in 1 ms pulses was tested in 1970 [44]. The results were encouraging. However, the expenditure needed to run these apparatus in continuous operation mode is so great that to this day only a plasma wind tunnel in Russia has been equipped with an applied field MPG [47].

Self-field MPGs of different sizes have been developed over the past few years at the IRS. They are employed successfully in the IRS wind tunnels PWK 1 and PWK 2 for investigating erosion properties as well as ablation of heat protection materials and they are therefore looked at more closely here.

The nozzle-type MPG plasma generators (dubbed RD), as shown in Fig. 4.9, consist of two coaxial electrodes, separated by neutral, water-cooled copper segments. The nozzle exit, which is also a water-cooled segment, forms the anode. The cathode, made of 2 % thoriated tungsten, is mounted in the center of the plenum chamber.

The arc is ignited by a Paschen breakdown. The current passes through the expansion nozzle from the cathode tip to the end of the nozzle. The test gas is dissociated and partly ionized. In order to avoid the oxidation of the cathode, only the nitrogen component of the test gas is fed in along the cathode into the plenum chamber, heated up by the arc and accelerated partly by the thermal expansion and partly by the electromagnetic forces due to the self-induced magnetic field in the nozzle. The magnitude of the magnetic acceleration force strongly depends on the current level of operation [46]. With this MPG, the oxygen needed for the duplication of high enthalpy air flows is fed in radially at a high velocity at the supersonic part of the nozzle, but still within the arc region. The various gas injection points enable the operation of the MPG with different gas mixtures. As pointed out earlier this capability is used for the investigation of entry maneuvers into the atmospheres of other celestial bodies such as Titan and Mars, containing $CH_4$ and $CO_2$, respectively.

Special efforts have been made to minimize the erosion of the plasma generator. In order to avoid a spotty arc attachment on the anode, which would cause a contamination of the plasma flow, a small amount of argon is injected tangentially along the anode contour. This method has been shown experimentally to eliminate anode erosion [2]. Within the whole region of operation the only contaminating part of the MPG is the cathode. The 2 % thoriated tungsten cathode reaches more than 3000 K during the steady-state operation [39]. The high temperature and the low work function of the cathode result in a diffuse arc attachment and, consequently, a very low cathode erosion rate at the order of sublimation. Furthermore, the very low cathode erosion results in operation periods of the MPG of hundreds of hours without refurbishment of the generator.

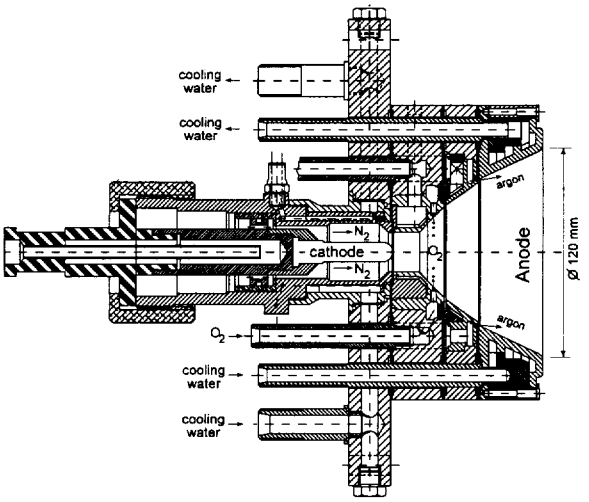


**Fig. 4.9: Magnetoplasmadynamic generator RD5**

The MPGs are operated at ambient pressures between 5 Pa and 5 kPa. For the MPG generator RD5, shown in Figs. 4.9 and 4.10, with a nozzle exit

diameter of 125 mm, the mass flows are between 0.3 g/s and 50 g/s at current levels between 200 A to 4000 A and power levels of 40 kW to 1 MW, while the average specific enthalpy $\bar{h}$ at the nozzle exit varies between 2 MJ/kg and 150 MJ/kg.

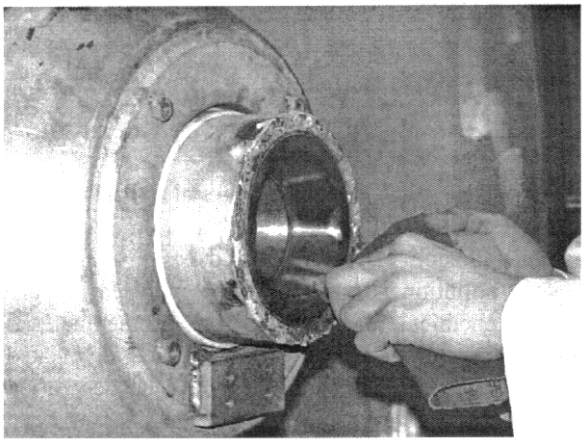

**Fig. 4.10: The RD5 generator installed in the PWK**

For testing large TPS structures an MPG generator with enlarged nozzle has been built. While the RD5 generator has a nozzle exit diameter of 125 mm (Fig. 4.9), the nozzle diameter of RD7 is 320 mm (Fig. 4.11), which enables the investigation of TPS materials up to 400 mm in diameter [48].

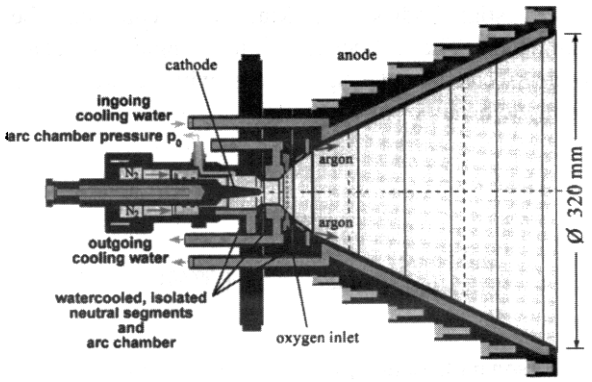


**Fig. 4.11: Scheme of the plasma generator RD7**

In Figs. 4.12 and 4.13 the current-voltage characteristic and the mean specific enthalpy $\bar{h}$ at the end of the plasma generator (Eq. 4.3) as a function of the current intensity are shown for various mass flows for the plasma accelerators RD5. Data of the RB3 performance are also included in these figures.

Since the degree of ionization decreases, the voltage increases with the mass flow. The specific enthalpies are dependent on the mass flow and the current intensity; low mass flow and high current intensity make it possible to reach specific enthalpies of up to 150 MJ/kg which can, for example, appear during return missions to Earth or during aerobreaking maneuvers. The specific enthalpies which are attainable with an MPG are high compared to those reached with a TAG. This can essentially be attributed to two reasons:

- additional acceleration of the gas through magnetic Lorentz forces $\vec{j} \times \vec{B}$;
- heating the gas up to the nozzle exit, which leads to a high enthalpy (and temperature) of the gas at the beginning of the free jet.

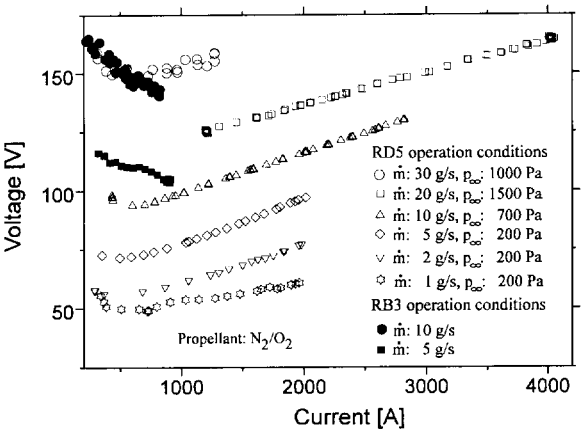


**Fig. 4.12: Current-voltage characteristic of the MPG RD5 and the TPG RB3**

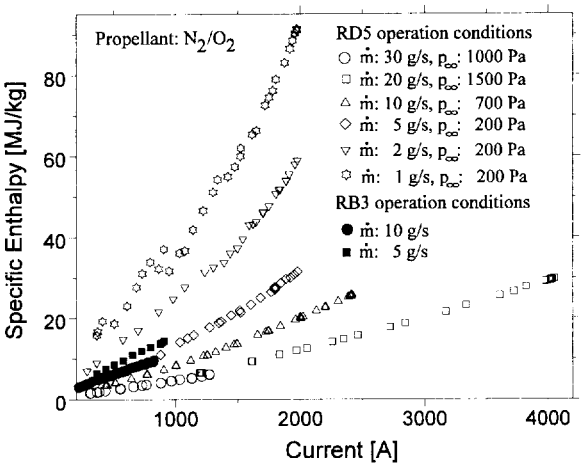


**Fig. 4.13: Specific enthalpy vs. current for the MPG RD5 and the TPG RB3**

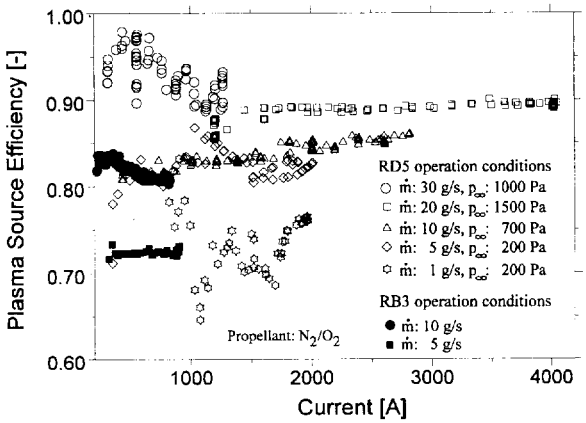


**Fig. 4.14: Plasma source efficiency of the MPG RD5 and the TPG RB3**

Compared to the TAG, the plasma source (or thermal) efficiency $\eta_{th}$ (see Eq. 4.2) of the MPG is high. It is almost independent of the current level and lies between 70 % and 90 % (see Fig. 4.14). This is

due to the low combustion chamber pressure in the RD generator, which is dependent on the electric power and the mass flow and lies between 2 and 40 kPa (Fig. 4.15). Radiation losses do not play a role at these pressure levels.

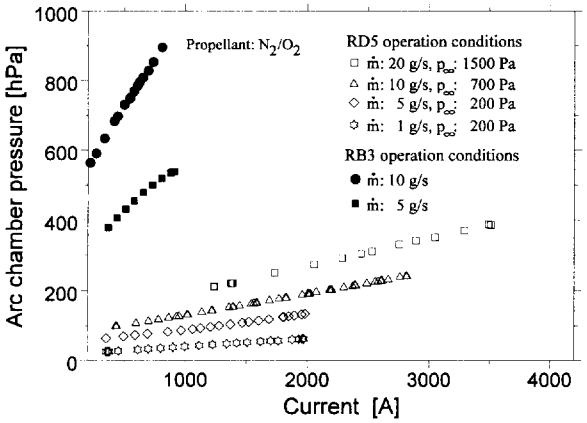


**Fig. 4.15: Arc chamber pressure vs. current for RD5 and RB3**

Since there are various possibilities for the gas supply for the RD-devices, these plasma sources are ideal for simulating the entry conditions into the atmospheres of other celestial bodies. In PWK 2, for example, the qualification tests were carried out for the heat shield of Huygens for the entry into the atmosphere of Saturn's moon Titan [7, 8] (Fig. 4.16). Currently, preparations are being made for a Mars mission. Both atmospheres contain carbonaceous gases.

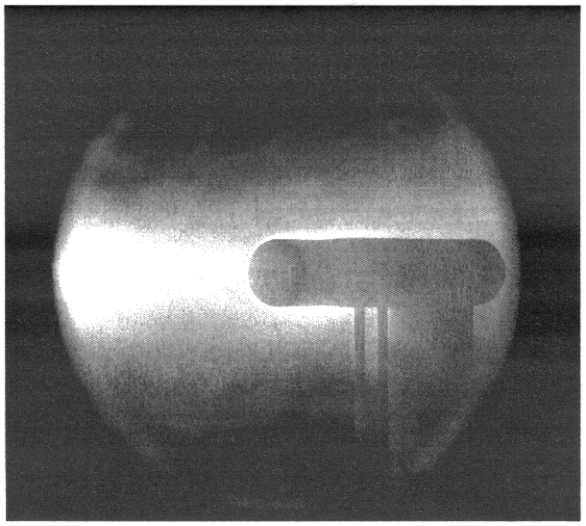

**Fig. 4.16: Material test for Huygens reentry**

The plasma source is also suitable for the systematic investigation of the influence of individual plasma components. Therefore, tests of kinetic effects and the influence of individual components on erosion can also be performed at the IRS. The plasma jet, created by an MPG, is neither in thermal nor in chemical equilibrium. Therefore, by investigating the plasma of different cross sections using experimental diagnostic methods, numerical non-equilibrium codes can be validated.

For further optimization of the MPGs and for the investigation of the local test conditions in MPG wind tunnels, a computational method is presently being developed [14]. This is based on numerical methods which have already been qualified for plasma thrusters [13].

## 4.3 The inductive plasma generator IPG

One basic aim of reentry material experiments is the investigation of the catalytic behavior. Due to the cathode erosion of the TAG and MPG generators, plasma pollution is present, which may lead to unwanted chemical reactions in front of the material probe. Therefore, an electrodeless, inductively heated plasma generator IPG, which enables the generation of metallic particle free plasma flows, has been developed at the IRS. The behavior of the probe and the plasma in front of it can be considered to be unadulterated. This means that it is possible to investigate the catalytic behavior of the TPS material and to make a comparison between the inductively heated plasma and the arc-heated plasma. The second advantage also results from the inductively coupled power input: Even rather reactive gases (oxygen, carbon dioxide) are applicable. Hence, atmospheres of celestial bodies like Mars or Venus can be simulated. The influence of the single gas components can be investigated e.g. with regard to the catalytic behavior of a material.

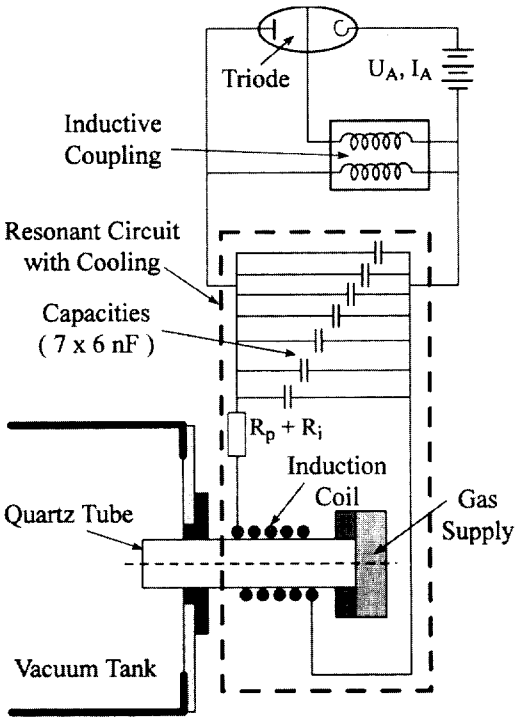


**Fig. 4.17: Scheme of the induction heated plasma generation**

An inductive plasma generator basically consists of an induction coil surrounding a quartz tube and

capacities, as schematically shown in Fig. 4.17. This resonant circuit is fed by an energy supply. The alternating current in the coil induces a mostly azimuthal electric field inside the quartz tube. This electric field initiates an electric discharge in the gas which is injected at one side into the tube (see Fig. 4.18). The produced plasma is expanded into the vacuum chamber. The electric discharge in the plasma is carried by mostly azimuthal currents. The current amplitude - and thus the Ohmic heating - strongly depends on the electric conductivity of the plasma and the resonant frequency of the electric circuit.

According to Lenz's law, the currents in the plasma produce a magnetic field to counteract the electromagnetic field of the induction coil. This gives rise to a limitation of the penetration depth of the external magnetic field. This so-called skin-depth $\delta$ depends on the electrical conductivity $\sigma$ and the frequency f [49, 50]:

$$\delta = \sqrt{\frac{2}{\mu_0 \sigma f}} \quad . \qquad (4.4)$$

The higher the electric conductivity of the plasma and the higher the resonant frequency, the lower the skin-depth, and thus, the penetration of the external electromagnetical field into the plasma.

The plasma generator IPG3 is shown in Fig. 4.18. The gas injection head enables different gas injection angles. The quartz tube contains the produced plasma, which leaves the generator through the water-cooled vacuum chamber adapter. The induction coil is connected to the external resonant circuit, which delivers power and high pressure cooling water. Furthermore, both the tube and the coil are surrounded by the external tube cooling, which protects the tube from overheating. The total length of IPG3 is about 0.35 m, its diameter about 0.08 m.

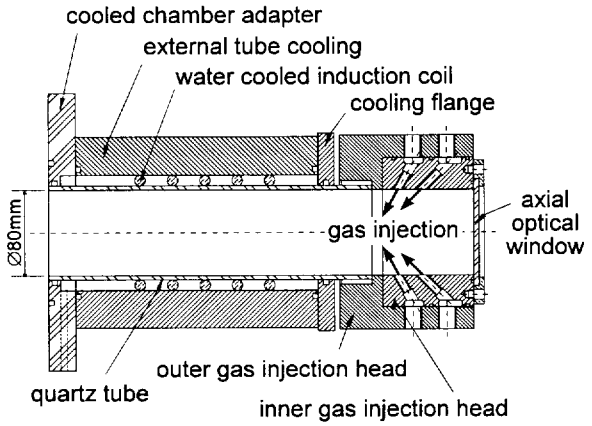


**Fig. 4.18: View of the plasma source IPG3**

As mentioned before, various gas injection angles are achievable by replacing the inner gas injection head with others which have different bore angles. Therefore, the influence of the injection angle on the operational behavior of IPG3 can be studied and optimized for certain applications. It is evident that the plasma is continuously swept away by an axially injected gas [49]. Using a tangential injection of the gas enables the plasma to be stabilized. Furthermore, lower pressure can be expected in the tube's center. So on the one hand the plasma recirculates, on the other hand it is kept away from the inner surface of the tube. Hence, a lower heat load of the tube can be achieved and higher power can be applied. An axial optical access through the inner injection head enables investigations of the plasma inside the generator. Figure 4.18 schematically shows the optical access and Fig. 4.19 the optical window of IPG3 while it is in operation with argon. The tube cooling system is transparent; therefore, the position of the "plasma flame" within the tube can be observed with regard to different operating parameters such as chamber pressure, gas, mass flow rate and anode power.

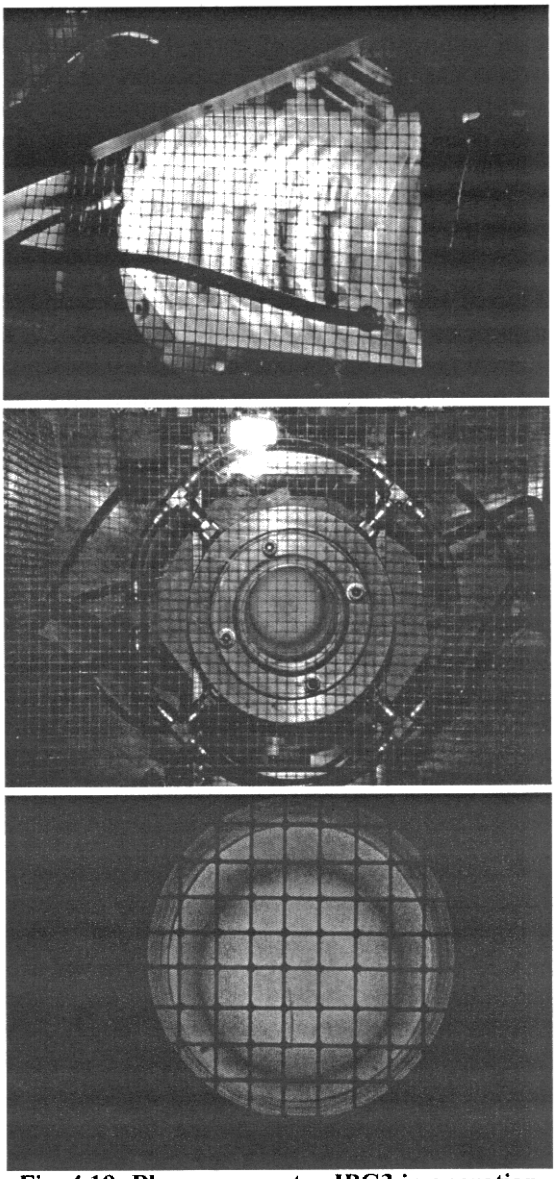

**Fig. 4.19: Plasmagenerator IPG3 in operation ( argon ); top: side view; middle and lower: axial optical window**

Additionally, this feature is supported by the axial optical window.

Figure 4.19 shows IPG3 and its tube cooling while operating with argon. The top picture in Fig. 4.19 is a side view of IPG3, the middle and lower pictures the axial optical access of IPG3.

As indicated in Fig. 4.17, the Meissner type resonant circuit is supplied by the DC anode power $P_a$, which is calculated from the measured anode voltage $U_a$ and the anode current $I_a$ during the operation of the device [24]. The anode voltage is controlled. Hence, the anode current results from the load of the resonant circuit (plasma) and the accompanying operating conditions.

The operational frequencies were measured using a Rogowski coil, which was wrapped around one of the inductor connections (see Fig. 3.4).

All measurements presented here were performed at an ambient pressure of about 100 Pa inside the vacuum chamber and with 7 capacitors switched in parallel (see Fig. 3.10). The measurements were made using air and argon with different anode powers. The gases were tangentially injected. Figure 4.20 shows the determined frequencies for argon and air versus the anode power $P_a$. The averaged value for the frequency in air operation is 510 kHz, the averaged value for argon is 528 kHz. The different frequencies can be most likely explained by the different field dampings due to the mutual inductions, which lead to a change of the inductivity. This again changes the operational frequency.

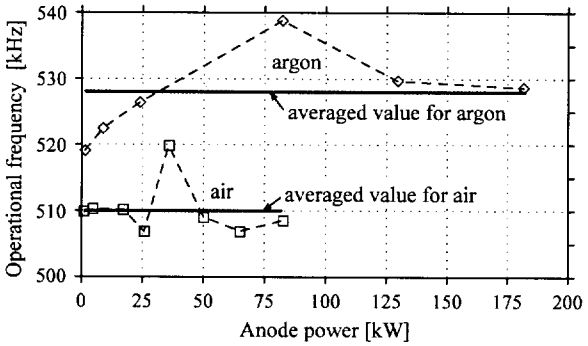


**Fig. 4.20: Operational frequencies (argon and air)**

A CID camera was used to investigate the discharge and to measure the radial intensity distribution of the plasma. The measurement was done through the axial optical window of IPG3. Its focus was about 0.05 m behind the closest coil winding; the camera's distance to the axial outlet was about 2.5 m. Therefore, the rf-protection cage meshes, as can be seen in Fig. 4.21, could be used as a geometric net enabling the introduction of the tube's diameter geometry. The camera has a spectral response in a wide wavelength range leading to an arbitrary intensity distribution; therefore, the data were normalized with respect to the measured maximum.

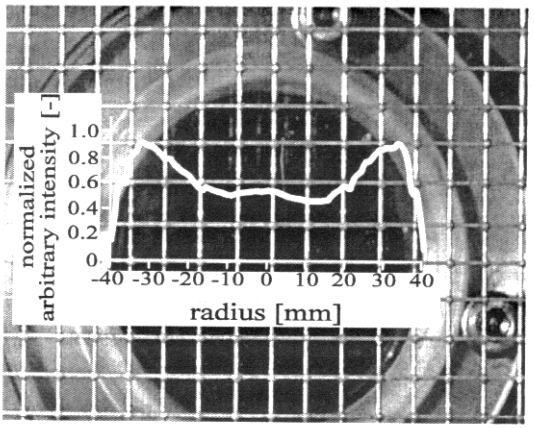


**Fig. 4.21: Arbitrary intensity history along the x-direction of the optical window of IPG3 (air)**

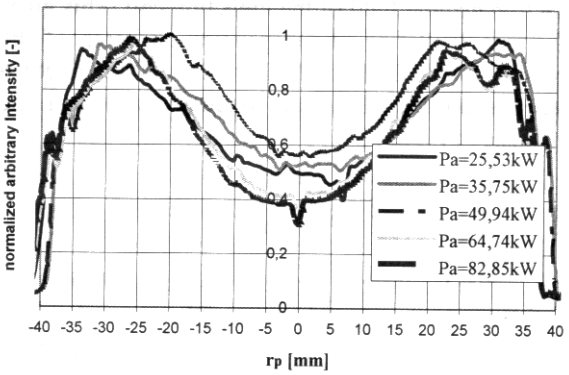


**Fig. 4.22: Normalized relative intensities of the discharge for different anode powers (air)**

Figure 4.22 shows the behavior of the arbitrary relative intensity curves of the discharge as a function of increasing power for air operation. Generally, the intensity of the discharge increases with the power. But the intensity "peaks" at the inner tube wall only slightly increase with increasing input power.

The anode power distribution can be written, for practical considerations, in the following form

$$P_A = f(U_A) + aU_A^2 \approx bU_A^c \quad . \qquad (4.5)$$

Here, $P_A$ is the anode power, $U_A$ is the measured anode voltage, the term $aU_A^2$ represents the real powers according to the Ohm's law, while $f(U_A)$ represents the remaining power losses such as the anode losses of the metal-ceramic triode. This leads to $P_A = bU_A^c$, with $c > 2$. This consideration is confirmed by the measured power lines (see Figs. 4.23 - 4.24), which are, in a first approximation, represented by polynomial functions depending on $U_A^c$. Hence, the anode powers in a double logarithmic scale appear approximately a straight lines.

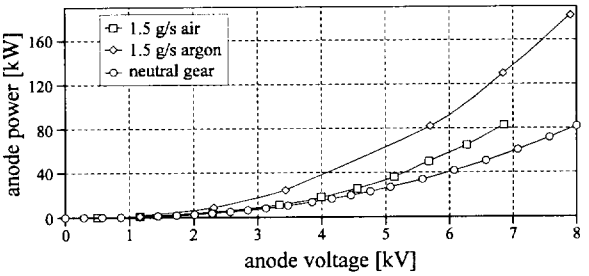


**Fig. 4.23: Anode power versus anode voltage for argon, air and "plasma-off" mode**

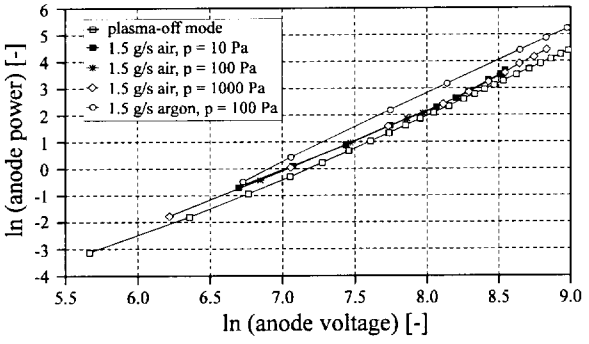


**Fig. 4.24: Anode powers in logarithmic scale**

## 4.4. Erosion of the Plasma Sources

When material tests are to be performed in a plasma wind tunnel, it is of the utmost importance that the plasma which is generated is free from impurities because they change the catalycity of the material and thus more than double the heat flux and significantly enlarge the erosion rate. Therefore, erosion on the electrodes or rather on the discharge vessel must be avoided or minimized.

Copper for example has a large catalytic effect, which means nitrogen and oxygen atoms are encouraged to form molecules on the surface releasing most of their combining energy at the surface. SiC on the other hand has a relatively small catalytic effect.

Erosion of the anode can be avoided in an MPG if the arc attachment is diffuse. In order to guarantee this with the, in some cases, relatively high pressures on the anode (to approx. 5 kPa), a small amount of argon is fed in tangentially to the anode (see Fig. 4.9). In a TAG spot formation at the anode cannot be avoided due to the high operating pressures (0.1 - 10 MPa). A destabilization of the anode attachment by means of a magnetic field and/or the turbulent movement of gas minimizes the erosion. In this way and with cooled copper anodes the erosion is minimal and a service life up to 100 hours can be achieved [46, 39].

In principle, erosion on the arc cathode is unavoidable. There are two possibilities for the arc's cathode attachment in the plasma generator: the focal spot with a cooled cathode and the diffuse attachment with primarily thermal electron emissions and a hot cathode (at cathode temperatures higher than 2000°C) [39]. In the case of the focal spot, the erosion rate of the cathode is up to three times higher than when it is operated in a hot state [39]. In both cases, the cathode erosion is almost proportional to the current intensity. Therefore, thermal arc sources are operated at a low current intensity.

Hot tungsten cathodes are in use for the small TAGs as at the IRS in order to run at the lowest possible erosion mode. The disadvantage in this case is that the gas has to be separated and only purified nitrogen may be in contact with the glowing cathode. Due to the high operation cost, this cannot be realized in large devices in the MW-level. Here undecomposed gases are used with cooled copper cathodes. The arc attachment in this case is not diffuse but rather it appears as a so-called focal spot with local melting [46]. The higher erosion, in this case copper, must be accepted.

MPGs must be operated with as high a current intensity as possible because the magnetic acceleration increases with the square of the current intensity [46]. Therefore, hot cathodes out of thoriated tungsten are always used with the MPG in order to nevertheless reach comparatively low erosion rates and good jet qualities. This is especially advantageous for material tests because tungsten oxidizes in air plasmas. Because tungsten oxide has a high vapor pressure, it doesn't settle on the hot material samples.

Figure 4.25 shows the contamination of the test gases from erosion products in various plasma wind tunnels [3]. The superiority of the PWKs equipped with MPGs is obvious. However, also the erosion rates for the RB plasma source at the IRS are rather low compared to the erosion rates of constricted and Huels-type arc generators. In addition, high productivity in the tunnel is a result of the low erosion rate because the life span of the electrodes is many hun-

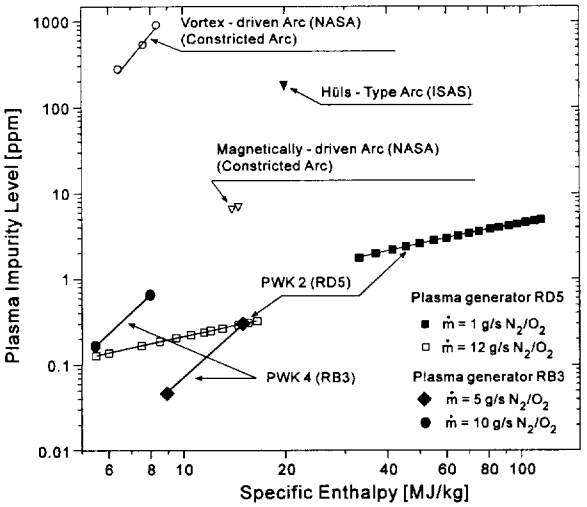


**Fig. 4.25: Diagram of the plasma impurity level in the MPG driven PWK [3], data partly from [51, 52]**

dreds of hours.

A disadvantage of the hot cathode is that oxygen must be kept away from it. Therefore, in the MPG purified nitrogen is fed in along the cathode while the oxygen is blown into the supersonic part of the nozzle. This part lies directly behind the narrowest cross section and consequently still within the arc. Cathode erosion tests with the MPG resulted in a significant decrease in the erosion rate down to the level of sublimation while avoiding remaining oxygen and dampness in the nitrogen [39].

In an IPG, which is operated without electrodes, indications of erosion can appear on the vessel or rather on the cooling elements which contaminate the plasma. In Russia such devices are operated with cooling inserts. Investigations of the plasma contamination are not available. At the IRS the TAG is operated without any cooling insert.

In addition to the importance of the absolute quantity of eroded material in the jet, one has to point out that different materials have different influences on the material tests. For example, copper particles ejected from arc spots are found to be partly deposited on the material probes, whereas no tungsten deposit eroded from MPG cathodes has ever been detected.

First results of a comparison of catalytic material behavior in a MPG and a TAG have shown no difference in the material behavior [3]. This indicates that the very small tungsten pollution has no influence.

## Acknowledgements

The authors would like to thank all colleagues who were involved in the set-up and operation of the plasma wind tunnel facilities at the IRS. Special thanks also to Mrs. Jennifer Baer-Engel for her help in writing this script.

## 5. References

[1] NASA Photo Gallery, Dryden Flight Research Center, 1997

[2] M. Auweter-Kurtz, H.L. Kurtz, S. Laure, "Plasma Generators for Re-entry Simulation", Journal of Propulsion and Power, Vol. 12, No. 6, pp. 1053 - 1061, Dec. 1996

[3] S. Laure, "Experimentelle Simulation der Staupunktsströmung wiedereintretender Raumflugkörper und deren Charakterisierung mittels mechanischer Sonden", Ph.D. Dissertation, Institut für Raumfahrtsysteme, Universität Stuttgart, Germany, May 1998

[4] M. Auweter-Kurtz, H. Habiger, S. Laure, E. Messerschmid, W. Röck and N. Tubanos, "The IRS Plasma Wind Tunnels for the Investigation of Thermal Protection Materials for Reentry Vehicles", Proceedings of the 1st European Symposium on Aerothermodynamics for Space Vehicles (Noordwijk, Netherlands), European Space Agency, SP-318, Paris, France, 1991, pp. 283 - 293

[5] M. Elsner, "Thermal Protection System - Comparison of Hermes Flight Environment and Test Facility Environment of the IRS Plasma Wind Tunnel", Messerschmidt-Bölkow-Blohm, TR H-NT-1B-0006-MBB, Munich, Germany, 1990

[6] S. Laure, M. Auweter-Kurtz, H. Kurtz, "Plasma Flows for Reentry Simulation", Proceedings of the 12th International Symposium on Plasma Chemistry, Vol. 3, Univ. of Minnesota, Minneapolis, MN, 1995, pp. 1749 - 1754

[7] W. Röck, M. Auweter-Kurtz, "Experimental Investigation of the Huygens Entry into the Titan Atmosphere within a Plasma Wind Tunnel", AIAA Paper 95-2112, July 1995

[8] W. Röck, "Simulation des Eintritts einer Sonde in die Atmosphäre des Saturnmondes Titan in einem Plasmawindkanal", Ph.D. Dissertation, Institut für Raumfahrtsysteme, Universität Stuttgart, Germany, Dec. 1998

[9] M. Auweter-Kurtz, H. Hald, G. Koppenwallner, H.-D. Speckmann, "German Reentry Experiments on EXPRESS", 45th Congress of the International Astronautical Federation, 94-1.3.192, Jerusalem, Israel, Oct. 1994; published in ACTA ASTRONAUTICA, Vol. 38, No. 1, pp. 47 - 61, 1996

[10] H. Habiger, M. Auweter-Kurtz, H. Früholz, G. Herdrich, "PYREX - Pyrometric Temperature Measurement on the Ceramic TPS of the Re-Entry Capsule MIRKA", Proceedings of the 3rd European Workshop on Thermal Protection Systems, WPP-141, pp. 353 - 361, ESTEC, Noodwijk, The Netherlands, März 1998

[11] G. Herdrich, M. Auweter-Kurtz, H. Habiger, M. Hartling, "Multi-Channel Temperature Measurements on Ceramic Heat Shields", IAF-97-I.5.06, 48th International Astronautical Congress, Turin, Italy, 6-10 October 1997

[12] G. Herdrich, M. Auweter-Kurtz, M. Hartling, T. Laux, "Present Design of the Pyrometric Sensor System PYREX-KAT38 for X-38", International Symposium on Atmospheric Reentry Vehicles and Systems, Arcachon, France, March 1999

[13] C. Sleziona, "Hochenthalpieströmungen für Raumfahrtanwendungen", Habilitation, Faculty

of Aerospace Technology, University Stuttgart, 1999

[14] C. Sleziona, M. Auweter-Kurtz, E.W. Messerschmid, "Evaluation of an Air Driven Plasma Wind Tunnel Source", AIAA 96-1854, 31st AIAA Thermophysics Conference, New Orleans, June 1996

[15] T. Grau, E. Messerschmid, "Numerical Investigation of a Partially Ionized Air Flow in a Plasma Wind Tunnel", AIAA 98-2955, 7th AIAA/ASME Joint Thermophysics and Heat Transfer Conference, Albuquerque, NM, USA, June 1998

[16] S. Lenzner, M. Auweter-Kurtz, J. Heiermann, C. Sleziona, "Energy Distribution in an Inductively Heated Plasma Wind Tunnel for Re-entry Simulations", AIAA-98-2947, 7th AIAA/ ASME Joint Thermophysics and Heat Transfer Conference, Albuquerque, NM, USA, June 1998

[17] Lukasiewicz, J., Whitfield, J.D., Jackson, R., "Aerodynamic Testing at Mach Numbers from 15 to 20", Proceedings of the ARS International Hypersonic Conference, Cambridge, Massachusetts, 1961

[18] Hornung, H., "High Enthalpy Wind Tunnel for the Simulation of Chemical Nonequilibrium Effects", HEG, DLR, Institut für Experimentelle Strömungsmechanik, Document Number IB222-86A43, 1986

[19] E. Messerschmid, S. Fasoulas, "Grundlagen der Raumfahrtsysteme", Vorlesung, Institut für Raumfahrtsysteme, Universität Stuttgart, 1998

[20] M. Auweter-Kurtz, G. Hilfer, H. Habiger, K. Yamawaki, T. Yoshinaka, H.-D. Speckmann, "Investigation of Oxidation Protected C/C Heat Shields in Different Plasma Wind Tunnels", IAF-96-1.3.06, 42nd International Astronau-tical Congress, Beijing, China, October 1996, accepted for publication in ACTA ASTRONAUTICA

[21] Y. Morino, T. Yoshinaka, M. Auweter-Kurtz, G. Hilfer, H.-D. Speckmann, A. Sakai, "Erosion Characteristics of SiC Coated C/C Materials in Arc Heated High Enthalpy Air Flow", IAF-97-I.4.02, 48th International Astronautical Congress, Turin, Italy, October 1997

[22] G. Hilfer, M. Auweter-Kurtz, "Experimental and Theoretical Investigation of the Oxidation Behavior of Thermal Protection Materials under Oxygen Attack", High Temperatures - High Pressures, 1995/1996, Vol. 27/28, pp. 435 - 448, also ESA/ESTEC 2nd Workshop on Thermal Protection Systems and 3rd European Workshop on High Temperature Materials, Stuttgart, October 1995

[23] G. Herdrich, M. Auweter-Kurtz, H. Kurtz, S. Lenzner, "A Test Facility with a Newly Developed Inductively Heated Plasma Generator for TPS Re-entry Simulations", Proceedings of the 3rd European Workshop on Thermal Protection Systems, WPP-141, pp. 109 - 115, ESTEC, Noodwijk, The Netherlands, März 1998

[24] G. Herdrich, M. Auweter-Kurtz, H. Kurtz, "A New Inductively Heated Plasma Source for Re-Entry Simulations", AIAA-98-3022, 20th AIAA Advance Measurement and Ground Testing Conference, Albuquerqu, NM, June 1998

[25] M. Fertig, A. Dohr, H.-H. Frühauf, "Transport Coefficients for High Temperature Non-equilibrium Air Flows", AIAA 98-2937, 7th AIAA/ASME Joint Thermophysics and Heat Transfer Conference, Albuquerque, NM, USA, June 1998

[26] M. Auweter-Kurtz, G. Bauer, K. Behringer, P. Dabalà, H. Habiger, K. Hirsch, H. Jentschke, H. Kurtz, S. Laure, T. Stöckle, G. Volk, "Plasma-diagnostics within the Plasma Wind Tunnel PWK", Zeitschrift für Flugwissenschaften und Weltraumforschung, Vol. 19, No. 3, pp. 166 - 179, June 1995

[27] M. Auweter-Kurtz, H. A. Habiger, Th. Wegmann, "Diagnostics of High Enthalpy Plasma Flows", AIAA 97-2495, 32nd Thermo-physics Conference, Atlanta, GA, USA, June 1997

[28] H. Hald, P. Winkelmann, "Post Mission Analysis of the Heat Shield Experiment CETEX for the EXPRESS Capsule", IAF-97-I.4.01, 48th International Astronautical Con-gress, Turin, Italy, October 1997

[29] J. Burkhardt, U. Schöttle, E. Messerschmid, "Mission and System Design Aspects of a Semi-Ballistic Reentry Experiment Vehicle", 48th International Astronautical Congress, Turin, Italy, October 1997

[30] M. Auweter-Kurtz, "Cassini-Huygens-Mission - Qualifikation des Hitzeschutzes für den Eintritt in die Atmosphäre des Titan", Revue Technique, Vol. 3, pp. 145 - 153, Luxemburg, March 1993

[31] M. Auweter-Kurtz, S. Laure, W. Röck, "Experimental Planet Entry Simulation within a Plasma Wind Tunnel", ESA SP-367, Proc. of the 2nd European Symposium on Aerothermo-dynamics for Space Vehicles, ESTEC, Noordwijk, The Netherlands, November 1994

[32] G. Francois, J.P. Ledy, A. Masson, "ONERA High Enthalpy Wind Tunnel F4", 82th Meeting of the Supersonic Tunnel Association, October 1994

[33] Finklenburg, W., Peter, T., "Kontinuierliche Spektren", Handbuch der Physik, Bd. XXVII, S. 100, Springer, Berlin, 1957

[34] F. Vilbig "Lehrbuch der Hochfrequenztechnik", Vol. 2, Akademische Verlagsges.m.b.H., Frankfurt am Main, 1958

[35] "Technical Specification of the rf-capacitors and the Triode RS 3300 CJ of the PWK3-IPG energy supply", Fritz Düsseldorf Ges. m. b. H., 1997

[36] W. Winovich, W.C.A. Carlson, "The 60 MW Shuttle Inetraction Heating Facility", Proceedings of the 25th International Instrumentation Symposium (Anaheim, CA), ISBN 97664-434-5, 1979

[37] M. Fiebig, K. Kindler, D.G. Papanikas, "Hochleistungsbrenner und Expansionsdüsen zur Untersuchung von Hochenthalpieströmungen", DLR-Mitteilung 75-06, 1975

[38] "Plasma Arc Heater", Firmenbroschüre, Aerospatiale, Les Mureaux, Frankreich, 1987

[39] M. Auweter-Kurtz, B. Glocker, H. L. Kurtz, O. Loesener, H. O. Schrade, N. Tubanos, Th. Wegmann, D. Willer, J. E. Polk, "Cathode Phenomena in Plasma Thrusters", Journal of Propulsion and Power, Vol. 9, No. 6, pp. 882 - 888, 1993

[40] R.B. Pope, "Measurement of Enthalpy in Low_density Arc-Heated Flows", AIAA Journal, Vol. 6, No. 1, pp. 103 - 109, 1968

[41] M. Auweter-Kurtz, H. Wilhelmi, D. Wagels, T. Laux, "Untersuchung der Stabilität von pulvermetallurgisch hergestellten, gradierten Thermalschutzkacheln, bei thermomecha-nischer Belastung von hochenergetischen Strömungen im Hochenthalpie-Windkanal", IRS-97-Ib-19, 1997

[42] H. Wilhelmi, D. Wagels, "Untersuchung der Stabilität von pulvermetallurgisch hergestellten, gradierten Thermalschutzkacheln, bei thermomechanischer Belastung von hochenergetischen Strömungen im Hochenthalpie-Windkanal", Zwischenbericht Wi 491/34-1, Institut für Industrieofenbau und Wärmetechnik, RWTH Aachen, 1996

[43] M. Auweter-Kurtz, F. Hammer, G. Herdrich, H. Kurtz, T. Laux, E. Schreiber, Th. Wegmann, "The Ground Test Facilities for TPS at the Institut für Raumfahrtsysteme", 3rd European Symposium on Aerothermodynamics for Space Vehicles, ESTEC, Noordwijk, NL, November 1998

[44] E. R. Pugh, R. M. Patrick, A. M. Schneiderman, "High-Pressure, High-Enthalpy Test Facility", AIAA Journal, Vol. 9, No. 2, 1971

[45] H. Hügel, "Arc-Heater for High-Enthalpy Plasma Flows", Third International Conference on Gas Discharges, London, 1974

[46] M. Auweter-Kurtz, "Lichtbogenantriebe für Weltraumaufgaben", B.G. Teubner Verlag, ISBN 3-519-06139-2, 1992

[47] N. Anifimov, "TSNIIMASH Capabilities for Aerogasdynamical and Thermal Testing of Hypersonic Vehicles", AIAA 92-3962, 17th Ground Testing Conf., Nashville, July 1992

[48] M. Auweter-Kurtz, H. Habiger, G. Herdrich, G. Hilfer, H. Kurtz, S. Laure, E. Schreiber, Th. Wegmann, "The Magnetoplasmadynamic Generator RD7 - A new plasma source for large structure testing", Proceedings of the 3rd European Workshop on Thermal Protection Systems, WPP-141, pp. 101 - 108, ESTEC, Noodwijk, The Netherlands, März 1998

[49] J. Mostaghimi, M. I. Boulos, "Two-Dimensional Electreomagnetic Field Effects in Induction Plasma Modelling", Plasma Chemistry and Plasma Processing, Vol. 9, No. 1, pp. 25 - 44, 1989

[50] M. P. Freeman, J. D. Chase, "Energy-Transfer Mechanism and Typical Operating Characteristics for the Thermal rf Plasma Generator", Journal of Applied Physics, Vol. 39, No. 1, p. 180, Jan. 1968

[51] M. Hinada, Y. Inatani, T. Yamada, K. Hiraki, "Performance Characteristics of the ISAS Huels-type Arc Heater", ISTS 94-d-37, 19th International Symposium on Space Technologie and Science, Yokohama, Japan, May 1994

[52] T.J. Stahl, W. Winovich, G. Russo, S. Caristia, "Design and Performance Characteristics of the CIRA Plasma Wind Tunnel", AIAA-91-2272, AIAA/SAE/ASME/ASEE 27th Joint Propulsion Conference, Sacramento, CA, 1991

# Diagnostic Tools for Plasma Wind Tunnels and Reentry Vehicles at the IRS

Monika Auweter-Kurtz, Markus Feigl, Michael Winter
Universität Stuttgart
Institut für Raumfahrtsysteme
Pfaffenwaldring 31
70550 Stuttgart
Germany

## Introduction

Various plasma wind tunnels have been built for developing reusable space transportation systems and space probes entering the atmospheres of celestial bodies. All together they cover almost the whole reentry trajectory of a space craft [I.1]. They generate continuous plasma flows of high specific enthalpy and velocity with thermal or magnetoplasmadynamic generators. Plasma wind tunnels are used for:

- development and qualification of radiation and ablative cooling materials and thermal protection systems,
- validation of numerical codes for reentry prediction and
- development and qualification of reentry measurement devices.

The accuracy of the simulation of reentry conditions strongly depends on the ability to determine the flow conditions. These three lectures give an overview of the diagnostic methods which are qualified and in use at the IRS. Both intrusive probe measurement techniques (part A) including mass spectrometry and non-intrusive, optical techniques (part B) such as emission spectroscopy and laser induced fluorescence (LIF) are used to investigate high enthalpy plasma flows. Several measurement techniques are being developed for flight application (see part C).

The minimum set of parameters which have to be duplicated during the tests for material qualification (see Fig. I.1) are the specific enthalpy of the gas, the stagnation pressure and the surface temperature in the case of a radiation cooling material, or the heat flux for an ablative material. This is a minimum set of parameters which has to be adjusted during the test. A whole series of probes and non-intrusive techniques were developed to determine these parameters.

The average specific enthalpy of the flow in the exit plane of the plasma generator nozzle can be derived for all kinds of plasma wind tunnels by an energy balance. Therefore, the electric power consumed by the plasma source, the mass flow rate and the heat losses within the plasma generator are measured. The average specific enthalpy at the end of the plasma generator is then derived as the difference of the electrical power and the total heat loss related to the mass flow rate. This result is very important for an initial estimation of the flow situation and even more so for the assessment of the plasma source condition and reproducibility of a test series. But without knowing the enthalpy distribution in the nozzle exit and due to the interaction between the free jet and the ambient gas in the wind tunnel, specific enthalpy near the material sample position can not be derived exclusively from this result. Direct enthalpy measurements with probes are necessary here or a calculation of the local enthalpy from the local pressure and heat flux profiles.

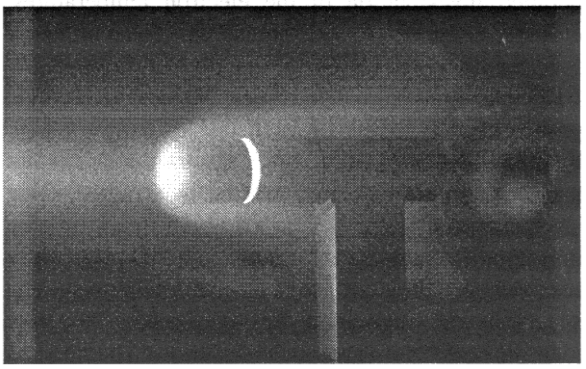

**Fig. I.1: TPS material sample in the beam**

However, the catalycity of the TPS materials strongly effects the surface temperature and the development of materials with the lowest possible catalycity is of great importance for future space vehicles. Plasma wind tunnels can be used to investigate the energy accommodation due to catalytic recombination near the surfaces of TPS materials. However, this requires detailed knowledge of the flow conditions within the shock layer. The measurement of the quantities of interest (temperatures, densities and velocities) is very difficult. The most significant problems are the high enthalpy and the chemically aggressive plasma, which limits probe measurements, and the fact that the flow is not in chemical and, in many instances, not in thermal equilibrium, which complicates the interpretation of measurement results. The non-equilibrium effects are more significant with lower pressure. With special probes, equipped with materials of various catalycities, the energy accommodation due to catalytic recombinations on the surface of the materials is being investigated [A2, A3, A4, A5]. LIF and emission spectroscopy are used

*Paper presented at the RTO AVT Course on "Measurement Techniques for High Enthalpy and Plasma Flows", held in Rhode-Saint-Genèse, Belgium, 25-29 October 1999, and published in RTO EN-8.*

to determine atomic and molecular density and velocity distribution in the boundary layer [I.6]. Very important information was obtained from boundary layer investigations by emission spectroscopy in front of water-cooled copper and hot, radiating material probes [I.7, I.8, I.9].

Important information about the erosive behavior, catalycity and the failure of surface protection layers has been obtained using a mass spectrometer positioned directly behind the material sample within the plasma wind tunnel [I.10, I.8]. The transition from active to passive oxidation of materials containing Si has been investigated by LIF [I.6]. Surface temperature measurement is of great importance for material qualification, therefore, several pyrometers, including LCD systems, are available at the IRS.

For code validation the high enthalpy plasma jet has to be completely characterized at no less than two cross sections (see Fig. I.2). For this purpose a lot of measurement techniques are in use and being developed at the IRS. These are, for example, miniaturized mechanical probes for pressure and heat flux measurements [I.4]. Cylindrical electrostatic probes working in the collisionless regime are used for the detailed investigation of the electron temperatures, electron densities, plasma potentials, electron energy functions and velocities of the plasma flows [I.11, I.12]. At very high enthalpies where electrostatic probes can no longer be used due to the very high thermal and chemical load, the electron densities are high enough so that they can be determined using Thomson scattering [I.13]. Emission spectroscopic investigations are performed for the spectrally resolved analysis of the plasma radiation. The spectroscopic measurements also allow for the identification of various plasma parameters (temperatures and densities) in regions where intrusive probe measurements are impossible [I.14]. A Fabry-Perot Interferometer is used as a high resolution spectrometer to determine the plasma velocity from Doppler measurements. From the broadening of specific emission lines the translational and kinetic temperatures of the heavy particles in the plasma flow can be determined [I.12, I.15]. LIF will be used as for the boundary layer to determine the atomic densities of oxygen and nitrogen, NO-density distribution and velocity distribution [I.6]. For very low densities a mass spectrometer as a probe positioned in the plasma flow allows the plasma composition and the distribution of ions, molecules and neutral components to be determined [I.16]. The comparison of the experimental results with numerical calculations and flow simulations, which are also conducted at the IRS, are very important for both the diagnostic and code development of high enthalpy flows [I.17].

For planetary entry missions the radiative heat flux plays a major role due to very high entry velocities or carbonaceous atmospheres. Therefore, a probe was developed at the IRS for overall radiation measurements [I.18, I.19].

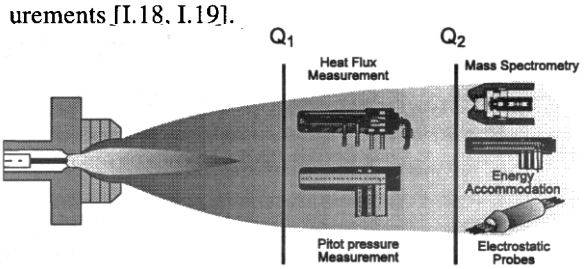


**Fig. I.2: Experimental set-up for numerical code validation**

Some diagnostic techniques which are in use in the PWKs can be further developed and qualified for flight applications on ballistic or winged reentry vehicles. A miniaturized pyrometric sensor system called PYREX [I.20, I.21] was developed and flight qualified for TPS temperature measurements. Furthermore, a catalytic sensor experiment is being developed [I.22]. An emission spectroscopic experiment is currently being prepared in conjunction with DASA [I.9]. Based on our experience with electrostatic probes in the wind tunnel environment, an electrostatic probe for space applications is being developed.

## References

[I.1] Auweter-Kurtz, M., Frühauf, H., Messer-schmid, E,. Schöttle, U., Sleziona, C., "Wieder-eintrittsprobleme von Raumflugsystemen", IRS-95-M-1, Institut für Raumfahrtsysteme der Universität Stuttgart, 1995.

[I.2] Stöckle, T., Winter, M., Auweter-Kurtz, M., "Simultaneous Spectroscopic and Mass Spectroscopic Investigation of Surface Catalytic Effects in High Enthalpy Gas Flows", AIAA-98-2845, 7th AIAA/ASME Joint Thermophysics and Heat Transfer Conference, Albuquerque, NM, 1998.

[I.3] Stöckle, T., Auweter-Kurtz, M., Laure, S., "Material Catalysis in High Enthalpy Air Flows", AIAA-96-1904, 31st AIAA Thermophysics Conference, New Orleans, LA, 1996.

[I.4] Laure, S., "Aufbau und Qualifikation von Versuchseinrichtungen zur Erzeugung von Hochenthalpie-Luftströmungen und deren Charakterisierung mittels mechanischer Sonden", Dissertation, Universität Stuttgart, 1998.

[I.5] Fasoulas, S., Stöckle, T., Auweter-Kurtz, M., "Measurement of Specific Enthalpy in Plasma Wind Tunnels Using a Mass Injection Probe", AIAA-97-2496, 32nd Thermophysics Conference, Atlanta, GA, June 1997.

[I.6] Auweter-Kurtz, M., Dabalà, P., Feigl, M., Habiger, H., Kurtz, H., Stöckle, T., Wegmann, T., Winter, M., "Diagnostik mit Sonden und optischen Verfahren", Teilprojekt A3, Sonderforschungsbereich 259 Arbeits- und Ergebnissbericht 1998, pp. 65-90.

[I.7] Winter, M., Auweter-Kurtz, M., Kurtz, H., Park, C., "Investigation of an Equilibrium Condition Boundary Layer in Front of a Material Probe in a Subsonic Plasma Flow", AIAA-96-1853, 31st Thermophysics Conference, New Orleans, LA, 1996.

[I.8] Dabalà, P., "Untersuchung des Erosionsverhaltens von Hitzeschutzmaterialien für Wiedereintrittsflugkörper unter Einsatz eines Massenspektrometers", Dissertation, Universität Stuttgart, 1998.

[I.9] Winter, M., Auweter-Kurtz, M., "Emission Spectroscopic Investigation of the Boundary Layer in Front of a Blunt Body in a Subsonic Air Plasma Flow", Proceedings of the 3rd European Symposium on Aerothermodynamics for Space Vehicles, ESTEC, Noordwijk, The Netherlands, 1998.

[I.10] Dabalà, P., Auweter-Kurtz, M., "Mass Spectrometric Erosion Measurements of Ceramic Thermal Protection Materials in High Enthalpy Plasma", AIAA-97-2590, 32nd Thermophysics Conference, Atlanta, GA, 1997.

[I.11] Habiger, H., Auweter-Kurtz, M., "Investigation of High-Enthalpy Air Plasma Flow with Electrostatic Probes", Journal of Thermophysics and Heat Transfer, Vol. 12, No. 2, April-June 1998, S. 198-205; also AIAA-96-1864, 31st AIAA Thermophysics Conference, New Orleans, LA, June 1996.

[I.12] Habiger, H., "Elektrostatische Sonden und Fabry-Perot Interferometrie zur Untersuchung von lichtbogenbeheizten Plasmen für Triebwerksanwendungen und Wiedereintritts-simulation", Dissertation, Universität Stuttgart, 1994.

[I.13] Schumacher, U., Hirsch, K., "Spektroskopie und Laser-diagnostik", Teilprojekt A2, Sonderforschungsbereich 259 Arbeits- und Ergebnissbericht 1998, pp. 39-63.

[I.14] Röck, W., Auweter-Kurtz, M., "Spectral Measurements in the Boundary Layer of Probes in Nitrogen/Methane Plasma Flows", AIAA-97-2525, 32nd Thermophysics Conference, Atlanta, GA, 1997.

[I.15] Habiger, H., Auweter-Kurtz, M., "Fabry-Perot Interferometry for the Investigation of a High Enthalpy Plasma Flow", AIAA-95-2040, 30th Thermophysics Conference, San Diego, CA, 1995.

[I.16] Schönemann, A., Auweter-Kurtz, M., "Mass Spectrometric Investigation of High Enthalpy Plasma Flows", Journal of Thermophysics and Heat Transfer, Vol. 9, No. 4, Oct.-Dec. 1995, pp. 620-628.

[I.17] Fay, J.A., Riddell, F.R., "Theory of Stagnation Point Heat Transfer in Dissociated Air", Journal of Aeronautical Sciences, Vol. 25, No. 2, February 1958.

[I.18] Röck, W., Auweter-Kurtz, M., "Experimental Investigation of the Huygens Entry into the Titan Atmosphere within a Plasma Wind Tunnel", AIAA-95-2112, 30th Thermophysics Conference, San Diego, CA, 1995.

[I.19] Röck, W., "Simulation des Eintritts einer Sonde in die Atmosphäre des Saturnmondes Titan in einem Plasma-windkanal", Dissertation, Universität Stuttgart, 1998.

[I.20] Auweter-Kurtz, M., Hald, H., Koppenwallner, G., Speckmann, H.-D., "German Experiments Developed for Reentry Missions". Acta Astronautica, Vol. 38, No. 1, 1996, pp. 47-61.

[I.21] Habiger, H., Auweter-Kurtz, M., Früholz, H., Herdrich, G., "PYREX - Pyrometric Measurement on the Ceramic TPS of the Reentry Capsule MIRKA", Proceedings of the 3rd European Workshop on Thermal Protection Systems, ESTEC, Noordwijk, The Netherlands, March 1998, pp. 353-362.

[I.22] Stewart, D.A, Rakich, J.V., Lanfranco, M.J., "Catalytic Surface Effects Experiment on the Space Shuttle", AIAA-81-1143, AIAA 16th Thermophysics Conference; also Progress in Aeronautics and Astronautics, Vol. 82: Thermophysics of Atmospheric Entry, pp. 249-272.

# A Intrusive Measurement Techniques

Besides the so-called mechanical probes, the mass spectrometry, electrostatic and radiation probes also belong to the group of intrusive measurement techniques. As the name already suggests, this diagnostic method is based on a suitably constructed probe being mounted in the plasma stream which is to be investigated. This differs from the optical measurement techniques which will be described in the second part of this lecture. The mechanical probes are among the most important instruments for plasma-diagnostic measurements and are therefore also often used. They can essentially be divided into five groups according to the parameters to be investigated. We differentiate between:

- material sample support,
- Pitot pressure probes,
- aerodynamic wedge probes,
- heat flux probes,
- enthalpy probes and
- solid-state electrolyte probes.

All of these probes can be installed at the IRS on four-axis platforms inside the plasma wind tunnels. Three of the axes are linearly oriented, notated as x, y and z; the fourth axis provides the possibility to rotate the probes around the z-axis.

The wedge probe is used to ascertain the static pressure and the Mach number of the supersonic flow. A solid-state electrolyte probe can determine the oxygen particle pressure in a stream. With a mass spectrometer probe, particle densities and the energy distribution of the particles can be investigated. In the case of the other four probes, they each measure what their name implies.

With the exception of the Mach number and the oxygen partial pressure measurements, all of the measuring techniques with mechanical probes are ultimately based on the measurements of pressure, flux and/or temperature, whereby the attempt must be made to ascertain these parameters with the highest possible exactness. In practice, these supposedly simple measurements are very difficult [A.1]. A more or less complex theory is hidden between determining the basic parameters and ascertaining the parameters which are actually of interest, especially in the case of enthalpy and heat flux.

Besides the enthalpy probes, all mechanical probes have one common denominator - they do not actively influence the plasma, but rather quasi passively register the effects of the plasma flow in an appropriate way. This information is then used to determine the important parameters.

Electrostatic probes are used to ascertain the plasma potential, electron density and temperature, energy distribution of the electrons, ion temperature, flow

velocity and direction. The measurement principle is based on an active influence on the plasma boundary layer which forms on the probe.

A mass spectrometer probe can be used with low pressure plasmas to investigate the composition of the plasma [A.2, A.3]. Due to catalytic effects and the large pressure reduction which is necessary, the possibility of this at pressures above 1 hPa is limited and it is only possible with a two-step system. However, a mass spectrometer probe can be used advantageously for on-line investigations of erosion behavior [A.4, A.5] and the catalytic behavior [A.6, A.7] of thermal protection materials.

The use of radiometric probes is unavoidable when the radiation heat flux can not be neglected compared to the convective part. This is the case when during sample return missions the entry speed into the Earth's atmosphere is especially high or when the atmosphere of another celestial body (which is to be entered) contains strong radiating species, as for example the atmosphere of Titan [A.8, A.9].

The outward appearance of a probe not only depends on the parameter to be measured, but rather also on whether for example the free jet conditions should be measured or whether the plasma composition on the surface of the material sample being investigated is important. In the last case, the outward appearance of all the probes is adapted to the form of the material probe.

## References


[A.1] Auweter-Kurtz, M., "Meßverfahren für strömende Plasmen", IRS-94-M1, Institut für Raumfahrtsysteme der Universität Stuttgart, 1994.

[A.2] Schönemann, A., Auweter-Kurtz, M., "Mass Spectrometric Investigation of High Enthalpy Plasma Flows", Journal of Thermophysics and Heat Transfer, Vol. 9, No. 4, Oct.-Dec. 1995, pp. 620-628.

[A.3] Schönemann, A., "Massenspektrometrie zur Untersuchung lichtbogenbeheizter Plasmen in Niederdruck-Plasmawindkanal", Dissertation, Universität Stuttgart, 1994.

[A.4] Dabalà, P., "Untersuchung des Erosionsverhaltens von Hitzeschutzmaterialien für Wiedereintrittsflugkörper unter Einsatz eines Massenspektrometers", Dissertation, Universität Stuttgart, 1998.

[A.5] Dabalà P., Auweter-Kurtz, M., "Mass Spectrometric Investigations of Erosion Behavior of Thermal Protection Materials", ESA 2nd European Workshop on Thermal Protection Systems, Stuttgart, Germany, October 1995.

[A.6] Stöckle, T., Winter, M., Auweter-Kurtz, M., "Simultaneous Spectroscopic and Mass Spectroscopic Investigation of Surface Catalytic Effects in High Enthalpy Gas Flows", AIAA-98-2845, 7th AIAA/ASME Joint Thermophysics and Heat Transfer Conference, Albuquerque, NM, 1998.

[A.7] Stöckle, T., Auweter-Kurtz, M., Laure, S., "Material Catalysis in High Enthalpy Air Flows", AIAA-96-1904, 31st AIAA Thermophysics Conference, New Orleans, LA, 1996.

[A.8] Röck, W., "Simulation des Eintritts einer Sonde in die Atmosphäre des Saturnmondes Titan in einem Plasmawindkanal", Dissertation, Universität Stuttgart, 1998.

[A.9] Auweter-Kurtz, M., Laure, S., Röck, W., "Experimental Planetary Entry Simulation within a Plasma Wind Tunnel", Proceedings of the 2nd European Symposium on Aerothermodynamics for Space Vehicle, ESTEC, Noordwijk, The Netherlands, November 1994, pp. 429-436.


# A1 Material Sample Support

Ablative materials are supported by water-cooled support systems of different sizes. An example is shown in Fig. A1.1.

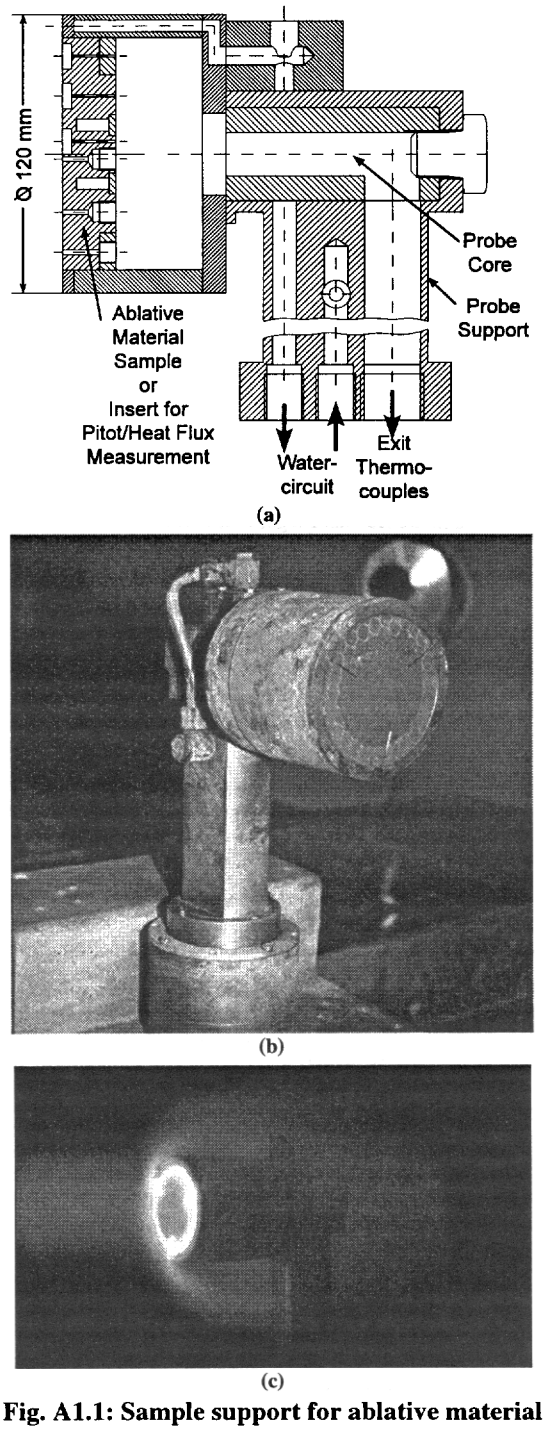


**Fig. A1.1: Sample support for ablative material**

The temperature distribution within the ablator is usually measured by thermocouples located at different distances from the front surface of the ablator.
A material sample support system which minimizes the heat exchange with the sample perpendicular to the flow is required for material qualification. In Fig. A1.2 the sample support for ceramic material in a stagnation point configuration is shown. The rear side temperature of the sample can be determined with a linear pyrometer (see also part B) via a fiber optic connection.

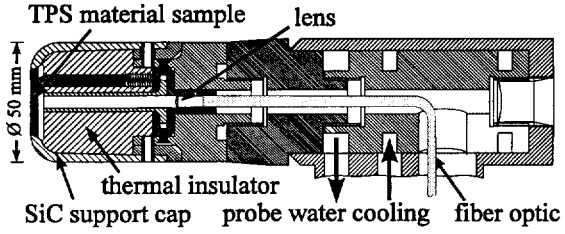


**Fig. A1.2: Scheme of a TPS material probe with integrated pyrometer fiber optics**

# A2 Pitot Pressure Probes

With Pitot probes it is possible to measure the dynamic or total stagnation pressure of the plasma flow by connecting them either to a differential pressure gauge inside or to a total pressure gauge outside of the vacuum tank.
Figure A2.1 shows the scheme of the 'spherical head' Pitot probe which has an identical geometry to the material support system shown in Fig. A1.2.

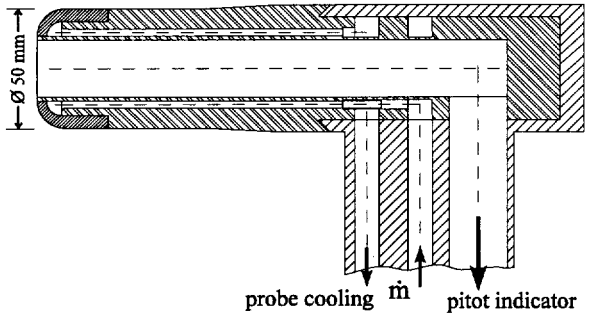


**Fig. A2.1: 'Spherical head' Pitot probe**

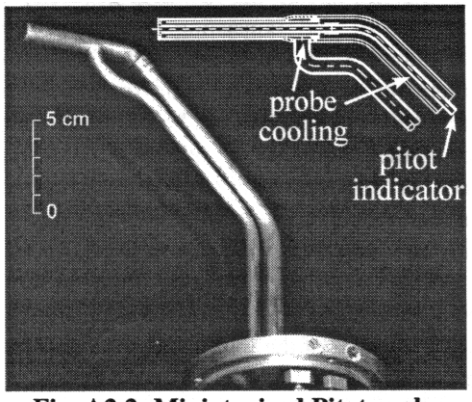


**Fig. A2.2: Miniaturized Pitot probe**

In Fig. A2.2 a miniaturized Pitot probe which is used for local measurements in the plasma flow can be seen. This probe is designed to determine very high heat fluxes of more than 10 MW/m$^2$ [A2.1].
When using Pitot probes, one must generally differentiate between two cases: pressure measurement in a subsonic flow and pressure measurement in a supersonic flow. In the first case, the conditions are relatively simple. The Bernoulli equation is valid whereby the simple equation

$$p_0 = p_\infty + \frac{\rho_\infty}{2} v_\infty^2 \qquad \text{(A2.1)}$$

at Mach numbers of $Ma > 0.3$ must be replaced by the Bernoulli equation for compressible flows. If friction effects are neglected and assuming that the changes in the condition run lengthwise isentropically along the lines, the following connection exists between the flow parameters:

$$p_0 = p_\infty \left( 1 + \frac{\kappa - 1}{\kappa} \frac{\rho_\infty}{p_\infty} \frac{v_\infty^2}{2} \right)^{\frac{\kappa}{\kappa - 1}} , \qquad \text{(A2.2)}$$

whereby $\kappa$ means the averaged adiabatic exponent, $p_0$ represents the pressure in the stagnation point and $p_\infty, \rho_\infty, v_\infty$ the quantities of the undisturbed flow. With that one can, for example, deduce the density from the pressure measurement when the speed and $\kappa$ are known.

In supersonic flows a compression shock forms in front of the probe which results in a loss of total pressure. The probe measures the total pressure $p_0$ after the shock. Assuming that the compression shock runs perpendicular to the initial direction of flow and the changes in the condition run isentropically in front of and behind the shock, then the following is valid for $p_0$:

$$p_0 = \frac{\kappa - 1}{2} Ma^2 \left[ \frac{(\kappa + 1)^2 Ma^2}{4\kappa Ma^2 - 2(\kappa - 1)} \right]^{\frac{1}{\kappa - 1}} p_\infty \ . \qquad \text{(A2.3)}$$

Here Ma is the Mach number in front of the shock and $\kappa$, on the other hand, is the averaged adiabatic exponent. If the Mach number is additionally determined with a wedge probe (see section A3) then the average adiabatic exponent can be calculated from this last equation.
However, one must be very careful when interpreting the measurement results from a Pitot probe. The viscosity effects of a flow affected by friction have to be considered. Two additional aspects must also be taken into account. These are the effect of the shape of the bore hole and the error which results when the longitudinal axis of the probe and the plasma stream axis are not aligned [see A2.2]. The size of the bore hole has to be large compared to the mean free path.

## References


[A2.1] Laure, S., "Aufbau und Qualifikation von Versuchseinrichtungen zur Erzeugung von Hochenthalpie-Luftströmungen und deren Charakterisierung mittels mechanischer Sonden", Dissertation, Universität Stuttgart, 1998.

[A2.2] Habiger, H., "Elektrostatische Sonden und Fabry-Perot Interferometrie zur Untersuchung von lichtbogenbeheizten Plasmen für Triebwerksanwendungen und Wiedereintritts-simulation", Dissertation, Universität Stuttgart, 1994.


# A 3 Aerodynamic Wedge Probe

Aerodynamic wedge probes can be used to ascertain the static pressure and Mach number of a supersonic flow. Their main component is a water-cooled copper wedge (see Fig. A3.1) which is placed in a supersonic flow, whereby attention must be paid to the parallel alignment of the probe surface to $\vec{v}_\infty$. With the help of a pressure measurement bore hole on the top side of the probe the static pressure can also be determined.

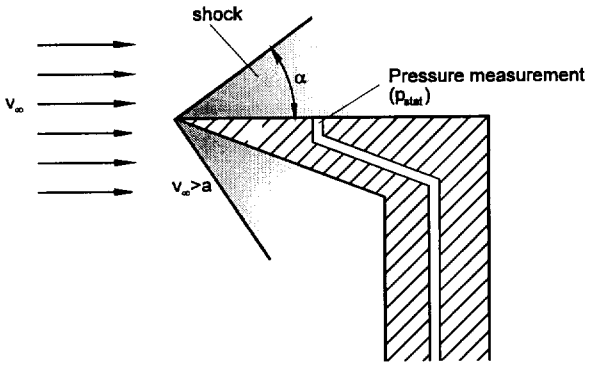


**Fig. A3.1: Wedge probe in a supersonic stream**

The tip of the wedge probe causes a disturbance in the flow which spreads analogously to the sound wave in the supersonic flow shown in Fig. A3.2. The effects of the disturbances are limited to the inside of a cone whose half open angle $\alpha$, recognizable in Fig. A3.2, can be calculated as follows:

$$\sin\alpha = \frac{at}{vt} = \frac{a}{v} = \frac{1}{Ma} \quad . \qquad (A3.1)$$

This cone is called a Mach cone.

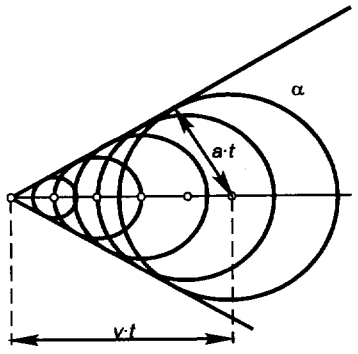


**Fig. A3.2: Spreading of supersonic sound waves**

From the measurement of the angle between the Mach line and the plasma stream axis the Mach number at this point can be determined.

When used in a high enthalpy flow (see Fig. A3.3), especially the cooling of the wedge tip causes problems. If the tip of the wedge is not sharp enough, the contour can not be discerned.

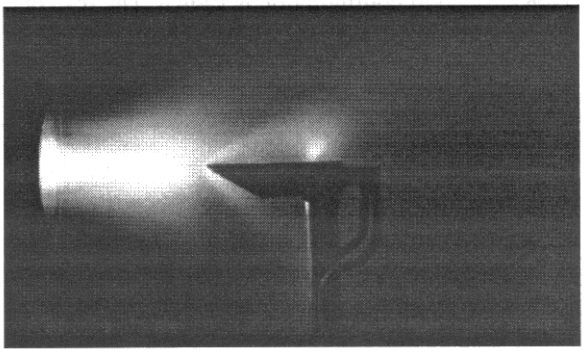

**Fig. A3.3: Wedge probe in a plasma stream**

# A4 Heat Flux Measurements

Heat transfer to a body exposed to the plasma flow is of great interest for reentry simulation in a high enthalpy flow. With the heat flux probes described in this section, the total heat flux is measured. A radiometer probe which can be used for measuring the radiative part exclusively is described in section A9.

However, for the total heat flux measurement the material of the probe itself is of great importance because the heat transfer may vary depending on the catalycity of the material of the body. In addition, the surface temperature of the probe may change the measurement result since it affects the recombination rate and its emission coefficient. As a standard reference material for heat flux probes copper is mostly used as it has a relatively high catalytic efficiency. However, it is not an ideal material as a standard because in an oxidizing atmosphere it forms two different oxides which change the catalycity.

At the IRS both stationary and non-stationary heat flux measurement devices are used. The actual probes are inserted into the front plate of a water-cooled support system, having the identical geometry of the material probe, and consisting of either a water-cooled tube or a Gardon Gage for stationary measurements or a heat sink slug for non-stationary measurements. The probes can be coated and the slug can be made of copper or other materials such as tungsten or SiC to investigate the influence of the surface catalycity [A4.1, A4.2].

The inserts, which can be seen in Figs. A4.1, A4.2, and A1.1a are thermally insulated from the surrounding support. Therefore, the heat flux onto the defined front area of the insert facing the plasma flow is measured.

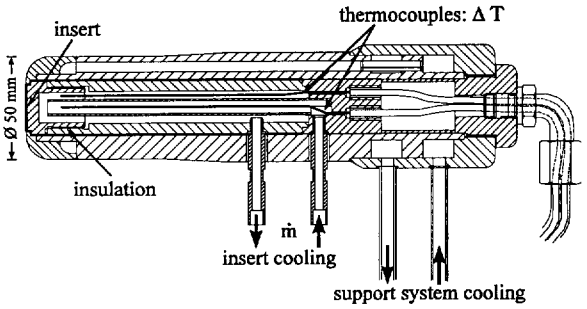


**Fig. A4.1: Stationary heat flux probe**

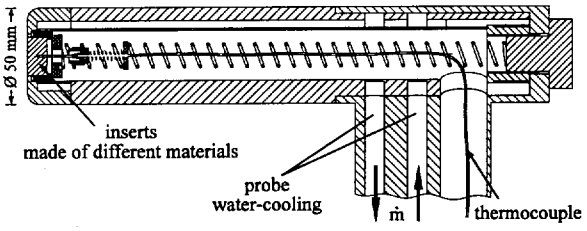


**Fig. A4.2: Non-stationary heat flux probe**

# A4.1 Stationary Heat Flux Measurement

Two different principles are in use for stationary heat flux measurement.

## A4.1.1 Calorimetric Probe

With this method the heat flux to a relatively cold surface is measured. Normally water is used for cooling the body of this type of probe (Fig. A4.1). From the heat which is carried off by the cooling water, one obtains the heat flux $\dot{q}$ onto the front surface $A_s$ by measuring the temperature difference between the cooling inflow and the outlet and its mass flow $\dot{m}_c$ according to the equation:

$$\dot{q} = \frac{\dot{m}_c}{A_s} c_c \, \Delta T \; . \qquad \text{(A4.1)}$$

Here $c_c$ represents the specific heat capacity of the coolant.

While operating the probe, one must keep in mind that the flow rate of the coolant is large enough to guarantee sufficient cooling on the one hand, and on the other hand small enough to keep the temperature difference between the inflow and outlet at a reasonable level so that it can still be measured.

## A4.1.2 Gardon Gage

With this method the heat flux is determined from the temperature gradient which forms between the center and the edge of a circular foil. A heat flux probe of this principle called the Gardon Gage, named after its inventor Robert Gardon, consists of a heat sink in the form of a hollow cylinder usually made of copper and a foil attached to the front side of the cylinder and typically made of constantan. The constantan foil is in turn connected with a copper wire in the center (Fig. A4.3). If the heat sink is kept at a constant temperature, for example by embedding it in a water-cooled sample, a radial temperature drop forms on the foil.

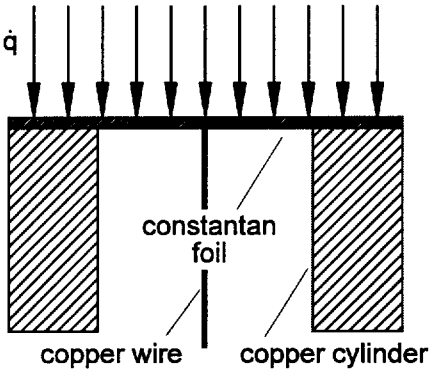


**Fig. A4.3: Construction of a Gardon Gage**

Assuming that the front and back of the foil do not give off any heat and that no temperature gradients are present across the thickness *s* of the foil, the following equation for stationary temperature distribution results from the parameters in Fig. A4.4:

$$\frac{\dot{q}}{s\lambda} + \frac{1}{r}\frac{dT_{stat}}{dr} + \frac{d^2 T_{stat}}{dr^2} = 0 \; . \qquad \text{(A4.2)}$$

Here $T_{stat}$ is the stationary temperature of the foil at the radius r and $\lambda$ is the heat conductivity of the foil.

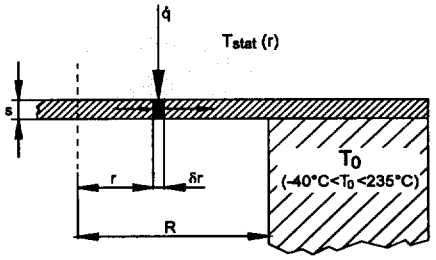


**Fig. A4.4: Geometric relations**

Considering the fact that the heat conductivity increases linearly when the temperature increases according to $\lambda = \lambda_o\left(1+\alpha(T-T_o)\right)$, the solution to the above differential equation results in the following equation:

$$\Delta T\left(1+\frac{\alpha}{2}\Delta T\right) = \dot{q}\,\frac{R^2}{4\lambda_0 s} \; , \qquad \text{(A4.3)}$$

where $\Delta T$ represents the temperature difference between the center point and the edge of the foil. With the values for $\lambda_0$ and $\alpha$ one obtains for constantan:

$$\dot{q} = \frac{1}{2026.25}\frac{s}{R^2}\Delta T\,(1 + 0.00115\,\Delta T)\left[\frac{W}{m^2}\right] . \qquad \text{(A4.4)}$$

It is evident that the dependence of the temperature difference on the heat flux to be measured is still not linear.

This disadvantage can, however, be compensated for. Figure A4.3 shows how two thermal element transitions form in the center and at the edge of the foil where the copper cylinder or rather the wire and the constantan foil are connected. The fact that the temperature difference calculated above exists between the two contact points leads to a resulting thermal voltage which can be expressed for a copper-constantan combination in the following equation:

$$U = 0.0381\,\Delta T\,(1 + 0.00117\,\Delta T) \quad [mV]. \qquad (A4.5)$$

The figures in brackets of the last two equations are practically identical so that the measured thermal voltage becomes directly proportional to $\dot{q}$:

$$U \approx 77.2\,\frac{R^2}{s}\,\dot{q} \quad [mV]\ . \qquad (A4.6)$$

Another advantage of the Gardon Gage is the compact design. The dimensions are usually only a few mm in diameter so that several sensors can easily be integrated into a probe body. As a result of their small size and low heat capacity the response times are also very short so that fast heat flux fluctuations, for example due to fluctuations of the plasma, can also be detected. The time constant $\tau$, that is the time that passes until the sensor's output signal reaches 63% of the total with a jump in the heat flux, can be approximated by:

$$\tau \approx 3.76 \cdot 10^{-6}\,R^2 \quad [s]\ . \qquad (A4.7)$$

At the IRS these heat flux sensors are equipped with surface layers of different materials to study catalytic effects. But the reduction of the heat flux from measured data is no longer as easy as for the copper-constantan case.

## A4.2 Non-Stationary Heat Flux Measurement

If one avoids a radial heat transport as in the stationary case, the axial heat flux can be calculated from the one-dimensional Fourier equation:

$$\frac{\partial T}{\partial t} = a\left(\frac{\partial^2 T}{\partial x^2}\right)\ . \qquad (A4.8)$$

For the boundary conditions the labels from Fig. A4.5 apply:

$t < 0$: temperature of the probe = $T_{w0}$ = *const.*, heat flux $\dot{q} = 0$

and

$$t > 0: \quad T = T(x, t)\ , \qquad (A4.9)$$
$$T(x=0, t) = T_w(t)\ .$$

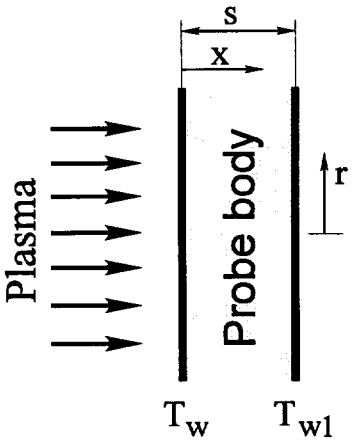


**Fig. A4.5: Explanation of the parameters**

One differentiates between two different methods - the thin wall and the thick wall method. These methods differ from each other in the realization of the last necessary boundary conditions.

### A4.2.1 Non-Stationary Thin Wall Method

With this method the heat flux is assumed to be constant throughout the entire thickness of the probe:

$$\dot{q}_{x=0} = \dot{q}_{x=s}\ . \qquad (A4.10)$$

The solution to the Fourier equation can be greatly simplified for Fourier numbers

$$F_o = \frac{a\,t}{s^2} > 0.3\ . \qquad (A4.11)$$

The temperature rise is measured and the heat flux can be directly determined from this:

$$\dot{q} = \rho\,c_p\,s\,\frac{dT}{dt}\ . \qquad (A4.12)$$

The $\rho$ and $c_p$ represent the density and specific heat capacity of the material, respectively. With a probe body made of copper with a thickness of 10 mm, the condition $F_0 > 0.3$ is for example fulfilled after a measurement time of $t_{min} > 0.27$ s.

Although the theory of the non-stationary thin wall method neglects heat fluxes in a radial direction (that is $d\dot{q}/dr \neq 0$), in practice this condition can not be completely fulfilled. A simple estimate shows, however, that these heat fluxes do not interfere with the measurement as long as the heating of the body does not last longer than a certain maximum time $t_{max}$. The following is valid for the maximum measurement time:

$$t_{max} << \left|\frac{\dot{q}}{\frac{d\dot{q}}{dy}\,s}\right|\frac{s^2}{a}\ . \qquad (A4.13)$$

A typical heat flux probe using the thin wall method is shown in Fig. A4.2.

### A4.2.2 Non-Stationary Thick Wall Method

With the non-stationary thick wall method one assumes that the temperature on the back of the sample body does not rise during the measurement. The solution to the Fourier equation while keeping this boundary condition in mind is:

$$\dot{q}(t) = \sqrt{\frac{\rho c_p \lambda}{\pi}} \left[ \frac{T(t)}{\sqrt{t}} + \frac{1}{2} \int_0^t \frac{T(t) - T(\tau)}{(t-\tau)^{3/2}} \, d\tau \right] \quad . \quad (A4.14)$$

If one can assume that the heat flux is constant over time, the solution to the Fourier equation for this case can be written as follows:

$$T(x = 0, t) - T_{w0} = \frac{2}{\sqrt{\pi}} \dot{q} \sqrt{\frac{t}{\rho c_p \lambda}} \quad . \quad (A4.15)$$

Contrary to the thin wall method, in using this equation there is no demand for a minimum test time $t_{min}$. On the other hand, it is only valid as long as the increase in temperature has not spread over the entire measurement element. That is $T(\infty,t)$ is no longer equal to $T_{w0}$.

In the thin wall method only the material constants $\rho$ and $c_p$ have to be known, while in the thick wall method the heat conductivity $\lambda$ of the sample body must also be known. Because this parameter is very difficult to determine in experiments, it can be viewed as a disadvantage. In contrast to this, the thick wall method used for heat flux measurements in a plasma wind tunnel offers the possibility while passing through the plasma stream of determing the entire profile at one time because it is possible to calculate back from the temperature-time course via Eq. (A4.14) to $q(t)$ or when the speed of the probe is known to $q(y)$. This is not possible with the thin wall method. Here the jet beam profile must be interpolated from individual measurements at various radial positions.

But the length of the thick wall sensor must be sufficient so that within the measurement time needed a rise in temperature does not occur at the back of the sensor. With metallic samples the minimum length can be approximately calculated according to the equation:

$$l_{min}\,[cm] = 4\sqrt{t_{meß}\,[s]} \quad . \quad (A4.16)$$

This means that with a typical measurement time in a plasma wind tunnel of approximately 8 s for a radial scan, the sensor length must be around 10 cm. This is one of several reasons that these kinds of sensors have mostly been used in shock tubes and shock tube wind tunnels up to now.

With this method the temperature of the front surface has to be observed. A simple measurement of the front surface temperature is possible when the sensor is designed as a thermocouple. Here the sensor is made of a round material which is inside a hollow cylinder. The material and the cylinder are separated from each other by a layer of insulation which runs along the sides. The front surface is, for example, dampened with a conductive layer (see Fig. A4.6). In this way, catalycity tests with different layers can also be carried out.

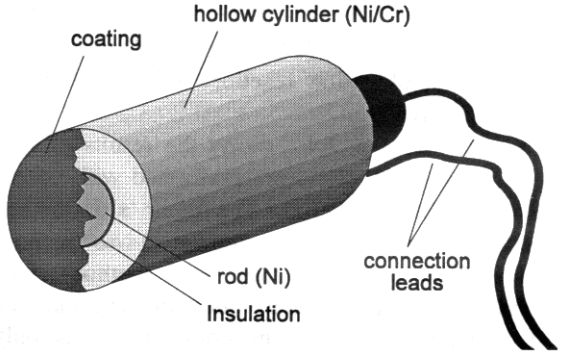


**Fig. A4.6: Non-stationary heat flux probe according to the thick wall method, Shock Wave Lab, RWTH Aachen**

## A4.3 Influence of Surface Catalycity on Heat Flux Measurements

Apart from the uncontrolled heat losses which have already been mentioned there is a far more important factor which can considerably influence the measurement results: the surface catalycity of the sample.

The heat flux on a sample in a dissociated gas (while neglecting the radiation portion) which is not chemically balanced consists of two parts joined together. The first part is supplied by the normal, molecular heat conductivity of the plasma. The second forms when atom pairs recombine on the surface. Here they transfer some of their recombination energy to the sample. The quantitative relationship between the two parts, heat conductivity and recombination, depends greatly on the length of time that the recombination partners are in the boundary layer. If the time necessary for the potential reaction partners to make their way to the sample surface by means of diffusion is much longer than the time needed by the partners for the recombination reaction, then one speaks of a *balanced boundary layer*. In this case the surface catalycity of the sample does not play a role because the particles already recombine beforehand and transfer their energy to the gas mixture. Contrary to this, the surface catalycity becomes important when a so-called *frozen boundary layer* prevails. In this case, the recombination time is much longer than the diffusion time through the boundary layer so that all potential reaction partners that enter the boundary layer also reach the front surface of the sample. If the nature of the surface encourages recombination, then the reaction energy will be set free on the surface and the heat flux onto the wall will increase. However, if

the surface is not conducive to recombination, then the particles leave the boundary layer again without having released their energy. This characteristic is quantitatively expressed by the so-called recombination coefficient of a material $\gamma$. Here $\gamma = 1$ means that all of the atoms that make it to the surface recombine (fully catalytic behavior), and $\gamma = 0$ that no catalytic recombination reactions take place (non-catalytic behavior).

As an example Fig. A4.7 shows the results of heat flux measurements that were performed with probes made of different materials. The 'n' or 's' in the key explains what kind of measurement it was (n: non-stationary, s: stationary, thin wall method). One assumes with the stationary measurement that the surface temperature remains constant and is only slightly higher than the temperature of the coolant (300 K). The temperature for the stationary measurements applies to the sample's average surface temperature when measuring in the middle of the beam (y = 0). One recognizes that the surface catalycity can increase the heat flux by more than a factor of 2 and that a material's catalycity increases as the temperature rises.

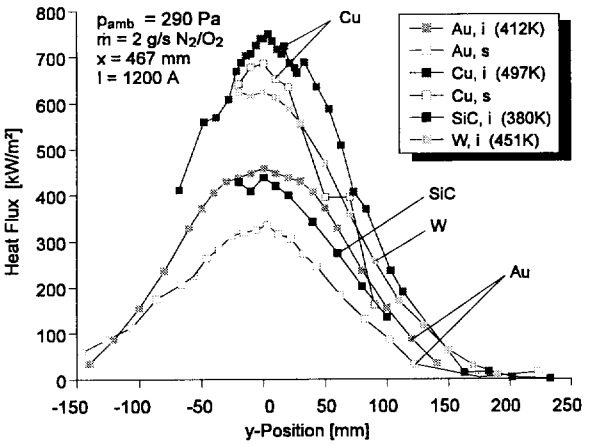


**Fig. A4.7: Results of heat flux measurements with various samples**

Copper has the highest catalycity of all the normal metals used. Its recombination coefficient is 0.2 - 0.5 and for gold between 0.04 and 0.09.

## References


[A4.1] Stöckle, T., Auweter-Kurtz, M., Laure, S., "Material Catalysis in High Enthalpy Air Flows", AIAA-96-1904, 31st AIAA Thermophysics Conference, New Orleans, LA, 1996.

[A4.2] Stöckle, T., Fasoulas, S., Auweter-Kurtz, M., "Heterogeneous Catalytic Recombination Reactions Including Energy Accommodation Considerations in High Enthalpy Gas Flows", AIAA-97-2591, 32nd Thermophysics Conference, Atlanta, GA, 1997.


# A5 Enthalpy Measurements

Due to the very high velocity of the plasma jet, the total specific enthalpy of the gas consists of two parts according to:

$$h_t = \frac{1}{2} v^2 + c_p T \quad . \qquad \text{(A5.1)}$$

As discussed in the introduction, due to the unknown enthalpy distribution in the nozzle end section and due to interaction of the jet with the ambient gas, the local enthalpy can not be derived from the averaged value in the nozzle exit plane. Therefore, at the IRS two different enthalpy probes are used depending on the pressure level. The main differences are that in one case the plasma is suctioned out and in the other case gas is injected. In addition to this, the specific enthalpy is calculated from the heat flux measurements.

## A5.1 Mass Suction Enthalpy Probe

If the total pressure is high enough, then the local specific enthalpy and the local mass flow rate of a supersonic flow can be determined by suctioning out mass using the probe pictured in Fig. A5.1.

The mass flow which corresponds to the probe opening is suctioned out with a pump and here $\dot{m}_g$ and the gas temperature $T_{g,2}$ at the end of the probe and consequently the enthalpy of the gas at this point can be determined. The suction power has to be adjusted so that the compression shock which forms in front of the probe is perpendicular to the inlet opening so that mass escaping or in-flow is avoided.

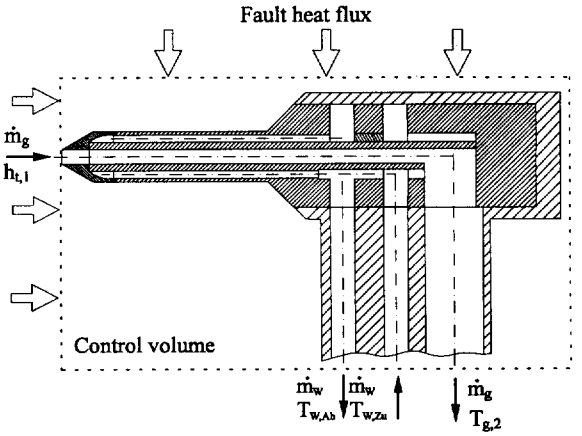


**Fig. A5.1: Set-up of a mass suction enthalpy probe**

The amount of heat which is carried off with the cooling water is measured with (V. open) as well as without (V. closed) suction and so the amount of heat extracted from the gas flow is determined by means of the difference. The energy balance reads as follows:

$$\dot{m}_g\, h_{t,1} = \dot{m}_W\, c_W \left(T_{W,outflow} - T_{W,inf\,low}\right)_{V.open}$$

$$\left| -\dot{m}_W\, c_W \left(T_{W,outflow} - T_{W,inf\,low}\right)\right|_{V.closed} + \dot{m}_g\, c_p\, T_{g,2} \quad . \tag{A5.2}$$

From here the unknown total enthalpy $h_{t,1}$ can be obtained.

Another error appears when the specific enthalpy and thereby the suction speed are very high. It is possible that as a result the heat transfer to the wall and herewith to the water circulation will be greatly reduced which makes itself noticeable in that the gas temperature $T_{g,2}$ rises quickly. Based on the high gas temperature and the slight temperature increase of the cooling water connected with it, determining the enthalpy under these conditions can result in a large error. Furthermore, with low pressure plasmas the problem arises that the very low mass flow rate $\dot{m}_g$ can only be measured correctly with great difficulty.

## A5.2 Mass Injection Enthalpy Probe

This diagnostic method, which was developed at the IRS [A5.1], can be used for plasma flows at low pressures. The measurement principle is based on the reduction of the heat flux to the wall due to mass injection through the surface of the probe (see Fig. A5.2).

The surface heat transfer in a viscous non-equilibrium high enthalpy flow is for this case obtained by:

$$\dot{q}_w = \underbrace{\left(\lambda \frac{\partial T}{\partial y}\right)_w}_{\text{conduction}} + \underbrace{\left(\rho D_{12} \sum_i h_i \frac{\partial c_i}{\partial y}\right)_w}_{\text{diffusion}} + \underbrace{\dot{q}_R}_{\text{radiation}} \quad , \tag{A5.3}$$

where the radiation is often negligible (also within this investigation).

A mass injection through the wall into the boundary layer now influences the layer and the transferred heat flux. It leads to a decrease of the temperature gradient on the surface and therefore to a decrease of heat flux due to conduction. Indeed, when the injection rate is high enough, the viscous layer is blown completely off the surface and the aerodynamic convective heat transfer becomes zero. Theoretical investigations by solving the transformed Navier-Stokes equations in the boundary layer show that the heat flux $\dot{q}$ in the stagnation point of the body being investigated is clearly dependent on the mass flow of the cooling gas which is emitted and can be expressed over a wide range of operations by

$$\frac{\dot{q}}{\dot{q}_0} = 1 - 0.72\, B + 0.13\, B^2 \tag{A5.4}$$

with the so-called mass addition factor B

$$B = \frac{\rho_w\, v_w}{\rho_\infty\, v_\infty\, St_0} = \frac{\rho_w\, v_w}{\dot{q}_0}\left(h_\infty - h_w\right) . \tag{A5.5}$$

Here $\dot{q}_0$ is the heat flux and $St_0$ is the Stanton number without the cooling gas mass flow. The Stanton number is defined as the relation between the heat flux which appeared and the maximum possible heat flux:

$$St_0 = \frac{\dot{q}_0}{\rho_\infty\, v_\infty \left(h_\infty - h_w\right)} \quad . \tag{A5.6}$$

Another investigation leads to nearly identical results by solving the viscous shock layer equations [A5.2]. By varying the specific mass flow rate $\rho_w\, v_w$ and measuring the heat flux ratio $\dot{q}/\dot{q}_0$ the enthalpy can be determined from the equation system above as follows:

The heat flux to the probe is measured by varying the mass flow rate of the injection within a wide range. Then the heat flux ratio $\dot{q}/\dot{q}_0$ is plotted against the mass addition factor as shown in Fig. A5.4. For this B has to be calculated.

In order to calculate the mass addition factor B, the effective area specific mass flow rate of the cooling gas $\rho_w\, v_w$ must be known. The mass flow rate $\dot{m} = \rho_w\, v_w\, A$ can easily be measured but determining the corresponding area A is difficult. This area can not simply be stated without further ado. (In no case is it identical to the sum of the profiles of the cooling gas bore holes.) In Fig. A5.2 one can recognize (although only weakly) that the cold boundary layer arches over the entire area of the cooling gas bore holes and beyond. Measurements in plasmas with a known enthalpy that consequently allow an inference of the effective discharge area show that in a first approximation the base of the cold boundary layer can be perceived as an effective injection area.

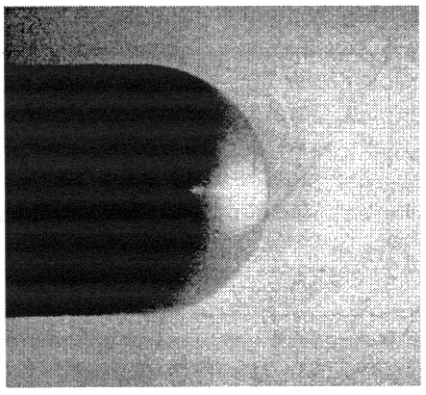

**Fig. A5.2: Cold boundary layer**

The second value needed to calculate B is the unknown enthalpy difference to begin with, and the enthalpy difference is arbitrarily chosen. The uncertainty in determining B results in a curve which will more or less deviate from the theoretical function. By varying a factor X the curve will approach the

theoretical curve when, for example, the least squares method is used. Figure A5.4 shows the result of such a regression calculation for various positions in the plasma stream. It is noticeable that from a mass addition factor of B ≈ 1.2 onward a sudden deviation of the measurements from the course of the theory appears. Numerical simulations have shown that at this point the emission speed of the cooling gas reaches sonic speed. Here effects obviously appear that can no longer be explained by the theory applied. However, this is unimportant in determining the enthalpy because the upper portion of the curve is sufficient for the regression analysis.

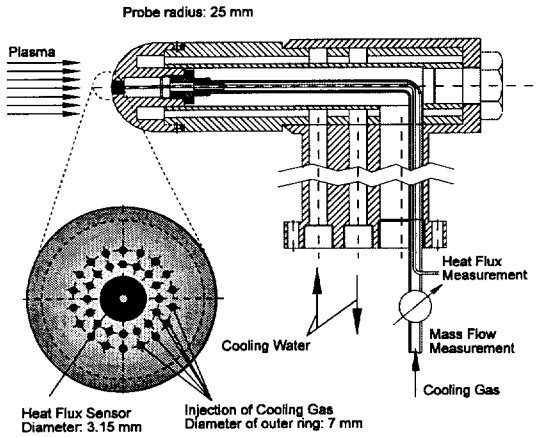


**Fig. A5.3: Experimental set-up of the mass injection probe**

The experimental set-up is shown in Fig. A5.3. In the hemispherical front part there are small bore holes through which the cooling gas flows and in the middle there is a Gardon Gage heat flux sensor. The front of the probe differs from the otherwise flat contour of the mechanical probes usually used in wind tunnels. The reason is that in a flat stagnation point the boundary layer's similarity to itself no longer exists. With that the decrease in the heat flow would no longer obey the form given in Eq. (A5.4).

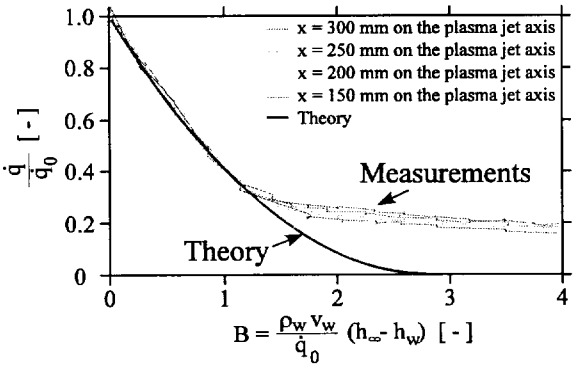


Fig. A5.4: Determining the enthalpy by adjusting the measurement curve to the theoretical course

# A5.3 Determining the Specific Enthalpy from Heat Flux Measurements

The local distribution of the specific enthalpy can be determined from measurements of the local heat flux distribution and the total pressure distribution. For this purpose, Fay and Riddell [A5.3] reformed the laminar boundary layer equations for chemically reactive flows. By comparing them with experimental results, semi-empirical equations could be formed for the following three cases:

- boundary layer in chemical equilibrium (independent of the surface catalycity),
- frozen boundary layer with a fully catalytic surface,
- frozen boundary layer with a non-catalytic surface.

As an example of this only the equation for the heat flux on a fully catalytic surface is given:

$$\dot{q}_{fc} = 0.763\,Pr^{-0.6}\left(\frac{\rho_w\mu_w}{\rho_\infty\mu_\infty}\right)^{0.1}\sqrt{\rho_\infty\mu_\infty\beta}\,(h_\infty - h_w)\left[1+\left(Le^{0.63}-1\right)\left(\frac{h_D}{h_\infty}\right)\right] \quad \text{(A5.7)}$$

With the help of Eq. (A5.7), the local enthalpy in the flow $h_\infty$ can in principle be determined by measuring the local heat flux. However, the density $\rho_\infty$, viscosity $\mu_\infty$, dissociation energy $h_D$, Prandtl number Pr, Lewis number Le and velocity gradient ß at the stagnation point have to be known.

In the case of a chemically frozen flow, an approximate solution was given by Pope [A5.4] which only requires that the Pitot pressure and the heat flux be known in order to calculate the enthalpy:

$$h_\infty = \frac{\dot{q}_{fc}}{K\sqrt{\frac{p_{tot}}{R_{eff}}}} \quad \text{(A5.8)}$$

Here K is a constant which has the value K = 108 W/(MJ/kg bar$^{0.5}$ m$^{1.5}$) for nitrogen, $R_{eff}$ is the effective leading edge radius of the probe which can be given by $R_{eff} = 2.9\,r_N$ ($r_N$: real leading edge radius) for the relatively low Mach numbers in the plasma wind tunnels.

Here $\dot{q}_{fc}$ represents the fully catalytic heat flux. For copper up to a specific enthalpy of approximately 50 MJ/kg it can be calculated from the actual heat fluxes $\dot{q}_{fc}$ with the help of measurements from Pope [A5.5] and Goulard [A5.6].

## References

[A5.1] Fasoulas, S., Stöckle, T., Auweter-Kurtz, M., "Measurement of Specific Enthalpy in Plasma Wind Tunnels Using a Mass Injection Probe", AIAA-97-2496, 32nd Thermophysics Conference, Atlanta, GA, June 1997.

[A5.2] Moss, J.N., "Reacting Viscous-Shock-Layer Solutions with Multi-Component Diffusion and Mass Injection", NASA TR R-411, June 1974.

[A5.3] Fay, J.A., Riddell, F.R., "Theory of Stagnation Point Heat Transfer in Dissociated Air", Journal of Aeronautical Sciences, Vol. 25, No. 2, February 1958.

[A5.4] Vojvodich, N.S., Pope, R.B., "The Influence of Ablation on Stagnation Region Convective Heating for Dissociated and Partially Ionized Boundary Layer Flows", Proceedings of the 1965 Heat Transfer and Fluid Mechanics In-stitute, Stanford University Press, California 1965; Marvin, J.G., Pope, R.B., "Laminar Convective Heating and Ablation in the Mars Atmosphere", AIAA Journal, Vol. 5, No. 2, February 1967; Pope, R.B., "Measurements of Enthalpy in Low Density Arc Heated Flows", AIAA Journal, Vol. 6, No. 1, January 1968.

[A5.5] Pope, R.B., "Stagnation Point Convective Heat Transfer in Frozen Boundary Layers", AIAA Journal, Vol. 6, No. 4, April 1968.

[A5.6] Goulard, R., "On Catalytic Recombination Rates in Hypersonic Stagnation Heat Transfer", Jet Propulsion, Vol. 28, No. 11, November 1958.

# A6 Solid State Electrolyte Probe

Solid state electrolyte probes were developed to determine the local oxygen content [A6.1]. The functional principle is the same as that of Lambda probes used in cars.

The basic idea is based on the principle of electrolysis, whereby, however, the electrolyte here does not exist in the typical liquid form but rather as a solid. Zirconium dioxide ($ZrO_2$) doped with yttrium oxide ($Y_2O_3$) is used as the solid state electrolyte (see Fig. A6.1).

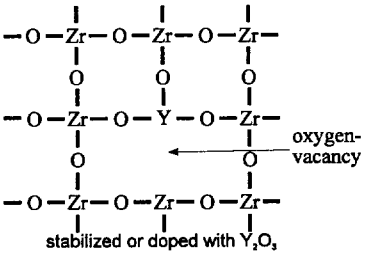


**Fig. A6.1: Two-dimensional representation of the mesh structure**

The presence of oxygen vacancies in the material make oxygen ion ($O^{2-}$) mobility possible. This conductivity is very low at room temperatures but reaches values of a wet electrolyte when the sensor is heated up to approximately 600°C. The conductivity due to electronic mobility can usually be neglected.

An oxygen sensor can be constructed by providing the solid electrolyte with porous electrodes and by separating two gas chambers with it as shown in Fig. 6.2. At higher cell temperatures the solid electrolyte conducts oxygen ions, thus an oxygen concentration difference between the sample and reference chamber results in a potential difference.

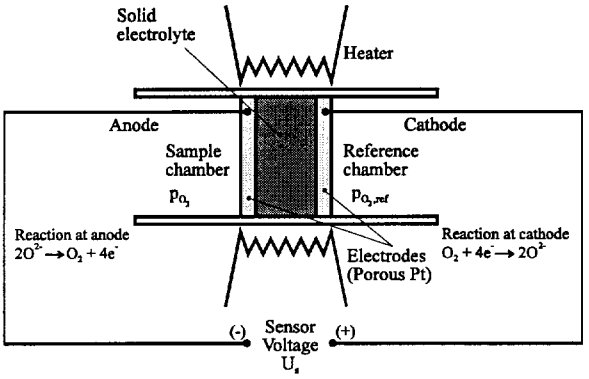


**Fig. A6.2: Basic construction of a potentiometric solid state electrolyte sensor**

In order to reach the necessary electrolyte temperatures, a heating element is integrated into the sensor. On the cathode the molecular oxygen is catalytically decomposed into two double negative oxygen ions. The reduction of the ions takes place at the cathode. The electromotive power of a concentration cell, as shown in Fig. A6.2, can be described by the so-called Nernst equation in a first approximation.

$$\Delta U_S = \frac{\Re T_s}{4F} \ln \frac{p_{O_{2,ref}}}{p_{O_{2,meas}}} \quad . \qquad \text{(A6.1)}$$

$T_s$ is here the sensor temperature, F the so-called Faraday constant with the value $F = 9.6485 \cdot 10^4$ As/mol and $p_{O_{2,ref}}$ or $p_{O_{2,meas}}$ the particle pressure of oxygen in the reference and the sample chamber, respectively.

Solid state electrolyte probes can be operated according to two different measurement principles. First, the voltage $\Delta U_P$ can be measured directly. Secondly, constant voltage can be applied externally so that a continuous current flows over the ceramic. In the first case one calls it a potentiometric and in the second an amperometric probe.

Potentiometric probes can cover a measurement area of 8 decades without any problems. Within this area the partial pressure can be described well with Eq. (A6.1). In comparison, with the amperometric sensors one intentionally creates a flux of oxygen ions, whereby the adjusted current is in turn an index for the oxygen concentration. With amperometric probes the determination of the oxygen concentration is more accurate; however, measurements are only possible within three decades.

Figure A6.3 shows the water-cooled probe used in the PWK. The reference chamber of the probe is connected with the environment outside the PWK by means of a hose line. That means that the reference partial pressure corresponds to the oxygen partial pressure of the laboratory atmosphere.

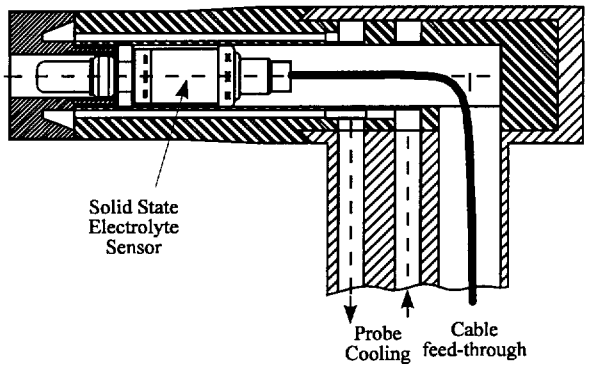


**Fig. A6.3: Solid state electrolyte probe for use in a PWK**

Due to the high catalycity of the surface, these solid state electrolyte probes can not differentiate between atomic and molecular oxygen. The oxygen distribution measured with solid state electrolyte sensors corresponds to the sum from the molecule portions of O and $O_2$. Moreover, additional electro-chemical reactions on the catalytic probe electrodes are brought about by oxidizable gases such as NO and CO which are often present in combustion gases and thereby influence the sensor voltage and may therefore falsify the measurement.

## References

[A6.1] Fasoulas, S., "Measurement of Oxygen Partial Pressure in Low Pressure and High Enthalpy Flows", AIAA-96-2213, 19th AIAA Advanced Measurement and Ground Testing Technology Conference, New Orleans, LA, 1996.

# A7 Electrostatic Probes

Electrostatic probes normally used in plasma wind tunnels consist of up to three electrodes which are electrically insulated from each other and from mass and are exposed to the plasma. By recording current-voltage characteristics or current-time developments, the various parameters of the plasma such as plasma potential, electron temperature and density, flow direction, electron energy function, plasma velocity or ion temperature can be determined at the position of the probe electrodes [A7.1, A7.2].

If one moves an electrostatic probe into a plasma beam, a plasma boundary layer forms around the probe. This layer can be altered by varying the bias voltage across the probe. Important plasma parameters can be deduced from the probe signal. For this purpose, the boundary layer must be described theoretically.

When moving a probe into a plasma assumed to be quasi-neutral, a negative charge of the probe takes place across from the surrounding plasma. This is because the higher thermal mobility of the electrons causes more electrons than ions to reach the probe electrode surface. The negative charge causes a repulsion of further electrons in the area around the probe. Therefore, a positive space charge layer forms which disturbs the ionization recombination equilibrium.

The higher ion density in the space charge layer around the probe, compared to the electron density, causes the formation of an electric field which decreases as the distance to the probe surface increases.

As a result of the recombinations on the probe surface, charge carriers from the quasi-neutral, undisturbed plasma have to subsequently be delivered to the space charge layer. This charge carrier drift requires the existence of a weak remaining field which must also be present outside of the space charge layer in the so-called transition region. Figure A7.1 shows the development of the potential in the entire plasma surface layer.

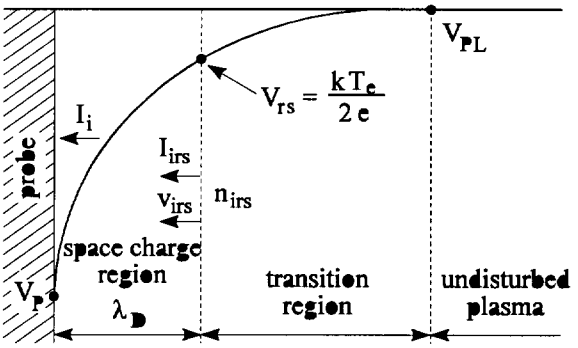


**Fig: A7.1: Potential development in the plasma surface layer**

The thickness of the space charge layer is given by the Debye length $\lambda_D$ which is dependent on the electron temperature and density by means of the equation

$$\lambda_D = \sqrt{\frac{\varepsilon_0 k T_e}{e^2 n_e}} \quad . \qquad \text{(A7.1)}$$

Figure A7.2 shows that, for example, in MPD tunnels the Debye length is several mm. In the adjacent transition region, a slight charge carrier concentration decline still exists which affects the drift. Despite the small, remaining electric field in the transition region, the plasma can be considered quasi-neutral for the theoretical treatment. For additional increasing distances from the probe surface, the undisturbed, quasi-neutral plasma with the potential $V_{PL}$ is finally reached. The border of the space charge layer is determined by the so-called Bohm criteria according to which the charge carriers entering the space charge layer have to apply the energy of

$$e V_{rs} = \frac{k T_e}{2} \quad . \qquad \text{(A7.2)}$$

Moreover, for the theoretical description of the boundary layer, the smallest mean free path is of great importance. It is the mean free path due to electron and ion collisions:

$$\lambda_{ei} = \frac{16\pi (\varepsilon_0 k T_e)^2}{e^4 n_e \ln \Lambda}$$

with $$\Lambda = 12\pi \frac{(\varepsilon_0 k T_e)^{3/2}}{n_e^{1/2} e^3} \quad . \qquad (A7.3)$$

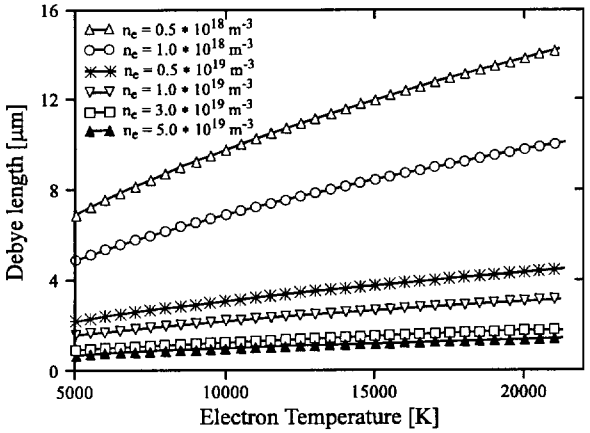


**Fig. A7.2: Debye length as a function of $n_e$ and $T_e$**

As can be seen in Fig. A7.3, in the MPD tunnels it is expressed in mm.

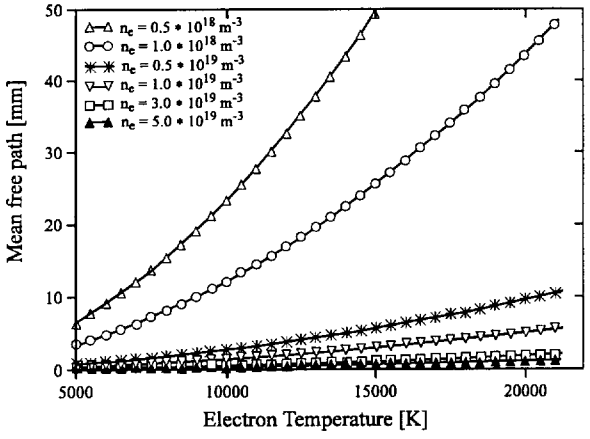


**Fig. A7.3: Mean free path as a function of $n_e$ and $T_e$**

The current that flows to a probe's surface depends on the mean free path $\lambda_{ei}$ of the charge carrier and the Debye length $\lambda_D$ in the space charge layer and on the probe radius r. The relationships between these parameters determine whether the movement of the charge carriers in the space charge layer is influenced by a shock.

If the probe radius can be chosen so that

$$\lambda_{ei} >> r >> \lambda_D \qquad (A7.4)$$

is fulfilled, then a so-called conventional shockless thin space charge layer can be assumed.

In an MPD tunnel partial densities of the charged particles in the investigated regions of the air plasma flow, ranging from x = 50 mm to 500 mm axial distance to the MPG, are in the range of $n_e = 10^{17}$ to $10^{21}$ $m^{-3}$. With electron temperatures $T_e$ of 5000 to 30000 K, this results in Debye lengths of $\lambda_D < 40$ µm.

The Coulomb mean free paths are in the range of $\lambda_{ei} \geq 1$ mm.

The shockless theories developed for stationary plasmas and cylindrical probes can also be applied to flowing, shockless plasmas when the cylindrical probes with a length $l$ are aligned with the plasma flow and $l/\lambda_D >> 1$ is fulfilled. In the case of larger Debye lengths the plasma layer is enlarged at the front surface of the probe and the ion current to this surface compared with the ion current to the cylindrical surface of the length $l$ can no longer be neglected. The ratio $l/\lambda_D$ is proportional to the so-called end effect parameter $\tau_l$ which is a criterion for the portion of current to the front surface of a cylindrical probe aligned with the plasma flow. For $\tau_l > 50$ this amount of current is negligible.

Table 7.1 gives an overview of the probes typically used for plasma diagnostics and the plasma parameters which can be determined with each one.

| Probe | Parameters |
|---|---|
| Single probe | Electron temperature $T_e$, electron density $n_e$, plasma potential, electron energy distribution |
| Double probe | Electron temperature $T_e$, electron density $n_e$ |
| Triple probe | Electron temperature $T_e$, electron density $n_e$ |
| Time of flight probe | Plasma velocity |
| Electrostatic angle probe | Plasma flow line |
| Rotation electrostatic probe | Plasma flow line |
| Electrostatic crossed probe | Plasma velocity at known ion temperature ion temperature at known plasma velocity |

**Tab. 7.1 Various probes and their determinable plasma parameters**

# A7.1 Electrostatic Single Probe

The measurement diagnostic while operating electrostatic single probes consists of determining the current-voltage characteristic. By applying external voltage between the single probe electrode and a reference electrode in contact with the plasma, the probe potential $V$ is varied with respect to the surrounding plasma and therefore the thickness of the space charge layer is changed. Figure A7.4 depicts a typical current-voltage characteristic.

Here the entire current to the probe consists of the ion current $I_i$ and the electron current $I_e$ components. The single probe characteristic curve can be divided into three areas: ion saturation A, transition region B and electron saturation C.

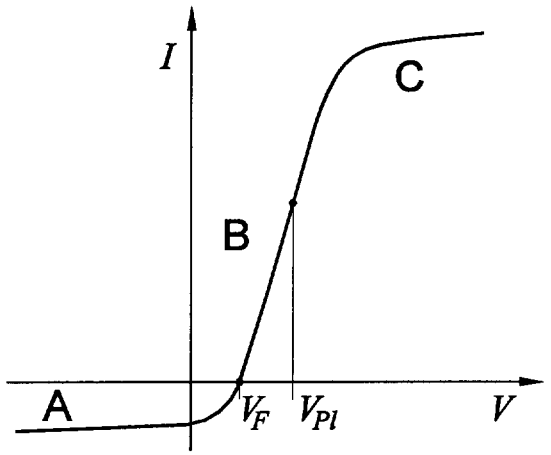


**Fig. A7.4: Typical single probe current-voltage characteristic**

For large negative probe voltages all electrons are rejected by the probe; only ions are drawn by the probe resulting in an ion saturation current. For lower negative probe voltages in the electron retarding region of the probe characteristics, an increasing amount of electrons contributes to the net current drawn by the probe while the ion current portion decreases. At the floating potential $V_F$ no net current is drawn since the ion current $I_i$ equals the electron current $I_e$. If the probe voltage reaches the point $V_{Pl}$, the space charge zone disappears because there is no longer a potential difference between the probe and the plasma. Therefore, $V_{Pl}$ is referred to as *plasma potential*. At probe voltages positive with respect to the plasma potential $V_{Pl}$ , the ions are rejected and only electrons contribute to the probe current. Saturation is reached when due to the electron mobility more electrons can no longer be supplied from the plasma.

The electron saturation current is substantially higher than the ion saturation current due to the higher mobility of the electrons. The ratio of the two currents is given by:

$$\frac{I_e}{I_i} \approx \sqrt{\frac{m_i T_e}{m_e T_i}} \quad . \qquad \text{(A7.5)}$$

### Electron Temperature

The shape of the probe characteristic especially in the electron retarding region, where the transition from ion to electron current occurs, is governed by the electron energy distribution function. If the electron current to the probe is calculated assuming Maxwell distribution, the result is a simple equation for determining the electron temperature:

$$\frac{d\,\mathrm{In}(Ie)}{dU} = \frac{e}{kT_e} \quad . \qquad \text{(A7.6)}$$

For a Maxwellian electron energy distribution function, the electron temperature $T_e$ can therefore be obtained by plotting the slope of the logarithmic electron current in the retarding region versus the probe potential.

The electron current plotted logarithmically against the probe potential in the transition area B has to result in an even integer (see Fig. A7.5). The value of the increase of these even integers is required to determine the electron temperature. In practice, however, an evaluation in the region of the floating potential $V_F$ has been proven to be most reliable.

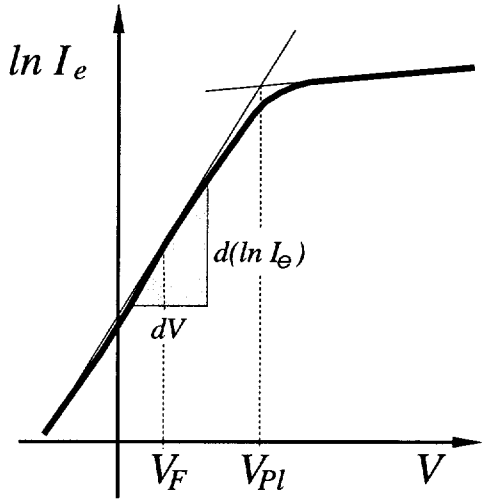


**Fig. A7.5: Determining the electron temperature**

The electron current in region B is determined from the current-voltage characteristic (Fig. A7.4) in that one first of all determines the ion current by means of a linear extrapolation from the ion saturation current. This is then subtracted from the measured total current.

### Plasma Potential

The plasma potential can also be determined from Fig. A7.5. The plasma potential $V_{Pl}$ is given by the crossing point of the extrapolated linear electron retarding region and the saturation region of the logarithmic electron current.

### Electron Density

The ion current is calculated to determine the electron density. Assuming quasi-neutrality Laframboise did this for a probe in a parallel flow taking the thermal non-equilibrium into account.

According to Laframboise's theory [A7.3], the ion current $I_i$ to a single probe aligned with the plasma is given by

$$I_i = A\,e\,n_e \sqrt{\frac{kT_e}{2\pi m_i}}\; i_i\left(\chi_p, \frac{T_i}{T_e}, \frac{r}{\lambda_D}\right). \qquad \text{(A7.7)}$$

The correction factor $i_i$ depends on the normalized plasma potential $\chi_p = e(V_{Pl} - V_P)/kT_e$, the Debye ratio $r/\lambda_D$ and the temperature ratio $T_e/T_i$. The correction factor can be set to 1 in good approximation if the Debye ratio is greater than 50, which can be achieved by choosing the corresponding probe radius r in accordance with this requirement and if the

ion current is obtained by the extrapolation of the saturation current region to values of small normalized probe potentials $\chi_p$ .

### Electron Energy Distribution

An essential requirement of the single probe theory introduced here is the assumption of a Maxwell distribution of the electron energies. The validity of this assumption in the plasma which has been examined can be proven rather easily based on the linearity of the logarithmized electron current in the transition region of the probe characteristic curve as shown in Fig. A7.5. Due to high local heat input, deviations from this energy distribution may occur so that it is no longer possible to exactly determine the electron temperature based on the electron current increase of a single probe measurement.

According to Fig. A7.6, the electrons on the center line at a distance of x = 117 mm to the exit of the MPG are non-Maxwellian. It can be clearly seen from Fig. A7.6 that for the other positions the electrons do have a Maxwellian energy distribution.

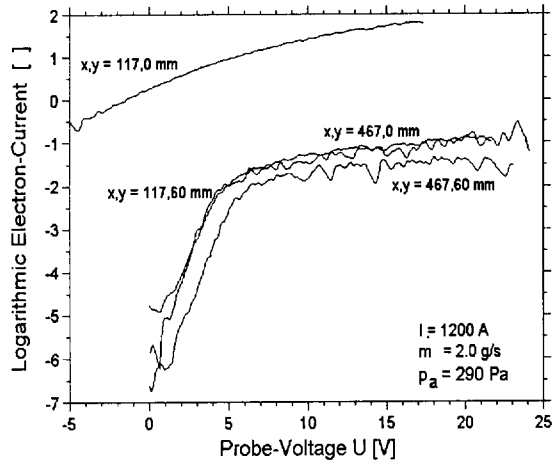


**Fig. A7.6: Semi-logarithmic plots of the electron currents to a single probe at different x, y positions to the MPG exit**

In the case of deviations from the Maxwellian electron velocity or distribution, i.e. one has a different isotropic distribution function, this distribution function can be obtained from the probe characteristic in the retarding region at $V_S < V_{PL}$. The shape of the second derivative of the electron current $I_e$ to a single probe with respect to the probe voltage U is proportional to the shape of the distribution function of the electrons which can be numerically fitted. To do this, the plasma potential $V_{Pl}$ must be known since the probe potential must be measured with respect to the plasma potential. In the electron retarding region of the probe characteristic, the change of probe current is mainly driven by the change in the electron current part which is much greater than the change in the ion current. Thus it can be assumed that the second derivative of the total probe current is essentially the same as the second derivative of the electron current.

If the electron current $I_e$ is differentiated twice with respect to U, one yields

$$[f(E)]_{E=-eU} = \frac{-1}{A\,2e\pi}\left(\frac{m_e}{e}\right)^2 \frac{d^2 I_e}{dU^2}; \quad U < 0 \quad \text{(A7.8)}$$

for the velocity distribution function f(E) and

$$F(E)\Big|_{E=eU} = -\frac{4}{Ae^2}\sqrt{\frac{-m_e U}{2e}}\,\frac{d^2 I_e}{dU^2} \quad \text{(A7.9)}$$

for the energy distribution function of the electrons.

In Figs. A7.7 and A7.8 the experimentally obtained electron energy distribution functions at two different positions in the air plasma are shown. For reasons of comparison, Fig. A7.7 also shows a theoretical Maxwell distribution function at an appropriate electron temperature $T_e$.

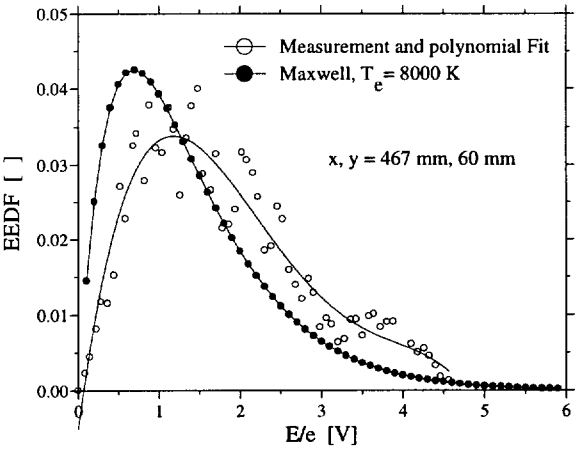


**Fig. A7.7: Experimental and theoretical (Maxwell) electron energy distribution function at x, y = 467mm, 60 mm**

Figure A7.8 shows the experimentally obtained electron energy distribution function on the plasma flow center line at x = 117 mm. High energy electrons are dominant.

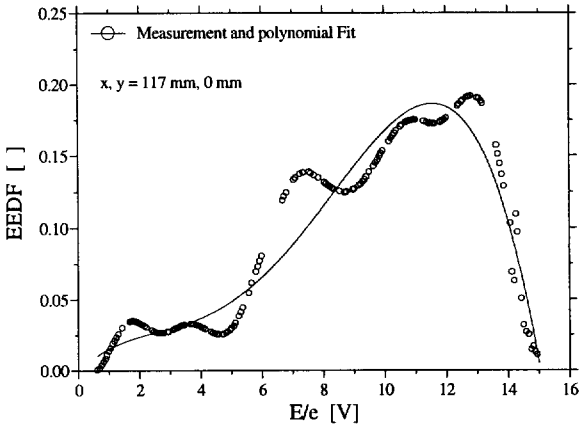


**Fig. A7.8: Experimental electron energy distribution function at x, y = 117 mm, 0mm**

### Experimental Set-up

Figure A7.9 shows the design of a typical single probe. For use in MPD tunnels the probe itself consists of a tungsten wire with a diameter of 0.1 to 1 mm and an effective length of 5 to 20 mm. The rest of the wire is insulated from the probe clamp by means of a small aluminum tube.

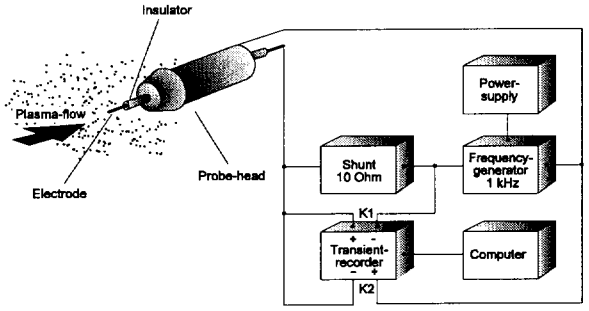


**Fig. A7.9: Experimental design for single and double probe measurements**

A power pack supplies voltage of ± 30 V which is modulated in the form of a sine or saw tooth signal from a portable generator. This voltage variation is established as probe potential. The modulation across the entire voltage region is done with a frequency of up to 10 kHz. The probe potential is measured directly and the probe current is measured at a precision resistance. The measurements are recorded with a oscilloscope or transient recorder.

## A7.2 Electrostatic Double Probe

A double probe consists of two cylindrical probe electrodes whose distance to each other has to be more than several Debye lengths so that any kinds of disturbances can be ruled out. Normally the surfaces of both electrodes are the same size. This condition should be assumed for the following.

Voltage is created between the two electrons and the flowing current is measured. Each electrode can be considered to be a single probe with the other electrode acting as the reference. The theory of the double probe characteristic can, therefore, principally be derived from the theory for single probes.

If the potential of a probe electrode (electrode 1) is negative compared to the plasma after applying external voltage $V$, then there is a continuous decrease of the electron current portion until ion saturation is reached. If the external voltage is 0, both probe electrodes float and the resulting total current disappears. In the case of polarity reversal of the double probe, electrode 2 becomes more and more negative compared to the plasma potential and finally reaches ion current saturation. Electrode 1 compensates for this ion current with an appropriately large electron current. In this way, contrary to the single probe, the double probe with equal surface areas never reaches the point of electron saturation. Figure A7.10 shows a typical double probe characteristic curve.

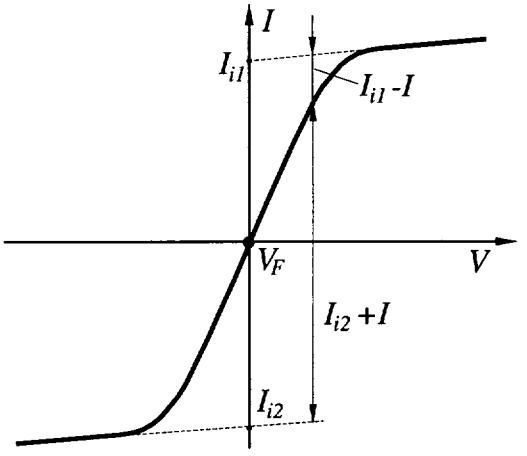


**Fig. A7.10: Double probe characteristic curve for electrodes with equal surface area**

Only high energy electrons penetrate the plasma sheath near the floating potential $V_F$ and contribute to the net current. This means that the double probe is less sensitive to low energy deviations from the assumption of Maxwell electron energy distribution (see Fig. A7.7).

### Electron Temperature

The electron temperature $T_e$ is obtained by the equation (A7.10):

$$\left.\frac{dI}{dV}\right|_{V=0} = \frac{I_{i1}\, I_{i2}}{I_{i1} + I_{i2}} \frac{e}{k T_e} \quad . \qquad \text{(A7.10)}$$

The ion currents $I_{i1}$ and $I_{i2}$ are extrapolated from the saturation regions of the characteristic to the floating potential $V_{PL}$ where no current is drawn (see Fig. A7.10).

### Electron Density

The electron density can be determined from a double probe measurement with the same equation as with a single probe measurement Eq. (A7.7). However, a mean ion current has to be determined. With a double probe with equal surface areas this is obtained from

$$\bar{I}_i = \frac{|I_{i1}| + |I_{i2}|}{2} \quad . \qquad \text{(A7.11)}$$

The decision whether one uses a single or a double probe is based on the advantages and disadvantages of each method. Single probe measurements and the evaluation can be performed quickly due to the low Debye lengths and the resulting negligible ion current correction factor. These probes are smaller and allow for a better local resolution of the plasma parameters. However, single probes used to determine the electron temperature and density reach their limits as soon as significant deviations of the electron energies

from the Maxwell distribution appear. An additional disadvantage is that the distance between the reference electrode and the single probe is usually quite large and therefore the probe characteristic can be influenced by changes in the plasma potential between the two electrodes. Moreover, a thermal overload and destruction can be easily caused by the high electron current load of a single probe which results in an increased burning off of the probe electrodes with erosive plasmas. With a double probe, the load from the current is lower due to the essentially smaller ion current saturation, which in this case is the maximum current load. The number of electrons in a double probe current is limited to the high energy electrons, i.e. a double probe measurement is less susceptible to deviations of the electron energy distribution. The disadvantages of the double probe, the larger size and lower local resolution of the measurement, can usually be compensated for with the smaller changes of the plasma potential between the electrodes. The technical performance and the construction of a double probe only differs from a single probe in that the voltage is established between the two probes.

## A7.3 Electrostatic Triple Probe

A major disadvantage of single and double probes for plasma wind tunnel applications is that the heat load during the measurement of the probes in the plasma jet is very high due to the time needed to obtain the full probe characteristics at any measurement point. In addition, the current to the probe often results in high thermal loads, leading to extensive erosion in the chemically reacting air plasma. With an electrostatic triple probe, for example, the whole radial distribution of the electron temperature and the electron density can be measured by a fast radial motion of the probe through the investigated plasma jet. No further evaluation of characteristics taken at specific radial test positions is necessary.

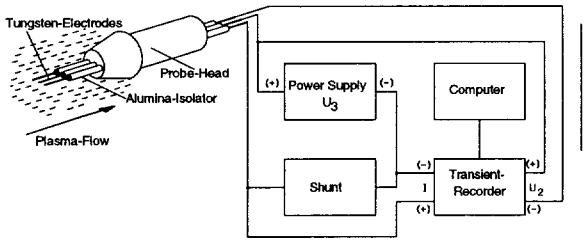


**Fig. A7.11: Triple probe measurement set-up**

As shown in Fig. A7.11, the electrostatic triple probe consists of three electrodes identical in surface area A, two of them (1, 3) connected to a double probe and a third (2) floating with respect to the plasma.

### Electron Temperature

In a collisionless thin sheath of plasma at the probe surface, the current to each electrode at a potential V can be expressed by:

$$-I_1 = A\, j_i\,(V_1) - A\, j_e \exp\,(-eV_1/kT_e)\ , \quad \text{(A7.12)}$$

$$I_2 = A\, j_i\,(V_2) - A\, j_e \exp\,(-eV_2/kT_e)\ , \quad \text{(A7.13)}$$

$$I_3 = A\, j_i\,(V_3) - A\, j_e \exp\,(-eV_3/kT_e)\ . \quad \text{(A7.14)}$$

Without an externally applied potential difference between the double probe circuit and the floating electrode, the current $I_2$ to the floating electrode will be zero. By assuming no variation in ion current density $j_i$ in the probe region, one obtains from the current ratio:

$$U_2 = \frac{kT_e}{e}\left[\ln 2 - \ln\left(1+\exp(-eU_3/kT_e)\right)\right], \quad \text{(A7.15)}$$

with $U_2 = V_2 - V_1$ and $U_3 = V_3 - V_1$. For an externally applied fixed potential difference $U_3$ in the double probe circuit, an electron temperature dependent potential voltage difference $U_2$ can be measured between the double probe and the floating electrode. By moving the probe through the plasma, direct radial or axial distribution of $T_e$ can be measured.

### Electron Density

Since the ion current density $j_i$ depends on the electrode potentials, the assumption of equal ion current densities is not quite correct even for the thin sheath case. Therefore, Chen and Sekiguchi derived an approximate expression for the ion current density which includes a correction factor ß [A7.4]. This correction factor scales the potential difference with respect to the floating potential $V_F$. The correction factor ß can be calculated from the equation

$$\exp\left(-\frac{eV_F}{kT_e}\right) = 0.6577\sqrt{\frac{m_i}{m_e}\left(1-ß\left(V_F-\frac{e}{2kT_e}\right)\right)} \quad \text{(A7.16)}$$

by using one of the triple electrodes as a single probe in order to determine the floating potential $V_F$ and the electron temperature as described in Eq. (A7.1). Using this correction, one obtains:

$$\frac{1}{2} = \frac{1-\left(\sqrt{1-ßU_2}+\sqrt{1+ß(U_3-U_2)}\right)}{1-\exp\left(-\frac{eU_3}{kT_e}\right)} * 0.5\exp\left(-\frac{eU_2}{kT_e}\right) \quad \text{(A7.17)}$$

to determine the electron temperature.

In Fig. A7.12 the correction factor ß is plotted as function of electron temperature for different gases. Without this correction the electron temperatures are overestimated by 20% at the most.

From the collisionless probe theory and the measured current I in the double probe circuit under the assumption of constant current density j, the electron number density is determined by:

$$n_e = \frac{\sqrt{m_i I}}{A}\,\frac{\sqrt{e}}{e\sqrt{kT_e}\left[\exp(-eU_2/kT_e)-1\right]}. \quad \text{(A7.18)}$$

Without this correction factor the electron density is overestimated by a maximum of 40% according to the theory of Chen and Sekiguchi with respect to Eq. (A7.15). The equation for the electron density changes to:

$$n_e = \frac{\sqrt{m_i I}}{A} \frac{1.05 \cdot 10^9 \left(1 - ß\left(V_F - e/2kT_e\right)\right)^{1/2}}{\sqrt{T_e}\left(\exp\left(eU_2/kT_e\right) - \left(1 - ßU_2\right)^{1/2}\right)}. \quad \text{(A7.19)}$$

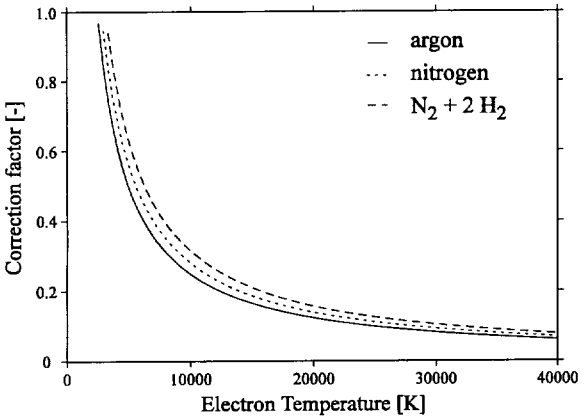


**Fig. A7.12: Correction factor β for various plasmas as function of the electron temperature $T_e$**

For the use of the formula given in section A7.3 the electron energy distribution has to be Maxwellian. A correction in the case of a non-Maxwellian energy distribution is impossible without losing the advantage of rapid mobility of this type of probe. In this case a single probe measurement is preferable because of its much higher local resolution.

The wiring of the probe can be seen in Fig. A7.11. Contrary to single and double probe measurements, a saw tooth generator is not necessary. This makes it possible to achieve a substantially higher transport speed of the probe in the plasma beam and therefore a lower thermal load.

Figures A7.13 and A7.14 show cross sections of the electron temperature and density, determined by a double and triple probe respectively, through the plasma beam at a distance of 467 mm from the nozzle end of the plasma generator in an MPD tunnel.

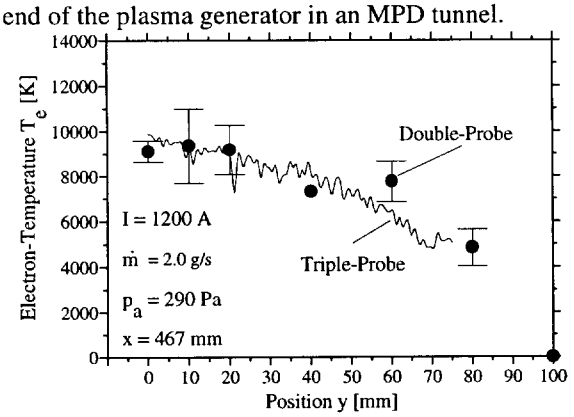


**Fig. A7.13: Electron temperature distribution**

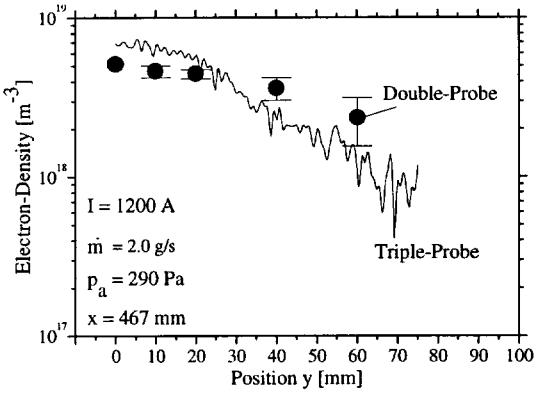


**Fig. A7.14: Radial electron density distribution**

## A7.4 Time of Flight Probe

Time of flight probes are in use for plasma flow measurements. They are electrostatic double probes separated at a known distance and aligned with the flow of the plasma particles as shown in Fig. A7.15.

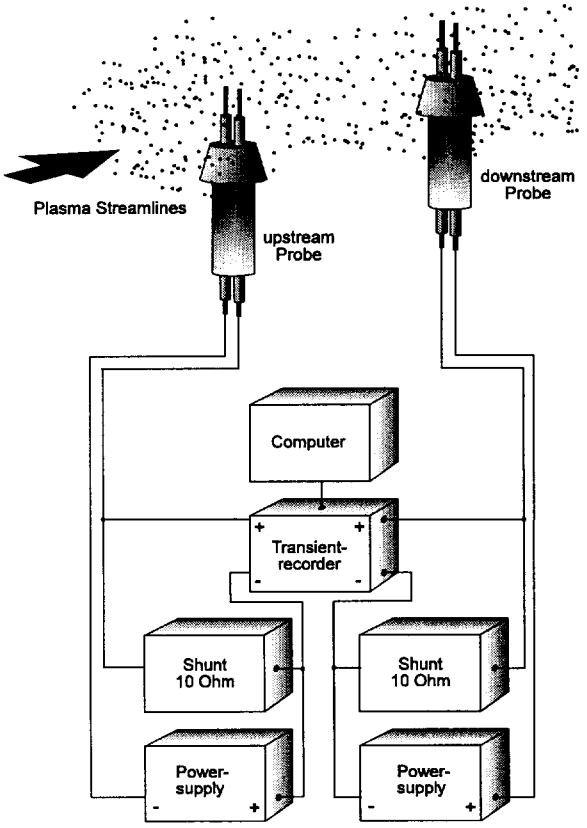


**Fig. A7.15: Design of a time of flight probe**

Upstream and downstream probes are both biased to draw ion-saturation current. Fluctuations in the local ion number density around a probe result in fluctuations in the detected ion current. By moving with the flow velocity v, those fluctuations are first detected at the upstream probe and then time-delayed at the downstream probe. The method of time of flight probes as described is only applicable within regions with moderate velocity gradients because a relatively large probe separation of about 25-50 mm is needed

to resolve the time delays in high speed plasmas. By performing an FFT-cross-correlation with the two signals, the value of the time shift in respect to the time of flight can easily be determined. With the known separation of the two probes, the velocity of the plasma particles can be calculated.
Within the air plasma of an MPD wind tunnel the natural plasma fluctuation is high enough to use this method. Figure A7.16 shows the axial velocity distribution at the center line of the plasma jet. The velocity measurements, especially those close to the plasma source, were compared to optical velocity measurements using the Doppler shift effect of a nitrogen NI emission line at 746.83 nm, detected with a Fabry-Perot interferometer described in section B4. In Fig. A7.17 the plasma velocity measurements were taken as input values for calculation of the stagnation pressures by the Bernoulli equation. The calculated results already agreed quite well with measurements of the pressure.

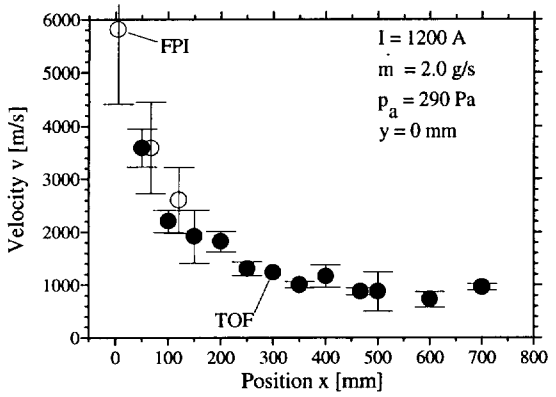


**Fig. A7.16: Axial velocity distribution measured with time of flight probes and Fabry-Perot interferometry**

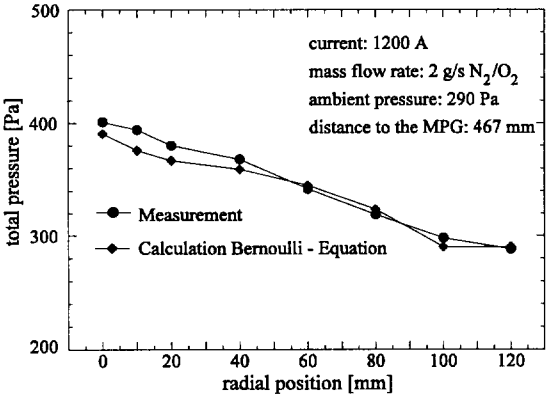


**Fig. A7.17: Total pressure distribution**

# A7.5 Electrostatic Angle Probe

Theoretically formulated and experimentally verified, the ion current to a cylindrical probe in a plasma flow depends strongly on the angle θ between the probe axis and the plasma flow vector [A7.5]. For a probe electrode not aligned with the plasma flow, the kinetic energy of charged particles moving towards the electrode results in a deformation of the potential sheath around the electrode, in which the charged particles are sampled and contribute significantly to the probe current. For electrodes aligned with the plasma flow vector, only those charged particles which enter the potential sheath by random thermal motion like in stationary plasma contribute to the probe current. In general the ion current to a probe at an angle θ with respect to the velocity vector can be described by the following equation:

$$I_i = \sqrt{\frac{kT_e}{2\pi m_i}} n_e e A \frac{2}{\sqrt{\pi}} \exp\left(-\left(\frac{v_i}{v_{th}}\right)^2 \sin^2\theta\right) \cdot \sum_{n=0}^{\infty}\left(\frac{\left(\frac{v_i}{v_{th}}\right)^n \sin^n\theta}{n!}\right) 2\Gamma\left(n+\frac{3}{2}\right) \quad \text{(A7.20)}$$

Here $v_i$ is the directed ion flow velocity, A the probe surface area and $v_{th}$ the thermal velocity given by:

$$v_{th} = \sqrt{\frac{2\,k\,T_i}{m_i}} \quad . \quad \text{(A7.21)}$$

With two different probes this current dependence of the angle is made use of at the IRS: in the case of the rotating electrostatic probe for determining the flow direction and in the case of the so-called electrostatic crossed probe for velocity or ion current measurement.

## A7.5.1 Rotating Electrostatic Probe

The flow direction in a diverging plasma flow can be determined based on Eq. (A7.20) using a cylindrical single probe which is rotated as shown in Fig. A7.18.

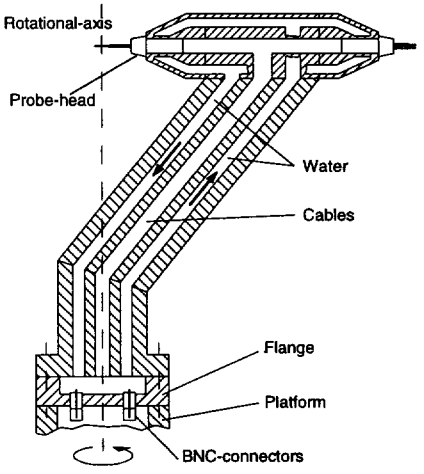


**Fig. A7.18: Rotating probe**

The variation of the probe angle θ with respect to the flow direction causes a change in the current to the probe which has a minimum in the case of a parallel alignment. In Fig. A7.19 the theoretical course of the probe current for constant values of the flow velocity

$v_i$ while varying the probe angle is shown. Likewise the constant values of the electron temperature $T_e$, the mass $m_i$ as well as the charge carrier density $n_e$ and the probe surface A influence the shape of the curve but do not change the location of its minimum. While the probe is being turned, a constant negative probe voltage to the ground is applied so that the probe draws ion saturation current.

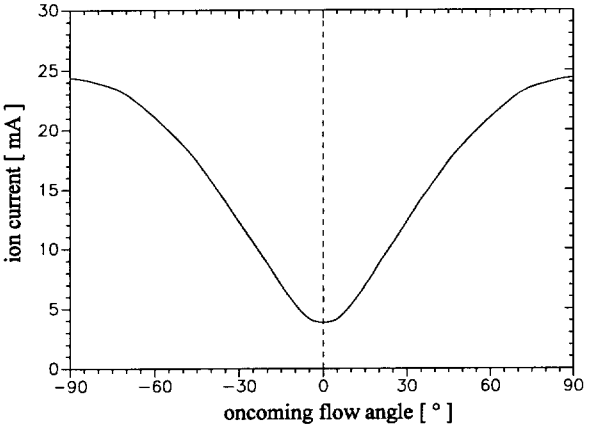


**Fig. A7.19: Calculated ion current to a cylindrical probe depending on the oncoming flow angle θ**

The current as function of the angle θ can be calculated from the constant rotation velocity of the probe. The angle θ which correspnds to the current minimum then gives the flow direction at the measurement position.

### A7.5.2 Electrostatic Crossed Probes

For two single probes with one oriented perpendicular to (sin θ = 1) and one aligned with the flow vector (see Fig. A7.20) the reaction of the two currents becomes:

$$\frac{I_{i\perp}}{I_{i\parallel}} = \frac{2}{\sqrt{\pi}} \exp\left(-\left(\frac{v_i}{v_{th}}\right)^2\right) \sum_{n=0}^{\infty} \left(\frac{(v_i / v_{th})^n}{n!}\right) 2\Gamma\left(n+\frac{3}{2}\right) \quad . \qquad \text{(A7.22)}$$

If the ion temperature and therefore with Eq. (A7.21) the thermal velocity is known, the directed ion velocity $v_i$ can be derived from the current ratio [A7.6]. By knowing the directed velocity of the plasma from time of flight measurements, for example, the ion temperature $T_i$ can be calculated using Eq. (A7.22).

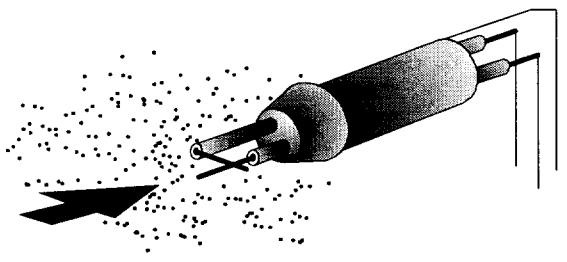

**Fig. A7.20: Measurement head with crossed single probes**

There are some crucial assumptions underlying the crossed probe method. To obtain the correct current ratio, the surface area of both probes must be known or assumed to be equal as in the case of Eq. (A7.22). Especially in chemically reacting air plasmas, a high erosion rate of the perpendicular electrode is observed, which has to be taken into account. Within supersonic flows like in MPG plasmas, the effective area of the perpendicular probe is reduced due to a shock effect. The errors are therefore quite large with this method. They are at about ± 50% of the absolute value for the ion temperature $T_i$ and at about 20% for the ion velocity $v_i$ based on experience at the IRS.

## References

[A7.1] Habiger, H., Auweter-Kurtz, M., "In-vestigation of High-Enthalpy Air Plasma Flow with Electrostatic Probes", Journal of Thermophysics and Heat Transfer, Vol. 12, No. 2, April-June 1998, S. 198-205; also AIAA-96-1864, 31st AIAA Thermophysics Conference, New Orleans, LA, June 1996.

[A7.2] Habiger, H., "Elektrostatische Sonden und Fabry-Perot Interferometrie zur Untersuchung von lichtbogenbeheizten Plasmen für Triebwerksanwendungen und Wiedereintritts-simulation", Dissertation, Universität Stuttgart, 1994.

[A7.3] Langmuir, I., "The Collected Works of Irving Langmuir", ed. by C. Suits, Pergamon Press Inc., New York 1961.

[A7.4] Chen, S.L., Sekiguchi, T., "Instantaneous Direct-Display System of Plasma Parameters by Means of Triple-Probe", Journal of Applied Physics, Vol. 36/8, 2363, August 1965.

[A7.5] Kanal, M., "Theory of Current Collection of Moving Cylindrical Probes", Journal of Applied Physics, Vol. 35, No. 6, June 1964, p. 1967.

[A7.6] Poisant, G., Dudeck, M., "Velocity Profiles in a Rarefied Argon Plasma Stream by Crossed Electrostatic Probes", Journal of Applied Physics, Vol. 58, No. 6, Sept. 1985.

# A8 Mass Spectrometer Probes

Mass spectrometry allows the particle densities and the energy distributions of the neutrons and ions in a free stream plasma to be determined and is used to determine the plasma flow composition [A8.1, A8.2] as well as to investigate the erosion behavior [A8.3, A8.4] and catalytic effects [A8.5, A8.6] of heat shield materials in the PWK plasma flows.

The mass spectrometer used at the IRS is based on a VG Quadrupole [A8.7] SXP300/CMA500 and consists of an open electron impact ion source, a cylindrical mirror energy analyzer (CMA, 0 - 50 eV), a triple filter quadrupole (0 - 300 amu) and a channeltron (see Fig. A8.1). In front of the ion source an ion transfer optic (ITO) is installed, a small aperture lens, with which external ions can be focused into the CMA while the ion source is switched off. In the case where neutrals are detected, a reflecting potential for

positive ions is applied to the ITO and the ion source is switched on. Thus, mass scans at a constant energy level and energy scans at a constant mass can be carried out for neutral as well as ionized plasma particles [A8.8].

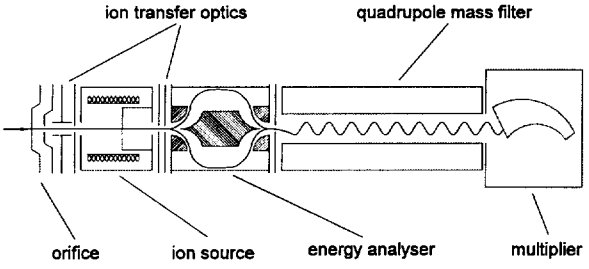


**Fig. A8.1: Set-up of the mass spectrometer**

The mass spectrometer is situated inside the vacuum chamber of the plasma wind tunnel (see Fig. A8.2). Therefore, the whole spectrometer is protected by a stainless steel housing and a water-cooled copper heat shield against the high heat loads and the erosive environment. All equipment is placed outside the vacuum chamber, i.e. the electrical support is made through a flexible tube under atmospheric pressure while the vacuum support is done with a CF100 bellow, which also serves the mobility of the spectrometer.

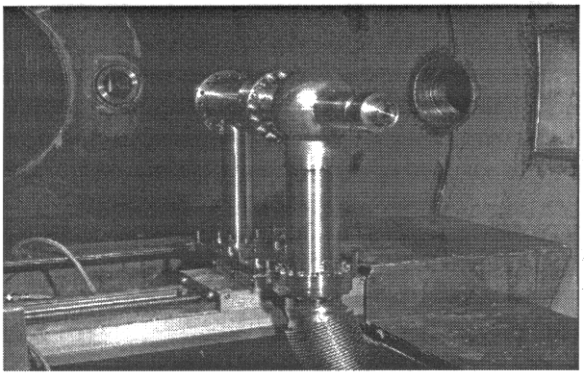

**Fig. A8.2: Mass spectrometer probe in PWK 1**

### One-Stage System

The spectrometer head MS-1 is shown in Fig. A8.3. This one-stage configuration is used to determine the plasma composition at low pressures. The orifice opening (diameter 100 µm, length 100 µm) is drilled into a tungsten plate (diameter 39 mm, thickness 4 mm) with an excimer laser. This plate is cooled by a special cooling body. The spectrometer head is electrically insulated from the rest of the housing, thus the orifice is floatable. In case of high pressures (> 100 Pa) a tungsten foil instead of the tungsten plate is used yielding again a length to diameter ratio for the orifice of L/d = 1 for all measurements (opening diameter 40 µm). The orifice opening also serves as a one-staged differential pumping system.

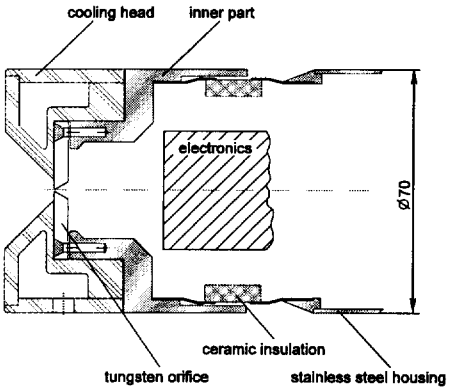


**Fig. A8.3: Set-up of the spectrometer head with orifice opening**

The ITO is placed 32 mm behind the orifice opening. Therefore, long paths inside the spectrometer leading to particle losses are avoided.

For calibration purposes a special test stand has been built at the IRS [A8.9]. The spectrometer was calibrated with neutrals, external atoms and external ions to show the function and accuracy of the CMA for energy analysis, the relative sensitivities of the spectrometer for different masses and to demonstrate the influence of the orifice opening on the sampling of atoms and ions as well as the influence of a space charge sheath in front of the orifice on the measured ion energies [A8.2].

The CMA was shown to measure with an error of ± 0.5 eV in the relevant energy region of 0 - 50 eV. The normal fluctuation of the signal within an energy scan of a neutral particle is around 10%. In contrast it was observed that for plasma ions, which have a very high intensity (e.g. $N^+$ with up to $10^6$ counts/s), these fluctuations can increase to 20%. The mass resolution of the quadrupole is set to $\Delta m/m = 1$, i.e. neighbored masses like water (m = 17, 18) can be resolved, but not that of certain molecules like $N_2$ and CO (m = 28). To distinguish between molecules with the same mass number and between particles which were produced inside the plasma and enter the spectrometer and those which were produced inside the ion source, the particles' ionization potentials can be used [A8.10]. Therefore, the electron impact energy of the ion source was lowered from 70 eV to 17 eV. Here, dissociation of a molecule, e.g. $O_2$, and subsequent ionization of the fragment, O, is not possible. Thus, O atoms detected inside the plasma jet at this electron energy can be attributed entirely to the plasma. Additionally, a reference spectrum of the residual gas inside the spectrometer can easily be subtracted from the data measured inside the plasma jet.

As a typical result, the composition of a nitrogen plasma at a stagnation pressure of 130 Pa is shown in Fig. A8.4.

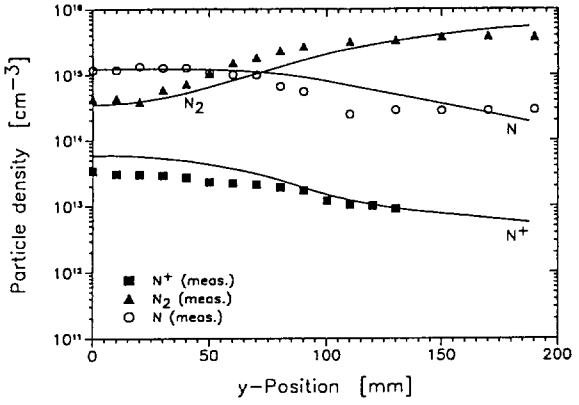


**Fig. A8.4: Comparison of mass spectrometric data and results of the numerical simulation of the 130 Pa test case [A8.6]**

One-stage configurations of different shapes were used for the investigation of catalytic effects [A8.6]. They allow operation at different surface temperatures and with different coatings of the orifice region. In Fig. A8.5 the distribution of nitric oxide with different coatings and configurations is shown as an example.

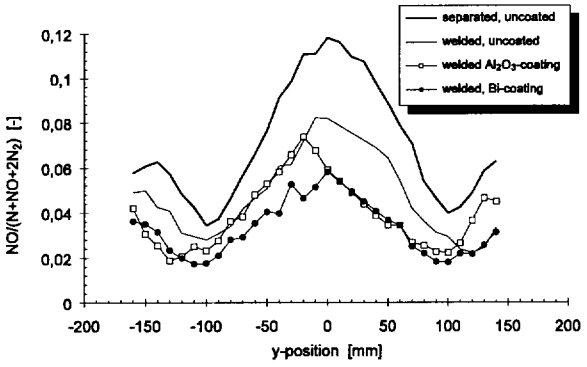


**Fig. A8.5: Distribution of nitric oxide with different cooling heads and coatings in air plasma**

### Two-Stage System

For measurements at higher ambient pressures, a two-staged system MS-II was designed for pressures up to 1 kPa [A8.5] which is shown in Fig. A8.6.

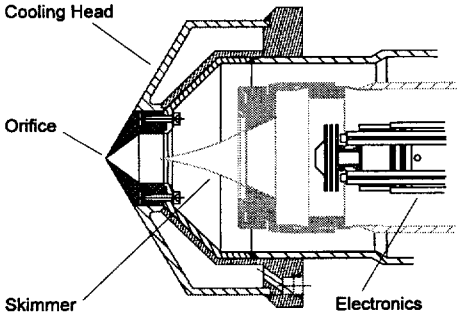


**Fig. A8.6: Two-stage mass spectrometer inlet system**

The inlet system was built with an additional pumping stage between the tungsten orifice and the spectrometer housing. With this two-stage design it was possible to increase the orifice diameter to 400 µm. The second stage is equipped with a nickel skimmer of 100 µm orifice diameter and a total wedge angle of 35°. Between the orifice and the skimmer a pressure of 0.01 - 1 Pa is achieved. According to the investigation of Pertel [A8.11], due to interactions with the residual gas molecules, the supersonic free jet generated from the orifice is enclosed by a shock barrel at the side and by a normal shock (Mach disk) at the front of the jet. To avoid changes of the chemical composition of the extracted plasma jet, it is absolutely vital that the tip of the skimmer be placed at a distance from the orifice smaller than the distance of the Mach disk $X_M$. Ashkenas and Sherman [A8.12] showed that this axial distance is given by

$$x_M = 0.67 \sqrt{\frac{p_0}{p_1}}\, d \quad . \qquad \text{(A8.1)}$$

For a chosen orifice diameter d and a total pressure of 290 Pa, for example, the equation above states that the orifice to skimmer distance must be less than 12 mm. The MS-II configuration was used for catalytic investigations with different orifice materials [A8.6]. In Fig. A8.7, the ratio of $NO/N_2$ is shown with a tungsten and an SiC orifice, respectively.

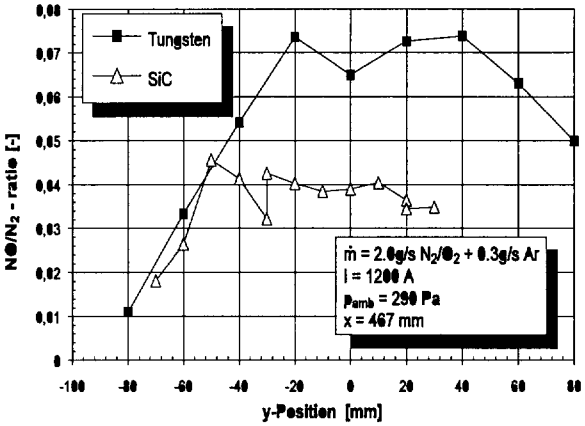


**Fig. A8.7: $NO/N_2$-ratio measured with a tungsten and a SiC-orifice, respectively**

### Configuration for Material Investigation

The third configuration of MS-III (Fig. A8.8) was built to examine the erosion behavior of ceramic heat shield materials. For this purpose, the material sample has to be arranged uncooled just in front of the spectrometer orifice [A8.13, A8.14]. The erosion products are extracted by the same pinhole diameters as in the MS-I configuration.

This configuration has been used for the on-line investigation of the erosion behavior of different coatings as well as for the investigation of the passive/active transition of the oxidation of SiC.

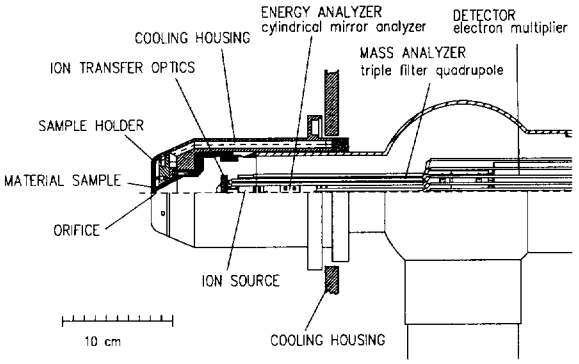


**Fig. A8.8: MS-III configuration**

As an example, Fig. A8.9a shows the time dependence of the ion percentage of mass 28 which represents Si and CO using a coated C/C-SiC sample. The corresponding temperature history of the sample is plotted in Fig. A8.9b. After 15s at a temperature of about 1400°C, a rapid increase of the signal can be seen. A surface temperature of 1670°C was reached after 30 seconds when the steep decrease of the signal occurs.

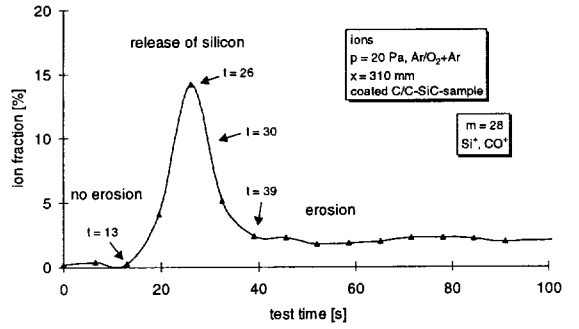


**Fig. A8.9a: Erosion behavior**

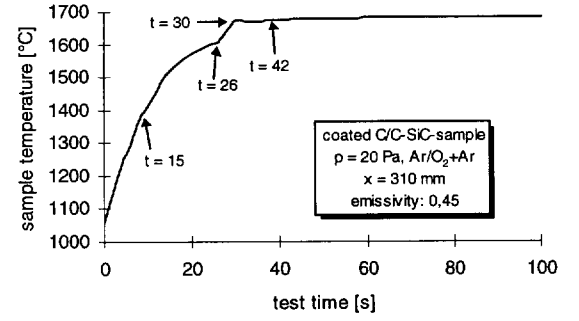


**Fig. A8.9b: Temperature history of a coated C/C-SiC sample**

## References


[A8.1] Schönemann, A., Auweter-Kurtz, M., "Mass Spectrometric Investigation of High Enthalpy Plasma Flows", Journal of Thermophysics and Heat Transfer, Vol. 9, No. 4, Oct.-Dec. 1995, pp. 620-628.

[A8.2] Schönemann, A., "Massenspektrometrie zur Untersuchung lichtbogenbeheizter Plasmen in Niederdruck-Plasmawindkanal", Dissertation, Universität Stuttgart, 1994.

[A8.3] Stöckle, T., Winter, M., Auweter-Kurtz, M., "Simultaneous Spectroscopic and Mass Spectroscopic Investigation of Surface Catalytic Effects in High Enthalpy Gas Flows", AIAA-98-2845, 7th AIAA/ASME Joint Thermophysics and Heat Transfer Conference, Albuquerque, NM, 1998.

[A8.4] Dabalà P., Auweter-Kurtz, M., "Mass Spectrometric Investigations of Erosion Behavior of Thermal Protection Materials", ESA 2nd European Workshop on Thermal Protection Systems, Stuttgart, Germany, October 1995.

[A8.5] Stöckle, T., Auweter-Kurtz, M., Laure, S., "Material Catalysis in High Enthalpy Air Flows", AIAA-96-1904, 31st AIAA Thermophysics Conference, New Orleans, LA, 1996.

[A8.6] Schönemann, A., Auweter-Kurtz, M., "Characterization of Nitrogen and Air Plasma Flows by Mass Spectrometry", ISPC 11, Proceedings of the 11th International Symposium on Plasma Chemistry, Loughborough, UK, 1993, pp. 458-463.

[A8.7] Batey, J.H., "Quadrupole Gas Analyzers", Vacuum 37/8, 1987, pp. 659-668.

[A8.8] Schönemann, A., Auweter-Kurtz, M., Habiger, H., Sleziona, C., Stöckle, T., "Experiment and Numerical Investigation of the Influence of Argon Used a Protection Gas in a Reentry Simulation Device", 28th Thermophysics Conference, AIAA-93-2829, Orlando, FL, 1993.

[A8.9] Auweter-Kurtz, M., "Meßverfahren für strömende Plasmen", IRS-94-M1, Institut für Raumfahrtsysteme der Universität Stuttgart, 1994.

[A8.10] Litzow, M.R., Spalding, T.R., "Mass Spectrometry of Inorganic and Organometallic Compounds", Elsevier Scientific Publishing Co., Amsterdam, 1973, chapter 3.

[A8.11] Pertel, R., "Molecular Beam Sampling of Dynamic Systems", Int. J. Mass Spectrom. Ion Phys., 16, (1975), 53.

[A8.12] Ashkenas, A., Sherman, F.S., "The Structure and Utilization of Supersonic Free Jets in Low Density Wind Tunnels", 4 RGD 84, 1966.

[A8.13] Dabalà, P., Auweter-Kurtz, M., "Mass Spectrometric Erosion Measurements of Ceramic Thermal Protection Materials in High Enthalpy Plasma", AIAA-97-2590, 32nd Thermophysics Conference, Atlanta, GA, 1997.

[A8.14] Dabalà, P., Auweter-Kurtz, M., "Investigation of the Erosion Behavior of Graphite and Silicon Carbide by Mass Spectrometry", 12th International Symposium on Plasma Chemistry, Minneapolis, MN, 1995.


# A9 Radiometer Probe

Radiometer probes are mainly used to determine the radiation heat flux. By using appropriate filters, however, conclusions about the gas composition can also be made. The radiation intensity of the plasma rises with the fourth power of the gas temperature when only the continuum part of the plasma radiation is taken into account. The following is approximately valid for the radiation heat flux. Whereby the degree of emission of the plasma can be smaller than that of the thermal protection material depending on the plasma condition:

$$\dot{q}_{radiation} \sim \varepsilon_{plasma} T^4_{plasma} - \varepsilon_{wall} T^4_{wall} \,. \quad \text{(A9.1)}$$

At plasma temperatures of 10000 K and higher and at pressures of up to 10 kPa, the radiation heat flux can generally no longer be neglected and reaches the same order of magnitude as the convective part. Figure A9.1 shows, for example, calculated heat fluxes for the entry of the Huygens probe into the atmosphere of the Saturn moon Titan.

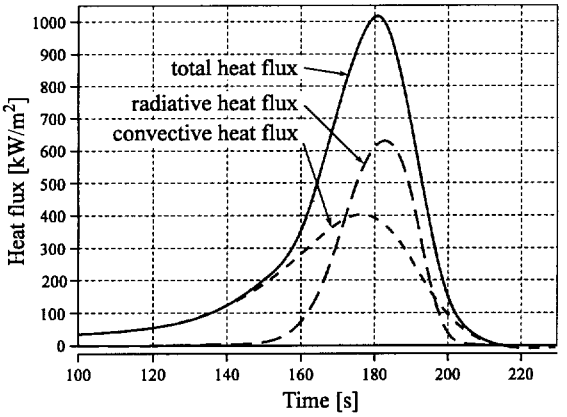


**Fig. A9.1: Calculated heat fluxes for the entry of the Huygens probe into the $N_2/Ar/CH_4$ atmosphere of the Saturn moon Titan (without catalytic effects)**

In ground test facilities a detector can be placed perpendicular to the plasma beam or to the shock front to measure the radiation heat fluxes. The measurement devices are then located outside of the evacuated test chamber and the optics are focused on the test point through windows or light wave conductors. This stipulates long distances to the measurement position along which radiation can be absorbed and the measurable wavelength region remains limited to the transmission area of the windows or the light wave conductors.

The more direct way is to place the radiometer in a probe which is directly exposed to the plasma. For this purpose a radiometer probe, shown in Fig. A9.2, was developed at the IRS. Various glass shields, filters and detectors can still be used as indicated in Fig. A9.2.

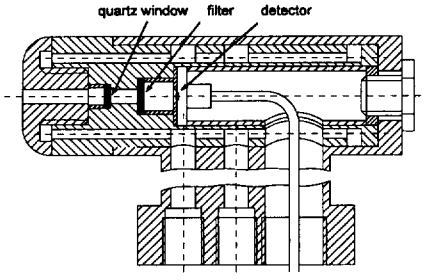


**Fig. A9.2: Radiometer probe with dismountable quartz window and filter**

Adding filters and lenses to protect the detector is possible. However, they greatly limit the usable spectral region as seen in Fig. A9.3. The goal, however, of radiometric measurements is to cover the entire radiation which appears.

However, the detectors may not touch the plasma because they can be damaged by the heat. This can be avoided by mounting the detector deep inside the cooled probe body. The radiation reaches the detector through an optical tunnel. Here a cold, stationary gas column forms because the detector completely closes off the end of the tunnel.

However, this method clearly narrows the visible solid angle. In order to get the entire radiation on the front side of the sample, the probe has to be rotated in the beam while being measured so that the complete solid angle is covered. A hemispherical numerical integration results then in the demanded radiation heat flux at the front opening of the radiometer [A9.1].

The detector and where applicable the filters and lenses must be suited to the task. Special attention must be paid to the choice of the detector. After that the most important characteristics are compiled.

The signal-noise ratio and the noise equivalent power (NEP) are used to assess and compare detectors.

The signal-noise ratio is the ratio between the output signal of a detector and the superordinated noise. It describes the maximum possible exactness of a measurement. With a signal-noise ratio of 100:1, the exactness of the measurement can in no case be better than 1 %.

In a radiometric detector the NEP indicates the radiation power which has to reach the detector in order to create a signal-noise ratio of 1. NEP is also the smallest measurable power which reaches the detector. The following applies:

$$NEP = \frac{I_n}{S} \quad . \qquad \text{(A9.2)}$$

Here $I_n$ is the noise voltage or the noise current of the detector and $S$ is the total sensitivity. Because $S$ depends on the relative spectral intensity distribution of the radiation source, when comparing various NEP values it must be taken into account that they were recorded with the same radiation source under the same conditions. Usually a black radiator with a temperature of 500 K is used.

Additional important characteristics are:

### Linearity

The linearity is one of the most important specifications of a detector for radiometric measurements. Linearity exists when in a certain range the output signal of a detector is exactly proportional to the incoming radiation or when the sensitivity of the detector does not depend on the incoming power.

### Time constant

The time constant $\tau$ of a detector reports the time that the detector signal requires to reach 63% of the final value after constant radiated power suddenly appears on the detector.

### Total sensitivity of a detector

The total sensitivity of a detector is the ratio between the detector output signal $I$ and the total incoming radiated power $\Phi$ in a certain wavelength region. It is a function of the detector, the radiation source and the transmission from windows and filters on the optical axis of the measurement arrangement. A certain detector has a different total sensitivity for each radiation source:

$$S = \frac{I}{\Phi} = \frac{\int_{\lambda_1}^{\lambda_2} \Phi_{e/\lambda}(\lambda) S_\lambda(\lambda) \tau(\lambda) d\lambda}{\int_{\lambda_1}^{\lambda_2} \Phi_{e/\lambda}(\lambda) d\lambda} \qquad \text{(A9.3)}$$

with:

$\lambda_1, \lambda_2$ = lower or upper boundary wavelength
$S$ = total sensitivity
$I$ = detector output signal
$\Phi$ = total incoming radiation
$\Phi_{e/\lambda}(\lambda)$ = absolute spectral intensity distribution of the radiation source
$S_\lambda(\lambda)$ = spectral sensitivity, known from the calibration
$\tau(\lambda)$ = transmission from windows and filters

Instead of the absolute spectral intensity distribution $\Phi_{e/\lambda}(\lambda)$ the relative or normalized spectral intensity distribution can be used:

$$\phi(\lambda) = \frac{\Phi_{e/\lambda}(\lambda)}{\Phi_{e/\lambda}(\lambda_0)} \quad . \qquad \text{(A9.4)}$$

$\lambda_0$ is here the normalized wavelength.
The radiation heat flux onto a detector surface A can be calculated as:

$$\dot{q}_{Strahlung} = \frac{I}{AS} \quad . \qquad \text{(A9.5)}$$

If in addition the measurement arrangement is divided by the visible solid angle, one obtains the radiation heat flux in [W/(m$^2$sr)].
Figure A9.3 shows several profiles of the radiation heat flux perpendicular to the beam axis at various $N_2/CH_4$ plasma combinations used to simulate the entry of the Huygens probe into Titan's atmosphere.

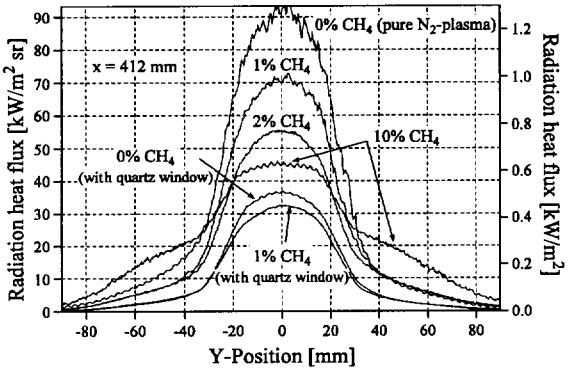


**Fig. A9.3: Radial profiles of various $N_2/CH_4$-plasmas with and without a protective window at a distance of 412 mm to the plasma generator**

## References

[A9.1] Röck, W., "Simulation des Eintritts einer Sonde in die Atmosphäre des Saturnmondes Titan in einem Plasmawindkanal", Dissertation, Universität Stuttgart, 1998.

# B Non-Intrusive Measurement Techniques

Most of the optical measurement techniques are non-intrusive techniques. The pyrometer commonly used for surface temperature measurements in plasma wind tunnels, the emission spectrometry and Fabry-Perot interferometry clearly meet this criterion. Emission spectroscopy enables identification of the heavy particles in the plasma and the determination of their temperatures. Furthermore, it has the potential to be used for density measurements. Fabry-Perot interferometry can be used to determine the plasma velocity and the kinetic temperature of the heavy particles.
All measurement techniques which are based on the investigation of the plasma reaction to light intensity radiated into the plasma technically do not belong to the non-intrusive techniques; they may locally change the plasma state and possibly its composition. However, they are generally included in this category. Absorption spectroscopy, laser induced fluorescence and Raman spectroscopy belong to this group. These methods can all be used to identify the particles as well as to determine particle densities and velocities. Another laser based technique is Thompson Scattering from which temperature and density of the free electrons can be derived.

## B1 Pyrometry

Determining the surface temperature of heat shield materials is of particular interest for the development as well as for the qualification of these materials. The erosion and ablation behavior are very sensitive to the surface temperature within the regarded temperature range. Temperature measurements during the re-entry itself give information about the material characteristics and the re-entry conditions representing the test conditions which should be used in ground test facilities.
Due to the sufficient thickness of the ablation materials and their low heat conductivity, thermo couples can be mounted at different material depths. The surface temperature, the heat flux and the time-dependent erosion can be determined in this way [B1.1].
The situation is different if fiber ceramic materials are used. Due to the wall thinness (between 0.5 up to only a few millimeters) and the high temperatures (between 1000 and 3000 K) the thermo couples cannot be embedded correctly without a risk of damaging the material. Even during the material production, the temperature rises over the bearable temperature of the thermocouples. If the thermo-

couples are mounted on the back side of the heat shield material, the measurement is adulterated and the material can be damaged by carbonization caused by the thermo couples. Therefore for fiber ceramic materials, a non intrusive measurement technique using a pyrometer remains as single solution.

# B1.1 Theoretical Basics

Each body with a surface temperature above absolute zero emits electro-magnetic radiation. Measurement instruments that determine the surface temperature from this thermal radiation are called radiation thermometers or pyrometers. The observed wavelength region reaches from $10^{-7}$ to $10^{-5}$ m, which also covers the narrow region of visible light.
The basic quantities are the *radiant energy flux* $\phi$ given by the emitted energy $dW$ during the time $dt$

$$\phi = \frac{dW}{dt} \qquad \text{(B1.1)}$$

and the *radiant exitance* $M$ which describes the radiation that is emitted by the surface element $dA$ into a solid angle of $2\pi$:

$$M = \frac{d\phi}{dA} \qquad \text{(B1.2)}$$

If the *radiant exitance* is observed at a single wavelength *spectral radiant exitance* $M_\lambda$ is obtained which can be calculated using *Planck's law*:

$$M_{\lambda S} = \frac{2\pi c^2 h}{\lambda^5 \left(e^{\frac{ch}{\lambda kT}} - 1\right)} \qquad \text{(B1.3)}$$

*h*: *Planck's constant* ($6.6256 \cdot 10^{-34}$ Js)
*c*: Speed of light in vacuum ($2.9979\ 10^8$ m/s)

The integration of $M_{\lambda S}$ of a black body over all wavelengths yields, according to the *Stefan Boltzmann law*, the *radiant exitance of a black body* $M_S$

$$M_S = \int_0^\infty M_{\lambda S} d\lambda = \sigma T^4 \qquad \text{(B1.4)}$$

$\sigma$: Stefan Boltzmann constant ($5.669 \cdot 10^{-8}$ $Wm^{-2}K^{-4}$)
The *emissivity* $\varepsilon$ is the ratio of the *radiant exitance* M of any given radiator and the *radiant exitance of a black body.*

$$\varepsilon = \frac{M}{M_S} \qquad \text{(B1.5)}$$

which depends on the temperature, the material itself and the condition on the surface such as roughness. Accordingly, the *spectral emissivity* $\varepsilon(\lambda,T)$ is defined:

$$\varepsilon(\lambda,T) = \frac{M(\lambda,T)}{M_S(\lambda,T)} \qquad \text{(B1.6)}$$

If the emissivity does not depend on T or $\lambda$, the emitting surface is called a *gray body.* Although gray bodies do not exist in reality, the assumption of a gray body gives a good approach for most real bodies.
While the integration of the spectral radiation over the total wavelength regime yields the *Stefan Boltzmann law* the first derivation gives the wavelength $\lambda_{max}$, which defines the wavelength where the emitted spectral radiation at a given temperature $T$ reaches its maximum value.
*Wien's Law* is obtained:

$$\lambda_{max} = \frac{2898}{T} \cdot 10^{-6}\ [m] \qquad \text{(B1.7)}$$

Figure B1.1 shows the spectral radiant exitance of a black body for different temperatures within the important wavelength region. If a non black body is observed, the spectral radiant exitance has to be reduced according to the spectral emissivity of the surface.

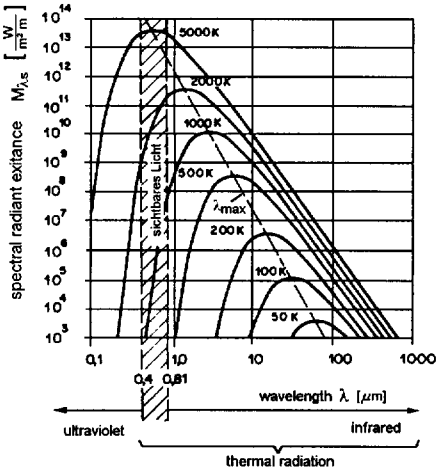


**Fig. B1.1: Spectral radiant exitance of a black body**

The above mentioned radiation laws already show the main problems of radiation thermometry:

- According to the *Stefan Boltzmann law*, the thermally emitted radiation remarkably decreases (proportional to $T^4$) with decreasing temperature.
- At low temperatures, the maximum of radiation is shifted to high wavelengths where disturbing influences on the measurement become high.
- The spectral emissivity of non black bodies depends not only on temperature and wavelength but also on the material itself and the surface structure (mainly the surface roughness) in an often not well-known matter.
- Besides the radiation emitted by the observed surface, disturbing radiation of reflected or transmitted radiation emitted by other radiators can influence the measurement.

If radiation interacts with a surface, reflection, absorption and emission occur. The ratios of absorbed, transmitted and reflected radiant energy fluxes to the incoming radiant energy flux are defined as:

absorptance transmittance reflectance

$$\alpha = \frac{\phi_a}{\phi}, \qquad \tau = \frac{\phi_{tr}}{\phi}, \qquad \rho = \frac{\phi_r}{\phi} \qquad \text{(B1.8)}$$

According to the above-mentioned definitions, the word spectral is added if these quantities refer to monochromatic radiation.

$$\alpha_\lambda = \frac{\phi_{\lambda,a}}{\phi_\lambda}, \qquad \tau_\lambda = \frac{\phi_{\lambda,tr}}{\phi_\lambda}, \qquad \rho_\lambda = \frac{\phi_{\lambda,r}}{\phi_\lambda} \tag{B1.9}$$

They are functions of the wavelength and depend on the material, its surface structure and the temperature. They are coupled by the relation

$$\alpha + \tau + \rho = 1 \qquad \alpha(\lambda) + \tau(\lambda) + \rho(\lambda) = 1 \tag{B1.10}$$

Additionally, according to *Kirchhoff* the emissivity is equal to the absorptance for all bodies:

$$\varepsilon(T,\lambda) = \alpha(T,\lambda) \tag{B1.11}$$

A black body will absorb all incoming radiation and has therefore an absorptance and due to equation (B1.11) also an emissivity of 1.

## B1.2 Measurement Principle

To determine the surface temperature the radiant energy flux emitted by the surface $A_1$ and received by $A_2$ has to be determined (see Fig. B1.2). The surface $A_1$ does not cover the solid angle of $2\pi$, so only a part of the radiant exitance $M$ (or $M_\lambda$, respectively) is received. This part is given by:

$$L = \frac{dM}{d\Omega \cos\vartheta} = \frac{d\left(\frac{d\phi}{dA_1}\right)}{d\Omega \cos\vartheta} = \frac{d^2\phi}{dA_1 d\Omega \cos\vartheta} \tag{B1.12}$$

L is the radiance in the dimension $Wm^{-2}sr^{-1}$. In Fig. B1.3 $A_1$ is the radiating surface which emits a radiance of $L_1$ and $A_2$ the receiving area which is represented by the measurement array of the pyrometer, which transfers the measured radiance into an electrical signal. According to the radiation laws and due to the geometrical relations given by $A_1$, $A_2$, $a$ and $b$, the radiant energy flux $\phi_{1,2}$ in the dimension of $Wsr^{-1}$ is given by:

$$\phi_{1,2} = L_1 A_2 \frac{A_3}{a^2} \tag{B1.13}$$

Normally, area $A_3$ is given by an iris which is part of the optical path inside the pyrometer. The values $A_2$, $A_3$ and $a$ are hardware parameters of the pyrometer and remain constant within the measurement. Therefore, the measured signal becomes independent of the distance to the measured surface $b$ and is a function of constructive parameters of the pyrometer and of the radiance $L_1$ emitted by the measured surface. Often a lens system which also acts like an iris is added to the optical setup to measure small areas in large distances to the pyrometer. According to the optical laws, the independence of the measured signal from the distance to the measured object remains valid.

Usually imaging factors between 10 and 100 are used which means that the measured spot on a surface at a distance of 1 m has a diameter of 10 cm or 1 cm.

With *linear pyrometers*, the measured signal is proportional to the radiance seen by the pyrometer and therefore also to that emitted by the measured surface. There are several classes of pyrometers which differ mainly in the evaluation of the measured signals [B1.1].

A *monochromatic radiation thermometer* measures only radiation within a narrow wavelength region (in effect at one wavelength), a *spectral-band radiation thermometer* measures within a much broader wavelength region while a *wideband radiation thermometer* (sometimes also called *total radiation thermometer* ) is able to detect more than 90 % of the emitted radiation by choosing suitable optics and detectors.

The *radiation ratio thermometer* compares the spectral distribution of the measured radiation with that of a black body. The best known type is the *two color pyrometer*, which uses the ratio of two spectral radiances measured at different wavelengths to determine the true temperature.

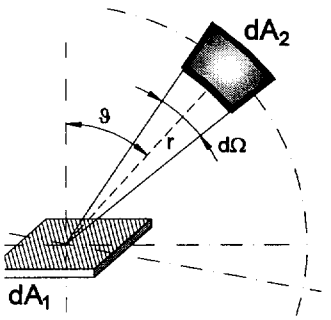


**Fig. B1.2: Geometrical relations**

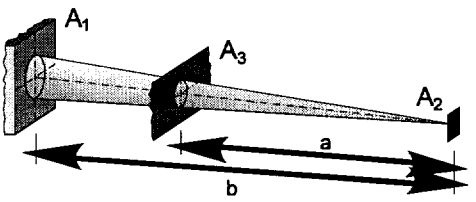


**Fig. B1.3: Measurement principle of a pyrometer**

To obtain temperature distributions on the surface of a sample, an image can be taken using a CID-camera. The same measurement method was used to determine the temperature distribution on the surface of the cathode of a MPD plasma generator [B1.2]. Similar to normal pyrometric measurements, the radiation emitted by a probe body is detected and evaluated. The main difference is the measurement of a whole array of detector elements which offers, in combination with different lens systems, a wide range of spatial variations.

With the camera, a kind of black and white image is obtained and read into a computer using a video adapter. The typical dynamic resolution of 8 bit offers different gray values from 0 (black) up to 255 (white). The spectral sensitivity of the detector elements limits the usable wavelength range from the visible up to the close infrared where it is possible to limit the radiation with suitable wavelength filters to enable a temperature determination. For this purpose, the camera has to be calibrated by a measurement of a black body radiator at different temperatures. So, different gray-levels can be transferred into temperature values.

# B1.3 Determination of the True Temperature

The measured radiant energy flux $\phi_m$ is a combination of the desired radiation $\phi_e$ emitted by the surface of the object of interest, of radiation which originates from the surrounding walls $\phi_S$ and is partly reflected at the surface and partly transmitted by the body as shown in Fig. B1.4.

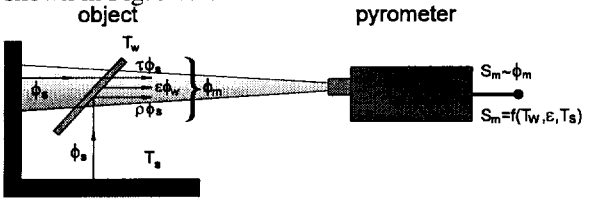


**Fig. B1.4: Experimental setup**

$\phi_e$ can be written as the radiation of a black body $\phi_w$ at the same temperature reduced by the emissivity $\varepsilon$ of the measured surface. The disturbing radiation of the surroundings $\phi_s$ is to be multiplied with the factors $\rho$ and $\tau$ to obtain the reflected and the transmitted radiation, respectively. For the measured radiant energy flux the equation

$$\phi_m = \varepsilon\phi_W + \rho\phi_S + \tau\phi_S \qquad \text{(B1.14)}$$

is valid. According to equation (B1.10), the sum of emissivity, reflectivity and transmission has to be 1. Thus follows:

$$\phi_m = \varepsilon\phi_W + (1-\varepsilon)\phi_S \qquad \text{(B1.15)}$$

According to equations (B1.3), (B1.4) and (B1.12) radiances can be calculated from the radiant energy fluxes and so, between the radiance $L_m$ and the temperature $T_m$ the relation

$$L_m = \int_{\lambda_1}^{\lambda_2} \frac{2\pi c^2 h R(\lambda) d\lambda}{\Omega_0 \pi \lambda^5 \left[\exp\left(\frac{hc}{k\lambda T_m}\right) - 1\right]} \qquad \text{(B1.16)}$$

can be obtained. $R(\lambda)$ is the relative spectral sensitivity of all optical components of the setup and can be regarded as remaining constant between $\lambda_1$ and $\lambda_2$.

Substituting the radiant energy fluxes with the radiation densities and assuming black body radiation for the wall emission to allow the usage of Planck's Law, one gets for a *monochromatic radiation thermometer* an equation to determine the true temperature $T_w$ for a measured temperature $T_m$:

$$T_W = \frac{1}{-\frac{\lambda k}{ch}\ln\left[\exp\left(-\frac{ch}{\lambda k}T_m\right) - (1-\varepsilon)\exp\left(-\frac{ch}{\lambda k}T_S\right)\right] + \frac{\lambda k}{ch}\ln\varepsilon} \qquad \text{(B1.17)}$$

The same procedure for a called *total radiation thermometer* yields:

$$T_W = \frac{T_m}{\sqrt[4]{\varepsilon}} \sqrt[4]{1-(1-\varepsilon)\left(\frac{T_S}{T_m}\right)^4} \qquad \text{(B1.18)}$$

In reality, the temperature of the surrounding $T_S$ is often clearly below the temperature which should be measured.

In this case, the equations can be simplified to:

$$T_W = \frac{1}{\frac{1}{T_m} + \frac{\lambda k}{ch}\ln\varepsilon} \quad \text{and} \quad T_W = \frac{T_m}{\sqrt[4]{\varepsilon}} \qquad \text{(B1.19)}$$

Obviously, the agreement between the displayed temperature $T_m$ with the true temperature $T_w$ is better the lower the wavelength used for the measurement and the closer the emissivity is to 1. Generally, the displayed temperature is lower than the true temperature. Furthermore, the influence of the emissivity becomes weaker with a decreasing difference between the temperatures of the measurement object itself and the surroundings.

With a *spectral-band pyrometer* the same equations as with a *monochromatic radiation thermometer* are valid if $\lambda$ is replaced by a characteristic wavelength at which the main part of the radiation is measured.

One important uncertainty is a result of requiring the emissivity to determine the temperature (see Fig. B1.5). One certain exception is given by the *two color pyrometer*. With this instrument, the ratio of the spectral radiation densities at two different wavelengths $\lambda_1$ and $\lambda_2$ is determined. The measured signal can be written as:

$$S_m = \frac{L_{m1}}{L_{m2}} = \frac{\varepsilon_1 L_{W1} + (1-\varepsilon_1)L_{S1}}{\varepsilon_2 L_{W2} + (1-\varepsilon_2)L_{S2}} \qquad \text{(B1.20)}$$

Figure B1.5 shows the spectral radiation densities $L_{m1}$ and $L_{m2}$ at the wavelengths $\lambda_1$ and $\lambda_2$. Similar to the *total radiation thermometer* $T_m$ is determined from $S_m$. *two color pyrometers* are used when $T_m \gg T_S$.

Under this assumption, the true temperature can be calculated from:

$$T_W = \frac{1}{\frac{1}{T_m} - \frac{k}{hc}\frac{\lambda_1 - \lambda_2}{\lambda_1\lambda_2}\ln\frac{\varepsilon_1}{\varepsilon_2}} \qquad \text{(B1.21)}$$

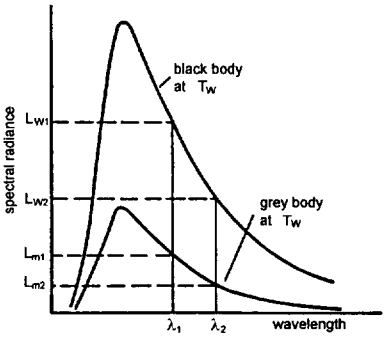


**Fig. B1.5: Description of the ratio pyrometry**

Under the assumption of a common emissivity at both wavelengths, the above equation can be reduced to $T_W = T_m$, which means that the measured temperature equals the true temperature with no need for any information about the quantitative value of the emissivity.

In reality, this assumption is rarely valid. Especially with metallic surfaces, $\varepsilon$ decreases with a rising wavelength (see table B1.1). With ceramic materials, the situation is worse because often not even a steady function of the wavelength can be given. The measured temperature is too high and $T_m$ has to be corrected according to equation (B1.22) to obtain $T_W$. Again, this requires the knowledge of at least the

qualitative course of the emissivity with a rising wavelength.
The possibility that the measured temperature can be higher than the true temperature is significant for *radiation ratio thermometer* because *linear pyrometers* typically show a temperature lower than the true temperature.

## B1.4 Emissivity

As shown in the previous section, the temperature measurement with pyrometers can only be correct if the emissivity of the surface is known. ε depends on many different factors such as wavelength, temperature and surface structure and has to be determined experimentally. For this purpose, a hole is drilled into a probe body and the true temperature is determined using thermo couples. The emissivity can be determined by a comparison with for example a pyrometrically measured temperature. Table B1.1 shows the emissivity of different metals.
Ceramic materials also show a wavelength dependent emissivity. Exemplarily, the ε(λ)-distribution of silicon carbide (SiC) at different temperatures is shown in Fig. B1.6.

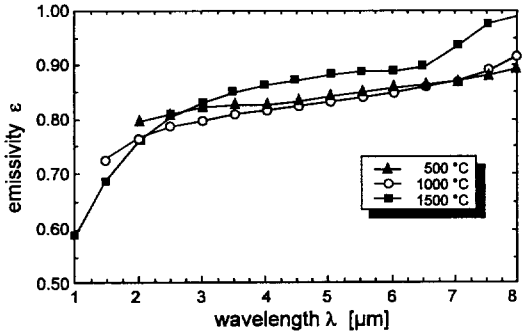


**Fig. B1.6: Emissivity of SiC as a function of wavelength and temperature**

Uncertainties in determining the emissivity cause errors in the transformation of the measured temperature into the true temperature which can rise up to some hundred K. Figure B1.7 shows the difference ΔT of a temperature $T_m$ determined by a spectral pyrometer and the true temperature $T_W$ for different emissivities at a wavelength of λ = 0.65 nm.

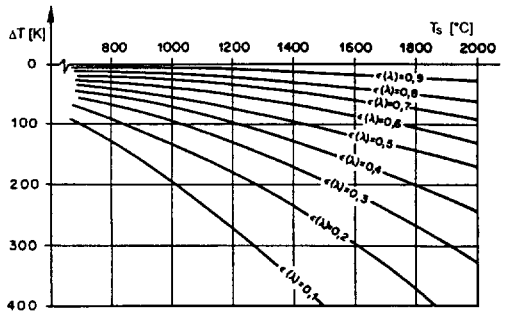


**Fig. B1.7: Difference between measured and true temperature for various emissivities**

## B1.5 Calibration Procedure

For calibration purposes a black body source is available at the IRS. The source which is shown in Fig. B.1.8 consists of an electrically heated graphite radiator with a cylindrical cavity. To approximate the black body, the cavity has a large length-to-diameter ratio and the cavity walls are designed to maintain an isothermal profile. This temperature uniformity is achieved by a variable heat source distribution which is realized by varying the cavity wall thickness. The outline of the graphite rod was therefore calculated using a numerical procedure [B1.3].

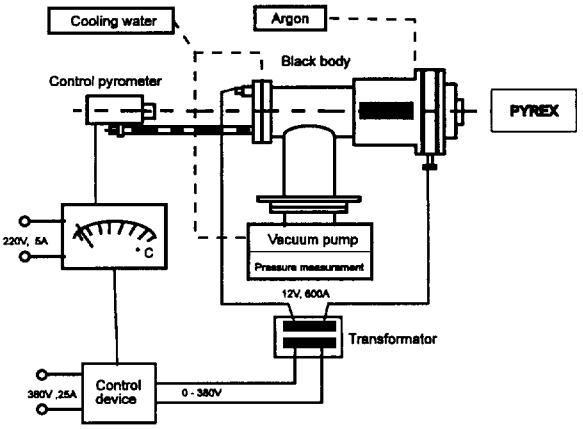


**Fig. B1.8: Schematic view of the IRS black body**

In order to provide high accuracy, three different geometries for three different temperature ranges are available. The black body's second radiation outlet is used for the calibration of pyrometers. The black body's temperature is varied using the control pyrometer; temperature and photo current are measured simultaneously. Figure B.1.9 shows a typical result of such a calibration measurement for the system (see part C).

| metal | temperature [K] | ε at λ = 540 nm | ε at λ = 660 nm |
|---|---|---|---|
| iron | 1300 / 1600 / 2000 | - | 0.39 / 0.37 / 0.35 |
| gold | 1000 / 1300 / 1600 | 0.41 / 0.44 / 0.40 | 0.11 / 0.16 / 0.21 |
| copper | 1000 / 1300 / 1600 | 0.40 / 0.40 / 0.38 | 0.11 / 0.11 / 0.15 |
| molybdenum | 1000 / 1500 / 2000 | 0.44 / 0.42 / 0.41 | 0.39 / 0.38 / 0.36 |
| nickel | 1000 / 1300 / 1600 | 0.42 / 0.42 / 0.42 | 0.38 / 0.38 / 0.38 |
| platinum | 1000 / 1300 / 1600 | 0.32 / 0.32 / 0.33 | 0.29 / 0.30 / 0.30 |

**Table B1.1: Spectral emissivity of different metals**

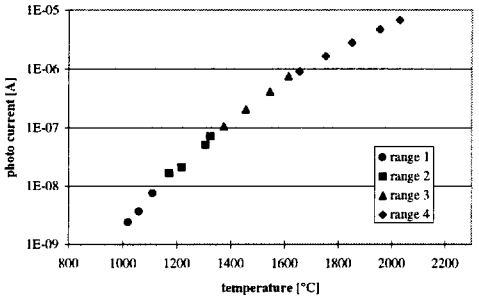


**Fig. B1.9: PYREX-LD photo current vs. black body temperature**

A photo current line versus the measured temperature is obtained. This photo current calibration curve is then used to calculate the temperature data. Within each of the four measuring ranges, the photo current signal is linear to the temperature with the measured radiance of the material as the only necessary input signal. The advantage of this linearity is that any disturbances as well as changes of the emission coefficient $\varepsilon$ can be taken into account by reprocessing the temperature data.

# B1.6 Pyrometers for Plasma Wind Tunnel Applications

The pyrometers in use at the IRS are listed in Table B1.2. The measurement head TMR85L is used for investigations of cathodes for the plasma devices. All other pyrometers are used in the plasma wind tunnels for material testing. Furthermore, the measurement head TMR95 is used for investigations at comparatively low temperatures between 150 °C and 650 °C. With the TMR105 the pyrometrical determination of surface temperatures of materials with high transmittance in the visible wavelength range such as $SiO_2$ is possible.

The first five instruments in Table B1.2 show a non-linear characteristic. The main disadvantage can be seen in the difficulty to extract influences of disturbing radiation such as reflected cathode radiation or plasma emission from the measured signal. Generally, it is almost impossible to perform such an extraction if some of the influences show up after the measurement or if a quantization of these effects is only possible afterwards. Also a wrong emissivity or a change in emissivity during the test can hardly be covered by these instruments.

The results of linear pyrometers as the better choice in this case can also be corrected after the measurement due to the direct proportionality of the measured signal to the spectral radiance. Thus, the linear pyrometer LP2-80/20 [B1.4] as shown in Fig. B.1.10 was optimized for the application to problems within the plasma wind tunnel investigations [B1.5]. One feature is the possibility to use different filter combinations with respect to the plasma radiation.

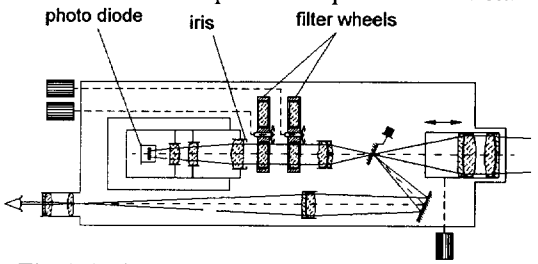


**Fig. B1.10: The linear pyrometer LP2-80/20**

Based on the good results obtained with the LP2-80/20, a miniaturized linear pyrometer called MP1 was designed and qualified at the IRS [B1.5]. This pyrometer is integrated into the sample support system as shown in Fig. B1.11. On the back of the sample, the temperature measurement is neither influenced by the plasma jet nor by possible changes in emissivity on the front during the test. The PYREX-pyrometer which is described in part C is a flight version of the MP1 [B1.6].

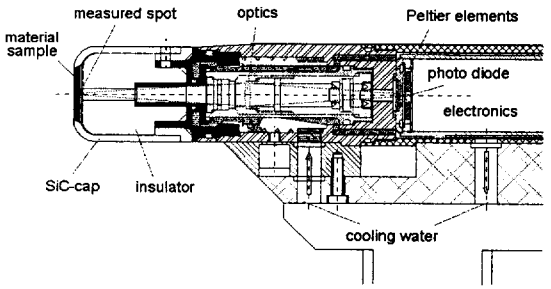


**Fig. B1. 11: Miniaturized pyrometer MP1**

| type | wavelength | measurement range [°C] | purpose |
|---|---|---|---|
| 1) spectral band pyrometers | | | |
| TMR85EA | 900 nm | 610 - 3050 | cathodes of electrical thrusters |
| TMR95EA | 1.5-2.6 µm | 150 - 650 | material tests in the PWK<br>electrode investigation with electrical thrusters |
| TMR105 | 7 - 7.5 µm | 800 - 2000 | material tests in the PWK |
| TMR85H | 900 nm | 610 - 2420 | material tests in the PWK<br>control of black body temperature |
| 2) linear pyrometers | | | |
| LP2-80/20 | 9 diff. wavelengths 560 - 960 nm | 800 - 3000 | precision measurements |
| MP1 | 630 nm | 1000 - 1900 | material tests in the PWK |
| PYREX | 630 nm | 1200 - 3000 | material tests in the PWK / reentry experiments |
| 3) CID camera | | | |
| CID | | 1000 - 3400 | surface temperature distributions |

**Table B1.2: Various pyrometers at the IRS**

## References


[B1.1] Auweter-Kurtz, M., Burkhardt, J., Fertig, M., Frühauf, H.-H., Habiger, H., Jahn, G., Messerschmid, E., Schöttle,U., "Flugdatenauswertung der MIRKA-Experimente HEATIN und PYREX", DGLR-JT98-203, Bremen, DGLR-Jahrestagung 1998.

[B1.2] DeWitt, D. P. and Nutter, G. D., "Theory and Practice of Radiation Thermometry", J. Wiley, New York, 1988.

[B1.3] Winter, M., Auweter-Kurtz, M. Kurtz, H.L. and Sleziona, P.C., "Evaluation of Cathode Temperature Distribution in a Cylindrical MPD Thruster", Proceedings of the 24th International Electric Propulsilon Conference, Moscow, Russia, September 1995.

[B1.4] Groll, M. and Neuer G., "A New Graphite Cavity Radiator as Blackbody for High Temperatures", in: Murray, H.P.( ed. ): "Temperature, its Measurement and Control in Science and Industry - Part 1", Vol.4; Instrument Society of America, Pittsburgh, 1971.

[B1.5] Schreiber, E., Neuer, G., Wörner, B., "Performance Tests with a Standardpyrometer", Proceedings of the Fourth Symposium on Temperature and Thermal Measurement in industry and Science, Helsinki, September 1990, pp. 292-305.

[B1.6] Loesener, O. R., "Pyrometrische Temperaturmessungen an Oberflächen von Hitzeschutzkeramiken im Plasmawindkanal", Dissertation am Institut für Raumfahrtsysteme, 1993 in: Fortschrittsberichte VDI, Reihe 6: Energieerzeugung, Nr. 294, VDI Verlag, Düsseldorf, 1993.

[B1.7] Habiger, H., Auweter-Kurtz, M., Früholz, H., Herdrich, G., "PYREX - Pyrometric Temperature Measurement on the Ceramic TPS of the Re-Entry Capsule MIRKA", 3rd European Workshop on Thermal Protection Systems, ESTEC, Noordwijk, The Netherlands, March 1998.


# B2 Emission Spectroscopy

Emission spectroscopy is based on the analysis of the radiation which is emitted by the investigated medium and evaluates the spectral distribution of the obtained radiation. Thus, information about the qualitative and quantitative chemical composition and about different thermodynamic quantities can be acquired.

# B2.1 Theoretical Basics

In gases and plasmas at low pressures which are excited to emit light, the emission is mainly caused by single atoms and molecules. Thus, the properties of the emitted radiation allow conclusions to be drawn about the emitting particles. In this case, radiation occurs mainly at single discrete wavelengths as so-called spectral lines. The number of lines for molecules of one species normally outnumbers the number of lines caused by a certain atom. The resulting intensity distribution as a function of the wavelength is called emission spectrum.
There are several possibilities to excite atoms and molecules to emit radiation:

- In flames, light arcs and sparks, the atoms are excited by collisions due to their high thermal energy.
- In discharges, the excitation is caused by collisions with electrons and ions which possess high kinetic energy due to acceleration processes within an electric field.
- Excitation induced by radiation at short wavelengths such as UV or Röntgen-radiation.

For the first two reasons, the plasma jet within a plasma wind tunnel is already excited which makes emission spectroscopic methods easily applicable.

## B2.1.1 Discrete Energy Levels of Atoms

This section gives an overview of the basic processes for the excitation of atoms. More detailed information is given in [B2.1, B2.2]. The emission and absorption at single lines is explained by the model of *Bohr*, who found that atoms can only exist at discrete energy values which correspond to special orbits of the electrons around the positively charged nucleus (see Fig. B2.1a).

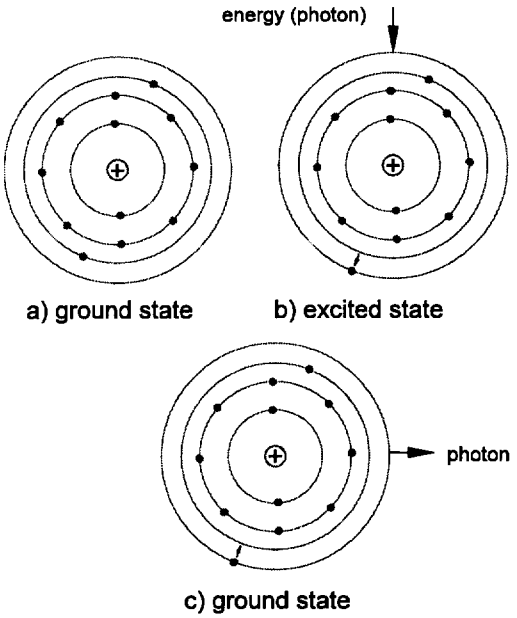


**Fig. B2.1: Model of the magnesium atom**

Energy can be absorbed or emitted if an electron changes its orbit from one energy level to another one. In this case the energy

$$E_{nm} = h\nu = \frac{hc}{\lambda} \qquad \text{(B2.1)}$$

is either absorbed or emitted in form of electromagnetic waves of the frequency $\nu$ which is equivalent to the wavelength $\lambda$. Here, $h$ is *Planck's constant* and $c$ the speed of light in the observed medium. Only transitions between allowed energy values are possible. The allowed energy values are called energy levels and are characterized by the indices $n$ and $m$ in the above equation. This means an atom can only absorb radiation if it passes the transition from the energy level $E_m$ to the higher

energetic level $E_n$ where its electron is at a higher energetic orbit (see Fig. B2.1b). On the other hand, an atom at the state $E_n$ emits radiation if its electron falls down to a lower energetic orbit with the energy $E_m$ (see Fig. B2.1c).
The time during which the electrons stay in the higher energetic state is limited to the life-time of the excited state which is characteristic for each excited state. This time, which is equivalent to the time between absorption and emission, is normally very short, in the range of nanoseconds or below.
An important quantity is the spectral emission coefficient $\varepsilon_\nu$ which is defined as the energy of the radiation per time and solid angle emitted at the frequency $\nu$ by a unity volume. For a spontaneous transition of an excited electron at an energy level $n$ to a lower level $m$, the emission coefficient $\varepsilon_{nm}$ can be calculated as:

$$\varepsilon_{nm} = \frac{1}{4\pi} h\nu_{nm} A_{nm} n_n \qquad \text{(B2.2)}$$

Here, $A_{nm}$ is the *Einstein transition probability* between the excited states $m$ and $n$ while $n_n$ is the number density of the particles in the excited state $n$.
According to equation (B2.1), the transition from the energy level $n$ to a lower level $m$ produces emission of the frequency $\nu$. In reality, the emission occurs within a frequency interval $\delta\nu$. This phenomenon is called line broadening. Therefore, the emission coefficient $\varepsilon_{nm}$ of a spectral line with the linewidth $\delta\nu$ has to be written as:

$$\varepsilon_{nm} = \int_{\nu}^{\nu+\delta\nu} \varepsilon_\nu d\nu \qquad \text{(B2.3)}$$

The different broadening mechanisms are described in section B2.1.2.
The basic mechanisms of atomic radiation can be seen most clearly in the most simple case of the hydrogen atom with only one electron.

### B2.1.1.1 The Optical Spectrum of the Hydrogen Atom

*Kirchhoff* and *Bunsen*, who laid the foundation for spectral analysis, realized already in the middle of the last century that each element emits its own characteristic spectrum. The spectral lines of one species can be sorted into series and are described formally by a so-called series formula. In the most simple case of the hydrogen atom with only one electron, each spectral line fulfills the equation:

$$\frac{1}{\lambda} = R_H \left( \frac{1}{n_1^2} - \frac{1}{n_2^2} \right) \qquad \text{(B2.4)}$$

Here, $R_H$ is the so-called *Rydberg-constant* ($R_H = 2\pi^2 m_e e^4/(h^3 c) = 109677{,}581\ \text{cm}^{-1}$), where the index H stands for hydrogen. $n_1$ and $n_2$ are natural numbers and represent the numbering of the energy levels where $n_1 < n_2$ and $n_1$ is constant within one series.

The emission spectrum of hydrogen consists of the following series:

| | |
|---|---|
| Lyman-Series (UV) | $n_1 = 1 \quad n_2 \geq 2$ |
| Balmer-Series (visible if $n_2<8$) | $n_1 = 2 \quad n_2 \geq 3$ |
| Paschen-Series (infrared) | $n_1 = 3 \quad n_2 \geq 4$ |
| Brackett-Series | $n_1 = 4 \quad n_2 \geq 5$ |
| Pfund-Series | $n_1 = 5 \quad n_2 \geq 6$ |

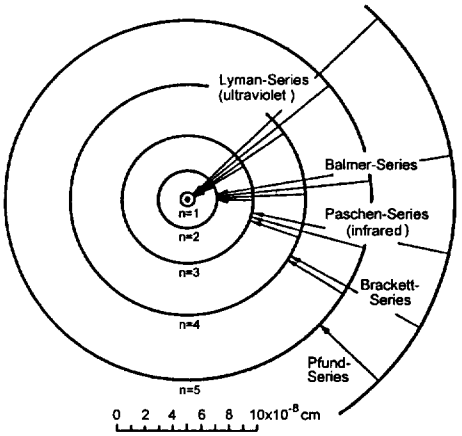


**Fig. B2.2: Bohr model of the hydrogen atom with the first five spectral series**

Figure B2.2 explains the origin of the different series. Normal hydrogen, where all atoms are at the ground level (n=1), can absorb radiation only in the Lyman-series. The absorption at other spectral lines requires the existence of excited states which means that atoms exist where the electron already stays in the levels $n_1 = 2$ or $n_1 = 3$ and so on.

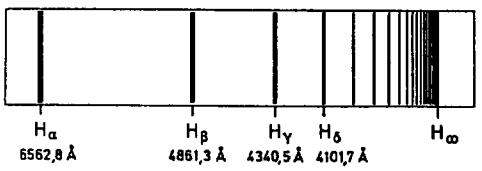


**Fig. B2.3: Balmer-series of hydrogen**

With rising $n_2$ the spectral distance between lines of one series decreases more and more. For $n_2 \rightarrow \infty$ the borders of the series are given by:

$$\lambda_\infty = \frac{n_1^2}{R_H} \qquad \text{(B2.5)}$$

Beyond this border, the spectrum is no longer characterized by single emission lines but by continuous emission. The radiation is now no longer caused by transitions of excited atoms. It originates when free electrons are captured by ions (radiation by recombination) or when ions or electrons are accelerated or decelerated by electric fields. The line emission is also called bound-bound radiation while radiation by recombination is called free-bound. Radiation caused by acceleration and deceleration processes is termed free-free.
If the excited states are highly enough populated, the emission spectrum of hydrogen always contains three characteristic lines in the visible wavelength region at 6563, 4861 and 4340 Å (1Å = $10^{-10}$m = 0.1nm) which

originate from the Balmer-series (compare Fig. B2.3). The strongest of these lines was already discovered by *Ångström* in 1853. Nowadays this line is called $H_\alpha$-line (6563 Å), the others were called $H_\beta$, $H_\gamma$ and so on corresponding to their rising frequency. For atoms other than hydrogen the formulation of analytic series formulas that cover all possible spectral lines becomes rather complicated due to the fact that more than one electron exists.

### B2.1.1.2 The Optical Spectra of Nitrogen and Oxygen

In the case of re-entry investigations, the emissions of nitrogen and oxygen as main components of an air plasma are of particular interest. As mentioned above, the definition of simple analytic series formulas like those for hydrogen is no longer possible. Although a more complicated analytic calculation of single emission lines is still possible, in most cases using values that are tabulated in literature like [B2.3, B2.4] is the better solution. Different numerical codes like NEQAIR [B2.5] or PARADE [B2.6] offer the possibility of computing a complete spectrum. Normally, the number densities of the desired species as well as different temperatures have to be added into the code. The working principle of the code will not be discussed in more detail but Figs. B2.4 and B2.5 show the emission of atomic nitrogen and oxygen and their ions computed with PARADE.

| species | number density [$m^{-3}$] |
|---|---|
| N | $6{,}4\ 10^{20}$ |
| O | $2{,}02\ 10^{20}$ |
| $N^+$ | $1{,}72\ 10^{21}$ |
| $O^+$ | $3{,}16\ 10^{20}$ |

**Table B2.1: Number densities used for PARADE computation**

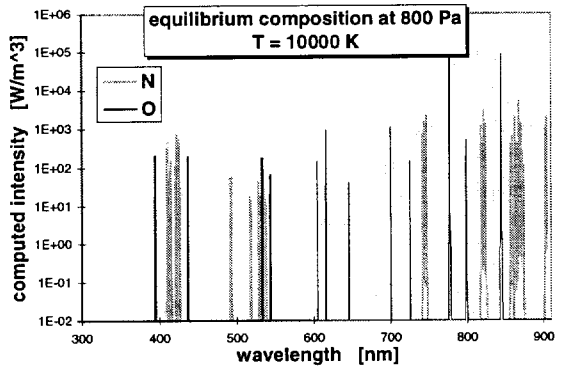


**Fig. B2.4: Emission of neutral atomic nitrogen and oxygen computed by PARADE**

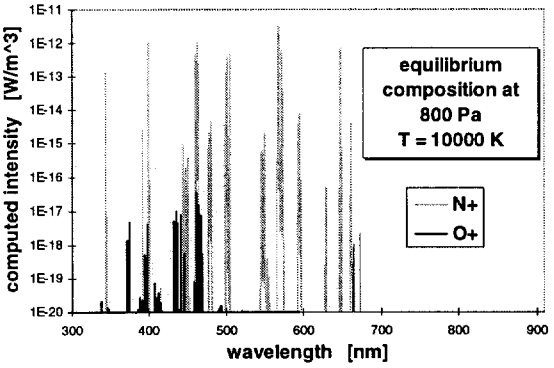


**Fig. B2.5: Emission of ionized atomic nitrogen and oxygen computed by PARADE**

Table B2.1 gives the number densities used for the computation. Although the number densities of the ions are even higher than those of the neutral particles, the computed intensities within the same wavelength region are weaker by factors of about $10^{20}$ and $10^{15}$. This factor shows the influence of the Einstein transition probability.

## B2.1.2 Line Broadening

The *natural line-width* in an almost motionless plasma at a low pressure (which means that collisions between particles are rare) is determined by *Heisenberg's law of uncertainty* and is in the dimension of $10^{-5}$ nm which normally can be neglected in comparison to the other broadening mechanisms.

The most important processes for line-broadening are:

- Doppler effect
- Interaction with other particles (pressure broadening such as resonance, Stark and Van der Waals broadening)
- Zeemann effect caused by disturbing magnetic fields
- Absorption within the plasma
- Contributions of the optical elements

The Zeemann effect gains importance if strong magnetic fields are used e.g. to control the plasma as in fusion reactors. The influence of absorption can be seen if the intensity profile has a local minimum value at the center of the line where the emission is re-absorbed. This effect gains importance at high pressures and at optically thick plasma states. The contributions of the optical elements are mainly caused by chromatic and spherical aberrations of lenses and mirrors. This effect has to be taken into account in the calibration procedure.
The first two effects can be used for diagnostics to determine thermodynamic quantities. Therefore, the Doppler broadening and the pressure broadening (here Stark broadening is the most important process) are discussed in more detail in this section.

### B2.1.2.1 Doppler Broadening

The motion of radiating particles causes a wavelength shifting of the emitted spectral line (Doppler shift). Within a non-flowing plasma, the velocity values and directions of the single particles are statistically distributed. A superposition of the different Doppler shiftings yields a broadened intensity profile. If the Doppler displacement is strong in comparison to the other broadening mechanisms, the translatory temperature of the emitting particles can be determined from the Doppler half width of the emission lines. For this purpose, a high resolution spectrometer is needed. A Fabry Perot interferometer fulfills this requirement (see section B4).

### B2.1.2.2 Broadening by Interaction with Other Particles

Neutral particles, electrons and ions in the plasma surrounding the emitting particles can cause disturbances of the emission which is proportional to the partial pressures of the emitting and disturbing particles. This pressure broadening can be divided into resonance, Stark and Van der Waals broadening. To describe this procedure, the disturbing particles are mostly regarded as classical particles which move in the most simple case on straight lines with the velocity $v$. From a distance $\rho$ to the emitting particle the effect of the disturbing particle can be noticed as illustrated in Fig. B2.6. Therefore, the time during which the disturbance occurs is in the magnitude of

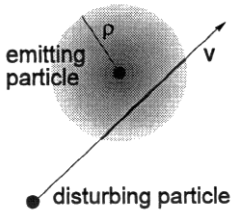


**Fig. B2.6: Illustration of the collision time**

$$\Delta t \approx \frac{\rho}{v} \qquad \text{(B2.6)}$$

If $\Delta t$ is short in comparison to the time between two disturbances (which is normally valid for fast particles such as electrons) the disturbances can be regarded as collisions and interpreted by collision theories. In this case, the emitting particle is regarded as a harmonic oscillator.

If a disturbing particle passes the emitting particle, the phase of the above-mentioned oscillation is changed. A Fourier analysis of the phase-disturbed oscillation gives a dispersion profile with the half width $\Delta\nu_H$ (see Fig. B2.7). The maximum value of this line profile is shifted by $\Delta\nu$ compared with the profile of the undisturbed line with the frequency $\nu_0$. At the regarded plasma states, the half-width is mainly determined by the Stark effect which covers the interaction of charged particles caused by the forces due to their electric field.

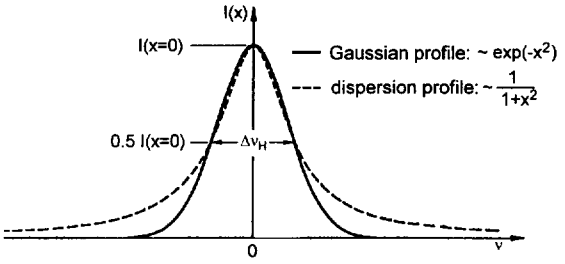


**Fig. B2.7: Gaussian and dispersion profile with the same half width**

In comparison to the emission without disturbing effects caused by an electric field, the emission of atoms in an electric field of the strength $E$ is shifted by the frequency $\Delta\nu$:

$$\Delta\nu(E) = \frac{1}{2\pi} C^* E^2 \qquad \text{(B2.7)}$$

Here, $C^*$ is the so-called Stark effect constant. A disturbing electron in the distance $r$ to the emitting particle produces an electric field at the location of the particle with the strength

$$E = \frac{1}{4\pi\varepsilon_0}\frac{e}{r^2} \qquad \text{(B2.8)}$$

and therefore causes a frequency displacement of the above described oscillator of:

$$\Delta\nu(r) = \frac{1}{2\pi}\left(\frac{e}{4\pi\varepsilon_0}\right)^2 C^* \frac{1}{r^4} = \frac{C_W}{r^4} \qquad \text{(B2.9)}$$

Therefore, the line broadening due to the Stark effect is proportional to $\sim r^{-4}$ with the constant $C_w$. So, the equations for the line displacement $\Delta\nu_V^{ST}$ and the half width $\Delta\nu_H^{ST}$ in a plasma with the electron density $n_e$ and the average thermal velocity $\bar{V}$ can be written as:

$$\Delta\nu_v^{St} = \frac{1}{2\pi} 9.85 C_W^{2/3} \bar{v}^{1/3} n_e$$

$$\Delta\nu_H^{St} = \frac{1}{2\pi} 11.37 C_W^{2/3} \bar{v}^{1/3} n_e \qquad \text{(B2.10)}$$

$$\text{with} \quad v = \sqrt{\frac{8}{\pi} kT\left(\frac{1}{m_e} + \frac{1}{M}\right)}$$

Here, $M$ is the molecular mass of the corresponding ion. In the above equations, only the influence of the electrons on the emitting particles is taken into account. Due to their higher mass and their therefore lower velocity, the influence of the heavy particles can often be neglected. Meanwhile, the simple model as described above has been refined by quantum mechanical considerations of the collision processes but the principal results remain valid.

Due to their large line width, especially the Balmer lines of the hydrogen atom are well-suited to determine the electron density from the line broadening due to the Stark effect. Figure B2.8 shows the $H_\alpha$-line at two different plasma states.

The line width of the Balmer line $H_\beta$ is even stronger than that of the $H_\beta$-line. At an electron density of

$n_e = 10^{23}\,m^{-3}$ and a temperature of $T = 10000$ K the half width of the $H_\beta$-line is 45 Å.

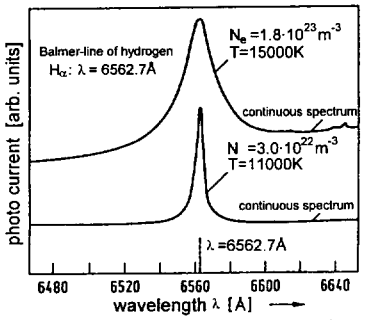


**Fig. B2.8: Line broadening due to the Stark-effect**

For plasmas without hydrogen, determining the electron density from the Stark broadening is often difficult or even impossible because the effects of other broadening mechanisms (especially the effect of Doppler broadening) are stronger than the Stark effect. Sometimes, small amounts of hydrogen can be added to the plasma to enable the determination of the electron density as described above.

## B2.1.3 Energy Levels of the Molecules

In this section, an overview of the basic principles will be given. For more detailed information the corresponding literature such as [B2.7, B2.8] is recommended. As seen above, the energy levels of atoms are defined by the electron orbits around the nucleus. In the case of molecules, there are additional energy levels caused by the degrees of freedom of rotation and vibration. Still, the emission occurs at discrete energies which results in an emission spectrum consisting of single emission lines. But in comparison to the atoms, the number of transitions allowed is much higher and the spectral distance between the single lines is much smaller. A measurement of single lines is only possible with extremely high resolution spectrometers. The wavelength of each emission line is not only a function of the upper and lower electronic states of the transition but also of the upper and lower rotational and vibrational energy levels. In molecular spectroscopy usually the wave number $\tilde{\nu}$ which is the inverse wavelength is used to characterize the single emission lines. The corresponding wave number for a molecular transition is proportional to the total change in energy:

$$\tilde{\nu} = \frac{1}{hc}\left(\Delta E_{el} + \Delta E_{vib} + \Delta E_{rot}\right) \qquad \text{(B2.11)}$$

Here, $\Delta E_{el}$, $\Delta E_{rot}$ and $\Delta E_{vib}$, are the changes in electronic, rotational and vibrational energy, respectively.

The effect of the electronic transition can be reduced to the corresponding energy difference of the upper and lower electronic state and is usually taken from literature such as [B2.8, B2.9]. The degrees of freedom for rotation and vibration can be described by analytical models which allow the calculation of the possible energy levels and the quantum physical interpretation of the obtained spectra.

### B2.1.3.1 Rotational Energy Levels

Figure B2.9 shows a simple model for a two-atomic molecule which is simulated as a dumb-bell. Here, the atoms are regarded as point masses $m_1$ and $m_2$, the connection with the length $r_0$ is regarded as boundless and rigid in a first approach. The molecule rotates around the center of mass $S$. In this system, the rotational energy can be calculated using the equations of classical mechanics:

$$E_{rot} = \frac{1}{2} j\omega^2 \qquad \text{(B2.12)}$$

Here, $j$ is the moment of inertia and $\omega$ the angular velocity of the rotation. For the simple model of the rigid rotation, $j$ becomes:

$$j = m_1 r_1^2 + m_2 r_2^2 \qquad \text{(B2.13)}$$

The assumption that $m_1 = m_2 = m$ and therefore $r_1 = r_2$ which is actually valid for homonuclear molecules results in:

$$j = \frac{m}{2} r_0^2 \qquad \text{(B2.14)}$$

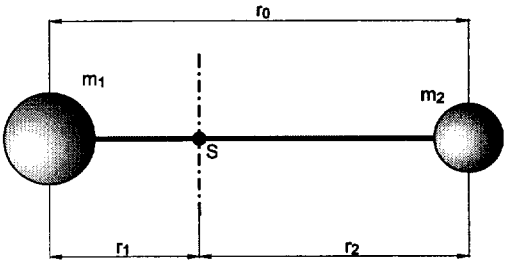


**Fig. B2.9: Molecule as rotating dumb-bell**

Equations of classical mechanics would say that the rotational energy can have any value. But again, in quantum mechanics only discrete energy levels exist. As not explicitly shown here, the solution to the so-called *Schrödinger equation* yields the relation:

$$E_{rot} = \frac{h^2}{8\pi^2 j} J(J+1) \qquad \text{(B2.15)}$$

with J = 0, 1, 2, ...

As already mentioned, $h$ is *Planck's constant* while $J$ is the *rotational quantum number.*

In molecular spectroscopy, the energy terms are usually given in terms of wave numbers which is done by a normalization by $hc$. Therefore, equation (B2.15) is equivalent to:

$$F(J) = \frac{E_{rot}}{hc} = B_e J(J+1) \qquad \text{(B2.16)}$$

The rotational constant $B_e$ is one of the most important constants in molecular spectroscopy. It is inversely proportional to the moment of inertia $j$ and gives for a known atomic mass the bonding length of the molecule which is a very basic piece of

information about the inner construction of the investigated molecule. The normalized rotational energy $F(J)$ is used within the temperature determination procedure of molecular temperatures (compare section B2.2.4).
The selection rules of quantum mechanics only allow transitions with neighboring rotational quantum numbers which means the maximum change in $J$ can be 1 or -1. The resulting series of emission lines are called branches and are named P-, Q- and R-branch. The possible changes in rotational energy become:

P-branch ($\Delta J=1$) $\Delta E_{rot} = \frac{h^2}{8\pi^2 j} 2(J+1)$ (B2.17a)

Q-branch ($\Delta J=0$) $\Delta E_{rot} = 0$ (B2.17b)

R-branch ($\Delta J=-1$) $\Delta E_{rot} = -\frac{h^2}{8\pi^2 j} 2J$ (B2.17c)

If the change in the total angle remains constant within the transition, the Q-branch is not allowed. The contribution of the rotational transition to the wave number of the emission line is given by:

$$\tilde{\nu}_{rot} = \Delta F(J) = \frac{\Delta E_{rot}}{hc} \qquad J = 0,1,2,... \qquad \text{(B2.18)}$$

In the model of the rigid rotating dumb-bell, the wave numbers within one branch increase linearly with a rising quantum number. This results in constant spectral differences between the single rotational lines in terms of wave numbers. In reality, the connection between the two nuclei is not rigid as assumed within the above equations. This yields a deformation of the molecule with rising centrifugal force which can be taken into consideration by implementing a second order correction term yielding the model of a non-rigid rotating dumb-bell. Here, the constant $D_e$ is implemented which considers the extension of the distance between the nuclei with increasing rotational energy. $D_e$ is an experimentally determined constant which varies for different species and for different electronic states. Equation (B2.16) transforms into:

$$F(J) = B_e J(J+1) - D_e[J(J+1)]^2 \qquad \text{(B2.19)}$$

## B2.1.3.2 Vibrational Energy Levels

In addition to the rotation around the center of mass, a vibration of both atoms along the molecular axis is possible. In the most simple way, this vibration can be described as the motion of a reduced mass $\mu$ around an equilibrium position $r_0$ with $\Delta r = r - r_0$. With

$$\mu = \frac{m_1 m_2}{m_1 + m_2} \qquad \text{(B2.20)}$$

and the spring constant $k$ the well-known differential equation of the harmonic oscillator is obtained:

$$\mu \frac{d^2(\Delta r)}{dt^2} + k\Delta r = 0 \qquad \text{(B2.21)}$$

The solution to this equation is an oscillation with the frequency:

$$\nu_{osz} = \frac{1}{2\pi}\sqrt{\frac{k}{\mu}} \qquad \text{(B2.22)}$$

Similar to the model of the rotating dumb-bell, the application of the Schrödinger equation on the harmonic oscillator yields again quantisized vibrational energies. The vibrational energy term becomes:

$$E_{vib}(\upsilon) = h\nu_{osc}\left(\upsilon + \tfrac{1}{2}\right) \qquad \text{(B2.23)}$$

with $\upsilon$=0, 1, 2, ...
Again, a normalization by hc can be done yielding:

$$G(\upsilon) = \frac{E_{vib}(\upsilon)}{hc} = \omega\left(\upsilon + \tfrac{1}{2}\right) \qquad \text{(B2.24)}$$

The energy scheme of a linear harmonic oscillator consists of equi-distant steps $h\nu_{osc}$ with a minimum energy value $h\nu_{osc}/2$. $\upsilon$ is the vibrational quantum number and $\omega$ represents the vibrational frequency
In contradiction to the rotation, transitions between vibrational energy levels with quantum number differences higher than 1 are also allowed. The wave numbers of pure vibrational lines (which means that both upper and lower level belong to the same electronic state and that no change in rotational energy occurs which is equivalent to $\Delta J = =0$) are given by:

$$\tilde{\nu} = \frac{\Delta E_{vib}}{hc} = \frac{\upsilon_1 - \upsilon_2}{c}\nu_{osc} \qquad \text{(B2.25)}$$

From this equation, the distances between the single lines are supposed to be multiples of the ground frequency divided by $c$. Again, this expectation is not fulfilled completely in reality which can be explained by the fact that a molecule has to be seen as a so-called *anharmonic oscillator*.
To illustrate this coherence, the potential curves for both harmonic and anharmonic oscillators are plotted in Fig. B2.10. They show the potential of the forces between the nuclei as a function of the nuclear distance. The quantisized vibrational energy levels $E_{vib}$ are added to the viewgraph.

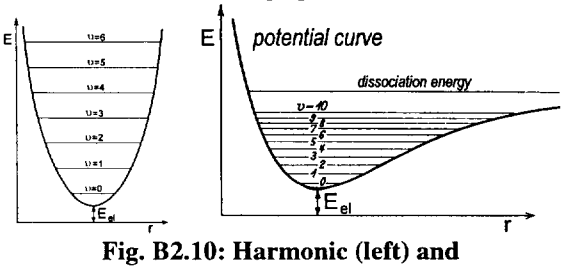


**Fig. B2.10: Harmonic (left) and anharmonic (right) oscillator**

In the case of a harmonic oscillator, the potential curve appears as a symmetrical parabolic function. If one nucleus is regarded as fixed, the other one would oscillate like a ball which rolls along the curve. The points where the energy levels cross the curve are the reversal points of this oscillation.
This model does not agree with reality in two essential points. First, in the simple model there is no theoretical reason that the distance between the nuclei

could not decrease to zero. In reality, this is physically not possible because the electrostatic forces between the two positively charged nuclei would rise very quickly. On the other hand, the potential is not allowed to rise until infinity with increasing distance between the nuclei. The force between the nuclei which is produced by the electrons is only decreasing with rising distance until the molecule becomes dissociated. As can be seen from the potential curves, reality is better represented by the model of the anharmonic oscillator. In this case, the energy levels are no longer equidistant.

## B2.1.4 The Molecular Spectrum

As already mentioned, the molecular emission spectra are based on a superposition of electronic, vibrational and rotational transitions. The wave number of each emission line is given by the total change in energy. From now on, the upper state of a transition is characterized by ´ and the lower state by ´´. Using this nomenclature, equation (B2.11) can be written as:

$$\tilde{\nu} = \Delta T^{el} + \Delta G + \Delta F \qquad \text{(B2.26)}$$

or

$$\tilde{\nu} = T'^{el} - T''^{el} + G'(\upsilon') - G''(\upsilon'') + F'(\upsilon', J') - F''(\upsilon'', J'') \qquad \text{(B2.26b)}$$

with: $T^{el}$ normalized electronic energy
$G(\upsilon)$ normalized vibrational energy
$F(\upsilon J)$ normalized vibrational energy
and $\Delta T^{el} >> \Delta G >> \Delta F$

Within each electronic state, the electronic, rotational and vibrational constants are different and the basic mechanisms described in sections B2.1.3.1 and B2.1.3.2 are coupled. If only the rotational energy changes ($\Delta T^{el} == \Delta G == 0$), the pure rotational spectrum in the far ultrared is obtained with:

$$\tilde{\nu} = +F'(J') - F''(J'') \qquad \text{(B2.27)}$$

If the vibrational energy changes but the electron energy remains unchanged, the rotational vibrational bands in the short ultrared are obtained.

$$\tilde{\nu} = G'(\upsilon') - G''(\upsilon'') + F'(\upsilon', J') - F''(\upsilon'', J'') \qquad \text{(B2.28)}$$

In section B2.1.1.2 the rotational constant $B_e$ was introduced for the model of a rotating dumb-bell. In the case of coupling between vibrational and rotational transitions, the model has to be extended to a rotating oscillator where B is also a function of the vibrational quantum number. Additionally, the bonding length of the molecules differs at different electronic levels. So Be has to be replaced by $B'_{\upsilon'}$ and $B''_{\upsilon''}$ for the upper and lower states of the transition. If the energy terms in equation (B2.26b) which are not a function of the rotational quantum numbers such as the normalized electronic and vibrational energies are combined to a wave number $\tilde{\nu}_0$, the wave numbers of the emission lines for a given electronic and vibrational transition within the different branches can be written as a function of the rotational quantum number:

P-branch ($\Delta J=1 \Rightarrow J'=J, J''=J+1$):

$$\tilde{\nu}_P = \tilde{\nu}_0 + \left(B'_{\upsilon'} - B''_{\upsilon''}\right)J^2 + \left(B'_{\upsilon'} - 3B''_{\upsilon''}\right)j - 2B''_{\upsilon''} \qquad \text{(B2.29a)}$$

Q-branch ($\Delta J=0 \Rightarrow J'=J''=J$):

$$\tilde{\nu}_Q = \tilde{\nu}_0 + \left(B'_{\upsilon'} - B''_{\upsilon''}\right)J^2 + \left(B'_{\upsilon'} - B''_{\upsilon''}\right)J \qquad \text{(B2.29b)}$$

R-branch ($\Delta J=-1 \Rightarrow J'=J+1, J''=J$)

$$\tilde{\nu}_R = \tilde{\nu}_0 + \left(B'_{\upsilon'} - B''_{\upsilon''}\right)J^2 + \left(3B'_{\upsilon'} - B''_{\upsilon''}\right)j + 2B'_{\upsilon'} \qquad \text{(B2.29c)}$$

These parabolic functions of the rotational quantum number give the spectral position of all rotational emission lines for one vibrational transition within a given electronic transition. If the rotational quantum numbers are plotted versus the wave number, the resulting graphs are called Fortrat parabolas.

Similar to the wave number, the intensity of an emission line is represented by a superposition of an electronic, a vibrational and a rotational transition. Under the assumption of a Boltzmann distribution (compare section B2.2.1) the intensity of each emission line is given by:

$$I_{\upsilon'J'-\upsilon''J''} = K\nu^4 S_J f_{alt} e^{\left[-T^{el}\frac{hc}{kT_e}\right]} e^{\left[-G'(\upsilon')\frac{hc}{kT_{vib}}\right]} e^{\left[-F'(\upsilon'J')\frac{hc}{kT_{rot}}\right]} \qquad \text{(B2.30)}$$

Here $K$ is a function of the electronic transition moment and the partition functions for the electronic, vibrational and rotational transition and therefore of electronic, vibrational and rotational temperature but not of rotational or vibrational quantum number. For a given plasma state, $K$ is a constant.

$S_J$ is the London-Hönl factor which describes the statistical weights for the transition. In the case of $N^2_+$ as a homonuclear diatomic molecule the London-Hönl factors for P- and R-branch of the First Negative band system become:

P-branch:
$$S_J^P = \frac{(J'+1)^2 - \frac{1}{4}}{(J'+1)} \qquad \text{(B2.31)}$$

R-branch:
$$S_J^R = \frac{J'^2 - \frac{1}{4}}{J'} \qquad \text{(B2.32)}$$

Due to effects of the atomic spin, an alternation between adjacent lines within the rotational spectrum occurs which is covered by the factor $f_{alt}$. In the case of $N^2_+$ the total spin is 2 and $f_{alt}$ becomes:

$$f_{alt} = \left(\frac{3+(-1)^{J'+1}}{2}\right) \qquad \text{(B2.33)}$$

To illustrate the appearance of a molecular spectrum, Fig. B2.11 shows the $N_2^+$ First Negative band system in low resolution with the different band heads and the fine structure of the $\Delta v=0$ band in high resolution including the 0-0 and the 1-1 band head.

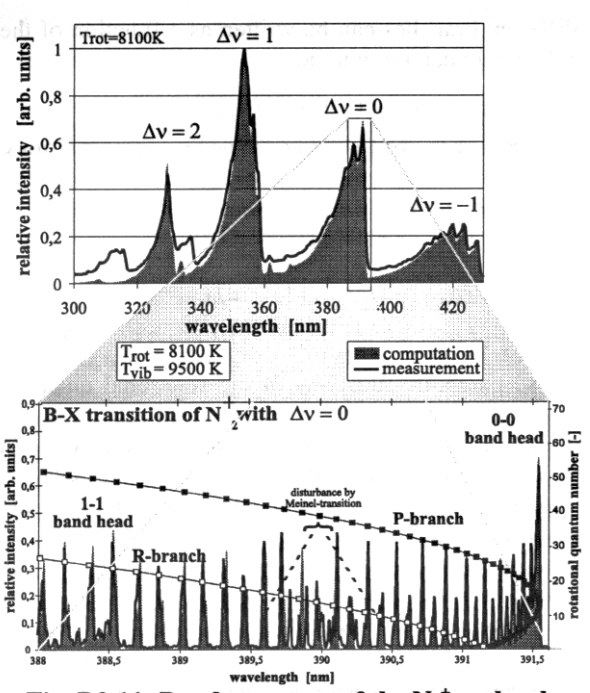


**Fig. B2.11: Band structure of the $N_2^+$-molecule**

The dark line represents a measurement, the gray areas are a numerical simulation of the emission. The Fortrat parabolas for the 0-0 vibrational transition are added to the fine structure diagram. The molecular band is divided into different parts which are formed by single rotational lines. In the case of $N_2^+$ these bands are degraded to the violet which means that rotational lines with rising rotational quantum number are shifted to lower wavelengths. All rotational lines which result from the transition from the vibrational level 0 to the vibrational level 0 lie close together and form the 0-0 vibrational band. The next band head at lower wavelengths belongs to the 1-1 transition. All higher vibrational transitions with Δv=0 are adjacent. Together they form the Δv=0 band system. Systems with other differences in vibrational quantum number such as Δv=-2, Δv=-1, Δv=1 and Δv=2 are similarly formed.

## B2.1.5 Spectral Appearance of an Air Plasma

The basic principles that determine the emission of atoms and molecules have been explained above. The spectrum emitted by a plasma can be regarded as a superposition of the emission of the different radiating species. Figure B2.12 shows a computation of the most important radiating species within an air plasma in the wavelength region between 200 nm and 900 nm in a low resolution of 0.5 nm. The spectral emission as a function of the wavelength corresponds to that of an equilibrium plasma state at a temperature of T = 11700K but the emissions of the different species have been scaled by different constant factors to enable a graphical representation in a common diagram. The emissions of the atomic species have been reduced by a factor of $10^{-6}$ and the emissions of the molecular species NO, $N_2$ and $O_2$ have been amplified by factors of 10, 100 and 300, respectively. Generally, the UV-region between 200 nm and 400 nm contains the radiation of most molecular species such as NO, $N_2$, $O_2$ and $N_2^+$ with the exception of the $N_2$ First Positive system. The strongest atomic radiation can be observed close to the infrared wavelength region above 700 nm.
It can be clearly seen that several wavelength regions are dominated by the emission of different species. The investigation of the molecular species mostly requires a separation of the desired species. For this purpose, best suited wavelength regions can be found for the detection of the different species such as the region below 250 nm which is dominated by the emission of NO, a region between 280 and 305 nm for the investigation of the $N_2$ Second Positive system and the region between 320 and 450 nm for the $N_2^+$ First Negative system although a separation of the $N_2^+$ and the $N_2$ emission is often not easy. In most cases, the emission of $O_2$ is too weak to remarkably disturb the measurements of the other species. The investigation of the atomic radiation as well as the measurement of the $N_2$ Second Positive emission has to be done in a wavelength range from the visible up to the close infrared.

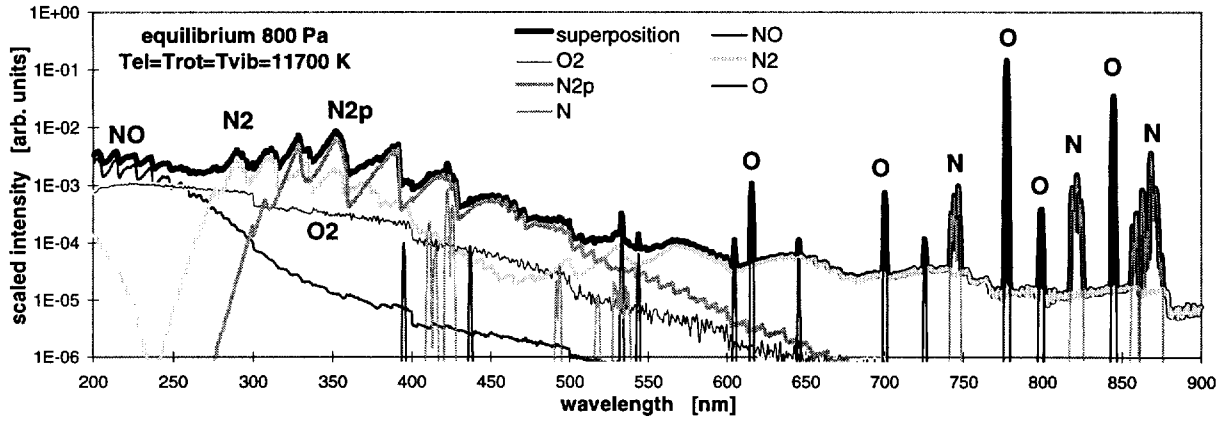


**Fig. B2.12: Superposition of the computed emission of the most important radiating species in an air plasma in the wavelength region between 200 nm and 900 nm**

The shape of the spectra contains information about the thermodynamic properties of the plasma. Temperatures can be obtained from the ratio of different emission lines; the particle density can be determined from the total intensities. The methods for determining these quantities are described in section B2.2.

## B2.2 Plasmadiagnostics

Emission spectroscopy is one of the most important methods of plasma diagnostic measurements with the great advantage of being completely nonintrusive. The emission spectrum contains information about

- the wavelength of the emitted radiation
- its intensity
- the intensity profile of each line
- the intensity distribution of the continuous radiation

To obtain information about thermo-chemical processes, the evaluation of the measured data can become rather difficult. Generally, the applications of emission spectroscopic measurements can be divided into three sections:

- The identification of different atoms and molecules within the plasma
- The determination of thermodynamic quantities such as temperatures and particle densities
- Gaining information about excitation and recombination processes within the plasma

For the applicability of emission spectroscopy as a plasma diagnostic method to determine thermodynamic quantities, the energetic conditions within the plasma are of special interest.
Therefore, this section first gives an overview about the basic assumptions for the different plasma states before the temperature determination from atomic radiation is explained. After that, the determination of $T_{rot}$ and $T_{vib}$ from molecular emission is shown and the determination of particle densities from the emission spectrum is discussed briefly.

### B2.2.1 Basic Definitions of the Plasma States

In the state of *complete thermodynamic equilibrium*, each elementary process (e.g. ionization) is in equilibrium with its complementary (in this case recombination) which means the numbers of both processes per unit time are equal. The most important properties of plasma in complete thermodynamic equilibrium are:

1) The spectral distribution of the emitted radiation is that of a black body radiator and follows Planck's Law.

2) The velocities of all particles follow *Maxwell's distribution function* with a common temperature $T$

$$f(v)=\frac{1}{N}\frac{dN}{dv}=\frac{4}{\sqrt{\pi}}v^2\left(\frac{m}{2kT}\right)^{\frac{3}{2}}\exp\left(-\frac{mv^2}{2kT}\right) \quad \text{(B2.34)}$$

$v$ is the velocity value, $m$ the particle mass and $N$ the number of particles per volume unit.

3) The ratio of the number of particles in an excited state $n_{i,n}$ and the number of all particles of the regarded species $n_i$ is given by a *Boltzmann-distribution*. For this case, the Boltzmann equation

$$\frac{n_{i,n}}{n_i}=\frac{g_{i,n}}{g_{i,o}}\exp\left(-\frac{E_{i,n}}{kT}\right) \quad \text{(B2.35)}$$

is valid. The quantities $g_{i,n}$ and $g_{i,0}$ are the statistic weights of the different excitation levels of the regarded ionization stage. They are always integers and can be derived from quantum mechanical laws or taken from spectroscopic tables. $E_{i,n}$ is the energy of the excited state $n$.

4) The chemical equilibrium which is also a part of the complete thermodynamic equilibrium is defined by the *law of mass action*. A reaction A + B ⇨ C is described by:

$$\frac{n_A n_B}{n_C}=K(T) \quad \text{(B2.36)}$$

Here, $n_A$, $n_B$ and $n_C$ are the concentrations of the reacting components and $K$ is the velocity constant of the particular reaction. $K$ is a function of the temperature and has to be determined experimentally.

5) The last important requirement is a relation for the ionization-recombination equilibrium which is given by the *Saha-Eggert equation* which is in fact the law of mass action for the ionization reaction. Limiting the possible ionization stages to 1 yields for the degree of ionization $\alpha$ for an atomic gas:

$$\frac{\alpha^2}{1-\alpha^2}=\frac{(2\pi m)^{\frac{3}{2}}}{ph^3}(kT)^{\frac{5}{2}}e^{-\frac{E_i}{kT}} \quad \text{(B2.37)}$$

Here, $E_i$ means the energy of ionization and $p$ is the pressure of the plasma.

In a real plasma there are always differences from complete thermodynamic equilibrium. If those differences are moderate and limited to single processes, the plasma state can often be described as close to equilibrium.
There are several possibilities to gain access to those plasma states but the most important one is probably the LTG-model (*local thermal equilibrium*). In this case, all properties of the complete thermodynamic equilibrium, with the exception of the requirement of a Planck distribution for the radiation, remain valid.
If we regard the energy equations, the influence of this difference on the particle densities can be neglected if the important processes such as excitation and heat transfer processes are dominated

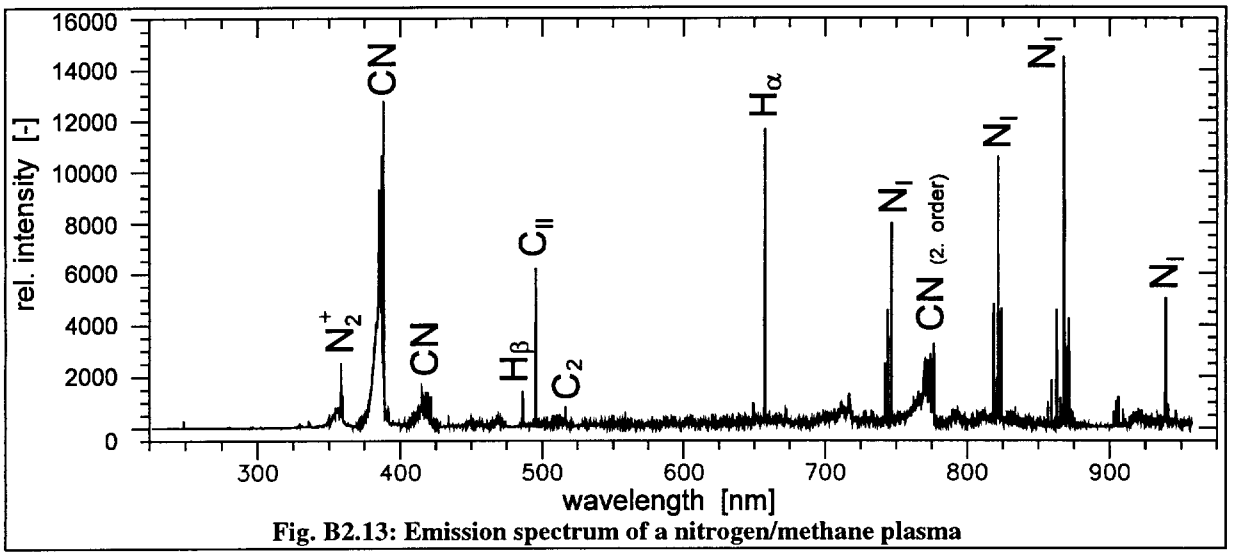


**Fig. B2.13: Emission spectrum of a nitrogen/methane plasma**

by collisions and not by radiation. For this reason a sufficient particle density of colliding particles is necessary. Due to their higher mobility in comparison to that of the heavy particles, electron number density is the important quantity. The electron number density required for LTG depends on the temperature and the excitation state up to which the LTG should be valid. Additionally, the highest ionization stage that is regarded is important. For example, a typical minimum electron density for LTG for argon up to complete single ionization and at a temperature of $T = 20000$K is given by $n_e = 4 \cdot 10^{17} \text{cm}^{-3}$.

Regarding plasma states within plasma wind tunnel experiments, not even LTG can be expected in every region of the jet and the plasma is in thermal and thermodynamic non-equilibrium. Here, thermal non-equilibrium means that the temperatures of the electrons and the heavy particles are different and that the molecules have different values for rotational, vibrational and electronic temperatures.

Even in these non-equilibrium cases, the Boltzmann distribution for the rotational and vibrational energy is often still valid with the corresponding temperature $T_{rot}$ or $T_{vib}$ as the determining parameter for the distribution function. In thermodynamic non-equilibrium, the chemical composition of the plasma does not correspond to the equilibrium composition because the changes in temperature are often so fast that the chemical reactions cannot follow.

## B2.2.2 Identification of Atoms and Molecules

Without a doubt, the identification of unknown elements using the wavelength of the emitted spectral lines is the oldest application of emission spectroscopic measurements. In plasma wind tunnels, the identification of different particles is of particular interest for:

- Proving the existence of ionized species
- Detecting erosion products of the electrodes which pollute the plasma
- Determining the plasma regions where recom bination, dissociation or ionization processes occur (e.g. NO-formation due to catalytic effects).
- Detecting erosion products of the heat shield materials.

As an example, Fig. B2.13 shows the emission spectrum taken from the experimental simulation of the entry conditions into the atmosphere of the Saturn moon Titan which was realized by using a mixture of nitrogen and methane as working gas in the plasma wind tunnel [B2.10].

For the atoms, the index $_{\text{I}}$ means that the neutral species is regarded while $_{\text{II}}$ means the first ionization stage. For molecules the ionization is characterized by $^+$ (for example $N_2^+$ is ionized molecular nitrogen).

## B2.2.3 Temperature Determination from Atomic Radiation

The information about the plasma temperature is contained within the intensity and the shape of the spectral lines of the radiating species. Replacing the number density of the excited state $n_n$ under the assumption of a Boltzmann distribution as introduced in equation (B2.35), the spectral emission coefficient $\varepsilon_{nm}$ of a spectral line as introduced in equation (B2.2) can be written as:

$$\varepsilon_{nm} = \frac{1}{4\pi} h\nu_{nm} A_{nm} n \frac{g_n}{g_0} exp\left(-\frac{E_n}{kT}\right) \qquad \text{(B2.38)}$$

If all quantities that remain constant for one species at the same plasma state are combined in the constant C which also contains common factors that influence the measured radiation such as the solid angle of the focusing system, an equation for the measured line intensity of the transition from state n to m is obtained:

$$I_{nm} = C\, \nu_{nm} A_{nm} g_n\, exp\left(-\frac{E_n}{kT}\right) \qquad \text{(B2.39)}$$

or $$\ln\left(\frac{I_{nm}}{\nu_{nm}A_{nm}g_n}\right)=\ln(C)-\frac{E_n}{kT} \qquad \text{(B2.40)}$$

Even without knowledge of the particle density, a determination of the temperature by a comparison of two emission lines can be performed. For this method, the fact is applied that the above equation formally appears as a straight line equation $y = b + mx$ with y and x being the logarithmic expression and the excitation energy respectively and where the slope contains the desired temperature. With only two points which means two emission lines the slope and therefore the temperature can be determined. To increase the quality of the measurement, usually more than two lines are used. This method is called Boltzmann plot and can be used both for determining atomic and molecular temperatures as explained in detail in the following section.

## B2.2.4 Determination of Molecular Temperatures

In most cases, the distribution of the number densities of the excited rotational and vibrational levels follows a Boltzmann distribution.

If single rotational vibrational lines can be spectrally resolved within the measurements of the molecular bands, the application of a Boltzmann plot is possible to determine the molecular temperatures.

A closer look at equation (B2.30) for the intensity of single emission lines gives the basic principles for temperature determination. Within one electronic transition the ratio of different emission lines is only a function of rotational temperature if the vibrational quantum number does not change.

Therefore, different rotational lines of the same vibrational transition can be used to determine the rotational temperature. Knowing $T_{rot}$, emission lines of different vibrational transitions can be used to determine the vibrational temperature if absolute intensities are measured. Determining the electronic temperature is only possible if different electronic transitions of the same molecule can be detected. But even in this case, the assumption of a Boltzmann distribution for the electronic states is necessary. Contrary to the rotational and vibrational states, this assumption is seldom fulfilled and has to be verified in any case.

Within real measurements, the spectral distance between corresponding lines of different vibrational transitions is rather large which causes severe problems in performing the necessary measurements. Thus, the usual application of the Boltzmann method is given by the determination of the rotational temperature.

If only emission lines of one vibrational transition are chosen, the terms which contain the electronic and vibrational quantities can be concluded in a constant *C*. Similar to the procedure in the case of the atomic radiation, equation (B2.30) can then be written as:

$$ln\left(\frac{I_{\upsilon'J'-\upsilon''J''}\lambda^4}{S_J}\right)=ln(C)-\frac{hc}{kT_{rot}}F'(\upsilon',J') \qquad \text{(B2.41)}$$

Here, $I_{\upsilon'J'-\upsilon''J''}$ is the intensity of the regarded rotational line at the wavelength λ. The *London-Hönl factor* $S_J$ gives the statistical weights of the different transitions as corresponds to the statistical weights $g_n$ used for the atoms. If the intensities of different rotational lines are measured and plotted over the rotational energy *F'*, in the case of a Boltzmann distribution a straight line is formed where the slope $-1/kT_{rot}$ contains the desired rotational temperature.

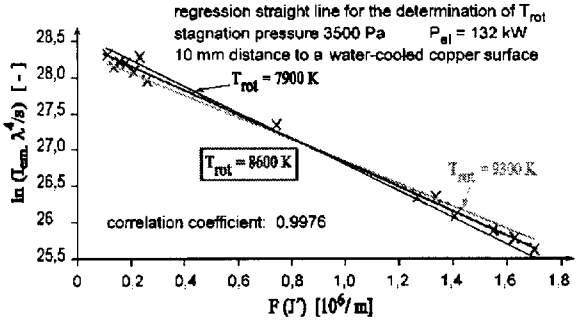


**Fig. B2.14: Typical Boltzmann plot used for determining $T_{rot}$**

In Fig. B2.14 the application of this method to the emission of a $N_2^+$-molecular band is shown [B2.11]. The theoretical linear relation can be seen clearly which validates the assumption of a Boltzmann distribution.

If different vibrational transitions are regarded, equation (B2.41) transforms into:

$$\ln\left(\frac{I_{\upsilon'J'-\upsilon''J''}\lambda^4}{S_J}\right)=\ln(C)-\frac{hc}{kT_{vib}}G'(\upsilon')-\frac{hc}{kT_{rot}}F'(\upsilon',J') \qquad \text{(B2.42)}$$

To obtain a straight line equation equivalent to (B2.41) the upper vibrational and rotational quantum numbers of the chosen emission lines have to be the same for all lines. This means that the lines which have to be evaluated are found in band systems with a different vibrational quantum number difference Δv (compare Fig. B2.11) yielding a large spectral distance. In the case of $N_2^+$, the band systems from Δv=-2 up to Δv=2 can typically be observed. Therefore, the maximum number of data points for each Boltzmann plot would be reduced to about five points.

If the measurement of spectrally resolved lines is possible only within a limited wavelength region, equation (B2.42), which no longer has the formal qualities of a straight line equation, has to be used directly for evaluation. It is no longer possible to use a Boltzmann plot to determine the rotational temperature. The vibrational temperature now has to be determined using the ratios of the intensities of different emission lines. In the logarithmic form, these ratios appear as differences. Still, the constant C which now includes only the partition functions and the terms due to the electronic transition is eliminated

from the equation. Solving for $T_{vib}$ yields for two different emission lines:

$$T_{vib} = -\frac{G'(\upsilon_1') - G'(\upsilon_2')}{\frac{F'(\upsilon_1', J_1') - F'(\upsilon_2', J_2')}{T_{rot}} + \frac{k}{hc}\ln\left(\frac{I_{\upsilon_1'J_1'-\upsilon''J'',1}\lambda_1^4 S_{J,2}}{I_{\upsilon_2'J_2'-\upsilon''J'',2}\lambda_2^4 S_{J,1}}\right)} \quad \text{(B2.43)}$$

Besides the Boltzmann plot, a low resolution temperature determination can also be done by comparing a simulation of the molecular bands with measured data. For this purpose, a simulation of the quantum mechanical processes has to be done. The spectra for different temperature couples (here $T_{rot}$ and $T_{vib}$) are computed and the numerically determined data are compared with the measurement. The spectrum which shows the highest resemblance to the measured spectrum gives the desired temperatures [B2.12]. One important presumption is that each simulated spectrum can be accurately related mathematically to a certain couple of the parameters of the model (in this case $T_{rot}$ and $T_{vib}$). Figure B2.15 shows a parameter variation for the selected molecular bands [B2.13]. The left diagram shows a variation of rotational temperature while electronic and vibrational temperatures were kept constant. The right diagram shows a variation of both $T_{rot}$ and $T_{vib}$.

The big advantage of this method compared to the Boltzmann plot is the much lower measurement time needed and the possibility for the simultaneous measurement of both $T_{rot}$ and $T_{vib}$. Only with this method is the determination of the temperature distribution within the boundary layer in front of a material probe as described in section B2.3.3 possible with a reasonable measurement time.

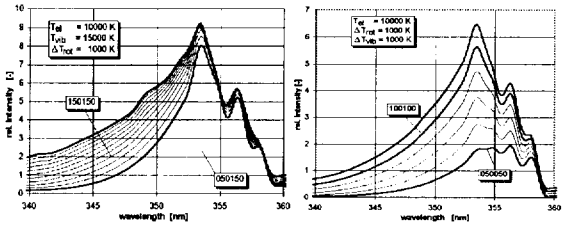

**Fig. B2.15: Influence of the different temperatures on the molecular band structure: left - variation of $T_{rot}$, $T_{el}$ and $T_{vib}$ kept const. right - variation of $T_{rot}$ and $T_{vib}$, $T_{el}$ kept const.**

Recently, the simulation has been extended from pure $N_2^+$ to a superposition of $N_2^+$ and $N_2$ emission [B2.14]. Figure B2.16 illustrates the data processing procedure and the temperature determination method in a flow chart.

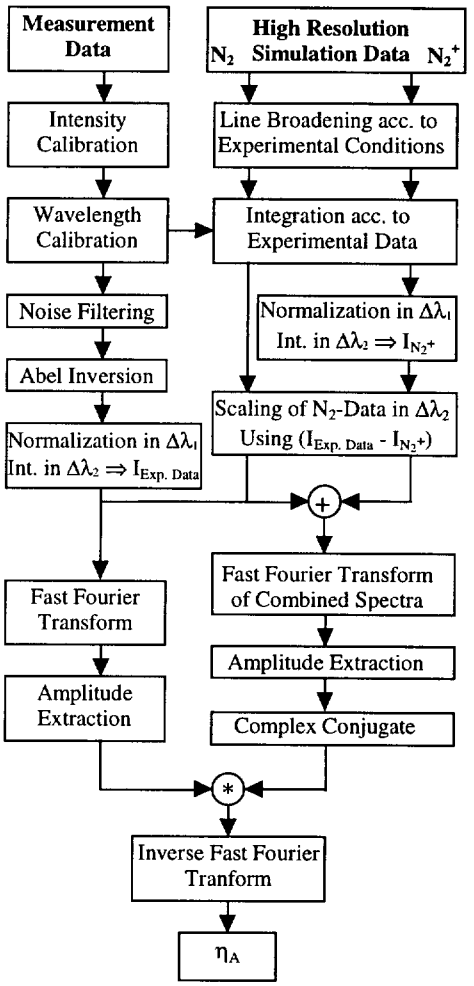


**Fig. B2.16: Flow chart of the data processing procedure and the temperature determination method.**

## B2.2.5 Determination of Particle Densities

Generally, the determination of particle densities from the measured emission spectra is also possible. Again, the most important assumption is the Boltzmann distribution. Additionally, the corresponding temperature must be accurately known and the measured data have to be calibrated to absolute intensities.

To determine atomic particle densities, the emission coefficient $\varepsilon_{nm}$ in equation (B2.38) (see section B2.2.3) has to be replaced by the intensity calibrated measured emission $I_{nm}$ and the equation has to be solved for the particle density $n$:

$$n = I_{nm}\frac{4\pi\, e^{\frac{E_n}{kT}}}{h\nu_{nm}A_{nm}}\frac{g_0}{g_n} \quad \text{(B2.44)}$$

Theoretically, the determination of molecular particle densities from the emission spectrum is also possible. The desired particle density is contained in the constant $K$ in equation (B2.30) (see section B2.1.4). Although the assumption of Boltzmann distributed

rotational and vibrational energies is often valid, an application to the electronic levels is not necessarily possible.
Therefore, the determination of molecular particle densities with other methods such as laser induced fluorescence (compare section B5.1) is better suited.

# B2.3 Plasma Wind Tunnel Application

During re-entry, as well as in the simulation in a plasma wind tunnel, thermal or chemical equilibrium can not be assumed in wide ranges. Sometimes not even a Boltzmann or Maxwell distribution is present. In this case, an interpretation of the measured data becomes rather complicated.
So an important task is the verification of the above-mentioned assumptions. The presence of a Boltzmann distribution can be verified by the linearity of a Boltzmann plot as described in section B2.2.4; the validation of a Maxwell distribution can be done using electrostatic probes (compare section A7.1). The equilibrium condition of the plasma state can be estimated using temperature measurements with electrostatic probes (A7.1) and emission spectroscopic temperature measurements of atomic and molecular temperatures (B2.2).
The next sections describe the experimental set-up for emission spectroscopic measurements, the intensity and wavelength calibration procedures and the Abel inversion as important factors for evaluating the measured data.

## B2.3.1 Experimental Set-up

The results of emission spectroscopic measurements are influenced by different factors. Generally, the measured data can not be used for further evaluation without any corrections. Although modern spectrometers and monochromators are normally wavelength calibrated, an additional wavelength calibration should be performed prior to each measurement because testing time is often limited and very expensive. In any case, a spectral intensity calibration (either relative or absolute) is necessary to enable a comparison of emission lines at different wavelengths or to determine thermodynamic quantities from the absolute intensity of the measured emission.
Measurements in different wavelength regions require different capabilities of the experimental set-up. For measurements of molecules in the ultraviolet wavelength region, the spectral transmittance of the optical elements of the experimental set-up and the spectral efficiency of the detector have to be optimized for utilization in the UV because at most plasma states the emission of the molecules is already weak. Fused silica lenses and windows as well as mirrors are the most commonly used optical elements. In any case, a spectral calibration of the set-up has to be done which will be described below.

At higher wavelengths up to the near infrared, the choice of materials for the optical elements is rather easy because most optical materials have sufficient characteristic properties in this wavelength region. On the other hand, most detectors suffer from decreasing efficiency close to the infrared especially if they are sensitive in the UV region. Another important disturbance is second order radiation. Due to self-absorption in air below 185 nm this effect gains importance only at wavelengths above 390 nm. To prevent the measured data from second order radiation, spectral filters are used to block radiation at wavelength below the region of interest.

Figure B2.17 shows a typical set-up for emission spectroscopic measurements. The emitted radiation is focused onto the entrance slit of a spectrometer where the spectral decomposition takes place. At the exit of the spectrometer, the transmitted light is collected by a detector. The focusing elements of the optical set-up have a remarkable influence on the results. In the set-up presented all lenses have been replaced by mirrors to minimize chromatic aberration which causes a shifting of the focus. If extensive wavelength ranges have to be detected, this shifting causes significant errors in the measured data.

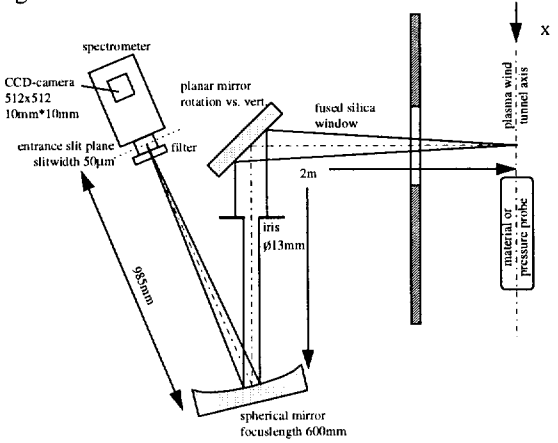


**Fig. B2.17: Typical experimental set-up for emission spectroscopic measurements**

The mirrors are used for focusing and for adjusting the measurement position inside the vacuum tank. Because of the comparatively large focal length of 650 mm, a precise adjustment of the optics is an important requirement for a successful measurement. For the adjustment procedure, the detector is replaced by a laser. The laser light has to take the reverse optical path and enables both an adjustment of the optical axis and of the measurement position.

If the available space is limited or if the direct optical path is somehow blocked, e.g. for measurements in the arc chamber of the plasma generator, the set-up shown above is not well-suited to perform emission spectroscopic measurements. In this case, the emission can be transferred to the spectrometer using fiber optics. The spectrometer needs no direct optical access to the measurement position. Figure B2.18 shows such a set-up.

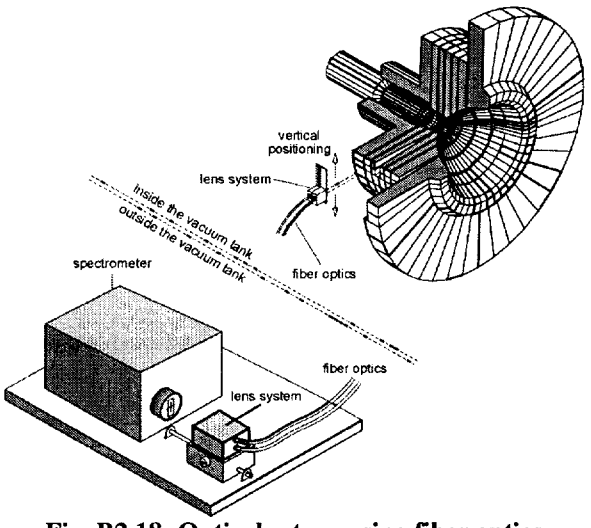


**Fig. B2.18: Optical set-up using fiber optics**

## B2.3.2 Measurement Grid

Emission spectroscopic measurements have been used to characterize the processes within the boundary layer in front of a probe in the plasma jet [B2.5-9]. Some results are given in section B2.4. Due to the non-intrusive character of the measurement method these kinds of measurements are well-suited for such an application.

For this purpose, a measurement grid in front of the probe as shown in Fig. B2.19 had to be developed.

To perform an Abel inversion, radial profiles over the whole radial extension of the plasma jet have to be recorded. The axial distances between the measurement positions are chosen smaller in regions of special interest (normally close to the probe surface) where the gradients are high and larger in regions with low gradients away from the probe surface to reduce the amount of data. The grid is adapted to the dimensions of the boundary layer.

During one test, 3000 to 7000 spectra are recorded. With a measurement time-optimized set-up including an imaging spectrometer and a CCD-camera used as detector which can detect all axial positions in one shot, the measurement of one complete scan requires a measurement time between 20 and 30 minutes.

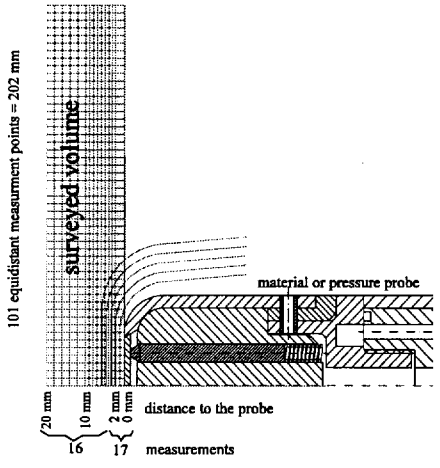


**Fig. B2.19: Measurement grid in front of a probe**

## B2.3.3 Wavelength Calibration

Generally, a wavelength calibration should be done. Most spectrometer software offers a procedure to calibrate the single detector elements although a manual calibration is also possible. For this purpose, the radiation of a calibration lamp with emission lines at known spectral positions is measured. Figure B2.20 shows the measured spectrum of an Hg-lamp which is one of the most commonly used calibration lamps.

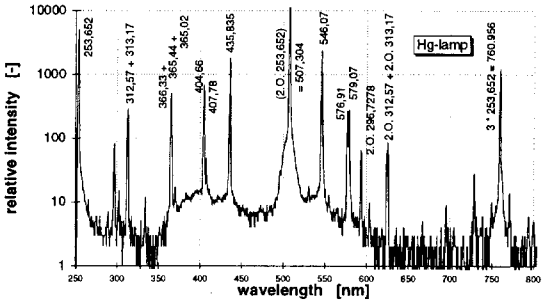


**Fig. B2.20: Spectrum of an Hg-calibration lamp**

Normally, the spectrometer is adjusted until one of the known emission lines appears in the center of the detector array. Other known lines are used to perform a polynomial fit (second order is most sufficient) for the wavelengths of the other pixels.

## B2.3.4 Intensity Calibration

If the absolute intensity of the emission lines has to be detected, it is obvious that the sensitivity of the detector has to be calibrated. But even if only relative intensities have to be compared, at least a relative calibration has to be done. The calibration is done by measuring a calibration lamp with already calibrated continuous emission (e.g. a tungsten band lamp for the visible wavelength region or a deuterium lamp for the UV).

Sometimes, only the spectrometer-detector couple is intensity calibrated which is done by illuminating the whole entrance slit of the spectrometer with the light of a calibration lamp. In this case, the calibration lamp is placed directly in front of the entrance slit. The advantage is that the spectrometer-detector combination has to be calibrated only once for a given wavelength range. The disadvantage of this calibration is that all spectral transmissions of windows, filters and lenses in the optical path have to be known accurately. Additionally, the solid angle and the imaging factor have to be included in the final evaluation.

The better but also more time consuming method is to place the calibration lamp at the measurement position and use the same optical path as in the measurement which has to be calibrated. In this case, all influences on the signal are included in the calibration procedure.

Figures B2.21 and B2.22 show the calibrated emission of two calibration lamps as tabulated by the manufacturer and the measured values. The

correction factors for the single detector elements are included in the diagram. The emission of the tungsten band lamp drops down in the ultraviolet wavelength region where the deuterium emission is rather strong. On the other hand, the emission of the deuterium lamp is no longer continuous in the visible wavelength range. Thus, only a combined calibration using both lamps gives a valid correction factor. Since the deuterium lamp itself is calibrated to spectral irradiance, the correction factors have to be scaled by a constant factor to those of the tungsten band lamp which is calibrated to spectral radiance.

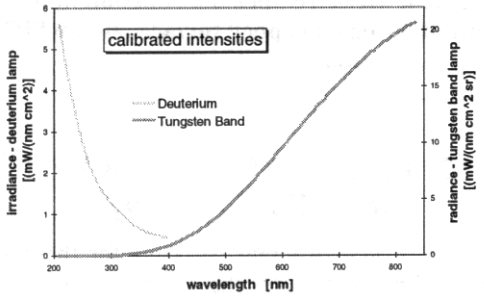


**Fig. B2.21: Calibrated intensities of the different calibration lamps**

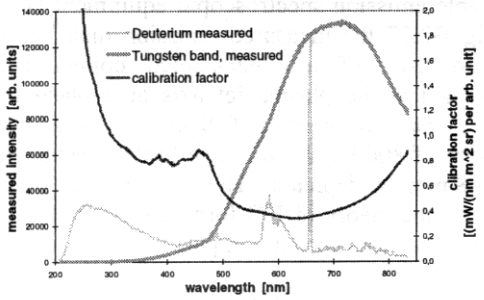


**Fig. B2.22: Calibration measurement with different calibration lamps**

## B2.3.5 Determination of Local Quantities

A main disadvantage of emission spectroscopic measurements is the fact that the measured signal always consists of an integration along the line of sight as illustrated in Fig. B2.23.

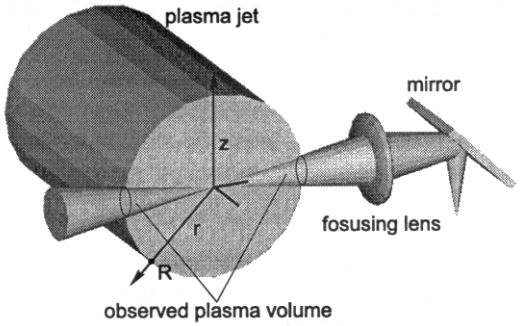


**Fig. B2.23: Typical geometrical configuration**

The Abel inversion is a mathematical technique which allows a reconstruction of the local values from a vertical profile of measured (that means integrated) intensities $I(z)$ as long as rotational symmetry of the radiation within the measured volume is given.

The radiation of the plasma volume is described by the emission coefficient $\varepsilon(r)$. The measured integrated intensity $I(z)$ is coupled to $\varepsilon(r)$ by the *Abel equation:*

$$I(z) = 2\int_{r=z}^{R} \frac{r}{\sqrt{r^2 - z^2}}\varepsilon(r)dr \qquad \text{(B2.1)}$$

$R$ is the radius of the measured volume while $r$ is the local radius. Solving for $\varepsilon(r)$ gives

$$\varepsilon(r) = -\frac{1}{\pi}\int_{z=r}^{\infty} \frac{(dI/dz)}{\sqrt{z^2 - r^2}}dz \qquad \text{(B2.2)}$$

In most cases an analytical solution is hard to find because a valid approximation of the integrated intensities is not available. Therefore, a numerical solution is used where the emission coefficient is considered to be constant over finite rings of the regarded volume. A refinement can be implemented if a linear transition between the measurement position is postulated to approximate the continuous course in the real plasma. Figure B2.24 illustrates the principle of the numerical Abel inversion.

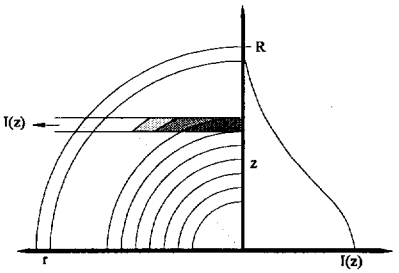


**Fig. B2.24: Principle of the Abel inversion**

Figure B2.25 shows the measured intensities I(z) and the Abel-inverted intensity i(r). The Abel-inverted intensities drop down to negative values at the borders of the plasma jet. Theoretically, this could be caused by absorption, but more likely these values are caused by numerical errors which can accumulate especially in the border region where intensities are rather low. Generally, the Abel inversion reacts very sensitively to functions which are not constantly differentiable. For this reason, a smoothing of the measured data often has to be performed first.

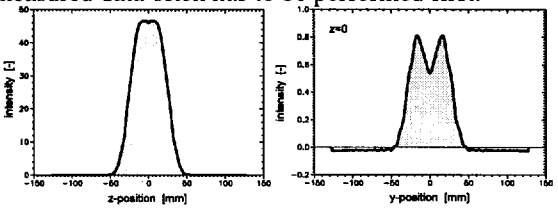


**Fig. B2.25: Measured (left) and Abel-inverted (right) intensity distribution**

The principle discussed is easily applicable if the local intensity distribution within the plasma is of particular interest as it was postulated for temperature determination methods. The problem becomes more complicated if, in addition to the intensity distribution, the line profile also has to be resolved, for example to determine electron densities from Fabry-Perot measurements (see section B4). Here, the

line broadening changes over the cross section as the electron density changes.
The measured intensity I(z) within the Abel integral equation is not only described by the emission coefficient ε(r) but also by the line profile of the emission lines. The Abel equation becomes:

$$\varepsilon(r)\Delta\lambda_B^2(r) = \frac{1}{\pi}\int_{z=r}^{\infty} \frac{\left(d\left(I(z)\Delta\lambda_B^2(z)\right)/dz\right)}{\sqrt{z^2-r^2}}dz \qquad \text{(B2.3)}$$

This expression gives a relation between the integrally measured broadening $\Delta\lambda_B(z)$ of an emission line at the wavelength λ with the local broadening $\Delta\lambda_B(r)$. If ε(r) is known from a conventional Abel inversion, the local broadening can be calculated.
The above-mentioned evaluation procedure is also applicable for Fabry-Perot measurements but one problem arises if plasma velocities are to be determined (see section B4.4). In this case, the optical path is no longer rectangular to the plasma axis. Here, the assumption of rotational symmetry is no longer given and the evaluation of the measured data becomes more difficult [B2.15].

# B2.4 Measurement Results

The emission spectroscopic measurements at the IRS concentrate on the investigation of the flow field in front of a probe in the plasma jet although investigations of the free stream are also carried out.
In this section, some overview spectra are presented before the investigation of the boundary layer region by the measurement of atomic and molecular emission, of molecular temperature distributions and of erosion products are discussed. All measurements were taken at the MPD-driven plasma wind tunnel PWK 2.

## B2.4.1 Overview Spectra

Figure B2.26 shows the radiating species measured at the plasma condition with a mass flow rate of 8 g/s and a stagnation pressure at the probe position of 800 Pa yielding a SiC surface temperature of 1700°C in front of a glowing probe and a water-cooled copper surface.
Generally, the emission spectra at the subsonic air flows typically investigated are dominated by the emission of the molecules NO, $N_2$ and $N_2^+$ in the ultraviolet and by the molecular emission of $N_2$ and the atomic emission of nitrogen N and oxygen O in the wavelength region from the visible to the near infrared. In front of a glowing material probe, strong emission of erosion products such as Si, CN and C can be seen in the UV.

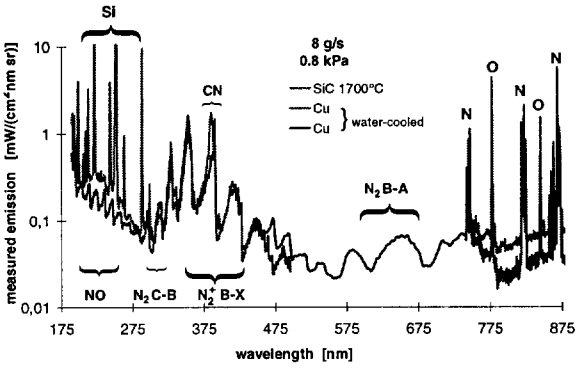


**Fig. B2.26: Measured plasma emission in front of a water-cooled copper surface and an SiC material probe at 1700°C**

## B2.4.2 Integrated Emission as Indicator for the Boundary Layer

There are several different purposes for these kinds of measurements. Besides the characterization of the boundary layer shape, a main purpose was the detection of NO inside the boundary layer with the available emission spectroscopic equipment [B2.16]. In Fig. B2.27 the measured emission distribution of NO in front of a water-cooled copper surface positioned at the plasma jet axis at a plasma state with a mass flow rate of 8 g/s and a stagnation pressure of 800 Pa at a distance to the plasma source of 368 mm is depicted. The rise in NO radiation supports the theory of NO formation in front of high catalytic surfaces such as copper.

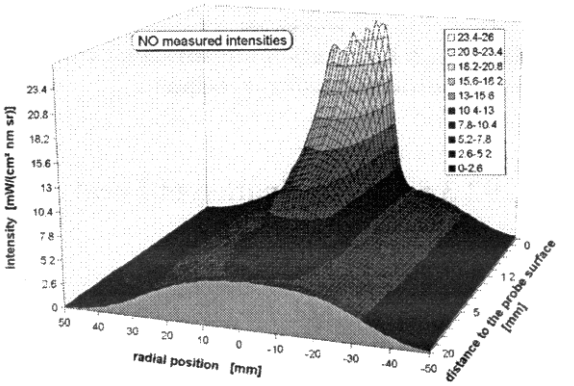


**Fig. B2.27: Measured NO intensities in front of a water-cooled probe**

The ratio of $N_I$ to $O_I$ is also regarded as a good indicator for the boundary layer borders. Figure B2.28 shows the intensity ratios obtained from the measured intensities of $O_I$ and $N_I$ [B2.16]. The profile indicates a location of the boundary borders at about 8 mm to the probe surface. The increase of this ratio at the borders of the plasma jet indicates an decrease of N atoms in relation to the O atoms due to their higher recombination energy.

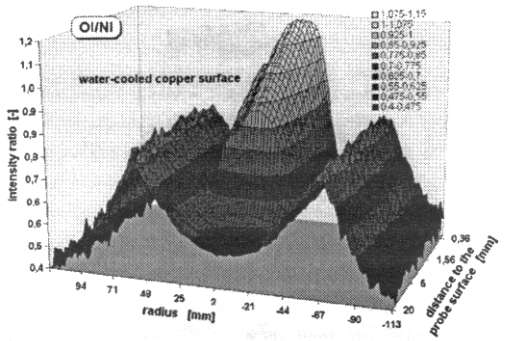


**Fig. B2.28: Ratio of $O_I/N_I$ obtained from measured intensities in a 3D-view**

## B2.4.3 Detection of Erosion Products

Strong radiation of erosion products has been detected in front of an SiC sample at 1700°C at a plasma state with a mass flow rate of 8 g/s and a stagnation pressure of 800 Pa at a distance of 368 mm to the exit plane of the plasma source.

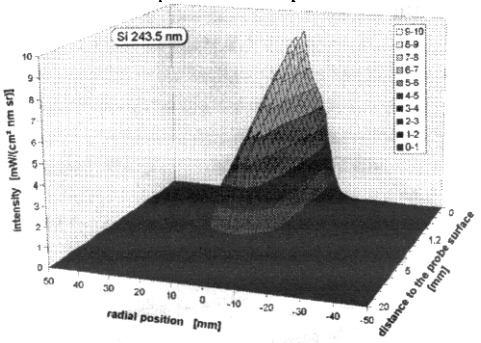


**Fig. B2.29: Si emission line intensity at 243.52 nm in the measured volume**

Figure B2.29 shows the measured line of sight emission of the silica emission line at 243.52 nm in the measured volume [B2.16]. The influence of the erosion products can be detected up to a distance of roughly 8 mm to the probe surface which corresponds to the boundary layer dimensions obtained from the ratio of $O_I$ and $N_I$ as shown in section B2.2.2.

## B2.4.4 Determination of $T_{rot}$ and $T_{vib}$ from $N_2^+$ and $N_2$ Emission

One important application of emission spectroscopic measurements as performed at the IRS is the determination of temperatures from the measured emission spectrum. As described in section B2.2.4, the rotational and vibrational temperatures are determined from the combined emission of the $N_2^+$ First Negative system and the $N_2$ Second Positive system. The temperatures presented are obtained from experiments at a plasma state with a mass flow rate of 2 g/s air and an ambient pressure of 290 Pa [B2.8]. At a distance of 467 mm to the exit plane of the plasma source, the stagnation pressure reaches 400 Pa yielding an SiC sample temperature of 1280°C. At this plasma state, erosion is rather low. Therefore all differences in the measured data between the experiments in front of a glowing SiC sample and in front of a water-cooled pressure probe show the influence of the much higher catalycity of the copper surface. Figures B2.30 and B2.31 show the spatially resolved distributions of rotational temperature in front of a water-cooled pressure probe with a copper surface and in front of a glowing SiC material probe at 1280°C. The strongly rising temperatures in front of the probe surface result from non-equilibrium effects such as deviations from the assumed Boltzmann distributions or disturbances of the emitted spectra by molecules other than $N_2^+$ or $N_2$ which are not included in the simulation. For this reason, the temperature values close to the surface are no longer reliable but clearly show the non-equilibrium effects and thus the shape of the boundary layer.

The same distributions for the vibrational temperature are given in Figs. B2.32 and B2.33. Here, the effects of the different materials on the temperatures are even stronger.

Figures B2.34 and B2.35 show the correlation factors obtained from the measured data in front of the different surfaces. Again, the non-equilibrium effects in front of the copper surface are much stronger than in front of the SiC surface. The boundary layer is thicker and the gradients are stronger in the case of a copper surface.

As clearly seen in the temperature distributions, the effects of surface catalycity on the boundary layer shape can easily be accessed by the temperature measurements. Thus, the correlation coefficient which expresses the degree of resemblance between the measured data and the computed spectra is a well-suited indicator for the boundary layer shape.

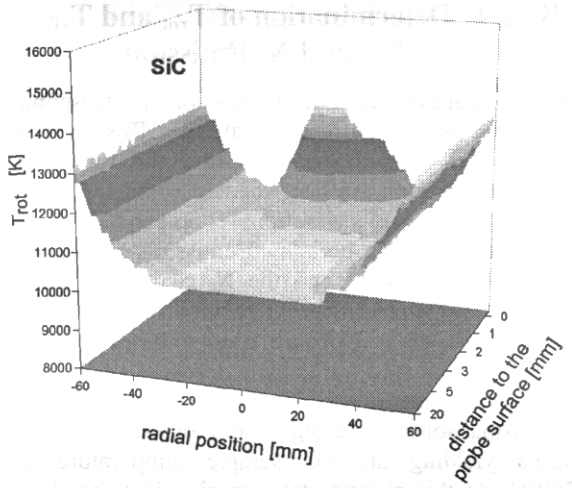


Fig. B2.14: Rotational temperature distribution in front of an SiC sample at 1280°C.

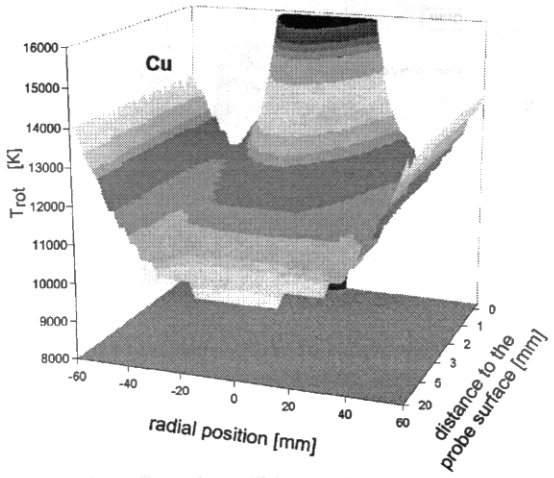


Fig. B2.15: Rotational temperature distribution in front of a water-cooled copper surface.

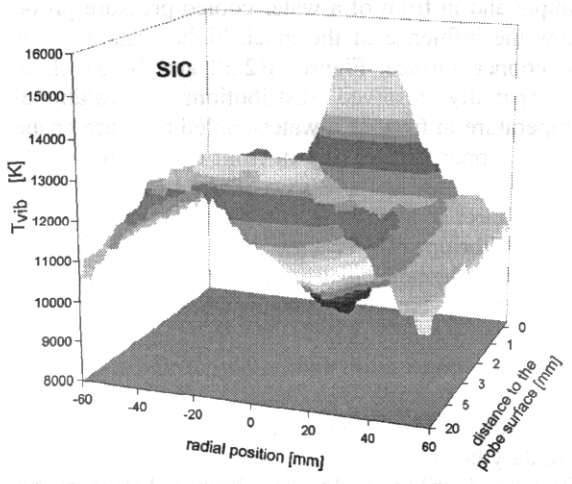


Fig. B2.16: Vibrational temperature distribution in front of an SiC sample at 1280°C.

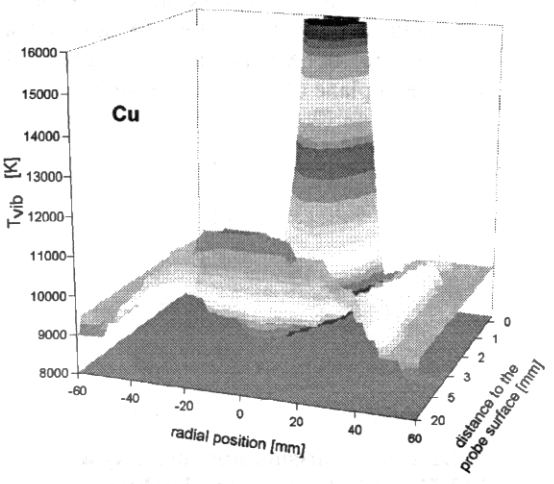


Fig. B2.17: Vibrational temperature distribution in front of a water-cooled copper surface.

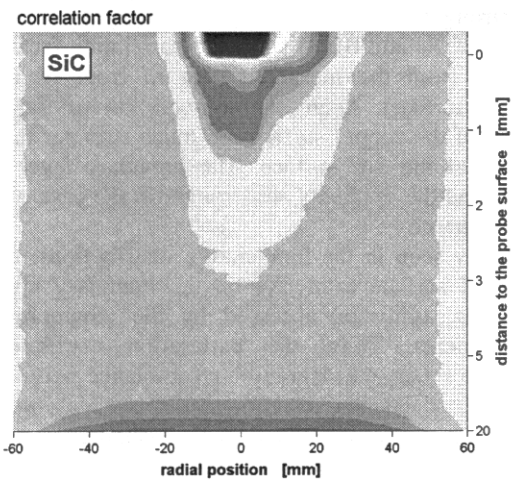


Fig. B2.18: Correlation factors in front of an SiC sample at 1280°C.

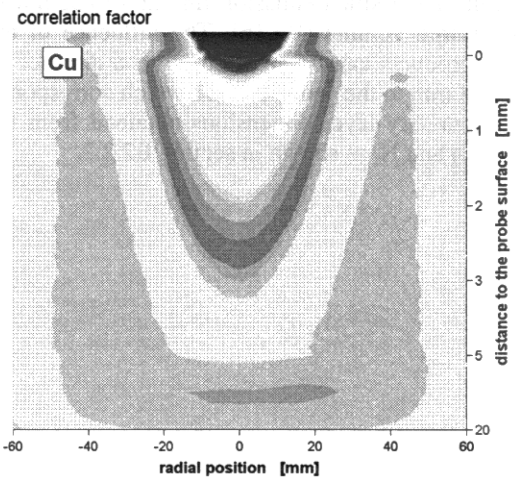


Fig. B2.19: Correlation factors in front of a water-cooled copper surface.

## References


[B2.1] Herzberg, G., "Atomic spectra & atomic structure", Dover Publications , New York, 1944.

[B2.2] Hellwege, K. H., "Einführung in die Physik der Atome", Springer-Verlag Berlin Heidelberg New York, 1974.

[B2.3] Striganov, A.R., Sventitskii, N.S., "Tables of Spectral Lines of Neutral and Ionized Atoms", IFI/Plenum, New York - Washington, 1968.

[B2.4] Wiese, Smith, Miles, "Atomic Transition Probabilities", Volume I+II, U.S. Department of Commerce, Washington D.C., 1969.

[B2.5] Park, C., "Calculation of Nonequilibrium Radiation in the Flight Regimes of Aeroassisted Orbital Transfer Vehicles" in Thermal Design of Aeroassisted Orbital Transfer Vehicles, Progress in Astronautics and Aeronautics, Volume 96, AIAA, 1985, pp. 395-418.

[B2.6] Smith, A.J., Gogel, T.H., Vandervelde, P., "Plasma Radiation Database PARADE", Final Report of the ESA/ESTEC TRP, Contract 11148/94/NL/FG, April 1996.

[B2.7] Hellwege, K. H., "Einführung in die Physik der Molekeln", Springer-Verlag Berlin Heidelberg New York, 1989.

[B2.8] Herzberg, G., "Molecular Spectra and Molecular Structure: Vol. I, Spectra of Diatomic Molecules, D. Van Nostrand Company, LTD, 1950.

[B2.9] Laux, C. O., "Optical Diagnostics and Radiative Emission of Air Plasmas", HTGL Report No. T-288, Stanford University, CA, USA, August 1993.

[B2.10] Röck, W., "Simulation des Eintritts einer Sonde in die Atmosphäre des Saturnmondes Titan in einem Plasmawindkanal", Dissertation, Fakultät Luft- und Raumfahrttechnik, Universität Stuttgart, 1998.

[B2.11] Winter, M.W., Auweter-Kurtz, M., Kurtz, H.L. and Park, C., "Investigation of an Equilibrium Condition Boundary Layer in Front of a Material Probe in a Subsonic Plasma Flow", 31st AIAA Thermophysics Conference, New Orleans, LA, June, 1996.

[B2.12] Winter, M.W., Auweter-Kurtz, M. and Kurtz, H.L., "Spectroscopic Investigation of the Boundary Layer in Front of a Blunt Body in a Subsonic Air Plasma Flow", AIAA 97-2526, 32nd AIAA Thermophysics Conference, Atlanta, GA, June 1997.

[B2.13] Fromm, M.A., "Charakterisierung der Probenumströmung einer Materialprobe im Plasmastrahl mit emissionsspektroskopischen Mitteln", Diplomarbeit IRS-97-S-12, Institut für Raumfahrtsysteme, Universität Stuttgart, Stuttgart, Germany, 1997.

[B2.14] Winter, M.W., Auweter-Kurtz, M., "Emission Spectroscopic Investigation of the Boundary Layer in Front of a Blunt Body in a Subsonic Air Plasma Flow", 3rd European Symposium on Aerothermodynamics for Space Vehicles, ESTEC, Noordwijk, The Netherlands, November, 1998.

[B2.15] Habiger, H., "Elektrostatische Sonden und Fabry-Perot Interferometrie zur Untersuchung von lichtbogenbeheizten Plasmen für Triebwerksanwendungen und Wiedereintrittssimulation", Dissertation, Institut für Raumfahrtsysteme, Fakultät Luft- und Raumfahrttechnik, Universität Stuttgart, 1994.

[B2.16] Winter, M.W. and Auweter-Kurtz, M., "Boundary Layer Investigation in Front of a Blunt Body in a Subsonic Air Plasma Flow by Emission Spectroscopic Means", AIAA 98-2460, AIAA 7th Joint Thermophysics and Heat Transfer Conference, Albuquerque, NM, June, 1998.


# B3 Absorption Spectroscopy

With absorption spectroscopy, the absorption of electromagnetic radiation by the particles of the transmitting medium is investigated. The method is based on the same quantum mechanical processes as emission spectroscopy, only that energy is absorbed and not emitted by the plasma.

As already seen, atoms and molecules emit energy in form of electromagnetic waves if they are thermally or electrically excited. Accordingly, light is absorbed at discrete lines if the radiation of a continuous light source is transmitted through a gas. These absorption lines correspond to the discrete energy levels necessary for the excitation of atoms and molecules in the gas [B3.1]. The continuous spectrum of the calibration lamp observed through the absorbing medium (e.g. the gas or plasma) therefore shows weaker intensities at these discrete lines. If the medium is regarded rectangular to the optical axis where the continuous radiation is not visible, an emission line at the same wavelength as the absorption line is visible due to the short life time of the excited state. It can be shown that not only the wavelength but also the amount of radiation is the same in emission and in absorption. This phenomenon is called resonance fluorescence. Figure B3.1 shows the absorption and the emission spectrum of sodium.

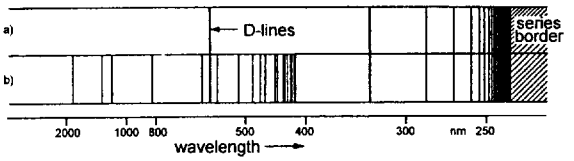


**Fig. B3.1: a) Absorption and b) emission lines of sodium**

Usually absorption spectroscopy is used at temperatures below 3000K. At these plasma states, the biggest part of the atoms and molecules ($\approx$ 99.9%) is in the ground state. In this case, only absorption from these ground states is possible. The resulting series are called main series, the lines themselves resonant lines. If there are remarkable amounts of excited states, the transitions already known from the emission spectroscopic formulas can be obtained and the absorption spectrum becomes very similar to the emission spectrum.

Due to the high temperatures in plasma wind tunnels, an application of absorption spectroscopy is seldom possible. A more common application is absorption spectroscopy in flames, where temperatures are lower [e.g. B3.2 and B3.8].

## B3.1 The Coefficient of Absorption

The total amount of energy absorbed per time and volume unit can be written as:

$$e_{abs} = B_{mn} n_m I_\nu h\nu \qquad \text{(B3.1)}$$

with:

$n_m$ number of particles in the absorbing state per volume unit
$h\nu$ radiation energy
$I_\nu$ spectral energy density

The factor $B_{mn}$ is the Einstein transition probability for absorption for the transition m → n and describes the number of absorbing particles per time unit and per spectral energy density in [$m^3J^{-1}s^{-2}$]. The product $B_{mn} I_\nu$ is an expression for the portion of particles in the state $m$ which absorb one photon with the energy $h\nu$ per time unit.

The total amount of energy absorbed per time and volume unit can also be expressed by the product of the number of absorbed photons and their energy:

$$e_{abs} = \kappa_{mn} n_m c I_\nu \qquad \text{(B3.2)}$$

where $\kappa_{mn}$ is the coefficient of absorption. Combining both equations yields:

$$\kappa_{mn} = \frac{h\nu}{c} B_{mn} \qquad \text{(B3.3)}$$

The coefficient of absorption has the unit [$m^2s$] and is a measure for the amount of radiation of the frequency $\nu$ that can be absorbed by one particle.

In reality, similar to the emission lines each absorption line has a certain line width which is produced by various effects (see section B2.1.2). Basically, the expression for coefficient of absorption represents an integration over this line width and can be written as:

$$\kappa_{mn} = \int \kappa'_{mn}(\nu) d\nu \qquad \text{(B3.4)}$$

## B3.2 Absorption Measurements of Particle Densities

Atoms are capable of absorbing radiation in only a very narrow frequency interval. For this reason, the radiation source has to meet some special requirements. Although continuous radiators emit a high total amount of radiation, the emitted intensity within the important spectral region is mostly too weak to stimulate remarkable absorption. A lamp which emits the same spectrum as the investigated element or a laser is often a better choice.

With such a set-up, the selected spectral line has to be separated from the other emission lines emitted by the same element using a spectrometer. Figure B3.2 shows an experimental set-up for these kinds of measurements.

A line radiator such as a hollow cathode lamp (or a laser if available) emits the spectrum of the investigated element. Within the plasma, part of the incoming radiation is absorbed at the resonant line. This part is directly proportional to the amount of particles in the corresponding state of excitation. Spectral lines that don't exist in absorption are transmitted without any reductions. The number of excited particles in the low temperature range (< 3000 K) is usually much smaller than the number of particles in the ground state. Therefore, in most cases the ground state particle density is determined by absorption spectroscopic measurements. After the spectral decomposition in the monochromator, the absorption line is separated and all other emission lines are eliminated. The detector „sees" only one line. The comparison with the originally emitted line gives the absorption.

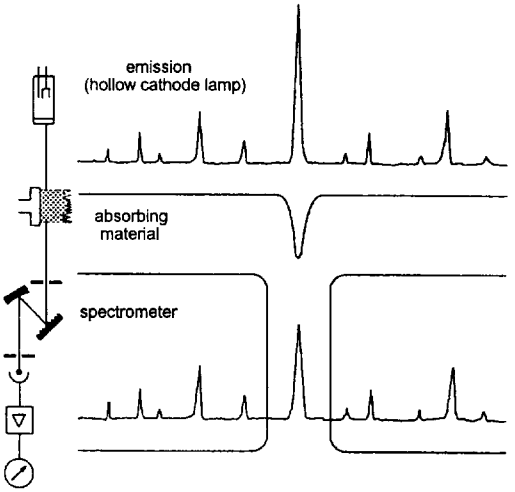


**Fig. B3.3: Principle of absorption measurements**

To determine $n_m$ , the radiant energy fluxes have to be regarded. According to Lambert's law the relation:

$$\phi_{D\nu} = \phi_{0\nu} e^{-\kappa_{mn} n_m d} \qquad \text{(B3.5)}$$

is given, where $\phi_{D\nu}$ and $\phi_{0\nu}$ represent the spectral radiative flux prior to and after the transmission through the absorbing region of the thickness $d$.

If $d$ is known and $\kappa_{mn}$ can be determined for the specified absorption line, the particle density in the state $m$ (usually the ground state) is obtained from:

$$n_m = \frac{1}{\kappa_{nm} d} \ln \frac{\phi_{0\nu}}{\phi_{D\nu}} = \frac{A}{\kappa_{nm} d} \qquad \text{(B3.6)}$$

The above equation is valid as long as the half width of the emission line of the radiation source is remarkably lower than that of the absorbing line. If not, a part of the emitted radiation at both (spectral) sides of the absorption line can not be absorbed which influences the results.

Furthermore, $n_m$ has to remain constant over d. Otherwise, an Abel-inversion of the measured data has to be performed to obtain local particle densities (see section B2.3.5).

## B3.3 Experimental Set-up

The principle set-up of an absorption spectrometer is rather simple and can be recognized in Fig. B3.2. But such a simple system has some important disadvantages:

As mentioned above, the number of excited particles in the low temperature range (< 3000 K) is usually much smaller than the number of particles in the ground state. In spite of that, the emission of the absorbing region is known to disturb the absorption measurements of such a simple setup, especially if other elements (for example molecules with numerous emission lines) exist. These effects can become important. If it is not possible to separate the investigated line from other emission lines, so called *spectral interferences* are obtained. In this case, the

ratio $\phi_D/(\phi_0+\phi_E)$ is measured instead of $\phi_D/\phi_0$, where $\phi_E$ is the intensity of an additional emission line of the frequency ν'. The observed absorption is smaller than its real value. In some cases, a negative absorption represented by a transmittance > 1.0 will result.

To eliminate disturbing emission lines, most absorption spectrometer work is based on the chopped-light (AC) principle which is illustrated in Fig. B3.3a and no longer on the simple continuous-light (DC) system. The experimental setup is almost the same but the radiation of the reference source is mechanically or electrically modulated with a certain frequency. The amplifier electronics are synchronized with this modulation frequency („selective amplifier"). Only the part of the radiation which is oscillating with the modulation frequency is amplified so that the disturbing emission, which does not oscillate, loses importance. Spectral interferences by disturbing emission are minimized.

Another refinement of this set-up which eliminates additional error sources is given by the two beam AC system, shown in Fig. B3.3b. With this system, the radiation of the primary radiation source is separated by a rotating mirror into a measured beam ($\phi_D$) and a reference beam ($\phi_0$). After $\phi_D$ has passed the absorbing volume, both beams are reunited. The electronics of the system builds the ratio of these two beams. Both beams are created by the same radiation source, pass the same monochromator, are detected by the same detector and are amplified by the same amplifier. If the rotation frequency of the mirror is higher than the expected disturbances, changes in the primary radiation source strength or fluctuations in detector sensitivity or amplifier power appear in both measured signals and no longer appear in the ratio of both signals.

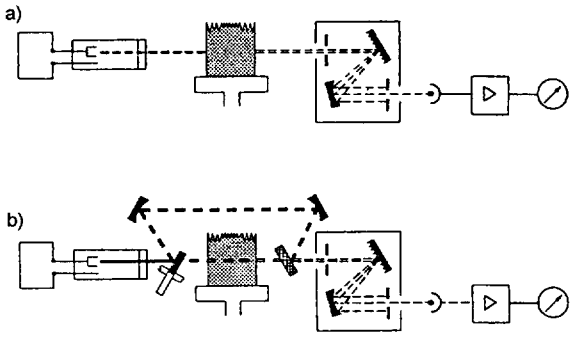


**Fig. B3.5: Working principle of absorption spectrometers: a) chopped-light-system b) two beam AC-system**

# B3.4 Applications

Some of the main applications for absorption spectroscopy are found in astrophysics. Here, numerous investigations of stars and the atmospheres of other planets have been done .

The concentration of atomic or molecular impurities in air can be determined using absorption spectroscopic methods [B3.3]. Molecular absorption spectroscopy in the far infrared wavelength region is used in shock tubes to investigate relaxation processes [B3.4 to B3.6]. For these applications, lasers are used as light source. Also the investigation of combustion processes by absorption spectroscopic measurements of flames at rather low temperatures offers another broad range of applications.

Further fields of applications are the tracing of metal estimations either in solid food stuffs or organic materials ( e.g. estimation of Mercury in water/fish by flameless Atomic Absorption Spectroscopy (A.A.S.), soil analysis ). Another growing field is the application of A.A.S. in Clinical Chemistry [ B3.8].

For plasma wind tunnel applications some restrictions to absorption spectroscopic methods appear. First, in most cases the temperatures are rather high yielding a highly excited plasma. Thus, the particle densities determined by absorption spectroscopy are no longer necessarily coupled to the ground state density.

Furthermore, the highest thermal loads on a reentering space vehicle occur at high altitudes and low pressures. Here the plasma usually can be regarded as optically thin which complicates absorption spectroscopic measurements.

If a laser is used instead of a continuous light source, a better sensitivity of the setup is provided but still the above mentioned restrictions are valid.

An exception is given if the absorbed energy is measured not by the attenuation of the laser beam but by the radiation of the stimulated emission. This method is called laser induced fluorescence and is described in section B5.1.

## B3.4.1 Determination of the Plasma Transmittance

Even if the application as described above is not possible, absorption spectroscopic measurements can be very useful for the correction of all other optical measurement methods. In this case, the spectral range as well as the apparatus used are defined mainly by the measurement method to which the correction will be applied. The knowledge of the plasma absorbance and transmittance over a certain wavelength range for example is of particular interest if the surface temperature of a material probe inside a plasma jet is determined using pyrometers. Absorption of the radiation emitted by the material probe in the surrounding plasma yields errors in the determined surface temperature if the absorbed part of the emitted radiation can not be quantified. Absorption spectroscopy is in use for the selection of suitable filters for linear pyrometers in order to avoid this error source. The required transmittance measurements do not necessarily have to be performed spectrally resolved and a pyrometer can be used instead of a spectrometer (see Fig. B3.4).

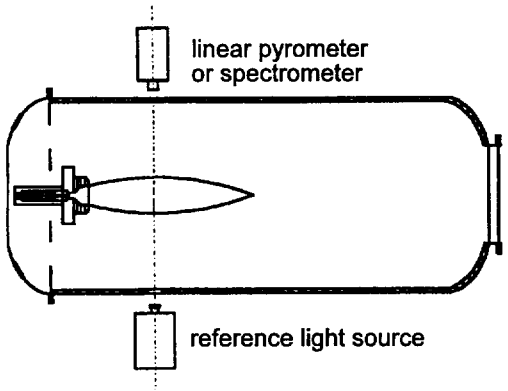


**Fig. B3.6: Determination of the plasma transmittance**

The reference source, which should radiate at the same magnitude of total radiation as the material to be measured, is placed outside the vacuum chamber and measured by the detector through the plasma. By comparing the measured signal without plasma $I_R$ with the signal transmitted through the plasma $I_{R+Pl}$ the transmittance can easily be obtained. If the plasma itself emits within the selected wavelength region, an additional measurement of the plasma without the reference source $I_{Pl}$ has to be performed and subtracted from the signal of plasma and radiation source. The transmittance of the plasma is given by:

$$\tau_{Pl} = \frac{I_{R+Pl} - I_{Pl}}{I_R} \qquad \text{(B3.7)}$$

If the measurement is performed using a spectrometer, the spectral transmittance is obtained.

## References


[B3.1] Welz, B., "Atomabsorptionsspektroskopie", Verlag Chemie, Weinheim, 1983.

[B3.2] Baer, D. S., Nagali, V., Furlong, E. R., Hanson, R. K., Newfield, M. E, "Scanned- and fixed-wavelength absorption diagnostics for combustion measurements using a multiplexed diode-laser sensor system", AIAA Journal, 34, 1996, pp. 489-493.

[B3.3] Unsöld, A., "Physik der Sternatmosphären: mit bes. Berücks. d. Sonne", Springer Verlag Berlin Heidelberg, 1955.

[B3.4] Demtröder, W., "Laserspektroskopie, Grundlagen und Techniken", Springer Verlag, Berlin, Heidelberg, 1993.

[B3.5] Klenk, W., "Spektroskopische Untersuchungen der Relaxationszone hinter Verdichtungsstößen in Luft mit einem Infrarot-Dioden-Laser", Berichte aus der Luft- und Raumfahrttechnik, D 93 Dissertation Universität Stuttgart, Shaker Verlag, Aachen, 1997.

[B3.6] Brandt, O. and Roth, P., "Temperature measurement behind shock waves using a rapid scanning IR-diode laser", Phys. Fluids, 30, 1987, pp. 1294-1298.

[B3.7] Moser, L. K. and Hindelang, F. J., "Shock-tube study of the vibrational relaxation of nitric oxide", in Proceedings of the 17th International Symposium on Schock Waves and Shock Tubes, 1989, pp.531-534.

[B3.8] Thompson, K.C., Reynolds, R.J., "Atomic Absorption, Fluorescence and Flame Emission Spectroscopy", Charles Griffin & Company LTD, London, 1978.


# B4 Fabry Perot Interferometry

A Fabry Perot interferometer is a high resolution spectral device based on the principle of multiray interference. It can be used to measure particle speeds and translational temperatures. Contrary to, for example, electrostatic probe measurements, this method provides the speed and temperature of the plasma by optical means. All of the necessary elements and devices for the measurements are located outside of the vacuum tank and therefore do not influence the plasma stream.

Axial and any azimuthal speed components of the accelerated plasma particles that appear are measured by means of the Doppler shift of their emission lines. The Doppler shift can be directly determined by simultaneously displaying the plasma line with a reference line which has not been shifted. With the conditions in the plasma wind tunnel PWK2 heavy particle velocities, for instance of atomic nitrogen, of approximately 1000 to 5000 m/s give Doppler shifts of approximately $\Delta\lambda_D \approx 0.002$ to 0.013 nm. To determine this shift, a high resolution spectrum is necessary. This spectrum can best be achieved by means of a so-called Fabry Perot Interferometer (FPI).

Futhermore, by determing the Doppler broadening the heavy particle translational temperature and if applicable the radial speed components of the plasma particles can be ascertained. As with emission spectroscopy, it is not a local measurement but a kind of average over the beam cross section that can be performed with this method. However, this disadvantage can also for the most part be eliminated with a subsequent mathematical resolution by means of an Abel inversion, as explained in section B4.5. The examined beam cross sections are, however, not axially symmetrical. This complicates the Abel inversion method explained in B2.3.5. A solution is given in [B4.1].

# B4.1 Theoretical Principles of Fabry-Perot Interferometry

The Fabry-Perot interferometer was introduced by two French opticians, Charles FABRY and Alfred PEROT, in 1897. It essentially consists of two glass plates with a reflective coating on one side of each plate. The plates are positioned parallel to each other and are a few micrometers to a few meters apart.

The function of an FPI is based on the interference of a smooth wave through multiple reflections on two mirror plates. This phenomenon can also be explained by the multiple reflections in a plane parallel plate. One differentiates between so-called constructive and destructive interference. Construc-

tive interference appears when the phase shift of two overlapping, smooth waves is an integer multiple of 2 π (see Fig. 4.1). Otherwise a destructive interference exists.

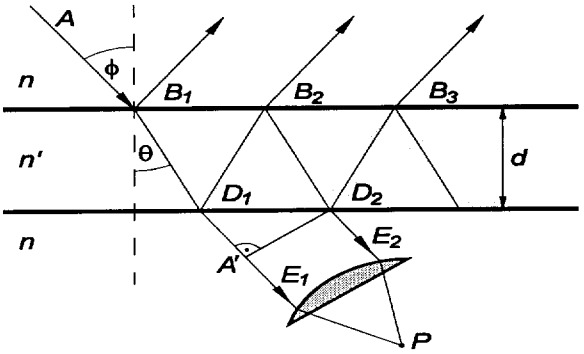


**Fig. B4.1: Reflection in a glass plate**

In the case of a Fabry-Perot interferometer the multiple reflection takes place on the translucent inner surfaces of two parallel glass plates. As Fig. B4.2 shows, an aperature partition on the optical axis in the focal point of lens 2 has the effect that only almost parallel light ($\theta \approx 0°$) makes it through the FPI. If the medium has the refractive index $n$ between the plates, the following condition for the intensity maximum of order m results:

$$m\lambda_0 = 2nd \qquad \text{(B4.1)}$$

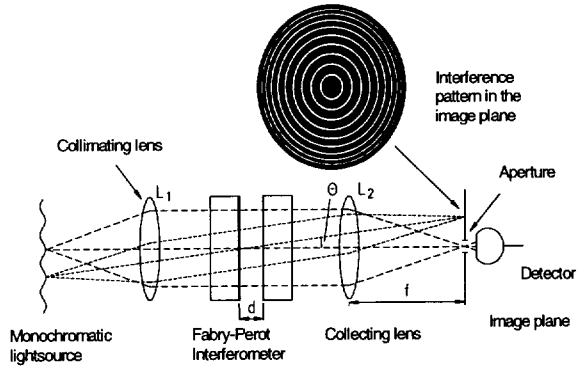


**Fig. B4.2: Schematic construction of a Fabry-Perot interferometer**

The Fabry-Perot interferometer can be adjusted to a declared wavelength by varying the parameters $n$ or $d$. Changing the refractive index of the medium between the plates, for example by changing the pressure, is difficult. Modern FPIs are, therefore, adjusted by changing the distance between the plates. With the instrument in use at the IRS, one of the plates is shifted by means of piezoelectric. The piezoelectric elements are steered through a ramp generator and in this way they create a linear, periodic translational movement. This kind of scanning makes it possible to represent several interference arrangements of a certain wavelength or rather makes it possible for a defined, narrow wavelength area to go through.

# B4.2 The Airy Function

The intensity $I_T$ of the waves penetrating the FPI is among other things dependent on the transmission $T$ of an FPI. The intensity is defined as the percentage permeability in the exact resonance distance of the mirror plates for a certain wavelength $\lambda_0$, that means as a quotient of the intensities with and without FPI in the path of the detecting optics. The reduction of intensity caused by the FPI is essentially determined by the absorption and the scattering losses on the layers of the mirror-coating substrata, expressed by the mirror depending constant $A_S$ and the reflection degree $R$ on the mirror layers. In order to describe the relationship of the transmitting to incoming intensity $I^T/I^i$, the so-called Airy function is used which is given by:

$$\frac{I^T}{I^i} = \frac{(1-R)^2}{(1-R)^2 + 4R\sin^2\frac{\delta}{2}} \cdot \qquad \text{(B4.2)}$$

Here δ is the phase shift of an electromagnetic wave, caused by the reflections on the mirrors' surfaces. If δ is a multiple of 2π, then constructive interference occurs. In this case

$$\delta = \frac{4\pi}{\lambda_0} nd\cos\theta = 2\pi \cdot m \qquad \text{(B4.3)}$$

is valid, with n as the refractive index inside the FPI, d as the spacing between the mirror plates, θ as the angle of the incoming wave, $\lambda_0$ as the wavelength of the transmitted light and m as the number of the interference order. The Airy function is shown in Fig. B4.2 for various degrees of reflection.

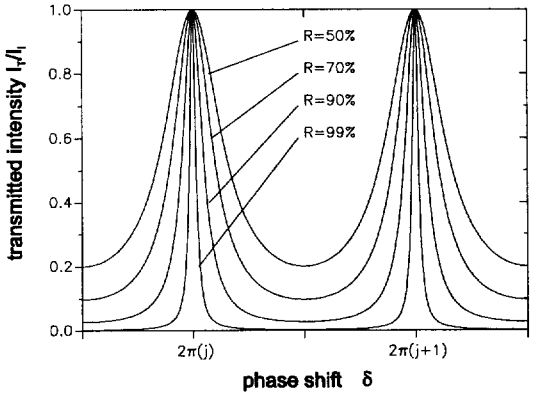


**Fig. B4.2: Intensity relationship $I_T/I_i$ for various degrees of reflection as a function of δ.**

For a given optical thickness $nd$ the Airy function describes a whole system of concentric interference rings when the order $m$ of the interferences is equivalent to a whole number ($m$ = 1, 2,...) according to Eq. B4.1. For small degrees of reflection $R$ wide interference rings result and the contours become more and more defined as the degree of reflection increases.

A measure for the definition of the interference rings is given by the so-called half-width χ, which means the width of the profile at half the height of the

intensity maximum. For an interference ring of the order m the intensity is reduced by half. Hence it follows that the half-width of the interference ring results in:

$$\chi = \frac{4}{\sqrt{\frac{4R}{(1-R)^2}}} \qquad \text{(B4.3)}$$

The mirror plates used in the FPI at the IRS have a dielectric wideband coating with a degree of reflection of $R$=94% and a transmission area of 400 nm to 800 nm.

# B4.3 Characteristic Quantities of a Fabry-Perot Interferometer

In order to effectively use an FPI as a high resolution spectrometer for a certain measurement task, one must optimize the system in order to maximize the resolution of the system.

## B4.3.1 The Resolution

The resolution of the FPI determines the ability to separate two spectral lines which are very close together. The resolution is of great importance for the plasma wind tunnel application. For the practical use of the FPI for the purposes of detecting and identifying spectral lines, the Rayleigh criteria can be used (for Rayleigh see chapter B5). This is shown in Fig. B4.3a. Two spectral lines must be clearly separated by means of a drop in intensitiy to at least 81%. To use the FPI to determine the Doppler shift and broadening, which is explained in sections B4.4 and B4.5, one is dependent on an exact determination of the central wavelength $\lambda_0$ related to the maximum intensity. It is only possible to determine this when the observable profile of two spectral lines can be clearly seperated at the height of their half-width.

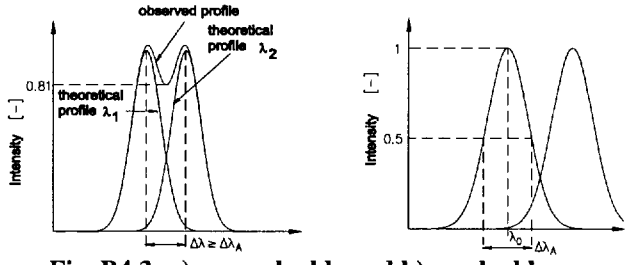


**Fig. B4.3: a) unresolvable and b) resolvable spectral lines related to the measurement of Doppler effects**

This is not the case in Fig. B4.3a. The central wavelength must be determined from the middle of the half-width as shown in Fig. B4.3b. According to this, the resolution $\Delta\lambda_A$ of the FPI is defined as the half-width of a perfectly monochromatic spectral line of the wavelength $\lambda_0$. The useful resolution $\Delta\lambda_A$ depends on two characteristic quantities of a Fabry-Perot interferometer: the usable finesse $F_N$ and the free spectral area $\Delta\lambda_F$. Both are explained below. I is calculated from the quotient of both according to:

$$\Delta\lambda_A = \frac{\Delta\lambda_F}{F_N} = \frac{\lambda_0^2}{2ndF_N} \quad . \qquad \text{(B4.7)}$$

## B4.3.2 The Finesse

The quality of an FPI is described by the so-called instrmental finesse $F$ of the interferometer. The finesse is used to measure the performance of the FPI and describes the ability to resolve the spectral lines which are very close together. The larger the finesse of an FPI, the higher the resolution. The instrumental finesse $F$ is determined by the indivual finesses of the degrees of reflection $F_R$ and the finesse $F_F$ of the smoothness of the mirror plates. If an FPI is operated as a spectral device, in addition to the instrumental finesse the characteristics of the collecting optics which follow the FPI must be taken into consideration. The useful finesse $F_N$ contains in addition the finesse of the aperature partition $F_P$ and the refraction finesse $F_D$. This can be calculated as follows:

$$\frac{1}{F_N^2} = \frac{1}{F^2} + \frac{1}{F_P^2} + \frac{1}{F_D^2} = \frac{1}{F_R^2} + \frac{1}{F_F^2} + \frac{1}{F_P^2} + \frac{1}{F_D^2} \quad . \qquad \text{(B4.5)}$$

The equation clearly shows that the useful total finesse $F_N$ worsens and the values decrease compared to the apparatus constants $F$. As a result, the collecting optics following the FPI should be subjected to an optimization to keep the useful finesse $F_N$ as close as possible to the value of the instrumental finesse $F$.

## B4.3.3 The Free Spectral Range

During movement of the FPI mirror plates, that is when the distance $d$ between them is varied, the various orders of interference of the wavelength under observation move across the detection apparatus, for example across the aperture partition in front of the detector in Fig B4.2. The free spectral range $\Delta\lambda_F$ of the FPI describes the wavelength interval in which light is represented under the same order. It is given by

$$\Delta\lambda_F = \frac{\lambda_0^2}{2nd} \qquad \text{(B4.6)}$$

The free spectral range of the FPI can therefore be influenced by the variation of the distance between the mirror plates $d$. In order to minimize the free spectral range, the mirror plates have to be far apart. But on the other hand, the useful total finesse $F_N$ decreases with increasing distance [B4.1]. The resolution finally approaches a minimum asymmetrically. It is already close to this value in the case of nitrogen ($N_1$) at a distance of approximately

3mm [B4.2]. The free spectral range can be determined experimentally by measuring two orders of a strictly monochromatic spectral line, for example of a laser.

## B4.4 Doppler Shift and Heavy Particle Speed

The Doppler effect was discovered by Christian Doppler in 1843 while investigating the propagation of sound. He found out that the frequency of a sound changes when a relative movement takes place between the acoustic source and the sound receiver. This effect can also be applied to optics. If a light emitting medium, for example a plasma, is moving with a speed v and the emitted light is observed by a stationary receiver under an angle $\alpha$ to the propagating medium, the following equation is valid between the wavelength $\lambda$ measured by the receiver and the actual emitted wavelength $\lambda_0$:

$$\frac{\lambda}{\lambda_0} = \frac{\sqrt{1-\frac{v^2}{c^2}}}{1-\frac{v}{c}\cos\alpha} \quad . \tag{B4.8}$$

Here $c$ represents the speed of light and $\alpha$ is the angle between the normal to the wave vector of the spreading light and the speed v of the emitting particle. For plasma wind tunnel applications $\alpha$ indicates the angle between the optical axis of the FPI and the flow vector of the plasma stream (see Fig. B4.4). Because v is generally very small compared to $c$, the root in the equation above can be set at approximately 1. If the denominator in the equation above is developed in a binomic row, while neglecting the term to the second and higher orders the result is finally the following equation for the Doppler shift $\Delta\lambda_D$:

$$\Delta\lambda_D = \lambda - \lambda_0 = \lambda_0 \frac{v}{c}\cos\alpha \quad . \tag{B4.9}$$

From this equation the plasma velocity v can be determined from the Doppler shift measurement. The chosen angle, however, must be large enough so that $\Delta\lambda_D$ is larger than the resolution $\Delta\lambda_A$ of the FPI.

## B4.5 Doppler Broadening and Heavy Particle Translational Temperature

While observing a plasma volume emitting radiation from any angle, a Doppler broadening of the spectral line being observed occurs due to the random thermal movement ($v_{th}$) of the plasma particles. This Doppler broadening $\Delta\lambda_T$ results from the overlapping of Doppler shifts $\Delta\lambda$ for which the following is valid:

$$\Delta\lambda = \pm\lambda_0 \frac{v_{th}}{c} \quad . \tag{B4.11}$$

Contrary to the speed v in Eq. B4.9, $v_{th}$ is not a directed speed and the change in the wavelength is therfore also not dependent on the angle. Because, however, the thermal speed is a function of the translational temperature $T_{tr}$ of the corresponding particle, the temperature $T_{tr}$ can be determined by determining $\Delta\lambda_T$.

A purely thermal movement of the emitting particle corresponds to the distribution of the thermal speeds of a Maxwell distribution. The particle concentration dn with a thermal speed in the interval between $v$ and $v + dv$ is given by:

$$\frac{dn}{n} = \sqrt{\frac{m}{2\pi k T_{tr}}} \exp\left(-\frac{mv^2}{2kT_{tr}}\right) dv \quad . \tag{B4.12}$$

Here $k$ is the Boltmann constant, $n$ is the concentration of the emitting particles and $m$ their mean mass. If $v$ is replaced by $dv$ using Eq. (B4.11) and its derivative the result is:

$$\frac{dn}{n} = \sqrt{\frac{mc^2}{2\pi k T_{tr}\lambda_0^2}} \exp\left(-\frac{mc^2}{2kT_{tr}}\left(\frac{\Delta\lambda}{\lambda_0}\right)^2\right) d(\Delta\lambda) \quad . \tag{B4.13}$$

In a so-called optically thin plasma the radiation absorption plays only a minor role and the intensities of the spectral lines being observed are proportional to the concentration of the emitting particles. In a low pressure plasma wind tunnel, an optically thin plasma can be assumed. Following Eq. (B4.13), the result for the intensity of a Doppler broadened spectral line is a distribution according to:

$$I(\Delta\lambda) = I_0 \sqrt{\frac{mc^2}{2\pi k T_{tr}\lambda_0^2}} \exp\left(-\frac{mc^2}{2kT_{tr}}\left(\frac{\Delta\lambda}{\lambda_0}\right)^2\right) \quad . \tag{B4.14}$$

Here $I_0$ is the entire intensity of the spectral line and herewith $I(\Delta\lambda)$ the intensity at a distance of $\Delta\lambda$ to the unshifted center $\lambda_0$. The width of the spectral line at half maximum counts as Doppler broadening. According to the equation above this is the case when the exponential term assumes the value 1/2. Therefore

$$\Delta\lambda = \sqrt{\frac{2kT_{tr}\ln 2}{mc^2}}\lambda_0 \tag{B4.15}$$

is valid. Because the distribution of the spectral line is symmetric under these assumptions, the entire Doppler broadening results in $\Delta\lambda_T = 2\Delta\lambda$, and herewith for the translational temperature of the emitting particles,

$$T_{tr} = \frac{mc^2\Delta\lambda_T^2}{8k\lambda_0^2 \cdot \ln 2} \tag{B4.16}$$

is attained.

## B4.6 Experimental Set-up

Two experimental set-ups are in use at the IRS for the Fabry-Perot interferometry. The first experimental set-up is completely outside the vacuum tanks and can be applied to every plasma wind tunnel in operation. The second experimental set-up uses fiber optics for sampling and monitoring the plasma emission on the FPI. For the first set-up, shown in Fig. B4.4, emitted light of the plasma jet is sampled with a collimating optic through an optical window. A plano-convex lens with a focal length of 2000 mm or 1500 mm is focused on the centerline of the plasma plume via a steerable mirror. Different angles of incidence are adjustable by turning the mirror and sliding the lens in order to keep the focus length. Keeping the focus in the centerline provides light intensity integration over equal volumes of the plasma plume to the right and left hand side of the centerline. The parallelized light of the plasma enters a cubic beam splitter where it is united with an unshifted and unbroadened but also parallelized light of an external lightsource, which could be a laser or also a broadened but unshifted light of the plasma plume sampled under perpendicular incidence with $\alpha$=90°. Behind the beam splitter the light enters the FPI. The light which passes through the FPI is focused by a f=84 mm focal length lens on the pinhole entrance of a monochromator. The monochromator works as a special filter and a fast single channel photomultiplier (PMT) is used as a signal detector. The monochromator is necessary to prevent stray light from entering the PMT which transforms the light intensity into a voltage signal to be detected with a storage oscilloscope.

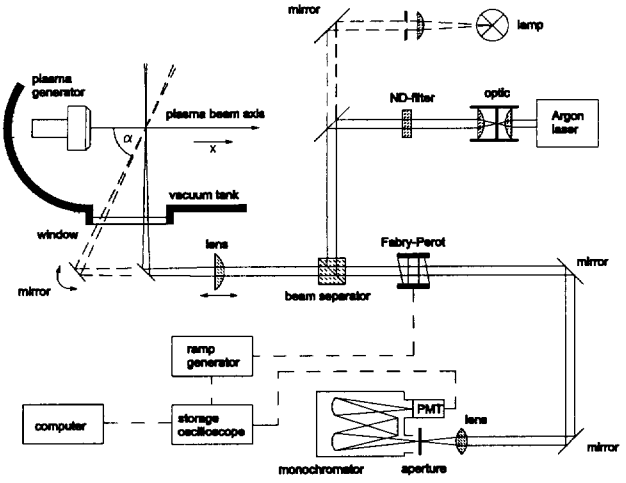


**Fig. B4.4: Experimental set-up of the Fabry-Perot interferometer**

The modified second experimental set-up is shown in Fig. B4.5. It provides easy access to the light emitted by the plasma plume without intensive calibration of the optical path to the FPI. Moreover, with this set-up there is no longer a limitation in the observation angle due to the window locations. Two fiber optics can be mounted on the positioning system in the plasma wind tunnel. The optical axes of both optics are orientated under a fixed angle of $\alpha$=45°. The focus of both optics is exactly at the same position in the plasma beam and can be moved to every position. Since one of the optics will always be mounted perpendicular to the plasma beam axis, the observation angle $\alpha$ is always 45°. A third fiber optic provides the possibility to feed laser light into the FPI for calibration purposes. Each of the three fiber optics can be plugged into an optical system which parallelizes and widens the light beam coming out of a fiber optic.

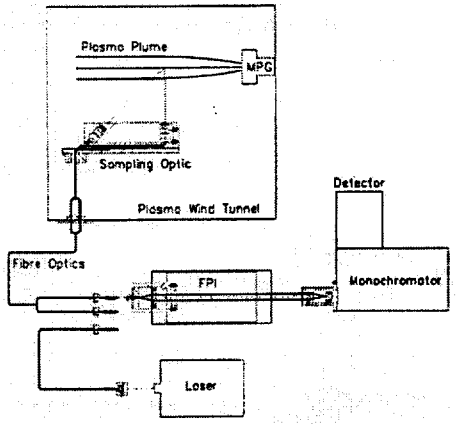


**Fig. B4.5: Schematic of the experimental set-up using fiber optics**

## B4.7 Measurement Results

To examine the Doppler effects, one has to choose an adequate spectral line emitted by the plasma. Taking an emission spectra with the FPI experimental set-up or with emission spectroscopy (see Fig. B2.13), strong lines can be identified. Furthermore, to achieve high resolution (see eq. B4.6), longer wavelengths are preferred. One of the strongest emission lines rises out of the transition of atomic nitrogen at $\lambda_0$=746.83 nm.

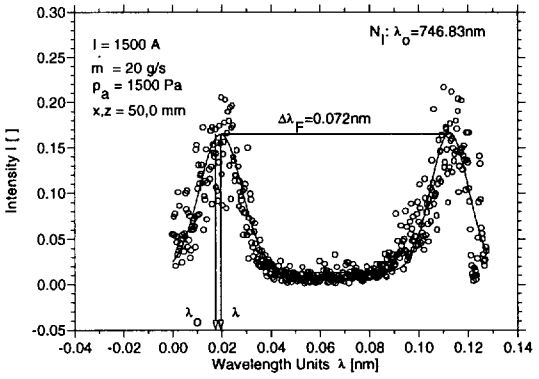


**Fig. B4.6: Doppler shifted $N_I$ emission line of an air plasma flow**

In Fig. B4.6, two orders of a typical shifted $N_I$ emission line are shown. The distance between the two line maximas represents the free spectral range $\Delta\lambda_F$ =0.092 nm. The plotted circles describe the signals of the photomultiplier, while the solid line is the fitted curve in order to determine the center of the full width at half maximum (FWHM). This center

represents the shifted wavelength $\lambda$. The FWHM gives the total line broadening $\Delta\lambda_G$ from which $\Delta\lambda_T$ is calculated (for line broadening see B2.1.2).
The axial distribution of the atomic nitrogen velocity in two air plasma flows of different conditions along the plasma plume center line axis can be seen in Fig. B4.7. These values are taken without Abel inversion. Due to the relatively flat velocity profile in the zone of high emission in this case, an Abel inversion does not change the result remarkably. The velocity distribution shows a "shock" behavior with decreasing velocity in the compression zone and acceleration in the expansion area for one of the test conditions.

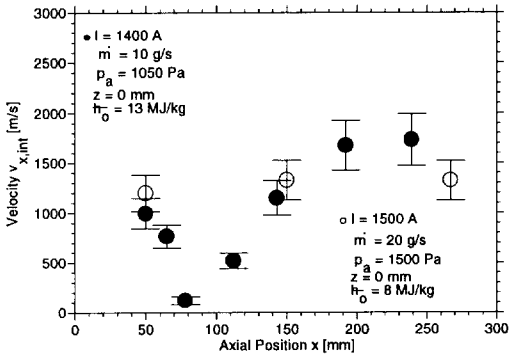


**Fig. B4.7: Axial distribution of the heavy particle velocity in air plasma flows of different conditions along the plasma plume center line axis**

Figure B4.8 shows the broadened profile of a $N_I$ emission line. The instrumental broadening $\Delta\lambda_R$ is illustrated to show the effect of the thermal broadening.

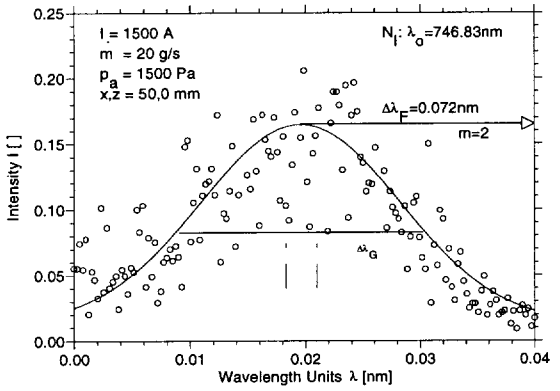


**Fig. B4.8: Broadened profile of a $N_I$ emission line of an air plasma flow**

The resulting temperatures in a radial scan for different plasma condition is pictured in Fig. B4.9 again taken without an Abel inversion (see section B2.3.5).

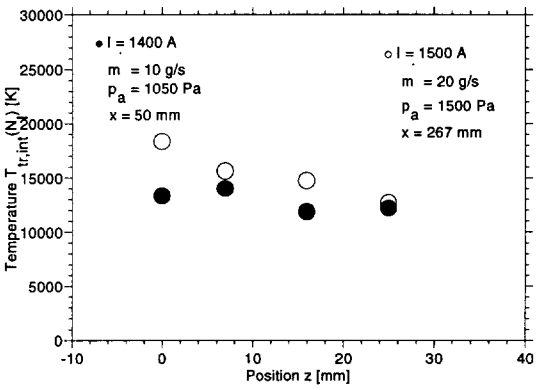


**Fig. B4.9: Radial temperature distribution**

## References

[B4.1] Habiger, H.,"Elektrostatische Sonden und Fabry-Perot Interferometrie zur Untersuchung von lichtbogenbeheizten Plasmen für Triebwerksanwendungen und Wiedereintrittssimulation", Dissertation, Universität Stuttgart, 1994.

[B4.2] Auweter-Kurtz M.,"Manuskript zur Vorlesung Messverfahren für strömende Plasmen", Institut für Raumfahrtsysteme, Universität Stuttgart.

[B4.3] Habiger H., Auweter-Kurtz M.,"Fabry-Perot Interferometrie for the Investigation of a High Enthalpy Plasma Flow", AIAA-5-2040, 30th AIAA Thermophysics Conference, San Diego, 1995.

# B5 Laser Diagnostics

Laser technics are in use in plasma wind tunnels for identifying particles, determining particle densities of atoms, molecules and electrons and for plasma velocity measurements. A big part of our knowledge of the structure of atoms or molecules could be gained by laser diagnostic measurement methods. Laser-based techniques offer the capability of performing spatially and temporally resolved measurements for a host of important parameters of the plasma jet and the boundary layer in front of heat shield materials, which can lead to an improved understanding of the material behavior. The interaction between the electromagnetic radiation of the laser and particles leads firstly to absorption and/or scattering and in consequence to emission spectra. The emission provides information about the behavior of species under investigation as explained in section B2.

## B5.1 Laser Induced Fluorescence

Laser induced fluorescence is a well-established, sensitive technique for detecting population densities of atoms and molecules in specific quantum states and offers the possibility of investigating species of interest in a selective way just by choosing the appropriate wavelength.

## B5.1.1 Basic Theory

With laser induced fluorescence, an upper electronic state is populated by a laser source with an emission frequency tuned to an optically allowed resonance between the electronically and rotationally vibrationally excited state and a discrete lower state, typically the electronic ground level. Fluorescence then denotes the following radiation emitted by molecules or atoms, decaying by spontaneous emission of a photon in an optically allowed transition from a higher to lower energy state. The fluorescence occurs parallel to other processes which act to de-excite the molecule, such as collisional energy transfer to other molecular states.

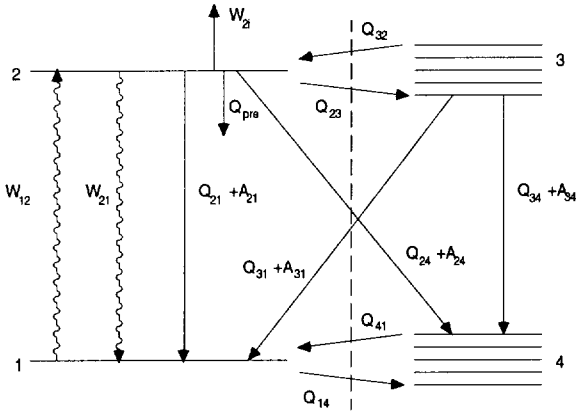


**Fig. B5.1: Energy level diagram of important populating and depopulating processes**

Figure B5.1 shows the excitation and de-excitation processes involved by exciting a molecule. After excitation ($W_{12}$), the laser-populated upper state may undergo a number of subsequent processes. Firstly, the molecule can be returned to its original state by stimulated emission ($W_{21}$). Secondly, absorption of an additional photon can excite still higher molecular states, including ionized levels ($W_{2i}$). Thirdly, the internal energy of the system can be altered in inelastic collisions with other molecules producing rotational and vibrational and also electronic energy transfer, the latter is often referred to as quenching ($Q_{ij}$). Fourthly, interactions between the separate atoms of the molecule, known as internal collisions, produce internal energy transfer and dissociation of the molecule. When the dissociation is produced by a change from a stable to a repulsive electronic arrangement in the molecule, it is called predissociation ($Q_{pre}$). Finally, there is the fluorescence signal ($A_{21}$) of the originally populated state and nearby states, indirectly populated through collisions [B5.1]. This signal can be captured with a photodetector and can be related to specific properties of the absorbing species through modeling of these state-to-state transfer processes. As the fluorescence is a function of the upper states population density, this requires solving the state dependent population dynamics. While quantum-mechanical density-matrix descriptions of the interactions involved in LIF are available, most treatments of LIF are based on a semi-classical rate equation analysis [B5.2]. The rate equations are conceptually and mathematically more traceable than the quantum approach, but fail to include possible coherence effects. Generally, the validity of the rate equation analysis holds true for laser pulses which rise slowly compared to the characteristic collision time. The time dependent population N(t) of a specific energy level j among a set of other levels i can be modeled with the set of rate equations, given by:

$$\frac{dN_j(t)}{dt} = \sum_{i \neq j} \left(N_i(t) Z_{ij}\right) - N_j(t) \sum_{i \neq j} Z_{ji} \quad . \quad \text{(B5.1)}$$

The first summation represents events which populate j while the second denotes loss processes. The total rate coefficient for all events transfering molecules from level i to j is $Z_{ij}$ ($s^{-1}$). A number of distinct rate coefficients are included in this overall coefficient: the collisional transfer coefficient $Q_{ij}$ ($s^{-1}$), encompassing both intermolecular and internal collisions, the Einstein coefficient $A_{ij}$ ($s^{-1}$) for spontaneous emission and the coefficient for laser stimulated processes $W_{ij}$ ($s^{-1}$). For single photon laser stimulated absorption or emission, $W_{ij}=B_{ij}I_\nu$, where $B_{ij}$ ($cm^2J^{-1}Hz$) is the Einstein B coefficient and $I_\nu$ is the laser spectral intensitiy. Applying equation (B5.1) for the energy levels involved gives a system of differential equations. The equations depend on the excitation and detection scheme used for a specific molecule or atom and have to be solved taking into consideration the special properties of the quantum mechanical behavior of the particle. For a simple two level model, where only the ground (index 1) and the directly excited state (index 2) are taken into account, the system of differential equations becomes:

$$\frac{dN_1}{dt} = -N_1 W_{12} + N_2 (W_{21} + A_{21} + Q_{21}) \,, \text{(B5.2)}$$

$$\frac{dN_2}{dt} = N_1 W_{12} - N_2 (W_{21} + A_{21} + Q_{21} + Q_{pre} + W_{2i}) \quad \text{(B5.3).}$$

Assuming that predissociation $Q_{pre}$ and photoionization $W_{2i}$ can be neglected and the population of the excited state prior to the laser excitation is negligible as well, the total population in the system is constant and for moderate temperatures in good approximation equal to the initial population of the ground state $N_1^0$ prior to laser excitation. This population can be calculated with the Boltzmann expression, according to equation (B2.35). The lower index of $N_1^0$ accounts for the state and the upper index indicates t=0, i.e. prior to the laser pulse, such that:

$$N_1 + N_2 = \text{constant} = N_1^0 \quad . \quad \text{(B5.4)}$$

The time dependent population for the excited state can then be written as:

$$N_2(t) = \frac{W_{12} N_1^0}{r} (1 - e^{-rt}) \quad , \quad \text{(B5.5)}$$

where

$$r=W_{12}+W_{21}+A_{21}+Q_{21}. \quad \text{(B5.6)}$$

For steady state assumption, i.e. the rates of the exciting and decaying processes reach a steady state behavior, the population in the excited state is then given by:

$$N_2 = N_1^0 \frac{B_{12}}{B_{12}+B_{21}} \frac{1}{1+\frac{I_{sat}^{\nu}}{I_{\nu}}}, \quad \text{(B5.7)}$$

where the saturation spectral irradiance $I^{\nu}_{sat}$, i.e. the laser irradiance which saturates a transition, is defined as:

$$I_{sat}^{\nu} = \frac{(A_{21}+Q_{21})c}{B_{12}+B_{21}}, \quad \text{(B5.8)}$$

with c as the speed of light. In the saturation regime the maximum number of molecules or atoms are in the excited state. Increasing the laser irradiance will not increase the fluorescence signal any more. At low laser excitation irradiances, i.e. $I_{\nu}<<I^{\nu}_{sat}$, the fluorescence is said to be in the linear regime, namely linearly proportional to the input laser irradiance. For $I_{\nu}>>I^{\nu}_{sat}$, the saturated regime is reached, where the fluorescence signal becomes independent of quenching processes and the laser irradiance. In the saturation regime, the rates of laser absorption and stimulated emission become so large that they dominate the state-to-state energy transfer into and out of the directly pumped levels. Saturation also maximizes the fluorescence signal. However, complete saturation is not easy to achieve, especially in the wings of the laser focus and during the entire duration of the laser pulse.

In the linear regime, the fluorescence signal depends on the laser irradiance. To make the measurement independent of the fluctuations of laser energy, one has to normalize the fluorescence signal to the laser irradiance. Additionally the quenching rate can be determined experimentally in the linear regime. In low pressure regimes and low laser irradiances, the quenching rate can be measured by monitoring the exponential decay rate, i.e. the time resolved decay of the excited molecules to the ground level. An excited level has a certain molecular dependent lifetime, which is described with: $\tau=1/(A+Q)$ [B5.2]. Here, Q stands for all de-excitation processes and A again for the spontaneous emission rate. By monitoring the time decay, one can extract the de-excitation rate, as seen in Fig. B5.2.

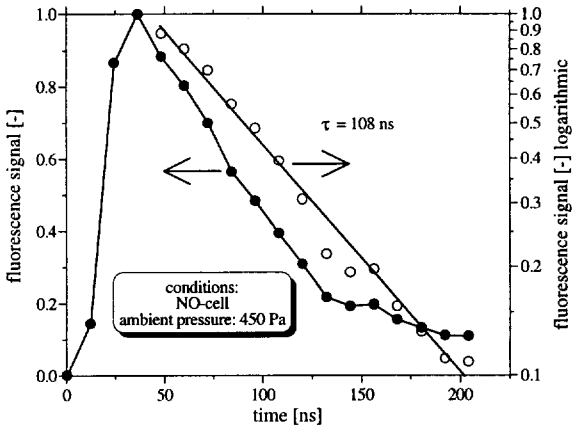


**Fig. B5.2: Lifetime measurement of NO in a cold gas cell [B5.3]**

## B5.1.1.1 Two-Photon Excitation

As will be explained in B5.1.2.1, with modern laser equipment tunable radiation can be generated in a continous spectral range down to about 200 nm. However, most atoms and several molecules possess absorption lines well below 200 nm. The spectral region below 200 nm is termed the vacuum ultraviolet (VUV), since radiation in this range will not propagate through air due to atmospheric absorption, initially by molecular oxygen. Transitions below 200 nm can be accessed and excited via the simultaneous absorption of two photons (or more). Most of the excitation schemes involve single wavelength multi-photon excitation and are of course favourable since one needs only one laser. An example of the excitation scheme of atomic nitrogen is illustrated in Fig B5.3. The two-photon excitation rate constant per molecule may be written as:

$$W_{12} = \frac{\alpha_{12} I^2}{h\nu} \quad \text{(B5.9)}$$

where $\alpha_{12}$ is the two-photon absorption cross section from state 1 (ground state) to state 2 (excited state). The two-photon cross sections are small which means that stimulated two-photon downward transitions can be neglected for moderate laser irradiances. The fluorescence signal will depend quadratically on the laser irradiance and on the quenching rate constant as in the linear fluorescence regime.

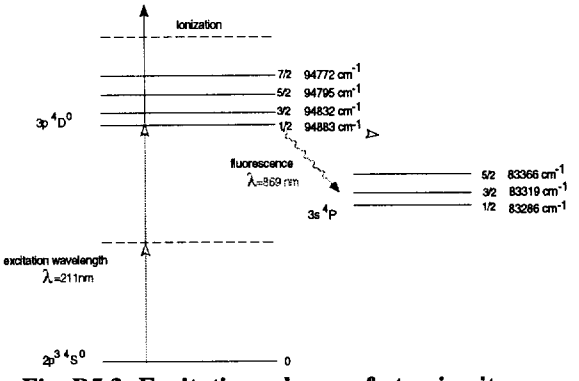


**Fig. B5.3: Excitation scheme of atomic nitrogen**

By absorption of a third photon, the particle can be ionized. Since this means a loss in fluorescence signal, one has to ensure that the laser energy is kept sufficiently low.

### B5.1.1.2 Fluorescence Detection and Temperature Considerations

The intensity of the fluorescence signal is proportional to the number density $N_2$ in the excited state and can in general be described with:

$$S = C_{KAL} h\nu N_2 A_{21} \qquad \text{(B5.10)}$$

The calibration constant $C_{KAL}$ has to be determined for the experimental set-up used and includes the transmission of the fluorescence through windows, filters, lenses and influences of the excitation and collection volume and the electronics in the data capturing process. The term hν describes the photon energy of the emitted photons. $N_2$ is determined with the rate equation model. The initial population prior to the laser pulse $N_1^0$ of the rotational quantum state is related to the total number density and temperature via the Boltzmann expression, see equation (B2.35). Therefore, the temperature has to be determined first. For molecules the temperatures which describe the population distribution in different rotational, vibrational and electronical levels are called the rotational, vibrational and electronical temperature, as explained in B2.1.4 and B2.2.4. Mostly one only has access to the rotational temperature which is coupled with the heavy particle temperature in plasma applications. If the temperature is high enough to populate different vibronic levels, the vibrational temperature can be determined with the so-called two line thermometry. The best access to the rotational temperature is given by doing an excitation scan over the rotational states in the ground state [B5.2]. The laser wavelength is changed continuously over the range of the rotational absorption lines of the electronical transition of the particle. If the fluorescence $F_J$ of each transition is monitored and normalized by the degeneracy (2J+1), fluorescence quantum yield (A/(A+Q) and line strength $B_{12}$, and plotted in semi-log fashion against the rotational energy $hcB_vJ(J+1)$, like

$$\ln\left(\frac{F_J \cdot B_{12}/(A/A+Q)}{2J+1}\right) = -B_v J(J+1)\frac{hc}{kT} + const. \qquad \text{(B5.11)}$$

a straight line is obtained with negative slope whose magnitude equals $(kT)^{-1}$ thus yielding the rotational temperature. If the exact temperature cannot be determined but the approximate value $\overline{T}$ is known, one can use a transition whose quantum number J* is least sensitive to temperature changes. Therefore, setting the derivative of the Boltzman expression over the temperature to zero leads to:

$$J^{*2} + J^* - \left(\frac{k}{hcB_v}\right)\overline{T} = 0 \ . \qquad \text{(B5.12)}$$

### B5.1.1.3 Calibration

In order to determine the number density from a LIF experiment, values for a number of parameters related to the employed excitation and detecting scheme are required. The exciting wavelength and the spectral width of the laser beam has to be determined as well as the laser pulse length and the laser pulse energy. The light collection efficiency, the collection solid angle and the sample volume have to be evaluated. In the linear fluorescence regime the fluorescence quantum yield has to be measured to account for quenching losses. The influence of the electronical data acquisition system has to be identified.
Calibrations are often performed by employing a gas cell filled with a known density and temperature of the examined gas in the observation volume and leaving any other part of the experimental set-up unchanged. Building the ratio with equation (B5.10) for the calibration measurement and the experiment ($N_2$ (Eq. B5.7) and the rotational and vibrational temperatures in the Boltzmann distribution equations (B2.35) are different), lead directly to the number density of the species. However, this procedure requires a stable molecule or atom, for instance nitric oxide. Since LIF is a method used mainly for monitoring reactive species (N, O, SiO, OH etc.) other calibration techniques have to be used. There are different methods established to approach the calibration process, like Rayleigh scattering [B5.4], absorption measurements [B5.5] and Raman scattering [B5.6]. Every process has advantages for certain applications. The calibration procedures used at the IRS will be discussed in B5.1.2.

## B5.1.2 Research at the IRS

The possibilities offered by LIF are tremendous. LIF can contribute solutions in almost all plasma relevant questions. It can help to identifiy the species involved in a material erosion process, provide data about the catalycity of a material and monitor plasma parameters. However, high operating expenditure is demanded. It is necessary to control and synchronize the laser with the monochromator, the data capturing electronics, e.g. the gated integrator and boxcar averager, the digital storage oscilloscope, the energy meter and the computer. Special care and further analysis has to be done when relating the fluorescence signal to absolute number densities by calibrating the detection optics. And finally the alignment of the optical paths are crucial for the quality and the precision of an experiment. The research so far has focused on determining number densities as well as on the characterization of erosion mechanisms of thermal protection materials. For the characterization of the plasma flow, the atomic densities of nitrogen (N) and oxygen (O) are of special interest. These quantities are also monitored together with nitric oxide in the boundary layer of a probe material for the investigation of the material

catalycity. The boundary between active and passive oxidation of silicon carbide (SiC) can be determined by exciting silicon oxide (SiO) molecules. Furthermore, the evaluation of the relative density of silicon oxide, carbon oxide and nitric oxide (absolute measurements planned as well) in front of a material probe will help us to better understand the erosion mechanism.

## B5.1.2.1 Experimental Considerations and Experimental Set-up

In general, the fluorescence wavelength is different from that of the incident excitation and occurs primarily, but not exclusively, at longer wavelengths. The photons emitted from the excited molecules radiate undirected. Therefore, the fluorescence signal can be detected under any angle, but it is advantageous to detect the fluorescence perpendicular to the propagation of the laser beam and perpendicular to the plasma flow under investigation because this provides the smallest observation volume and a non-Doppler shifted absorption line (see Fig. B5.4).

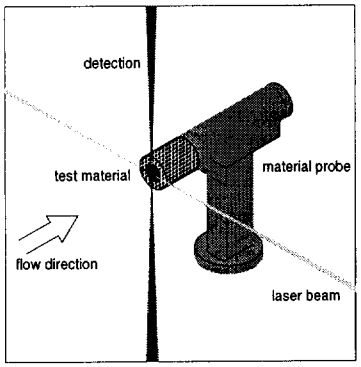


**Fig. B5.4: Principle of excitation and detection scheme**

There are two ways of setting up the experimental approach. In a single point measurement, the laser is focused into the observation area and the fluorescence is detected with a one-dimensional detector, generally a photomultiplier tube (PMT). The selection of the fluorescence wavelength can be achieved either with a monochromator or with an interference filter. The output signal of the PMT is then captured with a so-called gated integrator and boxcar averager. This device is designed to recover fast analog signals from noisy backgrounds. It consists of a gate generator, a fast gated integrator and exponential averaging circuitry. The gate generator provides an adjustable delay from a few nanoseconds to 100 milliseconds to an input trigger pulse before it generates a continuously adjustable gate of 2 ns to 15 µs. The fast gated integrator integrates the input signal during the gate. Figure B5.5 shows an example of setting the sampling gate of the boxcar averager (data acquisition device) in respect to the fluorescence signal. The position of the sampling gate is particularly important for density or temperature measurements as will be discussed in section B5.1.2.2.

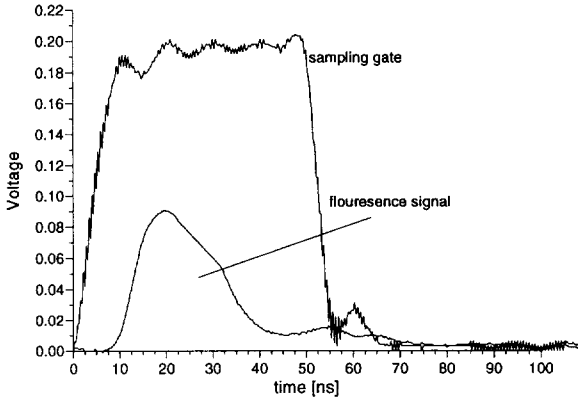


**Fig. B5.5: Example of setting a sampling gate**

For a planar LIF (PLIF) measurement, the excitation laser beam is optically spread into a thin sheet, and the resulting fluorescence from the illuminated plane is imaged through an appropriate filter onto a two-dimensional detector.

At the IRS, a laser system is available to experimentally examine plasma flows and boundary layers within the plasma wind tunnels. The laser system consists of an excimer laser Lambda Physik COMPex201, a dye laser Lambda Physik SCANmate 2E and a second harmonic generator to double the frequency. The excimer laser is filled with XeCl and emits radiation at around 308 nm. This laser light is passed to the dye laser to pump the circulating dye inside the oscillator / preamplifier and main amplifier cells of the dye laser. The oscillator determines the quality of radiation and is therefore the most important and sensitive part of the dye laser. It basically consists of a grating for wavelength selection and an etalon for ultra-narrow line width operation. If needed, the etalon can be moved in the laser beam path to improve the laser line width from 0.15 $cm^{-1}$ without etalon to 0.03 $cm^{-1}$ with etalon.

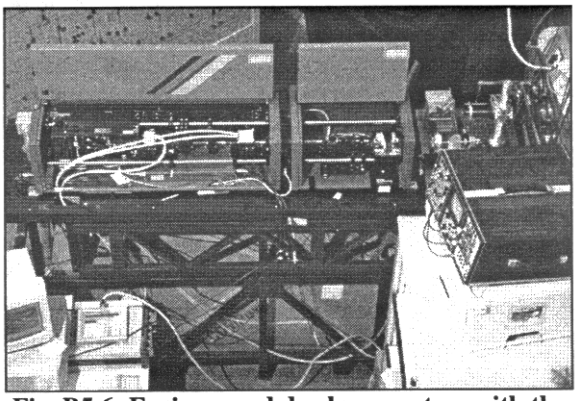

**Fig. B5.6: Excimer and dye laser system with the frequency doubling unit at PWK2**

This becomes particularly important for determining atomic or molecular velocities with Doppler shift measurements (see also section B4.4). Since many absorption lines of atoms or molecules are in the C-UV (C-ultraviolett, 180-280 nm) or even VUV (vacuum ultraviolett, below 180 nm) region and the different dyes cover a spectral range of 320-1050 nm, a frequency doubling unit was installed. It is a Beta Barium Borat (BBO) crystal followed by a quartz plate to compensate for the beam shift. In order to separate the UV and the fundamental beam with low losses and without beam displacement, four quartz Pellin-Broca prisms, set nearly to Brewster's angle (angle for which the transmission of vertically polarized light is the highest), are placed in the beam path. To provide the specific excitation wavelengths for the species of interest, different dyes, dissolved in Methanol, were used as shown in Table B5.1.

| Dye | For excitation of | Peak [nm] | Range [nm] | Efficiency [%] |
|---|---|---|---|---|
| Stilbene 3 | N | 425 | 412-443 | 9 |
| Coumarin 47 | NO O | 456 | 440-484 | 18 |
| Coumarin 102 | SiO | 480 | 460-519 | 18 |

**Table B5.1: Characteristic values for the dyes used with an XeCl-excimer laser excitation source**

With this laser system, it is possible to obtain wavelengths from around 200 nanometers up to 1050 nanometers by choosing the desired dye. Typical maximum laser energy outputs after the frequency doubling unit are about 3-4 mJ. The laser pulse length can be monitored by using the Rayleigh signal and is about 25 ns. Rayleigh scattering is an elastic process in which there is no energy exchange between the incident photons of light and the target molecules. Thus, the scattered light is unshifted from its initial incident frequency. This is explained in section B5.2. To make the measurement independent of the fluctuations of laser energy, one has to normalize the fluorescence signal to the laser irradiance, where the laser energy can be measured with a pyroelectric energy meter. In Fig. B5.7 the experimental set-up and the assignment of the axes are shown. The x-axis is the plasma beam axis, the y-axis is perpendicular in the horizontal, i.e. along the laser beam path and the z-axis is perpendicular in the vertical, here along the path of the collection optics. Fluorescence is detected perpendicular to the laser and the flow direction. It is monitored with a telescope consisting of two planoconvex fused silica lenses three inches in diameter and detected using photomultiplier tubes with a very short rise and transition time (usually less than 2 ns). The output current of the photomultiplier tube is terminated with a 50 Ohm load and passes through a preamplifier before it is sampled by a boxcar averager and transmitted via the GPIB interface to the computer for data processing.

### B5.1.2.2 Examination of Nitric Oxide

The formation of NO is a result of the recombination of N and O atoms on surfaces and contributes to the heat flux to which the material is exposed. This formation strongly depends on the material's catalycity which has to be minimized for thermal protection application. An attempt has been made to examine NO in the PWK. The γ-band of NO is used to excite molecules from the ground state.

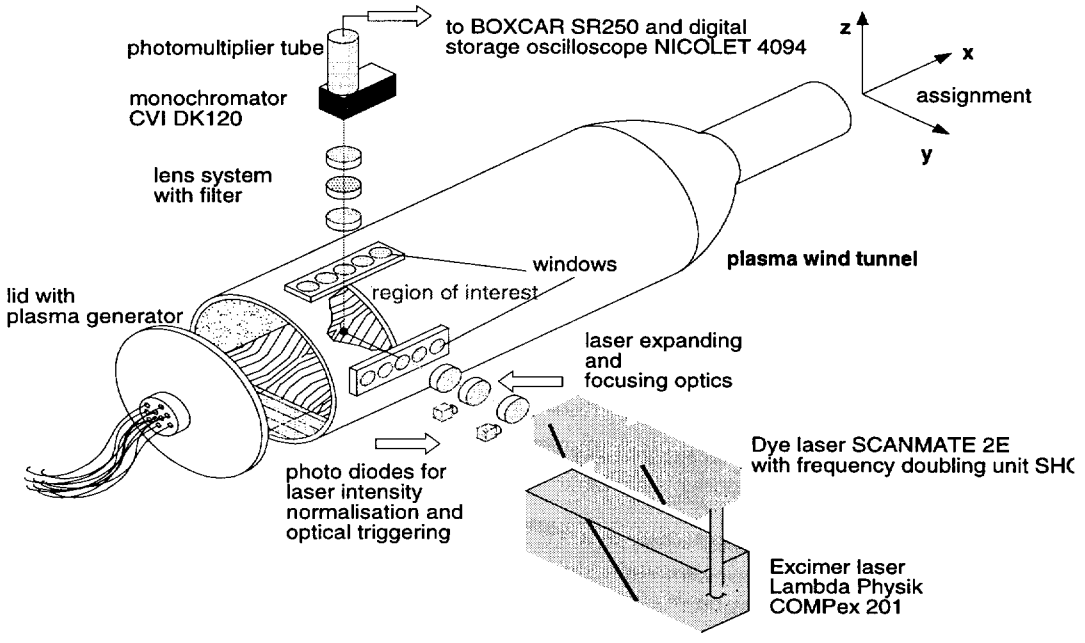


**Fig. B5.7: Experimental set-up at PWK2**

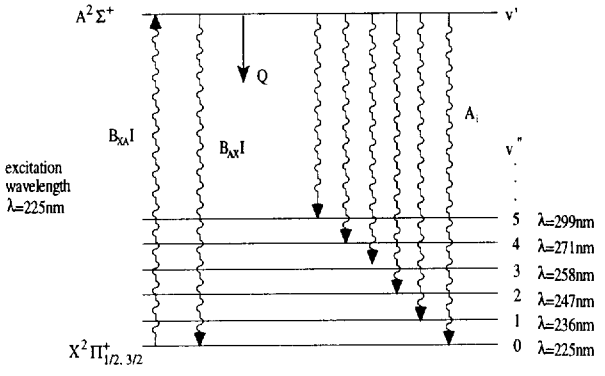


**Fig. B5.8: Energy level diagram for nitric oxide**

Figure B5.8 shows the radiation and collision processes involved. The monochromator was set at 260 nm with an exit slit of 4 mm, resulting in a detected range of 234 to 286 nm, so that fluorescence from (0,1) to (0,4) vibrational bands could be detected and scattered laser light at 225 nm is rejected. The sampling gate width was set to 200 ns to sample all the fluorescence for an acceptable signal-to-noise (S/N) ratio. Therefore, caution must be taken when calculating rotational temperatures. Rensberger et al. [B5.7] described the requirements for obtaining accurate temperatures. They proposed using small gate widths to account for rotational energy transfer. A gate width, which collects fluorescence over the exponential decay, leads to a measured temperature which is too high because excited states with high rotational quantum numbers can have a longer lifetime than states with low quantum numbers. For these PWK conditions it was necessary to detect any fluorescence signal in order to get a signal high enough to be used for data processing. The occurrence of NO in a plasma jet decreases with increasing enthalpy [B5.8, B5.25]. For operating conditions at high enthalpies of around 30 MJ/kg and pressures of approximately 300 Pa, as is of importance for the qualification of winged vehicles [B5.9], there is no LIF-detectable amount of NO concentration in the plasma beam axis of the free stream. Under these arc heater conditions, the mole fraction of NO is numerically estimated to be about $10^{-5}$ [B5.10]. But the situation is very different in front of a material probe positioned in the same plasma jet due to the material catalycity. Figure B5.9 shows an excitation scan with an arc current of 1200 A at an axial distance of 467 mm and 1 mm in front of a water-cooled copper probe. The scan is performed at laser irradiances in the linear fluorescence regime and the fluorescence is normalized to laser intensity. Fifty samples have been averaged to achieve a statistical result. The data are normalized to the maximum fluorescence signal from the overlapping $Q_2(35)$ and $R_1(28)$ lines and background subtracted. The line assignment is done by comparing the experimentally obtained spectra with a simulated spectra of LIFBASE [B5.11]. To acquire the fluorescence, the collection volume had to be made comparably large to get enough of a signal. Additionally, precautions have to be taken for the reabsorption of fluorescence since the occurrence of NO in the outer region of the plasma beam is comparably high.

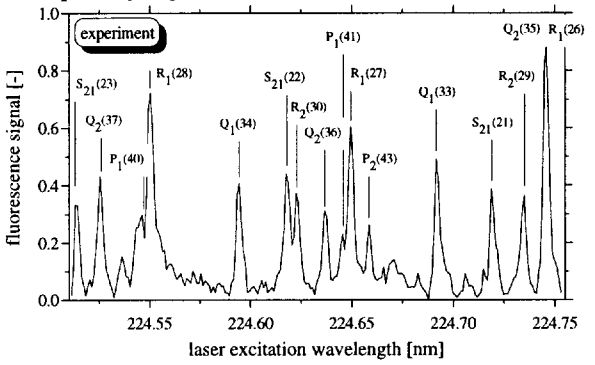


**Fig. B5.9: Excitation scans of NO 1 mm in front of a water-cooled copper probe, placed at an axial distance of x=467 mm in PWK with an arc current of 1200A and rotational assignment**

In Fig. B5.10 one can see that NO is produced as a result of a water-cooled copper probe placed in the plasma beam axis. It is apparent that the background noise at the beam axis is high compared to the fluorescence signal. The data are normalized to the fluorescence signal taken at 1 mm to the probe surface. There is no fluorescence signal in the free stream plasma flow. At a distance of 6 mm from the collected volume to the probe surface there is a detectable amount of NO, which increases as the distance to the probe decreases. Taking into account this fact together with the low rotational temperatures of ca. 1200 K, leads to the assumption that NO is produced by catalytic interactions with the probe surface and not because of adequate conditions in the boundary layer.

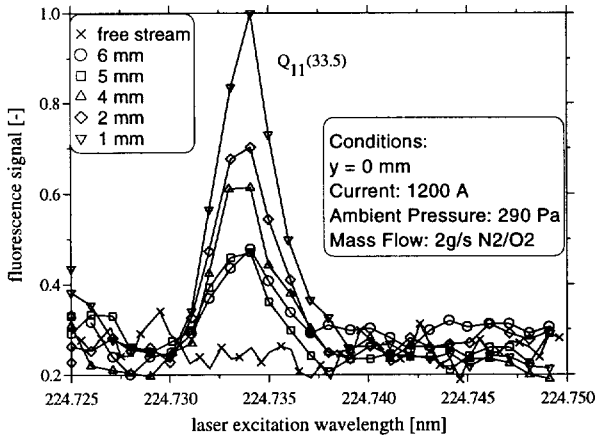


**Fig. B5.10: Integrated NO fluorescence at various distances to a water-cooled copper probe at an axial distance of x=467 mm**

Bismuth is known to have low catalycity. Therefore experiments with a bismuth coated surface were performed but signal levels are too weak for data processing. To get a profile for the y-axis, measurements were carried out in one direction of the y-axis from the center to the outer region, assuming rotational

symmetry. The spatial scan is seen in Fig. B5.11 which was taken with a cooled copper probe placed at y=0.

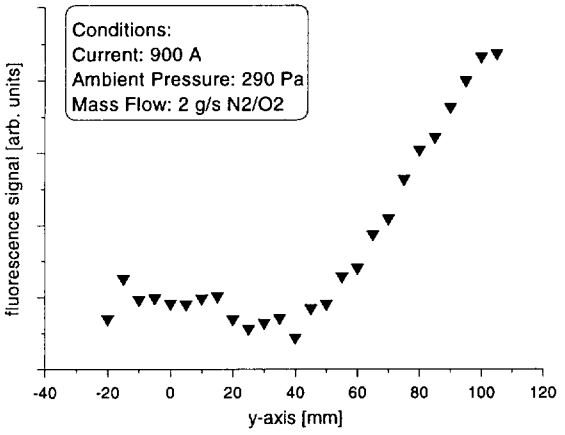


**Fig. B5.11: Radial profile of fluorescence signal of NO at an axial distance of x=467 mm**

The qualitative radial distribution of NO molecules is in agreement with mass spectroscopy measurements. The observation window of the PWK has a diameter of 100 mm. Therefore, the signal with a radial distance of more than y = 20 mm is not collected correctly perpendicular to the laser beam. But the effect on the collection volume is negligible since the angle varies only by about 1 to 4 degrees. To suppress the influence of the temperature, a ground rotational state which is least sensitive to an estimated rotational temperature is chosen to excite NO molecules. It was calculated from evaluating the derivative of the Boltzmann expression with respect to temperature and equating it to zero according to equation (B5.12). The molecular data were taken from LIFBASE [B5.11]. There is a very small amount of NO in the plasma beam axis compared to the outer region of the plasma beam. The heavy particle temperature in the center of the free stream at x = 467 mm is about 6000 K [B5.26] which is too high for NO to occur. In the satellite region (at y=80 mm) there is a temperature of about 2500 K and therefore good conditions for NO stability. The increasing NO occurrence in front of a water-cooled copper probe agrees with the numerical prediction using the SINA Code [B5.10]. The probe is placed at x = 467 mm (Fig. B5.12). It is evident that the amount of NO increases in front of a probe and the heavy particle temperature which is coupled with the rotational temperature decreases. Absolute measurements could not be performed yet. At the IRS the calibration for NO will be done with a heated dynamic gas cell which is currently under construction. Heating the NO gas of known density is necessary in order to populate higher rotational states and excite a rotational transition with the same quantum number as used in the experiment.

## B5.1.2.3 Examination of Silicon Oxide

Ceramics and composites based on silicon carbide (SiC) are prime canditates for reusable thermal protection materials. The erosion behavior of thermal protection materials is still not known in detail. The reactions, which lead to the reduction of the thermal protection material, involve a host of chemical combination products and depend on pressure, temperature, plasma velocity and plasma components. Of great importance is the oxidation behavior of the material. The oxidation regime is divided into a passive and an active oxidation regime. In a situation where the oxidant pressure is so low that a protective layer of $SiO_2$ cannot be formed, SiO (gaseous) forms and leads to rapid consumption of the SiC and $SiO_2$ if available. This behavior is termed "active oxidation". The other mechanism which occurs at higher oxidant pressures is the formation of $SiO_2$ (solid) and immediate reduction to SiO (gaseous) by reducing gases in the environment. At those oxidant pressures where $SiO_2$ volatility is negligible, typical "passive oxidation" behavior is observed [B5.13, B5.14]. The monitoring of SiO formation while changing plasma parameters can be used to evaluate the conditions for the passive-active transition. The basic spectroscopic data are calculated numerically [B5.15, B5.16].

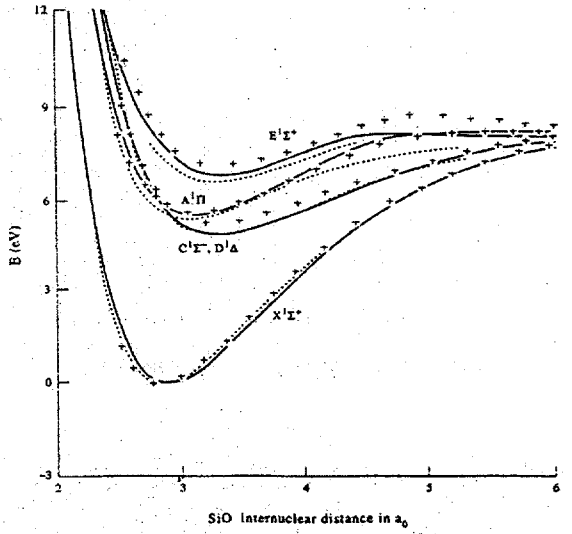


**Fig. B5.13: Energy levels of SiO [B5.15]**

Experimental data are available from the authors Heynes [B5.17] and Park [B5.18]. The known electronic states are shown in Fig. B5.13. The ground level is given with $X^1\Sigma^+$. The data, like the Franck-Condon-Factors and lifetimes, are only available for the electronically first excited level $A^1\Pi$ and the level $E^1\Sigma^+$. One can easily see that the $E^1\Sigma^+ \leftarrow X^1\Sigma^+$ transition can only be excited with a two-photon-absorption because the symmetry of the molecule does not change. The number of excited atoms or molecules are due to the probability of absorbing two photons almost instantaneously, less than with one photon absorption. Additionally the one-photon-excitation wavelength would be very close to the VUV (around 189 nm). Although this transition

offers a transition probability twice as high as the $A^1\Pi \leftarrow X^1\Sigma^+$ transition, it is advantageous to use the $A^1\Pi \leftarrow X^1\Sigma^+$ transition at around 235 nm because of the excitation wavelength and the one-photon absorption process. In order to identify SiO, an excitation scan (Fig. B5.14) is performed in front of the surface of a Si-probe material in an argon/oxygen plasma at an axial distance of 330 mm. The total pressure in front of the probe was 42 Pa and the front surface of the probe had a temperature of 1315°C. The fluorescence signal of the (0,4) vibrational band and parts of the (0,3) and (0,5) bands were monitored using an interference filter with 260±10 nm. Figure B5.15 shows the reaction zone of SiO in front of a silicon surface. Apparently with these plasma conditions, SiO is produced at the surface or at least close to the surface. It is planned to examine the behavior with the two-dimensional detection of the reaction zone. PLIF will be used to obtain relative concentrations of SiO, as well as from other erosion components (CO, CN, NO, SiN).

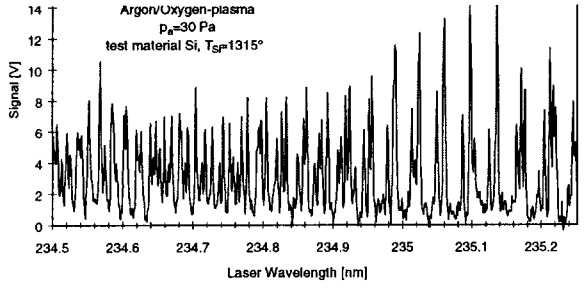


**Fig. B5.14: Excitation spectra of SiO**

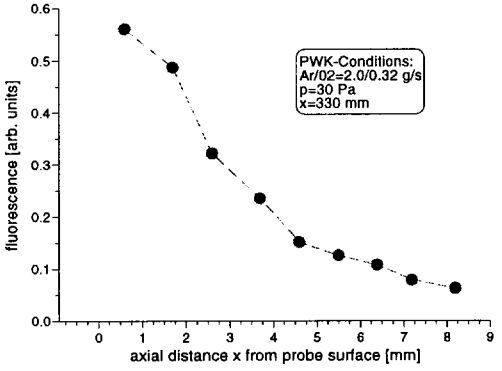


**Fig. B5.15: Reaction zone of SiO in front of a silicon wafer**

In a second step, the materials Si, $SiO_2$ and SiC were used and the surface temperatures were varied. The fluorescence signal was observed at a distance of 1 mm to the surface. With $SiO_2$ material, SiO is produced at a temperature of 1200°C whereas with SiC the onset takes place at 1500°C. An interesting result is seen with an SiC probe. Above 1750°C the process apparently seems to proceed with other dominant reactions. This will be examined in the near future.

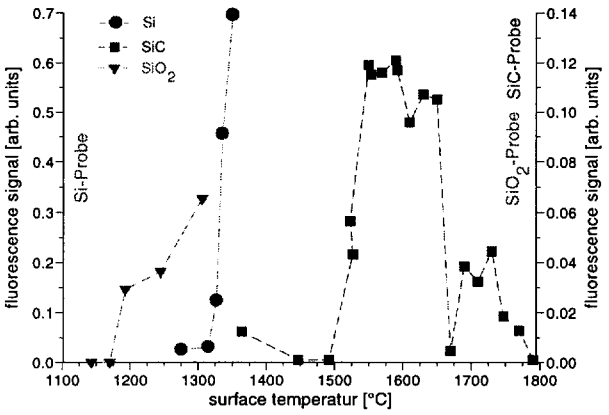


**Fig. B5.16: Temperature dependent erosion mechanisms of SiO for different materials at a total pressure of 42 Pa**

## B5.1.2.4 Examination of Atomic Oxygen and Atomic Nitrogen

There is great interest in determining atomic species concentration. This can contribute to gaining knowledge about plasma conditions created by the different generators and to evaluate phenomena of catalycity and erosion processes. The difficulties of atomic density measurement arise from calibration procedures. Since there are no reliable sources of atomic oxygen or atomic nitrogen production, it is very difficult and very complex to calibrate the measurements, i.e. to relate the fluorescence signal to a certain density. However, LIF can be used to determine N- and O-concentrations. The procedure follows experiments of Bamford et al. [B5.19], who developed an approach by carefully measuring all factors involved. As described in section B5.1.1.3, the spatial (dimension of the focus) and temporal spread (laser pulse length) have to be accounted for and the characteristics of the laser beam, the detection optics and electronics have to be calibrated. Furthermore, the fluorescence quantum yield has to be determined and for atomic nitrogen polarization (polarization explained in section B5.2) effects cannot be neglected. With these assumptions and by computing the system of differential equations, the number density can be calculated with:

$$N_0 = \left[ 4\pi^2 \left( \frac{S}{E^2} \right) \omega_v \omega_h \frac{(h\cdot\nu)^2}{\alpha} \phi_f \cdot D \cdot \int_{-\infty}^{\infty} F^2\left(t''\right) dt'' \right] \qquad \text{(B5.13)}$$

S is the measured voltage of the photomultiplier, E is the energy of a laser pulse, $\omega_v$ and $\omega_h$ are the focus sizes in vertical and horizontal directions, hν is the photon energy of the laser beam, α is the cross section for a two-photon absorption, $\phi_f = A/(A+Q)$ is the fluorescence yield and D is the calibration constant obtained with Raman spectroscopy. The constant includes the effective length of the light collection system, the solid angle of the collection lens, the transmission through

windows and filters, the quantum efficiency of the detector and the electronical conditions.

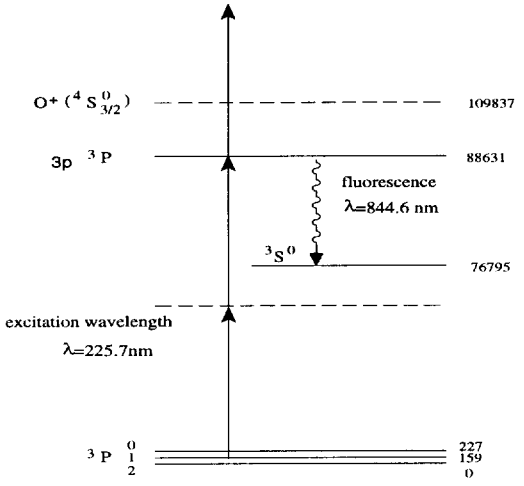


**Fig. B5.17: Excitation scheme of atomic oxygen**

The function F(t) accounts for the temporal profile of the laser beam. The fluorescence yield can be measured by monitoring the fluorescence decay curve, as explained in section B5.1.1. The excitation processes for atomic nitrogen and atomic oxygen are shown in Figs. B5.3 and B5.17, respectively. A spectra is shown in Fig. B5.18. The atomic oxygen was produced in a microwave discharge at low pressure. The three absorption lines arise out of the fine structure splitting, as can also be seen in the schematic excitation in Fig. B5.17.

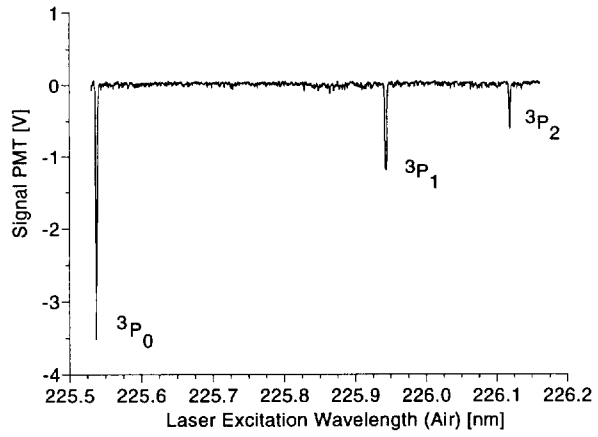


**Fig. B5.18: Excitation scan over the fine structure splitting of atomic oxygen**

As mentioned before, the requirements for an absolute measurement have to be satisfied. Raman scattering on $H_2$ is used to absolutely calibrate the photon collection efficiency of the detection optics [B5.6]. This calibration procedure has advantages over the other methods, mentioned in section B5.1.1.3. The collection efficiency can be calibrated for the exact laser focal volume used in the experiment at exactly the fluorescence wavelength. The influence of stray light from the laser beam (e.g. plays a role in calibrating with Rayleigh scattering technics) is greatly supressed since the transition used is shifted at 4155 $cm^{-1}$ to a higher wavelength than the incident laser wavelength. This Raman shift in $H_2$ at 4155 cm-1 is the largest of any molecular system and its spectroscopy is well known.
Furthermore, PWK2 can be operated with a mixture of $Ar/O_2$ and the inductive plasma generator PWK3 can be operated with pure oxygen. In the past an oxygen sensor was developed [B5.20 and see section A6] to monitor the partial pressure of oxygen. The difficulty is that the sensor cannot distinguish between atomic and molecular oxygen. Adjusting the PWK conditions in a manner that it can be assumed that all the oxygen is dissociated but not ionized offers a possibility to compare the results of both measurement methods.

## B5.2 Raman Spectroscopy

Raman scattering is the inelastic scattering of light from molecules and is termed rotational, vibrational or electronic, depending on the nature of the energy exchange which occurs between the incident light quanta and the molecules. Because polarization of light plays an important role in Raman spectroscopy, a short introduction to this topic is given. Optical radiation across the spectrum is in the form of transverse electromagnetic waves, that is, the directions of the oscillating electric and magnetic fields of any particular wave are perpendicular to the direction of travel and to each other. Polarization occurs when the electric field vectors for many waves in a beam assume a preferred direction rather than being randomly distributed. The electric field vector is used to describe the various states of polarization. Most incoherent sources emit rays that have electric fields with no preferred orientation and are therefore unpolarized. A beam is said to be linearly or plane polarized when all the electric field vectors are oriented in the same direction or plane of polarization. The plane of polarization is perpendicular to the direction of travel. When the plane of polarization is parallel to the plane of incidence, this is known as p-polarization. If the plane of polarization is perpendicular to the plane of incidence, this is known as s-polarization. The plane of incidence contains the direction of the incident beam and the normal to the surface. In addition to the linear polarization, cirular and elliptical polarization can occur.
Raman scattering essentially occurs instantaneously within a time of $10^{-12}$ s or less. The molecular polarizability, $\alpha$, relates the induced dipole moment, $\vec{p}$, to the incident electric field, i.e. $\vec{p} = \alpha\varepsilon_0\vec{E}$ and the dipole moment induced by an incident wave with frequency $\nu_0$ is then:

$$\vec{p} = \alpha_0\varepsilon_0\vec{E}_0\cos(2\pi\nu_0 t) + \left(\frac{\partial\alpha}{\partial Q}\right)_0 \varepsilon_0 \frac{Q_0\vec{E}_0}{2}\left[\cos(2\pi t(\nu_0 - \nu_\nu)) + \cos(2\pi t(\nu_0 + \nu_\nu))\right] \quad \text{(B5.14)}$$

with Q as the nuclear vibration coordinate. The subscript 0 stands for conditions in the equilibrium position of the atom nuclei. The first term leads to scattered radiation at the incident frequency, the Rayleigh process, while the second term leads to scattered radiation shifted from the incident wave by the characteristic frequencies of the medium, namely the Raman scattering. The radiation downshifted in frequency is termed Stokes, while that upshifted is termed anti-Stokes. The latter involves energy exchange from the molecule to the incident photon and occurs only at elevated temperatures when a sufficient excited state population exists [B5.2]. No specific laser wavelength is required and due to the quantization of the molecular energy states, the Raman spectrum resides at fixed frequency separation from the laser line and is characteristic for the molecule from which the scattering emanates. The Raman scattered signal is therefore species specific and linearly proportional to the species number density.

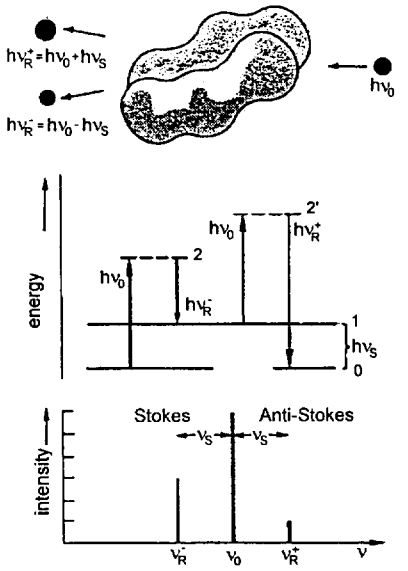


**Fig. B5.19: Schematical model of Raman scattering [B5.21]**

The energy model in Fig. B5.19 shows the transfer processes involved. State 0 describes the ground level, state 1 an excited vibration level. States 2 and 2' are imaginery states. The frequencies of the Raman scattering are $\nu_R^-$ and $\nu_R^+$. The Raman shift is described with $\nu_S$. The ground vibrational level is more highly populated than the excited levels due to the Boltzmann expression and therefore the intensity of Stokes shifted Raman scattering is mostly higher than the anti-Stokes shifted intensity.

Important factors of Raman scattering are the depolarization ratio and the cross section. The depolarization ratio ρ is defined by the ratio of the polarization of the scattered radiation and is:

$$\rho = \frac{I_{II} - I_{\perp}}{I_{II} + I_{\perp}} \quad , \tag{B5.15}$$

where $I_{II}$ and $I_{\perp}$ are the intensities of the scattered radiation with a polarization parallel or perpendicular to the polarization of the laser light. Raman scattering cross sections are necessary to determine the signal strength. In general, Raman cross sections and depolarization ratios depend on the species and are experimentally determined. Unfortunately, Raman scattering is very weak with small cross sections, thus requiring a certain number density of the species probed. In comparison with LIF, Raman requires concentration levels of 1% of the species mole fraction, whereas LIF can measure in the ppm (particle per million) range. For a small scattering solid angle, the radiant intensity $I_r$ may be expressed as:

$$I_r = I_i n \cdot \left(\frac{\partial \sigma}{\partial \Omega}\right) \cdot \Omega l \varepsilon \quad , \tag{B5.16}$$

where $I_i$ is the incident laser intensity, n is the number density of scattering species, $\partial\sigma / \partial\Omega$ is the differential cross section, Ω the collection angle, l the sampling extend and finally ε as the collection efficiency which has been included to account for losses in the optical collection system. Figure B5.20 shows a rotational Raman spectrum of $N_2$ as an example.

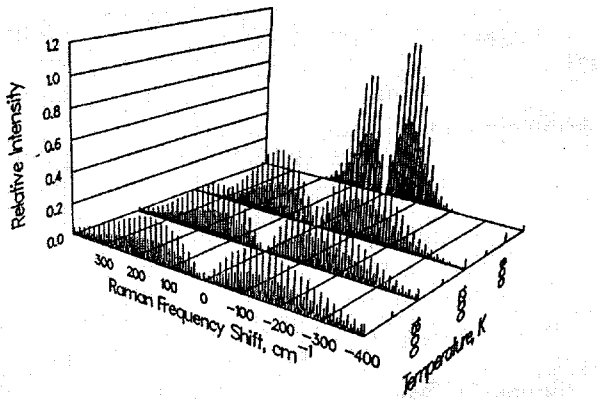


**Fig. B5.20: Temperature dependence of the rotational Raman of $N_2$ [B5.2]**

At the IRS, Raman spectroscopy is used for absolute calibration of the detection optics and electronics of the LIF experiments with Raman scattering in $H_2$. The molecular densities in the MPD wind tunnels are too small to obtain a sufficient signal.

## B5.3 Thomson Scattering

In recent years, the method of incoherent Thomson scattering has been applied to measure electron properties of plasma flows. When a laser beam is injected into a plasma, the laser radiation scatters non-resonantly from the free and bound electrons in the plasma. The total spectrum of the scattered light contains three main components: a Thomson scattering component which arises from scattering of free electrons, a Rayleigh scattering component which arises from incoherent scattering from the

bound electrons in the atoms and ions and a stray light component which arises from laser radiation scattering from the surfaces and windows of the chamber. The Thomson and Rayleigh components, which are both Doppler-broadened due to the motion of the scattering particles, have very different spectral widths because of the much higher thermal velocity of the electrons compared with the atoms and ions.

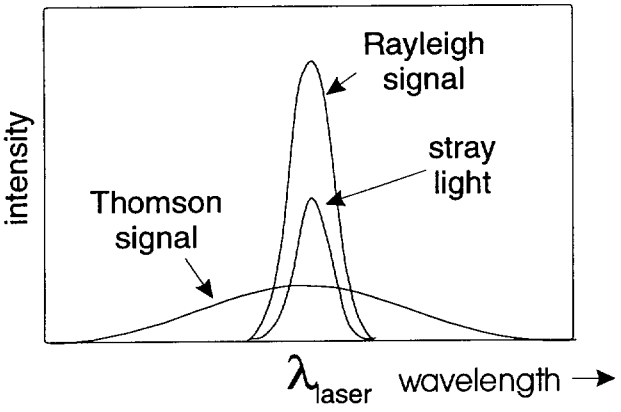


**Fig. B5.21: Different components of the total scattered spectrum [B5.22]**

If the entire spectrum is measured, the Thomson scattering component can be determined from wavelengths at which there is no contribution from the Rayleigh or stray components. Interpolation of the Thomson component in the central part of the spectrum then allows the Rayleigh and stray light components to be determined. Or the influence of the Rayleigh signal and the stray light are measured separately in a calibration and can then be substracted from the measured signal in a Thomson scattering experiment. When the electron temperature is low (i.e. below approximately 50000 K), the Doppler-broadened Thomson-scattered spectrum is directly related to the velocity distribution function of the scattering electrons. When the electron velocity distribution function is Maxwellian, the Thomson-scattered spectrum is Gaussian in shape and has a spectral half-width $\Delta\lambda_{Th}$ which is related to the electron temperature by:

$$\Delta\lambda_{Th} = 2\lambda_0 \sin(\theta/2)\sqrt{\frac{2kT_e}{m_e c^2}} \quad , \qquad \text{(B5.17)}$$

where $\lambda_0$ is the laser wavelength, $\theta$ is the scattering angle, i.e. the angle under which the scattered radiation is detected in respect to the laser beam, $T_e$ is the electron temperature and k, c and $m_e$ are the Boltzmann constant, the speed of light and the electron mass, respectively.

The total Thomson-scattered light intensity is directly proportional to the electron density $n_e$. Therefore, $n_e$ can be determined from the measured spectrum if the absolute sensitivity of the detection system is accurately calibrated. In practice, this calibration is easily done by measuring the Rayleigh-scattered intensity when the discharge chamber is filled with gas at a prefixed pressure without a plasma. In this situation the scattered signal intenstities $I_p$ (from a plasma with unknown electron density $n_e$) and $I_g$ (from a gas with known density $n_0$) are given by:

$$I_p = n_e \sigma_{Th} \Delta\lambda_p f_{system} \quad , \qquad \text{(B5.18)}$$

and

$$I_g = n_0 \sigma_R \Delta\lambda_g f_{system} \quad , \qquad \text{(B5.19)}$$

in which $\sigma_{Th}$ and $\sigma_R$ are the differential cross sections for Thomson scattering and Rayleigh scattering, respectively, $\Delta\lambda_p$ and $\Delta\lambda_g$ are the spectral FWHM-widths of the scattered spectra from the plasma and the gas and $f_{system}$ is a function of the laser energy and the efficiency of the detection system. The electron density is then given by [B5.22]:

$$n_e = n_0 \frac{I_p}{I_g} \frac{\sigma_R}{\sigma_{Th}} \frac{\Delta\lambda_g}{\Delta\lambda_p} . \qquad \text{(B5.20)}$$

Depending on the efficiency of the collecting optics and detectors, Thomson scattering measurements require electron densities of at least $10^{18}$ to $10^{21}$ $m^{-3}$ to achieve an acceptable signal level. Densities of $10^{21}$ $m^{-3}$ can only be achieved at low distances to the plasma generator and additionally near the plasma beam axis in the MPD wind tunnels at the IRS, as shown in Fig. B5.22. The method is applied with the IRS wind tunnel PWK2 and spatial profiles of the electron temperature and electron density were received from the plasma jet [B5.23].

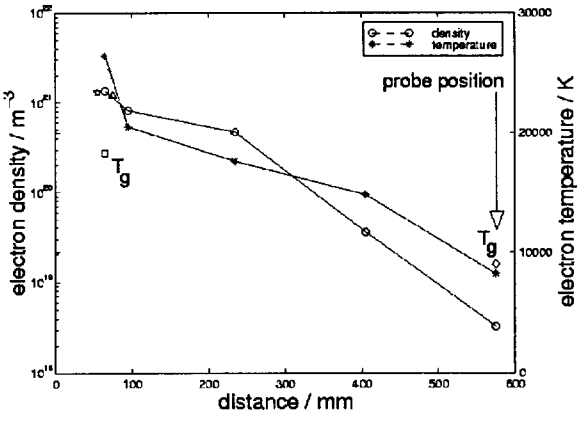


**Fig. B5.22: Electron density and temperature profile [B5.24]**

An axial scan for the electron density and electron temperature is shown in Fig. B5.22. The gas temperature is indicated with $T_G$. To achieve a signal in distances more than 200 mm to the plasma generator, one needs to integrate the Thomson scattering emission over thousand shots of the laser and the spatial radial resolution has to be decreased from 2 mm observation length in low distances to the plasma device to 5 mm observation length in higher distances.

## References


[B5.1] Seitzman, J.M.: "Quantitative Applications Of Fluorescence Imaging In Combustion", HTGL Rep. No. T-275, Stanford University, 1991.

[B5.2] Eckbreth, A.C.:Laser "Diagnostics For Combustion Temperature And Species", 2nd ed., Gordon and Breach Publishers, 1996.

[B5.3] Feigl M.: "Inbetriebnahme des LIF-Systems und erste Messungen am PWK", IRS 98-IB-08, 1998.

[B5.4] Salmon, J.T., Laurendeau, N.M.: "Calibration of laser-saturated fluorescence measurements using Rayleigh scattering", Applied Optics, Vol. 24, No. 1, 1985, pp. 65-73.

[B5.5] Hertz, H. M., Alden, M.: "Calibration of Imaging Laser-Induced Fluorescence Measurements in Highly Absorbing Flames", Applied Physics B 42, 1987, pp. 97-102.

[B5.6] Bischel, W.K., Bamford, D.J., Jusinski, L.E.: "Absolute calibration of a fluorescence collection system by Raman scattering in $H_2$", Applied Optics, Vol. 25, No. 7, April 1986, pp. 1215-1221.

[B5.7] Rensberger, K.J., Jeffries, J.B., Copeland, R.A., Kohse-Höinghaus, K., Wise, M.L. Crosley, D.R.: "Laser-induüed fluorescence determination of temperatures in low pressure flames", Applied Optics, Vol.28, No. 17, 1989.

[B5.8] Arepalli, S.: "Demonstration of the feasibility of laser induced fluorescence for arc jet flow diagnostics", NASA Johnson Space Center CR-185595, 1989.

[B5.9] Auweter-Kurtz M., Bauer G., Behringer K., Dabala P., Habiger H., Hirsch K., Jentschke H., Kurtz H., Laure S., Stöckle T., Volk G.: "Plasmadiagnostics within the Plasma Wind Tunnel PWK", Z. Flugwiss. Weltraumforsch. 19, pp. 166-179, 1995.

[B5.10] Grau, T., Messerschmid, E.: "Numerical Investigation of a Partially Ionized Air Flow in a Plasma Wind Tunnel", AIAA 98-2955, 7th AIAA/ASME Joint Thermophysics and Heat Transfer Conference, Albuquerque, NM, June 1998.

[B5.11] Luque, J., Crosley, D.R.:LIFBASE: "Database and Spectral Simulation Program (Version 1.1)", SRI International Report MP 96-001 (1996).

[B5.12] Habiger, H.: "Elektrostatische Sonden und Fabry-Perot Interferometrie zur Untersuchung von lichtbogenbeheizten Plasmen für Triebwerksanwendungen und Wiedereintrittssimulation", Dissertation, Universität Stuttgart, 1994.

[B5.13] Hilfer G.: "Experimentelle und theoretische Beiträge zur Plasma-Wand-Wechselwirkung keramischer Hitzeschutzmaterialien unter Wiedereintrittsbedingungen", Dissertation, Institut für Raumfahrtsysteme, Universität Stuttgart 1998.

[B5.14] Opila, E.J., Jacobsen, N.S.: "SiO(g) Formation from SiC in Mixed Oxidizing-Reducing Gases", Oxidation of Metals, Vol. 44, Nos. 5/6, 1995, pp 527-544.

[B5.15] Drira, I., Spielfiedel, A., Edwards, S., Feautrier, N.: "Theoretical study of the $A^1\Pi$ - $X^1\Sigma^+$ and $E^1\Sigma^+$ - $X^1\Sigma^+$ bands of SiO", J. Quant. Spectrosc. Radiat. Transfer, Vol. 60, No.1, 1998, pp. 1-8.

[B5.16] Langhoff, S.R., Arnold, J.O.: „Theoretical study of the $X^1\Sigma^+$, $A^1\Pi$, $C^1\Sigma$- and $E^1\Sigma^+$ states of the SiO molecule", J.Chem. Phys. 70 (02, 1979), pp. 852-863.

[B5.17] Heynes, A.J.: "Laser-induced fluorescence of silicon monoxide in a glow discharge and an atmospheric pressure flame", Chemical Physics Letters, Vol. 181, No. 2,3 1991, pp.237-244.

[B5.18] Park,C.S. ,Crosley, D.R., Eckstrom D.J., Heere K.R.: "Measurement of the $A\ ^1\Pi$- $X\ ^1\Sigma^+$ electronic transition moment of SiO using a shock tube", J.Quant.Spectrosc.Radiat.Transfer, Vol.49, No.4, 1993, pp. 349-360.

[B5.19] Bamford, D.J., O'Keefe, A., Babikian, D.S., Stewart, D.A., Strawa, A.W.: "Characterization of Arcjet Flows Using Laser-Induced Fluorescence", Journal of Thermophysics and Heat Transfer, Vol.9, No.1, January-March 1995.

[B5.20] Fasoulas S.: "Measurement of Oxygen Partial Pressure in Low Pressure and High-Enthalpy Flows", 19th AIAA Advanced Measurement and Ground Testing Technology Conference, New Orleans, LA, June 1996.

[B5.22] Muraoka, K., Uchino, K., Bowden, M.D.,: "Diagnosics of low density glow discharge plasmas using Thomson scattering", Plasma Phys. Control. Fusion 40, 1998, pp.1221-1239.

[B5.23] Hirsch, K., Volk, G.: "Thomson scattering with a gated intensified charge-coupled device camera using frequency doubled periodically pulsed Nd:YAG laser", Rev. Sci. Instrum. Vol. 66, No. 11, 1995, pp. 5369-5370.

[B5.24] Schinkoeth D., Hirsch K., Bauer G., Jentschke H., Schumacher U.: Verhandl. DPG (VI) 3414, 357, P20.15, 1999.

[B5.25] Feigl M., Auweter-Kurtz M.: "Investigation of nitric oxide in a high enthalpy air plasma flow using laser-induced fluorescence", AIAA 98-2459, 7th Joint Thermophysics and Heat Transfer Conference, Albuquerque, June 1998.

[B5.26] Fasoulas S.: "Experimentelle und theoretische Charakterisierung einer hochenthalpen Stickstoffströmung zur Wiedereintrittssimulation", Dissertation, Institut für Raumfahrtsysteme, Universität Stuttgart, June 1995.


# C Reentry Measurement Techniques

For more than a decade, intensive investigations of reentry conditions for spacecraft have been under way in Europe in view of the development of reusable spacecraft. Ground test facilities have been developed and built for this purpose [C.1-C.7] and a lot of effort has been put into developing numerical simulation processes [C.8-C.11]. Due to the complex physical-chemical relationships - there is in a large area neither chemical nor thermodynamic equilibrium - we are still not in a position today to predict the chemical and physical processes near the surface which can essentially influence the material behavior and therefore also the heat flux and the change from laminar to turbulent flow. However, this is a necessary precondition to qualify thermal protection systems (TPS. On the one hand the TPS can not be allowed to fail and on the other hand its mass must be minimized to gain pay load capacity. Especially the US has used its numerous return flights and entries into the atmospheres of other celestial bodies to validate calculation methods. However, only a small portion of these data is available to us in Europe. That is why we are largely dependent on our own experiments. In view of this, a great effort has been

made at the IRS in the last few years to develop and qualify flight measurement equipment and to then use it in actual flights. In the framework of a national mission (MIRKA) [C.12] and participation in return missions (EXPRESS [C.13] and X-38 [C.14]) the IRS was able and continues to be able to gather valuable experience. The following measurement techniques have been or are being developed: a pyrometer system for measuring the temperature distribution on ceramic thermal protection shields, catalytic sensors for determining the heat flux and the degree of dissociation, electrostatic probes for determining the boundary layer density, a boundary layer probe for determining the boundary layer thickness and position and a spectrometer experiment for examining the gas composition. For future interplanetary missions an ablator experiment for determining the recession rate and heat flux and a radiometer probe for determining the radiation heat flux are planned.

## References


[C.1] Auweter-Kurtz, M., Kurtz, H.L., Laure, S., "Plasma Generators for Re-entry Simulation", Journal of Propulsion and Power, Vol. 12, No. 6, December 1996, pp. 1053 - 1061.

[C.2] Auweter-Kurtz, M., Wegmann, Th., "Overview of IRS Plasma Wind Tunnel Facilities", RTO AVT/VKI Special Course on 'Measurement Techniques for High Enthalpy and Plasma Flows', von Karman Institute for Fluid Dynamics, Belgium, October 1999.

[C.3] Gülhan, A., "Qualification of TPS-Components in the Arc Heated Facility L3K of DLR", Proceedings of the 3rd European Workshop on Thermal Protection Systems, ESTEC, Noordwijk, The Netherlands, March 1998, pp. 121-130.

[C.4] Caristia, S., et. al., "Scirocco Project: Construction Phase Progress Report", CIRA, Italy, Proceedings of the 3rd European Workshop on Thermal Protection Systems, ESTEC, Noordwijk, The Netherlands, March 1998, pp. 91-100.

[C.5] Bottin, B., et. al., "Aerothermodynamic Design of an Inductively-Coupled Plasma Wind Tunnel", AIAA-97-2498, 32nd Thermophysics Conf., Atlanta, GA, June 1997.

[C.6] Weiland, M.K.H., Beck, W.H., Mee, D.J., Paull, A., "Comparison of Force Measurements in the HEG and T4 Shock Tunnels", Proceedings of the 3rd European Symposium on Aerothermodynamics for Space Vehicles, ESTEC, Noordwijk, The Netherlands, November 1998, pp. 631-636.

[C.7] Willian, J., Sagnier, P., Verant, J.-L., "Effects of Free Electrons in the Onera High Enthalpy Wind Tunnel F4", Proceedings of the 3rd European Symposium on Aerothermodynamics for Space Vehicles, ESTEC, Noordwijk, The Netherlands, November 1998, pp. 637-648.

[C.8] Frühauf, H.-H., Fertig, M., Kanne, S., "Validation of the Enhanced URANUS Nonequilibrium Navier-Stokes Code", AIAA 99-3683, 33rd Thermophysics Conference, Norfolk, VA, June/July 1999.

[C.9] Heiermann, J., Auweter-Kurtz, M., Sleziona, P.C., "Air and Argon RF Plasma Flow Simulation on Structured and Unstructured Meshes", AIAA-99-3496, 33rd Thermophysics Conference, Norfolk, VA, June/July 1999.

[C.10] Kordulla, W., Brück, S. (Eds.), "DLR Contribution to the Fourth European High Velocity Database Workshop", Forschungsbericht 97-34, ESTEC, Noordwijk, The Netherlands, November 1994.

[C.11] Hirschel, E.H., "Thermal Surface Effects in Aerothermodynamics", Proceedings of the Third European Symposium on Aerothermodynamics for Space Vehicles, ESTEC, Noordwijk, The Netherlands, November 1998, pp. 17-31.

[C.12] Schmitt, G., Pfeuffer, H., Kasper, R., Kleppe, F., Burkhardt, J., Schöttle, U.M., "The MIRKA Re-entry Mission", IAF-98-V.2.07, 49th International Astronautical Congress, Melbourne, Australia, September/October 1998.

[C.13] Auweter-Kurtz, M., Hald, H., Koppenwallner, G., Speckmann, H.-D., "German Experiments Developed for Reentry Missions", Acta Astronautica, Vol. 38, No. 1, 1996, pp. 47-61.

[C.14] Herdrich, G., Auweter-Kurtz, M., Hartling, M., Laux, T., "Present Design of the Pyrometric Sensor System PYREX-KAT38 for X-38", AAAF International Symposium: Atmospheric Re-entry Vehicles and Systems, Arcachon, France, March 1999.


# C1 Pyrometer

The miniaturized linear pyrometer PYREX was designed at the IRS for flight application. PYREX (**Py**rometer **R**e-entry **Ex**periment) was specially designed to determine the temperature on the back of ceramic heat shield materials during reentry without any contact to the surface. Knowing the temperature as a function of time, valuable conclusions about the heat flux and the catalycity (see section C2) of the ceramic material can be made. A one-channel version of PYREX was developed and qualified within the German reentry technology program from DARA [C1.1, C1.2].

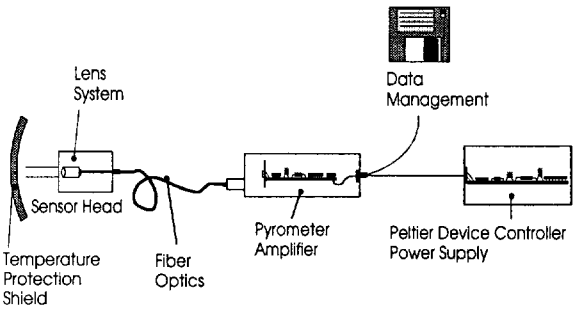


**Fig. C1.1: Schematical set-up of PYREX**

As shown in Fig. C1.1, the PYREX system consists of five components: the sensor head with the optics, the optical fiber with its connectors, the pyrometer itself with the photodiode and the amplifier, the additional housing for the control electronics and the data processing unit.

The transfer of the radiation into the pyrometer is done by the measurement head which has to image the emitted radiation onto the fiber optics. Essentially, it consists of an SiC-tube which is guided through the structure of the capsule and the ablator/isolator beyond the heat shield tile. The SiC-tube is mounted onto the structure with an inconel flange. The fiber optics with their collecting lenses are

mounted at the measurement head and transfer the signals to the photodiode. The wavelength of the measured signals is limited to a narrow region around 630 nm using a suitable filter combination. The photodiode together with the amplifier electronics are placed in a housing made of aluminum. To guarantee the high accuracy of the measured signal, the temperature of the photodiode has to remain constant (for example at 20°C). This is done by Peltier elements. A thermocouple which is placed directly beside the photodiode delivers a control signal for the Peltier elements. The heat is conducted to the pyrometer housing and the structure. Figure C1.2 shows the integration of the PYREX measurement head into the structure of the EXPRESS capsule behind the ceramic shield.

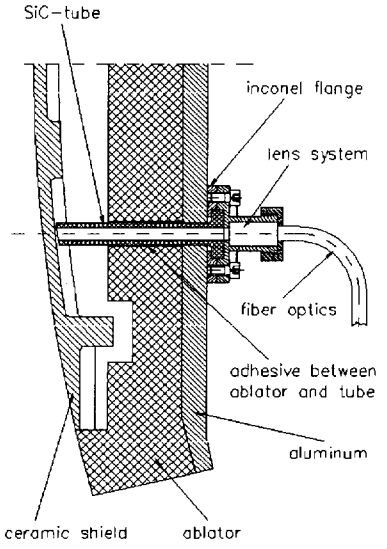


**Fig. C1.2: Integration of the measurement head into the structure of the EXPRESS capsule**

A two-channel system of PYREX was qualified during the MIRKA mission [C1.3]. With this mission the system successfully measured the temperature profile at two different positions. The instrument disintegrated after the mission and the black body radiator described in section B1.5 was used to compare the signal with the calibration curve prior to the flight.

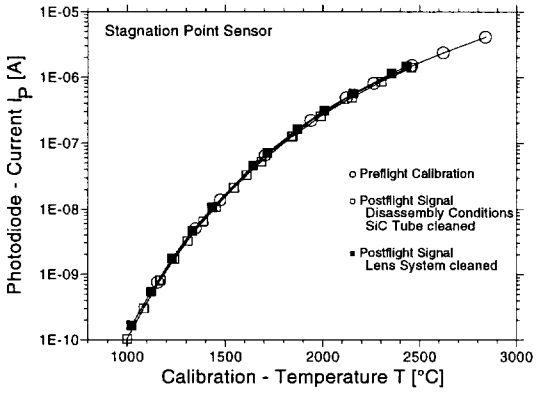


**Fig. C1.3: Comparison of preflight calibration and the postflight signal**

Figure C1.3 shows the good correlation between the postflight signal and the calibration curve.
For the X-38 mission a five-channel system is being developed [C1.4]. Three channels are foreseen for the temperature measurements and two will be used for a catalytic experiment (see section C2).

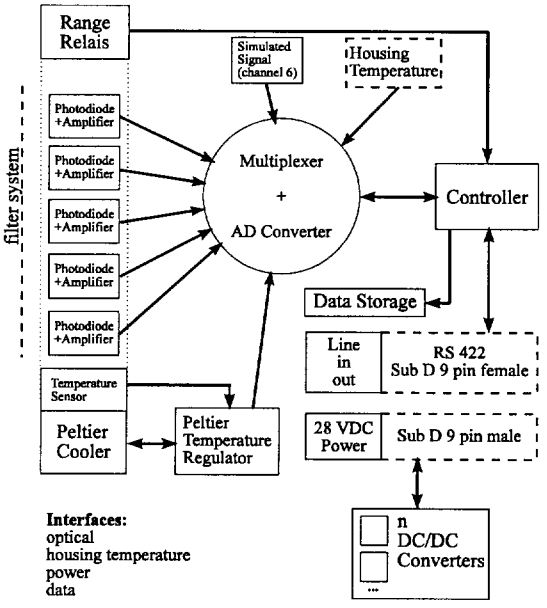


**Fig. C1.4: PYREX-KAT38/EM sensor unit**

The system PYREX-KAT38 consists of several subdevices. A schematic view of PYREX-KAT38 is shown in Fig. C1.4. Each of the five sensor heads carries a lens system to focus the incoming radiation on the fiber optics entrance. The fiber optics are attached to the sensor heads and transmit the radiation to the sensor units which contain the electronics. Data transfer, power and control signals are transmitted to the Vehicle Analysis Data Recording (VADR) System, which is being developed by OHB-System GmbH in Bremen, Germany. A portable computer, which can be switched to the sensor unit, enables external data management and preflight tests. Both the X-38 power system and the VADR system are attached to the sensor unit. For PYREX-KATR38 an independent memory bank has been added.

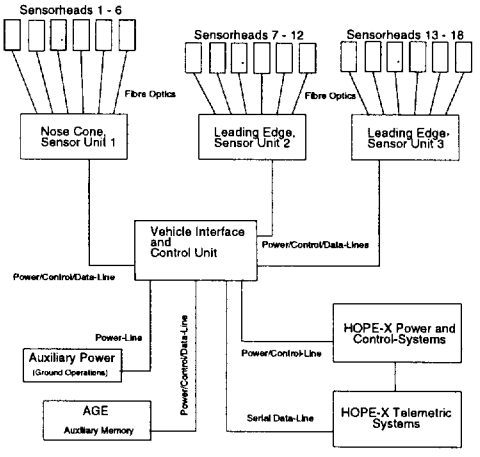


**Fig. C1.5: Schematic view of the PYREX-HX system**

For the Japanese space plane HOPE-X, three pyrometer systems with six channels each are foreseen (see Fig. C1.5). Six channels will be used for determining the temperature distribution in the nose cap and 12 channels are foreseen for the leading edge (see Fig. C1.6).

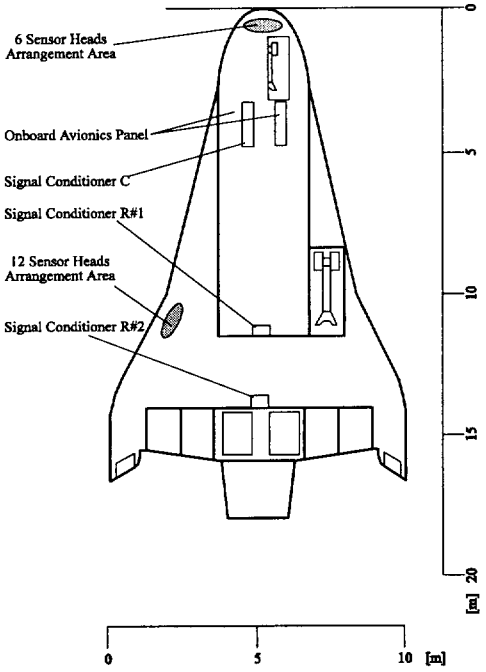


**Fig. C1.6: HOPE-X**

The graduation has been chosen with respect to the geometries in the nose cone and wing leading edge and the environmental requirements for the sensor units. In addition, it is useful to manufacture three identical sensor units in order to decrease the qualification efforts as only one sensor unit engineering model has to be qualified.

Due to the large distance between the sensor head and the nose cap a special effort is necessary in this mission to calculate the effective emittance for these measurements and to determine the measurement location.

To calibrate the pyrometer sensors the calibration device described in section B1.5 is used. To qualify the pyrometers for reentry application, the numerically predicted heat loads were simulated within the IRS plasma wind tunnels. For EXPRESS, for example, temperatures between 1200°C and 2600°C could be measured For the EXPRESS mission additional extensive qualification procedures have been performed using various ground test facilities for simulating heat, chemical, thermomechanical, vibration and acceleration loads [C1.1].

In order to improve the accuracy of the measurements in the system, an intrusive postflight program is foreseen. Postflight operations will consist of the readout of the internally stored PYREX-HX data to an auxiliary memory system of the air-ground-equipment (AGE), which is a portable computer, and a preliminary flight data evaluation. A detailed mechanical and optical inspection will be performed after the mission.

During this inspection, the performance of the systems will be checked in comparison to the preflight status. The system will be checked for mechanical and electronic damage. A verification of the previously performed calibration of the system will be carried out using the calibration device described in section B1.5 in order to take possible damage and performance changes into account for an exact flight data processing and temperature evaluation. A functional test in the plasma wind tunnel will be performed to look for reproducibility under acceptance test levels. The system will be generally analyzed to determine improvements for future missions.

The final flight data evaluation will consider all aspects of the postflight inspection. With the known preliminary temperature data of the HOPE-X reentry, the actual emissivity distribution of the C/C structure during the reentry phase and the influence of the thermal behavior of the hardware parts of PYREX-HX must be considered for a final and reliable evaluation of the measured C/C structure temperatures.

## References

[C1.1] Auweter-Kurtz, M., Hald, H., Koppenwallner, G., Speckmann, H.-D., "German Experiments Developed for Reentry Missions", Acta Astronautica, Vol. 38, No. 1., 1996, pp. 47-61.

[C1.2] Auweter-Kurtz, M., "PYREX - Ausbau und Postflight-Untersuchung von PYREX auf EXPRESS", Fördervorhaben 50TT9302, IRS-96-P8, Institut für Raumfahrtsysteme, Universität Stuttgart, December 1996.

[C1.3] Habiger, H., Auweter-Kurtz, M., Früholz, H., Herdrich, G., "PYREX - Pyrometric Temperature Measurement on the Ceramic TPS of the Re-Entry Capsule MIRKA", Proceedings of the 3rd European Workshop on Thermal Protection Systems, ESTEC, Noordwijk, The Netherlands, March 1998, pp. 353-362.

[C1.4] Herdrich, G., Auweter-Kurtz, M., Hartling, M., Laux, T., "Present Design of the Pyrometric Sensor System PYREX-KAT38 for X-38", AAAF International Symposium: Atmospheric Re-entry Vehicles and Systems, Arcachon, France, March 1999.

# C2 Catalytic Sensor

Catalytic sensors are used to gather information on atomic species concentrations in front of the heat shield using materials of different catalycities. The sensors are based on the experience gained from intensive investigations of the catalytic behavior of high temperature materials using plasma wind tunnel facilities.

For years the catalycity of various metallic and ceramic materials has been closely investigated in the IRS plasma wind tunnels (see also section A4.3). Using stationary heat flux probes coated with different materials of known catalycity and calibrated in plasma wind tunnels, information about the atomic concentrations can be qualitatively obtained during reentry. For this purpose sensors based on the Gordon Gage principles (see section A4.1.2) are being

developed at the IRS. The Gardon Gages can be coated using physical vapor deposition (PVD) [C2.1]. Figure C2.1 shows a possible feed-through design for a reentry probe being developed at the IRS. For the calibration of these sensors the atoms species concentrations have to be determined. This will be possible at the IRS in the near future using LIF (see section B5.1).

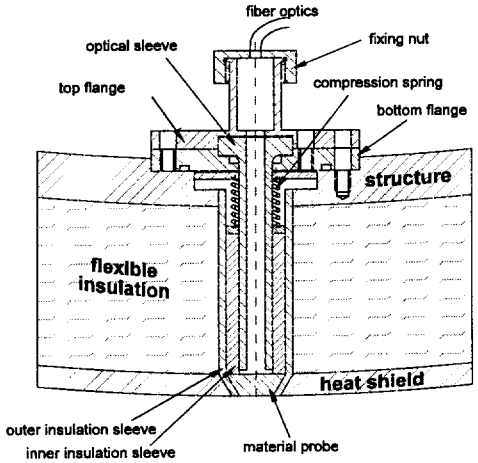


**Fig. C2.1: Feed-through from structure to heat shield for a catalytic based sensor**

Due to a lack of the time and money necessary for qualification, it was impossible to use such a sensor with the X-38 mission and to insert this kind of probe into the heat shield in the stagnation point region. Because of the expected high temperatures (approx. 2000K), a local increase in the catalycity had to be avoided for safety reasons.

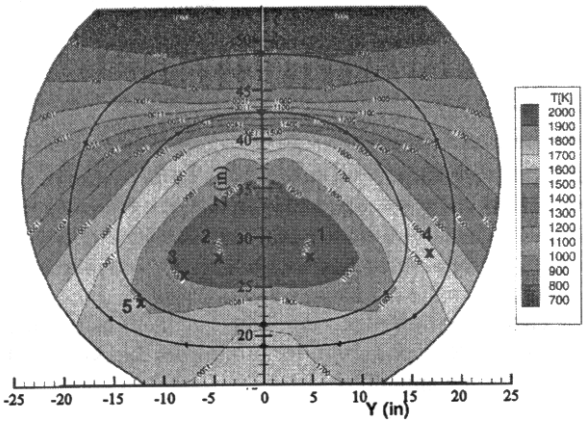


**Fig. C2.2: Nose cap (DLR-S) and nose skirt (DASA-B, MAN-T) maximum temperature distribution with PYREX-KAT38 sensor positions**

Therefore, it is now planned to apply a layer of low catalycity to the protection shield near the stagnation point 1 (see Fig. C2.2) and to pyrometrically observe the temperature curve on the back of this shield at point 1 and point 2, which are supposed to see the same flow condition due to the symmetrical location. These temperature curves and tests in the plasma wind tunnel will be used to determine the heat flux curve and evaluate the atomic particle densities.

## References

[C2.1] Auweter-Kurtz, M., Dabalà, P., Feigl, M., Habiger, H., Kurtz, H., Stöckle, T., Wegmann, T., Winter, M., "Diagnostik mit Sonden und optischen Verfahren", SFB Arbeits- und Ergebnisbericht 1998, pp. 65-90.

# C3 Heat Flux Determination for Ablators

Thermocouples can generally be used for missions with ablative heat shields due to the low heat conductivity of the material and the large wall thickness. If they are inserted at various depths near the surface, the recession rate and the development of the carbonization layer can be determined. Furthermore, as long as the heat conductivity in addition to the degree of emission of the ablator, the heat capacity of the material and its energy consumption for ablation are known, not only can the temperature curve in ablator probes be determined but also the heat flux to the probe surface.

This task, however, is made more difficult with many materials by a non-isotropic heat conduction and heat capacity and conduction both dependent on the depth. In addition, it is in principle possible to determine the ablation energy consumption in plasma wind tunnels, but requires great effort. In addition, the degree of emission of an ablator can change over time due to a change in the chemical composition of the surface and has to be taken into account. In the framework of the reentry mission MIRKA, a corresponding experiment, the so-called HEATIN experiment, was planned, qualified in a plasma wind tunnel at the IRS and successfully tested in flight [C3.1, C3.2].

The main objective of the flight data evaluation of the HEATIN experiment was to determine the transient heat fluxes along the MIRKA surface. The calculation of the areal heat flux density $\dot{Q}$ from measured in-depth temperature histories implies the solution of the inverse heat conduction problem. For this purpose a method has been developed, qualified and successfully applied in order to process flight data [C3.3].

## References

[C3.1] Schmitt, G., Pfeuffer, H., Kasper, R., Kleppe, F., Burkhardt, J., Schöttle, U.M., "The MIRKA Re-entry Mission", IAF-98-V.2.07, 49th International Astronautical Congress, Melbourne, Australia, September/October 1998.

[C3.2] Reich, G., Jahn, G., "MIRKA Heat Shield Experiment HEATIN - Theoretical and Experimental Approach to the Surface Protected Ablator", 26th International Conference on Environmental Systems, Monterey, CA, July 1996.

[C3.3] Jahn, G., "Theoretische und experimentelle Untersuchung des Hitzeschutzverhaltens einer Rückkehrkapsel", Dissertation, Universtität Stuttgart, 1998.

# C4 Boundary Layer Probe

To determine the boundary layer thickness and the pressure, a new probe, shown in Fig. C4.1 is in the process of being developed at the IRS. A retractable probe is used to measure the pressure in the flight body boundary layer perpendicular to the material surface. The pressure curve can be used to determine the position and thickness of the shock front. After a fundamental study [C4.1], the next steps are to choose an appropriate material with temperature stability for the probe head and to build an engineering model for qualification in a plasma wind tunnel. Accompanying flow simulations of the pressure probe in the plasma wind tunnel high enthalpy flow are planned using the numerical methods developed at the IRS [C4.2]. For the qualification of the experiment, emission spectroscopy will be used (see section B2.3).

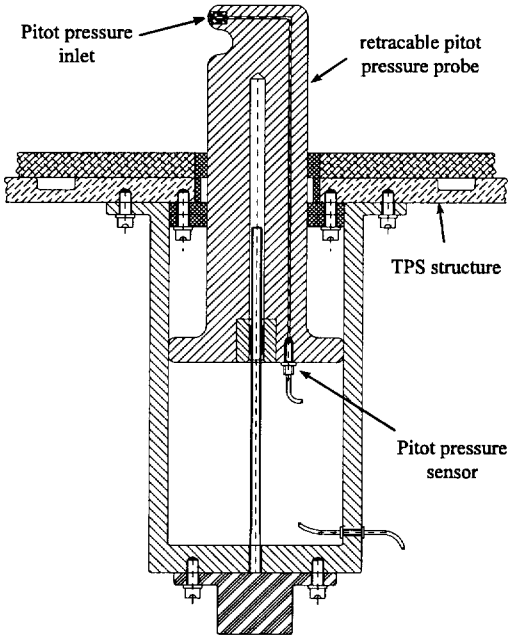


**Fig. C4.1: Pressure probe for determining the shock front**

## References

[C4.1] Alting, J., "Entwurf eines Flugexperimentes zur Bestimmung der Stoßfrontposition beim Widereintritt", IRS-97-S23, Institut für Raumfahrtsysteme, Universität Stuttgart, 1997.

[C4.2] Sleziona, P.C., Auweter-Kurtz, M., Boie, C., Heiermann, J., Lenzner, S., "Numerical Code for Magneto-Plasma Flows" in: Hyperbolic Problems: Theory, Numerics, Applications, 7th International Conference in Zürich, February 1998, Vol. II, Eds. M. Fey, R. Jeltsch, International Series of Numerical Mathematics, Vol. 130, 1999, Birkhäuser Verlag, Basel, pp. 905-914.

# C5 Spectrometer Probe

The thermal and mechanical loads onto a space vehicle surface during re-entry are mainly defined by the plasma state and its chemical composition close to the wall. Although various numerical codes have been developed to simulate these conditions, the experimental data which can be used to verify the numerical simulation are still poor. The existing experimental data concentrate on single species such as NO-radiation. Experiments that give information about multiple important species within the post-shock layer at the same time have not been performed yet.

One way to gain access to the required data is given by emission spectroscopic measurements during the re-entry flight. Figure C5.1 shows the measurement principle of the proposed experiment.

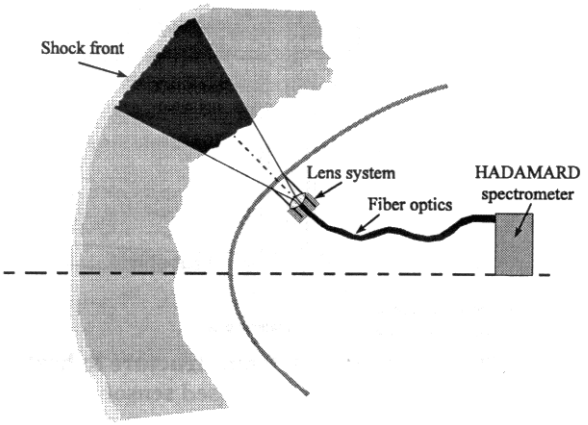


**Fig. C5.1: Measurement principle of the proposed experiment**

A newly developed spectrometer which operates according to the HADAMARD principle is planned to gain spectral data in the flow field around a space vehicle re-entering the earth's atmosphere [C5.1]. Data collection is foreseen during the entire flight trajectory.

Due to the integrating character of the measurement, a direct extraction of temperatures or densities from the measured data does not seem possible; however, the desired information can be obtained by a comparison with numerically simulated data.

A spectrometer for use in space has to fulfill special requirements. Besides the optical qualities, it has to be small and light and withstand the mechanical, thermal and chemical loads. The proposed spectrometer shown in Fig. C5.2 uses the HADAMARD principle to minimize the size and weight of the apparatus.

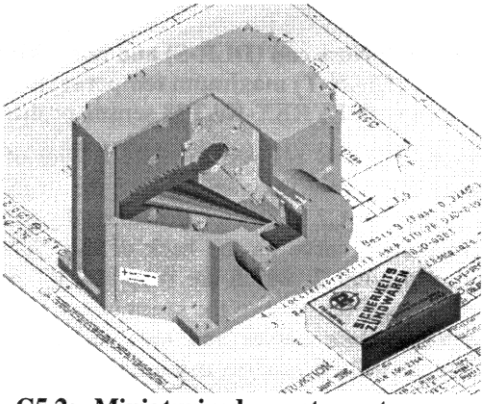

**Fig. C5.2: Miniaturized spectrometer operated according to the HADAMARD principle**

The HADAMARD principle is based on the use of different entrance slits into the spectrometer. These slits are used in various combinations to perform the measurements. A transformation of the obtained data results in a higher effective resolution than with conventional spectrometers [C5.2]. This allows for a smaller configuration of the spectrometer itself. The obtained data will cover a wavelength range from 200 nm up to 800 nm with a resolution of approximately 0.5 nm. Thus, it will contain the emission of all relevant radiating air species such as $N_2$, NO, N, O and $N_2^+$.

The functional qualification procedure will be performed in the plasma wind tunnels of the IRS [C5.3, C5.4]. Magnetoplasmadynamic as well as thermal plasma generators creating sub- and supersonic flows, respectively, will be used to simulate the condition along the flight path at lower and higher stagnation pressures.

Emission spectroscopic experiments have already been carried out to investigate the boundary layer in front of a blunt body in a subsonic high enthalpy plasma flow at total pressures between 0.1 kPa and 3.5 kPa representing the first part of re-entry (see section B2.3.3). The ratios of the emission of different species were found to be a valuable indicator for chemical processes, especially within the boundary layer. Although within a flight mission Abel inversion or temperature determination techniques as used in the plasma wind tunnel experiments are not possible, a comparison with numerically simulated spectral data will provide valuable information about the chemical and thermodynamic processes in the plasma flow.

The numerical data for the comparison with the measurement will be provided by the numerical flow solver URANUS (**U**pwind **R**elaxation **A**lgorithm for **N**onequilibrium Flows of the **U**niversity of **S**tuttgart) [C5.5], the radiation transport code HERTA (**H**igh **E**nthalpy **R**adiation **T**ransport **A**lgorithm) [C5.6] and the radiation database PARADE (**P**lasma **Ra**diation **D**atabase) [C5.7]. In recent years, URANUS has been validated for different flow cases, such as Shuttle, FIRE II, MIRKA, RAMCII, BSUV I & II and Stardust. Compared to these cases, however, the proposed experiment will perform more detailed spectroscopic measurements by offering the emission of multiple radiating species measured at the same time. This will enable a more specific investigation of the physical processes in the plasma.

Using the radiation codes, the chemical model of the flow field solver can be verified by a comparison of measured and calculated radiation. Different models can be tested and the influence of chemical reactions on radiation signals can be shown. For example, the modeling of the NO production can be checked by this method.

The requirements for the spectrometer are mainly defined by a wavelength range which allows the detection of the main radiating species in the flow as presented in Fig. C5.3 and Fig. B2.26 in section B2.4.1. The experimental data were measured within experimental investigations of the boundary layer in front of a blunt body in the subsonic air plasma flow in the IRS plasma wind tunnel PWK2. The numerical data result from a simulation with PARADE for a shuttle reentry at a distance of 77 km to the ground.

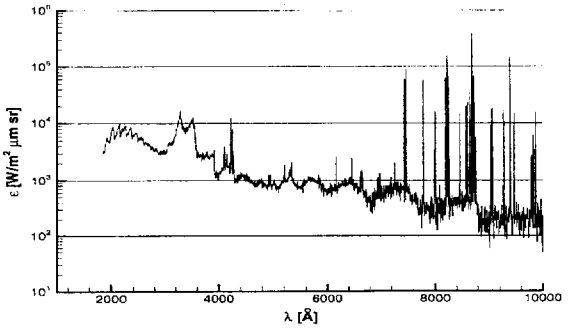


**Fig. C5. 3: Numerically simulated spectrometer signal during a shuttle reentry at a distance of 77km to the ground**

The lower border of the wavelength range is defined by the emission of NO in the UV from 200 nm up to 250 nm. The upper border is defined by the emission of atomic oxygen with strong emission lines at 776 nm. For this reason, a wavelength region from 200 nm to almost 800 nm has to be covered. According to the plasma wind tunnel measurements, a resolution of about 1 nm is sufficient to separate the emission of the different species.

The dynamic range of the detector has to be chosen as high as possible to take both varying intensities within one spectrum and the variation along the flight trajectory into account. At the same time, a sufficient readout frequency has to be guaranteed to minimize the integration along the flight path. A measurement time of 100 ms is considered to give both sufficient time resolution and measured intensity. For these reasons, a dynamic range of 16 bit is proposed.

Because the spectrometer has been proposed for a flight mission, the dimensions and weight have to be minimized.

The demonstrator of the spectrometer has already been built and tested at Jena Optic. It is the first demonstration of the HADAMARD principle with a double-array-arrangement in the world. Functionality and performance of the spectrometer were demonstrated with a device having dimensions of 150 mm × 150 mm × 50 mm. The next step in the project is the development of a prototype. The design and materials for the optical head have already been prepared for use in space. Minimization of the volume to 80 mm × 80 mm × 50 mm is foreseen. An enlargement of the wavelength range from 200 nm up to 800 nm by a resolution goal of about 0.5 nm is planned.

Although most specifications for the coupling to the space vehicle itself will have to be specified by the requirements of the flight mission, some basic requirements have to be fulfilled in any case.

It will surely not be possible to mount the spectrometer directly behind the thermal protection material. The transmission of the radiation to the spectrometer inlet has to be done using optical fibers. For the coupling of the fibers to the surface material a feed-

through has to be used to couple the fiber optics to the heat shield.
This phase is of particular importance for the success of the whole project. The design and construction of the feed-through will be done in cooperation with the DLR-Stuttgart. Furthermore, the focusing system has to be protected from both plasma influences and erosion products of the heat shield.
At the IRS, several flight missions have been performed with experiments like PYREX, measuring the material temperature with a minimized pyrometer (see section C1). The experience gained from these flight experiments will be used for the construction of the required coupling device.

## References


[C5.1] Winter, M., Kanne, S., Lonschinski, J., Auweter-Kurtz, M., Frühauf, H.-H., "Proposal for a Reentry Experiment Using a Newly Developed Spectrometer", Proceedings of the 3rd European Symposium on Aerothermodynamics for Space Vehicles, ESTEC, Noordwijk, The Netherlands, November 1998, pp. 711-716.

[C5.2] Riesenberg, R., Voigt, W., Schöneich, J.,"Kompakt-Spektrofotometer mit Mikro-systemtechnik", SENSOR 97, Nürnberg, 1997.

[C5.3] Auweter-Kurtz, M., Kurtz, H.L., Laure, S., "Plasma Generators for Re-entry Simulation", Journal of Propulsion and Power, Vol. 12, No. 6, December 1996, pp. 1053 - 1061.

[C5.4] Auweter-Kurtz, M., Wegmann, Th., "Overview of IRS Plasma Wind Tunnel Facilities", RTO AVT/VKI Special Course on 'Measurement Techniques for High Enthalpy and Plasma Flows', von Karman Institute for Fluid Dynamics, 1999.

[C5.5] Kanne, S., Knab, O., Frühauf, H.-H., Messerschmid, E., "The Influence of Rotational Excitation on Vibration-Chemistry-Vibration-Coupling", AIAA-96-1802, 31st AIAA Thermophysics Conference, New Orleans, LA, June 1996.

[C5.6] Gogel, T., "Numerische Modellierung von Hochentalpieströmungen mit Stahlungsverlusten", Dissertation, Universität Stuttgart, 1994.

[C5.7] S. Kanne, T. Gogel, M. Dupius, E. Messerschmid, "Simulation of Radiation Experiments on Reentry Vehicles Using the New Radiation Database PARADE", AIAA-97-2562, 32nd AIAA Thermophysics Conference, Atlanta, GA, June 1997.


# C6 Electrostatic Triple Probe

An electrostatic triple probe is being developed to determine the electron density and electron temperature during reentry. With reentry missions from low earth orbit the densities of charged particles close to the surface is very low. This is no longer the case for sample return missions which now also being planned in Europe. For these missions the knowledge of the electron density close to the surface is of great importance due to the high reactivity of these particles and a possible impact on radio communication.

Triple probes offer the possibility of monitoring this quantity on-line with a high time resolution (as described in section A7.3). A drawing of this experiment is shown in Fig. C6.1.

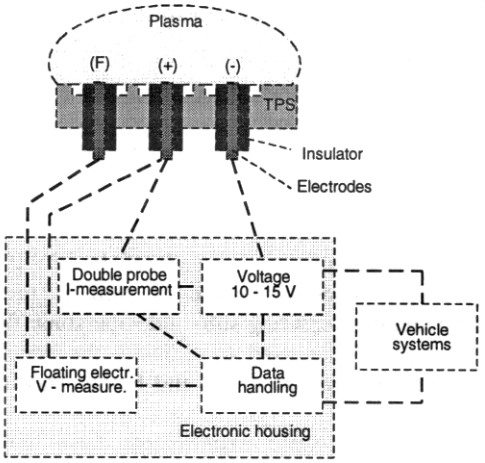


**Fig. C6.1: Flight experiment with an electrostatic triple probe**

# C7 Radiometer Probe

During high enthalpy reentries and many interplanetary missions, the radiative portion of the heat flux to a vehicle can no loner be neglected. The high gas enthalpy and high radiative intensities of some carbonaceous molecules cause high radiation intensities. This is, for example, the case for the Huygens mission. At the IRS the heat shield material for Huygens was tested and the final qualification for this mission was carried out. Within this context a radiometer probe (see section A9) for wind tunnel application was developed at the IRS [C7.1]. Based on this knowledge, it is planned to develop a flight version for future European interplanetary missions which can be qualified in the plasma wind tunnels of the IRS [C7.2].

## References


[C7.1] Röck, W., "Simulation des Eintritts einer Sonde in die Atmosphäre des Saturnmondes Titan in einem Plasmawindkanal", Dissertation, Universität Stuttgart, 1998.

[C7.2] Auweter-Kurtz, M., Wegmann, Th., "Overview of IRS Plasma Wind Tunnel Facilities", RTO AVT/VKI Special Course on 'Measurement Techniques for High Enthalpy and Plasma Flows', von Karman Institute for Fluid Dynamics, 1999.


# C8 Acknowledgements


The authors would like to thank all colleagues who were involved in the development and qualification of the diagnostic techniques at the IRS during the last decade. Special thanks also to Mrs. Jennifer Baer-Engel for her help in writing this script.

# Measurement Requirements for Improved Modeling of Arcjet Facility Flows

*Presented by*
*Douglas G. Fletcher*
*Reacting Flow Environments Branch*
*NASA Ames Research Center*
*Moffett Field, CA, 94035-1000*

**1. Introduction** ..... 3A-2

**1.1** Historical Development of NASA Ames Arcjet Facilities ..... 3A-2
**1.2** Overview of Current NASA Arcjet Facilities ..... 3A-4
**1.3** Ames Aerodynamic Heating Facility Arcjet ..... 3A-4
**1.4** Arcjet Characterization Using Conventional Instrumentation ..... 3A-5

**2. CFD for Arcjet Flows** ..... 3A-8

**2.1** Motivation for Arcjet Flow Modeling ..... 3A-8
**2.2** CFD Requirements for Arcjet Flow Simulations ..... 3A-8
**2.3** Strategies for Arcjet Flow Simulations ..... 3A-9

**3. Measurement Requirements for Arcjet Flow Modeling** ..... 3A-10

**3.1** Enthalpy ..... 3A-11
**3.2** Arc Heater ..... 3A-11
**3.3** Arcjet Nozzle and Free-Stream Flow ..... 3A-12
**3.4** Blunt-Body Shock-Layer Flow ..... 3A-12
**3.5** Measurement Accuracy Requirements ..... 3A-13

**4. Experimental and Computational Investigation of Shock-Layer Flows** ..... 3A-14

**4.1** Objectives of Investigation ..... 3A-14
**4.2** Experimental and Computational Approach ..... 3A-14
**4.3** High Pressure Case ..... 3A-16
**4.4** Low Pressure Case ..... 3A-20
**4.5** Spatially Resolved Measurements ..... 3A-23
**4.6** Lessons Learned ..... 3A-23

**5. Summary and Recommendations** ..... 3A-24

**6. Acknowledgements** ..... 3A-25

**7. References** ..... 3A-25

*Paper presented at the RTO AVT Course on "Measurement Techniques for High Enthalpy and Plasma Flows", held in Rhode-Saint-Genèse, Belgium, 25-29 October 1999, and published in RTO EN-8.*

## 1. Introduction

Current efforts to develop new reusable launch vehicles and to pursue low-cost robotic planetary missions have led to a renewed interest in understanding arcjet flows. Part of this renewed interest is concerned with improving the understanding of arcjet test results and the potential use of available computational-fluid-dynamic (CFD) codes to aid in this effort. These CFD codes have been extensively developed and tested for application to nonequilibrium, hypersonic flow modeling. It is envisioned, perhaps naively, that the application of these CFD codes to the simulation of arcjet flows would serve two purposes: first, the codes would help to characterize the nonequilibrium nature of the arcjet flows; and second, arcjet experiments could potentially be used to validate the flow models. These two objectives are, to some extent, mutually exclusive. However, the purpose of the present discussion is to address what role CFD codes can play in the current arcjet flow characterization effort, and whether or not the simulation of arcjet facility tests can be used to evaluate some of the modeling that is used to formulate these codes.

This presentation is organized into several sections. In the introductory section, the development of large-scale, constricted-arc test facilties within NASA is reviewed, and the current state of flow diagnostics using conventional instrumentation is summarized. The motivation for using CFD to simulate arcjet flows is addressed in the next section, and the basic requirements for CFD models that would be used for these simulations are briefly discussed. This section is followed by a more detailed description of experimental measurements that are needed to initiate credible simulations and to evaluate their fidelity in the different flow regions of an arcjet facility. Observations from a recent combined computational and experimental investigation of shock-layer flows in a large-scale arcjet facility are then used to illustrate the current state of development of diagnostic instrumentation, CFD simulations, and general knowledge in the field of arcjet characterization. Finally, the main points are summarized and recommendations for future efforts are given.

### 1.1 Development of NASA Ames Arcjet Facilities

Development efforts that led to what we now classify as arcjet test facilities began in the late 1950's with the goal of producing a continuously operable hypersonic ground test facility. This need was driven by both US Department of Defense and NASA mission planning requirements. From the NASA side, planetary missions and the manned space program were pushing aerospace vehicles to higher aerothermodynamic heating rates. Several excellent texts have been written that include a much broader treatment of the historical development of arcjet facilities and plasma arc devices for propulsion.[1,2] However, for the purpose of introducing the current topic, a brief recapitulation of arcjet facility development activities at NASA Ames Research Center is given below.

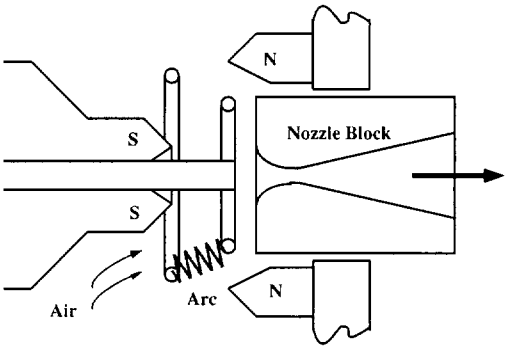


Fig. 1. NASA Ames concentric ring arcjet.

The rather ambitious target capabilities for developing the first Ames arcjet were: 1) 32 MJ/kg enthalpy; 2) 100 atm pressure; 3) 1 MW input power; and 4) continuous and contaminant-free operation. The first successful arcjet that even partially met some of these goals was the Ames Concentric Ring Arcjet,[3] which is depicted in Fig. 1. While the device could operate at the intended high pressures, it had a very low efficiency in terms of coupling the electrical energy to the flow. As can be seen in Fig. 1, the arc region is quite small, and most of the incoming air stream bypasses the arc. This resulted in relatively low deposition of energy into the test gas stream.

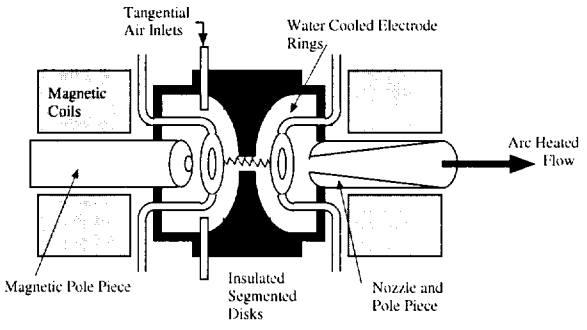


Fig. 2. Early Ames constricted-arc heater.

To improve the coupling of electrical energy into the flow, the next round of heater configurations featured more widely spaced electrodes separated by an orifice plate that is intended to constrict the arc to a relatively small region. It was hoped that forcing the flow and arc through the same small region would improve the electrical energy deposition and raise the stream enthalpy. Figure 2 shows an example of this device, which did show an improvement in energy deposition. However, it proved to be nearly impossible to prevent the arc from attaching at the edge of the orifice plate,

and excessive arc-induced failures produced further design modifications.

Subsequent efforts resulted in the development of supersonic arcjets,[4] which achieved high enthalpies and low heat loss by extending the arc through the throat region before attachment downstream in the low pressure, expanded flow region. A schematic of one of the earlier versions is shown in Fig. 3. Erosion of the downstream attachment point was minimal for this type of arcjet because of the diffuse nature of the arc at the low pressures of the supersonic flow region. The constrictor diameter was only 6.4 mm, but the heater performance was pretty much as predicted, and there appeared to be a substantial gain in electrical energy deposition. Shortly thereafter a second supersonic arcjet was developed with a 25.4 mm diameter constrictor and this device delivered enthalpies on the order of 900 MJ/kg on the flow centerline.[5] Unfortunately, the stream was highly nonuniform and the excessive radial gradients limited the application range of this heater.

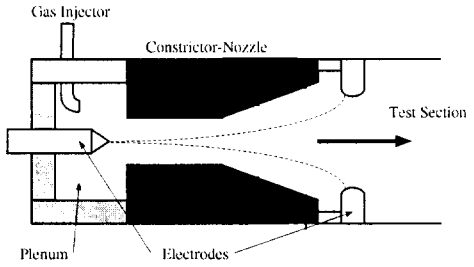


Fig. 3. NASA Ames supersonic, constricted-arc facility.

In one of the more interesting developments that has particular relevance to the current discussion, the ARCFLO code was developed in 1967 to model proposed arc heater configurations.[6] For the instrumental technology available at the time, comparisons between arcjet performance measurements and ARCFLO predictions were satisfactory. This led to the use of the code in the development of new heater configurations.

Although impressively high enthalpy levels were generated in some of these early devices, there was no great demand for routine operation at those conditions. Instead, the emergence of the shuttle as the primary launch and payload capability for NASA generated a significant demand for test capability in the 20 to 30 MJ/kg range to develop and qualify shuttle-related thermal protection materials. With the exception of meteor ablation studies and work involved with the development of heat shields for planetary-entry missions,[7] this test condition range has proven satisfactory for a majority of the aerospace community's needs. Progress in providing robust test facilities in the required performance range was enabled by timely improvements in magnetically driven electrode technology.[8] All of the successful heater designs relied on magnetic fields to spin the arc attachment point around the electrode to reduce the local heating. However, an optimal combination of geometry, current load, and magnetic field strength leading to extended electrode lifetime could only be found through trial and error, since theoretical models of the combined fluid and plasma dynamics of the electrode were inadequate at that time.

Using the new magnetically driven electrodes, the Ames 20 MW Constricted Arc Jet was built in 1972. A schematic rendering of the constrictor, downstream electrode package and nozzle configuration is shown in Fig. 4. This basic constricted-arc heater configuration has been used continuously, with relatively little variation, in the Ames arcjet facilities since that time. An excellent description of the electrode and constrictor design and performance evaluation is given as part of the report on the Ames 60 MW arcjet,[9] which is still in use today.

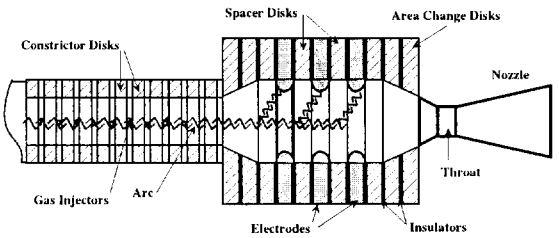


Fig. 4. Current version of Ames constricted-arc heater.

In the late 60's and early 70's arcjets were in use at aerospace companies and research centers around the world. It appeared that arcjets would find extensive use as aerothermodynamic test facilities where fundamental investigations of real gas phenomena could be conducted. Although they did not provide perfect simulation of atmospheric flight environments, arcjets had a significant advantage over impulse facilities in that they could be operated at high enthalpy levels for long periods of time. Unfortunately, it proved to be very difficult to establish just what operating enthalpy level was actually reached. In fact, the inability to characterize the arcjet stream conditions ultimately limited arcjets mainly to applications where complete knowledge of stream conditions was not a requirement for evaluating test results.

In a review of ground-test facility simulations of poorly understood real-gas phenomena, Park[10] identified seven important problems: 1) determining aerodynamic parameters; 2) viscous/shock interactions; 3) boundary layer transition; 4) understanding leeward or base region flows; 5) nonequilibrium radiation; 6) nonequilibrium ionization; and 7) surface catalysis. Park then examined the capabilities of three types of hypersonic ground-test facilities that could be used for fundamental investigations of these problems: 1) impulse facilities (including shock tunnels); 2) ballistic ranges; and 3) arcjets. Arcjets were only deemed suit-

able for studies of nonequilibrium radiation and surface catalysis, and even then adequate specification of the stream conditions was mentioned as a requirement for improving the analysis of test results.[10]

Before discussing the issue of stream conditions further, it is useful to examine the current status of large-scale arcjet facilities and their role in thermal protection material test and development. In addition, it is instructive to examine the use of conventional stream characterization instrumentation and how it is used in the interpretation of test measurements.

### 1.2 Overview of Current NASA Arcjet Facilities

Today, NASA's large-scale arcjet facilities are used mainly to simulate aerothermal heating environments, although there is still some limited use in evaluating supersonic air-breathing propulsion concepts. Our discussions will focus exclusively on facilities, modeling, and measurements that relate to the principal application: aerothermal heating simulation. Two NASA Centers, Johnson and Ames, are currently operating segmented-type constricted-arc heater facilities for this application. This facility is the workhorse for the 20 to 30 MJ/kg enthalpy range of long-duration thermal testing.

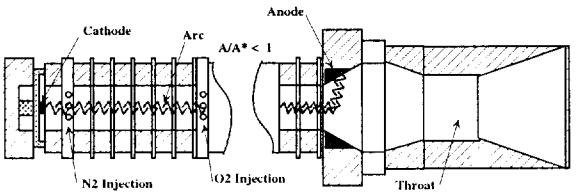


Fig. 5. Current version of JSC TP-1 constricted-arc heater and nozzle.

Arcjet facilities at Johnson Space Center support TPS testing requirements for manned missions. All of the thermal protection materials for shuttle, including tiles, coatings, and fillers, are qualified for use on the basis of tests in these arcjets. Johnson has two 10 MW facilities JSC TP-1, which became operational in 1973, and JSC TP-2, which was upgraded to 10 MW in 1991.[11] Both facilities have segmented, constricted-arc heaters. The TP-1 facility is usually arranged with a conical nozzle configuration for stagnation-point testing, while TP-2 is typically configured with a rectangular channel for flat-plate testing. A schematic of the Johnson TP-1 heater and nozzle is presented in Fig. 5, and it shows two noteworthy features. First, because of the tungsten cathode, $O_2$ is injected separately from $N_2$ further downstream in the heater to prolong the useful life of the electrode. Although they are injected separately, the two gases are thought to be mixed by the time the downstream electrode package is reached. The second interesting feature is that the throat diameter is larger than that of the constrictor, which causes some uncertainty regarding the sonic location. Axial velocities in the arc column could actually be quite high, which may inhibit mixing of the $O_2$ and $N_2$ streams. The facility is equipped with energy balance instrumentation, which provides a measure of the bulk enthalpy for each test.

The Arcjet Complex at Ames Research Center supports Ames' role as lead NASA Center for thermal protection material development. There are currently three operating segmented, constricted-arc facilities: the Aerodynamic Heating Facility (AHF) and the Panel Test Facility (PTF) are both rated at 20 MW ; and the Interactive Heating Facility (IHF) is rated at 60 MW. There are also two operable Huels-type heater facilities, 2x9 Turbulent Flow Facility (TFF) and the Direct Connect Arcjet Facility (DCAF). Two arcjet facility buildings house the different arcjets, which share common steam-ejector vacuum and water-cooling systems. With a shared vacuum system, only one facility can operate at a time. However, facilities can operate sequentially throughout the day with up to 8 runs during a single operating shift. Note that the operating frequency for an arcjet is greater than that of typical large-scale impulse facilities.

A cross section of a typical Ames constricted-arc heater configuration was shown above in Fig. 4. The configuration is different from the JSC TP-1 configuration that was shown in Fig. 5. For the Ames heater, the throat diameter is smaller than the constrictor diameter, so the sonic point will always be located between the converging and diverging sections of the nozzle. Also, both the upstream and downstream electrodes are copper, so oxygen does not need to be injected separately for air tests. Since the overwhelming majority of arcjet tests at Ames Research Center are performed using segmented-type, constricted-arc heaters, Huels-type heaters will not be discussed further.

Even though they are both classified as segmented, constricted-arc heaters, the different designs of the JSC and Ames heaters illustrate the variety of electrodes and nozzles that are in use today. There is no standard design. Consequently, performance will vary widely from facility to facility and characterization of the performance of one facility is by no means applicable to others unless the configuration is exactly duplicated.

### 1.3 Ames Aerodynamic Heating Facility Arcjet

The Aerodynamic Heating Facility (AHF) Arcjet at NASA Ames Research Center is an example of current large-scale, constricted-arc heater test facilities. A schematic of the facility is shown in Fig. 6. Facility operation is initiated by evacuating the arcjet and then striking an arc in a low-pressure argon stream.[12]

The test gas flow, usually air or nitrogen, is then introduced through the segmented disks along the column, and the arc current is adjusted to achieve the test conditions. Within the arc column, heating by the electrical discharge causes substantial dissociation and ionization of the test gas. The argon start-gas stream is maintained during operation, and additional argon is injected to protect the downstream electrode. Each electrode package is made up of a series of alternating copper rings and spacer disks. The rounded rings are the actual electrodes, and they protrude into the stream to move the arc attachment away from the wall (see Fig. 4). Magnetic windings inside the electrodes rotate the arc attachment point to reduce the heat load on the electrodes. Each electrode can carry up to 500 A of current. Typically, the anode is placed at the upstream end of the arc column to benefit from further cooling by the test gas.

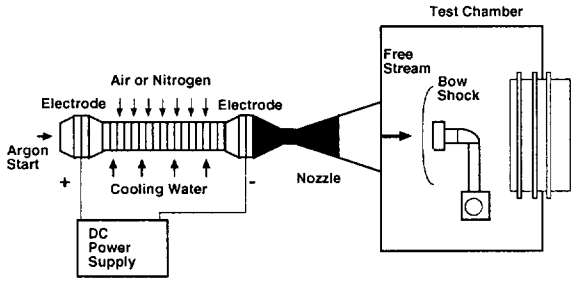


Fig. 6 Schematic of the NASA Ames AHF Arcjet.

Upon leaving the heater, the flow is accelerated to hypersonic speed through a conical, converging-diverging nozzle. During the expansion-driven acceleration, the collision frequency decreases rapidly in the nozzle and the thermochemical state of the flow departs from equilibrium. At some point, the flow chemistry becomes frozen, and this may be followed by freezing of the internal energy distribution of the molecular species. Various nozzle sections can be used to provide expansion ratios ranging from 64 to 576. The flow exits the nozzle and continues expanding into a cabin where material tests are conducted. Material samples are typically inserted into the stream 36 cm downstream of the nozzle exit. Test durations of up to 20 minutes are possible, depending on the particular conditions. During the tests, the stagnation pressure, cabin pressure, and arc heater conditions are continuously monitored.

In a typical test cycle, a preliminary analysis of the expected heat load in a flight application has been performed and a candidate thermal protection material has been selected for testing in an arcjet flow. The test conditions are chosen to attempt to match the expected heat flux for a particular point on a predicted trajectory, such as the peak heating point. Conventional instruments, which will be discussed below, are used to verify the test conditions. The test results are then interpreted without the benefit of full knowledge of the stream conditions. Currently, relating test results from the arcjets to the intended flight application is more of an art than a science, because the arcjet stream conditions are not sufficiently characterized.

### 1.4 Arcjet Characterization Using Conventional Instrumentation

The words "Arcjet Characterization" are typically understood to mean specifying the state of the arcjet test stream, and they are referred to throughout this discussion in that context. Although it is important in flow modeling, the need for arcjet characterization is driven primarily by the needs of thermal protection material developers, who need better specification of the stream conditions to relate the results to flight environments. In addition, an improved understanding of arcjet stream conditions in general may also make arcjets more suitable for fundamental studies of real gas phenomena.

The state of arcjet stream characterization in the early 90's was summarized in an excellent and thoughtful review article by Scott.[13] Both established and novel instrumental techniques were critically reviewed in the article. The article focused mainly on how various diagnostic techniques could be used to characterize the most important stream variables: enthalpy and the degree of nonequilibrium in the stream. Rather than repeat this review, some of the more widely used conventional diagnostics are reviewed briefly below. The limitations of these measurement techniques are discussed to provide background for considering what measurements are required to improve arcjet flow modeling. Newer, less widely used spectroscopic techniques, such as multiphoton spectroscopy will be mentioned later, and are discussed more fully in the second article.

Traditional instruments that are used to obtain flow property measurements include pitot probes and calorimeters. Additional instruments, such as thermocouples and flow meters are used to measure coolant flow rates and temperature rise to perform an energy balance on the facility. Stream surveys are usually performed with a traversing, sting-mounted probe, since the facility can operate continuously and at a level where the instrument can give an equilibrated response to the quantity being measured.

Pitot measurements yield the stagnation pressure behind a shock wave that is generated by the probe. For much of the operating range of today's large-scale arcjet facilities, the pitot, or impact, pressure can be related to the dynamic pressure of the flow, $\rho v^2/2$, through the Rayleigh supersonic pitot relation [14],

$$p_p = \frac{\rho\, v^2}{\gamma}\left(\frac{2\gamma}{\gamma+1}\right)^{\frac{\gamma}{\gamma-1}}\left(\frac{\gamma+1}{2}\right)^{\frac{\gamma}{\gamma-1}}, \text{for} \quad M >> 1. \tag{1}$$

In the above expression, $\gamma$ is the ratio of specific heats for the gas, $M$ is the Mach number, $p_p$ is the pitot pressure, $\rho$ is the stream density, and $v$ is the velocity. Although $\rho$ and $v$ are both important stream variables for arcjet flow characterization, a determination of each variable cannot be made without an additional measurement. For typical facility operating conditions the flow velocity is a considerably larger quantity than the stream density, so a strategy for determining both variables should involve a velocity measurement.

**Energy Balance -** Most arcjet facilities are equipped with instruments that can be used to perform an energy balance on the arcjet facility as a whole. Owing to its simplicity, the energy balance approach remains by far the most commonly used for characterizing the arcjet stream. The basic principle of the measurement is illustrated in Fig. 7, which shows the arc-jet operation measurements that must be acquired to perform the energy balance. A simple first law relationship is invoked for the system,

$$\dot{m}\, h_{\text{avg}} = VI - \dot{m} c_p \left(\Delta T_{\text{on}} - \Delta T_{\text{off}}\right), \qquad (2)$$

where $\dot{m}$ is the mass flow rate, $h_{\text{avg}}$ is the bulk enthalpy, $V$ is the arc voltage, $I$ is the arc current, $T$ and $c_p$ are the coolant temperature and specific heat, and the subscripts of $\Delta T$ refer to a measurement of the temperature rise with the arc on and with the arc off. This is required to account for the coolant temperature rise that results from pumping a viscous fluid through the cooling lines. An uncertainty analysis for typical measurement errors can be performed, and this indicates that the average total gas enthalpy can be determined fairly accurately.[15] However, there are some important considerations. First, the larger the facility, the more difficult it is to accurately measure the coolant temperature rise. Either a large number of measurements must be made in the smaller coolant lines or the temperature distribution in a large manifold must be resolved to determine the coolant temperature rise. Second, the energy balance does not account for further heat losses beyond the nozzle that may reduce the bulk enthalpy value of the free stream. Finally, although knowledge of the enthalpy determined from an energy balance is important and useful from a facility perspective, it is still an average, or bulk value. This average enthalpy value may not be representative of that part of the test stream actually impinging on the test article since gradients in flow enthalpy that may develop in the arc column persist owing to short residence times in the high pressure region of the nozzle. Perhaps more importantly, the energy balance approach provides no information about the degree of nonequilibrium or how the energy is apportioned in the free stream.

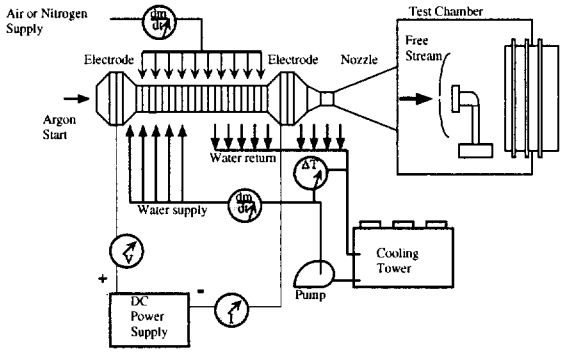


Fig. 7. Energy balance on a large-scale, constricted-arc arcjet test facility.

Energy balance measurements can also be used to determine heater efficiency values during facility operation. The heater efficiency, which is generally a function of arc pressure and current, is defined as

$$\eta_H(p, I) = \dot{m}\, h_{\text{avg}}/(VI). \qquad (3)$$

Once this is determined for the particular heater configuration, it can be used to quickly estimate the bulk enthalpy using the mass flow rate of the gas and the arc voltage and current by simply rearranging the equation. Because the efficiency is a function of the arc current and the stagnation pressure, this measurement must be carried out over the full range of facility operation to develop an empirical correlation that accounts for the dependence.[16] It is important to understand that changes in electrode configuration, or indeed, variation in electrodes themselves will directly influence the heater efficiency. Moreover, the electrodes are typically the most frequently replaced component of the facility, so efficiency values, and this approach to estimating bulk enthalpy, should be used with caution.

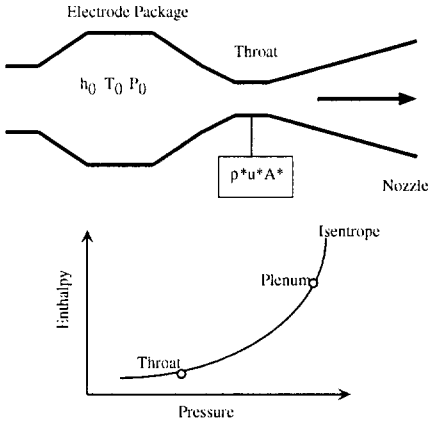


Fig. 8. Sonic flow method for determining enthalpy in an arcjet facility (after Winovich[17]).

**Sonic Flow -** Another method used to determine the total enthalpy is the sonic-flow method that was developed by Winovich.[17] The basic physical principle of this method is that for any given equilibrium thermodynamic state there is a unique value of the sonic mass flow. Thus for a given enthalpy and pressure there is

only one value of the choked mass flow. Conversely, for a known pressure a measurement of the mass flow determines the enthalpy. The graphical representation of this approach is shown in Fig. 8. Assuming that the flow is one-dimensional and in equilibrium, then for both real and ideal gases a simple expression relating mass flow and reservoir enthalpy can be derived from the equations governing the flow from a reservoir through a choked nozzle,

$$\frac{\dot{m}}{(A\ p_0)} = \frac{\sqrt{2\ h_0}}{(R\ T_0)} \left[ \frac{\rho^*}{\rho_0} \left( 1 - \frac{h^*}{h_0} \right)^{1/2} \right] \quad . \qquad (4)$$

In the above expression, $A$ is the cross-sectional area, the subscript 0 refers to stagnation conditions, and the superscript $*$ refers to conditions at the throat.

Simplified versions of this equation can be derived for the case of thermally and calorically perfect gases, as well as for calorically imperfect gases. For real gases both $\gamma$ and $R$ vary with temperature and pressure and there are no simple closed form expressions that represent this variation. Consequently, the governing equations for the choked nozzle flow were solved iteratively using an equation of state representing a dissociating gas for a range of pressures and enthalpies. For the range of pressures investigated (0.25 to 100 atm) all solutions for the mass flow fell within 4 % of a mean curve. A curve fit procedure was then used to develop the empirical correlation,

$$\frac{\dot{m}}{(A\ p_T)} = \frac{C}{h_T^{3.97}} \quad , \qquad (5)$$

where $C$ is a constant factor whose value depends on the system of units. The effects of boundary layer, nonequilibrium (or frozen) chemistry, and variable heat loss to the nozzle walls were examined in the original work pertaining to this measurement approach.[17] While boundary layer and heat loss effects appear to be small, the existence of nonequilibrium flow at the throat leads to a systematically low estimate of the flow enthalpy. As with the energy balance approach, the total enthalpy determined with the sonic-flow method represents an average value, and there is no information about the degree of nonequilibrium where testing takes place beyond the nozzle exit.

**Stagnation Point Heat Flux -** With certain assumptions the total stream enthalpy can be inferred from a simultaneous measurement of heat transfer and impact pressure at the stagnation point of a blunt body, such as a sphere or cylinder as depicted in Fig. 9. Boundary layer equations for stagnation point heat transfer were developed by Fay and Riddell,[18] and a subsequent modification of these results to include nonequilibrium boundary layer chemistry and surface catalytic effects was given by Goulard.[19] Later, Pope[20] presented an experimental investigation of Goulard's theoretical results for arcjet flows. During the same time period, empirical correlations for stagnation point heat transfer in any gas were published:[21,22]

$$\Delta h = \frac{q}{\kappa} \sqrt{\frac{R_{eff}}{p_p}}, \qquad (6)$$

where $\kappa$ is a gas species dependent constant, $R_{eff}$ is the effective radius of the blunt-body article, and $\Delta h$ is the difference between the stream and cold wall enthalpy. A clear advantage of this approach is that it gives a spatially resolved measure of the stream enthalpy at the test location. However, an important assumption in the use of the above correlation is that the catalycity of the surface of the heat flux gauge is essentially full, i.e. all atoms impinging on the surface recombine and deposit the excess energy from the exothermic reaction on the surface as heat. It should be noted that full catalycity is rarely achieved for calorimeters, and heat flux measurements with gauges of different catalycity show wide variation.[23,24] Oxidized, uncleaned surfaces, which are typical on calorimeters that are in service, have significantly lower catalycity. This means that calorimeters will generally under-measure the incident heat flux when significant dissociated species are present at the calorimeter surface. Since the inferred enthalpy is linearly dependent on the measured heat flux, this approach will lead to a lower estimate of the stream enthalpy level.

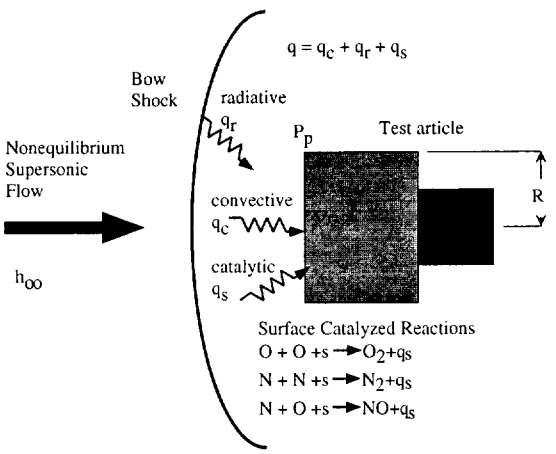


Fig. 9. Stagnation point heat transfer measurements.

All of the conventional approaches to arcjet stream characterization that have been discussed in this section share common attributes in that they infer enthalpy from other flow property measurements and they provide no information on the degree of nonequilibrium. The ability of measurements made using these approaches to guide and inform flow modeling is therefore limited. Furthermore, it is not possible to use these measurements to relate the arcjet stream conditions to the intended flight application, because

they do not address the nonequilibrium state of the free stream.

New spectroscopic techniques that are currently under development may improve this situation, and some of these approaches will be discussed in the second lecture. Judicious application of CFD codes may also improve this situation by providing more insight into the thermochemical state of the flow. However, any CFD codes that are developed for this purpose must be guided by experimental results, and this topic is addressed in the following sections.

## 2. CFD for Arcjet Flows

Today, CFD is an important resource for aerospace vehicle design, testing, and development. Investigations into new, or poorly understood, flow problems are often undertaken with a combined experimental and computational approach. Both the experiment and the modeling benefit from the collaboration, since the CFD simulations can evaluate a wide parameter space quickly and efficiently, while the experimental results provide guidance for developing assumptions and improving model fidelity. The general state of CFD for a particular discipline in the wider field of aerospace applications is periodically reviewed. Recent reviews that are relevant to simulating arcjet facility flows can be found in Refs. 25 and 26, which examine CFD for high enthalpy test facilities and external flows, respectively.

The present discussion is concerned mainly with the impact of experimental measurements and instrumentation on modeling, so detailed examinations of numerical methods, particular models, and grid resolution, which are familiar topics in the literature regarding CFD, will not be covered. Rather, the intent is to discuss shortcomings in current instrumentation and available experimental data that make the task of producing credible arcjet flow simulations exceedingly difficult, if not impossible. Although the conservation equations and general numerical method are discussed briefly below, they are invoked only to frame the discussion about what must be measured and how well. The perspective is that of an experimental approach to flow modeling that examines assumptions, model inputs, and constraints in order to propose better experimental tests to resolve ambiguities and uncertainties.

### 2.1 Motivation for Arcjet Flow Modeling

A major driving force behind arcjet flow modeling is the desire to extract the most information from tests of thermal protection systems in large-scale arcjet facilities. Testing costs are always a concern, and an investment in computational resources to avoid test article failures or to conduct a more efficient test cycle represents a prudent strategy. Computational investigations can often be undertaken at lower expense than experimental efforts. Unless a complete computational capability is being started from scratch, the costs of employing state-of-the-art instrumentation for experimental investigations is usually much higher, assuming that manpower for both efforts is equivalent. If more and better information could be obtained from arcjet testing, then substantial development cost savings may be realized from a reduced dependence on flight experiments (e.g. FIRE[27,28] and Apollo[29]) that are often required to establish thermal protection system effectiveness.

Minimizing thermal protection mass for current, low-budget planetary missions is also an important motivation for generally improving the state of knowledge of arcjet flow stream conditions. For these missions there is neither time nor budget for flight testing a prototype before launching. If results from arcjet tests can be extrapolated to flight conditions with quantifiable uncertainties, then it may be possible to reduce the design safety margins that currently added to heat-shield thickness.[30] It may ultimately be possible to establish flight performance of thermal protection materials through arcjet testing if a sufficient understanding of arcjet flows is developed. CFD modeling would play an indispensable and enabling role in this effort.

Facility improvements and optimization for particular test configurations could also benefit from the development of CFD tools tailored to arcjet flow modeling. As noted above, ARCFLO played an important role in the early development of large-scale arcjet test facilities, and there is a need for modern computational tools to improve electrode designs, optimize heater configurations, and design new nozzles for flat-plate test configurations. These tools could also be used to design test configurations that would provide the necessary information at reduced cost and effort.

Additional motivation derives from the desire to improve the general state of nonequilibrium flow modeling and the understanding of real gas effects. As mentioned above, the stable, relatively long-duration arcjet operation at high enthalpies creates opportunities for studying complex chemical and thermal interactions that cannot be easily analyzed in impulse facilities.

### 2.2 CFD Requirements for Arcjet Flow Simulations

Before discussing measurement requirements for improving computational simulations of arcjet facility flows, it is useful to examine the CFD requirements that have evolved from previous and ongoing efforts to model arc-heated flows in large-scale facilities. Arcjet flows are typically not in thermal and chemical equilibrium, except possibly in the constrictor and electrode

package regions. Consequently, any attempt to model the flow requires a CFD code that models nonequilibrium processes.

The conservation equations for hypersonic flows in thermal and chemical nonequilibrium that are solved by the LAURA CFD code[31] have been compiled in a single reference publication by Gnoffo and his coworkers.[32] Eleven species that are typically encountered in simulations of hypersonic air flows were included in the model: $N_2$, $O_2$, NO, N, O, $N_2^+$, $O_2^+$, $NO^+$, $N^+$, $O^+$, and $e^-$. Thus, eleven species continuity equations and three momentum equations must be solved by the code. For this particular CFD code, three separate energy equations are modeled to account for nonequilibrium effects: vibrational energy, electronic energy, and total energy. Thermodynamic data for the eleven species and reaction rates for two different models, Park [33] and Dunn and Kang[34], were also given in the report. In this CFD approach, which is representative of those currently in use for nonequilibrium, hypersonic flows, only the ground electronic states of each species are modeled. When radiative energy flux is important, it is typically treated separately or in a loosely-coupled fashion. It should be emphasized that there is no universally agreed upon model formulation, particularly when it comes to nonequilibrium processes and chemical reaction and energy transfer rates. Interested readers are referred to Refs. 35-38 for other computational model formulations.

For arcjet flows in large scale facilities, argon must also be considered since it is often added to the test gas flow to protect electrode surfaces. If only the neutral state is considered, this brings the total number of species for air/argon flows to twelve. In addition, thermodynamic and chemical reaction rate data must also be included for argon. [39]

### 2.3 Strategies for Arcjet Flow Simulations

Just as there is no universally accepted model for nonequilibrium, hypersonic flows, there is no single CFD code that can simulate the complete arcjet facility flow from the heater to the test article. Thus, some reasonable modeling strategy must be developed that matches available CFD models to flow regions in an advantageous manner. To illustrate this point, several modeling efforts that were concerned with either arcjet characterization or interpretation of arcjet test results are surveyed below. The presentation is organized by flow region, starting from the heater and moving through the nozzle to the test article.

**Arc Heater -** The flows within the arc heater and electrode packages are special cases, since the electrodynamic processes occurring within these typically subsonic flow regions are usually absent in hypersonic flows (with the exception of MHD device flows). However, a discussion of numerical studies of arc heaters is included here for two reasons: first, the flow may be in thermal and chemical equilibrium within the downstream electrode package; and second, if the flow and discharge physics can be modeled correctly, then it may be possible to compute inlet conditions for use in nozzle calculations.

Within an arc-heater, the flow is typically subsonic and is more properly described as a plasma owing to the presence of the electrical discharge. To model this portion of the flow accurately, a coupled solution of the fluid dynamics, radiation, and electrodynamics is required. The development of a CFD model for the arc heater that included the necessary coupling was undertaken at Ames Research Center several years ago,[40,41] but the effort was eventually abandoned. Instead, the flow within constricted-arc heaters is still modeled with either the ARCFLO code, which was mentioned above, or a derivative. One of the derivative codes, SWIRLARC,[42,43] has been modified to include the tangential component of gas injection that is typically used to help stabilize the discharge in high-pressure facilities. It should be noted that in any form, ARCFLO does not attempt to fully simulate the physical processes within the heater. Rather, ARCFLO and its derivatives employ a semi-empirical approach to perform comparative studies and indicate trends that might be useful for design studies.

Recently, there has been renewed interest in improving computational models of constrictors. A Navier-Stokes formulation for a constrictor was developed and implemented by Kim et al,[44] and an improved, fully-coupled radiation model was applied to the study of an arc heater by Sakai et al.[45] The main motivation for this renewed activity is the need to increase the efficiency and performance capabilities of existing arcjet facilities. Obviously, measurements will be required to validate these newer flow models.

**Nozzle and Free Stream -** For studies relating to arcjet characterization, arcjet test interpretation, or general nonequilibrium flow modeling, the expanding flow in an arcjet facility nozzle presents a challenge to the computational community. The general strategy for modeling arcjet nozzle flows relies on some means for estimating the inlet conditions for the nozzle, particularly the stagnation enthalpy, and then using whatever experimental information is available from the free stream to assess the fidelity of the simulation. Depending on the particular computational model, the inlet conditions can be specified either in the subsonic flow region upstream of the throat or in the supersonic portion of the nozzle. As was mentioned in the description of a typical arcjet facility, the nozzle flows are not in thermal or chemical equilibrium. Therefore, the computational approach must model the thermodynamic and chemical kinetic processes that govern hypersonic, nonequilibrium flows.

There have been several efforts aimed at simulating flows in arcjet nozzles. At Ames Research Center alone, three different numerical approaches have been used recently to simulate nozzle flows in conical[46–48] and semi-elliptic[49] geometries. These particular studies were undertaken specifically to address arcjet characterization issues. Additional investigations of conical nozzle flows have been carried out in support of arcjet surface catalysis experiments.[50] Details of the different numerical approaches are given in each of the references. However, it is interesting to note the progression of the numerical models used in these studies. Babikian used a quasi-one-dimensional, multitemperature flow model, NOZNT,[51] to compare with free stream temperature measurements in the Ames AHF Arcjet Facility.[46] Gökçen performed simulations of the nozzle flow with an axisymmetric, nonequilibrium Navier-Stokes solver in support of shock layer experiments.[47] More recently, Loomis and his coworkers used GASP, which is a general three-dimensional, flow solver to simulate both conical and semi-elliptic nozzle flows in support of thermal protection material tests for the X-33.[49]

Concurrent experimental and computational studies of expanding, $N_2$/Ar plasma flows have also been carried out by Schönemann and coworkers.[52] The noteworthy aspect of this particular investigation was the use of experimental measurements at one axial location to start the calculations and predict the rapidly expanding flow properties at a second, downstream location. This approach has the advantage of avoiding some of the uncertainties that result from estimating inflow conditions.

**Flow Over a Test Article -** As the current use of large-scale arcjet facilities is aimed primarily at simulating aerothermal heating, it is extremely important to be able to model the flow over a test article accurately. Test article flows can be classified into two basic types: shock-layer flows over a test article in a conical nozzle flow and boundary-layer flow over a flat plate for semi-elliptic, or rectangular, nozzle flow. Since the flat plate is usually an extension of the nozzle wall, the modeling requirements for simulating boundary layer flows are identical to those for nozzle flows, although the angle of attack is typically varied as part of an experimental investigation. Shock-layer flows are different, particularly for studies of stagnation point heating. For this configuration, the flow undergoes compression by a shock wave, whose strength depends on the particular test conditions and geometry, before impinging on the test-article surface. Thus, the free stream conditions, which largely determine the characteristics of the shock layer flow, must somehow be known to carry out the simulation.

Typically, there are no stream measurements, other than pitot pressure and heat flux, that could be used to specify the stream conditions. For certain arcjet test conditions, it is possible to estimate the stream conditions using a combined equilibrium and frozen-flow analytical approach, and then carry the analysis through the shock layer based on measurements of the pitot pressure, heat flux, and model surface temperature.[50] However, a more general approach involves simulating the nozzle flow (again, an estimate of the initial enthalpy is required) with a numerical model and then using those conditions as input to a shock layer calculation. An example of this latter approach can be found in the work of Gökçen,[47,48] which will be discussed in detail below. Inevitably, inaccuracies in modeling the expanding nozzle flow affect the simulations of shock-layer and boundary-layer flows in arcjet facilities.

The response of the test article to the shock layer flow is also of considerable interest to the arcjet test and material development communities, where much can be gained by understanding the interaction between the shock layer flow and the material. A review article by Milos and Rasky[53] outlines the importance of properly defining the boundary conditions that govern the interactions at the fluid/surface interface. The authors also point out that since boundary processes define the interaction of the fluid and solid computational models, their boundary conditions must agree. This issue is especially important for understanding the performance of charring and ablating thermal protection materials. Although it is very interesting, this topic is outside the scope of the present discussion.

| Measurement Requirements for Arcjet Flow Modeling | | |
|---|---|---|
| Arcjet Flow Measurements | | Model Development Measurements |
| *Starting Conditions* | *Simulation Validation* | |
| Enthalpy<br>Pressure<br>Mass flows of test gases<br>Inflow velocity<br>Contaminant level<br>Turbulent or laminar?<br>Gradients<br>Assessment of equilibrium | Velocity<br>Species concentrations<br>Density<br>Pressure<br>Translational T<br>Rotational T<br>Vibrational T<br>Electronic state populations<br>Post-nozzle expansion rate<br>Stream profiles | Three-body recombination rates<br>Third-body efficiencies<br>Spontaneous emission rates<br>Laser-excitation rates<br>Collisional-radiative model rates<br>Species thermodynamic data<br>Energy Transport Rates |

Fig. 10. Classification of measurements for arcjet flow modeling.

## 3. Measurement Requirements for Arcjet Flow Modeling

Measurements that can be used to improve computational models of arcjet flows can be separated into general categories, which are illustrated in Fig. 10. The first classification distinguishes between direct measurements of properties of arcjet flows and more generic measurements that can influence the development of models for nonequilibrium, hypersonic flows. Measurements of thermodynamic properties, species concentrations, velocity, and enthalpy in arcjet flows

would all fall into the first category of direct measurements. More accurate determinations of important reaction or energy transfer rates, which need not be measured in arcjet flows, would fall into the second category. While this category is probably of equal importance in the improvement of arcjet flow modeling, the majority of the discussion below is concerned with direct measurements of primary arcjet flow quantities.

Within the first category of direct arcjet flow property measurements, a further distinction can be made between measurements that would be used to define starting, or inflow-boundary, conditions and measurements that could be used to assess the fidelity of the simulation. Since the success of any flow modeling effort is inextricably linked to the accuracy with which the starting conditions for the calculation are defined, measurements of the input parameters are considered to be of greater importance. Of the inflow parameters for arcjet flows, the total enthalpy is the most important because it defines the total flow energy and the initial composition and temperature. Despite its importance, enthalpy has proven to be the most difficult parameter to characterize accurately, as discussed above. Typically, the settling chamber pressure is measured to reasonable precision for most arcjet tests, so it is assumed herein that pressure is given. Other primary measurements that define the starting conditions are the mass flows of the test gases and the configuration and geometry of the facility.

Velocity, species concentrations, temperature(s), static pressure, and density are examples of flow property measurements that can be made at various locations in the arcjet to assess the performance of a computational model. Flow quantities that are derived from measurements of primary flow variables, such as the dynamic pressure, specific heat ratio, Mach number, and Reynolds number, are less important from the perspective of evaluating computational models. However, these quantities are quite useful in specifying the performance of the arcjet facility and for relating the test conditions to the expected flight environment.

### 3.1 Enthalpy

It is readily apparent from even a casual reading of the previous section on modeling requirements that all simulations of the most important arcjet regions, the nozzle and shock-layer, or boundary-layer, flows, require knowledge of the stagnation enthalpy. The state of enthalpy determination using conventional instrumentation was examined in the introductory section, and it was found to be inadequate for several reasons. First, the conventional means for determining the flow enthalpy can only give an estimate of the total value, which does not specify the state of the essentially frozen free-stream flow. Second, for the energy balance and sonic flow approaches, only the bulk enthalpy value can be determined. While this is useful for monitoring facility performance, the enthalpy value probably does not represent the free-stream core flow, where stagnation-point tests are conducted, unless there are no spanwise enthalpy gradients. The assumption of gradient-free flow appears to be questionable.[25] Third, even when great care is taken with the treatment of the calorimeter surface, enthalpy values derived from heat flux measurements are likely to be systematically low.

It should be noted that the measurements required for determining flow enthalpy vary with flow region. Moreover, the influence of the enthalpy determination on the outcome of the flow simulations also depends on where the enthalpy measurement is made. For arc heater and nozzle flow simulations, a measurement of the stream enthalpy within the downstream electrode package, which also functions as a nominal settling chamber, is appropriate. However, for shock layer simulations, inaccuracies are accumulated from simulating both the nozzle flow and the shock layer flow. A more appropriate enthalpy measurement location would be the free stream, provided that the measurement could quantify both the total enthalpy and the nonequilibrium state of the gas. With this information about the free stream, the shock layer flow could be simulated independently of the nozzle flow. Obviously, owing to the nonequilibrium nature of the flow, more flow property measurements are required to determine the thermodynamic and chemical state of the flow in the free stream.

Finally, any enthalpy measurement must be spatially resolved, and enthalpy gradients must be quantified to remove potential ambiguity from the specification of the starting conditions. This issue will be discussed further below and the applicability of nonintrusive optical diagnostics to enthalpy measurements will be addressed fully in the following lecture.

### 3.2 Arc Heater

The flow within the arc heater and electrode package is usually subsonic and the enthalpy is mostly static, being comprised of thermal and chemical mode contributions. Because pressure is reliably known, a measure of total density or temperature would permit a determination of the total enthalpy. Of the two variables, temperature is more amenable to measurement through optical means. Assuming that the flow is in thermal equilibrium, then determination of a single temperature is sufficient for determining enthalpy. If there is optical access to either the heater or electrode package region, then a spectrally resolved emission measurement can be used to determine temperature. The specific procedures for determining temperatures from spectrally resolved emission are discussed in the following lecture.

Useful information could also be derived from additional measurements of other flow variables in the electrode package. These other flow properties include: the axial flow velocity; the azimuthal velocity component, which would quantify the amount of swirl at the nozzle inlet; the total heat flux and radiative heat flux to the wall; the amount of copper, which is introduced into the stream by the process of electrode erosion;[54] and the electron number density downstream of the arc. Although the axial extent of the electrode package region is usually not that large, the flow is cooling as it moves toward the throat. Consequently, a determination of the axial variation in any flow quantity would provide some insight into the evolution of the flow as it begins to accelerate.

Owing to limited accessibility, flow probes are not a viable option. Their survival at typical large-scale arcjet facility operating conditions is also an issue. Optical access to the downstream electrode package can often be realized,[55] and measurements in this region are particularly useful because this region provides the inflow to the nozzle. It may be possible to implement optical measurements at two different axial locations downstream of the arc termination to assess the rate of evolution of the stream properties. Furthermore, since large fluctuations in the magnitude of emission from atomic transitions have been observed in the electrode package,[55] it may be possible to develop a two point correlation approach for velocity measurement.

### 3.3 Arcjet Nozzle and Free-Stream Flow

**Nozzle -** For the purposes of this discussion, the starting point for nozzle flow is defined as the end of the electrode package. Unlike the segmented arc heaters and electrode packages of todays constricted-arc facilities, the nozzle assemblies are typically fabricated in a more monolithic manner. Because they are fabricated with integral water cooling, there is little hope for instrumenting existing large-scale arcjet nozzles. This essentially precludes *in situ* monitoring of the onset of chemical and thermal freezing, which could then be used as a starting point for frozen flow analysis.

Using smaller scale arcjet devices fabricated with segmented nozzles it may be possible to address the onset of chemical, and possibly thermal, freezing for flow conditions of interest in aerothermal testing applications. Note that the fluid dynamic expansion rate plays an important role in determining the location at which the flow freezes. Whatever studies are undertaken in smaller facilities must address this issue.

**Free Stream -** Although the flow is usually chemically and thermally frozen by the time it exits the nozzle, the free stream region is often optically accessible, and measurements of many flow properties are possible. Spatially resolved measurements of velocity, translational temperature, density, pressure, and species concentrations have all been made using laser-induced fluorescence (LIF) techniques.[56–59] Recently, measurements of enthalpy and its distribution among thermal, chemical, and kinetic modes, were demonstrated in $N_2/Ar$[58] and air/Ar[59] flows using two-photon LIF of atomic nitrogen. Although more property measurements are required to determine enthalpy for nonequilibrium flow, the approach of using LIF of the dissociated species to determine multiple flow parameters appears capable of providing this information with the aid of certain assumptions. Fortunately, the validity of the assumptions that are currently invoked can be evaluated experimentally.[59] Flow property measurements using LIF techniques will be discussed extensively in the second lecture.

Although further development of this approach is required to assess the assumptions and establish the range of applicability, LIF based stream property measurements may ultimately prove sufficient to establish the enthalpy and degree of nonequilibrium of the free stream flow. This would provide a set of inflow conditions that could be used to calculate the shock-layer flow. A computational simulation of the flow over a test article that was started from known free stream conditions and compared to shock-layer property measurements would allow a better assessment of the computational modeling. Determinations of free stream rotational and vibrational temperatures and assessments of possible metastable atomic state populations are needed to establish the validity of the LIF-based approach.[59]

In addition to establishing inflow conditions for shock layer simulations, the two-photon LIF measurements provide stream property information that can be used to evaluate the fidelity of nozzle flow simulations. Since total enthalpy is specified by the LIF measurements, with a quantified uncertainty, that value can be used along with the constrictor pressure to start the nozzle simulation. If the model used in the nozzle flow simulation is accurate, it should reproduce the measured distribution of the total enthalpy into kinetic, thermal, and chemical contributions in the nonequilibrium free stream. Comparisons between nozzle simulations and free stream measurements are underway for the chemically simpler $N_2$/argon flow cases.

### 3.4 Blunt-Body Shock-Layer Flow

Even with the free stream conditions specified, much is required in order to improve the general understanding of shock-layer flows in the stagnation-point heating configuration for aerothermal test applications. Finite rate effects that vary in significance depending on the test conditions and model geometry still control the chemical and thermal state of the shock layer and impact issues such as the difference in catalytic heating between the arcjet test conditions and the flight environment. Moreover, depending on the test geometry

and conditions, merged shock layer and rarified flow effects may be important, and may complicate the interpretation of heat transfer data.

Instrumentation and techniques for making spatially resolved flow property measurements are therefore required to establish the thermochemical state of the gas in the shock layer as it moves toward the surface of a test article. Spatial resolution is important because the flow is generally evolving from a nonequilibrium state toward an equilibrium state as it approaches the surface. Understanding this evolution is important from a modeling perspective as well as for aiding in the interpretation of test results. Again, for nonequilibrium situations, multiple flow properties, including velocity, species concentrations and temperatures must be measured to specify the flow state. In contrast to free steam conditions, shock layer temperatures ($T_r$, $T_v$, and $T_e$) can reach levels in excess of 5000 K and pressures can be orders of magnitude higher. Many internal energy levels of a number of species will be populated, and the distributions of populations over these energy levels may differ for different species (and possibly electronic states). With an ablating material, the situation is even more complex.

However, the goal of understanding the shock layer thermochemistry is important because that is the environment that must ultimately be related to flight conditions. In addition, if instrumental approaches that determine the thermochemical state of the shock-layer can be developed, then it may be feasible to test all-body vehicle configurations in the long-duration, arcjet flow facilities.

### 3.5 Measurement Accuracy Requirements

The uncertainty in experimental measurements and in computational predictions is an important consideration in arcjet flow investigations. For the present discussion, only uncertainties in experimental measurements are considered. Experimental uncertainties are estimates of errors in measurements that typically arise from either systematic or random contributions, or more typically, both. The systematic and random contributions are manifestations of the more general measurement attributes: accuracy and precision. Definitions of measurement accuracy and precision, which are frequently confused, can be found in a variety of reference publications, including a text on the subject by Bevington.[60] In the introductory discussion, Bevington indicates that the accuracy relates to how close a measured value is to the "true" value, while precision provides information on how well something can be measured, regardless of what that measurement means. For arcjet flow property measurements that would be used to improve flow modeling capabilities, both accuracy and precision are important. However, because flow properties are generally unknown, instrumentation must be developed to make measurements with a minimal reliance on assumptions that cannot be tested; otherwise it is impossible to assess accuracy. How closely a measured flow property represents the real situation is important from the perspective of predicting absolute flow property magnitudes, as in the simulation of a single arcjet test.

In contrast, it is often easier to establish the precision of a particular measurement from a number of different observations at similar conditions. This can be done without evaluating all of the assumptions that may go into a particular measurement, and it may then be possible to use the measured quantity constructively without knowing the absolute accuracy. Once the precision is established, then the measurement could be made for a number of different flow conditions where a single control parameter, such as the arc current, is varied. Simulations of these different flow conditions and comparisons with the experimental results would test the ability of the model to predict trends and might ultimately do more to establish confidence in the modeling than single-condition comparisons. Obviously, the model would have to be optimized for an appropriately chosen test condition. This approach may prove to be more effective in advancing both modeling and instrumentation development, especially when one considers the number of measurements required to document a single test case completely. As the instrumental techniques mature and as more is learned from parametric comparisons, then it may be feasible to pursue a single, well-documented test case.

From an experimental perspective, given the scarcity of data and the fact that measurement results from one facility cannot be directly transferred to another unless the configuration is identical, any property measurements that also have quantified uncertainty estimates are useful in advancing the general state of knowledge. Enthalpy measurements, as well as other inflow conditions that are required to initiate simulations, are examples of this type of flow property. Measurements that are used to evaluate the validity of computational models must be held to a higher standard, since their determination may influence changes in the model formulation. It is difficult to formulate a general statement as to how high the standard should be, given the complexity of present day CFD models. For some parameters an accuracy requirement can be postulated easily. As an example, consider LIF-measured atomic nitrogen concentrations, which currently have an estimated uncertainty of $\approx 30\ \%$ .[59] Although this uncertainty appears to be large, the recombination rate for the reaction,

$$N + N + M \rightarrow N_2 + M \quad ,$$

which largely determines the N atom concentration in the chemically frozen free stream, is currently uncertain by up to a factor of three.[62] Clearly even the

relatively uncertain N atom concentration measurement can be used to evaluate flow model performance. To determine accuracy requirements for other flow properties, an effort should be made to evaluate uncertainties in quantities currently used in the models and parametric studies with the computational model should be performed to evaluate sensitivities.

## 4. Experimental and Computational Investigation of Shock-Layer Flows

Recent attempts to simulate arcjet flows and compare the numerical predictions with experimental measurements illustrate the current status of both simulations and measurements. Knowledge gaps that affect the comparisons between simulations and measurements are readily apparent. The combined experimental and computational investigation of blunt-body, shock-layer flows in the Ames AHF Arcjet Facility was chosen for this purpose because the investigation was motivated by the need for improved characterization of arcjet flows, and understanding the shock-layer flow is directly relevant to aerothermal testing of thermal protection materials. Although experimental investigations have also been undertaken in the electrode package and free stream regions of the same arcjet facility, comparisons between measurements and simulations for those studies are ongoing. Consequently, more can be learned from examining the process and the results of the documented shock-layer flow property comparisons, and from the results of those comparisons.

**4.1 Objectives of Investigation** The objectives of this investigation were to: 1) determine whether a region of thermal and chemical equilibrium exists in the shock layer formed over a flat-faced cylinder; 2) determine the conditions required to establish the equilibrium region; and 3) determine whether or not enthalpy measurements could be derived from spectrally resolved emission emanating from the equilibrium region.

Early investigations of arcjet facility flows included efforts to characterize the shock layer flow using emission spectroscopy.[62,63] If the flow is in thermal and chemical equilibrium, then a measurement of the temperature from spectrally resolved emission and a concurrent pressure measurement would uniquely specify the thermochemical state of the flow and its enthalpy. A relatively recent analysis of shock-layer emission appeared to indicate the presence of an equilibrated region within the shock layer at a lower pressure than had been expected.[46] Therefore, a major goal of the present investigation was to verify the existence of the equilibrated region, and begin the task of defining the conditions that produce the equilibrium flow. By undertaking this investigation, issues associated with the development of an "enthalpy meter" based on measurements of shock layer emission could also be assessed.

At the outset, several areas of uncertainty were identified that had to be addressed in the investigation. These areas included: 1) what criteria are used to identify a region of thermal and chemical equilibrium; 2) how to interpret emission measurements with certainty; and 3) the effects of spatial intensity gradients on measurements that are integrated along the line-of-sight. It quickly became apparent that computational-flow modeling could address some of these issues and help guide the experimental investigation. Conversely, it was realized that the experimental measurements might also provide some assessment of the computational model validity, but this was not the primary objective.

### 4.2 Experimental and Computational Approach

**Experiment -** The shock layer emission experiments were carried out in the Ames AHF Arcjet Facility, which was previously described in the introductory section. To generate the highest shock layer pressure values the facility was configured with the 30.5 cm diameter nozzle, which produces the least free stream expansion. A 15.2 cm diameter, flat-faced cylinder made of copper was placed in the stream to generate the shock layer. Two different test conditions were surveyed, and these are referred to as the high pressure and low pressure cases. Test conditions for the two cases are summarized in Table 1.

**Table 1.** Arcjet test conditions for shock layer investigation.

| Test Conditions | | | |
|---|---|---|---|
| Case | Pressure | Current | Voltage |
| | atm | A | V |
| Low | 1.70 | 1141 | 2657 |
| High | 6.80 | 2075 | 5630 |

To obtain as much information from a single facility run as possible, line-of-sight emission spectra were acquired from multiple axial locations along the central stagnation streamline using a spectrograph and CCD camera. The model was placed at two different axial locations in the stream, 34.5 and 36.9 cm downstream of the nozzle exit (forward and back positions, respectively), to allow full coverage of the shock layer emission with the finite viewing area of the CCD and spectrograph system. Thus, two separate facility runs at the same nominal operating conditions were required to obtain the full shock layer emission profile for each test case.

Emission spectra were acquired at several grating positions covering the UV to near-IR wavelength range and the measured signals were converted to absolute intensities through calibration with standard spectral lamps. Each grating position was chosen to measure

certain spectral features that could be used to ascertain temperature or species information using spectral analysis techniques.[64,65] Particular attention was given to developing methods for determining rotational and vibrational temperatures using spectral feature ratios that minimized the influence of uncertainties in the measurements. This was desirable because agreement between the measured temperature values was thought to be a good indicator of the presence of a thermally equilibrated flow region. Portions of the $N_2^+$ (1,2), (0,1), and (0,0) vibrational bands were found to yield vibrational and rotational temperatures with minimum uncertainty based on spectral simulations. Note that the temperature values are derived from emission that is integrated along the line-of-sight, so the inferred flow properties actually represent intensity-weighted, spatially averaged values. Further details of the experimental configuration and the spectral analysis can be found in Refs. 65 and 66.

**Computational Modeling Approach -** The experimental measurements consisted of spectrally resolved, absolute intensities from multiple axial locations within the shock layer during a single facility run. Consequently, the computational simulation had to be able to address issues relating to emission, which required the use of a radiative transport code. In addition, two different CFD models were required to predict the shock layer flow. The first model was used to simulate the nozzle flow to determine the free stream conditions ahead of the shock layer, which was then simulated with a second, separate computational model. Flow properties predicted by the shock layer model were then used to calculate the radiative transport.

The two flow models that were used for the simulation were developed by Gökçen.[67,68] Both models use an axisymmetric formulation, which is appropriate for the conical nozzle flow and the shock layer flow over a flat-faced cylinder. Twelve chemical species: $N_2$, $O_2$, NO, N, O, $N_2^+$, $O_2^+$, $NO^+$, $N^+$, $O^+$, $e^-$, and Ar; are modeled for these flows, and three temperatures: translational, rotational, and vibrational; are used to represent the thermal state of the gas mixture. The reactions and rate coefficients that are used in the model are derived from the multi-temperature model of Park and Lee.[51] Turbulence is not included in either flow model; the flow is assumed to be laminar throughout the facility. Further details of the computational models can be found in Refs. 67 and 68, and more information about the nozzle and shock layer computations can be found in Refs. 47 and 48.

To calculate the emissive flux for the shock layer flow, the NEQAIR[69] radiative transport model was used. Inputs to the model, which include species concentrations and temperatures, were obtained from the flow solution by interpolating between calculated quantities at the known measurement locations. For all of the calculations, the emitting level populations were assumed to follow Boltzmann distributions, albeit with potentially differing values of rotational and vibrational temperatures. The electronic temperature was assumed to equal the vibrational temperature.

**Starting Conditions for the Calculations** The most important inputs to the CFD model are the starting conditions, and, as discussed above in the introductory section, the flow enthalpy and its spatial distribution are not known in the free stream or at the entrance to the nozzle. Therefore, some means of estimating the starting conditions based on facility measurements was required for the nozzle and shock layer simulations. For this investigation, measurements of stagnation point heat flux and shock layer pitot pressure were used to estimate the total stream enthalpy based on an empirical correlation of the form presented in Eq. (6). At the time of this work, the argon mass flow rate had not been recently measured, so it was assumed to be equal to 5 % of the total mass flow for the high pressure case. Using the estimates of flow enthalpy and argon mass flow along with the facility measurement of the arc heater pressure, the nozzle flow could be calculated. Based on the low level ($\approx$ 3 ppm)measured in the stream of the 60 MW arcjet facility,[9] copper was not included in the simulations of the AHF arcjet nozzle and shock layer.

Upon exiting the nozzle, the flow regions that are within the local Mach angle near the periphery expand into the test box at a rate that is different from that in the nozzle, unless the nozzle exit static pressure matches the ambient pressure. Owing to this further expansion, the calculated flow property values at the exit of the nozzle could not be used directly as the inflow conditions for the shock layer simulations. This effect is well documented for perfect gas flows,[70] but the rates of expansion for the nonequilibrium arcjet flows at various operating conditions are not known. Therefore, the calculations were continued in the axial direction at the nozzle expansion rate until the calculated dynamic pressure matched the value derived from the shock layer pitot pressure measurement using Eq. (1). Although this procedure does not exactly reproduce the fluid dynamics of the full free stream, it produced acceptable inflow conditions for the shock layer simulations without requiring a complete simulation of the flow in the test box.

It should be noted that the enthalpy value that was ultimately used in the simulations was greater than the value derived from the stagnation point heat flux and pressure measurements for both the high and low pressure test cases. After performing initial comparisons between the calculated and measured emission spectra, the enthalpy was increased for both test cases to bring the calculated spectra into closer agreement

with the measurements. The total increase for the high pressure case was limited arbitrarily to 10 %, although it could have been increased further, as will be seen below. Adjusting the total flow enthalpy estimate to a higher value is justified if the calorimeter surface has a low catalycity and the recombining atom flux is significant, because correlations such as Eq. (6) apply to fully catalytic surfaces. While the catalycity of the particular calorimeter used for these measurements is not precisely known, the surface of the constantan foil was known to have a ceramic oxide coating, so the gauge was considerably less than fully catalytic. Given the uncertainty in the total flow enthalpy, the poor agreement found in the initial comparisons between calculated and measured spectra could not be attributed to the flow model. This clearly illustrates the importance of quantifying the stream enthalpy, since using the experimental measurements to guide the adjustment of the input conditions compromises any assessment of the flow model.

### 4.3 High Pressure Case

**Calculated Shock-Layer Properties -** Using the inflow conditions and two-model computational approach the flow properties were calculated for the shock layer at the high pressure case conditions. Axial profiles of the flow properties along the central streamline where the measurements were made are shown in Fig. 11 and 12. The axial distributions of pressure and temperature are shown in Fig. 11 as a function of nondimensionalized distance from the test article surface. Note that the nozzle solution predicts that the flow is vibrationally frozen ahead of the shock, but the rotational energy is predicted to be in equilibrium with translation. The rotational and translational temperatures rise significantly near the shock and decrease as the blunt-body surface is approached. A lesser increase is exhibited by the vibrational temperature, and all three temperatures are seen to converge to a value that is very close to the equilibrium temperature for these conditions at about 0.1 R upstream of the surface. Thus, the calculations suggest that there is a region of thermal equilibrium within the shock layer at the high pressure conditions.

Axial profiles of species mass fractions are shown in Fig. 12, also as a function of the normalized distance upstream of the test article surface. Outside of the surface boundary layer, at the point where the temperature values converge, the species mass fractions are quite close to their equilibrium values, which are indicated on the right-most vertical axis. According to the simulation, the flow is also very nearly in chemical equilibrium at these test conditions.

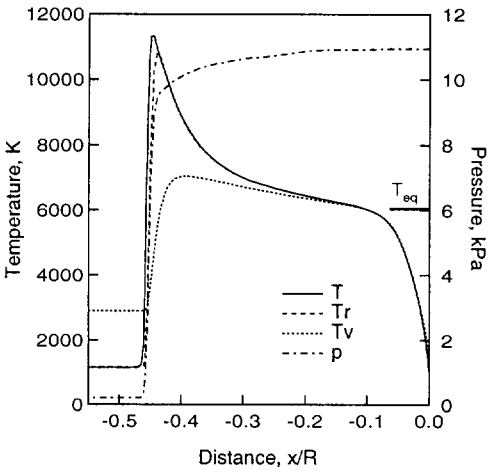


Fig. 11. Temperature and pressure profiles within the shock layer for the high pressure case.

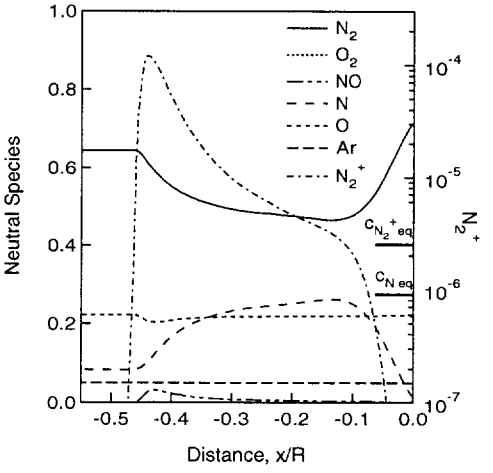


Fig. 12. Species mass fraction profiles within the shock layer for the high pressure case.

In the description of the experimental effort above, the use of $N_2^+$ spectral features to determine vibrational and rotational temperature values within the shock layer was noted. For an isolated rovibrational transition, the measured intensity for thermal equilibrium conditions can be expressed as

$$I_\lambda = \frac{K_\lambda n L}{Q} e^{-E_u/kT} \quad , \tag{7}$$

where $I_\lambda$ is the spectral intensity, $K_\lambda$ represents the line shape function and the transition strength, $n$ is the species density, $Q$ is the partition function, $L$ is the line-of-sight path length, and $E_u$ is the total upper state energy. This expression shows that the intensity has a linear dependence on the emitting species density and an exponential dependence on temperature. From the computed axial property profiles of Figs. 11 and 12, it is apparent that all temperatures and the $N_2^+$ concentration are higher near the shock front. Consequently, the measured $N_2^+$ emission could

easily be dominated by contributions from emission at the shock front, where nonequilibrium effects are more likely to be present. Temperatures are derived from intensities with the implicit assumption that the rotational and/or vibrational level populations are each thermally equilibrated. If the measured intensity is dominated by emission from nonequilibrium regions, then this assumption is untenable.

The prediction of significantly higher temperatures and $N_2^+$ concentrations near the shock front led to a further analysis of the flow property distributions along the emission measurement sight lines. Recall that one of the objectives was to use temperature measurement comparisons to determine whether or not the flow reached thermochemical equilibrium. This requires that the temperature values derived from the spectral analysis actually represent the central, core-flow region, rather than the shock front. To assess this potential problem in interpreting the spectral data, computed flow property profiles along the spanwise flow direction were extracted from the shock layer solution at selected axial measurement locations.

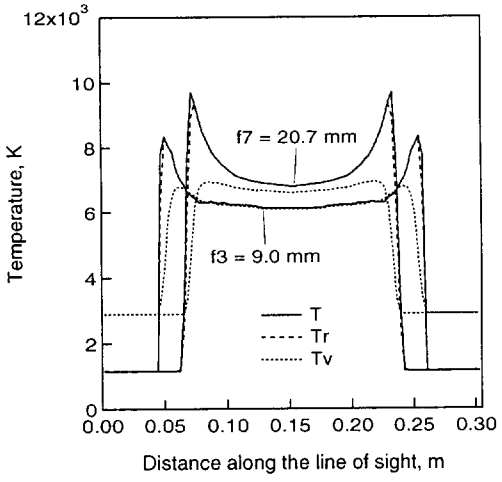


Fig. 13. Temperature variation along the line-of-sight for the high pressure case.

Profiles of rotational and vibrational temperatures along the line-of-sight direction, which is normal to the flow axis, are shown in Fig. 13 for two of the measurement positions. The axial location of the sightlines is given on the figure in terms of the distance from the surface of the test article. Again, this will make it difficult to draw conclusions about the state of the flow from temperatures derived from the emission spectra.

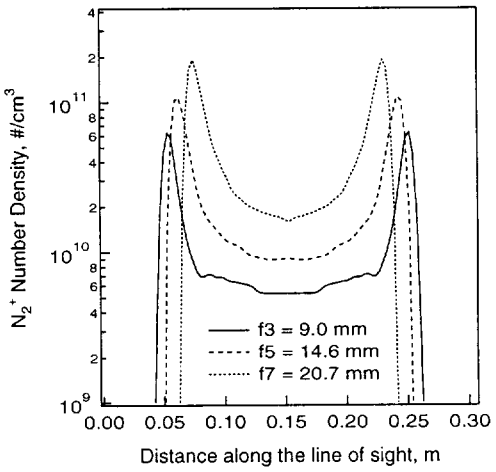


Fig. 14. $N_2^+$ number density along the line-of-sight for the high pressure case.

Computed $N_2^+$ number densities are shown in Fig. 14 as a function of distance along the line-of-sight at three different axial measurement locations, two of which correspond to the locations of the temperature profiles in the previous figure. As with temperatures, there is a significant increase in $N_2^+$ number density near the shock front. For the two flow properties that govern emission from $N_2^+$, the shapes of the spanwise profiles are predicted to be far from the idealized top hat distribution that is assumed to exist in the spectral analysis.

**Comparisons With Measurements -** Despite the indication that strong spatial gradients would compromise the derivation of flow properties from the measured intensities, values of line-of-sight integrated rotational temperature, vibrational temperature, and number density values were extracted from the spectral data. To make a meaningful comparison, the calculated flow field emission was averaged in the same manner as the measured intensity. The approach used to derive these values from the flow property and emission calculations is described at length in Ref. 47.

Comparisons of the measured and calculated line-of-sight (LOS) averaged temperatures are shown in Fig. 15. Measured and calculated vibrational and rotational temperatures are shown as a function of the normalized distance from the surface of the test article. Despite the predicted strength of the shock-front region emission, the computed, LOS-averaged temperatures still appear to nearly converge near the test article surface. Compared to the measured temperature values, the computed LOS averaged values appear to approach convergence faster and to a greater degree. Although the overall trends appear to be consistent between the measured and calculated values, the two sets of LOS-averaged temperatures do not agree. In view of this disparity and because the measured temperature values do not converge, the existence of an

equilibrated flow region could not be ascertained from the comparison.

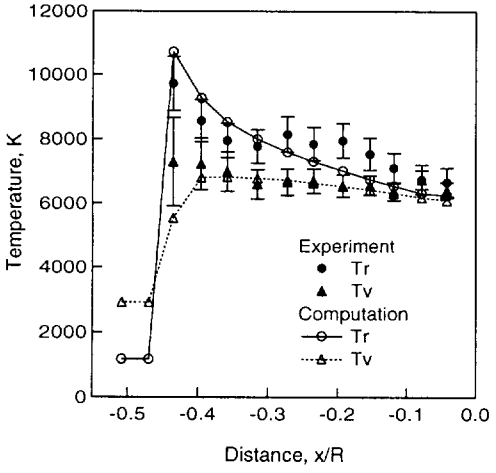


Fig. 15. Predicted and measured line-of-sight averaged temperatures for the high pressure case.

By assuming that the vibrational temperature determined from the spectral analysis of the measured intensities represented the electronic temperature, values of LOS-integrated $N_2+$ number density could be determined. As was done for temperature, an approach for deriving a comparable quantity from the calculated flow properties was also developed.[71] Measured and calculated values of the LOS-integrated $N_2^+$ number density are compared in Fig. 16. Some of the disagreement between the two sets of number densities can be attributed to differences in spatial gradients along the line-of-sight. Until the spatial gradient effects are investigated experimentally, it is not possible to determine whether the difference seen in the comparison nearer the test-article surface is caused by spatial averaging from the optical system or by inaccurate modeling of the $N_2^+$ dissociative recombination processes.

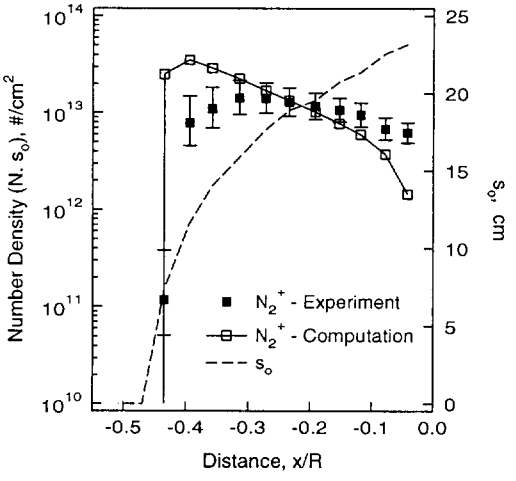


Fig. 16. Predicted and measured LOS-integrated $N_2^+$ number density for the high pressure case.

Based on the comparisons between the measured and calculated flow properties above, it was not possible to determine whether an equilibrated flow region exists within the shock layer for these conditions. Such a determination clearly requires an approach that resolves the spatial intensity gradients to extract information from the relevant flow region in the core of the shock layer. Once that is done, then the impact of other assumptions can be examined, and the processes that lead to equilibration can be investigated. Although the question of an equilibrated region was not conclusively resolved, it was still possible to address whether or not emission-based measurements could be used to determine the thermochemical state of the flow.

For these investigations, the experimental instrumentation did not actually measure flow properties. Instead, flow property information was derived from an analysis of measured emissive intensities. To address the issue of using emission to evaluate the flow enthalpy and to understand how the experimental approach and the computational modeling might be improved, comparisons were made between calculated and measured spectral data at selected measurement locations.

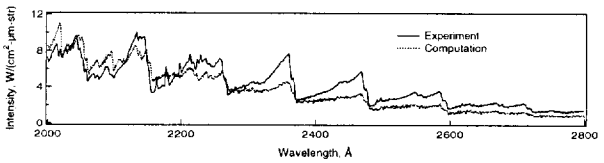


Fig. 17. Measured and computed emission spectra for the 240 nm grating position, 20.7 mm upstream of test article.

Comparisons between the measured and calculated emission spectra are presented below at several grating positions for a single axial location, 20.7 mm upstream of the test article. For the 240 nm grating position, the comparison is shown in Fig. 17. At this spectral location, the emission is mainly from NO $\gamma$ and $\delta$ with probable contributions from the $\beta$ and $\epsilon$ systems. Owing to the overlap of the emission from the different electronic states of NO, extracting temperature information from this spectral region is not feasible. Except for emission below 2100 Å, the calculated intensity is less than the measured value.

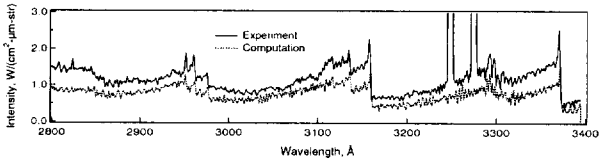


Fig. 18. Measured and computed emission spectra for the 310 nm grating position, 20.7 mm upstream of test article.

A similar comparison of measured and calculated emission spectra at the 310 nm grating position is shown in Fig. 18. The off-scale spectral features are Cu atom

transitions. Copper is present in the stream because of electrode erosion, and it is not included in the computational model. Emission from molecular species in this spectral region is mainly from NO at shorter wavelengths, and $N_2$ (2+) and $N_2^+$ (1-) systems at the longer wavelengths. The strongest emission peaks aside from those due to Cu emission are from $N_2$ (2+). Agreement between the calculations and the measurements is reasonable good in shape, but the overall signal level from the computational spectra appears to be low. Recall that the calculated signal levels are exponentially dependent on the electronic temperature. If the calculated electronic temperature, which is nearly 6000 K at this measurement location, was increased by 200 K, the $N_2$ (2+) emission would nearly double.

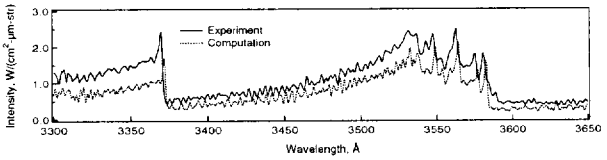


Fig. 19. Measured and computed emission spectra for the 345 nm grating position, 20.7 mm upstream of test article.

For the 345 nm grating position comparison, which is shown in Fig. 19, the emission is mainly from molecular species: $N_2$ (2+), $N_2^+$ (1-), and CN violet. The CN in the flow comes from dissociation of $CO_2$ that is present naturally in air and the subsequent recombination of C and N. Although it is truly a minor species, the transition strength is large and it is a significant emitter, as seen in the region near 3550 Å where several of the measured peaks are not reproduced by the calculated spectra. Cyanogen was not included as a species in the computational model. Some of the under-prediction of the intensity magnitude can therefore be attributed to the exclusion of CN from the calculation. For the $N_2^+$ (1-) emission, a 200 K increase in the electronic temperature would produce a roughly 20 % increase in the calculated intensity.

Comparisons were also done for the 415 and 450 nm grating positions, which contained mostly molecular emission, and the agreement between the measured and calculated intensity magnitude is better, although the calculated levels are still low. The improved agreement for these grating positions is likely due to their use to guide the adjustment of the estimated stream enthalpy.

The shock layer flow also contained significant O and N atom populations, and atomic transition intensities were recorded at two near-IR grating positions. The measured and computed emission from O atomic transitions at 777 nm and 845 nm are compared in Figs. 20a and 20b. As with the grating positions at the shorter wavelengths, the calculated intensity is generally lower than the measured intensity. At a calculated electronic temperature of 6000 K, an increase of 200 K would nearly double the atomic emission.

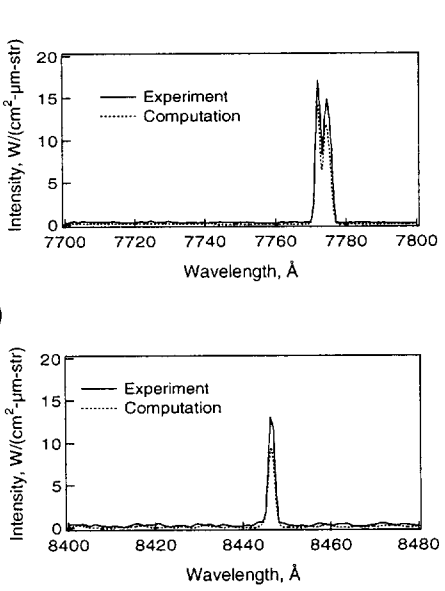


Fig. 20. Measured and computed emission from the a) 777 nm O transitions and from the b) 845 nm O transition, 20.7 mm upstream of test article.

Similar comparisons were done for N atom transitions and these are shown in Fig. 21a and 21b for the 744 and 868 nm N transitions, respectively. The calculated emission for the N atom transitions is also low and because the emitting states are at energy levels that are similar to those of the O atom transitions above, an increase in the electronic temperature of 200 K would also result in a near doubling of the intensity for these transitions.

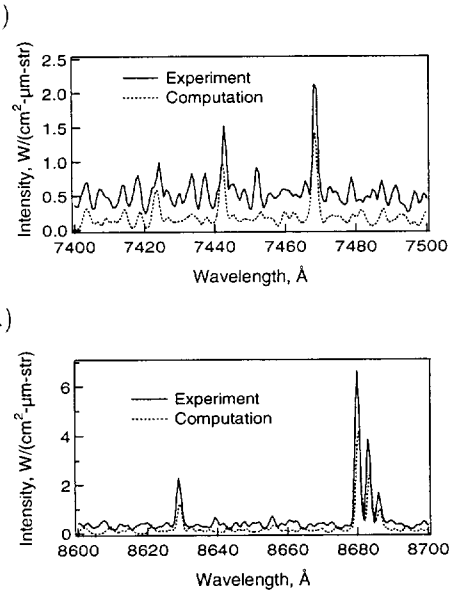


Fig. 21. Measured and computed emission from the a) 745 nm N transition and from the b) 868 nm N transition, 20.7 mm upstream of test article.

Based on these spectral comparisons, it appears that the calculated emission was generally low for all grating positions at this measurement location. Since the emission is exponentially dependent on temperature, it is likely that the calculated flow temperature was low. Again, the most likely culprit for this discrepancy is the enthalpy, which was probably not raised to the proper level. Clearly, the exponential dependence of the emission on temperature makes emission a very sensitive indicator of flow temperature. From an instrumentation development perspective, this implies that emission-based measurements have both the signal magnitude and sensitivity that are necessary to measure temperature, and ultimately flow enthalpy (with the assupmtion that velocity is negligible within the shock layer), reasonably well. However, the spatial gradients must be resolved for this approach to succeed.

A different perspective on the LOS-integrated $N_2^+$ number density distribution that was presented in Fig. 16 can be obtained by comparing measured and calculated $N_2^+$ (1-) emission for a single grating position at each of the measurement locations on the central stagnation streamline. This comparison is shown for the 426 nm grating position in Fig. 22a for the back position of the test article, and in Fig. 22b for the forward position. There is an easily distinguishable difference between the evolution of the measured signal and the calculated signal. By performing a direct comparison of measured and calculated emission spectra, uncertainties introduced in the analysis that was performed to derive flow properties from measured intensities are avoided. However, possible differences between measured and calculated flow property gradients are still present and will influence the comparison. Of particular concern is the possibility of additional averaging of the measured intensities that may have been caused by the optical collection system.[65] This possibility has not been accounted for in these comparisons, so only qualitative statements can be made regarding the differences between the calculated and measured spectra.

a.)

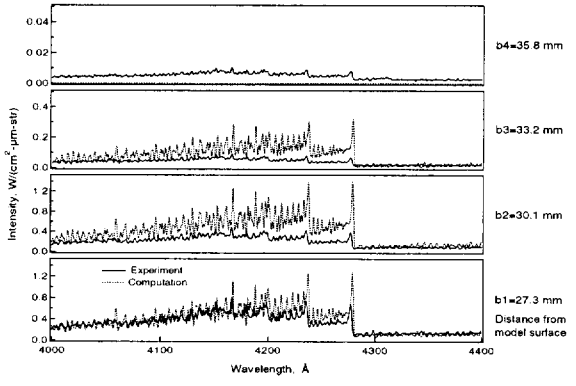


b.)

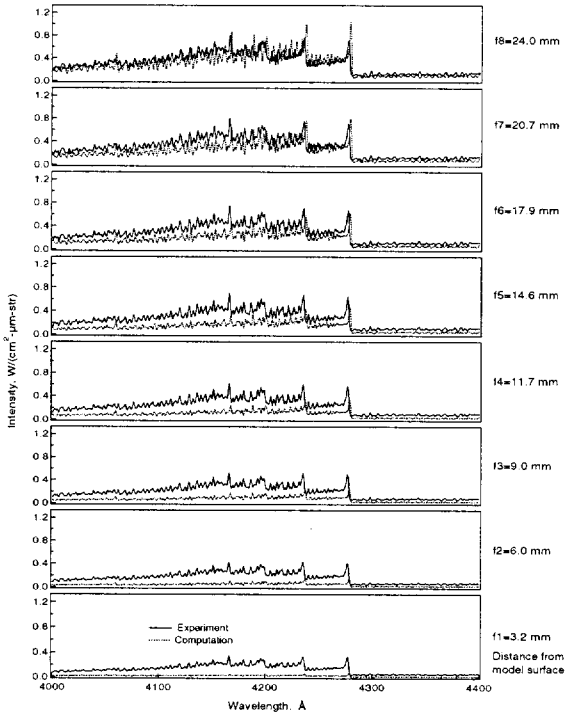


Fig. 22. $N_2^+$ emission at 420 nm grating position for all of the axial measurement locations for the high pressure case: a.) back position; b.) forward position.

In Figs. 22a and 22b, it is apparent that the measured rate of evolution and decline of the $N_2^+$ emission as the flow goes from the shock to the test article is less rapid than predicted by the calculations. Although the limitations in the spatial resolution of the optical system preclude further statements about the axial distribution of the $N_2^+$ emission, the comparison does illustrate the possibility of using emission spectra to evaluate the population dynamics of important shock layer species.

### 4.4 Low Pressure Case

**Starting Conditions -** The lower pressure case test conditions were chosen to maximize the change in shock layer pressure, which was reduced by a factor of $\approx 3$. At the lower pressure, the collision frequency in the shock layer is reduced significantly. Consequently, the flow is less likely to be in thermal or chemical equilibrium. If the degree of departure from equilibrium could be determined at these test conditions, then progress could be made in defining the test conditions that lead to equilibration within the shock layer.

As was found in the comparisons between the simulated and measured emission spectra for the high pressure case, the comparisons for the low pressure case indicated that the stream enthalpy value derived from the stagnation point heat flux and pressure measurements was probably low. Therefore, additional calculations were performed at total enthalpy values that were 14 % and 32 % higher than the estimated values.

In addition to the uncertainty in the stream enthalpy that was present for both the high and low pressure test cases, the uncertain argon mass flow rate became an issue for the simulations of the low pressure conditions. The total mass flow rate for the low pressure case was reduced by a factor of $\approx 4$, based on the reduction in pressure, while the start and shield argon mass flow remained constant. For the high pressure case, the argon mass flow was assumed to be 5 % of the total mass flow. This implied that the relative argon mass flow could be 20 % of the total mass flow for the low pressure case. At this level, the uncertainty in the argon mass flow becomes more important because of its increased participation in the reaction kinetics. For example, in three-body recombination reactions, Ar is less efficient than $N_2$ as the third body.[61] To address this additional uncertainty and attempt to bound its influence, flow simulations were performed for three different argon mass fractions: 5 %, 10 %, and 30 %.

Thus, owing to the uncertain starting conditions a total of five different simulations of the shock layer flow for the low pressure case were computed. The starting conditions and computed free stream properties for each of these simulations are summarized in Table 2. At nearly constant enthalpy, increased argon mass flow is seen to increase the temperatures and free stream velocity slightly, while increasing the dissociation fraction for nitrogen substantially. Comparing cases that have the same argon mass fraction, increasing the total enthalpy produces results that are similar to increasing argon mass fraction at constant enthalpy. This uncertainty in the starting conditions clearly create difficulties for comparisons of simulations and experimental measurements.

**Table 2.** Starting conditions and free stream properties for the low pressure test case simulations

| Parameter | Case 1 | Case 2 | Case 3 | Case 4 | Case 5 |
|---|---|---|---|---|---|
| $p_0$, atm | 1.7 | 1.7 | 1.7 | 1.7 | 1.7 |
| $h_0$,MJ/kg | 15.2 | 15.15 | 17.15 | 17.26 | 20.07 |
| $w_{Ar}$ | .05 | .30 | .05 | .30 | .10 |
| $u_\infty$, km/s | 4.12 | 4.19 | 4.29 | 4.39 | 4.53 |
| $p_\infty$, Pa | 62. | 57.5 | 58.5 | 57.1 | 57.6 |
| $T_\infty$, K | 727 | 775 | 741 | 823 | 786 |
| $T_{v\infty}$, K | 2960 | 3360 | 3100 | 3550 | 3370 |
| $w_{N_2}$ | .67 | .45 | .63 | .42 | .53 |
| $w_N$ | .06 | .09 | .10 | .12 | .16 |
| $w_O$ | .22 | .16 | .22 | .16 | .21 |

**Calculated Shock-Layer Properties -** Using the Case 3 conditions, axial profiles of temperatures and pressure for the shock layer flow were computed, and these are shown in Fig. 23 as a function of the normalized distance from the test article surface. While the rotational and translational temperatures are still higher near the shock, the increase over the levels nearer the test article is not as great as was seen for the high pressure case (see Fig. 11). At the lower shock layer pressure, the vibrational and translational-rotational temperatures do not appear to converge outside of the boundary layer of the test article. This is in contrast to the results of the simulation for the high pressure case, where the temperatures clearly converged as the model surface was approached. According to the simulation, the shock layer is not in thermal equilibrium, except within the boundary layer at these simulated conditions.

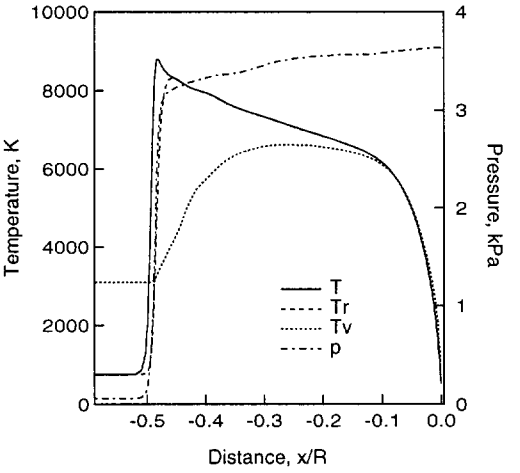


Fig. 23. Axial profiles of temperature and pressure in the shock layer.

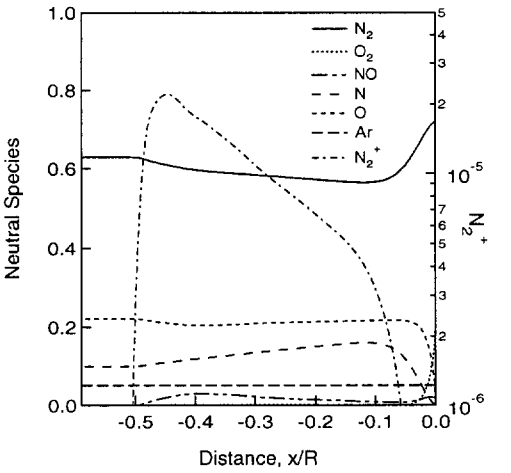


Fig. 24. Axial profiles of species populations in shock layer.

For the same starting conditions, the axial profiles of the neutral species and $N_2^+$ are plotted in Fig. 24, again as a function of the nondimensional distance from the surface. As was seen in the high pressure case, there appears to be a significant peak in the $N_2^+$ concentration near the shock front. However, for the low pressure conditions of this simulation, the mass fraction near the shock front is only $\approx 5$ times higher than the mass fraction nearer the test article surface (as opposed to $\approx 50$ times for the high pressure case, see

Fig. 12). The mass fractions of N and $N_2$ do not reach a limiting value as the surface is approached, so the simulation indicates that the shock layer is also not in chemical equilibrium.

a.)

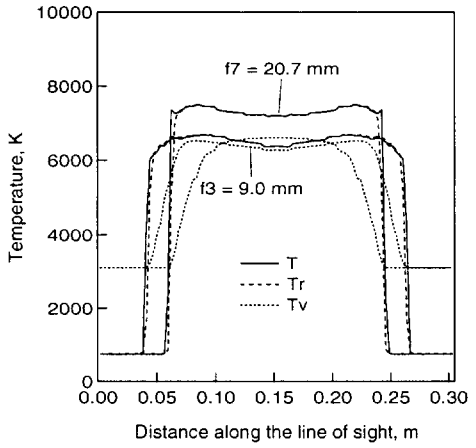


b.)

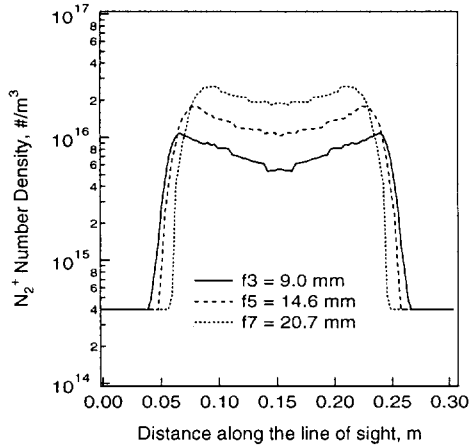


Fig. 25. Computed flow property profiles for Case 3 conditions at selected axial locations for a) temperatures and b) N2+ number density.

Although the starting enthalpy and argon mass flow values were less certain for the low pressure case, the gradients in the $N_2^+$ and temperature profiles appeared to be less severe than found for the high pressure case. To assess the spatial gradients along the optical sight lines at the measurement locations, temperature and species profiles were extracted from the shock layer solutions, and these are shown for selected axial locations in Figs. 25a and 25b, respectively. For both temperatures and $N_2^+$ number density, the computed profiles along the lines-of-sight are much closer to the idealized top-hat distributions that are required to derive temperatures that are representative of the core flow region from the spectral analysis of the measured intensities. Unfortunately, it appears that the majority of the shock layer flow is likely to be in nonequilibrium, which may violate the other major assumption of the spectral analysis. The degree of departure from equilibrium and its impact on the distributions of populations over the various energy levels is difficult to quantify.

**Comparisons With Measurements -** As with the high pressure case, rotational and vibrational temperature values were derived from an analysis of $N_2^+$ spectral features.[66] Using an intensity-weighted averaging approach,[47] temperature values that could be compared with the experimental values were extracted from the computed flow properties at the axial measurement locations for some of the different simulation cases. Comparisons between the computed and measured LOS-averaged temperatures are shown in Figs. 26 and 27, for the simulation conditions of Case 3 and Case 4, respectively. For these two cases, the enthalpy levels were in the middle of the range of simulations and were nearly in agreement. However, for Case 3 the argon mass fraction was 0.05, while for Case 4, the argon mass fraction was 0.3. In Fig. 26, for the Case 3 condition, there are significant differences in both trends and magnitudes between the computed and measured temperatures. First, for the experimental values, the rotational and vibrational temperatures do not appear to overlap, except perhaps accidentally at one or two measurement locations. Owing to low signal levels near the shock front, the measured values are highly uncertain. Consequently, the discussion of trends will be restricted to the positions nearer to the surface than $x/R$ = -0.4. For those locations, the trends in the computed and measured vibrational temperatures appear to be reasonably similar, although the measured values are generally greater in magnitude. In contrast, the measured rotational temperatures do not appear to decrease significantly from the values near the shock front, while the computed rotational temperatures clearly show evidence of relaxation going toward the test article.

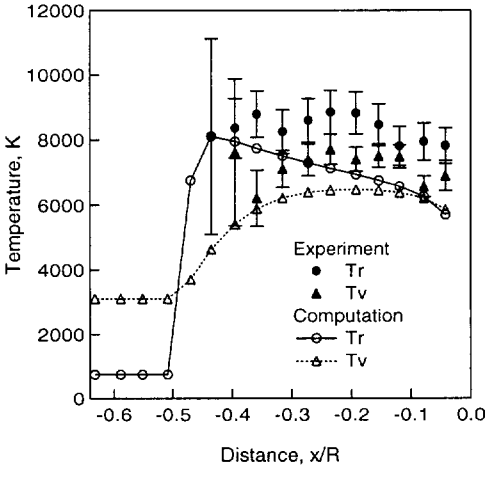


Fig. 26. Computed and measured LOS-averaged temperatures for the conditions of Case 3 ($h_0$ = 17.15 MJ/kg, $w_{Ar}$ = 0.05).

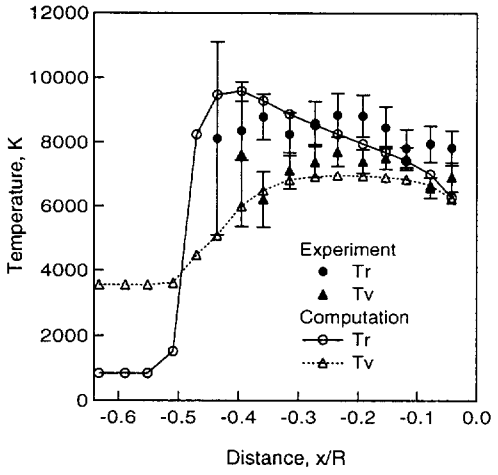


Fig. 27. Computed and measured LOS-averaged temperatures for the conditions of Case 3 ($h_0$ = 17.26 MJ/kg, $w_{Ar}$ = 0.30).

At the high argon mass flow conditions of Case 4, the comparison between measured and computed LOS-averaged vibrational temperatures shows improved agreement on the magnitude, while maintaining reasonable agreement on the shape of the distribution at locations closer than $x/R$ = -0.4. The agreement between magnitudes of the computed and measured LOS-averaged rotational temperatures also appears to be improved with the increased argon mass flow, but the difference between the distributions is unaffected. It should be noted that the influence of streamwise and spanwise spatial averaging by the optical collection system on the measured values has not been fully accounted for in these comparisons. Considering the uncertainty in the starting conditions for the simulations and the uncertainty in the unresolved spatial intensity gradients for the experiment, the general lack of agreement is not surprising.

### 4.5 Spatially Resolved Measurements

In a recent set of experiments conducted at the low pressure test conditions, Park acquired emission spectra from multiple locations along the spanwise direction as a single axial position within the shock layer.[71] Several separate emission measurements were recorded simultaneously by the spectrograph and CCD system, and a series of adjusted collection mirror positions were used to cover the radial extent of the shock layer during a single facility run. An Abel-inversion was then used to obtain spatially resolved emission spectra from the LOS-integrated intensities. Finally, temperatures were derived from the Abel-inverted spectra using an analytical method that involved ratios of $N_2^+$ spectral features and ratios of O atom transitions. A fuller description of the experiment and the analytical approach is given in Ref. 71.

Radial distributions of the rotational, vibrational, and electronic temperatures that were derived from the spectrally resolved emission are shown in Fig. 28. The rotational and vibrational temperatures were determined using the same analytical approach that was used to derive temperatures from the line-of-sight intensities, above. As explained in Ref. 71, two sets of atomic oxygen transitions were used to calculate electronic temperature. Thus, the two electronic temperature distributions are labeled by the shorter wavelength transition used in each intensity ratio. Owing to an unresolved background contribution at the 8446.5 Å transition, electronic temperatures derived from the intensity of that transition are systematically low. Electronic temperature values obtained using the 7773.4 Å transition are believed to be valid.

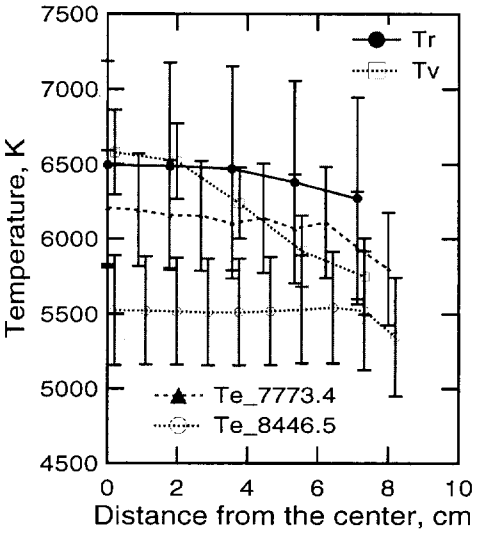


Fig. 28. Radial temperature profiles in the shock layer at 12.7 mm upstream from the test article. Labels for $T_e$ indicate the shorter wavelength O transition of the pair.

The most striking aspect of the radial temperature distribution shown in Fig. 28 is that the rotational, vibrational, and electronic (for the 7773.4 Å pair) temperatures appear to overlap within their respective uncertainties. This may indicate a region of thermal equilibrium within the shock layer for the low pressure conditions, contrary to the prediction of the computational simulation. The shapes of the rotational and vibrational temperature distributions are reasonably similar to the shapes of the predicted radial temperature distributions at 9 mm that were shown in Fig. 25a. (Note that the 9 mm axial location of the predictions was closest to the 12. 7 mm axial position of the measurements.) The temperatures and the emission spectra from these experiments are still being analyzed

### 4.6 Lessons Learned

First, and foremost, the futility of attempting to perform detailed computational simulations of arcjet flows without adequate specification of the starting conditions, mainly the enthalpy, has to be recognized. Un-

til this issue is resolved, the knowledge gained from performing combined experimental and computational investigations will be marginal. The limitations of using stagnation point heat flux and impact pressure measurements to estimate enthalpy were clearly illustrated. Although the unspecified argon mass flow rate did affect the low pressure test simulations, this inflow parameter is a more tractable problem. Most large-scale arcjet facilities routinely measure the mass flows of the test gases, and the Ames Research Center Arcjet Facilities have recently been equipped with improved mass flow sensors and control capability.

The second important lesson to derive from this exercise concerns the use of diagnostic techniques and approaches that do not resolve spatial gradients. Attempts to compare simulation predictions with measurements of spatially integrated quantities can lead to misleading conclusions. For the low pressure case, the LOS-averaged temperature distributions suggest that the flow is not in thermal equilibrium, while the radial distribution of spatially resolved temperatures suggest the opposite. An investment of additional effort into acquiring emission spectra in the radial direction to obtain Abel-inverted intensities has a far better (and more certain) return than deriving the comparable integrated flow properties from a number of computational simulations. It was fortunate that the comparisons between the predicted and measured LOS-averaged temperatures agreed so poorly for the high and low pressure cases; otherwise, the temptation to "correct" the measurements using the computational results may have proven overwhelming.

Finally, the possibility that a portion of the shock layer is in thermal equilibrium at the low pressure test conditions contradicts the computational predictions, which showed extensive thermal nonequilibrium for all of the different low pressure simulations. Further knowledge of the chemical state of the shock layer, which is currently under investigation, and verification of equilibrium would provide much-needed insight into the nature of the shock layer flow.

## 5. Summary and Recommendations

The question of the state of CFD simulations of arcjet flows is still dominated by the lack of knowledge about the flow enthalpy. Any other consideration is secondary. Conventional methods for estimating the flow enthalpy, including energy balance, sonic flow, and stagnation point heat transfer, all provide insufficient specification of the flow enthalpy for simulation purposes. If adequate resources and dedicated effort are brought to bear on this problem, then eventually it will be resolved and arcjet facility simulations will become much more meaningful. New LIF-based approaches to enthalpy measurement may improve this situation.[58,59]

Although this premise cannot be rigorously tested until enthalpy can be more accurately determined, it appears that current nonequilibrium, hypersonic-flow computational models are able to provide reasonable simulations of arcjet flows. This observation is based on a qualitative assessment of the comparisons between the shock layer measurements and predictions, combined with the fact that no obvious shortcomings in the flow models could be identified. Despite having to estimate the enthalpy and use two CFD models and a radiative transport code to predict intensity, the comparisons with measured values were generally favorable; particularly for the high pressure case.

While the flow enthalpy must be accurately specified to enable detailed comparisons between simulations and measurements for a single arcjet facility test condition, measurements and simulations of relative trends in arcjet characteristics are not similarly constrained. Measurements and simulations of the response of sensitive flow properties to changes in arcjet control parameters during a single facility test can add substantial information to the knowledge base at the present time. The approach to this involves using diagnostic instrumentation to monitor stream parameters, when conditions have stabilized, as a single control variable, such as the arc current, is changed. (Examples of this type of experiment will be discussed extensively in the second lecture.) Making the best possible estimate of the total enthalpy for a single condition, a computational simulation is essentially calibrated at that condition. Subsequent conditions are then simulated using further estimates of the total enthalpy, without changing the other parameters of the model. Comparisons are then made between the measured and predicted trends. This approach avoids the larger uncertainties that pertain to measurements of absolute quantities.

Some of the more obvious parametric studies to perform include: 1.) varying pressure to assess impact on chemistry; 2.) varying the arc current, which varies the initial ionization level; and 3.) varying the test gas composition to investigate relative third-body efficiencies in $N_2$ recombination.

To establish the validity of diagnostic approaches, comparisons between measurements made using multiple independent instruments would be extremely useful. This observation is particularly relevant to developing new approaches for determining the flow enthalpy, which is the most important parameter to measure accurately, and which ultimately determines how useful and relevant arcjet testing will become.

At present, it is too early to propose code validation experiments for large-scale arcjet facility flows. However, it is appropriate to begin thinking about how to develop diagnostics and strategies that may eventually enable code validation experiments in these facilities. The most important advantage that arcjets have over

impulse facilities is the test duration. Steady state flow conditions and material response can be achieved and documented. The long test time allows for multiple property measurements that can be temporally averaged. Because there is no diaphragm, these measurements can be repeated in multiple runs to assess facility repeatability with a rapid turn-around time between tests.

Test guidelines for validation experiments have been suggested by Mehta in his descriptions of methods for producing credible computational simulations.[72] Performing validation experiments in arcjet facilities will require considerable maturation of currently available diagnostic techniques to ensure adequate specification of inflow conditions for either nozzle or shock-layer flow simulations. In addition to improving the accuracy of inflow condition measurements, sufficient spatial coverage must be attained to allow approximate integration of the flow properties for comparison with other measurements of mass flow, energy balance, etc. Without this type of internal accuracy check of the experimental results, confidence in the measurements would not be sufficient to motivate extensive computational simulations or efforts to improve physical models.

## 6. Acknowledgements

Many colleagues have contributed to the lecture material contained herein, but special thanks are due to Tahir Gökçen and Chung Park of Thermosciences Institute (Eloret), Mark Newfield of Ames Research Center, and James Donohue of UTRC for their excellent work on the combined computational and experimental investigation of arcjet flows. John Balboni of the Thermophysics Facilities Branch at Ames Research Center provided many useful references on arcjet facilities in general. The entire staff of the Aerodynamic Heating Facility Arcjet provided vital test support and Frank Hui's efforts as test engineer deserve special recognition. Many of the thoughts expressed in this document resulted from conversations with colleagues about arcjet flows and testing. While any erroneous statements are attributable solely to the author, the contributions of Chul Park, Joan Pallix, Raj Venkatapathy, Ellis Whiting, and Jochen Marschall of Thermosciences Institute (Eloret) to what has been written are greatly appreciated. Similar conversations with Paul Kolodziej, Jeff Bull, Dave Stewart, Joe Hartman, Joe Olejniczak, Dave Olynick, Stephanie Langhoff, Surrendra Sharma, and George Raiche of NASA Ames Research Center have also proven to be very helpful in writing this document.

## 7. References

1. P. R. Dennis, C. R. Smith, D. W. Gates, and J. B. Bond, Editors, Plasma Jet Technology, NASA Report SP-5033, National Aeronautics and Space Administration, Washington, DC, October, 1965.
2. D. A. Gerdeman and N. L. Hecht, Arc Plasma Technology in Materials Science, Springer-Verlag, New York, 1972.
3. H. A. Stine, "The Hyperthermal Supersonic Aerodynamic Tunnel", presented at International Symposium on High Temperature Technology, Asilomar, CA, 8-11 September, 1963.
4. C. E. Shepard, V. R. Watson, and H. A. Stine, "Evaluation of a Constricted-Arc Supersonic Jet", NASA Technical Note TN D-2066, 1964.
5. C. E. Shepard, "Advanced High-Power Arc Heaters for Simulating Entries into the Atmospheres of the Outer Planets", AIAA Paper No. 71-263, AIAA $6^{th}$ Aerodynamic Testing Conference", (1971).
6. V. R. Watson and E. B. Pegot, "Numerical Calculations for the Characteristics of a Gas Flowing Axially Through a Constricted Arc", NASA TN D-4024, 1967.
7. C. Park, J. H. Lundell, M. J. Green, W. Winovich, and M. A. Covington, "Ablation of Carbonaceous Materials in a Hydrogen-Helium Arcjet Flow", *AIAA J.*, **22**, pp. 1491-1498, October, (1984).
8. J. R. Jedlicka, "The Shape of a Magnetically Rotated Electric Arc Column in an Annular Gap", NASA Technical Note TN D-2155, 1964.
9. W. Winovich and W. C. A. Carlson, "The 60-MW Shuttle Interaction Heating Facility", presented at the $25^{th}$ International Instrument Symposium, Anaheim, ISBN 87664-434-5, May, (1979).
10. C. Park, "Laboratory Simulation of Aerothermodynamic Phenomena: A Review", AIAA Paper No. 92-4025, AIAA $17^{th}$ Aerospace Ground Testing Conference, Nashville, TN, (1992).
11. R. K. Smith, D. A. Wagner, and J. W. Cunningham, " A Survey of Current and Future Plasma Arc-Heated Test Facilities for Aerospace and Commercial Applications", AIAA Paper No. 98-0146, 36th Aerospace Sciences Meeting, Reno, NV, 12-15 January, 1998.
12. A. Balter-Peterson, F. Nichols, B. Mifsud, and W. Love, "Arc Jet Testing in NASA Ames Research Center Thermophysics Facilities", AIAA Paper No. 92-5041, $^{th}$ *AIAA International Aerospace Planes Conference*, (American Institute of Aeronautics and Astronautics, New York, 1992).
13. C. Scott, "Survey of Measurements of Flow Properties in Arcjets",*Journal of Thermophysics and Heat Transfer*,**7**, pp. 9-24, (1993).
14. H. W. Leipmann and A. Roshko, Elements of Gasdynamics, John Wiley & Sons, New York, 149, (1957).
15. D. A. Gerdeman and N. L. Hecht, Arc Plasma Technology in Materials Science, Springer-Verlag, New York, pp. 94-97, (1972).
16. J. Balboni, Thermophysics Facilities Branch, NASA

Ames Research Center, private communication, (1997).
17. W. Winovich, "On the Equilibrium Sonic-Flow Method for Evaluating Electric-Arc Air-Heater Performance", NASA TN D-2132, NASA, Washington, DC, 1964.
18. J. A. Fay and F. R. Riddell, "Theory of Stagnation Point Heat Transfer in Dissociated Air", *J. Aeronautical Sciences* , **25**, pp. 73-85, (1958).
19. R. Goulard, "Catalytic Recombination Rates in Hypersonic Stagnation Heat Transfer",*Jet Propulsion*, **28**, pp. 733-745, (1958).
20. R. B. Pope, " Stagnation-Point Convective Heat Transfer in Frozen Boundary Layers", *AIAA Journal*, **6**, pp. 619-626, (1968).
21. E. V. Zoby, "Empirical Stagnation-Point Heat-Transfer Relation in Several Gas Mixtures at High Enthalpy Levels", NASA TN D-4799, NASA, Washington, DC, (1968).
22. R. B. Pope, "Measurements of Enthalpy in Low-Density Arc-Heated Flows", *AIAA J.*, **6**, pp. 103-110, (1968).
23. E. L. Winkler and R. E. Sheldahl, "Influence of Calorimeter Surface Treatment on Heat-Transfer Measurements in Arc-Heated Test Streams", *AIAA J.*, **4**, pp. 717-716, (1966).
24. L. A. Anderson, "Effect of Surface Catalytic Activity on Stagnation Heat-Transfer Rates", *AIAA Journal*, **11**, pp. 649-656, (1973).
25. C. Park, "Evaluation of Real-Gas Phenomena in High-Enthalpy Aerothermal Test Facilities: A Review", *J. Thermophysics and Heat Transfer*, **11**, pp. 330-338, (1997).
26. G. Candler, "Chemistry of External Flows", in Aerothermochemistry for Hypersonic Technology, VKI Lecture Series 1995-04, von Karman Institute for Fluid Dynamics, Rhode Saint Genese, (1995).
27. D. L. Cauchon, "Project Fire Flight I Radiative Heating Experiment", NASA TM X-1222, (1966).
28. D. L. Cauchon, "Radiative Heating Results from the Fire II Flight Experiment at a Reentry Velocity of 11.4 Km/s", NASA TM X-1402, (1967).
29. D. B. Lee and W. D. Goodrich, "The Aerothermodynamic Environment of the Apollo Command Module During Suborbital Entry", NASA TN D-6792, (1972).
30. D. Olynick, Y.-K. Chen, and M. E. Tauber, "Forebody TPS Sizing with Radiation and Ablation for the Stardust Sample Return Capsule", AIAA Paper No. 97-2474, June, (1997).
31. P. A. Gnoffo, "Application of the Program LAURA to Three-Dimensional AOTV Flowfields", AIAA Paper NO. 86-0565, January, (1986).
32. P. A. Gnoffo, R. N. Gupta, and J. L. Shinn, "Conservation Equations and Physical Models for Hypersonic Air Flows in Thermal and Chemical Nonequilibrium", NASA TP-2867, February, (1989).
33. C. Park, "Assessment of a Two-Temperature Kinetic Model for Ionizing Air", AIAA Paper No. 87-1574, June, (1987).
34. M. G. Dunn and S.-W. Kang, "Theoretical and Experimental Studies of Reentry Plasmas", NASA CR-2232, (1973).
35. J.-H. Lee, "Basic Governing Equations for the Flight Regimes of Aeroassisted Orbital Transfer Vehicles", in Thermal Design of Aeroassisted Orbital Transfer Vehicles, H. F. Nelson, ed., Volume 96 of Progress in Astronautics and Aeronautics, AIAA, New York, pp. 3-53, (1985).
36. G. V. Candler and R. W. MacCormack, "The Computation of Hyperonsic Ionized Flows in Chemical and Thermal Nonequilibrium", AIAA Paper No. 88-0511, Jan., (1988).
37. K. G. Brown, "Chemical and Thermal Nonequilibrium Heat Transfer Analysis for Hypervelocity, Low Reynolds Number Flows", AIAA Paper No. 85-1033, June, (1985).
38. C. Park, Nonequilibrium Hypersonic Aerothermodynamics, John Wiley & Sons, New York, (1990).
39. R. J. Gessman, C. O. Laux, and C. H. Krueger, "Experimental Study of Kinetic Mechanisms of Recombining Atmospheric Pressure Air Plasmas", AIAA Paper No. 97-2364, AIAA $28^{th}$ Plasmadynamics and Lasers Conference, Atlanta, GA, June, (1997).
40. P. Durgapal, "Electrode Phenomena in High Current, High Pressure Arc Heaters", *J. Thermophysics and Heat Transfer*, **7**, pp. 412-417, (1993).
41. P. Durgapal, "Strongly Coupled Radiative Transfer and Joule Heating in an Arc Heater Cathode", *J. Thermophysics and Heat Transfer*, **8**, pp. 730-736, (1994).
42. S. F. Shaeffer, "SWIRLARC: A Model for Swirling, Turbulent, Radiative Arc Heater Flowfields", AIAA Paper No. 78-68, (1978).
43. W. N. MacDermott and E. J. Felderman, "Arc Heater Scaling Parameters Predicted with the SWIRLARC Code", AIAA Paper No. 93-2797, AIAA $28^{th}$ Thermophysics Conference, July, (1993).
44. K. H. Kim, O. H. Rho, and C. Park, "Assessment of ARCFLO Code and Computations of Arc Heater Using Navier-Stokes Code", AIAA Paper No. 99-0736, AIAA $37^{th}$ Aerospace Sciences Meeting, Jan., (1999).
45. T. Sakai, K. Sawada, and M. Mitsuda, "Application of Planck-Rosseland-Gray Model for High Enthalpy Arc Heaters", AIAA Paper No. 98-2838, (1998).
46. D. S. Babikian, N. K. J. M. Gopaul, C. Park, "Measurement and Analysis of Nitric Oxide Radiation in and Arcjet Flow", *J. Thermophysics and Heat Transfer*, **8**, pp. 737-743, (1994).
47. T. Gökçen, C. S. Park, M. E. Newfield, and D. G. Fletcher,"Computational Simulation of Emission Spectra from Shock Layer Flows in an Arc-Jet Facility", *J. Thermophysics and Heat Transfer* **12**, 180-

189, (1998); also AIAA Paper No. 97-0135.

48. T. Gökçen, C. S. Park, and M. E. Newfield, "Computational Analysis of Shock Layer Emission Measurements in an Arc-jet Facility", AIAA Paper No. 98-0891, AIAA $36^{th}$ Aerospace Sciences Meeting, Jan., (1998).
49. M. P. Loomis, S. Polsky, E. Venkatapathy, D. K. Prabhu, and F. C. L. Hui, "Arcjet Semi-Elliptic Nozzle Simulations and Validation in Support of X-33 TPS Testing", AIAA Paper No. 98-0864, AIAA $36^{th}$ Aerospace Sciences Meeting, Jan., (1998).
50. D. A. Stewart, Y.-K. Chen, D. J. Bamford, and A. B. Romanovsky, "Predicting Material Surface Catalytic Efficiency Using Arc-Jet Tests", AIAA Paper No. 95-2013, AIAA $30^{th}$ Thermophysics Conference, June, (1995).
51. C. Park and S. H. Lee, "Validation of Multitemperature Nozzle flow Code", *J. Thermophysics and Heat Transfer*, **9**, pp. 9-16, Jan.-March, (1995).
52. A. T. Schönemann, M. Auweter-Kurtz, H. A. Habiger, P. C. Sleziona, and T. Stöcle, "Analysis of the Argon Additive Influence on a Nitrogen Arcjet Flow", *J. Thermophysics and Heat Transfer*, **8**, pp. 466-472, (1994).
53. F. S. Milos and D. J. Rasky, "Review of Numerical Procedures for Computational Surface Thermochemistry", *J. Thermophysics and Heat Transfer*, **8**, pp. 24-34, (1994).
54. W. N. MacDermott, D. D. Horn, and C. J. Fisher, "Flow Contamination and Flow Quality in Arc Heaters Used for Hypersonic Testing", AIAA Paper No. 92-4028, (1992).
55. J. M. Donohue, D. G. Fletcher, and C. S. Park, "Emission Spectral Measurements in the Plenum of an Arc-jet Facility", AIAA Paper No. 98-2946, $7^{th}$ AIAA/ASME Joint Thermophysics and Heat Transfer Conference, June, (1998).
56. D. J. Bamford, A. O'Keefe, D. S. Babikian, D. A. Stewart, and A. W. Strawa, "Characterization of Arc-Jet Flows Using Laser-Induced Fluorescence", J. Thermophysics and Heat Transfer **9**, 26-33, (1995).
57. D. J. Bamford and A. Romanovsky, "Velocity and Chemical Composition Measurements in an Arc Jet Flow", AIAA Paper No. 95-2039, AIAA $30^{th}$ Thermophysics Conference, June, (1995).
58. D. G. Fletcher, "Arcjet Flow Properties Determined from Laser-Induced Fluorescence of Atomic Nitrogen", AIAA Paper No. 98-0205, $36^{th}$ Aerospace Sciences Meeting, (1998).
59. D. G. Fletcher and D. J. Bamford, "Arcjet Flow Characterization Using Laser-Induced Fluorescence of Atomic Species", AIAA Paper No. 98-2458, $7^{th}$ AIAA/ASME Joint Thermophysics and Heat Transfer Conference, (1998).
60. P. R. Bevington, Data Reduction and Error Analysis for the Physical Sciences, McGraw-Hill, New York, pp. 3-7, (1969).
61. D. L. Baulch, D. D. Drysdale, D. G. Horne, and A. C. Lloyd, Evaluated Kinetic Data for High Temperture Reactions, Vol. 2, Butterworth Group, London, pp. 25-53, (1973).
62. W. Winovich, "Total Radiation Measurements at the Stagnation Point of Blunt Bodies at Stagnation Temperatures to 15000 K", AIAA Paper No. 68-405, AIAA *3rd* Aerodynamic Testing Conference, April, (1968).
63. A. F. Okuno and C. Park, "Stagnation Point Heat Transfer Rate in Nitrogen Plasma Flows: Theory and Experiment", *Journal of Heat Transfer*, pp. 372-384, August, (1970).
64. C. O. Laux, "Optical Diagnostics and Radiative Emission of Air Plasmas", Stanford High Temperature Gasdynamics Laboratory Report No. HTGL T-288, Stanford University, August, (1993).
65. C. S. Park, M. E. Newfield, D. G. Fletcher, T. Gökçen, and Sharma, S. P., "Spectroscopic Emission Measurements within the Blunt Body Shock Layer in an Arc-Jet Flow", AIAA Paper No. 97-0990, Jan., 1997; also *J. Thermophysics and Heat Transfer*, **12**, pp. 190-197, (1998).
66. C. S. Park, M. E. Newfield, D. G. Fletcher, and T. Gökçen "Spectroscopic Measurements of the Flows in an Arc-Jet Facility", AIAA Paper No. 98-0893, $36^{th}$ Aerospace Sciences Meeting; also *J. Thermophysics and Heat Transfer*, **13**, pp.60-67, (1999).
67. T. Gökçen, "Computation of Nonequilibrium Viscous Flows in Arc-Jet Wind Tunnel Nozzles", AIAA Paper No. 94-0254, $32^{nd}$ Aerospace Sciences Meeting, (1994).
68. T. Gökçen, "Effects of Freestream Nonequilibrium on Convective Heat Transfer to a Blunt Body", *J. Thermophysics and Heat Transfer*, **10**, April-June, pp.234-241, (1999).
69. E. E. Whiting, J. O. Arnold, and G. C. Lyle, "A Computer Program for a Line-by-Line Calculation of Spectra from Diatomic Molecules and Atoms Assuming a Voigt Line Profile", NASA TN D-5088, March, (1969).
70. E. Venkatapathy, J. W. Naughton, and D. G. Fletcher, "Experimental and Computational Study of Sonic and Supersonic Plumes", AIAA Paper No. 95-3496, AIAA Atmospheric Flight Mechanics Conference, August, (1995).
71. C. S. Park, D. G. Fletcher, and J. M. Donohue, "Spatially Resolved Shock Layer Emission Measurements and Analysis in an Arc-Jet Facility", AIAA Paper No. 99-1046, $37^{th}$ Aerospace Sciences Meeting, Jan., (1999).
72. U. B. Mehta, "Guide to Credible Computer Simulation of Fluid Flows", *J. Propulsion and Power*, **12**, pp. 940-948, (1996).

# Nonintrusive Diagnostic Strategies for Arcjet Stream Characterization

*Presented by*
*Douglas G. Fletcher*
*Reacting Flow Environments Branch, MS 230-2*
*NASA Ames Research Center*
*Moffett Field, CA, 94035-1000*

**1. Introduction** ..... 3B-2

**1.1** Ames AHF Arcjet Facility ..... 3B-2

**1.2** Nonintrusive Diagnostics ..... 3B-3

**2. Emission Measurements in Large-Scale Arcjet Facilities** ..... 3B-4

**2.1** Emission Spectroscopic Measurements ..... 3B-4

**2.2** Arc Column & Electrode Package ..... 3B-8

2.2.1 Experimental Configuration for Electrode Package Measurements ..... 3B-9
2.2.2 Electrode Package Results and Discussion ..... 3B-10

**2.3** Nozzle and Free Stream ..... 3B-11

2.3.1 Experimental Configuration for Free-Stream Measurements ..... 3B-12
2.3.2 Free Stream Results and Discussion ..... 3B-12

**2.4** Shock Layer Flows ..... 3B-14

2.4.1 Experimental Configuration for Shock-Layer Measurements ..... 3B-15
2.4.2 Flow Properties from Emission ..... 3B-15
2.4.3 Shock Layer Results and Discussion ..... 3B-17

**2.5** Summary of Emission Measurements ..... 3B-20

**3. LIF Measurements in Large-Scale Arcjet Facilities** ..... 3B-21

**3.1** Laser-Induced Fluorescence ..... 3B-21

**3.2** Single-Photon LIF of Cu and NO ..... 3B-23

**3.3** Two-Photon LIF of O and N ..... 3B-23

3.3.1 Experimental Configuration for Free Stream LIF ..... 3B-24
3.3.2 Flow Properties from Two-Photon LIF ..... 3B-25
3.3.3 Two-Photon LIF Measurements in $N_2$/Argon Flows ..... 3B-26
3.3.4 Two-Photon LIF Measurements in Air/Argon Flows ..... 3B-30

**3.4** Summary of LIF Results ..... 3B-33

**4. Summary of Arcjet Characterization Using Nonintrusive Diagnostics** ..... 3B-34

**5. Acknowledgements** ..... 3B-34

**6. References** ..... 3B-34

*Paper presented at the RTO AVT Course on "Measurement Techniques for High Enthalpy and Plasma Flows", held in Rhode-Saint-Genèse, Belgium, 25-29 October 1999, and published in RTO EN-8.*

## 1. Introduction

In the previous lecture, the issues related to arcjet flow modeling were introduced, and the limitations of conventional instrumentation in addressing these issues were discussed. The general level of understanding of the arcjet flows was seen to preclude the use of arcjets as aerothermodynamic test facilities beyond the current role in aerothermal material testing, despite their long test duration capability. In this section, the focus will be on new developments in spectroscopic instrumentation and techniques that can be brought to bear on the fundamental problem of arcjet stream characterization. Although a wide selection of arcjet facilities were introduced in the previous section, the discussion of nonintrusive diagnostic instrumentation will be restricted to the large-scale, segmented, constricted-arc heater facilities that are most widely used in thermal protection material testing for aerospace applications.

After a brief review of the important features of arcjet flows, the topic of nonintrusive, optical diagnostics is introduced with a discussion of some of the basic aspects of radiative transitions. The lecture is then organized into two sections covering emission measurements and laser-induced fluorescence measurements. Emission measurements are presented next for different regions of arcjet flows, while the fluorescence measurements are presented for the free stream region only. Summaries are given for each of the two main sections, and observations on arcjet characterization by optical diagnostics in general are given at the end.

Characterization of arcjet flows involves determining the thermodynamic state of the test gas. To do this in any particular flow region requires an evaluation of the distribution of energy among the kinetic, chemical, and thermal modes of the gas, which also quantifies the degree of departure from thermochemical equilibrium. As opposed to other high enthalpy ground-test facilities, the total enthalpy of an arcjet flow is not always known, so characterization will also involve determining the total enthalpy. Although the measurement objectives can be clearly and simply stated, the nonequilibrium nature of typical arcjet flows makes arcjet characterization difficult to accomplish by requiring measurements of multiple species and multiple temperatures in addition to the flow velocity.

### 1.1 Ames AHF Arcjet Facility

The Aerodynamic Heating Facility (AHF) Arcjet at NASA Ames Research Center is one example of a large-scale, constricted-arc heater test facility. It consists of a segmented, constricted-arc heater, a conical nozzle section, and a test cabin.[1] The arrangement of these components is shown in Fig. 1. Facility operation is initiated by evacuating the arcjet facility and then striking an arc in a low-pressure argon stream. The test gas flow, which typically consists of air or nitrogen, is then added and the arc current is adjusted to achieve the desired test conditions. Within the arc heater, the incoming test gas flow is heated by the electrical discharge to a level that causes substantial dissociation of the molecular species. The argon stream used to initiate the arc is maintained during operation and an additional argon stream is injected in the downstream electrode package to minimize erosion. This electrode package also serves as a plenum that reduces the gas velocity before it enters the nozzle. The flow is then accelerated to high velocity through a conical, converging-diverging nozzle. Owing to the decrease in density during the expansion, the collision frequency decreases rapidly in the nozzle and the thermochemical state of the flow departs from equilibrium. At some point in the nozzle, depending on the test conditions, the flow chemistry becomes frozen, and remains frozen through the remainder of the expansion. Various nozzle sections can be used to provide expansion ratios ranging from 64 to 576. The flow exits the nozzle and continues expanding into a cabin where material tests are conducted. Material samples are typically inserted into the stream ≈36 cm downstream of the nozzle exit.

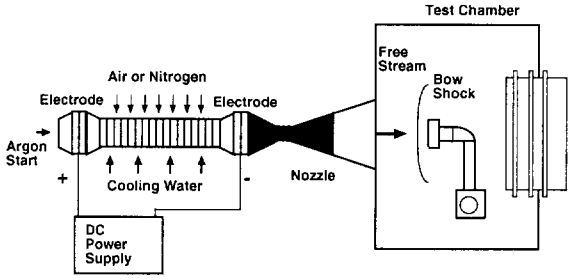


Fig. 1 Schematic of the NASA Ames AHF Arcjet.

The constrictor chamber pressure and arc current are adjusted to achieve the desired operating condition, which is usually defined by a predetermined surface temperature or heat flux level impinging on the test article. Test durations of up to 20 minutes are possible, depending on the particular conditions. During the tests, the stagnation pressure, cabin pressure, and arc heater conditions are continuously monitored. Stagnation-point heating and pitot pressure measurements are typically performed during a run to verify test conditions. These measurements are also frequently used to determine the stream enthalpy based on an empirical correlation for stagnation point heating. The limitations of this approach for characterizing the arcjet stream were discussed in the previous lecture.

The general state of arcjet stream characterization in the early 90's was summarized in an excellent and thorough review article by Scott.[2] Both conventional instrumentation and nonintrusive, spectroscopic techniques that were being developed for arcjet flow characterization were critically reviewed in the article.

Particular attention was given to how various diagnostic techniques could be used to characterize the most important stream variables: enthalpy and the degree of nonequilibrium. Instead of revisiting all of the instrumental approaches that have been used for making measurements in arcjet flows, this lecture will focus on recent developments in nonintrusive optical techniques that have been implemented in large-scale arcjet facilities. Progress made in arcjet characterization using these optical diagnostics will be discussed in detail.

### 1.2 Nonintrusive Diagnostics

Stated in the most general terms, optically based, nonintrusive diagnostic strategies attempt to determine flow or thermodynamic properties from an analysis of light that is emitted from either a thermally-induced or laser-induced process. Optical techniques have been used for many years in spectroscopic investigations and aerospace diagnostic applications. Most of the earlier applications involved radiative emission and absorption in addition to interferometric and shadowgraph instrumentation. In fact, early in the development stage of large-scale arcjet facilities, emission spectroscopy was investigated as a means for characterizing a nitrogen shock-layer flow.[3] Newer spectroscopic diagnostic techniques that take advantage of recent advances in laser instrumentation are gaining wider acceptance in the aerospace ground-test community.[4] Much of the development of these instruments, particularly those based on laser spectroscopy, has been driven by research into combustion processes.[5]

Although all of the nonintrusive diagnostic techniques that will be discussed in this paper are derived from the same physical principles, each technique will be examined separately. In addition, mathematical descriptions will be given to illustrate the relation between the measured quantity and the flow variables. To do this adequately requires a brief examination of background material that will be common to all of the techniques. More information on basic principles and on specific diagnostic techniques can be found in books by Eckbreth[5] and Demtröder[6].

**Background Physics -** Atoms and molecules have discrete, quantized energy levels. For atoms, these energy levels are only electronic, while molecules have rotational and vibrational energy levels in addition to the electronic energy levels. If certain selection criteria, which are established from quantum mechanical considerations,[7] are met, then atoms and molecules can undergo radiative transitions between these levels. These transitions can involve the scattering, absorption, or emission of a photon. Because applications of optical diagnostics to arcjet stream characterization is a major focus of this paper, only processes involving photon emission and absorption will be considered further.

For absorption and emission, the photon energy matches the difference between the two internal (atomic or molecular) states connected by the radiative transition,

$$h\nu = E_u - E_l \quad , \tag{1}$$

where $h$ is the Planck constant and $\nu$ is the transition frequency. For atomic species, the energies correspond to electronic levels directly, while for molecules the upper and lower state energies are comprised of electronic, vibrational, and rotational terms,

$$E = T_E + G(v) + F(J) \quad , \tag{2}$$

where $v$ and $J$ are the vibrational and rotational quantum numbers, respectively. For diatomic molecules that are modeled simply as vibrating rotators the vibrational and rotational term energies are represented by polynomial expansions[7] that take into account interactions between these energy modes,

$$G(v) = \omega_e(v+\frac{1}{2}) - \omega_e x_e(v+\frac{1}{2})^2 + \omega_e y_e(v+\frac{1}{2})^3 + \ldots \tag{3}$$

$$F(J) = [B_e - \alpha_e(v+\frac{1}{2})]J(J+1) - [D_e + \beta_e(v+\frac{1}{2})J^2(J+1)^2 + \ldots \tag{4}$$

For most species of interest related to arc-heated or shock-heated air, the vibrational and rotational constants $(\omega_e, B_e, D_e, \alpha_e, \beta_e)$ in the above expressions, and in higher order terms, are accurately known. Recommended constants for many diatomic species are given in Huber and Herzberg[8], while Laux[9] has a compilation of more recently reported constants for high temperature air.

The amount of light absorbed or emitted by atoms or molecules in a particular energy level depends on the population in that particular level. If the system is in thermal equilibrium, then the populations of atoms or molecules in the energy levels follow a Boltzmann distribution,[10]

$$N_i = N\frac{g_i e^{(-E_i/kT)}}{\sum_i g_i e^{(-E_i/kT)}} \quad , \tag{5}$$

where $g_i$ is the level degeneracy. The summation in the denominator is over all energy levels, and it is called the partition function, $Q = \sum_i g_i e^{(-E_i/kT)}$. For molecules, the total partition function can be expressed as the product of the partition functions for the individual internal energy modes,

$$Q = Q_R\, Q_V\, Q_E \quad . \tag{6}$$

An approximate closed form expression for the vibrational partition function is

$$Q_V = (1 - e^{-\theta_v/T})^{-1} \quad , \tag{7}$$

where $\theta_v = hc\omega_e/k$ is the characteristic vibrational temperature[10] of the particular molecule under consideration, $c$ is the speed of light, and $k$ is the Boltzmann constant. For room temperature and higher, an approximate closed form expression can also be derived for the rotational partition function,

$$Q_R = \frac{T}{\sigma\theta_r} \quad , \tag{8}$$

where $\theta_r = hcB/k$ is the characteristic rotational temperature of the molecule, and $\sigma = 1$ or 2 depending on whether the diatomic molecule is heteronuclear or homonuclear.

With the aid of these expressions for partition functions, analytic expressions for the fractional populations in particular rotational ($J$) and vibrational ($v$) levels can be written as

$$\frac{N_J}{N} = \frac{\sigma(2J+1)\theta_r}{T} e^{-J(J+1)\theta_r/T} \quad , \tag{9}$$

if nuclear spin degeneracy is ignored, and

$$\frac{N_v}{N} = e^{-v\theta_v/T}(1 - e^{-\theta_v/T}) \quad . \tag{10}$$

It should be noted that Eqs. (5), (9), and (10) govern the population distributions of atoms and molecules under thermal equilibrium conditions. By inspection of the exponential terms, it is apparent that the higher energy levels become substantially populated only at very high temperatures.

**Uncertainty in Measured Quantities -** Both approximate and exact analytical expressions are developed in subsequent sections to relate particular flow properties to either emission or LIF signals. In addition to illustrating how a particular flow property is measured, these expressions provide a means for estimating the sensitivity of the optical signal to that flow property, which is then used to determine the uncertainty. All flow properties determined from optical measurements in this paper include estimates of the experimental uncertainty. These estimates are derived from the combined effect of multiple, statistically independent contributions, which is expressed as

$$\sigma_M = \sqrt{(\frac{\partial M}{\partial W_1}\sigma_{W_1})^2 + (\frac{\partial M}{\partial W_2}\sigma_{W_2})^2 + \ldots.} \quad , \tag{11}$$

where $M = f(W_1, W_2, \ldots)$ and $\sigma$ represents the uncertainty in a particular parameter. Sensitivity of the measured parameter to a particular variable is reflected in the value of the partial derivative taken with respect to that variable in the above expression.

Some contributions, such as uncertainties in spectroscopic constants, are evaluated analytically, while others, such as unresolved background signal contributions, are evaluated numerically using a spectral model. Detailed discussions of the uncertainty estimates are given in each of the referenced publications that describe a particular experiment. The importance of estimating uncertainties for the measured values cannot be understated, since knowledge of the uncertainty values guides the use of the measurements and informs improvements in instrumentation and diagnostic approach.

## 2. Emission Measurements in Large-Scale Arcjet Facilities

Emission measurements are the simplest optically based, nonintrusive diagnostics that can be used in arcjet test facilities. These measurements are truly nonintrusive, since only light is taken from the flowfield. No external mechanism is invoked to populate excited atomic or molecular states that would lead to observable radiative transitions. Rather, thermal excitation within the flow region continuously replenishes populations in radiating electronic levels for the constituent atoms and molecules. This excitation mechanism necessarily constrains measurable populations to regions having sufficient thermal excitation, such as shock layers over test articles placed in the stream and regions within and adjacent to the arc heater.

### 2.1 Emission Spectroscopic Measurements

When the spontaneous emission rate for a particular radiative transition, $A_{ul}$, is known, then the radiant power density emitted by a unit volume of gas can be expressed as

$$E = n_u A_{ul} h\nu_{ul}/4\pi \quad , \tag{12}$$

where $n_u$ is the number density of the emitting level. The spectral power density of spontaneous emission can be obtained by multiplying the above expression by a line-shape function, $\phi(\lambda)$,

$$E_\lambda = n_u A_{ul} h\nu_{ul}\phi(\lambda)/4\pi \quad , \tag{13}$$

where $\phi(\lambda)$ is defined such that

$$\int_{-\infty}^{+\infty} \phi(\lambda)d\lambda = 1.$$

An optically thin gas, which has negligible self-absorption, is essentially emission dominated. For this special case, stimulated emission is also negligible and the specific intensity (also called spectral radiance) is given by the integral of the spectral power density over

an optical path, which might be defined by a line-of-sight, as

$$I_\lambda = \int_0^L E_\lambda dx \quad .$$

This latter quantity, the specific intensity, is the quantity actually measured by a radiometric sensor (after applying a slit or filter function). Note that the expressions above apply only to atomic and bound-bound molecular radiative transitions. If significant absorption is occurs within the observation volume, then the combined effects of stimulated absorption and emission must be taken into account, and the radiative transport equation takes on a more complex form,[11]

$$I_\lambda = \int_0^L \alpha_\lambda (I_\lambda - B_\lambda) dx \quad ,$$

where $\alpha_\lambda$ is the effective volumetric absorption coefficient that includes stimulated emission and absorption and $B_\lambda$ is the Planck function.

For either case, quantitative emission measurements require that the detection system be calibrated with standard spectral lamps. Also, for both cases the intensity measured by the detector is integrated along the optical path and spatial resolution in the line-of-sight direction is therefore lost.

An emission dominated, optically thin gas and an isotropic emitting volume with constant properties represents an optimal diagnostic situation for emission measurements, since the light levels can be interpreted directly in terms of the local thermodynamic properties of the emitting volume. Generally, this is not the case even when the gas is optically thin; usually there are spatial property gradients along the viewing direction and the recorded emission signal represents the intensity-weighted integral sum of the emitted light.[12] For the worst case, which is also quite common, gradients along the line of sight and self-absorption in the optically thick gas require a solution of the radiative transport equation with a numerical model, such as NEQAIR.[13]

For applications of emission spectroscopy to arcjet flow property measurements in large-scale facilities, the test gas is usually a mixture of air and argon (or $N_2$/argon) and the wavelength range of interest typically covers the region between 2000 and 9000 Å. An example of a measured emission spectrum for this range is shown in Fig. 2a-d. The temperature of the gas was between 7000 and 8000 K, based on an analysis of the spectrally resolved emission. The thermochemical state of the flow was not specified, although it should be close to equilibrium, because the spectrum was acquired in the high pressure region of the arcjet within the downstream electrode package. The emission is a mix of bound electronic transitions from molecules, as evidenced by the band structure at the shorter wavelengths, and from atoms, which appear as isolated lines with increasing intensity at longer wavelengths. There is also an underlying background emission that is at least partly due to bound-free continuum emission, and there may possibly be some black-body emission collected from reflections of the arc in the constrictor region. It will be useful to refer to this spectrum as the relationships between atomic and molecular emission and thermodynamic properties are developed below.

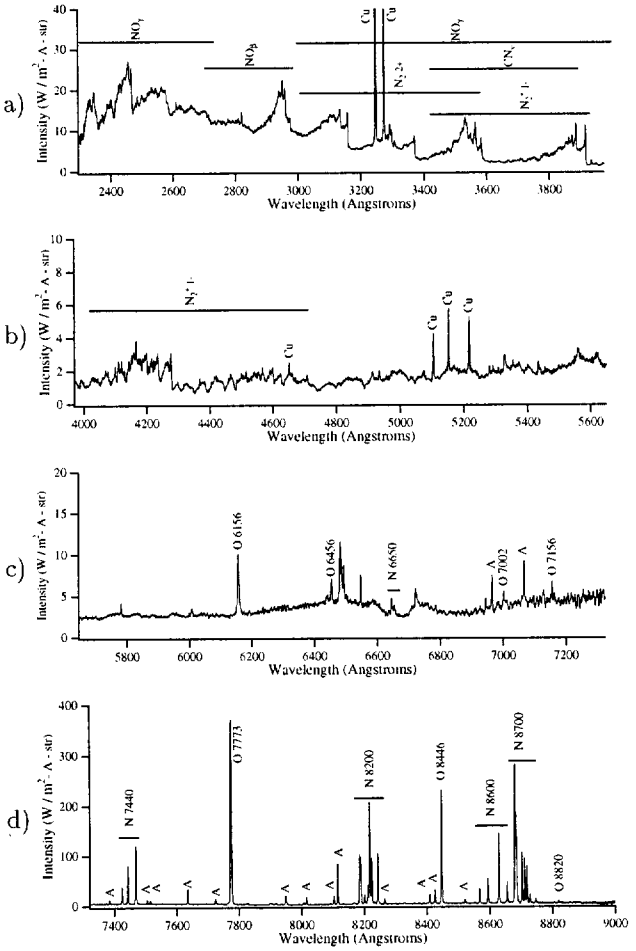


Fig. 2a-d. Spectrally resolved emission from a high temperature mixture of air and argon.

**Temperature Measurement -** In Eq. (13), the thermodynamic dependence of the emission is due to the upper state population, $n_u$, which is a function of species density and temperature. Under conditions of thermal equilibrium, the temperature dependence is given by the Boltzmann fraction expression and the specific intensity for emission dominated radiation integrated along the line-of-sight is

$$I_\lambda = \frac{n A_{ul} h\nu_{ul}}{4\pi} \phi(\lambda) \frac{g_u}{Q} e^{-E_u/kT} L \quad . \qquad (14)$$

At modest temperatures, where $E_u/kT > 1$, emission is more sensitive to temperature than to density. The degree of temperature sensitivity is determined by the

energy of the radiating level. If the system is in thermal equilibrium, then in principle, the measurement of two spectral features with different upper state energies is sufficient to determine temperature.

**Electronic Temperature -** For example, the electronic temperature can be determined from the ratio of the spectrally integrated intensities emanating from two different thermally populated electronic levels of an atomic species. By taking the natural log of the intensity ratio and rearranging the terms, an analytic expression for electronic temperature is obtained,

$$T_e = \frac{(E_1 - E_2)/k}{\ln\left(\frac{I_2 A_1 g_1 \nu_1}{I_1 A_2 g_2 \nu_2}\right)} \quad , \tag{15}$$

where $I_1, I_2$ are the spectrally integrated intensities,

$$I = \int_{\lambda_1}^{\lambda_2} I_\lambda d\lambda \quad .$$

Note that the number densities and partition functions cancel in the ratio, since both spectral features are emitted by the same species.

The sensitivity of the ratio of intensities to temperature is found by taking the derivative of the intensity ratio with respect to temperature, and rearranging the expression to give,

$$\frac{\Delta R}{R} = \frac{E_1 - E_2}{k\ T_e} \frac{\Delta T_e}{T_e} \quad , \tag{16}$$

where $R = I_2/I_1$ For the two most commonly observed transitions of atomic oxygen at 7773 and 8446 Å, the sensitivity term $\Delta E/kT_e = 2880/T_e$. At temperatures above 6000 K, this ratio will be less than .5 and large changes in $T_e$ will produce only small changes in the measured ratio. Greater sensitivity to temperature occurs with larger energy differences between emitting levels. Often, a compromise must be reached between the enhanced temperature sensitivity of higher energy levels and signal-to-noise ratio. In this regard, spectroscopic diagnostics are no different from ordinary laboratory instrumentation.

To overcome the low temperature sensitivity that arises from small energy differences between emitting levels, spectrally integrated signals from multiple transitions are used to develop a Boltzmann plot for a particular species. By taking the natural log of Eq. (14), an expression that represents the Boltzmann plot mathematically is obtained,

$$\ln\left(\frac{I}{A_{ul} g_u h \nu_{ul}}\right)_i = \frac{-1}{kT_e}(E_u)_i + C \quad , \tag{17}$$

where $C$ contains the terms that are common to all the transitions. Temperature is then obtained from a least squares linear fit to the data and the precision of the measurement improves with the number of transitions used, provided that the energy levels and spontaneous emission rates, $A_{ul}$, are known accurately.

**Molecular Spectra -** Emission from molecular species is typically comprised of overlapping spectral features from multiple energy levels that are less completely resolved, as seen in the band structure at shorter wavelengths in Fig. 2. Despite the spectral overlap, similar analytical approaches can be used to determine temperature values. These approaches also involve taking ratios of spectral features that are reasonably well defined. Specific approaches for determining vibrational and rotational temperatures from molecular spectra have been developed by Laux[9] and Park et al[14]. The methods of Park are shown graphically in Figs. 3 and 4. The figures show emission spectra from vibrational bands of the $N_2^+$ (1-) system and the shaded regions indicate the spectrally integrated areas used to determine temperatures. Approximate analytical expressions for vibrational and rotational temperatures as functions of these intensity ratios are derived below. For the derivations, it is assumed that: vibrational and rotational modes are in thermal equilibrium (but $T_v \neq T_r$ is allowed); the radiation field is emission dominated; effects of nuclear spin on degeneracy are ignorable; and the individual ro-vibrational transitions are fairly isolated spectrally (in reality, the spectral resolution of the detecting instrument convolves contributions from multiple transitions, as discussed below). Also, each derivation makes use of the Born-Oppenheimer approximation to separate the electronic, vibrational, and rotational contributions to the spontaneous emission rate, which can then be written as[15]

$$A_{ul} = c\nu^3 R_e^2 q_{v_u v_l} \frac{S_{J_u J_l}}{(2J_u + 1)} \quad , \tag{18}$$

where $c$ represents the group of constants, $R_e$ is the electronic transition moment, $q_{v_u v_l}$ is the Franck-Condon factor, which represents the vibrational band strength, and $S_{J_u J_l}$ is the Hönl-London factor, or rotational line strength.

**Vibrational Temperature -** For vibrational temperature, spectrally integrated intensities near two band heads, (1,2) and (0,1) are ratioed. The two spectral regions are shown on Fig. 3, and the difference in upper state vibrational quantum number gives a difference in energy level analogous to the explicit $\Delta E$ for the two-line electronic temperature measurement that was discussed above. Emission at the vibrational band head is comprised of contributions from a number of rotational transitions, and the spectrally integrated

intensity for each band head is

$$I_i = \int_{\lambda_{i1}}^{\lambda_{i2}} I_\lambda d\lambda = \frac{cnh\nu^4}{4\pi} R_e^2(q_{v_u v_l})_i \left(\frac{n_{vi}}{n}\right) \sum_{Ji} \frac{(S_{J_u J_l})_i}{(2J_u+1)_i} \frac{n_{Ji}}{n} \quad , \tag{19}$$

where $i = 1, 2$. The ratio of the two intensities obtained from the spectral integration of the emission at the two bandheads is then

$$\frac{I_2}{I_1} = \frac{(q_{v_u v_l}\nu^4)_2}{(q_{v_u v_l}\nu^4)_1} \frac{e^{-v_2\theta_v/T_v}}{e^{-v_1\theta_v/T_v}} \frac{\sum_{J_2}(S_{J_2 J_l})_2 e^{J_2(J_2+1)\theta_r/T_r}}{\sum_{J_1}(S_{J_1 J_l})_1 e^{J_1(J_1+1)\theta_r/T_r}} \quad , \tag{20}$$

where the Boltzmann expressions for vibrational and rotational distributions have been used and the vibrational and rotational temperatures are explicitly identified. Ideally, if the rotational transitions comprising the sum for each band head had the same range of $J$ values, then the intensity ratio would be insensitive to rotational temperature. In practice, this is not achieved, and although the rotational temperature sensitivity can be minimized, an iterative solution is required that includes a concurrent, but separate, determination of rotational temperature.

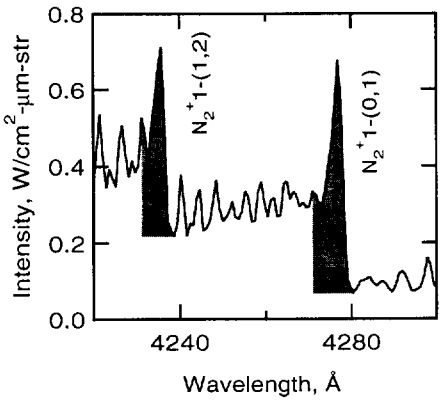


Fig. 3. Spectral integrals used to determine $T_v$.

The above intensity ratio can be rearranged and solved for vibrational temperature,

$$T_v = \frac{(v_1 - v_2)\theta_v}{\ln\left[(I_2 q_1 \nu_1^4)/(I_1 q_2 \nu_2^4 f(T_r))\right]} \quad . \tag{21}$$

The sums of rotational terms, which do not cancel in the ratio, are now represented by $f(T_r)$. As with the electronic temperature, the greater the difference in vibrational energies of the two levels, the greater the sensitivity to temperature.

**Rotational Temperature -** By taking the ratio of two spectrally integrated intensities that contain different rotational transitions, but arise from a single vibrational band, the rotational temperature can be determined. One approach is shown schematically in Fig. 4, where the ratio of the two spectrally integrated regions gives

$$\frac{I_2}{I_1} = \frac{\sum_{J_2}(S_{J_2 J_l}\nu^4)_2 e^{-J_2(J_2+1)\theta_r/T_r}}{\sum_{J_1}(S_{J_1 J_l}\nu^4)_1 e^{-J_1(J_1+1)\theta_r/T_r}} \quad , \tag{22}$$

and all common terms have been canceled. Note that this is again an idealized case, since in practice the integrated intensities include signal contributions from adjacent vibrational band transitions and from other species. In Fig. 4, the merging of spectral features caused by finite slit resolution is evident, and contributions from other radiative transitions are evident in the nonzero baseline level at the edge of the band head near 3917 Å.

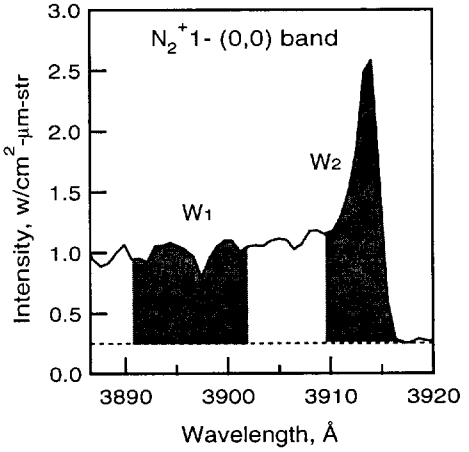


Fig. 4. Spectrally integrated regions used to determine $T_r$.

To illustrate the temperature sensitivity of the above relation, average values, $\overline{S_{JJ}}$ and $\overline{J}$,can be defined such that

$$\sum_{J=Ja}^{Jb} S_{JJ_l} e^{-J(J+1)\theta_r/T_r} = (\Delta J_{ab}+1)\overline{S_{JJ}} e^{-\overline{J}(\overline{J}_1)\theta_r/T_r} \quad . \tag{23}$$

With the average rotational strength and quantum numbers, the expression for rotational temperature becomes

$$T_r = \frac{(\overline{J_1}(\overline{J_1}+1) - \overline{J_2}(\overline{J_2}+1))\theta_r}{\ln\left[(I_2 \overline{S_{JJ}}_1 \nu_1^4)/(I_1 \overline{S_{JJ}}_2 \nu_2^4)\right]} \quad . \tag{24}$$

This result is analogous to the two previous derivations for determining vibrational and electronic temperatures from the ratio of spectrally integrated intensities. Here however, it is the difference in rotational energies that determines the rotational temperature sensitivity of the intensity ratio. As before, greater sensitivity to temperature is found for larger differences in rotational quantum numbers and the same considerations apply regarding a trade between sensitivity and signal level.

For all of the temperature determinations above, it is assumed that the gas is optically thin. If this is not the case, then self-absorption, or radiative trapping, must be considered. To interpret emission spectra emanating from an optically thick gas, a radiative transport model, such as NEQAIR, is required. An iterative procedure must be used to interpret and correct the spectra for self-absorption, since the absorbing populations depend on density and temperature in the same manner as the emitting populations (see Eqs. (9) and (10)). Some modeling must also be done to properly account for the coupling between rotational and vibrational temperatures for molecular spectra and for finite instrument resolution.

**Species Densities -** Species concentrations that are integrated along the line-of-sight can be estimated if the electronic temperature is known from one of the methods outlined above. This implies that the population of the excited electronic state is in Boltzmann equilibrium with the ground state. By rearranging the spectrally integrated form of Eq. (13), the line-of-sight integrated concentration of an atomic species in an emission dominated radiation field can be expressed as

$$nL = \frac{I 4\pi Q}{g_u A_{ul} h\nu_{ul}} e^{E_u/kT_e} \quad . \tag{25}$$

Owing to the exponential dependence of density on electronic temperature, small uncertainties in electronic temperature cause large uncertainties in the $nL$ product. The temperature uncertainty contribution to the $nL$ uncertainty is amplified by the factor $E_u/kT_e$, where $E_u$ is the energy of the emitting level. To illustrate this aspect, consider an electronic temperature of 10000 K and the 7773 Å transition of O, which has an average upper state energy of 86630 $cm^{-1}$ (from Wiese et al[16]). In this case $E_u/kT_e = 12.5$. Thus, integrated species density values will be considerably more uncertain than temperatures.

**Abel Inversion** The path-integrated nature of emission measurements limits the amount of information that can be obtained from the flow. This is a serious drawback to emission-based property measurement since typical flow situations involve spatial gradients; they are not simply one-dimensional. However, if the flow gradients are axisymmetric and emission spectra are recorded from multiple spatial locations, then an Abel inversion of the recorded signals can yield localized emission intensities.

In an optically thin gas, the radiation intensity measured by an observer is an integrated sum of volumetric emission that varies with lateral displacement, $x$, of the viewing line. In Fig. 5, a cross section of the axisymmetric flow under consideration is shown. The measured integrated intensity $I(x)$ is an Abel transformation of a radial distribution of emissive intensity $E(r)$

$$I(x) = 2 \int_x^R \frac{E(r) r dr}{\sqrt{r^2 - x^2}}. \tag{26}$$

The reverse of this transformation, i.e., the Abel inversion, relates $E(r)$ to the measured intensity $I(x)$:

$$E(r) = -\frac{1}{\pi} \int_r^R \frac{(dI/dx) dx}{\sqrt{x^2 - r^2}}. \tag{27}$$

If the radiating flow region is axially symmetric, then even-power polynomials can be used to represent $E(r)$ and $I(x)$, thereby simplifying the analysis. Further information on the Abel inversion can be found in Refs. 9 and 17.

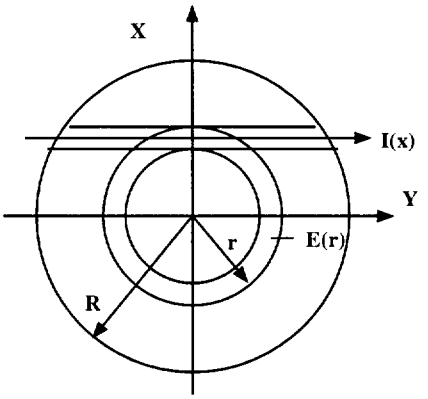


Fig. 5. Cross section of axially symmetric , optically thin radiation source.

Flow properties derived from emission spectroscopic measurements in large-scale arcjet facilities are discussed below. The discussion is organized by arcjet flow region, beginning with the arc column and ending with the shock layer over a blunt-body test article. Specific measurement examples, including experimental configuration and analysis details, are given for each flow region.

### 2.2 Arc Column & Electrode Package

Although optical access is limited, acquisition of emission spectra from the arc heater and electrode region can give a direct indication of the total flow conditions. Pressures are relatively high in this region, typically greater than atmospheric, and despite the high temperature, the collision frequency should be sufficient to ensure that the flow is in thermochemical equilibrium. If this is the case, then an optical measurement of temperature along with a concurrent pressure measurement would uniquely determine the total flow enthalpy. Numerical simulations of arcjet facilities often start with assumed equilibrium conditions in the electrode package region and then model the nozzle flow to calculate test conditions in the free stream. Knowledge of the flow properties in this region could specify

the input parameters and thereby enable a better evaluation of nonequilibrium, expanding flow simulations. This reasoning has motivated several investigations of arc-column and electrode package emission.

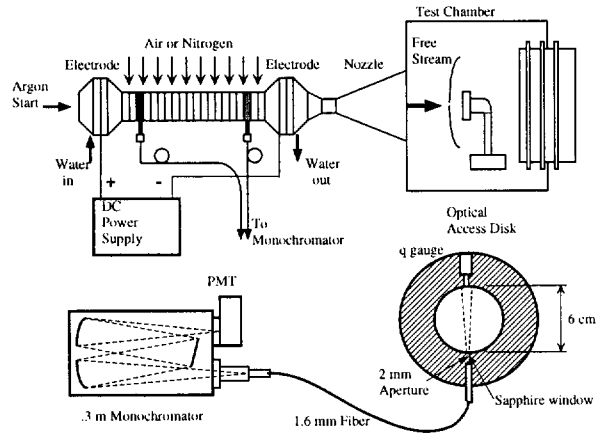


Fig. 6. Experimental setup for arc column emission measurements.

One of the earlier investigations involved the installation of a window on different segments of an arc column at AEDC.[18] The visual characteristics of the discharge were studied over a range of facility operating conditions for several locations along the column. Later, a heater segment disk with fiber-optic access was developed at Ames Research Center for installation in an arc column.[19] Using a fiber-based light collection system similar to the one that will be discussed in more detail below, Terrazas-Salinas et al[20] acquired emission spectra from the disk when it was installed in a 20 MW constricted-arc heater at two locations on the column, as shown in Fig. 6.

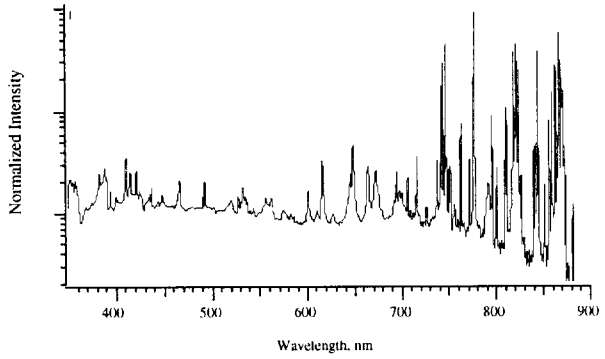


Fig. 7. Typical emission spectrum from cathode end of arc column.

A typical emission spectrum from the arc column is shown in Fig. 7. The spectrum is dominated by atomic lines with some $N_2^+$ ion emission seen at the shorter wavelength region where fiber attenuation begins to limit signal collection. Treating the gas as optically thin, Boltzmann plots of the atomic transition intensities were used to estimate electronic temperatures for O and N and these were compared with predictions from a numerical model of the flow in the constrictor section[21] and NEQAIR.

More recently, a series of investigations into emission from the downstream electrode region of a constricted arc heater were conducted at Johnson Space Center in their 10 MW arc heater.[22] Again, a fiberoptic collection system was used to bring the light to a spectrograph and the emission spectra were analyzed to infer electronic temperatures assuming that the gas was optically thin. A wide disparity between electronic temperatures derived from O and N transition intensities was noted for these measurements. Although the authors attributed the disagreement between the two temperatures to uncertainties in transition probabilities for N,[23] it is also possible that the assumption of an optically thin gas is inappropriate, since there will be some population in absorbing electronic states if the plenum region is filled with hot gas. It is also possible that nitrogen and oxygen are not completely mixed since they are injected separately in the Johnson arcjet. More recently, this group has acquired plenum region spectra along multiple lines-of-sight in an attempt to resolve the radial intensity gradients that are most likely present.[24]

Each of these investigations invoked the assumption that the gas was optically thin in the interpretation of the spectra. While this may be reasonable in the arc column, it may not be appropriate in the electrode package, or plenum, region. This question of self-absorption was explicitly considered in a recent investigation of electrode package emission in a 20 MW arcjet facility at Ames Research Center.[25] Findings from a preliminary analysis of the data are discussed below.

### 2.2.1. Experimental Configuration for Electrode Package Measurements

The current investigation of plenum radiation involves the use of a spacer disk in the electrode package to provide optical access to the flow. Based on the design of similar disks for the constrictor section,[19] this particular disk was sized to fit within the downstream electrode package and to accommodate a pressure tap and a heat transfer gauge in addition to the optical fiber. Figure 8 shows the location of the fiber view port in the downstream electrode package along with the optical layout for the experiments. The tests that are discussed below were conducted in the Ames 20 MW AHF Arcjet Facility that was described in the introductory section.

Hot gas emission from the plenum was collected through a sapphire window in the optical disk and imaged onto a 0.94 mm diameter, 30 m long, fiberoptic cable. The fiber, which delivered the light to a monochromator in a remote laboratory, was recessed

from the inside surface of the disk and viewed the emitting gas through a 2 mm aperture. A fused silica lens assembly was used to couple the fiber output with f-number matching to a 0.32 m scanning monochromator with a PMT mounted at the exit slit. The monochromator was equipped with a 1200 line/mm holographic grating blazed at 250 nm and the entrance and exit slits where both set at 50 $\mu$m. To cover the 2000 to 9000 Å spectral range during a single facility run, the monochromator was scanned at 1800 Å/min. Measured signals were converted to absolute intensities by determining the spectral response of the light collection system using standard tungsten and deuterium lamps. Further details about the optical instrumentation can be found in Ref. 25.

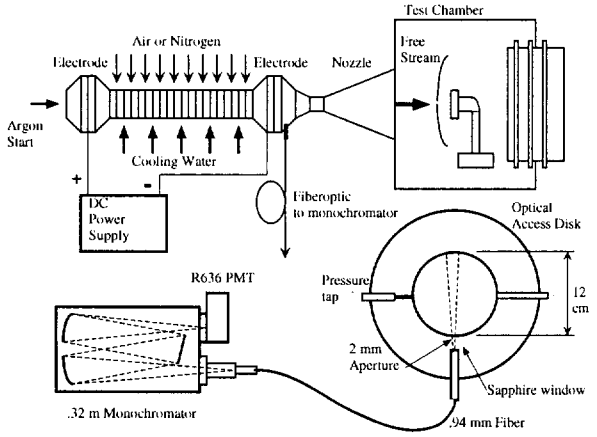


Fig. 8. Experimental setup for electrode package emission measurements.

During the facility tests PMT signals showed strong temporal fluctuations, on the order of +/- 30 %, across the spectrum. To reduce the fluctuations in the measured signals the PMT output was filtered with a 30 Hz, 12 dB/octave low pass filter. The combination of monochromator scan rate and electrical low pass filtering caused an artificial broadening (the Full-Width at Half-Maximum (FWHM) increased from 2 to 2.6 Å) and slight skewing of the line shapes. The settings chosen were considered necessary to reduce the rapid fluctuations and still scan over the desired wavelength range during a 4 min facility run. Integrated line intensities, which were used in the data analysis, were negligibly affected.

Test gases were either air/argon or $N_2$/argon mixtures and measurements were performed over a wide range of facility operating conditions. A compilation of the test conditions is given in Table I of Ref. 25. Results from a preliminary analysis of some of the data are discussed below.

### 2.2.2. Electrode Package Results and Discussion

The raw signal from a typical spectral scan recorded during a single facility run is shown in Fig. 9a. This raw signal was then corrected for the instrumental spectral response that was determined from the tungsten and deuterium lamp calibration, which is shown in Fig. 9b. The resulting calibrated, absolute intensity is shown in Fig. 9c and the predominance of atomic line emission over molecular band emission is evident. Despite differences in relative strengths stemming from different thermodynamic conditions, the spectral features seen in Fig. 9c are the same as seen in the spectrum from the arc column that was presented in Fig. 7. Assignments of some of the more important spectral features of the electrode package spectrum are given in Fig. 2 for an expanded wavelength scale.

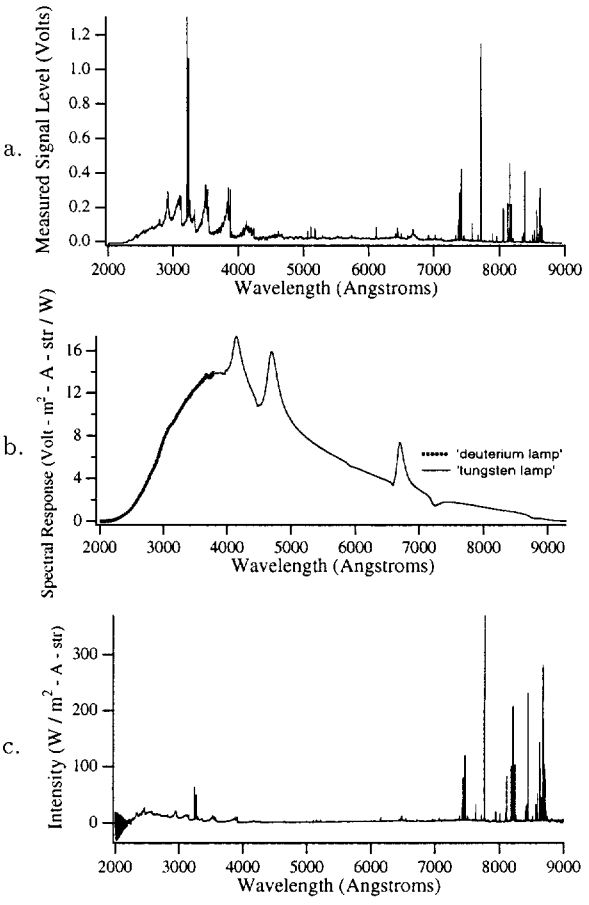


Fig. 9a-d. Example emission spectrum from electrode package measurements showing: a, raw signal from electrode package; b, system spectral response; and c, calibrated emission spectrum.

Using the basic procedure outlined in the introductory section, Boltzmann plots of the spectrally integrated atomic transition intensities were constructed to determine electronic temperatures assuming that the flow region was in local thermal equilibrium. NEQAIR simulations were performed to evaluate self-absorption since it is possible that hot gas entirely fills the electrode package region. Example Boltzmann plots for N and O are shown in Fig. 10 for a single facility test. Two plots are shown for each species; one assuming the

gas is optically thin, and a second plot with signals corrected for radiation trapping based on NEQAIR simulations of the radiative transport. Instead of assuming an arbitrary temperature profile within the electrode package, the simpler assumption of uniform conditions over the measurement domain was made. Note that the correction for self-absorption improves the agreement between the electronic temperatures that were determined from the slopes of the N and O distributions.

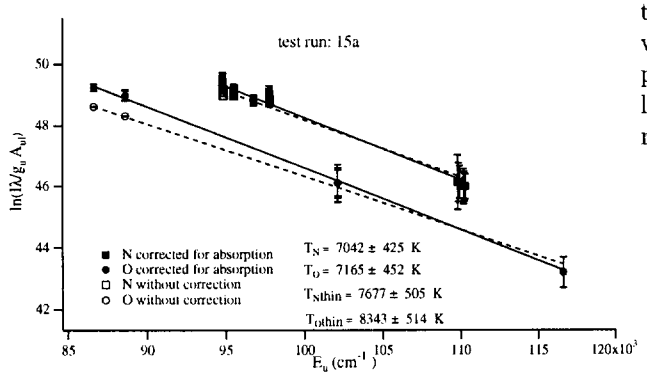


Fig. 10. Example Boltzmann plots for N and O, with and without correction for self-absorption.

Electronic temperatures deduced from O and N intensities are presented in Fig. 11 as a function of specific heater energy ($= VI/\dot{m}$) for a range of test conditions. Two sets of temperatures are shown for each condition: with and without correction for self-absorption. The temperatures show little variation as heater power ($VI$) is increased. Agreement between the electronic temperatures determined from O and N transitions is consistently better when self-absorption from a uniform absorber distribution along the line-of-sight is taken into account. Also, the temperature values derived from the absorption corrected intensities are consistently lower than the uncorrected values.

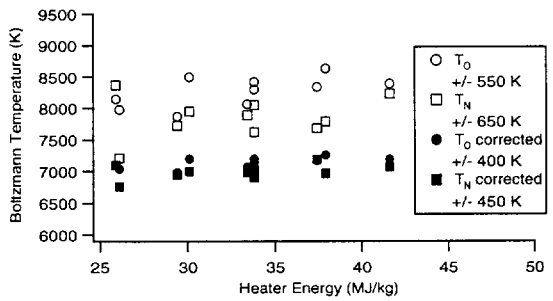


Fig. 11. Plenum temperatures derived from the analysis of the emission spectra for 2.4 atm pressure.

Despite the relatively low signal levels, the molecular band emission was also analyzed for rotational and vibrational temperature using the approach of Park[14], which was based on spectrally-integrated intensities of $N_2^+$ (1-) band features. Values of $T_r$ that were obtained from the analysis were compared with $T_e$ values and were found to be consistently higher for all test conditions. Vibrational temperatures that were determined from the spectrally integrated intensity ratios were even higher and appeared to be unreasonable. All of the temperature values were determined from spectra that were corrected for self-absorption assuming that the thermodynamic conditions and species distributions were uniform across the viewing region. This assumption may not hold for all species; in fact, it is possible that the molecular species are absent near the center of the flow where the absorbing atomic populations may be greatest. Likewise, the excessively high vibrational temperatures may indicate that the band populations may not be equally distributed along the line of sight. However, the possibility of nonequilibrium conditions can not yet be ruled out.

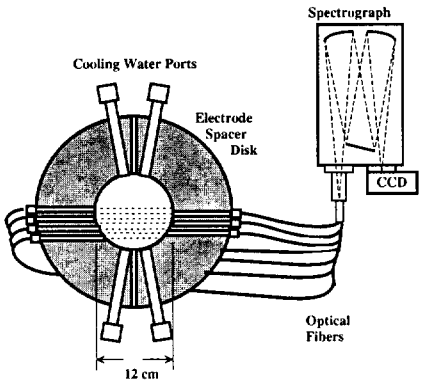


Fig. 12. Multiple line-of-sight optical disk for electrode package emission measurements.

Interpretations of emission spectra from the electrode package and plenum regions are severely constrained by a lack of knowledge about spatial gradients in flow properties and species distributions that may exist. To gain further insight, an improved optical disk with multiple line-of-sight detection capability has been fabricated for installation as a spacer disk in the electrode package of the 20 MW arcjet facility. The arrangement of the seven viewports is shown in Fig. 12 and the assumption that the flow is, on average, axisymmetric has been exploited in the design.

Measurements in the electrode region are still in the development stage at this time. There is not yet sufficient information to definitely establish the existence of thermal equilibrium within the electrode package, and the question of chemical equilibrium has not been attempted. Consequently, the impact of electrode package and arc column emission measurements on arcjet flow modeling is currently negligible.

### 2.3 Nozzle and Free Stream

In most large-scale arcjet facilities, optical access exists at the exit of the nozzle, which is usually attached to an enclosure where material tests are conducted.

Provided that populations in excited electronic levels exist, it is possible to acquire emission spectra from the free stream at the entrance to the test chamber. Normally, one would expect little or no population in excited states based on credible estimates of stream temperatures and the widely held belief that the flow is thermally and chemically frozen for most test conditions. However, if excited state populations exist, then it may be possible to use emission spectroscopy to assess the degree nonequilibrium of the free stream.

As part of an earlier spectroscopic investigation of the Ames AHF Arcjet Facility, Gopaul[26] recorded emission from the $\gamma$ $(A^2\Sigma^+ - X^2\Pi)$ and $\delta$ $(C^2\Pi - X^2\Pi)$ systems of NO in the free stream. Only rotational transitions from the lowest vibrational level of the two electronic states were detected. Using NEQAIR simulations to fit the vibrational bands by varying the rotational temperatures, values of rotational temperatures for several free stream test conditions were obtained. Since no emission was measured from levels having $v' > 0$, no assessment of the free stream vibrational temperature could be made (recall that emission from two different vibrational levels is required to determine vibrational temperature). With the assumption that the upper electronic state population was in Boltzmann equilibrium with the ground state, large NO $(X)$ populations in the free stream were inferred from the measurements. Additional CFD simulations of the nozzle flow were conducted to attempt to understand the NO populations.[27] As will be discussed below in the section on LIF measurements, it is likely that the NO $(X)$ state is not in equilibrium with the $A$ and $C$ electronic states.

In more recent measurements with a different nozzle and with different facility operating conditions, Park et al [14,28] reconfirmed the findings of Ref. 26 regarding the emitting states and vibrational levels of NO. Surveys over a wide wavelength range with long accumulation times on a CCD camera gave no indication of appreciable excited state populations for other species in the free stream flow. However, this does not rule out possible populations in metastable electronic states such as $N_2$ $(A)$, O $(^1S)$ and $(^1D)$, or N $(^2D^o)$ and $(^2P^o)$. In a second experiment, the radial distribution of excited-state NO was investigated in the free stream flow.[29] These investigations and their findings are discussed below.

### 2.3.1 Experimental Configuration for Free-Stream Measurements

A typical optical configuration for the free steam measurements is shown in Fig. 13. The spherical collection mirror was positioned to give an object to image magnification of 0.25 and a mask with eight apertures was used to image eight separate (about 3 mm apart) 0.2 mm x 0.5 mm object areas in the flow onto a CCD camera. The spatial dimension of the camera could be aligned with either the flow axis or the spanwise (radial) direction of the conical flow.

The spectrograph was equipped with a 1200 g/mm, 300-nm-blaze ruled grating and the entrance slit width was set to 50 $\mu$m. This produced a reciprocal linear dispersion of 3 nm/mm. Emission spectra were captured by a $1024 \times 256$ 2-D CCD camera array mounted at the exit plane of the spectrograph with the 1024 pixel side in the wavelength direction. The 27 $\mu$m square pixels limited the spectral coverage of the array to approximately 800 Å and the total spatial coverage to roughly 25 mm. The spectral resolution on the array and instrumental broadening were determined to be 0.8 Å/pixel and 1.6 Å FWHM, respectively.

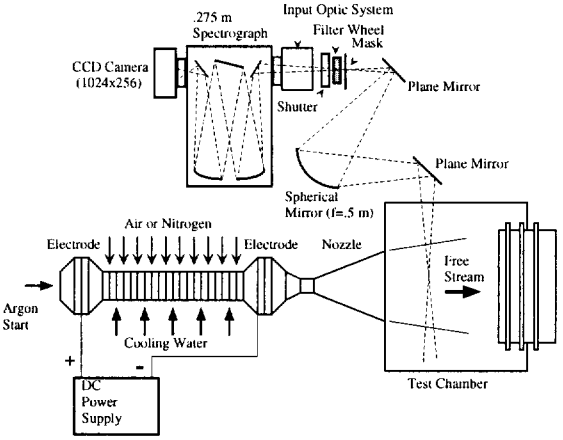


Fig. 13. Experimental setup for free stream emission measurements.

**Calibration of Optical System** The measured emission spectra were corrected for the spectral response of the mirrors, filters, grating, and CCD array. Two National Institutes of Standard and Technology (NIST) traceable standards of spectral radiance, a deuterium lamp and a tungsten ribbon-filament lamp, were used to calibrate the optical system in units of $W/cm^2 - \mu m - sr$. Details of the procedure are given in Ref. 14.

**Facility** For these tests, the arcjet nozzle was configured with a 3.81 cm diameter throat and an exit diameter of 30.48 cm. The arc heater was operated at two different test conditions that are identified as the low pressure and high pressure cases. For the low and high pressure cases the heater pressure, arc current, and arc voltage were: Low) 1.7 atm, 1141 A, and 2657 V and High) 6.8 atm, 2075 A, and 5630 V; respectively. The test gas consisted of air and argon ($\dot{m}_{Ar}$ =.03 kg/s).

### 2.3.2 Free Stream Results and Discussion

A typical free stream emission spectrum for the 2000 to 2800 Å grating position is shown in Fig. 14. This spectrum was taken on the free stream centerline, and

is representative of the eight separate spectra acquired by the CCD-based system. As mentioned in the introductory section, only emission from $v' = 0$ levels was evident for both the $\gamma$ and $\delta$ bands. As indicated in Fig. 14, the detected spectra were identified as belonging to the NO $\gamma$ and $\delta$ systems.

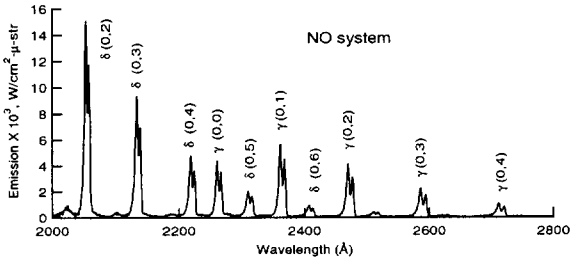


Fig. 14. Free stream spectra taken at the center of free stream and 30 cm downstream from the nozzle exit.

The rotational temperature, $T_r$ was determined from the well resolved vibrational bands in Fig. 14. The FWHM of the band intensity was calculated for different $T_r$ values using NEQAIR. In Fig. 15, the FWHM of the NO $\gamma$ (0,1) band is plotted as a function of $T_r$ with a fixed instrumental line width of 1.6 Å. Using this correlation and the measured FWHM of the NO $\gamma$ (0,1) band, a $T_r$ value was obtained for each test condition for the eight spectra along the flow axis.

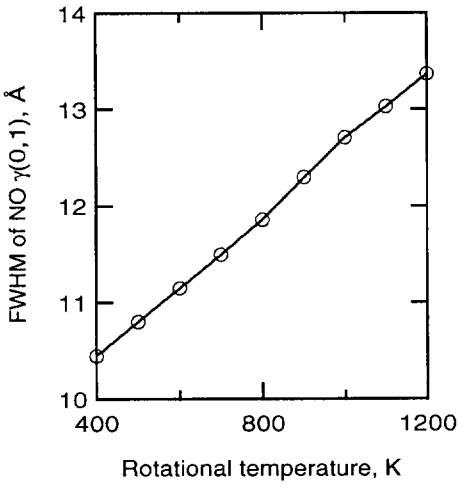


Fig. 15. FWHM of NO-$\gamma$ (0,1) band as a function of $T_r$.

Rotational temperatures for two different facility operating conditions are summarized in Table I along with the facility operating conditions for the tests. The reported values represent the average of the three rotational temperatures determined from the NO $\gamma$ (0,1), (0,2), and (0,3) features. As expected, the rotational temperature from the higher pressure, higher current test case is greater than that for the lower pressure and current case. Because the $T_r$ determination does not rely on absolute intensity, the leading contribution to the uncertainty comes from unresolved background emission underlying the NO spectral features rather than uncertainty in the intensity calibration. The cause of this background emission has not been identified. Although the level of this background signal is small, it does affect the temperature determination. A secondary contribution stems from the finite spectral resolution and its influence on the determination of the FWHM. This contribution was quantified by evaluating the scatter in the eight separate free stream measurements that were simultaneously acquired by the CCD camera. Thus, the uncertainty value indicated in the table includes both contributions.

**Table I.** Arcjet test conditions and measured rotational temperatures from free stream emission experiments.

| Run Condition & Rotational $T$ | | | | |
|---|---|---|---|---|
| Run | Pressure | Current | Voltage | Temp. |
| | atm | A | V | K |
| A | 1.70 | 1141 | 2657 | 618±38 |
| B | 6.80 | 2075 | 5630 | 989±75 |

It should be noted that the $T_r$ values given in Table I represent line-of-sight intensity averaged values for the free stream. Thus, the distribution of the NO emission in the stream must be relatively uniform for the $T_r$ values to be representative of the free stream.

**Radial Distribution of NO $\gamma$-** To ascertain the distribution of the NO emission in the free stream, a radial intensity survey was performed. For this experiment, the image was rotated 90° to align with the radial, or spanwise, direction and a modified mask was used to define four object areas separated by 8.9 mm in the flow. By tilting the first plane mirror of the collection system, four spatially distinct spectra were acquired at 6 locations spaced at 35.6 mm apart to cover the stream during a single run.

Results from the radial survey of the NO emission are shown in Fig. 16 for the low pressure, low current condition. Peak values of NO $\gamma$ (0,2) band emission are plotted as a function of radial distance for one of the four object areas that were imaged at each measurement location. Also shown on the figure is an Abel-inverted emission distribution derived from the radial measurements. As this shows a large, relatively uniform region in the central portion of the flow, it appears that the $T_r$ of NO $\gamma$ and $\delta$ states is representative of a large portion of the inviscid flow. Whether or not the rotational temperature of these excited NO states represents the rotational temperature of the ground state molecular populations has not yet been established.

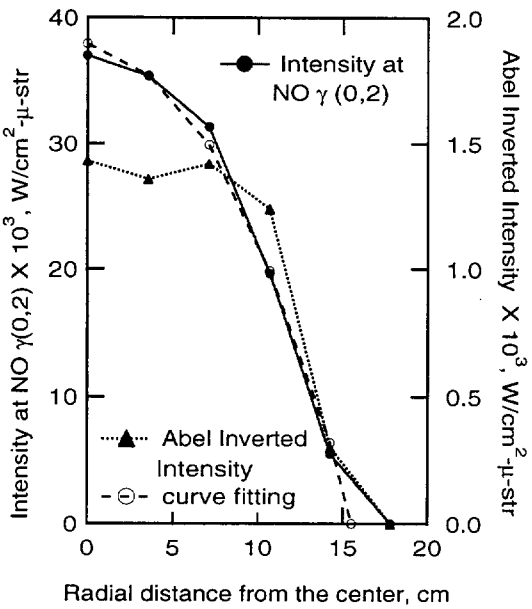


Fig. 16. NO $\gamma$ (0,2) intensity as a function of radial position.

Based on the results of these and earlier investigations, it appears that measurements of free stream rotational temperature can be made with relatively low uncertainty. This presents opportunities for instrumentation development that can enable real-time monitoring of the free stream rotational temperature with a small, dedicated spectrometer and detector.

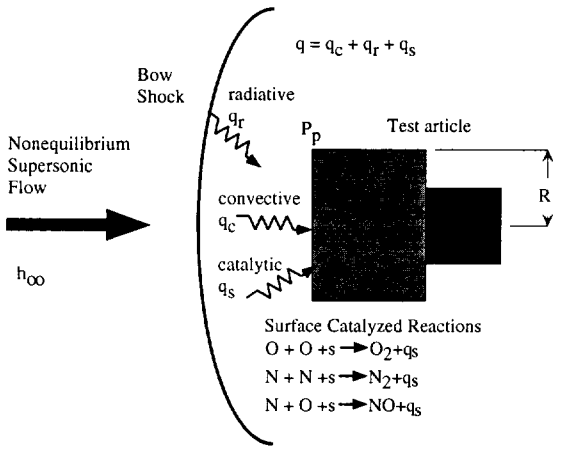


Fig. 17. Stagnation point heating configuration for a blunt-body test article.

## 2.4 Shock Layer Flows

A stagnation point heating configuration is frequently used in the development and testing of thermal protection materials in large scale arcjet facilities. With the stagnation point configuration and a supersonic free stream flow, a bow shock is formed over the test article, as depicted in Fig. 17. Flow compression by the shock causes a significant temperature rise, which populates many emitting states. For modest enthalpy levels, significant visible emission can be observed emanating from the shock layer. Thus, the potential use of shock-layer emission to characterize the flow has been investigated extensively.[3,28–34] Although similar investigations of subsonic boundary layer flows formed over blunt bodies have also been undertaken,[35,36] the discussion in this section will be restricted to shock layer measurements.

Characterization of the shock layer enthalpy by spectral analysis of emission measurements is possible if equilibrium conditions are reached within the shock layer. If equilibrium is attained, then the spectral features of radiation are a function only of pressure and enthalpy. Pressure measurements in the shock layer are routinely performed, as mentioned in the introduction. If a spectral measurement of temperature can be obtained under equilibrium conditions, then the flow enthalpy can be specified.

In recent shock layer emission experiments carried out at the Ames AHF Arcjet Facility, tests were conducted at conditions deemed likely to generate a region of thermochemical equilibrium within the shock layer; i.e., at higher stagnation pressure and with a large diameter test model.[14,28,29] In these experiments, spectrally resolved emission measurements were acquired simultaneously from multiple spatial locations along the central stagnation streamline for two different facility operating conditions. Analytical methods were developed to determine $T_r$, $T_v$, and $T_e$ of the shock layer using the $N_2^+$ 1- system and atomic oxygen lines. For one test condition, the spectrally determined temperatures were used to obtain line-of-sight averaged number densities of $N_2^+$, $N_2$, CN, and O from the shock layer emission spectra. An additional experiment was performed to evaluate the extent and influence of radial intensity gradients for the low pressure, low current condition. The experimental configuration, analytical approach, and flow property measurement results for these investigations are discussed below.

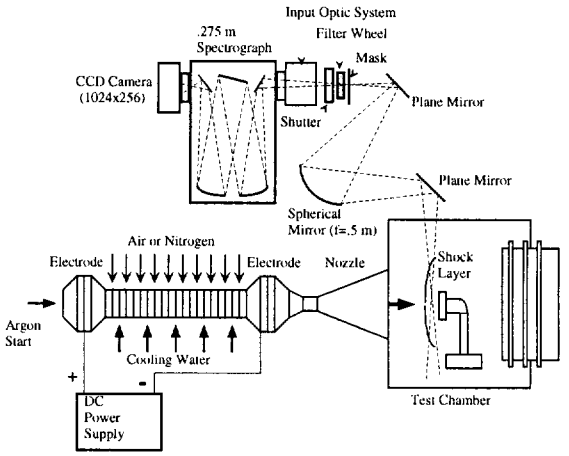


Fig. 18. Optical configuration for shock layer emission measurements in the AHF Arcjet Facility.

### 2.4.1 Experimental Configuration for Shock-Layer Measurements

For the shock layer investigations, the experimental configuration is basically the same as that given above for the free stream emission measurements. However, a 15.24 cm diameter blunt-body test article is placed in the stream and a shock layer is formed, as shown in Fig. 18. The eight apertures of the mask are now used to define eight distinct object areas, which are spaced roughly 3 mm apart, within the shock layer. The arrangement of the aperture images in the object region is shown in Fig. 19. The total distance imaged onto the CCD camera from the shock layer was limited to 25 mm, which did not allow complete shock layer coverage in a single facility run for the test conditions. Therefore, two axial positions of the test article, 34.5 cm and 36.9 cm downstream of the nozzle exit, were used to obtain spectra from the full shock layer. Facility test conditions for these experiments were the same as given above in Table I for the free stream measurements.

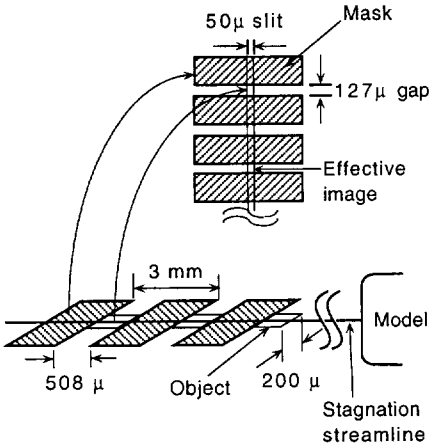


Fig. 19. Object and image planar areas defined by the mask used in the collection system for the axial shock layer survey.

### 2.4.2 Flow Properties from Emission

Before discussing the flow properties derived from the analysis of the emission spectra, it is useful to review a typical emission spectrum acquired at one of the eight spatial locations within the shock layer. This spectrum is shown in Figs. 20a-d, and it was acquired at a position 17.9 mm upstream from the face of the test article for a high current, high pressure test condition. In some of the figures, measured emission from multiple separate grating positions are joined.

In the 2000-3000 Å range, as shown in Fig. 20a, NO $\gamma$ was the most significant with some weaker emission from higher vibrational levels of the $N_2$ (2+) system. Emission from the NO $\beta$ system could also be present even though there is no distinct evidence of NO $\beta$ spectral features.

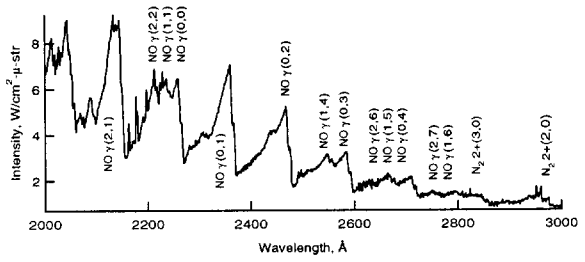


Fig. 20a. Shock-layer emission spectrum in the 2000 -3000 Å range for a flat-faced, cylindrical test article of 15.24 cm diameter.

In the 3050-3650 Å and the 3950 - 4820 Å spectral ranges, as shown in Figs. 20b and 20c, the identified transitions were attributed to NO ($\gamma$), $N_2$ (2+), $N_2^+$ (1-), and CN Violet systems. Also, several Cu atomic transitions are identified. These were expected, because copper electrodes were used in the AHF Arcjet Facility for these tests and copper is present in the stream due to arc-induced erosion.

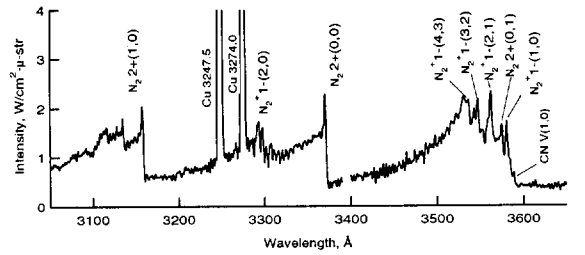


Fig. 20b. Shock-layer emission spectrum in the 3050 - 3650 Å range for a flat-faced, cylindrical test article of 15.24 cm diameter.

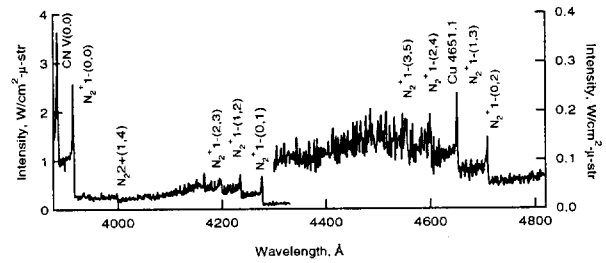


Fig. 20c. Shock-layer emission spectrum in the 3950 - 4820 Å range for a flat-faced, cylindrical test article of 15.24 cm diameter.

Example spectra for the 7500 to 9500 Å range are shown in Fig. 20d. The dominant emission features are O and N atomic lines, with a broad background contribution from $N_2$ (1+) emission. Transitions that were used to determine electronic temperatures within the shock layer are identified by their upper and lower electronic states.

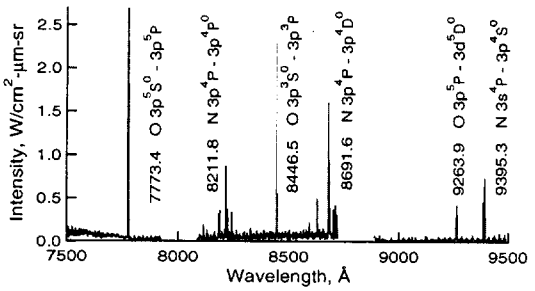


Fig. 20d. Shock-layer emission spectrum in the 7500 - 9500 Å range for a flat-faced, cylindrical test article of 15.24 cm diameter.

**Temperatures from Spectra-** As shown in Figs. 20b and 20c, the $N_2^+$ 1- band system was the most dominant one and it proved to be the most reliable for determining line-of-sight averaged values of $T_r$ and $T_v$.[24] The analytical approach is based on the use of ratios of spectrally integrated intensities in well-resolved spectral regions that are largely free of interfering emission from other species. Although peak intensity ratios were also evaluated, area ratios were selected because of their reduced sensitivity to the limited spectral resolution of the CCD camera.

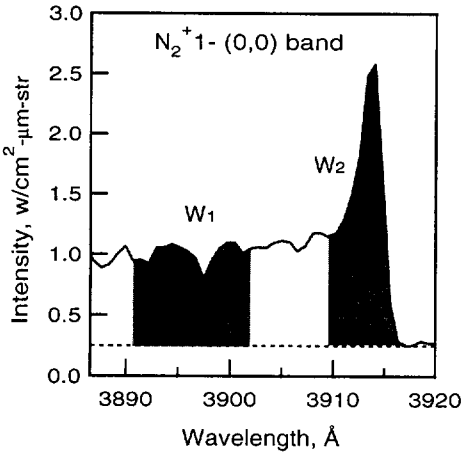


Fig. 21. A pair of areas used in $T_r$ determination.

**Rotational Temperature -** In contrast to the relatively cool free stream conditions, $T_r$ of the shock layer is quite high, and the vibrational bands are no longer completely resolved. Therefore, to evaluate $T_r$ from the shock layer spectra, an approach based on the ratio of spectrally integrated areas within a single vibrational band was developed. Details of this analysis were presented in the introductory section above, and an approximate expression relating $T_r$ to the ratio of spectrally integrated intensities was derived,

$$T_r = \frac{(\overline{J_1}(\overline{J_1}+1) - \overline{J_2}(\overline{J_2}+1))\theta_r}{\ln\left[(W_2\overline{S_{JJ}}_1\nu_1^4)/(W_1\overline{S_{JJ}}_2\nu_2^4)\right]} \quad .$$

In Fig. 21, the spectral intervals $W_1$ and $W_2$ of the $N_2^+$ 1- (0,0) band system that were used to determine $T_r$ are shown by the shaded regions. The baseline signal was taken from the minimum near the band head rather than absolute zero of the spectral intensity to reduce the contribution of any unresolved background light to the integrals.

While the approximate expression given above is useful for assessing rotational temperature sensitivity to changes in intensity ratios, it is not sufficiently accurate for determining $T_r$ values. Instead, NEQAIR simulations were run to develop correlations between the intensity ratio values and $T_r$.[14] As an example, the ratio of integrated spectral intensities from the two regions is shown in Fig. 22 as a function of $T_r$ and $T_v$. Although the intensity ratio shows some sensitivity to $T_v$ at higher rotational temperature, it appears to be relatively insensitive to $T_v$ over most of the range of temperatures anticipated in the shock layer.

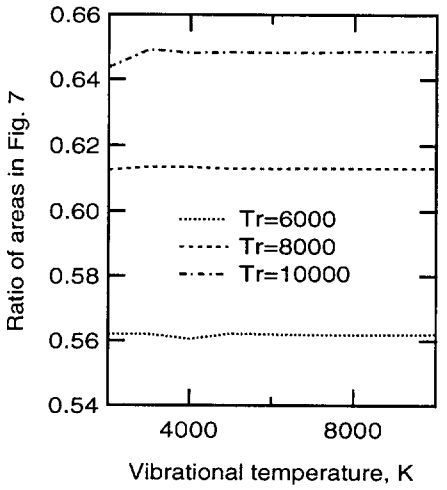


Fig. 22. The ratio of spectral integrals from the $N_2^+$ 1- (0,0) band as a function of $T_r$ and $T_v$.

**Vibrational Temperature -** The determination of $T_v$ from $N_2^+$ 1- system emission involves an approach similar to that used in $T_r$ evaluation, except now the spectral integrals are taken from two different vibrational bands with $v_1' \neq v_2'$. In Fig. 23, what were determined to be the optimum intervals for this application[14] are shown by the extent of the shaded region. To maximize signal levels and permit easy identification, the intervals were restricted to the band-head spectral regions. Again, to reduce the contribution of background signal, each area was measured from the minimum close to the band head. As with $T_r$, the simplified analytical expression that was developed in the introductory section above to relate $T_v$ to the measured intensity ratio,

$$T_v = \frac{(v_1 - v_2)\theta_v}{\ln\left[(I_2 q_1 \nu_1^4/(I_1 q_2 \nu_2^4 f(T_r))\right]} \quad ,$$

is only useful for evaluating differences in uncertainty for different spectral features. Accurate determination

of $T_v$ requires the use of NEQAIR, or a similar spectral model to account for the coupling between $T_r$ and $T_v$ as well as possible interfering emission from other species. Using NEQAIR, correlations were developed between $T_v$ and the spectrally integrated band intensities.

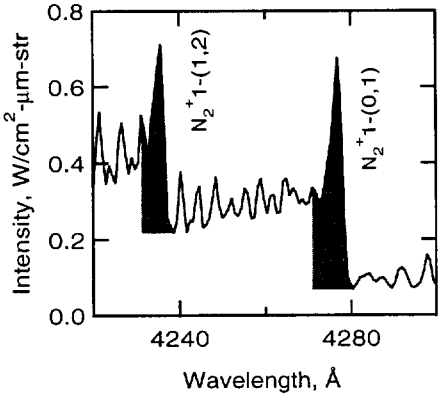


Fig. 23. A pair of areas used in $T_v$ determination.

**Electronic Temperature** - Two sets of atomic oxygen transitions were used to determine electronic temperatures in the analysis of spectra from these experiments, and their wavelengths were: 1) 7773.4 and 9263.9 Å, 2) 8446.5 and 9263.9 Å. These transition pairs had adequate signal-to-noise ratios and their difference in upper-state energy levels is greater than other possible two-line combinations in this spectral region. As discussed in the introductory section on emission measurements, the uncertainty in $T_e$ due to the uncertainty in intensity decreases as the difference in energy levels increases (see Eq. (16)). For $T_e$, the analytical expression that was derived in the introductory section,

$$T_e = \frac{(E_1 - E_2)/k}{\ln[(I_2 A_1 g_1 \nu_1)/(I_1 A_2 g_2 \nu_2)]} \quad ,$$

was used to determine electronic temperature values from the shock layer emission spectra. However, the influence of the unresolved background emission that underlies the atomic transitions was evaluated using NEQAIR.

**Line-of-sight Integrated Species Densities** - With the assumption that $T_e = T_v$ for the molecules, the integrated species densities along the line-of-sight could be determined from the relation,

$$nL = \frac{I 4\pi Q}{g_u A_{ul} h\nu_{ul}} e^{E_u/kT_e} \quad , \qquad (28)$$

which was derived by spectrally integrating Eq. (14) and solving for $nL$. Values of $nL$ were obtained for $N_2$, CN, and $N_2^+$ using $T_v$ determined from the $N_2^+$ band head ratios.

**Uncertainty of Spectral Analysis** - For the temperatures derived from emission measurements, the leading contributions to the uncertainties were typically: 1) the background signal that is thought to consist of stray light and contributions from unidentified species; 2) finite instrumental resolution of the important spectral features, which can be seen in Figs. 21 and 23; 3) coma from the off-axis reflectors in the spectrograph, which shifted the spectra in wavelength for different locations on the CCD camera; and 4) uncertainties in spectroscopic constants.

Uncertainties arising from the absolute intensity calibration are considerably smaller than the contributions listed above for temperatures because ratios of spectral features were used instead of absolute intensities. Whenever possible, ratios of spectral features from a single grating position, or, in the case of electronic temperatures, adjacent grating positions were used to minimize uncertainty contributions from the instrumental calibration. For integrated species densities, however, the absolute calibration uncertainty does contribute, but it is still less important than the uncertainty in electronic temperature (or $T_v$, depending on what was assumed). Possible additional uncertainty contributions from facility operation and spatial averaging are discussed below.

### 2.4.3 Shock Layer Results and Discussion

Results are presented for shock layer temperature and species density measurements that were derived from spectrally resolved emission emanating from multiple locations within the shock layer. All of the measured quantities represent time-averaged values obtained during the steady operation of the facility. Spectral surveys of the shock layer emission were performed for two different optical configurations. In the first configuration, multiple spectra were acquired along the central stagnation streamline for the high and low pressure flow conditions given in Table I. A different optical arrangement was used to perform a survey of the shock layer emission at the lower pressure condition of Table I to assess the radial intensity gradients within the shock layer.

**High Pressure Case** - Line-of-sight averaged flow temperatures for the high pressure test case are shown in Fig. 24, which presents shock layer profiles of $T_r$ and $T_v$ for two separate facility runs at the same nominal test conditions. Uncertainties in the measured values are indicated by error bars. For both $T_v$ and $T_r$, the measurements indicate a general trend of decreasing temperature as the test article surface is approached. Agreement between the two different sets of $T_v$ and $T_r$ measurements is generally quite good, which indicates that the facility performance is reasonably repeatable. For each test, the line-of-sight averaged $T_v$ and $T_r$ values do not overlap within their estimated uncertainties; $T_r$ is consistently higher than $T_v$. While this difference may indicate the absence of thermal

equilibrium, it may also be indicating the influence of differential averaging effects along the line-of-sight. This latter effect is important, since contributions to the measured intensity come from the vicinity of the shock front at all spatial locations. Near the shock, the flow is more likely to be in nonequilibrium and this nonequilibrium contribution to the line-of-sight averaged intensity may be significant. Finally, the uncertainty in $T_r$ is greater than in $T_v$. This arises from the difference in sensitivities of the temperatures to the respective intensity ratios. Electronic temperatures are not shown in Fig. 24 because it was found that one of the transitions used in determining $T_e$, the 8446 Å transition of O, has a large, unresolved background contribution that cannot be properly accounted for in the analysis. This issue is discussed further below.

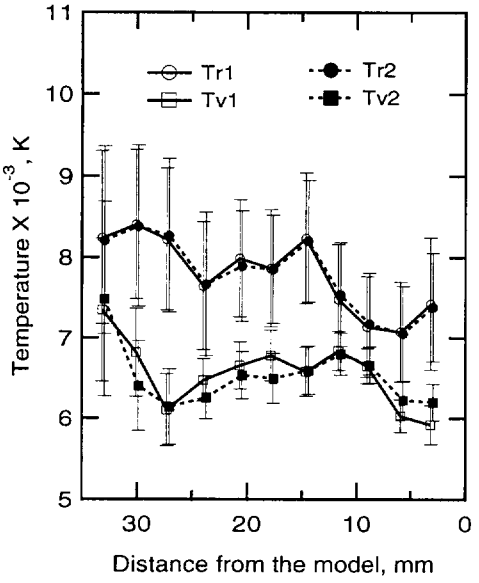


Fig. 24. Shock layer $T_r$ and $T_v$ profiles for the high pressure case. Note that data are shown for two different facility runs and that the flow goes from left to right. Lines are drawn to guide the eye.

**Species Densities for High Pressure Case -** Line-of-sight integrated species densities, $nL$, of $N_2$, CN, and $N_2^+$ are shown in Fig. 25 for one run of the high pressure case. The electronic temperature for these species was assumed to be equal to the line-of-sight averaged vibrational temperature that was measured using the $N_2^+$ intensity ratio (see Eq. (28)). All of the integrated species densities appear to increase moving from the shock front into the shock layer and then decrease as the test article surface is approached. The uncertainties are again indicated by the size of the error bars. Uncertainty is greatest for $nL$ for $N_2$, owing to the use of (2+) system emission, which has a high upper state energy level, to determine the integrated density. Recall that for species densities, the uncertainty in electronic temperature is amplified by $E_u/kT_e$. The upper state energy levels of CN and $N_2^+$ are approximately half of that of the $N_2$ C state. Consequently, the uncertainty in $T_e = T_v$ has less impact on those species.

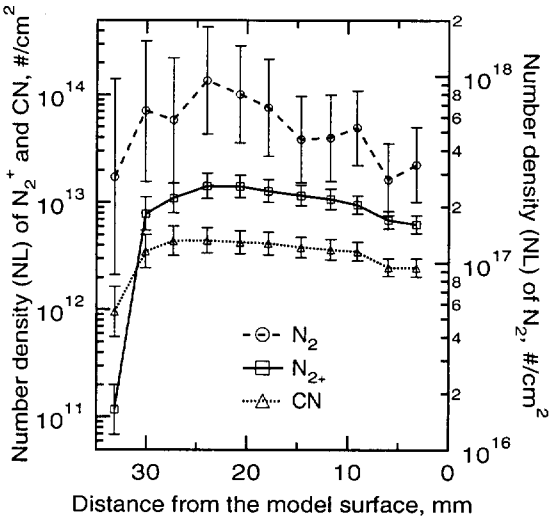


Fig. 25. LOS integrated number densities of $N_2^+$, $N_2$, and CN along the stagnation streamline.

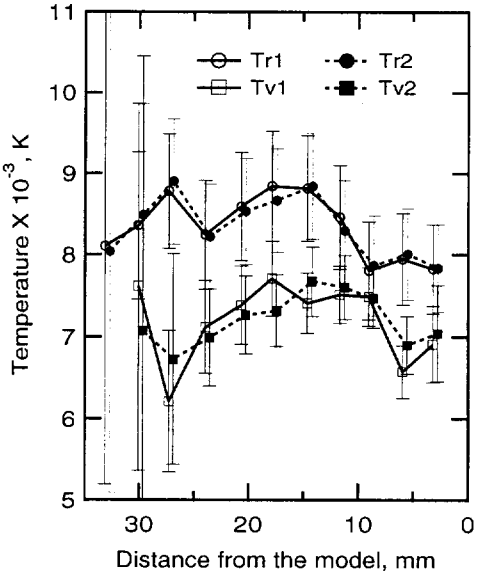


Fig. 26. Shock layer $T_r$ and $T_v$ profiles for the low pressure cases. Note that data are shown for two different facility runs.

**Low Pressure Case -** Line-of-sight integrated $T_r$ and $T_v$ values for the lower current, lower pressure case are shown in Fig. 26. Again, results from two different facility runs are shown, and the agreement between the measurements from the two different runs is reasonable. The agreement is generally better for the rotational temperatures and improves for the measurement locations nearer to the test article. The uncertainties are largest near the shock, owing to relatively weak $N_2^+$

emission signals superimposed on a larger background signal. Although $T_v$ and $T_r$ appear to nearly converge at 10 mm, the two temperatures do not overlap near the test article surface. As in the high pressure case, this could indicate thermal nonequilibrium, or it could indicate differential averaging effects along the line-of-sight. Further analysis of the emission has indicated that the temperatures near the shock may be less reliable owing to differences in intensities between the two separate runs.[29]

**Radial Temperature Profiles -** To better understand the spatial averaging of intensity within the shock layer, a radial survey was conducted at the low pressure conditions using the test article and optical components described above. However, as noted in the discussion of the free stream survey, the mask was modified to reduce the number of imaged areas to four and the image was rotated to align with the radial flow direction. For the shock layer survey, four spatially distinct spectra were acquired at intervals of 17.8 mm to cover the entire shock layer. The survey was conducted at a location 12.7 mm upstream of the test article surface. Details of the experiment are given in Ref. 29. The emission spectra that were acquired at multiple locations in the radial direction during a single facility run were analyzed by performing an Abel inversion, as described in the introductory section on emission diagnostics above. Rotational, vibrational, and electronic temperature values were then derived from the spatially resolved emission distribution using the analytical methods that were described above.

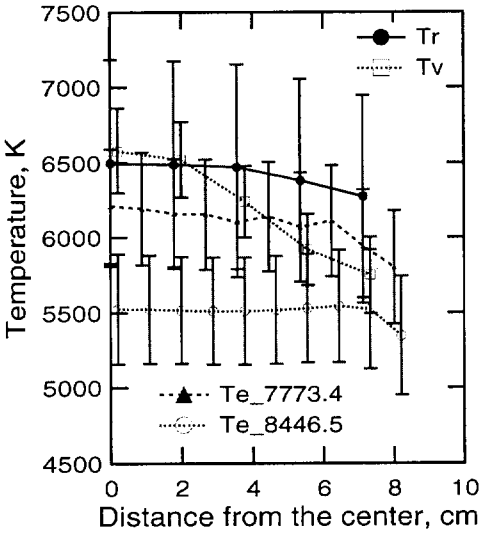


Fig. 27. Radial temperature profile in the shock layer at 12.7 mm upstream from the test article. Labels for $T_e$ indicate the shorter wavelength O transition of the pair.

Electronic, vibrational, and rotational temperatures that were determined for each radial position for the shock-layer flow are shown in Fig. 27, where they are plotted as functions of distance from the central flow axis along the radial direction. Although the three temperatures were all measured at the same location, the values are offset slightly from each other to improve clarity. Twice as many electronic temperatures are shown, because values were determined for the first and third object areas at each location. Only the first object area was used to derive vibrational and rotational temperatures. As before, error bars for each temperature are used to indicate uncertainties. Recall that two different $T_e$ values were determined using two sets of oxygen transitions: 1) 7773.4 and 9263.9 Å, and 2) 8446.5 and 9263.9 Å. Electronic temperatures from these transition pairs are identified by the shorter wavelength transition.

The measured temperatures presented in Fig. 27 can be seen to agree within their error bounds, except $T_e$ based on the oxygen lines at 8446.5 and 9263.9 Å. Since this $T_e$ is consistently lower than the value derived from the other atomic lines, it is likely that even after background subtraction there is still significant emission from other species in the spectrally integrated signal. Supporting evidence was found by comparing the inferred $nL$ densities of atomic oxygen using the two different $T_e$ values. The value obtained using the 7773.4 and 9263.9 Å line pair was more consistent with estimates of O densities based on the impact pressure measurement and the known oxygen mass flow.[29]

Excluding the $T_e$ values derived from the 8446.5 Å transition pair, the three different measured temperatures agree within their error bounds, which indicates that the flow could be in thermal equilibrium. Further analysis to assess the chemical state of the shock layer flow at the measurement locations is currently underway.

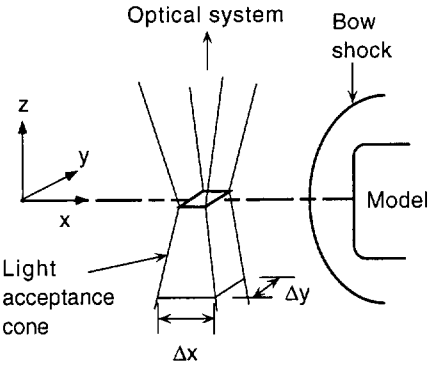


Fig. 28. Schematic representation of the light collection cone.

**Spatial Averaging -** In an attempt to better understand the averaging of the emission signals along the line-of-sight, a ray tracing analysis of the light collection geometry was performed for the initial f/50 experimental configuration that was used in the axial shock layer survey. The analysis indicated that the spatial

resolution of the light collection system was not what had been designed. An idealized representation of the light acceptance cone for a single object area defined by the optical components is shown in Fig. 28. In reality, the planar cross section depicted on the figure at the flow centerline is distorted by astigmatism introduced by the off-axis orientation of the spherical mirror of the collection system. Light rays in the local x and y directions are actually focused at different locations along the line-of-sight dimension because of this astigmatism.

Using ray-tracing software, the dimensions of the light collection cone were calculated at different locations along the line-of-sight and the results are shown in Fig. 29. Calculations of $\Delta x$ and $\Delta y$ were done from 8 cm above to 12 cm below the stagnation streamline. Separation of the focal points for $\Delta x$ and $\Delta y$ is apparent, and the size of the imaged area extends to roughly .28 cm for $\Delta y$ and .43 cm for $\Delta x$ near where the sight line crosses the shock wave. These dimensions are on the order of the shock stand-off distance for these experiments, and it is likely that additional spatial averaging along the spanwise and streamwise directions was introduced into the measurements. In view of this result, the aperture was closed further in the radial survey experiment to increase the system f/# to 100 and thereby minimize this effect.

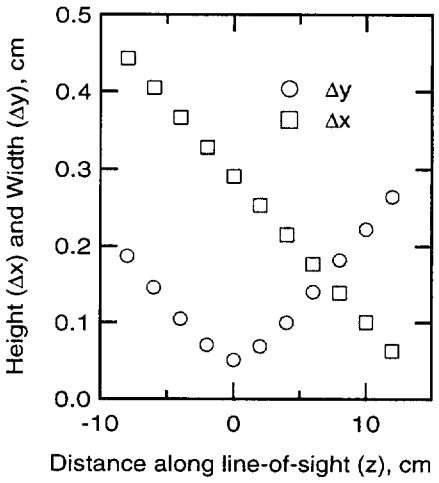


Fig. 29. Dimensions of the light cone of Fig. 28 as a function of distance along the line-of-sight direction.

**Uncertainty in Arc-Jet Conditions** - In all of the work discussed thus far, the operating condition of the facility is assumed to be constant. However, fluctuations in shock-layer emission could be observed visually during the experiments. For one electrode package experiment, the temporal variation of the 7773.4 Å atomic oxygen transition intensity was monitored. A running-averaged signal value was calculated over a fixed time interval. The standard deviation of this averaged signal indicated the fluctuation level of the raw data. For $t_{exp}$ >2 s, the fluctuations became negligible. Thus, in the more recent experiments several neutral density filters were used so that the shutter could be opened longer than 5 s without saturating the CCD camera. This was not done for the axial shock-layer emission surveys, which may help explain the large scatter in $T_e$ values near the shock front for those experiments.[14]

## 2.5 Summary of Emission Measurements

Results of the analysis of emission signals acquired in the electrode package region indicate that the gas is probably optically thick and that radiative transport must be taken into account. However, by assuming that the flow property and species distributions are uniform across the line-of-sight, a correction for self-absorption was developed and the $T_e$ values derived from O and N emission exhibited good agreement.

Line-of-sight integrated values of $T_r$, $T_v$, and $T_e$ were obtained within the shock layer formed over a blunt-body placed in the stream. Profiles were obtained in the axial direction, normal to the blunt-body surface for two different operating conditions and in the radial, or spanwise, direction for the low pressure condition. Simplified interpretations of the emission spectra based on the assumption that the intensity gradients are negligible along the line-of-sight appear to be in error. Results from the radial survey at a single axial location within the shock layer indicate a large region of thermal equilibrium when the temperatures are derived from Abel-inverted intensities. This shock-layer result was obtained at relatively low stagnation pressure with a 15.24 cm diameter flat-faced cylinder. A similar radial survey conducted with the test article out of the stream indicated that the NO $\gamma$ band emission is relatively uniform over a large spanwise distance. Thus, the rotational temperatures derived from the FWHM of NO-$\gamma$ bands can be considered to be representative of the stream.

An additional observation from this work is that a ray-trace analysis of the light collection system is required to understand additional degradation of spatial resolution that may result from setting the system f/# too low. This type of analysis can also be used to guide the alignment the system to optimize the distribution of object area dimensions about the target focal location, and thereby minimize off-axis contributions to the light collection. Finally, knowledge of the light collection volume defined by the ray tracing is required in order to reliably compare measured emission spectra with calculations.

Further work will include completing the analysis of the Abel-inverted emission results to assess chemical equilibrium within the shock layer. This analysis is important for determining the state of the shock-layer

flow and may help improve current analytical methods used to relate the arcjet test conditions to flight environments.

## 3.0 LIF Measurements in Large-Scale Arcjet Facilities

**Introduction -** The discussion of flow properties derived from emission measurements in large-scale arcjet facilities mentioned two drawbacks to emission-based property measurements: the quantity of measurements required to obtain spatially resolved emission intensities, and the required assumption that the thermodynamic behavior of the sparsely populated excited electronic states is representative of the ground states. Concerns about these issues have motivated investigations of laser-spectroscopic techniques, such as laser-induced fluorescence (LIF). Laser-induced fluorescence techniques offer an attractive alternative to emission-based measurements, because of their ability to probe ground state populations with high spatial resolution. Following a brief introduction to the basic principles of LIF measurements, recent results from applications of LIF to large-scale arcjet facilities are presented and discussed.

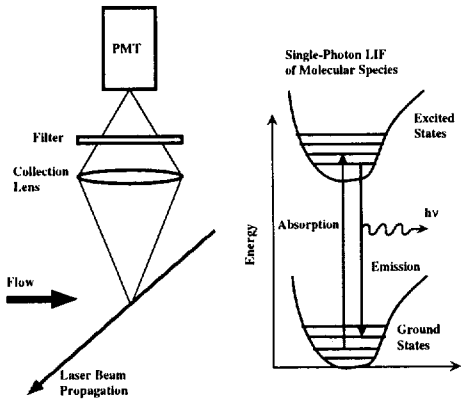


Fig. 30 Single-photon LIF process for a molecular species.

### 3.1 Laser-Induced Fluorescence

The LIF process involves two steps, absorption and fluorescence. Provided that the allowed absorption transitions for a particular species are optically accessible, then LIF can be used to probe ground state populations. This is important for arcjet flow applications because the ground electronic states of the major species are the most heavily populated. A simplified diagrammatic rendering of LIF is shown in Fig. 30 for a diatomic molecule. At the right of the figure, two bound electronic states with vibrational energy levels are indicated by the potential curves. The LIF process is indicated by the vertical arrows with the upward arrow representing absorption of a photon from the laser and the downward arrow representing fluorescence, which is accompanied by the emission of a photon. Other depopulating mechanisms, such as quenching and predissociation, can also operate on the upper state population.

A generic experimental configuration is shown at the left of Fig. 30 to illustrate the spatially resolved nature of the LIF measurements. Unlike absorption and emission diagnostics, LIF provides localized measurements, since only the volume defined by the intersection of the image of the detection aperture and the laser beam produces the recorded signal. Flow axisymmetry is therefore not required for making spatially resolved LIF measurements. Before discussing how specific flow properties are measured, some background information about the LIF process is required.

**Single-Photon LIF Rate Equations -** The first step of the LIF process involves the absorption of a photon. Absorption is described by Beer's law,[6] which states that the change in intensity of light at a certain frequency through an optically thin absorbing medium is

$$\frac{dI_\omega}{dz} = -\alpha_\omega \, I_\omega ,$$

which can be integrated directly and rearranged to yield

$$I_\omega = I_{0\omega} e^{-\alpha_\omega z} \quad . \tag{28}$$

Species and thermodynamic information is contained in the absorption coefficient $\alpha_\omega$, which can also be expressed in terms of an absorption cross section[6]

$$\alpha_\omega = n \, f(T) \, \sigma_{12} \phi(\omega) \quad . \tag{29}$$

In the above expression, we have introduced the spectrally integrated cross section $\sigma_{12}$, a line shape function $\phi(\omega)$, and shorthand notation for the Boltzmann population fraction $f(T)$.

$$f(T) = \frac{n_i}{n} \frac{g_i e^{-E_i/kT}}{Q} \quad ,$$

which was discussed extensively in the description of emission measurements.

A model of the LIF process is required to determine gasdynamic quantities from measured fluorescence signals. This model can be derived by solving the equations that govern the populations of the energy levels involved in the LIF process. For a simple system consisting of only two, nondegenerate energy levels, the appropriate rate equations are[37]

$$\frac{dn_1}{dt} = -b_{12} n_1 + (b_{21} + A_{21} + Q_{21}) n_2 \tag{30}$$

for the lower level population and

$$\frac{dn_2}{dt} = b_{12} n_1 - (b_{21} + A_{21} + Q_{21}) n_2 \tag{31}$$

for the upper level. In the above equations, $n_1$ and $n_2$ are the number densities of the two levels, which

are related through the total population in the initial level before the laser is switched on, $n_1^0 = n_1 + n_2$; $b_{12}$ and $b_{21}$ are the stimulated absorption and stimulated emission rates; $A_{21}$ is the spontaneous emission rate; and $Q_{21}$ is the collisional quenching rate. Predissociation from the upper level is assumed to be negligible. The stimulated absorption rate can be expressed as the product of the spectral absorption cross section, $\sigma_\omega$, and the photon flux, $\Phi$,[38]

$$b_{12} = \sigma_\omega \Phi \quad , \tag{32}$$

where $\sigma_\omega = \sigma_{12}\phi(\omega)$ and $\Phi = I/\hbar\omega_{12}$.

By using the total population relation to eliminate $n_1$ from Eq. (31) and integrating directly, the time-dependent expression for the upper state population is obtained,

$$n_2 = \frac{b_{12}n_1^0}{r}\left(1 - e^{-rt}\right) \quad , \tag{33}$$

where $r = (b_{12} + b_{21} + A_{21} + Q_{21})$ is the sum of all the rates. The measured LIF signal depends on the upper state population, and can be expressed in general terms as

$$S(t) = \hbar\omega_{21} n_2(t) A_{21} \frac{\Omega}{4\pi} V_c \quad , \tag{34}$$

where $\Omega$ is the solid angle of the collection system that is used to observe the probe volume, $V_c$, which is defined by the collection optics (often it is the product of the beam area, $A_p$, times observed length, $L$).

A pulsed laser system is often employed in arcjet diagnostic applications, and the detection electronics integrate the LIF signal over the laser pulse duration,$\tau_p$. The only time-dependent term in the expression above is the upper state population, so the integral involves

$$\int_0^{\tau_p} n_2(t)dt = \frac{b_{12}n_1^0}{r}\int_0^{\tau_p}\left(1 - e^{-rt}\right)dt \quad .$$

The resulting expression,

$$\int_0^{\tau_p} n_2(t)dt = \frac{b_{12}n_1^0}{r^2}\left(e^{-r\tau_p} - 1\right) + \frac{b_{12}n_1^0\tau_p}{r} \quad ,$$

can be simplified by considering the magnitudes of the rates and the temporal interval. For a pulsed, UV laser system operating near 225 nm, with 0.1 mJ pulse energy, a 1 mm beam diameter at the probe volume and a 10 ns temporal pulse length, the pulse intensity is $\approx 10^6$ W/cm$^2$. For 225 nm wavelength photons, the photon flux $\Phi$ for this intensity is $\approx 10^{24}$ cm$^{-2}$ sec$^{-1}$. The absorption cross section can be derived from the Einstein A coefficient for spontaneous emission[38]

$$\sigma_\omega = \frac{g_2}{g_1}\frac{\pi^2 c^2}{\omega_{21}^2} A_{21}\phi(\omega) \quad .$$

Using the value published by Eckbreth[37] for $A_{21}$ for the (0,0) band of the NO $\gamma$ system, and assuming that the combined laser and transition line width has a FWHM of $\approx .3$ cm$^{-1}$ at 225 nm, then $\sigma_\omega(0,0) \approx 5(10)^{-14}$ cm$^2$. The pumping rate for a NO $\gamma$ (0,0) transition is then $b_{12} \approx 5(10)^{10}$ sec$^{-1}$ from Eq. (32). This rate dominates all others in the total rate expression, $r = (b_{12} + b_{21} + A_{21} + Q_{21})$, used in this two level analysis. For a typical gate integration time on the order of 100 ns,

$$\left(e^{-r\tau_p} - 1\right) << r\tau_p \quad ,$$

and the following simplified result is obtained,

$$\int_0^{\tau_p} n_2(t)dt \cong \frac{b_{12}n_1^0\tau_p}{r} \quad .$$

With this result, the expression for the temporally integrated energy incident on a photodetector becomes

$$\begin{aligned} S &= \int_0^{\tau_p} S(t)dt \\ &= \hbar\omega_{21}A_{21}\frac{\Omega}{4\pi}V_c n_1^0 \tau_p \frac{b_{12}}{(b_{12} + b_{21} + A_{21} + Q_{21})} \end{aligned}$$

By rewriting the total rate expression as

$$b_{12} + b_{21} + A_{21} + Q_{21} = (b_{12} + b_{21})\left(1 + \frac{(A_{21} + Q_{21})}{(b_{12} + b_{21})}\right)$$

and by replacing the stimulated absorption and emission rates with their definitions, (*i.e.*, $b_{12} = B_{12}^\omega I_\omega/c$), the temporally integrated signal can be expressed as,

$$S = \hbar\omega_{21}A_{21}\frac{\Omega}{4\pi}V_c n_1^0 \tau_p \frac{B_{12}^\omega}{B_{12}^\omega + B_{21}^\omega}\frac{1}{1 + \frac{I_{sat}}{I_\omega}} \quad ,$$

where $I_{sat} \equiv (A_{21}+Q_{21})c/(B_{12}^\omega + B_{21}^\omega)$ is the saturation intensity[37] and $B_{12}^\omega$, $B_{21}^\omega$ are the Einstein coefficients for stimulated absorption and emission. For modest laser intensities, $I_\omega << I_{sat}$, and the expression for the energy incident on the photodetector simplifies further to

$$S = \frac{\Omega}{4\pi}V_c \frac{A_{21}}{A_{21} + Q_{21}} n_1^0 (I_\omega \tau_p)\hbar\omega_{21}\frac{B_{12}^\omega}{c} \quad .$$

Finally, if the spectral intensity of the pump laser is defined such that $I_\omega = I\phi(\omega) = \phi(\omega)\int I(t)dt/\tau_p = \phi(\omega)E_p/A_p$, where $E_p$ is the pulse energy, then the detected signal can be written as,

$$S = \frac{\Omega}{4\pi}V_c \frac{A_{21}}{A_{21} + Q_{21}}\frac{E_p}{A_p}\sigma_{12}\phi(\omega)f_1(T)n \quad , \tag{33}$$

where the substitution, $n_1^0 = f_1(T)n$, for the population of the initial level has also been made.

In Eq. (33), the dependence of the LIF signal on thermodynamic parameters is manifested in several terms. The initial population in the pumped level depends on species density, $n$, and on temperature through the Boltzmann population fraction, $f_1(T)$, while the collisional quenching rate, $Q_{21}$, depends on the pressure, temperature, and collision partner. Except in rare cases, such as for highly predissociated species or extremely broad laser band widths, the absorption line shape function, $\phi(\omega)$, also depends on temperature and pressure through the mechanisms of Doppler and collisional shift and broadening, which are discussed below for two-photon LIF measurements.

### 3.2 Single-Photon LIF of Cu and NO

Demonstrations of single photon LIF measurements in arcjet facilities using Cu as the target species have been reported at NASA Johnson Space Center[39,40] (JSC) for pointwise configurations and at ISAS,[41] in Japan, for a planar laser sheet configuration. In the JSC arcjet experiments, the measured LIF signals were analyzed to determine velocity and translational temperature from the Doppler shift and Doppler broadening of the excitation profile at a single location in the arcjet stream.[40] The planar measurements using Cu-LIF at ISAS were used to determine a two-dimensional map of the flow velocity.

Copper is present in most arcjet flows as a result of arc-induced erosion of the copper electrodes, but it is usually (hopefully) a minor species. The two applications of Cu-LIF above indicate the ubiquitous nature of copper in arcjet flows, since the JSC facility is a constricted-arc heater and the ISAS facility used a Huels-type heater. Estimates of copper loading on the order of 100 to 1000 ppm in the test gas flow have been derived from mass loss analyses of electrodes (see Ref. 41, for example) Unfortunately, the copper erosion process is difficult to characterize because electrode erosion is inherently unpredictable. It is likely that copper is introduced into the flow in multiple phases owing to liquefaction of the electrode surface from the intense heating at the arc attachment point. This raises questions about both the spatial and temporal uniformity of the copper distribution in the stream and its fidelity as a tracer atom for velocity measurements.

Nitric oxide has also been used as a fluorescing species in arcjet streams by the same researchers[39,42], as well as the research group at IRS,[43] in Germany. No quantitative measurements of flow properties from NO-LIF were reported from the JSC group, but the other groups used NO-LIF to derive temperature and species information. The enthalpies determined from energy balance methods were typically $< 10$ MJ/kg for the JSC and ISAS investigations.

For air flows, NO is also a minor species, and depending on the stagnation enthalpy, pressure, and expansion process, concentrations in the free stream vary widely. Results of an investigation of NO LIF in the Ames AHF Arcjet Facility illustrate this point. Based on earlier free-stream emission measurements in the same facility, instrumentation was implemented to probe NO in the free stream flow[44] using LIF to confirm the implied NO ($X$) populations that were predicted by a computational flow simulation.[27] Despite the sensitivity of LIF for NO ($X$) population measurements using ro-vibrational transitions of the $\gamma$ system, no detectable signal was found from the flow centerline. An assessment of the [NO] detectivity of the LIF instrumentation that was used in the investigation[44] indicated that the NO ($X$) population was $\leq 10^{13}$ cm$^{-3}$. The absence of a measurable NO ($X$) population is not surprising, since the enthalpy levels in this facility are typically $> 10$ MJ/kg. Given that the free stream flow is not in thermochemical equilibrium, the discrepancy between observed NO ($A$) state emission and absence of NO ($X$) state absorption is also not surprising. It is possible that the ground state NO population is due entirely to radiative transitions, and therefore may only be on the order of the ($A$) state population. Alternative mechanisms for producing NO ($\gamma$) and ($\delta$) band emission in the free stream are being investigated.

### 3.3 Two-Photon LIF of O and N

**Introduction** - Although the single-photon LIF measurements discussed above have yielded useful information about arcjet flows, the two target species most commonly used, NO and Cu, are minor flow constituents. As such, it is impossible to characterize the arcjet test stream from NO or Cu measurements alone. More useful information would be obtained from LIF measurements of the major species, which include atomic oxygen, atomic nitrogen, di-nitrogen, and argon for air flows. For example, it is important to know the degree of dissociation in nonequilibrium arcjet flows, because considerable energy can reside in oxygen and nitrogen chemistry. If the mass flows of the facility gases are known at any point, and atomic species concentrations are measured in the free stream, then the degree of dissociation and chemical energy level can be determined. Unfortunately, single-photon transitions for N and O require an excitation source at VUV wavelengths, which is difficult to implement in large-scale facilities. LIF excitation of O and N is still feasible, however, if two UV photons are used to provide the transition energy.[45]

Two-photon LIF measurements in large-scale arcjet facilities were demonstrated by Bamford and his coworkers in a series of pathfinding investigations conducted in the Ames AHF Arcjet Facility.[46,47] The two-photon

LIF of N technique has been developed further to obtain more information from the flow.[48,49] Results from these more recent investigations are discussed below.

A schematic representation of two-photon LIF is given in Fig. 31, where the excitation process is indicated by the vertical arrows and a single radiative transition from the upper level is shown for both O and N. Note that the experimental configuration is no different from that of single-photon LIF; both single- and two-photon strategies provide spatially-resolved, species-selective information. As was the case for quantitative, single-photon LIF measurements, a mathematical model of the two-photon LIF process for the target species is required to derive gasdynamic flow properties from the measured signals.

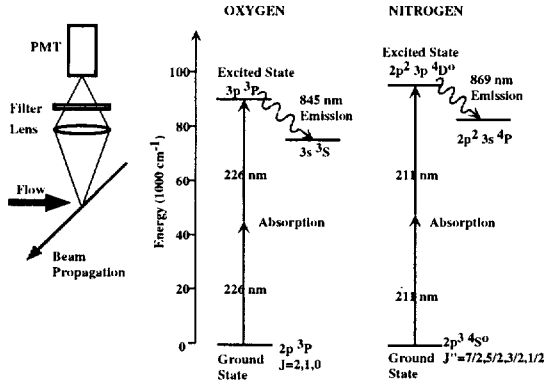


Fig. 31. Two-photon LIF technique and energy levels for O and N that are used in this work.

A complete derivation of the expression for the measured fluorescence signal resulting from two-photon excitation of atomic oxygen is given by Bamford et al.[50] The two-photon nature of the excitation process is manifested primarily in the stimulated absorption rate,

$$b_{12}^{(2)} = \sigma_{\omega}^{(2)} \Phi^2 \quad ,$$

which now depends on the square of the photon flux $\Phi$. In the above expression the two-photon excitation cross section, $\sigma_{\omega}^{(2)}$, is related to the spectrally integrated cross section, $\sigma_{12}^{(2)}$, by

$$\sigma_{\omega}^{(2)} = \sigma_{12}^{(2)} G^{(2)} \phi(\omega) \quad ,$$

where $G^{(2)}$ is the second-order coherence factor that contains the effects of unresolved, ultrafast fluctuations of the laser excitation pulse on the temporally integrated signals.[51]

Using the same UV laser parameters specified in the discussion of rate magnitudes for single-photon LIF above, the stimulated absorption rate can be estimated for two-photon LIF. For the $J = 2$ level of atomic oxygen, the spectral two-photon excitation cross section for line center excitation[50] is $\sigma_{\omega}^{(2)} = 4.8(10)^{-46}$ cm$^4$ sec. As before the photon flux is $\Phi \approx 10^{24}$ cm$^{-2}$ sec$^{-1}$, and the stimulated absorption rate is therefore $b_{12}^{(2)} \approx 630$ sec$^{-1}$. This is roughly eight orders of magnitude lower than the stimulated absorption rate for single-photon excitation of NO, and this rate magnitude disparity illustrates why two-photon LIF strategies are used only when absolutely necessary.

Since the process of deriving the two-photon LIF signal expression is similar to that followed above for the single-photon case, only the result is given here. The expression for the temporally integrated two-photon LIF signal is

$$S = \frac{\Omega}{4\pi} V_c \frac{A_{21}}{A_{21} + Q_{21}} \frac{E_p^2 \int F^2(t) dt}{A_p^2 (\hbar\omega)^2} G^{(2)} \sigma_{\omega}^{(2)} f_1(T) n \quad , \tag{39}$$

where $\int F^2(t) dt$ represents the integral of the square of the laser temporal profile, and the initial population term $f_1(T)n$ accounts for fine level population distributions.

Flow properties derived from LIF signal measurements are usually obtained by comparing, and thereby calibrating, the flow signals with simultaneously measured LIF signals from a reference cell at known thermodynamic conditions.[47–49] For the experiments described below, the reference cell is a flow reactor that uses a microwave discharge to dissociate a fraction of the molecular gas stream at a known pressure and temperature. The beam propagation path is oriented perpendicular to the velocity vector so that the transition line center seen by the reference cell detector is not Doppler-shifted. Signals are acquired from the flow and the reference cell simultaneously by scanning the laser through the transition and recording the measured fluorescence as a function of the scan wavelength.

Following a brief description of the optical configuration for the experiments, discussions of specific methods for measuring velocity, translational temperature, and species density using two-photon LIF of atomic nitrogen are given. Results of flow property measurements, along with estimated experimental uncertainties are then presented for two separate arcjet experiments; one with $N_2$/Ar flow and the other with air/Ar flow. For each test series, further data analysis is performed to characterize the flow of the free stream based on the LIF measurements. Although LIF measurements have been made in the shock layer,[44] the discussion below will be restricted to free stream measurements. Finally, findings from the stream characterization experiments are summarized.

### 3.3.1 Experimental Configuration for Free Stream LIF

Although Fig. 31 depicts the elemental components required for making LIF measurements, the actual installation is more complex. The optical configuration for the two-photon LIF experiments in the Ames AHF

Arcjet Facility is shown in Fig. 32. During the arcjet experiments, a frequency-doubled, Nd:YAG-pumped dye laser is scanned through the absorption transition (near 211 nm for N or 226 nm for O) and the resulting fluorescence signal is recorded as a function of wavelength, once the appropriate test conditions have been attained. Approximately 3 minutes are required to scan a single transition, so the measurements represent time-averaged quantities obtained during steady operation of the continuously running arcjet. For the arcjet optical path, the beam is delivered to the test cabin through a series of fused silica prisms and a Galilean telescope. The beam is then transmitted through a fused silica window onto a two-mirror positioner that orients the beam probe volume at an angle relative to the main flow axis. A PMT with a fast preamplifier detects the LIF signals through a side window with f/18 optics and a narrow bandpass filter to reduce background light. For these experiments, LIF measurements were made $\approx$ 15 cm downstream of the nozzle exit, and owing to the 1/6 magnification of the collection optics, the 3 mm aperture restricts the viewed length of the laser beam to 18 mm about the central streamline. Typically, the beam diameter is 1 - 2 mm and only about 150 $\mu$J of laser pulse energy is delivered to the measurement location.

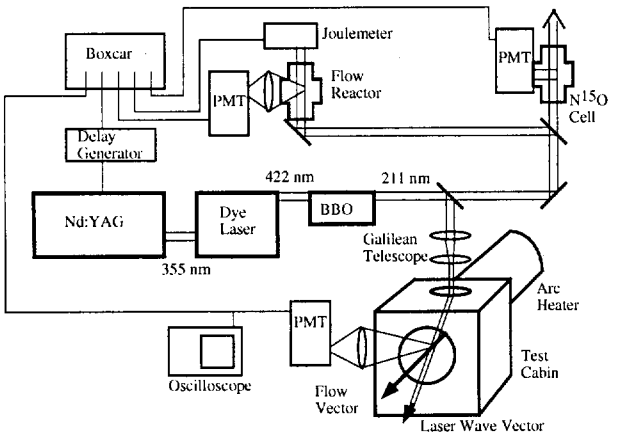


Fig. 32. Optical configuration for the arcjet two-photon LIF experiments.

Two other beam paths are shown on Fig. 32. The first path shows a small portion of the beam being used to excite single-photon LIF in a room temperature, low pressure isotopic nitric oxide, $N^{15}O$, cell. Nitric oxide is a useful wavelength reference molecule in the ultraviolet, and the isotopic form is used in this application to obtain a closer spectral overlap between the $N^{15}O$ and atomic transitions.[44] The second additional beam path in Fig. 32 is directed to the flow reactor, which is used as a temperature and velocity measurement reference, as described above. Fluorescence signals from the cell and reactor are also detected with PMTs. Signals from the laser pulse energy meter and all PMTs are processed by a computer-controlled preamplifier and boxcar unit. Further details on the instrumentation can be found in Ref. 48.

### 3.3.2 Flow Properties from Two-Photon LIF

Example two-photon LIF signals from atomic nitrogen obtained from the arcjet flow and from the low pressure flow reactor are shown in Fig. 33. The fluorescence signals, which arise from pumping the J= 7/2, $3p^4D^\circ \leftarrow 2p^4S^\circ$ transition of N, are shown as a function of the dye laser fundamental wavelength. The broader, noisier LIF signal was obtained from the arcjet flow and the narrower signal was detected in the flow reactor. Both LIF signals were five-pulse averaged by the data acquisition system. A nonlinear, least-squares fit to the data using a model of the two-photon absorption line shape is also shown for both the reactor and flow signals. The flow reactor conditions given on the figure were measured with a pressure transducer and thermometer at the reactor, while the arcjet flow conditions were determined from the spectra using analytical methods that are described below.

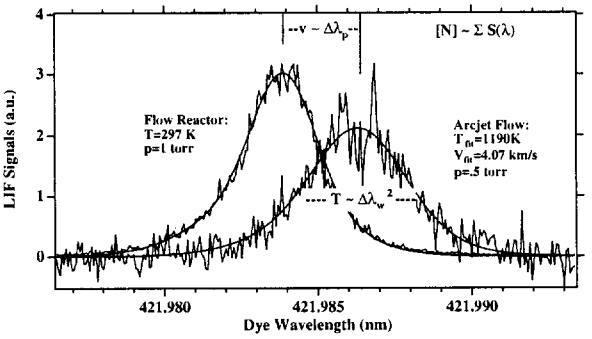


Fig 33. Example spectra from two-photon LIF of N in the flow reactor and the arcjet free stream.

**Velocity** - In Fig. 33, the central absorption wavelength of the transition for the arcjet flow is shifted relative to the transition location in the flow reactor. This Doppler shift is due to the angular orientation of the beam path relative to the axial flow velocity of the arcjet centerline. Provided that there is no collision-induced shift and the beam angle relative to the velocity vector is known, the gas velocity can be determined from the wavelength shift of the absorption line center using the following relation:

$$v = \frac{c\Delta\lambda}{\lambda \cos\theta}. \tag{35}$$

In the above expression, $v$ is the flow velocity, $c$ is the speed of light, $\Delta\lambda$ is the difference between the arcjet flow transition wavelength and the unshifted reference wavelength from the flow reactor, and $\theta$ is the angle between the light wave vector and the velocity vector.

**Translational Temperature** - The translational temperature can be inferred from the Doppler width of the excitation line profile. Referring again to Fig. 33, the spectral width of the transition measured in the arcjet flow is considerably broader than that measured

in the flow reactor, which indicates that the arcjet flow temperature is greater than the reactor flow temperature. Generally, multiple broadening mechanisms contribute to the total spectral width of the excitation line profile. For the arcjet and flow reactor test conditions however, the profile is dominated by the combined effect of the laser line width and Doppler broadening. The Doppler broadening contribution for an unknown flow temperature can be deconvolved from the total transition line width by determining the laser line width from an excitation profile measured at a known temperature. Once the transition line widths have been derived from spectral fits to the line shapes, the translational temperature is obtained from the following relation

$$T = \frac{M_N c^2}{8ln(2)kn_A\hat{\nu}^2}\left[\Delta\hat{\nu}^2_{T,F} - (\Delta\hat{\nu}^2_{T,R} - \Delta\hat{\nu}^2_{D,R})\right], \quad (36)$$

where $M_N$ is the molecular weight of N, $k$ is Boltzmann's constant, $n_A$ is Avogadro's number, $\hat{\nu}$ is the transition central wavenumber in $cm^{-1}$, the $\Delta\hat{\nu}_{I,J}$ are the relevant line width values (FWHM), and the subscripts identify the widths as either Flow, Reactor, Total, or Doppler.

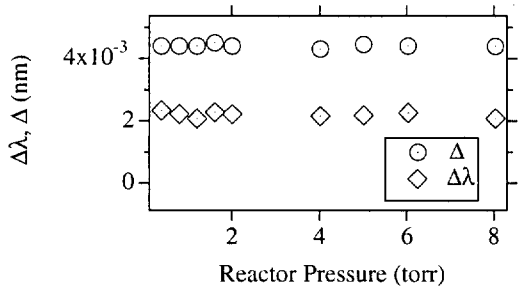


Fig. 34. Measured transition spacing, $\Delta$, and width, $\Delta\lambda$, in the $N/N_2$ flow reactor as a function of the cell pressure. Note that there is no increase in either parameter with increasing pressure.

**Collisional Effects -** Since velocity and translational temperature are determined from spectral fits to the measured two-photon excitation line shape, the influence of collisional effects was investigated by recording the excitation line shape in the room temperature, $N/N_2$-flow reactor at various pressures. The excitation line shapes were then fit with the spectral model, and the location and width of the N atom transition were determined from the fit. The transition location was measured relative to the wavelength of the $P_1$ (6) rotational transition of the $N^{15}O$-$\beta$ (2←0) vibrational band. Results from these tests are shown in Fig. 34, where the relative N atom transition location, $\Delta$ (nm), and transition width, $\Delta\lambda$ (nm), are shown as function of cell pressure. Neither the location or the width change significantly as the pressure is varied from 0.4 to 8 torr at room temperature. If the dominant collisional mechanism arises from dispersion forces, then the collisional broadening and shift should scale thermodynamically as $pT^{-.7}$.[52] Thus, for typical conditions within the arcjet free stream where $pT^{-.7} << 8(293)^{-.7}$ (torr/$K^{.7}$), collisional processes should have negligible influence on the excitation line shape.

**Species Concentration -** The spectrally integrated LIF signal is proportional to the concentration of the absorbing species in the laser probe volume. In previous publications of AHF arcjet LIF measurements, the N atom concentrations were presented as relative values, because there had been no measurement of the absolute two-photon excitation cross section for the transition.[47] In a series of recent experiments, both the excitation cross section for this transition, $\sigma^{(2)}_{12}$, and the second order coherence factor, $G^{(2)}$, for the laser used in these experiments have been measured. A preliminary value of the spectrally integrated $\sigma^{(2)}_{12}G^{(2)}$ product for the J= 7/2, $3p^4D^\circ \leftarrow 2p^4S^\circ$ transition of N in the favorable detection orientation $(2.81(10)^{-35}$ $cm^4$-rad) is used in this work to convert relative N atom concentration measurements to absolute values. The orientation of the detection optics must be considered because the N atom fluorescence is polarized.[53]

Additional measurements that quantify the pump laser characteristics, light detection efficiency, and upper state lifetime are required to convert the spectrally integrated fluorescence signals to absolute species concentrations. The upper state lifetime, $\tau_{obs}$ is used to account for collisional quenching of the fluorescence signal, and it is measured during the excitation scan using a fast digital oscilloscope. Other parameters, including the laser pulse energy in the cabin, $E_P$, its spatial distribution, $A_P$, and the laser pulse temporal profile, $\int F^2(t)dt$, were measured daily. Finally, the detection system calibration factor, $D$, was measured in a Raman scattering experiment (in the manner described in Ref. 54) once the flow measurements were completed. With these additional measurements, the absolute N density can be obtained by rearranging the rate equation solution for two-photon excitation given in Eq. (34) above,

$$n_N = \frac{4\pi}{D}\frac{\tau_{rad}}{\tau_{obs}}\frac{A_P}{\int F^2(t)dt}\frac{(h\nu)^2}{G^{(2)}\sigma^{(2)}_{12}}\int\frac{S_N}{E_p^2}(\omega)d\omega, \quad (37)$$

where $\tau_{rad}$ is the radiative lifetime ($43 \pm 3$ ns)[55] of the transition, and $S_N$ is the LIF signal in V.

### 3.3.3 Two-Photon LIF Measurements in $N_2$/Argon Flows

**Test Conditions -** Two-photon, N atom LIF measurements were conducted during three different facility runs at two different heater pressures for $N_2$/Ar flows. The two different pressures were nominally 2.4 and 4.8 atm, and the currents were varied from about

1200 A at the lower pressure to about 2200 A at the higher pressure. An attempt was made to acquire measurements at four different arc current values during a single facility run at each of the two heater pressures. However, at the lower pressure two separate runs were required to obtain the measurements owing to operational instability of the steam vacuum system during extremely hot weather. Geometrically, the arcjet was configured with a 6 cm diameter heater, a 3.8 cm diameter throat, and a 30.5 cm nozzle exit diameter, which gave an area expansion ratio of 64. Facility operating conditions for these tests are summarized in Table II, and the uncertainty in the parameters is currently estimated to be $\approx 5\%$ of the listed value.

**Table II.** Arcjet test conditions for LIF experiments in $N_2/Ar$ flow.

| Arcjet Run Conditions | | | |
|---|---|---|---|
| Run | Pressure | Current | Voltage |
| | atm | A | V |
| 21 | 2.44 | 1165 | 3732 |
| | 2.50 | 1388 | 3565 |
| 22 | 2.35 | 1563 | 3263 |
| | 2.39 | 1771 | 3165 |
| 23 | 4.78 | 1556 | 5626 |
| | 4.86 | 1782 | 5408 |
| | 4.73 | 1964 | 4981 |
| | 4.80 | 2197 | 4826 |

For each measurement, the arc current was adjusted and a scan was taken when the facility condition stabilized. Once the spectral scan was acquired for a current setting, the next condition was set. Flow property measurements from these tests are presented below as functions of the arcjet control variables, pressure and arc current. Uncertainty estimates for each flow property measurement were obtained using the approach outlined in the introduction along with the expressions derived above that relate the properties to the measured signals.

**Velocity Measurements -** Velocities measured in the free stream of the arcjet flow at each operating condition are shown in Fig. 35. Measured values were obtained from the excitation spectra using Eq. (35). On the figure, the velocities are shown as a function of the arc current, and the circular symbols represent measurements at the 2.4 atm heater pressure, while the diamond symbols represent 4.8 atm pressure values. The measured velocities range from about 3.8 to 4.8 km/s, and two interesting trends are apparent in the data. First, for a given heater pressure, there does not appear to be a significant increase in the stream velocity as the arc current is increased. Second, when pressure is increased, flow velocity appears to increase. Currently, the estimated uncertainty in the velocities is about 6% of the measured value, owing mainly to the uncertainty in determining the difference between the Doppler-shifted and unshifted wavelengths from the spectral fits to the data.

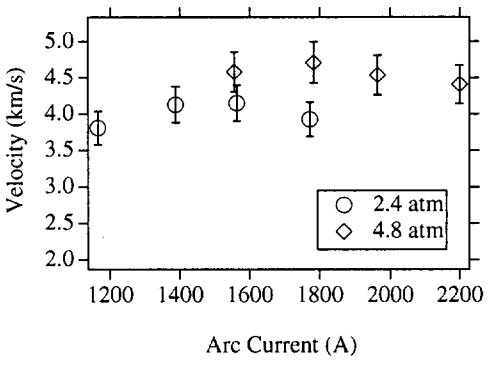


Fig. 35. Arcjet free stream velocities as a function of arc current at two different heater pressures.

**Translational Temperature Measurements -** Translational temperatures obtained from the measured spectral width of the two-photon transition of N are presented in Fig. 36. The measured values were derived using Eq. (36), and are shown as a function of the arc current for the two different heater pressures. As before, the circles denote the 2.4 atm values and the diamonds represent the 4.8 atm measurements. Measured translational temperatures range from about 800 to 1800 K. Given the estimated uncertainty level, which is 25% of the measured value, it is difficult to distinguish trends for temperature as a function of arc current. Generally, the temperatures at the higher pressure are greater than those at the lower pressure, which would be consistent with the greater sound speed indicated by the velocity measurements (assuming the local Mach number does not change significantly with pressure). The ability to accurately determine the spectral widths of somewhat noisy LIF signals is again the leading contribution to the uncertainty.

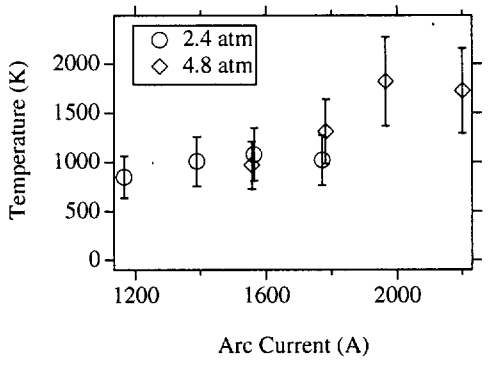


Fig. 36. Measured translational temperatures in the arcjet free stream as a function of arc current.

**Table III**. Beam and collection parameters for [N] measurements.

| Parameter | Value | Units |
|---|---|---|
| $G^{(2)}\ \sigma^{(2)}$ | $2.81(10)^{-35}$ | $cm^4 rad$ |
| $D$ | $1.93(10)^{-8}$ | V-cm-sr |
| $A_p$ | .029 | $cm^2$ |
| $\int F^2(t)dt$ | $1.91(10)^8$ | $s^{-1}$ |
| $h\nu$ | $9.415(10)^{-19}$ | J |

**N Concentrations** - Absolute and relative N atom number density measurements are shown in Fig. 37 for the variable current, constant pressure arcjet tests. The absolute [N] values (circles and diamonds) are shown as a function of arc current, while the relative values (squares and triangles) are shown at currents that are shifted by 40 A for clarity. The measured absolute [N] values were obtained from the spectrally integrated, free-stream LIF signals using Eq. (37). Values of the laser pulse spatial and temporal characteristics, the detection calibration constant, and other parameters used to convert the integrated signals from these measurements to absolute N concentrations are given in Table III. Observed fluorescence lifetimes that were recorded during the measurements at each condition are given in Table IV. Measured values of [N] range from $4(10)^{15}$ to $11(10)^{15}$ $cm^{-3}$. Currently, the uncertainty in the [N] measurements is estimated to be about 28%. Nearly all of this uncertainty is introduced in the conversion of relative to absolute values, with the uncertainty in $G^{(2)}\sigma^{(2)} \approx 25\%$ as the leading contributor. In contrast, the uncertainty in the relative [N] values is only about 5% of the measured value; therefore, trends in the measurements can be inferred from the variation in the relative values. For both the low pressure (squares) and high pressure (triangles) cases, there appears to be a trend of increasing [N] with arc current. At the higher pressure, for which the total mass flow has also increased, the [N] values are all consistently greater than the values for the lower pressure case.

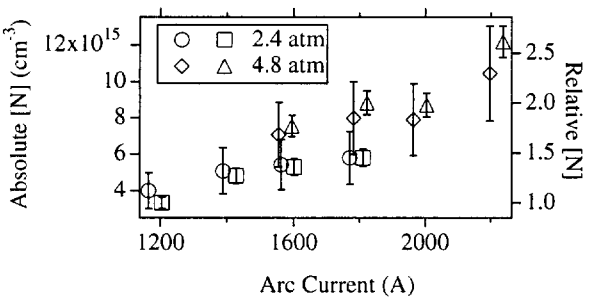


Fig. 37. Absolute and relative [N] as a function of arc current. The relative values, denoted by the squares and triangles, are shifted by 40 A from the absolute values.

For the two flow properties measured with the lowest uncertainty, $v$ and relative [N], trends in the data may provide information about the chemical freezing process that occurs in the nozzle. As current is increased at constant pressure, [N] increases in the free stream, which may indicate that changing the arc current at these conditions does not change the point at which [N] freezes. Energy added to the flow by increasing the discharge current increases $N_2$ dissociation rather than increasing the kinetic energy of the stream. When pressure is increased, $v$ increases, which may indicate that the [N] freeze point in the nozzle changes due to the increased collisional frequency at the higher pressure. This change in the chemical freezing location may provide more kinetic energy to the flow. Although [N] clearly increases with increasing pressure, some of this increase can be attributed to the increased stream density. With additional information from facility instrumentation, these LIF-based measurements can provide further information about the thermochemical state of the free stream.

**Table IV**. Fluorescence lifetimes, pitot pressures, and mass flow rates for the arcjet tests.

| Lifetimes & Facility Measurements | | | | |
|---|---|---|---|---|
| Run | $\tau_{obs}$ | $p_p$ | $\dot{m}_T$ | $\dot{m}_{Ar}$ |
| | ns | torr | kg/s | kg/s |
| 21 | 36.2 | 40.4 | 0.10 | 0.03 |
| | 33.8 | 41.2 | 0.10 | 0.03 |
| 22 | 33.3 | 39.7 | 0.11 | 0.03 |
| | 34.7 | 40.1 | 0.11 | 0.03 |
| 23 | 33.7 | 69.0 | 0.19 | 0.03 |
| | 34.5 | 70.0 | 0.19 | 0.03 |
| | 36.3 | 68.0 | 0.20 | 0.03 |
| | 37.0 | 67.9 | 0.20 | 0.03 |

**Stream Characterization** - To calculate N mass fractions and other flow properties from the LIF-determined stream properties requires additional information from facility measurements of mass flow and pitot pressure. These quantities are summarized in Table IV for each run and the uncertainties are currently estimated to be between 5 and 10% of the values given. The total mass flow rate, $\dot{m}_T$, and the argon mass flow rate, $\dot{m}_{Ar}$, were determined from the manifold pressures based on earlier facility tests.[56] Also, a flat-faced cylinder with a pressure tap was placed in the test stream to measure the impact, or pitot pressure behind the shock. By rearranging the supersonic Rayleigh formula for pitot pressure[57] and making use of the LIF measurement of velocity, the total stream density, $\rho$, can be obtained,

$$\rho = \frac{p_p}{v^2}\gamma\left(\frac{2\gamma}{\gamma+1}\right)^{\frac{1}{\gamma-1}}\left(\frac{\gamma+1}{2}\right)^{\frac{-\gamma}{\gamma-1}}, \text{ for } M >> 1. \tag{38}$$

Note that density is only a weak function of $\gamma$, and that $\gamma$ only changes by about 30% going from a molecular to completely dissociated gas. Thus from the measured pitot pressure, velocity, and an estimate of $\gamma$ ($\approx 1.45$)

the stream density can be calculated. This allows a determination of the N mass fraction, $w_N$, from

$$w_N = \frac{n_N M_N}{\rho n_A}. \tag{39}$$

Assuming that the ion and excited electronic level populations are negligible, the mass fractions of the remaining flow constituents can be determined from

$$w_{Ar} = \frac{\dot{m}_{Ar}}{\dot{m}_T}, \tag{40}$$

and

$$w_{N_2} = 1 - w_{Ar} - w_N.$$

Using the constituent mass fractions, a closer estimate of $\gamma$ can be developed by iterating between Eq. (38) and the above relations, although there is no information on $N_2$ vibration, as discussed below.

**Table V.** Constituent specific heats, gas constants and molar masses used in Eqs. (39),(41), and (42).

| $N_2$/Ar Flow Species Thermodynamic Properties | | | |
|---|---|---|---|
| Species | $c_{pi}$ | $R_i$ | $M_i$ |
| | MJ/kg-K | MJ/kg-K | kg/mol |
| Ar | $2.5R_{Ar}$ | 208 | .040 |
| N | $2.5R_N$ | 594 | .014 |
| $N_2$ | $4.5R_{N_2}$ | 297 | .028 |
| O | $2.5R_O$ | 519.6 | .016 |

Assuming that $N_2$ vibration is fully excited, the total flow enthalpy can then be calculated from the measured values of velocity, translational temperature, and the derived mass fractions,

$$h_T = \sum_i w_i c_{pi} T + \frac{v^2}{2} + w_N R_{N_2} \Theta_{dN}, \tag{41}$$

where $c_p$ is the specific heat and $\Theta_{dN}$ is the characteristic dissociation temperature of N (113,000 K, Ref. 58). As will be shown below, the contribution of the thermal mode, which includes vibrational energy, to the total flow enthalpy is quite small. Note that the free stream LIF-based approach to determining the enthalpy provides the apportionment among the chemical, thermal, and kinetic modes directly.

Using the above relations and values for the constants that are given in Table V, values of the mass fractions and total enthalpies were determined for the arcjet tests. The N mass fractions are shown in Fig. 38 as a function of arc current for the tests at the two different heater pressures. Now the effect of the increased stream density at the higher chamber pressure is more apparent, and $w_N$ may actually decrease as pressure is increased at constant current. This would support the earlier suggestion of increased N recombination arising from the greater collision frequency at higher chamber pressure. Note that the degree of N dissociation, $\alpha_N = w_N/(w_N + w_{N_2})$,[58] on the free stream centerline is substantial, ranging from .33 to .56 for these test conditions.

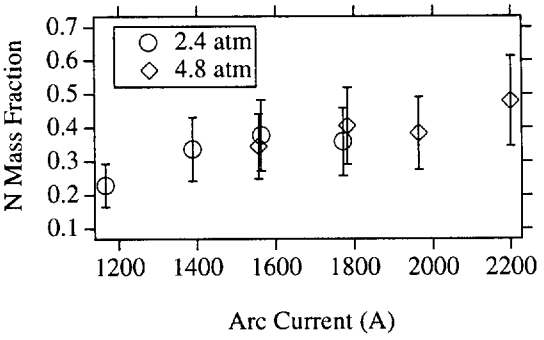


Fig. 38. Atomic nitrogen mass fraction as a function of arc current in the arcjet free stream.

The total flow enthalpies determined from the measured flow properties using Eq. (41) are given in Fig. 39. Values range from 16 ± 3 MJ/kg at the lowest current of the low pressure test to 28 ± 6 MJ/kg at the highest current of the high pressure test case. For both values of the heater pressure, the total enthalpy appears to increase with increasing arc current, as expected.

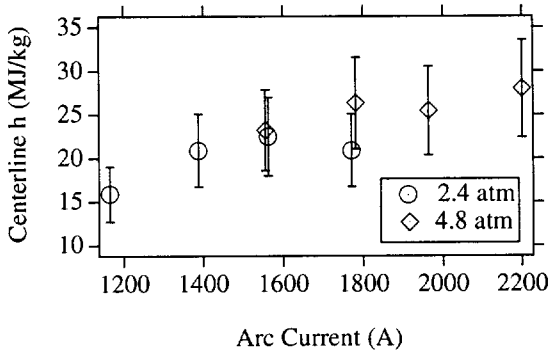


Fig. 39. Total enthalpy on the arcjet free stream centerline as a function of the arc current.

The fractional contributions of the separate modes to the total enthalpy are plotted in Fig. 40. For these test conditions, the dominant contributions to the total enthalpy come from the $N_2$ dissociation, or chemical mode, and the kinetic mode. The total thermal contribution to the free stream flow enthalpy is always less than 10% . This suggests that even a fully-excited $N_2$ vibrational contribution (with $T_v = 2T_{tr}$) to the total enthalpy would be less than 1%, so the penalty for the assumption of full excitation in the preceding analysis appears to be small. This plot also shows which flow properties need to be measured most accurately, $v$ and [N], to improve the precision of the enthalpy determination.

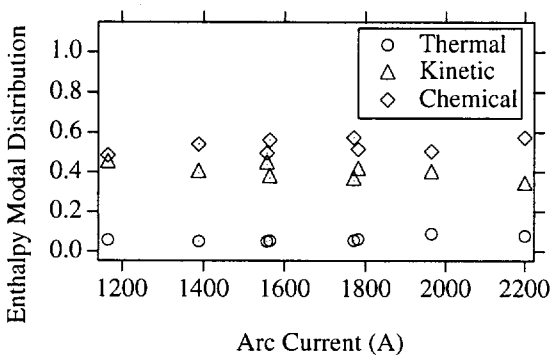


Fig. 40. Fractional distribution of the total centerline enthalpy as a function of the arc current.

Additional properties that were determined for the tests are the flow Mach number, $M = v/\sqrt{\gamma RT}$, which ranged from 4.2 to 6.2, and the static pressure, $p_s = \rho RT$, which varied from 0.9 to 2.8 torr.

### 3.3.4 Two-Photon LIF Measurements in Air/Argon Flows

Flow property and stream characterization measurements obtained using two-photon LIF of N have also been performed for air/Ar test gas flows in the same arcjet facility. Results from these experiments are discussed below.

**Test Conditions** - Two sets of LIF measurements in air/argon gas mixtures were obtained for variable current settings at two different nominal constrictor pressures, 2.4 and 4.8 atm. An additional set of measurements was acquired at the lower pressure. For all three runs, the geometric configuration of the arcjet facility was identical to that mentioned earlier for the $N_2$/Ar tests. Facility operating conditions for the three tests are summarized in Table VI.

**Table VI**. Test conditions in the AHF Arcjet for the variable current, constant pressure LIF experiments in air/Ar flows.

| Arcjet Run Conditions | | | |
|---|---|---|---|
| Run | Pressure | Current | Voltage |
| | atm | A | V |
| 11 | 2.44 | 1149 | 3198 |
| | 2.51 | 1333 | 3115 |
| | 2.58 | 1556 | 3067 |
| 15 | 2.43 | 1130 | 3218 |
| | 2.37 | 1357 | 2991 |
| | 2.43 | 1545 | 2926 |
| | 2.46 | 1761 | 2855 |
| 19 | 4.78 | 1836 | 4454 |
| | 4.86 | 2016 | 4309 |
| | 4.80 | 2237 | 4206 |

For the results reported below, the uncertainties in the measured flow properties are greater than those for the $N_2$/Ar flow results owing to the reduced signal levels that resulted from dilution of the N population by atomic oxygen.

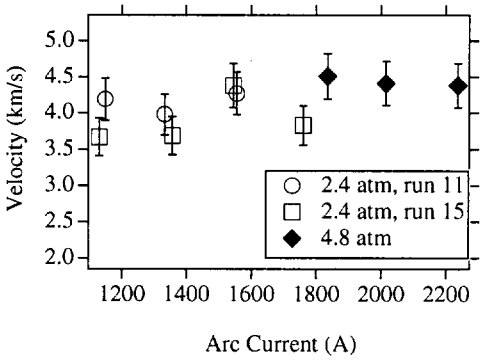


Fig. 41. Arcjet free stream velocities as a function of arc current at two different heater pressures.

**Velocity Measurements** - Velocity measurements as a function of arc current are shown in Fig. 41 for the three runs at constant pressure. The lower pressure (2.4 atm nominal) results from two different runs are denoted by the open circles and squares, while the results from the higher pressure run are represented by the solid diamonds. Uncertainties for the velocity measurements are about ± 7%, and measurements from the two lower pressure runs agree to within this amount. The lower pressure data appear to indicate increasing velocity with increasing current for each run, while the higher pressure measurements appear to indicate the opposite trend. This suggests that the arc current has little effect on flow velocity. However, all of the velocities from the higher pressure run are greater than for the lower pressure cases. Both observations are consistent with trends noted in previous experiments.[48,49]

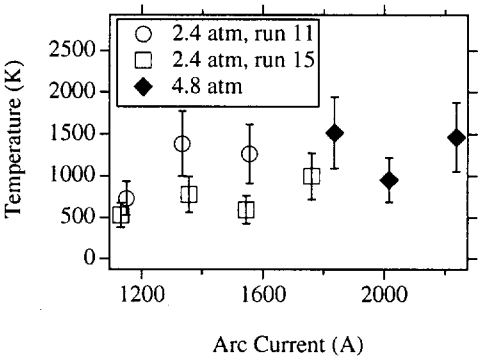


Fig. 42. Measured translational temperatures in the arcjet free stream as a function of arc current.

**Translational Temperature Measurements** - Measured flow translational temperatures that were derived from the N atom transition line width are shown in Fig. 42, using the same symbol convention to denote the separate runs. Owing to the high uncertainty, which is 30 % of the measured value, it is difficult to discern trends in translational temperature with increasing arc current, although the mean value

of measured translational temperature is higher for the higher pressure, higher current conditions than for the lower conditions. Measured values from the two lower pressure tests generally agree to within their estimated uncertainty.

**N Concentration Measurements -** In contrast to the velocity and translational temperature, consistent trends of increasing relative N atom concentration with increasing arc current were observed for both lower pressure and higher pressure tests, as shown in Fig. 43. Relative N concentrations that are normalized to the value measured at the lowest current are shown as a function of arc current. Because [N] is determined from the spectral integration of the absorption line shape, the lower N atom LIF signal for air/argon flows has less of an impact on the concentration measurements. The low pressure test results show a lower rate of increase in relative concentration with increasing current than the 4.8 atm results. At the lowest current of the high pressure test case, the relative [N] is lower than that of the highest current of the lower pressure test. This may be attributed to increased recombination in the nozzle resulting from the higher pressure.

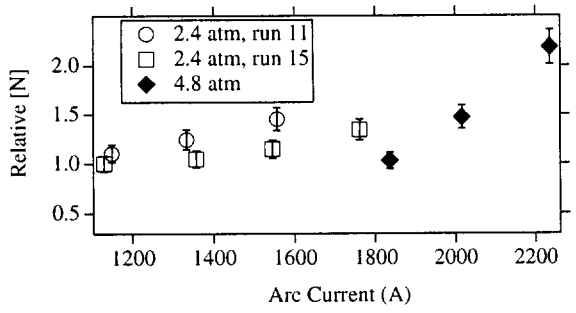


Fig. 43. Relative [N] as a function of arc current.

Absolute N concentrations are plotted as a function of arc current in Fig. 44 using symbol conventions that are consistent with the preceding figures. Upper state observed lifetime measurements, which are required to account for collisional quenching in calculating the [N] values, are given in Table VII. For these experiments, only a limited number of lifetime measurements were made, so mean lifetime values were calculated for the lower and higher pressure cases and applied to all the measurements. As noted in earlier work,[48] the observed lifetimes indicate that collisional quenching is relatively weak at these test conditions. Uncertainty in the product of the two-photon absorption cross section and the second order coherence factor for the laser was again the leading contributor to the total uncertainty in the absolute N concentration measurements. Currently, the uncertainty in these absolute [N] measurements is estimated to be about 30 %, which is considerably greater than the uncertainty in the relative [N] values. Despite the relatively large uncertainty, the absolute concentration values are a critical component of the further analysis of the thermochemical state of the flow.

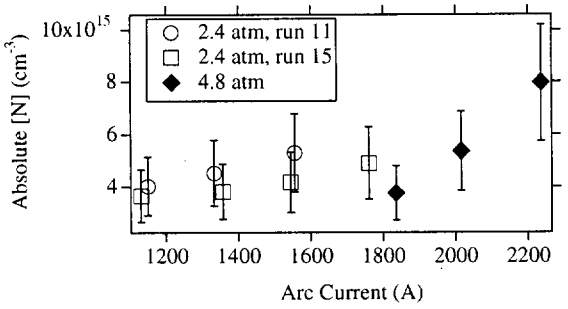


Fig. 44. Absolute [N] as a function of arc current.

**Stream Characterization -** With the aid of certain assumptions, it is possible to make an assessment of the total stream enthalpy on the flow centerline using the LIF measurement results. The approach is similar to that outlined above for $N_2$/Ar flow experiments. However, the expression for the free stream enthalpy given by Eq. (41) must be modified to account for the presence of atomic oxygen,

$$h = v^2/2 + w_N R_{N_2} \Theta_{dN} + w_O R_{O_2} \Theta_{dO} + \sum w_i c_{p_i} T. \quad (42)$$

This expression again represents the sum of the contributions of the different modes; kinetic, chemical, and thermal; to the total enthalpy. The characteristic dissociation temperature used in the above expression is $\Theta_{dO} = 59{,}500$ from Ref. 57. As with $N_2$/argon flows, the velocity and translational temperature are obtained directly from the LIF measurements, while the mass fractions require input from additional facility measurements. Values of total mass flow and argon mass flow that were derived from manifold pressures for the current tests are given in Table VII, along with pitot pressure measurements.

**Table VII.** Fluorescence lifetimes, pitot pressures, and mass flow rates for the air/argon flow tests.

| Lifetimes & Facility Measurements | | | | |
|---|---|---|---|---|
| Run | $\tau_{obs}$ | $p_p$ | $\dot{m}_T$ | $\dot{m}_{Ar}$ |
| | ns | torr | kg/s | kg/s |
| 11 | 35.0 | 40.4 | 0.110 | 0.030 |
| | 35.0 | 42.3 | 0.110 | 0.030 |
| | 35.0 | 44.1 | 0.110 | 0.030 |
| 15 | 35.0 | 42.6 | 0.105 | 0.030 |
| | 35.0 | 42.1 | 0.105 | 0.030 |
| | 35.0 | 42.5 | 0.105 | 0.030 |
| | 35.0 | 42.6 | 0.105 | 0.030 |
| 19 | 33.1 | 70.7 | 0.200 | 0.030 |
| | 33.1 | 70.1 | 0.200 | 0.030 |
| | 33.1 | 69.8 | 0.200 | 0.030 |

The argon mass fraction values for these tests were determined from the ratio of measured argon mass flow to the total mass flow. For all of the tests conducted

to date there has been no evidence to suggest that any oxygen-bearing molecular species are present in the stream. Therefore, the assumption is made that oxygen is completely dissociated, $w_{O_2} = 0$, which allows the O atom mass fraction to be determined from the total mass flow,

$$w_O = .21(M_{O_2}/M_{air})(1 - w_{Ar}), \qquad (43)$$

where $M_i$ are the species molar masses. A further discussion of oxygen dissociation is given below.

Atomic nitrogen mass fraction values were determined using the same method presented above for $N_2$/Ar flows, which involved determining the stream density from the pitot pressure measurements using Eq. (38) and then using the stream density and [N] measurements in Eq. (39). The $N_2$ mass fraction is then calculated from

$$w_{N_2} = 1 - w_{Ar} - w_N - w_O.$$

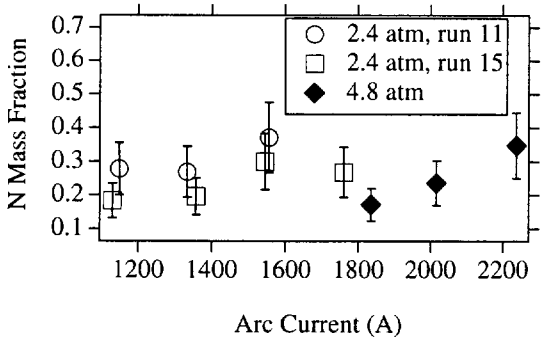


Fig. 45. Nitrogen atomic mass fraction as a function of arc current in the arcjet free stream.

Atomic nitrogen mass fractions derived from the absolute [N] and velocity measurements are shown in Fig. 45 for the three air/Ar runs. Trends for each of the runs are similar to those described in the [N] measurements. However, the effect of the increased stream density at the higher chamber pressure is more apparent, and $w_N$ may actually decrease as pressure is increased at (nearly) constant current. This is consistent with the idea of increased N recombination arising from the greater collision frequency at higher nozzle pressure. Note that the degree of N dissociation, $\alpha_N$, on the free stream centerline is again substantial, ranging from .26 to .62 for these test conditions.

As with the $N_2$/Ar flow case, there is no information about the vibrational state of $N_2$ in the nonequilibrium air/Ar flow. However, the same assumption is made here that the $N_2$ vibrational energy mode is fully excited, which gives the maximum possible specific heat for $N_2$.

Total centerline flow enthalpies near the nozzle exit were determined from the measured flow properties using Eq. (42) and the constants given in Table VIII. The results are shown in Fig. 46. Values range from 16 MJ/kg at the lowest current of the low pressure test to 26 MJ/kg at the highest current of the high pressure test case. As with the $N_2$/Ar results, the total enthalpy appears to increase with increasing arc current. Uncertainties in the total enthalpies are currently estimated to be about ± 30 % of the derived values, based on the propagation of the primary variable uncertainties through Eq. (42). Since the uncertainty contributions from the measured parameters are weighted by their fractional contribution to the total enthalpy, the leading contributors to the uncertainty are the velocity and absolute nitrogen concentration.

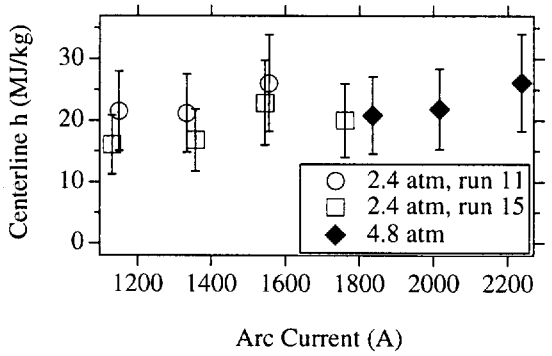


Fig. 46. Total enthalpy on the arcjet free stream centerline as a function of the arc current.

For these air/Ar flow test conditions, the dominant contributions to the total enthalpy come from the $N_2$ dissociation ($w_N R_{N_2} \Theta_{dN}$), and the kinetic energy ($v^2/2$). The total thermal contribution ($\sum w_i c_{p_i} T$) to the free stream flow enthalpy is again less than 10% at all of the test conditions. This suggests that the vibrational contribution is also negligible for air/Ar flows at these conditions.

**Oxygen Dissociation Level -** The recent LIF measurements have been directed toward developing and demonstrating the ability to measure enthalpy in the free stream using two-photon excitation of N.[48,49] To use this approach for air/Ar flow mixtures, oxygen is assumed to be fully dissociated. Based on the results of the [N] measurements and the derived dissociation levels, the amount of nitrogen dissociation is substantial ($\alpha_N = .26 - .62$). Since it is energetically easier to dissociate oxygen, the degree of oxygen dissociation should be greater than that of nitrogen.

Additional information on the state of oxygen in the arcjet free stream can be found from the results of experiments undertaken to assess NO populations.[44] During those tests, no laser-induced emission was detected from either the NO-$\gamma$ system or the $O_2$ Schumann-Runge bands, which both have a large number of ro-vibrational transitions near 226 nm.[59] Based on their single-photon LIF detectability, a conservative

estimate of approximately $10^{13}$ cm$^{-3}$ can be placed on the upper population limits for NO and $O_2$.

From these observations, it was expected that all of the oxygen population would appear as ground state ($^3$P) atomic oxygen. Thus, a comparison between the absolute [O] measurements from the earlier LIF experiments of Ref. 47 and values calculated from the facility mass flow correlations should support this premise. These [O] measurements were carried out by measuring the total LIF signal of a single fine-level transition (J"=2) and using the Doppler width based temperature measurement to account for the fractional population residing in the other fine levels of the $^3$P ground state. Results from the measurements are shown in Fig. 47, along with calculated population levels derived from the facility mass flow correlations (Eq. (38), above). Both measured and calculated [O] values are shown as a function of chamber pressure, to be consistent with the original presentation of the data.[47] At all but the lowest pressure conditions, the LIF measurements indicate a lower [O] value than expected from the facility data.

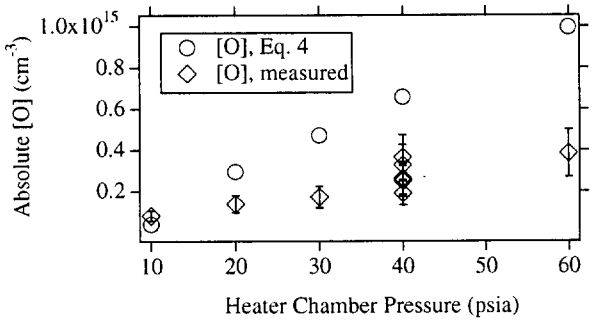


Fig. 47. Comparison of measured and calculated [O] as a function of the heater pressure for tests in the 61 cm diameter nozzle. (Note that Eq. (4) refers to Eq. (38).)

Assuming that the facility correlations are reliable, it is possible that the total O atom population may be under-measured by the LIF approach owing to populations in the two low-lying, metastable singlet states, $^1$D and $^1$S. Since these two states do not have an allowed optical transition path to the $^3$P state, populations can build up as a result of optical transitions from higher electronic levels and remain trapped due to the essentially collisionless free stream environment. Significant metastable state populations would not affect the assumption of full $O_2$ dissociation, but would affect the overall energy balance since the amount of energy carried by the O atoms is greater for the $^1$D and $^1$S levels. If all of the [O] difference is assumed to lie in the highest energy state, then the centerline enthalpy values calculated using Eq. (42) would increase by up to 6 %. While this amount is within the current uncertainty of the centerline enthalpy values, the possibility of O atom metastable state populations should be investigated further.

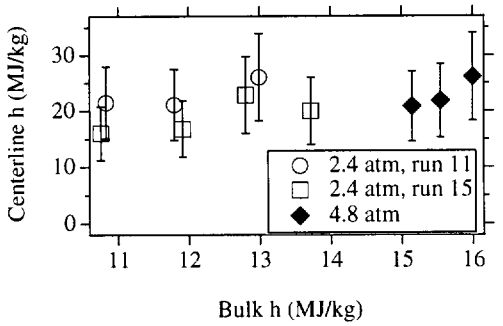


Fig. 48. Measured centerline enthalpies as a function of calculated bulk enthalpies for the air/Ar flows.

**Comparison with Bulk Enthalpy** - Although the efficiency of the constricted arc heater has not been measured recently for the AHF, measured values obtained from a similar constricted arc heater were used to estimate the bulk flow enthalpy, using the following relation,

$$h_B = \frac{\eta_H V I}{\dot{m}_T} \tag{44}$$

Figure 48 shows the LIF-measured centerline enthalpies as a function of the bulk enthalpy values calculated from the facility correlations for the three different constant pressure, variable current test cases. For each test, the measured centerline enthalpy value appears to increase with increasing bulk enthalpy. The change in measured centerline enthalpy from the lowest current, lowest pressure condition to the highest current, highest pressure condition is 62 %, while the change in bulk enthalpy calculated over these same conditions was 60 %. While this agreement in the relative enthalpy change is noteworthy, the measured enthalpy values on the flow centerline are typically 30 to 50 % greater than the corresponding bulk enthalpy values. This may indicate a nonuniform enthalpy distribution in the stream, but further confirmation by off-centerline measurements is required.

### 3.4 Summary of LIF Results

The stream information derived from the LIF experiments illustrates the advantage of making spatially resolved measurements using a major flow species. For arcjet flows in particular, probing the most energetic dissociation product allows a determination of the chemical energy in the stream. Moreover, in combination with the species concentration, the additional LIF-based flow property measurements yield a measure of the stream enthalpy and the distribution of energy among the kinetic, chemical, and thermal modes. A measurement of the total enthalpy alone is important, because credible flow simulations and analyses are not possible without it. By knowing the distribution of energy and the flow mass fractions, the degree of nonequilibrium of the free stream in an arcjet flow

can be largely quantified, although there is as yet no information on the vibrational temperature.

From the analysis of the LIF measurements obtained in the Ames AHF Arcjet Facility, it appears that there is more stream energy in the kinetic and chemical modes that in the thermal mode. When the current is increased at nearly constant pressure, only the N concentration appears to change significantly. Comparisons between measured and calculated O concentrations indicate that the flow may be even more energetic than the N LIF measurements imply, since some of the metastable, singlet states of O may be populated in high-enthalpy air flows.

Future work with the LIF instrumentation will be directed toward assessing the magnitude of possible flow property gradients in the radial direction in the free stream. In addition, excitation strategies are being developed to attempt to quantify possible metastable state populations and vibrational temperatures.

## 4. Summary of Arcjet Characterization Using Optical Diagnostics

Recall that one of goals of these lectures was to argue a case for aerothermodynamic testing in arcjet facilities. In this context, the term aerothermodynamic refers to testing that involves more than simply measuring the thermal response of a material to a measured, but not necessarily known heat flux. Where does this argument stand in light of results from recent experiments performed using optical diagnostics? First, the results from the 2-photon LIF measurements indicate that characterization of the arcjet free stream is feasible. However, further measurements are required to establish the appropriateness of assumptions invoked in the use of the measured quantities and the validity of the approach. Although it is only a limited validation, some insight may be gained by comparing enthalpies derived from the free stream LIF measurements with enthalpies derived from electrode package emission measurements. Each approach relies on different assumptions to determine enthalpy, so the comparison can be useful, and this is currently being investigated.[25]

The second issue involved in using arcjet facilities for aerothermodynamic simulation concerns the state of the gas within the shock layer. In arcjet flows, a highly dissociated free stream gas passes through a relatively weak shock, while in flight the undissociated gas is processed by a strong shock. Depending on the conditions, the result of the relaxation processes may be similar. In fact, if the combination of pressure and shock stand-off distance is similar and the relaxation processes are common, then the gas may reach the same thermochemical state as it approaches the surface in both cases. There is much to be done to establish the validity of this hypothesis, but the spatially resolved radial temperature profile measurements in the shock layer represent an important first step in this process. These measurements showed agreement between the three temperatures; $T_r$, $T_v$, and $T_e$; over a fairly large shock layer region at the low pressure, low current condition. This suggests that the gas is in thermal equilibrium at a lower shock layer pressure than was expected. As mentioned above, further work to assess the chemical state of the gas in this region of the shock layer is ongoing, and some of this effort is directed toward relating the conditions of this test to the appropriate flight environment. Finding a region of thermal equilibrium, and possibly chemical equilibrium, within the shock layer provides a foundation for further characterization of the shock layer flow, and, more importantly, a basis for interpreting test results without having to make assumptions about the state of the test gas reaching the surface.

These admittedly intermediary and preliminary findings have not yet made a convincing case for the use of arcjets as aerothermodynamic ground test facilities. It also appears likely that the possibility of performing aerothermodynamic tests in arcjet facilities will depend on the operating conditions and the test configuration. However, the results acquired from the optical diagnostic measurements in a prototypical large-scale arcjet test facility argue strongly for further careful measurements to continue toward this goal.

## 5. Acknowledgements

A number of talented and dedicated researchers have contributed to this work, and their efforts are greatly appreciated. Special thanks are owed to Chung Sik Park, James Donohue, Mark Newfield, Tahir Gökçen, Imelda Terazzas-Salinas, John Balboni, Chul Park, Doug Bamford, Jochen Marschall, George Raiche, and Frank Hui. The support of the Reacting Flow Environments Branch and the Space Technology Division at Ames Research Center are gratefully acknowledged. Finally, the efforts of the technical staff of the Thermophysics Facilities Branch ensured reliable and repeatable arcjet facility performance, without which this work would not have been possible.

## 6. References

1. A. Balter-Peterson, F. Nichols, B. Mifsud, and W. Love, "Arc Jet Testing in NASA Ames Research Center Thermophysics Facilities", AIAA Paper No. 92-5041, $^{th}$ *AIAA International Aerospace Planes Conference*, (American Institute of Aeronautics and Astronautics, New York, 1992).
2. C. Scott, "Survey of Measurements of Flow Properties in Arcjets",*Journal of Thermophysics and Heat Transfer*,**7**, pp. 9-24, (1993).
3. A. Okuno and C. Park, "Stagnation Point Heat Transfer Rate in Nitrogen Plasma Flows: Theory

and Experiment", *Journal of Heat Transfer*, pp. 372-384, August, (1970).
4. R. L. McKenzie, "Progress in Laser Spectroscopic Techniques for Aerodynamic Measurements: An Overview", *AIAA J.*, **31**, pp. 465-477, (1993).
5. A. C. Eckbreth, Laser Diagnostics for Combustion Temperature and Species, Abacus Press, Tunbridge Wells, (1988).
6. W. Demtröder, Laser Spectroscopy, $2^{nd}$ Ed., Springer-Verlag, Berlin, (1996).
7. G. Herzberg, Molecular Spectra and Structure, Vol. I - Spectra of Diatomic Molecules, $2^{nd}$ Edition, Krieger Publishing Company, Malabar, (1989).
8. K. P. Huber and G. Herzberg, Constants of Diatomic Molecules, Van Nostrand Reinhold, New York, (1979)
9. C. O. Laux, "Optical Diagnostics and Radiative Emission of Air Plasmas", Stanford High Temperature Gasdynamics Laboratory Report No. HTGL T-288, Stanford University, August, (1993).
10. W. G. Vincenti and C. H. Krueger Jr., Introduction to Physical Gas Dynamics, R. E. Krieger, Malabar, 108-109, (1982).
11. ibid, pp. 448-460.
12. T. Gökçen, C. S. Park, M. E. Newfield, and D. G. Fletcher, "Computational Simulation of Emission Spectra from Shock Layer Flows in an Arc-Jet Facility", J. Thermophysics and Heat Transfer **12**, 180-189, (1998).
13. E. E. Whiting, J. O. Arnold, and G. C. Lyle, "A Computer Program for a Line-by-Line Calculation of Spectra from Diatomic Molecules and Atoms Assuming a Voigt Line Profile", NASA TN D-5088, March, (1969).
14. C. S. Park, M. E. Newfield, D. G. Fletcher, T. Gökçen, and Sharma, S. P., "Spectroscopic Emission Measurements within the Blunt Body Shock Layer in an Arc-Jet Flow", AIAA Paper No. 97-0990, Jan., 1997, also *J. Thermophysics and Heat Transfer*, **12**, pp. 190-197, (1998).
15. E. E. Whiting, C. Park, Y. Liu, J. O. Arnold, and J. A. Paterson, "NEQAIR96, Nonequilibrium and Equilibrium Radiative Transport and Spectra Program: User's Manual", NASA Reference Publication 1389, and references therein, (1996).
16. W. L. Wiese, J. R. Fuhr, and T. M. Deters, "Atomic Transition Probabilities of Carbon, Nitrogen, and Oxygen: A Critical Compilation", *J. Phys. Chem. Ref. Data*, Monograph No. 7, (1994).
17. C. Park and D. Moore, "A Polynomial Method for Determining Local Emission Intensity by Abel Inversion", NASA TN D-5677, Feb., (1970).
18. W. E. Bruce and D. D. Horn, "AEDC Arc Column Diagnostic Measurements", ISA Paper No. 92-0190, (1992).
19. J. S. Taunk, C. E. Shepard, and A. Carrasco, "Design and Verification of a Copper Disk for Radiation Measurement in the Constrictor Region of an Arcjet", ISA Paper No. 94-3025, Baltimore, MD, (1994).
20. I. Terrazas-Salinas, C. Park, A. W. Strawa, N. K. J. M. Gopaul, and J. S. Taunk, "Spectral Measurements in the Arc Column of an Arc-Jet Wind Tunnel, AIAA Paper No. 94-2595, (1994).
21. V. R. Watson and E. B. Pegot, "Numerical Calculations for the Characteristics of a Gas Flowing Axially Through a Constricted Arc", NASA TN D-4022, June, (1967).
22. M. A. Rob, L. H. Mack, S. Arepalli, and C. D. Scott, "Spectral Measurements in the Plenum of an Arcjet Wind Tunnel", AIAA Paper No. 95-2126, $30^{th}$ AIAA Thermophysics Conference, San Diego, CA, (1995).
23. M. A. Rob, L. H. Mack, S. Arepalli, and C. D. Scott, "Characterization of Plenum Spectra in an Arcjet Wind Tunnel", *J. Thermophysics and Heat Transfer*, **11**, pp. 339-345, (1997).
24. L. H. Mack, M. A. Rob, S. Arepalli, C. D. Scott, J. D. Milhoan, and C. O. Laux, "Radial Spectral Measurement in the Plenum of an Arc-Jet Wind Tunnel", AIAA Paper No. 96-1897, (1996).
25. J. M. Donohue, D. G. Fletcher and C. S. Park, "Emission Spectral Measurements in the Plenum of an Arcjet Wind Tunnel", AIAA Paper No. 98-2946, $7^{th}$ AIAA/ASME Joint Thermophysics and Heat Transfer Conference, June, (1998).
26. N. K. J. M. Gopaul, "Spectral Measurement of Nonequilibrium Arc-Jet Free Stream Flow", ISA Paper No. 93-144, *$39^{th}$ International Instrumentation Symposium*, (International Society for Measurement and Control, Research Triangle Park, 1993).
27. D. S. Babikian, N. K. J. M. Gopaul, C. Park, "Measurement and Analysis of Nitric Oxide Radiation in and Arcjet Flow", *J. Thermophysics and Heat Transfer*, **8**, pp. 737-743, (1994).
28. C. S. Park, M. E. Newfield, D. G. Fletcher, and T. Gökçen "Spectroscopic Measurements of the Flows in an Arc-Jet Facility", AIAA Paper No. 98-0893, *$36^{th}$ Aerospace Sciences Meeting*, (American Institute of Aeronautics and Astronautics, New York, 1998),also *J. Thermophysics and Heat Transfer*, **13**, pp.60-67, (1999).
29. C. S. Park, D. G. Fletcher, and J. M. Donohue, "Spatially Resolved Shock Layer Emission Measurements and Analysis in an Arc-Jet Facility", AIAA Paper No. 99-1046, *$37^{th}$ Aerospace Sciences Meeting*, (American Institute of Aeronautics and Astronautics, New York, 1999).
30. H. E. Blackwell, F. A. Wierum, and C. D. Scott, " Spectral Determination of Nitrogen Vibrational Temperatures", AIAA Paper No. 87-1532, AIAA $22^{nd}$ Thermophysics Conference, June, (1987).
31. H. E. Blackwell, F. A. Wierum, S. Arepalli, and

C. D. Scott, "Vibrational Measurements of $N_2$ and $N_2^+$ Shock Layer Radiation", AIAA Paper No. 89-0248, AIAA $27^{th}$ Aerospace Sciences Mtg., January, (1989).

32. G. A. Raiche, "Molecular Ultraviolet and Visible Emission from an Air Arc Jet Bow Shock", ISA Paper No. 94-3020, *$40^{th}$ International Instrumentation Symposium*, (International Society for Measurement and Control, Research Triangle Park, 1994).
33. D. S. Babikian, C. Park, and G. A. Raiche, "Spectroscopic Determination of Enthalpy in an Arc-Jet Wind Tunnel", AIAA Paper No. 95-0712, *$33^{rd}$ Aerospace Sciences Meeting*, (American Institute of Aeronautics and Astronautics, New York, 1995).
34. H. E. Blackwell, C. D. Scott, and S. Arepalli, "Measured Nonequilibrium Temperatures in a Blunt Body Shock Layer in Arc Jet Nitrogen Flow", AIAA Paper No. 97-2522, AIAA $32^{nd}$ Thermophysics Conference, June, (1997).
35. M. W. Winter, M. Auweter-Kurtz, H. L. Kurtz, and C. Park, "Investigation of an Equilibrium Condition Boundary Layer in Front of a Material Probe in a Subsonic Plasma Flow", AIAA Paper No. 96-1853, $31^{st}$ AIAA Thermophysics Conference, June, (1996).
36. M. W. Winter, M. Auweter-Kurtz, and H. L. Kurtz, "Spectroscopic Investigation of the Boundary Layer in Front of a Blunt Body in a Subsonic Air Plasma Flow", AIAA Paper No. 97-2526, AIAA $32^{nd}$ Thermophysics Conference, June, (1997).
37. A. C. Eckbreth, Laser Diagnostics for Combustion Temperature and Species, pp. 304-310, Abacus Press, Tunbridge Wells, (1988).
38. R. C. Hilborn, "Einstein Coefficients, Cross Sections, $f$ Values, Dipole Moments, and All That", *American Journal of Physics*, **50**(11), pp. 982-986, November, (1982).
39. S. Arepalli, E. H. Yuen, and C. D. Scott, "Application of Laser-Induced Fluorescence for Flow Diagnostics in Arc Jets", AIAA Paper No. 90-1763, AIAA/ASME $5^{th}$ Joint Thermophysics Conference, Seattle, WA, June, (1990).
40. W. J. Marinelli, W. J. Kessler, M. G. Allen, and S. J. Davis, "Copper Atom Based Measurements of Velocity and Turbulence in Arc Jet Flows", AIAA paper No. 91-0358, AIAA $29^{th}$ Aerospace Sciences Meeting, Reno, NV, (1991).
41. K. Itagaki, T. Yamada, Y. Inatani, and K. Suzuki, "Measurement of Two-Dimensional Velocity Distribution of Arc-Heated Flow by Cu-LIF", Paper No. 96-d-19, $20^{th}$ International Symposium on Space Technology and Science, Gifu, Japan, May, (1996).
42. T. Takahashi, T. Yamada, and Y. Inatani, "Measurement of NO Rotational and Vibrational Temperatures in Arc Heated Air Flow by LIF Spectroscopy", Paper No. 96-d-18, $20^{th}$ International Symposium on Space Technology and Science, Gifu, Japan, May, (1996).
43. M. Feigl and M. Auweter-Kurtz, "Investigation of Nitric Oxide in a High Enthalpy Air Plasma Flow Using Laser-Induced Fluorescence", AIAA Paper No. 98-2459, $7^{th}$ AIAA/ASME Joint Thermophysics Conference, Alburquerque, NM, June, (1998).
44. D. J. Bamford, "Remote Measurement System for Arcjet Temperature and Density", Deacon Research Phase II SBIR Final Report, Contract No. NAS2-13469, (1993).
45. W. K. Bischel, B. E. Perry, and D. R. Crosley, "Detection of Fluorescence from O and N Atoms Induced by Two-Photon Absorption", *Applied Optics*, **21** (8), pp. 1419-1429, April, (1982).
46. D. J. Bamford, A. O'Keefe, D. S. Babikian, D. A. Stewart, and A. W. Strawa, "Characterization of Arc-Jet Flows Using Laser-Induced Fluorescence", J. Thermophysics and Heat Transfer **9**, 26-33, (1995).
47. D. J. Bamford and A. Romanovsky, "Velocity and Chemical Composition Measurements in an Arc Jet Flow", AIAA Paper No. 95-2039, *$30^{th}$ AIAA Thermophysics Conference*, (American Institute of Aeronautics and Astronautics, New York, 1995).
48. D. G. Fletcher, "Arcjet Flow Properties Determined from Laser-Induced Fluorescence of Atomic Nitrogen", AIAA Paper No. 98-0205, *$36^{th}$ Aerospace Sciences Meeting*, (American Institute of Aeronautics and Astronautics, New York, 1998).
49. D. G. Fletcher and D. J. Bamford, "Arcjet Flow Characterization Using Laser-Induced Fluorescence of Atomic Species", AIAA Paper No. 98-2458, *$7^{th}$ AIAA/ASME Joint Thermophysics and Heat Transfer Conference*, (American Institute of Aeronautics and Astronautics, New York, 1998).
50. D. J. Bamford, L. E. Jusinski, and W. K. Bischel, "Absolute two-photon absorption and three-photon ionization cross sections for atomic oxygen", Phys. Rev. A **34**, 185-198, (1986).
51. R. Loudon, The Quantum Theory of Light, $2^{nd}$ Ed., Clarendon Press, Oxford, pp. 344-347, (1986).
52. D. G. Fletcher and J. C. McDaniel, "Collisional Shift and Broadening of $I_2$ Spectral Lines in Air Near 543 nm", JQSRT **54**, 837-850, (1995).
53. J. B. Jeffries, R. A. Copeland, and D. R. Crosley, "Intramultiplet energy transfer in the collisions of $3p^4D^o$ nitrogen atoms with nitrogen molecules", J. Chem. Phys. **91**, 2200 - 2205, (1989).
54. W. K. Bischel, D. J. Bamford, and L. E. Jusinski, "Absolute calibration of a fluorescence collection system by Raman scattering of $H_2$", Appl. Opt. **25**, 1215-1221, (1986).
55. R. A. Copeland, J. B. Jeffries, A. P. Hickman, and D. R. Crosley, "Radiative lifetime and quenching of the $3p^4D^o$ state of atomic nitrogen", J. Chem.

Phys. **86**, 4876-4884, (1987).
56. J. Balboni, Thermophysics Facilities Branch, NASA Ames Research Center, private communication, August, 1997.
57. H. W. Leipmann and A. Roshko, Elements of Gasdynamics, John Wiley & Sons, New York, 149, (1957).
58. W. G. Vincenti and C. H. Krueger Jr., Introduction to Physical Gas Dynamics, R. E. Krieger, Malabar, 152-158, (1982).
59. I. J. Wysong, J. B. Jeffries, and D. R. Crosley, "Laser-Induced Fluorescence of O(3p $^3$P), $O_2$, and NO Near 226 nm: Photolytic Interferences and Simultaneous Excitation in Flames", *Optics Letters*, **14**, pp. 767-769, (1989).

# Overview of Measurement Techniques at CORIA

(October 1999)

**L. Robin***, P. Boubert, A. Bourdon, A. Bultel, B. van Ootegem and P. Vervisch

CORIA / CNRS UMR 6614
Université de Rouen
Place Emile Blondel
76821 Mont Saint Aignan Cedex
France
Lionel.Robin@coria.fr

## SUMMARY

At CORIA, three wind tunnels have been built up to simulate reentry conditions of different planetary atmospheres. They have been implemented by numerous optical and probe measurement techniques to carry out flow parameters to improve understanding of the aerodynamic behavior and chemical processes.

## 1. INTRODUCTION

The overview of measurement techniques at CORIA presented in this paper do not have the aim to provide, nor an extensive catalog of diagnostic tools devoted to the characterization of the plasma flows, neither an extensive catalog of the more suitable lines or molecular species which can be used for characterization of the plasma flows. It will be presented the diagnostic techniques developed at CORIA for plasma flow studies and the major difficulties encountered with measurement techniques used on species of interest, to drawn information of the signing of the flow. The presentation will be support by works and results issued from experimental studies performed on the wind tunnels developed at the CORIA, and operating under different working conditions simulating reentry conditions of different planetary atmospheres

This review starts with a fast overview of the facilities built at CORIA for simulating reentry conditions of different planetary atmospheres. The next part is dedicated to emission and absorption techniques. Then diagnostic methods based on Laser diagnostic will be presented in the third part. Finally, imaging and in situ measurement techniques are reviewed.

## 2. FACILITIES AND ANALYSIS DEVICES

### FACILITIES AND PLASMA FLOWS

At CORIA, the three main facilities consist mainly on two arc-jets and a high frequency inductive torch. They are in operation to generate high enthalpy flows up to 50 MJ/kg for different gas mixtures. Experiments are performed in test chamber with stagnation pressure from 50 Pa up to atmospheric pressure. Working with different gas mixtures, oxidizing or not such as Ar, $N_2$, $N_2$-$CO_2$, Air…., these facilities are well adapted first to simulate the conditions met during reentry of spacecraft in numerous planetary atmospheres and second to improved understanding of the aerodynamic behavior and chemical processes.

- In the two first facilities, the plasma source is a 10-15 kW dc arc-jet facility. The arc is initiated between the tip of a cathode and a nozzle shaped anode. The nozzle is conical both upstream and downstream. The plasma is expanded in test chamber.
  To reduce the contamination of the flow and increase the lifetime of the electrodes, the materials of the electrodes vary depending the gas used. With $N_2$-$CO_2$ mixture, carbon electrodes are preferred to the ones generally used with non-oxidizing gas and made of tungsten or copper.
  To increase the temperature and the degree of dissociation, a second stage may be added below the first anode. A secondary arc therefore heats up the primary plasma. This amounts the total electric power of about 30%.

- The third wind tunnel is an high frequency inductive plasma torch (ICP torch, 100 kW, 1.7 MHz). The plasma is ignited in a quartz tube (discharge chamber) placed into inductor before its expansion in the test

*Paper presented at the RTO AVT Course on "Measurement Techniques for High Enthalpy and Plasma Flows", held in Rhode-Saint-Genèse, Belgium, 25-29 October 1999, and published in RTO EN-8.*

chamber. In subsonic regime, the jet is 80 mm in diameter. By addition of a shaped-nozzle at the exit of the quartz tube, the wind tunnel works in supersonic regime.

On the one side of the discharge chamber the gas former introduces the working gas. Its conception allows proceeding the reliable stabilization of the discharge, to direct the gas flow and to protect the walls of the discharge chamber against an overheating, thus affording the flow purity. The external part of the quartz tube is water cooled to rule out overheating of the quartz tube by the plasma radiation emission.

With no electrode purity of the flow is expected and experiments may be performed with non-oxidizing as well as oxidizing gas mixture such as $CO_2$, air...

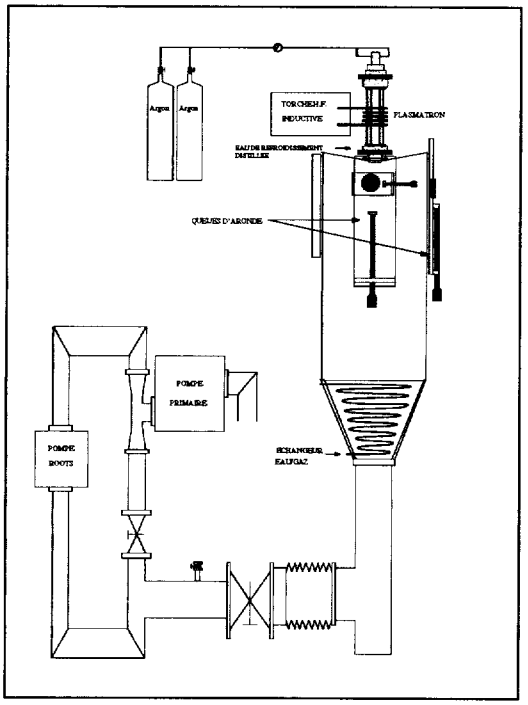


*Figure 1. ICP wind tunnel*

Experimental works are devoted to characterize flow stream impinging simple models as well as to analyze the transfer processes between gas and wall material. Facilities have been implemented for studies such as, analysis of a low pressure plasma in boundary layer situation [1],[2], study of $N_2$-$CO_2$ plasma interaction with a C-SiC tile in low pressure condition [3], analyze of a supersonic turbulent low pressure plasma flow generated for simulating the recombination of charged species [4]...

## 3. MEASUREMENT TECHNIQUES

For the description and explanation of phenomena occurring in a plasma, it is necessary to determine as many parameters of the plasma as possible with the help of the as many as possible mutually independent methods, as accurately as possible. Among the relevant parameters is the composition of the plasma, the temperature and density of the different atoms and molecules and flow velocities of the individual components of the plasma.

Through the emission, absorption and laser spectroscopy of plasma flows, investigation of the plasma parameters may be done by numerous methods of analysis. The study of intensity of spectral lines emitted by atoms, ions and molecules is extensively used with assumption that level population satisfied a Boltzmann distribution law and that the medium is optically thin. With plasma displaying an appreciable absorption, the determination of temperature and number density is drawn from the absorption coefficients of resonance lines.

Among the methods of plasma diagnostics cited above and used at CORIA, attention is done to carry out measurements with the well-adapted method suitable to the operating plasma flow condition of interest.

### 3.1. Diagnostics devices

- DETECTION DEVICES

Different spectrometers and gratings are available at CORIA to spectrally analyze emission and absorption spectra of plasma flow in the spectral range of 120 nm to 10 µm. Species such as N, $N_2$ , O, $O_2$ C, $C_2$, CO, $CO_2$, NO, SiO, $SiO_2$.....are well identified. In the UV and far UV with holographic grating (4230 groves/mm), the highly resolving spectrometer has permit to record the resonance line of nitrogen ($^4P \rightarrow {}^4S^0$: 119.955 nm) with a resolution of 1/100 Å. In the UV-visible spectral range, the molecular spectra of numerous species have been well observed with high resolution of the vibrational and rotational structures. Spectra analysis allowed the signing of the flows and identification of species. Depending of the structure of molecular spectra, the spectra are recorded with highly or partially resolution, or are fully degraded to be matched with synthetic spectra for temperature and density measurements [5].

For single point measurement the light intensity of emitting species is generally recorded on a photomultiplier. For light-of-sight and 2D measurements, the used of Intensified Charged Coupled Detector (ICCD) is commonly used. Time resolved light emission (LIF diagnostics) for single point or integrated light emission

may be easily analyzed by means of 2 GHz numerical oscilloscope.

- LIGHT EMISSION SOURCES

Numerous emission and absorption continuous sources (tungsten, mercury, xenon, deuterium lamps and a krypton pumped monomode Dye laser,...) are available from Ultra-Violet to InfraRed spectral range. They are used for spectrometer wavelength calibration and laser wavelength calibration. In the UV from 180 to 300 nm, the large continuum of the W, Hg, Xe and $D_2$ lamps provide useful sources for absorption spectroscopy.

On the other hand because of the low radiation emission of such lamps especially in the far-UV down to 120 nm, the plasma team develops particular UV sources adapted to particular experimental works (see § Emission and absorption sources).

The highly resolving Dye Laser with a spectral resolution of $10^{-4}$ *nm* is suitable for line broadening measurement by absorption in the visible spectral range (680 –780 nm). In addition, it permits an accurate velocity measurement by Doppler shift.

Laser induced fluorescence (LIF) is a powerful technique which provides local information of the flows parameters with a much lover detection limit than the usual absorption sources. The LIF technique is well known at CORIA and has been extensively used and developed to study high enthalpy flows. The different sources available, not only for LIF, but also for Rayleigh and Raman measurements are:

- The Krypton pumped monomode Dye (SPECTRA PHYSICS) laser. It has been recently modified at CORIA. The slow motorized wavelength scanning has been replaced by an electro-optic LiNBo (Boro-Silicate of Lithium) photo-refractive crystal whose optical index varies with the applied voltage. Then, the ring cavity length changes and the laser is tilted in wavelength. The method will allow scanning frequency in the turbulent time scales. Up to now, this device is under-development. With this method we expect to measure simultaneously the temperature, number density of excited states and velocity by laser induced fluorescence in a turbulent plasma flow.

- The excimer laser (LPX 150/50T LAMBDA PHYSIK) used with ArF (193.4 nm) or KrF (248.0 nm) gas mixture. The radiation is of about 180 mJ at 193.4 nm and 250 mJ at 248 nm, with a pulse duration of 10 ns at FWHM. The excimer laser consisting in two separate cavities may be used indifferently in broadband mode or narrow-band mode, respectively with resolution of 0.5 nm FWHM and 1.2 $10^{-3}$ *nm* at HWHM. In narrow-band mode, the pulsed radiation can be tuned with a step increment of 2.2 $10^{-4}$ *nm* on the full spectral range of the broadband emission.
The coupling of the excimer laser with a high pressure Raman Shifter Cell filled with suitable gas ($H_2$, $D_2$...) allows to shift the incident laser radiation to wavelength of interest, corresponding to excitation wavelengths of molecules on both sides from the initial 193.4 and 248 nm excitation wavelength. The excimer laser working with ArF and KrF gas mixture provide a fruitful diagnostic tool for the whole species present in air plasma and at the vicinity of materials such as C-C, SiC-SiC and C-SiC immersed in plasma flow.

- A pulsed Optical Parametric Oscillator (OPO SPECTRA PHYSICS) pumped by Nd:YAG. The OPO provides a powerful and monochromatic radiation (0.3 $cm^{-1}$ *FWHM*) from IR (2 μm) down to UV (15 mJ at 226 nm). The spectral range can be extended further in the UV using a Raman Shifter Cell.

- A Raman Shifter Cell filled with specific gases and coupled with the excimer laser at 193 or 248 nm allows to enlarge the spectral range of the excitation wavelengths from the excimer laser radiation.

### 3.2. Emission and absorption

Emission and absorption spectrometry of atomic and molecular species has been extensively study in plasma flows from VUV to IR spectral range to provide information on number density species and temperature. Although emission and absorption spectrometry provides information on the medium, attention is done on the on the relevance of the deduced parameters.

- INTEGRATED LIGHT EMISSION AND ABSORPTION

Emission or absorption measurements are not punctual measurements and the recorded intensities have to be considered as integrated along the light-of-sight of the observed signal. In a non-absorbing medium without number density and temperature gradient, the local intensity may be easily drawn from the recorded intensity signal. The main difficulty encountered appears in an inhomogeneous medium, in presence of a non-axis-

symmetric flow and of an optical thick medium. For emission or absorption measurements, the light intensity recorded is providing from the light emitted along the line-of-sight and is resulting from the summation of numerous individual locations which are different in density and temperature. Local measurement can be only derived with an axis-symmetric geometry if an Abel's inversion is applied:

$$i(x) = 2\int_{x}^{R} \frac{i(r)rdr}{\sqrt{r^2 - x^2}}$$

The reverse relation is given as:

$$i(r) = -\frac{1}{\pi}\int_{x}^{R} \left(\frac{di}{dx}\right) \frac{1}{\sqrt{x^2 - r^2}} dx$$

where i(x) is the integrated light-of-sight signal intensity and i(r) the radial (or local) signal intensity.

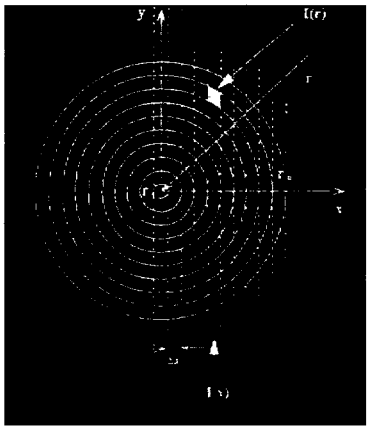

*Figure 2. Abel's inversion*

A Beer's law may be added to the Abel's inversion to correct the self-absorption of the medium. For that, a separate absorption measurement have to be done.

- MEASUREMENT OF THE GROUND AND EXCITED STATES

While emission spectroscopy provides information on the upper excited levels of atoms, molecules and radicals, the absorption spectroscopy allows to probe the metastables and fundamental ground states.

As a general rule, emission or absorption measurement gives only information on the population density of the emitting or absorbing levels of atoms and molecules. If the collisional coupling between the various energy levels of the atoms or molecules is very efficient, then a Boltzmann equilibrium assumption may be assessed to deduce from emission or absorption measurements the whole concentration of species of interest and the temperature.

As the emitting or absorbing levels concerned in the visible or near UV spectrum are generally issued from excited electronic levels of atoms and molecules, the population density is only representative of a finite proportion of the entire species population density. The main part of the particles are on the fundamental level or on the nearest electronic levels such as the metastable states. In expanding flow, emissive levels are populated either by recombination of the parent ions or by exchange of excitation with another molecule. So, they are highly weakly coupled with the fundamental level and then more representative of the whole species population density. Then, by emission and absorption measurement, it isn't relevant to deduce the species population density according to a Boltzmann equilibrium distribution. We have also to notice that the emissive levels being weakly populated, the rotational distribution can be very sensitive to selective rotational population rate by chemical reaction and even measurement of the ground and nearest excited states. As mentioned above, only absorption measurement on the fundamental or nearest electronic levels may provide with a good confidence the species concentration. Generally, the radiative transition taken into account are in the VUV region. The difficulty provides mainly from the lack of efficient absorbing source, added to the difficult operating conditions in the UV spectral range imputed to the $O_2$ molecular Schumann Runge absorption band.

- EMISSION AND ABSORPTION SOURCES

The usual calibration sources and absorption lamps available (W, Hg, Xe and De) are used to provide absolute calibration of number density and absorption spectroscopy. Attention has been done in the UV spectral range because of the high resolution suitable to the analysis of rovibronic structure of molecular spectra and broadening of line. By this way, UV detection and particular UV sources has been developed for emission spectrometry and overall, UV absorption down to 120 nm. As it has been yet noticed, the main difficulty for these UV source and more generally for UV spectrometry, is the strong absorption by the $O_2$ Schumann-Runge absorption band and transmitivity of optical glasses down to 250 nm. So, it is required the use of specific optical windows (MgF2 and LiF below 180 nm) and to set optical arrangement and detection device in vacuum or in low-pressure conditions, or in inert gas atmosphere.

Different UV-sources have been developed for particular experimental works, to produce stable and reproducible media with a continuous or discontinuous highly light emission spectrum on a broad spectral range.

An example of a discontinuous UV source with a specific optical arrangement is presented here. It consists in an atmospheric Argon-plasma seeded with nitrogen in low concentration [5]. This source has been used as high emission UV source to involve absorption of the resonant and metastable states (120 to 180 nm), in a low pressure nitrogen plasma flow. The high-pressure Ar-$N_2$ medium provides suitable N-atomic lines broadening to be used as absorption source on the N-atomic spectrum emitted from the low-pressure nitrogen plasma. The complete optical arrangement is set at 3 $10^3$ *mbar*, and optical windows and lenses are made of $MgF_2$, 2 mm thick. In the 120-200 nm spectral range, the UV emission spectrum points out neither the presence of the Lyman-Birge-Hopfield, nor the Vegard-Kaplan system. The spectrum is a discontinuous spectrum of atomic nitrogen lines. The hydrogen line $L\alpha$ set at 121.6 nm, the resonant oxygen line (130 nm) and carbon lines (165 and 193.1 nm) are also observed. From the atomic nitrogen highly resolved absorption lines (down to 1/1000ème nm), the number density of the metastable states $2P \rightarrow {}^2P^0$ (174.272, 174.525 nm) and $2P \rightarrow {}^2D^0$ (149.262, 149.267 and 149.467 nm) has been determined. On the other hand, the self-absorption in the UV atmospheric source precludes direct measurement on the resonant transition ${}^4P \rightarrow {}^4S^0$ (119.955, 120.022, 120.071 nm). In this case, populations have been determined using a model including first the emission measurements after an Abel's inversion and second a correction from the self absorption by the medium, in agreement with the absorption lines profiles recorded.

An other example is the development of experimental source to increase the potentiality of studies in the UV down to 120 nm. It consists of a dielectric barrier discharge (DBD) in rare gas to produce excited dimmers sources as $Ar_2$, $He_2$, $Ne_2$ and $Kr_2$. De-excitation of these molecules produces intense radiation in the ultra-violet spectral range 100 – 300 nm. At low pressure conditions, the DBD source emits a discontinuous spectrum mainly constituted by the resonant lines of the rare gas. With increasing pressure, the spectrum is shaded off in a continuum highly lightening favorable to absorption spectroscopy. The DBD is made of a quartz tube (500 mm length and 5 mm) used as dielectric with two metallic electrodes painted on its external surface. Micro-discharges are generated with a power supply generator (7 kV – 20 kHz) and provide a high electronic number density $\left(10^{20}-10^{21}\ m^{-3}\right)$ with electron energy levels up to 20 eV and a lifetime of about 100 ns, depending from the gas mixture. The integrated light emitted by the DBD source produces thus high radiation (few mW) in the sight-of-light of the quartz tube. It is noted that from the quality of the gas mixture will depend the light emission from the DBD source. It has been observed that presence of impurities may produce an abundant spectrum of the impurity itself, and releases the excimer emission. The future of DBD sources is promising and always under development at CORIA. It is driven by the opportunity to probed the ground levels of atomic species (O, N, C...) and molecules (CO, SiO...) in planetary atmospheres such as the Earth and Martian ones in order to better understand the chemical mechanisms in heterogeneous and homogeneous situations.

### 3.3. Laser diagnostics

By comparison with usual emission and absorption methods, the laser diagnostics present advantage of local and/or 2D measurements with high selectivity of species of interest. Laser diagnostics are extensively used for temperature and density measurements by comparisons with computed synthetic spectra.

Molecular spectra are calculated for the main species observed in reentry conditions such as the earth or mars atmospheres (i.e.: $N_2$, $O_2$, $C_2$, CO, $CO_2$, NO, CN...), and for the main species observed in studies of plasma/surface interactions (i.e.: SiO, SiC, $SiO_2$ ...).

From high monochromatic light emission laser source adds to the possible spectral tilting in wavelength, velocity measurements may be carried out.

The main laser diagnostics used to probe the plasma flows are summarized hereafter.

- RAYLEIGH SCATTERING

The Rayleigh scattering is the elastic interaction between the incident laser radiation and gas molecules, so without excitation wavelength dependence in regard to the molecule probe and thus without interaction with the internal energy molecular mode. Because intensity of the scattered light is proportional to the number density of gas molecules, the Rayleigh scattering is a suitable method to determine the gas number density.

One of the advantages of Rayleigh scattering in comparison with the Raman light scattering is that Rayleigh cross sections are in three orders of magnitude greater than the corresponding vibrational Raman cross sections. Thus the Rayleigh scattering is the strongest of the molecular light scattering techniques well adapted to the number density measurement, as well as at low gas density than in higher pressure conditions. In an other

side, one disadvantage of the Rayleigh scattering is that it is an elastic process, and thus not species specific. In addition, Rayleigh scattering may occur at any excitation wavelength, the shorter wavelength being more efficient because of the Rayleigh scattering cross section evolution with $\nu^4$. Since the Rayleigh light scattering is observed in coincidence with the excitation wavelength, the signal can be overlapped with Mie scattering (20-fold greater than the Rayleigh signal) and parasite reflections from surfaces surrounding the incident radiation.

Rayleigh scattering has been used extensively in low-pressure high enthalpy wind tunnel for total number density measurements and also in well identified medium for calibration of the fluorescence signal intensity. For example, the used of high energy density of excimer laser in the far UV is well suitable to achieve total number density measurements in medium with pressure down to 1 mbar.

Depending on species present in the plasma flow and operating conditions, attention has to be done with Rayleigh measurements. It is necessary to tune the excitation source wavelength out of absorbing transitions of species present in the flow, in order to avoid overlapping of LIF and Rayleigh (for example with ArF excitation in presence of NO molecule). It is also noticed that as total number density is directly proportional to the Rayleigh signal and determined at the same wavelength than the excitation source, the reflection of the incident excitation radiation may enhances the effective Rayleigh scattering signal and thus provides an erroneous value of the total number density.

- SPONTANEOUS RAMAN SCATTERING

The Raman scattering is the inelastic interaction between the incident light and the electronic-mediated vibrational-rotational modes of the molecules. The inelastic process is described by an energy exchange between the incident photon and internal energy modes of the scattering molecule. Thus implies that the scattered photon may gain or loss energy and that the Raman signal can be spectrally observed at different wavelengths, shifted from the incident radiation. The spacing energy between the incident and scattered photon corresponds to the excitation energy of the molecule, and thus is specific of the molecule excited.

The scattering light spectrum consists of Raman Stokes, Rayleigh and Raman Anti-Stokes lines. The incident photon excites a molecule from rovibronic levels of the electronic ground state, from the lower vibrational levels to a upper virtual one. This level de-excites to rovibronic levels of the electronic ground state with radiation emission at shorter, identical and higher wavelengths than the one corresponding to the excitation energy of the molecule, respectively named the Raman Stokes, Rayleigh and Raman Anti-Stokes scattering. Only the Rayleigh scattering remains unshifted in regard to the excitation radiation.

Intensity of the Raman scattering is dependent from the vibrational number density of the probed molecule, and then depends from the rovibronic levels thermally populated. The scattered spectrum, spectrally resolved allows to identify molecular species according to the energy spacing between the incident and scattering radiation. This implies that Raman scattering may provide simultaneously, multiple species concentration and temperature measurements. Since Raman scattering may occur at any excitation wavelength and because spontaneous Raman scattering involves only transitions from the electronic ground states, it is possible to measure the number densities of stable species, such as $N_2$, $O_2$, CO, $CO_2$, SiO, $SiO_2$.... The only limitation to this technique is the weak light emission imputes to the lower values of the Raman scattering cross sections. Thus, accurate Raman scattering measurement will depend first on the energy spacing between the excitation wavelength and the scattering Raman signal, and second from the relative ratio between Rayleigh and Raman scattering cross sections.

- LASER INDUCED FLUORESCENCE

Laser induced fluorescence is an electronic absorption process that produces relatively high signal intensity with high spatial resolution. Except the resonant fluorescence emitted at the same wavelength than the excitation one, the fluorescence spectrum is normally red-shifted from the excitation wavelength and thus easier to discriminate. Fluorescence intensity is directly proportional to the molecular number density and can be used to measure the concentration. However, quenching effects imputed to collisional partners present in the gas mixture, pressure and temperature can reduce the fluorescence signal intensity.

Up to now, in the spectral range of the ArF laser at 193.4 ± 0.5 nm, experiments were performed extensively on $O_2$ , $NO_\varepsilon$. For molecules such as CO, $NH_3$ and $H_2O$, the fluorescence may also be observed via the multi-photons photo-dissociation processes. For CO molecule, it has been pointed out that through the different CO excitation pathways by means of an ArF excitation source, only the three photons process may be retained. The difficulty provides in this case to an absolute number density measurement.

The spectral energy distribution of the excimer shows us strong absorption region dues mainly to absorption of the laser radiation by the intense $O_2$ Schumann-Runge bands and by absorption of HF and C molecular species, HF and C being considered as intra-cavity impurities. Gaps in the spectral energy distribution takes on particular importance in the excitation process of atomic or molecular species, because they prevent or degrade excitation of the species of interest, and modify the general feature of the fluorescence or excitation spectra. For example, a good knowledge of laser radiation spectral energy is needed to understand and improve some particular fluorescence phenomena such as the photo-dissociation of the carbon monoxide. In addition, as usually done, the matching of experimental spectra with computed ones may be greatly influence by a non-constant energy density of the laser source and provides non negligible discrepancies inherent only to the badly knowledge of the excitation mode. This may be harmful to number density determination and temperature when this latter is drawn from line ratio.

- RAMAN SHIFTER

As a result of the Raman lines emission is the use of the incident laser emission as a pump laser to provide via the Raman Stokes and Raman Anti-Stokes scattering of a suitable molecule, a new set of excitation wavelengths shifted from the incident one, to induce fluorescence of molecules such as CO, SiO, O. It is noticed that the Raman Shift effect may be observed only in gas with high Raman cross section such as $H_2$, $D_2$, HD and $CH_4$ (respectively, 4155, 2987, 3628 and 2917 $cm^{-1}$). The efficiency of the process remains lower, less than 10% on the first stokes and is decreasing for higher components.

For experiments performed at CORIA on interaction plasma/surface studies, interest has been focussed on the CO, SiO, O molecules excited via a Raman Shifter Cell pumped by an ArF excimer laser

Carbon monoxide fluorescence (CO)

The carbon monoxide fluorescence is induced at 230.1 nm from the $H_2$ 2nd Stokes issued from the Raman Shifter Cell pumped with ArF excimer excitation source. Efficiency is less than 10%, but only few mJ are necessary to induce the CO fluorescence $\left(B^1\Sigma^+,\ v'=0 \leftarrow X^1\Sigma^+,\ v''=0\right)$ in low pressure conditions set at 50 mbar. Fluorescence is detected in the visible spectral range from 450 to 560 nm.

Oxygen fluorescence (O)

The oxygen fluorescence is induced at 226 nm from a two-photon process, from the fundamental $2p^3P$ to the atomic excited state $3p^3P$. The fluorescence light is detected in the visible from direct de-excitation, either from the transition $3p^3P \rightarrow 3s^3S$ at 845 nm, or from the transition $3p^5P \rightarrow 3s^5S$ at 777 nm, after collisional transfer from the $3p^3P \rightarrow 3s^5P$. The usual excitation may be provided from a doubled and mixed Nd:YAG; the radiation is closed to 226 nm, with energy of about few mJ. Whatever the gas used in the Raman Shifter Cell pumped by ArF or KrF excimer laser, no light is emitted at the wavelength of interest. On the other hand, if we consider the summation of the second and third stokes generated from the Raman Shift Cell filled with Deuterium (8 bars) and pumped by ArF excitation source, then light emitted from the Raman Cell is tuned on the oxygen transition $2p^3P \rightarrow 3p^3P$ which one may be excited. The major difficulty is imputed to the filtering of both transitions among the other stokes, and to the focussing two transitions of different wavelengths at the same measurement point. The method is promising in plasma studies and in catalysis studies in which oxygen is considered as major specie.

Monoxide silicate fluorescence (SiO)

In the spectral range 230-232 nm, the SiO absorption spectrum via the $\left(A^1\Pi,\ v'=1 \leftarrow X^1\Sigma^+,\ v''=0\right)$ transition is in coincidence with the second stokes of Hydrogen ($H_2$) pumped with ArF excimer laser. Because of high transition probability, this vibrational sequence can be easily excited at 231 nm. The more critical point for the SiO molecule provides from the spectral range of fluorescence de-excitation at 240 nm, in coincidence with the emission band of NO$\gamma$. The SiO spectrum shape is well characteristic and defined with a bandhead set at lower wavelengths and rotational structure varying extensively with the rotational temperature. SiO molecule expected to be produced by catalytic parietal recombination in air plasma / SiC interaction, may be a suitable specie for temperature measurement.

### 3.4. Measurement from molecular spectra

Analysis of molecular spectra provide information on the signing of species present in the flow and information on temperatures and densities. The band spectrum of diatomic molecules allows:

- the determination of the temperature and particles densities from absolute intensity of individual bands.

- determination of the rotational temperature from the relative intensities of the rotational lines within a band.
- determination of the vibrational temperature via the relative intensities of several bands belonging to the same electronic transition.

When temperatures and densities are drawn from comparison with computed synthetic spectrum, accuracy will depend on the bands system analyzed, the temperature levels considered and accuracy of the computed spectrum in regard to the particular recording experimental conditions. The computed spectrum have to be as accurate as possible and include correction for apparatus function of the optic detection device, constituted mainly by the monochromator used as a narrow or broad band-pass filter over the full spectral range of the molecular of interest.

At CORIA, the synthetic spectra of numerous diatomic molecules met in re-entry conditions have been calculated in emission and are also available in absorption. For species probed by laser excitation, excitation and fluorescence spectra have been built. It is important to note that generally comparisons between experimental and synthetic spectra are carried out for flows at low or moderate temperature. For high temperature medium, the high rotational and vibrational levels have to be considered for a best synthetic spectra description.

As previously mentioned, with a nom-homogeneous flow, numerous spectra will be necessary to calculate from the Abel inversion the spectrum in a single point measurement. High or low resolution spectra may be used to determinate the temperature value.

The rotational temperature is determined from the relative intensities of the rotational lines within a molecular band. When frequency of heavy particles collisions with an upper excited state of molecule is at least 5-fold greater than the radiative transition probability, then a Boltzmann equilibrium between rotational levels and the upper electronic excited states of molecules may be expected. Taken into account the strong coupling between translational and rotational energy states, the rotational temperature derived from experiment will be then given as the kinetic gas temperature.

The vibrational temperature is determined from the relative band intensities of the same electronic state. A Boltzmann equilibrium between the vibrational energy levels of the upper excited state is expected if the frequency of inelastic collisions (energy exchange between vibrational level) is higher compare to the electronic transitions probability.

For non resolved rotational structure, an experimental spectrum is commonly spectrally degraded to record the general envelop shape of the spectrum. It is then compared with a synthetic spectrum computed with identical apparatus function. Rotational and vibrational temperatures of the synthetic spectrum are adjust up to the general feature of the computed spectrum coincides exactly to the experimental one.

In non equilibrium plasma, it is commonly observed that $T_{gas}<T_{vib}<T_{elec}$ because molecular vibrational energy levels are both influenced by heavy particle collisions and by electronic collisions.

### 3.5. Velocity measurement

Velocity measurements are performed considering a Maxwell velocity distribution of emitting species which move according to the mean velocity of the flow. The light emitted from species and observed along a line of sight different from the direction of the flow, is shifted by the quantity corresponding to the mean velocity component of the molecule in the direction of observation. For observation in the direction of the particle mean velocity, the light emitted (or line profile) is blue-shifted. Conversely, it is red-shifted with the same absolute shift value for observation in the direction opposite to the mean movement of the flow stream. For observation perpendicularly to the flow axis, the light emitted is unshifted. The shift in wavelength is given as the Doppler shift and expressed as:

$$\frac{\Delta\nu}{\nu}=\frac{v}{c}\cos\theta$$

where $\nu$ is the frequency, v the velocity and c the light speed. $\theta$ is the difference angle between the flow axis and the light of sight of observation in a direction such as $0<\theta<\pi/2$. Experiment may be carried out either from lines emission, or from absorption or fluorescence analysis.

## 4. OTHER DIAGNOSTICS

- LANGMUIR PROBES

The Langmuir probes are used to determine the behavior of the electrons in plasma flows. With plasma out of equilibrium with the different energy modes, electronic temperature as well as electronic number density may be determined from electrostatic Langmuir probe measurement.

When an electrode is immersed in an ionized gas, an electrostatic sheath is formed if its potential is set at a different potential than the plasma one. Due to the electric field perturbation, charged species are repulsed or attracted, collide with the electrode and provide an induced current. The study of this current provides the charged species characteristics. The electrostatic probes consist of two cylindrical metallic wires shielded with a thin ceramic sleeve. Their dimensions are such that assumption of uncollisional sheath surrounded the probe is respected (ratio to the Debye length (sheath thickness) to the mean free path of the medium of interest), to apply the Laframboise theory. Typically probes are 0.05 mm radius and are aligned on the flow axis. Measurement close to model surface is provided with wires implanted on the surface as flush probes. The small size provides local measurements and reduces depletion of low energy electrons. One probe yields the plasma floating potential. A sawtooth voltage is applied with a low frequency (1-2kHz) to the other probe. The temperature of thermal electron is drawn from the second derivative of the intensity versus voltage probe characteristic, represented with a straight line for a Maxwellian electron energy distribution. The electron number density is calculated from the probe current value at plasma potential.

It is noticed that electrostatic probes have been adapted to work at high frequencies in order to reach the small time scales of turbulent plasma flows. Indeed, for higher sweeping frequency up to 90 kHz, the noise induced by the RC characteristics of coaxial cables becomes non-negligible and prevents probe measurements of weak current. So, an original setup has been developed for high frequency. The noise reduction is obtained by doubling the measuring circuit by a compensatory one. On one side, the circuit supplies the real probe immersed in the plasma flow, on the other side, one supplies a dummy probe, identical to the first one, placed outside the plasma. The RC cable induced noise removal is obtained by analogic subtraction of both signals. This device was used at 90 kHz to measure the plasma number density fluctuations in turbulent flow and determine the turbulent integral scale of large structures.

Flow velocity may be also provided from crosses Langmuir probes, setting at right angle. The ionic drift current is inefficient on the current for the probe aligned to the direction of the flow axis, but added to it when the probe is placed in the direction perpendicular to the flow. With assumption than the Debye shield is collisionless and that it thickness is smaller than the probe radius, the ratio of the perpendicular to parallel probe current component is given as proportional to the ratio of the flow velocity to the most probable ions thermal speed.

- HEAT FLUX PROBE

The local measurements of the parietal net heat flux exchanged is obviously, a very important parameter for studies of plasma / surface interaction for simulation of reentry conditions in different planetary atmospheres.

The homemade thermo-gauge consists of a constantan foil (Radius 3.8 mm, thickness 0.2 mm) brazed on a copper tube and insert in an insulator shield. Immersed in a radian medium, the heat flux is continuously drained from the sensor to the surrounding body. Due to the low conductivity of the constantan, a difference of temperature occurs between the center and the edge of the foil, which is measured by a thermocouple. The relationship between the thermocouple value and the spectral net heat flux is calibrated by means of a monochromatic source and points out a linear response for net heat flux up to 80 $kW.m^{-2}$. The time rise up is estimated to about one second.

This device satisfies well flux measurements up to 10-100 $kW.m^{-2}$, in the same order of magnitude than those encountered in reentry plasmas. On the other hand, value of the incident flux as to be considered as a mean value when plasma parameters such as the spectral range of plasma emission and thermal conductivity and local kinetic temperature of the plasma are not accurately determined.

- THERMOGRAPHY

The facility devoted to analysis on the parietal net heat flux exchange and to comparative studies on the catalytic behavior of C-C and C-SiC TPS materials immersed in a plasma flow simulating the Martian atmosphere, has been implemented by Infra-Red thermography detection. The Infra-Red camera is cooled with Peltier effect and it analysis spectral range is 2 μm – 5 μm. It is pointed out that accurate 2D temperature field measurement depends mainly from the accurate knowledge of the material emissivity at the detection wavelength.

Analysis of medium may also be performed in the I.R. spectral range by means of classical I.R. plasma emission.

- OTHERS INTRUSIVE METHODS

Others intrusive methods such as pitot probe and thermocouple are also used in plasma flows. In our experimental working conditions and considering the weakness spatial resolution, these devices do not allow to provide more than an order of magnitude of the parameters of interest.

## 5. SYNTHETIC SPECTRA

Temperatures and densities are derived from the comparison of synthetic spectra with experimental ones [6]. These comparisons also allow to point out the non-Boltzmann distributions of vibrational and rotational populations. At CORIA, the synthetic spectra of all the diatomics species met in reentry conditions have been calculated in emission. Absorption spectra are also available for the same molecules, radicals and ions. It is important to note that generally comparisons between experimental and synthetic spectra are carried out for flows at low or moderate temperatures. At CORIA, we have particularly studied the extension of synthetic spectra to high rotational and vibrational temperatures (for example see Figure 3).

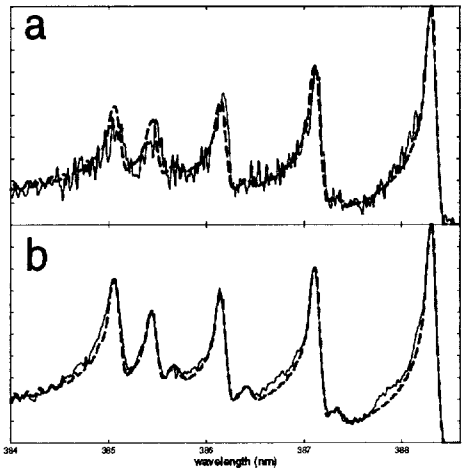


*Figure 3. Experimental (solid lines) and synthetic (dashed lines) spectra of CN violet system in alow pressure $CO_2N_2$ plasma.*
*(a) exit of the plasma generator $T_{rot}$=7000 K, $T_{vib}$=9500 K, FWHM =0.092 nm*
*(b) over a C-SiC tile $T_{rot}$=7500 K, $T_{vib}$=13200 K, FWHM=0.092 nm*

These section presents two molecular systems of interest studied in the $N_2CO_2$ [6] plasma flows analyzed in the different wind tunnels at CORIA.

- CN – red system

CN is one of the most emitting molecules in plasma media produced from mixtures as $CO_2$-$N_2$ and $CH_4$-$N_2$. Within the visible range of wavelengths, its red system is the main source of molecular radiation with the Swan bands of $C_2$.

That red system gathers all the rovibronic transitions between the $A^2\Pi$ excited state and the $X^2\Sigma^+$ fundamental state. Its structure is close to the $\gamma$ and $\varepsilon$ bands of NO and to the ultraviolet bands of OH. The spectrum involves 6 main branches and 6 satellite branches. One of the main distinctive features of that kind of system is the signification level of the satellite branches. The high number of branches leads to a real complexity of the spectra. According to the experimental resolution, there is no main bandhead but several secondary bandheads corresponding to the main branches.

The $\Delta v=0$ sequence is located in the infrared while the first bands of the $\Delta v=+3$ sequence and upper sequences take place in the visible range of wavelengths. Vibrational and rotational structures develop both towards large wavelengths.

The significant emission through this system is more a population effect rather than caused by a short lifetime of the state; indeed, the highest transition probabilities remain lower than $10^5$ $s^{-1}$. $A^2\Pi$ state may be populated by electron collisions if the ionization rate is high enough or by excitation transfer with vibrationaly excited partners such as CO and N2 (v>3).

- CO – fourth positive system

With atomic emission, CO fourth positive system is the more significant source of radiation during a spacecraft entry in the atmosphere of planets such as Mars and Venus. This system is made of transitions between two single states: the excited state $A^1\Pi$ and the fundamental state $X^1\Sigma^+$. The wavelength of the first band origins ($\Delta v=0$) is close to 155 nm but in vibrationaly excited media, it is possible to detect some band in absorption over 200 nm. Vibrational and rotational structures develop both towards large wavelengths. In spite of numerous overlapping, the spectra remain little complex since there is only three main branches. Lifetime of state A is very short and thus the fourth positive system owns high transition probabilities. These features make this system very interesting for studies in emission as well as in absorption spectroscopy because of the very low detection limit. However, the location of (A-X) transitions in the wavelength range complicate the experiments. Problems are connected to the absorption of light by Schumann-Runge bands of molecular oxygen below 190 nm. This phenomenon prevents to work with an optical axis under atmospheric air. Vacuum conditions are needed which are different according to the wavelength. A pressure lower than 1 Pa is rated to avoid oxygen absorption problems.

## 6. STUDIES AT CORIA AND ON SITE CAMPAIGNS

In this section, we present briefly the different studies carried out at CORIA on high enthalpy flows. The objective is to illustrate the potentialities of the techniques developed at CORIA. Further details may be found in the given references.

We show also that the techniques developed at CORIA may be implemented on other facilities with very different working conditions.

### 6.1. Numerical simulations

In parallel to experiments, different numerical codes have been developed at CORIA:

- Two 2D Navier-Stokes codes for laminar and turbulent flows,
- a 2D parabolic boundary layer code.

The objective is to carry out thorough experiment/modeling comparisons in order to better understand the studied flows. Discrepancies observed between computations and experiments have led us to study in more detail the modeling of numerous terms in conservation equations. New models have been proposed for different rate coefficients (see for example [7]) and energy exchange terms (see for example [8]).

### 6.2. Experiment/modeling comparisons in a nitrogen plasma jet and boundary layer

Numerous measurements have been carried out in a partially ionized nitrogen flow generated in one of the arc-jet facility of the CORIA [1]. In parallel, two codes have been developed: one for the laminar supersonic free jet [9] and a second one for the boundary layer [10] developed over a flat plate set along the jet axis. The interest and the difficulty of this experiment/modeling comparison was that a good agreement had to be obtained on numerous parameters. This has led us to study in detail the modeling of different terms in the conservation equations. For example, Fig.4 shows the density of atomic nitrogen on the fundamental state (derived from UV emission and absorption spectroscopy) on the jet axis downstream the nozzle exit [5].

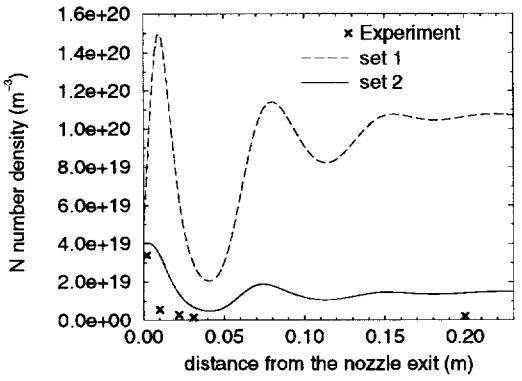


*Figure 4. Influence of the kinetic scheme on the calculated N density on the axis of a nitrogen plasma jet.*

These experimental data were in total disagreement with classical kinetic schemes (set 1), which predict a strongly dissociated flow. A thorough study of the kinetic scheme and recent measurements of poorly known reaction rates (set 2) have been taken into account, and finally, a fairly good agreement has been obtained with experiments.

### 6.3. Experimental investigation of the interaction of a C-SiC wall with a low pressure $CO_2$-$N_2$ jet

Reentry conditions in the Martian atmosphere have been simulated at CORIA to study the behavior of thermal protection systems (TPS). The model was a C-SiC tile, and the initial composition of the mixture was 50% $N_2$ and 50% $CO_2$. The main problem in that kind of study is to generate a plasma which contains atomic and molecular oxygen by means of an arc between two electrodes. Indeed, due to the erosion of electrodes by oxygen, metallic species may be present in the jet. These species as copper or tungsten may modify the chemistry of the jet and even the catalycity of the tile. The solution offered by the use of hafnium or zirconium for the cathode is valid as an insert of these metals at the end of a water-cooled copper rod, and with high flow rates. Indeed, first, at low flow rates, the arc is not carried enough by the gas and is hung on the copper structure of the cathode and second, as zirconium has a low thermal conductivity, a whole zirconium cathode would have a very short life time. So a plasma generator was realized with high-purity carbon electrodes, the low erosion of which, does not pollute the jet. Currently, a new generator using plasma cutting torch technology is developed to work at higher flow rates with a better stability of the jet.

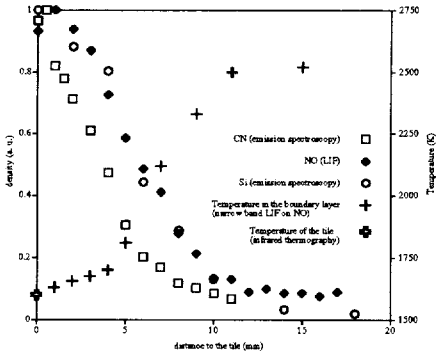


*Figure 5. Measured species concentration profiles in the boundary layer over a C-SiC tile in a $CO_2$-$N_2$ plasma.*

The boundary layer over the C-SiC plate (and for comparison over a carbon plate) was analyzed at a pressure of 100 Pa. Figure shows the measured profiles of NO, CN, Si of and the temperature [3]. Measurements are underway to probe other species as CO, O, N, C, SiO. The ionization degree of the flow is close to 0.05% and the temperature of the tile is 1600 K (measured by thermography).

### 6.4. Study of a supersonic turbulent low pressure argon plasma jet

In the after-body trailing wake of a ballistic missile, abnormal electron density fluctuations are generally observed. To study this phenomenon, we have considered at CORIA a simplified situation: an under-expanded argon jet which becomes turbulent [4]. The inductive plasma torch conditions are: gas flow rate 2.6 g/s, input power 45 kW, pressure in the chamber 17 mbar. Classical measurement techniques have been used to measure mean parameters in the flow, and fast methods have been developed to reach the turbulent time scales. For example, the electron temperature and density have been measured simultaneously and locally using the fast sweeping method developed at CORIA. It is also interesting to note that the different lasers at our disposal allow us to carry out measurements in extreme conditions.

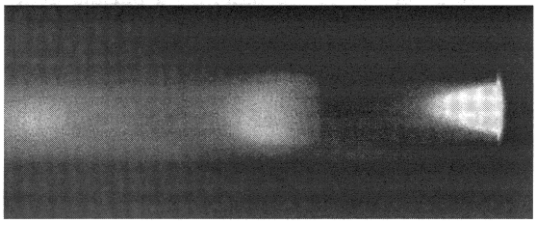

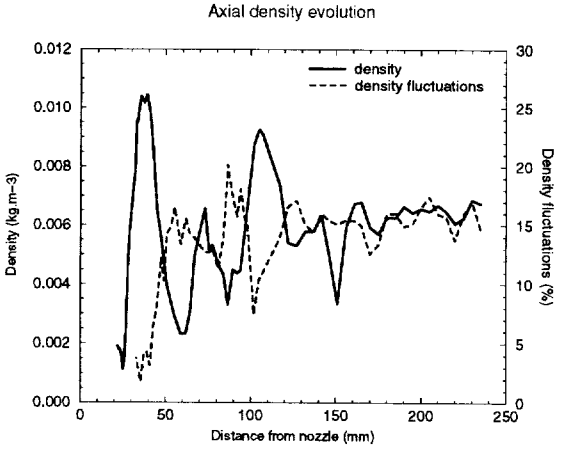


*Figure 6. Total density and its fluctuation of an argon plasma jet on the jet axis. Flow conditions are given in the text.*

For example, using a UV ArF laser, Fig 6. shows the total density and its fluctuations measured on the jet axis by Rayleigh scattering with a detection limit lower than 100 Pa. In parallel to experiments, a numerical code has been developed to simulate this flow [11]. Comparisons with experiments are underway.

### 6.5. Study at the Tsniimach Center - Moscow

A measurement campaign cite [12] has been carried out at the central research institute of machine building (TSNIIMACH Moscow) on two facilities:

- the ground experimental Y13PHF high frequency facility devoted to characterize the physico-chemical phenomena encountered in reactive flow/surface interactions,

- the TT1 arc jet facility designed to study the aerodynamics and the heat transfer of supersonic and hypersonic spacecrafts.

The main purpose of this work was to implement the LIF technique to measure species concentrations, velocity and temperature in the incoming flow, boundary layers and shock layers lying at the vicinity of a thermal protection system (TPS) model simulating a misalignment of tiles. The objective of this study was twofold : first to obtain reliable data for validation of numerical codes, second to point out the great potentialities of the LIF technique to study continuous high enthalpy air-flow/body interaction. The technical challenge of the test campaign was the exportation from CORIA to the TSNIIMACH center of the

complete set of equipment needed for laser measurements and their implementation on different facilities with an experimental set up, as the whole diagnostic apparatus, fully automated and operating under an industrial environment. The experimental challenge has been to implement a new experimental methodology able to draw simultaneously local parameters in continuous high enthalpy supersonic air flow set for Hermes flight conditions at altitude 50 km and Mach 15.

Fluorescence was induced by a narrow band tunable ArF Excimer laser on NO epsilon-band. Rotational temperature and NO number density have been determined. Moreover, the spatial resolution of the LIF technique permitted accurate characterization of velocity distribution of the impinging free stream as well as in the flow field around specific shaped models. Thickness of the boundary layer and shock were also determined.

On the Y13PHF High frequency 1MW torch (15 MJ/kg, Mach 2.5) more devoted to catalycity studies on TPS materials, it has been determined that, due to the shape of the nozzle, the flow was 3D, and not 2D as expected.

Second, it has been pointed out that presence of N in the boundary layer participates to a non negligible growing of NO and CN at the vicinity of the plasma surface interaction, which is never taken into account in wall catalycity modeling. In the TT1 arc jet facility 10 MW (7.5 MJ/kg and Mach 4.5) studies have been carried out over a shaped model simulating a misalignment of tiles. First, experiments have been performed in the free jet to locate a sufficient homogeneous region to put the wide $SiO_2$ model and assure subsequently a 2D aerodynamic description of the boundary conditions with flat NO number density, temperature and velocity profiles. Then the spatial resolution of the LIF experimental set up has allowed to carry out a fine description of the velocity, temperature and NO concentration in the boundary layer and in the shock layer down to the surface of the model. This test campaign has demonstrated the potential of the LIF technique for the instrumentation of continuous high enthalpy facilities.

In parallel to experiments, a numerical code has been developed at CORIA to study the flow in the nozzle of the TT1 facility, and the downstream free jet.

On the axis at the nozzle exit, a fairly good experiment/modeling agreement is obtained on velocity, but computations underestimate by about 30 % the translational temperature and overestimate by more than one order of magnitude the NO number density [13]. Similar results have been obtained in the F4 hot shot wind tunnel. In fact, to explain experimental results, a much higher recombination rate of O atoms than the one given currently in the literature, would be necessary. Then, to improve the experiment/modeling comparison, complementary measurements of the O concentration would be of great interest.

### 6.6. Study at the TCM2 shock tube - Marseille

A measurement campaign was carried out during last summer on TCM2 free piston facility in Marseille (IUSTI-Université de Provence). The main purposes of this campaign were first, to prove the cleanness of the flow during the useful gust, and second to measure the density of nitrogen monoxide in the bow shock layer in front of a 2D model. The challenge was to excite nitrogen monoxide and to record the fluorescence image on an intensified CCD camera in the range of 0.3 ms corresponding to the useful gust. Results and details are presented at this conference in the paper [14].

## 7. CONCLUSION.

From numerous experiments performed in the wind tunnels available at CORIA and on industrial sites, it is pointed out that the measurement techniques developed at CORIA, and always under development, are well adapted to carry out information on the flow parameters during reentry conditions of different planetary atmospheres. It is also pointed out that in parallel to experiments, the experiments / numerical simulations comparisons are needed to improve the understanding of the aerodynamic behavior and chemical processes in planetary reentry condition.

## bibliography

[1] L. Robin, B. Chéron and P. Vervisch, "Measurements in a nitrogen plasma boundary layer: the boundary conditions of charged species", Phys. Fluids B, vol.5, no.2, pp.610-620, 1993.

[2] L. Robin, P. Vervisch and B. Chéron, "Experimental study of a supersonic low pressure nitrogen plasma jet", Phys. Plasmas, vol.1, no.2, pp444-458, 1994.

[3] P. Boubert, L. Robin, and P. Vervisch, "Experimental investigation of the interaction of a C-SiC wall with a low pressure $CO_2N_2$ plasma jet", in Proceedings of the 23rd International Conference on Phenomena in Ionized Gases, (Toulouse, France), 1997.

[4] B. van Ootegem, L. Leborgne; and P. Vervisch, "Experimental study of a supersonic turbulent low pressure argon jet", in Proceedings of the 3rd European Symposium

on Aerodynamics for Space Vehicles, (Noordwijk, The Netherlands), ESA-ESTEC, 1998.

[5] A. Bultel, B. Chéron and P. Vervisch, "Measurements of the ground state and metastable atomic nitrogen number density in a low pressure plasma jet", Plasma Sources Sci. Technol., vol.1, no.2, pp.597-605, 1995.

[6] P. Boubert, B. van Ootegem, L. Robin, B. Chéron and P. Vervisch, "The use of synthetic spectra for temperature measurements in different kinds of plasma", in Proceedings of the 21st International Symposium on Rarefied Gas Dynamics, (Marseille, France), 1998.

[7] A. Bourdon and P. Vervisch, "Three-body recombination of atomic nitrogen in low pressure plasma flows", Phys. Rev. E, vol.54, no.2, pp.1888-1898, 1996.

[8] A. Bourdon and P. Vervisch, "Electron-vibration energy exchange models in nitrogen plasma flows", Phys. Rev. E, vol.55, no.4, pp.4634-4641, 1997.

[9] P. Domingo, A. Bourdon and P. Vervisch, "Study of a supersonic low pressure nitrogen plasma jet", Phys. Plasmas, vol.2, no.7, pp2853-2862, 1995.

[10] A. Bourdon and P. Vervisch, "Study of a supersonic low pressure nitrogen plasma boundary layer over a metallic plate", Phys. Plasmas, vol.4, no.11, pp4144-4157, 1995.

[11] P. Domingo and T. Benazzouz, "Studying turbulent plasma using direct numerical simulation and probability density function", AIAA Paper 98-0982,1982.

[12] L. Robin, D. Honoré and P. Vervisch, "Laser Induced Fluorescence measurements in high enthalpy facilities: application to the study of air plasma/surface interaction", in Proceedings of the 20th International Symposium on Shock Waves, (Pasadena, California), 1997.

[13] A. Bourdon, A. Leroux, P. Domingo and P. Vervisch, "Experimental modeling comparison in a non equilibrium supersonic air nozzle flow", J. Thermophys. Heat Transfer, vol.13, no.1, pp.68-75, 1999.

[14] P. Boubert, A. Chaix, A. Chikhaoui, L. Robin, and P. Vervisch, "TCM2 a ground test facility: spectroscopic measurements in a bow shock layer", in Proceedings of the International Symposium on Atmospheric Reentry Vehicles, (Arcachon, France), 1999.

# Laser Induced Fluorescence in high enthalpy facilities in the Tsniimach Center (Moscow – Russia)

**L. Robin**
CORIA / CNRS UMR 6614
Université de Rouen
Place Emile Blondel
76821 Mont Saint Aignan Cedex
France

## SUMMARY

The requirements for accurate measurements, the higher sophistication in the design, the need for monitoring, control and diagnostics in difficult circumstances and the request for data bases to validate numerical codes have incited the advanced measurement techniques to the investigation of ground test facilities.

This lecture presents an experimental work and the results obtained by Laser Induced Fluorescence (LIF) in continuous high enthalpy supersonic airflows. The test campaign is performed at the Central Research Institute of Machine Building (Tsniimach, Moscow region) in ground experimental facilities designed for aerodynamics and heat transfer studies of supersonic and hypersonic aircrafts. The main objective of this test campaign was to perform measurements of species concentrations, temperature and velocity in the incoming flow, and in the boundary and shock layers over a Thermal Protection System (TPS) model simulating a misalignment of tiles, by means of techniques developed by the plasma team from the University of Rouen. So, an original method using LIF diagnostic has been implemented to measure simultaneously the three parameters. Fluorescence of NO was induced in the high enthalpy air plasma flow by a tunable ArF-excimer laser via the ε-band system $D^2\Sigma^+_{(v'=0)} \leftarrow X^2\Pi_{(v''=1)}$. Measurements of the rotational temperature and NO number density have been performed. The spatial resolution of the LIF technique permitted accurate characterization of the boundary and shock layer, as well as shock thickness. Finally, flow velocity is deduced from the Doppler-shift measurements of excited rovibrational NOε band. Analysis of the results will allow to assess the validity of the computational tools in order to control the representativity of future industrial tests devoted to local aerodynamic studies.

## 1. INTRODUCTION

Re-entry trajectories for spacecrafts include large regions where the flow surrounding the vehicle is in high thermo-chemical non-equilibrium and behaves differently from a perfect gas. Molecules become vibrationally excited, dissociated and even ionized, and the hot gas may emit or absorb radiation. When the atoms produced by dissociation reach the wall surface, chemical reactions, including recombination, may occur. The thermo-chemical phenomena of vibration, dissociation, ionization, surface chemical reaction and radiation are referred to commonly as a high-temperature real-gas phenomena, and thus induce changes in the dynamic behavior of the flow and provide a strong and complex gas/surface interaction. To develop and verify phenomenological models, as well as to validate high enthalpy flows with CFD (Computed fluids Dynamics) tools, ground test facilities are required to generate such reacting gas flow over configurations of interest, and have to be implemented with sufficient diagnostics to describe the character and behavior of the flow. Although ground facilities have serious limitations in simulating full-scale flight conditions, they are capable of examining selected aspects which are expected to be vital to success in the full-scale flights, then offer the advantage of observations, such as optical flow visualization, which are not realistic in real flight.

Fine measurements in high enthalpy flows represent a technological challenge and research is done in this way to develop new methods and new instruments to probe the physical-chemical and aerodynamics states of re-entry plasmas. So, in the purpose of the framework of the Hermes program, to validate and improve CFD tools, experimental test cases has been planned on high enthalpy flows generated in different facilities of the Tsniimach Institute.

*Paper presented at the RTO AVT Course on "Measurement Techniques for High Enthalpy and Plasma Flows", held in Rhode-Saint-Genèse, Belgium, 25-29 October 1999, and published in RTO EN-8.*

In the test campaign conducted in the Tsniimach Center, Hermes flight conditions at altitude 50 km and Mach 15 has been covered in different continuous supersonic high enthalpy air flow ground test facilities. As real flight requirements are not fulfilled at the whole for chemistry and aerodynamic studies, the strategy adopted was to work on different facilities of which experimental conditions satisfy as much as possible the relevant problem of interest to validate and improve the numeric tools upon fixed flight conditions. The TT1 arc jet facility and a high frequency facility (Y13PHF-plasmatron) were devoted respectively to local aerodynamics problems arising in supersonic high temperature flow and physico-chemistry phenomena encountered in reactive-flow / surface interaction. The aim of the complete program was twofold. First, to improve reliable data for validation of chemical non-equilibrium shock and boundary layer and Navier-Stocke codes to compute a new test case of supersonic air-heated flow impinging on a TPS surface, and second to point out the potentiality of the LIF technique for instrumentation of continuous high enthalpy facilities.

The lecture is intend to present the LIF diagnostic tools developed for application to this specific study, to highlight its advantages and weaknesses, and to illustrate it with an experiment performed in an industrial environment. Before discussion on the experimental work is given, the general feature of the implemented facility and generalities on LIF measurements will be presented.

In the state of the art, the results presented here are drawn from LIF experiments performed on the TT1 arc jet facility for studies on the aerodynamic properties encountered in high temperature air flow impinging a shaped model designed for simulate a misalignment of tile. The ground test facility has been implemented by LIF technique to draw measurements of NO density, rotational temperature and velocity evolutions of the medium. Experiments are performed by means of a ArF-excimer laser in free jet as well as in numerous test sections within the boundary and shock layer down to the TPS surface model.

## 2. DIAGNOSTIC BASED ON LASER INDUCED FLUORSCENCE

### 2.1 Generality

The early development of Laser Induced Fluorescence (LIF) method was driven by single–point measurements, but application of LIF as non-intrusive method to probe complex flows in a short time exposure has been dominated by multi-point planar imaging. Planar Laser Induced Fluorescence (PLIF) may be considered as an advanced method of flow visualization. In common with methods such as Schlieren and Shadowgraph, the planar LIF is extremely used for quantitative and qualitative or semi-qualitative characterization of complex flow fields, providing spatially resolved information in a plane rather than integrated over a line-of-sight. The LIF has been extensively developed in the characterization of combustion processes and flames diagnostics for temperature and radical species measurements. The great capacity of LIF, which lies both to the strength of the fluorescence process and to the selectivity of species detection has demonstrated its applicability in high temperature medium under drastic pressure conditions associated with high enthalpy flow simulations. Well adapted to probe non-equilibrium airflow such as those generated in ground test facilities, LIF has become a powerful diagnostic tool for physico-chemical and aerodynamic property studies.

Laser Induced Fluorescence is the result of light emission incoming from an atom or a molecule excited by a laser beam. In a LIF measurement, the molecule is initially at its lower electronic state before it is excited to an upper electronic energy level by a laser source. When the beam is directed into the gas, the molecule absorbs a laser photon and undergoes transition from the populated electronic ground state to an upper electronic state of the absorbing species. The wavelength of the laser excitation needs to be tuned in coincidence with an absorption transition of the molecule of interest. Typically, the lower states probed are depending from the broadening of the excitation wavelength and correspond either to a single or to a set of rovibrational levels of the ground electronic state. Then, the originally upper populated states return to lower states of the ground state by radiative process in agreement with the selection rules and collisional processes, fluorescence and collisional quenching respectively.

The emitted fluorescence signal is detected at right angle from the incident laser beam pathway either onto a high-speed photo-multiplier (spot measurement) or a CCD intensified camera (1D or 2D planar measurement).

When the excitation wavelength of the laser could not be tuned on the absorption band of single species of a complex mixture, the selectivity of species can be done in detection, by tuning the spectral resolution through spectral filter (or monochromator), on the selected fluorescence signal of species of interest.

The fluorescence intensity provides information on the concentration of the emitting species. For quantitative interpretation of LIF experiment, a model involving the

population and competitive depopulation mechanisms is required.

In the following section, we will describe the basic physical processes involved in LIF experiment. First, a simplified two-level model will be presented, then extended to a multi-levels model. The second part will be devoted to the development of the method for simultaneous measurement of temperature, species concentration and velocity by LIF on NO in high enthalpy airflow. The calibration process associated will be presented to draw the absolute values of the measured flow properties. Finally, results from experiments on TT1 will be presented.

## 2.2 Simplified two level model

The two-level model illustrates the principal mechanisms involved in LIF of molecular species and allows to point out the important processes following its excitation by a monochromatic laser source. This model is a simplified one, and considers a single lower rovibrational level probed by the monochromatic radiation and the upper excited level populated by absorption and depopulated by spontaneous emission (fluorescence), stimulated emission and collisional quenching rate. The model doesn't take into account, neither the complete set of rotational levels involved by the selection rules at excitation, nor the complete fluorescence de-excitation observed from the upper excited vibrational level down to the various vibrational levels of the ground state.

Let us $U_v$, the spectral density energy of the incident laser radiation corresponding to a transition of the molecule, from the rovibrational level ($E_1$, $N_1$, $v_1$) of the lower electronic state to the rovibrational level ($E_2$, $N_2$, $v_2$) from the upper electronic excited state. Let us the total gas number density is given by $N_0=N_1+N_2$.

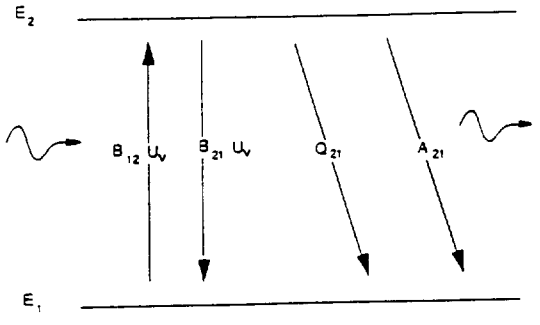


Fig(1): The two-level model

The dynamic to populate the upper excited state $N_2$ is driven as follow

- Absorption ($N_1B_{12}U_v$): the molecule absorbs a photon whose energy hv corresponds to the suitable transition $E_2$-$E_1$. Increasing of the $N_2$ population is proportional both to the $N_1$ population density of the lower state and to the laser intensity.
- Spontaneous emission ($N_2A_{21}$): the originally populated level $N_2$ return to the lower fundamental rovibrational state and light is emitted first at the same wavelength than the excitation laser radiation (resonant fluorescence).
- Stimulated emission ($N_2B_{21}U_v$): the molecule can be returned to its original quantum state by laser induced stimulated emission. This process is observed in the same direction as the light-of-sight of the incident laser beam, on the contrary to the spontaneous emission or fluorescence, which can be detected in the $4\pi$ steradians.
- Quenching ($N_2Q_{21}$): this non-radiative de-excitation process is imputed to the inelastic collisions with other molecules which results in electronic energy transfers between the different electronic states of the molecule.

The Einstein balance of population and de-population of the $N_2$ upper excited rovibrational level excited by laser radiation is expressed by the differential equation:

$$\frac{dN_2}{dt} = N_1B_{12}U_v - N_2B_{21}U_v - N_2(A_{21} - Q_{21}) \qquad (1)$$

$A_{21}$= Einstein coefficient for spontaneous emission (fluorescence emission)
$B_{12}$= Einstein coefficient for stimulated absorption
$B_{21}$= Einstein coefficient for stimulated emission
$Q_{21}$= the collisional transfer coefficient or quenching
$U_v$= the spectral energy density of the laser source
The Einstein balance includes the fluorescence emission and quenching terms, which depend from the selection rules existing between an excited rotational level ($N_2$) and the rotational levels of the ground state.

With assumption that at t=0 the $N_2$ level is not populated, and than $U_v(t) = Cte$, the solution of the differential equation is given as:

$$N_2(t) = \frac{N_1B_{12}U_v\left(1 - e^{-((B_{12}+B_{21})U_v + A_{21} + Q_{21})t}\right)}{(B_{12}+B_{21})U_v + A_{21} + Q_{21}} \qquad (2)$$

Depending on the pulse laser intensity and in regard to the characteristic time $\tau$, function of the intrinsic parameters of the molecule, the quenching rate and the energy density of the excitation source,

$$\tau = ((B_{12}+B_{21})U_v + A_{21} + Q_{21})^{-1} \qquad (3)$$

the equation of $N_2(t)$ can be rewritten as:

$$N_2(t) = N_1 B_{12} U_\nu \tau \left(1 - e^{-t/\tau}\right) \quad (4)$$

For the limiting case corresponding first to a low laser intensity or linear fluorescence regime given by

$$U_\nu \leq U_\nu^{sat} = \frac{A_{21} + Q_{21}}{B_{12} + B_{21}} \quad (5)$$

and assuming a pulse duration shorter than the characteristic time $\tau$, the $N_2$ population can be considered as stationary and expressed as:

$$N_2 = N_1 B_{12} U_\nu \quad (6)$$

Finally, the fluorescence signal detected can be expressed as:

$$P_{21}^{fluo} = N_2 A_{21} \varepsilon_c V_c \frac{\Omega}{4\pi} h\nu \quad (7)$$

where $\varepsilon_c$, $V_c$, $\Omega_c$ are constants.
$\varepsilon_c$ is a calibration constant, including the transmitivity characteristics of optics and the sensitivity of the detector, in the spectral range of the detection of interest.
$V_c$ is the volume of gas probed by the laser.
$\Omega_c$ is the solid angle in collection.

From the measurement of the fluorescence signal and from knowledge of the emission probabilities of the emitting level considered, population of the upper excited level may be determined. With assumption of equilibrium at the temperature T, the Boltzmann equation will provide the total ground state population of the molecule.

The two-level model developed above is extended to the general analysis to express the fluorescence signal in different experimental situations, depending from the order of magnitude of the quenching term $Q_{21}$ in regard to the Einstein coefficient for spontaneous emission $A_{21}$, and depending from the intensity and pulse laser duration. Because rotational energy transfer process (RET) acts to replenish the population of the laser excited states and at the opposite acts to drain the population from the laser-populated states to lower states, they have to be considered in the collisional quenching rate.

- In a weak energy density laser excitation with $(B_{12} + B_{21})U_\nu << A_{21} + Q_{21}$, the fluorescence emission is described simply with identical assumptions than the two-level model, and fluorescence emission simplifies to:

$$P^{fluo} \propto N_1 B_{12} U_\nu \frac{A_{12}}{A_{12} + Q_{12}}$$

If the quenching rate is in the same order of magnitude or greater than the radiative one, then it is possible to measure directly the temporal evolution of the fluorescence to extrapolate the quenching term. In the opposite, for to stronger quenching rate it had to be compared to the laser pulse duration.

## 2.3 Multi-levels model

For diatomic molecules, the simplified two-level model is not expected to be widely applicable to take into account the rotational and vibrational energy redistribution (RET and VET). Molecular models including three or four-levels have been developed to expressed the rapid coupling between rotational and also vibrational levels. However uncertainty persist in such model, because of lack of reliable data between levels involved in the fluorescence scheme of interest, and because quantitative detection of a single radical species by LIF therefore requires an enormous amount of information on collisions process. The RET and VET are generally approximated by a mean value averaged for a set of rotational and vibrational levels and more often compared to the electronic quenching term. Since the energy spacing between rotational and vibrational levels are closed to the translational energy of heavy particles, the RET and VET are more efficient than the electronic one, and remains the predominant process. Since the fast redistribution of the rovibronic levels between neighboring state takes place, the history of the excited level is lost in the fluorescence spectrum and lines are not necessary redistributed with a Boltzmann distribution.

The rotational (RET) and vibrational (VET) redistributions with neighbouring levels, in which inelastic collisions with the other molecules of the medium produce internal rotational and vibrational energy transfers of the molecule. We have to note that, the difficulty of LIF measurement remains in the absolute value determination of species density and is mainly imputed to this quenching term. Its value is highly depending from the collisional partners, temperature and pressure conditions, and is usually difficult to estimate and not well known for complex experimental working conditions.

In the model, the term of pre-dissociation, related to a change from a stable electronic state to a repulsive unstable one, has not been taken into account. Observed for some molecules excited with a high-energy laser source, the pre-dissociation is a non-radiative process, which can compete highly with the fluorescence emission. It is commonly imputed to interactions between atoms of the molecules with production of internal energy transfer following by the dissociation of the molecule. The molecules pass from an electronic excited state to the Continuum State of a neighbouring electronic state with the same or thermally accessible energy level. The pre-dissociation rate is shorter than the quenching rate. So, for a quantitative measurement of species concentration, it ids necessary to determine the quenching value.

## 2. 4 Quantitative measurements and calibration

The calibration of fluorescence signal to provide the absolute value of concentration is obtained by comparison between fluorescence light intensity of the molecule of interest and the Rayleigh scattering light recorded in a reference medium whose temperature and total density are well determined.

### 2.4.1 Rayleigh scattering

The fundamental principle governing the Rayleigh scattering is that the elastic collisions between gas molecules and incident laser light. The scattered light has the same wavelength as the incident light. The scattered light signal, in general, is directly proportional to the laser power, the gas density and a differential cross-section on the gas that is probed. For experiments with Rayleigh scattering detected at 90° in the direction perpendicular to the incident laser beam pathway and a minimized scattering volume defined by the intersection of the incident laser beam (polarized perpendicular to the detection) and the image of the aperture placed in front of the collection device, the Rayleigh scattering signal $P_{\nu_0}^{rayleigh}$ is given as:

$$P_{\nu_0}^{rayleigh} = (\varepsilon_c \Omega_c V_c) I_{\nu_0} N_{Ref} \sigma_{\nu_0}^{rayleigh} \tag{8}$$

with

- $\varepsilon_c$, $V_c$ and $\Omega_c$ are calibration constant, respectively the efficiency of the collection device, the volume of gas probed by the laser and the solid angle in collection.
- $I_{\nu_0} = E_{\nu_0}^{laser}/S$ = incident laser intensity ($W.cm^{-2}$), expressed by the ratio of laser energy at $\nu_0$ with section of the laser beam.
- $N_{Ref} = PA_o/RT$, the total number density of the gas molecule ($cm^{-3}$) related to the pressure, temperature and Avogadro's number: $A_o$=6.023 $10^{23}$ molecules.$mol^{-1}$.

The term $\sigma^{rayleigh(\nu_0)}$ is the differential Rayleigh scattering cross section given by:

$$\sigma^{rayleigh(\nu_0)} = \left( \partial \sigma_{\nu_0}^{rayleigh} / \partial \Omega \right) = \frac{4\pi^2 \nu^4}{c^4} \left( \frac{n-1}{N} \right) \sin^2 \theta \tag{9}$$

with

- $n$ = the real part of the refractive index of the gas.
- $N$ = the molecular number density.
- $\theta$ = the scattering angle for detection

For a gas mixture, the formulation of the Rayleigh scattered cross section may be expressed as:

$$\sigma^{rayleigh(\nu_0)} = \sum_k \chi_k \sigma_{k,\nu_0}^{rayleigh} \tag{10}$$

with

- k the number of species present in the gas mixture.
- $\chi_k$ is the mole fraction of each species k ($\Sigma\chi_k$=1).
- $\sigma_{k,\nu_0}^{Rayleigh}$ its associated Rayleigh cross section.

### 2.4.2 Fluorescence de-excitation

In a complete radiative de-excitation scheme, it will be consider, first the summation on the numerous rovibrational levels involved by the selection rules at excitation then at de-excitation (rotational branches P, Q, R ...) which participate to the radiative de-excitation according to the allowed selection rules from the upper excited rovibrational state to a single ground rovibrational state), and second, the summation on the numerous vibrational levels involved ($\Delta v$=0,±1,2), from the upper excited vibrational level down to the numerous vibrational level of the ground state:

$$P_{total}^{fluo} = \sum_{\Delta v} \sum_{N_2} \sum_i P_{2i}^{fluo} \tag{11}$$

For most experiments and in presence of a gas mixture, different species or molecules may be excited at the same wavelength with the excitation source. The fluorescence resulting has to be filtered to allow a separate analysis of the different species present in the medium of interest. The use of a selective band-pass filter allows to limit the spectral range in detection to a single vibrational de-excitation corresponding to a selected molecule and then provide a selective analysis of the medium. For the molecule of interest, the intensity of fluorescence is then given as:

$$P_{\Delta v}^{fluo} = \sum_{N_2} P_{2i}^{fluo} \tag{12}$$

The ratio of $P_{total}^{fluo} / P_{\Delta v}^{fluo}$ is inversely proportional to the ratio of the vibrational emission probabilities between the vibrational level considered and all the vibrational levels participating to the global radiative de-excitation of the molecule of interest.

### 2.4.3 Fluorescence cross-section

In this section, let us consider only that the intensity of fluorescence is depending to a single rotational transition of the molecule, from the upper excited vibrational level to a single rovibrational i-level of the ground state.:

$$P_{2i}^{fluo} = \varepsilon_c V_c \frac{\Omega_c}{4\pi} h\nu N_2 A_{2i} \tag{13}$$

Considering the particular transition between the lower ($E_1$, $N_1$) and the upper ($E_2$, $N_2$) rotational leve, the absorption process induced by the laser radiation and expressed by the Einstein balance between the de-populated of lower rotational state and the populated upper rotational states is given by:

$$\left(\frac{dN_2}{dt}\right)^{abs} = N_1 B_{12} U_{\nu_{12}} \tag{14}$$

with $U_{\nu_{12}}$ the spectral density energy, so that $h\nu_{12} = E_2 - E_1$ and $B_{12}$ the Einstein absorption coefficient of the transition considered.

With assumption of the drift movement of particles carry out with disorderly velocities and according a Maxwell velocity distribution, line are Doppler broadened and the cross section profile of the excited transition may be described by a gaussian shape such as:

$$\sigma_{12}^{abs} = \int_{\delta\nu_D} \sigma_{12}^{abs}(\nu)d\nu = \int_{\delta\nu_D} \sigma_{12}^{abs}(\nu_{12}) \exp\left(-\left(4\ln 2\left(\frac{\nu-\nu_{12}}{\delta\nu_D}\right)^2\right)\right) d\nu \tag{15}$$

$$= \sigma_{12}^{abs}(\nu_{12}) \left(\frac{\pi}{4\ln 2}\right)^{1/2} \delta\nu_D \tag{16}$$

with $\sigma_{12}^{abs}$ the total absorption cross section, $\sigma_{12}^{abs}(\nu)$ the monochromatic absorption cross section, and $\sigma_{12}^{abs}(\nu_{12})$ the absorption cross section value on the center line. $\delta\nu_D$ is the Doppler broadening $\delta\nu_D = \nu_{12}\sqrt{\frac{8kT\ln 2}{mc^2}}$ and c is the speed of light.

Let us $U_{\nu_{12}} = Cte$, the spectral energy density of the radiative excitation, the differential equation related to the photon absorption process in the spectral range $\nu,\nu+\delta\nu$ can be expressed as:

$$\left[\frac{dN_2}{dt}\right]_{\nu+\delta\nu}^{abs} = \frac{cU_{\nu_{12}}}{h\nu} N_1 \sigma_{12}^{abs}(\nu) \frac{U_{\nu_{12}}}{h\nu} N_1 \tag{17}$$

With integration in the spectral range of ν, ν+Δν of the absorbing transition, the populated upper $N_2$-level by photon absorption can be rewritten as:

$$\left(\frac{dN_2}{dt}\right)^{abs} = \frac{cU_{\nu_{12}}}{h\nu} N_1 \sigma_{12}^{abs}(\nu_{12}) \left(\frac{\pi}{4\ln 2}\right)^{1/2} \delta\nu_D \tag{18}$$

The comparison with the Einstein balance equation thus provides the relationship between the absorption cross section and the Einstein coefficient for the transition of the molecule of interest:

$$\sigma_{12}^{abs}(\nu_{12}) = \frac{h\nu_{12}}{c} B_{12} \left(\frac{4\ln 2}{\pi}\right)^{1/2} \frac{1}{\delta\nu_D} \tag{19}$$

From relations between Einstein coefficients and degeneracy between the two levels involved in the transition:

$$B_{12} = \frac{\varpi_2}{\varpi_1} B_{21} = \frac{\varpi_2}{\varpi_1} \frac{c^3}{8\pi h\nu_{12}^3} A_{21} \tag{20}$$

Finally, the absorption cross section is expressed as:

$$\sigma_{12}^{abs}(\nu_{12}) = \frac{\varpi_2}{\varpi_1} \frac{c^3}{\nu_{12}^3} A_{21} \left(\frac{1}{4\pi^2}\right) \sqrt{\frac{m}{8kT}} \tag{21}$$

### 2.4.4 Calibration method

The calibration method for absolute concentration measurement is provided by the ratio of the intensity of fluorescence of the molecule probed with the Rayleigh intensity of a reference gas mixture probed in the same experimental condition. Both measurement is performed assuming , a given operating condition for the exciting source and identical optical setup and detection device. With such operating conditions, the incident laser radiation $I_{\lambda_0}$, the transmitivity of optical setup $\varepsilon_c$, and the size and probed volume $V_c\Omega_c$ are constants, and are ruled out in the expression of the ratio of fluorescence with Rayleigh given by:

$$\frac{P_{21}^{fluo}}{P^{rayleigh(\nu_0)}} = \frac{\alpha N_1 \sigma_{21}^{fluo}}{N_{Ref}\sigma^{rayleigh(\nu_0)}}$$

The ratio $P_{21}^{fluo}/P^{rayleigh(\nu_0)}$ is experimentally measured. The term $N_{Ref}\sigma^{rayleigh(\nu_0)}$ is calculated for the calibration medium used as the reference medium. The term $\sigma_{21}^{fluo}$ is the fluorescence cross section and can be calculated easily from the absorption cross section term. $N_1$ is the unknown parameter to determine. The term α is a constant.

The variations of the Rayleigh scattered light signal are the result of the mixture number density (i.e. the variation of temperature or pressure or both) or the species variations, or even both. Hence, an unambiguous interpretation of the Rayleigh scattered light signal requires that experiment has to be conducted in reference mixture for which the term $N_{Ref}\sigma^{rayleigh(\nu_0)}$ is well known. The ratio of intensities given above is expressed for a single transition and a monochromatic detection. Depending on the spectral range at excitation and detection of fluorescence, the term $N_1\sigma_{21}^{fluo}$ have to be summed on all the rovibronic considered.

## 2.5 Temperature measurement with LIF

With density measurement, the temperature is one of most important flow parameters to be determined for simulation of kinetic processes with numerical models and comparisons between model predictions and experimental test case. One of the advantages of LIF is that measurement of number density and temperature may be performed together with the same spatial resolution at the location of the measurement point.

The rotational temperature is determined from the relative intensity of less two rotational lines within a molecular band with assumption of Boltzmann equilibrium. At the opposite of number density measurement, the temperature value is drawn from comparison of the relative experimental lines ratio with the calculated one by means of synthetic spectra computed at different temperatures. For lines recorded with the same operating experimental conditions, no information on the size of the probed volume and detection solid angle are to be known. Accuracy of the measurement will be provided by accuracy of the synthetic spectrum, the knowledge of the exact excitation laser radiation, the lines involved in the fluorescence process (energy spacing between rotational level, transition probability, quantum yield...) and spectral range in detection. Whatever the excitation source used, the two levels model presented above has to be completed to include the selection rules between the rovibrational levels involved at excitation and de-excitation, to take into account the possible overlapping of lines.

For two levels involved, the temperature is drawn from the ratio of the relative intensity of the two lines, but for several lines involved, more accuracy can be obtained from the semi-logarithmic Boltzmann plot of fluorescence intensity weighted by the Einstein transition probability $P_k$ and degeneracy $g_k$ of the considered k levels, versus its energy $E_k$:

$$Ln\left(\frac{\phi_{fluo}}{P_k g_k}\right) = -\left(\frac{E_k}{kT}\right) + Cte$$

The accuracy on the temperature value will depend first, on the energy spacing between the rotational levels involves and on the relative rovibronic population in regard to the medium temperature. Secondary, it will depend on the radiative process observed in detection: i.e. either radiation from an excitation spectrum or from a fluorescence spectrum.

For a broadband laser excitation (i.e. fluorescence spectrum), numerous rovibronic transitions are simultaneously excited from the low energy states to the upper excited one according to the selection rules of individual excited transition. The lines intensity ratio is drawn from the fluorescence spectrum spectrally resolved through a high resolving monochromator set at a selective $\Delta v$ vibrational fluorescence de-excitation. By this way, the temperature is measured from the upper excited state and is greatly dependant from the population equilibrium of this level by the RET process. Accuracy on the temperature will then depend on the efficiency of the RET to provide a Boltzmann distribution on the upper excited.

The use of a single laser source working in broadband at excitation and coupled in detection with a monochromator and a CCD camera allows to perform a 1D-temperature measurement on a light of sight of the laser beam if assumption of efficient RET is done. The 2D description of the CCD camera is thus devoted, in one direction along the beam pathway for the spatial resolution of the medium, and in the second direction for the spectral resolution through the monochromator.

For a narrow band excitation (excitation spectrum), the laser is tuned separately on the maximum peak intensity of each rovibronic transition of interest and thus provides the spectral resolution at excitation. In detection an excitation spectrum is recorded for both rovibronic transition considered. Without filtering, the complete radiative de-excitation depends only on the lower rovibronic state excited by the laser radiation, and thus on the population equilibrium of the ground state.

In case of short run duration of the test facilities, the two-line thermometry is used to probe simultaneously the maximum intensity of two rotational lines from the same excited vibrational level. This method is commonly used for planar temperature field determination with a CCD camera (or for spot temperature measurement with two photo-multipliers tuned on each line). However and as a general rule, it required to focus at the same location two planar laser beams tuned respectively on the maximum peak intensity of each transition of interest, with an identical energy density. Accuracy on the temperature determination thus depends mainly from accuracy of the excitation wavelength in regard to the rovibrational lines selected. In the case of weak or strong laser excitation (non-saturated or saturated LIF), the fluorescence signal is solely dependant from the initial-ground state populations which may be assumed as function of the temperature alone (i.e. ground state populated with a Boltzmann distribution). In the intermediate case, between weak and strong laser excitation, the transitions are only partially saturated and uncertainties on temperature may provide from the ratio of intensity.

The detection limit of a photo-multiplier being in some order of magnitude lower than the detection limit of a CCD camera, the use of a single spot measurement is preferred in medium with low absorbing properties or with low number density. Add to the wish to increase the signal to noise ratio, the single spot LIF is commonly used, when difficult experimental geometry conditions doesn't allow to implement the ground test facility or the medium with planar diagnostic. This implies that, for short run duration of the facility or non-continuous flow, the temperature measurement can be achieved with two wavelength excitations. For continuous facility, the problem is less drastic. With assumption that the medium is in stationary state, the use of a single excitation laser source may be conceivable. Here, the temperature measurement is obtained from an excitation spectrum. The excitation wavelength of the laser is tuned twice, respectively on each of two absorbing transitions considered and ratio of line intensities drawn from the excitation spectrum recorded through a spectral band-pass filter set at a fixed $\Delta v$ vibrational de-excitation sequence. As it has been noted here above, accuracy on the maximum peak intensity determination will depend essentially from the accuracy of the excitation wavelength spectral tuning. As it is not so easier to scale the maximum peak intensity of the monochromatic exciting radiation together with the absorbing line, the two absorbing lines chosen for the ratio will be both spectrally described by tuning the laser radiation over entire spectral range corresponding to the line profiles. Although the recording time necessary to perform the temperature measurement by this way is greater than the time needed to performed experiment with two laser sources (set at the two wavelengths), this method remains well adapted to the temperature measurement in stationary medium generated by continuous facilities.

### 2.6 Velocity measurement with LIF

The narrow band radiation of the exciting laser source can be devoted to evaluate the flow velocity via the Doppler shift of the highly resolved excitation spectrum.

In this section we consider emitting molecules excited by the laser radiation and a Maxwell velocity distribution of emitting species which move with a the mean velocity of the flow. The light emitted from species and observed along a line of sight different from the direction of the flow, is shifted by the quantity corresponding to the mean velocity component of the molecule in the direction of observation. For observation in the direction of the particle mean velocity, the light emitted (or line profile) is blue-shifted. Conversely, it is red-shifted with the same absolute shift value for observation in the direction opposite to the mean movement of the flow stream. For observation perpendicularly to the flow axis, the light emitted is unshifted. The shift in wavelength is given as the Doppler shift and expressed as:

$$\frac{\Delta v}{v} = \frac{v}{c}\cos\theta$$

where v is the frequency, v the velocity and c the light speed. $\theta$ is the difference angle between the flow axis and the light of sight of observation in a direction such as $0<\theta<\pi/2$. Experiment may be carried out when the laser is spectrally wider than the probed line and requires high resolution in detection, thus damageable for the signal detection. With a monochromatic excitation, it is preferred to resolve the line by absorption.

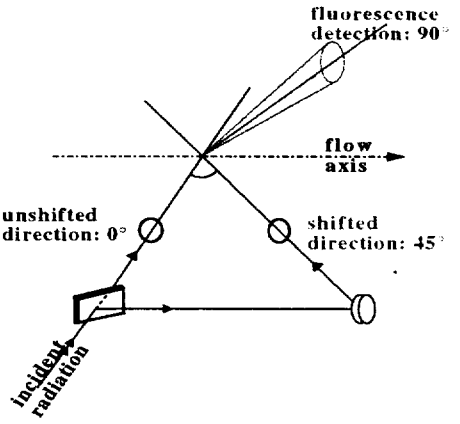


Fig(2): velocity measurement

Let us the flow excited with a laser radiation in the two excitation pathways, respectively in the direction 0° normal to the flow axis (unshifted line) and in the direction 45° upward the flow axis (shift line). In the direction 0°, the molecule will be excited if the laser excitation frequency coincides exactly to a rovibronic transition of the molecule. In the direction 45°, the molecule will be excited if the laser excitation frequency is shifted from the quantity corresponding to the Doppler shift. So, with two successive excitation pathways (0° and 45°) and a monochromatic excitation tilted on a spectral range corresponding to the Doppler shift, since the whole fluorescence signal is proportional to the monochromatic absorption coefficient.

## 3. $NO_\varepsilon$ SYNTHETIC SPECTRUM

Synthetic spectrum of the NO ε-band is computed to carry out information on lines distribution and lines intensity. These information complete the experimental basis work necessary to tilt the excitation laser radiation on lines of interest and also necessary for the temperature

determination in case of lines are not sufficient resolved, and than the overlapping of rovibrational lines may provide uncertainties on lines ratio measurement.

The fluorescence intensity distribution observed depends on the rotational levels involved first at excitation by the spectral distribution of the incident light, and second on the detection by the spectral range analyzed.

The excimer excitation source avoids simultaneous excitation of numerous rovibrational levels, depending first on the narrow or broad-band excitation and second, depending from the selection rules between the rovibrational levels involved at excitation, from the electronic ground state of NO ε-band $X^2\Pi_{(v''=1)}$ to the upper electronic state $D^2\Sigma^+_{(v'=0)}$. The upper state belongs to the Hund's case b, the lower state is a Hund's case a, with a spin orbit coupling constant. Each of the two sub-bands consists of twelve branches, whose the P, Q, R, $^PQ$, $^QR$ and $^RP$ are the major ones, well separated for low rovibrational levels but merged for higher rotational numbers.

The selective absorption cross sections of the rovibrational transitions are computed in the spectral range of the exciting source, just as fairly from a discret excitation and absorption molecular spectrum of NO. Thus, absorption spectrum is computed assuming a Doppler broadening for the rovibrational lines (low pressure conditions of the experiment) , the experimental energy distribution of the exciting source which includes the intensity gaps resulting from the $O_2$ Schumann-Runge absorption band in the spectral range of the laser at 193.1, 193.3, 193.5, 193.7 nm and geometric factors corresponding to apparatus function of the optical arrangement. Calculation is done assuming for the population number density of the ground state $X^2\Pi_{(v''=1)}$, a Boltzmann distribution at the rotational temperature. Finally, the absorption spectrum provides the number density of the particles absorbed and then the relative population number density of the numerous rotational levels of the upper state $D^2\Sigma^+_{(v'=0)}$, populated from the $X^2\Pi_{(v''=1)}$ state by the incident laser radiation.

The fluorescence associated to the radiative de-excitation from the upper $D^2\Sigma^+_{(v'=0)}$ state to the ground state $X^2\Pi$ is also computed accurately. This radiative de-excitation includes the radiative cascading process between rovibrational levels from the upper state $D^2\Sigma^+_{(v'=0)}$, down to the numerous vibrational levels of the ground state which satisfied the selection rule $\Delta v=0, 1, 2....$ The fluorescence cross section is calculated line by line for all the transitions observed and selected in detection through a spectral filter. Finally, an averaged fluorescence cross section value is calculated for the whole rotational transitions considered and will be used for an absolute calibration of the NO number density.

## 4. MODEL DESIGN AND FLOW CONDITIONS

Because of the high enthalpy levels required, the difficulties to reproduce high-speed flight conditions in wind tunnel are increasing. With the non-equilibrium flow conditions expected, analysis implies to test full-scale models. In regard to these working conditions, the TT1 facility (fig.*) is well adapted with its large experimental test section, its high enthalpy and air mass-flow rates.

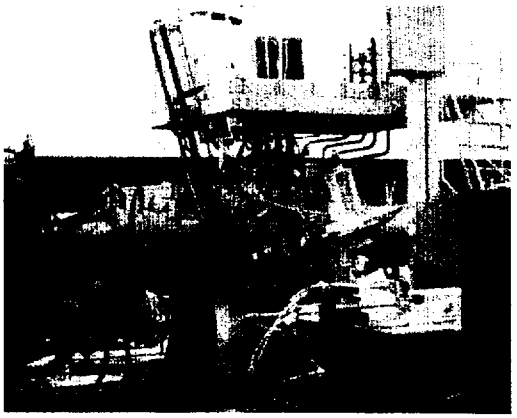

The air plasma source is a classical D.C. arc jet with a classical electrode configuration. The arc is generated between the tip of a copper cathode and a cylindrical anode corresponding to the convergent part of the reservoir chamber. Expanding high enthalpy gas through a water-cooled convergent-divergent nozzle generates the supersonic flow, before expansion in the low-pressure experimental test chamber set at $10^3$ Pa. The well-shaped divergent part of the nozzle has been calculated to provide a homogeneous air plasma flow at Mach 4.5, over the entire section of the nozzle exit of about 300 mm wide.

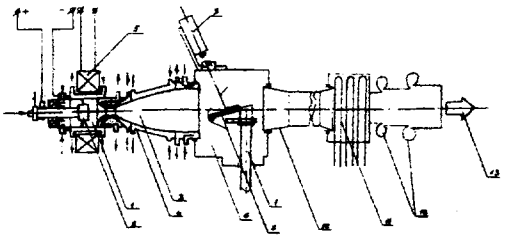

Fig(3): TT1 wind tunnel

The flow conditions in the stagnation chamber are $P_o \approx 1.6\ 10^5$ Pa, $H_o \approx 6.3$ MJ/kg and $T_o \approx 4100$ K with an input electric power supply of about 4 MW and an airflow rate of 0.5 kg/sec. The test conditions of the four runs retained in the test campaign to validate and improve CFD tools are summarized in Table 1.

At the nozzle outlet, the enthalpy leads to a thermo-chemical non-equilibrium flow. The pressure and temperature is estimated of about 2 $10^4$ Pa and 1000 K with a Reynolds number of $Re_{unit}=10^6$. The enthalpy leads to a supersonic vibrationaly excited, weakly dissociated and even ionized air plasma flow.

| | | Test run | #1 | #2 | #3 | #4 |
|---|---|---|---|---|---|---|
| $T_0$ | °K | hot gas stagnation heater | 4100 | 4159 | 4117.7 | 3910 |
| $P_0$ | $kg.cm^{-2}$ | hot gas pressure heater | 6.991 | 7.114 | 7.079 | 7.100 |
| $P_{02}$ | $kg.cm^{-2}$ | cold gas pressure heater | 1.640 | 1.642 | 1.637 | 1.697 |
| $M_a$ | | Mach number | 4.913 | 4.691 | 4.762 | 4.867 |
| V | $m.s^{-1}$ | Velocity nozzle exit | 3143.5 | 3345.9 | 3332.5 | 3205.4 |
| $R_e$ | $m^{-1}$ | Reynolds number | 121823 | 101498 | 98579.3 | 114805 |
| G | kg.s | Mass flow rate | .514 | .497 | .495 | .513 |
| $P_1$ | $kg.cm^{-2}$ | Static P test chamber | .006 | .007 | .006 | .006 |
| $H_1$ | $kcal.kg^{-1}$ | Static enthalpy | 263.3 | 361.8 | 342.8 | 287.3 |
| $H_0$ | $kcal.kg^{-1}$ | Total enthalpy | 1443.6 | 1699.1 | 1669.3 | 1514.6 |
| W | MWatt | Heater total power | 3.813 | 3.959 | 3.941 | 4.002 |
| $P_{01}$ | $kg.cm^{-2}$ | Stagnation Pshock | .180 | .191 | .177 | .180 |
| $M_1$ | $kg.c.m^{-2}$ | Gas viscosity flow | - | - | - | - |
| $T_{01}$ | °K | Static T | 920.3 | 1221.4 | 1163.3 | 993.6 |
| $R_{01}$ | $g.c^2.m^{-4}$ | Gas density nozzle exit | .182 | .167 | .158 | .175 |

Table 1: TT1 wind tunnel conditions

Add to the main characteristics of such facility is the long duration of the runs which can be maintain up to 15 minutes and thus allow to performed numerous tests during one run with unchanged operating conditions. In comparison with tests performed during short runs as in shock tube, the long run of TT1 facility makes easier implementation of continuous diagnostic as the LIF method developed for this specific test campaign.

Aerodynamics studies are performed radialy in the free stream, 190 mm downstream from the nozzle exit, then in numerous sections of the shock layer developed around a TPS model simulating a misalignment of tiles. In regard to the real flight conditions and to the difficulty to transpose the size and the shape of the tiles overlapping to a resized model dedicated for testing in experimental ground test facility, the used of a full-scaled model has been chosen. So, in such experimental situation, the huge diameter (300 mm in diameter) of the TT1 plasma flow is well adapted and representative of the test case of interest.

The model is made of insulating material like BOURAN (mainly $SiO_2$)and it looks like to a flat plate 200 mm length and 100 mm spanwidth, with a step of 3 mm height located 100 mm downstream from the blunt leading edge (Fig.*). The model is aligned on the jet axis with a 15 degrees incidence to reproduce the required parietal heat flux conditions. Most critical seems to be the high temperature expected on the leading edge, so it as been proposed to build the leading edge as a water-cooled copper cylinder of 20 mm radius.

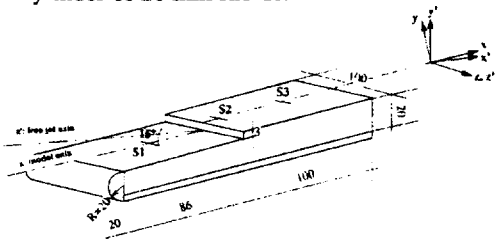


Fig(4): The $SiO_2$ model

## 5. EXPERIMENT DESCRIPTION

This paper deals with the experiments achieved in the TT1 wind tunnel. The small changes in the heater total power, the mass flow rate, the stagnation pressure in the heater and the static pressure in the test chamber provide weak changes of experimental working conditions for each run, despite efforts to maintains identical test conditions from run to run. The challenge of this test campaign was then to perform in the duration of each run sufficient measurements in the flow field (without then in presence of the model), to provide the best description of the flow parameters related to a particular test condition.

The two excitation mode of the ArF excimer source are used. The plasma flow is first implemented in broad-band mode to provides signing of species and information on the thickness evolution of the shock layer from the bow shock up the step of the model. In narrow band mode, the laser is tuned to excite single rovibrational levels of NO molecule. These experiments are devoted to the measurement of NO number density and temperature. Finally, the high resolved excitation spectra is used to determine the flow velocity via the Doppler shift of excitation lines.

An accurate description of the flow parameters has been allowed by the original LIF methodology developed for the test campaign on the High enthalpy air flow TT1. It consists in measuring simultaneously the number density, temperature and velocity using Laser Induced Fluorescence on NOε-band $D^2\Sigma^+_{(v'=0)} \leftarrow X^2\Sigma^+_{(v''=1)}$. Briefly, the number density will measured from line intensity after calibration of the fluorescence intensity with a reference medium. The temperature will be drawn from the ratio of two lines intensity after comparison with a computed fluorescence

spectrum (including the experimental optical arrangement, essentially the laser emission and optical apparatus functions). The velocity will be determined by tilting the monochromatic excitation line of the laser over the spectral range corresponding to the Doppler effect.

It is so required that the ArF laser have first, to excite the NO-molecule to resolve first, the rovibrational lines structure of the NOε-spectrum and second, to describe the Doppler shifted effect resulting from an excitation of the plasma flow in a direction along the line-of-side of the drift movement of the flow stream

In order to provide simultaneously the three parameters, the working conditions for excimer laser excitation and fluorescence detection have to satisfy some requirements listed hereafter:

1- Number density will be measured with a narrow band mode excitation centered on the center line of a NO-rovibrational line well identified. So an accurate scaling of the excitation wavelength of the laser is needed and will be provided by the 50mbar NO-reference cell. Experimental data on lines positions will be used first for experiment and second, to adjust lines positions of the NOε synthetic spectra in order to provide an accurate tool of comparison for simulation. It is note here that methodology carried out for the temperature measurement (next part) is based on the accuracy of line position and even on overlapping of lines, and thus need the used of a well representative synthetic spectrum to provide the expected accuracy on the temperature measurement. The absolute concentration value for NO will be drawn from calibration of the Rayleigh light intensity measured in a well known medium (air STP for example) with the same operating condition (laser power, probe volume and solid angle in detection and detection device).

2- Temperature will be drawn from the ratio of two lines intensity at their maximum intensity (center line of each transition considered). The NOε-synthetic spectrum allows to select the transitions of interest in the spectral range of the narrow-band excimer excitation. The rovibrational transitions have to be close to each other (low energy spacing between the lines) to limit the tilting of the laser between the lines and then to limit the time of measurement. Accurate measurement will be obtained with an accurate positioning of the excitation wavelength on the center line of the two or group of rovibrational levels chosen. In order to increase the accuracy of measurement, the two rovibrational transitions considered have to satisfy the following criteria: one of the two transitions considered have to be greatly dependent with the temperature in the range of interest (500-2000 K), and the other one without dependence (unit line intensity). The choice of the better transitions which satisfied these requirements are driven according to the evolutions observed from computed spectra.

3- Velocity measurement will be provided by the shift in wavelength at excitation and not by the shift observed at detection. Considering the two excitation pathways of the optical arrangement (named respectively the unshifted or 0°incidence and unshifted or 45°incidence), the fluorescence detection of a single rovibrational level would be observed at a only one wavelength if, the wavelength between the two excitation pathways is tuned at excitation by the amount corresponding to the Doppler shift value. The Doppler shift value is proportional to the velocity of the medium probed following the two particularly excitation pathways. The lower limit of the Doppler shift value is estimated to 1.8 $10^{-4}$nm and corresponds to a velocity of about 300 $m.s^{-1}$ in the air plasma flow (accuracy is given by the step by step increment of the excitation wavelength)

4- In addition to these requirements, the fluorescence detection has to be tuned on the more intense vibrational fluorescence de-excitation, except the resonant one, in order to rule out reflection and Rayleigh scattering. It is also required nor overlapping with the $O_2$ Schumann-Runge band, neither other band systems (excited by the laser or observed from plasma emission). For calibration of number density and velocity, the operating conditions have to be maintained constant for each measurement point (excitation pathways, probed volume, laser intensity, and so on ...).

Before implementation of the TT1 facility, some experiments were conducted in a high frequency plasmatron of the TSNIIMACH (Y13PHF) to improve the methodology and record reliable data on the rovibrational structure of the NOε-band, and particularly to calibrate the energy level (or lines position) of the NOε-rovibrational lines in regard to the reference lines of the well known $NO_\beta$ system $B^2\Pi_{(v'=7)} \leftarrow X^2\Pi^+_{(v''=0)}$.

## 6. EXPERIMENTAL ARRANGEMENT

### 5.1 The laser source

A tunable ArF excimer laser (Lambda Physik LPX 150/T) is used to induce fluorescence of NO-molecule in the high enthalpy airflow of the TT1 facility. With an excitation at 193.4 nm, the excitation source is tuned on the rovibrational lines of the ε-band $D^2\Sigma^+_{(v'=0)} \leftarrow X^2\Sigma^+_{(v''=1)}$.

The excimer laser consists of two separate cavities to work independently in broadband mode or narrow band-mode. The broadband radiation is centered at 193.4 nm with a 0.5 nm FWHM. In narrow band-mode, the 1.2 $10^{-3}$ nm FWHM pulsed radiation can be tuned with a step increment of 2.2 $10^{-4}$ nm on the full spectral range of the broadband ArF emission. A 10 ns pulse is achieved up to 120 mJ/pulse energy and a 1-50 Hz repetition rate.

In narrow-band mode, the excimer laser has to be calibrated in wavelength to be tuned on the wavelength of interest. Thus, a weak part of the laser radiation is directed in an external reference source made of a home-made static cell filled with 50 mbar of pure NO at 300K. In these operating conditions the calibration cell allows to provide the excitation spectrum of the $NO_\beta$ system $B^2\Pi_{(v'=7)} \leftarrow X^2\Pi^+_{(v''=0)}$ whose lines are well identified. From the good knowledge of the β-lines wavelengths, the correspondence between the excitation wavelength and the tilting of the ArF grating (which selects the monochromatic excitation radiation) is provided with accuracy (1.2 $10^{-3}$ nm).

A pin silicon photocell (Hamamatsu S1722-02) is added at the laser source exit to correct the pulse to pulse energy variations of the laser.

## 5.2 Setup and optical arrangement

The TPS model designed to simulate a misalignment of tiles is immersed in the flow stream, its blunt leading edge centered on the jet axis and its surface set at 15°deg upward. It is fixed on a 1D displacement and may be translated during the run, by step of 10 mm in the direction of the jet axis. This device allows to analyze numerous test sections in the shock layer from the bow shock to the step, during a single run.

A scheme of the experimental setup is depicted in Fig(*). The optical setup consists of the laser, its reference cell (filled with 50 mbar of NO) and dielectric high reflection coating mirrors set to direct the laser beam in the test chamber. An optical periscope is fastened by a stepper motor with accuracy of 10 µm and directed 15° downward the vertical direction. It is equipped with a beamsplitter to divide the excitation beam in two excitation beams, one for the unshifted excitation, the second one for the shifted excitation. The two preferential pathways for Doppler shift measurement are respectively at 0° and 45°deg incidence in regard to the flow axis. The velocity or Doppler shift measurement is performed by recording first the unshifted line, the shifted pathway being close. When the maximum line intensity is recorded, the shifted pathway is closed and the unshifted one automatically open.

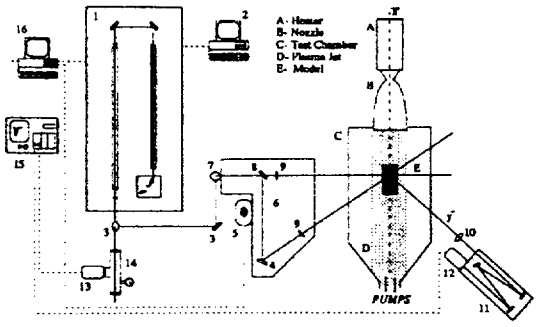


Fig(5): Optical setup

1- laser, 2- PC control, 3- 90°mirror, 4- 45°mirror, 5- vertical translation, 6- optical table, 7-optical periscope, 8-beam splitter, 9-lens, 10-focalisation lens, 11-spectrometer, 12-photomultiplier, 13- photomultiplier, 14- numerical oscilloscope, 15- PC control

The free jet radial and shock layer analysis perpendicularly to the surface of the model are carried out by translation of this optical arrangement (focussing lens, beamsplitter and mirrors) set on the 1D displacement device. Whatever is the altitude probed in the test of interest, the crossing point of the two excitation pathways always coincides and the probe excitation volume is maintains constant. In the directions where the most significant gradients are expected. Fine spatial resolution down to 200 µm is achieved with the focussing lenses f1000 mm (radially in the free jet and normal to the surface of the model).

The test chamber (1m*1m*1m) is equipped with tree optical access. Their location is forced first, by the incidence of the model aligned 15° upward the jet axis, and second, by the method of Doppler shift measurement used. For detection of fluorescence, the top of test chamber is equipped by an optical window, UV-fused silica 100 mm in diameter. To induce fluorescence, two optical access are set on the side part of the test chamber to provide the two excitation pathways for Doppler shift measurement. The first one is centered on the jet axis, at 190 mm from the nozzle exit. It allows the laser to enter the test chamber perpendicularly to the flow axis and to provide the orthogonal access required for the unshifted Doppler measurement. The shifted measurement is provided by the second window set at 15° upward the free jet axis and 45° incidence from the previous optical window. Its positioning in regard to the previous one allows to cross the shifted excitation pathway with the unshifted excitation pathway in the free jet section of interest defined at 190 mm from the nozzle exit. Optical access at excitation are limited by

the size of the windows (UV fused silica, 100 mm in diameter) and allow analysis of the flow stream 50 mm on either side.

The fluorescence signal is collected on the top of the test chamber, at right angle from the two-excitation beam pathways. The signal is recorded through a monochromator used as a spectral filter (Jobin-Yvon, f588 mm, 3600 groves/mm holographic UV grating), onto a UV sensitive photomultiplier (RTC XP2020Q). The probe volume is imaged with a f50 mm fused silica lens onto the entrance slit (600 μm) of the monochromator used as a tuning 0.4 nm FWHM band-pass filter. Because the detection device is fixed (and couldn't be displaced), the solid angle in collection have not to be too large in order to make assumption that the measurement volume is unchanged when the focussing point of both excitation pathways are displaced across the entire section of the flow stream.

The time resolved fluorescence is detected in the plasma flow and in the reference cell, then recorded on a 2 GHz numerical oscilloscope (Tektronic DSA 602A). Data are transferred to a PC computer simultaneously with information on the laser intensity of the incident pulse monitored via a power-meter and positioning of the measurement point provided by the optical periscope device.

The experimental setup as the whole (optical periscope, monochromator, detection device and the excimer laser) are fully automated and are operated under remote control. During the run, the NO reference cell provides the accurate positioning in wavelength of the laser which can be tilted on the wavelength of interest. The location of the measurement point which can be adjusted as well as the positioning of the model along the jet axis. In detection, the spectral range for fluorescence detection can be adapted to the spectral range of interest.

## 7. OPERATING CONDITIONS

### 7.1 Introduction and positioning of the model

At the ignition of the wind tunnel, the model is removed to avoid impact with metallic particles coming from electrodes erosion and maintains apart from the flow as long as the input power, gas flow rate and static pressure in the test chamber are not set to their nominal value. When the working conditions are reached, the model is immersed in the flow at its nominal position, so that its rounded leading edge is located on the jet axis, at a distance of 190 mm from the nozzle exit. The surface is 15° upward the jet axis.

To perform measurements in a given section, the model is displaced parallel to the flow axis by step increment of 10 mm, up to that the section of interest coincide with the optical direction defined by the incident laser beam pathways, oriented perpendicularly to the flow axis. Measurements in the section perpendicularly to the surface of the model will be provide by the optical periscope 1D-displacement, with step increment down to 10 μm.

### 7.2 Operating conditions for LIF diagnostic

The huge span width of the model coupled with the solid angle of the input laser excitation and the size of the laser spot doesn't allow to focus the laser down to 1 mm from the surface of the model whitout increase a parasite reflection damageable to the fluorescence signal. Thus no data have to be considered in the last millimeter over the model, and no measurement will be possible at the foot of the step of the model. The reflection provides a high level of light emission centered at the excitation wavelength which can be rule out from fluorescence emission, except if a narrow band-pass filter is set in detection on a vibrational sequence of the complete fluorescence radiative de-excitation different from the resonant fluorescence .

Before to start the run, the detection is tuned on the excitation wavelength to record the signal issued from the reflection of the laser on the model, and to determine the absolute location of the model, first in the flow and second, location of its surface in regard to the reference position of the 1D-displacement of the optical periscope.

When the model is immersed in the flow, the Infra-red record points out that 60 seconds are necessary to reach a thermo-equilibrium of its surface (up to 95%). LIF will be carried out after this delay time.

The long run duration (15 mn) is convenient to multiply points of measurement. Notably in experiments with the model, the long run allow to probe the free flow before to introduce the model and then, to provide with the identical experimental working condition of the wind tunnel, both data set from the flow and from the shock layer .

### 7.3 Data acquisition

(see §8.2 : Transitions for the simultaneous measurements of number density, temperature and velocity)

Considering first, the criteria retained for the simultaneous measurement of number density, temperature and velocity and second, the long duration of the run, the LIF experiments are conducted as follow:

a) Fluorescence is filtered in detection. The filter is a narrow band one, but can be consider as a broadband filter in regard to the number of rovibrational lines involved in the narrow band mode excitation. Thus, shifted and unshifted lines will be detected.

b) The first fluorescence record is to determine the spectral spacing between the reference βNO line ($R_2$(30.5) measured in the reference NO-cell, and the ε-NO line $Q_1$(31.5) measured in the air plasma flow with the unshifted beam pathway (0°). The laser radiation is tuned over the entire exact spectral range of the reference βNO line ($R_2$(30.5) and the ε-NO line $Q_1$(31.5), then stopped.

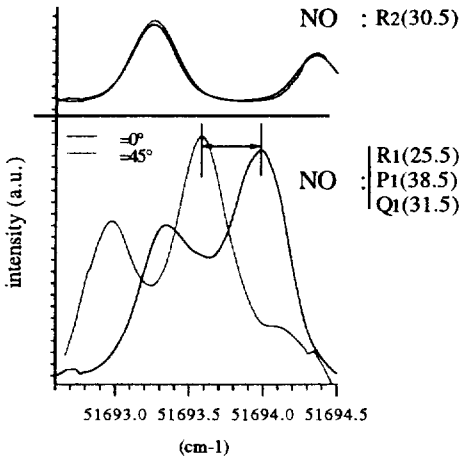


Fig(6): Doppler shift measurement

c) The second fluorescence records is carried out with the shifted excitation beam pathway set at 45°deg incidence. The laser radiation is tuned over the βNO line ($R_2$(30.5) used always as the common reference line and over the ε-NO lines $P_1$(38.5), $R_1$(25.5), $Q_1$(31.5) previously determined. For this record, the spectral spacing of the record will be identical to the previous one but spectral range to consider has to be brought forward to take into account the Doppler shift effect

d) The velocity will be drawn from the spectral spacing measured with the two records between the NOβ line ($R_2$(30.5) and the NOε line $Q_1$(31.5).

The temperature will be drawn from the ratio intensity of the lines from the group of NOε lines after comparison with synthetic spectra.
The integrated fluorescence intensity will provide the absolute number density, after calibration by intensity of Rayleigh scattering.

## 8. LIF MEASUREMENTS

### 8.1 The resolved NOε spectrum

A high enthalpy air flow generated in the high frequency plasmatron Y13PHF of the TSNIIMACH has been implemented in order to provide reliable data on the NOε spectrum. The working conditions of such facility in which the plasma is generated in a quartz tube without electrode, thus provides a flow without impurity. In addition, the stability and reproducible flow has been verified and provides a convenient high enthalpy air plasma source for basis experimental.

The NO fluorescence is induced in the air plasma flow by pumping the $D^2\Sigma^+_{(v'=0)} \leftarrow X^2\Sigma^+_{(v''=1)}$ ε-band with the incident ArF laser radiation tuned in narrow-band mode on the ArF tuning wavelength range from 192.8 to 193.8 nm. The fluorescence emission is collected through the monochromator from the (0-2) vibrational band (198 to 202 nm). The only excitation spectrum observed is the NOε band system, via the $D^2\Sigma^+_{(v'=0)} \leftarrow X^2\Sigma^+_{(v''=1)}$ excitation scheme. Nor rovibronic transition from the hot Schumann Runge lines, neither the γ-NO band $A^2\Sigma^+ \leftarrow X^2\Pi$ (3-0) and (4-1) are observed. The radiative fluorescence is detected at right angle from the straight line of the incident beam is recorded through a monochromator used as a broad-band filter. The spatial resolution is minimized in order to provide a probe volume in which the density and temperature evolutions are expected to be constant. From analysis of fluorescence emission at different height in the section of the plasma flow, the line intensity with the temperature dependence may be observed on the records.

### 8.2 Transitions for the simultaneous measurements of number density, temperature and velocity

The spectrum presented fig* is described by the P, Q and R-branches of the NOε band $D^2\Sigma^+_{(v'=0)} \leftarrow X^2\Sigma^+_{(v''=1)}$. Tilting of the laser narrow-band emission and positioning of more than 40 rovibronic lines of the NOε band has been allowed in agreement with the positioning of the lines from the NOβ band $B^2\Pi_{(v'=7)} \leftarrow X^2\Pi^+_{(v''=0)}$, recorded

simultaneously in a static cell filled with 50 mbar of NO. Accuracy in wavelength positioning is only dependent from the step by step increment of the laser tilting, and estimated of about 2.2 $10^{-4}$ nm.

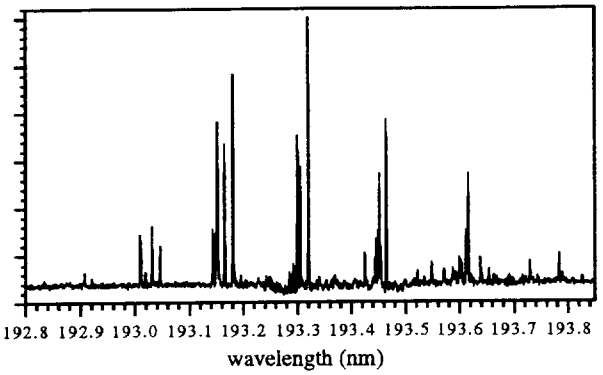


Fig(7):NOε band $D^2\Sigma^+_{(v'=0)} \leftarrow X^2\Sigma^+_{(v''=1)}$

Measurements are completed in a heated home made static (up to 1200 K) to record intensity lines evolutions versus temperature, and to chose the more sensitive transitions. The comparison with synthetic spectrum allows to complete the analysis for higher temperatures.

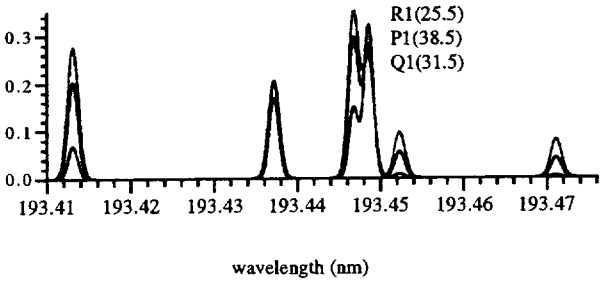


Fig(8): Temperaure measurement

From experiments and computed synthetic spectrum at numerous temperature, we can conclude that:

The $P_1(38.5)$, $R_1(25.5)$, and $Q_1(31.5)$ group of rotational lines of the NOε band, respectively at 51692.50, 51693.25 and 51693.75 $cm^{-1}$, is well identified to satisfy the requirements for the simultaneous measurement of density, temperature and velocity.

- Lines are closed to each other to minimized time of tilting of the excitation radiation to describe the entire profile of the group of lines.

- Lines are close to a reference line of the reference β-NO spectrum ($R_2(30.5)$ at 51693.25 $cm^{-1}$), which one will be used first to scale the tilting of the excitation before the recording of the lines profile, and second as the reference unshifted line for both laser excitation beam pathway used for Doppler Shift measurement.

- The intensity ratio of these transitions is sufficiently sensitive with the temperature in the temperature range of interest.

- The integrated intensity of the group of lines will be used for the absolute number density measurement after calibration with Rayleigh light scattering.

8.3 Interference with NOε band $D^2\Sigma^+_{(v'=0)} \leftarrow X^2\Sigma^+_{(v''=1)}$.

First, it has been observed that signal from plasma emission is in some order of magnitude weaker than fluorescence induced by the excimer laser, and thus can be neglected.

Secondary, the air flow of the TT1 wind tunnel has been probed with a broad-band laser excitation and detection has been tuned through a narrow-band filter (0.4

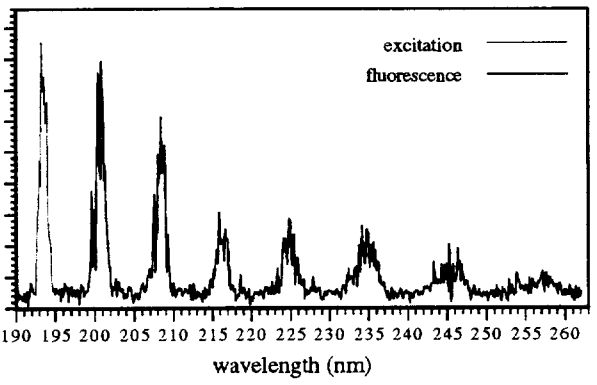


Fig(9): NO vibrational fluorescence de-excitation

nm FWHM) over a large spectral range in order to detect all the fluorescence of species present in the medium and excited with the ArF source. As a result of the broad-band excitation, only the NOε $\left(D^2\Sigma \rightarrow X^2\Sigma\right)$ fluorescence has been observed, from the resonant fluorescence centered on the excitation wavelength at 193.3 nm (Δv=0) up to 256.0 nm (Δv=7).

Because of all the potential interfering optical signals, it is important to verify that signals acquired are those from the NO fluorescence. We have to take into account

the possible reflection of the laser beam in the test chamber and close to the model, when measurements are performed in the shock layer at the vicinity of its surface. So, The fluorescence emission will be collected through the monochromator either from the (0-2) vibrational band (198 to 202 nm), or from the (0-3) vibrational band (206 to 210 nm). Less intense than the (0-1) but sufficiently far away from the Rayleigh peak, these fluorescence pathways are selected in order to maximize the fluorescence signal, minimize emission from the plasma flow and because its allows rejection of the elastically scattered laser light and reflection from the test chamber and surface of the model.

### 8.4 Absolute calibration of NO

For absolute calibration, the Rayleigh scattering is recorded in the test chamber with air at STP. Experiment is carried out with the complete optical setup and detection device, but precautions are taken to avoid reflection in the test chamber as the monochromator is tuned on the excitation laser radiation. By this way, fluorescence records and Rayleigh scattering are provided under identical experimental conditions. Thus, the terms related to the transmitivity of optical setup $\varepsilon_c$, and the size and probed volume $V_c\Omega_c$ may be ruled out in the expression of the ratio of fluorescence with Rayleigh scattering.

The air number density at STP and the differential Rayleigh cross section at the excitation wavelength are $N_{air}^{STP} = 2.4110^{19}\ part.cm^{-3}$ and $\sigma_{v_0}^{rayleigh} = 4.94810^{-26}\ cm^2$, respectively.

## 9. FLOW PARAMETERS MEASUREMENT

### 9.1 Analyze in the free plasma flow

Experiments are performed on both sides of the free jet axis and reveal a sufficient homogeneous region to locate the wide $SiO_2$ model and assure subsequently a 2D aerodynamic description of the boundaries conditions.

The unchanged rotational lines distribution and the constant fluorescence intensity point out a flat NO number density and temperature profiles in the free air flow section, 50 mm on either side from the jet axis.

The rotational temperature is estimated of about 1200 K and NO mole fraction of about $3.8\ 10^{-3}$ .

The Doppler-shifted fluorescence signals provide a flat velocity radial distribution in the test section located at 190 mm from the nozzle exit. The constant value of 3325 $m.s^{-1}$ is corresponding to a supersonic flow with a Mach number close to Mach=4.9.

These results are in good agreement with the calculated parameters: v=3300 $m.s^{-1}$ and Mach=4.75, computed with the stagnation chamber conditions, the nozzle shape and assumption of a perfect gas flow in equilibrium upstream of the critical convergent throat and followed by a frozen expansion downstream in the nozzle divergent region.

No real discrepancy is observed between the four selected run

| | Test run number | #1 | #2 | #3 | #4 |
|---|---|---|---|---|---|
| Trot | Rotational temperature (K) | 1150 | 1200 | 1200 | 1150 |
| [NO] | NO concentration | $3.8\ 10^{-3}$ | $4.1\ 10^{-3}$ | $3.7\ 10^{-3}$ | $3.8\ 10^{-3}$ |
| v | Velocity (m/s) | 3325 | 3325 | 3275 | 3300 |

Table 2: TT1 wind tunnel results

### 9.2 Analyze in the shock layer

The flat plat model simulating a misalignment of tile with a step 3 mm height is placed on the homogenous region previously analyzed. The aerodynamic behavior of the supersonic high-enthalpy air flow impinging on a TPS $SiO_2$ model is shown in Fig(*). One observes mainly the bow shock which originates from the rounded leading edge and propagates laterally away from the surface. On the leading edge of the step, another less intense shock originates and rises up downstream the step.

Infra-red thermography doesn't reveals modification of bow shock in front of the model, at the location of the transition zone between the water cooling rounded leading edge and the $SiO_2$ surface. The picture reveals an important temperature gradient on the $SiO_2$ surface, up to 1500 K in the first part of the model and at the top of the step. On the contrary, in the last millimeters before the step, the temperature decreases down to 1100 k, just in the dark region at the foot of the step where a re-circulation zone can be expected. No LIF measurement has been done in front of the step because of the height reflection level of the laser beam on the step leading edge.

Fig(10): ombroscopy

Three sections located at 56, 112 and 156 mm from the rounded leading edge are investigated. The section $S_{56}$ is 44 mm upstream the step, the $S_{112}$ and $S_{156}$ sections are downstream the step. On the two first sections reported on this picture, the two marks point out the place where a rise up of fluorescence has been observed by LIF at the boundary of the shock layer.

At the separation region between the free jet and the shock layer (estimated at $35 \leq y \leq 38$ mm), the NO-fluorescence signal increases exponentially because of NO vibrational excitation, i.e. a higher vibrational temperature and thus a higher number density of the of NO(v=1). As the transition considered in the NOε excitation process via $D^2\Sigma^+_{(v'=0)} \leftarrow X^2\Sigma^+_{(v''=1)}$ imply the v=1 vibrational level, increasing of the vibrational temperature is favorable to populate higher vibrational level, and thus increase the absorption process and the intensity of fluorescence detected at the crossing of the shock layer.

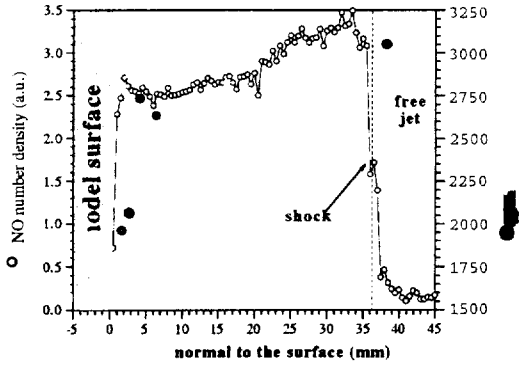


Fig(11): Profile of NO in the section $S_{56}$

The Fig(*) shows the fluorescence signal profile from the section $S_{56}$. Measurements are carried out with a spatial resolution of a 500 μm, from the free jet ($y > 0$) down to the surface ($y = 0$).

In the shock layer, intensity of fluorescence evolves weakly down to the surface of the model, and no rotational temperature gradient is observed. The number density thus do not vary significantly, indicating that NO number density is frozen into the shock layer.

In the two last millimeters ($0 \leq y \leq 2$ mm), the loss of signal is attributed to the cut of the spot size which is imputed to the intersection of the solid angle of the focused incident laser radiation with the surface of the model.

For $y \leq 5$ mm and down to the surface of the model, the weak rise up doesn't allow to conclude about a parietal recombination and indicate no signifiant creation of NO at the wall.

In the weakly dissociated flow, the current results do not confirm a predominant effect of wall recombination in comparison to the compression effect of the shock layer near the surface. The equilibrium conditions in the free jet upstream are 1200 K and $10^2$ Pa, and the stagnation pressure behind the shock is evaluated to 1.9 $10^3$ Pa, namely 20-fold greater than the free jet static pressure. The same order of magnitude is observed on the fluorescence signal jump crossing the shock propagating laterally away from the model. If one considers first the fluorescence intensity with respect to the distribution of the NO $\left(X^2\Sigma^+_{(v''=1)}\right)$ in the absorbent rotational levels, and secondly, the very slight variation of the rotational temperature crossing the shock, then the NO concentration jump is in order of 22-fold greater in the shock layer than in the free jet. This value is assumed to be directly proportional to the difference of pressure crossing the shock layer.

The spatial resolution of 5 measurement points per millimeter allows to have an accurate description of the location and intensity of the shock. However, we have to consider than the real thickness of the shock is overestimated because of the vibrational excitation time lower than the rotational one.

The fluorescence emission results in the first section $S_{56}$ are in good agreement with the ombroscopy picture which reveals only the shock location without giving information on the intensity ratio from both sides of the boundary shock layer.

The same results are obtained for the location of the second shock originating from the step, 15 mm behind the step (section $S_{112}$, see Fig(*)). Its lower intensity indicates

no real change in the vibrational relaxation and is confirmed by no significant evolution of the NO number density and rotational temperature.

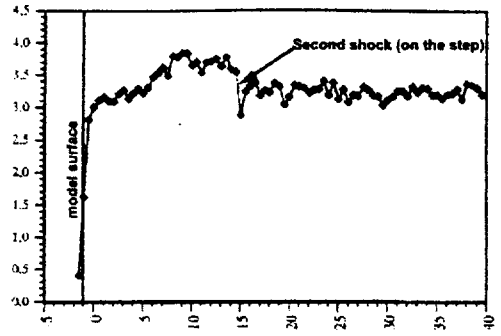


Fig(12): Profile of NO in the section $S_{112}$

The axial component of velocity is affected by the presence of the model. The profiles drawn from the three test sections of interest show a velocity gradient mainly located in the last millimeters close to the surface, in the region where a slight decrease of fluorescence has been previously observed.

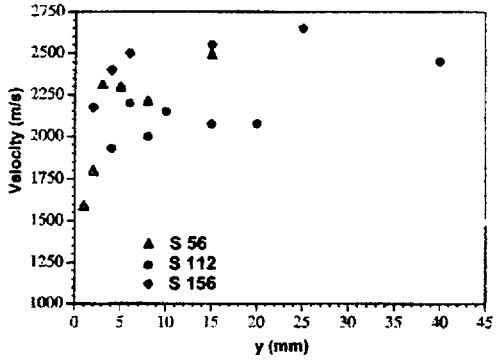


Fig(13): velocity in the shock layer

No discrepancy is observed for the axial component of the velocity across the shock front. Its value is estimated to 3300 ± 150 $m.s^{-1}$, which correspond to the initial free jet velocity. Upstream of the step, the thickness of the dynamic boundary layer is given at y = 5 mm in the first section. Under this limit, the velocity decreases continuously down to y = 1 mm to reach its lower value 1900 $m.s^{-1}$. The thickness of the dynamic boundary layer in front of the step can be expected to be of the same order of magnitude than the step height. One of the main feature of the velocity distribution in this section $S_{112}$, lies in the continuous increase in velocity, up to the limit of the shock generated at the top of the step. The lower value measured near the wall may be imputed to a deflection of the flow impinging on the step and a normal component of velocity non-negligible in comparison to the lower axial one. The most important gradient is observed 5 mm above the surface. For y > 5 mm, the axial value is approximately constant (2500$m.s^{-1}$) up to the limit of the secondary shock, then increases far off to reach its maximum value corresponding to the velocity of the free jet.

## 10. CONCLUSION.

The potential of LIF technique for instrumentation of continuous high enthalpy facilities has been demonstrated. NO number density, temperature and velocity has been measured in the supersonic air plasma free jet, as well as on a TPS model, allowing characterization of the aerodynamic behavior of the flow, especially at the misalignment of tiles.

# Molecular Diagnostics for the Study of Hypersonic Flows

**F. Grisch**
Office National d'Etudes et de Recherches Aérospatiales
Département Mesures Physiques
29, Avenue de la DivisionLeclerc
92320 Châtillon Cedex
France

## Summary

New laser-based diagnostic techniques offer considerable promise for measurements in hypersonic flows. In this paper , we overview optical techniques such as Rayleigh and Raman scattering, laser-induced fluorescence, electron beam fluorescence, coherent anti-Stokes Raman scattering and diode laser absorption. These methods have unique capabilities for nonintrusive measurements of flowfield parameters such as temperature, density, species concentration and velocity. The applicability of these techniques for the study of hypersonic flows is also presented.

## Introduction and Scope

The interest in reentry of space vehicles, in high speed transportation, and in single stage-to-orbit concepts continues to stimulate the research into supersonic and hypersonic aerodynamics. This research is conducted in facilities that basically simulate flight at high altitude and high velocity.

Short-duration test facilities such as the hypersonic shock tunnel, however, have afforded a means for extending research study capabilities into the high velocity flight regime. The development of ground test facilities to simulate the flow about hypersonic vehicles is nevertheless very challenging because of the high total enthalpies required. The stagnation enthalpies encountered in flight at hypersonic velocities result in flowfield temperatures high enough to dissociate and even ionize the chemical species in air. The reservoir state in a short duration test facility, which then undergoes expansion to high velocity is, of course, at comparable enthalpies to the flight case. The test gas in reservoir is therefore also dissociated and ionized. In the subsequent expansion to hypersonic speeds, the flow can depart from thermal and chemical equilibrium.

It is in the test flow environments that perfect gas reciprocity is lost since, at comparable velocities, the freestream in the high enthalpy facility test section differs from that existing for flight in the atmosphere. The static pressures and temperatures (and hence the Mach numbers) differ and the composition of the air contains oxygen atoms and nitric oxide, in addition to the $O_2$ and $N_2$ molecules. At higher enthalpies, nitrogen is also appreciably dissociated and ionized species begin to appear in significant concentration. The ionization introduces plasma properties into the flow environment which can leads to additional interaction phenomena associated with the presence of a free electron concentration in the flowfield. The effect of the nonequilibrium free stream composition on flowfield measurements around a test model must then be understood in order to relate to the flight case. Computer codes exist, of course, for the prediction of nonequilibrium flow expansions, and for flows about high velocity vehicles. The important questions are the followings: Is the chemistry fully specified? Are the reactions reliable?

In high enthalpy facility operations, therefore, it is necessary that consideration must be given to the diagnostic methods and techniques available for independent measurement of species compositions. A description of such complementary techniques will comprise the substance of the lecture discussions. The methods to be discussed have all appeared, in various forms, in the literature on research studies covering a range of different flow environments and gas mixtures.

With the advent of laser light sources, light scattering spectroscopic diagnostic techniques are assuming an ever-increasing role in a broad spectrum of physical investigations. There is a large variety of diagnostic processes potentially applicable to the remote, nonintrusive, point and imaging probing of hypersonic flows. The subject of hypersonic diagnostics has received a great deal of attention in the past few years. A review of the techniques for hypersonics that were available a

*Paper presented at the RTO AVT Course on "Measurement Techniques for High Enthalpy and Plasma Flows", held in Rhode-Saint-Genèse, Belgium, 25-29 October 1999, and published in RTO EN-8.*

few years ago can be found in Ref. 1. A special issue of the AIAA Journal has been devoted to advanced measurements technologies [2].

Attention will be directed ultimately only to those laser techniques which can permit the determination of local species concentration, temperature and velocity measurements. In the first part of this review, we present potential optical techniques such as the Rayleigh scattering, the spontaneous Raman spectroscopy (SRS), the coherent anti-Stokes Raman spectroscopy (CARS) and the laser induced fluorescence (LIF) which allows points measurements. These techniques provide good spatial resolution, either via the use of the configuration of the laser beams (CARS) or by monitoring a small elemental length of the laser beam (SRS, LIF,...). We also present the electron beam fluorescence (EBF), which is also a suitable technique to determine the number density and velocity.

Other optical techniques to be discussed involve emission or absorption phenomena which exploit the idea that air species in real-gas flows are optically active and allow emission or absorption spectroscopic techniques to be used. These latter are integrated line of sight measurements which are appropriate, for instance, for the characterization of the quasi one-dimensional flows in a nozzle expansion. In particular, diode laser absorption spectroscopy has a potential for great accuracy in the acquisition of the translational temperature and velocity.

From this exhaustive list, three techniques, which are mainly used at ONERA for the study of high-enthalpy flows will be selected for a detailed evaluation including: Coherent anti-Stokes Raman Spectroscopy, electron beam fluorescence and Diode laser absorption spectroscopy.

## Review of potential hypersonic diagnostic techniques

Measurements are primarily performed by using laser scattering off the molecules or particles seeded into the flow. They can be implemented using their incoherent scattering of a laser beam or coherent, nonlinear optical arrangements; the molecules can also be excited by electrons beams of several kiloelectron volts, which can induce fluorescence in the visible, ultraviolet and X ray regions.

### *Incoherent Scattering*

Incoherent scattering is observed by illuminating the gas with a focused laser beam. The light scattered at right angles by the gas molecules is collected by a lens, spectrally analyzed using a spectrograph, and detected by means of PM tubes or detector arrays. Three sorts of scattering processes in molecules are commonly recognized and schematically depicted in the energy-level diagrams in Figure 1. Commercial pulsed lasers can be employed, giving a typical time resolution of 10 ns, which is suitable for short-duration facilities. The energy per pulse needed is in the range 10-100 mJ. Continuous wave lasers also can be used for steady state flows, and the spatial resolution is typically 0.1-1 $mm^3$.

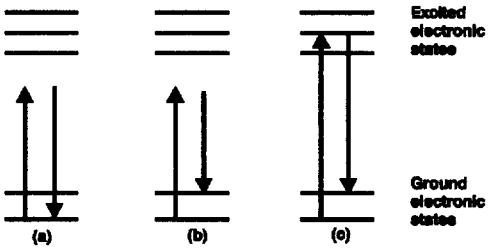


*Figure 1* Energy level diagram for Rayleigh (a), Raman (b), and fluorescence (c) scattering.

### *Rayleigh Scattering*

The elastic scattering of light quanta from molecules is termed Rayleigh scattering and is the phenomenon giving rise to the blue appearance of the sky. Because the scattering process is elastic, the photons are scattered in all directions and have the same energy as the laser photons. the scattered light is unshifted in frequency and, hence, not specific to the molecule causing the scattering. Thus the technique can be used for total density measurements but not for individual species concentrations. From a practical viewpoint, Rayleigh scattering is a weak process that requires total absence of stray light at or near the laser wavelength. Also, the laser should not impact any solid surface near the volume under probe to avoid strong interference. Particles suspended in the flow also cause Mie scattering (see below) that constitutes another form of interference. This problem actually limits the sensitivity of the method to densities of the order $10^{-1}$-$10^{-2}$ normal at best. Its potential use is thus restricted to classical subsonic and low supersonic tunnels. Proximity of a wall is also a major source of interference because the laser light scattered off the surface is many orders of magnitude stronger than that from the molecules. Rayleigh scattering is thus proscribed in boundary layers studies. Filtered Rayleigh scattering can solve that problem [3].

*Mie Scattering*

Elastic scattering of light quanta from particulate matter is termed Mie scattering. Mie scattering designates the signal scattered by particles with sizes comparable to or larger than the wavelength of the illuminating laser (0.4-0.6 nm, typically). It is a close parent of Rayleigh scattering. It is not dependent on molecular number density or temperature and, hence, cannot be used to provide such information. It is the basic effect underlying the Laser Doppler Velocimetry (LDV) [4]. While LDV works remarkably well in subsonic and low supersonic flows, it has met with mixed success in hypersonic, because the low density is too low to carry the particles, especially through shocks. An interesting assessment is found in Ref.1. It can be a very strong process depending on particle number density and particle size, and is a potential source of interference in high enthalpy flows.

*Spontaneous Raman Scattering*

Raman scattering is the inelastic scattering of light from molecules as illustrated in Fig.1 and is termed rotational, vibrational or electronic depending on the nature change which occurs in the molecule. The process is essentially instantaneous occurring within a time of $10^{-12}$ s or less. The molecule may either become excited or deexcited depending on its original state prior to the interaction. Due to the quantization of the molecular energy states, the Raman spectrum is located at fixed frequency separations from the laser line characteristic of the molecule from which the scattering emanates. This property is extremely interesting, because it offers chemical selectivity, since the frequency difference, which is proportional to the vibrational quanta, differs from molecule to molecule. Spectroscopy of the scattered light thus reveals the presence of the various chemicals and allows concentration measurements. It also offers temperature measurement capacity: the energy of the vibrational quantum slightly depends on the rotational state of the molecule. Each rotational state thus gives a specific line, which is separable from its neighbors under high spectroscopic resolution. The states being populated according to Boltzmann's law, spectral analysis yields the rotational temperature; the latter is generally equal to the static temperature of the gas. Measurement accuracy is of the order of 50-100 K if the signal-to-noise ratio is good. Even better performance seems attainable under special conditions using a variant called rotational Raman scattering.

Unfortunately, Raman scattering is weaker than Rayleigh scattering, typically by a factor of 100-1000. Its use, in spite of its other attractive characteristics, is thus restricted to aerodynamic flows above or close to normal density, and to weakly luminous flames. Its effective detection sensitivity with state-of-the-art lasers and detection optics is in the range $10^{15}$-$10^{16}$ molecules $cm^{-3}$ for a spatial resolution set at 1 $mm^3$. Thus, it has a little future in hypersonics with today's lasers and detectors unless densities as high as at least $10^{-1}$ normal are achieved in the free stream, and stray light and flow luminosity are kept very low. Some applications of Raman scattering to aerodynamics flows can be found in [5, 6].

*Fluorescence Scattering*

Fluorescence is the emission of light from an atom or molecule following promotion to an excited state by various means: heating, chemical reaction (chemiluminescence), electron bombardment, or absorption. Here only the two last means will be considered. The precise definition of fluorescence requires that emission occur between electronic energy states of the same multiplicity, i.e. the same electronic spin states. Emission between states of different electronic spin is called phosphorescence. In general, fluorescence lifetimes are between $10^{-10}$ and $10^{-5}$ s, much shorter than the phosphorescent lifetimes of $10^{-4}$ s to seconds. The light emission may be shifted in wavelength from the incident light (fluorescence) or occur at the same wavelength (resonance fluorescence). In general, it is desirable to examine shifted emission to avoid potential from particles (Mie scattering) or spurious laser scattering.

Fluorescence is of diagnostic interest since it combines the species selectivity of Raman scattering with far stronger signal intensities. It is closely related to Raman, but with the exciting laser tuned onto resonance with the one-photon absorption lines of the molecule of interest. This trick enhances the scattering cross section – and therefore the signal strength – by many orders of magnitude and makes it possible to detect parts-per-million-level traces in flames as the OH radical and the NO pollutant. Detection sensitivities lie in the range $10^{10}$-$10^{12}$ $cm^{-3}$.

The principles of LIF are well-known (see refs. 7-8 and articles cited herein for an up-to-date review) and need not to be repeated in detail here. In brief, a laser source is tuned to excite a specific electronic absorption transition in the species of interest. Following the absorption process, collisional redistribution in the electronically excited state may occur prior to either collisional quenching or radiative de-excitation (fluorescence) of the molecule back to a lower electronic state. The emission, which occurs over a range of wavelengths, is usually collected at right angles

and filtered spectrally at the photodetector. For a given species, the variables in the LIF process are the transition pumped, the detection spectral bandpass, the spectral intensity of the laser, and, in the case of narrow linewidth laser, the location of excitation within the absorption line profile. LIF may be thought of as potentially with the intersection of the illumination and collection beam paths controlling the spatial resolution of the measurement. In the case of sheet beam illumination and detection with an array detector, the size of the detector pixels and the magnification of the collection optics controls the size of the measurement volume at each image "point" [9].

The governing equation of the LIF signal, S, is based on a simple two-level model with weak (unsaturated) excitation, for a single detector pixel, is [10-11]

$$S = CEVN_s BF_{vj}(T)[A/(A+Q)]$$

Here, C is a group of constants specific to the experimental set-up. E is the laser energy per pulse per unit area per unit frequency, V is the measurement volume for the detector element, $N_S$ is the number density of the absorbing species, $F_{vj}$ is the population fraction for the pumped state, B is the Einstein coefficient for absorption, and A is the appropriate (for the transitions monitored) Einstein coefficient for spontaneous emission. The parameter Q represents the sum rate of all other transfer processes which eliminate into the detection bandwidth. In the most common case, these processes are: dissociation, energy transfer to other internal energy states within the same molecule, and chemical reaction. These processes competitive with fluorescence, termed quenching processes, reduce the signal strength which can be obtained and complicate interpretation of the data. In principle, if all the quenching species densities are known, and if all of the appropriate quenching rate is available, analytical quenching corrections to the data would be possible [12, 13].

LIF was at first used for point measurements, particularly in flames and in supersonic, low pressure streams (for mixing studies using traces of iodine gas as a seeder). For the past 5-10 years, however, it has primarily been employed for flame and flowfield imaging (see below), thanks to the introduction of intensified two-dimensional charge-coupled device (CCD) detector arrays. Several applications to hypersonics are compiled in Ref. 1. Recent work has focused on concentration measurements of copper [14] and oxygen atoms [15-16]. By scanning the absorption lines with their tunable lasers, these authors were also able to detect the Doppler shift resulting from the flow motion and to deduce the flow velocity with an accuracy on the order of 10-15 %.

A good application of such work is shown in the following example which illustrates the capabilities of this technique to study high enthalpy flows [17]. The flowfield of the high enthalpy facility L2K of the Deutsche Forshungsanstalt für Luft and Raumfahrt (DLR) have been explored using the LIF technique in order to characterize the conditions in the test section free stream flow and also to probe the shock layer induced by a model placed in the flow. The arc heated facility, which is mainly used for testing thermal protection materials, offers a wide choice of flow conditions to simulate the stagnation conditions during shuttle re-entry. The L2K facility can be operated during several hours without interruption. It uses two hollow copper electrodes and is powered by a direct current power supply. The high enthalpy gas flows through a small settling chamber then through a conical nozzle toward a vacuum chamber. The mass flow rate is 50 g/s. The total enthalpy delivered to the gases is 6.7 MJ/Kg and the stagnation pressure and temperature are 1.3 $10^5$ Pa and 3910 K respectively. The flow field in this facility is dominated by nonequilibrium phenomena.

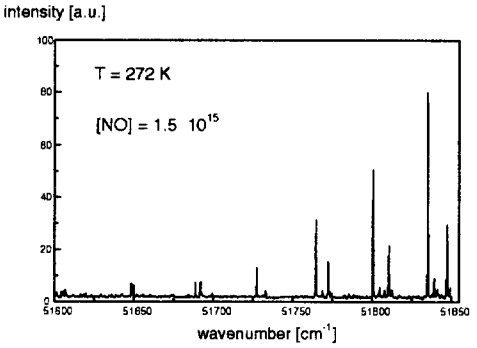


***Figure 2*** Excitation spectrum of NO recorded in the free stream at the LBK facility.

NO has been used as a natural tracer for the LIF experiments. A tunable excimer laser (lambda Physics LPX 150) is operated with ArF to generate light pulses with a duration of 20 ns and a power of up to 240 mJ at the wavelengths of NO transitions in the 192.8 nm–193.8 nm spectral range. Because of the L2K continuous flow, characterization of the free stream flow has been made by recording the excitation spectrum of NO in the flow. For instance, a typical free stream excitation spectrum is shown in Fig 2. The analysis of the line intensities allows the determination of the rotational temperature. The absolute number

density of NO can be also deduced from the comparison of the fluorescence signals with those measured in a calibration experiment where all the physical parameters are known.

Two-dimensional laser induced fluorescence images of NO upstream of the model are also recorded by tuning the laser to a NO transition (excitation frequency of 51625 $cm^{-1}$). Figure 3 shows clearly the shock shape with a shock stand off of 13-14 mm at the model axis. The increase of the NO fluorescence signal behind the shock front is related to the increase of the number density and to the temperature elevation. Due to quenching effects, the fluorescence intensity decreases in region close to the model.

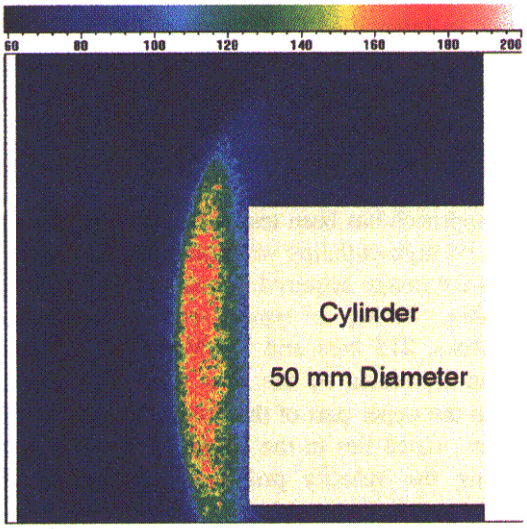


***Figure 3*** Two-dimensional LIF image of NO recorded upstream of the model at the LBK facility

***Electron beam Fluorescence***

Electron beam fluorescence (EBF) bears some resemblance to LIF excepted that the laser beam is replaced by a high energy electron beam. Electron guns such as those employed in electron microscopy are used, but even more powerful sources like pseudo-sparks are sometimes utilized. The high energy electrons induce broadband excitations onto the molecules under probe and eventually ionize them. For nitrogen at $10^{-4}$ normal density, the main process is

$$N_2 + e_p^- \rightarrow N_2^{+*} + e_p^- + e_s^-$$

Where $e^-_p$ is a primary electron (from the electron beam) and $e^-_s$ a secondary electron of an energy of a few electron volts emitted during the formation of the $N_2^+$ ion. This ion, which is excited by the collision on one of its vibronic states, denoted by the * symbol, promptly loses its energy via emission of a photon,

$$N_2^{+*} \rightarrow N_2^+ + h\nu$$

in the near ultraviolet. The luminescence is interesting because its intensity is proportional to the $N_2$ number density and its spectral content reveals the original population distribution on the quantum states of the $N_2$, allowing temperature measurements to be performed. The secondary electrons remain confined in the immediate vicinity of the ions by the space charge and continue to have low-energy collisions with them; these collisions reexcite them and maintain a luminescence by the processes

$$N_2^+ + e_s^- \rightarrow N_2^{+*} + e_s^-$$

$$N_2^{+*} \rightarrow N_2^+ + h\nu$$

This causes the luminescence to persist several microseconds or tens of microseconds after the high-energy electron beam has been turned off. This phenomena can be exploited for free stream velocity measurements by flow tagging, followed by time-of-flight detection [18]. EBF also measures rotational and vibrational temperatures by dispersing the spectrum of the emitted fluorescence.

Typical applications of EBF can be found in ref. 1. Both point measurements and imaging (see below) are used. The spatial resolution is of the order of 1 $mm^3$; it is usually a little worse than in the laser scattering techniques. Recently, encouraging results were reported using a pseudo-spark mounted on a model [19]. However, EBF suffers from a difficulty associated with quenching:

$$N_2^{+*} + N_2 \rightarrow N_2^+ + N_2$$

Quenching reduced the fluorescence yield and interferes with the concentration measurements at densities above a few $10^{-4}$ normal. Detection of the X-ray emission, which results from a Brehmstrahlung process and suffers no quenching, offers an interesting alternative [20].

EBF has so far been used primarily in low and medium enthalpy facilities for imaging. Illumination is achieved by rastering the continuous-wave beam emitted by the electron gun, giving a triangular field. Mohamed et al. have done interesting studies using this method on shock-shock interaction configurations between a flat plate and a cylinder [18]. In spite of the quality of such images, work at high enthalpy facilities is impaired by the weakness of the scattering and the strength of the stray light. Higher-current electron

beams are thus required. Recently, a new electron-beam source based on a pseudospark electron gun and capable of delivering a thin-pulsed sheet 45 cm in length has been developed at Onera. This source shows great promise for future work in high-enthalpy facilities. However, the main constraint is that flows should not exceed densities of $10^{-3}$ normal to avoid excessive electron-beam blowup.

The pseudospark technology consists of two electrodes in the form of coaxial disks, each with a central hole, separated by a gap of a few millimeters. (Fig 4). The upper disk forms the cathode, whereas the lower one acts as the anode. Injection of $10^9$-$10^{10}$ electrons to the back of the cathode induces the electrical breakdown of the gap between the two electrodes. The standing voltage that can exceed 60 kV for a single-stage apparatus then, typically, collapses to zero in 20-50 ns. This is simultaneously accompanied by emission of a very bright pinched electron beam along the axis of the disks. The maximum current is then 300-1000 A, the mean section is in the square millimeter range, and the electron energy is related to the instantaneous voltage between the electrodes. The fast electrons exit the anode disk orifice and can propagate for a few tens of centimeters in a low-pressure medium. In practice, the pseudospark, which operates in a same gas as the flow, is provided with its proper gas-pressure control device and communicates with the wind tunnel through a reduced hole of 0.3 mm diameter. This allows one both to achieve a narrower electron beam for the
gas ionization trace and to maintain a low pressure inside the pseudospark.

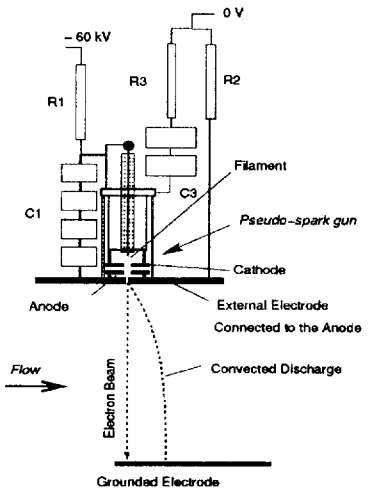


***Figure 4*** Schematic diagram of the pseudo-spark electron gun for velocity measurement

A solution avoiding the important problem of the ionization of the gas leading to the production of the conductive plasma of ions and secondary electrons has been elaborated to maintain the electron beam elsewhere in the wind tunnel. The proposed strategy was to use simultaneously the fast electron emission by the pseudospark, together with its high-voltage breakdown capability, to sustain across the plasma column a supplementary discharge current of much longer duration than the pulsed-electron beam. This induces an intense fluorescence that persists for some microseconds, as long as an electrical current of a few amperes feeds the conductive trace. During this time, the column is convected and deformed by the flow following the velocity profile that is present.

Using an intensified CCD camera, the column of the gas can be photographed after some delay, showing its displacement. One can then visualize the velocity field along a line, over a length of about 25 cm.

This approach has been tested successfully recently at the F4 high-enthalpy wind tunnel [21]. Figure 5 shows the image acquired 90 ms after the onset of the shot, during a typical run at stagnation conditions, 215 bars and 7.8 MJ/kg. The plasma column convected by the flow after 5 μs can be seen at the upper part of the image. The top of the column, which lies in the boundary layer, is bent, showing the velocity profile. Fig 6 shows the velocity profile deduced by the best fit of the image of Fig. 6. The highest velocity, i. e., 4100 m/s (± 5%) at 150 mm from the external boundary of the stream, correlates well with the theory.

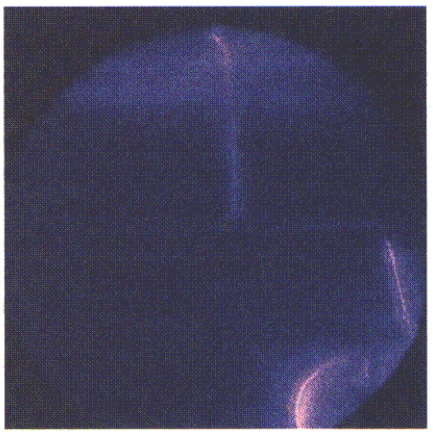

***Figure 5*** Typical F4 run, flow at 90 ms, convection imaged 5 μs after beam emission.

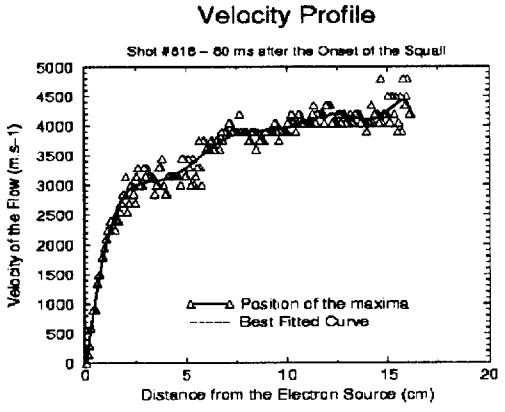


***Figure 6*** Velocity profile at 90 ms for run of Fig.5.

## *Coherent scattering*

***Coherent anti-Stokes Raman Scattering***

The possibility to carry out concentration and temperature measurements by Raman spectroscopy was proved since the seventies. A non linear coherent signal optical process was proposed to solve analysis problems which remain inaccessible using incoherent scattering. This technique, named Coherent anti-Stokes Raman spectroscopy, was observed initially in aromatic liquids in 1965 by Maker and Terhune [22]. The CARS process involves the mixing of four coherent waves, three of them are incident and the fourth one is created in the medium under study. At the beginning, CARS was used for spectroscopic purposes. The idea to employ it to carry out non intrusive analysis in reactive gaseous mixtures was born at ONERA shortly after the seventies.

***a) Principle***

The interaction of light with matter is represented by the classical Maxwell's equations. When the bulk material has no free charges and no magnetization, we obtain (in Gaussian units):

$$\nabla\times(\nabla\times\vec{E}(\vec{r},t))+\frac{1}{c^2}\frac{\partial}{\partial t^2}\vec{E}(\vec{r},t)=-\frac{4\pi}{c^2}\vec{P}(\vec{r},t)$$

Where E(r,t) is the total electric field of the incident waves, c is the speed of light, and P(r,t) the electronic polarization vector. With weak incident electric fields, P responds linearly in terms of E. With more intense fields, P is written in terms of a power series in the field amplitudes:

$$\vec{P}(\vec{r},t)=\vec{P}^{(1)}(\vec{r},t)+\vec{P}^{(2)}(\vec{r},t)+\vec{P}^{(3)}(\vec{r},t)+...$$

Using the following expression for the incident electric field E(r,t) as a function of monochromatic planes waves of frequency $\omega_i$ and of wave vectors $k_i$, the spectral components of the polarization can be written like:

$$\vec{P}^{(n)}(\vec{r},\omega_q)=\left(\frac{1}{2}\right)^{n-1}\chi^{(n)}(-\omega_q,\omega_i,\omega_j,\omega_k)\,\vec{E}(\vec{r},\omega_i)\vec{E}(\vec{r},\omega_j)\vec{E}(\vec{r},\omega_k)$$

with $\omega_q=\Sigma\omega_i$

$\chi^{(1)}$ is the linear susceptibility. This term accounts for the classical phenomena like absorption and refraction. $\chi^{(2)}$ is the second-order susceptibility. This latter vanish in isotropic media and centrosymmetric crystals. In isotropic media, the first non-linear term is $\chi^{(3)}$. This term is responsible for CARS. CARS is observed when three waves with frequencies $\omega_1$ and $\omega_2$ pass through a gas. Incident laser beams at frequencies $\omega_1$ and $\omega_2$ (often termed the pump and the Stokes beams respectively) interact through the third order non linear susceptibility $\chi^{(3)}$ to generate a polarization field which produces coherent radiation at frequency $\omega_3=2\omega_1-\omega_2$. When the frequency difference $(\omega_1-\omega_2)$ is close to the Raman-active vibrational frequency $(\omega_P)$ of a molecular species of the gas, the magnitude of the radiation at $\omega_3$ become very large. Large enough, for instance, that with typical pulsed experimental arrangements, the CARS signal from room air on $N_2$ is visible.

CARS offers very promising potential for the diagnostic probing of hypersonic flows. First, in contrast to spontaneous Raman phenomena, CARS is fairly strong process leading to signal levels typically several orders of magnitude larger than those from Raman scattering. Second, The CARS signals are coherent. Consequently, all of the CARS signal can be collected. Contrast this with the situation pertaining in the incoherent processes where photons are scattered over $4\pi$ steradian and are collected only over a limited solid angle $\Omega$. Furthermore, since the CARS signal can be collected in an small solid angle, discrimination against interference signals like background luminosity, florescence, ... is greatly facilitated. Thus, CARS is expected to produce signal to noise ratio improvements of many orders of magnitude over spontaneous Raman scattering.

The expression of the intensity of the CARS signal at the $\omega_3$ frequency is given by:

$$I_3 = 1.910^{-25}\omega_3^2\left|\chi^{(3)}(-\omega_3,\omega_1,\omega_1,-\omega_2)\right|^2 I_1^2 I_2 z^2$$

where $I_1$and $I_2$ are the beam intensities ($W.cm^{-2}$) at frequency $\omega_1$ and $\omega_2$ respectively and z is the probe length. When the incident beams are focused at the same point, the CARS signal is created mainly in the focal zone. The CARS power depends on those of the incident beams by

$$P_3 = 2.210^{-47}\omega_3^4\left|\chi^{(3)}(-\omega_3,\omega_1,\omega_1,-\omega_2)\right|^2 P_1^2 P_2$$

The expression is obtained assuming that the beams have the same diameter and that their divergence is limited by diffraction. It is independent of the focal strength of the lenses and of the beam diameter. We note also that the signal is proportional to $P_1^2P_2$ which explains the use of high power pulsed lasers.

The susceptibility can be written in terms of a resonant and non-resonant part

$$\chi = \chi_r + \chi_{nr}$$

$\chi^{nr}$ is the contribution from electrons and remote resonances. The resonant susceptibility associated with a homogeneously broadened Raman transition, j is given by

$$\chi_r = \frac{N}{\hbar}\sum_{if}(\omega_{if} - \omega_1 + \omega_2 - \Gamma_{if})^{-1} \times (\rho_{ii}^{(0)} - \rho_{ff}^{(0)}) \times \alpha_{if}^2$$

The subscripts i and f refers to initial and final states respectively. Purely collisional damping is assumed in the eqn., where $\Gamma_{if}$ is the half width and f of the collisional Raman linewidth. Note that the populations appears as a difference between the initial states and the final states. $\alpha_{if}$ is the polarizability matrix element of a specific transition and is related to the well-known Raman cross section by

$$\alpha_{if} = \left(\frac{d\sigma}{d\Omega}\right)_{if}^{1/2}\left(\frac{c}{\omega_2}\right)^2$$

For efficient CARS signal generation, the incident pump and Stokes laser beams must be combined in order to fulfil the phase matching condition

$$\vec{k}_3 = \vec{k}_1 + \vec{k}_1 - \vec{k}_2$$

where $\mathbf{k}_i$ denotes the wave factor at frequency $\omega_i$. This condition stipulates that the anti-Stokes field created at any location by the two laser beams will be phased properly with the anti-Stokes wave coming at upstream positions. The spatial resolution is of the order of 1 cm if one uses collinear beams at the diffraction limit which are focused at the same point of interest under a f–number of 50. For some applications, particularly in turbulent flows, this is insufficient. A better resolution can be obtained with a crossed-beam geometry called BOXCARS [23]. In this configuration, an additional beam of frequency $\omega_1$ is focused at the same point, thus generating a new signal beam in its direction. The latter is generated from the volume common to all the laser beams. The spatial resolution obtained is then of the order of several mm.

All the CARS experiments aim at recording the variations of $P_3$ versus the frequency difference ($\omega_1$-$\omega_2$). The CARS spectrum allows both the chemical and temperature analysis of the gas mixture:

- The spectral positions of the lines or bands are characteristic of the molecular species;
- The line strengths permit the measurement of the molecular densities;
- The population distributions on the diverse quantum states yield the temperature.

Several methods are possible to record CARS spectra. The first one, called scanning CARS, uses a monochromatic laser and a narrow band tunable laser. The spectra are recorded step by step by scanning ($\omega_1$-$\omega_2$), the fixed frequency laser being usually the $\omega_1$ laser. Scanning CARS gives an excellent spectral resolution and a good sensitivity of the order of $10^{14}$ $cm^{-3}$ but, because several minutes are often requested for data recording, only stable or reproducible media can be studied. The second method, called broadband CARS, is well suited to study fluctuating or transient phenomena. It requires a monochromatic laser and a laser covering a wide range of frequencies. The entirety of the CARS spectrum is generated during a single shot laser. The laser energy being now spread over a wide spectral domain, the CARS signal intensity is reduced by several orders of magnitude. The detection limit increases to $10^{17}$ $cm^{-3}$. The third technique, called the dual-line CARS is used to study short-duration low density phenomena., when neither broadband CARS or scanning CARS can be used. It requires a monochromatic laser and two tunable narrow band lasers tuned so that ($\omega_1$-$\omega_2$) and ($\omega_1$-$\omega'_2$) are in resonance with two Raman frequencies of the molecule. Spectra are no longer recorded but the temperature is obtained from the ratio of the two CARS intensities and the density from the line strengths.

***b) experimental setup***

CARS set-up are made up of an emission part and of a reception part separated by the measuring and reference channels. We will describe successively the emission block, a typical arrangement of the measuring and reference channels, and finally the detection system. This later differs according to the type of spectroscopy which is implemented. The instrument developed at ONERA has been conceived to be reliable, transportable and versatile. It allows the three CARS techniques. All the optics, laser sources and mixing optics, are mounted on a transportable table. The main element of the set-up is the Nd:YAG laser chain. The frequency doubled Nd:YAG laser is operated in single longitudinal and transverse mode. This property is felt to be quite important for CARS in the gas phase. A pockels cell is used to trigger the Nd:YAG oscillator. Because there is then no way to maintain the less efficient mode below the threshold, the single mode operation is forced by seeding the oscillator with a CW single mode diode-pumped micro Nd:YAG laser. With one amplifier and a KDP-type 2 frequency doubler, the YAG chain delivers 400 mJ at 532 nm in 11 ns pulses. Using a second KDP crystal like above, gives 70 mJ at 532 nm. This beam is used to pump a dye laser oscillator.

For scanning CARS experiments, the dye laser chain is composed of a dye laser and one amplifier. The oscillator comprises an uncoated wedged output mirror, a 2100 groves/mm grazing incidence grating, a four prism expander and a flat rotating back mirror. The linewidth is 0.07 $cm^{-1}$ (FWHM). The tuning is driven by steeping mirror which allows both a continuous sweep from 500 to 800 nm in coarse steps of 0.07 $cm^{-1}$, and limited sweeps of 6 nm around the coarse drive setting in fine steps of 0.007 $cm^{-1}$. After the amplifier cell, pumped by 1/3 of the main 532 nm beam, the dye chain energy ranges between 1 and 10 mJ depending on the dye and the pump energy.

For broadband CARS experiments, the dye laser chain is also composed of a dye laser and one amplifier. The oscillator is formed by a 100 % back mirror and an uncoated wedged output mirror. A 3 µm-thick Fabry-Perot etalon is used for the tuning. The oscillator is pumped by the second part of the 532 nm generated by the second KDP. The laser linewidth is of the order of 100 $cm^{-1}$. After the amplifier cell, pumped by 1/3 of the main 532 nm beam, the dye chain energy is 5 mJ.

For dual line CARS, both dye lasers are used simultaneously. The linewidth of the broadband laser is narrowed by an interference filter and two intracavity Fabry-Perot etalons. They are 0.1 mm and 1 mm thick respectively. The linewidth is then 0.2 $cm^{-1}$.

Prior leaving the CARS table, the beams are expanded to 6-7 mm by means of telescopes. The Nd:YAG beam passes through a tilted parallel plate which splits the beam into two parallel beams of equal energy. A simple translation of the plate transmits the collinear and BOXCAR arrangements. $\lambda/2$ and $\lambda/4$ wave plates can also be inserted for proper background cancellation at the signal probe volume. Finally, a dichroic mirror is used to align the $\omega_1$ beams along with the $\omega_2$ beam.

It is well known that CARS suffer large shot to shot fluctuations, larger than those due to Poisson statistics. CARS signals usually vary between 1 and 3 successive laser shots which makes it difficult to use CARS without care. The origin of these fluctuations are two fold, apart from those given by the analyzed media:

- the directions and the aberrations of the laser beams vary slightly; this modifies the phase and intensity distribution within the probe volume and consequently changes the signal intensity.
- the mode frequencies and mode amplitudes of the multimode dye lasers are random. The modes excite more or less resonantly the Raman lines. This constitutes the main source of fluctuations when the Raman linewidth is smaller than the free spectral range between the modes as it is encountered in low density media.

The solution, now currently used, consists in dividing the measuring signals by a reference CARS signal measured simultaneously. The optical arrangement of the referencing and measuring channels depends on the experiment. Referencing signal is usually created in a cell filled with one atmosphere of a non resonant gas like Argon. For dual-line CARS, the rare gas referencing is replaced by referencing in the gas analyzed in the measuring channel in order to take into account more precisely the effects of the mode structure of the dye laser.

In scanning CARS, the anti-Stokes signals are filtered by means of compact double monochromators, preceded by dichroic filters to prevent breakdown of the monochromator slits and detected by PM tubes. The latter are mounted in the same rack as the electronic signal processing unit to reduce pick up problems. The light is thus piped from the monochromator to the detectors by means of 1 mm diameter fibers. The photocurrent pulses are treated by a computer-controlled home-

made electronic unit, which gates them, calculates their ratios square roots and averages for a fixed numbers n of shots (n=1 to 50 in practice). The code rejects shots which do not fall within 35 % of the mean reference leg. It also maintains the signal in the upper half part of the AD converter by changing electronics attenuators and PM high voltages. Moreover, it tunes the dye laser after the n shots have been collected.

For multiplex CARS, the anti-Stokes signals are dispersed by spectrographs and detected with intensified photodiode arrays (EGG 512). The dispersive element in the spectrographs is a 2100 lines/mm, aberration-corrected concave holographic grating with curvature radius of 750 mm. The spectrum is imaged with a 4× magnification optics onto the detector target. The net spectral resolution is 0.8 $cm^{-1}$ and the dispersion is 0.12 $cm^{-1}$ per diode. Both signal and reference spectra are recorded simultaneously on the signal and reference arrays and ratioed channel by channel; square roots, and averages if necessary, are subsequently processed.

*c) data processing*

For multiplex CARS, the data processing is performed by comparing the experimental profiles to the theoretical ones. Because the calculation of theoretical spectral is time consuming even with the faster computers, the use of a library of pre-calculated theoretical contours has been adopted. The different parameters like the rotational temperature, the vibrational temperature (when a nonequilibrium regime exist) are determined by using a least squares routine giving the best fit between the profiles. With this data processing, the standard deviation of the temperature remains less than 4 % for conditions of temperature and pressure equal to 3200 K and 1 bar respectively.

Scanning CARS is usually set up to analyze low density media such as hypersonic flows, discharges, low pressure CVD reactors.. As often when scanning CARS is used to analyze a low-pressure medium, the spectrum is composed of isolated lines. The logical way to process the data has been fully explained in Ref 27: The rotational temperature, the vibrational temperature and finally the density are successively inferred. The rotational temperature $T_R(V)$ of the vibrational band V is measured by plotting the natural logarithm of the lines amplitudes versus the energies of the lower states of the Raman transitions. From the expression of $\chi^{(3)}$, it can be seen that the line amplitude is proportional to the rotational population difference and so to the rotational population if one assumes that the rotational temperature does not depend on the vibrational band. The diagram is called a Boltzmann diagram. $T_R(V)$ is obtained from a linear regression with an accuracy $\Delta T_R$. $\Delta T_R$ depends on :

- the number of rotational lines and the energy gap between the lower and the upper energy levels which have been probed,
- the signal to noise ratio at peak intensity of each rotational line
- $T_R(V)$. A simple calculation shows that $\Delta T_R$ is proportional to the square of $T_R(V)$ for fixed above conditions.

As a consequence, $\Delta T_R$ ranges generally from 10-50 K for low V and increases rapidly for high V when the signal strength decreases. Furthermore, it is found that $\Delta T_R$ is in good agreement with the standard deviation of repetitive measurements.

The total population difference between the V and V+1 vibrational states are calculated assuming a Boltzmann distribution at $T_R$ on the entire vibrational bands. Each vibrational band strength is corrected for the dependence of the Raman cross section on (V+1) and the line profile through the Doppler effect.

Once the signal strength dependence have been taken into account, the vibrational population is then obtained from

$$N_V = \sum_{V'=V}^{V_{max}} \Delta N_{V'} + N_{V_{max}+1}$$

Where $V_{max}$ is the quantum number of the upper level of the last observed band. The population of this level may be extrapolated from the lower populations. Its value does not modify appreciably the vibrational population distribution. A Boltzmann diagram of the vibrational populations yields the vibrational temperature if existing. Summing the vibrational populations gives the total number density of the species.

Using dual-line CARS, one no longer obtains a spectrum. Supposing the $\omega_2$ and $\omega'_2$ lasers are tuned on the rotational Q-lines J and J', the electronic system delivers four signals: two signals from the reference channel R(J) and R(J'); two signals from the measuring channel S(J) and S(J'). The software calculates the ratios $Q_1$=S(J)/R(J), $Q_2$=S(J')/R(J') and $Q=Q_1/Q_2$. First, the rotational temperature $T_R$ is inferred from the following expression

$$T_R = \frac{\Delta E/k}{\frac{1}{2}LnQ + \frac{\Delta E}{kT_{ref}} - \frac{1}{2}LnA}$$

Where k is the Boltzmann constant, ΔE is the energy difference between the rotational levels J and J', $T_{ref}$ is the temperature in the reference cell and A is a constant deduced from an experiment carried out in a gas at known temperature. In the derivation of the latter expression, it is assumes that the rotational population distribution is Boltzmann-like and identical for the vibrational states coupled by the Raman transitions. Then once $T_R$ is known, the density is deduced from $Q_1$ or $Q_2$.

*d) practical applications*

While CARS has been primarily used in combustion research, work at lower pressures in plasmas, gas laser media, and aerodynamic flows has been performed. To our knowledge, the only research in practical hypersonic wind tunnels have been obtained, including frees streams and shock layers.

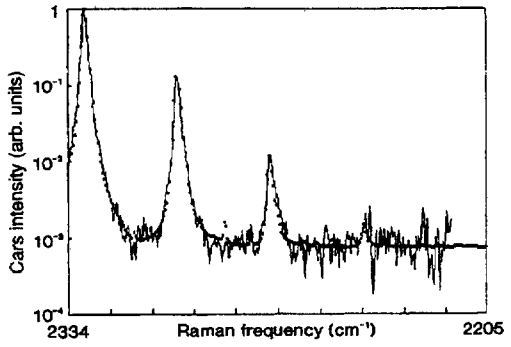


***Figure 7*** Typical single-shot multiplex coherent anti-Stokes Raman scattering (CARS) spectrum of the plume of decomposition products of a lead azide pellet 33 mm above the pellet and 9 ms after ignition

In particular, the multiplex CARS, mainly used in combustion media [24, 25] where density is relatively high, was recently used in the expanding plume of the decomposition products of lead azide, exposing a nonequilibrium gas and demonstrating, a priori, the feasibility of this technique for short-duration flows at static pressures a few $10^{-3}$ normal [26]. Figure 7 show a typical single-shot experimental spectrum of $N_2$ following the detonation of lead azide and its best fit. The theoretical spectrum is calculated for $T_R$ =200 K for all the vibrational states. The vibrational temperature of V=0 to 4 is Boltzmann-like with a vibrational temperature of 2000 K. Time sequential behavior of the $N_2$ product obtained from detonation of lead azide is also shown in Figure 8. $T_V$ decreases while $T_R$ increases as the CARS pulses is delayed. The cloud velocity is estimated to be 4000 $m.s^{-1}$. The behavior of $N_2$ is then characteristic of a product at high temperature and at high density formed near the surface of the explosive and expanding at a supersonic velocity. As a result, the rotational temperature rapidly decreases. The vibrational degree of freedom of $N_2$, remains poorly coupled to translation and rotation with a higher temperature than rotational temperature.

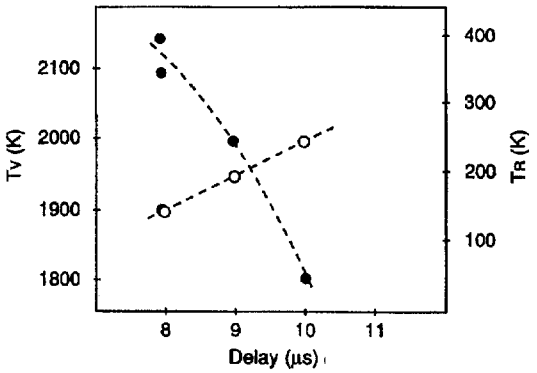


***Figure 8*** Rotational (○) and vibrational (●) temperatures evolution versus time obtained from spectra such as of Figure 7.

An illustration of the capability of the scanning CARS spectroscopy on nitrogen can be shown from the experimental study conducted in the arc driven wind tunnel L2K described previously [27]. The objective of this study was to investigate the nonequilibrium shock layer air flow induced by a two dimensional body (disk model). Preliminary measurements were carried out at a position of 555 mm downstream the nozzle exit and on the centerline region of the nozzle flow to determine the free stream conditions. Figure 9 shows a sample nitrogen CARS spectrum recorded in the free stream using the scanning CARS technique. The spectral bands detected are identified as the Q branches of the vibrational transitions (0,1) and (1,2). For each transition, clearly resolved are the rotational distributions of the two states of the molecule; the para-$N_2$ and the ortho-$N_2$ corresponding to the odd values of J and the even values of J respectively. The rotational distributions in each vibrational transition gives a rotational temperature of 330 K ± 6 K and 334 K ± 9 K for the (0,1) and (1,2) transitions respectively and demonstrates a non-dependence of the rotational distributions versus V. The vibrational temperature, measured from the ratio between V=1 and V=0 populations is 2510 K ± 130 K where the

accuracy reflects the uncertainty on the vibrational populations. A number density of nitrogen of 2.25 $10^{15}$ molecules.cm$^{-3}$ is found from the intensity of the nitrogen spectrum.

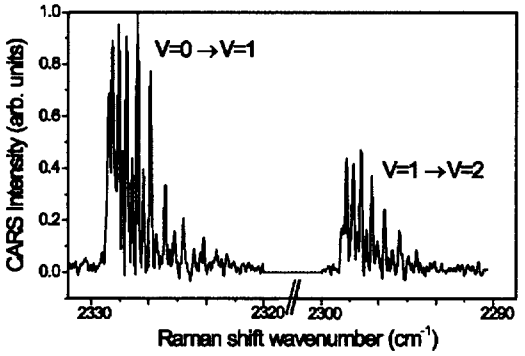


*Figure 9* Scanning coherent anti-Stokes scattering (CARS) spectrum of $N_2$ in the free stream at the LBK wind tunnel facility.

CARS measurements are then performed between the shock layer and the model. For instance, Figure 10 shows a typical nitrogen CARS spectrum recorded at 2 mm from the model where rotational lines up to J=50 are detected in each vibrational band. As previously, rotational and vibrational temperatures and $N_2$ number density have been measured. The two resulting distributions are still found in equilibrium and the rotational temperatures associated to the two vibrational bands are equal to 4200 K ± 150 K. The vibrational temperature is found less than the rotational temperature (≈2800 K).

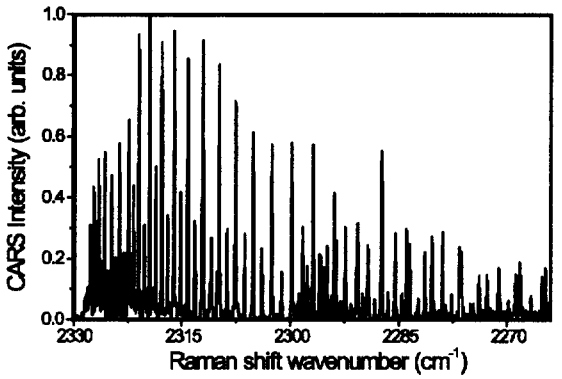


*Figure 10* Scanning coherent anti-Stokes scattering (CARS) spectrum of $N_2$ behind the shock layer induced by a disk model.

Figure 11 shows a comparison between the experimental and theroretical temperature distributions on the symmetry axis in the shock layer. The experimental results brings into evidence the important increase of the rotational temperature through the shock wave. The rotational temperature, assumed to be also the translational temperature displays then a flat profile in a large portion of the shock layer before decreasing strongly close to the wall. On the contrary, the vibrational temperature varies slowly in the shock layer. Good agreement is achieved between these profiles and theoretical ones simulated by a Navier-Stokes solver, demonstrating the potential of this technique.

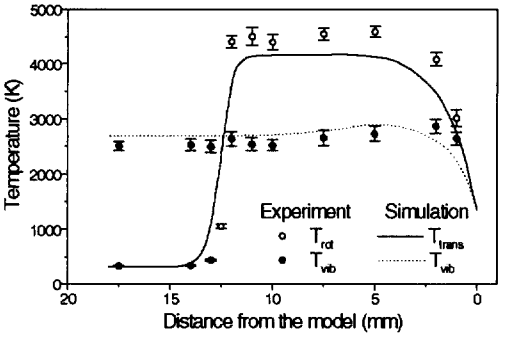


*Figure 11* Comparison between the axial temperature distributions recorded by CARS downstream from the bow shock and the numerical predictions.

At last, dual-line CARS is shown to be well adapted to study media having low density and short run time. This is demonstrated by the spatially resolved and time-resolved rotational temperature and $N_2$ number density measurements which have been recorded in several configurations. In particular, the case of the interaction between the boundary layer and the shock wave in the vicinity of a two-dimensional compression corner has been studied [28]. The experiment was performed in the R5Ch low enthalpy blow down wind tunnel. This facility produces a Mach 10 flow for a stagnation pressure of 2.5 $10^5$ Pa. Under these conditions, the free-stream pressure, static temperature and total density are 5.9 Pa, 52.5 K and 3.9 $10^{-4}$ Kg.m$^{-3}$ respectively. Figure 12 presents the rotational temperature and density profiles measured using the dual-line CARS at five sections located between X/L=0.4 and X/L=1.2. The first two positions are located upstream of the separation line. At X/L=0.4, the temperature and the density are those of the free stream for Y=0.017 m. The temperature and the density found at Y=0.017 m are due to the shock-wave created by the leading edge interaction. For Y=0.017 m, the temperature increases through the boundary layer due to the viscous effects which decelerate the flow, and then decreases to reach the wall. Meanwhile, the density decreases and then is nearly constant in the part of the boundary layer close to the wall. At X/L=0.6, the same behavior is observed. At the

other positions, the profiles present the same features and reflect the evolution of the boundary layer along the model. The density profiles show clearly the effect of the shock induced by the ramp. For instance, the density jump observed at X/L=1.0 and located above Y=0.035 m is mainly due to the leading-edge shock and the density jump located at Y=0.026 m is due to the separation shock. As illustrated on the fig. 12, these experimental results can be used as a data bank to validate calculations performed using a Navier-Stokes solver.

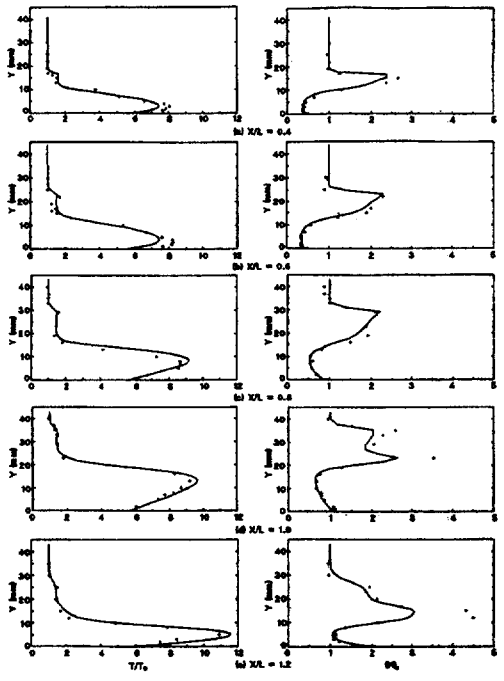

*Figure 12* Rotational temperature (left) and total density (right) distributions normalized by the free stream conditions (-)Homard2 code;(+) experiment.

## *Line-of-Sight techniques*

Line of sight methods essentially rest on emission and absorption spectroscopy.

***Emission***

In emission, one collects the light coming from the flow or from some boundary layer. This light is passed and dispersed through a spectrograph for analysis. Spectral lines are generally detected that reveal the presence of chemicals like metal vapors (in the visible or ultraviolet) or of vibrationally excited molecules. Presence of these lines indicates presence of the compound. The method suffers from major drawbacks, such as the impossibility of determining the position of the radiating species along the line of sight of the collection optics; this is fatal if zones of different temperature and concentration is contributing. In addition, it is also impossible to determine temperature concentrations in a quantitative manner, even if only a homogeneous zone contributes. The latter difficulty stems from the fact that the radiating quantum states are populated via complex collisional mechanisms with electrons or hot species in the nonequilibrium flow and are depopulated by both radiative and collisional (quenching) processes with other species. Emission is this primarily for establishing the presence of trace species or contaminants.

***Absorption***

Absorption techniques are capable of measuring populations of the ground rovibrational states, which are the most populated. Therefore, concentrations can be measured (at least if the absorbing medium is homogenous or presents some spatial symmetry). Technically, the best measurements are performed with laser tunable sources having a spectral resolution capable of resolving the molecular or atomic lines. Currently, the diode laser absorption spectroscopy (DLAS) technique in the infrared is attractive to perform measurements in a wide variety of aerodynamic flows [29, 30, 31]. Measurements in hypersonic flows are usually performed on heteronuclear molecules like CO, NO and $H_2O$ which have strong absorption line strengths due to their high dipole moments. The fundamental level absorption lines for these molecules are usually in the mid infrared region (wavelength > 4 μm).

***a) Principle***

The technique is based on semiconductor diode lasers which are well adapted to absorption spectroscopy. These lasers have very narrow line width emissions (a few tens of MHz) which can be tuned precisely (with a resolution close to $10^{-4}$ $cm^{-1}$ ) around absorption lines, allowing one to visualize the temperature and pressure broadening without any disturbance broadening from the laser linewidth itself. Therefore, this high spectral resolution feature allows linewidth measurements of temperature and concentrations of trace molecules in low pressure (less than 1000 Pa) chemically reacting media such as in hypersonic flows where the lines are mainly broadened by temperature effects with typical Doppler line widths of $10^{-2}$ $cm^{-1}$. The gas velocity can also be determined from the Doppler shift induced in the line positions of the absorbing species when the beam is not perpendicular to the flow axis. The Doppler shift is on the order of $10^{-2}$ $cm^{-1}$ at 5 μm for bulk velocities above 1000 m/s. The allowed measurements are illustrated in Figure 13 from a spectrum presenting an NO absorption line with its Doppler-shifted component. The unshifted line results from absorption of molecules at low velocities which are in the boundary layer of the flow or outside the

flow. For $H_2O$, there is also a contribution from the ambient humidity of air outside the test section.

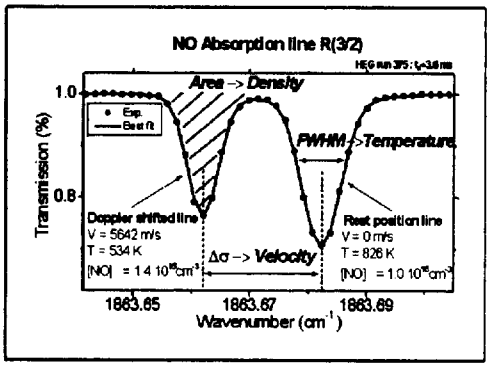


*Figure 13* Usual parameters which can be deduced from pressure-free absorption lines

A major disadvantage of this technique is its line-of-sight nature which gives integrated or averaged data over the absorption path through the medium crossed. The Doppler shifting helps to discern the flow core properties from other zones with molecules absorbing at lower velocities. Another drawback of the technique, carried out in the mid infrared (>2.5 μm), is the requirement to use cryogenic technology: liquid nitrogen cooling for both the diode laser (working around 100 K) and HgCdTe detectors. The main advantages are its sensitivity and its capability to perform measurements at relatively high frequency. Spectra recording can be repeated up to several tens of kHz, which is a very attractive feature for high enthalpy blow-down facilities where the flow runs for short periods (about 200 ms for arc-driven facilities like F4), and where the thermodynamic parameters change over characteristic times of about 10 μs to 1 ms.

***b) Experimental setup***

The laser emission bench and detection setup has been described in detail elsewhere [32]. It can be equipped with two diodes working at temperatures around 100 K. Usually, these diodes emit only over allowed modes covering spectral windows about 1 $cm^{-1}$ wide. With proper tuning of the temperature and current of the diode, some of the spectral windows can be made to come into coincidence with absorption lines of the molecules to be probed. Out of these, only a few lines showing absorption above the detection limit and below saturation can be used, after proper evaluation from the expected densities and temperature of the flow to be probed. A typical emission mode covering some NO absorption lines is presented in Figure 14. This "1864 $cm^{-1}$" mode is the most widely used to probe NO or $H_2O$ in F4 because of the absorption lines contained in it allowing a probe of nearly all the flow conditions. A few hundred sets of flow absorption spectra are acquired together with their corresponding calibration spectra, during each run. Each spectrum is sampled with 1000 spectral points spaced at less than $10^{-3}$ $cm^{-1}$, so that a pressure-free FWHM line profile, which is typically $10^{-2}$ $cm^{-1}$ wide, is described by about 20 spectral points. After wavelength and intensity calibration with the help of the calibration channels, the useful segment of each corrected spectrum is matched to simulated spectra through an iterative non-linear least-squares fitting procedure [32] to retrieve the velocity, the kinetic temperature, and the concentrations of the absorbing species.

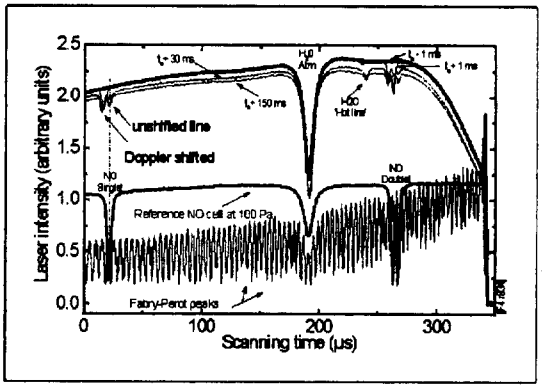


*Figure 14* Typical flow absorption spectrum together with associated calibration spectra

A simple two-layer model is assumed for the flow to perform the data reduction [32]. One layer corresponds to the core flow with a constant free stream velocity v and is usually called the Doppler layer. The other layer (called external or 'rest position' layer) includes all the gases outside the flow core with no bulk velocity that contribute to rest-position lines in the absorption spectrum. This model has been justified experimentally by the use of pipes to protect absorption of the laser beam through the boundary layer (see sections 3 and 4 below) : the comparison of the absorption with and without pipes show that molecules with intermediary velocities in the boundary layer contribute very little to the absorption spectra. Thus, the Doppler shifted and the unshifted line corresponds to only two zones : respectively, the flow core at high velocity and the region outside the flow at thermal velocity.

***c) practical applications***

We present here some applications in the F4 wind tunnel generating high enthalpy flows where molecules like CO, NO, $H_2O$ are naturally present as a result of real gas effects or trace pollution species. Measurements on $H_2O$ in a low enthalpy hypersonic wind tunnel (S4MA) is also presented to illustrate the wide range of application of this technique. Figure 1

summarizes the principal reservoir characteristics and the flow duration times of the wind tunnels probed. The F4 arc-driven, hot-shot, high enthalpy facility was built to simulate part of the re-entry trajectory of space vehicles in the upper atmosphere. It has been extensively described elsewhere [33, 34].

The S4MA facility is a cold blow-down hypersonic wind tunnel operating at Mach numbers of 6.4, 10 or 12 [35]. For reentry studies, it is a common use to obtain reference points where there are no real gas effects. In order to avoid liquefaction, the stagnation conditions (up to 15 MPa for pressure and up to 1800K for temperature) are obtained by passing compressed air in an accumulation heater containing 11 tons of alumina pebbles heated by propane combustion before a run. The run can last up to 100 s, but usually the first 10 to 25 s are used to stabilize all flow parameters at the expected values. This stabilization time is suspected to be due to air liquefaction and water vapor condensation at the beginning of the run.

• *F4 experiments*

The laser beam from the emission bench enters the vacuum chamber through $CaF_2$ windows and crosses the flow at the smallest possible angle to the flow axis (around 63°, given the distance between nozzle and diffuser ) so as to induce the largest Doppler shift for velocity measurements. The portion of the flow which is probed is roughly a cylindrical volume of about 670 mm in diameter (nozzle n° 2 exit diameter with a 400 mm diameter flow core) over a path length of about 400 mm.

The laser beam was guided through profiled sealed pipes to avoid the absorption contribution from lower velocity and higher temperature molecules in the flow boundary layer which can disturb the absorption line shapes in the flow core. The tube ends generate a boundary layer of their own, but its contribution to the absorption lines was assumed to be negligible as it does not exceed a thickness of a few millimeters. It was too difficult to have such sealed pipes on the whole path of the laser beam inside the test section because of the mirrors used to obtain the necessary angle of the beam with respect to flow axis for the Doppler-shift velocity measurements. Nevertheless, this configuration reduced the absorbing molecules to only two groups : molecules of the flow core at bulk velocity of the flow giving the Doppler shifted lines and molecules only at thermal velocities giving the unshifted absorption lines. The data reduction is therefore easier and justifies completely the two layer model mentioned in section 2 above. In fact, comparisons of results for similar runs with and without protection pipes shows that the protection pipes only bring a decrease in the intensity of the non-shifted absorption lines, but little or no difference for velocity and temperature measurements, confirming that boundary layers have indeed little impact on the measurements [36].

The flow can last up to 400 ms, with its thermodynamic parameters rapidly changing as the gas is expelled out of the arc chamber (about 1%/ms decrease of total pressure and enthalpy). The spectra acquisition is therefore set in this facility to 1 kHz for a total measurement time of 1 second. Usually, the data reduction on the absorption spectra is performed for the first 120 ms of the run, because the Doppler shifted absorption line in the flow becomes too small or the results to be reliable after this period.

The typical values of free stream velocity, temperature and NO density versus time for a type III flow using nozzle n°2 are shown in Figure 15. These values are also compared to results obtained from several numerical flow models [37]. The velocities inferred from the spectra are lower than the values calculated from heat flux measurements using frozen and equilibrium flow assumptions in the first 40 ms but the theoretical/experimental agreement is good after 40 ms. Note that the first 30-40 ms of F4 runs are considered as a flow establishment period due to the nozzle plug and wires expelling phase. The other gas parameters do not compare well: the DLAS temperature is higher even than the equilibrium one, whereas the NO density is lower than the frozen one. Some attempts to explain these discrepancies are described in ref. 37.

Experiments are carried out with a diode laser tuned on a CO absorption line (the R8 line at 2176.2835 $cm^{-1}$). Figure 16 shows the corresponding results of free stream velocity, temperature and CO density for a run having a lower enthalpy condition than for a type III condition. These results are still being analyzed and will be published shortly. The CO is presently believed to result, first, from organic material (seals, silicon paste...) ablation with pure nitrogen runs, second, from combustion processes taking place in the arc chamber where the temperature is very high (up to 8000 K) and where the thermal protection elements are mostly in carbon materials. Further tests with nitrogen will allow to quantify these two contributions.

The least-squares fit, using the two-layer model, gives uncertainties of about 1% for velocity and 10% for both temperature and density. We must add to this, uncertainties from spectrum calibration and setup configuration (for example the angle of the laser beam to the flow axis is known with only 1 degree accuracy resulting in an uncertainty of 4% on velocity). The overall uncertainties are then estimated, for both

probed molecules, to be less than 10% for velocity and 30% for both temperature and density.

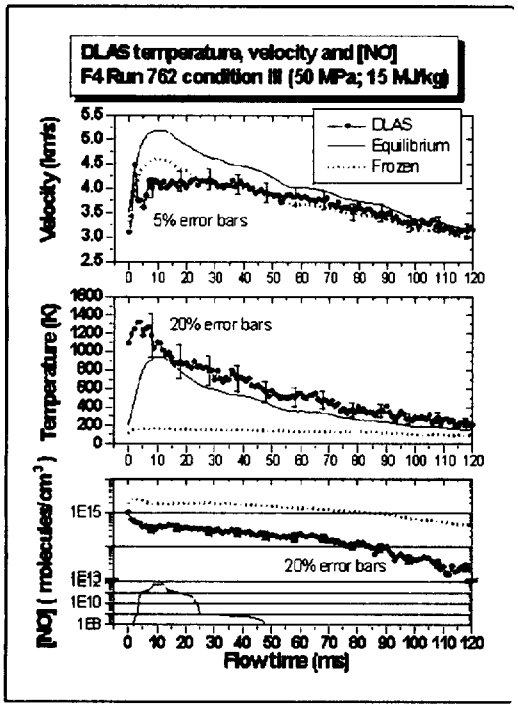


*Figure 15* Velocity, translational temperature and NO density from DLAS in F4 air run.

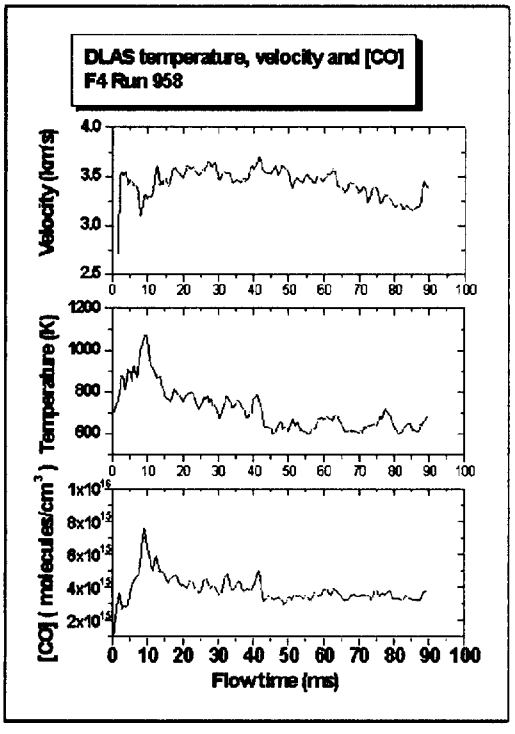


*Figure 16* Velocity, translational temperature and CO density from DLAS in F4 air run.

• *S4MA experiments*

The aim of the diode laser measurements was to measure the water vapor in the flow so as to see the impact of its concentration on the stagnation conditions stabilization time encountered in this wind tunnel.

The laser diode used here has been specifically chosen to emit in a spectral window covering two of the most intense absorption lines of $H_2O$ (1616,1135 $cm^{-1}$ and 1653.2671 $cm^{-1}$ ). This was required to measure the quite low water vapor density expected in the free stream : about $10^{12}$ molecules/$cm^3$, which makes about 13 ppm in the free stream of total mass density of 0.01 kg/$m^3$ and at the temperature of 50K. One of the main problems in the experimental setup is to avoid saturation of the absorption line from ambient water vapor and from the low pressure contribution in the test section outside the flow.

These feasibility experiments were done with the laser beam crossing perpendicularly to the flow in order to check if the signal-to-noise ratio is sufficient to obtain measurements. This of course denies the possibility of velocity measurements as there is no Doppler shift in the absorption lines.

The probed zone was a cylinder of diameter 8 mm and of length ranging from 0,6 meter (flow core only) to 1 meter (flow core and boundary layer). The rest of the laser path is protected in tubes (of variable length) flushed with dry nitrogen in order to avoid absorption by low pressure water vapor absorption outside the flow or in the boundary layer. The emission and detection benches are also flushed with dry nitrogen to avoid absorption from atmospheric water vapor outside the test section.

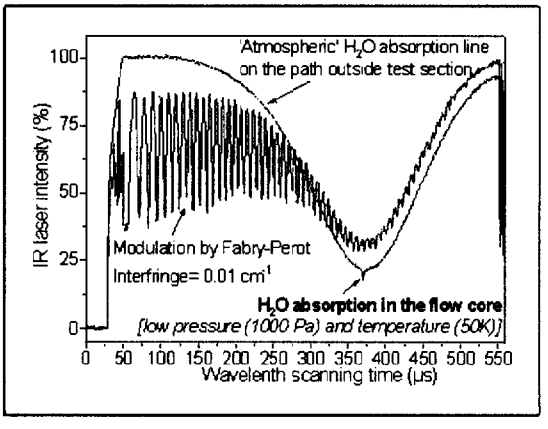


*Figure 17* Typical flow absorption spectrum recorded together with associated calibration spectra

The unwanted absorption from outside the test section was the most difficult to eliminate : the $N_2$ flushing only reduced this saturated absorption to an 80-90% absorption. Fortunately, this was enough to allow us to see the small absorption (a few %) of the water vapor in the flow. The width of this absorption line is narrower (because of the low pressure and low temperature) than the atmospheric $H_2O$ line. The absorption spectrum in Figure 17 illustrates this difference in the line widths. As the atmospheric $H_2O$ absorption line can be considered to be constant during the flow time of 100 seconds, it was also considered as a mere emission envelope during the data reduction.

Spectra were acquired every 0.1 seconds for a total time of 100 seconds which was more than enough to cover the total flow time set to about 60 seconds for these experiments. After calibration and inversion, the time evolution of water vapor density in the flow can be traced as illustrated in Figure 18 where three runs at three different reservoir temperatures (nominal values of 980, 1030 and 1120 K for runs R3063, R3064 and R3065 respectively) are compared. These density curves are also compared to the Mach number and temperature temporal evolution of the flows considered. It was not possible to measure the water vapor density for very low temperatures as the absorption line was below the detection limit of our instrument. The curves in Figure 18 show that there is a threshold temperature (~46K) above which the absorption line could be detected.

These results show that the water vapor content in the free stream is very low as expected. Its density increases with flow time and has the same temporal trend as for Mach number or temperature. A possible explanation is that at the beginning of the run, the water is not only in vapor form, but also in liquid and solid form; after the first seconds of the run, as the temperature increases, the increase of water vapor content can indicate a decrease of the water vapor condensation, and appears to be a positive sign for good flow parameters. Also, there can be other reasons for the stagnation conditions stabilization time, like air liquefaction, or dust due to ablation of the heating pebbles coming mostly at the beginning of the flow. Other types of experiments are now being planned to measure water in form of solid or liquid as well as to measure dust particles which can enhance air liquefaction at the beginning of the blow down.

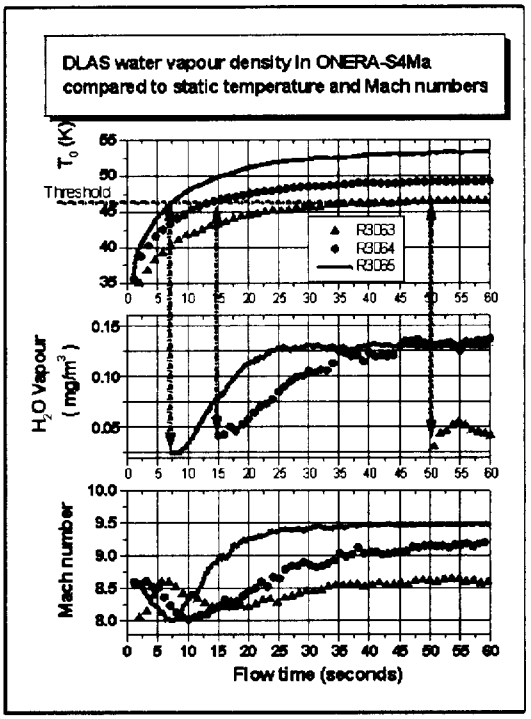


*Figure 18* Time evolution of the temperature, water vapor density and Mach number during three runs at S4MA.

## Conclusion

With the new laser sources now available, there are numerous approaches to acquisition of the flow parameters for probing hypersonic flows in ground testing facilities.

In high-enthalpy facilities, diode laser absorption spectroscopy is well suited for free stream measurement of velocity, static temperature and trace species concentration measurements. However, it requires the flow to be quite homogeneous. CARS is a good tool for point measurement of rotational and vibrational temperatures and of number density. Electron beam fluorescence and Laser Induced fluorescence can be employed for qualitative imaging and visualization. Visualization of shocks and in particular the convection of a plasma column can be used to measured the velocity profiles.

In low-enthalpy flows, the same methods can be also employed. However, if density is higher, Diode laser absorption will lose ground in the velocity measurements and seeding with NO or other species may become necessary. EBF will also lose all of its applications, while the optical techniques like Rayleigh and Raman scattering will become applicable.

**Acknowledgments**
I am indebted to the many members of the ONERA research group who have contributed to the research described in this article. In particular, I am grateful to A. Mohamed and S. Larigaldie for permission to cite aspects of their research works. I am grateful also to U. Koch and A. Gülhan from DLR for permission of their results and J.P. Taran from Onera for helpful discussions.

## References

[1] Boutier A., "News trends in Instrumentation for hypersonic research". Proc. NATA Adv. Res. Workshop Instrum. Hypersonic Res., ONERA Le Fauga-Mauzac Center, France, Series E: Applied Sciences, Vol 224, 1992.

[2] "Aerodynamic measurement technologies", AIAA J, 34 (3), pp 433-526 ,1996.

[3] Miles R.B., Lempert W.R., "Quantitative flow visualization in unseeded flows", Ann. Rev. Fluid. Mech. 29, pp 285-326, 1997.

[4] Byer R.L., "Review, remote air pollution measurement", Opt. Quant. Elect. 7, pp 147-177, 1975.

[5] Bobin L., "Experimental investigation of a jet in a cross flow by spontaneous Raman scattering", ICIASF, ISL, Saint Louis, France, EEE Publ. 93CH3199-7, 1993.

[6] Gillepsie W.D., Bershader D., Sharma S.P., Ruffin S.M., "Raman scattering measurements of vibrational and rotational distributions in expanding nitrogen", AIAA paper 93-0274, 1993.

[7] Palmer J.L., McMillin B.K., Hanson R.K., "Planar Laser-Induced fluorescence Imaging of velocity and temperature in Shock tunnel free jet flow", AIAA 92-0762, 1992.

[8] Hanson R.K., "Combustion diagnostics: Planar Flowfield Imaging" twenty First Symposium (International) on Combustion, The Combustion Institute, pp 1677-1691, 1986.

[9] Kychakoff G., Howe R.D., Hanson R.K., "Use of Planar Laser Induced Fluorescence for the study of Combustion Flowfields", AIAA paper 83-1361, 1983.

[10] Lucht R.P., "Laser Spectroscopy and its applications", Eds. L.J. Radziemski, Solanz R.W., Paisner J.A., Marcel Dekker, New York, pp 623-676, 1986.

[11] Bechtel, J.H., Dasch, C.J., Teets R.E., Laser Applications, Academic Press, New York, 1984.

[12] Cattolica R.J., Vosen S.R., Twentieth Symposium (International) on Combustion, The Combustion Institute, pp 1273, 1985.

[13] Seitzman J.M. , Hanson R.K., "Quantitative Fluorescence Imaging: A Comparison of Linear, Predissociative and Saturated Pumping Techniques", AIAA paper 92-0879, 1992.

[14] Marinelli W.J., Kessler W.J., Allen M.G., Davis S.J., Arepalli S., Scott C.D., "Copper atom based measurements of velocity and turbulence in arc jet flows" AIAA paper 91-0358, 1991.

[15] Bamford D.J., O'Keefe A., Babikian D.S., Stewart D., Strawa A.W., "Characterization of arc-jet flows using laser-induced fluorescence", AIAA paper 94-0690, 1994

[16] Meyer S., Sharma S., Bershader D., Whiting E., Exberger R., Gilmore J., "Absorption line shape measurement of atomic oxygen at 130 nm using a Raman-shifted excimer laser", AIAA paper 91-0358, 1991.

[17] Koch U., Gülhan A., Esser B., Grisch F., Bouchardy P., "Rotational and Vibrational temperature and density measurements by planar laser induced NO-fluorescence spectroscopy in a nonequilibrium high enthalpy flow", RTO/AGARD fluid dynamics panel symposium, Advanced aerodynamic measurement technology, Seattle, USA, 22-25 September 1997.

[18] Mohamed A.K., Pot. T., Chanetz B., "Diagnostics by electron beam fluorescence in hypersonics", Int. Congr. Aerosp. Sim. Facil., 16 th, Dayton, OH, 1995.

[19] Lufty F.M., Muntz E.P., "Initial experimental study of pulsed electron beam florescence", AIAA J., 34, pp 478-482, 1996.

[20] Voronel E.S, Kuznetsov L.I., Parfenov M.V., Yarygin V.N., "Electron X ray method for measuring the local density in pulsed erosion jets", Quantum Electron., 24, pp 1010, 1994.

[21] Larigaldie S., Bize D., Mohamed A.K., Ory M., Soutadé J., Taran J.P., "Velocity measurement in hypersonic flows using electron beam-assisted glow discharge", AIAA J., 36, pp1061-1064, 1998.

[22] Maker P.D., Terhune R.W., "Study of optical effects due to an induced third order polarization in the electric field strength", Phys. Rev., 137A, pp 801-818, 1965.

[23] Greenhalgh, D.A., "Comments on the use of BOXCARS for gas-phase CARS spectroscopy", J. Raman Spectrosc., 14, 150-153, 1983.

[24] Eckbreth, A.C., Dobbs G.M., Stufflebeam, J.H., Tellex P.A., "CARS temperature and species measurements in augmented jet engine exhausts", Appl. Opt., 23, pp 1328-1338, 1984.

[25] Magre, P., Moreau P., Collin G., Borghi, R., Péalat M., "Further studies by CARS of premixed turbulent combustion", Combustion and flame, 71, 147-153, 1988.

[26] Rosenwaks T., Arusi-Parpar T., Bar I., Bouchardy P., Cohen Y., David D., Grisch F., Heflinger D., Péalat M., Strugano A., Taran J.P., Valentini J.J.,"Application of stimulated Raman excitation and Coherent anti Stokes Raman spectroscopy to Molecular dynamics and Gas dynamics", Nonlinear Optics, 5, pp33-44, 1993.

[27] Grisch F., Bouchardy P., Koch U., Gülhan A., Esser B., "Rotational and Vibrational temperature and density measurements by coherent anti-Stokes Raman spectroscopy in a nonequilibrium shock layer flow", RTO/AGARD fluid dynamics panel symposium, Advanced aerodynamic measurement technology, Seattle, USA, 22-25 September 1997.

[28] Grisch F., Bouchardy P., Péalat M., Chanetz B., Pot T., Coët M.C., "Rotational temperature and density measurements in a hypersonic flow by Dual-Line CARS", Appl. Phys. B., 56, pp 14-20, 1993.

[29] Arroyo M. P., Langlois S., Hanson R. K., "Diode laser absorption technique for simultaneous measurements of multiple gas dynamic parameters in high speed flows containing water vapor", Appl. Opt., vol 33, n°15,1994.

[30] Mohamed A. K., Rosier B., Henry D., Louvet Y., Varghese P. L., "Tunable diode laser measurements on nitric oxide in a hypersonic wind-tunnel", AIAA Paper 95-0428, 1995.

[31] Upschulte B. L., Miller M. F., Allen M.G., Jackson K., Gruber M., Mathur T., "Continuous water vapor mass flux and temperature measurements in a model scramjet combustor using a diode laser sensor", AIAA paper 0518, 1999.

[32] Mohamed A. K., "MSTP Phase 2 Progress Report. Infrared Diode Laser Absorption Spectroscopy in Wind Tunnels. I-Experimental Setup, II-Data Reduction Procedures" (ESA -HT-TN-E34-701&702&703-ONERA),ONERA Technical Report n° 8 and 9 /7301 PY, 1996.

[33] François G., Ledy J.P., Masson A., "ONERA high enthalpy wind-tunnel F4", 82nd Meeting of the Supersonic Tunnel Association, Wright Patterson AFB, Ohio, Oct. 16-18, 1994

[34] Vardavas I..M., "Modeling reactive gas flows within shock tunnels", Australian J. Chem., 37, pp157-177, 1984.

[35] Ledy J.P., Prieur J., "Improvement of the ONERA hypersonic facility S4MA exhaust at the atmosphere at M = 6.4", 89th Supersonic Tunnel Association International Meeting (VKI), Brussels, 26-28 April 1998.

[36] Mohamed A. K. , Rosier B., Sagnier P., Henry D., Louvet Y., Bize D., "Application of Infrared Diode Laser Absorption Spectroscopy to the F4 High Enthalpy Wind Tunnel", Aerospace Science and Technology, 4, pp 241-250, 1998.

[37] Sagnier Ph., Vérant J. L., "Flow characterization in the ONERA F4 high enthalpy wind tunnel", AIAA J., 36, pp 522-531, 1998.

# The VKI Plasmatron Characteristics and Performance

**B. Bottin, O. Chazot, M. Carbonaro, V. Van Der Haegen, S. Paris**
The von Kármán Institute for Fluid Dynamics
72 Chaussée de Waterloo
B-1640 Rhode-Saint-Genèse
Belgium

## Abstract

The von Kármán Institute (VKI) recently completed the commissioning of a new inductively-coupled plasma wind tunnel ("Plasmatron") devoted to the simulation of thermal re-entry conditions as applicable to TPS materials used on real flight trajectories. In the context of the commissioning, two main intrusive measurement techniques, the Pitot tube and the calorimetric heat flux probe, were developed and extensively used to record the performance in order to compare them with the specifications. During the commissioning phase, other techniques were being developed in another VKI facility, the Minitorch, a small inductively-coupled plasma torch used as the instrumental test bench for the Plasmatron. This paper presents the Plasmatron facility to the reader, then describes in detail the probes that were used, the test methodology that was followed, and the results that were obtained during the commissioning phase. The technique of laser Doppler velocimetry (LDV), which is currently developed in the Minitorch and envisaged as one of the standard Plasmatron techniques in the near future, is also described in detail.

# 1. The Plasmatron facility

## 1.1 Inductively-coupled plasma heaters

The concept behind plasma generation by induction is sketched on figure 1. A coil surrounds a quartz tube in which cold gas is injected. This coil is connected to a high-frequency generator and is traversed by high-voltage, high-frequency current (a few thousand volts with frequencies from 400 kHz to several MHz).

Due to these conditions, induced electric and magnetic fields exist inside the quartz tube, with induction lines parallel to the axis, as in a classical solenoid. The periodic time variation of the induction creates circular, oscillating electric fields in planes perpendicular to the tube axis. These fields can move the free electrons existing in the gas, creating current loops (*eddy currents*) heating the gas by Joule effect. Once the gas heats up, it dissociates and ionises into a plasma. Conceptually, the torch is actually a transformer (as illustrated on figure 2), with the coil as primary winding and the induced current loops in the gas as secondary windings.

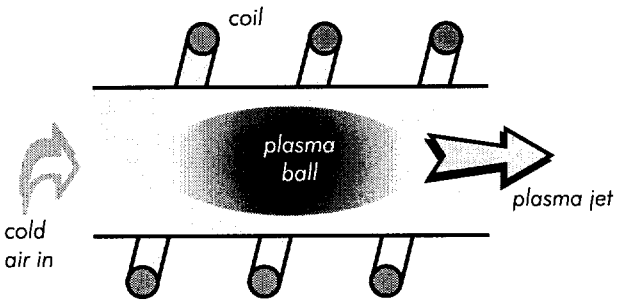


*Figure 1. Concept of the inductively-coupled plasma torch*

The first free electrons can be obtained by introducing an electrode into the plasma torch or, preferably, by reducing the pressure under 0.1 mbar and applying voltage on the coil. Electric field gradients appearing in the vicinity of the coil (between turns) are strong enough to cause a local ionisation of the gas in the tube. Once the first free electrons have appeared, the whole gas is rapidly heated by Joule effect. Argon is used in order to facilitate the initial electric discharge because of the longer lifetime of the free electrons at low pressure compared to the air plasma case. By these means plasma can be generated from low to atmospheric pressures with temperatures of the order of 6000 K to 12000 K. The operation of such ICP devices can be maintained as long as desired, provided that electricity, gas supply and adequate cooling are not interrupted.

## 1.2 Motivation and requirements

The Plasmatron project was originally devised towards the end of 1992 as part of the European Hermes reusable space vehicle programme, and later became part of the MSTP (Manned Space Transportation Programme) research program of the European Space

*Paper presented at the RTO AVT Course on "Measurement Techniques for High Enthalpy and Plasma Flows", held in Rhode-Saint-Genèse, Belgium, 25-29 October 1999, and published in RTO EN-8.*

Agency. Indeed, future European space missions have brought the need of specific tools for the development and testing of new thermal protection systems within Europe. As presented above, no ICP facility of high power was available in Europe to satisfy those needs. This fact led, towards the end of 1994, to the financing by ESA and the Belgian Federal Office for Scientific, Technical and Cultural Affairs (OSTC) of the design, fabrication and assembly of a 1.2 MW Plasmatron at the VKI. This facility is, at the present time, the most powerful of its kind in the world. It was inaugurated on December 8, 1997 by Belgian Minister Yvan Ylieff and by the ESA Director of Manned Space Flight and Microgravity, Jorg Feustel-Buechl.

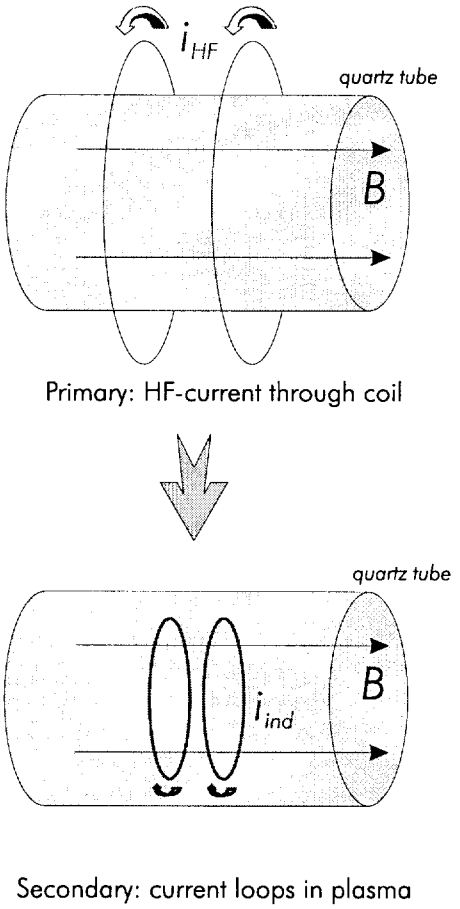


*Figure 2. The inductively-coupled plasma torch seen as a transformer*

The specifications for the facility are matched to the flight envelope of the Hermes vehicle (although the project was abandoned, it is a good representative of a typical lifting re-entry). They are given in terms of stagnation point heat flux and stagnation pressure, as shown on figure 3. It must be noted that the heat flux rates have to be reached on a catalytic cold wall in order to avoid uncertainties due to catalytic effects. This operating envelope has been achieved during the commissioning phase of the facility, as will be presented later.

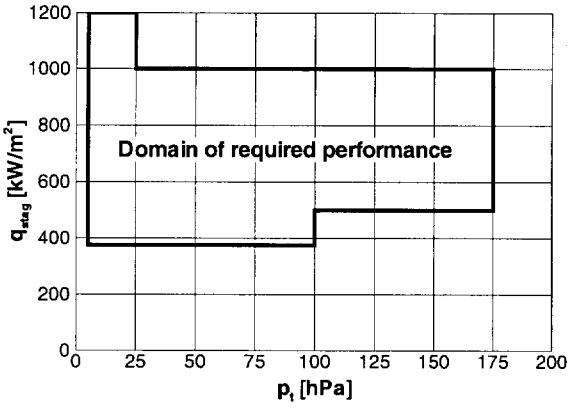


*Figure 3. ESA specifications diagram for the VKI Plasmatron*

## 1.3 The Plasmatron facility

### 1.3.1 The ICP torch

The ICP torch designed for the Plasmatron facility is of the latest double flux cold crucible technology. Its principle is illustrated on figure 4. Compared to the basic design (figure 1), the torch features an additional quartz tube, located inside the outer tube, which serves to divide the gas between central and peripheral injections. The purpose is explained below.

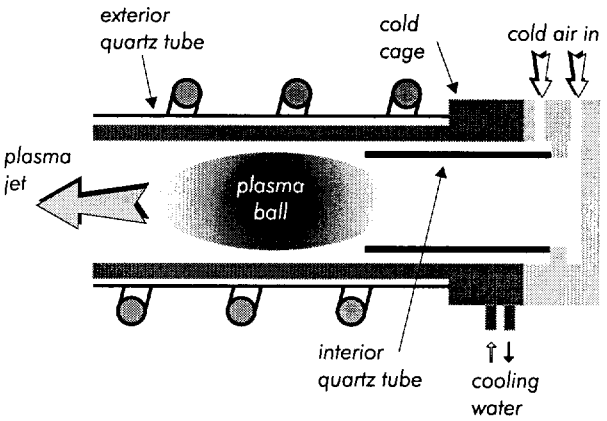


*Figure 4. Concept of the double flux, cold crucible, ICP torch*

It is understandable from the basic principle of an ICP torch that the plasma ball remains in the centre of the tube, confined by electromagnetic forces. However, in some conditions, the ball could expand and touch the wall, melting the quartz tube. To prevent this, a thin layer of cold air flows along the inner side in the discharge region. This peripheral gas flux shields the tube wall and feeds the plasma ball. The inner tube is used to bring the flow close to the discharge. It is thus also close to the plasma ball and may sometimes be in direct contact. The central gas flux is used to push the plasma ball away from the inner tube [1]. The fine tuning of these two injections is essential to obtain a stable plasma with relatively high-power.

Inside the torch is inserted a cold cage made of water-cooled copper segments, which serves as an additional protection for the quartz tube. One might think that the copper cage could be a source of flow pollution. However, the presence of metallic parts is a necessary but not a sufficient condition for erosion. Since the copper cage is water-cooled to a wall temperature less than the boiling point of water, there simply cannot be a direct contact between the copper and the hot plasma (otherwise the copper cage would overheat, melt and be destroyed, preventing continuous operation).

Figure 5 shows a picture of the ICP torch in operation, with the plasma glow showing through the segments of the copper cage. This segmentation is necessary to avoid screening of the high-frequency electric field by Faraday cage effect. The single-turn inductor (made of seven parallel rings) with internal water cooling can clearly be seen on the photograph. The tubes on the left provide gas supply, those on the right are used to inject cooling water into the cold cage and other parts of the metallic casing enclosing the ICP torch.

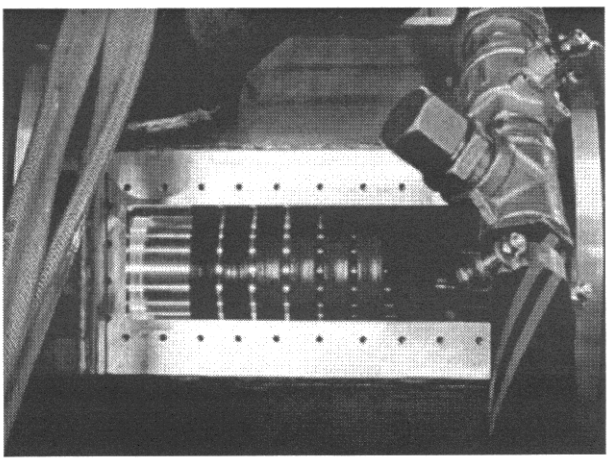

*Figure 5. The Plasmatron ICP torch in operation*

### 1.3.2 The facility

The complete Plasmatron facility schematic [2] is sketched in figure 6. It is equipped with two interchangeable ICP torches, one of 80 mm diameter for the test of small samples and one of 160 mm diameter suited to samples as well as to full TPS tiles. Each torch is mounted inside a support casing, which is fixed on a side of the test chamber, a 2.5 m long, 1.4 m diameter vessel (figure 7) equipped with multiple portholes and windows to allow maximal flexibility and unrestrained optical access for plasma diagnostic techniques.

Inside the test chamber, the samples and probes are supposed to be mounted on a three-axis fast-injection and support system. However, this subsystem is not yet operational at the present time. Instead, probes can be mounted on a traversing mechanism fixed on a porthole. Up to now, low speed plasma jets have been generated (figure 8 shows an air plasma jet from the 80 mm diameter torch). Accelerated subsonic flows and supersonic flows will be obtained in the near future by insertion of nozzles at the outlet of the torch.

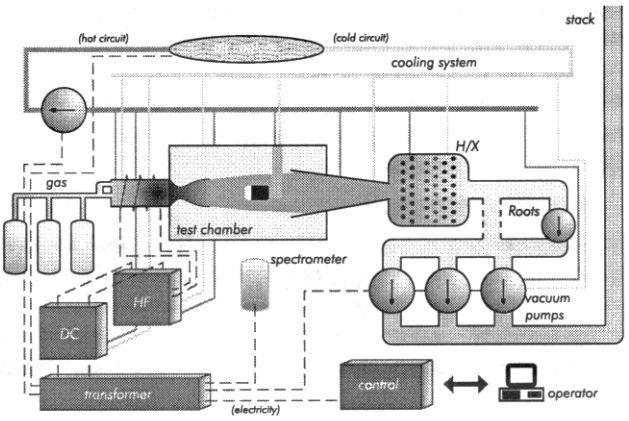


*Figure 6. The Plasmatron facility (schematic drawing)*

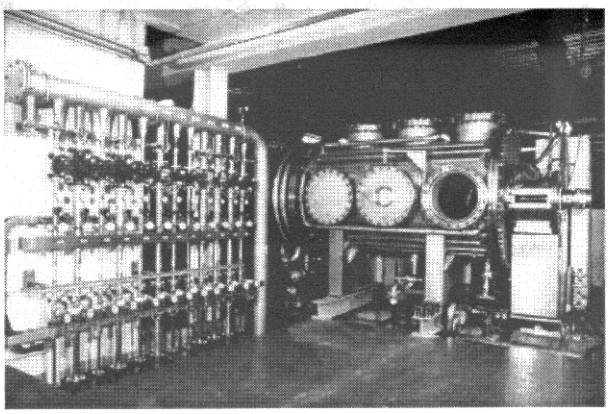

*Figure 7. The Plasmatron viewed from the left*

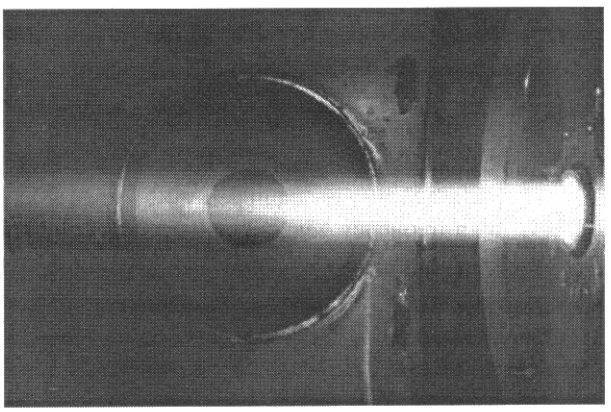

*Figure 8. Air plasma jet from the 80 mm torch*

The jet of plasma is collected at the outlet of the test chamber and cooled in the heat exchanger to a temperature of 50 °C to protect the vacuum plant from overheating damage. Figure 9 shows the heat exchanger vessel, which is as big as the test section. Inside are two modules, each with its own cooling line. The front

module has two rows of 28 tubes and faces the maximal heat load from the jet. The back module has 16 rows of 28 tubes, with the last 14 rows made of flattened tubes in order to reduce the pressure loss. The vacuum plant consists of three volumetric vacuum pumps which allow operating pressures between 1 hPa and atmospheric pressure with a maximum flow rate of 3000 $m^3/h$. A Roots pump can be inserted in the circuit to bring the pressure down to 4 Pa without any volume flow penalty. Exhaust gases are vented to the atmosphere through a stack.

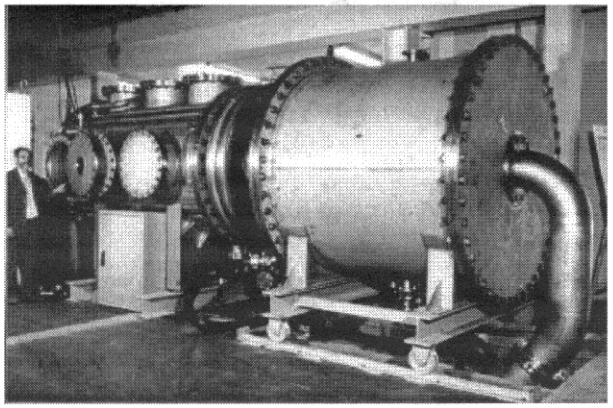

*Figure 9. The Plasmatron viewed from the right*

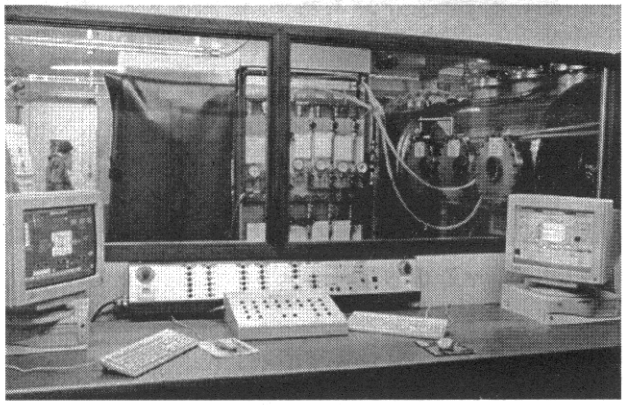

*Figure 10. The Plasmatron viewed from the control cabin*

The Plasmatron is equipped with a 1.2 MW, 400 kHz, high-frequency generator of the new solid-state technology, using thyristors and MOS inverters instead of vacuum tubes. A closed circuit cooling system using de-ionised water protects all facility parts from melting due to the plasma heat, which is evacuated through three dry air coolers located on the roof. The total water flow rate is about 2088 l/min. Figure 7 shows the individual cooling lines and the collection manifold. The working pressure of this cooling system is 3 bar, but specific cooling lines (inductor, copper cage and test probes) are fed at a 10 bar pressure to compensate for the very small size of internal cooling passages encountered within the subsystems. Test gases can be injected from carboys in order to duplicate the required chemical composition. A separate carboy provides argon for ignition purposes. For air plasma, the facility is connected to the VKI compressed air supply. The full facility is computer-controlled from a remote cabin. Figure 10 shows the facility as seen from the control cabin, with the gas supply panel in the background.

# 2. Performance measurements

## 2.1 Introduction

The performance matrix imposed by the European Space Agency (figure 3) needed to be experimentally confirmed by performing total pressure and heat flux measurements. To that effect, specific probes have been designed, built and used. However, the probes allow to obtain much more information than simply the values of total pressure and heat flux. Coupled with a specific data reduction procedure, the experimental results can be used to obtain significant information on the flow.

The data reduction procedure cannot be applied without some model of the plasma state. It requires the use of several numerical tools, as outlined on figure 11. These models include of course adequate thermodynamic and transport properties modules, the input from the measurements, and a stagnation-point heat transfer computation. This module is the most sensitive as far as data reduction is concerned, because the capability to relate stagnation properties to flow properties directly depends from the quality of this module.

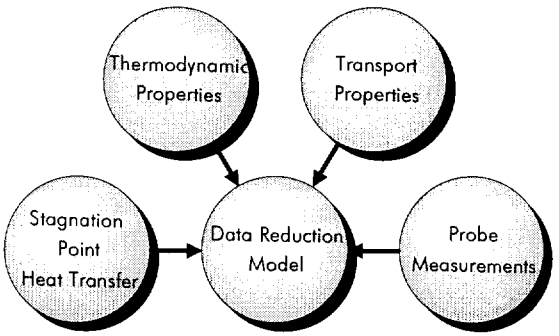


*Figure 11. Elements to take into account in the data reduction model of the Pitot and heat flux probes measurements*

## 2.2 The Pitot probe

### 2.2.1 Description

The Pitot probe used in the Plasmatron is similar to classical Pitot probes, except that it is water-cooled to resist the plasma heat. It is made out of brass and has a hemispherical head of 12 mm diameter, with a pressure-sensing orifice of 2 mm diameter. The size of the Pitot is imposed by the requirements of installing the water passages for the water. The design of the

probe has been inspired by the example of the Pitot probe used in the LBK arc-jet facility at DLR Köln. The conceptual drawing of the Pitot probe is shown on figure 12 and a picture of the probe is shown on figure 13 [2]. The probe is connected to the Plasmatron cooling system and receives water at a pressure of 10 bars and a flow rate of 8 l/min.

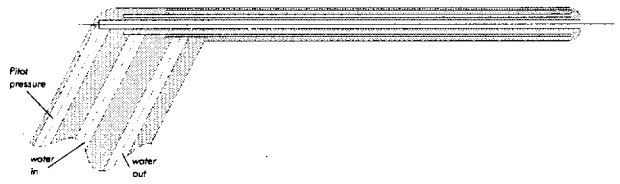


*Figure 12. Conceptual drawing of the Pitot ptobe*

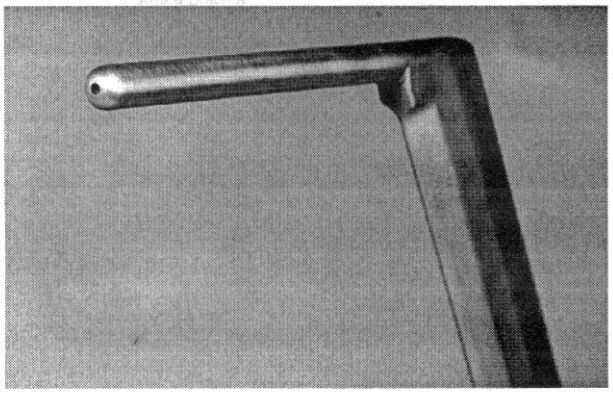

*Figure 13. The Pitot probe as built*

### 2.2.2 Measurements and accuracy

The Pitot probe is used to perform stagnation pressure measurements. The required experimental set-up is shown conceptually on figure 14. The static pressure $p_s$ of the Plasmatron chamber is measured by an absolute pressure transducer of 0.3% full-scale uncertainty (Leybold ceramic capacitance diaphragm transducer DI200). The Pitot tube is connected to a differential pressure transducer (Valydine variable reluctance transducer DP45), calibrated using a Betz precision micro-manometer. The transducer output is read on a pen plotter.

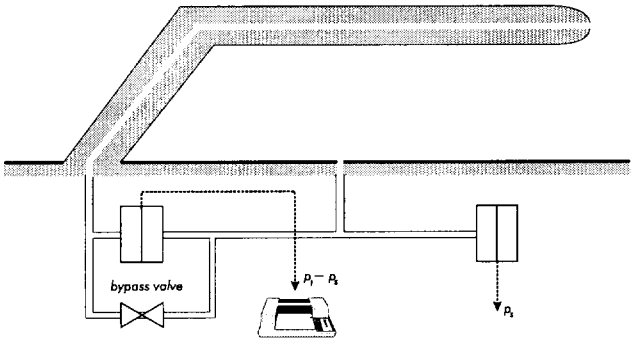


*Figure 14. Pitot pressure measurement set-up (schematic drawing)*

The accuracy of each component is indicated on table 1 according to the manufacturer's specifications (reading accuracy is assessed based on the capability of the user to distinguish half of the interval between two lines on the plotter paper). The global error can be obtained either by summing up each error ("highest error possible" approach) or by using the square root of the sum of the squares of the successive errors ("most probable error" approach). We obtain:

- Final absolute error on the static pressure: $\Delta p_s = 0.6$ hPa.
- Final absolute error on the Pitot differential pressure reading: $\Delta(p_t - p_s) = 0.022$ hPa (most probable).
- Final absolute error on the Pitot pressure: $\Delta p_t = 0.6$ hPa (most probable).

| Component | Quoted uncertainty | Absolute error |
|---|---|---|
| Plasmatron transducer DI200 | 0.3 % on 200 hPa | 0.6 hPa |
| Validyne pressure transducer | 0.25 % on 86 mm $H_2O$ | 0.021 hPa |
| Betz micro-manometer | 0.02 mm $H_2O$ | 0.002 hPa |
| Pen plotter | 0.3 % on 1 V (10 inches) | 0.003 hPa |
| Reading accuracy | 0.05 inches | 0.005 hPa |

*Table 1. Uncertainty of the Pitot probe measurement chain*

## 2.3 The heat flux probe

### 2.3.1 Working principle

The heat flux measurement is carried out by heat balance between power inflow from the plasma and power outflow through the cooling water:

$$q\,S = \dot{m}\,c_p\,(T_{out} - T_{in}) \qquad (1)$$

In this equation, the left side represents power brought from the plasma jet into the probe, with $q$ the stagnation-point convection heat flux rate (unknown) and $S$ the area of the sensing element. The right side represents power evacuated by the cooling circuit of the probe, with $\dot{m}$ the mass flow rate of the water and $c_p$ its specific heat. $T_{in}$ and $T_{out}$ are the water temperatures at respectively the inlet and outlet of the sensing element.

### 2.3.2 Description

The heat flux probe has been specifically designed at VKI [3]. Its concept is shown on figure 15. The probe is shaped exactly as the standard TPS sample holder of the European Space Agency, so that the stagnation-point velocity gradient at the edge of the boundary layer can be the same in both cases (hence, there is no change

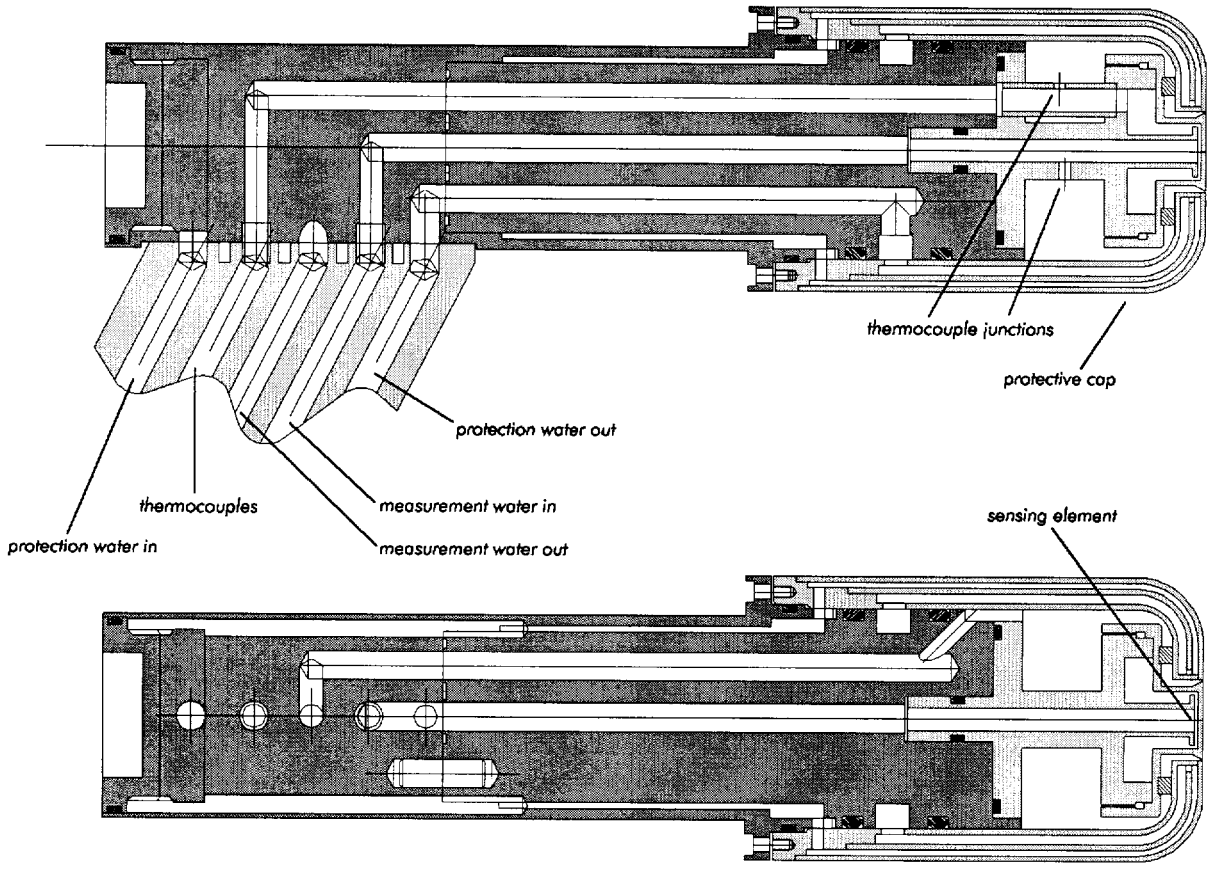


*Figure 15. Conceptual drawing of the heat flux probe*

in heat flux due to the geometry). The front part of the probe is made of copper, which is a highly catalytic material and is used as a reference material in many facilities. The sensing element is 14 mm in diameter. Cold water flows against its inner wall, coming from the probe centreline. A thermocouple junction is inserted to measure $T_{in}$ close to the sensing element. Water flows radially outwards and is mixed in the collector before flowing back into the stem. Another thermocouple junction is inserted after the collector to measure $T_{out}$.

The external shape of the probe is obtained by the protective cap, in which cold water is also flowing to avoid damage by the plasma flow. This protective cooling water circuit is completely separated from the measurement circuit (the water is taken from the Plasmatron cooling system at 10 bar and 10 l/min). The external wall of the cap is made of copper as well, in order to avoid changes in wall catalycity around the sensing element (such differences in wall catalytic properties can cause local heat flux overshoots of 10% [4] that perturb the measurements considerably). There is a small gap between the sensing element and the cap, to avoid contact causing heat losses by conduction. As a consequence, the interior space around the sensing element is under the same low pressure than the Plasmatron chamber. This increases the insulation between the sensing element and other parts of the probe.

### 2.3.3 Measurements and accuracy

Figure 16 shows the measurement chain required for the measurement of heat flux rate. The two thermocouple junctions measuring the temperature difference are part of the same thermocouple. The signal then directly gives a measure of the temperature difference ($T_{out} - T_{in}$). Besides a greater accuracy (it eliminates the need of calculating a small difference between two large quantities), doing so also removes the need of compensating wires.

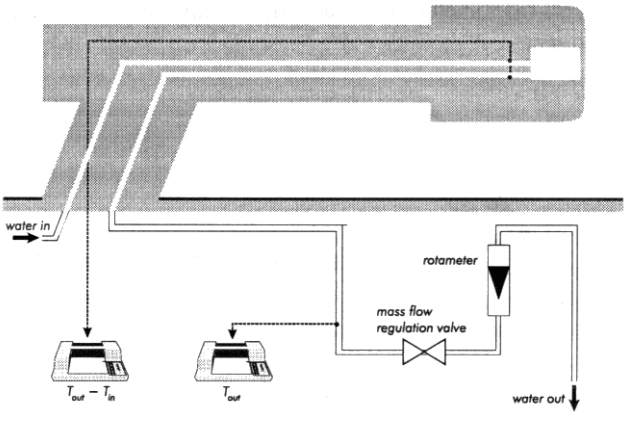


*Figure 16. Heat flux measurement set-up (schematic drawing)*

Another thermocouple is installed to measure the water temperature in the measurement circuit at the exit of the probe, where the mass flow rate has to be measured. A rotameter is used to measure the mass flow rate, which can be adjusted manually by a regulating valve (changing the amount of mass flow changes the temperature difference at a given heat flux rate). Both temperature records are made using a pen plotter. The mass flow determination from the rotameter float height involves reading the calibration curves provided by the manufacturer. In order to obtain reduced processing times, a small computer program was written to interpolate the calibration curves automatically, in such a way that no additional error is performed.

From (1) it is seen that the accuracy depends on the mass flow measurement, temperature difference measurement and sensing element area (neglecting uncertainties on the water $c_p$). The uncertainties associated with the individual elements of the measurement chain are given by table 2 and can be combined using classical error analysis, to give a highest error of:

$$\frac{\Delta q}{q} = \frac{\Delta S}{S} + \frac{\Delta (T_{out} - T_{in})}{T_{out} - T_{in}} + \frac{\Delta c_p}{c_p} + \frac{\Delta \dot{m}}{\dot{m}} \qquad (2)$$

and a most probable error of:

$$\frac{\Delta q}{q} = \left[ \left(\frac{\Delta S}{S}\right)^2 + \left(\frac{\Delta (T_{out} - T_{in})}{T_{out} - T_{in}}\right)^2 + \left(\frac{\Delta c_p}{c_p}\right)^2 + \left(\frac{\Delta \dot{m}}{\dot{m}}\right)^2 \right]^{1/2} \qquad (3)$$

The value of heat flux involves many variables and a value of uncertainty cannot be obtained in such a straightforward way as was done in the Pitot probe case. In particular, the measurements of temperature and mass flow rate are related: if the mass flow rate increases, the temperature difference decreases, and so the error on the former decreases but the error on the latter increases.

More in-depth error analysis requires to examine the actual operating conditions of the heat flux probe in the plasma flow. As is shown by figure 17, pen plotter recordings of the temperature show high-frequency oscillations. When the mass flow is too small (e.g. 60 mm float height – 4.3 g/s ), the oscillations are big. They first decrease with increasing mass flow (e.g. 70 mm, 5.4 g/s) then increase again (not shown). In the example, the oscillations at 70 mm and 80 mm (6.4 g/s) are comparable in amplitude, but the mean signal was steadier at 70 mm. Of course, as the mass flow rate increases, the temperature difference decreases, so the height of 70 mm was chosen, except when the heat flux was too high, in which case the mass flow was increased.

This behaviour could be interpreted as follows: at low mass flow, the flow is laminar; as it increases, the flow can get turbulent in the sensing element of the probe, causing greater oscillations in the output traces. Consequently, increasing the mass flow causes an increase in signal noise. The decrease in signal noise which is first observed when the mass flow is increased can indicate that, when the mass flow is too low, the convection coefficient is not high enough to prevent local boiling of the water. The bubbles will cause signal noise when passing over the thermocouple.

| Component | Quoted uncertainty | Absolute error |
|---|---|---|
| Rotameter | 1.6 % full scale | 0.37 $10^{-3}$ kg/s |
| Sensing element area | 1/10 mm on diameter | 8.83 $10^{-6}$ $m^2$ |
| Water specific heat | 0.1 J/(kg K) | 0.1 J/(kg K) |
| Thermocouple coefficient | 1 % | 0.25 K |
| Pen plotter ($\Delta T$) | 0.3 % on 1 V (10 inches) | 0.075 K |
| Pen plotter ($T$) | 0.3 % on 1 V (10 inches) | 0.15 K |
| Reading accuracy ($\Delta T$) | 0.05 inches | 0.125 K |
| Reading accuracy ($T$) | 0.05 inches | 0.25 K |

*Table 2. Uncertainty of the heat flux probe measurement chain.*

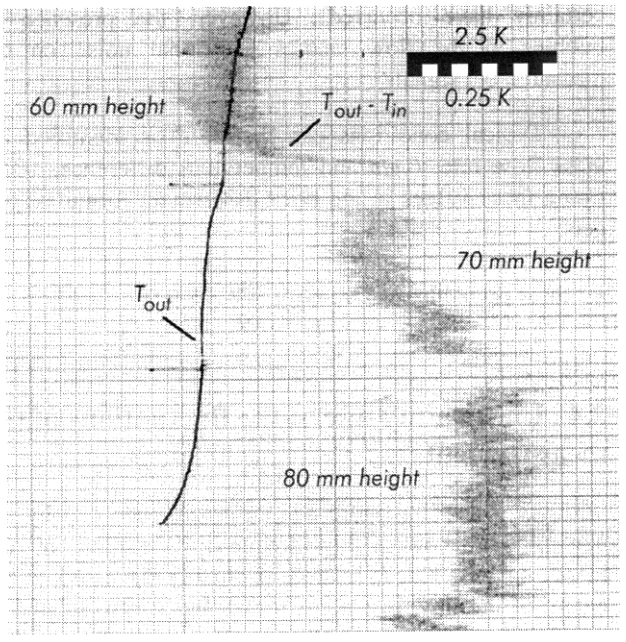


*Figure 17. Typical traces recorded when the heat flux probe is in the plasma jet*

The probe study that was performed[1] [3] has allowed to obtain a relationship between the mass flow rate in the probe and the heat flux rate:

[1] Numerical simulation of the flow inside the sensing element have been performed to obtain the Nusselt-Reynolds relationship for the particular geometry.

$$\dot{m} = \frac{\pi \mu_{in} D_{in}}{4} \left( \frac{\frac{q D_{in}}{\lambda_{wall} (T_{wall} - T_{in})} - 5.848}{2.047 \left( \frac{\mu_{wall}}{\mu_{in}} \right)^{0.1}} \right)^2 \quad (4)$$

with $\lambda_{wall}$ the wall thermal conductivity. Based on a wall temperature equal to the boiling point at 10 bar (440 K), the minimum mass flow rate necessary to avoid boiling is obtained. In the range of the Plasmatron original specifications, i.e. heat flux values up to 1200 kW/m$^2$, the minimal mass flow rate was compatible with values yielding significant temperature differences (about 15 K at 1200 kW/m$^2$). As the next chapter will show, the Plasmatron performances quite exceed the original specifications. Because the necessary mass flow rate varies with the square of the heat flux, the mean temperature increase $(T_{out} - T_{in})$ varies as the inverse of the heat flux and drops down to values much too small to be of practical use. For this reason, the probe was used with lower mass flow rates, corresponding to risks of boiling in the probe. It is known that a small amount of boiling causes *nucleated boiling*, a condition that increases the local convective heat transfer coefficient. Apparently, up to the maximal measured heat flux of 3.5 MW/m$^2$, the DNB point[2] has never been reached in the performed experiments (if not, damage to the probe would certainly have occurred). However, the presence of bubbles in the flow creates additional noise on the measurement signals.

Typical conditions can therefore be identified as: mass flow rate, 6 g/s and temperature difference, 10 K. Using these values in the error assessment formulas, one gets:

- most probable relative error: $\frac{\Delta q}{q} = 8.9\ \%$

## 2.4 Uncertainty due to the fluctuations of the measurements

As shown by figure 17, the traces recorded by the pen plotter show a high-frequency variation of the measurements. This is related, as already discussed, to the nature of the flow inside the probe, but is also related to the fluctuations of the facility operating conditions. The uncertainty of the measurements must take this phenomenon into account. In order to do so, the standard uncertainty assessment procedure used at VKI (Kline & McClintock, [5] ) has been applied.

Pen-plotter records of a heat flux traverse have been used. The mean value of the heat flux has been recorded at each 1 mm interval, by locating the minimal and maximal value of the high-frequency temperature variations around the sampled time position, and taking the middle value of the interval. This has been converted to heat flux. The reference heat flux value has then been taken as the mean value of all the means. An uncertainty band of ± 4.07% can be obtained for the bulk of the measurements (20 to 1 odds). Combining this uncertainty with the instrumental error of the heat flux measurements, one finally obtains a most probable relative error of 9.8 % (20 to 1) on the heat flux.

The same kind of studies have also been made for the Pitot probe. The uncertainty band is found to be 2.05 Pa (20:1). This uncertainty band can be coupled with the instrumental uncertainty determined above, to yield final values of the uncertainty:

- Most probable absolute error on the Pitot pressure reading: $\Delta(p_t - p_s) = 0.03$ hPa (20 to 1).
- Most probable absolute error on the Pitot pressure: $\Delta p_t = 0.6$ hPa (20 to 1).

## 2.5 Correctness of heat flux measurements

The heat flux probe yields a measurement of the heat flux received at the stagnation point, with an accuracy of about 10% based on the errors and uncertainties of the measurement chain. However, the question of the correctness of this result remains to be addressed. In other terms, how accurate is the measurement with respect to the real heat flux yielded by the flow?

### 2.5.1 Heat flux balance on the probe

The principle of the heat flux probe relies on a steady-state equilibrium of heat fluxes at the stagnation point: the probe is subject to the convective heat flux $q_f$ from the flow, which can be split into the radiated heat flux $q_r$ from the probe surface, the transmitted heat flux $q_c$ conducted through the probe wall and the conduction losses $q_l$ to the probe sides. The measured heat flux corresponds to $q_c$, and hence has a value equal to:

$$q_c = q_f - q_r - q_l \quad (5)$$

The radiated heat flux is that of a black body surface at a temperature which cannot exceed the boiling point of water at 10 bars, i.e. 440 K. Hence, one obtains:

$$q_{r,max} = \sigma T^4 = 2125.4 \text{ W/m}^2 \quad (6)$$

The radiated heat flux is equal to 0.6% of the minimal heat flux requirement of 350 kW/m$^2$. Hence, the radiated heat flux is negligible.

[2] *Departure from Nucleated Boiling*, when the gas phase settles in a film flowing close to the wall, forming an insulation layer that causes a severe drop in the heat transfer coefficient (a condition known as *film boiling*).

The lateral conduction losses in the probe are much limited by the gap which lies between the sensing element and the protective cap. This gap creates a layer of low-pressure air which acts as an insulator with respect to lateral heat flux losses.

Another source of conduction losses would be heat travelling in the outer walls of the sensing element. However, the mechanical design of the sensing element is such that these walls are in contact with the cooling water over several diameters before the outlet temperature is measured (figure 15). Therefore, it can be safely assumed that all the incoming heat flux has been absorbed by the water before the temperature measurement is made.

### 2.5.2 Outlet temperature measurement

Another source of error can come from the outlet temperature measurement in the sensing element. Indeed, numerical simulations of the first design [3] had shown that there was a significant temperature gradient at the thermocouple junction, meaning that the measured outlet temperature could be different than the mean outlet flow temperature. The design has been accordingly modified to include a mixing chamber before the outlet flow passes in the measurement region, in order to reduce this source of error to maximum extent.

# 3. Data reduction procedure

## 3.1 Thermodynamic and transport properties model

In the temperature and pressure range of ICP torches (i.e. $T < 15\,000$ K and $p < 1$ atm), air dissociates and ionises, giving rise to a mixture of chemically-reacting thermally perfect gases which can be accurately described by the 13-species model ($O_2$, O, $O^+$, $O_2^+$, $N_2$, N, $N^+$, $N_2^+$, NO, $NO^+$, Ar, $Ar^+$, $e^-$) [6]. Bottin, Vanden Abeele and Barbante have developed an efficient computer library called *PEGASE*, used to compute thermodynamic and transport properties of arbitrary mixtures [7]. As indicated by figure 18, it is made of three modules which can be individually called from any CFD application that requires it, such as the program performing the data reduction procedure described in the present notes.

The thermodynamic module computes the thermodynamic properties of individual species using the statistical thermodynamics relations for atoms and harmonic or anharmonic oscillator diatomic molecules. It computes the equilibrium composition of the mixture using the law of mass action, through an efficient algorithm solving the system in a partly analytical, partly numerical (Newton) approach. The mixture properties are obtained from the species properties and the composition.

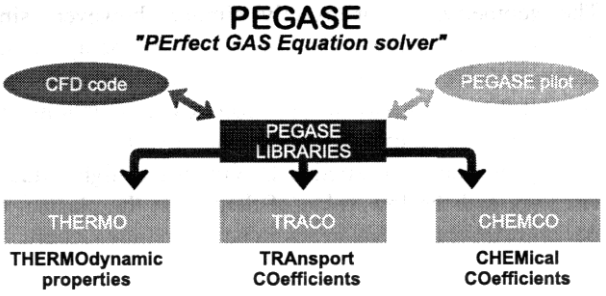


*Figure 18. Constituents of the thermodynamic model* PEGASE

The transport properties module uses the kinetic theory of gases to compute viscosity, thermal conductivity and diffusion in the mixture. It relies on recent values of collision integrals data and includes second-order treatment of the electron properties and rigorous computation of both the ambipolar diffusion and the reactive thermal conductivity through the Stefan-Maxwell equations.

The chemical kinetics module produces the source terms arising from the finite-rate chemistry air models available in the literature. It is not used in the present data reduction procedure, since we are assuming local thermodynamic equilibrium.

## 3.2 Low-Reynolds correction to the measured Pitot pressure (Barker effect)

At very low Reynolds numbers, it is no longer possible to ignore the effects of viscosity. The radial velocity gradient close to the stagnation point causes momentum to be transferred to the stagnation streamline from the neighbouring streamlines. This leads to an increase of total pressure in the stagnation point with respect to the ideal, isentropic deceleration case. This effect[3] appears for Reynolds numbers lower than 1000, based on the external Pitot tube diameter, but only becomes significant under $Re = 100$. The increase of Pitot pressure is usually expressed as a function of the dynamic pressure of the flow:

$$C_p = \frac{p_{Pitot} - p}{\frac{1}{2}\rho U^2} \tag{7}$$

This pressure coefficient depends of the Pitot tube shape, as clearly shown on figure 19, taken from [8]. All Pitot probes used by the various researchers had a cylindrical geometry with a flat end facing the flow. Only Pitot tube B had a round nose and yields data of interest for the present probe.

[3] Named according to its discoverer, M. Barker (1922).

The geometry is not exactly similar, however, since Sherman used source-shaped probes but no hemispherical probes [9]. Nevertheless, he obtained results which could be well fitted with Homann's theoretical calculations [10] for a sphere. The expression obtained by Homann almost exactly fits the data labelled B. Given the high value of viscosity and the low value of density in the plasma, the Barker effect obviously needs to be taken into account.

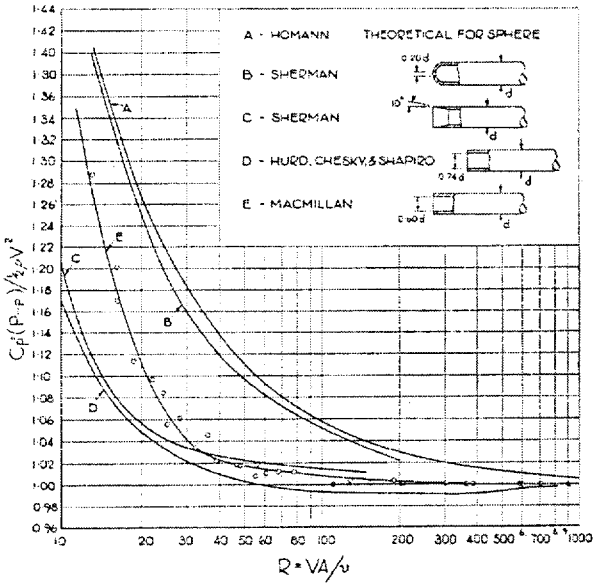


*Figure 19. Pitot pressure correction for Barker effect as a function of Reynolds number and Pitot probe shape (from [8] - A = tube external diameter)*

Homann's computation yields the following correction term for incompressible Barker effect:

$$p_t = p_{Pitot} - \frac{1}{2}\rho U^2 \left[ C_p(Re) - 1 \right] \qquad (8)$$

with

$$C_p = 1 + \frac{6}{Re + 0.455\, Re^{1/2}} \qquad (9)$$

where the Reynolds number is expressed in terms of the probe nose radius $R$:

$$Re = \frac{\rho u R}{\mu} \qquad (10)$$

We cannot be sure that this relation holds true even for low-velocity plasmas, because of the density variation due to temperature. However, it is the only existing relation that we found in the literature and which offers a sound theoretical basis. More in-depth studies of the Barker effect in plasma flows may be necessary to improve the correction.

## 3.3 Exact computation of the stagnation point heat transfer

### 3.3.1 Introduction

The exact solution of the stagnation-point heat transfer on the heat flux probe can be obtained through the numerical integration of the compressible axisymmetric boundary layer equations for chemically-reacting gas mixtures. It is important, for such problems, to understand the effect that wall catalycity can have on the solution.

Figure 20 shows the difference between a non-catalytic and a fully catalytic surface. In the former case, the speed with which dissociated species recombine at the surface (noted $k$, catalytic recombination speed) is zero. Consequently, there is no reaction taking place on the surface. In the latter case, that speed tends to infinity and the dissociated species will recombine at the surface. In so doing, they free up their formation energy, which goes into the wall. Thus, as wall catalycity increases, the conductive heat transfer is increased too, and so is the equilibrium surface temperature.

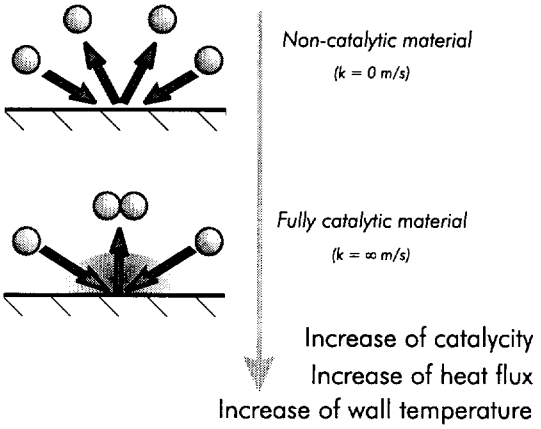


*Figure 20. Effect of surface catalycity on heat flux*

### 3.3.2 The limiting solutions: equilibrium and frozen boundary layers

Three limiting solutions can be of interest. The frozen boundary layer on a non-catalytic wall is the simplest problem to treat, since no chemical reactions take place in the boundary layer or on the wall surface. However, the copper heat flux probe has a surface which is much closer to full catalycity than to no catalycity. Therefore, the case of a catalytic wall must be considered.

A catalytic wall imposes recombination of ions and atoms in the vicinity of the wall. Hence, in a frozen boundary layer on a catalytic wall, there is no chemistry source term in the flow, but there are chemical reactions near the wall and the species concentration varies across

the boundary layer, reaching a steady-state distribution in accordance to diffusion effects due to concentration gradients. In the equilibrium boundary layer case, the chemical composition is imposed by the temperature and pressure profile across the boundary layer. In that limiting solution, the wall catalycity does not play any role. Diffusion effects are negligible in the boundary layer but not near the wall, since diffusion of chemical energy adds to the heat flux just like in the case of the frozen boundary layer with catalytic wall. However, this effect can be taken into account by means of the equilibrium thermal conductivity. Under this hypothesis, one simply writes:

$$\vec{q} = -\lambda_{equ}\, \vec{\text{grad}}\, T \qquad (6.11)$$

At this point, we should note that there is not much difference in species concentration near the wall between an equilibrium boundary layer and a frozen boundary layer with a fully catalytic wall. The values of heat flux in both cases will then be almost identical [11]. The simplifying assumption of an equilibrium boundary layer then seems reasonable for the purpose of the calculation.

### 3.3.3 Governing equations

The governing equations of the axisymmetric, compressible equilibrium boundary layer equations are written as follows [12]:

$$\frac{\partial \rho u R}{\partial x} + \frac{\partial \rho v R}{\partial z} = 0 \qquad (12)$$

$$\rho u \frac{\partial u}{\partial x} + \rho v \frac{\partial u}{\partial z} = -\frac{\partial p_e}{\partial x} + \frac{\partial}{\partial z}\left(\mu \frac{\partial u}{\partial z}\right) \qquad (13)$$

$$\rho u \frac{\partial h}{\partial x} + \rho v \frac{\partial h}{\partial z} = u \frac{\partial p_e}{\partial x} + \mu \left(\frac{\partial u}{\partial z}\right)^2 + \frac{\partial}{\partial z}\left(\lambda_{eq} \frac{\partial T}{\partial z}\right) \qquad (14)$$

### 3.3.4 Change of variables

A combination of the Mangler transformation[4] and Howarth, Illingworth, Stewartson transformations[5] are used, in which the outer edge of the boundary layer is used as reference condition [13], unlike Fay and Riddell's choice of wall conditions. The Levy-Lees change of variables is given by [14]:

$$\xi(x) = \int_0^x \rho_e \mu_e u_e R^2 \, dx' \qquad (15)$$

$$\eta(x, z) = \frac{R u_e}{\sqrt{2\xi}} \int_0^z \rho \, dz' \qquad (16)$$

[4] Transforming axisymmetric to equivalent 2D boundary layer equations.

[5] Transforming compressible to equivalent incompressible boundary layer equations.

and the new functions $f$, $g$ and $V$ are introduced such as:

$$f' = \frac{\partial f}{\partial \eta} = \frac{u}{u_e} \qquad (17)$$

$$g = \frac{T}{T_e} \qquad (18)$$

$$V = \frac{2\xi}{\left(\frac{\partial \xi}{\partial x}\right)}\left(f' \frac{\partial \eta}{\partial x} + \frac{\rho v R}{\sqrt{2\xi}}\right) \qquad (19)$$

It can be easily verified that all variables and functions are non-dimensional. The function $V$ is introduced in order to reduce the order of the equations. If it was not done, terms proportional to the third derivative of $f$ would appear in the equations.

### 3.3.5 Non-dimensional equations

Using the Levy-Lees transformation outlined above and performing the necessary substitution and algebra, the following equations are obtained for the stagnation-point solution:

$$\frac{\partial V}{\partial \eta} + f' = 0 \qquad (20)$$

$$V \frac{\partial f'}{\partial \eta} = \frac{1}{2}\left(\frac{\rho_e}{\rho} - (f')^2\right) + \frac{\partial}{\partial \eta}\left(\chi \frac{\partial f'}{\partial \eta}\right) \qquad (21)$$

$$V \frac{\partial g}{\partial \eta} = \frac{1}{C}\frac{\partial}{\partial \eta}\left(\frac{\chi C}{Pr}\frac{\partial g}{\partial \eta}\right) - \frac{E}{C}\left[\frac{\rho_e f'}{2\rho} - \chi\left(\frac{\partial f'}{\partial \eta}\right)^2\right] \qquad (22)$$

The following non-dimensional symbols have been introduced, with $c_p$ and $\lambda$ taken as *equilibrium* values:

$$\chi = \frac{\rho \mu}{\rho_e \mu_e} \qquad (23)$$

$$C = \left(\frac{c_p}{c_{p,e}}\right) \qquad (24)$$

$$E = \frac{u^2}{c_{p,e} T_e} \qquad (25)$$

$$Pr = \frac{\mu c_p}{\lambda} \qquad (26)$$

The equations can be simplified to self-similar form (i.e. dependent on $\eta$ only) because, by definition of the stagnation point, $\xi = 0$. This alone does not guarantee that all terms function of $\xi$ vanish, however. In addition, the derivatives of $u_e$ and $T_e$ at the stagnation point can be shown to have the following limiting values:

$$\lim_{\xi \to 0} \left( \frac{2\,\xi}{u_e} \frac{\partial u_e}{\partial \xi} \right) = \frac{1}{2} \tag{27}$$

$$\lim_{\xi \to 0} \left( \frac{2\,\xi}{T_e} \frac{\partial T_e}{\partial \xi} \right) = 0 \tag{28}$$

### 3.3.6 Boundary conditions

The following boundary conditions for the transformed variables are used:

(wall, $\eta = 0$) $\quad f' = 0$ (29)

(wall, $\eta = 0$) $\quad g = \frac{T_w}{T_e}$ (30)

(outer edge, $\eta \to \infty$) $\quad f' = 1$ (31)

(outer edge, $\eta \to \infty$) $\quad g = 1$ (32)

### 3.3.7 Resolution scheme

The above system of equations is solved in a loosely coupled manner. Supposing that $f'$ is given, the continuity equation (20) can be integrated in a straightforward way along the $\eta$ co-ordinate. A uniform spacing has been chosen for the discretisation in $\eta$ so that Simpson's rule can be used in the integration.

Supposing $V$ known, the momentum (21) and energy (22) equations can then be solved. These equations are non-linear, but they can be cast in a general pseudo-linear form:

$$a\,y'' + b\,y' + c = 0 \tag{33}$$

with, for the momentum equation ($y = f'$):

$$a = \chi \tag{34}$$

$$b = \frac{\partial \chi}{\partial \eta} - V \tag{35}$$

$$c = \frac{1}{2}\left( \frac{\rho_e}{\rho} - f'^2 \right) \tag{36}$$

and for the energy equation ($y = g$):

$$a = \chi / Pr \tag{37}$$

$$b = \frac{1}{C}\frac{\partial}{\partial \eta}\left( \frac{\chi C}{Pr} \right) - V \tag{38}$$

$$c = \frac{E}{C}\left( \frac{\rho_e f'}{2\,\rho} - \chi \left( \frac{\partial f'}{\partial \eta} \right)^2 \right) \tag{39}$$

The coefficients $a$, $b$ and $c$ are function of $f$ and $g$, but for the sake of solving the equations will be considered constants, computed using the results of the previous iteration. The derivatives are replaced by 4th-order central finite differences[6] [15] and the value of the unknown functions are obtained at each discretised point along the $\eta$ co-ordinate by solving the resulting linear system.

The solution method differs from what was outlined above for the sake of numerical efficiency [13]. The unknowns are actually replaced by 4th-order Lagrange polynomials of which the coefficients are computed so that the polynomial matches the exact solution of the differential equations in several arbitrary points [16].

### 3.3.8 Computation of heat flux rate

Based on the definition (11) of the heat flux rate and the transformation of the equations in non-dimensional space, the magnitude of the heat flux rate is simply given by:

$$q = \sqrt{\frac{2\,\beta}{\rho_e\,\mu_e}}\, T_e\, \rho_w\, \lambda_w\, g'_w \tag{40}$$

The value of the derivative $g'_w$ at the wall comes from the boundary layer computation. The outer edge parameters come in the picture from the Levy-Lees transformation.

### 3.3.9 Stagnation-point velocity gradient

For the typical geometry of the ESA sample holder, idealised by a cylinder of radius $R_m$ with a flat face placed perpendicularly to the flow, it is not possible to obtain an expression for the velocity gradient based on theory alone. Kolesnikov [17] proposed the following relation, based on computations and experimental observations:

$$\frac{\beta\,R_m}{U_e} = \frac{1}{2 - \zeta - 1.68\,(\zeta - 1)^2 - 1.28\,(\zeta - 1)^3} \qquad (\zeta \le 1) \tag{41}$$

$$\frac{\beta\,R_m}{U_e} = \zeta \qquad (\zeta > 1) \tag{42}$$

with $\zeta = R_m / R_j$, $R_j$ being the plasma jet radius.

For other, simpler geometries, like the cylinder or sphere, potential flow results can be used to provide a reasonably accurate value of the stagnation-point velocity-gradient in inviscid flow.

---

[6] Forward and backwards 4th-order finite differences are used on the sides of the discretised space, where a central formula cannot be applied.

## 3.4 Relating flow properties to experimental measurements

### 3.4.1 Principle of the method

Let us suppose that the models described above are available to compute the stagnation-point heat flux rate $q$ and the stagnation pressure on the Pitot tube $p_{Pitot}$. The flow properties in which we are interested are the pressure $p$, density $\rho$, temperature $T$ and velocity $u$, from which all other flow properties can be computed. Since the measurements are performed in a subsonic plasma jet, the static pressure in the jet is constant and equal to the test chamber pressure. Then, only temperature is required before the chemical composition can be computed. The computation of the heat flux rate requires a knowledge of the equivalent outer flow values on the probe, i.e. the total pressure and temperature, to serve as boundary conditions:

$$q = q\,(p_t,\, T_t,\, u) \tag{43}$$

If the full exact solution of the boundary layer equations cannot be implemented or for first analysis, the stagnation-point heat transfer formula of Fay and Riddell for the equilibrium boundary layer [11] can be used. It yields a heat flux accurate within 10%:

$$q = 0.76\, Pr_w^{-0.6}\, (\rho_e\, \mu_e)^{0.4}\, (\rho_w\, \mu_w)^{0.1} \sqrt{\beta}\, (H_t - h_w) \times \left(1 + (Le - 1)\frac{h_D}{H_t - h_w}\right)^{0.48} \tag{44}$$

### 3.4.2 Set of equations without correction for the Barker effect

In this case, the Pitot probe is supposed to exactly measure the total pressure of the flow. The probe measurements thus provide values of total pressure $p_t°$ and heat flux $q°$. The static pressure $p°$ in the chamber is known. Then, the following system of three equations can be written, expressed in three unknowns $T_t$, $T$ and $u$ which yield the aerothermodynamic state of the gas ahead of the probe:

$$\begin{cases} q\,(p_t°,\, T_t,\, u) - q° = 0 \\ H_t\,(p_t°,\, T_t) - [h\,(p°,\, T) + 0.5\, u^2] = 0 \\ S_t\,(p_t°,\, T_t) - s\,(p°,\, T) = 0 \end{cases} \tag{45}$$

This system can be solved using a Newton-Raphson iterative procedure.

### 3.4.3 Set of equations with correction for the Barker effect

The above system supposes that the total and stagnation pressures are equivalent, a hypothesis which is probably hardly verified in practice. If the low-Reynolds correction to Pitot pressure (known as the "Barker effect") has to be included, then the total pressure becomes an additional unknown [18]. Hence, (45) must be transformed into a system with four unknowns by way of the total pressure correction defined in terms of a coefficient $C_p$, function of the Reynolds number, which is itself a function of pressure, temperature and velocity:

$$\begin{cases} q\,(p_t,\, T_t,\, u) - q° = 0 \\ H_t\,(p_t,\, T_t) - [h\,(p°,\, T) + 0.5\, u^2] = 0 \\ S_t\,(p_t,\, T_t) - s\,(p°,\, T) = 0 \\ p_{Pitot} - p°_{Pitot} = 0 \end{cases} \tag{46}$$

with

$$p_{Pitot} = p_t + 0.5\, \rho\,(p°,\, T)\, u^2\, [C_p\,(p°,\, T,\, u) - 1] \tag{47}$$

The final system, solved using the Newton-Raphson procedure, is written out as follows, with the elements of the Jacobian matrix computed, as usual, using numerical finite differences[7]:

$$\begin{pmatrix} 0 & \frac{\partial q}{\partial u} & \frac{\partial q}{\partial T_t} & \frac{\partial q}{\partial p_t} \\ -\frac{\partial h}{\partial T} & -u & \frac{\partial H}{\partial T_t} & \frac{\partial H}{\partial p_t} \\ -\frac{\partial s}{\partial T} & 0 & \frac{\partial S}{\partial T_t} & \frac{\partial S}{\partial p_t} \\ \frac{\partial p_{Pitot}}{\partial T} & \frac{\partial p_{Pitot}}{\partial u} & 0 & \frac{\partial p_{Pitot}}{\partial p_t} \end{pmatrix} \begin{pmatrix} \Delta T \\ \Delta u_t \\ \Delta T_t \\ \Delta p_t \end{pmatrix} = \begin{pmatrix} q° - q\,(p_t,\, T_t,\, u) \\ [h\,(p°,\, T) + 0.5\, u^2] - H_t\,(p_t,\, T_t) \\ s\,(p°,\, T) - S_t\,(p_t,\, T_t) \\ p°_{Pitot} - p_{Pitot} \end{pmatrix} \tag{48}$$

The iterative process is continued until the residuals (right-hand side vector) have reached a sufficiently low value (in our case, $10^{-9}$, usually reached in 10 to 20 iterations – a few cases were tougher to compute, not converging beyond 5 orders of magnitude).

## 3.5 Facility and data reduction charts

The development of the data reduction model using the stagnation-point heat transfer and Pitot probe models allows us to numerically build *performance maps*, i.e. charts that relate the Plasmatron parameters and the flow stagnation properties. Since three boundary conditions are needed to completely determine the conditions of each run, it is impossible to represent the facility performance on a single diagram. One possible choice, which comes naturally, is to freeze the test

[7] There are no practical closed-form explicit analytical expressions for these derivatives, due to the chemistry.

chamber pressure and to represent the facility performance as a function of the two remaining parameters, mass flow rate and power. The sample geometry and temperature must also be defined for the heat flux computation. The heat flux probe geometry (figure 15) has been used with a wall temperature of 400 K. This is about 50 K lower than the boiling point of water at 10 bars, the maximal temperature that the cooling water can reach in the probe. The low values of heat flux are then underestimated because the probe will actually be colder.

Figure 21 (a to e) shows the performance maps at pressures of 15, 25, 75, 125 (the four pressure levels used in the tests) and 175 hPa respectively. The maps are drawn with Mach number and flow temperature as axes. Each figure comes with two maps: the one on the right is used to determine the operating conditions (Mach number and temperature) from the testing conditions (stagnation point heat flux and total pressure). The other on the left is used to determine the values of equivalent mass flow rate (tilted right) and power (tilted left) of the flow.

It should be noted that the power and mass flow rate indicated by the charts above do not correspond to the facility settings, but are computed based on constant flow properties across the jet, as in a quasi-one-dimensional model. The difference is shown on figure22, where it is readily seen that the mean value of any real flow property is lower than the equivalent quasi-one-dimensional value taken for that property.

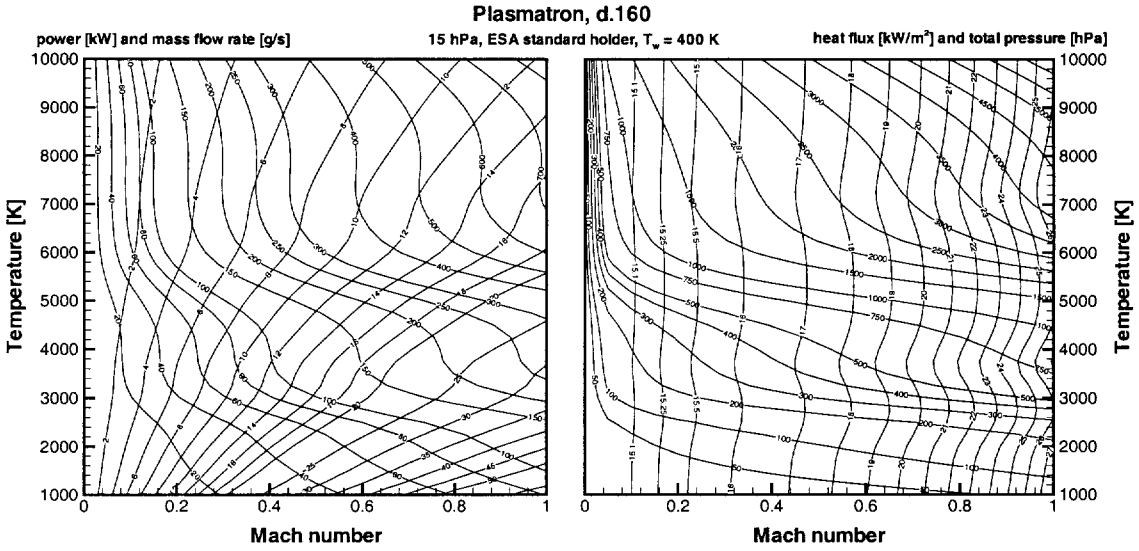


*(a)*

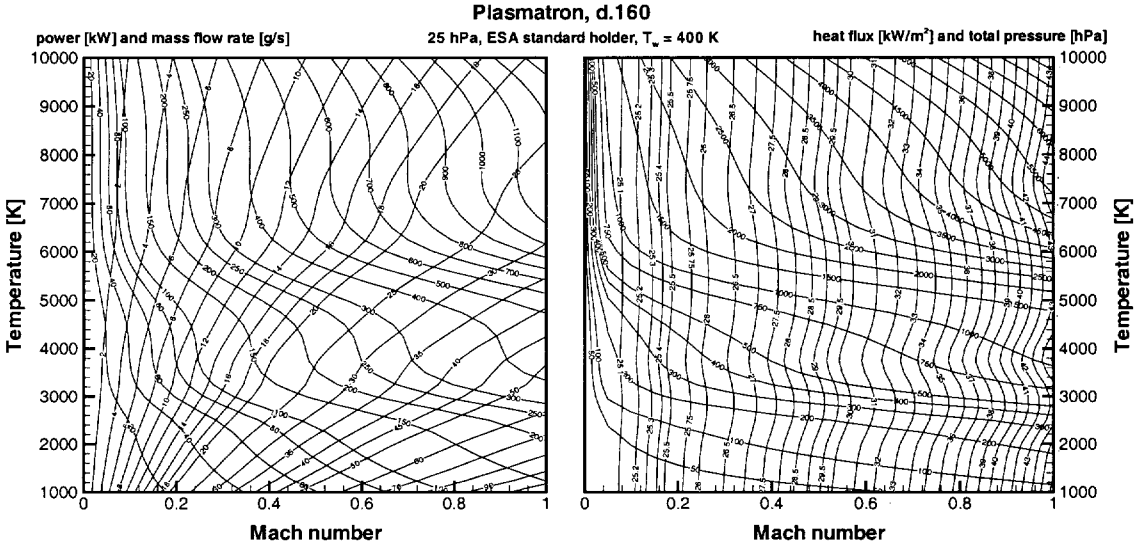


*(b)*

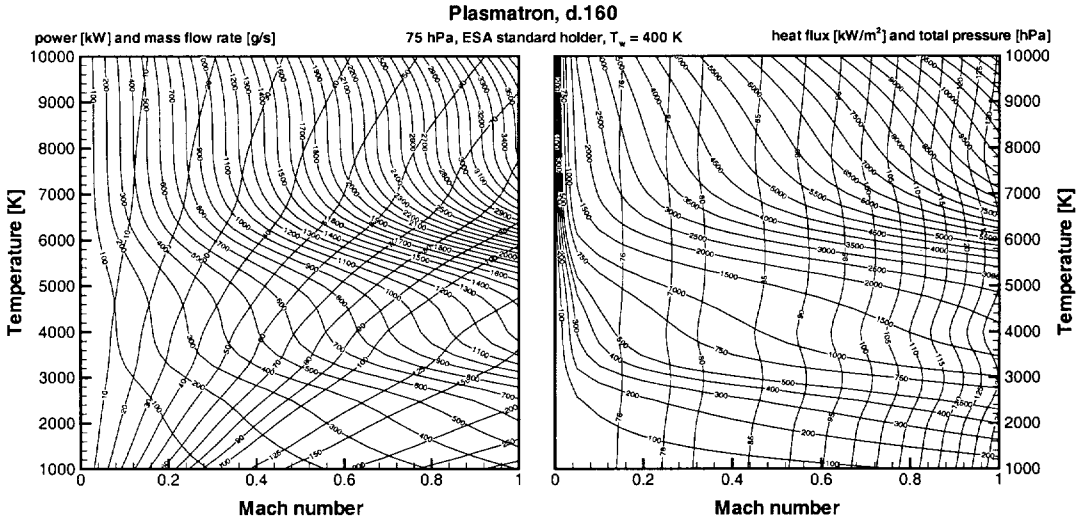


*(c)*

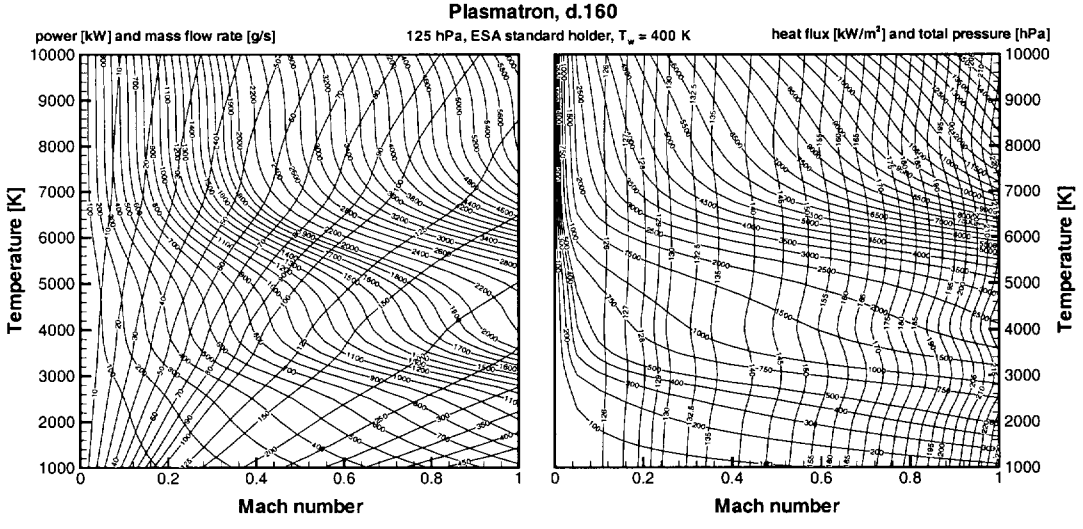


*(d)*

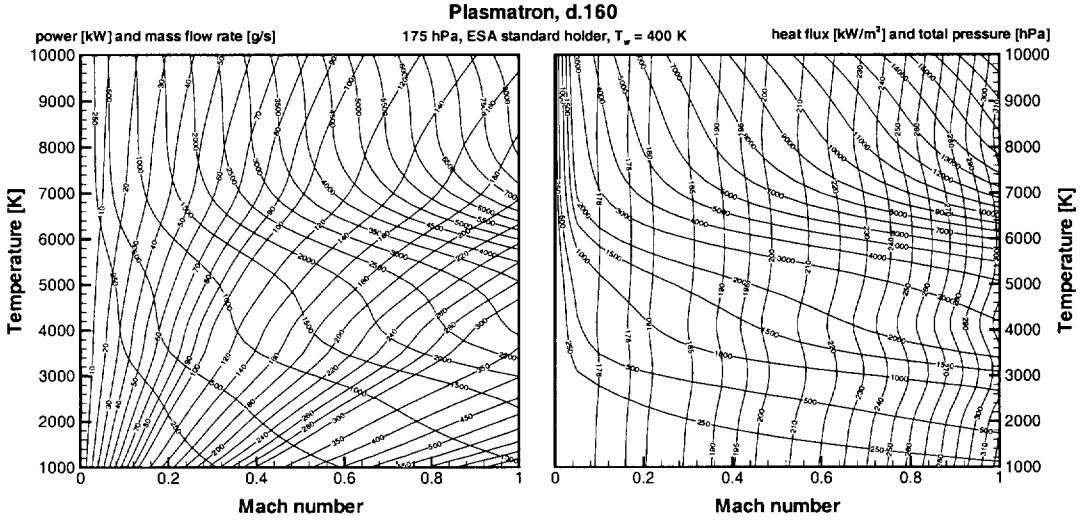


*(e)*

*Figure 21. Plasmatron performance maps at various chamber pressures – 160 mm diameter torch. (a) 15 hPa – (b) 25 hPa – (c) 75 hPa – (d) 125 hPa – (e) 175 hPa*

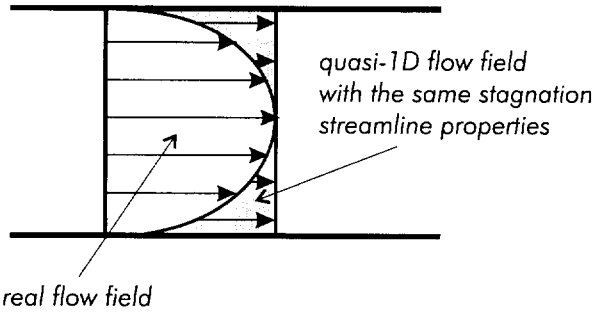


*Figure 22. Difference between the real field and the quasi-1D flow field used in the performance maps*

Detailed calibration of the facility is required to be able to relate the two values one to another. We have shown [18] that it was generally not possible to do so in the Plasmatron facility because the equivalent value for the mass flow rate does not vary according to a simple function of the mean mass flow passing through the facility. However, the charts presented above can still be used to obtain, at a glance, the values of temperature and Mach number on the measurement streamline from the measured values given by the probes.

# 4. Facility performance

## 4.1 Performance tests versus the heat flux versus static pressure diagram

### 4.1.1 Introduction

Global performance measurements were carried out in the scope of the preliminary calibration, as a verification of the compliance of the facility to ESA requirements (as outlined on figure 3. During that first phase, heat flux measurements were carried out at different axial positions with many different facility settings.

### 4.1.2 Axial position of the probes

The test conditions considered in the present work are defined as follows. The Plasmatron SMIM[8] allows only a limited number of measurement positions in the test section. Table 3 shows the nomenclature associated with each position and the distance between the torch exit and the tip of the probe. The heat flux probe or the Pitot probe can be mounted on the SMIM, but only one probe can be used at the same time.

[8] *Side Model Injection Mechanism*, a temporary probe support system that can be fixed on the side portholes. It will be replaced in the future by the MITM, *Model Injection and traversing Mechanism.*

| designation | distance (mm) |
|---|---|
| AA1 | 39 |
| AA2 | 139 |
| AA3 | (189) |
| AC1 | 193 |
| AC2 | 293 |
| AC3 | (343) |
| AR1 | 347 |
| AR2 | 447 |
| AR3 | (497) |

*Table 3. SMIM probe positions at the first porthole (distances between parentheses require additional equipment not manufactured at the time of writing)*

The first measurements were carried out from the second porthole, at 1100 mm from the torch, as a precaution against overheating. Measurements were then taken at more forward positions from the first porthole. Four positions were considered in this work: AR2, AR1, AC1 and AA1 (as defined in table 3). Given the results of the heat flux measurements at AC1, it was decided that testing in the AA1 position, closest to the torch, could not safely be conducted with the present heat flux probe design, and positions closer than AC1 were dropped out of the study.

### 4.1.3 Facility settings

Facility settings used to control the test conditions are generator power, gas mass flow rate and chamber static pressure. For the first series of test, which involved illustrating the performances, a wide combination of the parameters were used. In second and more detailed calibration phase, only 4 pressure levels were considered: 15, 25, 75 and 125 hPa. Power levels were chosen to be 150, 250 and 300 kW, mass flow rate levels 8 and 16 g/s. All their combinations lie in the domain of stability of the 160 mm diameter plasma torch and are easily related one to another by simple ratios, except the condition at 8 g/s and 300 kW, which is out of the domain at low pressure and has therefore not been tested.

### 4.1.4 Results of the first heat flux measurements

The first series of heat flux measurements are summarised on figure 23 in function of static pressure. As it is seen, the original requirements are largely exceeded, as indicated by the high heat flux rates observed in all the pressure range, up to 2.8 $MW/m^2$. This is beneficial to the future use of the facility: not only does it give more flexibility in testing capabilities, but it also ensures that reasonable tests can be carried out on many different re-entry configurations. Indeed, the heat flux measured here are recorded on a fully catalytic surface. Real TPS samples are subject to lower heat fluxes for the same value of stagnation enthalpy. Therefore, they require a testing environment with more

enthalpy for the same value of heat flux. The peak heat flux of 2.8 MW/m$^2$ has been measured at a power setting of 250 kW and at 193 mm from the torch exit. Extrapolating the value to the torch exit, one finds that the peak heat flux close to the torch might be of 3500 kW/m$^2$. Taking into account the power still available, still higher heat fluxes are conceivable.

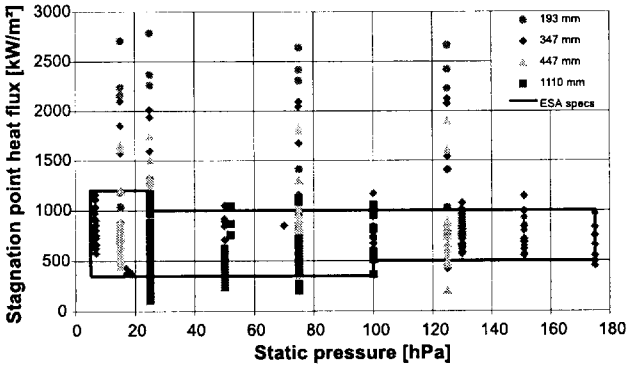


*Figure 23. Heat flux performance of the Plasmatron compared to the original ESA requirements*

## 4.2 Use of Pitot and heat flux traverses as a validation tool

### 4.2.1 Introduction

Although the Pitot and heat flux probes have been designed primarily to record the contractual performance of the facility, they can be used to obtain other data as well. We have performed traverses of Pitot and heat flux across the jet, in order to obtain radial profiles of dynamic pressure and heat flux. Figures 24a and b show photographs of the probes in the 160 mm diameter jet. The pictures clearly show that the blockage of the Pitot probe is relatively small but that the blockage of the heat flux probe is quite important. Therefore, heat flux probe traverses are used only to obtain an order of magnitude confirmation of the jet enthalpy. They cannot yield extremely accurate measurements.

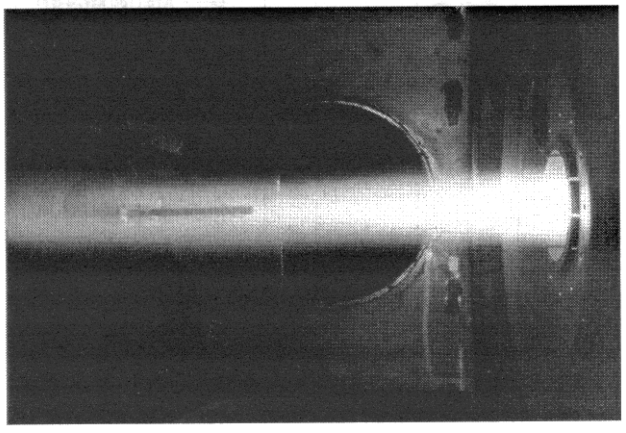

*(a) Pitot probe*

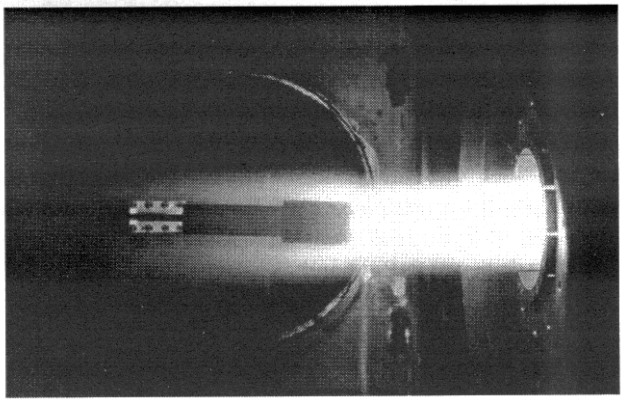

*(b) Heat flux probe*

*Figure 24. Pitot and heat flux probes in the plasma jet*

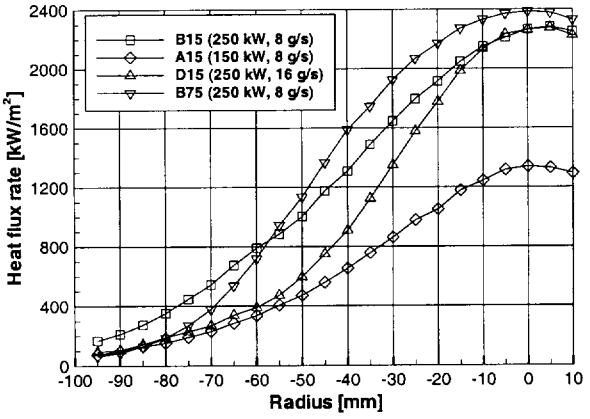


*(a) measured traverses*

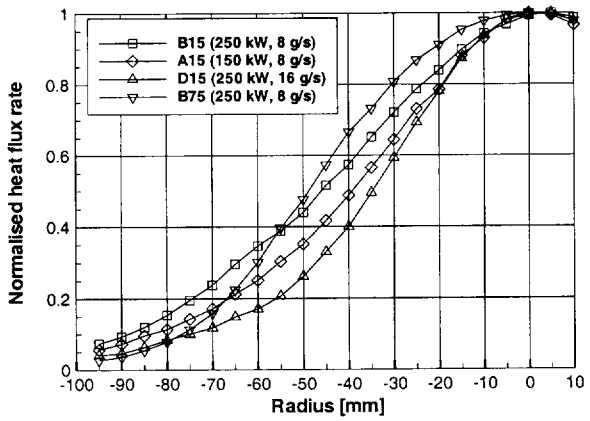


*(b) non-dimensional traverses*

*Figure 25. Heat flux traverses across the plasma jet at position AC1 (193 mm)*

### 4.2.2 Analysis of the traverses regarding two-dimensional flow characteristics

Only four traverses were made in order to observe the effect of each parameter. The reference condition was chosen as B15 (8 g/s, 250 kW, 15 hPa). From there, the three other conditions were obtained by doubling

the mass flow (D15), using 150 kW power (A15) and increasing the pressure to 75 hPa (B75). All traverses have been done at 193 mm from the torch exit. Figure 25 shows the results of the heat flux probe traverses, in dimensional (a) and non-dimensional (b) form. In the latter case, the values have all been divided by the corresponding centreline value. Figure 26 shows the same type of plot for the measured Pitot pressure, i.e. the difference between Pitot and static pressure.

The heat flux traverses confirm the linear dependence of heat flux on power: the A15 peak value has about 0.6 times the value of the B15 peak, and the non-dimensional heat flux curves of A15 and B15, although not superimposed, are closest one to another. The same trend is found for the Pitot reading. This can be understood by expressing the Pitot reading in function of the Mach number (assuming here incompressible flow):

$$p_{Pitot} - p = \frac{\gamma}{2} p M^2 \qquad (49)$$

As total enthalpy increases linearly, so temperature does, and therefore so does $M^2$.

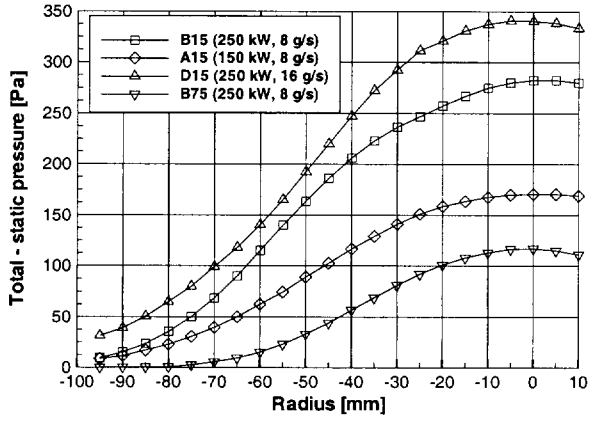


*(a) dimensional traverses*

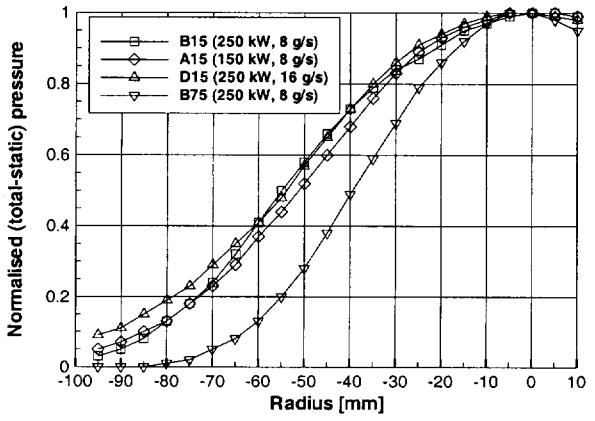


*(b) non-dimensional traverses*

*Figure 26. Traverses of Pitot measurements across the plasma jet at position AC1 (193 mm)*

The effect of increasing pressure creates a more full heat flux profile and a more empty Pitot profile. Increasing the pressure increases the density, therefore at constant mass flow and power the velocity drops accordingly. The jet is also smaller, which partly explains why this profile is not similar to the others.

The effect of doubling the mass flow rate does not even double the Pitot pressure, and more surprisingly it does not affect the heat flux rate on the centreline. A probable explanation for this closeness of the results at 8 and 16 g/s can be drafted as follows: when the mass flow increases at constant power, the total enthalpy should decrease accordingly. However, the inductive heating still requires a high temperature close to the torch centreline, in the coupling region. The relative constancy of total enthalpy on the centreline can therefore be a direct result of this constant high temperature in the torch. Since less total enthalpy is globally available, the heat flux must be lower on the edges if energy is to be conserved

### 4.2.3 Corrections applied to the traverse measurements

The traverses can be processed using the same technique as the one used to process the centreline measurements. This allows to obtain computed traverses of temperature, velocity and total enthalpy. The integration on the jet section of the mass flow and power should yield values close to the mass flow and power used in the torch.

The process is not of extreme quantitative precision, however. If a traverse made in a 160 mm diameter jet by a 12 mm diameter Pitot can still be thought of as reasonable, it is certainly not the case of the heat flux traverses. As said before, the blockage of the probe (50 mm diameter) is such that the displacement effect and the change in stagnation-point velocity gradient become considerable.

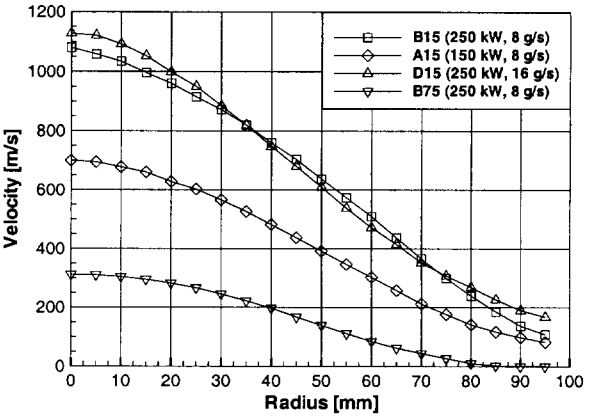


*Figure 27. Computed velocity traverses at position AC1 (193 mm)*

Figure 27 shows the computed velocity traverses and figure 28 the total enthalpy traverses. The latter clearly shows an artefact effect from the size of the heat flux probe: as the heat flux does not go sufficiently down close to the edge of the jet, the total enthalpy is overestimated, even more so as velocity drops down.

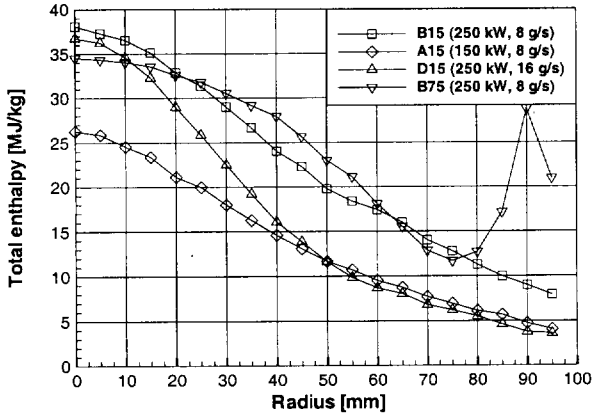


*Figure 28. Computed total enthalpy traverses at position AC1 (193 mm)*

The velocity results show that the traverse has not been carried out to the edge of the jet, as a residual velocity is measured, in some cases of hundreds of meters per second. This could be due to the fact that the jet has opened beyond or to the fact that the high heat flux on the edge automatically gives a significant velocity. Both explanations are equally valid, as figure 26a shows a significant dynamic pressure at the edge in some cases.

The traversing mechanism does not allow to explore radial positions below −95 mm. Hence, a possible correction scheme is to smoothly extrapolate the readings to a reasonable jet edge. Based on a fair extrapolation of the curves, the traverses were extended to −110 mm in the 8 g/s case and −120 mm in the 16 g/s case (see figure 29a for heat flux and b for dynamic pressure).

It is also necessary to apply a displacement effect correction to the measurements, which takes into account the fact that the flow upstream of either probe is non-uniform. The gradient of incoming velocity in the flow has two effects: (1) because the dynamic pressure is proportional to the square of the velocity, its integration over the orifice or sensor does not yield the same value as the exact value in the geometrical centre (this *velocity head correction* is usually negligible with respect to the other effect); (2) the streamlines in front of the Pitot probe and, to a greater extent, in front of the heat flux probe, are deflected towards the region of low velocity, causing the probe to record a higher stagnation pressure or heat flux than the one existing at the probe location. This second effect has been theoretically studied by Lighthill, who proposes the following correction for a Pitot probe [19]:

$$\frac{\delta}{D} = 0.45\,a - 1.35\,a^3 \qquad (50)$$

with $\delta$ the correction to the radial position of the measurement (towards the centre of the jet), $D$ the probe diameter and $a$ a parameter based on the gradient of velocity in the jet, defined as:

$$a = \frac{\Delta u}{\overline{u}} \qquad (51)$$

with $\overline{u}$ the mean velocity of the gradient $\Delta u$. This expression was used to correct both Pitot and heat flux measurements.

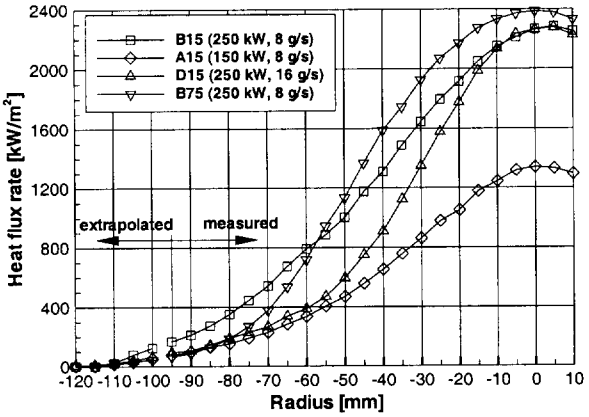


*(a) heat flux probe reading*

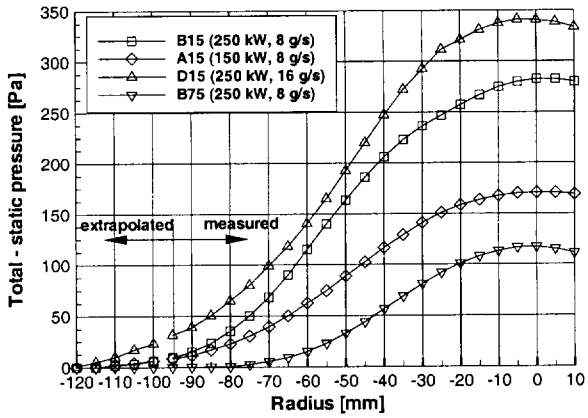


*(b) Pitot probe reading*

*Figure 29. Extrapolated traverses of Pitot pressure and heat flux rate*

### 4.2.4 Integration of the traverses and comparison with facility settings

It is possible to integrate the computed traverses of density, velocity and total enthalpy in order to compute the mass flow rate and the plasma power in the jet, according to:

$$\dot{m} = 2\,\pi \int_0^R \rho(r)\ u(r)\ r\,dr \qquad (52)$$

$$P = 2\,\pi \int_0^R \rho(r)\ u(r)\ H_t(r)\ r\,dr \qquad (53)$$

If these values have to be compared to the mass flow rate and power settings of the facility, the correction for jet entrainment must also be taken into account. The values of mass flow have been corrected using following formula, derived by Schlichting [20] for laminar entrainment, using a mean value of viscosity:

$$\frac{\partial \dot{m}}{\partial x} = 8\,\pi\,\mu \qquad (54)$$

The entrained mass flow rate is subtracted from the measured mass flow rate to obtain the final corrected mass flow rate. The entrained power is also subtracted from the measured power, although the contribution in this case is quite small as the surrounding air is supposedly cold.

Results of the integration of mass flow and power with and without taking into account the corrections are summarised in table 4. The displacement effect causes a shift of up to 4.7 mm (heat flux probe) and 1.2 mm (Pitot probe) on the edge of the jet. The entrainment mass flow rate is of the order of 0.6 g/s in all cases.

Table 4 indicates that the global mass flow is accurately computed in the 8 g/s case, and less so in the 16 g/s case. However, the jet was rather arbitrarily extended to 120 mm radius; if it is extended to 115 mm, the corrected mass flow is then 15.49 g/s (–3.2 %), which yields a much better agreement. It seems reasonable to conclude, from this example, that integration of the traverses yield mass flow values close to those used in the facility.

| | facility | | uncorrected | | | |
|---|---|---|---|---|---|---|
| | $\dot{m}$ [g/s] | P [kW] | $\dot{m}$ [g/s] | error [%] | P [kW] | error [%] |
| **A15** | 8 | 90 | 7.81 | –2.37 | 87.61 | –2.60 |
| **B15** | 8 | 150 | 8.63 | 7.87 | 167.90 | 11.93 |
| **D15** | 16 | 150 | 13.39 | –16.31 | 147.06 | –1.96 |
| **B75** | 8 | 150 | 6.78 | –15.25 | 167.57 | 11.71 |

| | facility | | corrected | | | |
|---|---|---|---|---|---|---|
| | $\dot{m}$ [g/s] | P [kW] | $\dot{m}$ [g/s] | error [%] | P [kW] | error [%] |
| **A15** | 8 | 90 | 7.89 | –1.41 | 82.48 | –8.35 |
| **B15** | 8 | 150 | 8.04 | 0.51 | 156.84 | 4.56 |
| **D15** | 16 | 150 | 17.1 | 6.90 | 145.58 | –2.94 |
| **B75** | 8 | 150 | 7.93 | –0.83 | 164.75 | 9.83 |

*Table 4. Results of the integration of mass flow and power using the computed traverses*

The values of power are in slightly worse agreement, although they all lie within the experimental uncertainty of the heat flux probe measurements. These results seem to indicate that the methodology used here is valid. It also means that the flow is not far from chemical equilibrium or that chemical non-equilibrium does not play a significant role on total pressure and stagnation-point heat flux.

The comparison above can be performed on any facility and should be one of the first tests to be performed in order to assess the overall quality of the developed measurement techniques. However, it can be carried out only if some knowledge of the efficiency is available. Indeed, the power settings is applied to the power generator, which is different from the power in the plasma jet due to numerous losses. If the facility cooling system is properly instrumented, an indicative value of the efficiency can be deduced from the conservation of power. In the case of the Plasmatron facility, we obtained a global efficiency of about 60% [6].

# 5. measurement techniques in development

## 5.1 Introduction

### 5.1.1 The VKI Minitorch

The VKI inductively coupled plasma "Minitorch" was first ignited in December 1996. It is a small facility, operating at gas flow rates of the order of 1 g/s, and using a 30 mm diameter plasma torch, supplied by a high frequency (27.12 MHz) vacuum triode oscillator which delivers up to 15 kW anode power at anode voltage up to 6 kV (figure 30).

The Minitorch was designed as a pilot facility during the design and construction at VKI of the bigger and more powerful 1.2 MW Plasmatron. Changes in torch geometry and operating conditions can very easily be made to study the effect of the various torch parameters and gain experience in ICP torch operation. This plasma facility is also used as a test bench to test and validate the measurement techniques and methods, before their implementation on the plasmatron.

### 5.1.2 Measurement developments

The latest measurement technique implemented in the Minitorch is the Laser Doppler Velocimetry (LDV). This technique is non-intrusive and provides accurate detailed measurements of the flow field of the plasma jet. It is not the aim of this note to present in details the principles of the LDV technique, but to show its

adaptation for plasma flow characterisation. Briefly, it consists in measuring the plasma flow velocity by recording the scattered signal of a seeding particle passing trough the interference region of two coherent laser beams (figure 31).

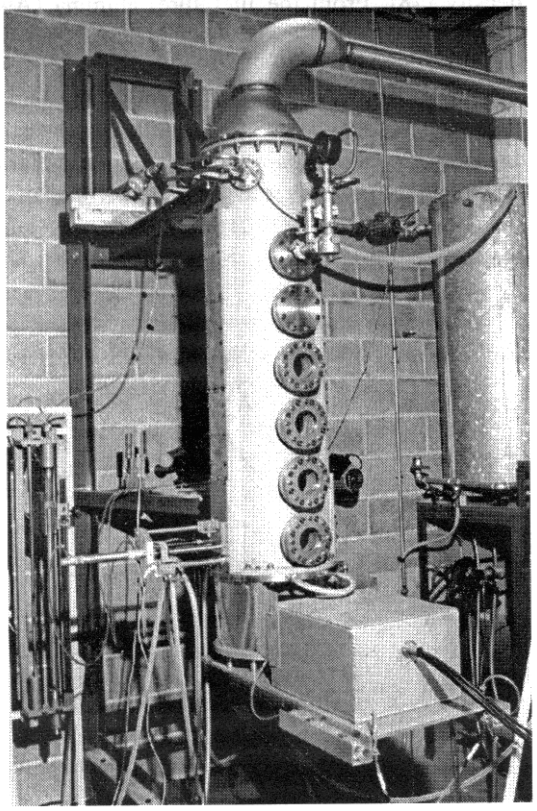

*Figure 30. The minitorch facility*

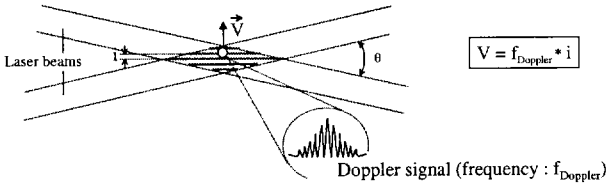


*Figure 31. Basic principles of LDV measurements*

## 5.2 LDV measurements

### 5.2.1 Introduction

The classical set-up for LDV measurements, which is used with forward scattering, is shown in figure 32. It contains a laser, a beam splitter, lenses, filter, photo-multiplier, particle generator and an electronic device. In a severe environment like a plasma flow, preliminary studies on the optical device used and on the behaviour of the chosen particles are needed in order to define good conditions for such measurements.

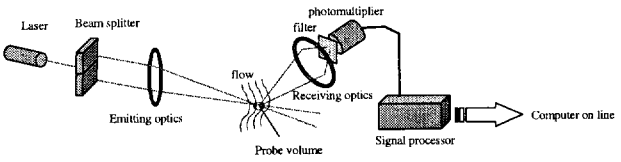


*Figure 32. Classical LDV set-up*

### 5.2.2 Optics

The plasma discharge is a very bright source which emits on a large wavelength spectrum. One has to check if the wavelengths of the laser beam used for the measurement are not corresponding with a peak of the plasma spectrum. When working with an air plasma, we can avoid overlaps of the LDV signal by using an argon laser (figure 33). Nevertheless one has to use an interference filter because the plasma is an intense source of light and leads to a saturation of the photo-multiplier.

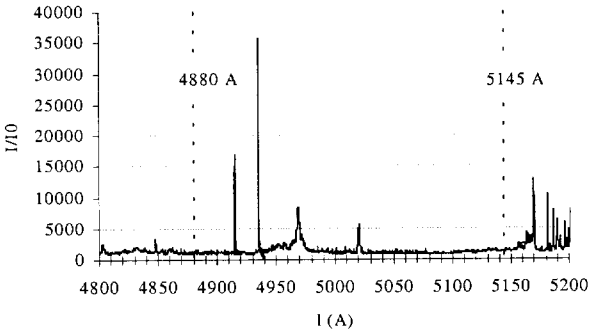


*Figure 33. Air plasma wavelength spectrum (4800 < λ < 5200 Å)*

The filter allows to reduce the perturbation due to the thermal emission of the particle heated in the high enthalpy flow which can lead to noisy signals. Another problem concerns the presence of temperature gradients which can introduce variations of the refraction index and disturb the interference pattern in the probing volume. From experiments with Schlieren photography in plasma jets at low pressure [21] and from literature about LDV measurements in hot gases [22], one can consider this effect as negligible in general cases. On the other hand one has to worry about the optical accessibility of the plasma flow to realise a good optical alignment.

### 5.2.3 Seeding

The seeding conditions in plasma flows are one of the worst that can be encountered as they consist in a gas at high temperature under low pressure. The particle generator must allow to work in such conditions. Previous experiments in combustion [23] and in argon plasma [24] can guide us to choose a convenient

apparatus. The solid particles are the most adapted ones, but their polydisperse nature appears to be a problem. Filters or special selection in or before the particle generator are usually needed. The cyclone aerosol generator seems to be a good candidate since it is a simple device. It has already been used successfully for $Al_2O_3$ particles to seed flames [25]. Other more sophisticated particle generators can be used for specific applications [23]. It has to be noticed that seeding problems can appear before reaching the plasma discharge. Actually, during the process of particle transport in pipes, the seeding can decrease drastically because of particle deposition on the tube wall. The powder has to be in good condition to be injected in the flow. Possible electrostatic charge or humidity have to be removed.

### 5.2.4 Particles behaviour

It is out of the scope of this report to study in detail the behaviour of particles in a high enthalpy flow. We just want to indicate the relevant parameters that have to be checked to be in good conditions for LDV measurements. The particles are exposed to a low-density fluid with high temperature. They have to be small enough to follow the fluid, but big enough to resist to the strong heat transfer at which they are exposed. The motion of the particles and their thermal resistance have to be inspected.

The ability of a particle to follow the flow depends on its shape, size, relative density with respect to the density of the fluid and particle concentration. An easy way of characterising particle dynamics effects is to examine the Stokes number:

$$St = \frac{\tau_p}{\tau_f} \qquad (55)$$

where $\tau_p$ is the characteristic particle response time and $\tau_f$ is the time scale of the flow variations. For $St << 1$, the particles will effectively follow the fluid motions to be measured. $\tau_f$ is evaluated as the diameter of the torch over the mean velocity of the flow for the working condition of the torch. The particle time $\tau_p$ is defined by [26]:

$$\tau_p = \frac{\rho_p d_p^2}{18\,\mu} \qquad (56)$$

In order to check the particles ability to support the heating from the plasma flow during their flight we have to estimate their total evaporation time. The complete solution of the evaporation of a material in a plasma discharge has been already examined [27]. This unsteady problem is not trivial and takes into account many effects of heat and mass transfer phenomena. A rough calculation of this consumption time $\tau_c$ can be considered assuming a pure heat transfer conduction to the particle [21]. A non-dimensional life duration number can be defined as the ratio between the consumption time and the time of flight of the particle in the discharge ($\tau_r$):

$$L_d = \frac{\tau_c}{\tau_r} \qquad (57)$$

Others authors take into account a "heating number" $S_p$ to select the particle to be used. It represents the ratio between the heat which is contained per unit volume of the particle at its melting point and its density [28]. From the literature, alumina ($Al_2O_3$), zirconium oxide ($ZrO_2$) and porous zirconium oxide ($ZrO_2$') appear to be adapted for LDV measurements in high enthalpy flows [28], [29]. $ZrO_2$' presents the advantage to be lighter with a good thermal resistance. As an example, the Stokes number and life duration number for $Al_2O_3$, $ZrO_2$ and $ZrO_2$' are calculated for typical plasma conditions ($T$ = 6000 K, $\dot{m}$ = 0.5 g/s) on figures 34 and 35.

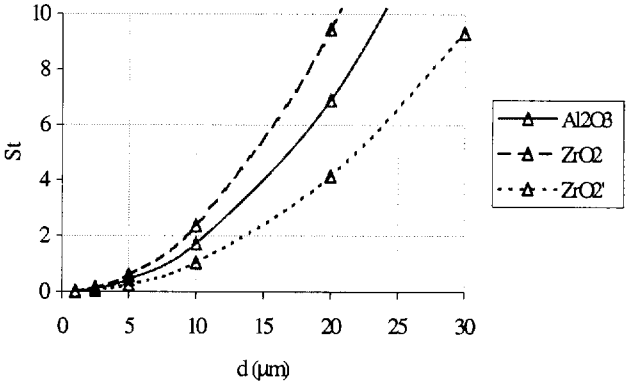


*Figure 34. Stokes number of particles in a plasma flow*

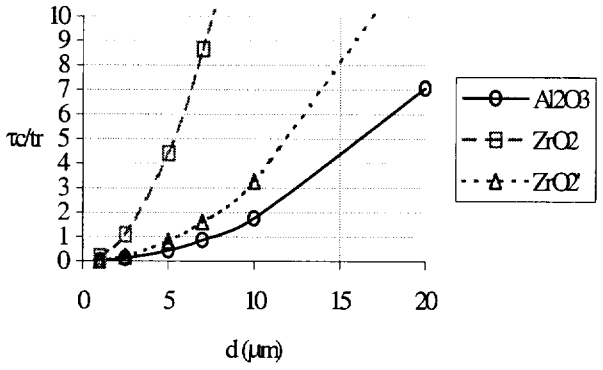


*Figure 35. Non-dimensional life duration of a particle in a plasma flow*

A remark has to be done for seeding realised with metallic powders. When the static pressure increases in the test chamber, the time residence of the powder become larger and the evaporation rate increases. The presence of the metallic vapour in the coil region significantly changes the electrical properties of the discharge. This change of impedance leads to electrical instabilities and it becomes difficult to control the power transferred to the plasma charge. Moreover, we

have to mention that thermophoresis forces can be notable because of temperature gradient [24].

### 5.2.5 Signal processing

Once the optical adjustment and a good seeding have been achieved, the signal from the particle scattering must be processed to get the flow velocity. This signal is then firstly collected in a pinhole through an objective and guided by an optic fibre to a photo-multiplier. The electrical signal is filtered and analysed in the signal processor device. Its role is to select the valid signal which contains relevant information to deduce the flow velocity. The main parameter to measure is the signal frequency ($f_{Doppler}$) since the particle velocity ($V$) is given by:

$$V = f_{Doppler}\ i \tag{58}$$

where $i$ is the fringe spacing.

In many cases the signal to measure, usually called "Doppler burst", can easily be affected by several sources of disturbances. A faraday cage has to be placed around the ICP torch to limit its electromagnetic radiation to the surroundings. The alteration of the signal can also be caused by a slight misalignment in the laser beam cross section or by a bad intensity balance between the beams. These problems can be checked by the operator. The disturbance coming from the particles are more difficult to control. Actually the dispersion in particle diameter can lead to big differences in light scattering. The thermal emission of the particles, heated in the high enthalpy flow, can induce noisy signals. Moreover the particles which cross the control volume partially or in a bad way have to be removed in order to process a correct value for the velocity. Since we measure relatively high velocities, few light is scattered and the voltage of the photomultiplier has to be increased. This amplifies the noise level as well. Figure 36 shows typical non-filtered and filtered signals from $SiO_2$ particles in the plasma jet of the Minitorch facility.

### 5.2.6 Experiments

The measurements have been done for two static pressures in the test chamber and two average total enthalpies of the jet. This represents four working conditions for the ICP torch reported in table 5. Let us remember that the average total enthalpy is defined by the ratio between the electrical power transfer to the discharge ($P_w$) and the mass flow ($\dot{m}$).

$$\Delta H = \frac{P_w}{\dot{m}} \tag{59}$$

The torch works with a straight annular injection. The axisymmetry of the configuration has been checked with a flow visualisation technique in cold condition [30].

| Test case | Mass flow | Average total enthalpy | Pressure |
|---|---|---|---|
| C1 | 0.55 g/s | 3.2 MJ/kg | 50 mbar |
| C2 | 1.0 g/s | 1.8 MJ/kg | 50 mbar |
| C3 | 0.55 g/s | 3.2 MJ/kg | 200 mbar |
| C4 | 1.0 g/s | 1.8 MJ/kg | 200 mbar |

*Table 5 Working conditions considered in the Minitorch*

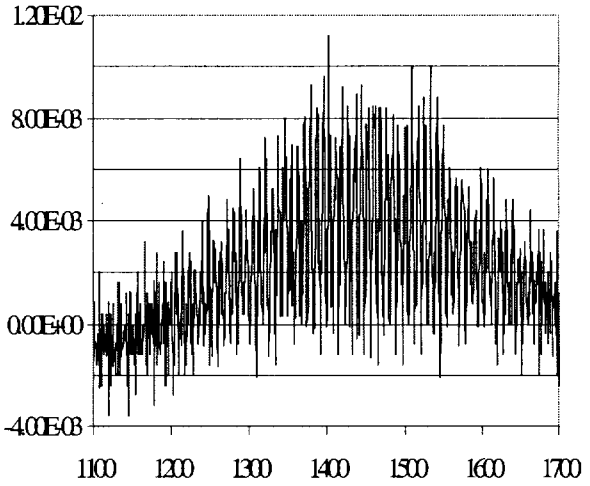


*(a) Non-filtered signals*

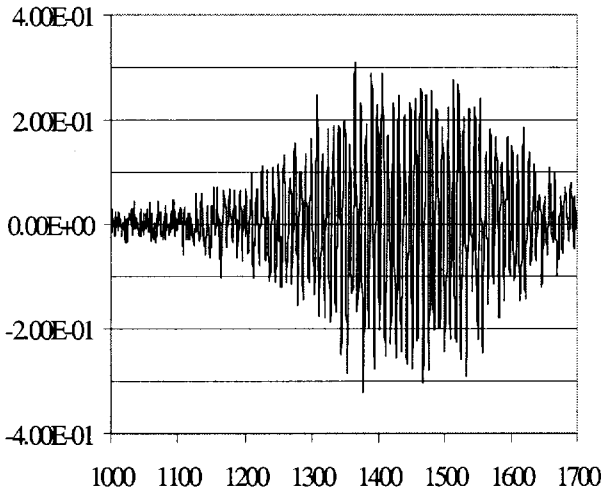


*(b) Filtered signals*

*Figure 36 Typical Doppler signals*

The LDV measurements have been implemented in the plasma jet, 20 mm downstream of the torch exit. They are taken along the radius since the axisymmetry of the jet has been checked. All the optical set-up of the LDV system is fixed to a table that can move in the three directions. In our case, the intersection of the laser beams is located on the axis of the jet (figure 37). This location is taken as marking the reference plane and the traverses are performed across the jet in that plane. The

position of the table is checked by a ruler which has an accuracy of half a millimetre for each displacement.

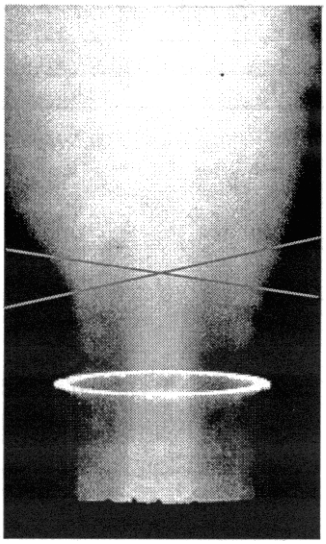

*Figure 37. Crossing laser beams in the plasma jet*

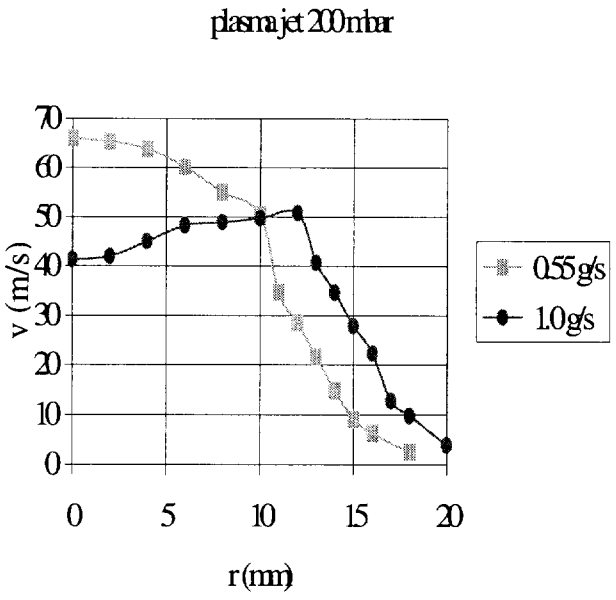


*Figure 38. Velocity profiles of the plasma jet, cases C3 & C4*

At each step the Doppler signals are measured with an oscilloscope. The band-pass filter is chosen and we control the data rate and the validation rate. A measurement corresponds to a recording of one thousand valid signals. The velocity profiles of the plasma jet are shown in figures 38 and 39. The seeding of the plasma was performed at 200 mbar with particles of silica, less than 1 μm in diameter, and at 50 mbar, with particles of aluminium with a diameter of 5 to 10 μm.

The trends of the velocity profile for the two ranges of pressure are similar. The differences between the curves are more pronounced at higher pressure. As a result of the coupling between the temperature and the velocity profiles in the plasma jet, the maximum velocity is decreasing when increasing the mass flow rate. For the higher-pressure ranges the velocity gradient at the border of the jet is larger than for the lower pressure cases. This is coherent with the visual inspection of the jet which appears more open at higher pressure. This corresponds to a more extended mixing layer.

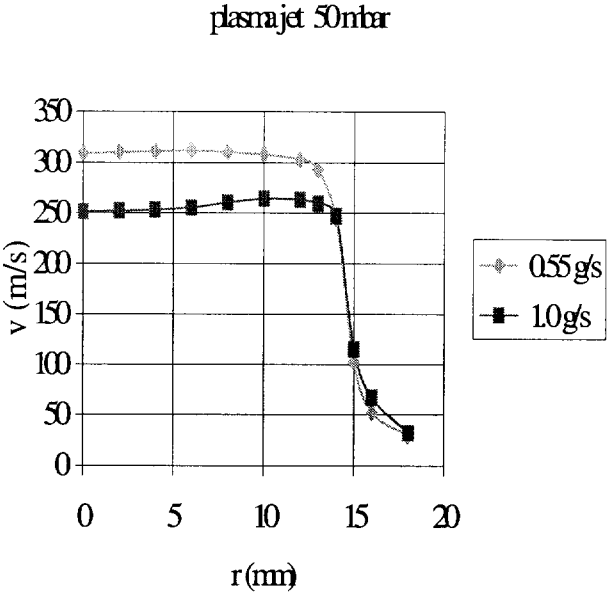


*Figure 39 . Velocity profiles of the plasma jet, cases C1 & C2*

## 5.3 Final remarks

As a non-intrusive and space-resolved technique, LDV measurements bring detailed information about the plasma flow. The implementation can be realised with a classical set-up using adapted interference filters. Nevertheless the seeding appears as the most important problem and has to be carefully examined to achieve accurate measurements. It can lead to some limitations because of the agglomeration and sedimentation of the particles to the tube wall. Particle evaporation in the coil region can induce plasma instabilities which drastically disturb the flow field. Once these problems are solved by selecting an appropriated seeding particle, LDV measurements provide precise results to assess the accuracy of more global high enthalpy measurement techniques, such as presented earlier in this review.

# List of References


[1] CHAZOT, O.; PEREIRA GOMES, J.M.; CARBONARO, M.: Characterization of a "mini-plasmatron" facility by Pitot probe measurements.
In *AIAA 29th plasmadynamics and lasers conference, AIAA paper 98-2478,* Albuquerque (USA), 15-18 June 1998.

[2] BOTTIN, B., CARBONARO, M., VAN DER HAEGEN, V., PARIS, S.: Predicted and measured capability of the VKI 1.2 MW Plasmatron regarding re-entry simulation.
In *3rd European symposium on aerothermodynamics for space vehicles, ESA SP-426,* ESTEC, Noordwijk (The Netherlands), 24-26 November 1998, pp 553-560.

[3] LUMENS, J.F.; BOTTIN, B.; CARBONARO, M.: Design of a steady-state heat flux probe for measurements in an induction-heated plasma flow.
In *ICIASF '97 Record (Ed. F. Kevin Owen), IEEE Publication 97CH36121,* Pacific Grove (USA), September 29 - October 2, 1997, pp 410-418.

[4] BARONETS, P.N.; KOLESNIKOV, A.F.; KUBAREV, S.N.; PERSHIN, I.S.; TRUKHANOV, A.S.; YAKUSHIN, M.I.: Overequilibrium heating of the surface of a heat-shield tile in a subsonic jet of dissociated air.
*Fluid Dynamics (Soviet Research),* **26** (3), May 1991, pp 319-476.

[5] KLINE, S.J. & MCCLINTOCK, F.A.: Describing uncertainties in single-sample experiments.
*Mechanical Engineering,* **75** (1), January 1953, pp 3-8.

[6] BOTTIN, B.: Aerothermodynamic model of an inductively-coupled plasma wind tunnel.
*Ph.D. Dissertation, Université de Liège & von Karman Institute for Fluid Dynamics,* October 1999.

[7] BOTTIN, B.; VANDEN ABEELE, D.; CARBONARO, M.; DEGREZ, G.; SARMA, G.S.R.: Thermodynamic and transport properties for inductive plasma modeling.
*Journal of Thermophysics and Heat Transfer,* **13** (3), July 1999, pp 343-350.

[8] MACMILLAN, F.A.: Viscous effects on Pitot tubes at low speeds.
*Journal of the Royal Aeronautical Society,* **58** (8), August 1954, pp 570-572.

[9] SHERMAN, F.S.: New experiments on impact-pressure interpretation in supersonic and subsonic rarefied air streams.
*NACA Technical Note 2995,* September 1953.

[10] HOMANN, F.: The effect of high viscosity on the flow around a cylinder and around a sphere.
*NACA Technical Memorandum 1334,* July 1952.

[11] FAY, J.A. & RIDDELL, F.R.: Theory of stagnation point heat transfer in dissociated air.
*Journal of the Aeronautical Sciences,* **25** (2), February 1958, pp 73-85.

[12] ANDERSON, J.D.JR.: Hypersonic and high temperature gas dynamics.
McGraw-Hill Book Company, New York, 1989.

[13] PETERS, N.: Lösung der Grenzchichtgleichungen für chemisch reagierende Gase mit einem Mehrstellenverfahren.
*DLR report 72-58,* August 1972.

[14] FLETCHER, C.A.J.: Computational techniques for fluid dynamics, vol. 2.
Springer-Verlag, Berlin, 1991.

[15] HOFFMANN, K.A. & CHIANG, S.T.: Computational fluid dynamics for engineers.
Engineering Education Systems, Wichita, 1993.

[16] BARBANTE, P.: Chemically reacting high-temperature gas flow around a stagnation point.
*VKI Project Report 1996-03,* June 1996.

[17] KOLESNIKOV, A.F.: Conditions of simulation of stagnation point heat transfer from a high-enthalpy flow.
*Fluid Mechanics (in Russian),* **1**, January 1993, pp 131-137.

[18] BOTTIN, B.; PARIS, S.; VAN DER HAEGEN, V.; CARBONARO, M.: Experimental and computational determination of the VKI Plasmatron operating envelope.
In *30th AIAA Plasmadynamics and Lasers Conference, AIAA paper 99-3607,* Norfolk (USA), June 28 - July 1, 1999.

[19] VAN DEN BRAEMBUSSCHE, R.; ARTS, T.; BOERRIGTER, H.; CARBONARO, M.: Pressure Measurements.
In *Introduction to Measurement Techniques, VKI Lecture Series 1994-01,* Rhode-Saint-Genèse (Belgium), (annual lecture), pp 41-138.

[20] SCHLICHTING, H.: Boundary-layer theory.
McGraw-Hill, New York, 1955.

[21] CHAZOT, O.: Global characterisation of plasma flow in an ICP torch by intrusive measurements.
*VKI Internal Note 117,* June 1999.

[22] PFEIFER, H.-J.: Measurements in gas and flames.
*VKI Lecture Series 1981-03,* 1981.

[23] MELLING, A.: Particle behaviour in flows and suitable particles for LDA measurements.
*VKI Lecture Series 1981-03,* 1981.

[24] GOUSBET, G. & TRINITE, G.: Anémométrie laser doppler interférentielle dans une torche à plasma haute fréquence.
*J. Phys. E. Sci. Instrum.,* **10**, 1977, pp 1009-1016.

[25] GLASS, M. & KENNEDY, I.M.: An improved seeding method for high temperature laser doppler velocimetry.
*Combustion and Flame,* **29**, 1977, pp 333.

[26] MUNGAL, M.G.: Experiments in combustion (lecture 3).
In *Introduction to Turbulent Combustion, VKI Lecture Series 1999-04,* Rhode-Saint-Genèse, March 22-26, 1999.

[27] BONET, C., DAGUENET, M., DUMARGUE, P.: Etude théorique de l'évaporation d'une particule sphérique d'un matériau réfractaire dans un plasma thermique.
*International Journal of Heat and Mass Transfer,* **17**, 1974, pp 643-654.

[28] GOUSBET, G.: A review on measurements of particle velocities and diameters by laser techniques, with emphasis on thermal plasmas.
*Plasma Chemistry and Plasma Processing,* **5** (2), 1985, pp 91-117.

[29] MOREAU, P. & LABBE, J.: Laser velocimetry in high velocity combustion flow.
*ONERA-TP-1978-75,* 1978.

[30] CHAZOT, O.: Qualitative description of the flow field of an ICP torch with a cold model.
*VKI Internal Note 114,* January 1999.

# Spectroscopic Techniques for Measurement of Velocity and Temperature in the DLR High Enthalpy Shock Tunnel HEG

**W. H. Beck**
Aerothermodynamics Section,
Institute of Fluid Mechanics,
German Aerospace Center (DLR),
Bunsenstraße 10,
37073 Göttingen
Germany

## ABSTRACT

The theory of absorption techniques, including line broadening and shifts, along with a brief description of the spectroscopy of the seed species Rb, will be given. A brief overview of the diode laser itself and the experimental setup for the technique follow. Results are split into two parts: preparatory and calibration work in a test cell and a small test shock tube, followed by results in HEG, are presented. Here time profiles for gas temperature $T_{trans}$ and velocity u are given for various HEG run conditions.

## 1. INTRODUCTION

As in any wind tunnel, the free stream flow in the High Enthalpy Shock Tunnel HEG of the DLR in Göttingen needs to be characterised (i.e. calibrated) properly in order to carry out measurements on small test models. Standard techniques are bulk techniques, whereby pressures (Pitot or static) and stagnation point heat transfer rates are measured at various radial and axial positions after the nozzle exit, to be then compared with CFD results from which other flow properties can be calculated. However, this represents experimentally a very limited data set with which to validate the CFD codes - measurement of other physical properties such as gas temperatures (either inner or translational $T_{trans}$), velocities u and species concentrations are hence highly desirable. For example, a measurement of u is the best way to determine whether the enthalpy of the gas is as high as expected and calculated from shock speed and/or CFD of the nozzle flow. Spectroscopic techniques such as LIF and CARS can deliver rotational $T_{rot}$ and vibrational $T_{vib}$ temperatures, and in some cases also species concentrations. (For the former, one usually *assumes* that $T_{rot} = T_{trans}$.) They can't measure $T_{trans}$ or in most cases u.

The aim of this lecture is to present the diode laser absorption technique, which can deliver $T_{trans}$, u and, depending on the probed species, also concentration by a measurement of line broadening, line shift and line area, respectively. As used on HEG, a seed species rubidium Rb was introduced into the test flow in minute concentrations, thereby not itself influencing the flow properties in any way. Another naturally occurring species in HEG, NO, has also been probed using this technique (Ref. 1), only in that case measurements were performed in the IR, whereas the Rb work was carried out in the visible. The technique has one drawback, however, compared with LIF or CARS; it is a line-of-sight technique, meaning that the signal is integrated over the pathlength of the laser beam through the test region. As will be shown, in the case of HEG, the free stream flow is assumed to be homogeneous in a radial direction, so that this drawback is not severe. The technique in its present form has, therefore, limited applicability to flows where property gradients are large relative to the laser beam path length (e.g. around a test model).

The theory of absorption techniques, including line broadening and shifts, along with a brief description of the spectroscopy of the seed species Rb, will be given. A brief overview of the diode laser itself and the experimental setup for the technique follow. Results are split into two parts: preparatory and calibration work in a test cell and a small test shock tube, followed by results in HEG, are presented. Here time profiles for gas

*Paper presented at the RTO AVT Course on "Measurement Techniques for High Enthalpy and Plasma Flows", held in Rhode-Saint-Genèse, Belgium, 25-29 October 1999, and published in RTO EN-8.*

temperature $T_{trans}$ and velocity u are given for various HEG run conditions.

## 2. THEORY

### 2.1 Absorption spectroscopy

The transmission $T(\bar{\nu})$ of light (wavenumber $\bar{\nu}$) through an absorbing medium is given by the Beer-Lambert law (see Ref. 2, and references therein):

$$T(\bar{\nu}) = \frac{I(\bar{\nu})}{I_0} = e^{-\int k(\bar{\nu})\, d\bar{\nu}},$$

where $I(\bar{\nu})$ and $I_0$ are the light intensity after and before entering the absorbing medium, respectively, and $k(\bar{\nu})$ is the spectral absorption coefficient. This coefficient can be written as:

$$k(\bar{\nu}) = h \,.\, \bar{\nu} \,.\, n_i \,.\, \frac{B_{ik}}{c} \,.\, \left(1 - e^{-h\bar{\nu}/kT}\right) \,.\, \Phi(\bar{\nu})$$

where h is Planck's constant, $n_i$ the population density in the lower energy level i, $B_{ik}$ the Einstein coefficient for transition from level i to k, c speed of light, k Boltzmann's constant, T the temperature and $\Phi(\bar{\nu})$ the line shape function. This function is the key to the absorption technique; a knowledge of its shape, broadening mechanisms and shift in wavelength will be used to deliver the temperature and velocity of the gas.

### 2.2 Line broadening

Four mechanisms leading to broadening of absorption will be discussed:

*1. Natural linewidth.* Although one may expect that the absorption line width for the transition from level i to k, occurring at $\bar{\nu}_0$, is infinitely narrow, this is not possible since it would violate the Heisenberg Uncertainty Principle, one form of which relates the energy uncertainty $\Delta E_k$ to the lifetime $\tau_k$ of the upper excited state k by $\Delta E_k \cdot \tau_k \geq h / 2\pi$. For example, for the lifetime $\tau_k$ = 10 ns of the upper state of the Rb $D_2$ transition ($5^2S_{1/2} \rightarrow 5^2P_{3/2}$, see chapter 2.4 and Fig. 1), the natural line broadening of the Rb absorption line is only 0.5 x $10^{-3}$ $cm^{-1}$. Natural line broadening is represented by a Lorentzian line shape.

*2. Pressure broadening.* Also called collisional broadening, this is brought about by perturbations of the quantum energy states involved in the transition due to collisions, leading to a smearing of the energy levels and therefore a broadening of the lines. It usually only plays a role at high pressures, and is not important at HEG free stream pressures of about 500 Pa. (For comparison, the $D_2$ line of sodium, which is in the same column of the Periodic Table as Rb and therefore has similar spectroscopic properties, would experience a line broadening at HEG conditions of only $1x10^{-3}$ $cm^{-1}$.

*3. Doppler broadening.* This is the major broadening mechanism in the HEG free stream, and is what is used to determine the translational temperature $T_{trans}$ of the gas. It arises from the movement of the absorbing species in directions towards and away from the direction of the laser beam, leading to small Doppler shifts which manifest themselves as line broadening. For Rb at HEG conditions ($T_{trans} \approx$ 1000 K), the broadening amounts to about 30 x $10^{-3}$ $cm^{-1}$, and so has about 30 times more influence than pressure broadening. Doppler broadening is represented by a Gaussian line shape.

*4. Stark broadening.* This mechanism is very important in ionised flows or plasmas, where electron concentrations are quite high. As in pressure broadening, a perturbation of the energy levels arises from species-electron collisions, only for these types of collisions their cross sections are much larger. Electron concentrations in HEG are unkown; CFD calculations of the nozzle flow predict very low values, so that, if correct, this mechanism should not play a major role here.

Doppler broadening leads to a Gaussian line shape $g_D(\bar{\nu})$, whose FWHM (full width at half maximum height) line width $\delta\bar{\nu}_D$ is a function of the temperature T of the excited atom:

$$g_D(\bar{\nu}) = \exp\left[-4 \cdot \ln 2 \cdot \frac{(\bar{\nu} - \bar{\nu}_0)^2}{(\delta\bar{\nu}_D)^2}\right],$$

$$\delta\bar{\nu}_D = \frac{2 \cdot \sqrt{2 \cdot R \cdot \ln 2}}{c} \cdot \bar{\nu}_0 \cdot \sqrt{\frac{T}{M}}.$$

R is the universal gas constant, M the atomic weight, other symbols as before. In the above equation, one can see that, apart from some

constants or quantities, $\delta\bar{\nu}_D$ is a function only of $\sqrt{T}$. Hence, by measuring $\delta\bar{\nu}_D$, one can determine the temperature, albeit not very accurately due to the square root dependence. It should be noted that this is measurement of a translational temperature, and as such is independent of the population of the atomic energy levels, and is not plagued by quenching problems (as in LIF).

In fitting experimentally determined line shapes to theoretical profiles, one usually uses a Voigt profile, which is a composite of the Gaussian profile from Doppler broadening and the Lorentz profile from natural broadening. However, since the Doppler broadening is some 30 times stronger than natural broadening (see before), in HEG free stream flows it is sufficient to use just the Gaussian form, as given in the above equations.

### 2.3 Line shifts

Whereas line broadening delivers information on temperature, a shift in the line position (in wavelength or wavenumber) due to the Doppler effect can give the relative velocity between the moving atom and the laser beam. This Doppler shift is a direct linear function of the velocity u of the atoms and the angle θ between atom velocity vector and laser beam direction:

$$\Delta\bar{\nu}_{line} = \bar{\nu}_0 \cdot \frac{u}{c} \cdot \cos(\theta).$$

For the $D_2$ line of Rb, and taking the range of HEG free stream velocities (~4300 - 6200 m $s^{-1}$), quite large line shifts of about 0.11 - 0.16 $cm^{-1}$ would be expected. This makes the velocity determination much more accurate than that for temperature, since these large shifts can be measured quite accurately.

### 2.4 The rubidium atom Rb

Rb posseses two naturally occurrring isotopes, $^{85}$Rb and $^{87}$Rb, with relative proportions of 72% and 28%, respectively. Both contribute to the absorption and so they must both be considered in calculating line shapes. As with all alkali metals, Rb possesses a very strong resonant transition where an electron is promoted from an s to a p orbital. This single electron in the 5s orbital leads to a ground state symbol $5^2S_{1/2}$. The next level, an electron in a 5p orbital leads to the state $5^2P_{3/2}$. Both of these levels are further split due to spin/orbit interactions into hyperfine structure levels, designated by a quantum number F. This hyperfine splitting is quite large for the $5^2S_{1/2}$ ground state - 0.1007 $cm^{-1}$ for $^{85}$Rb and 0.2262 $cm^{-1}$ for $^{87}$Rb - whereas for the excited state $5^2P_{3/2}$ it is only 0.0072 $cm^{-1}$ for $^{85}$Rb and 0.0166 $cm^{-1}$ for $^{87}$Rb. Fig. 1 shows on the left a term energy level diagram for Rb, with the strong $D_2$ transition at 780.2 nm indicated. To the right the sublevel structure of both Rb isotopes is shown.

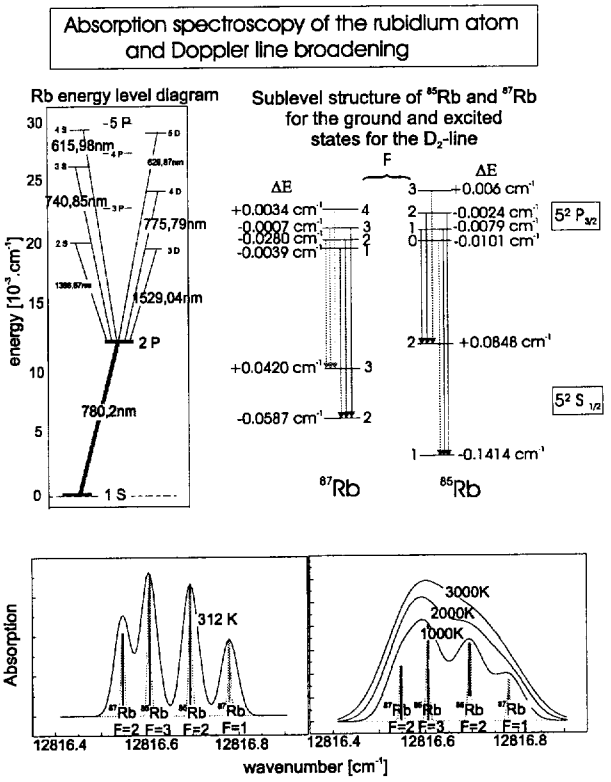


*Fig. 1 Energy level diagram and calculated spectra for Rb*

With the Doppler broadening to be expected here, transitions from lower states to the upper states F = 0 - 4 cannot be resolved; however, transitions from each of the lower states F = 2, 3 ($^{87}$Rb) and F = 1,2 ($^{85}$Rb) can, so that in all four absorption lines will be measured (see calculated spectra in Fig. 1).

The effect of Doppler broadening on the naturally broadened lines can be seen in Fig. 1, lower traces. In both traces the naturally broadened lines have been calculated and are shown in grey; they are designated by the hyperfine level quantum number F from the lower energy level for both isotopes. The left plot shows also calculated Doppler-broadened lines at 312 K; one can see immediately

that the hyperfine structure due the levels F in the upper state merge together, even at this "low" temperature. For higher temperatures, 1500, 2500 and 3500 K, shown right, eventually even these four lines merge into one. It is clear with this example that this method of temperature determination becomes quite inaccurate at higher temperatures, or at the very least requires experimental data of high quality (low S/N).

This broadening as a function of temperature is further exemplified in Fig. 2. Here calculated spectra are shown for temperatures above 3000 K (3000 - 5000 K) and in the range of expected temperatures for HEG free stream flows (700 - 1300 K). Above 3000 K the method is virtually useless! In the range 700 - 1300 K the situation is quite good - it will be shown later that here temperature measurements can be carried out with a (conservative) accuracy of better than ±20%.

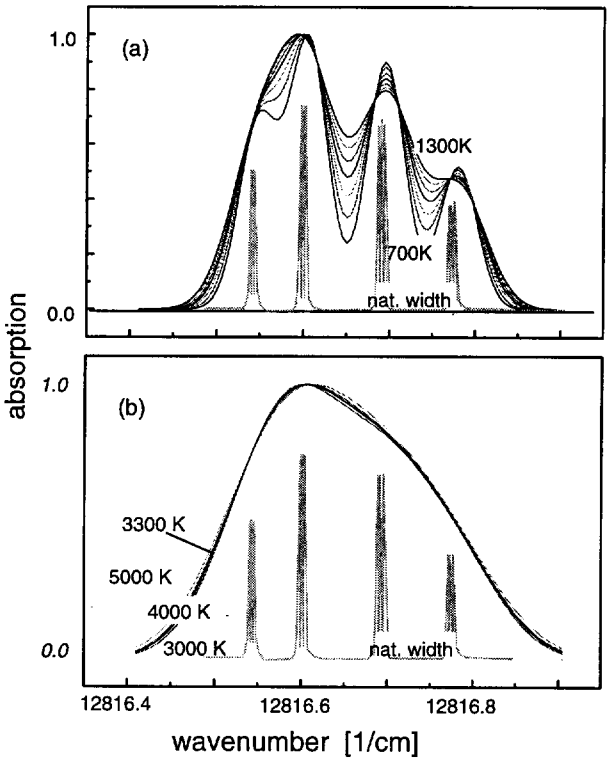


*Fig. 2 Calculated Rb spectra (a) 700 - 1300 K; (b) 3000 - 5000 K*

## 3. EXPERIMENTAL TOOLS

### 3.1 The diode laser

The GaAlAs semi-conductor diode lasers used here are of type III-IV (elements of periodic columns III and IV) and emit in the range 720 - 895 nm. In CW (continuous wave) operation they emit a single longitudinal mode, so that, since their geometry is very small, they have a very narrow bandwidth (~3 x $10^{-3}$ $cm^{-1}$). The wavelength of the emitted light is dependent on the temperature and injection current for the diode, although not in a continuous way, but rather step-wise, see Fig. 3.

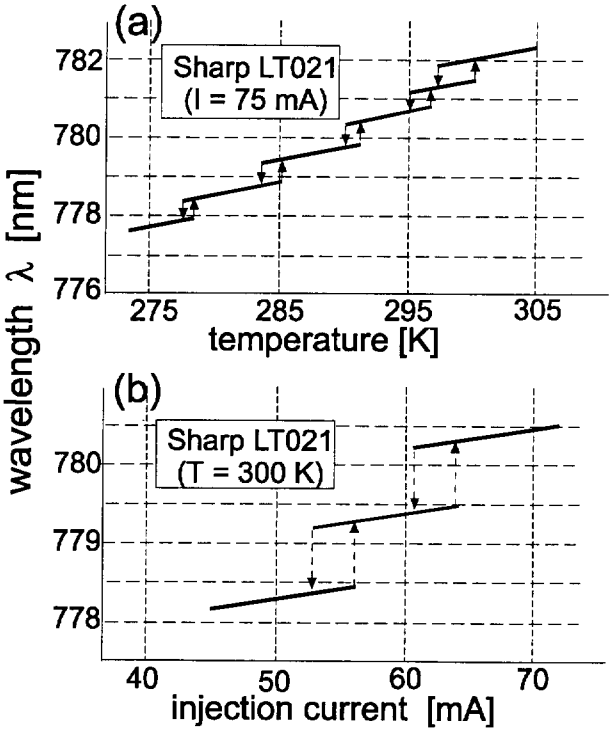


*Fig. 3 Dependence of laser diode wavelength on temperature and current*

In Fig. 3 the wavelength (in nm) of the emitted light is plotted as a function of (a) temperature (from 275 to 305 K) at constant current, and (b) injection current (from 45 to 70 mA) at constant temperature for Sharp LT021 laser diodes. Wavelength is tunable continuously over a single step over a range of 0.05 to 0.5 nm, depending on laser type; this is wide enough to encompass completely the Rb absorption lines discussed in chapter 2.4. In doing this it is important to be not too close to the edge of one of the steps shown in Fig. 3, otherwise the laser may hop from one mode (step) to another. This can be seen in Fig. 4, where

measured intensity of a ROHM RLD-78NP laser diode is plotted against wavelength for a constant temperature of 15°C and for injection currents between 45.85 and 45.90 mA (in steps of 0.01 mA). The bandwidth of the measured emission is not that of the laser diode, but rather due to the resolving power of the spectrometer used in the measurement.

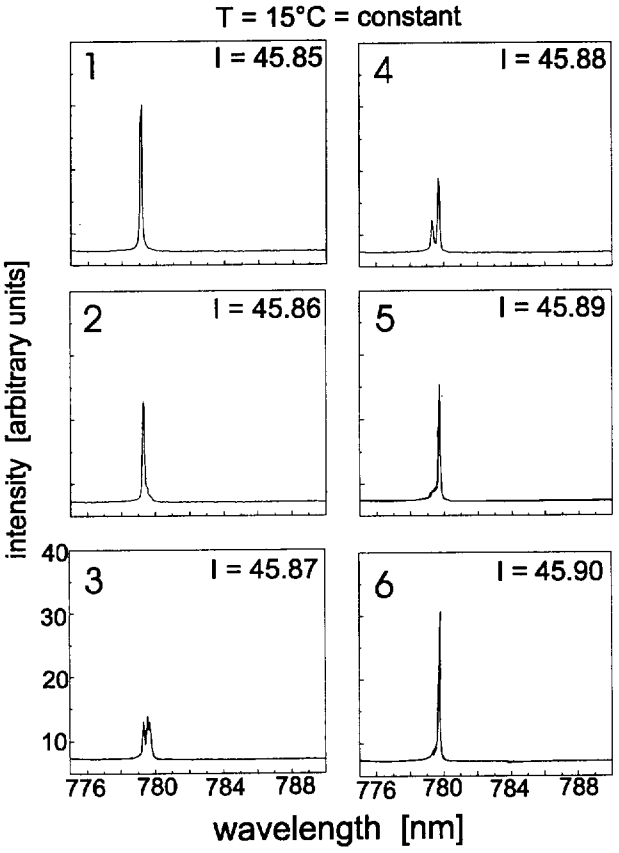


*Fig. 4 Laser diode output at different injection currents, showing mode hopping*

The figure shows that at currents of 45.87 and 45.88 mA mode hopping must be occurring, so that with the combination of this temperature and these currents, the laser diode is not suitable for scanning work.

Operating conditions which are suitable for Rb absorption work are shown in Fig. 5. At a constant temperature of 281.90 K, a plot of emitted wavelength against injection current is shown. Also included in the figure is the wavelength region (narrow grey region) where the four Rb absorption lines occur. The laser diode mode between 37 and 42 mA nicely encompasses the Rb absorption lines, so that here there is no danger of mode hopping occurring.

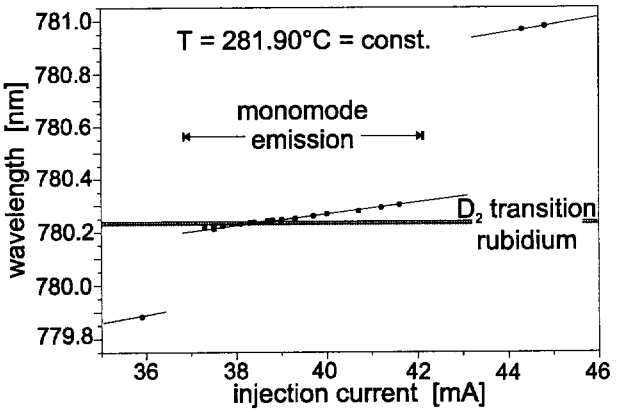


*Fig. 5 Single ramp of laser diode output, compared with Rb absorption region*

The measurement shown in Fig. 5 was carried out by varying the current step-wise and recording the wavelength. It is also possible to vary this current very rapidly - the laser diode can respond equally rapidly up to 100 kHz. If the injection current is modulated as a sawtooth or triangular function, then the laser will also follow this modulation in both wavelength and intensity of emission. This is done here in measurements on HEG, so that during the available flow test time a multitude of ramps from the triangular-modulated current provide as many absorption spectra, which can each be analysed to give the time dependence of the flow development. (See Ref. 2)

### 3.2 The rubidium calibration cell

A reference cell is needed to calibrate the wavelength of the laser diode using the accurately known absorption lines of Rb. This cell is made of glass, having a length of 8 cm and a diameter of 1.5 cm, and is sealed at both ends with planar-parallel windows. It is filled with 5 g of high purity Rb und a protective atmosphere of argon. The cell can be heated up to temperatures of 370 K. Rb metal melts at 312 K and has an equilibrium vapour pressure and concentration at this temperature of ~8 x $10^{-5}$ Pa and ~1.5 x $10^{10}$ $cm^{-3}$, respectively. An absorption spectrum of Rb at 273 K recorded with a laser diode is shown in Fig. 6.

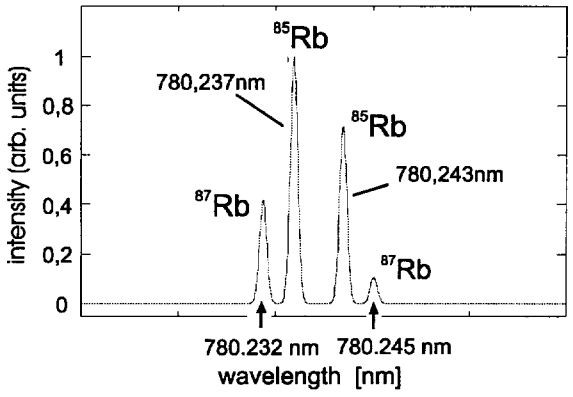


*Fig.6 Measured absorption spectrum of Rb using a laser diode*

### 3.3 The test shock tube

Development of the seeding technique, recording of emission spectra and testing of the set-up for recording absorption spectra were all carried out in a small test shock tube. This consists of 1.37 m driver (ø 21.9 cm)and 3.13 m driven (ø 6 cm) tubes separated by a plastic diaphragm. Driver gas was helium at 810 kPa, test gas air or $N_2$. A small test section (length 13.3 cm) at the end of the driven (shock) tube contains windows for emission and absorption work and pressure sensors. Temperatures here of up to 3000 K were attained.

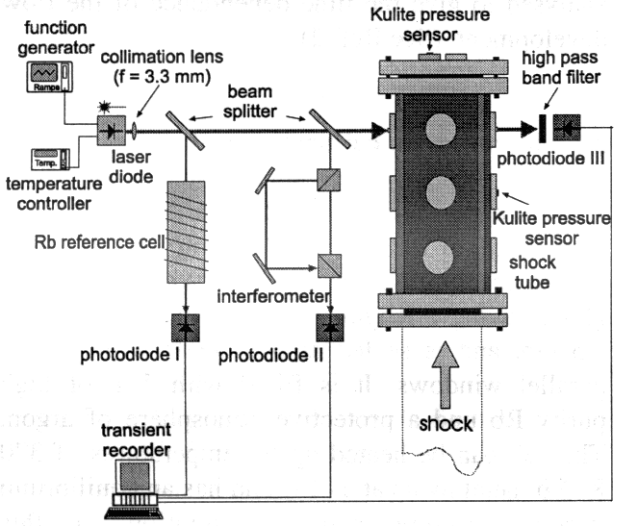


*Fig.7 Diode laser absorption setup on the small test tube*

The experimental set-up at the test shock tube is shown in Fig. 7. Small portions of the diode laser beam are split off and sent through the reference cell and to an interferometer, where the two beams are recorded by two photodiodes. (The interferometer provides a wavelength calibration over the laser diode scanning range, i.e. one ramp of the triangular modulation.) The main part of the beam passes through the shock tube test section, where it also is recorded by a photodiode. All photodiode outputs are stored in a transient recorder.

### 3.4 The high enthalpy shock tunnel HEG

The HEG is a free-piston driven shock tunnel operating in the reflected shock mode. It has been described in greater detail elsewhere (ref. 3). As shown in Fig. 8, a reflected shock creates high temperature and pressure conditions in the reservoir (before the nozzle entrance), after which the test gas expands through the nozzle to deliver the free stream conditions in the test section. The test time is about 1 ms. Also shown in Fig. 8 are nominal conditions which have been calculated using a non-equilibrium Euler code for the free stream and the reservoir - these conditions apply to the old contoured nozzle in HEG, with which most of the testing was carried out. Conditions I and III are low pressure, with high and low specific enthalpy, respectively, and II and IV are high pressure, also with respectively high and low enthalpies. Free stream temperatures are calculated to lie between about 500 and 1100 K and flow velocities between 4800 and 6200 m $s^{-1}$.

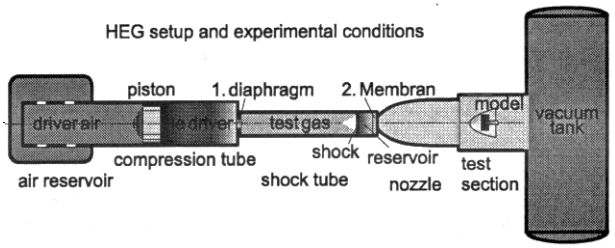


Nominal conditions for the contoured nozzle

| Conditons | | I | II | III | IV |
|---|---|---|---|---|---|
| $p_0$ | [MPa] | 40 | 90 | 45 | 110 |
| $T_0$ | [K] | 9100 | 9700 | 7300 | 8100 |
| $T_\infty$ | [K] | 790 | 1040 | 550 | 720 |
| $h_0$ | [MJ/kg] | 21 | 22 | 13 | 15 |
| $u_\infty$ | [km/s] | 5,9 | 6,2 | 4,8 | 5,1 |
| N2 | [$10^{15}$cm$^{-3}$] | 26,1 | 56,6 | 44,0 | 95,6 |
| O2 | [$10^{15}$cm$^{-3}$] | 1,1 | 4,3 | 7,6 | 18,0 |
| NO | [$10^{15}$cm$^{-3}$] | 1,1 | 3,0 | 3,9 | 8,4 |

*Fig.8 The high enthalpy shock tunnel HEG*

### 3.5 Diode laser set-up on HEG

The set-up for HEG is shown in Fig. 9.

The basic set-up is as in Fig. 7, except that the beam is split into two halves, one of which passes through the HEG test section at 90° and the other at 53° to the flow. Photodiodes I - IV record laser beam signals through the reference cell, the interferometer, and the HEG test section at 90° and at 53°, respectively. Inset plots upper left and mid right show the intensity of the laser output as a function of time (i.e. wavelength) with and without absorption by Rb. Upper right are two emission spectra recorded in HEG with and without seeding with Rb (see chapter 5.1).

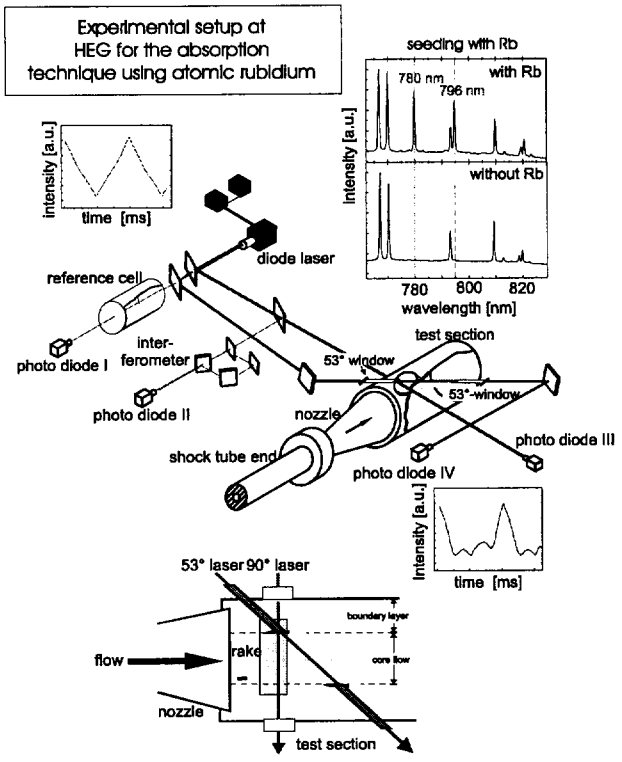


*Fig. 9 Diode laser setup in HEG*

To avoid influences on the measurement from boundary layer effects (remembering that the technique is line-of-sight integrating), the 53° laser beam path is protected by light guiding pipes, as shown at the bottom of Fig. 9. Here the laser beam "sees" only the core flow. This is shown graphically in Fig. 10.

Here calculated radial profiles at the HEG nozzle exit for temperature and velocity are shown (Ref. 4). The core flow and boundary layer regions are indicated at the top, as are the regions excluded by use of the light guiding pipes. These regions are characterised by very high temperatures and a negative velocity gradient.

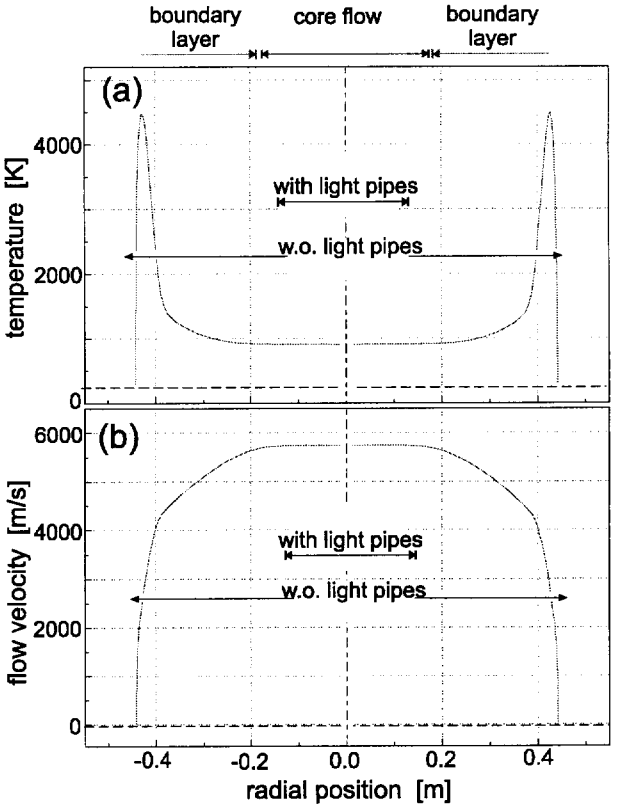


*Fig.10 HEG radial temperature (a) and velocity (b) profiles, showing exclusion of boundary layer effects by the light pipes*

### 3.6 Seeding Rb in HEG

Rb is a reactive alkali metal, is not stable in air and so is not suited to be used directly and quantitatively as a seed species. However, its nitrate $RbNO_3$ is readily water soluble and decomposes to its oxide $Rb_2O$ at 550 K, which itself melts at 1500 K. At the high temperatures in the HEG reservoir (up to 9700 K), $Rb_2O$ further decomposes within the flow time to its constituent parts, including atomic Rb. Seeding was carried out with very low concentrations of $RbNO_3$ in water by applying the solution with a brush to surfaces both at the shock tube end and in the compression tube near the diaphragm position (see Fig. 8). Total Rb amounts were around only 1 µg!

## 4. RESULTS IN THE TEST SHOCK TUBE

Fig. 11 shows a typical shock tube result (test gas air), with: (a) photodiode I signal with Rb absorption in the reference cell; (b) photodiode signal III with Rb absorption in the shock tube; (c) pressures measured at shock tube test section end and side walls. In (b) one can clearly see the initial undisturbed triangular emission trace of the laser diode, followed after arrival of the reflected shock at the test window by superimposed absorption peaks due to Rb. (The gas behind the incident shock in this run was too low to vaporise the $Rb_2O$, explaining the absence of an absorption signal here.)

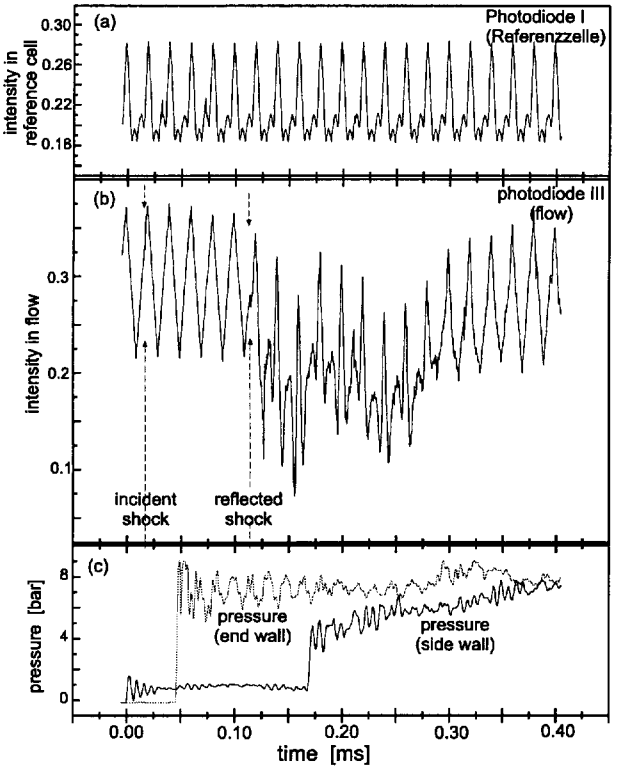


*Fig. 11 Measurement in small test shock tube: (a) reference; (b) shock tube ;(c) pressures*

The reflected shock region should have a temperature of about 3300 K, according to calculations derived from the shock tube fill pressure and shock Mach number. One of the spectra (one of the ramps) shown in Fig. 11 in the reflected shock regime, after appropriate correction for changing laser beam intensity and conversion to absorption units, is shown in Fig. 12 (dark line plot). Superimposed are calculated (simulated) spectra for temperatures 3000, 3500, 4000 and 4500 K. (For reference, a spectrum for 312 K is also plotted.)

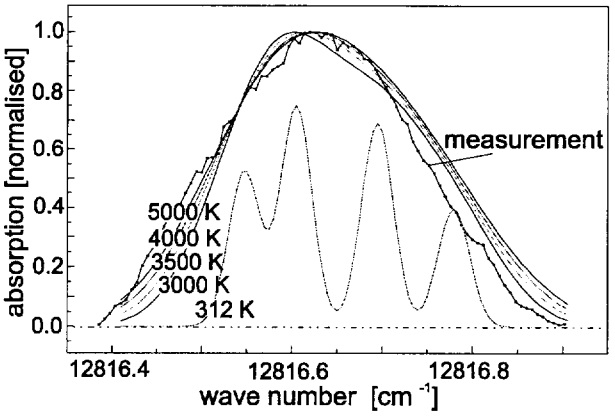


*Fig. 12 Comparison of measured and calculated absorption profiles in the test shock tube*

One sees here a confirmation of the problem referred to in Fig. 2; the differences between the simulated spectra for this wide temperature range are too small to be resolved by the available experimental data. At these temperatures the method is very inaccurate and not suited.

## 5. RESULTS IN HEG

### 5.1 Emission spectra

In order to analyse absorption spectra recorded in HEG correctly, one needs to be sure that absorption is occurring only through the presence of Rb, and not overlapped by other disturbing absorbing species. Before the first introduction of Rb into HEG, emission spectra in front of a flat plate (of area 20 $cm^2$) placed in the HEG test section normal to the flow direction were recorded using an optical multichannel analyser. The reservoir region was then seeded and another spectrum recorded. Both spectra were shown in Fig. 9, upper right. Here it is clear that the only emitting (and therefore absorbing) species at 780.2 nm is Rb.

### 5.2 Seeding results

*Core vs boundary layer regions.* After the first seeding experiment, there remain for future shots always small amounts of Rb compounds at the shock tube end and nozzle inlet, present as "dirt" on the walls. This Rb does not enter the core

region, as can be seen in Fig. 13(b). Shown in this figure for a shot at condition I are (a) Pitot pressure in the test section; (b) Absorption from an experiment without prior Rb seeding for both 90° and 53° laser beams, where the latter was protected by the light guiding pipes; (c) Absorption for 53° laser beam from an experiment where Rb was seeded into the flow (dark line trace), compared with the unseeded experiment (grey).

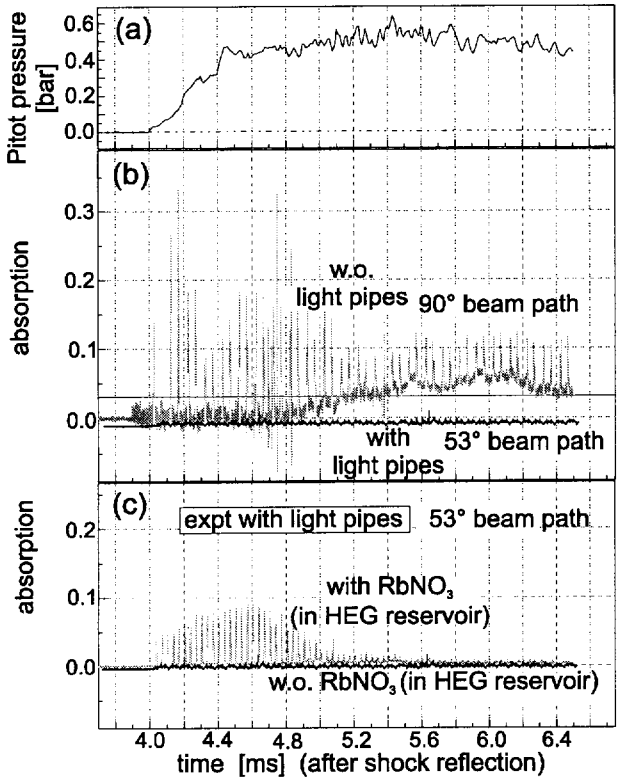


*Fig. 13 Rb absorption spectra in HEG, showing contributions of core and boundary layer regions*

(b) shows clearly that for the unseeded experiment, the only Rb absorption signal is in the boundary layer region outside the core flow, due to the dirt. This absorption also persists for quite long times - >2.5 ms after flow arrival. In the case of Rb seeded immediately before the shot (upper trace in (c)), there is absorption from the core region for the 53° laser beam; this Rb does not remain very long (<1 ms).

This effect can be further clearly seen in Fig. 14, where both laser beam transmission traces ((a) and (b)) are shown plotted versus time for an HEG shot at condition I (as before, in Fig. 13, gas arrival occurs at about 4.0 ms). Note how the absorption from the unprotected 90° laser beam persists for a long time. A small time excerpt from both traces (a) and (b) for the time window 4.875 - 5.00 ms is shown in (c). The Doppler shift of the 53° laser beam absorption spectrum relative to that for the 53° beam is obvious. This will be analysed later (chapter 5.4).

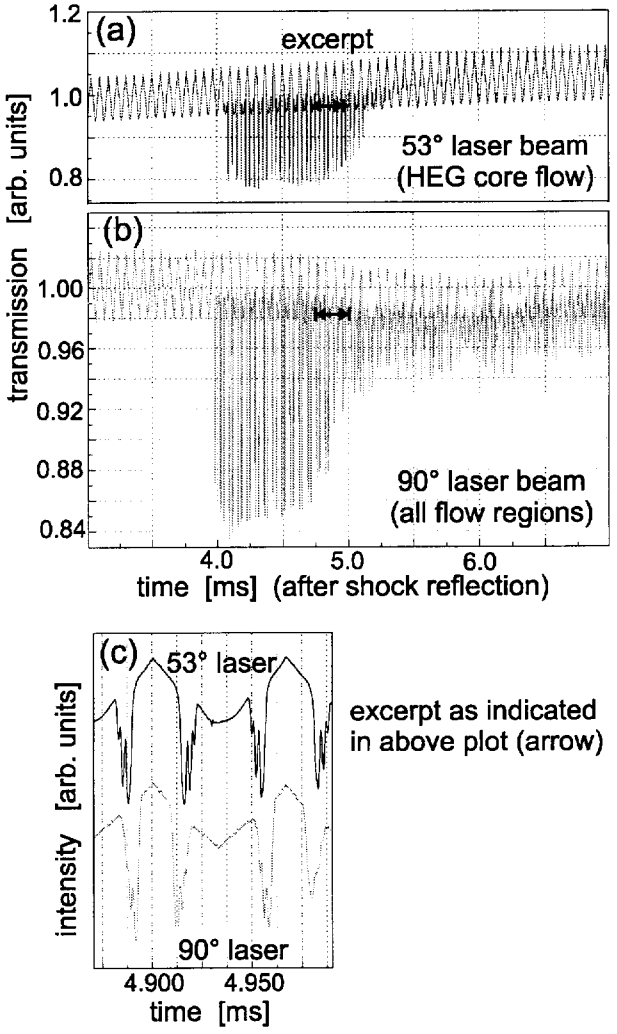


*Fig. 14 Rb absorption spectra in HEG (as in Fig.13), showing Doppler-shifted absorption lines*

*Quantity of seeded species.* The influence of quantity of seeded species can be seen in Fig. 15. Both absorption results (a) and (b) were carried out at the same HEG run condition I, only the quantity of $RbNO_3$ seeded into the flow in the reservoir was different; (a) 0.15 µg , and (b) 2.0 µg. Both absorption axes are plotted to the same scale, allowing a direct comparison. (Pitot pressure traces are shown for reference at the top of (a) and (b).)

Note that in both cases there is little Rb left during the indicated test window.

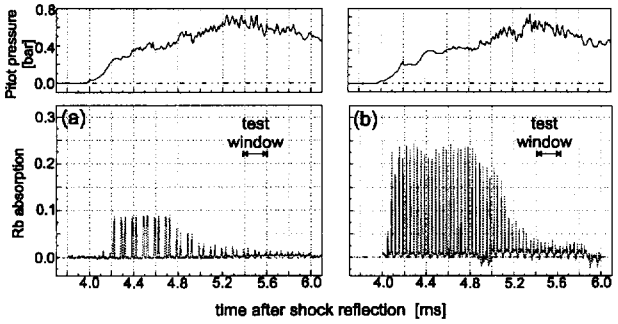


*Fig. 15 Effect of Rb seeding amounts on absorption spectra: (a) 0.15μg; (b) 2.0μg*

*Seeding in shock vs compression tubes.* Fig. 16 compares the result shown in Fig. 15 with 0.15 μg $RbNO_3$ seeded into the reservoir (dark grey trace) with a result where 5.0 μg $RbNO_3$ were seeded into the flow upstream of the diaphragm in the compression tube (light grey). Both shots were at condition I. Both traces have a similar form until about 4.5 ms, after which a new charge of Rb, originating from the compression tube, enters the probed region (light grey trace).

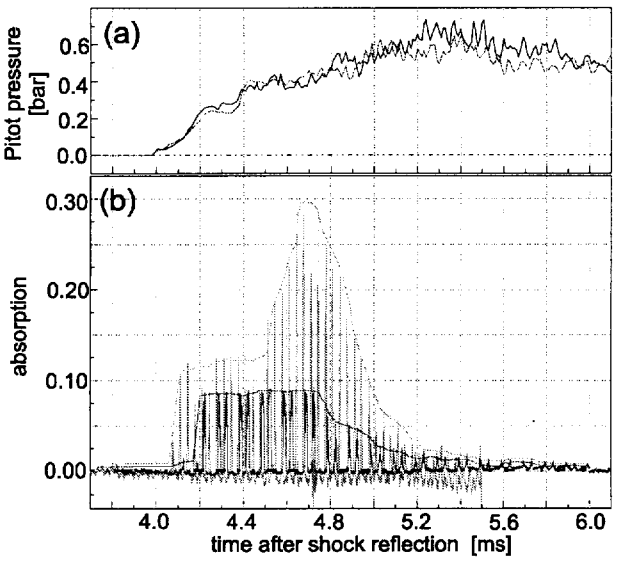


*Fig. 16 Effect of seeding in shock and compression tubes: (a) pressure; (b) absorption*

Since the Rb seeded in the compression tube can only be carried downstream by the helium driver gas, its presence thus signals the arrival of the first He in the test gas at about 4.5 ms. This early arrival of He has since been confirmed by other techniques and by CFD. Furthermore, in both results there are only weak absorption signals at later times, making analysis difficult. The main advantage of the seeding in the compression tube is to spread the Rb (as some compound) through the *whole* shock tube, so that for the following shots the *whole* test gas (air) slug is seeded more or less equally.

## 5.3 Time-resolved absorption measurements in HEG

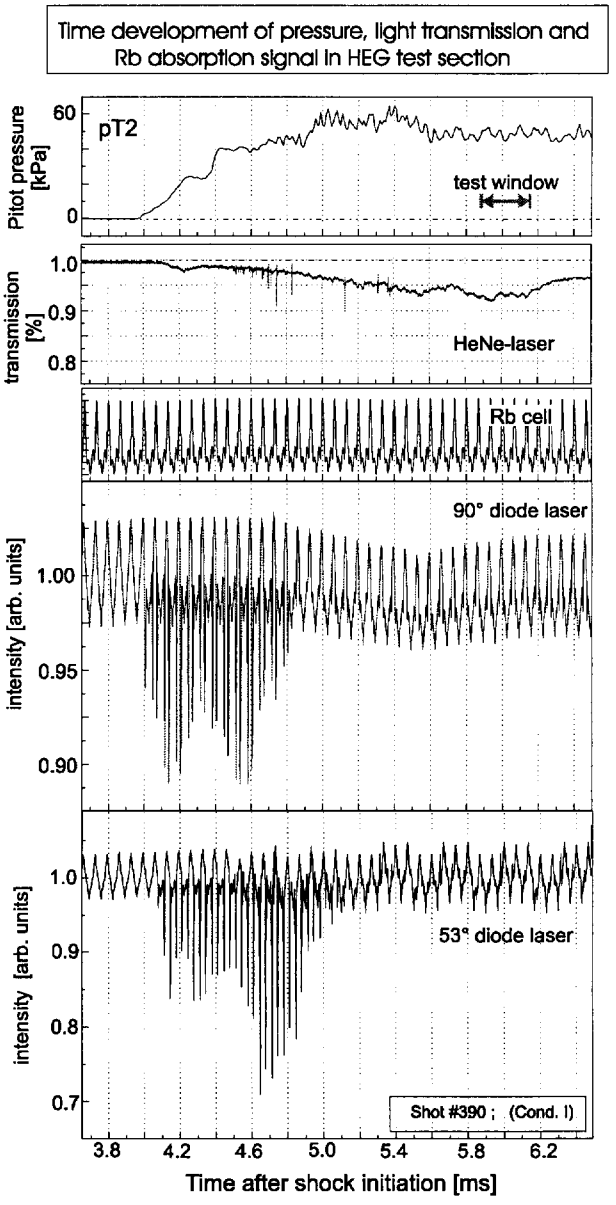


*Fig. 17 Rb absorption in HEG at condition I (see text)*

The time development of Rb absorption in a typical condition I shot, such as will be used later in an analysis for temperature and velocity, is shown in Fig. 17. Plotted from top to bottom are:

Pitot pressure pT2, showing the test window; extinction measurement through the HEG test section using a HeNe laser beam; reference Rb absorption spectrum from the calibration cell; absorption spectrum in HEG with 90° laser beam; absorption spectrum in HEG with 53° laser beam.

Note that for this shot condition there is at most a laser beam extinction of about 7%. This is quite small, but nevertheless the laser diode beam transmission traces need to be corrected for this. At higher shot pressures (conditions II and IV) the extinction is much larger, making the correction more difficult and the result less accurate. (There are no species here that absorb at the HeNe laser wavelength, so that this measured extinction is thought to be due to particulate matter in the flow.)

### 5.4 Determination of line broadening and shifts

*Line broadening.* Two of the many ramps that were shown in Fig. 17 for the 53° laser beam absorption result are shown in Fig. 18(a). Here two absorption spectra are plotted overlapped with zero absorption spectral traces (used for base line correction). For reference, a typical interferometer trace is also shown (used for wavelength linearity check over the ramp). After applying base line and linearity corrections, and converting to a scale in units of absorption, the experimental trace (grey curve) shown in Fig. 18(b) is obtained. A $\chi^2$-fitting procedure with temperature $T_{trans}$ as fit parameter is then used to fit the theoretical (Gaussian) lineshape function, as discussed in chapter 2.2, to the experimental trace. This result is also shown in the figure (dark trace). The resulting temperature is $T_{trans}$ = 1120 ± 300 K; even at these lower temperatures, the method is not very accurate.

*Line shifts.* Even though the 90° laser beam cannot be used to deliver useful temperatures (they represent an average integrated over different flow regions, see Fig. 10), it does however provide a very useful reference for line shifts in the 53° laser beam spectra. Two such absorption spectra from both laser beams (shown in Fig.17) are plotted overlapped on the same axis in Fig. 19.

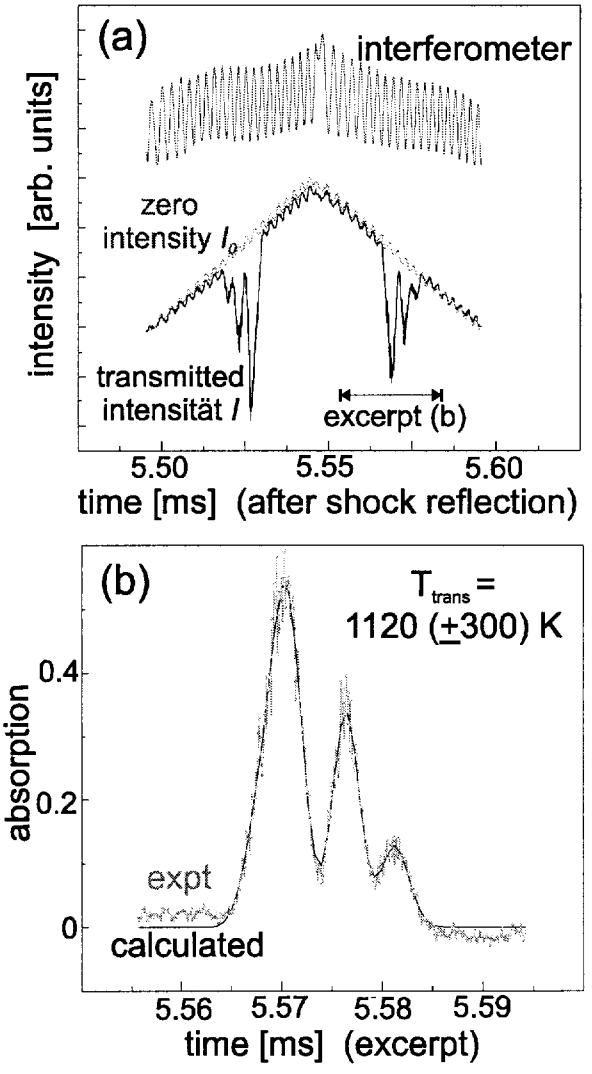


*Fig. 18 Measured single Rb absorption spectra in HEG: (a) Two ramps; (b) comparison with theory*

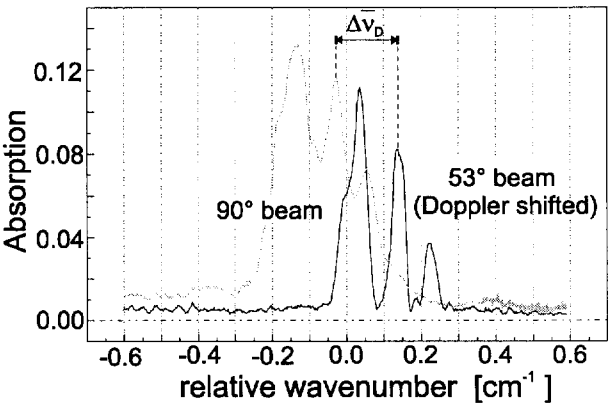


*Fig. 19 Orthogonal and 53° Doppler-shifted Rb absorption spectra in HEG*

The abscissa is in units of line shift in wavenumbers, taken relative to an arbitrary origin. The line shift $\Delta\bar{\nu}_D$ was measured as 0.1638 ± 0.0035 $cm^{-1}$. Using the method outlined in chapter 2.3, a flow velocity of 6370 ± 130 m $s^{-1}$ could be determined.

### 5.5 Accuracy of measurements (goodness of fit)

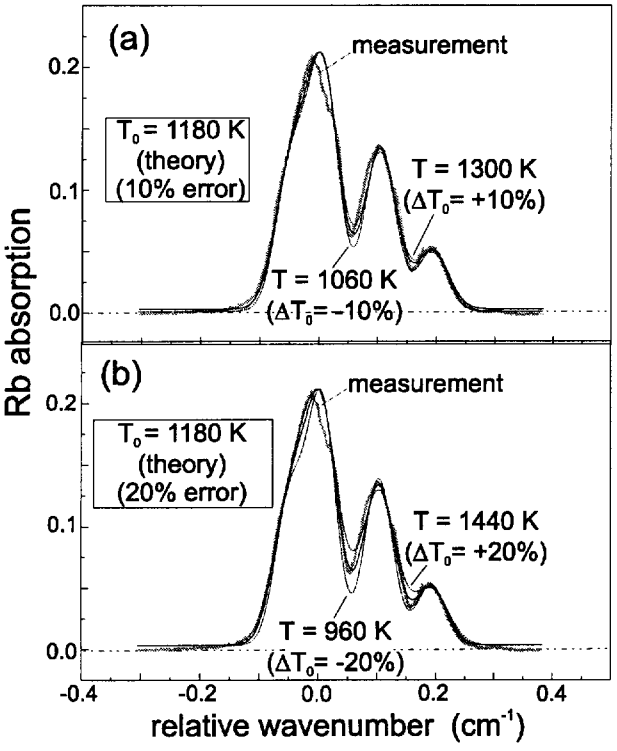


*Fig. 20 Comparison of measured and theoretical absorption spectra in HEG, with temperature ranges of ±10% (a) and ±20% (b)*

The accuracy of the results of temperature and flow velocity presented in chapter 5.4 for a typical spectrum is limited in part due to considerations already discussed beforehand (chapters 2.2 and 2.3). This will be clarified by a few further examples.

Figs. 20 and 21 show measured Rb absorption spectra compared with simulated spectra for temperature ranges of ±10% and ±20% (Fig. 20) and a velocity range of ±5% (Fig. 21). It can clearly be seen that velocity fits are more accurate than temperature fits.

This is further exemplified by the ±5% $\chi^2$ plots for temperature and velocity shown in Fig. 22. Note here also the difference in ordinate scales for temperature and velocity!

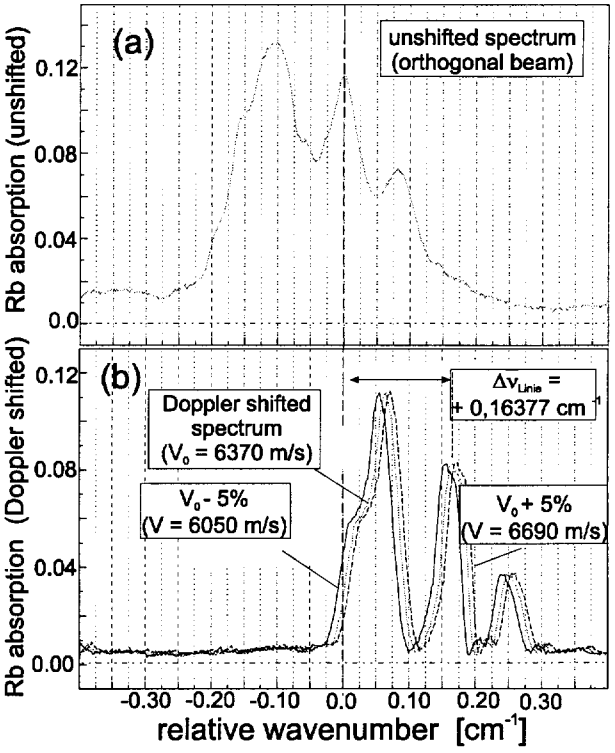


*Fig. 21 Unshifted (a) and shifted (b) measured spectra, compared with theoretical spectrum for velocity range of ±5%*

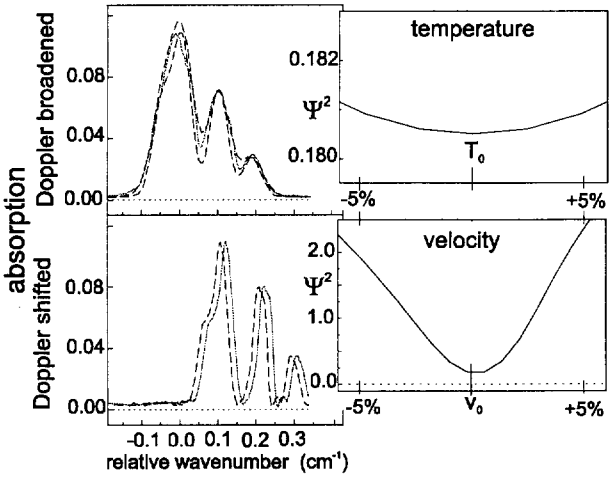


*Fig. 22 $\chi^2$ plots for temperature and velocity, showing relative sensitivity of both*

## 5.6 Temperatures and velocities in the HEG free stream

Fig. 23 shows a comparison between experimental and simulated absorption plots for HEG shot 390 (condition I). The agreement is very good.

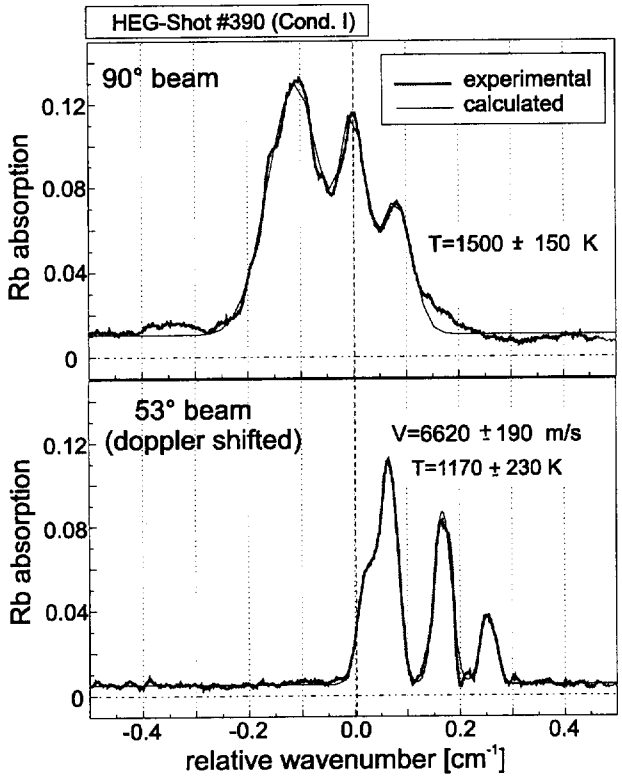


*Fig.23 Comparison of measured and simulated spectra for 90° and 53° beams in HEG*

When all spectra obtained during the duration of the flow test time in shot 390 are analysed in a similar way, one obtains the time-dependent development of temperature and flow velocity, as shown in Fig. 24. From top to bottom are shown: Pitot pressure trace in the test section (for reference, the test window is also shown); Raw absorption trace for the 53° laser beam; Temperature and velocity time profiles for two cases, with and without positioning of a measurement rake in the test section. (These studies were carried out during calibration measurements of the HEG free stream flow using a rake in the form of a cross equipped with pressure and temperature sensors and placed at the nozzle exit - this could lead to some disturbances in the downstream region, over some of which the 53° laser beam passed.)

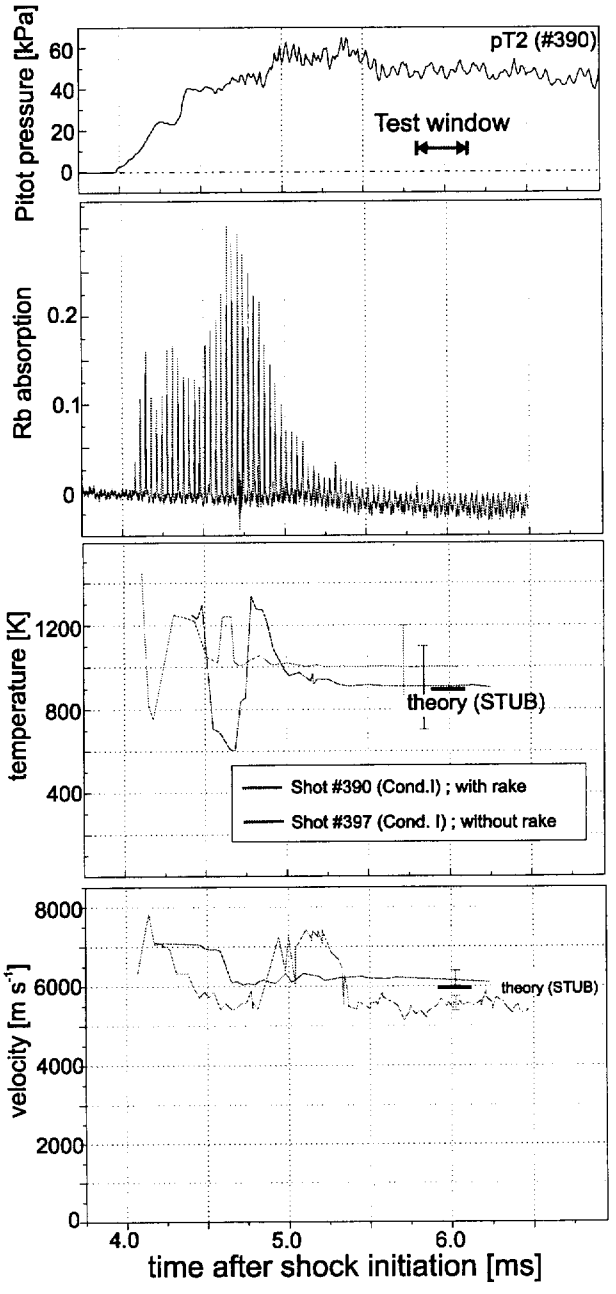


*Fig.24 Time development of temperature and velocity in HEG at condition I*

Values of temperature and velocity calculated using an Euler chemical non-equilibrium code (STUB) for the HEG nozzle flow are also shown. Both temperature and velocity traces show considerable oscillation at early times when the flow is still being established. With the rake, velocities are lower and temperatures are higher. This is as expected if the measurement rake blocks some of the flow. However, there were too few shots carried out with and without rake to be certain of its influence.

The results obtained from all HEG shots (at conditions I, II, IV, V and VI) are summarised in the following table. Shown is the measured value of temperature and velocity, taken as the average value in the time plots over the designated test time window (as shown in Fig. 24) Theoretical values from STUB, and the differences between STUB and measured values are also shown.

| Cond. | $T_{expt}$ (K) | $T_{STUB}$ (K) | $\Delta T$ (%) | $u_{expt}$ (m $s^{-1}$) | $u_{STUB}$ (m $s^{-1}$) | $\Delta u$ (%) |
|---|---|---|---|---|---|---|
| I | 1000 | 807 | +24 | 5600 | 5939 | -6 |
| II | 1410 | 1036 | +36 | 5500 | 6157 | -11 |
| IV | 1100 | 722 | +52 | 3900 | 5148 | -24 |
| V | 1010 | 503 | +100 ! | 4100 | 4382 | -7 |
| VI | 910 | 536 | +70 | 3830 | 4582 | -20 |

Temperature values lie systematically above the theoretical results (in one case, 100%! higher), velocities systematically below. The differences between experiment and theory in the velocities are much less than with the temperatures; this is not unexpected, in view of the discussions on accuracy of this method. Furthermore, the simplified approach taken in the Euler calculations may also be suspect and would definitely be more reliable using a full non-equilibrium (thermal and chemical) Navier-Stokes solution. Since the differences between measured and theoretical results are in the right direction to be explained by the presence of the measurement rake, more results in a non-disturbed free stream are needed.

## ACKNOWLEDGEMENTS

This technique was implemented at HEG initially by Dr. W. Gillespie to look at O atom absorption. The rubidium seeding technique was developed and all subsequent tests in HEG were carried out by O. Trinks in the framework of his Diplom thesis; this thesis forms the basis for this lecture. Financial support of the ESA through CNES for much of the testing is gratefully acknowledged.

## REFERENCES

1. Mohamed A.K., Henry D., Bize D. and Beck W.H. (1998) Infrared Diode Laser Measurements in the HEG Free Stream Flow, *AIAA Paper 98-2870.*

2. Trinks O. and Beck W.H. (1998) Application of diode-laser-absorption technique with the $D_2$ transition of atomic Rb for hypersonic flow-field measurements, *Appl. Optics 37 (30), 1-6.*

3. Eitelberg G. (1993) Calibration of the HEG and its Use for Verification of Real Gas Effects in High Enthalpy Flows, *AIAA Paper 93-5170.*

4. Hannemann K. (1997) *Private communication.*

# Rotational and Vibrational Temperature Measurements in the DLR High Enthalpy Shock Tunnel HEG Using LIF and Flash Lamp Absorption

**W. H. Beck**
Aerothermodynamics Section,
Institute of Fluid Mechanics,
German Aerospace Center (DLR),
Bunsenstraße 10,
37073 Göttingen
Germany

## ABSTRACT

Use of LIF in two line thermometry TLT and of flash lamp absorption to examine high enthalpy flows is presented. The aim is to measure rotational and vibrational temperatures of nitric oxide NO in high temperature air in the Göttingen High Enthalpy Shock Tunnel HEG. Theory of NO (energy levels, spectroscopy, level populations), LIF and TLT are discussed. Results are given from a test cell to validate TLT with NO LIF as a quantitative technique. HEG results for rotational and vibrational temperatures in the free stream and around models are presented. Finally, flash lamp absorption results yielding these temperatures are given.

## 1. INTRODUCTION

High enthalpy flows such as in the High Enthalpy Shock Tunnel HEG of the DLR in Göttingen are characterised by very high temperatures where the test gas (usually air) is dissociated and where the concentrations of the atomic and molecular species may not correspond to those pertaining to the translational temperature of the gas - this is chemical non-equilibrium. Furthermore, the gas may also not be in thermal equilibrium, i.e. internal temperatures (electronic, vibrational and in some cases even rotational temperatures) may be different from each other and from the translational temperature. In the worst case, the levels may not be occupied according to a Boltzmann distribution, so that an internal temperature is not even defined. To examine and understand the properties of such gases, it is no longer adequate to measure just bulk properties such as pressure or temperature; one must examine the gas at its molecular level, and preferably using a technique which is non-intrusive and does not influence or alter the gas propereties. Laser induced fluorescence LIF is such a technique. It has the further advantage of enabling 2D spatially resolved measurements of temperatures, as opposed to other techniques which measure line of sight (absorption techniques) or at a point (CARS).

A common component of high temperature air is nitric oxide NO. In HEG it is present up to levels of 10%. NO is a species which is quite well studied and understood (its energy levels, spectroscopy), and is well suited to LIF and absorption studies. This lecture will deal with basic theory of the NO molecule - its structure, energy levels, level populations, spectroscopy and its use in two line thermometry TLT using LIF. Although this theory is universal, pertaining not only to LIF work, it will be presented with mainly this aim in mind. Experimental apparatuses for LIF (laser apparatus, test cell) and the facility HEG will be described. Emission spectra in HEG are shown to prepare the way for use of planar LIF (PLIF) around models in the gas flow. A discussion of detailed experiments in a heated test cell containing NO, necessary to establish the requirements for quantitative TLT, follows. HEG LIF results are presented in two groups: LIF measurements of rotational and vibrational temperatures in the HEG free stream, and in flows around models (HERMES, cylinder, sphere, blunted cone, HOPE). Finally, results using flash lamp absorption in the HEG will be presented.

*Paper presented at the RTO AVT Course on "Measurement Techniques for High Enthalpy and Plasma Flows", held in Rhode-Saint-Genèse, Belgium, 25-29 October 1999, and published in RTO EN-8.*

## 2. THEORY

This chapter will overview some important theoretical concepts concerning the energy levels and spectroscopy of the NO molecule, the laser induced fluorescence technique and its use to determine internal (rotational and vibrational) temperatures via two line thermometry TLT. It will and cannot be an exhaustive overview, but rather will summarise the basics (there are several texts and literature references given in Ref. 1 which go into far greater detail). Above all, an attempt will be made to stress those points which are important in applying TLT to high enthalpy flows.

### 2.1 The NO molecule

The linear combination of atomic orbitals approach to forming the molecular orbitals (MO) of NO leads to an electron configuration in the electronic ground state (GS) where the last (outermost) electron resides in an anti-bonding $\pi^*_{(g)}$ molecular orbital. This is a single unpaired electron, so that the multiplicity of the GS is 2. The promotion of this electron can occur to higher (in energy) MO's, for example through absorption of a photon of light. The excited NO molecule can relax back to its GS via several processes, including emission of a photon of either the same or lower energy (fluorescence); all these processes are important in using LIF for TLT, and will be discussed later.

When an electron is boosted to a higher electronic level, it is also possible for the molecule to experience a change in its rotational and vibrational energies. (All internal energy changes are subject to certain selection rules, which arise out of parity and symmetry considerations pertaining to dipole transitions.) The energy of the molecule, or rather the energy change following a particular transition, can be broken down into electronic n, vibrational v and rotational J components - the so-called term energies T(n,v,J). Each state of the molecule, and its term energy, are uniquely defined by so-called quantum numbers, numbers which arise out of the wave function solutions (eigen functions) of the Schrödinger equation.

It is customary to represent pictorially these term energies, including the vibrational (and rotational) manifolds, in a potential energy level diagram such as in Fig. 1 for NO (see Ref. 1).

Here the energy (in units wavenumbers $cm^{-1}$, 1 ev ≡ 8067 $cm^{-1}$) of the level is plotted against internuclear separation (in Angstroms Å, 1 nm ≡ 10 Å) between N and O atoms in the molecule. The various electronic states are given term symbols, starting with X for the GS, and then A, B, C, ... for the higher lying states. Each electronic energy level is represented by either direct or projected quantum numbers, and given either a Greek symbol or value; e.g. the GS $^2\Pi^+_{mJ}$ has total spin ½, therefore multiplicity 2, total orbital angular momentum L = 1, hence Π state, and a projection of the summed orbital and spin quantum numbers $m_J$, with values of 1/2 or 3/2.

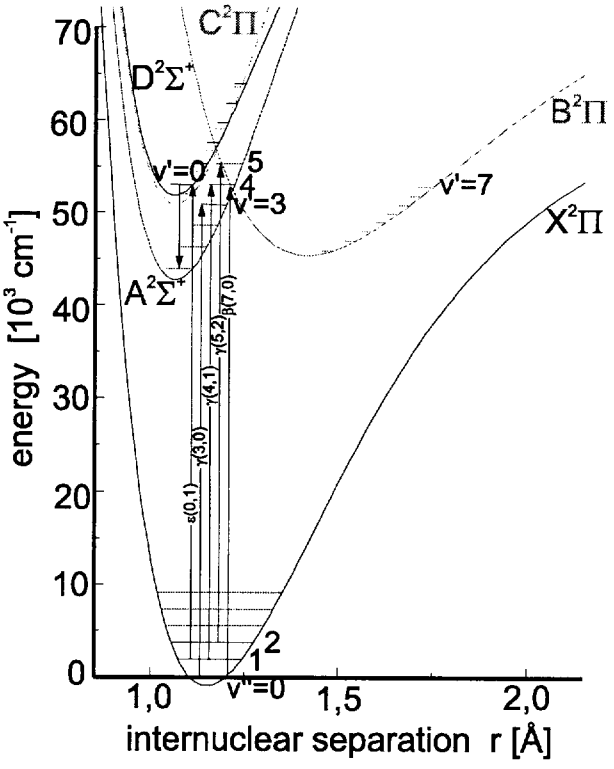


*Fig.1 Potential energy level diagram for NO.*

The above picture considers only the electronic, and not the rotational energy levels; there exists a coupling between the nuclear rotation and the electron movement, leading to a further splitting of the energy levels, the so-called Λ-splitting. Hence, when considering transitions from a particular

rotational level in the GS, they can arise from four energy levels, each having a (sometimes only slightly) different energy. Selection rules for rotational transitions allow only quantum number changes $\Delta J$ of -1, 0, +1 ($J \neq 0$), and only transitions to states of opposite parity, so that in all 12 separate transitions (spectral lines) to a $\Sigma$-excited state (where $m_J = 0$) can arise from one GS rotational level. This can be seen in Fig. 2. Of the four major NO electronic energy levels, X, A, B. C and D, as shown in Fig.1, only the X, A and D will be of main interest here. Whereas the vibrational energy levels (v = 0, 1, 2,....) are shown, the rotational manifolds (see Fig. 2) superimposed on each vibrational level, with their even smaller energy spacings, are not shown.

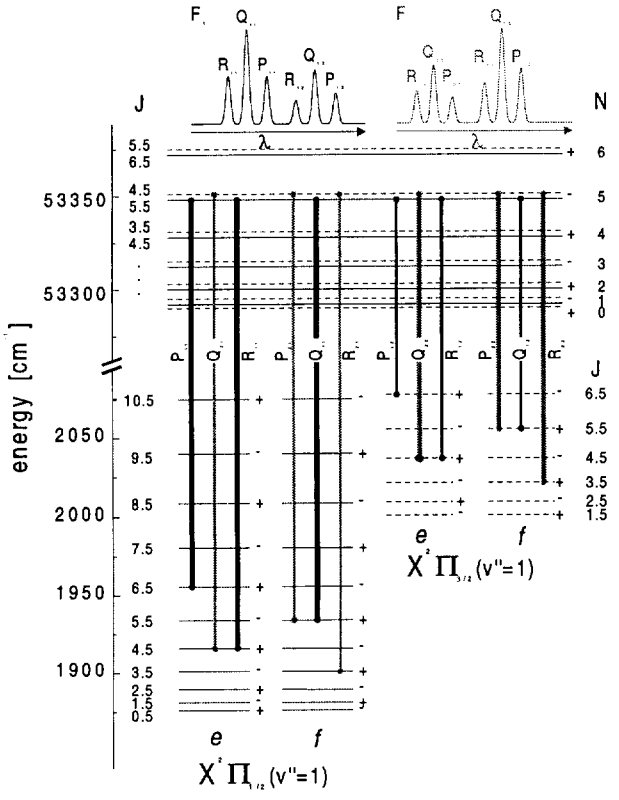


*Fig. 2 $\Sigma \leftarrow \Pi$ transitions in NO, showing 12 branches.*

Transitions between the states D ← X and A ← X are given designations $\varepsilon$ and $\gamma$, respectively, with the upper and lower vibrational quantum numbers v being given in brackets; e.g. $\varepsilon(0,1)$ refers to the transition between the X ground state, v = 1, to the excited state D, v = 0. No information regarding the change in rotational quantum number J is included yet. This is represented as $\Delta J_{F,F'}(J")$, where $\Delta J$ = -1, 0 or +1 (see before) is represented by the letter P, Q or R, F' and F" represent the two $m_J$ values 1/2 and 3/2, respectively, and J" represents the rotational level in the GS from which the transition arises. (The energy levels and transitions of NO are summarised in some more detail in ref. 1, where literature references can be found.) The two laser-excited transitions used for the LIF to be discussed later are $\varepsilon(0,1)$ $R_{22}(27.5)$ and $\varepsilon(0,1)$ $(R_{21}(17.5) + P_{11}(35.5))$; whereas the first transition is a single line, the second is an overlap of two lines which can lead to errors at temperatures above 1000 K, if not properly accounted for - see later. In the case of flash lamp absorption, where both low resolution vibrational bands (rotational envelopes) and high resolution rotationally-resolved lines are measured from broadband absorption experiments, vibrational transitions (0,0), (1,0) and (0,1) and low-lying rotational levels ($J \approx 4.5$) are involved.

## 2.2 Thermal populations

Given that thermal equilibrium between the electronic, vibrational and rotational levels exists, the fraction f of the total population in a given energy level |n,v,J> is given by:

$$f(n,v,J,T_{int}) = g_n \frac{g_{rot}}{Q(T_{int})} e^{-\left[\frac{T(n,v,J,T_{int})}{kT}\right]}$$

where $g_n$ is the electronic degeneracy, $g_{rot}$ the rotational degeneracy (= 2J + 1), k Boltzmann's constant, $Q(T_{int})$ the total partition function and $T_{int}$ the internal temperature, so called to distinguish it from the translational temperature $T_{trans}$, which may or may not be the same - see later. Hence, for a given known molecule with known properties and energy levels, the thermal distribution can be represented by just one variable, the temperature $T_{int}$. For the case of the rigid rotor, the term energy can be split into a sum of electronic, vibrational and rotational components and the partition function into a product of components from these modes. The fraction f can be redefined as:

$$f(n,v,J,T_{el},T_{vib},T_{rot}) =$$

$$g_n(2J+1)\frac{e^{-\left[\frac{T_{el}(n)}{kT_{el}}\right]}}{Q(T_{el})}\frac{e^{-\left[\frac{T_{vib}(v)}{kT_{vib}}\right]}}{Q(T_{vib})}\frac{e^{-\left[\frac{T_{rot}(J)}{kT_{rot}}\right]}}{Q(T_{rot})}$$

Hence, as can be seen from the above equation, it is possible that $T_{el}$, $T_{vib}$ and $T_{rot}$ are different, and also different from $T_{trans}$. However, the existence of a temperature as a variable requires a Boltzmann distribution - no Boltzmann distribution, no temperature defined! All spectroscopic methods used to determine internal temperatures rely on this assumption. Given that it holds, one can also see how to measure internal temperatures - measure the population in two different (e.g. rotational) levels, from which the (e.g. rotational) temperature can be determined.

To see how these populations change as a function of temperature can best be seen using two examples for NO, one for vibrational and one for rotational population distributions. Fig. 3 is a plot of fraction of vibrational level population (normalised to v = 0 at 300 K) plotted against temperatures up to 6000 K.

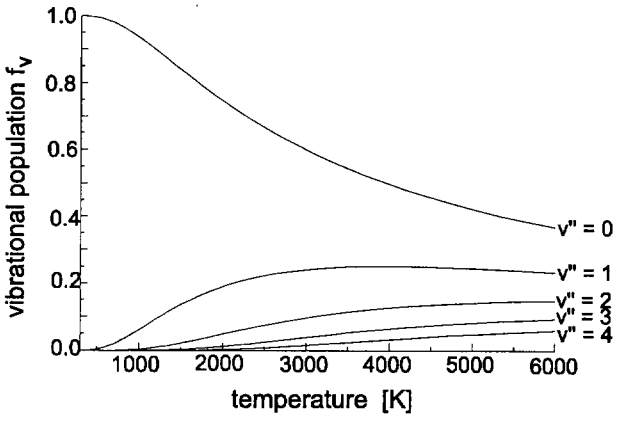


*Fig. 3 Vibrational population fraction $f_v$ for various NO vibrational levels as a function of temperature.*

At HEG free stream temperatures of less than about 1100 K, one can see that only levels v = 0 and 1 are substantially populated. In fact, the aforementioned ε-bands arise from v = 1, so that these transitions cannot be used at temperatures below about 600 K. Behind shocks in HEG temperatures can be as high as 9000 K, but at these high temperatures one sees another problem, which is best exemplified by the following: if one measures populations in levels, say, v = 2 and 3 at temperatures around 5000 K, one can see that the ratio of the populations in these levels is quite temperature insensitive. Or put another way, the demands on accuracy in measuring these populations are very high.

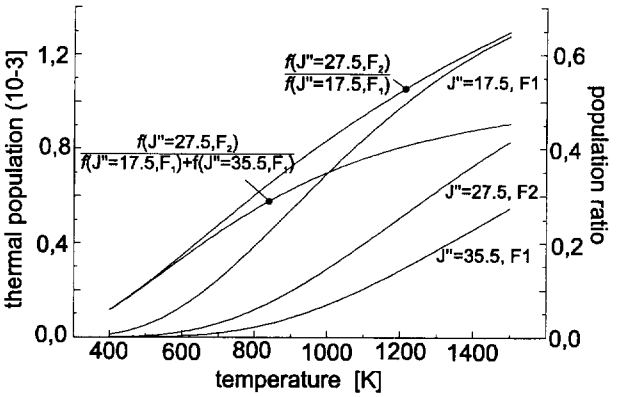


*Fig. 4 Rotational population fractions and ratios for two NO rotational levels as a function of temperature.*

The second example, shown in Fig. 4, is a plot of population fraction of the two NO rotational levels J" = 17.5 and 27.5 discussed in chapter 2.1 (and of the level J" = 35.5) against temperatures up to 1500 K. Also plotted are the ratios of the two populations with and without consideration of the J" = 35.5 level ($f_{27.5}/(f_{17.5}+f_{35.5})$ and $f_{27.5}/f_{17.5}$, respectively).

Neglecting the contribution from J" = 35.5, one can estimate from the ratio $f_{27.5}/f_{17.5}$ the accuracy of rotational temperature $T_{rot}$ determination: taking the ratio for the case $T_{rot}$ = 1000 K, and assuming an error in ratio measurement of 10% (quite good for single shot measurements - see later), one obtains an error in $T_{rot}$ of about 7%. Hence, these two transitions, based on only this criterion, are quite good for measurements at around 1000 K, although it is clear from Fig. 4 that the J" = 35.5 contribution cannot be neglected at higher temperatures. These matters will be further discussed in chapter 2.4.

## 2.3 LIF - two and three level approaches

The method whereby one obtains the abovementioned level populations needs to be looked at more closely. This is best done using the two level LIF model: in brief, a laser is used to excite NO from a lower level to an excited state, from whence a measurement of the intensity of re-emitted fluorescence can be related to the original population in the ground state. The requirements for this to apply, and the complications that may arise, will be discussed here briefly. Fig. 5 shows a two level system involving two states |1> and |2>, representing (v,J) levels in the NO X and D electronic states, respectively

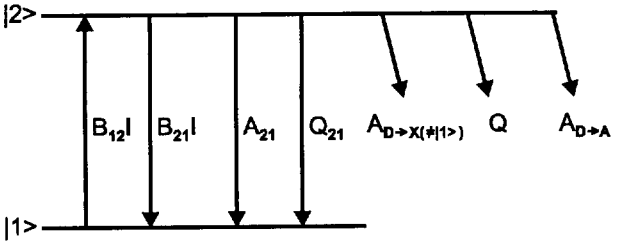


*Fig. 5 Two-level LIF model for NO.*

In the case of weak laser excitation, where the fluorescence signal $F_{lin}$ is proportional to laser intensity, one can write (see ref. 1, and references therein):

$$F_{lin} = B_{21} E^{las} g N f \frac{A_{21}}{A_{21} + Q_{21}},$$

where where $B_{21}$ and $A_{21}$ are Einstein coefficients for stimulated and spontaneous emission from state |2> to |1>, respectively, $Q_{21}$ is the radiationless channel for level |2> de-population, $E^{las}$ is the laser energy, g is the spectral overlap integral for absorption (representing the coincidence and bandwidths of spectral transition and laser - $g = g(\nu_{abs}, \Delta\nu_{abs}, \nu_{las}, \Delta\nu_{las})$), N the NO density and f the Boltzmann fraction for the lower level. The term

$$q_F = \frac{A_{21}}{A_{21} + Q_{21}}$$

is called the quantum yield, and lies between 0 and 1, depending on how strongly the fluoresence radiation is reduced (quenched) by other processes. In the two level model, $Q_{21}$ in the above equation actually represents all processes not leading to re-emission back to level |1>, viz. $Q_{21}$, $A_{D\text{-}X(\neq|1>)}$, Q and $A_{D\text{-}A}$ in Fig. 5.

In the LIF experiments fluorescence signals $S_f$ are recorded using either image-intensified cameras or photomultipliers. $S_f$ is related to $F_{lin}$ by

$$S_f = F_{lin} V \eta \frac{\Omega}{4\pi},$$

where V is the measurement volume, $\eta$ is the detection sensitivity (gain, filter losses, etc.) and $\Omega/4\pi$ is the detection solid angle.

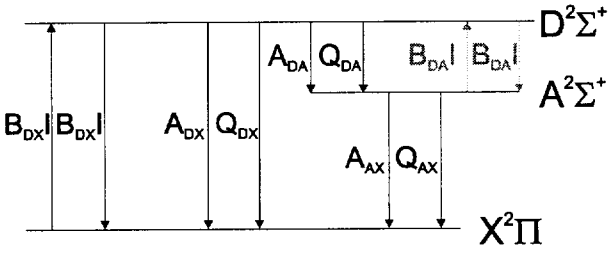


*Fig. 6 Three-level LIF model for NO.*

The proximity of the NO A state to the D state, shown in Fig. 1, complicates the situation, since it is also involved in energy transfer and removal processes - $A_{D\text{-}X(\neq|1>)}$, and $A_{D\text{-}A}$ - which influence the proportionality of fluorescence signal to level population. A three level system including the NO A state is shown in Fig. 6.

Here all processes for populating (absorption $B_{DA}I$) and depopulating (spontaneous emission $A_{DA}$, stimulated emission $B_{DA}I$ and collisional quenching $Q_{DA}$) the upper D state, and also corresponding processes between the A and X states (spontaneous emission $A_{AX}$ and quenching $Q_{AX}$) need to be considered. Furthermore, at higher laser power densities and higher NO densities, a particularly efficient process called amplified spontaneous emission ASE provides an efficient channel for energy removal from the D state. (This process arises from the strong pumping of the D state, leading to a population inversion between D and A states, which produces an amplification of D $\rightarrow$ A transitions in the direction of the D $\leftarrow$ X

pump laser beam.) Clearly all this can become quite complex if all processes occur, but on the other hand, if one is not aware of them, using LIF to do quantitative TLT can lead easily to erroneous results.

### 2.4 Two line thermometry TLT

To determine temperatures, fluorescence signals $S_f$ arising from excitation from two different lower energy levels |1> and |2> are measured, e.g. using the transitions $\varepsilon(0,1)$ $R_{22}(27.5)$ and $\varepsilon(0,1)$ ($R_{21}(17.5)$ + $P_{11}(35.5)$) one would obtain a rotational temperature. A ratio of energy and wavelength corrected signals is formed:

$$R = \frac{S_{f,1} / E_1^{las} g_1}{S_{f,2} / E_2^{las} g_2} = \frac{B_{21,1} N f_1(E_1,T) V_1 \eta_1 \frac{\Omega_1}{4\pi} q_{F,1}}{B_{21,2} N f_2(E_2,T) V_2 \eta_2 \frac{\Omega_2}{4\pi} q_{F,2}}$$

Cancelling, grouping together temperature-independent constants (molecular and apparatus constants) and assuming there is no quantum level dependence of quenching ($q_{F,1} = q_{F,2}$) leads to

$$R = c\, e^{-\frac{\Delta E}{kT}},$$

where $\Delta E = E_2 - E_1$ is the energy separation of the two states from which excitation occurred. To obtain the temperature T, a calibration measurement in a test cell at known NO concentration and temperature $T_{cal}$ and using the same experimental setup as for HEG is carried out: $R_{cal} = c e^{-(\Delta E/kTcal)}$. Setting the value $T_0$ for the characteristic temperature of the two states ($T_0 = \Delta E/k$), one obtains the measured temperature T:

$$T = \left\{ \frac{1}{T_{cal}} - \frac{1}{T_0} (\ln R - \ln R_{cal}) \right\}^{-1}.$$

For the case that $T_{vib} \neq T_{rot}$, the expression for R becomes

$$R = c\, e^{-\frac{\Delta E_{vib}}{kT_{vib}}} e^{-\frac{\Delta E_{rot}}{kT_{rot}}}.$$

If one temperature is known, the other can be determined in a measurement as described above.

One needs to ask the question: under which conditions and with which assumptions do the above equations apply when carrying out single shot TLT in high enthalpy flows? They are:

1. *Linear fluorescence* - requires laser excitation to be weak.
2. *No unaccounted-for loss processes* - mass balance between the two levels must apply: $N_1+N_2$=constant.
3. *No RET* - rotational energy transfer (RET) in the ground state, falsifying the required thermal population, must be low (this needs be considered behind strong shocks in HEG).
4. *Rotational dependence of quantum yields* - should not exist, or must be known and quantified.
5. *Laser pulse time form* - should be as near to rectangular as possible (does not apply fully to the ArF excimer lasers used in HEG).
6. *Fluorescence reabsorption* - in the path through the HEG test gas from excitation volume to the detection system must be negligible (hence any fluorescence ending in the v = 0 level of the X ground state must be suspect).
7. *Laser beam absorption* - from the HEG test section window to the excitation volume must not occur (exciting the ε-bands originating from v = 1 reduces this problem, but even v = 1 becomes populated at T > 600 K - see Fig. 3).
8. *Calibration cell conditions* - must be such that the calibration results can be carried over and used for comparison with the HEG results.
9. *Boltzmann distributions* - must exist! This assumption is the crux of both LIF and flash lamp absorption measurements.

The sensitivity of TLT is given quite simply by

$$\frac{\Delta T}{T} = \frac{T}{T_0} \frac{\Delta R}{R} = \frac{T}{1310} \frac{\Delta R}{R},$$

where the value $T_0$ = 1310 K has been inserted for the two rotational levels J" = 17.5 and 27.5 for the transitions $\varepsilon(0,1)$ $R_{22}(27.5)$ and $\varepsilon(0,1)$ $R_{21}(17.5)$. One sees immediately that at temperatures above about 1000 K the relative accuracy of the ratio R measurement approaches that of the temperature sensitivity, so that, for a 5% temperature accuracy, one needs an accuracy of 5% in R or about 3-4% in $S_f$. This is not difficult in cases where signal averaging can be used, but for single shot work as

in HEG where the short test time of 1 ms allows only one laser shot from each of the two lasers, this is most demanding. A general requirement for greater temperature sensitivity arises out of the above: $T << T_0$. This is desirable, but, as in the case of HEG (see later), not always possible to achieve.

## 3. EXPERIMENTAL TOOLS

### 3.1 The High Enthalpy Shock Tunnel HEG

The HEG is a free-piston driven shock tunnel operating in the reflected shock mode. It has been described in greater detail elsewhere (ref. 2). As shown in Fig. 7, a reflected shock creates high temperature and pressure conditions in the reservoir (before the nozzle entrance), after which the test gas expands through the nozzle to deliver the free stream conditions in the test section. The test time is about 1 ms. Also shown in Fig. 7 are nominal conditions which have been calculated using a non-equilibrium Euler code for the free stream and the reservoir - these conditions apply to the old contoured nozzle in HEG, with which most of the LIF testing was carried out. Conditions I and III are low pressure, with high and low specific enthalpy, respectively, and II and IV are high pressure, also with respective high and low enthalpies. Free stream temperatures are calculated to lie between about 500 and 1100 K and NO concentrations are quite high, lying between about 1 and 8 x $10^{15}$ $cm^{-3}$.

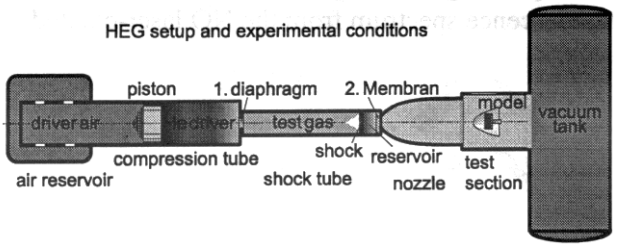


Nominal conditions for the contoured nozzle

| Conditons | | I | II | III | IV |
|---|---|---|---|---|---|
| $p_0$ | [MPa] | 40 | 90 | 45 | 110 |
| $T_0$ | [K] | 9100 | 9700 | 7300 | 8100 |
| $T_\infty$ | [K] | 790 | 1040 | 550 | 720 |
| $h_0$ | [MJ/kg] | 21 | 22 | 13 | 15 |
| $u_\infty$ | [km/s] | 5,9 | 6,2 | 4,8 | 5,1 |
| N2 | [$10^{15}cm^{-3}$] | 26,1 | 56,6 | 44,0 | 95,6 |
| O2 | [$10^{15}cm^{-3}$] | 1,1 | 4,3 | 7,6 | 18,0 |
| NO | [$10^{15}cm^{-3}$] | 1,1 | 3,0 | 3,9 | 8,4 |

*Fig. 7 The High Enthalpy Shock Tunnel HEG.*

### 3.2 The heated calibration and test cell

A special NO-containing test cell was designed and constructed to carry out NO spectroscopy measurements, to check the various assumptions and approximations in using TLT, to carry out time resolved measurements on NO quenching and to check imaging techniques when using 2D spatially resolved PLIF (Planar LIF). Several design criteria had to be met: 1. Temperatures encompassing the HEG free stream range - the cell can be heated up to 1300 K, 2. NO concentrations as in HEG free stream, and even lower to check quench-free conditions; 3. Optical access through large windows to permit laser beam traversal and imaging of 2D LIF signals using image intensified CCD cameras (ICCD's); 4. A flow system to ensure NO in the test volume is replenished regularly; 5. Appropriate gas path and sizing to make sure the gas temperature is as high as the heated ceramic tubing (where the thermoelement temperature is measured) and is homogeneous; 6. Design of cell geometry to enable it to be placed in the HEG test section for LIF calibration purposes. (5. is difficult at very low NO pressures.) The test and calibration cell is shown in Fig. 8 in position in the HEG test section.

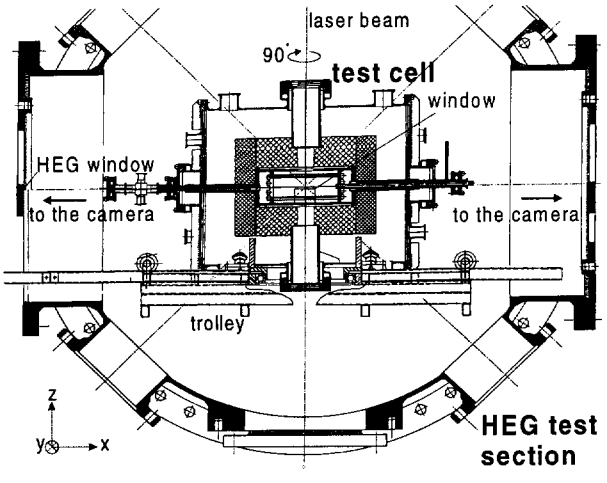


*Fig. 8 Calibration and test cell shown installed in the HEG test section.*

The view is shown in flow direction in HEG. The cell is introduced via a trolley into the test section and rotated 90° so that both windows face the test section openings left and right. Laser beams enter top and bottom. More details on the test cell are to be found in Ref. 3.

### 3.3 The LIF laser apparatus for HEG

The LIF apparatus, as used on HEG, is shown in Fig. 9. (It is described in more detail in Ref. 1.)

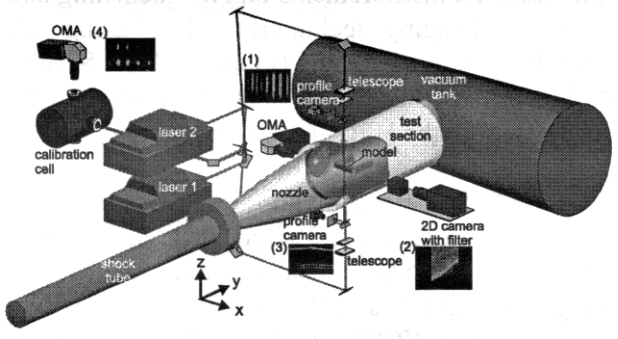


*Fig.9 The HEG LIF apparatus.*

Two formed (e.g. as sheets) laser beams from tunable ArF excimer lasers, operating at a wavelength tunable in the range around 192.9 - 193.9 nm, counter propagate through the test section in the vertical direction. Some percentage of each beam is split from the main beam and diverted into the calibration cell for spectroscopy checks and calibration purposes. A small proportion of each beam is also split off and recorded on an energy monitor (CCD camera). The lasers are thereby tuned to appropriate NO transitions and are fired one after the other with a small time delay (~µs), and the ensuing fluorescence is imaged with a UV lens either directly onto an ICCD for 2D fluorescence images or onto the slit of a spectrometer coupled to an ICCD (functioning as an optical multichannel analyser OMA) for spectrally resolved images (see images (2) and (1), respectively, in Fig. 9).

### 3.4 The LIF laser apparatus for the test cell

Much testing of TLT for HEG was carried on an HEG mock-up, consisting of the calibration cell discussed in chapter 3.2 representing HEG and a further simpler test cell as calibration and reference cell. Energy momitors, as described in chapter 3.3, are also installed here. The setup with just one laser is shown in Fig. 10.

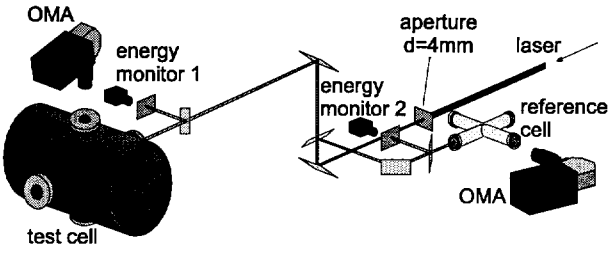


*Fig,10 The LIF apparatus for tests in the calibration cell.*

### 3.5 Filter for LIF measurements behind shocks

The captured NO fluorescence signals after laser excitation at ~193 nm extend over a UV wavelength range of about 193 - 300 nm. To reduce influences in HEG from emission behind shocks (see chapter 4), it was necessary to have special optical filters made which are tunable over a small range in the deep UV, have high suppression factors (~$10^6$) and avoid fluorescence signal distortion so that imaging can be carried out. The compound filters consist of four reflection interference filters in a configuration as shown in Fig. 11; by varying the angle α over the range 30 to 50°, the reflection band width profile shifts as shown the figure, lower left. The corresponding change of the measured fluorescence spectrum from the NO laser-excited

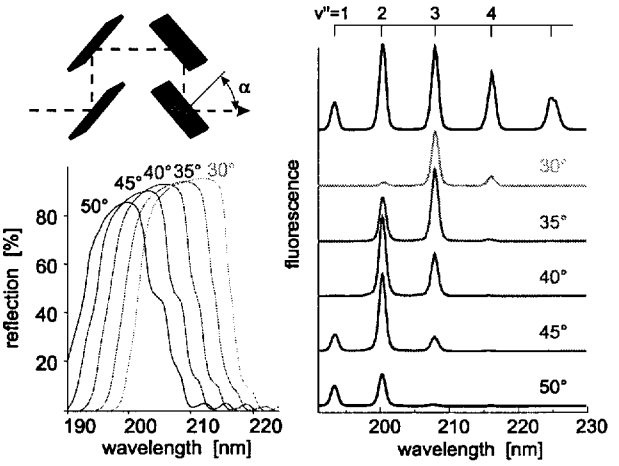


*Fig.11 Filter to reduce background radiation in HEG LIF measurements.*

transition $\varepsilon(0,1)$ $R_{22}(27.5)$ for these filter angles can be seen to the right of the figure.

## 4. EMISSION SPECTRA IN HEG

The gas temperature in the shock-heated region in front of a cylinder at enthalpies of 22 MJ $kg^{-1}$ can be as high as 9000 K. The gas radiates very strongly. To examine this emission, and to ascertain what needs to be done to carry out LIF in this difficult region, emission spectra in front of a cylinder in an $N_2$ flow were measured over a set of HEG runs at high enthalpy. The spectra were normalised and packed together to give a composite emission spectrum over the total wavelength range of 180 - 850 nm. This measured spectrum is shown as 1 in Fig. 12.

Superimposed (2) is the NO fluorescence spectrum shown in Fig. 11 (not to scale), with an arrow (↓) indicating the excitation wavelength. One can see that at wavelengths above about 220 nm the emission is so strong that it would make extracting NO fluorescence signals nigh to impossible. The role of the filters discussed in chapter 3.5 and shown in Fig. 11 is to suppress substantially this emission above about 220 nm.

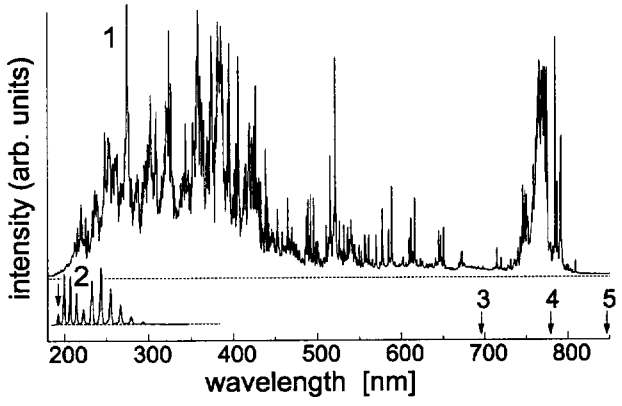


*Fig.12 Emission spectrum (1) of radiating gas behind the shock in front of a cylinder in a high enthalpy $N_2$ flow in HEG. An unscaled NO fluorescence spectrum is shown for comparison.*

If one can identify the source of the profuse emission seen in Fig. 12 between about 220 and 600 nm, one may be able to reduce it. Fig. 13 (upper trace, 1) shows an excerpt from the spectrum in Fig. 12 over the wavelength range of 350 - 390 nm. Shown below are calculated spectra for iron FeI and FeII species at temperatures of 6000 (2a), 9000 (2b) and 12000 K (2c).

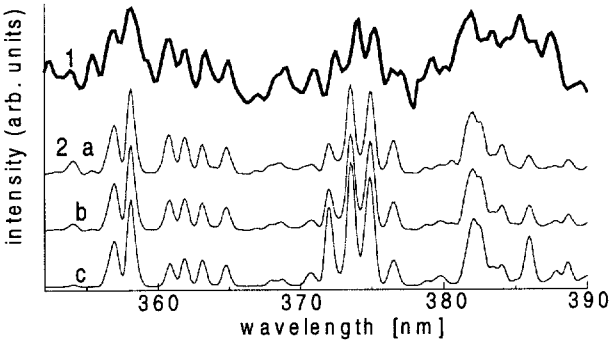


*Fig.13 Measured emission spectrum (1) compared with calculated Fe spectra at different temperatures: 2a. 6000 K; 2b. 9000 K; 2c. 12000 K.*

The coincidence of line wavelengths is quite good (e.g. 355 - 365 nm; 370 - 377 nm), but there are clearly unidentified lines still present (e.g. 379 nm; 388 nm). The relative insensitivity of the calculated spectra to vast changes in temperature suggests that the technique of emission spectroscopy is not suited to temperature determination in these shock heated gases. The abundance of Fe lines is not surprising; in *any* hypersonic facility at high enthalpies there is ablation of material (in HEG in the shock tube), which is carried by the gas flowing through the nozzle and into the test section. The presence of this material in the flow is an unavoidable evil in shock tunnels, making optical work difficult (depending on wavelength) and affecting heat transfer measurements at high reservoir pressures. The effect can be reduced somewhat by using other materials than steel (the source of Fe), such as copper alloys, but generally it can't be fully removed and has to be contended with.

## 5. LIF RESULTS FROM THE TEST CELL

The spectroscopy of NO after laser excitation at 193 nm and most of the assumptions and approximations discussed in chapter 2.4 on TLT

have been exhaustively studied using an experimental setup as shown in Fig. 10. All this work will be exemplified by a few cases to be discussed here; much more detail is to be found in Ref. 1.

### 5.1 NO spectroscopy

A glance at the NO molecular energy levels in Figs. 1 and 2 shows that excitation at 193 nm is quite complex. Indeed, over the tuning range of the ArF excimer laser (~193.9 - 192.9 nm ≡ 51575 - 51850 $cm^{-1}$), some 400 transitions have been observed and identified in LIF measurements in the test cell (Ref. 1). Excitation spectra measured at temperatures 300, 500, 700 and 1000 K are shown in Fig. 14. At temperatures below 500 K only the v=0 vibrational state is appreciably populated, so that the β(7,0) (and γ(3,0)) transitions predominate. Above 500 K the ε(0,1) and γ(4,1) (and at even higher temperatures even γ(5,2)) transitions become stronger.

The transition line strengths for the ε-bands are about 10x stronger than either the β- or γ-bands, making them a logical choice for single shot work in HEG. (Their disadvantage lies in their quicker saturation at moderate laser power densities.)

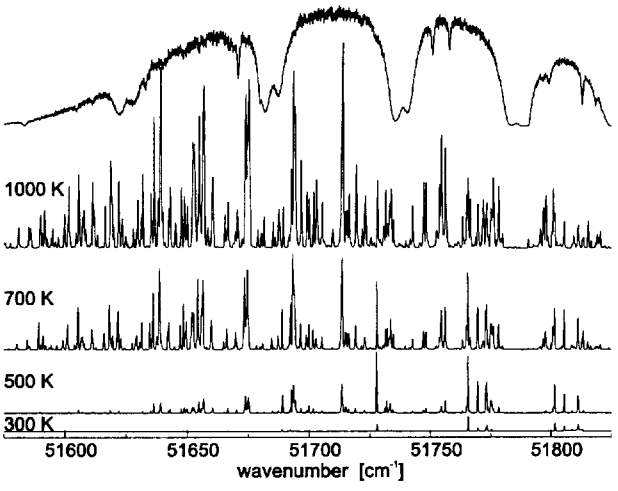


*Fig.14 NO excitation spectra at various temperatures (upper trace - laser output showing $O_2$ absorption "holes").*

Having identified the lines, one needs to establish the major criteria for suitable candidates for TLT in HEG:

1. *Laser energy* -the lines must lie in a wavelength region where there is sufficient laser energy, away from $O_2$ absorption bands;
2. *Electronic states* - due to their different fluorescence yields, these should be the same for both transitions;
3. *Line intensities* - should be high enough to be detected in single shot work, i.e. high Einstein coefficients and sufficiently populated levels;
4. *Single lines* - the lines should consist preferably of just one transition;
5. *Energy separation* - ΔE between the two lower quantum levels of the transitions must be as large as possible (see chapter 2.4);
6. *Vibrational temperatures* - can only be obtained from lines having different lower vibrational levels (obvious, but not trivial, since the tuning range of the lasers is very limited).

With these criteria, and taking into account the 400 identified transitions, not too many candidates appear: Two line pairs were chosen for TLT measurements in HEG, one for rotational temperatures $T_{rot}$:-

| | |
|---|---|
| 1. ε(0,1) $R_{22}(27.5)$ | 51696.2 $cm^{-1}$ |
| 2. ε(0,1) ($R_{21}(17.5) + P_{11}(35.5)$) | 51636.5 $cm^{-1}$ |

and the other for vibrational temperatures $T_{vib}$:-

| | |
|---|---|
| 3. γ(3,0) $R_{11} + Q_{21}$ (45.5) | 51746.7 $cm^{-1}$ |
| 4. γ(4,1) $R_{11} + Q_{21}$ (27.5) | 51746.7 $cm^{-1}$ |

Wavenumbers of each transition are shown. The two transitions for $T_{vib}$ determination are exactly coincident, so that both transitions are excited by the one laser pulse.

### 5.2 Fluorescence signal correction

In TLT using two lasers there will be differences in the energy, spatial and spectral (!) distribution of the two laser beams. These must be known or measured, and used to correct the fluorescence signals. 145 separate LIF measurements were carried using the setup of Fig. 10 with the test cell containing 100 Pa NO and at a thermoelement temperature $T_{therm}$ of 980 K for each of the two

transitions 1. and 2. identified before in chapter 5.1. Fluorescence signals were either left uncorrected, corrected with an energy monitor or corrected with the fluorescence signal obtained from the second reference cell (with 500 Pa NO and $T_{therm}$ = 610 K). Each of the fluorescence signals from the one transition was combined with each of the other transition, so that $145^2$ (=21025) fluorescence ratios and therefrom temperatures could be determined. These are plotted as temperature histograms in Fig. 15.

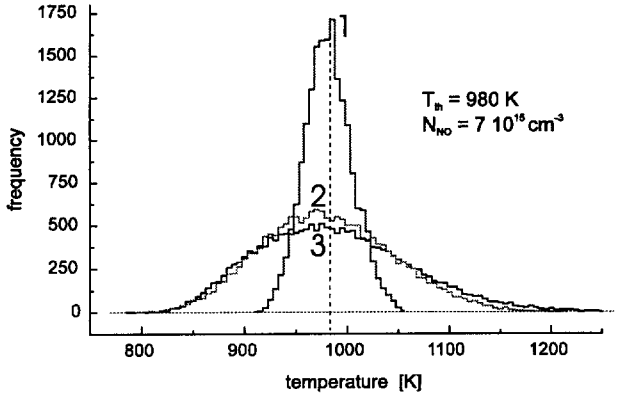


*Fig.15 Temperature histograms for corrected and uncorrected LIF signals.*

Histograms 1, 2 and 3 pertain to correction using reference cell fluorescence, energy correction and no correction, respectively. An energy correction alone obviously is hardly an improvement, so that, especially in single shot work, a reference fluorescence correction is mandatory.

### 5.3 Fluorescence reabsorption

The fluorescence from the laser excited NO in the test volume must usually pass through regions containing NO which can reabsorb the fluorescence, hence falsifying the signals. Its effect must be known. To examine this, transmission of fluorescence through the test cell at various NO densities and at a temperature of 1050 K was measured for emission to the lower vibrational levels v" = 1, 2, 3 and 4. The laser-excited transition 1. (chapter 5.1) was used. Results are shown in Fig. 16, where fluorescence normalised to the value for v" = 4 is plotted against NO density.

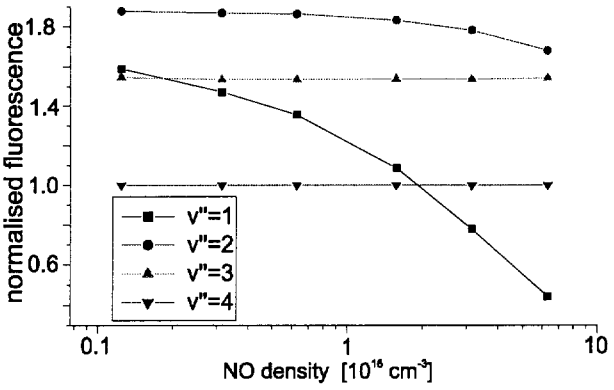


*Fig.16 Normalised fluorescence versus NO density showing reabsorption effects for lower v''.*

One sees here that while the strong reabsorption for emission to v" = 1, even at low densities, makes fluorescence measurements to this level unsuitable for TLT, fluorescence to levels v" = 3 and 4 is unaffected. In fact, for the estimated HEG NO densities lying in the range 1 - 8 x $10^{15}$ $cm^{-3}$ (Fig. 7), and for the given HEG test section geometry, reabsorption of fluorescence to the levels v" = 2, 3 or 4 is at most 1%. To be sure of minimising these effects, only v" = 3 and 4 fluorescence is used in all further TLT work.

### 5.4 Linear fluorescence

Fig. 17 shows reference cell corrected fluorescence signals in the test cell (setup as in Fig. 10) at three temperatures as a function of NO pressure for transitions 1. (open symbols) and 2. (closed symbols), as defined in chapter 5.1. Symbols: circles and diamonds refer to measurement of fluorescence transitions $D^2\Sigma^+(v' = 0) \rightarrow X^2\Pi(v" = 3,4)$ and $A^2\Sigma^+(v' = 0) \rightarrow X^2\Pi(v" = 3,4)$. Even though there is a linear relationship between fluorescence intensity and NO density in the range relevant for the HEG free stream (0.1 - 0.8 x $10^{16}$ $cm^{-3}$), one can see that this relationship is not held at higher densities. Here quenching and, especially at high laser power densities, ASE (see chapter 2.3) play a role.

The lesson here for HEG free stream TLT work is that low laser power densities should be used, even at the trade-off of spatial resolution (no laser

sheets). This will be further exemplified in chapter 5.6.

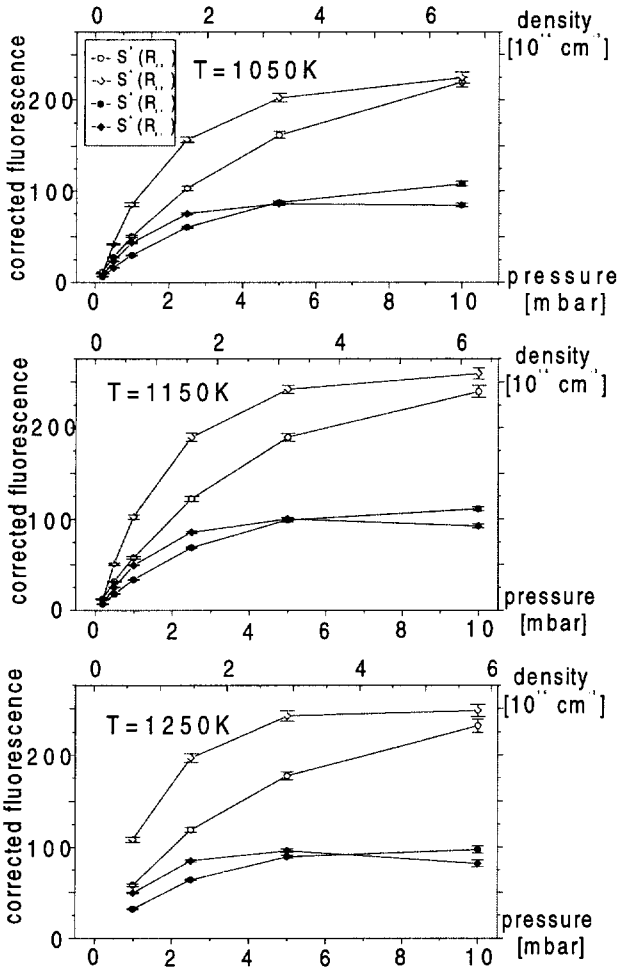


*Fig. 17 Corrected fluorescence signals versus NO pressure for three temperatures (Ref. 5).*

## 5.5 Quantum yields

Quantum yield was defined in chapter 2.3 as $q_F = \frac{A_{21}}{A_{21} + Q_{21}}$. Fig. 18 shows a calculation of $q_F$ as a function of NO density for three temperatures for the states $D^2\Sigma^+$ (v' = 0) and $A^2\Sigma^+$ (v' = 0). Literature values (see Ref. 1) for quenching cross sections $\sigma(A)$ = 44 Å$^2$ and $\sigma(D)$ = 83 Å$^2$ were used. This shows that $q_F[\varepsilon(0,v'')] \geq 0.95$ for all temperatures for HEG free stream NO concentrations.

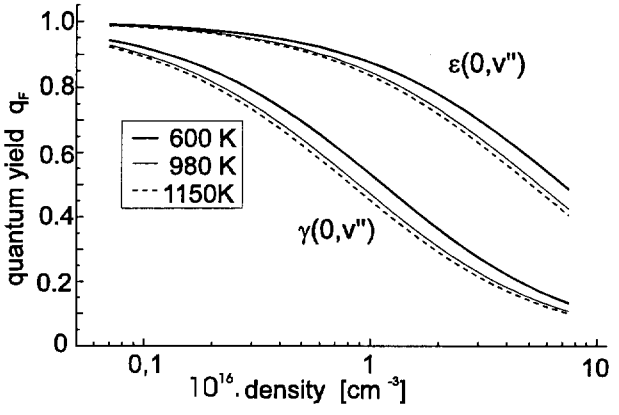


*Fig.18 Calculated quantum yields for NO D and A states versus NO density at three temperatures (Ref. 5).*

Even if $q_F << 1$, a glance at the derivation of the equations for TLT in chapter 2.4 had assumed that $q_{F,1} = q_{F,2}$, so that the actual values of $q_F$ didn't matter, as long as they were the same for both states |1> and |2>. This is an important requisite for use of TLT as used here. Unfortunately very little is known about quantum level dependence on quenching of these NO excited states, so that tests had to be carried out to determine $\sigma(A)$ and $\sigma(D)$, using our familiar transitions 1 and 2.

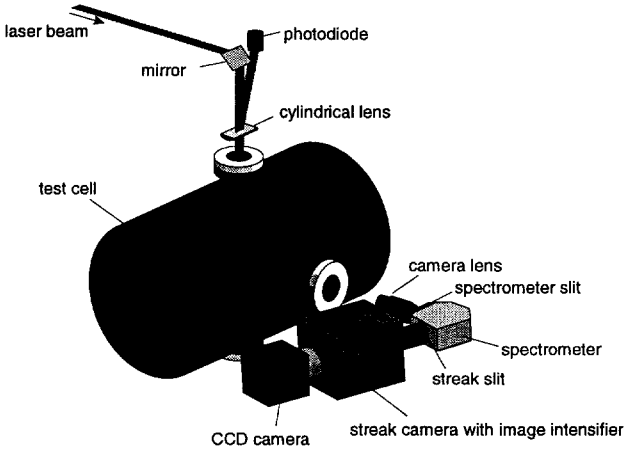


*Fig.19 Apparatus to measure NO fluorescence lifetimes and quenching using a streak camera.*

To do this, the experimental setup, shown in Fig. 19, coupled the test cell with a detection system consisting of a UV lens, a spectrometer and a fast streak camera capable of time resolved

fluorescence measurements with nanosecond resolution (Ref. 4). With this setup time resolved fluorescence measurements of NO at two temperatures (1157 and 1277 K) and various gas pressures (100 Pa- 20 kPa) for mixtures of NO and $N_2$ between 1 and 100% were carried out. Typical results are shown in Fig. 20.

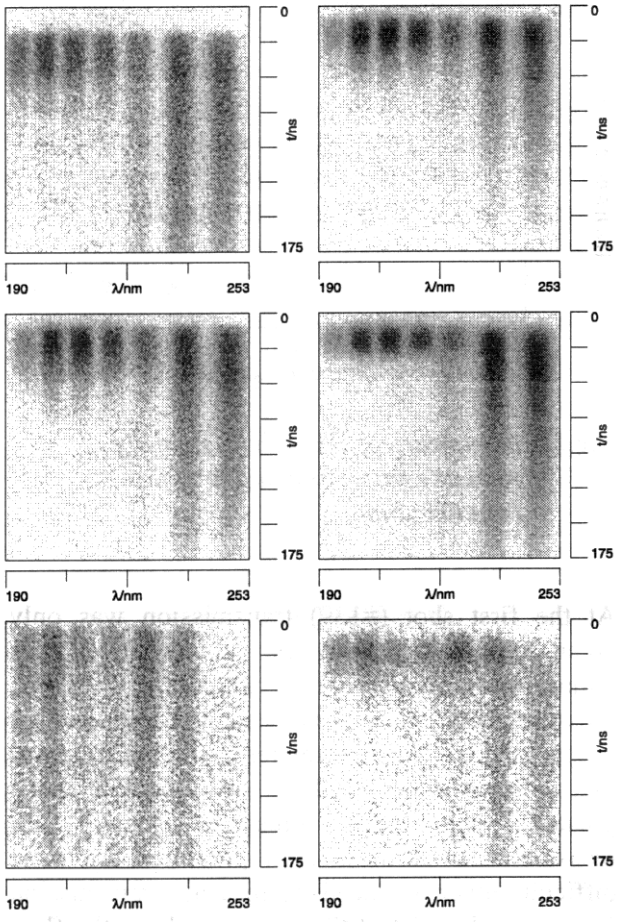


*Fig.20 NO quenching seen in different time resolved fluorescence measurements (see text).*

Here the horizontal axes represent wavelength from 190 - 250 nm, the vertical axes time from 0 to 175 ns. *Upper traces*: transition 1, 1227 K, NO 200 Pa (left), NO 1 kPa (right). *Middle traces*: transition 2, 1157 K, NO 500 Pa (left), NO 500 Pa + $N_2$ 19.5 kPa (right). *Lower traces (for comparison)*: transition (3,0) R11 (43.5), 1157 K, NO 500 Pa (left), NO 500 Pa + $N_2$ 19.5 kPa (right). Functions of the form $f_{theor}(t) = I_0 e^{-t/\tau_{nat}} + B$ ($I_0$ is the original fluorescence signal intensity at t = 0, $\tau_{nat}$ the natural fluorescence lifetime and B the background signal) were fitted to the experimental plots in Fig. 20 at late times to avoid having to carry out complex deconvolutions with the laser pulse form ($\tau_{1/e}^{laser} \cong$ 17 ns). Fluorescence lifetimes $\tau$ are then plotted logarithmically versus NO pressure (mbar) (Stern-Volmer plots), from which the natural upper state lifetimes $\tau_{nat}$ and quenching cross sections $\sigma_X$ (X = NO, $N_2$) can be determined (see Ref. 4). A typical Stern-Volmer plot for measurement of fluorescence $A^2\Sigma^+(v' = 0) \rightarrow X^2\Pi(v'' = 1,2)$ after excitation using transition 1 at temperature 1157 K and with pure NO is shown in Fig. 21. The following table shows the results for $\tau_{nat}$, $\sigma_{NO}$ and $\sigma_{N2}$ for the $D^2\Sigma^+$ (v' = 0) state for the two rotational levels J = 27.5 and 17.5, obtained from an analysis of a multitude of Stern-Volmer plots as in Fig. 21.

| | **ε(0,1) $R_{22}$(27.5)** | | **ε(0,1) $R_{21}$(17.5)** | |
|---|---|---|---|---|
| | *1157 K* | *1277 K* | *1157 K* | *1277 K* |
| **$\tau_{nat}$ (ns)** | 16.5 | 17.5 | 20.7 | 18.8 |
| **$\sigma_{NO}$ (Å$^2$)** | 46 | 64 | 75 | 62 |
| **$\sigma_{N2}$ (Å$^2$)** | 42 | 42 | 30 | 50 |

One sees that $\sigma_{NO}$ and $\sigma_{N2}$ are different for the two rotational levels! Having obtained these experimental values, and using calculated values of NO and $N_2$ concentrations in the HEG free stream, one can now finally assess the inaccuracy introduced by the assumption $q_{F,1} = q_{F,2}$ made in chapter 2.4. The quench rate of NO by species i is given by $Q_{21}^i = \sum_i N_i \sigma_i v_i$, where $N_i$ = concentration of species i, $\sigma_i$ = quenching cross section and $v_i$ = average velocity of species i ($v_i = \sqrt{8kT/\pi\mu_{NO-i}}$, k = Boltzmann's constant, T = temperature, $\mu_{NO-i}$ = reduced mass of collision pair NO and species i). Using measured values of $\sigma_{NO}$ and $\sigma_{N2}$ to determine $Q_{21}$ and therefrom $q_F$, then ratios of $q_{F,1}/q_{F,2}$ can be determined for the HEG run conditions. These are summarised in the following table:

| **HEG condition** | | **I** | **II** | **III** | **IV** |
|---|---|---|---|---|---|
| **$q_{F,1}/q_{F,2}$** | 500 K | 1.05 | 1.08 | 1.05 | 1.09 |
| | 1157 K | 1.08 | 1.12 | 1.08 | 1.12 |
| | 1277 K | 1.08 | 1.13 | 1.09 | 1.13 |

It can be seen here that the assumption that $q_{F,1} = q_{F,2}$ would lead to errors in forming fluorescence ratios of about 5 - 13%; in the best case, one can ignore this effect and accept the larger error, in the worst a correction for $q_{F,1}/q_{F,2}$ would need to be made.

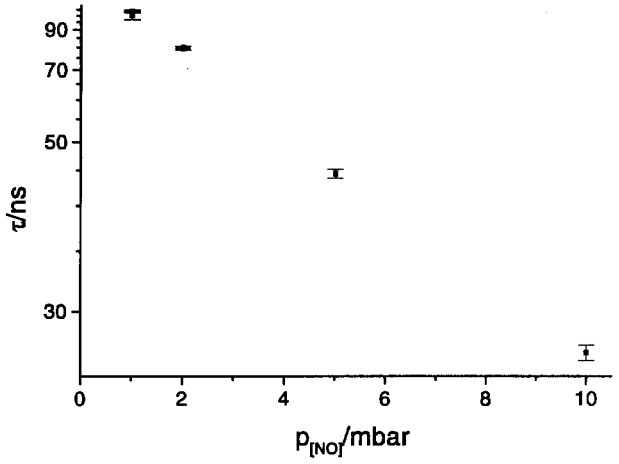


*Fig.21 Stern-Volmer plot for NO A → X fluorescence at 1157 K.*

22, where percent transmission for the two transitions 1 (open circles) and 2 (filled circles) are plotted for eight shots in sequence of performance in HEG at low (~40 MPa) and high (~100 MPa) pressure conditions. (The high pressure conditions are identified in the figure with Roman numerals II and IV.)

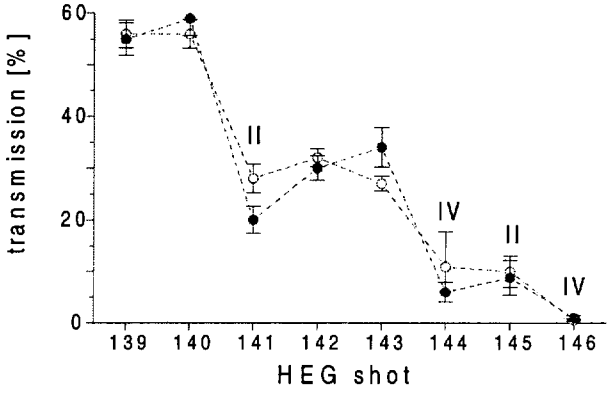


*Fig.22 A sequence of HEG shots showing reducing transmission due to flow contamination.*

### 5.6 Laser beam transmission

Absorption of the laser beam on its path to the test volume not only falsifies results, but, if severe enough, can reduce fluorescence signals to below detectable levels. Laser beam transmission measurements for transitions 1 and 2 in the test cell with NO densities below 1 x $10^{16}$ $cm^{-3}$ and at the highest temperature (1150 K) showed that there is a negligible effect. This is mainly due to the use of NO transitions arising from high vibrational (v" = 1) and rotational (J" = 17.5, 27.5) levels, which, even at 1150 K, are thermally not strongly populated (see chapter 2.2). This is one advantage of using ε-band rather than γ-band excitation of NO - the latter originates from the v" = 0 level, where considerable laser beam absorption occurs.

There is another source of laser beam extinction which causes problems - scattering by particulate matter in the flow. This is a typical problem with high enthalpy facilities and was referred to before (chapter 4) as producing the strong emission behind shocks. Its effect is the same as that due to absorption - less of the laser beam reaches the test volume. This is illustrated most graphically in Fig.

At the first shot (#139) transmission was only about 55%, and by the last shot (#146) it was almost down to 0%. The drastic effect of high pressure shots can also be seen; the transmission drops rapidly. This correlates with the findings that ablation of materials in the tunnel is much greater with high pressure shots. LIF measurements at these high pressures are most difficult, either one needs to measure transmission *in situ*, or choose test times very early in the flow before the contamination arrives.

### 5.7 Saturation of fluorescence

If one pumps an NO transition too hard (laser power density is too high and/or quantum level population is very low and/or transition moments (Einstein coefficients) are very large), it is possible to empty the level during the time of the laser pulse, so that further incoming photons don't lead to a further excitation of NO. The linear dependence between fluorescence signal and laser power no longer holds, and, in the worst case, further increases in laser power lead to no further fluorescence signal increase - complete saturation has occurred. Our transitions 1 and 2 have Einstein

B coefficients of 999 and 406 cm $J^{-1}$ , respectively, and both rotational levels J" = 17.5 and 27.5 are quite high and therefore not highly populated (see Fig. 4). Therefore, at higher laser power densities, one may expect saturation effects to occur, more so for the transition 1 than 2. This is indeed the case, as is shown in Fig. 23 (from Ref. 5), where fluorescence signal measured in the test cell (1100 K with 500 Pa NO) is plotted against laser energy density for both transitions 1 and 2 (for comparison, the dashed line shows the expected behaviour for linear LIF).

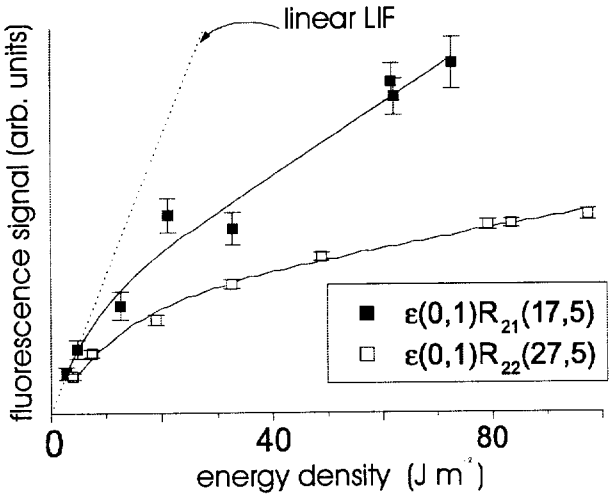


*Fig.23 Fluorescence signal vs. laser energy density for NO at 1100 K and 500 Pa (Ref. 1).*

Deviation from linear LIF starts to become severe at energy densities above about 10 J $m^{-2}$ (which corresponds to a laser power density of ~700 MW $m^{-2}$). To avoid saturation effects, energy densities below this value should be used. The trade-off for linear LIF, especially for transition 2, is the reduced fluorescence signal intensity, which may be critical with single shot TLT in environments such as HEG where signals are quite weak anyway.

### 5.8 Fluorescence signal Boltzmann plots

Armed with what has been learnt so far, the best proof of TLT in the test cell is to plot fluorescence signal ratios for transitions 1 and 2 logarithmically against inverse temperature (Boltzmann plot) - the slope should be equal to ΔE/k, where ΔE is the energy separation of the two energy levels from which excitation occurred. For our transitions 1 and 2, ΔE/k = 1310 K. Fluorescence measurements were carried out (Ref. 5) at four different NO concentrations $n_{NO}$ (1, 3, 5 and 8 x $10^{15}$ $cm^{-3}$) and with 5, 10 and 100% $NO/N_2$ mixtures. Boltzmann plots are shown in Fig. 24 for only two $n_{NO}$ (upper plot - $n_{NO}$ = 3 x $10^{15}$ $cm^{-3}$; lower plot - $n_{NO}$ = 8 x $10^{15}$ $cm^{-3}$). Lines of best fit for each mixture are

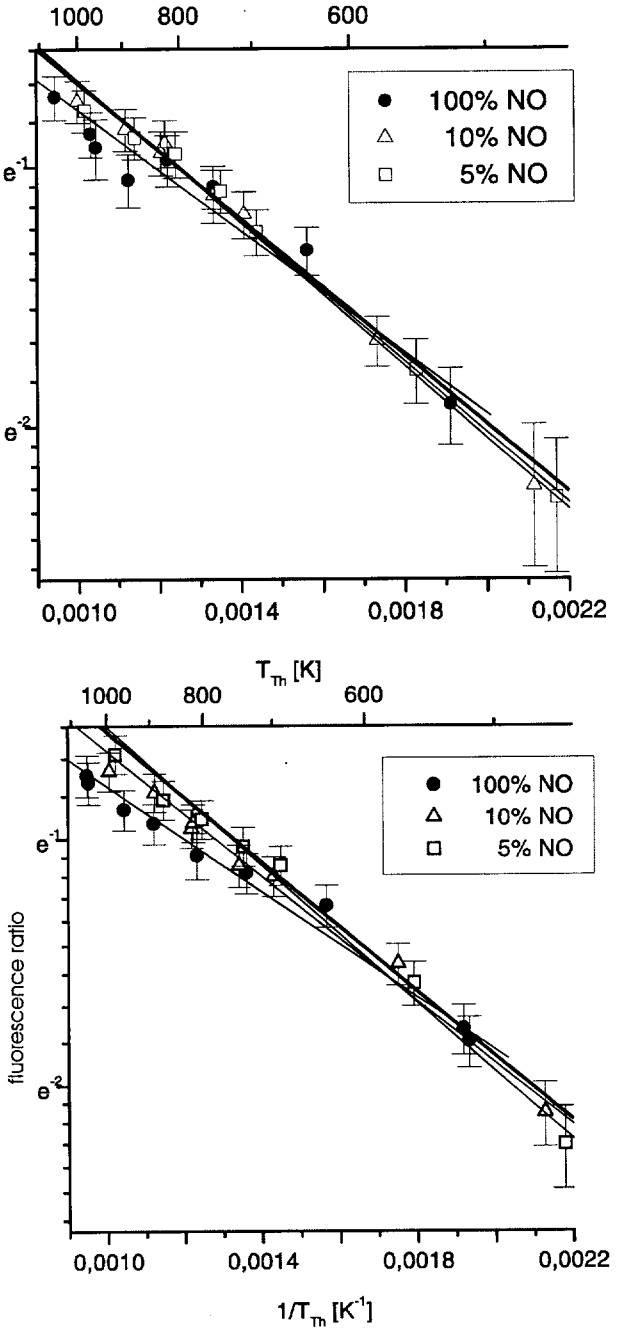


*Fig.24 Boltzmann plots for two NO densities (upper - 3 x $10^{15}$ $cm^{-3}$; lower - 8 x $10^{15}$ $cm^{-3}$) and different $NO/N_2$ percentages.*

shown, as is the expected result with the slope 1310 K. Deviations can be seen to be larger for the higher $n_{NO}$.

If one now plots the slopes of the fitted lines in Fig. 24 for each mixture as slope (in K) versus NO density, one obtains the result in Fig. 25. This encouraging result shows that over the $n_{NO}$ range 1 - 8 x $10^{15}$ $cm^{-3}$ (HEG free stream), the deviation from 1310 K is quite small for 5 and 10% mixtures (which also corresponds to the HEG case). The 100% mixture result lies furthest from the expected line; the reasons are not clear, but may be due to experimental difficulties in dealing with low gas pressures in the test cell and concommitant uncertainties in the temperature.

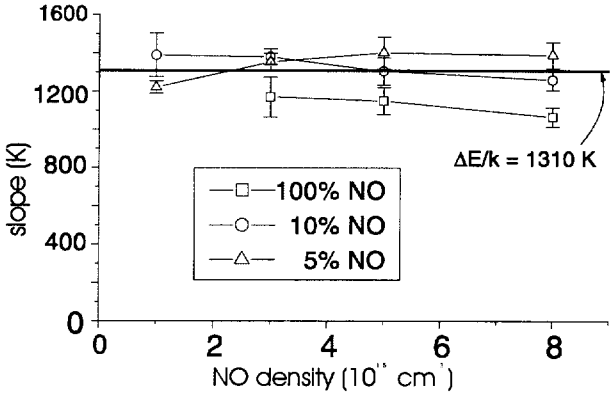


*Fig.25 Measured Boltzmann plot slopes from Fig. 24 versus NO density at different $NO/N_2$ percentages.*

## 6. LIF RESULTS IN HEG - FREE STREAM FLOW

LIF measurements were carried out in the HEG free stream flow with various run conditions to determine rotational and vibrational temperatures using TLT. $T_{rot}$ is of interest since it represents the "inner" temperature most likely to mirror the gas translational temperature $T_{trans}$, which is difficult to measure with any accuracy by other means (although line-of-sight absorption techniques using laser diode absorption of NO and of a seed species rubidium have delivered translational temperatures, albeit only to an accuracy of ±20% - see Ref. 6). For $T_{vib}$, based on nozzle flow calculations using a simple Landau-Teller approach for vibrational relaxation of NO, $T_{vib}$ is believed to lie above $T_{trans}$; vibrational relaxation freezes early in the nozzle flow.

### 6.1 Rotational temperature $T_{rot}$

Using the experimental setup shown in Fig. 9, and with the two detection systems (one for each laser) configured as OMA's, spectrally resolved fluorescence spectra were obtained in the HEG free stream at various run conditions after laser excitation of NO using transitions 1 and 2. Measured fluorescence spectra are shown as fluorescence intensity in counts against wavelength for transition 1 (left hand side) and 2 (right hand side) in Fig. 26. Also indicated are shot conditions (I - IV - see Fig. 7) and shot numbers 139 - 146.

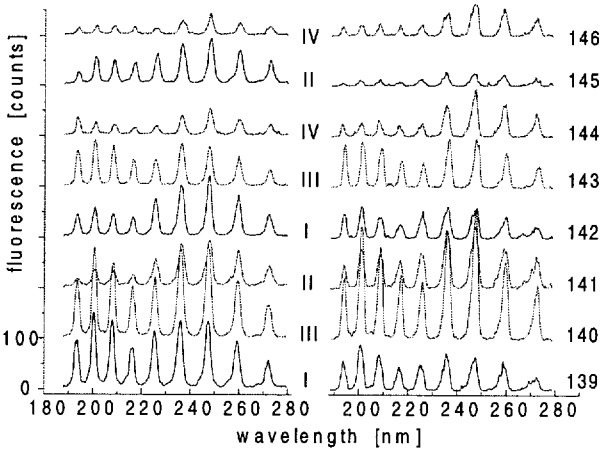


*Fig. 26 Measured NO fluorescence spectra in HEG for eight shots at four conditions.*

These results were analysed using the method outlined in chapter 2.4 for TLT to yield $T_{rot}$ in the HEG free stream, as shown in the following table:

| shot | cond | $p_0$ (MPa) | $h_0$ (MJ $kg^{-1}$) | $N_{NO}$ ($10^{15}$ $cm^{-3}$) | $T_{theor}$ (K) | $T_{rot}$ (K) |
|---|---|---|---|---|---|---|
| 139 | I | 38.8 | 21.8 | 0.96 | 763 | 710 |
| 140 | III | 44.7 | 13.2 | 3.85 | 552 | 620 |
| 141 | II | 84.9 | 22.7 | 2.61 | 1026 | * |
| 142 | I | 38.8 | 21.0 | 1.10 | 791 | 980 |
| 143 | III | 40.0 | 12.0 | 3.86 | 475 | 630 |
| 144 | IV | 105 | 11.6 | 1.04 | 559 | * |
| 145 | II | 68.3 | 21.0 | 2.48 | 903 | * |
| 146 | IV | 97.3 | 14.4 | 7.63 | 703 | 480 |

(* temperature evaluation not possible.)

Reservoir pressure $p_0$ and $T_{rot}$ were measured, specific enthalpy $h_0$, NO concentration $N_{NO}$ and temperature $T_{theor}$ were calculated using a chemical non-equilibrium computer code for nozzle flows (see Ref. 1). The agreement between $T_{rot}$ and $T_{theor}$ is not good, there being scatter in both directions. The main reason for this is that these measurements were performed before the substantial tests on TLT in the test cell (chapter 5) had been carried; these latter tests were indeed triggered by the poor agreement between measured and theoretical temperature results.

### 6.2 Vibrational temperature $T_{vib}$

As mentioned in chapter 5.1, there is a chance overlap of two NO transitions, one originating in the v" = 0, the other in the v" = 1 vibrational states:

3. $\gamma(3,0)\ R_{11} + Q_{21}$ (45.5) 51746.7 $cm^{-1}$
4. $\gamma(4,1)\ R_{11} + Q_{21}$ (27.5) 51746.7 $cm^{-1}$

Both transitions 3 and 4 are excited by tuning the laser to 51746.7 $cm^{-1}$. This is shown pictorially in Fig. 27 in an energy level diagram which includes the rotational manifolds.

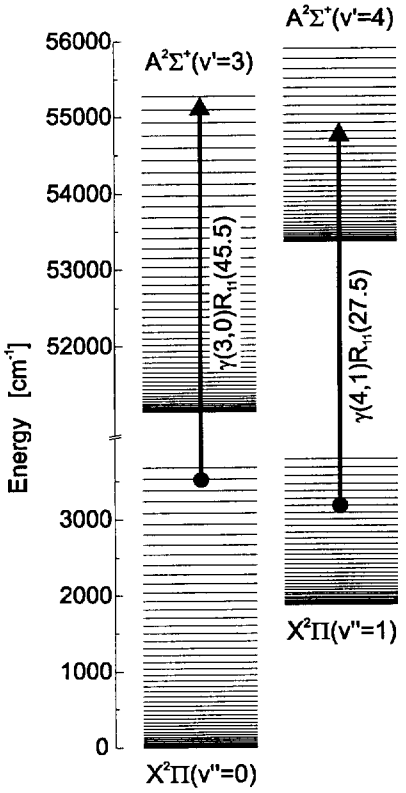


*Fig. 27 Chance overlap of two NO transitions used for vibrational temperature determination (Ref. 1).*

The measured fluorescence spectrum $F_\gamma(\lambda)$ is made up of the sum of components from the $A^2\Sigma^+$ (v' = 4) and $A^2\Sigma^+$ (v' = 3) upper states, $F^{27.5}_{\gamma(4,v")}(\lambda)$ and $F^{45.5}_{\gamma(3,v")}(\lambda)$, respectively, weighted with linear, temperature-dependent factors $\beta'(T)$ and $\alpha'(T)$:

$$F_\gamma(\lambda) = \alpha'(T)\, F^{45.5}_{\gamma(3,v")} + \beta'(T)\, F^{27.5}_{\gamma(4,v")}.$$

Since the two transitions 3 and 4 are coincident, it is not possible to measure them separately. However, neighbouring transitions from the same band can be used to measure similar single line spectra at various temperatures in the test cell, from which the factors $\alpha'(T)$ and $\beta'(T)$ can be determined. A further complication is the possible difference (thermal non-equilibrium) between $T_{rot}$ and $T_{vib}$ in HEG (in the test cell they are the same, of course). The relative population $\xi(T_{vib}, T_{rot})$ of the two lower (v",J") states, $X^2\Pi$(v" = 1, J" = 27.5, $F_1$ and $X^2\Pi$(v" = 0, J" = 45.5, $F_1$ is related to $T_{vib}$ and $T_{rot}$ by the following equation (where the constant is to be determined from the test cell calibration measurements at different temperatures):

$$\xi(T_{vib}, T_{rot}) = \frac{f(v=1, J=27.5, F_1)}{f(v=0, J=45.5, F_1)} = const.\frac{\beta(T)}{\alpha(T)} = 0.61 \cdot e^{\left[\frac{\Delta E_{vib}}{kT_{vib}} + \frac{\Delta E_{rot}}{kT_{rot}}\right]}$$

Fig. 28 shows a calculation for $T_{rot}$ = 800 K and various $T_{vib}$ between 800 and 2500 K, where one can see how the fluorescence spectra change. Also indicated in the figure with two arrows (↓) are two fluorescence lines, one being sensitive, the other insensitive to temperature variation.

A comparison between a measured fluorescence spectrum in the HEG free stream and one calculated using the above-described method is shown in Fig. 29. The arrow (↓) shows the excitation wavelength.

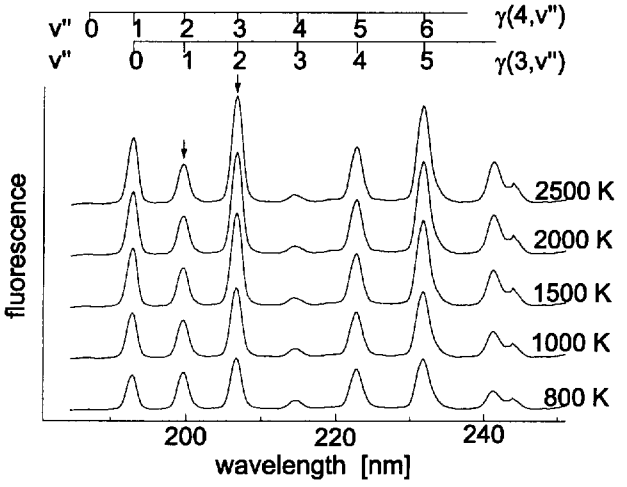


*Fig.28 Calculated NO fluorescence spectra at $T_{rot}$ = 800 K at various vibrational temperatures.*

The agreement between measured and calculated spectra is quite good. From this fit a value for the relative populations of both levels could be determined:

$\xi(T_{vib}, T_{rot}) = 0.7 \pm 0.2.$

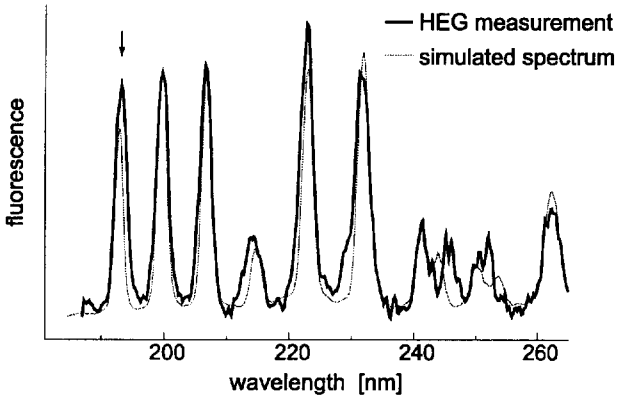


*Fig.29 Comparison between measured (in HEG) and calculated NO fluorescence spectra obtained from simultaneous excitation by one laser.*

If $T_{rot}$ were known in HEG, then $T_{vib}$ could be determined. Since both for the present must be treated as unknowns, one can represent this result pictorially as a contour plot of $\xi(T_{vib}, T_{rot})$ as a function of $T_{vib}$ and $T_{rot}$. This is done in Fig. 30.

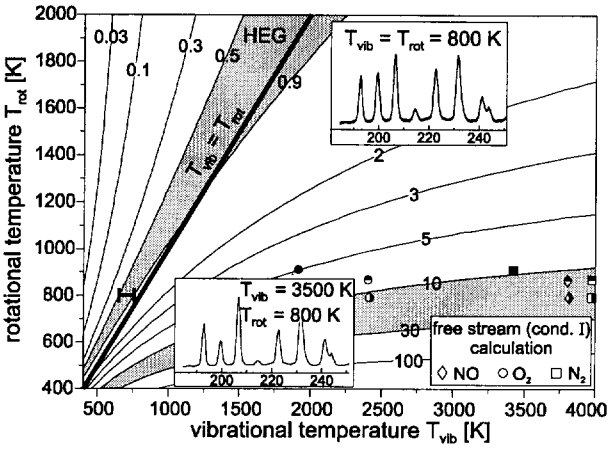


*Fig.30 Contours of relative populations $\xi(T_{vib}, T_{rot})$ as a function of $T_{vib}$ and $T_{rot}$.*

In this figure a family of contours for values of $\xi(T_{vib}, T_{rot})$ lying between 0.03 ($T_{rot} >> T_{vib}$) and 100 ($T_{rot} << T_{vib}$) has been plotted. The thermal equilibrium case, $T_{vib} = T_{rot}$, is plotted as a straight line, along with an inserted spectrum for the case $T_{rot} = T_{vib} = 800$ K. The grey region labelled HEG represents the result as measured (0.7 ± 0.2) with no assumption regarding the value of $T_{rot}$. If one assumes $T_{rot} = 800$ K, the error bar (|—|) represents the range of measured and predicted values of $T_{vib}$. The symbols in the figure for ($T_{vib}$,$T_{rot}$) represent values calculated by various workers (see Ref. 1) for NO, $O_2$ and $N_2$ vibrational non-equilibrium - all predict $T_{vib} >> T_{rot}$. For comparison, the calculated fluorescence spectrum for the case where $T_{vib}$ = 3500 K and $T_{rot}$ = 800 K is inserted in the figure. Here values for $\xi(T_{vib}, T_{rot})$ would lie between 5 and 100 (!), which is well above the measured value of 0.7 ± 0.2. Although the results would seem to indicate thermal equilibrium, there are some reservations: above all, only two levels with two low v" (with small Δv") and two high J" (with large ΔJ") could be interrogated. Whether these are representative of the distribution over all levels is not known. Furthermore it is known that non-equilibrium distributions amongst vibrational and rotational levels exist in rapidly expanding gas flows (see Ref. 1).

## 7. LIF RESULTS IN HEG - MODEL FLOWS

Many LIF measurements have been carried out in HEG, leading either to spectrally-resolved fluorescence spectra or 2D field measurements of fluorescence. The former have been used to study the free stream and also to ascertain how to obtain sufficient fluorescence signals from behind strong shocks; the latter have yielded information on flow visualisation (shock positions) and 2D resolved temperature field measurements around models in the HEG test flow. The results of tests with these models - HERMES space glider, cylinder, sphere, blunted cone (planetary probe) and the Japanese space glider HOPE (HII orbital plane) - are presented here.

### 7.1 HERMES - European space glider

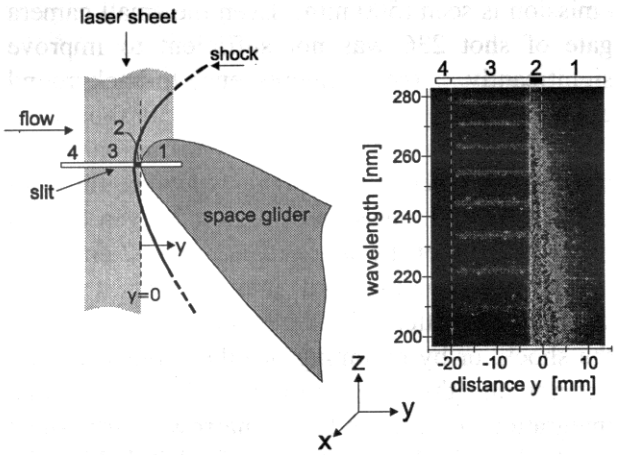


*Fig.31 LIF measurements on HERMES in HEG (condition II).*

In the late 1980's and early 1990's HERMES was a joint European development for a space transporter. Tests with models were carried out in HEG at conditions I and II. One laser, formed to a sheet, was made to pass in front of the model, tuned to a strong NO absorption line. The fluorescence emission was captured with a UV lens and focussed onto the OMA entrance slit (as in Fig. 9), which was placed transverse to the sheet. Fig. 31 (left hand side) shows the experimental setup.

This configuration affords a 1D spatial resolution along the slit. In the results of these measurements for an HEG shot at condition II, four regions can be identified, as shown in Fig. 31 in the experimental setup and in the experimental results (right hand side): 1. Region of shock heated gases where laser is blocked by model; 2. Behind the shock with laser excitation of NO; 3, In the free stream, with laser beam; 4. In the free stream, no laser beam. (The experimental result is an image, as recorded on the ICCD camera, with spectrometer dispersion (i.e. wavelength) in the vertical direction and spatial resolution (along the slit) in the horizontal.) The expected NO fluorescence spectrum can clearly be seen in region 3, whereas region 2 is harder to resolve.

By laying vertical profiles through the regions 1, 2 and 3 for the result shown in Fig. 31 and for two other HEG shots, the spectra shown in Fig. 32 were obtained.

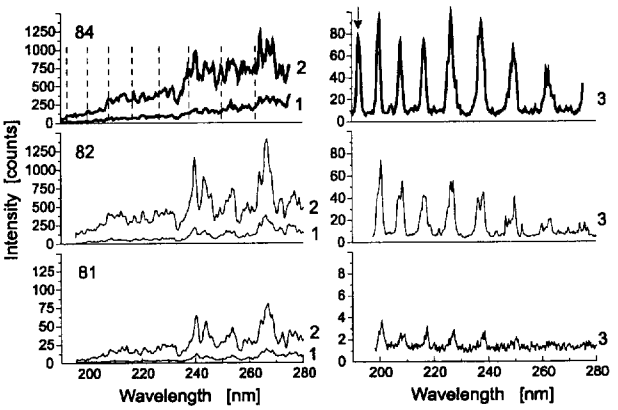


*Fig.32 Spectra from HERMES for regions 1, 2 and 3 (see Fig. 31) for three HEG shots.*

Shots 81, 82 and 84 were at conditions I, I and II, respectively. Camera gates were between 30 and 50 ns. Laser excitation occurred at the line wavelength shown in the top right hand spectrum by a vertical arrow (↓). In shots 82 and 84 (and less so in 81) one can clearly see the NO fluorescence spectrum after exciting transition 1 in region 3. For all three shots there is no indication of a fluorescence signal in region 2 at those wavelength positions (indicated by dashed lines) where it should occur. There are a few possible reasons for this: first, the very limited resolution afforded by the OMA setup (slit width was 280

μm) coupled with the very small shock stand-off distance (<3 mm) in the stagnation region in front of HERMES may prevent the weak fluorescence lines from being seen. Secondly, at the higher densities behind the shock, fluorescence quenching would also play a more major role. Finally, the strong emission behind shocks (see chapter 4) may mask any weak NO fluorescence signals. To overcome the spatial resolution problem, tests with a cylinder having a larger shock stand-off distance were carried out.

## 7.2 Circular cylinder

A cylinder with diameter 90 mm and length 500 mm was placed in the flow with its axis perpendicular to the flow direction. The optical set-up was identical to that shown for HERMES (chapter 7.1). Laser excitation occurred either via transition 1 or 2, or via a strong group of mixed lines ($\varepsilon(0,1)$ $Q_{11}(32.5)$ + $P_{21}(32.5)$ + $R_{21}(21.5)$ + $R_{11}(26.5)$ + $Q_{21}(26.5)$). Gates were either 50 or 300 ns. The experimental set-up and one of the recorded results (shot 236, group of lines, 150 mJ, 50 ns gate) are shown in Fig. 33.

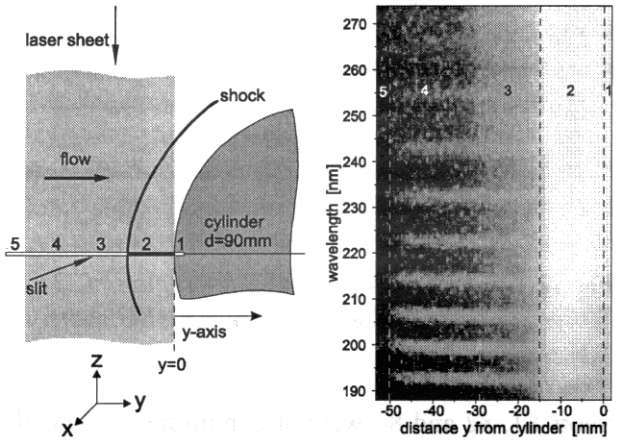


*Fig.33 LIF measurements on a cylinder in HEG.*

Here five regions are identified, the free stream flow region with laser beam (region 3. In Fig. 31) being further split into two regions. In region 3, even though one can see the NO fluorescence lines, they start to become overlapped with background emission at the higher wavelengths. For two shots 235 (transition 1, laser energy 50 mJ, 300 ns gate) and 236 (group of lines, 150 mJ, 50 ns), vertical spectral profiles for regions 2, 3 and 4 are shown in Fig. 34.

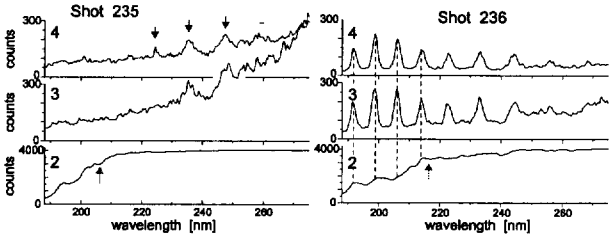


*Fig.34 Spectra from the cylinder for regions 2., 3. And 4. (see Fig. 33) for two HEG shots.*

Region 2 in both shots 235 and 236 is sooner or later saturated (commencing at position of vertical arrow ↑); even before saturation, no fluorescence lines are to be seen. One reason for this is the width of the laser sheet (0.5 mm) relative to the integrated length over which the background emission is seen (500 mm). Even the small camera gate of shot 236 was not sufficient to improve significantly the fluorescence-to-background emission ratio. Region 3 for shot 236 shows the free stream florescence lines, as in region 4, but overlapped especially at higher wavelengths with the background emission of region 2, even though one is in front of the shock! The region 2 emission is so overpowering and intense that it either scatters off matter in the free stream upstream of the shock, or by blooming or other optical effects extends into the upstream region. Due to its long integration length and the narrow laser sheet depth, the cylinder is not suited for LIF behind the shock.

## 7.3 Sphere

To reduce the long integration lengths of the cylinder (chapter 7.2) and increase the laser depth, sphere (radius 80 mm) tests with expanded laser beams were carried out. Three shots, all at condition I, all with one laser (90 mJ) fixed on the group of lines (see chapter 7.2) and with gates from 5 to 20 ns were carried out. In shot 259 the laser sheet was focussed to a sharp waist, in 260 and 261 the beam was expanded to a size of 50 x 21 $mm^2$, with the 50 mm being in the direction of integration with the cameras. This is shown in Fig. 35, side-on view top right, and front-on view

bottom left. Two OMA slit configurations were used, one transverse to the laser beam (as in Figs. 31 and 33), and one along the beam direction.

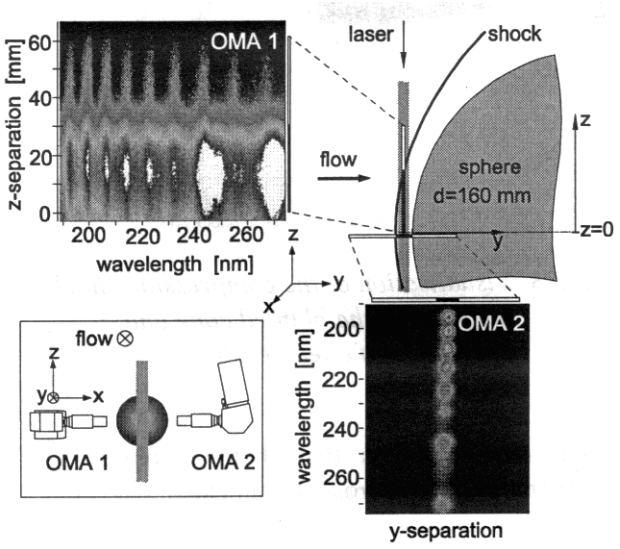


*Fig.35 LIF measurements on a sphere in HEG using two different OMA slit alignments.*

The results for shot 261 are also shown for both OMA configurations, where, in both cases, one can see NO fluorescence behind the shock. This is especially evident where the slit is in laser beam direction, where fluorescence from the free stream can also be clearly seen. This is the first recorded case of measured NO fluorescence behind a strong shock at high enthalpies.

Spectral profiles for the free stream (1), for the transition region between free stream and shock in the slit configuration along the beam (2), as in (2) but in the shock region, and with slit configuration transverse to the laser beam (4) are shown for shots 259 (thin line), 260 (medium line) and 261 (bold line) in Fig. 36. Downward arrows (↓) indicate onset of partial camera saturation. Asterisks (*) indicate spectral regions where the emission is largely due to the background emission.

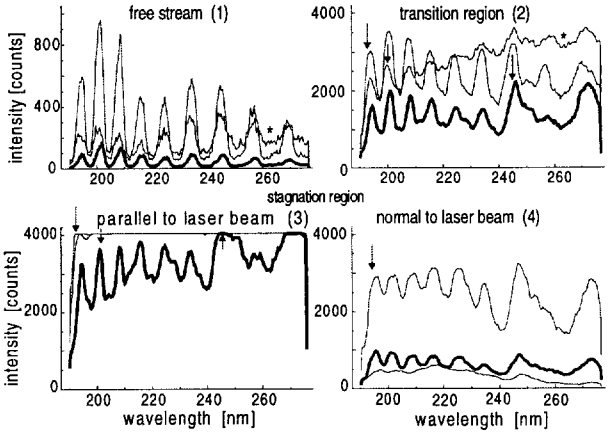


*Fig.36 LIF spectral profiles for the four regions in three HEG shots.*

These spectra show all too clearly the disadvantage of focussed (shot 259) compared with defocussed (shots 260 and 261) laser beams. An improvement in NO fluorescence/background emission intensity ratio by about a factor of 20 was chiefly due to: 1. Defocussing the laser beam; 2. Using a strong group of excitation lines; 3. Using very short camera gates; 4. Use of a sphere rather than a cylinder.

These tests were carried out with just one laser, so that an attempt at TLT could not be undertaken. Furthermore, to use TLT behind a shock with temperatures of over 6000 K, the presently available transitions 1 and 2 with their small $\Delta E/k$ value of only 1310 K are not suitable, Other transitions are needed, and since these are not accessible to the tunable ArF excimer lasers, other lasers will need to be used.

### 7.4 Blunted cone (planetary probe)

The blunted cone represents the forebody shape of a planetary probe. LIF was used (Ref. 7) to examine the flow wakes behind the cone; these are regions of interest since it is here that sensitive and delicate instrumentation is placed. There is also some concern regarding the influence of the model holder (sting) on the wake flow. The set-up for TLT measurements behind the cone is shown in Fig. 37. A shear layer separates the strong expansion at the edge of the cone from a re-circulation region in the corner formed by cone

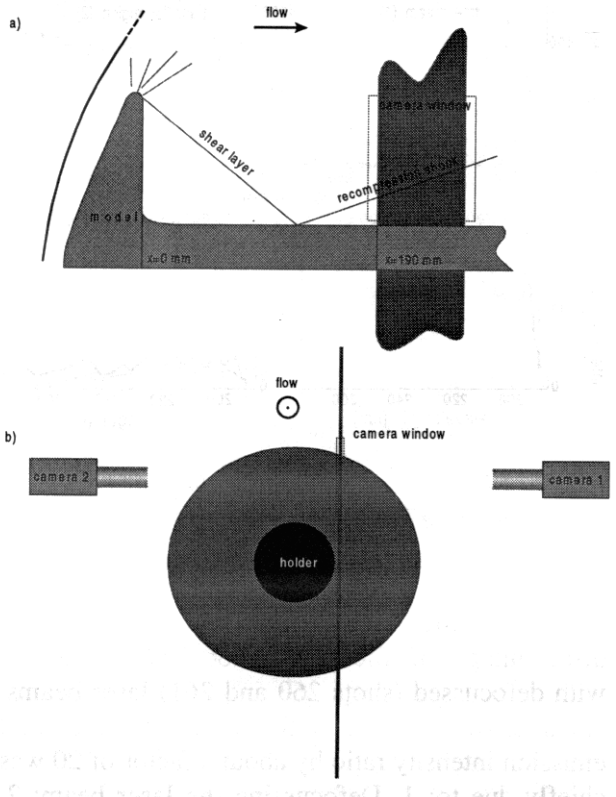


*Fig.37 Experimental setup for LIF measurements in the wake of a blunted cone in HEG.*

rear surface and sting. This shear layer impinges on the sting, where, to turn the flow, a weak re-compression shock is formed. PLIF measurements were performed in this region of the re-compression shock, with the configuration as shown. (Early tests in the region immediately behind the cone were not successful, even with the use of filters, due to the very strong background emission from behind the bow shock - at that stage, the methods leading to the successful results behind the sphere shock were not yet known.)

A 2D temperature plot and profile for the region shown in Fig. 37 is shown for shot 220 (condition III, test gas 30% $N_2$ + 70% $CO_2$) in Fig. 38.

One can faintly see the shock position in the inset 2D image (the shock is weak, the gas is quite "cold" and NO concentrations are quite low, so that fluorescence signals are very weak, leading to low S/N ratios are therefore poor signal quality). For the temperature determination a value of 1000 K has been assumed for the region upstream of the shock - this value has been obtained from calculations. Given this assumption, the LIF

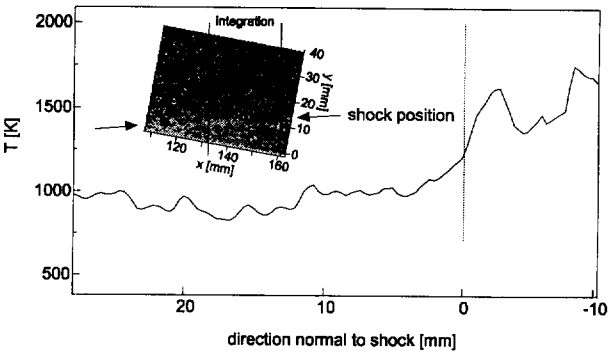


*Fig.38 Visualisation of the compression shock in the wake of the blunted cone and evaluation of a temperature.*

measurement shows that there is about a 1.6 temperature jump across the shock.

## 7.5 Japanese HII Orbital Plane (HOPE)

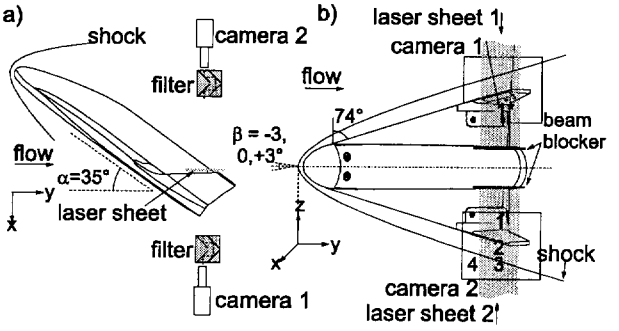


*Fig.39 Experimental setup for LIF measurements on the HOPE power delta model.*

PLIF measurements were carried out (Ref. 1, 4, 7, 8) on power delta and double delta shaped models as candidate shapes for the Japanese space glider HOPE. (This work was performed under contract to Kawasaki Heavy Industries.) Model angle of attack was 35°, three yaw angles of +3°, 0° and -3° were used, run conditions were I, II and IV, and laser transitions 1 and 2 were used in a two-laser set-up (Fig. 9) to record 2D NO fluorescence images. The experimental set-up for LIF for the power delta model, showing the configuration of the two laser sheets and the two ICCD's, is given in Fig. 39.

Here the laser sheets are brought in parallel to the flow direction just above the wing tip fins. Typical flow visualisation LIF images from both cameras (transitions 1 and 2) at yaw angles β of -3° (shot 198, condition IV) and +3° (shot 200, condition II) are shown in Fig. 40. The relative placement of the shock to the wing tip fin as β is changed can readily be seen.

The experimental set-up here doesn't allow both laser beams to probe the same region of the flow (see Fig. 39). Hence, to do TLT, one must either do repeat shots and hope for shot reproducibility, or use two symmetrical (β = 0°) regions in the one shot, and hope for flow homogeneity. Here the latter was chosen. A 2D result for shot 195 (condition I) for $T_{rot}$ in the vicinity of the power delta wing tip fin is shown in Fig.41a and a plot of temperature as a function of distance from the shock front is shown in Fig. 41b.

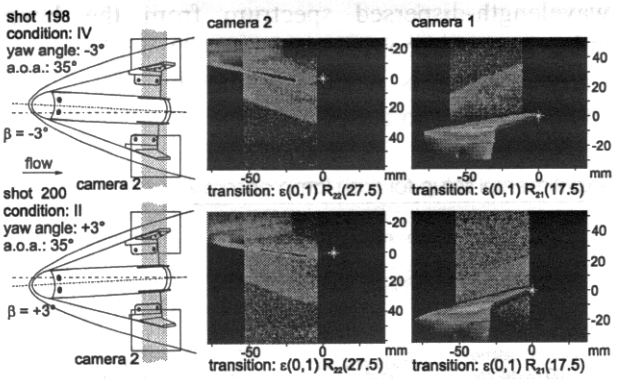


*Fig.40 LIF flow visualisation for yaw angles +3 and -3° for the power delta model.*

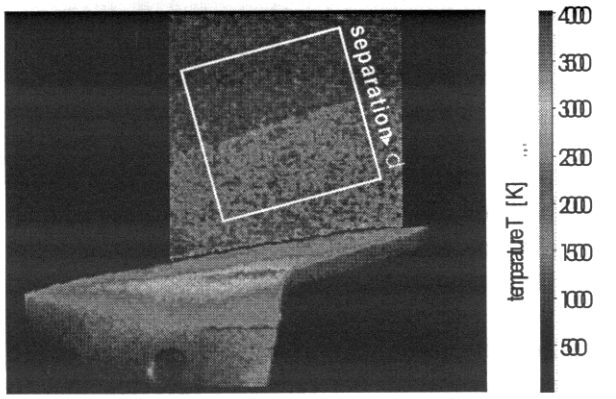


*Fig.41a 2D temperature measurement using LIF in the vicinity of the HOPE power delta wing tip fin.*

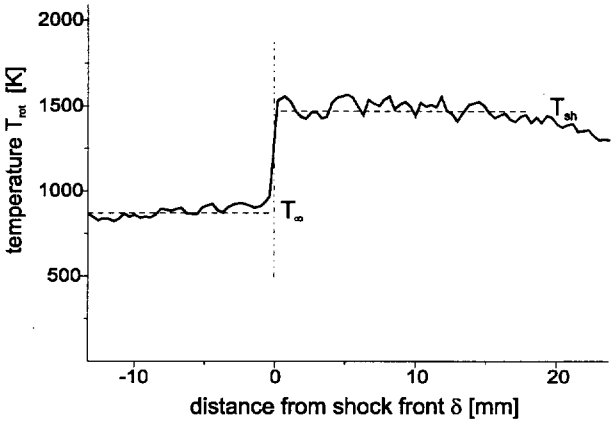


*Fig.41b Temperature jump across the shock shown in Fig. 41a.*

To obtain these temperature values, a free stream value of $T_{rot}$ of 700 K (based on calculations for this condition) has been assumed.

A double delta model was also tested, but with a different laser beam configuration - here the laser beam was brought to pass just upstream of the wing leading edge, which meant that the laser beam and therefore the cameras had to be tilted. This is shown in Fig. 42.

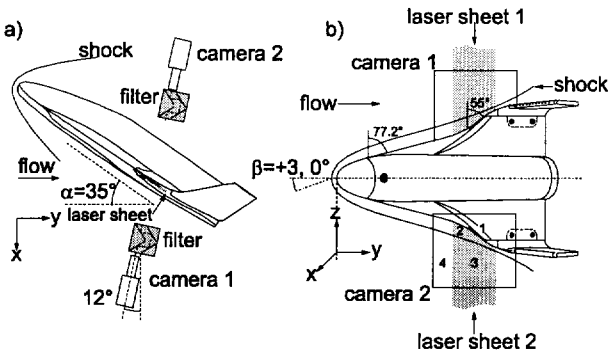


*Fig. 42 Experimental setup for LIF measurements on the HOPE double delta model.*

Typical results are shown in Fig. 43 for two shots at two different yaw angles: shot 204 (condition I, β = 0°) and 201 (condition I, β = +3°).

The shock stand-off distance from the wing leading edge as a function of β was measured over many HEG runs (shots 201 to 209) with different conditions. A summary of all double delta results is given in Fig. 44, where shock distances (in mm)

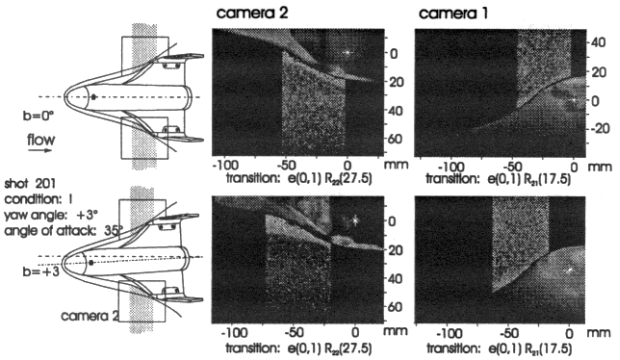


*Fig.43 LIF flow visualisation for yaw angles 0 and 3° for the double delta model.*

are plotted for the different HEG shots. (Yaw angles β = -3°, 0° and +3° are identified. Open symbols - condition I; half open symbols - condition II; filled symbols - condition IV. Squares - right wing camera 1; circles - left wing, camera 2. a, b -shock distance could not be determined.)

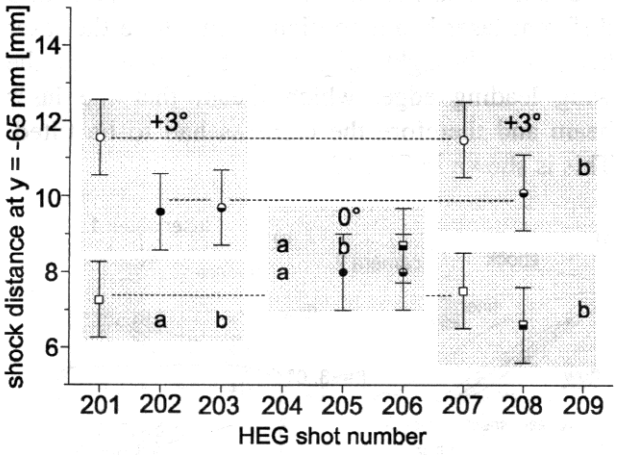


*Fig.44 Distance from shock to wing leading edge for the double delta model for various HEG shots.*

## 8. FLASH LAMP ABSORPTION IN HEG FREE STREAM FLOWS

The theoretical considerations in chapter 2 concerning the NO molecule, its spectroscopy, its level populations, considerations of thermal equilibrium, and TLT also apply here with this method. There are some major differences, however:- 1. It's an absorption technique, meaning line-of-sight integration along the direction of the flash lamp beam (LIF is spatially resolved); 2. Since the exciting source is broad-band, many NO absorption lines are probed, so that several level populations can be determined; 3. The flash lamp can operate at high repetition rates, so that time resolved spectra can be recorded during the flow.

Fig. 45 shows the University of Bielefeld experimental set-up for flash lamp absorption measurements of the HEG free stream flow. The flashlamp delivers a small (1 mm) 1 mJ pulse of short duration (100 ns) and at high repetition rates (100 kHz), with a sizeable proportion of its output in the UV. The beam is collimated, passed through the HEG test section normal to the flow axis and then focussed onto the entrance slit of an f9 spectrometer. This spectrometer contains an echelle grating as its dispersive element, which is used at very high order dispersion (>100), giving a very good wavelength resolution (0.0075 nm). Hence rotational lines can be resolved. The wavelength-dispersed spectrum from the lamp pulse is then recorded on an ICCD while a half frame transfer is occurring, thereby allowing a series of pulses to be recorded.

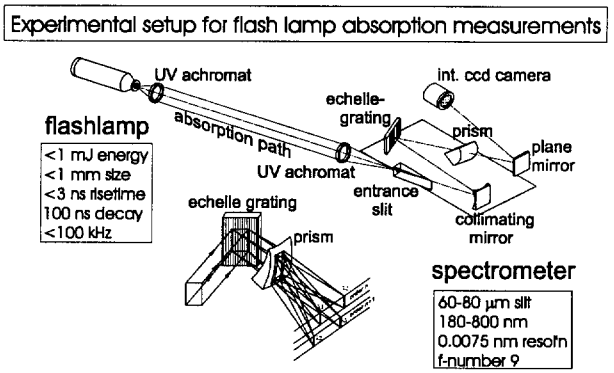


*Fig. 45 Experimental setup for flash lamp absorption measurements in HEG.*

Both low and high resolution spectra were recorded for two HEG shots, both at condition I. Fig. 46 shows a low resolution result for the wavelength range 210 - 240 nm.

At this resolution the rotational line structure cannot be resolved, but rather merges together to give the familiar vibrational band structure of NO. Three vibrational bands are seen in the measured spectrum (middle of figure), arising from γ(1,0),

γ(0,0) and γ(0,1) transitions. (This spectrum has been integrated over several flash lamp pulses to improve the S/N.) Inserted into the figure at lower

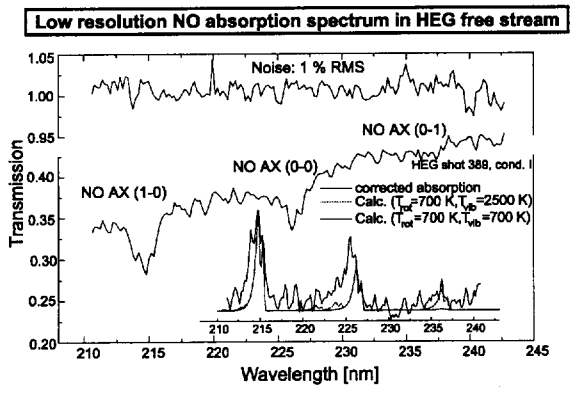


*Fig.46 Low resolution flash lamp absorption measurement of NO in the HEG free stream.*

right is the corrected measured absorption spectrum and two theoretical spectra for NO, one calculated for $T_{rot} = T_{vib} = 700$ K, and the other for $T_{rot} = 700$ K and $T_{vib} = 3500$ K. The major difference between the two calculated spectra is the appearance of the hot band at 236 nm when $T_{vib} = 3500$ K. (Hot bands arise from higher vibrational levels - here v" = 1 - which usually are only occupied when the gas is hot.) Even though the positions of the bands are predicted quite well, the agreement (goodness of fit) between experimental and calculated spectra is not very good - the top trace in Fig. 46 shows the residuals (least square differences) between calculated and experimental spectra. Furthermore, the hot band at 236 nm is not well enough resolved to be sure that $T_{vib}$ is high.

A measured high resolution spectrum is shown in Fig. 47 (bold line plot). The wavenumber range as shown corresponds to a wavelength range of 227.0 - 225.5 nm.

Here the rotational structure of the γ(0,0) vibrational band is resolved. Also shown is a simulated spectrum for NO absorption calculated for $T_{rot} = 700$ K (grey line plot). The agreement is quite good, as shown in the $\chi^2$ residuals plot in the lower right hand corner of Fig. 47; herefrom one would give a value for $T_{rot} = 650 \pm 50$ K. This can

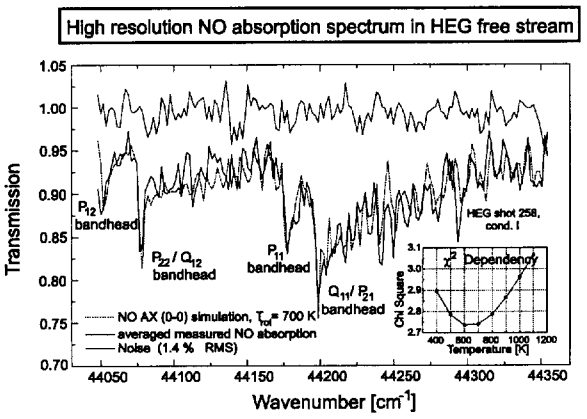


*Fig.47 High resolution flash lamp absorption measurement of NO in the HEG free stream.*

be compared with LIF values for $T_{rot}$ of 710 K and 980 K (see chapter 6.1) and the theoretical value for $T_\infty$ of 790 K (see Fig. 7).

## ACKNOWLEDGEMENTS

The LIF work was carried out by a host of people working at the DLR: Dr. M. Wollenhaupt (who coordinated the LIF activities at HEG over several years and whose doctoral thesis forms the core part of this lecture), Dr. M. Scheer, M. Rosenhauer, T. Müller, J. Jourdan, J. Scholz and S. Hartung. The original laser apparatus for LIF was provided by LaVision 2D Meßtechnik GmbH (Göttingen, Germany). The flash lamp absorption technique, as used here, originates from the group of Prof. P. Andresen (University of Bielefeld) and was implemented in HEG by Dr. C. Niederbäumer (previously University of Bielefeld). Much of the funding for the LIF work, as well as for the LIF apparatus, was provided by the ESA through CNES.

## REFERENCES

1. Wollenhaupt M. (1997) Einzelpuls Zwei-Linien-Thermometrie mit planarer laserinduzierter Fluoreszenz an NO-Molekülen in Hochenthalpieströmungen. *Dissertation, Faculty of Physics, University of Bielefeld.*

2. Eitelberg G. (1993) Calibration of the HEG and ist Use for Verification of Real Gas Effects in High Enthalpy Flows. *AIAA Paper 5170.*

3. Scheer M. (1994) Temperature and density measurements on hypersonic wind tunnels using laser induced fluorescence of NO, including a study of NO spectroscopy in the range 193 - 4 nm, using a novel heated cell. *Diplom thesis, Faculty of Physics, University of Göttingen. (DLR IB 223-96 A 32).*

4. Jourdan J. (1998) Zeitaufgelöste Messung der laserinduzierten Fluoreszenz von heißem NO zur Validierung der Zwei-Linien-Thermometrie für die Anwendung in Hochenthalpieströmungen. *Diplom thesis, Faculty of Physics, University of Göttingen. (DLR-IB 223 98 A 37.*

5. Hartung S. (1999) Laserinduzierte Fluoreszenz an heißem NO zur Anwendung der Zwei-Linien-Thermometrie an einer beheizbaren Zelle. *Diplom thesis, submitted to Faculty of Physics, University of Göttingen.*

6. Beck W.H. (1999) Spectroscopic Techniques for Measurement of Velocity and Temperature in the DLR High Enthalpy Shock Tunnel HEG. *Lecture in this RTO AVT/VKI Special Course on „"Measurements techniques for high enthalpy and plasma flows", 25. - 29. October, 1999.*

7. Rosenhauer M. (1996) Laserfluoreszenz Messungen an heißem NO im Göttinger Hochenthalpiekanal (HEG) und einer Kalibrierzelle. *Diplom thesis, Faculty of Physics, University of Göttingen.*

8. Müller T. (1996) Laserinduzierte Fluoreszenz von NO: Strömungsuntersuchung am Hochenthalpiekanal Göttingen (HEG) und Temperaturmessungen in einer heizbaren Kalibrierzelle. *Diplom thesis, Faculty of Physics, University of Göttingen.*

# Combined Measurements and Computations of High Enthalpy and Plasma Flows for Determination of TPM Surface Catalycity

**A.F. Kolesnikov**
Institute for Problems in Mechanics RAS
Prospect Vernadskogo 101/1
117526 Moscow
Russia

**Summary**

The paper presents the method for the TPM catalycity prediction on the basis of high enthalpy plasmatron heat transfer tests, performed in subsonic regimes, and appropriate CFD modeling of the whole plasma flow field in the plasma wind tunnel (1), viscous reacting gas flows around a test model (2), a nonequilibrium boundary layer near the stagnation point of a test model (3) and analysis of the the heat transfer for test conditions at the small Reynolds and Mach numbers (4). In general, the methodology was developed during the study of the catalytic efficiencies of the Buran TPM - the black ceramic tile and the C-C material with antioxidation coating - in dissociated nitrogen and air reacting flows. This experimental-theoretical methodology has been modified recently for the determination of TPM catalycity in subsonic carbon dioxide and pure oxygen flows from high enthalpy tests performed by using the 100-kW inductive IPG-4 plasmatron. The interaction between combined ground test measurements and CFD modeling is considered as genesis for catalytic effects duplication, plasma flow field rebuilding and the extraction of the quantitative catalycity parameters from the measured high enthalpy flow parameters, surface temperature and stagnation point heat fluxes.

## 1. Introduction

Apparently it was Bonhoeffer who first observed the heat effect of atoms heterogeneous recombination exposing the thermometer with bulb, covered with a thin layer of the catalyst, in the dissociated hydrogen flow [ref. 1]. The thermometer indicated different temperatures for different catalysts. More then 40 years ago Fay and Riddell [ref. 2], and Gulard [ref. 3] for the first time numerically estimated the catalysis heat effect on heat transfer from hypersonic flow to stagnation point of a blunt body.

It is well known now that surface catalysis plays a key role in the heat transfer to space vehicles with the reusable thermal protection system (TPS) such as the Space Shuttle [refs. 4-6], the Buran and Bor [refs. 7, 8]. *Fig. 1* shows the calculated temperature distribution along the lower surface of the Bor vehicle for the altitude 72.4 km and velocity 6450 m/s and flight test data [ref. 8]. The temperature jump on the thermal protection tile, covered with high catalytic black platinum, reached

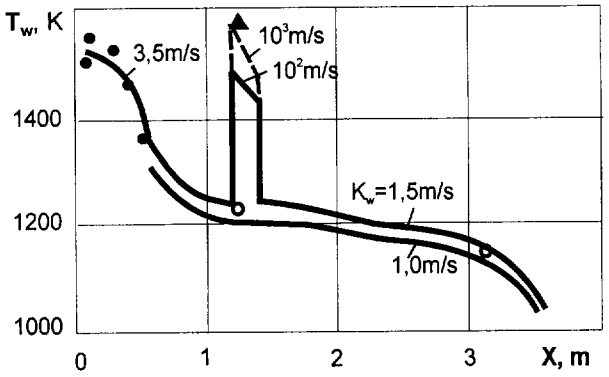


*Fig. 1. Surface temperature distribution along the windward center line of the Bor vehicle [ref. 8]. Dots - the flight test data: 1 - C-C material with antioxidation coating; 2 - ceramic tile; 3 - ceramic tile covered with black platinum. Curves - computations at different catalytic recombination rates $K_W$.*

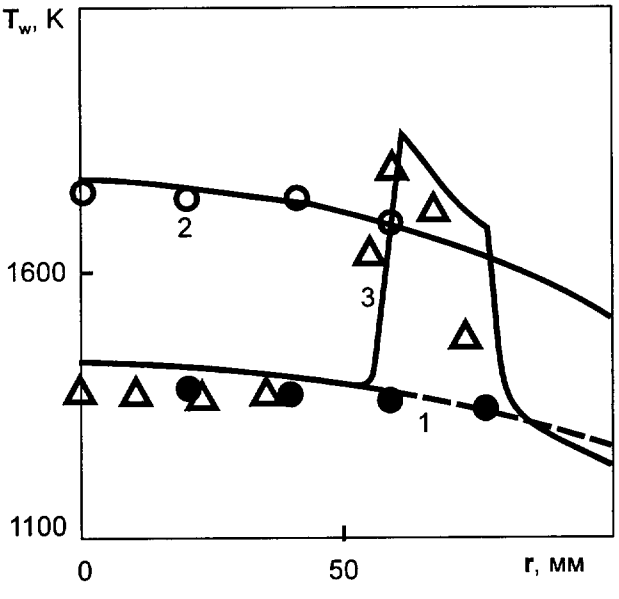


*Fig. 2. Effect of the "overequilibrium" heating of the ceramic tile with nonuniform catalytic coating [ref. 9]. Dots - test in subsonic air flow at the pressure 0.015 atm, enthalpy 23.5 MJ/kg, velocity 650 m/s: 1 - clean tile, 2 - tile fully covered with spinel, 3 - tile with a high-catalytic spot (nickel-chrome spinel ring). Curves - numerical solution of Navier-Stokes equations for nonequilibrium dissociated nitrogen: 1 - $K_{WN}$=1 m/s, 2 - $c_{WN}$=0, 3 - surface with a discontinuity of catalycity.*

*Paper presented at the RTO AVT Course on "Measurement Techniques for High Enthalpy and Plasma Flows", held in Rhode-Saint-Genèse, Belgium, 25-29 October 1999, and published in RTO EN-8.*

almost 400 K. Similar effects of the high catalytic spots "overheating" were observed before in the flight experiment on the Space Shuttle [ref. 5] and in ground test performed in the 1-MW IPG-3 plasmatron (IPM) in subsonic high enthalpy air flow [ref. 9] (see *Fig. 2*).

Surface catalysis may contribute essentially in heat transfer to a vehicle surface during a hypersonic entry into the Martian atmosphere. According to calculations [refs. 10, 11], the predicted stagnation point heat fluxes to the Mars Pathfinder aeroshell and Mars Probe are 3 times greater for the case of a fully catalytic surface in comparison with a noncatalytic surface case for the peak-heating points of the entry trajectories.

It is necessary to understand that surface catalycity can not be measured directly in an experiment. The catalytic recombination of atoms at the TPM surface has complex poorly-defined kinetics which include the following processes [ref. 12]:

- activation and deactivation of the surface sites;
- atoms adsorption and desorption: $A+S \leftrightarrow A_S$;
- adatoms $A_S$ surface migration;
- catalytic recombination of atoms through Eley-Rideal mechanism $A+A_S \rightarrow A_2+S$ and Langmuir-Hinshelwood mechanism $A_S+A_S \rightarrow A_2+2S$;
- formation and quenching of exited molecules.

No theories yet exist to predict the TPM catalycity beyond experiment. The only answer is to determine effective catalytic properties of the TPM from the ground test and to extrapolate accurately to flight conditions [ref. 13].

The method of the inductive heating of gases revealed the efficient way of the production of the unpolluted plasma flows with a temperature level close to gas temperatures at the outer edge of boundary layer at a blunt body when it moves in atmosphere at a hypersonic velocity [refs. 14-16]. This feature combined with a high stability of inductive coupled plasmas provided a basis for the development of the inductive plasmatrons [refs. 17-24] for the studies of the high-enthalpy flows, TPM testing, and real gas effects and plasma/surface interaction, including the contribution of the catalytic effects in surface heating.

The plasmatrons of the IPG family at IPM RAS appeared to be very efficient tools for the ablative TPM samples testing [ref. 25], and the prediction of the TPM catalycity, the testing of the full-scale TPS elements and the studies of TPM behavior in high enthalpy air flows in the course of the Buran program in 1978-1988 [refs. 9, 17, 18, 26, 27]. The efficient capabilities of the 100-kW IPG-4 plasmatron for the simulation of physico-chemical processes accompanying the hypersonic entry of a vehicle aeroshell in the Martian atmosphere have been demonstrated recently [refs. 24, 28-30].

This paper is focused on the method for the TPM catalycity prediction which was developed in refs. 13, 26, 27 in the framework of the Buran vehicle development till 1988 and which is developing now for the TPM catalycity prediction for entry conditions in the Martian atmosphere [refs. 28-30]. Previously accumulated test experience and current capabilities of the IPG-4 plasmatron from the point of view related to the problem of TPM catalycity are presented. Special attention is paid to the CFD codes as the standard diagnostic tools and to measurements/computations interaction. The previous most important results connected with measured and calculated heat transfer to different test models in high-enthalpy subsonic flows of air, nitrogen, oxygen and carbon dioxide are analyzed. The lessons learned from the development of the combined experimental/numerical methodology, current activities in the field of the thermochemical simulation for re-entry issues and perspectives are discussed.

## 2. Philosophy of the Methodology

The general philosophy of the method for the TPM catalycity prediction on the basis of an induction plasmatron heat transfer experiment developed in refs. 26-30 consists in the tight connection of the catalycity tests with heat transfer simulation for the atmospheric entry conditions. The logic of the surface catalycity determination is based on the stagnation point heat flux measurements in high-enthalpy subsonic flows and the sophisticated techniques of the extraction of the heat flux part, caused by the recombination of atoms, by using the CFD modeling of the heat transfer for test conditions (*Fig. 3*).

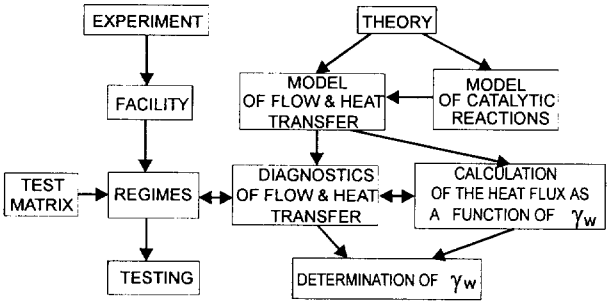


*Fig. 3. The logic tree of the methodology for the surface catalycity determination.*

This scheme was developed for the study of the catalytic effects in subsonic dissociated air and nitrogen flows in refs. 26, 27, 13 and has been recently applied to the prediction of the catalytic efficiencies of recombination of the $O$ atoms and $CO$ molecules on metals, quartz surface, tile coating and antioxidation coating of the carbon-carbon material on the basis of heat transfer experiment curried out in high enthalpy carbon dioxide and oxygen flows [refs. 28-30].

In fact, the method is quite laborious (see the logic scheme on *Fig. 3*), but it reveals a fair way of extrapolation of the surface catalytic effects from ground to flight, at least for the stagnation point heat transfer [refs. 13, 31, 32].

The IPM methodology of the TPM catalycity determination includes the following essential parts:

1) production of the highly dissociated subsonic stable gas flows and optimization of the test regimes;
2) experimental study of the steady-state heat transfer in the stagnation point configuration;
3) tests with different gases;
4) precise characterization of the high-enthalpy flows;
5) search and application of materials with standard catalytic properties;
6) CFD modeling of reacting plasma and gas flows within plasma torch and around a model;
7) numerical rebuilding of the free stream enthalpy;
8) model of the surface catalysis;
9) numerical computations of the nonequilibrium multicomponent boundary layers and design of the heat flux charts for test conditions;
10) analysis of uncertainties;
11) extrapolation from ground test to the atmospheric entry conditions.

## 3. Facilities

At the middle of the 1970's the plasmatron technology development was turned out from the atmospheric pressure plasmatron IPG-1 [ref. 25] toward low pressure domain due to the Buran program challenges including problem of the TPM catalycity. The development went in directions of the power increasing, the expanding of the pressure range and the enlargement of the discharge channel size. Philosophy of the development at this phase was based on the solution to build two IPG facilities: the first one - oriented on airheating problem coupled with the TPM catalycity, cost-effective samples tests and TPM selection, and the second one - powerful plasmatron for resource tests of the full-scale TPS elements at reentry heating conditions [ref. 17].

The 75-kW IPG-2 plasmatron with the discharge channel 60 mm in diameter produced sub- and supersonic high-enthalpy air and nitrogen flows in the stagnation pressure range 0.05-1 atm and total enthalpy range 10-40 MJ/kg. This facility was used to study of the nonequilibrium heat transfer effects and the TPM catalycity in subsonic dissociated air and nitrogen flows in the pressure range 0.05-1 atm during the period 1978-1988. Few catalycity tests with pure oxygen were performed by the IPG-2. The powerful (1-MW) IPG-3 plasmatron with the discharge channel of 200 mm in diameter has been operating with air plasma in subsonic regime in the pressure range 0.015-0.1 atm and the same total enthalpy range [ref. 17]. The multipurpose 100-kW IPG-4 plasmatron with the channel of 80 mm in diameter (mass flow rate 1.5-6 g/s) covers the stagnation pressure range 0.01-1 atm in sub- and supersonic regimes with air, nitrogen, oxygen, carbon dioxide and hydrocarbons as working gases.

The inductive plasmatrons IPG-3 and IPG-4 meet requirements [ref. 33] for R&D facilities to simulate reacting flow physics, real surface processes and to carry out code validation. The plasmatron capabilities provide potential possibilities to define well the flow conditions on the basis of judiciously combined surface and flow field measurements and CFD modeling.

## 4. Subsonic Test Regimes

From the standpoint of the TPM catalycity prediction, the subsonic regimes possess three significant advantages over the supersonic ones. Firstly, for hypersonic vehicles with a blunt nose radius $R_N$~1 m subsonic regimes reveal the way to the duplication of the stagnation point heat transfer if the conditions of a local simulation are satisfied [refs. 13, 31, 32].

Secondly, supersonic plasma flows normally are quite far from equilibrium, whereas the thermodynamic state of subsonic dissociated molecular gas flows in a core is close to LTE at pressures $\geq$ 0.1 atm. Thus, the oxygen flows are completely dissociated in the core, so in fact there is chemical equilibrium in this part of flow. For the carbon dioxide flow at the pressure 0.1 atm the Landau-Teller relaxation time for the CO molecules is $\tau_{VT} \sim 2 \cdot 10^{-5}$ s, so the relaxation zone length $\sim 2 \cdot 10^{-3}$ m is much shorter than the distance from the channel exit section to the model ($6 \cdot 10^{-2}$ m). At the same time the mixing layers and boundary layers near the model should be far from equilibrium.

Finally, in subsonic regimes the boundary layer on a model is quite thick, therefore if the exited molecules are produced on the surface due to the catalytic recombination of atoms those molecules are quenched efficiently within the boundary layer due to collisions [ref. 34]. In this case it is possible to take this effect into account by using the effective rate of catalytic reaction without actual consideration of the process of exited molecules formation.

The choice of the optimal test conditions is very important for reducing flow uncertainties and the contraction of margins. *Fig. 4* taken from ref. 13 shows in the pressure-surface temperature variables the map of the degree of a boundary layer nonequilibrium at the stagnation point of a model with the radius $R_m$=1.5 cm flown by a subsonic dissociated nitrogen jet. It is seen, that the conditions within boundary layer can be changed smoothly by pressure variation from frozen boundary

layer toward equilibrium one. The equilibrium region *5* is optimal for calibration, the optimal conditions for catalycity tests could be realized in the region *3* (equilibrium free stream & frozen boundary layer), the influence of the gas-phase reactions on the heat transfer can be studied in the region *4*.

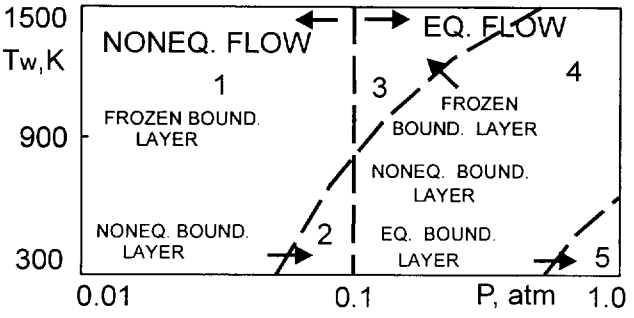


*Fig. 4. The map of the degree of a free stream and boundary layer nonequilibrium for subsonic regimes with nitrogen for a model with radius 1.5 cm [ref. 13].*

## 5. Test Configuration and Models

In the optimal regimes used, the inductively coupled plasma is forced back from the wall of the quartz tube of the discharge channel by a sublayer of the cold gas, the discharge is stable and exists for a long time. This offers the possibility of studying the heat transfer in the steady-state regimes.

Two main types of the models are used in the heat transfer tests (*Fig. 5*): 1) the water-cooled copper model with the water flow steady-state heat probes for the stagnation point heat flux measurements; and 2) the model made from SiC material for the TPM testing. The cylindrical models with a flat face of 30-50 mm in diameter are widely used for subsonic tests. During the last 5 years the standard form of the euromodel of 50 mm in diameter with a rounded edge of 11 mm in radius was widely used for high-enthalpy tests [refs. 35, 36, 28-30].

Under typical subsonic test conditions the optimum distance $Z_m$ between the model and the discharge channel exit can be estimated as $D_m < Z_m < 2D_c$, where $D_m$ is the model diameter and $D_c$ is the discharge channel diameter. For the IPG-4 tests $30 \le Z_m \le 60$ mm. In the optimum zone the following optimum conditions for the studying of the steady-state heat transfer are realized:

1) flow perturbations induced by the model do not reach the discharge channel;
2) the flow past the model exposed in the central part of the jet, is close to axisymmetric;
3) the high stability of the free jet parameters;
4) the uniform heat loading on the sample face;
5) the stagnation point heat flux and the surface temperature of the sample are well reproducible;
6) the flow enthalpy and velocity along the free-jet axis decrease only slightly.

The variation of the flow parameters and the stationary heat transfer conditions are achieved by the control of the anode power $N_{ap}$ supplied to the inductor. With the $N_{ap}$ increasing, the power input in plasma rises, and the flow enthalpy, velocity, stagnation point heat flux and temperature of the sample surface increase respectively.

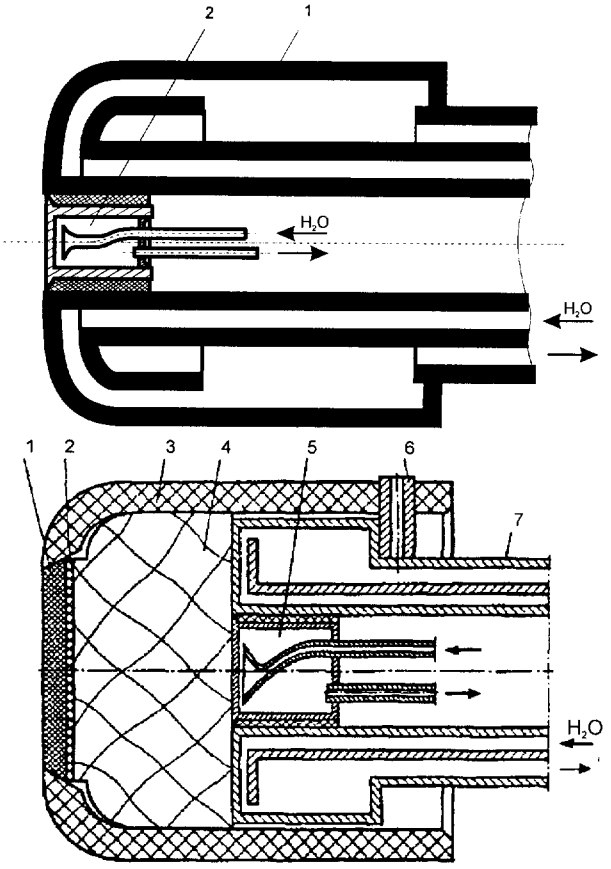


*Fig. 5. Models for heat transfer tests in subsonic regimes. upper - model for cooled wall test (refs. 28, 29): 1 - copper body, 2 - water flow stationary heat flux probe; lower - model for catalycity and oxidation tests: 1 - sample, 2 - spacer, 3 - SiC material, 4 - heat insulation, 5 - water flow stationary heat flux probe, 6 - zirconium pin, 7 - water-cooled holder.*

## 6. Measurements of the Heat Fluxes to Cooled Surfaces

The water flow steady-state probes made of copper monolith, nickel, monocrystalline molybdenum, quartz of high chemical purity and those made of copper with the heat reception faces covered with silver, platinum, titanium and tantalum were used in cooled wall tests [refs. 26-30]. Those heat-adsorbing surfaces of 14 mm in diameter were polished to a mirror quality. To vary quartz surface temperature at a constant plasmatron operating regime, the quartz probes with the different thickness of the heat reception wall in the range 0.63-2.26 mm are used. In order to improve the reproducibility the probe surface should be cleaned in the plasma flow in the course of a few minutes.

The stagnation point heat flux is calculated by the measured water flow rate through the probe and the water temperature difference between the probe outlet and inlet sections. The water flow rate is measured by the float rotameter with an error of ±1.5 %. The water temperature in the probe is measured by the thermocouples and mercury thermometers with the accuracy of 0.1°C. The accuracy of the measurement of the stagnation point heat flux to the cooled surface ($T_W$~300 K) is ±5 %.

For the quartz probes the surface temperature $T_W$ is obtained by the solution of the 1D heat transfer problem within the heat reception quartz wall taking into account the well documented quartz thermal conductivity [ref. 37]. The well-defined spectral and total quartz surface emissivity for the different wall thickness [refs. 38, 39] are necessary to determine the heat flux $q_W$.

The measurements of the heat fluxes to cooled surfaces is one of the key points of the methodology for the TPM catalycity prediction due to two main reasons:

Firstly, cooled wall tests demonstrate the heat effect of the heterogeneous catalysis in dissociated gases [ref. 30]. The difference between the measured values of the heat fluxes to different metals appears as a result of the difference between their surface catalytic activities with respect to atoms recombination. The difference increases with the power input in plasma and, respectively, with the increasing of flow enthalpy, velocity and the degree of dissociation. Since the heat flux to silver wall is higher then that for molybdenum in the dissociated oxygen and carbon dioxide flows, the silver surface is more catalytic then the molybdenum one in those gases.

In the dissociated air and nitrogen the copper and platinum showed the highest catalytic activity but molybdenum also manifested itself as metal with the lowest catalycity [refs. 26, 27] (see *Fig. 6*).

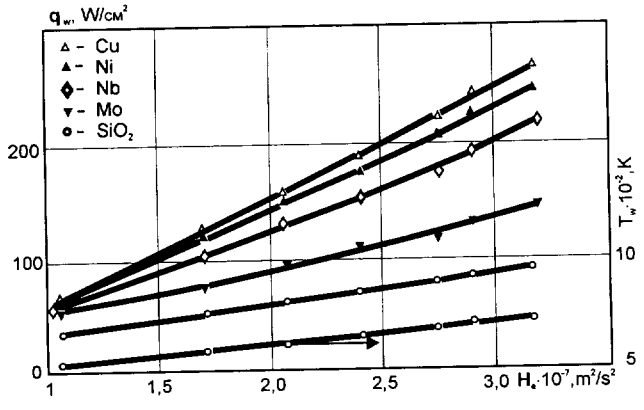


*Fig. 6. Catalytic heat effect on cooled metallic surfaces in subsonic dissociated air flows[ref. 26]:p=0.1 atm, $R_m$=1.5 cm.*

Secondly, more data for cold surfaces are collected then the experimental heat flux envelope is wider and more information for the validation of the CFD codes can be used. The key point of the methodology is the search of materials with maximum and minimum catalytic efficiencies for the different gas environment. Among the measured heat flux values the maximum one is used for the rebuilding of the flow enthalpy, the minimum one - for the verification of the gas-phase chemistry implemented in the CFD codes for modeling of nonequilibrium flows and heat transfer computations.

## 7. Heat Transfer Measurements for TPM Samples

It should be noted that the convective heat flux to the hot wall can not be measured directly. The stagnation point heat flux to the high temperature surface is rebuilt by the formula:

$$q_W = \varepsilon_{th}\sigma T_W^4 + q_C$$

where $\varepsilon_{th}$ is the total hemispheric emissivity of the surface, $\sigma$ is the Stefan-Boltzmann constant, $T_W$ is the surface temperature, $q_C$ is the density of the heat loss from the rear sample surface measured by using the water-cooled probe.

The brightness surface temperature of the sample $T_b$ has to be measured by using optical pyrometers on the basis of the radiation from the heated surface. The operating temperature range should be chosen taking into account the spectral emissivity $\varepsilon_\lambda$ as a function of the surface temperature. For example, in the temperature measurements for the ceramic tile and quartz surfaces the application of the infrared thermovision system AGA-780 is quite efficient for the brightness temperature record at the wavelength 5 μk where the spectral emissivity $\varepsilon_\lambda$=0.98 at $T_W$=300-1700 K [ref. 38].

The intrinsic surface temperature $T_W$ is determined taking into account the spectral emissivity $\varepsilon_\lambda$ of the sample and the spectral transparency $\tau_\lambda$ of the optical quartz window of the testing chamber by the following formula:

$$T_W = \frac{T_W}{1+(\lambda T_b/C_2)\ln\varepsilon_{eff}}, \varepsilon_{eff} = \varepsilon_\lambda \tau_\lambda, C_2 = 14380 \mu k \cdot K$$

In the measurements of the surface temperatures of the quartz sample and the ceramic black tile ($\varepsilon_{th}$ =0.89-0.82 at $T_W$=1200-1700 K) by using the POV-80 and APIR-C pyrometers, and the infrared thermovision system AGA-780 the average error is ±20 K [ref. 28].

In the optical surface temperature measurements the crucial point is the accuracy of the spectral and the total surface emissivity data. The additional uncertainties are connected with the influence of an operational angle of the pyrometric measurements. For the quartz-based borosilicate coating used in the Buran TPS the error in the determination of the heat flux to the surfaces of this kind does not exceed 7%.

## 8. Dynamic Pressure Measurements

The high enthalpy subsonic flow characterization must include the dynamic pressure $\Delta p$ measurements by using water-cooled Pitot probes at least along the flow axis. In IPM practice the water-cooled Pitot probe made of the same shape as the euromodel for the heat flux measurements (*Fig. 5*) is used. The dynamic pressure is measured as the difference between stagnation pressure and static pressure at the wall of the test chamber.

The static pressure in the test chamber and the dynamic pressure at the subsonic high-enthalpy flows are measured by using the transducers of "САПФИР" (sapphire) type. The pressure transducer "САПФИР 22М-ДА" model 2030 with the upper limit 125 hPa and the accuracy ±0.4 hPa is used for the static pressure measurements. The pressure transducer "САПФИР 22МД-ДД" model 2410 with the upper limit 16 hPa and the accuracy ±0.02 hPa is used for the dynamic pressure measurements. The physical principle of the operation is based on the accurate determination of a sensitive sapphire element deformation which is proportional to the measured pressure (or pressure difference). *Fig. 7* shows quite specific features of the measured dynamic pressure in subsonic high enthalpy flows [ref. 24]: $\Delta p$ is a linear function of $N_{ap}$ and $\Delta p$ is inversely proportional to $p$.

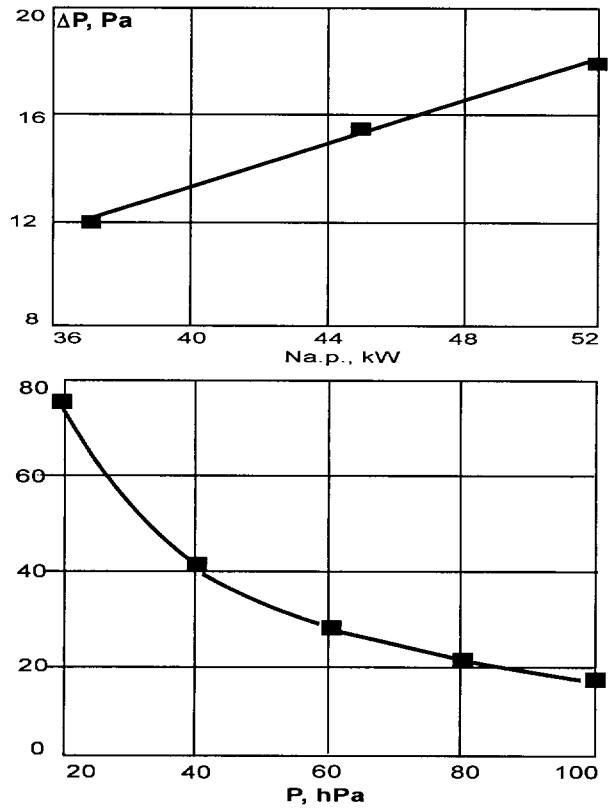


*Fig. 7. Dynamic pressure in subsonic carbon dioxide flows as function of the IPG-4 anode power (p=100 hPa) and pressure ($N_{ap}$=45 kW) at the mass flow rate 1.8 g/s, z=60 mm [ref. 22].*

## 9. Logic of the CFD Modeling

At the beginning of the 1980's the general problem of the subsonic high enthalpy test data analysis was the absence of any analytical theory for the stagnation point heat transfer in contrast with super- and hypersonic tests where Fay and Riddell or Gulard's theories [refs. 2, 3] and Newton's solution for a thin shock layer provided sufficient results. So, the application of the full Navier-Stocks equations for the computations of high enthalpy reacting flows for the test conditions at small Reynolds and Mach numbers was the only choice.

The numerical computations of the subsonic plasma and high-enthalpy reacting flows and heat transfer for the plasmatron test conditions is the essential part of the flow characterization and the surface catalycity prediction method [refs. 13, 26, 29, 40]. On the whole, the problem is rather tricky. Up to now the computations of the nonequilibrium molecular plasma flow coupled with the RF electromagnetic field are not in fact. So, our main idea consists in the separation of the whole flow field into three computation zones, where the distinctive flow features can be used for the efficient approach. For the considered plasmatron operating conditions ($p \geq 0.1$ atm) the main CFD problem for the modeling of the plasma and high-enthalpy oxygen and carbon dioxide reacting flows is divided in the following three problems:

1) the equilibrium inductively coupled swirling plasma flow within the cylindrical discharge channel;
2) the equilibrium subsonic axisymmetric high-enthalpy laminar jet flow past a cylindrical model;
3) the nonequilibrium multicomponent boundary layer with the finite thickness at the stagnation point.

The developed appropriate data base for thermodynamic and transport properties, and soft ware provide efficient numerical modeling for the subsonic regimes of the IPG-4 with different gases (air, nitrogen, oxygen, carbon dioxide, argon).

## 10. Inductive Plasma Modeling

The problem of the inductive plasma flow [ref. 41] is being treated for the case of equilibrium plasmas on the basis of the full Navier-Stokes equations coupled with the simplified Maxwell equations for the RF electromagnetic field [refs. 42, 43]. The statement of the problem includes the plasmadynamics effect of the Lorentz force and the Joule heat release. The 2D Navier-Stokes equations written for the total enthalpy and three velocity components including the tangential component due to the flow swirling and the simplified quasi 1D Maxwell equations for the complex amplitude of the electric field tangential component generating vortical electric currents are used for the computations of reacting plasma flows within the discharge channel. The input parameters of the problem are: the gas composition, the gas flow rate $G$, the coil geometry, the

electric current frequency $f$, and the power input in plasma $N_{pl}$ .

The boundary conditions at the inlet section and the channel wall should be specified in accordance with the torch design and the system of heat exchange between the torch and the ambient environment. The two main cooling systems are now in use: one self-cooling system with free quartz tube (the IPM plasmatrons, [ref. 17]) and the other with water cooled quartz tube (the VKI plasmatron, [ref. 23]).

In our methodology the finite difference analogies of the Navier-Stokes equations written for the control volumes of the staggered grid are used. The obtained equations are being solved by a method analogous to the SIMPLE method by Patankar and Spalding [ref. 44]. The final system of the linear algebraic equations is being solved by the modified method of incomplete factorization. The simplified equation for the complex amplitude of the electric field is being solved by an effective technique based on the Thomas algorithm.

The transport properties - viscosity, thermal conductivity and electrical conductivity - have to be calculated in advance as the functions of pressure and temperature by the precise formulae of the Chapman-Enskog method in the second approximation by the Sonine polynomials for the plasma viscosity and in the third approximation for the plasma thermal conductivity and electrical conductivity according- to well known requirements formulated in ref. 45. The formulation of the plasma transport properties proposed in ref. 46 is very efficient for inductively coupled plasmas computations.

The recent code-to-code validation for the test case with the argon inductively coupled plasma for the IPG-4 plasmatron geometry [ref. 47] has shown rather good agreement between 1D electric field approach [refs. 42, 43] and complete 2D formulation for the plasma induced electric field within the plasmatron channel and in the space beyond the torch itself [ref. 48] for the plasma flow and temperature fields in the whole discharge channel including the plasmatron exit section.

The computed flow and temperature fields for oxygen and carbon dioxide plasmas in the IPG-4 plasmatron discharge channel are shown in *Fig. 8* for $N_{pl}$=25 kW, $G$=2.8 g/s. The complicated structure of the flow with embedded vortical zones is formed due to the interaction of a swirling gas flow with Joule heat release and magnetic pressure. For both plasmas the flow patterns are quite similar, but the temperature fields are rather different at the same energy input in plasma due to the clear reason: in a carbon dioxide flow the great deal of input energy is spent on dissociation while in fully dissociated oxygen flow an essential part of input energy is pumped in the translational temperature of the monatomic gas.

The calculated flow parameters at the exit section of the discharge channel are the inflow boundary conditions for the second problem of reacting gas flow around a model. Due to the reason mentioned above, in the jet core the velocity and temperature profiles are more smooth for air and carbon dioxide then for oxygen (*Fig. 9*).

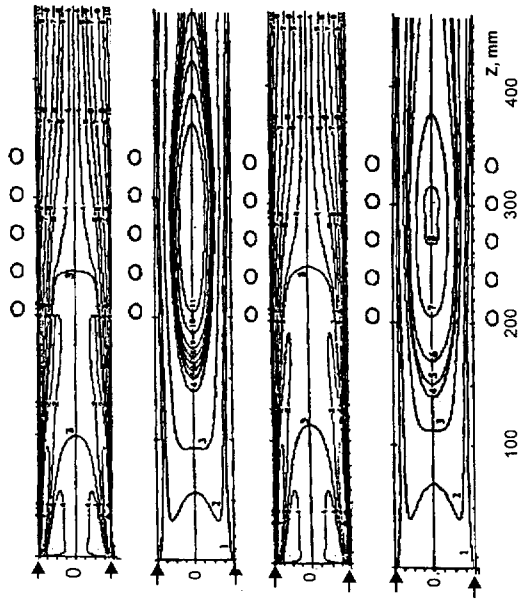


*Fig. 8. Flow and temperature fields in the IPG-4 discharge channel for oxygen (left) and carbon dioxide (right) plasmas. Dimensionless stream function values: -0.04, -0.02, 0, 0.01, 0.05, 0.1, 0.2, 0.4, 0.6, 0.8; temperature values for the isotherms in 1000 K [ref. 30].*

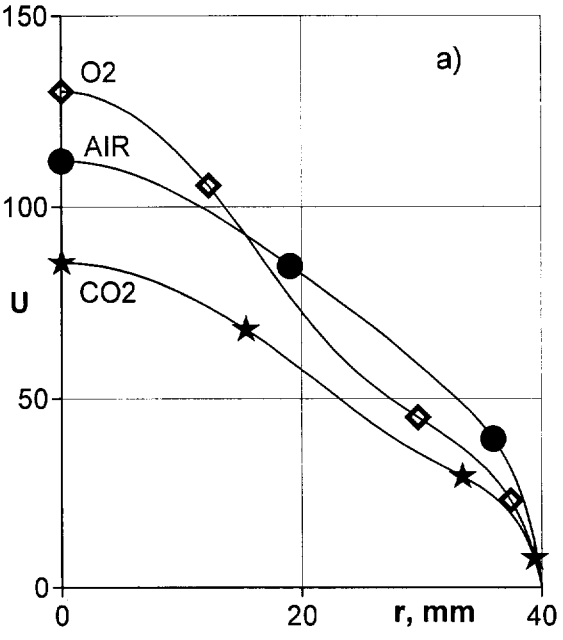


*Fig. 9a. Velocity profiles at the exit of the IPG-4 discharge channel for oxygen, air and carbon dioxide plasmas.*

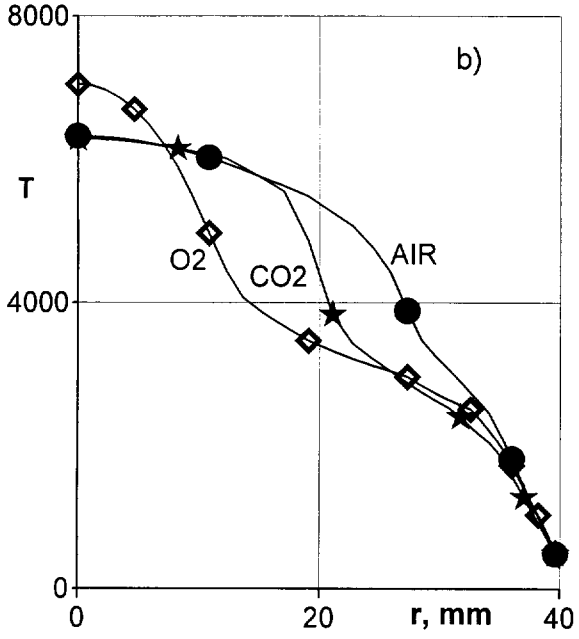


*Fig. 9b. Temperature profiles at the exit of the IPG-4 discharge channel for oxygen, air and carbon dioxide plasmas.*

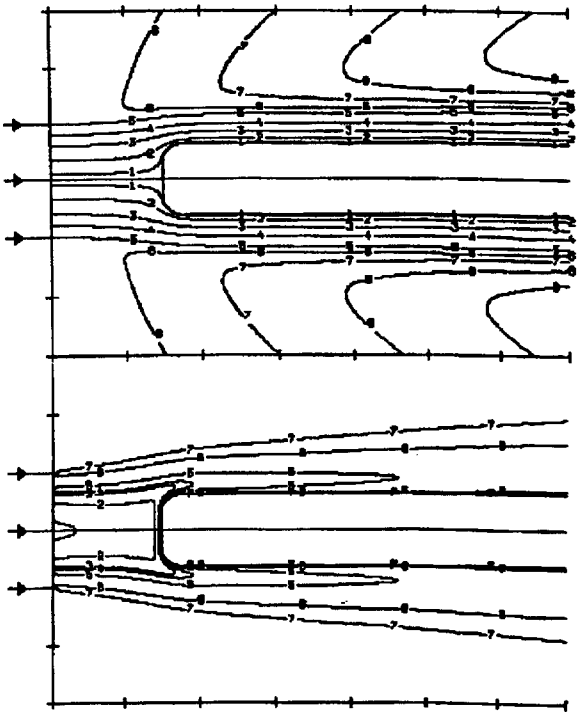

*Fig. 10. Flow and temperature fields of reacting carbon dioxide gas flow past a model at p=0.1 atm and $N_{pl}$=25 kW. Dimensionless stream function values: 0.01, 0.1, 0.3, 0.6, 1.0, 1.2, 1.4, 1.6, 1.8. Temperature values for isotherms: 6500, 6000, 5000, 4000, 2000, 1000 K [ref. 29].*

### 11. Flow around a Test Model

For the subsonic reacting flow after the plasmatron exit section we can assume that the flow is in equilibrium at pressure $p \geq 0.1$ atm. In the considered enthalpy range the flow ionization influence on heat transfer is negligible and weak traces of flow vorticity are also not taken into account.

The grounds for the equilibrium approach stand on the specific features of subsonic high-enthalpy flows in plasmatron at pressures $p \geq 0.1$ atm (see chapter **3** above). The approach consists in the use of equilibrium computations for the incoming subsonic plume serving only as the external solution for the nonequilibrium boundary layer problem. So, the surface catalycity is not an input parameter for this problem.

The full 2D Navier-Stokes equations for the enthalpy, two velocity components and pressure are used for the modeling of the laminar hyposonic (M<<1) equilibrium high-enthalpy flows over a model (flow swirling is not essential here). It is reasonable to use for computations the same numerical method [ref. 44] which is exploited for the previous problem. *Fig. 10* shows the calculated flow and temperature fields of reacting carbon dioxide gas around the model, *Fig. 11* - the enthalpy distributions along the jet axis for four different gases. These data confirm (qualitatively) the assumption on the chemical equilibrium in the core of the subsonic jet. In fact, we observe a large isothermal, isobaric zone between the exit section of the discharge channel and the model - favorable conditions for fast relaxation.

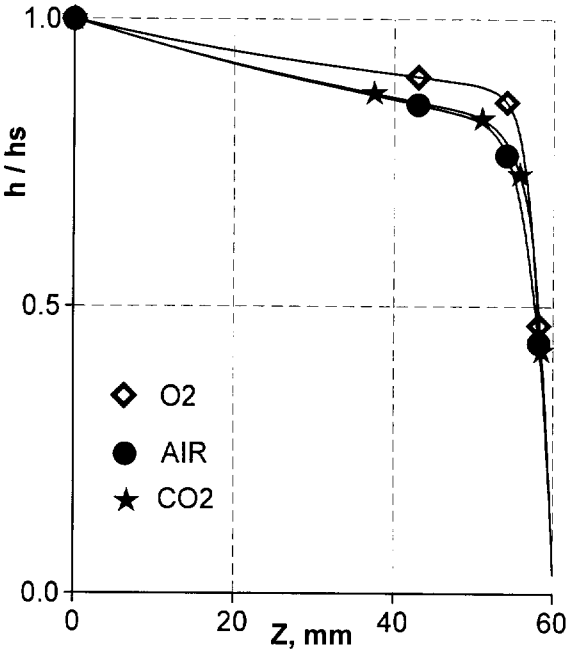


*Fig. 11. Dimensionless enthalpy distributions along jet axis from plasmatron exit to a cooled model at p=0.1 atm and $N_{pl}$=20 kW for different gases.*

At low pressures the displacement from equilibrium could be quite essential. The relaxation time $\tau_{VT} \sim p^{-1}$, but the hydrodynamic time for inductively coupled plasma has an opposite trend $\tau_{hyd} \sim p$ and at $p \sim 0.01$ atm those times are quite comparable.

## 12. Boundary Layer Problem for Subsonic Test Conditions

The analysis of experimental data concerning heat transfer and the procedure of surface catalycity rebuilding require a lot of computations for multiparameter models of the flow and the heat transfer. In spite of the capabilities of the modern PC, the application of the full Navier-Stokes equations, as a standard wind tunnel instrument, for modeling of the nonequilibrium flows in the whole computational field and computations of the heat transfer rates with sufficient accuracy, still does not look effective enough.

In order to find a compromise between requirements to take into account the main features of subsonic viscous reacting jets and heat transfer in plasmatron and to minimize computational efforts, the author developed in the early 1980's the 1D concept of the nonequilibrium boundary layer with finite thickness. This concept made it possible to efficiently separate the problem of the accurate computations of the stagnation point heat transfer rates and the solution of the full Navier-Stokes equations for the flow bulk.

The mathematical model of the 1D flow and heat transfer in the boundary layer for the reacting multicomponent gas presented in refs. 26-30 takes a finite thickness of the boundary layer and flow vorticity at the outer edge of the boundary layer into account by means of the three dimensionless parameters and provides accurate computations of the stagnation point heat flux. These three parameters at the outer edge of the boundary layer have to be obtained from the numerical solution of the full Navier-Stokes equations for the equilibrium subsonic flows around the model. At the fixed value of a gas flow rate those parameters actually slightly depend on the pressure and power input in plasma and should be calculated, as input parameters for the 1D boundary layer code, in advance. After that 1D code can run autonomously in the wide domain of test conditions, surface temperature and catalytic efficiency.

The following assumptions have been made in the physical model of the nonequilibrium boundary layer: 1) gas is a multicomponent mixture of molecules and atoms; 2) molecules vibrations are in equilibrium excitation, chemical kinetics is one-temperature. The data on rate constants for gas-phase reactions have been taken from ref. 49.

The finite difference scheme of the high order of approximation should be used for the fast numerical solution of the 1D boundary layer problem.

## 13. Model of the Surface Catalysis

As we mentioned above, the processes of the formation of molecules due to collisions of atoms on a surface have complex kinetics [ref. 12]. In general, these processes are poorly studied although the kinetics of the oxygen and nitrogen atoms recombination on silica has been investigated in refs. 6, 50, 51. The mechanisms of the Eley-Rideal and Langmuir-Hinshelwood recombination of the oxygen atoms on silica have been studied within a framework of molecular dynamics in ref. 52. Kinetic studies of the catalytic reaction $CO+O \rightarrow CO_2$ on the quartz-based surfaces, which is important for heat transfer to a vehicle surface during entry into Martian atmosphere, are practically absent.

In our methodology the parameters which characterize surface catalycity have to be determined form the comparison of the measured heat fluxes and surface temperatures with the results of parametric computations (inverse problem). Therefore, the model of surface catalysis has to contain a consistent number of parameters - actually one, or more, if possible to separate contributions of different catalytic reactions in heat transfer by performing tests in different gases.

Here we present the macrokinetic model for the catalytic recombination of the $O$ atoms and $CO$ molecules, reactions which accompany the heat transfer from dissociated carbon dioxide to TPM surface, formulated before in ref. 29.

The following assumptions are taken in this rather simple model:

- adsorption of oxygen atoms dominants over other species adsorption;
- adsorption of oxygen atoms and desorption of the products are fast reactions;
- recombination reactions $O+O \rightarrow O_2$ and $CO+O \rightarrow CO_2$ follow the Eley-Rideal mechanism $O+S \rightarrow O_S$, $O+O_S \rightarrow O_2+S$, $CO+O_S \rightarrow CO_2+S$, where $S$ is the site, $O_S$ is the adsorbed oxygen atom (adatom);
- recombination reaction $C+2O \rightarrow CO_2$ follows the Langmuir-Hinshelwood mechanism $C+O_S \rightarrow CO_S$, $CO_S+O_S \rightarrow CO_2+S$.

This scheme leads to the first order reactions of the $O$ atoms, $CO$ molecules and $C$ atoms with three independent effective parameters - catalytic efficiencies $\gamma_{WO}$, $\gamma_{WCO}$ and $\gamma_{WC}$ ($0 \le \gamma_W \le 1$). The case $\gamma_{WO} = \gamma_{WCO} = \gamma_{WC} = 0$ corresponds to a noncatalytic wall, the case $\gamma_{WO} = \gamma_{WCO} = \gamma_{WC} = 1$ - to a fully catalytic wall.

If $\gamma_{Wi}$ is identified with effective probability of catalytic recombination of atoms with the number $i$, then the boundary conditions for mass fraction of $i$-atoms at the wall has the following form

$$-J_i = \rho K_{wi} C_i \qquad (13.1)$$

$$K_{wi} = \frac{2\gamma_{wi}}{2-\gamma_{wi}}\sqrt{\frac{kT_w}{2\pi M_i}} \qquad (13.2)$$

Here $J_i$ is the mass diffusion flux and $K_{Wi}$ is the effective rate of catalytic recombination of $i$-atoms (the diffusion velocity of $i$-atoms at the wall). If $\gamma_{Wi} \ll 1$, then

$$K_{wi} = \gamma_{wi}\sqrt{\frac{kT_w}{2\pi M_i}} \qquad (13.3)$$

In literature the last expression occurs more frequently, then the exact expression.(13.2). For a low catalytic wall it is quite accurate, practically if $\gamma_{Wi} \le 0.1$. But in the full range of $\gamma_{Wi}$ the formula (13.3) is incorrect, because it was obtained for the case when the distribution function of atoms was assumed to be Maxwell function. If the wall is sufficiently catalytic, it disturbs the Maxwell distribution due to the gradient of atomic fraction and diffusion velocity becomes different from the thermal velocity of atoms.

In addition to the boundary conditions (13.1) the conditions of the total mass balance and mass balance of atoms at the surface must be added. For example, for 5-species dissociated carbon dioxide mixture ($CO_2$, $CO$, $O_2$, $O$, $C$) the following necessary conditions of the $O$ and $C$ atoms balance must be implemented in the 1D boundary layer code:

$$J_{O_2} + \frac{2M_O}{M_{CO2}} J_{CO_2} + \frac{M_O}{M_{CO}} J_{CO} + J_O = 0,$$

$$\frac{M_C}{M_{CO2}} J_{CO_2} + \frac{M_C}{M_{CO}} J_{CO} + J_C = 0$$

### 14. Numerical Rebuilding of Flow Parameters

The characterization of the free stream conditions (velocity, pressure, enthalpy, chemical composition) is the crucial point in the problem of the TPM catalycity prediction from the heat transfer test. The diagnostic of high-enthalpy reacting gas flows still is a quite challenging problem. In fact, we have to predict reliable data on the TPM catalycity on the basis of incomplete information on a plasma flow in facility.

It is essential to understand that the quality of the result is quite sensitive to the choice of the test regimes. For subsonic tests the main flow uncertainties are connected with the jet nonuniformity and displacement from equilibrium. So, it is vital to find optimal test regimes and then to determine profiles of the parameters (not only local or average values).

For the subsonic test conditions located in the optimal region (see *Fig. 4*) it is necessary to measure at least two flow parameters - the enthalpy and head velocity. The direct enthalpy measurements still are not in fact because there are not standard conditions for calibration, and any theory of an enthalpymeter with an accurate analysis of coupled effects of a nonequilibrium boundary layer does not exist.

The experimental key point of our methodology is a measurement of the stagnation point heat flux to the cooled surface with a standard high catalytic efficiency. The search of surfaces with such extreme property is an indispensable step for TPM catalycity prediction. After a considerable number of plasma tests performed with different metals it was found that in dissociated air and nitrogen flows the copper and platinum are the best catalysts [refs. 26, 27, 17], in dissociated oxygen and carbon dioxide flows the silver has the same feature [refs. 29, 30]. So, the measurements of heat transfer to the cooled wall is one of the stepping stones to TPM catalycity prediction.

The next one - the steady state measurements of the dynamic pressure of the high-enthalpy subsonic flow which were discussed in the chapter **8**. Those two measured parameters are necessary and sufficient for the rebuilding of flow conditions if the flow core is in equilibrium, the measured maximum heat flux is related to a fully catalytic wall and hydrodynamic parameters are derived from the CFD modeling. In this case the free stream velocity and thermodynamic parameters at the flow axis can be determined from the numerical solution of the following nonlinear algebraic equations:

$$q_W = 0.763\, Pr^{-0.6}(\rho_e\mu_e)^{1/2}\left(\frac{V_S}{R_{eff}}\right)^{1/2}\left(\frac{\rho_W\mu_W}{\rho_e\mu_e}\right)^{0.1}(h_e - h_W)$$

$$\Delta p = k(Re)\rho_e V_S^2/2,\quad p = \rho_e R T_e / m_e,\quad F(p, T_e, c_{ie}) = 0$$

Here, the first formula is the Fay-Riddell formula [ref. 2] adapted and verified for subsonic flows, the last formulae are the chemical equilibrium equations for the considered gas mixture, $q_W$, $\Delta p$ are the measured parameters, $k(Re)$ is the coefficient which takes into account the effect of the viscosity at low Reynolds numbers $Re$, $R_{eff}$ is the effective radius of the model which depends on the flow geometry, the model and channel radii $R_m$ and $R_c$.

The geometrical parameter $R_{eff}$ is expressed in term of the velocity gradient at the model stagnation point $R_{eff} = V_S\,(dU_e/dr)_0^{-1}$ and must be determined from the numerical solution of the Navier-Stokes equations for the subsonic flow past a model.

For the IPG-4 plasmatron with the discharge channel of 80 mm in diameter and the standard euromodel with a flat face and 50 mm in diameter at the stagnation point

configuration $R_{eff}$ =1.28 $R_m$. The formulae of kinetic theory for transport properties should be included in the procedure described above.

The results of this procedure application for the rebuilding of the subsonic high enthalpy carbon dioxide flow conditions as the functions of the generator anode power at the pressure 0.1 atm are presented in *Fig. 12*.

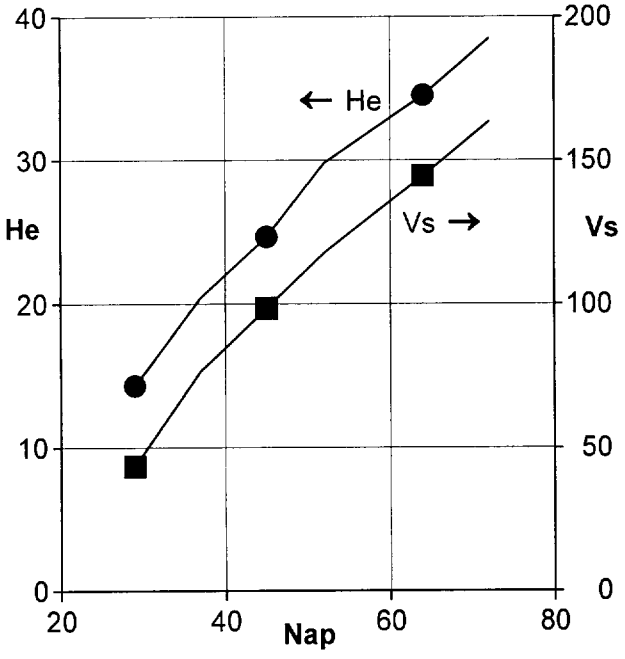


*Fig. 12. Enthalpy (MJ/kg) and velocity (m/s) of carbon dioxide flow at the center of the plasmatron exit as functions of anode power at p=0.1 atm and G=1.8 g/s.*

### 15. Procedure of the TPM Catalycity Determination

Let's consider the catalycity determination technique for the case when the surface is being flown by high enthalpy gas which is a binary mixture of atoms and molecules (dissociated nitrogen or oxygen). The first step consists in the study of the heat transfer to a cold wall from both sides - experimental and numerical. In the experimental part it is important to perform tests with different cooled metallic surfaces - as many as possible - and to put the data in the order of catalytic efficiency. At this step the traditional presentation of the calculated heat fluxes as the functions of $\gamma_W$ in *S*-like curves is required (see *Fig. 13* with data for tests in high enthalpy nitrogen flows in the IPG-2 plasmatron).

The search of the standard material with the minimal catalytic efficiency is also a key point. The heat flux from a nonequilibrium boundary to a noncatalytic wall ($\gamma_W$=0) is quite sensitive to gas-phase recombination of atoms. So, the comparison of numerical data for this case with the measured minimal heat flux reveals the way to verify the data on the rates of the atom-atom recombination implemented in the CFD codes. If an experimental point drops out of the numerically predicted heat flux range, bounded below with the minimum corresponding to $\gamma_W$=0, that means that the rate of atom-atom recombination is the excessive one. In this way we found [refs. 27, 30] that the data for nitrogen and oxygen atom-atom recombination from ref. 53 had provided the excessive rates. So, standard noncatalytic materials are indispensable tools for the validation of data base for the gas-phase chemistry.

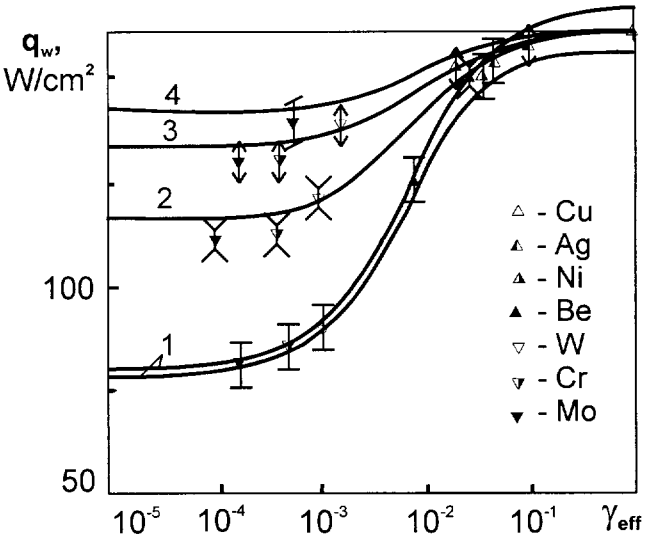


*Fig. 13. Stagnation point heat fluxes to cooled surfaces in dissociated nitrogen flows as functions of catalytic efficiency at different pressures [ref. 26]. Dots - measurements, curves - calculations: 1 - 0.1 atm, 2 - 0.2 atm, 3 - 0.3 atm, 4 - 0.4 atm. IPG-2, $h_e$=21 MJ/kg, $R_m$=1.5 cm.*

The CFD modeling produces a lot of information and a quite important question about the presentation of numerical data in the way mostly convenient for the experimental data analysis turns up. Concerning the TPM catalycity prediction, the method of a heat transfer chart, proposed by the author at the beginning of 1980's, still remains very efficient. A whole spectrum of the heat transfer conditions can be presented by the one heat flux chart in $q_W$-$T_W$ coordinates (measured parameters) for the given test regime and model geometry.

As an example, *Fig. 14* presents the heat flux chart for the subsonic test with pure nitrogen performed by the IPG-2 plasmatron at the pressure 0.1 atm, enthalpy $h_e$=20 MJ/kg and for a cylindrical model with a flat face of 30 mm in diameter. The solid curves are the dependencies $q_W(T_W)$ at constant $K_W$ values ($0 \le K_W \le \infty$). The upper curve *1* corresponds to a fully catalytic surface ($K_W=\infty$), the lower curve - to a noncatalytic surface ($K_W$=0). The dash curve presents the heat transfer rate to the noncatalytic surface calculated for the frozen boundary layer, i.e. the lower theoretical limit for the heat flux. The actual calculated heat flux envelope is bounded from the right side by the curve $q_W=\varepsilon_{th}\sigma T_W^4$, which corresponds to radiative-equilibrium wall, so, the right border is depended from the TPM optical properties.

The location of an experimental point is determined by two measured coordinates $q_W$ and $T_W$. The measured heat fluxes to the cooled copper surface ($T_W$=300 K) were used as a caliber value of the heat flux to the fully catalytic wall. So, the upper left corner of the chart in *Fig. 14* is matched with the experimental point, presented the copper cooled surface. Each experimental point gives one value of surface catalycity (for one measured temperature value), which is determined by the point position relative to curves $\gamma_W$=*const*.

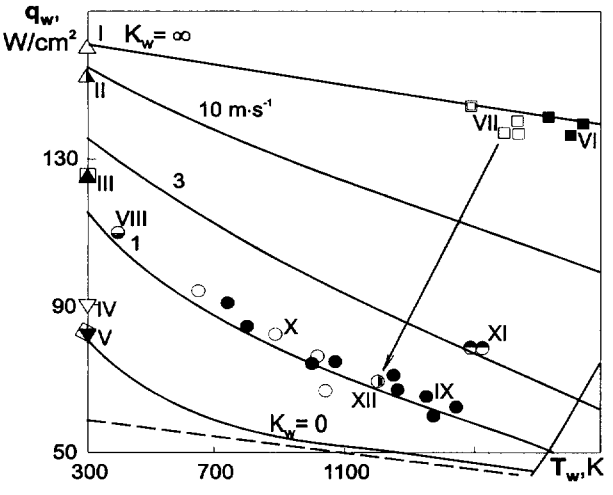


*Fig. 14. Heat flux chart and experimental data for the subsonic test with pure nitrogen [ref. 17]. IPG-2: p=0.1 atm, $h_e$= 20 MJ/kg, $V_S$=160 m/s, $R_m$=1.5 cm. I - Cu, II - Ni, III - Be, IV - W, V - Mo, VI - pyrographite, VII - carbon, VIII -$SiO_2$ coating, IX - ceramic tile, X - quartz, XI - C-C with antioxidation coating, XII - $SiO_2$ coating on carbon; dash line - frozen boundary layer with $K_W$=0.*

All data for cold metals are located along the left border of the heat flux envelope in the *Fig. 14*. The minimum of the measured heat flux corresponds to molybdenum. The data for quartz and tile coating are gathered along the curve which corresponds to $K_W \approx$1m/s ($\gamma_W \approx 3 \cdot 10^{-3}$), which means that the catalytic efficiency of the quartz-based surfaces does not depend sufficiently on surface temperature in the case of atomic nitrogen recombination.

The heat flux chart for the subsonic test with pure oxygen performed recently by using the IPG-4 plasmatron at the pressure 0.1 atm, for the euromodel configuration looks quite similar (*Fig. 15*). We can find from *Fig. 14* and *15* that the catalytic efficiencies of the quartz-based materials in dissociated nitrogen and oxygen flows are rather close.

For a multicomponent mixture the several catalytic efficiencies should be determined from catalycity tests: at least two for 5-species dissociated air and carbon dioxide to characterize the catalytic reactions $O+O \rightarrow O_2$ ($\gamma_{WO}$), $N+N \rightarrow N_2$ ($\gamma_{WN}$) in air and $O+O \rightarrow O_2$ ($\gamma_{WO}$), $CO+O \rightarrow CO_2$ ($\gamma_{WCO}$) in carbon dioxide. In fact, it is possible to rebuilt only one parameter of the surface catalycity using the present methodology.

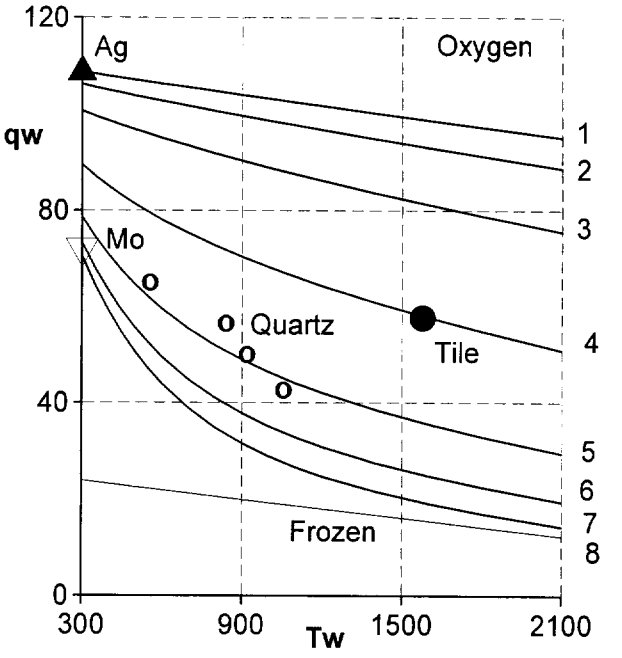


*Fig. 15. Heat flux chart and experimental data for the subsonic test with pure oxygen [ref. 30]. IPG-4: p=0.1 atm, $h_e$= 20 MJ/kg, euromodel with $R_m$=2.5 cm; curves 1-7: $\gamma_W$=1, $10^{-1}$, $3 \cdot 10^{-2}$, $10^{-2}$, $3 \cdot 10^{-3}$, $10^{-3}$, 0.*

Therefore, for those mixtures one parameter must be specified in advance on the basis of tests performed in simple gases, or we have to introduce some average catalytic efficiency for the two or more reactions. We see from the data presented in *Fig. 14* and *15* that we can use such effective catalycity assuming that $\gamma_{WO}=\gamma_{WN}$ for the quartz-based materials in dissociated air.

The one calculated chart of the stagnation point heat flux is shown on *Fig. 16* for the subsonic test with carbon dioxide performed by the IPG-4 plasmatron at $p$=0.1 atm, $N_{ap}$=45 kW ($h_e$=21,2 MJ/kg). The equality $\gamma_{WCO}=\gamma_{WO}=\gamma_W$ was assumed in the surface catalysis model. The upper solid curve *1* corresponds to a complete $CO_2$ reduction ($\gamma_W$=1), the lower curve *7* - to a noncatalytic surface ($\gamma_W$=0). All experimental data for quartz are spaced along the curve 5 ($\gamma_W=3 \cdot 10^{-3}$). Those data and the data shown in *Fig. 15* justify the above mentioned assumption $\gamma_{WCO}=\gamma_{WO}$ for the quartz-based materials.

But in general, one should be careful when an average catalytic efficiency is being introduced. For example, it is incorrect for the surface catalysis on a cold titanium surface in dissociated air. As was found in ref. 26, the catalytic recombination of the *O* and *N* atoms on titanium have quite different efficiencies: $\gamma_{WN}$=0, $\gamma_{WO}=10^{-2}$. Due to this difference the effect of the anomalous increasing of

heat transfer to the titanium surface exposed in dissociated nitrogen flow was observed when oxygen was slightly injected from surface into the boundary layer (*Fig. 17*, [ref. 54]).

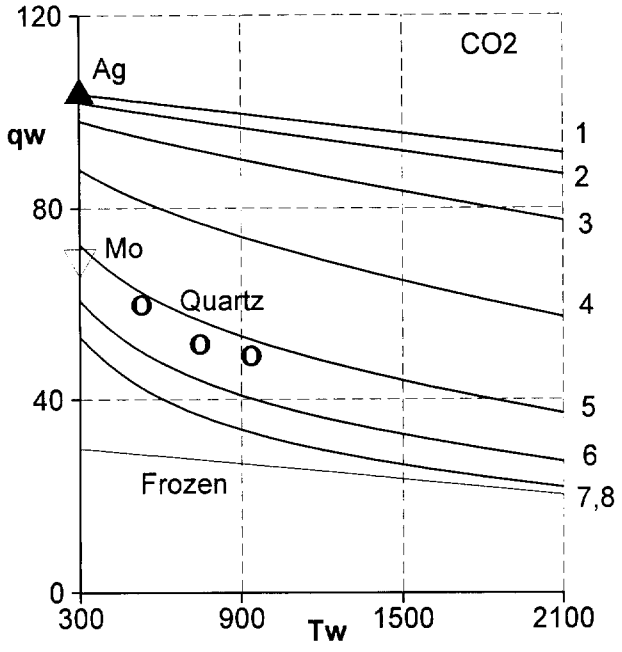


*Fig. 16. Heat flux chart and experimental data for the subsonic test with carbon dioxide [refs. 29, 30]. IPG-4: p=0.1 atm, $h_e$= 30 MJ/kg, euromodel with $R_m$=2.5 cm; curves 1-7: $\gamma_W$=1, $10^{-1}$, $3\cdot10^{-2}$, $10^{-2}$, $3\cdot10^{-3}$, $10^{-3}$, 0.*

This effect was caused by the formation of oxygen atoms near the surface and their diffusion toward surface which was quite catalytic to *O* atoms recombination. Therefore, heat flux was increasing in comparison with heat flux to noncatalytic wall (in pure nitrogen).

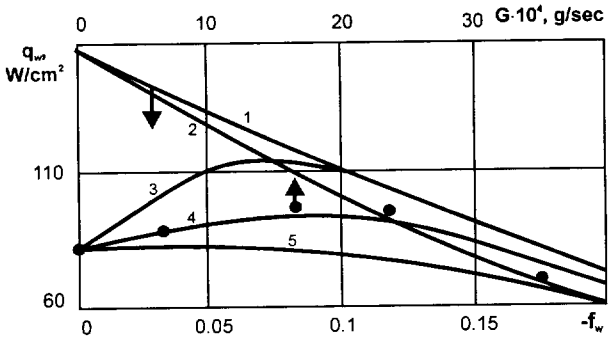


*Fig. 17. Effect of the stagnation point heat flux increasing at a weak injection of the oxygen into nonequilibrium boundary layer near the titanium surface exposed in flow of the dissociated nitrogen [ref. 50]; G - mass flow rate of oxygen, $f_w$ -dimensionless stream function; 1 - $K_{WO}=K_{WN}=10^4$ m/s; 2 - $K_{WO}=0$, $K_{WN}=10^4$ m/s; 3 - $K_{WO}=10^4$ m/s, $K_{WN}=0$; 4 - $K_{WO}=2$ m/s, $K_{WN}=0$; 5 - $K_{WO}=K_{WN}=0$.*

## 16. Discussion

On the basis of the presented self-consistent experimental-theoretical methodology the efficiencies of the catalytic recombination of the *N* and *O* atoms, and *CO* molecules were extracted from high enthalpy tests with dissociated nitrogen, air, oxygen and carbon dioxide flows performed by using the IPG-2 and IPG-4 plasmatrons in subsonic regimes at pressure $p\geq0.1$ atm, when free streams in the core were close to the thermal and chemical equilibrium. The appropriate CFD codes and methodology for the modeling of the whole flow field in the plasmatrons and the rebuilding of the free stream conditions were developed.

Normally, one test regime gives one value of $\gamma_W$ for the appropriate surface temperature. In order to obtain the dependence $\gamma_W(T_W)$ the variation of the free stream parameters, the different test models and heat probes were used in experiment. A lot of computations were carried out in order to analyze the test data. As an example, *Fig. 18* presents in the Arrhenius coordinates data for $\gamma_{WO}$ and average efficiency $\gamma_W$ obtained in pure oxygen and carbon dioxide subsonic gas flows for quartz and tile coating [refs. 28-30]. Taking into account some scattering of the data we can see that the presented data are in satisfactory agreement with the well known data on the recombination of oxygen atoms on quartz from ref. 55 and on RCG presented in ref. 5.

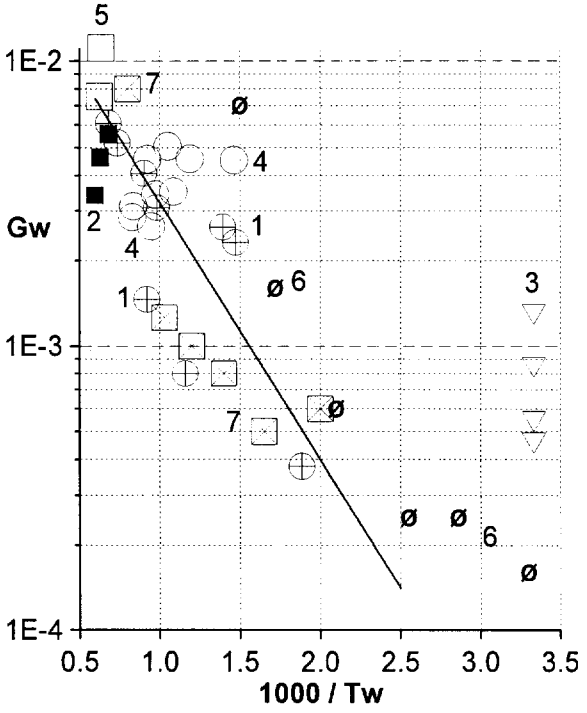


*Fig. 18. Surface catalytic efficiency versus temperature in carbon dioxide and oxygen [refs. 28-30]. Carbon dioxide: 1 - quartz, 2- tile, 3 - molybdenum; Oxygen: 4 - quartz, 5 - tile, 6 - quartz (ref. [55]), 7 - RCG (ref. [5]).*

The data on the quartz average catalytic efficiency in carbon dioxide flows have a slight temperature dependency and almost Arrhenius like behavior. On the

whole, the data for $\gamma_{WO}$ are quite close to the data for the average efficiency $\gamma_W$ obtained from tests with carbon dioxide. A good agreement between the efficiency of the catalytic reaction $O+O \rightarrow O_2$ and the average efficiency of the catalytic reactions $O+O \rightarrow O_2$, $CO+O \rightarrow CO_2$ on a quartz surface confirms the simple model of catalysis proposed in ref. 29.

It appeared that catalytic efficiencies of the Buran tile coating in dissociated air and carbon dioxide flows are quite close. Our recent data on atomic oxygen and carbon monoxide catalytic recombination [refs. 29, 30] have shown the maximum in the dependence $\gamma_W(T_W)$ at $T_W \approx 1670$ K and the decreasing $\gamma_W$ at higher temperatures due to the high efficiency of the atomic oxygen surface desorption. The numerical analysis of the experimental data obtained from tests with dissociated air, carbon dioxide and pure oxygen flows has revealed the similarity between the heterogeneous recombination mechanisms on the ceramic tile surface in the dissociated air and carbon dioxide gas flows and pointed out the atomic oxygen adsorption-desorption and recombination as dominant factors in catalytic processes accompanying the vehicles entry in the Earth and the Martian atmospheres.

## Conclusion & Outlook

The inductive plasmatrons of the IPG family appeared as necessary and capable ground tools for the simulation of the real gas phenomena and plasma/surface interaction during the Buran vehicle campaign in 1978-1988. The catalytic efficiencies of the black ceramic tile surface and antioxidation coating of the C-C material theoretically predicted from the IPG-2 and IPG-4 plasmotrons tests were completely confirmed in flight experiments with the Bor and Buran vehicles. Recent researches [refs. 24, 28-30, 32] have revealed good capabilities of the IPG-4 plasmatron for the simulation of thermochemical loads on heat shields of the Mars Pathfinder and future Mars Probe vehicles [ref. 56], including surface catalysis effects.

One of the main lessons learned from the previous experience in inductive plasma applications in the atmospheric reentry problem - the necessity of the CFD codes implementation as standard tools for the characterization of the high-enthalpy facilities and for the prediction of the surface catalycity. Another lesson: CFD models must be verified in the whole possible operating domain. Any disagreement between the measured and computed data should be accepted as a positive motivation for the validation of both parts of the collected information on flow conditions and heat transfer parameters.

Apparently inductive plasmatrons have powerful potential capabilities for future challenges. The nearest problems are connected with uncertainties of nonequilibrium inductively coupled plasma flows and TPM catalycity prediction at low pressures ~ $10^{-2}$ atm. Judicious CFD codes for multi-temperature sub- and supersonic reacting plasma flows computations must be developed and combined with precise measurements of the enthalpy and flow fields including the emission spectroscopy analysis within the flow core and boundary layers. Precise techniques for the characterization of the TPM optical properties at high temperatures should be included into the list of standard plasmatron measurements. For the promising inductive plasma applications to sample return missions the operating envelope has to be expanded toward the pressures above 1 atm. In this field the coupled problem of the RF discharge plasmadynamics and radiative gasdynamics is coming fast.

## Acknowledgements

The preparation of this paper was supported by RTA contract 4329A and the work performed in part under the ISTC project 036. The author would like to express his gratitude to Prof. J.F. Wendt, Prof. M. Carbonaro and Prof. J.-M. Charbonnier for inviting to the VKI at the RTA/AVT Special Course, and to thank Dr. S. Vasil'evskii, V. Mysova and N. Mamyrkina and for help in figures design.

## References

1. Bonhoeffer, K. F., Zeits. f. Physik. Chemie. 1924, v. 113, No. 3, p. 199.
2. Fay, J. A. and Riddell, F. R., "Theory of Stagnation Point Heat Transfer in Dissociated Air," J. Aeronaut. Sci., 1958, v. 25, No. 2, p. 73.
3. Goulard, R., "On Catalytic Recombination Rates in Hypersonic Stagnation Heat Transfer," Jet Propulsion, 1958, v. 28, No. 11, p. 737.
4. Scott, C. D., "Catalytic Recombination of Nitrogen and Oxygen on High Temperature Reusable Insulation," Progress in Astronautics and Aeronautics, 1981, v. 77, ed. by A. L. Crosbie, AIAA, New York, p. 192.
5. Stewart, D. A., Rakich, J. V., and Lanfranco, M. J., "Catalytic Surface Effects Experiment on the Space Shuttle," Progress in Astronautics and Aeronautics, 1982, v. 82, ed. by T. E. Horton, AIAA, New York, p. 248.
6. Jumper, E. J., "Recombination of Oxygen and Nitrogen on Silica-Based Thermal Protection Surfaces: Mechanism and Implications," in: Molecular Physics and Hypersonic Flows, 1996, NATO ASI Series, v. 482, ed. by M. Capitelli, Kluwer, p.203.
7. Lozino-Lozinskii, G. E., "Buran Flight," in: Gagarin Scientific Studies in Aviation and Cosmonautics, 1989 (in Russian), Nauka, Moscow, 1990, p. 6.
8. Voinov, L.P., Zalogin, G.N., Lunev, V.V., and Timoshenko, V.P., "Comparative Analysis of Laboratory and Full-Scale Data Concerning "Bor"

and "Buran" Space Vehicles Thermal Protection Material Catalycity," Cosmonautics and Rocket Engineering (in Russian), TSNIIMASH, 1994, No. 2, p. 51.

9. Baronets, P.N., Kolesnikov, A.F., Kubarev, S.N., Pershin, I.S., Trukhanov, A.S., Yakushin, M.I., "Overequilibrium Heating of the Surface of a Heat-Shield Tile in a Subsonic Jet of Dissociated Air," Fluid Dynamics, Plenum, (tr. from Russian), 1991, v. 26, No. 3, p.437.
10. Gupta, R.N., Lee, K.P., Scott, C.D., "Aerothermal Study of Mars Pathfinder Aeroshell," J. of Spacecraft and Rockets, 1996, v. 33, No.1, p. 61.
11. Gromov V.G., Afonina N.E., "Thermochemical Nonequilibrium Computations for a Mars Probe," 3rd European Symposium on Aerothermodynamics for Space Vehicles, ESTEC, Noordwijk, The Netherlands, 24-26 November 1998, ESA SP-426, 1999, p. 179.
12. Hardy W.A., Linnett J.W., "Mechanism of Atom Recombination on Surface," Proc. of 11-th Int. Symp. on Combustion. Berkley, Ca., 1966, p.167.
13. Kolesnikov, A.F., "The Aerothermodynamic Simulation in Sub- and Supersonic High- Enthalpy Jets: Experiment and Theory," Proc. of the Second European Symposium on Aerothermodynamics for Space Vehicles, ESTEC, Noordwijk, The Netherlands, November 1994, ESA SP-367, 1995, p. 583.
14. Babat, G.I., "Electrodeless Discharges and Some Allied Problems," J. of Inst. of Electr. Engineers, III, 94, issue 27, 1947, p.27.
15. Reed, T.B., "Induction-coupled Plasma Torch," J. of Appl. Phys., v. 32, 1961, p.821.
16. Yakushin, M.I., "Production of the High Temperature Gas in Electrodeless Induction Discharge," Pricl. Mech. Tech. Phys. (in Russian), No. 3, 1969, p.143.
17. Gordeev, A.N., Kolesnikov, A.F., Yakushin, M.I., "An Induction Plasmatron Application to 'Buran's' Heat Protection Tiles Ground Tests," SAMPE Journal, v. 28, No. 3, 1992, p. 29.
18. Anfimov, N.A., "TsNIIMASH Capabilities for Aerogasdynamical and Thermal Testing of Hypersonic Vehicles," AIAA 92-3962, 1992.
19. Labaste, V., Kolesnikov, A., Ferenbach, L., Guegan, H., Guigue-Joguet, P., "Influence of Aging upon Catalycity of C/C Material Protected Against Oxydation", Proc. of the Intern. Symposium on Advanced Materials for Lightweight Structures '94. ESTEC, Noordwijk, The Netherlands, 22-25 March 1994, p. 273.
20. Auweter-Kurtz, M., Kurtz, H.L., Laure, S., "Plasma Generators for Re-Entry Simulation", J. Propulsion and Power, v. 12, No.6, November 1996, p. 1053.
21. Auweter-Kurtz, M., Hammer, F., Herdrich, G., Kurtz, H., Laux, T., Schreiber, E., Wegmann, T., "The Ground Test Fasilities for TPS at The Institut Fur Raumfahrtsysteme", 3rd European Symp. on Aerothermodynamics for Space Vehicles, ESTEC, Noordwijk, The Netherlands, November 24-26, 1998, ESA SP-426, 1999, p. 529.
22. Bascele, J.M., Conte, D., Leroux, R., "A New Test Facility for Experimental Characterization of High Temperature Composites and Ceramics", 3rd European Workshop on TPS. ESTEC, Noordwijk, The Netherlands, 25-27 March 1998.
23. Bottin, B., Carbonaro, M., Paris, S., Van Der Haegen, Novelli, A., Vennemann, D., "The VKI 1.2 MW Plasmatron Facility for the Thermal Testing of TPS Materials", 3rd European Workshop on TPS. ESTEC, Noordwijk, The Netherlands, 25-27 March 1998. Netherlands, 25-27 March 1998.
24. Bykova, N. G., Vasil'evskii, S. A., Gordeev, A. N., Kolesnikov, A. F., Pershin, I. S., and Yakushin, M. I., "An Induction Plasmatron Application for Simulation of Entry into Martian Atmosphere," 3rd Int. Symp. on Environmental Testing for Space Programmes, ESTEC, Noordwijk, The Netherlands, 24-27 June 1997, SP-408, 1997, p. 195.
25. Georg, E.B., Yakushin, M.I., "Thermal Boundary Layer on Models Disintegrating in a High-Enthalpy Gas Stream," Fluid Dynamics, Plenum, (tr. from Russian), v. 11, No. 1, 1976, p. 21.
26. Kolesnikov, A.F. and Yakushin, M.I., "Determination of Heterogeneous Recombination Effective Probabilities of Atoms from Heat Fluxes to the Surface in Dissociated Air Flow," Matematicheskoe Modelirovanie (in Russian), 1989, v. 1, No. 3, p.44.
27. Vasil'evskii, S.A., Kolesnikov, A.F., and Yakushin, M.I., "Determination of the Effective Probabilities of the Heterogeneous Recombination of Atoms When Heat Flow is Influenced by Gas-Phase Reactions," High Temperature, Plenum, (tr. from Russian), 1991, v. 29, No. 3, p. 411.
28. Bykova, N.G., Vasil'evskii, S.A., Gordeev, A.N., Kolesnikov, A.F., Pershin, I.S., and Yakushun, M.I., "Determination of the Effective Probabilities of Catalytic Reactions on the Surfaces of Heat Shield Materials in Dissociated Carbon Dioxide Flows", Fluid Dynamics, Plenum, (tr. from Russian), 1997, v.32, No. 6, p. 876.
29. Kolesnikov, A.F., Pershin, I.S., Vasil'evskii, S.A., and Yakushin, M.I., "Study of Quartz Surface Catalycity in Dissociated Carbon Dioxide Subsonic Flows," 1998, AIAA 98-2847.
30. Kolesnikov, A., Yakushin, M., Vasil'evskii, S., Pershin, I., and Gordeev, A. "Catalysis Effects on Quartz Surface in High-Enthalpy Oxygen & Carbon Dioxide Flows", 3rd European Symposium on Aerothermodynamics for Space Vehicles, ESTEC, Noordwijk, The Netherlands, 24-26 November 1998, ESA SP-426, 1999, p. 537.
31. Kolesnikov, A.F., "Conditions of Simulation of Stagnation Point Heat Transfer from a High-Enthalpy

Flow," Fluid Dynamics, Plenum, (tr. from Russian), 1993, v. 28, No. 1, p. 131.

32. Kolesnikov, A., "The Concept of The Local Thermo-Chemical Simulation for Re-Entry Problem: Validation & Applications", presented in 9th Thermal & Fluids Analysis Workshop, August 31 - September 4, 1998, NASA Lewis Research Center and Ohio Aerospace Institute, Cleveland, Ohio.
33. Wendt, J.F., Muylaert, J.M., "Status of Hypersonic Testing Capabilities in Europe", Proc. of the Second European Symposium on Aerothermodynamics for Space Vehicles, ESTEC, Noordwijk, The Netherlands, November 1994, ESA SP-367, 1995, p. 165.
34. Berkut V.D., Doroshenko V.M., Kovtun V.V., and Kudryavtsev N.N. Nonequilibrium Physico-Chemical Processes in Hypersonic Aerodynamics. Moscow, Energoatomizdat (in Russian). 1994, 400p.
35. Gulhan, A., Vennemann, D., Yakushin, M., and Zhestkov, B., "Comparative Oxidation Tests on Reference Material in Two Indution Heated Facilities," 46th Int. Astronautical Congress, October 2-6, 1995, Oslo, Norway.
36. Vennemann, D., and Yakushin, M., "Oxidation Tests on SiC Reference Material in an Indution Heated Facility under Sub- and Supersonic Flow Conditions," 1996, AIAA 96-4566.
37. Spirin, G.G., Vinogradov, Yu.K., Belyaev, O.V., "Experimental Study of Molecular Thermal Conductivity of Quartz," Teplofizika Vysokih Temperatur, v.34, No.1, 1996, p. 29.
38. Dvurechensky, A.V., Petrov, V.A., Reznik, V.Yu., "Experimental Study of Quartz Glass Spectral Emissivity at High Temperatures," Teplofizika Vysokih Temperatur, v.16, No.4, 1978, p. 749.
39. Petrov, V.A., Reznik, V.Yu., "Total Normal Emissivity of Quartz Glass of 'QR' Type at High Temperatures," Teplofizika Vysokih Temperatur, v.10, No.4, 1972, p. 778.
40. Vasil'evskii, S.A., Kolesnikov, A.F., Yakushin, M.I., "Mathematical Models for Plasma and Gas Flows in Induction Plasmatrons," In: Molecular Physics and Hypersonic Flows, ed. by M.Capitelly, NATO ASI Series, v. 482, 1996, Kluwer, p. 495.
41. Boulos, M.I., "The inductively coupled radio-frequency plasma," J. of Pure and Appl. Chem., 1985, v. 57, No. 9, p.1321.
42. Kolesnikov, A.F., Vasil'evskii, S.A., "Some problems of numerical simulation of discharge electrodynamics in induction plasmatron," Proc. of 15th IMACS World Congress, Berlin, August 1997. v.3, Computational Physics, Chemistry and Biology. Ed. by A.Sydov, p.175.
43. Kolesnikov, A.F., Vasil'evskii, S.A., "Results and Problems of Inductively Coupled Plasma Flows Modeling," IPM RAS, Preprint No. 610, Moscow 1998, 28 p.
44. Patankar, S.V., Spalding, D.B., Heat and Mass Transfer in Boundary Layers. Intertext Books, London, 1970.
45. Capitelli, M. and Devoto, R. S., "Transport Coefficients of High-Temperature Nitrogen," Phys. Fluids, 1973, v. 16, No. 11, p. 1835.
46. Kolesnikov, A. F. and Tirskii, G. A., "Equations of Hydrodynamics for Partially Ionized Multi-Component Mixtures of Gases, Employing Higher Approximations of Transport coefficients," (tr. from Russian), in: Fluid Mechanics-Soviet Research, 1984, 1985 Scripta Technica, Inc., v. 13, No. 4, p. 70.
47. Vanden Abeele, D., Vasil'evskii, S. A., Kolesnikov, A. F., Degrez, G., and Bottin, B., "Code-to-Code Validation of Inductive Plasma Computations," 1998, VKI, Reprint 1998-26.
48. Vanden Abeele, D. and Degrez, G., "An Efficient Computational Model for Inductive Plasma Flows," 1998, AIAA 98-2825.
49. Park, C., Candler, G.V., Howe, J.T., Jaffe, R.T., "Chemical-Kinetic Problems of Future NASA Missions," AIAA 91-0464.
50. Kovalev, V.L., Suslov, O.N., Tirskiy, G.A., "Phenomenological Theory for Heterogeneous Recombination of Partially Dissociated Air on High Temperature Surfaces," In: Molecular Physics and Hypersonic Flows, ed. by M.Capitelly, NATO ASI Series, v. 482, 1996, Kluwer, p.193.
51. Daiβ, A., Frühauf, H.H., Messerschmid, E.W., "Chemical Reactions and Thermal Nonequilibrium on Silica Surfaces," In: Molecular Physics and Hypersonic Flows, ed. by M.Capitelly, NATO ASI Series, v. 482, 1996, Kluwer, p.203.
52. Cacciatore, M., Rutigliano, M., and Billing, G. D., "Energy Flows, Recombination Coefficients and Dynamics for Oxygen Recombination on Silica Surfaces," 1998, AIAA 98-2843.
53. Lin, S. Ch., and Teare, J. D., "Rate of Ionization behind Shock Waves in Air. II. Theoretical Iterpretations," Phys. Fluids, 1963, v. 6, No. 3, p. 355.
54. Vasil'evskii, S. A., Kolesnikov, A. F., and Yakushin, M. I., "Increased Heat Transfer to a Titanium Surface with Oxygen Injection into the Nonequilibrium Boundary Layer," Fluid Dynamics, Plenum, (tr. from Russian), 1991, v. 26, No. 4, p. 598.
55. Greaves, J.C, Linnett, J.W., "Recombination of Oxygen Atoms on Silica from 20C to 600C," Trans. of the Faraday Society, 1955, v. 55, p.1355.
56. Rubio Garcia, V., Marraffa, L., Scoon, G., Roumeas, R., "Mars Mini-Probes. Elements of Aerothermo-dynamics & Entry Trajectories," 3rd European Symposium on Aerothermo- dynamics for Space Vehicles, ESTEC, Noordwijk, The Netherlands, 24-26 November 1998, ESA SP-426, 1999, p. 155.

# Extrapolation from High Enthalpy Tests to Flight Based on the Concept of Local Heat Transfer Simulation

**A.F. Kolesnikov**
Institute for Problems in Mechanics RAS
Prospect Vernadskogo 101/1
117526, Moscow
Russia

## Summary

The concept of the local heat transfer simulation (LHTS) of the high enthalpy flow action on a vehicle stagnation point formulated in refs. 1, 2 is based on the requirement to locally provide in a ground test the same boundary layer on the model at the stagnation point as at the re-entry conditions. The present methodology of the extrapolation from ground to flight consists of the three main parts: 1) the recalculation of the test conditions to flight parameters, 2) the prediction of the test conditions for the given hypersonic flight parameters and 3) the validation of the extrapolation procedure.

The application and validation of this concept are carried out through the comparative analysis of the computed heat transfer rates and profiles of the gas temperature and atoms fractions within boundary layers near the model in the subsonic high enthalpy air flow and near the blunt body in the hypersonic air flow, whose parameters are extrapolated from the inductively heated air plasma experiment. It is established that the LHTS concept provides an excellent accuracy if air temperatures at the outer edges of both boundary layers near a model and a body are close to equilibrium values, or if the surface has a high or moderate catalycity.

The algorithm of determination of the trajectory point for which the complete local duplication of the heat transfer is possible is presented. Another examples of the LHTS concept applications are shown through an analysis of the capabilities of the IPG-4 plasmatron for thermochemical simulation at the Mars probe entry conditions, and through the prediction of the plasmatron subsonic test parameters for the duplication of the stagnation point heat transfer to the Mars Pathfinder aeroshell at the peak-heating conditions in the Martian atmosphere. The computed stagnation point heat flux range for the model in the subsonic dissociated carbon dioxide flow in the whole range of surface catalycity is found in sufficient agreement with the viscous-shock layer analysis carried out in ref. 3 for the Mars Pathfinder aeroshell without the surface ablation.

## 1. Introduction

In fact, only partial heat transfer simulation for atmospheric entry conditions could be achieved by using high enthalpy wind tunnels [ref. 4]. The stagnation point configuration is most important for the TPM samples testing and surface catalycity rebuilding [refs. 5-14]. In particular, the catalytic properties of the TPM for the Buran space vehicle were studied by using the inductive plasmatron IPG-2 on cylindrical models of the 30 mm in diameter with a flat face [ref. 7]. In subsonic high-enthalpy flows of dissociated nitrogen, oxygen and air, the effective probabilities $\gamma_{WN,O}$ of the catalytic recombination of the $N$ and $O$ atoms on the ceramic tile coating and the antioxidation coating of the carbon-carbon material were determined at the enthalpy 20-22 MJ/kg in the pressure range 0.1-0.3 atm and the surface temperature up to 1750 K: it was found that for the tile surface $\gamma_{WN,O} \leq 3 \cdot 10^{-3}$, for the antioxidation coating of the C-C material $\gamma_{WN,O} \approx 7 \cdot 10^{-3}$ [refs. 2, 7]. Those ground data were completely confirmed by the Bor and Buran space vehicles flight experiments [refs. 15, 16].

The first data on catalytic efficiencies of quartz-based materials and C-C materials have been recently predicted from heat transfer tests in dissociated carbon dioxide flows performed by using the 100-kW inductive plasmatron IPG-4 in subsonic regimes [refs. 12-14]. The question appears how we can extrapolate those data for entry conditions in the Martain atmosphere?

It is almost obvious now that the requirements to duplicate in tests only full-scale values of stagnation pressure and surface temperature [ref. 9] or total enthalpy [ref. 10] are insufficient for the complete simulation of the heat transfer and oxidation and we still need to answer the key question: for what hypersonic flight conditions can we substantially use the ground tests data on the TPM catalytic properties or thermo-chemical resistance for the prediction of the full-scale heat transfer or vehicle surface aging?

For the case of the stagnation point heat transfer (most important from the practical point of view) this question can be solved on the basis of the LHTS concept formulated in refs. 1, 2. This concept includes the requirements to provide in high-enthalpy tests the same values of the total enthalpy, the stagnation pressure and the velocity gradient at the stagnation point of the model as in a hypersonic flow around the vehicle at the given reentry trajectory point. By means of this rather simple theory the ground test data could be extrapolated to flight conditions if we know flow fields around a model and a body (practically - effective radii of a model and a body

*Paper presented at the RTO AVT Course on "Measurement Techniques for High Enthalpy and Plasma Flows", held in Rhode-Saint-Genèse, Belgium, 25-29 October 1999, and published in RTO EN-8.*

nose). Undoubtedly, an accuracy of such extrapolation should be estimated.

In this paper some results of application and validation of this concept are presented. The validation is carried out through the direct comparison of the numerical solutions of the 1D boundary layer problem for the high-enthalpy experiment and the corresponding 1D thin shock layer problem for the extrapolated flight parameters. The well documented experimental and numerical results for subsonic high enthalpy air flow parameters in the inductive plasmatron IPG-2 [ref. 2] are used.

By means of the LHTS theory the test parameters are recalculated to hypersonic flight conditions and then the nonequilibrium boundary layer near the model and the shock layer near the body along the stagnation line are computed for a 5-species dissociated air. Then stagnation point heat fluxes, temperature and the profiles of *N* and *O* atoms mass fractions within two boundary layers are compared.

It is shown that the surface catalycity and the displacement of air temperature from the equilibrium values at the outer edges of boundary layers are the factors in the actual accuracy of the presented test-to-flight extrapolation.

The algorithm of the determination of the trajectory point for which the local thermochemical simulation could be realized by using plasmatron is described. Two another examples of the applications of the LHTS concept are demonstrated through analysis of the Mars probe trajectory [ref. 17] and test parameters required for the stagnation point heat transfer simulation for the Mars probe and the Mars Pathfinder aeroshell at the trajectory peak-heating point in the Martian atmosphere [ref. 3] by using the 100-kW inductive plasmatron IPG-4 [refs. 11-14] and the standard European model configuration [refs. 9, 12-14]. The numerically predicted heat transfer range for the experiment in a subsonic high-enthalpy carbon dioxide flow is found in good agreement with computations for the Mars Pathfinder aeroshell from ref. 3 in the whole range of the surface catalycity.

## 2. Concept of the Local Heat Transfer Simulation

Our way to study the problem of the ground-to-flight extrapolation lies in the use of the theory of the local heat transfer simulation formulated in refs. 1, 2. At least for the case of the stagnation point heat transfer we can point out the hypersonic flow parameters and a blunt body radius which are in direct correspondence with high enthalpy subsonic flow parameters and a model radius (*Fig. 1*) if both surfaces have the same catalycity and emissivity and also the same heat transfer boundary conditions (for example, radiative-equilibrium walls).

The analysis is based on the boundary layer theory for dissociated reacting gases. Fay and Riddell theory [ref. 18] gives the following expression for the heat flux at the

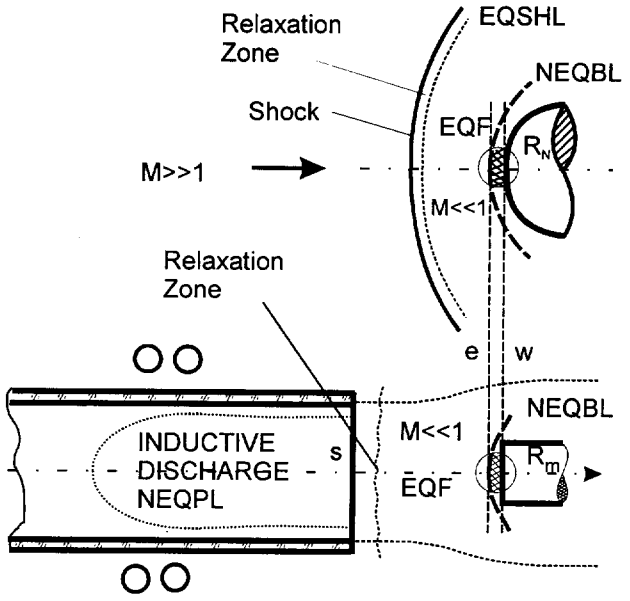


*Fig. 1. Schemes of hypersonic flow around a blunt body and the stagnation point heat transfer simulation in subsonic high enthalpy flow in plasmatron.*

stagnation point of a blunt body with a fully catalytic surface which is being flown by a hypersonic flow:

$$q_W = 0.763\, Pr^{-0.6}(\rho_e\mu_e)^{1/2}\left(\frac{dU_e}{ds}\right)_0^{1/2}\left(\frac{\rho_W\mu_W}{\rho_e\mu_e}\right)^{0.1}\times \times(h_e - h_W) \qquad (2.1)$$

For the case of the frozen boundary layer the Goulard's solution of the boundary layer problem [ref. 19] gives the following formula for the stagnation point heat flux to the wall with arbitrary catalycity:

$$q_W = 0.66\, Pr^{-2/3}(\rho_e\mu_e)^{1/2}\left(\frac{dU_e}{ds}\right)_0^{1/2}(H_e - h_W)[1+ +(Le^{2/3}\Phi - 1)\frac{h_A^0(c_e - c_W)}{H_e - h_W}], \qquad (2.2)$$

$$\Phi = \left(1+\frac{0.47Sm^{-2/3}(2(dU_e/ds)_0\rho_e\mu_e)^{1/2}}{\rho_W k_W}\right)^{-1}$$

Here $H$ is the total enthalpy, $h$ is the enthalpy, $h_A^0$ is the enthalpy of formation of atoms, $c$ is the mass fraction of atoms, $\rho$ is the density, $\mu$ is the viscosity, $(dU_e/ds)_0$ is the velocity gradient, $Pr$ is the Prandtl number, $Le$ the Lewis number, $Sm$ is the Schmidt number. The subscripts $e$ and $w$ denote the outer edge of the boundary layer and the body surface, respectively.

The analysis of the formulae (2.1) and (2.2) has revealed the three independent factors which control the heat flux: $H_e$-$h_W$, $\rho_e$ and $(dU_e/ds)_0$. In the case when the flow at the outer edge of the boundary layer is in equilibrium, $\rho_e$ is the function of $h_e(=H_e)$ and $p_e$, and accordingly to

Goulard's solution [ref. 19] $h_W$ appears to be a parameter dependent on $h_e$, $p_e$, $(dU_e/ds)_0$ and $T_W$. Therefore, the stagnation point heat flux $q_W$ is completely determined by the boundary condition on the body and the three parameters at the outer edge of the boundary layer: the enthalpy, the stagnation pressure and the velocity gradient.

We see, that the sufficient conditions of equality of the heat fluxes in flight and in ground test are the equalities of these three parameters in the two flows:

$$H_S=H_\infty,\ p_{eS}=p_{e\infty}=p_W,\ (dU_e/ds)_{0S}=(dU_e/ds)_{0\infty} \quad (2.3)$$

where the subscripts $\infty$ and $S$ relate to the flight and ground conditions.

Let's consider the conditions of duplication of the stagnation point heat transfer to a blunted body of radius $R_W$, which is being flown by a hypersonic flow with velocity $V_\infty$ and density $\rho_\infty$, in an axisymmetric high enthalpy subsonic flow with velocity $V_S$ and static pressure $p_S$ by using a cylindrical blunted model of radius $R_m$ (*Fig. 1*).

From the first equality (2.3) the equality of the total enthalpies of the two flows follows:

$$\frac{1}{2}V_S^2 + h_S = H_\infty \quad (2.4)$$

The second necessary condition reduces to the relation between the static pressure of the free stream in a plasma wind tunnel and the given stagnation pressure $p_W$, which is described by the approximate Poisson's adiabat equation for a real gas [ref. 20]:

$$p_S\left(1+\frac{\gamma_{*S}-1}{2}M_S^2\right)^{\gamma_{*S}/(\gamma_{*S}-1)} = p_W, \quad (2.5)$$

$$\gamma_{*S} = \frac{1}{1-p_S/\rho_S h_S}$$

where $\gamma_{*S}$ is the effective specific heat ratio, and $M_S<1$ is the Mach number of the simulating flow.

Let's represent the third condition - the equality of the stagnation point gradients - in the form

$$V_S/R_m^* = V_\infty/R_N^*, \quad (2.6)$$

$$R_{m,N}^* = V_{S,\infty}/(dU_e/ds)_{0S,\infty}$$

where $R_m^*$ and $R_N^*$ are the effective radii of the model and the body at the stagnation points. Assuming the parameters $V_\infty$, $H_\infty$, $p_W$, $R_m^*$, and $R_N^*$ to be known from (2.4)-(2.5) we obtain the parameters of the ground free stream in the following form:

$$V_S/V_\infty = \xi,\ h_S/H_\infty = 1-\zeta^2, \quad (2.7)$$

$$p_S/p_W = (1-\zeta^2)^{\gamma_{*S}/(\gamma_{*S}-1)}, \quad (2.8)$$

$$M_S^2 = \frac{2}{(\gamma_{*S}-1)}\frac{\zeta^2}{1-\zeta^2}, \quad (2.9)$$

$$\xi = R_m^*/R_N^*,\ \zeta = (V_\infty^2/2H_\infty)\xi^2, \quad (2.10)$$

$$\xi \le \frac{\sqrt{2H_\infty}}{V_\infty}\zeta_*,\ \zeta \le \zeta_* = \sqrt{\frac{\gamma_{*S}-1}{\gamma_{*S}+1}}$$

The expressions for calculating the velocity, enthalpy, pressure and Mach number of the simulating flow (2.7) are universal in form: they contain only two dimensionless parameters $\xi$ and $\zeta$. For the hypersonic flight in an atmosphere $V_\infty^2/2H_\infty \cong 1$, then $\xi=\zeta$.

Thus, for high-enthalpy flows in which the stagnation point heat fluxes at the body and the model are equal, the ratios $V_S/V_\infty$ and $h_S/H_\infty$ are completely determined by the elementary universal relations (2.7). The relations (2.8) and (2.9) for high-enthalpy flows are the universal implicit relations of the functions $p_S'(\zeta)=p_S(\zeta)/p_W$ and $M_S(\zeta)$, since $\gamma_{*S}$ depends on the values of $p_S$ and $h_S$.. In *Fig. 2* we have plotted the functions $p_S'(\zeta)$ and $M_S(\zeta)$ calculated for equilibrium air at $H_\infty$=32 (*a*), 16 (*b*) and 8 (*c*) MJ/kg. The curves *1-3* correspond to $p_W$ =$10^{-3}$, 1 and $10^2$ atm. The broken curves correspond to a perfect gas with constant $\gamma$=1.4.

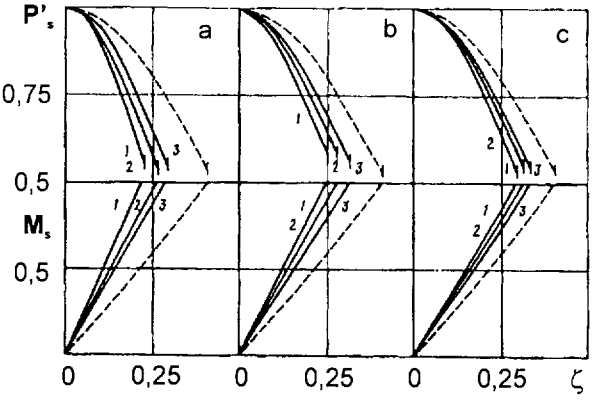


*Fig. 2. Universal dependencies of the dimensionless static pressure and Mach number of simulating subsonic air flow versus similarity parameter $\zeta$ [ref. 1].*

As may be seen from *Fig. 2*, the real properties of highly dissociated air essentially affect the functions

$p_S'(\zeta)$ and $M_S(\zeta)$, which are quite important for the analysis of the test conditions.

### 3. Recalculation of Test Parameters to Flight Conditions

For the experimental practice of the heat transfer simulation the case $\zeta<<1$ is very important: practically, this case occurs when $R_m<<R_N$. Let's consider this case in detail taking into consideration that for a hypersonic axially symmetric flow around a smooth blunted body we have the following well-known formulae (ref. 20):

$$H_\infty = \frac{1}{2}V_\infty^2, \quad p_W = \rho_\infty V_\infty^2, \tag{3.1}$$

$$\left(\frac{dU_e}{ds}\right)_0 = \left(\frac{8}{3}\frac{\rho_\infty}{\rho_e}\right)^{\frac{1}{2}} \frac{V_\infty}{R_N} \tag{3.2}$$

Then for the ground subsonic free stream conditions we have:

$$h_S = \frac{1}{2}V_\infty^2, \quad p_S = \rho_\infty V_\infty^2, \tag{3.3}$$

$$V_S = \left(\frac{8}{3}\frac{\rho_\infty}{\rho_e}\right)^{1/2} \frac{R_m^*}{R_N} V_\infty \tag{3.4}$$

In the case of subsonic jet the subscript $S$ denotes the center of the flow.

The conditions (3.3) are rather simple, but the condition (3.4) is not trivial and contains the geometrical parameter - effective radius $R_m^*$, which depends on the channel radius $R_c$, the model radius $R_m$ and should be computed for the test configuration by using CFD methods. For subsonic jets over cylindrical models with a flat face we obtained the following approximation for $R_m^*$ from numerical solutions of the Navier-Stokes equations [ref. 1]

$$R_m^* = \begin{cases} R_m\left[2 - l - 1{,}68(l-1)^2 - 1{,}28(l-1)^3\right], & l \le 1 \\ R_c, \ l > 1 \ (l = R_m / R_c) \end{cases} \tag{3.5}$$

In accordance with (3.3), (3.4) there is one-to-one correspondence between subsonic jet parameters $h_S, p_S(\approx p_W), V_S$ and the given dimensions $R_C$ and $R_m$, on the one hand, and the parameters of the hypersonic flow and the nose radius of a blunt body, on the other

$$V_\infty = \sqrt{2h_S}, \quad \rho_\infty = \frac{p_S}{2h_s}, \tag{3.6}$$

$$R_N = \left(\frac{8}{3}\frac{\rho_\infty}{\rho_e}\right)^{1/2} \frac{V_\infty}{V_s} R_m^*$$

As an example, let's analyze the well characterized subsonic regime performed in the IPG-2 plasmatron for the air flow at the pressure 0.1 atm , the generator anode power 37.4 kW and the mass flow rate through the discharge channel 2.8g/s [ref. 2]. At the distance of 30 mm from the plasmatron exit section, the enthalpy $H_e$=2.19·10$^7$ m$^2$/s$^2$ , the velocity $V_s$=180 m/s, the density $\rho_s$=3.86 10$^{-3}$ kg/m$^3$, Reynolds number $Re_s=\rho_s V_s R_m/\mu_s \cong$ ≅58.6, Mach number $M_S$=0.14. The radius of the IPG-2 plasmatron channel $R_c$=3·10$^{-2}$ m and for the cylindrical model of the radius $R_m$=1.5·10$^{-2}$ m we have $R_m^*$=1.2$R_m$=1.8·10$^{-2}$ m, in accordance with (3.5).

For these subsonic air flow parameters we have determined the parameters of the hypersonic air flow and the nose radius of a blunt body from expressions (3.6): $V_\infty$=6620 m/s, $\rho_\infty$=2.28·10$^{-4}$ kg/m$^3$, $R_N$= 0.265 m. The density value corresponds to the altitude 62.4 km in the Earth atmosphere. Correspondingly, the flight Reynolds number $Re_\infty$=1750 and the Mach number $M_\infty$=20. We see, that Reynolds and Mach numbers are quite different for those ground test and hypothetical flight regime. That means that Reynolds and Mach numbers are not the similarity parameters for the stagnation point heat transfer.

### 4. Method of the LHTS Concept Validation

The proposed method of the LHTS concept validation consists in the direct comparison of the calculated heat transfer rates and the profiles of the temperature and species fractions within the boundary layers near the stagnation points of the model and the body for subsonic and hypersonic flows conditions linked by the correlation (3.6). Such a comparison is carried out below.

A method for the calculation of the heat transfer rates at the stagnation point of a model with a flat face exposed to a subsonic jet of a viscous multicomponent reacting gas was developed in refs. 2, 7, 21, 22, 13. Here we also use the concept of a boundary layer with finite thickness in the vicinity of the stagnation point. The thickness δ of the boundary layer and the hydrodynamic parameters at its outer edge, including the flow vorticity, which are given below in the formulation of the problem, are determined from the numerical solution of the full Navier-Stokes equations, which is considered as an outer solution.

In the case of a one-temperature multicomponent mixture of atoms and molecules in the equilibrium excitation of the vibrational degrees of freedom, the system of the ordinary differential equations describing the flow within the boundary layer near the stagnation point of the model has the following form (ref. 21):

$$\left(lu'_\eta\right)'_\eta + fu'_\eta - \frac{u^2}{2} + \frac{1+\alpha_e}{2\rho} = 0, \qquad (4.1)$$

$$\left(\frac{l}{Pr}H'_\eta\right)'_\eta + fH'_\eta + \left[\frac{l}{Pr}\sum_{i=1}^{N}(h_i - h_i)^*(Le_i - 1)c'_i{}_\eta\right]'_\eta = 0,$$

$$\left(\frac{l}{Sc_i}c'_{i_\eta}\right)'_\eta + fc'_{i_\eta} + w_i = 0\ (i = 1,\ldots < N - N_e),$$

$$f'_\eta = u, \quad y'_\eta = \Delta_\rho^{-1}\chi^{-1}, \quad 1/\rho = T/m,$$

$$c_j^\bullet \equiv c_{j_e}^\bullet, \quad J_j^\bullet \equiv 0 (j = 1,\ldots,N_e), \quad H = \sum_{i=1}^{N} c_i h_i,$$

$$l = \frac{\mu\rho}{\eta_e^2}, \quad \eta_e = \frac{\Delta}{\chi}\sqrt{2Reu_{1e}}, \quad \chi = \int_0^1 \frac{d\eta}{\rho}, \quad Re = \frac{\rho_S V_S R_m}{\mu_e},$$

$$\Delta = \delta / R_m, \quad u = u_1 / u_{1e}, \quad u_1 = \partial u / \partial x, \quad \upsilon = -V^0 / V_s,$$

$$\alpha_e = -\upsilon_e(\partial u_1 / \partial y)_e / u_{1e}^2, \quad U = U^0 / V_s, \quad x = x^0 / R_m,$$

$$y = y^0 / R_m, \quad \rho = \rho^0 / \rho_e, \quad T = T^0 / T_e, \quad h_i = h_i^0 / H_e.$$

The boundary conditions at the outer edge of the boundary layer and on the surface of the model are:

$$\eta = 1: \quad u = H = 1, \quad c_i = c_{i_e}\ (i = 1,\ldots, N - N_e) \qquad (4.2)$$

$$\eta = 0: \quad u = f = 0, \quad T = T_w, \quad y = 0,$$

$$\frac{\mu}{Sc_i\eta_e}c'_{i_\eta} = \frac{K_{w_i}}{V_s u_{1e}}\sqrt{\frac{Reu_{1e}}{2}}\ c_i \qquad \left(K_{w_i} = \frac{2\gamma_i}{2-\gamma_i}\sqrt{\frac{kT_w}{2\pi m_i}}\right)$$

In (4.1), (4.2) $U^o$, $V^o$ are the velocity components in the cylindrical coordinate system $x^o$, $y^o$ which is related with a flat face, $\rho$ is the density, $c_i$ is the mass fraction, $h_i$ is the enthalpy, $h_i^*$ is the energy of formation of the species $i$; $c_j^*$, $J_j^*$ are the mass fraction and the diffusive flux of the chemical element $j$; $H$ is the enthalpy of the gas mixture, $T$ is the temperature, $m$ is the molecular weight, $K_{Wi}$ and $\gamma_i$ are the effective heterogeneous recombination rate constant and the catalytic efficiency; $k$ is the Boltzmann constant, $m_i$ is the molecular weight of the species $i$, $N$ is the number of species, $N_e$ is the number of chemical elements, and $\eta$ is the Dorodnitsyn's variable. The circle superscript denotes dimensional quantities.

In the momentum equation the parameter $\alpha_e$=const takes into account the vorticity of the flow at the outer edge of a boundary layer of the thickness $\delta$. Parameters $\alpha_e$, $U_e$ and $u_{1e}$ are determined from the profiles of the velocity components obtained from the numerical solution of the Navier-Stokes problem for a viscous reacting gas jet flow past a cylinder with the flat face at $M$ <<1 [refs. 2, 7, 19].

For our case $\Delta=\delta/R_m$=0.4, $\upsilon_e$=0.52, $u_{1e}$=0.445, $\alpha_e$=2.626. It was assumed in calculation that $Pr$=0.71, $Sc$=0.65 and $\mu \sim T^{0.77}$.

We assume that the following gas-phase reactions in a 5-species air occur within the boundary layer: *1)* $O_2+M \leftrightarrow O+O+M$, *2)* $N_2+M \leftrightarrow N+N+M$, *3)* $NO+M \leftrightarrow N+O+M$, *4)* $O+N_2 \leftrightarrow N+NO$, *5)* $O+NO \leftrightarrow N+O_2$. The chemical equilibrium is supposed to be at the outer edge of the boundary layer: $p_S$=0.1 atm, $H_e$=2.19·10$^7$ m$^2$/s$^2$, $T_e$=5960 K, $C_{N2}$=0.4576, $C_{O2}$=0.3513·10$^{-3}$, $C_{N2}$= 0.2922·10$^{-2}$, $C_N$= 0.3091, $C_O$=0.2304.

The thin viscous shock layer model was used independently for the computation of the hypersonic air flow ($V_\infty$=6620 m/s, $\rho_\infty$=2,28·10$^{-4}$ kg/m$^3$) past a sphere of the radius $R_W$=0,265 m. At the formulation of this problem the same boundary conditions at the wall and the same chemical reactions rates, as for the subsonic flow, were used. For the numerical solutions of the problem (4.1), (4.2) and the viscous shock layer problem the fourth-order-accurate finite-difference scheme was used. All computations were made for the surface temperature $T_W$=1500 K.

## 5. Results of Validation for Subsonic Air Test

*Fig. 3* shows the calculated dependencies of the stagnation point heat fluxes $q_W$ to the model ($M$<<1) and the body ($M$>>1) as the functions of the heterogeneous recombination rate constant $K_W$ for the case $K_{WO}=K_{WN}=K_W$ at test and flight conditions specified above.

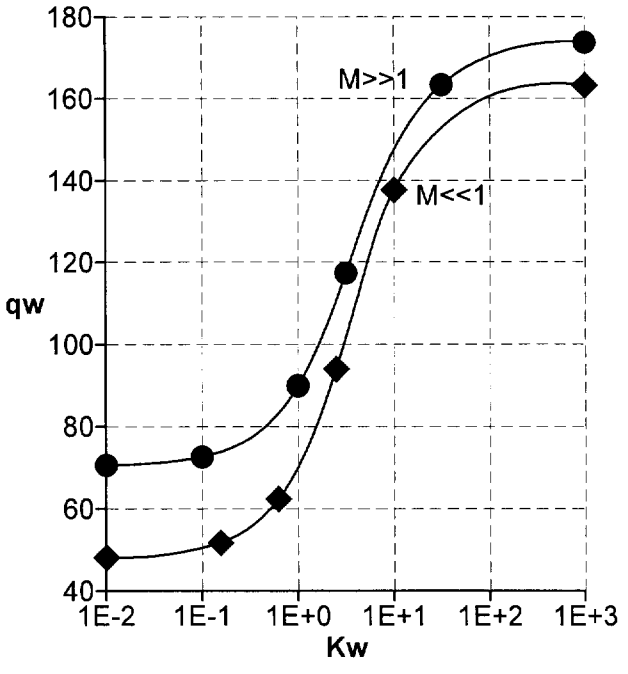


*Fig. 3. Stagnation point heat transfer rates $q_W$,(W/cm$^2$) versus effective rate constant of surface atom recombination $K_W$,(m/s) for plasmatron test (M<<1) and extrapolated to flight (M>>1).*

For a highly catalytic surface the difference in the heat fluxes $q_W$ under corresponding conditions for the subsonic and the supersonic flows is only about 5%. As $K_W$ decreases, this difference increases and for a noncatalytic surface in the subsonic jet the heat flux is 30% less then the heat flux in the corresponding hypersonic flow.

So, we see, that the accuracy of the heat transfer simulation on the basis of the LHTS theory developed in refs. 1, 2 depends on the surface catalytic efficiency. The accuracy is rather good for surfaces with high and moderate catalycity but it looks insufficient for a noncatalytic one. Nevertheless, both curves in *Fig. 3* are functionally similar and they have the same practically important interval $10^{-1}<K_W< 10^{2}$ m/s, where the heat transfer rates drastically depend on wall catalycity.

Moreover, it is easy to find by using *Fig. 3* that at least one function exists, which is duplicated with a quite perfect accuracy - the normalized heat flux

$$q_W^* = \frac{q_W - q_{Wn}}{q_{Wk} - q_{Wn}}, \qquad (5.1)$$

where $q_{Wk}$ is the heat flux to a fully catalytic wall and $q_{Wn}$ is the heat flux to a noncatalytic wall.

From here we can conclude that the data on the effective catalytic rates for atomic oxygen and nitrogen recombination on the Buran TPM $1\le K_W\le 3$ m/s, obtained in subsonic jets [refs. 2, 7, 20], are quite applicable to hypersonic re-entry conditions in the Earth atmosphere with flight parameters of the same orders of magnitude that calculated above.

For the more clear understanding of the LHTS capabilities we will compare the profiles of the air temperature, $N$ and $O$ atoms fractions across the boundary layer near the model and across the shock layer near the body at the same conditions for two limiting cases: fully and noncatalytic walls.

*Fig. 4* shows the temperature profiles within the boundary layer near the model and within the shock layer near the blunt body for a fully catalytic wall case. We see that temperature profiles are rather different at the outer edges of two boundary layers. For the hypersonic flow the temperature $T_e$ considerably (~ by 2000 K) exceeds the equilibrium value because the shock layer is fully nonequilibrium in this case, but at the same time the two temperature profiles are quite close to each other near the walls. This leads to good agreement between thermal conductive parts of the heat fluxes to fully catalytic surfaces of the body and the model.

Within the hypersonic shock layer we can see some displacement of the $N$ atoms mass fraction from the equilibrium value at the outer edge of the boundary layer (see *Fig. 5*): the mass fraction $c_N$ is significantly less then the equilibrium value in the subsonic flow. On the other hand, close to fully catalytic surfaces (*Fig. 5*), the profiles of the $N$ atoms fractions for the considered subsonic and hypersonic air flows are quite similar

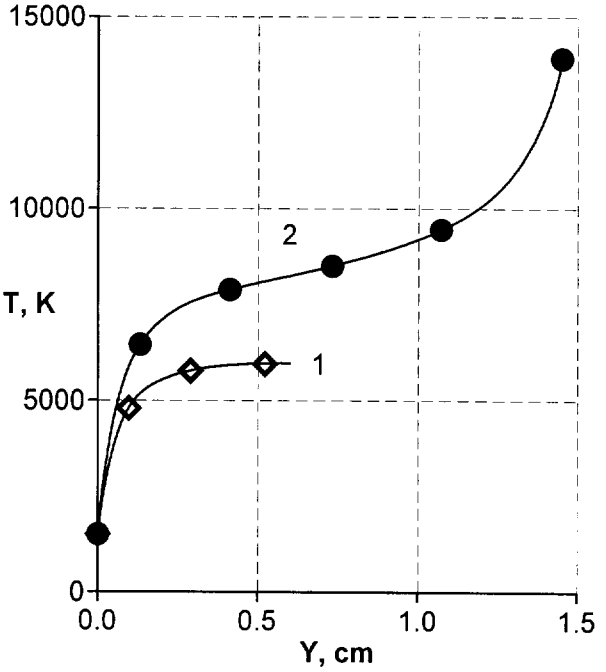


*Fig. 4. Temperature profiles along stagnation line (fully catalytic wall): 1 - the boundary layer near the model in subsonic flow ($R_m$=1.5 $10^{-2}$ m); 2 - the hypersonic shock layer near the body ($R_N$=0.265 m).*

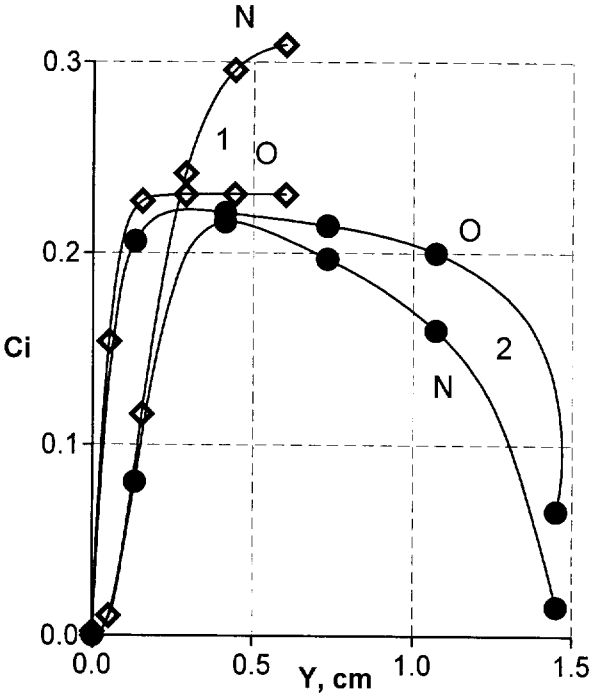


*Fig. 5. Profiles of the mass fractions of N and O atoms along stagnation line (fully catalytic wall): 1 - the boundary layer near the model in subsonic flow, 2 - the hypersonic shock layer near the body.*

including the fine details of different behavior of the profiles of *N* and *O* atoms due to the exchange reactions in dissociated air and mentioned above in the chapter **4**. In fact, the contributions in the heat fluxes due to nitrogen atoms diffusion are insignificant in this case. Also we can see on *Fig. 5* that the excellent simulation accuracy is achieved for the atomic oxygen fraction profile within the whole boundary layer because oxygen is completely dissociated at the outer edges of both boundary layers. As a result the contributions in the heat fluxes due to the atomic oxygen diffusion for both flows are equal within 5%. The same is correct for the total heat fluxes to a fully catalytic wall.

For the noncatalytic wall case the situation is more dramatic as we can see in *Fig. 6* and *7*. The temperature profiles across boundary layers are different exterior to the nearest vicinities of stagnation points and the heat flux caused by the to thermal conductivity is 30 % higher in the supersonic flow, then in subsonic one.

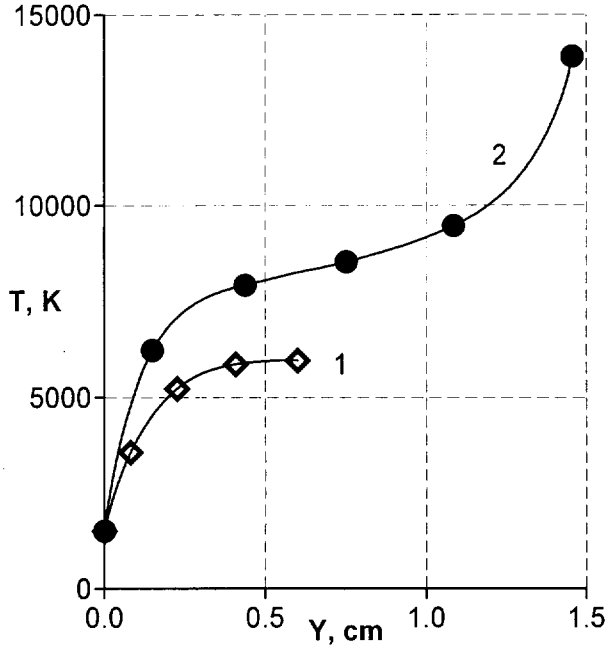


*Fig. 6. Temperature profiles along stagnation line (non-catalytic wall): 1 - the boundary layer near the model in subsonic flow, 2 - the hypersonic shock layer near the body.*

Both boundary layers are almost frozen and diffusion does not influence heat transfer. The atomic nitrogen fraction near the surface of the model is higher in the plasmatron test, but the atomic oxygen fraction profiles within boundary layers are quite close in test and hypothetical flight (*Fig. 7*). That means the formulae (3.6) for ground-to-flight extrapolation should provide a complete simulation of the diffusion flux and the partial pressure of atomic oxygen and, therefore, surface catalysis and oxidation processes. These are the arguments for using here the term "thermochemical" simulation.

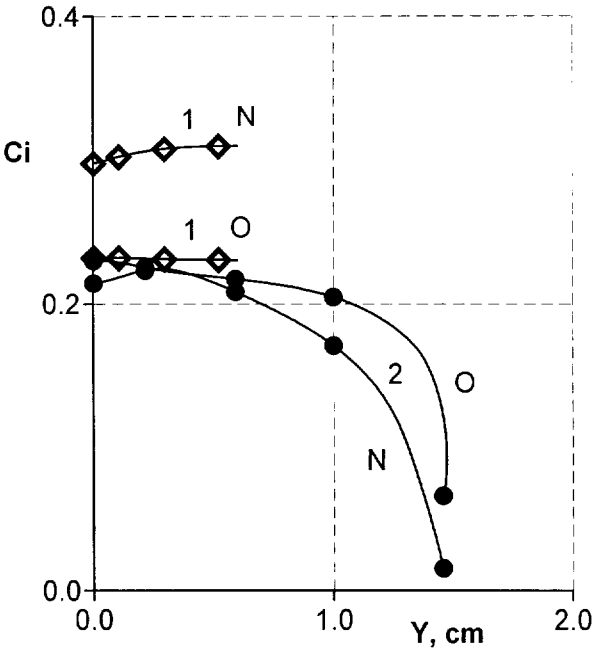


*Fig. 7. Profiles of the mass fractions of N and O atoms along stagnation line (noncatalytic wall): 1 - the boundary layer near the model in subsonic flow, 2 - the hypersonic shock layer near the body.*

It was established in ref. 23, that an accuracy of the heat transfer duplication for low catalytic surface was improving when the pressure in subsonic high enthalpy flow was increasing. When $p_S \geq 0.2$ atm the difference in the $q_W$ for subsonic and hypersonic flow was not more 5% for surfaces with $K_W \geq 1$ m/s (the quite practical case). The example of the excellent duplication of the temperature distribution across the boundary layer for hypersonic flow conditions we can see on *Fig. 8* for high enthalpy subsonic test in dissociated nitrogen [ref. 23].

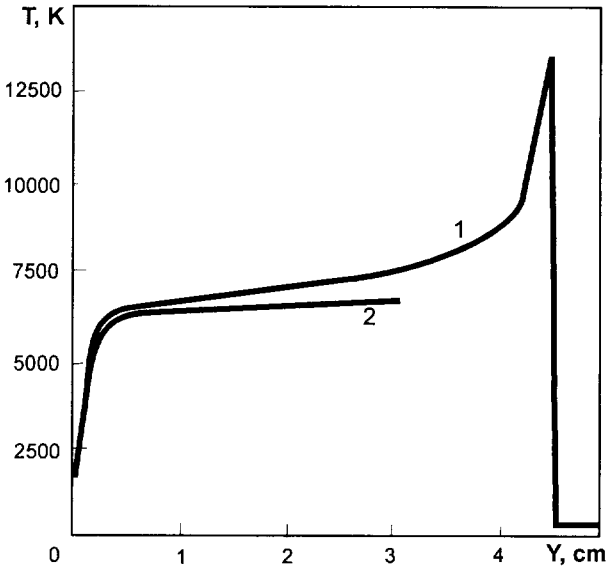


*Fig. 8. Temperature distributions along stagnation line in hypersonic shock layer (1: $M_\infty$=20, $V_\infty$=6490 m/s, Z=62 km, $R_W$=0.95 m) and in subsonic jet (2: $M_S$=0.04, $V_S$=50m/s, $p_S$=0.3 atm, $H_S$=21 MJ/kg, $R_m$=1.5·10$^{-2}$m).*

We can conclude that the displacement of air temperature from the equilibrium value at the outer edges of boundary layers in high-enthalpy tests or in flight is a factor in actual accuracy of the LHTS concept. One should expect that the agreement between the heat fluxes and two boundary layer structures will be improved when the air temperatures outside boundary layers are closer to equilibrium, for example, - for higher values of the pressure as has already been predicted for the high-enthalpy nitrogen experiment in ref. 23.

## 6. The Trajectory Point for the Complete Local Duplication of Heat Transfer

One in the main features of the subsonic high enthalpy jets is the nonuniformity of the enthalpy and velocity profiles at the plasma generator channel exit and the decreasing of these characteristics along the flow axis. In order to take these effects into account, in relations (2.7) instead of $V_S$ and $h_S$ we should substitute the velocity and enthalpy values on the axis of the free stream corresponding to the distance $L$ from the plasmatron channel exit to the model.

For the modeling in a hyposonic flow ($M<<1$), taking into account the above we can generalize relations (3.3), (3.4) in the following form

$$h_S = \frac{1}{2}\varphi_H^{-1}(L)V_\infty^2, \quad p_S = (1-\kappa)\rho_\infty V_\infty^2, \kappa = \frac{\rho_\infty}{\rho_e} \quad (6.1)$$

$$V_S = \varphi_V^{-1}(L)\left(\frac{8}{3}\kappa\right)^{1/2}\frac{R_m^*}{R_N}V_\infty \quad (6.2)$$

Here, the factors $\varphi_H(L)$ and $\varphi_V(L)$ take into account the decreasing of the enthalpy and velocity along the axis of the free subsonic stream, the subscript $S$ relates to the center of the plasmatron channel exit.

As we mentioned above, the parameters $h_S$, $p_S$ and $V_S$ are in functional coupling. For a wide range of the subsonic tests conditions in the optimum discharge burning regime these parameters could be presented with a functional relationship

$$p_S V_S = \chi(h_S, Q, p_S) \quad (6.3)$$

where Q is the mass flow rate and $\chi(h_S, Q, p_S)$ is the specific functional characteristic of the plasmatron. This characteristic should be determined for each facility which is used for the heat transfer duplication.

If function $\chi$ is known, we can eliminate $p_S$ and $V_S$ in (6.3) using (6.1) and (6.2) and obtain the following relationship between the hypersonic flow parameters $\rho_\infty$ and $V_\infty$

$$\rho_\infty = \left(\frac{8}{3}\kappa\right)^{-1/2}(1-\kappa)^{-1}\varphi_V^{-1}(L)\frac{R_N}{R_m^*}V_\infty^{-3} \times \times\chi\left(\frac{V_\infty^2}{2\varphi_H(L)}, Q, (1-\kappa)\rho_\infty V_\infty^2\right) \quad (6.4)$$

For the following step of the procedure, it is necessary to present the trajectory of the body in the atmosphere in the parametric form $V_\infty = F(\rho_\infty)$. The intersection of this curve with the curve (6.4) in the plane $\rho_\infty$-$V_\infty$, if it exists, gives us the trajectory point for which the complete local heat transfer duplication could be achieved.

For the specified parameters $V_\infty$, $\rho_\infty$, and $R_N$, the complete local simulation of the heat transfer is possible for the appropriate model (or channel) dimension. In this case the test conditions can be predicted in accordance with the following algorithm. The free stream parameters $h_S$, $p_S$, and $V_S$ are calculated from (6.1) and (6.3), and then the effective radius $R_m^*$ is calculated from (6.2). The necessary value of $R_m^*$ is insured by choosing a model or channel with the appropriate geometry (for models with flat face in accordance with expression (3.5)).

## 7. Analysis of the Mars probe trajectory and Requirements for Plasmatron Tests

Let's apply the LHTS concept in order to estimate the IPG-4 plasmatron capabilities for complete local duplication of the stagnation point heat transfer for the Mars probe trajectory parameters in a subsonic test with carbon dioxide. The IPG-4 operating envelope for the subsonic regime with carbon dioxide as a working gas (*Fig. 9*) contains the peak-heating parts of the Mars probe trajectory [ref. 17].

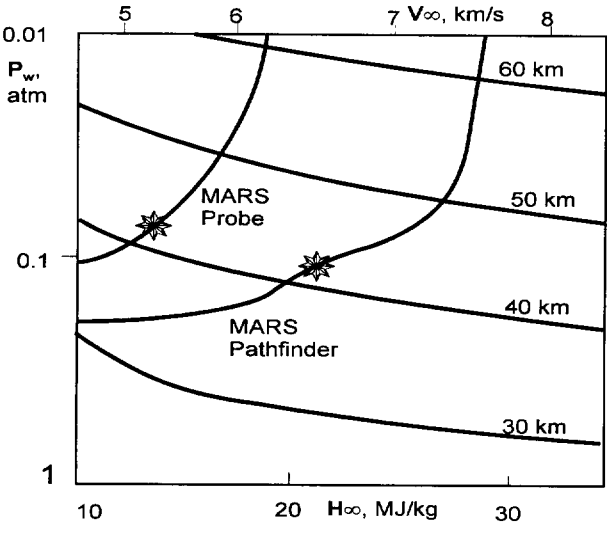


*Fig. 9. The IPG-4 operating envelope in the stagnation pressure-enthalpy coordinates for subsonic regime with carbon dioxide, and the Mars Pathfinder and the Mars Probe trajectories; the stars indicate the peak-heating points [ref.24].*

The velocity $V_\infty$, the altitude $H$ and the calculated convective heat flux to fully catalytic radiative-equilibrium wall $q_w$ at the stagnation point for the probe with $R_N$=0.8 m are presented in *Fig. 10* as functions of the entry time [ref. 17].

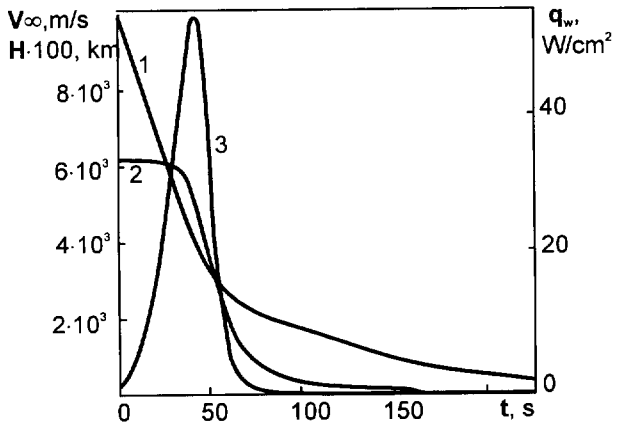


*Fig. 10. Mars probe trajectory and convective heat flux at stagnation point to fully catalytic radiative-equilibrium wall ($R_N$=0.8 m, $\varepsilon_{th}$=0.85) [ref. 24]: 1 - H·100, 2 - $V_\infty$, 3 - $q_W$.*

In accordance with these data and the density distribution in the Martian atmosphere from ref. 17 we have calculated, by using (3.3), the dependencies $p_s(t)$ and $h_s(t)$ that are presented in *Fig. 11* by the curves *1* and *2*. Also, in *Fig. 11* the part of the IPG-4 operating envelope in coordinates $p_s$-$h_s$ for the carbon dioxide gas is shown.

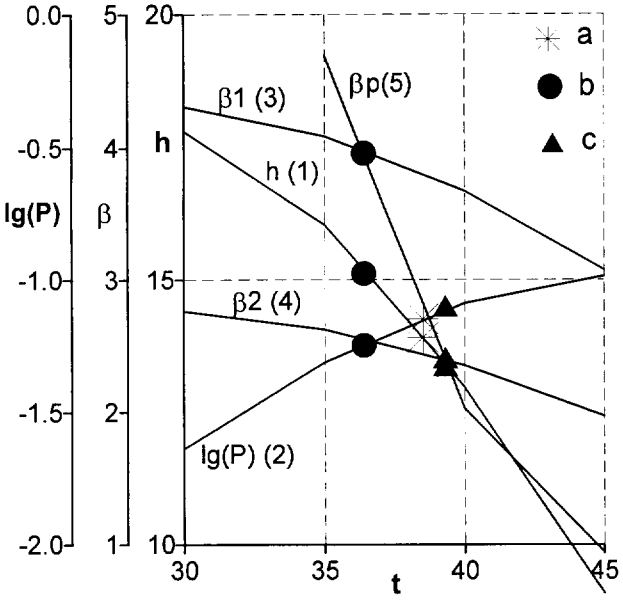


*Fig. 11. Heat transfer parameters for the Mars probe within the IPG-4 operating envelope as the functions of the entry time t (sec) [ref. 24]. Curves: 1 - enthalpy (MJ/kg), 2 - normalized stagnation pressure (p0=1 atm), 3, 4 - velocity gradients ($10^3$ $s^{-1}$) in hypersonic flow for $R_N$=0.8 and 1.25 m, 5 - velocity gradient ($10^3$ $s^{-1}$) in subsonic jet for the euromodel; points: a - the peak heating point, b and c -the points of the complete thermochemical simulation.*

We see, that the IPG-4 envelope contains the both curves $p_s(t)$ and $h_s(t)$ within the entry time interval $25 \le t \le 44$ s. This interval includes the heat-intensive part of the probe trajectory during the period $30 \le t \le 44$ s (*Fig. 10*). The maximum value of a heat flux should be achieved at the point $t^*$=38.5 s where $Z$=43.0 km and $V_\infty^*$=5995 m/s. One could expect that for an accurate simulation the heat transfer at that most important trajectory point it is necessary to have the subsonic flow in the IPG-4 with the enthalpy $h_s^*$=14.02 MJ/kg and the static pressure $p_s^*=6.7\cdot10^{-2}$ atm.

Taking into account, that in the IPG-4 subsonic regimes the pressure $p_s$ and the enthalpy $h_s$ could be controlled independently by using the vacuum pump system and by the variation of energy input in plasma [refs. 12-14], from *Fig. 11* we can conclude that it is possible to duplicate simultaneously both functions $p_s(t)$ and $h_s(t)$ in the real time scale during 19 seconds.

But in fact this way of the duplication of only two heat transfer parameters would not be the complete simulation of heat transfer because the satisfaction of conditions (3.3) does not guarantee the satisfaction of the condition (3.4). Let us emphasize that two parameters of the heat transfer simulation presented on *Fig. 11* by the curves *1* and *2* depend neither on a body shape nor on a model geometry. On the contrary, the equality of the two velocity gradients $V_s/R_m^* = V_\infty/R_N^*$ depends on subsonic and hypersonic flows geometry, shapes and dimensions of a body and a model.

In accordance with *Fig. 10*, along the Mars probe trajectory within the interval $25 \le t \le 44$ s the velocity gradient at the shield stagnation point $\beta_{ef}=V_\infty(t)/R_N^*$ decreases monotonously in the range $4.4\cdot10^3$–$3.2\cdot10^3$ $s^{-1}$ for $R_N$=0.8 m and in the range $2.8\cdot10^3$–$2.1\cdot10^3$ $s^{-1}$ for $R_N$=1.25 m (see the curves *3* and *4* on *Fig. 11*).

Let's consider now the variation of the velocity gradient $\beta_{ep}=V_s(t)/R_m^*$ at the stagnation point of the euromodel (the cylindrical model of 50 mm in diameter with a flat face and the rounded edge of 11 mm in radius with $R_m^*=3.2\cdot10^{-2}$m) if the parameters $p_s$ and $h_s$ change in the way, as *Fig. 11* requires.

It is very important to understand that in the plasmatron flow velocity $V_s$ is not an independent parameter - it is definitely linked with the gas flow rate through the discharge channel $Q$, the enthalpy $h_s$ and the pressure $p_s$. For further estimations we need to have some approximation for the dependence $V_s=V_s(Q,h_s,p_s)$. As a next step on the basis of the previous experimental and numerical data we assume the following approximation at pressures $p_s$<0.1 atm

$$V_s\left(h_s, p_s\right) = \frac{p_s^0}{p_s} V_s^0\left(h_s\right), \quad p_s^0 = 0.1 \text{ atm} \quad (7.1)$$

The experimental dependency $V_s^0(h_s)$ at the pressure 0.1 atm is taken from refs. 11, 12.

For the cylindrical model of 50 mm in diameter with the rounded edge of 11 mm in radius (the euromodel) and the subsonic flow configuration in the IPG-4 ($R_c$=40 mm) on the basis of the previous numerical solution of the Navier-Stokes equations [ref. 12] we have the following approximations for the velocity gradient and effective radius

$$\left(\frac{dU_{ep}}{dr}\right)_0 \cong 0.78\frac{V_s}{R_m}, \qquad (7.2)$$

$$R_m^* = 1.28R_m \cong 3.2\cdot 10^{-2}\ \text{m}$$

In *Fig. 11* the curve *5* shows the velocity gradient $\beta_{ep}(t)=V_s(t)/R_m^*$ that has been calculated from formula (7.2) taking into account (7.1) and dependencies $p_s(t)$and $h_s(t)$. We can see, that this velocity gradient $\beta_{ep}(t)$ decreases monotonously within the time interval $35\le t\le 44$ s from $4.7\cdot 10^3$ to $1.15\cdot 10^3$ $s^{-1}$. The curve *5* crosses the curves *3* and *4* at the points $t$=36.5 and 39.5 s.

That means that for the given value of the probe nose radius it is possible to duplicate in the IPG-4 plasmatron all three conditions (3.3), (3.4) for the one trajectory point only. For the nose radius $R_N$=0.8 m the point of the complete heat transfer simulation is: $t_1$=36.5 s, $H$=45.4 km, $V_\infty$=5524 m/s ($M_\infty$=28.9); the corresponding subsonic jet parameters are the following: $p_s$=5.8·10$^{-2}$atm and $h_s^o$=15.3 MJ/kg. For the nose radius $R_N$=1.25 m the desired point is: $t_2$=39.5 s, $H$=41.8 km, $V_\infty$=5163 m/s ($M_\infty$=26.7); the corresponding subsonic jet parameters are the following: $p_s^o$=7.8·10$^{-2}$ atm and $h_s^o$=13.3 MJ/kg. We see that both points $t_1$ and $t_2$ are close to the point $t^*$ where the heat flux has a maximum value and $t_1<t^*<t_2$. At these two trajectory points the stagnation point heat fluxes to the probe would be less than the maximum values of the heat fluxes but these differences would be within 1% (see *Fig. 10*). So, in fact, a remarkable opportunity for complete simulation of the heat transfer to the Mars probe quite close to the most important point of the entry into Martian atmosphere by using the IPG-4 plasmatron and the euromodel arises.

We should emphasize once more that partial duplication of only two parameters $p_s$ and $h_s$ along a trajectory in the real time scale would be not acceptable. In this way in test we shall have excessive heat fluxes if $t<t^o$ and underestimated heat fluxes if $t>t^o$, where $t^o=t_1$ if $R_N$=0.8 m and $t^o=t_2$ if $R_N$=1.25 m. Therefore, the most correct test technique for the study of the thermochemical resistance of the TPM for the vehicle during his entry into Martian atmosphere would be tests at constant values $p_s^o$ and $h_s^o$ during 15 s.

## 8. Prediction of Subsonic Carbon Dioxide Test for Mars Pathfinder

Let us consider another application of the LHTS concept to a prediction of the high-enthalpy test conditions in the IPG-4 plasmatron for precise simulation of the stagnation point heating for the Mars Pathfinder aeroshell which is a 70-deg sphere cone with a nose radius of 0.6625m [ref. 3]. In accordance with ref. 3 the maximum of the heat flux is achieved at the altitude 40.7 km and the following free stream conditions in the Martian atmosphere ($C_{CO2}$=0.97, and $C_{N2}$=0.03): $V_\infty$=6590 m/s and $\rho_\infty$=3.23·10$^{-4}$ kg/m$^3$. The IPG-4 operating envelope for the subsonic regime with carbon dioxide as a working gas contains the peak-heating parts of the Mars Pathfinder [ref. 3] trajectory (*Fig. 9*).

The desired test conditions are determined for a subsonic dissociated carbon dioxide flow around the cylindrical model of 50 mm in diameter with a flat face and the rounded edge of 11 mm in radius which is supposed to be exposed for testing in the 100-kW IPG-4 plasmatron with the quartz discharge channel of 80 mm in diameter [refs. 11-14].

Now we can recalculate the entry parameters specified above to plasmatron test conditions by using formulae (3.3), (3.4) and (7.2). This simple technique (when the effective radius $R_m^*$ is known) gives the following test conditions: the enthalpy $H_e$=21.73 MJ/kg, the static pressure $p_s$=0.14 atm, the flow velocity $V_s$=184 m/s. For the considered test configuration the calculated dimensionless parameters in equations (4.1) are: $\Delta$=0.4, $u_{1e}$=0.39, $\alpha_e$=2.10.

For these flow parameters and test geometry described above the stagnation point heat transfer rates have been calculated as a function of the surface temperature $T_W$ and the effective catalytic efficiency $\gamma_W$ from the numerical solution of the 1D boundary layer problem (4.1), (4.2) for a 5-species dissociated carbon dioxide mixture ($CO_2$, $O_2$, $CO$, $O$, and $C$).

The next assumptions have been made: 1) the following reactions are running in the mixture: $CO_2+M\leftrightarrow CO+O+M$, $O_2+M\leftrightarrow O+O+M$, $CO+M\leftrightarrow C+O+M$, $CO+O\leftrightarrow C+O_2$,, $CO_2+O\leftrightarrow CO+O_2$;, 2) the surface catalytic recombination of the $CO$ molecules in the reaction $CO+O\rightarrow CO_2$ and $O$ atoms in the reaction $O+O\rightarrow O_2$ are the reactions of the first order with equal efficiencies $\gamma_W$, and the $C$ atoms are not involved in surface reactions. The same fourth-order-accurate finite-difference scheme was exploited for the numerical solution of the boundary layer problem (4.1), (4.2).

The computed stagnation point heat flux envelope for the predicted subsonic test is shown in *Fig. 12*. The upper border of this envelope (the curve *1*) corresponds to the fully catalytic surface ($\gamma_W$=1), the lower border (the curve *7*) - to the noncatalytic surface ($\gamma_W$=0). The

solid curves *2-6* correspond to the constant values of $\gamma_W$, $=10^{-1}$, $3\cdot10^{-2}$, $10^{-2}$, $3\cdot10^{-3}$, $10^{-3}$, the line *8* corresponds to the theoretical minimum of the heat flux from the frozen boundary layer to the noncatalytic wall.

The heat flux envelope is limited from the right side by the curve $q_W=\varepsilon_{th}\sigma T_W^4$, where $\varepsilon_{th}$ is the total hemispherical emissivity, $\sigma$ is the Stefan-Boltzmann constant. The curves *9* and *10* correspond to radiative-equilibrium walls with $\varepsilon_{th}=1$ and 0.78.

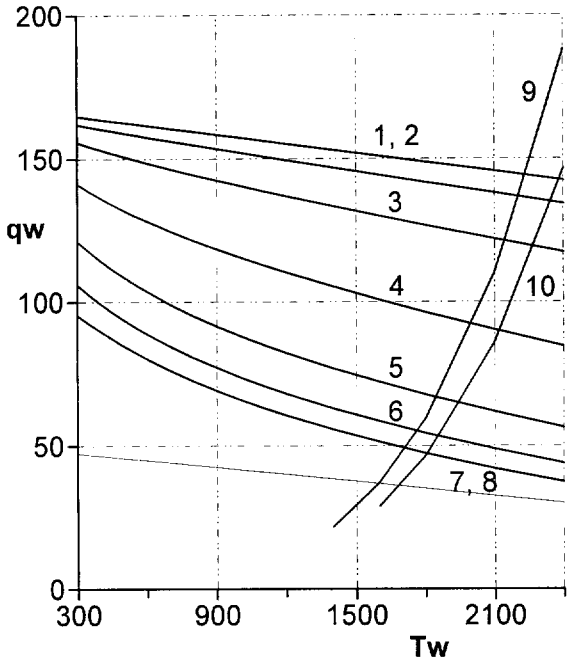


*Fig. 12. Heat flux envelope for the IPG-4 plasmatron subsonic regime for the duplication of the stagnation point heat transfer to the Mars Pathfinder aeroshell ($R_N$=0.6625 m) at the peak-heating point (h=40.7 km, $V_\infty$=6.59 km/s) by using an euromodel ($R_m=2.5\cdot10^{-2}$m).*

Now it is very easy to determine the heat flux and the radiative-equilibrium surface temperature for the given values of $\varepsilon_{th}$ and $\gamma_W$: $q_W$ and $T_W$ are just the coordinates of the intersection point for two curves - $q_W=q_W(T_W, \gamma_W=\text{const})$ and $q_W=\varepsilon_{th}\sigma T_W^4$. Thus, in the predicted test at $\varepsilon_{th}$=0.78 for the fully catalytic wall we have $q_W$=142 W/cm$^2$ and $T_W$=2380 K, for the noncatalytic wall - $q_W$=47 W/cm$^2$ and $T_W$= 1800 K.

For the heat transfer rates at the stagnation point of the Mars Pathfinder aeroshell and the radiative-equilibrium wall we have the maximum values $q_W$=127 W/cm$^2$ and $T_W$=2315 K at the wall condition of fully recombined $CO_2$ and $q_W$=42 W/cm$^2$ and $T_W$=1755 K in the non-catalytic wall case [ref. 3].

So, we observe quite sufficient agreement between the numerically predicted whole heat flux ranges for the Mars Pathfinder aeroshell at the trajectory peak-heating point and for test with an euromodel in the subsonic high-enthalpy carbon dioxide jet, which could be performed in the IPG-4 plasmatron with free stream parameters determined on the basis of the LHTS concept.

It is important that the enthalpy and pressure values determined above belong to the operating envelope of the IPG-4 plasmatron in a subsonic mode (*Fig. 9*) and the maximum of the thermochemical load on the stagnation point of the Pathfinder aeroshell could be duplicated precisely enough.

Recently it was shown in ref. 24 that quite precise duplication of the stagnation point heat flux to the Mars Probe [ref. 17] also could be achieved by using the IPG-4 plasmatron in subsonic regime with carbon dioxide as working gas.

This analysis was performed without taking into account the surface ablation, but in general the LHTS concept validated here can be applicable to a heat transfer problem with ablation effects if the influence of injection into the incoming flow is not very strong.

## 9. The Range of Applicability of the LHTS Concept

The derivation of conditions (2.7) - (2.9) of the local heat transfer simulation was based on the boundary layer theory and the assumption of local thermodynamic equilibrium in the subsonic flow (outside the boundary layer), which is fairly accurately satisfied for molecular gases (air, nitrogen, oxygen, carbon dioxide) in inductive plasmatrons at pressures $p\geq0.1$ atm.

It was found in ref. 25 that the boundary layer theory is applicable for calculating stagnation point heat transfer in subsonic high enthalpy flows at Reynolds numbers $Re_S = \rho_S V_S R_m^* / \mu_S \geq 30$, if the velocity gradient at the stagnation point on the model is determined with making allowance for the finite thickness of the boundary layer. Practically, for the models used in the heat transfer tests in the IPG plasmatrons $30<Re_S<3\cdot10^2$.

Thus, the general conditions of the LHTS concept formulated above are applicable for subsonic high enthalpy molecular gas flows in plasmatrons when $p\geq0.1$ atm and $Re_S$ >30. For the surfaces with a high catalycity the LHTS concept is valid in the full range of the pressure, for the surfaces with moderate catalycity the lower border of the pressure range should be estimated. For the accurate computations of the velocity gradient or effective radius for subsonic test conditions the numerical solution of the Navier-Stokes equations must be used.

The accuracy of the prediction of ground test parameters or extrapolation to flight could be improved if the velocity gradient for flight conditions is calculated more accurately directly from the numerical solution of the hypersonic shock layer problem.

## 10. Comments to Thermochemical Simulation in Supersonic Tests

Traditionally, in high enthalpy tests practice, especially in tests performed by using arc-jet facilities, supersonic regimes are used more often, then subsonic ones. The LHTS concept gives us the strict inequalities for the similarity parameters $\xi$ and $\zeta$ (see (2.10)), when supersonic high enthalpy flow should be performed for the providing of the correct duplication of the stagnation point heat transfer:

$$\frac{\sqrt{2H_\infty}}{V_\infty}\zeta_* \le \xi \le 1, \quad \zeta_* = \sqrt{\frac{\gamma_{*S}-1}{\gamma_{*S}+1}} \le \zeta \le 1 \qquad (10.1)$$

These inequalities mean that some supersonic test is necessary, if the nose radius and the model radius are comparable, although $R_m \ll R_N$ : practically, for the simulation of the hypersonic heating of a vehicle with a small nose radius.

For the case of duplication of the heat transfer to a nose cap with small radius the simulation conditions for velocity and enthalpy (2.7) remain valid, but the conditions for pressure (2.8) must be modified. For supersonic simulating flow, in which the gas between the shock wave and the outer edge of the boundary layer near the flow axis is in the equilibrium state, this modification consists in the following. In the approximate Poisson adiabatic equation (2.5), applied to the equilibrium gas moving behind the shock, the pressure and Mach number are eliminated by means of the Rankine-Hugoniot conditions on the shock wave, and equations (2.7). As a result we obtain

$$\frac{p_S}{p_W} = \frac{(1-\zeta^2)(1-\varepsilon_S\zeta^2)^{\tau_{*Sh}}}{1+(2\tau_{*S}(1-\varepsilon_S)-1)\zeta^2}, \qquad (10.2)$$

$$\varepsilon_S = \frac{\rho_S}{\rho_{Sh}}, \qquad \tau_* = \frac{\gamma_*}{\gamma_*-1}$$

Where $\gamma_*$ is the effective specific heat ratio, subscripts $S$ and $Sh$ relate to the parameters in the plasmatron free stream and behind the shock.

The validation of the conditions (2.7) and (10.2) as the basis of the LHTS concept for supersonic tests is not in fact yet, because the corresponding procedure requires the computations of the high enthalpy reacting supersonic flows in thermal and chemical nonequilibrium in the framework of the full Navier-Stokes equations.

## 11. Discussion

The accuracy of the prediction for the thermochemical action of the reacting gas on a vehicle surface for a hypersonic flight conditions, based on the LHTS concept, depends on the surface catalycity and the displacement of gas temperatures from the equilibrium values at the outer edges of the boundary layers on a body and a model. For surfaces with high and moderate catalycity the satisfaction of the conditions (3.3), (3.4) or (3.6) ensures the accurate duplication of the convective heat fluxes and the diffusive fluxes of atoms in subsonic high-enthalpy jets, when $R_m \ll R_N$.

For the real TPM with catalytic efficiency $\gamma_W \gg 3\cdot10^{-3}$ the above mentioned conditions of a local heat transfer simulation can guarantee in test not only full-scale heat transfer rates, but real nonequilibrium chemistry within boundary layer as well. If the states of the dissociated gas flow at the edge of the boundary layer in the test or hypersonic flow conditions are significantly non-equilibrium, ground test parameters, predicted by using of the LHTS concept in order to simulate the heat transfer to a noncatalytic surface, may be applied as support values.

The LHTS concept makes an analysis of heat transfer parameters along trajectory rather simple and gives clear algorithm of the determination of the trajectory point for which stagnation point heat transfer could be accurately duplicated without taking into account the actual information about TPM catalycity.

As we have seen, the computed heat flux range for simulation of the stagnation point heat transfer rate to the Mars Pathfinder aeroshell at the trajectory peak-heating conditions in the subsonic high-enthalpy carbon dioxide flow is found in sufficient agreement with the study carried out through the full viscous shock layer computations in ref. 3.

## Conclusion & Outlook

It is common knowledge now that modern ground facilities are unable to produce all flight conditions above Mach 8. At the same time the quantitative heat transfer could be duplicated in plasmatron quite precisely at least for a vehicle stagnation point. The LHTS concept reveals the new capabilities in the planning of a high-enthalpy experiment and the new approach to the extrapolation from ground to flight. For the complete stagnation point thermo-chemical simulation the triad of parameters - *total enthalpy-stagnation pressure-velocity gradient* - must be duplicated in a high-enthalpy test. In this kind of the heat transfer simulation the pairs of the parameters *M-Re* and $\rho L$-*V* [ref. 26], which are widely used in aerodynamics, are not the similarity parameters in the stagnation point heat transfer.

The conditions of the hypersonic flow past a blunt body and the desired conditions of the free stream in ground test could be easily linked on the basis of the LHTS concept if one knows or can calculate an effective model radius by using CFD for the test configuration. For the typical entry trajectory, if the geometry of a model is specified, those conditions determine only one trajectory point, for which the complete local simulation could be achieved. If the trajectory point and the nose radius are

specified, conditions of the heat transfer duplication determine the test conditions and the effective radius of a model.

In the more dramatic noncatalytic surface case, we have to solve numerically not only the nonequilibrium shock layer problem for flight conditions, but also to compute the nonequilibrium plasma flow within a plasmatron discharge channel and a subsonic (or supersonic) reacting gas flow past a model for the prediction of the well-documented test conditions. So, CFD modeling is an indispensable tool for the construction of the bridge from ground test to flight and for the verification of the quality of flight parameters duplication in plasmatron tests. The interaction between ground testing and CFD modeling is a genesis for real gas effects duplication and extrapolation to flight.

Above examples of the LHTS concept applications clearly shown that the maximum thermochemical load on a vehicle surface at the stagnation point and TPM behavior can be directly duplicated for the wide range of the reentry and entry conditions in the Earth and the Martian atmospheres by using the inductive plasmatrons in the subsonic regimes.

### Acknowledgements

The preparation of this paper was supported by RTA contract 4329A and the research has been performed in part under the INTAS-RFBR grant 95-1329 and the ISTC project 036. The author would like to express his gratitude to Prof. J.F. Wendt, Prof. M. Carbonaro and Prof. J.-M. Charbonnier for inviting to the VKI at the RTA/AVT Special Course, and to thank Dr. V.Shchelin for providing the shock layer parameters from his own code and Dr. S.Vasil'evskii for help in computations and figures design.

### References

1. Kolesnikov, A.F., "Conditions of Simulation of Stagnation Point Heat Transfer from a High-Enthalpy Flow," Fluid Mechanics, Plenum, (tr. from Russian), v. 28, No. 1, 1993, p. 131.

2. Kolesnikov, A.F., "The Aerothermodynamic Simulation in Sub- and Supersonic High-Enthalpy Jets: Experiment and Theory," Proc. of the Second European Symposium on Aerothermodynamics for Space Vehicles, ESTEC, Noordwijk, The Netherlands, November 1994, ESA SP-367, 1995, p. 583.

3. Gupta,R.N., Lee, K.P., Scott, C.D., "Aerothermal Study of Mars Pathfinder Aeroshell," J. of Spacecraft and Rockets, 1996, v. 33, No. 1, p. 61.

4. Wendt, J.F., Muylaert, J.M., "Status of Hypersonic Testing Capabilities in Europe", Proc. of the Second European Symposium on Aerothermodynamics for Space Vehicles, ESTEC, Noordwijk, The Netherlands, November 1994, ESA SP-367, 1995, p. 165.

5. Anderson, L.A., "Effect of Surface Catalytic Activity on Stagnation-Point Heat Transfer Rates," AIAA J., 1973, No. 11, p. 649.

6. Scott, C.D., "Catalytic Recombination of Nitrogen and Oxygen on High Temperature Reusable Surface Insulation," Progress in Astronautics and Aeronautics, v. 77, edited by A.L. Crosbie, AIAA, New York, 1981, p. 192.

7. Vasil'evskii, S.A., Kolesnikov, A.F., Yakushin, M.I., "Determination of the Effective Probabilities of the Heterogeneous Recombination of Atoms When Heat Flow is Influenced by Gas-Phase Reactions," High Temperature, Plenum, (tr. from Russian), 1991, v. 29, No. 3, p. 411.

8. Stewart, D.A., Chen, Y., Bamford, D.J., Romanovsky, A.B., "Predicting Material Surface Catalytic Efficiency Using Arc-Jet Tests," 1995, AIAA 95-2013.

9. Gulhan, A., Vennemann, D., Yakushin, M., Zhestkov, B., "Comparative Oxidation Tests on Reference Material in Two Induction Heated Facilities," presented at the 46th International Astronautical Congress, Oslo, Norway, October 1995.

10. Eitelberg, G., Krek, R., Beck, W., "Stagnation Point Heat Transfer Testing in Non-Equilibrium Flow Produced by the HEG,"1996, AIAA 96-4504.

11. Bykova, N.G., Vasil'evskii, S.A., Gordeev, A.N., Kolesnikov, A.F., Pershin, I.S., Yakushin, M.I., "An Induction Plasmatron Application for Simulation of Entry into Martian Atmosphere," Proc. of the Third International Symposium on Environmental Testing for Space Programmes, ESTEC, Noordwijk, The Netherlands, June 1997, ESA SP-408, p. 195.

12. Bykova, N.G., Vasil'evskii, S.A., Gordeev, A.N., Kolesnikov, A.F., Pershin, I.S., Yakushin, M.I., "Determination of the Effective Probabilities of Catalytic Reactions on the Surfaces of Heat Shield Materials in Dissociated Carbon Dioxide Flows," Fluid Mechanics, Plenum, (tr. from Russian), 1997, v. 32, No. 6, p. 876.

13. Kolesnikov, A.F., Pershin, I.S., Vasil'evskii, S.A., Yakushin, M.I., "Study of Quartz Surface Catalycity in Dissociated Carbon Dioxide Subsonic Flows," 1998, AIAA 98-2847.

14. Kolesnikov, A., Yakushin, M., Vasil'evskii, S., Pershin, I., and Gordeev, A. "Catalysis Effects on Quartz Surface in High-Enthalpy Oxygen & Carbon Dioxide Flows", 3rd European Symposium on Aerothermodynamics for Space Vehicles, ESTEC, Noordwijk, The Netherlands, 24-26 November 1998, ESA SP-426, 1999, p. 537.

15. Lozino-Lozinskii, G. E., "Buran Flight," in: Gagarin Scientific Studies in Aviation and Cosmonautics, 1989 (in Russian), Nauka, Moscow, 1990, p. 6.

16. Voinov, L.P., Zalogin, G.N., Lunev, V.V., Timoshenko, V.P., "Comparative Analysis of Laboratory and Full- Scale Data Concerning "Bor" and "Buran" Space Vehicles Thermal Protection Material Catalycity," Cosmonautics and Rocket Engineering, TSNIIMASH, (in Russian), 1994, No. 2, p. 51.

17. Rubio Garcia, V., Marraffa, L., Scoon, G., Roumeas, R., "Mars Mini-Probes. Elements of Aerothermo-dynamics & Entry Trajectories," 3rd European Symposium on Aerothermo- dynamics for Space Vehicles, ESTEC, Noordwijk, The Netherlands, 24-26 November 1998, ESA SP-426, 1999, p. 155.

18. Fay, J. A. and Riddell, F. R., "Theory of Stagnation Point Heat Transfer in Dissociated Air," J. Aeronaut. Sci., 1958, v. 25, No. 2, p. 73.

19. Goulard, R., "On Catalytic Recombination Rates in Hypersonic Stagnation Heat Transfer," Jet Propulsion, 1958, v. 28, No. 11, p. 737.

20. Lunev, V.V. Hypersonic Aerodynamics, (in Russian), Moscow, Maschinostroenie, 1975, 328 p.

21. Kolesnikov, A.F. and Yakushin, M.I., "Determination of Heterogeneous Recombination Effective Probabilities of Atoms from Heat Fluxes to the Surface in Dissociated Air Flow," Matematicheskoe Modelirovanie (in Russian), 1989, v. 1, No. 3, p.44.

22. Vasil'evskii, S.A., Kolesnikov, A.F., Yakushin, M.I., "Mathematical Models for Plasma and Gas Flows in Induction Plasmatrons," Molecular Physics and Hypersonic Flows, ed. by M.Capitelli, NATO ASI Series, v. 482, Kluwer, 1996, p. 495.

23. Kolesnikov, A.F., Shchelin, V.S., "Numerical Analysis of Simulation Accuracy for Hypersonic Heat Transfer in Subsonic Jets of Dissociated Nitrogen," Fluid Dynamics, Plenum, (tr. from Russian), 1990, v. 25, No. 2, p.278.

24. Kolesnikov, A., Marraffa L., "An Analysis of Stagnation Point Thermochemical Simulation by Plasmatron for Mars Probe," 1999, AIAA 99-3564.

25. Kolesnikov, A.F., Yakushin, M.I., "Modeling of Convective Nonequilibrium Heat Transfer for Bodies in Hypersonic Flows by Plasmatrons," High Temperature, Plenum, (tr. from Russian), 1988, v. 26, No. 4, p. 569.

26. Vennemann, D., "Hypersonic Aerodynamic/Aero-thermal Test Facilities available in Europe to support Space Vehicle Design," AGARD Symposium on Space Systems Design and Development Testing, Cannes, France, Oct. 1994.

# Heat Flux Measurements in High Enthalpy Flows

**A. Gülhan**
German Aerospace Center (DLR)
Institute of Fluid Mechanics
Wind Tunnel Division in Cologne
Porz-Wahnheide, Linder Höhe
D-51147 Cologne, Germany

## Summary

This document describes the fundamentals of heat transfer measurement techniques in high enthalpy flows. After description of basic relations for the stagnation point heat flux rate to a spherical surface in a high enthalpy flow field, different heat flux measurement techniques are discussed. Attention is paid to design aspects, mathematical model for the heat flux rate evaluation and application limits of each sensor type, in order to provide a useful and practical script for the reader with respect to the choice of an adequate sensor type for different requirements. Sensor calibration and comparative measurements using different heat flux sensors in the arc heated facility LBK are described in the last two chapters.

## 1. List of symbols

| | |
|---|---|
| $A$ | cross section area |
| $C_p$ | specific heat |
| $D_{12}$ | binary diffusion coefficient for atoms and molecules |
| $h$ | enthalpy |
| $h_D$ | enthalpy of dissociation per unit mass for the gas in the external flow |
| $K$ | thermal conductivity |
| LBK | arc heated facility of DLR |
| $Le$ | Lewis number |
| $\dot{m}$ | mass flow rate |
| $Nu$ | Nusselt number |
| $p$ | pressure |
| $Pr$ | Prandtl number |
| $\dot{q}$ | heat flux rate |
| $Re$ | Reynolds number |
| $s$ | wall thickness |
| $T$ | temperature |
| $u$ | flow velocity component in the direction parallel to the body surface |
| $\varepsilon$ | emissivity |
| $\rho$ | density |

### Subscripts

| | |
|---|---|
| $c$ | coolant |
| $e$ | boundary layer edge |
| $s$ | stagnation point |
| $w$ | wall |
| 0 | stagnation condition |
| 1 | inlet side |
| 2 | outlet side |
| $\infty$ | ambient, free stream |

## 2. Introduction

Intrusive measurement techniques in supersonic and hypersonic flows have been a challenging task for engineers for decades. Recent progresses in non-intrusive measurement techniques and numerical codes have led to a better understanding of local flow phenomena and to further improvement of intrusive measurement techniques in aerodynamics. Because of its complexity the measurement of the

*Paper presented at the RTO AVT Course on "Measurement Techniques for High Enthalpy and Plasma Flows", held in Rhode-Saint-Genèse, Belgium, 25-29 October 1999, and published in RTO EN-8.*

heat flux rate remains one of the key techniques, which have to be improved with respect to measurement accuracy and repeatability. The heat flux rate is usually determined from the measured temperature development on the surface or inside the probe and applying a mathematical model with some assumptions. Any deviation from a perfect contact between the temperature sensor and probe or other satisfaction of assumptions leads to inaccuracies.

Heat flux determination in high enthalpy flow fields is accompanied with some additional effects. Since the flow field of most of the high enthalpy facilities is in thermo-chemical non-equilibrium, the gas surface interaction phenomena influence the heat flux rate significantly. Surface catalysis and emittance, which are a function of the surface temperature, play an important role in such environments. The boundary flow around the probe is also influenced by these effects and there is a continuous coupling between the flow and model structure. Differences in the operation of different high enthalpy facilities give rise to different requirements on the heat flux sensors. Short duration high enthalpy facilities like shock tunnels, impulse facilities, etc. have a very short testing time of several milliseconds. Therefore only heat flux sensors with a very short response time can be used in these facilities. Because of short flow exposure time of the sensor the surface temperature is low. Arc heated and induction heated facilities have a longer testing time, which would lead to higher surface temperature of the stationary and uncooled probes. The practical realisation of the cooling and insulation of the probe influences the measurement. Another option is the application of uncooled transient heat flux probes, whose reliability depend on some further parameters like sweep speed, flow homogeneity, etc..

Because of above mentioned diversity in the requirement on heat flux sensors different types of measurement techniques will be described and compared in this document. Since some techniques can be used in both short and long test duration facilities, the layout of this script is chosen in such a way that similar techniques are described in the same chapter.

### 3. Heat flux at high surface temperatures

The heat transfer process at hypersonic velocities is complicated by high temperature effects, which are not present at low speed flights. The shock wave in front of the critical components of a hypersonic vehicle like nose cap, wing leading edge, etc. heats air to high temperatures at which dissociation and ionization of the gas species take place (**Fig. 1**).

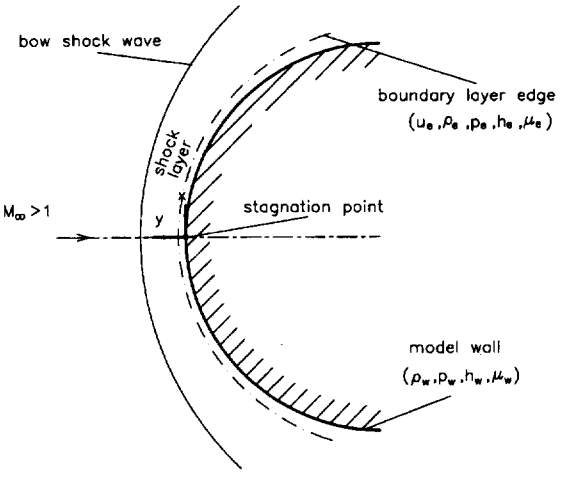


**Figure 1. Stagnation region flow field**

Since the dissociation and ionization processes proceed at finite rates and the relaxation length behind a bow shock is small the thermochemical

equilibrium is not necessarily be achieved in the stagnation point region. Depending on the shock strength, i.e. flight Mach number, the gas at the boundary layer edge consists of different composition of molecules, atoms and ions. The vibrational rotational and translational excitations of molecules are not in equilibrium. Due to viscous forces in the boundary layer the gas is decelerated and recombination reactions are initiated. Since atoms and ions recombine with a high specific energy release the heat transfer rate is enhanced. If a fully thermochemical equilibrium of the gas is not achieved in the boundary layer, the heat flux rate to the body depends on the catalysis of the surface.

The stagnation point heat transfer rate to a spherical body in a dissociated viscous boundary flow with thermochemical equilibrium was described by Fay and Riddell [1,2] as follows:

$$\dot{q}_s = 0.76\, Pr^{-0.6}(\rho_e\mu_e)^{0.4}\,(\rho_w\mu_w)^{0.1}\sqrt{\left(\frac{du_e}{dx}\right)_s}\,(h_{0_e}-h_w)\left[1+\left(Le^{0.52}-1\right)\left(\frac{h_D}{h_{0_e}}\right)\right] \quad (1)$$

The non-dimensional parameters appearing in this formula are defined as

Prandtl number

$$Pr = \frac{\mu C_p}{K} \quad (2)$$

Lewis number

$$Le = \frac{\rho C_p D_{12}}{K}. \quad (3)$$

The other notations used in the equation (1) are

$C_p$: specific heat

$D_{12}$: binary diffusion coefficient for atoms and molecules

$h$: enthalpy

$h_D$: enthalpy of dissociation per unit mass for the gas in the external flow

$K$: thermal conductivity

$\dot{q}_s$: stagnation point heat flux rate

$u$: flow velocity component in the direction parallel to the body surface

$x$: radial distance along the body surface from the stagnation point

$\mu$: viscosity

$\rho$: density

The subscript notation is:

0: conditions at the stagnation point

$e$: conditions at the boundary layer edge

$w$: conditions at the body surface

The stagnation point velocity gradient is given by Newtonian theory as:

$$\left(\frac{du_e}{dx}\right)_s = \frac{1}{R}\sqrt{\frac{2(p_e - p_\infty)}{\rho_e}} \quad (4)$$

where $R$ is the radius of the sphere, $p_e$ and $p_\infty$ are the pressure at the stagnation point of the boundary layer edge and the pressure ahead of the shock, respectively.

The heat flux rate of a fully catalytic spherical wall in a frozen boundary layer is given as

$$\dot{q}_s = 0.76\, Pr^{-0.6}(\rho_e\mu_e)^{0.4}\,(\rho_w\mu_w)^{0.1}\sqrt{\left(\frac{du_e}{dx}\right)_s}\,(h_{0_e}-h_w)\left[1+\left(Le^{0.63}-1\right)\left(\frac{h_D}{h_{0_e}}\right)\right] \quad (5)$$

The heat flux rate to a non-catalytic surface in a frozen boundary layer is approximated with $Le = 0$ as:

$$\dot{q}_s = 0.76\, Pr^{-0.6}(\rho_e\mu_e)^{0.4}\,(\rho_w\mu_w)^{0.1}\sqrt{\left(\frac{du_e}{dx}\right)_s}\left(1-\frac{h_D}{h_{0_e}}\right). \quad (6)$$

The equations (1) and (5) describing the heat flux rate to an arbitrary surface in an equilibrium flow and the heat flux rate to a fully catalytic surface in a frozen flow field, respectively, are essentially the same. They differ only in the slightly different exponent on the Lewis number. That means that the surface heat flux rate is nearly the same whether the flow is in local thermochemical equilibrium or is frozen with a fully catalytic wall. In the case of an equilibrium flow recombination reaction takes place in the colder region of the boundary layer itself, releasing chemical energy, which is transported by thermal conductance to the surface. In the frozen boundary layer flow recombination occurs on the catalytic wall surface. **Figure 2** shows the heat transfer coefficient $Nu/\sqrt{Re}$ as a function of the recombination rate parameter $C_1$ [3]. Nusselt number ($Nu$), Reynolds number ($Re$) and $C_1$ are defined as:

$$Nu = \frac{\dot{q}_s C_{p_w} x}{K_w(h_e - h_w)} \quad (7)$$

$$Re = \frac{\rho_w u_e x}{\mu_w} \quad (8)$$

$$C_1 = K_1 p_s^2 T_s^{-3.5} R^{-2}\left(\frac{du_e}{dx}\right)_s^{-1}. \quad (9)$$

$R$ is the universal gas constant.

The solid lines show the total heat flux rate for both catalytic (1) and non-catalytic (2) surfaces. The heat flux rate by conduction alone to a catalytic wall is shown by the dotted curve (3). Large values of $C_1$ corresponds to an equilibrium boundary layer flow. At this range the total heat transfer is dominated by conductive heating. As mentioned before in an equilibrium flow the heat flux rate to both catalytic and non-catalytic surfaces is the same since the recombination is completed in the boundary layer flow. In contrast the heat flux rate to a non-catalytic wall depends strongly on the flow regime. By moving from high $C_1$ values (equilibrium) to smaller $C_1$ values the flow becomes progressively more non-equilibrium and it is frozen at the left end of the curves. It can be seen clearly that the heat flux rate to a non-catalytic wall (curve 2) in the frozen flow field drops by a factor of more than two compared to the equilibrium flow. The difference between the curves 1 and 3 represents the heat transfer due to diffusion. It can be seen clearly that at decreasing $C_1$, i.e. freezing boundary layer chemistry, the conductive heat transfer rate to the wall is decreasing. Although for equilibrium flows the total heat transfer is essentially all conductive, the diffusion becomes a larger part of the heat transfer to a catalytic wall in strong non-equilibrium flow.

The influence of the non-equilibrium phenomena in the gas-surface-interaction in high enthalpy flow field has to be considered in the measurement techniques of the heat flux rate determination in high enthalpy facilities.

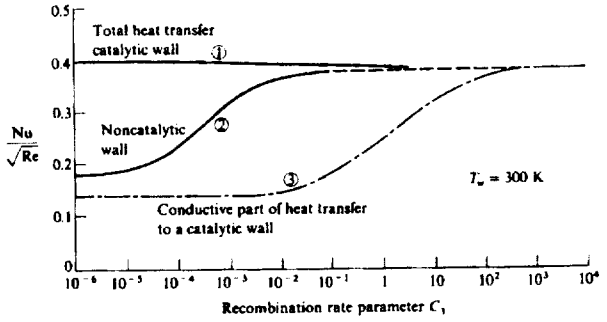


**Figure 2. Heat transfer parameter $C_1$ for different wall catalysis [1,2]**

## 4. Heat flux measurement techniques

Fay and Riddell equation for the stagnation point heat flux rate does not include radiation effects. Since the radiance of a surface is a strong function of the surface temperature and its development depends also on the thermal properties of the vehicle or model materials, it has to be considered by the analysis of heat balance of a solid surface. Although especially in high density gas with high temperature, radiation processes may affect the heat transfer from the gas to the model significantly, thermal radiation of the surface at high temperatures is more important. Therefore thermal radiance of the surface is considered in the analysis of the heat balance on the model surface.

Let us consider a test model, which is exposed to a high enthalpy flow field (**Fig. 3**).

The heat balance on the model surface can be expressed as

$$\dot{q}_g = \dot{q}_c + \dot{q}_r \tag{10}$$

where $\dot{q}_g$, $\dot{q}_c$ and $\dot{q}_r$ represent the heat flux rate from the gas to the surface, conduction inside the model and thermal radiation of the model surface, respectively. The thermal radiance is a strong function of the surface temperature

$$\dot{q}_r = \varepsilon\sigma\left(T_w^4 - T_\infty^4\right) \tag{11}$$

where $\varepsilon$ and $\sigma$ (= $5.67 \cdot 10^{-8}$ [W/(m$^2$ · K$^{-4}$)]) are the surface emissivity and the Stefan-Boltzmann constant, respectively.

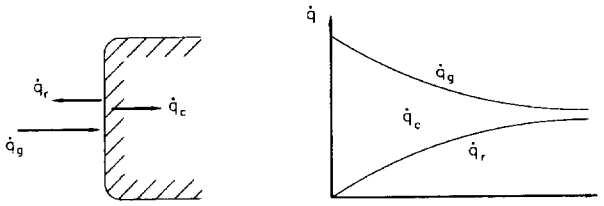


**Figure 3. Heat transfer balance at the model wall**

At low temperatures of the model in a high enthalpy flow field the thermal radiance ($\dot{q}_r$) is negligible compared to the gas heating (Fig. 3). Since the difference of the gas and surface temperatures is a driving factor of the heat transfer from the gas surface to the model surface (eqs. (1), (2) and (3)), it is high at cold surfaces in a high temperature gas flow. Therefore the heat conduction into the model, i.e. temperature increase in the model structure, is high. Since the gas heating to the surface and radiation cooling of the model have an opposite development with increasing temperature, a so-called radiative equilibrium establishes at high surface

temperatures. At that point the gas heating rate and radiation cooling rate are equal. The heat flux rate to a surface in radiative equilibrium can be determined by measuring the surface temperature and applying the equation (11). The surface temperature can be measured with non-intrusive measurement techniques like pyrometer or IR-camera. Besides an accurate temperature measurement a correct value of the surface emissivity ε is essential for the determination of the so-called hot wall heat flux rate. This technique can only be applied in arc heated or induction heated facilities with long testing time (several minutes), where radiative equilibrium can be achieved.

In order to determine the heat flux rate to models without radiative equilibrium conditions which are achieved in long duration high enthalpy facilities, shock tunnels or hot shot facilities use different measurement techniques.

### 4.1 Heat storage and conduction sensors

#### 4.1.1 Transient heat flux probe of DLR

The transient heat flux probe designed by DLR [4] consists of a copper cylinder with two embedded thermocouples at both ends of the cylinder (**Fig. 4**). It is integrated in a water cooled probe holder almost adiabatically.

The probe is swept through the flow field at constant flow conditions. Since the probe temperature is mostly lower than 500 K and copper surface is catalytic, this probe provides cold wall heat flux rate to a catalytic surface. The heat flux rate is determined from measured temperature development at two locations and applying one dimensional heat conduction equation. The measured temperature developments are the boundary conditions of this equation.

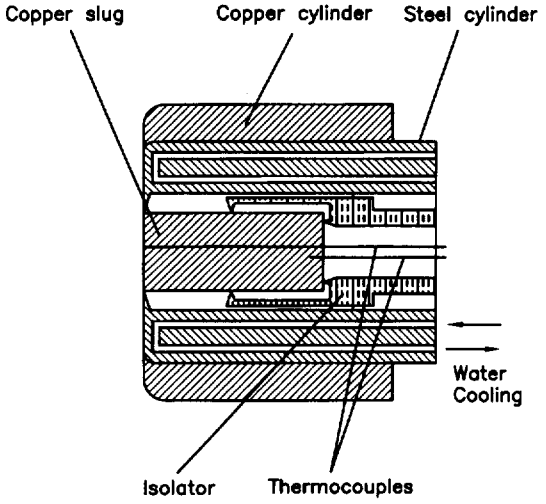


**Figure 4. Transient heat flux probe of DLR**

Based on the description in the **Fig. 5** the heat conduction equation can be written as below:

$$\frac{\partial T}{\partial t} = \frac{K}{\rho C_p} \frac{\partial^2 T}{\partial x^2} \tag{12}$$

where $T$, $t$ and $x$ are the temperature, the time and the axial distance from the front of probe surface. The parameters $K$, ρ and $C_p$ represents the thermal conductivity, the density and the specific heat of the copper cylinder, respectively.

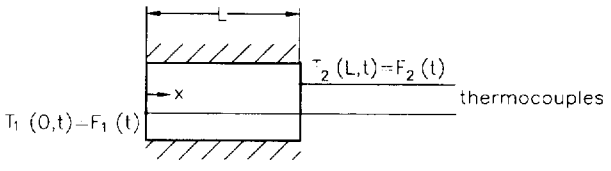


**Figure 5. Mathematical model of the transient heat flux probe**

The initial condition is

$$T(x,0) = T_0 . \tag{13}$$

The boundary conditions are given by two functions $F_1(t)$ and $F_2(t)$:

$$T(0,t) = F_1(t) \tag{14}$$

$$T(L,t) = F_2(t) \tag{15}$$

where $L$ is the length of the cylinder.

Since the solution of the equation (12) requires complicated Laplace transformations, it is not described here in details. Using the determined temperature development along the cylinder by solving equation (12), the heat flux rate to the front surface of the probe can be calculated from equation:

$$\dot{q}(0,t) = K\left(\frac{\partial T}{\partial x}\right)_{x=0} . \tag{16}$$

Transient heat flux measurement technique assumes that no heat is lost by conduction in radial direction and thermocouple wires. The first assumption is generally justified by keeping the contact surface of the probe to the probe holder as small as possible (three points around the circumference of the cylinder and use of an insulation material as interface surface). Since the heat conductivity of copper is nearly four times higher than that of Nickel or Chromium (NiCr-Ni thermocouples are used) [5] and the cross section area of thermocouples is very small compared the cylinder surface area the heat sink effect of thermocouples is small. The main uncertainty of this technique is correlated to the quality of vacuum brazing of thermocouples into the copper cylinder. Even small cavities at the measurement spot of thermocouples in the cylinder can influence the accuracy of the probe remarkably. Therefore all braze spots have to be analysed using X-ray before the calibration and use of the probe. The temperature dependency of the material properties ($\rho$, $C_p$, $K$) is considered to achieve a good accuracy of the measurement. This technique also allows to measure the spatial distribution of the heat flux rate.

### 4.1.2 Heat flux sensor of NAL

National Aerospace Laboratory (NAL) in Tokyo has developed a heat flux sensor for high temperature application using tile material [6]. This sensor was successfully applied during the flight of the HYFLEX vehicle in 1996 [7]. It consists of tile material with a high temperature coating of 0.3 mm thickness (**Fig. 6**). The sensor is attached to the substructure of the vehicle via an aluminium flange and screws.

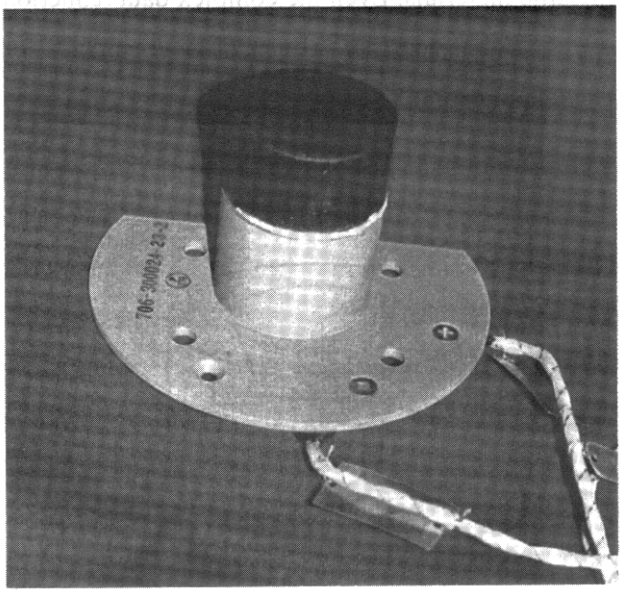

**Figure 6. NAL heat flux sensor [6]**

Three thermocouples are integrated in the sensor to measure the temperature history at three locations along the axis of the plug (**Fig. 7**). The first thermocouple is attached to the rear surface of the high temperature glass coating layer. The measured temperature is assumed to be the surface temperature of the sensor. The much higher thermal conductivity of the glass coating compared to the ceramic tile justifies this assumption. Using measured temperatures with three thermocouples as boundary conditions under the assumption of two dimensional plane symmetry and applying two dimensional heat conduction equation the heat flux rate is calculated.

NAL sensor is one of the few sensors, which can be used at high temperatures up to 1700 K for flight experiments. It has a response time of about one second. Since it is made of tile materials of the vehicle, the transferability of the data to the thermal behaviour of other TPS components of the vehicle is more reliable compared to sensors consisting of metallic materials. Even the complex data reduction of this sensor does not influence its advantages for flight application.

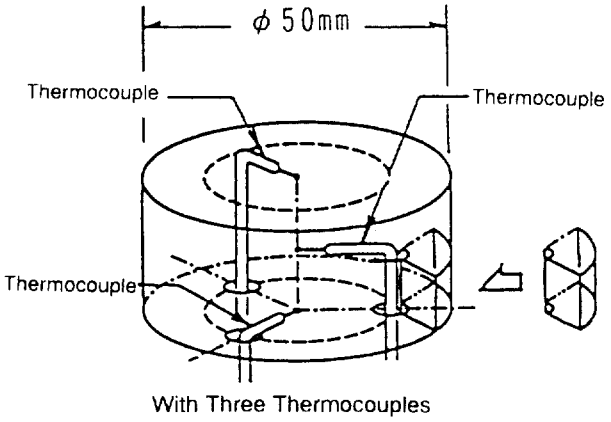


**Figure 7. Principle sketch of NAL heat flux sensor [7]**

### 4.2 Sensors based on thick wall technique

The principle of thick wall heat flux sensors is based on the measurement of the surface temperature of a model structure, which can be considered to be a semi-infinite solid (**Fig. 8**). It means that during the measurement time period the conductive heating does not reach the rear surface of the model, i.e. the surface temperature at that location remains constant.

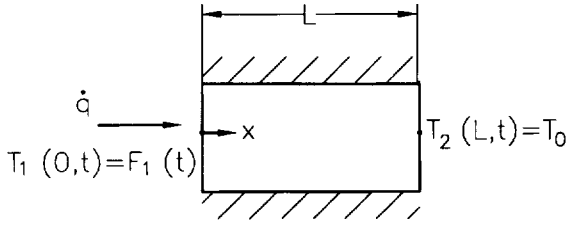


**Figure 8. Boundary temperatures of a semi-infinite model**

The boundary conditions for the one-dimensional heat conduction equation (eq. (12)) would be:

$$T(0,t) = F_1(t) = T(t) \tag{17}$$

$$\dot{q}_s(t) = K\left(\frac{\partial F_1(t)}{\partial x}\right)_{x=0} = K\left(\frac{\partial T(t)}{\partial x}\right)_{x=0} \tag{17'}$$

$$T(L,t) = T(\infty,t) = T_0. \tag{18}$$

The solution of the equation (12) under these boundary conditions leads to the following expression for the heat flux rate to a semi-infinite probe:

$$\dot{q}(t) = \sqrt{\frac{\rho C_p K}{\pi}}\left[\frac{T(t)}{\sqrt{t}} + \frac{1}{2}\int_0^t \frac{T(t)-T(\tau)}{(t-\tau)^{3/2}}d\tau\right] \tag{19}$$

In the case of a constant heat flux rate equation (19) takes a simpler form:

$$\dot{q} = \frac{\sqrt{\pi}}{2}\sqrt{\frac{\rho C_p K}{t}}\,[T(0,t) - T_0]. \qquad (20)$$

This technique requires a short exposure time of the sensor to the flow. The duration is defined by the constancy of the rear surface temperature of the slug. Therefore it is mainly used in shock tunnels, impulse tunnels or hot shot facilities. The transition phase of the flow after the start makes the heat flux evaluation in these facilities difficult.

### 4.2.1 Coaxial surface thermocouple

The principal of the application of the coaxial surface thermocouple for the heat flux rate measurement is the measurement of the surface temperature of a body, which can be considered as a semi-infinite solid. One thermoelectric material is installed in a second tube of thermoelectric material concentrically with an electrical insulation of ceramic base (**Fig. 9**). The hot junction of the thermocouple is created by abrading the center conductor and outer tube together. The coaxial thermocouple assembly is completed by attaching thermocouple lead wires to the coaxial thermoelements.

The heat flux rate is determined from the measured surface temperature history by solving equation (19) or (20) using a numerical integration technique.

In order to achieve a representative heat flux rate to the model surface, the material properties of the thermocouple (i.e. $\sqrt{\rho C_p K}$ value) has to match with the model parameters. This technique is applied in short duration wind tunnels, continuous wind tunnels and arc jet facilities. The main advantages of the coaxial thermocouple technique are its fast response time (~ 50 µs) and very good durability. Since the output is self-generating, no calibration is required. It's application is restricted more or less to metal models. Weak output signal and complex data reduction are the disadvantages of this technique.

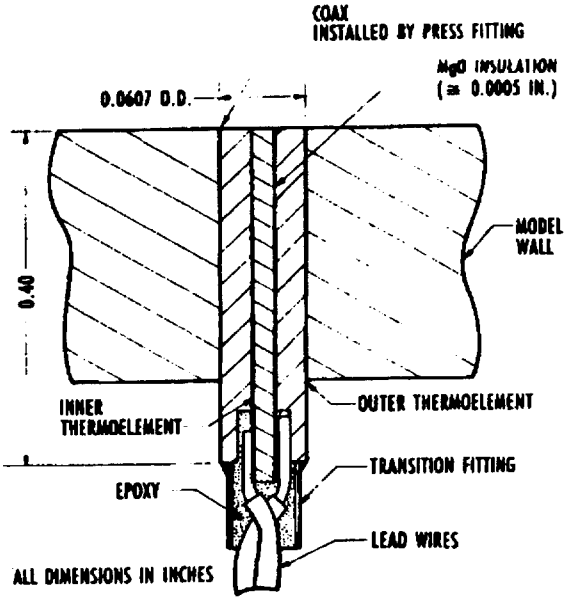


**Figure 9. Sketch of coaxial surface thermocouple [8]**

Based on already available coaxial thermocouples, a coaxial thermocouple with integrated pressure gauge has been developed at the Technical University of Aachen (RWTH Aachen) (**Fig. 10**) [9]. It allows to measure the temperature, i.e. heat flux rate, and pressure almost at the same location (spatial deviation between two sensors is about 1.5 mm). The sensor properties are matched for its application in short duration facilities.

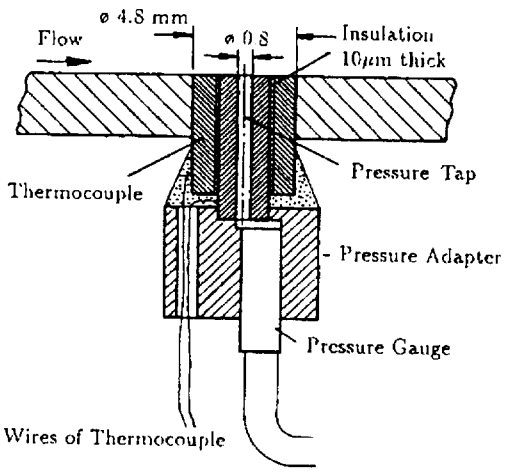


**Figure 10. Coaxial surface thermocouple with integrated pressure gauge [9]**

### 4.2.2 Thin-film gauge

Thin film gauges have been extensively used in the aerodynamic research for decades. Mainly a platinum film is applied in a thickness of several nanometers on the substrate by sputtering, vacuum deposition or painting. Pyrex, fused Quarts or MACOR are mainly used as substrate. Because of its high positive temperature-resistance coefficient Platinum provides an excellent output signal. The temperature data deduced from the measured resistance change is reduced to the heat flux rate using semi-infinite heat flux equation (eq. (19) or (20)). **Figure 11** shows a thin film gauge developed at RWTH Aachen [10]. Thin film gauges are very convenient for aerothermodynamic application, since they have a negligible heat capacity compared to the substrate. In contrast to coaxial surface thermocouples thin film gauges find a broad application on non-metallic materials. The other remarkable advantage is their easy use in surface curvatures of small radius. The response time is very short (less than 5 μs). But these sensors are very sensitive even to small particles. The calibration is time consuming. The influence of the heat conduction on the results has to be considered in the evaluation of the data.

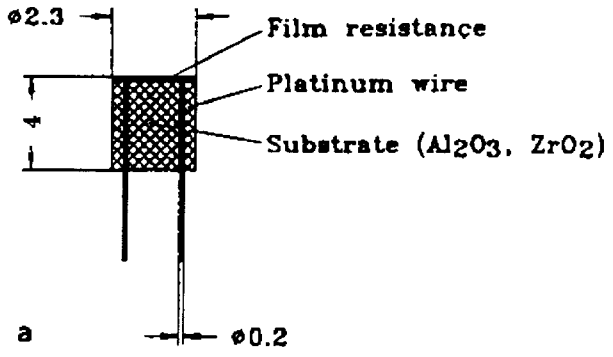


**Figure 11. Thin film gauge of RWTH Aachen [10]**

### 4.2.3 Null-point calorimeter

The null-point calorimeter was developed by AEDC [8]. **Figure 12** shows a sketch of this sensor. A thermal mass with a length of several centimetres is drilled from the backside to a few millimetre distance from the front surface.

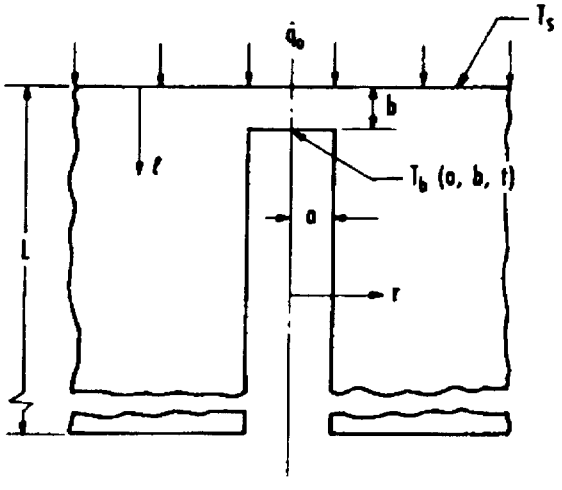


**Figure 12. Concept of null-point calorimeter [8]**

The location 0, *b* on the radial centerline of the cylinder cavity is defined as the null point. The

measured temperature development of this point is assumed to be identical to the surface temperature history on the outside surface of the same thermal mass without cavity. In order to justify this assumption the geometry of the sensor is specified by a very detailed thermal analysis. According to null point, analysis states that the temperature history at the null point would be very close to the surface temperature history in the absence of the hole, if the ratio of the hole radius to the axial distance of the point about 1.4. Therefore, the measured null point temperature with a Chromel-Alumel thermocouple can be inserted into the equation (19) to determine the heat flux rate to a semi-infinite mass. The thermocouple wires are normally attached by vacuum brazing. As it is shown in **Fig. 13** the null-point body has a slight chamber at the top and bottom, which creates an effective circumferential dead air space along the length of the cylinder to enhance one-dimensional heat conduction and prevent radial heat transfer.

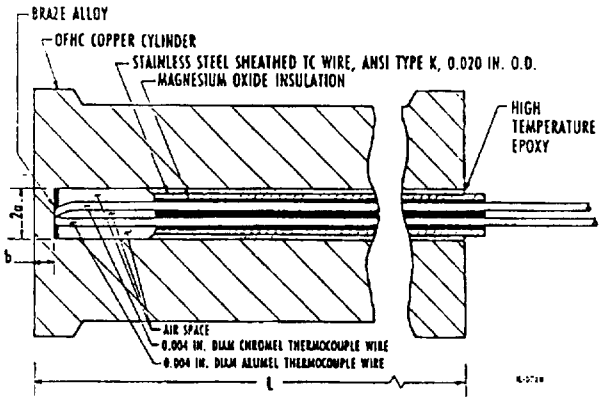


**Figure 13. Cross section view of null-point calorimeter [8]**

This sensor is mainly used at the stagnation point test configuration of arc heated facilities. Its response time is 1-2 ms. Very high heat flux rates up to 284 MW/m$^2$ can be measured with this sensor. Shortcomings of the null-point calorimeter are the difficulty in the achievement of consistency in thermocouple wire attachment, difficult calibration procedure and its limitation to high heat flux rates at short time duration.

### 4.3 Calorimetric sensors

#### 4.3.1 Thin-skin technique

The operation principle of the thin-skin technique involves measuring the slope of the back surface temperature history of a thin skin model.

The heat flux rate can be calculated using the relation:

$$\dot{q} = \rho C_p s \frac{dT}{dt} \tag{21}$$

where $s$ is the thickness of the thin wall.

This technique assumes that the heat conduction to adjacent structures is negligible during the measuring time. The exposure time of the sensor has to be specified in dependence on the material properties and heat flux rate level, i.e. temperature gradient on the back surface. Simple data reduction is a big advantage of this technique. But the influence of the lateral heat conduction and temperature dependency of the material properties on the measurement accuracy is a problem. Therefore the fabrication of a thin-skin model is expensive.

#### 4.3.2 Slug calorimeter

The slug calorimeter technique is based on the storage of all the heat which enters upon the sensor surface in a calorimetric mass during the measuring

time. A metallic disc is mostly used as calorimetric mass. The slug is integrated in a thermal insulator to avoid radial heat losses (**Fig. 14**).

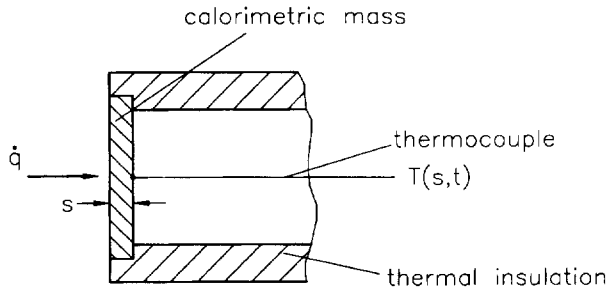


**Figure 14. Sketch of slug calorimeter**

Again equation (21) is applied for the calculation of the heat flux rate from the measured temperature history on the backside of the disc. The accuracy depends strongly on the quality of the insulation, i.e. prevention of radial heat conduction.

### 4.3.3 Water cooled calorimeter

The Institute of Mechanical Problems (IPM) in Moscow developed a water cooled calorimeter to measure the heat flux rate in steady state flow conditions [11]. This technique is based on the measurement of the energy absorbed by cooling water, which removes the incident heat from the back surface of the thin metallic disc of a hollow cylinder (**Fig. 15**).

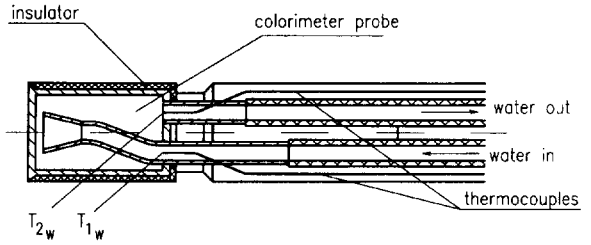


**Figure 15. Sketch of water cooled steady state calorimeter**

The water mass flow rate and the temperature increase of the water are measured precisely. The heat flux rate is calculated using following relation:

$$\dot{q} = \frac{\dot{m}_c C_{pc} (T_{2c} - T_{1c})}{A} \tag{22}$$

where

$A$: cross section area of the probe

$C_{pc}$: specific heat of water

$\dot{m}_c$: water mass flow rate

$T_{1c}$: water inlet temperature

$T_{2c}$: water outlet temperature

Material of different catalysis can be used as probe material. DLR and VKI have manufactured calorimeter probes based on IPM-concept (**Fig. 16**).

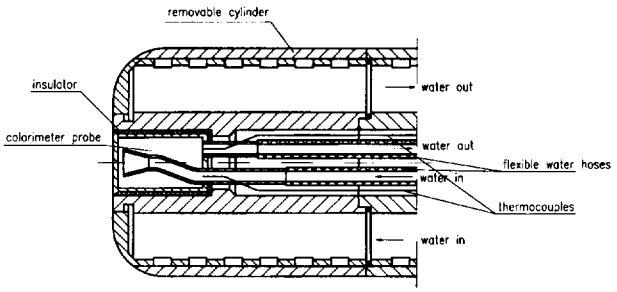


**Figure 16. Water cooled calorimeter probe of DLR based on IPM concept**

## 4.4 Heat conduction gauges

### 4.4.1 Gardon gauge (asymptotic calorimeter)

Gardon gauges consist basically of a thin metallic foil suspended over a cavity in a heat sink. It is thermally and electrically attached to the heat sink at the periphery of the cavity using metallurgical bonding techniques (**Fig. 17**). The metallic foil as

the first thermoelectric material (mostly constantan) creates together with to the second thermoelectric material of periphery (copper) one junction of the thermocouple. A wire of second thermoelectric material is attached to the rear surface center of the foil to form a differential thermocouple. It measures the temperature difference between the center and the edge of the foil.

The one-dimensional heat conduction in radial direction can be described in polar co-ordinates as:

$$\frac{\rho C_p}{K}\frac{\partial T}{\partial t} = \frac{1}{r}\frac{\partial T}{\partial r} + \frac{\partial^2 T}{\partial r^2} + \frac{\dot{q}}{s.K} \qquad (23)$$

with boundary conditions

$$T(r,0) = T_s \quad \text{at} \quad 0 < r < R \qquad (24)$$

and

$$T(R,t) = T_s \quad \text{for} \quad 0 < t < \infty. \qquad (25)$$

The steady state solution of the equation (23) under these boundary conditions is:

$$\dot{q} = \frac{4sK}{(R^2 - r^2)}(T - T_s). \qquad (26)$$

The heat flux rate at the foil center ($r = 0$) would be

$$\dot{q} = \frac{4sK}{R^2}(T - T_s). \qquad (27)$$

Equations (26) and (27) show that the temperature difference between the center and edge of the foil is directly proportional to the heating rate $\dot{q}$. A further thermocouple is usually integrated inside the cylinder to provide absolute gauge temperature for the calculation of heat transfer coefficient in aerodynamic application. The influence of the heat sink temperature should be considered by the specification of the sensor. Copper-Constantan combination meets the requirements with respect to the linearity of the sensor.

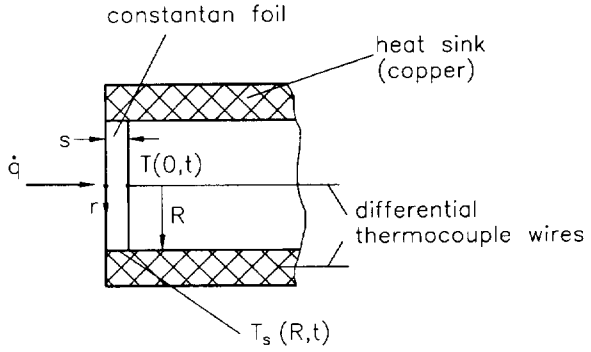


**Figure 17. Principle scheme of Gardon gauge**

Gardon gauges have a broad application in wind tunnel heat flux measurements and heat transfer determination during flight. Uncooled sensors can only be applied at surface temperatures up to 1100°C. The response time of these sensors is about 1 second. Since the heat flux rate is directly proportional to the temperature difference, the data reduction is very easy. Low sensitivity and limited surface temperature are main disadvantages. Gardon gauge signal in high enthalpy facilities is noisy.

### 4.4.2 Thin thermopile sensors

The thermopile measurement technique is based on the measurement of the temperature change across the thermal resistance elements, which are deposited on a heat sink material. The thermopile consists of multi thermocouple pairs to achieve measurable voltage drop across the sensor.

Vatell Corporation has developed a micro-sensor (HFM) based on this technique. Two different thin films are deposited on the aluminium nitride substrate of HFM. A thin film of less than 2 microns of the heat flux sensor HFS allows to achieve very fast response of about 10 microseconds. The heat flux sensor is surrounded by a temperature sensor made of platinum resistors (RTS). Temperature is determined by passing a small constant current through the resistance and measuring the resulting voltage. Substrate surface temperature is used to consider the change of the material properties with the temperature in the heat flux determination. It may also be used to check the calibration of the HFM sensor and measure the heat transfer coefficient in aerodynamic application.

In order to use the linear range of the temperature dependency of substrate material properties, the heat transfer to the surrounding model is forced by using nickel or copper housing, which is bonded to the substrate with high grip. The surface of the thin films can be coated with layers of different emissivity, which is very essential for the calibration of the sensor using radiation sensors. HFM sensors can be used at temperatures up to 1125 K without cooling.

In the frame of X-38 programme OHB will use a HFM sensor integrated in a flexible insulation material (FEI) and perform heat flux measurement on the Lee side of the vehicle during the first flight of the X-38 demonstrator (**Fig. 18**) [12].

The OHB set-up including HFM sensor has been qualified at flight conditions of X-38 demonstrator in the arc heated facility LBK of DLR (**Fig. 19**) [13].

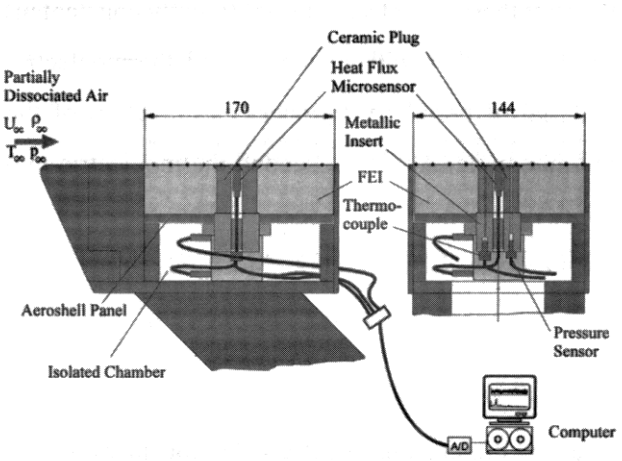


**Figure 18. HFM sensor integrated in the OHB flight component [12]**

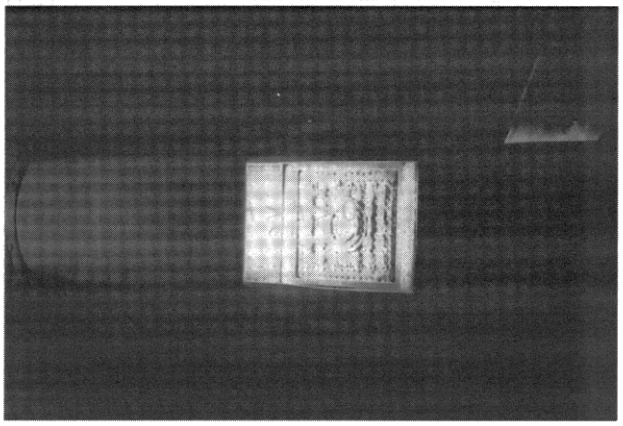

**Figure 19. Qualification test on OHB flight component with a HFM sensor in LBK**

## 5. Calibration of heat flux sensors

Calibration of heat flux sensors is a sophisticated work for engineers. Since heat sources based on convective heating is difficult to handle with respect to their repeatability, mostly radiative calibration sources are used. AEDC has developed two such calibration sources. The first source uses a 1.6 kW xenon arc lamp focussed on a small area to achieve high heat flux rates up to 28.4 MW/m$^2$. To improve the uniformity of the radiant intensity, which is a general problem of most of the radiant heat sources, an integrator consisting of an alu-

minium tube with a highly polished inside surface was installed with its entrance at the focal plane of the calibrator. Another portable calibrator for lower heat flux rate up to 1.4 MW/m$^2$ has a 200 W tungsten filament lamp as heat source. The radiant energy of the lamp is focussed on a small spot of about 7.6 mm at one of the focal point of the ellipsoidal reflector with polished surface (**Fig. 20**). The sensor is placed at this focal point.

Both calibration techniques require a reference sensor in addition to the sensor, which has to be calibrated.

The calibration unit of Vatell uses the radiation of a electrically heated thin graphite plate as heat source [12]. The reference and calibration sensor are installed at each sides of the plate and heated with same radiance intensity. In order to avoid any convection and oxidation processes, the complete furnace is set evacuated down to 1 hPa pressure level. Heat flux rate up to 3.4 MW/m$^2$ can be achieved in this heat flux calibration source.

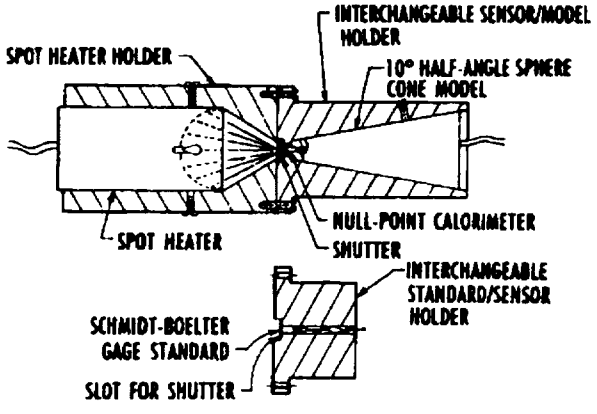


**Figure 20. Sketch of portable calibrator of AEDC [8]**

## 6. Comparative heat flux measurements in LBK

Transient heat flux probe and water cooled steady state calorimeter of LBK (Figs. 4 and 16) are used for the measurement of cold wall heat flux rate to a copper surface at same test conditions. Tests were performed in the stagnation point test configuration of LBK. Both flow conditions were chosen in such a way that moderate heat flux rates can be set. A SiC model with the same geometry as heat flux probes was also tested to determine the hot wall heat flux rate. The duration of the tests on the SiC probe was long enough to reach radiative equilibrium. As mentioned before the hot wall heat flux is determined from the measured surface temperature with a pyrometer. Measured cold and hot wall heat flux rates are listed in **Table 1**.

| **Test condition** | **I** | **II** |
|---|---|---|
| $\dot{q}_{c,t}$ [kW/m$^2$] | 725 | 1080 |
| $\dot{q}_{c,s}$ [kW/m$^2$] | 680 | 1210 |
| $\dot{q}_h$ [kW/m$^2$] | 303 | 351 |

**Table 1. Cold wall heat flux rates to a copper surface measured using transient and calorimeter probes in comparison with hot wall heat flux rates to a SiC model in LBK**

Although at test condition I the agreement between cold wall heat flux rates measured with the transient and calorimeter probes ($\dot{q}_{c,t}$ and $\dot{q}_{c,s}$, respectively) is acceptable, a deviation of around 11% is noticed at the test condition II. A systematic study including a detailed parameter variation is underway to clarify this discrepancy. Another very important results, which is strongly related to non-

equilibrium effects of high enthalpy flow on model surfaces with different catalycity, is the difference between cold and hot wall heat flux rates. As it can be seen in the Table 1 the cold wall heat flux rate is more than twice of the hot one. Since the gas temperature at the stagnation point in the boundary layer flow of the model of more than 4000 K is remarkably higher than the model surface temperature and the difference in the surface temperature of SiC and copper cylinder of cold wall heat flux probes is about 1500 K, this big difference has to be caused by additional gas surface interaction effects. At temperatures beyond 2500 K molecular oxygen in the flow field of LBK is completely dissociated. Spectroscopic measurements and numerical results state that the flow field in the free stream and behind bow shock ahead of the model is in thermochemical non-equilibrium (nearly frozen). Therefore the surface catalysis has an significant influence on the heat flux rate. It is well known that at above specified test condition a $SiO_2$ layer develops due to passive oxidation on the SiC surface. This leads to a low catalytic surface. In contrary copper surface is nearly fully catalytic. Therefore strong exothermic recombination reaction takes place on the copper surface and enhance the heat flux rate. Especially non-equilibrium effects on the gas surface interaction keeps heat flux measurements in high enthalpy flow fields very challenging and require further improvements.

## 7. Concluding remarks

Parallel to the progress in material science, electronics, and spectroscopic techniques the accuracy and application range of heat flux sensors has been improved in the last decades. But compared to other parameters in aerothermodynamics like pressure, flow rate, etc., where accuracy and repeatability values are specified within 1%, usually an accuracy value within 5% cannot be guaranteed for heat flux sensors, yet. Another challenge for engineers is the development of sensors of high accuracy for high temperature application in a reactive environment.

## 8. References

[1] Fay, J. A.; Ridell, F. R.; *Theory of Stagnation Point Heat Transfer in Dissociated Air.* Journal of Aeronautical Sciences, vol. 25, no. 2, pp. 73-85, February 1958.

[2] Andreson, J. D.; *Hypersonic and High Temperature Gas Dynamics.* McGraw-Hill Inc., 1989.

[3] Dorrance, W. H.; *Viscous Hypersonic Flow.* McGraw-Hill Inc., 1962.

[4] Kindler, K.; *Ermittlung einer zeitlich veränderlichen Wärmebelastung auf einen endlichen Zylinder.* 5. Jahrestagung der DGLR in Berlin, Vortrag Nr. 72, 1972.

[5] Grönig, H.; *Kurzzeitmeßtechnik.* Vorlesungsmanuskript der RWTH Aachen.

[6] Fujii, K.; *Thermal Model of the Sensor Plug and Derivation of Heat Transfer Rate from TC Temperature.* TN of NAL, Tokyo, 1996.

[7] Inouye, Y. et.al.; *Quick Report of HYFLEX Onboard Measurements.* 20th International Symposium on Space Technology and Science, Gifu, Japan, May 19-25, 1996.

[8] Kidd, C. T.; *Recent Developments in High Heat-Flux Measurement Techniques at the AEDC.* ISA Paper No. 90-156, presentation at 36th ISA International Instrumentation Symposium, Denver, Col., pp. 477-492, May 1990.

[9] Olivier, H; Grönig, H.; *Instrumentation Techniques of the Aachen Shock Tunnel TH2.* Paper at International Congress on Instrumentation in Aerospace Simulation Facilities (ICIASF), Ohio, USA, 1995.

[10] Jessen, C; Grönig, H.; *A new method for manufacture of thin film heat flux gauges.* Shock Waves, 1, 161-164, Springer Verlag, 1991.

[11] Yakushin, M. I.; *Test Report on Oxidation Tests in IPG-Facility.* IPM RAS, Moscow, April 1995.

[12] Janovsky, R.; Tausche, M.; Romberg, O.; *A Contribution to the Aerothermodynamic Measurement System of the X-38.* Proceedings of the International Symposium on Atmospheric Reentry Vehicles and Systems, Arcachon, March 1999.

[13] Gülhan, A.; Esser, B.; *Qualification Tests on the OHB Aerothermodynamic Measurement System in the Arc Heated Facility LBK.* TET-DLR-21-TN-3401, May 1999.

# Application of Pyrometry and IR-Thermography to High Surface Temperature Measurements

**A. Gülhan**
German Aerospace Center (DLR)
Institute of Fluid Mechanics
Wind Tunnel Division in Cologne
Porz-Wahnheide, Linder Höhe
D-51147 Cologne, Germany

**Summary**

In this document the non-intrusive temperature measurement techniques like pyrometry and IR-thermography and their application at high temperatures are described. For a better understanding first some basic relations of thermal radiation are discussed followed by the absorption behaviour of the atmosphere and optical glasses. Main properties of different IR detector types follows this chapter. Chapters five and six are devoted to the description of pyrometers and IR-cameras including a comparison of different detectors, data reduction and imaging techniques. Based on the experience from application of IR devices at the arc heated facility LBK, some requirements on an IR-system for its use at high enthalpy facilities are defined. Results of comparative and complementary measurements of the surface temperature of several thermal protection materials using pyrometers and IR-cameras are presented in chapter nine.

## 1. List of symbols

| | |
|---|---|
| $A$ | surface area |
| *CCD* | charge coupled device |
| *C-SiC* | carbon fibre reinforced silicon carbide |
| $c$ | speed of light in vacuum |
| $c_1, c_2$ | radiation constants |
| $D$ | detectivity |
| $d$ | distance |
| $E$ | energy |
| *FPA* | focal plane array |
| $h$ | Planck's constant |
| $I$ | photo current |
| *IR* | infrared |
| $k$ | Boltzmann's constant |
| $L$ | radiant intensity |
| *LBK* | arc heated facility of DLR |
| $L_\lambda$ | spectral radiance |
| *NEP* | noise equivalent power |
| $R$ | reflectance |
| $r$ | radius |
| *SiC* | silicon carbide |
| $T$ | temperature |
| *TPS* | thermal protection system |
| $W$ | radiance |
| $\alpha$ | absorption coefficient |
| $\varepsilon$ | emissivity |
| $\Phi$ | radiant flux |
| $\lambda$ | wavelength |
| $\tau$ | transmittance |
| $\nu$ | frequency |
| $\Omega$ | solid angle |

**Subscripts**

| | |
|---|---|
| $b$ | black body |
| *cal* | calibration |
| $D$ | detector |
| $F$ | filter |
| $G$ | geometric |
| $M$ | media |
| $m$ | measured |
| $O$ | optics |
| $p$ | primary |
| $S$ | stop |
| $s$ | secondary |
| $t$ | total |

*Paper presented at the RTO AVT Course on "Measurement Techniques for High Enthalpy and Plasma Flows", held in Rhode-Saint-Genèse, Belgium, 25-29 October 1999, and published in RTO EN-8.*

## 2. Introduction

The measurement of the surface temperature of test models in high enthalpy and hypersonic flows has been a big challenge for engineers. Because of chemical reactions between the solid and gas phases at high temperatures, mechanical temperature sensors like thermocouples, thermo-resistance sensors, etc. find only a limited application in such environments. In these cases and some other applications, where mechanical sensors can disturb the flow field as a result of interaction with the supersonic flow, non-intrusive temperature measurement techniques provide more reliable data. These techniques find a broad application in rotating systems as well.

IR-thermography and pyrometry are two well developed non-intrusive techniques for the measurement of the surface temperature. Because of their relatively simpler hardware, and lower costs mostly pyrometers are used for the measurement of local surface temperatures up to 3000°C. A simultaneous surface temperature distribution, which is sometimes essential for the interpretation of physical phenomena, can only be measured with more complex IR-cameras. Parallel to the developments in electronics and materials for optical components significant progress has been made recently with respect to the temperature resolution, quick response and good accuracy of IR-devices.

In this document, basic relations of thermal radiation, the properties of IR components and different applications of pyrometers and IR-cameras will be discussed.

## 3. Basic relations of thermal radiation

Each object at a temperature of higher than absolute zero emits light in the visible and infrared wavelength ranges. The glowing of materials heated to temperatures above 500°C is the optical manifestation of this radiation. The change in colour of the emitted light with increasing temperature shows the dependence of thermal radiation on wavelength.

Some main parameters of the thermal radiation are defined below [1]:

The radiant flux $\Phi$ is the radiance $dW$ emitted during a time duration $dt$ into a hemisphere:

$$\Phi = dW / dt \ [\mathrm{W/m^2}]. \tag{1}$$

Consider a radiation source element $A_1$ and a detector element $A_2$ in a hemispherical optical space (**Fig. 1**).

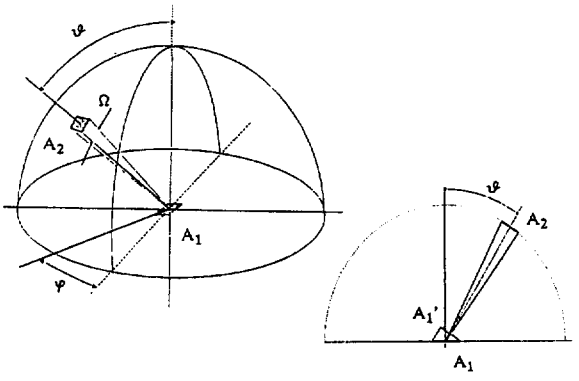


**Figure 1. Beam geometry in a hemispherical space**

Let $\Omega$ be the solid angle subtended by $A_2$ at $A_1$. We then have:

$$\Omega = A_2 / r^2 \left[ m^2 / m^2 \triangleq Steradiant \right]. \tag{2}$$

Using the above mentioned parameters $\Phi$ and $\Omega$ the radiant intensity can be derived as:

$$L = \frac{d^2\Phi}{dA_1 \cdot d\Omega \cdot \cos\Theta}\left[W / m^2 \cdot sr\right]. \quad (3)$$

Since only a limited spectral range of radiation is used in IR-thermography, it is necessary to introduce the spectral radiance (intensity) $L_\lambda$:

$$L_\lambda = \frac{dL}{d\lambda} = \frac{d^3\Phi}{dA_1 \cdot d\Omega \cdot d\lambda \cdot \cos\Theta}. \quad (4)$$

In order to keep the surface energy of an arbitrary body exposed to radiation constant, the sum of the reflected, absorbed and transmitted parts of light must equal the incident radiant intensity. The absorption coefficient $\alpha$, reflectance $R$ and transmission factor $\tau$ of a body are defined as:

$$\alpha = L_{\lambda_{absorbed}} / L_{\lambda_{total}} \quad (5)$$

$$R = L_{\lambda_{reflected}} / L_{\lambda_{total}} \quad (6)$$

$$\tau = L_{\lambda_{transmitted}} / L_{\lambda_{total}}. \quad (7)$$

The condition of constant energy leads to the following relation

$$\alpha + R + \tau = 1. \quad (8)$$

In general, these three parameters are functions of the temperature $T$, the wavelength $\lambda$, the azimuth angle $\varphi$ and the zenith angle $\Theta$ of the radiation:

$$\begin{aligned} \alpha &= \alpha(T, \lambda, \varphi, \Theta) \\ R &= R(T, \lambda, \varphi, \Theta). \\ \tau &= \tau(\lambda, T, \varphi, \Theta) \end{aligned} \quad (9)$$

There are no reliable theoretical relations to describe the dependence on all these parameters. A sophisticated and very complex set-up is necessary to investigate this problem experimentally. Only for special conditions, like for a black body, can the dependence between different radiation parameters be expressed analytically. A black body absorbs the incident light totally. This means the absorption coefficient $\alpha$ is independent of temperature, wavelength and light incident angles and has the value $\alpha = 1$, i.e. $R = \tau = 0$. A cavity surrounded with a cylindrical or spherical body with nontransmittive walls in thermal equilibrium is a common black body. Kirchhoff experimentally found that the ratio of the absorption coefficient $\alpha$ and emission coefficient $\varepsilon$ of an arbitrary surface has a constant value 1 (Kirchhoff's law):

$$\alpha / \varepsilon = 1. \quad (10)$$

According to the Kirchhoff's law the spectral radiance of an arbitrary surface $L_\lambda$ is a product of its emissivity $\varepsilon$ and the radiant intensity of a black body $L_{\lambda_b}$:

$$L_\lambda = \varepsilon \cdot L_{\lambda_b}. \quad (11)$$

The emissivity of a surface also depends on the temperature and the wavelength (the influence of angles $\varphi$ and $\Theta$ is weak and neglected here):

$$\varepsilon = \varepsilon(\lambda, T). \quad (12)$$

Based on quantum mechanics Planck analytically derived the following equation to describe the spectral radiance of a black body (Planck's law):

$$L_{\lambda_b}(\lambda,T)=\frac{c_1}{\Omega\pi\lambda^5}\cdot\frac{1}{e^{c_2/(\lambda\cdot T)}-1} \qquad (13)$$

where

$c_1 = 2\pi c^2 h = 3.7414\cdot10^{-16}$ [Wm²]

$c_2 = ch/k = 1.4388\cdot10^{-2}$ [mK]

and

| | |
|---|---|
| $c = 2.997925\cdot10^{8}$ [m/s] | the speed of light in vacuum |
| $h = 6.6256\cdot10^{-34}$ [J s] | the Planck's constant |
| $k = 1.38054\cdot10^{-23}$ [J/K] | the Boltzmann's constant |

are universal constants.

Thus, the thermal emission of a real body can be described by the following equation:

$$L_\lambda(\lambda,T)=\varepsilon(\lambda,T)\frac{c_1}{\Omega\pi\lambda^5}\cdot\frac{1}{e^{c_2/(\lambda\cdot T)}-1}\,. \qquad (14)$$

For temperatures up to about 2700 K:

$$\lambda T << c_2,\ i.e.,\ e^{c_2/(\lambda\cdot T)} >> 1. \qquad (15)$$

Thus, the Planck's equation can be approximated by the Wien's equation:

$$L_\lambda(\lambda,T)=\varepsilon(\lambda,T)\frac{c_1}{\Omega\pi\lambda^5}\cdot e^{-c_2/(\lambda\cdot T)}. \qquad (16)$$

This equation shows good agreement with the Planck's law within an accuracy of 0.1% and can therefore be applied at low temperatures.

The temperature of a real surface can be determined using the definition of a "black temperature" $T_b(\lambda)$. $T_b(\lambda)$ is the temperature of a black body, which at the wavelength $\lambda$ has the same radiance as the real surface

$$L_\lambda(\lambda,T)=L_{\lambda,b}(\lambda,T_b(\lambda)) \qquad (17)$$

where $T$ is the "true temperature" of the real surface. Planck's law leads to

$$\frac{1}{T}=\frac{1}{T_b}+\frac{\lambda}{c_2}ln\,\varepsilon(\lambda,T)-\frac{\lambda}{c_2}ln\frac{1-e^{-c_2/(\lambda\cdot T)}}{1-e^{-c_2/(\lambda\cdot T_b(\lambda))}}\,. \qquad (18)$$

Using the black temperature, which can be determined from the spectral intensity directly, the temperature of the real body with the same radiance can be calculated using eq. (18).

In practical applications, however, the influence of the measurement environment on the components of the IR-device have to be taken into account for a reliable temperature measurement.

## 4. Optical components of pyrometers and IR-cameras

IR-devices use mainly quantum or thermal detectors and provide photo currents as output signals, which are correlated to the intensity of the emitted light. A principal set-up is shown in **Fig. 2.**

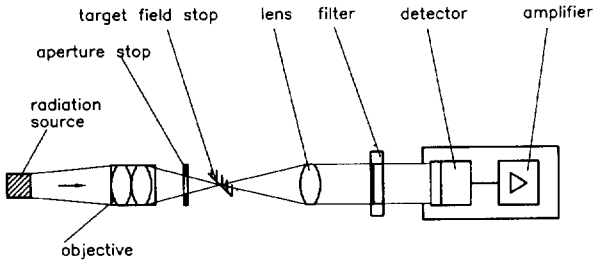


**Figure 2. Main components of an IR-device**

### 4.1 Aperture and field stops

Any element, be it the rim of a lens or a separate diaphragm, which determines the amount of light passing it, is called an aperture stop. At the same time it prevents the light emitted from foreign objects from entering the pyrometer. However highly oblique rays can still enter a system of this sort. Further improvement can be reached using a field stop, which determines the field of view of the instrument.

The spectral response of an IR-device is determined by the spectral behaviour of all its optical and opto-electronic components, i.e. the spectral transmittance of the medium, optical lenses, optical filters and the spectral response of the radiation detector.

### 4.2 Absorption of thermal radiation by the atmosphere

The atmosphere between the radiation source and the detector can partly absorb the emitted light and cause perturbations in temperature measurement. The transmission of optical radiation by the atmosphere depends mainly on two phenomena: self-absorption by the gas species and deflection due to scattering of the light by particles in the gas atmosphere.

**Figure 3** shows the transmission spectrum of the air atmosphere for the given distance under well-defined weather conditions [2]. Since the thermal radiation at temperatures up to 3000°C mainly occurs in the near and middle infrared spectral range, the transmittance $\tau_M$ of atmospheric air in this region is important for IR-measurements. Water vapour in air has strong absorption bands in the infrared spectrum. The main absorption bands due to water vapour lie at about 2.6 µm and between 5.5 µm and 7.5 µm. This fact has to be considered in the frame of the characterization of spectral properties of a IR-devices. Compared to water vapour, the absorption of infrared radiation due to carbon dioxide ($CO_2$) is weaker. Other species in atmospheric air have negligible influence on the transmission of the air for infrared radiation.

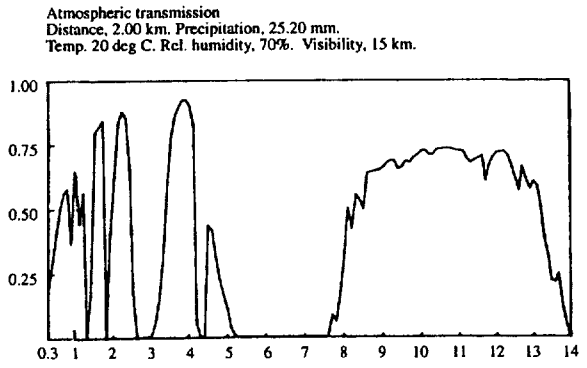


**Figure 3. Spectral transmittance of air atmosphere [2]**

### 4.3 Optical glasses and filters

Beside its optical properties the physical characteristics of an optical system are to be taken into account for its specification. The manufacturing and optical polishing of glasses is only possible above a certain hardness. Another important factor is the matching of optical glasses and their support sys-

tems in terms of their thermal expansion behaviour. Additionally their resistance to physical abrasion and chemical corrosion must be high.

Most optical glasses are not transparent beyond about 3 µm because of strong absorption by OH-ions. Fused quartz or fused silica glasses transmit satisfactorily up to 5 µm. Absorption above this limit is caused due to the vibration of the Si-O band. During the fabrication of glasses particular care is necessary to avoid any water diffusion into the glass, since, as previously shown, water vapour has strong absorption lines in this spectral range. Some special glasses, due to their material properties or fabrication processes can transmit in a much broader spectrum (**Fig. 4**).

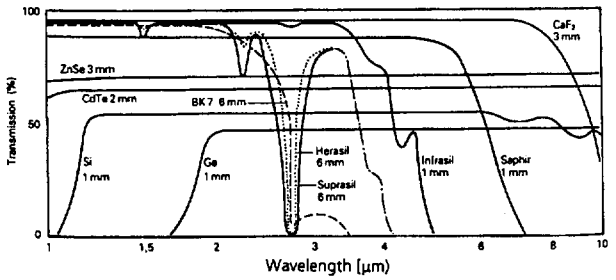


**Figure 4. Transmittance of different optical glasses**

The transmittance of glasses with highly reflective surfaces can be improved by the deposition of an anti-reflective thin film. Using multilayer anti-reflective coatings the reflectance can be reduced (i.e. the transmittance can be increased over a wider spectral range).

Depending on the spectral properties of the detector, different types of filters can be used, in order to provide well-defined spectral intervals of the radiative beam reaching the detector. Low pass filters absorb the light at wavelengths beyond a certain wavelength. High pass filters are transparent only at wavelengths beyond a certain limit. Band-pass filters can be considered as a combination of both these filters and transmit only in a defined wavelength interval. High selectivity can be achieved by means of interference filters. These filters consist of a transparent material with a multilayer surface coating. To achieve strong interference between incident and reflected waves, high reflectivity at the interface is required. Multilayer surface coating of alternate films with high and low refraction indices (mostly metal - dielectric-metal films) provide high and selective reflectance.

### 4.4 Detectors

A radiation detector transforms electromagnetic radiation into an electrical signal. There are two basic types of detector: thermal detectors and quantum detectors.

#### 4.4.1 Thermal detectors

Thermal detectors change their energy level, i.e. temperature, due to absorption of the incident radiation flux. These do not respond to photons but to radiant flux. The output signal of the detector is proportional to the temperature change and is independent of the wavelength.

Bolometers are thermal detectors in which the incident radiation produces a change in the temperature, i.e. in resistance of the sensitive surface (**Fig. 5**) [3]. Due to the constant voltage across the bolometer surface this resistance change leads to a current change. Compared to quantum detectors the response time of bolometers is remarkably longer

(several milliseconds). Metals or semiconductors are used as bolometer materials. The fact that bolometers can be used without detector cooling makes them very interesting for several applications.

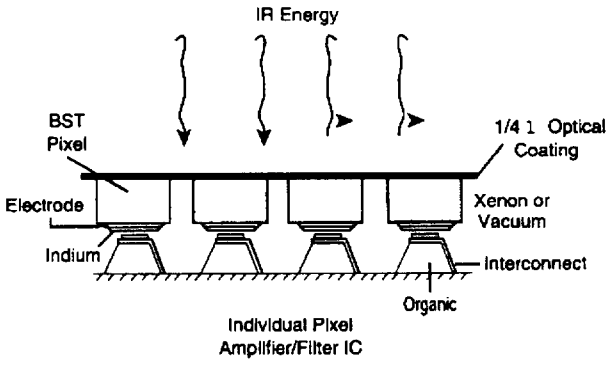


**Figure 5. Bolometer detector [3]**

Thermopiles consisting of several thermocouples, which are connected in series, are also used in IR-devices. As it is known, heating of one junction of a thermocouple compared to other one produces a voltage across the thermoelement. The multijunction of thermopiles allows to achieve sufficient signal even at low heating rates. Thermopiles do not need energy input and therefore find application in IR-systems of satellites.

Pneumatic thermal detectors use the effect of pressure change in a gas chamber due to radiation heating. Two chambers are separated by a membrane and have a capillary connection for pressure equilibrium. The radiance absorption through a sensitive element in the first chamber causes a pressure increase, i.e. deformation of the membrane. It changes electrostatic capacitance of a condenser, which use the membrane as one of the electrodes. Some pneumatic detectors use optical interference method instead of condenser technique.

### 4.4.2 Quantum detectors

Quantum detectors measure the direct excitation of electrons to conduction states by incident photons and are also called photo-electric detectors. There are different types of photo-electric detectors.

Photo emissive detectors consist of a metal photo cathode at a negative voltage and an anode at a positive voltage level. Both electrodes are integrated in an evacuated glass tube. If the energy of incident photons is higher than the electron band energy, they leave the cathode and accelerate to the anode in the vacuum and create a current. The spectral sensitivity of these detectors depends on the optical properties of the photo cathode. Some photo emissive detectors, so-called photo multipliers, consist of a set of electrodes (dynodes), each of them held at a different potential. Each electron colliding with a dynode produces new electrons, which accelerates to the next dynode like a chain reaction and a large number of electrons reach the anode. Photo emissive detectors are sensitive in the ultraviolet, the visible and the near infrared spectra.

The second group of quantum detectors is based on the change of the conductivity of the detector by absorbing photons. In some materials, like semiconductors, electrons excited by the photons do not leave the material but jump to another energy level. At absolute zero temperature, electrons occupy the lowest energy levels in a band called the valence band (**Fig. 6**). When the electrons absorb sufficient energy they can jump to the highly energetic con-

ductive band after passing the forbidden Fermi level. This process is coupled with current creation between those two regions of the material. The difference between the conduction band energy and valence band energy is called the activation energy. If the activation energy of the material is smaller than the energy $h\nu$ of the incident photon, sufficient electrons can cross the forbidden band and the material becomes conductive. These types of materials are called intrinsic semiconductors (PbS, InSb, HgCdTe, etc.). The conductivity of a semiconductor can be increased by doping some foreign particles with different valence levels. The application of photo conductive detectors is restricted by the recombination noise due to the electron-hole pairs by absorption of radiation.

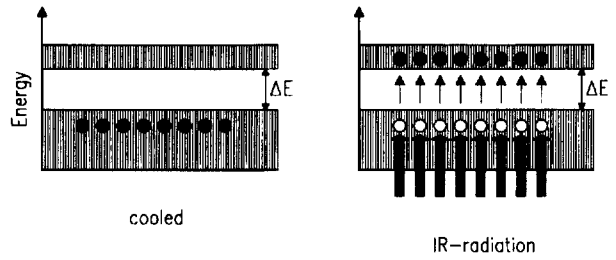


**Figure 6. Photoconductive detector.**

In the case of photovoltaic detectors, the photon absorption changes the potential distribution in the junction area of an inhomogeneous semiconductor. The local change of the electrical field $E$ due to the junction distorts the conduction and valence bands between the $n$ and $p$ regions. The absorption of photons, with sufficient energy, release some electrons and holes which then diffuse across the junction under the influence of the field $E$ and create a current. Photo-electric detectors behave as energy generators and can produce signals even in the absence of bias. Photo voltaic detectors have a faster response than photo conductive detectors. The photo voltaic effect is widely used in photo diodes, photo transistors and infrared detectors such as InAs, InSb and TeCdMg. These types of detectors have a lower noise level than photo conductors. The diffusion of electrons and holes prevents recombination.

### 4.4.3 Detector cooling

The main advantage of thermal detectors is their operation without active cooling. Depending on the application this aspect could be essential. In contrary quantum detectors has to be cooled to achieve a good signal to noise ratio. Each detector has a permanent noise level resulting from the thermal vibrations and the particle nature of light and electricity. The signal power equal to the noise power of the detector is called the noise equivalent power (NEP). It strongly depends on the temperature. The detectivity of a detector $D$ is inversely proportional to the NEP. **Figure 7** shows the detectivity of some detectors at different temperature levels. By reducing the temperature from 295 K to 193 K or 77 K, the noise level can be decreased, i.e. the detectivity can be improved.

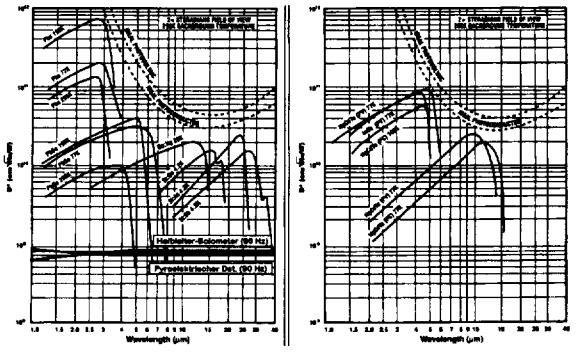

**Figure 7. Spectral detectivity of different detectors [4]**

Depending on the required temperature level, different types of systems can be used for detector cooling: Liquefied gas, Joule-Thomson expansion, cryogenic machines and thermoelectric techniques. Liquid nitrogen keeps the temperature constant at 77 K and is widely used in IR-thermography. The Joule-Thomson effect is used for cooling to temperatures below about 150 K [2]. The thermoelectric technique is applied in a temperature range between 160 K and 320 K. The Peltier thermoelectric effect is the result of the absorption or release of heat at the junction of two different metals with an electrical current flowing across it. In practical applications, a side from the Peltier effect, the thermal conductivity of metals and Joule heating of conductors, which are proportional to the resistance of the metals have to be taken into account.

## 5. Pyrometer technique

Because of their relatively easier imaging and signal processing compared to IR-cameras pyrometers find a broad application in the measurement of local temperatures on objects. Spectral pyrometers and total radiation pyrometers have nearly the same set-up, except for different characteristics of the filter and detector. A typical pyrometer set-up is shown in **Fig. 8**. The spectral transmittance of the filter and the spectral detector response have to match in the chosen wavelength interval.

In general, the radiance emitted by the radiation source can arrive at the detector directly or along other paths due to reflection from foreign objects $(R_k)$ (**Fig. 9**). In addition the radiance of some other light sources or daylight $L_{\lambda_E}$ has to be taken into account. The radiation intensity decreases according to the transmittance of surrounding media $\tau_M$, lenses $\tau_0$, filter $\tau_F$ or stop $\tau_G$ before reaching the detector.

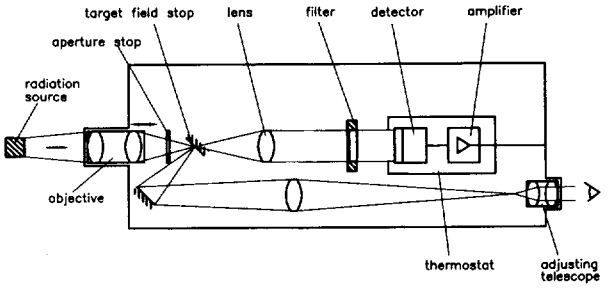


**Figure 8. Set-up of a spectral pyrometer**

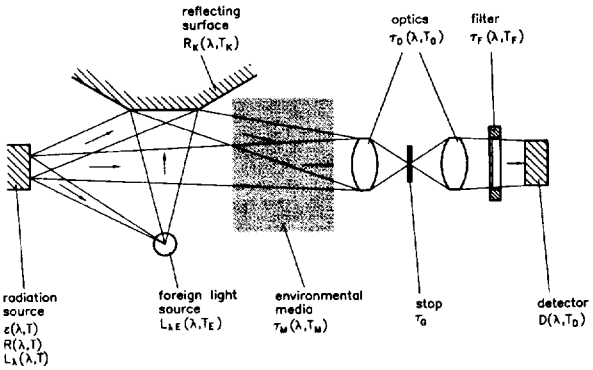


**Figure 9. Beam path of a spectral pyrometer**

If we neglect multiple reflections, the temperature dependence of the reflectance and transmittance of the components, the total radiance can then be expressed by:

$$L_{\lambda_r} = \tau_M(\lambda)\cdot\tau_0(\lambda)\cdot\tau_F(\tau)\cdot\tau_G \cdot\left[\begin{matrix} L_\lambda(\lambda,T)\cdot(1+R_k(\lambda))+ \\ L_{\lambda_E}(\lambda,T_E)\cdot(1+R(\lambda,T)+R_k(\lambda)) \end{matrix}\right] \tag{19}$$

or it can be written in another form:

$$L_{\lambda_r} = \tau_M(\lambda)\cdot\tau_0(\lambda)\cdot\tau_F(\lambda)\cdot\tau_G \cdot\left[L_{\lambda_p}(\lambda,T)+L_{\lambda_s}(\lambda,T_E)\right] \tag{20}$$

where

$$L_{\lambda_p}(\lambda,T) = L_{\lambda}(\lambda,T)\cdot(1+R_k(\lambda))$$

$$L_{\lambda_s}(\lambda,T_E) = L_{\lambda_E}(\lambda,T_E)\cdot(1+R(\lambda,T)+R_k(\lambda)).$$

The spectral radiance of the radiation source $L_{\lambda}(\lambda,T)$ and foreign light sources $L_E(\lambda,T_E)$ are defined by the eq. (14) and (16).

The effective radiance at the detector surface is:

$$L_D = \int_{\lambda_1}^{\lambda_2} \tau_M(\lambda)\cdot\tau_0(\lambda)\cdot\tau_F(\lambda)\cdot\tau_G \cdot\left[L_{\lambda_p}(\lambda,T)+L_{\lambda_s}(\lambda,T_E)\right]d\lambda \quad . \tag{21}$$

The detector itself is characterized by its spectral detectivity $D(\lambda,T_D)$. Since its temperature is usually kept at a constant level, the temperature dependence can be neglected.

The signal of the detector $I_D$ is:

$$I_D = \int_{\lambda_1}^{\lambda_2} \tau_G\cdot\tau_M(\lambda)\cdot\tau_0(\lambda)\cdot\tau_F(\lambda) \cdot\left[L_{\lambda_p}(\lambda,T)+L_{\lambda_s}(\lambda,T_E)\right]D(\lambda)\cdot d\lambda \quad . \tag{22}$$

In practical applications, it is very difficult to describe all parameters as a function of wavelength analytically.

The most efficient way to overcome this problem is to use the linear range of a detector, where the output signal current is proportional to the incident light intensity. After accounting for the optical system of the pyrometer, the current and radiance ratios can be equated as follows:

$$\frac{I_{D_1}}{I_{D_2}} = \frac{L_{D_1}}{L_{D_2}} \quad . \tag{23}$$

Since spectral pyrometers use a narrow wavelength interval, one can write using Planck's equation:

$$\frac{I_{D_1}}{I_{D_2}} = \frac{L_{D_1}}{L_{D_2}} = \frac{e^{c_2/(\lambda_{1,2}\cdot T_2)}-1}{e^{c_2/(\lambda_{1,2}\cdot T_1)}-1} \tag{24}$$

where $\lambda_{1,2}$ is the "mean effective wavelength" of the system relating to temperatures $T_1$ and $T_2$ of a black body. The temperature $T_2$ can be expressed as follows:

$$T_2 = \frac{c_2/\lambda_{1,2}}{ln\left[\frac{I_{D_1}}{I_{D_2}}\left(e^{c_2/(\lambda_{1,2}\cdot T_1)}-1\right)+1\right]} \quad . \tag{25}$$

The data $I_{D_1}$ and $T_1$ are determined by measuring the photo current of the detector $I_{D_1} = I_{cal}$ at a black body of known temperature of $T_1 = T_{cal}$ as a reference point. Using eq. (25) for any measured current level the corresponding surface temperature $T_2 = T$ can be calculated, if $\lambda_{1,2}$ is known.

The "mean effective wavelength" $\lambda_{1,2}$ can be determined by means of any pair of two temperatures [4]. Since $\lambda_{1,2}$ varies slightly with temperature $(\lambda_{1,2}(T))$ some iterative measurements and calculations are required.

For a real radiation source the temperature of the surface can be calculated using the modified form of the eq. (25):

$$T = \frac{c_2/\lambda_{1,2}}{ln\left[\frac{\varepsilon\cdot\tau_t\cdot I_{cal}}{I}\left(e^{c_2/(\lambda_{1,2}\cdot T_{cal})}-1\right)+1\right]} \tag{26}$$

where $\varepsilon$ and $\tau_i$ are the emission coefficient of the surface and the correction of the transmittance of the media between the source and detector, respectively. In practical application the calibration of pyrometers as well as IR-cameras is performed using a more straightforward procedure, which will be explained later.

The emissivity of a surface depends on its temperature and wavelength, as well as on its roughness and state of oxidation. This fact makes it difficult to specify the emission coefficient of a surface accurately. One method of resolving this problem is the two colour pyrometry. The basic idea is that, if the emissivity is not wavelength dependent, then taking a ratio of radiation intensities at two different wavelengths should eliminate the emissivity. Therefore the two colour technique is also called the intensity ratio method. A detailed description of two colour pyrometry is given in different documents [1,6].

## 6. IR-thermography

As it is mentioned before pyrometers are used only for the measurement of the local temperature of object surfaces. In order to measure the temperature distribution of the whole surface, IR-cameras with more complicated set-up are necessary. For both pyrometers and IR-cameras the same basic relations and calibration techniques are applied for the determination of the surface temperature from the measured thermal radiance. Therefore all basic equations (eqs. (1) - (26)) are also valid for IR-cameras.

### 6.1 Scanning and imaging

The thermal radiance of each point of the target has to reach the surface of the IR-detector. The scanning and imaging are performed using two different basic techniques: Image scanning technique and focal plane array (FPA) technique.

#### 6.1.1 Image scanning IR-cameras

Image scanning IR-cameras have a single detector. Using opto-mechanical scanners the radiance intensity of each object surface point is detected successively (**Fig. 10**). To achieve a high image frequency (50-60 Hz) the scanning has to be fast. Since the accuracy of the temperature measurement and the image quality are very essential, the detector properties have to meet the requirements of high scanning speed. Therefore mainly quantum detectors with a response time of several microseconds are used in image scanning IR-cameras. But high frequency imaging reduces the radiance intensity on the detector. Especially at low signal intensity the noise level of detectors has an strong influence on the measurement accuracy. Quantum detectors have a permanent noise level, which depends on the detector temperature. A negative influence of the detector noise on the accuracy of the measurement can only be avoided by detector cooling.

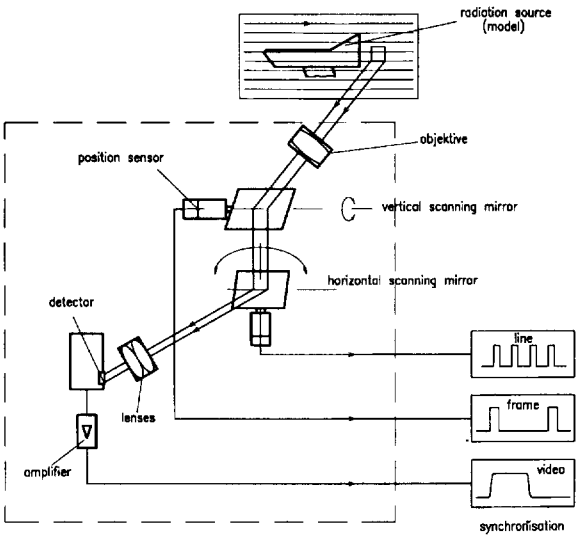


**Figure 10. Image scanning of an IR-camera**

Usually spinning mirrors or refracting prisms are used for scanning. The inertia of these components, light aberration and the geometrical continuity of the image are key parameters of the scanner components. The line scanning technique, which has a fast horizontal pixel by pixel scanning, finds application in most of the scanning cameras. An IR-frame is created by slower line scanning in vertical direction, which is usually performed at lower speed.

The detector provides an electrical signal corresponding to the infrared image. If the IR-camera use the linear range of the detector, this analogue video signal in the form of voltage or current is proportional to the radiance of the object within the spectral range of the IR-equipment. To yield the radiance intensity distribution at each pixel, synchronisation of the scanning with the radiation beam is necessary. Therefore the deflection of the scanner mirrors or prisms is measured by position sensors. These sensors deliver signals, which mark the begin of lines of the frame. The synchronisation signals can be transmitted to the signal processor separately or in multiplex form. The corresponding temperature to each radiance intensity of each pixel is deduced using calibration curves, which are created experimentally (**Fig. 11**).

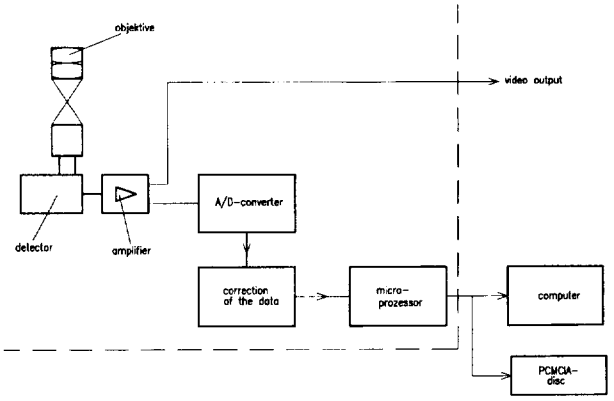


**Figure 11. Signal processing of an IR-camera**

The analogue output signal of the IR-camera is comparable with the television signal and can be monitored easily. The signal can be divided into steps corresponding to different temperature levels, which are marked on the screen.

For further analysis of the large data field the digitisation of the data is necessary. Fast analogue/ digital converters with a resolution between 8 Bits and 14 Bits are used for this process. The digitised data with a well described structure allows a flexible analysis and correction of the data with respect to emissivity, transmittance, etc. easily.

### 6.1.2 Focal Plane Array (FPA) IR-cameras

Each moving component of devices has a limited life duration and is sensitive to misalignment. To overcome such problems focal plane array (FPA) detectors have been developed recently. Comparable to CCD-chips of video cameras FPA detectors

consist of several thousands of small detector elements (for example 320 pixel per each of the 240 lines). The thermal radiance distribution of the object is detected simultaneously. Each detector element has to be compensated individually to gain a high image quality. Most of the FPA IR-cameras use quantum detectors, which require active cooling, in order to keep the noise level low. Stirling cycle cooling consisting of two moving pistons and a regenerator is usually used in recent developments.

Last year AGEMA (now Flir Systems) developed a new type of FPA-camera. The detector consists of 76800 microbolometers made of Si-elements coated with a $VO_x$ thermal resistance layer. As we have seen before bolometers are thermal detectors and are operated without cooling. But besides the thermal radiance of the target, the radiation of components inside the camera may be detected by the uncooled detector arrays, which can influence the measurement accuracy. Therefore the inside case temperature is measured at several locations and is used in the automatic re-calibration of the camera at defined time intervals. In addition to avoid any convective heat transfer to the detector elements, they are placed in a vacuum chamber and their temperature is kept close to the ambient temperature using Peltier elements. Even when the response time of bolometers is remarkably longer than quantum detectors, an image frequency of 60 Hz is achievable with this system. The absence of moving parts makes the operation of the Thermovision 570 S IR-camera of AGEMA more comfortable and safely. Although bolometers are not selective with respect to the spectral range, using optical filters this camera is optimised for a spectral range of 7.5-13 μm.

## 7. Calibration of pyrometers and IR-cameras

Since the radiance of a black body is independent from the surface roughness, the angle of incidence, etc. ($\varepsilon = 1$), black body sources are one of the common calibration devices. One method for realisation of a black body is to develop a perfect absorber by means of some special treatments and surface painting. But this method is limited in the accuracy and temperature range. A second and widely used method is to use a cavity with a very small hole compared to the surface area of the cavity. Due to the multiple reflection of radiation beams inside the cavity, thermal equilibrium is reached after a certain time depending on the cavity wall temperature. Mostly electrical heating technique is used to set different temperature levels in the cavity. Tungsten ribbon lamps consisting of an electrically heated tungsten strip in a glass tube, are also used for the calibration of pyrometers and IR-cameras for the wavelength range up to 2 μm.

As it can be seen in eq. (22) the output signal of the detector of an IR-device is a complex function of the spectral properties of the detector and other optical components. Since an analytical description of this function is very difficult, the relation between the output signal and thermal radiance is determined by calibration data. The output current of the detector can be approximated by the equation:

$$I = \frac{a}{e^{b/T} - 1}. \tag{27}$$

The black body calibration source is heated to different temperature levels and corresponding output signals (current or voltage) are registered. From the so obtained couples ($T_i$, $I_i$) the validation parameters $a$ and $b$ are calculated using the method of least squares approximation. In order to correct the influence of the thermal drift, which may be caused due to the heating of electrical circuits and mechanical components of the camera or change in the ambient temperature, these temperatures have to be recorded during the calibration.

## 8. Requirements on an IR-system at high enthalpy facilities

The choice of an IR-camera or pyrometer for the application at high enthalpy facilities has different priorities depending on the test duration of the facility. The response time of the IR-system is essential for shock tunnels or impulse facilities. Because of the short test duration of several milliseconds only quantum detectors can be used for the IR-application at these facilities. Even the IR-cameras with quantum detectors are limited with the imaging frequency of 50-60 Hz. Therefore the use of IR-cameras at short duration facilities is only possible by the modification of the system for each special case. Because of their faster response time some pyrometers are more convenient for this application.

At arc jet and induction heated facilities with long test duration of several minutes other aspects become more important. Since these facilities are mainly used for the qualification of thermal protection system (TPS) components, surface temperatures up to 3000 °C are achieved. At such high temperatures gas and solid particles with very different spectral properties can be formed around the test model. Especially the deposition of solid particles on the optical windows may change their transmittance in some spectral ranges remarkably. These phenomena influence also the surface emittance of the model. In the transition phase of an oxidation process on the model surface the emissivity may change significantly and lead to problems in the measurement accuracy of the surface temperature by a pyrometer and an IR-camera.

The operation of arc jet and induction heated facilities is coupled to high voltage, high current and strong electromagnetic fields. Besides its possible influence on the measurement device, such environments require special care concerning the safety of the facility operation team. Therefore a flexible remote control of the IR-systems in long duration high enthalpy facilities is very important.

Based on the facts mentioned above the specification of an IR-camera or a pyrometer for high temperature measurements could be performed according to following aspects:

- **Detector properties**

The differentiation of the Planck's relation (eq. (13)) leads to the so-called Wien's law:

$$\lambda_{max} = \frac{2898}{T} \quad [\mu m]. \tag{28}$$

This relation states that the maximum of the spectral radiance moves to shorter wavelengths as the temperature increases (**Fig. 12**).

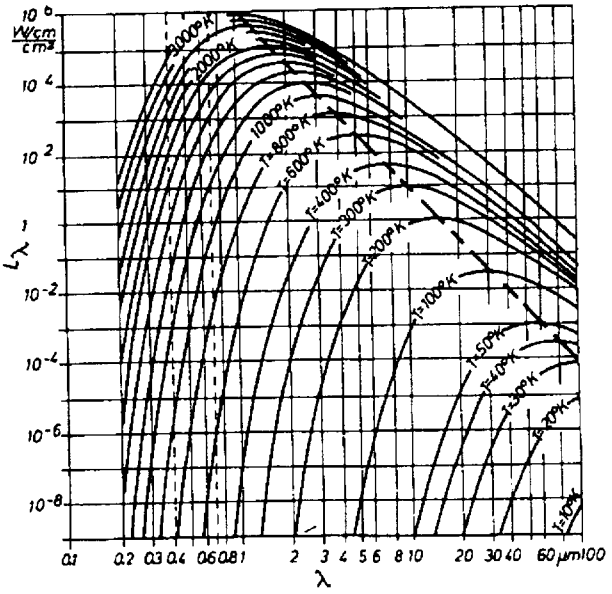


**Figure 12. Black body spectrum at different temperatures [7]**

According to Wien's law the maximum spectral radiance at a surface temperature of 290 K is around 10 μm. At high surface temperatures around 2800 K a detector with a spectral range around 1 μm would provide the maximum output signal. At that point two main properties of the detector are important. The first one is the sensitivity (*S*), which is defined by the relation between the output signal and incident radiance flux. The minimum detectable radiance energy, which is equivalent to the noise level of the detector, is called the noise equivalent power (NEP). The detector detectivity (*D*) is the reverse value of NEP ($D = 1/\text{NEP}$). Both sensitivity and detectivity of the sensor should have a high value in the chosen spectral range. Material properties, coating and the cooling of the detector define *S* and *D*.

- **Thermal and spatial resolution of the IR-system**

The thermal resolution is the minimum detectable difference between the temperatures of different object elements or between the object and its environment. The spatial resolution is the smallest distance between two detectable neighbour object elements. It is usually defined by the elementary solid angle of the system, which results from the combination of different factors like transfer functions of the optics, electronics and visualization system. Both thermal and spatial resolution of an IR-system should be as small as possible.

- **Transmittance of optical components**

The spectral property of optical lenses and filters combined with the detector behaviour define the complete spectral range of an IR-camera or a pyrometer. As defined in the chapter 4.3 most of the optical glasses with OH-ions have a very low transmittance beyond 3 μm. Because of its several absorption lines around in the spectral range of 1-8 μm any water diffusion into the optical glasses has to be avoided. In the spectral range between 7.5-14 μm special glasses with anti-reflective films have to be used.

- **Transmittance of the atmosphere**

As it is described in the chapter 4.2 the atmosphere inside and outside the test chamber have to be considered by the specification of the spectral range of the camera.

- **Radiance of foreign surfaces**

In the case of any other facility component with a significant thermal radiance in the chosen spectral range, the measurement accuracy can be influenced by this foreign radiance source. A proper choice of the spectral range, objective angle and placement

of the camera could allow to overcome this problem.

- **Emissivity of the model surfaces**

The spectral emittance of different materials can vary significantly. Therefore it is very difficult to cover the spectral behaviour of all materials with one IR-system. Since the long duration high enthalpy facilities are mainly used for the qualification of TPS-materials the spectral emissivity of these materials in the high temperature region could be used in the specification of the spectral range of the IR-system.

- **Safety aspects**

As mentioned before the high voltage-current level and strong electromagnetic fields of arc jet and induction heated facilities require special care of the personal safety. Therefore a flexible remote control of the IR-devices is an important aspect for the specification.

## 9. Application different of pyrometers and IR-cameras at LBK

The arc heated facility LBK consisting of two test legs L2K and L3K has been playing an important role in the qualification and testing of TPS components and materials in the frame of different space programmes like Hermes, X-38, etc. The test facility L2K with a maximum electrical power of 1.4 MW is equipped with a Huels type arc heater and allows to achieve cold wall heat flux rates up to 2 MW/m² at stagnation pressures up to 150 hPa. The L3K facility has a segmented arc heater with a 6 MW power supply. Models with a size of 300 mm (W) x 300 mm (L) x 50 mm (H) can be tested in this facility. In the stagnation point configuration cold wall heat flux rates up to 4 MW/ m² at pressures up to 400 hPa can be set on models with a diameter of 150 mm. A detailed description of the facility can be found in several documents [8,9].

### 9.1 Measurement configuration of IR-systems at LBK

Based on the fact that mainly high surface temperatures from 500°C up to 2600°C are achieved in LBK and specification criteria for an IR-system defined in the chapter 8, IR-devices with a spectral range in the near IR-region are more convenient for this facility. The temperature measurement using an unique pyrometer or IR-camera in a wide range between the room temperature and temperatures up to 3000°C with a high accuracy is very difficult. Therefore several spectral pyrometers with different measurement ranges are installed at LBK. All these pyrometers have a spectral range around 1 µm. In addition to spectral pyrometers two two colour pyrometers with a measurement range of 800-2000°C and 900-3000°C are used to perform complementary measurements and to determine the emissivity of materials with grey surface properties. Compared to a pyrometer the hardware and software of an IR-camera is more complicated and expensive. Therefore the type and variety of these systems are limited. As mentioned before the safety of the facility operation team of LBK is a very important issue. As a result of these aspects a FPA-camera with an uncooled bolometer detector and remote control system (AGEMA TV 570 S) has been used at LBK. The spectral range of the camera with a measurement range of –20°C–2000°C is

7.5-13 μm. In order to achieve high accuracy the calibration of the camera has been performed for three different measurement ranges (-20-120°C, 80-500°C, 350-2000°C). **Figure 13** shows the experimental set-up to measure the model surface temperature in LBK using pyrometers and IR-camera.

As shown in Fig. 13 the front surface temperature of the stagnation point model is measured with pyrometers placed outside the test chamber via an optical window. The measurement of the rear surface temperature is also important to investigate the influence of the flow radiation and temperature gradient in the sample. Thermocouples integrated in the insulator part behind the sample have been used to measure the rear surface temperature. But at high temperatures beyond 1600°C chemical interactions between particles released from the sample rear surface and thermocouple limit reliable temperature measurements. Therefore a pyrometer with miniaturized optics was developed for the measurement of sample rear surface temperature [10]. Since the test chamber is exposed to high thermal loads at low pressure levels the pyrometer is placed outside the test chamber and the radiation is transferred to the pyrometer via a fibre-optics connection. The miniaturized optical system is shown in the **Fig. 14.** A lens with a focal length of $f = 20$ mm is used. The distance between the lens and the sample rear surface is about 70 mm. A protective glass is used in front of the lens, in order to avoid any hazard to the lens in the case of a crack in the sample causing high enthalpy flow into the system. The fibre-optics inside the test chamber have a metallic coating and is applicable at temperatures up to 400°C.

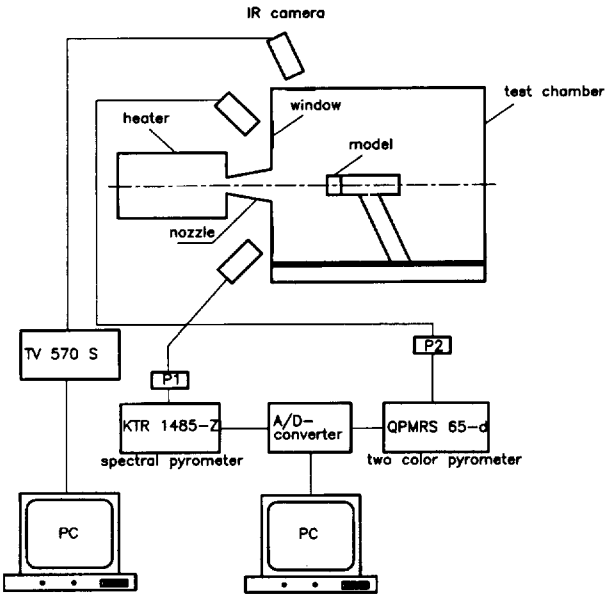


**Figure 13. Experimental set-up of pyrometers and IR-camera at LBK**

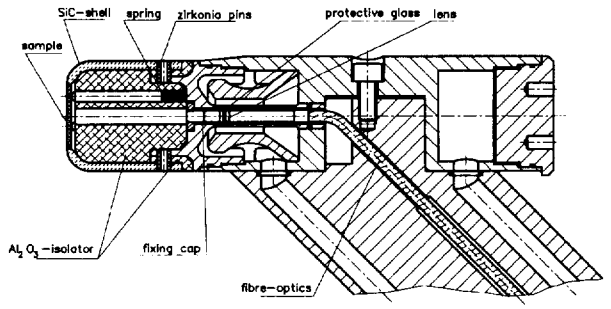


**Figure 14. Miniaturized pyrometer optics integrated in the stagnation point model holder**

## 9.2 Comparative temperature measurements in LBK

Since several parameters like the change of the emissivity due to the oxidation processes on the model surface, modification of the transmittance of the optical windows and test ambient during a test in LBK, comparative measurements using different pyrometers and an IR-camera is very important.

During comparative measurements of the front and rear surface temperatures of a stagnation point model with integrated miniaturized optics several temperature levels were set in L2K. The surface temperature of the sample was varied setting different reservoir flow conditions or moving the sample holder in axial direction to different distances from the exit of a conical nozzle. An unexpected behaviour between surface temperatures measured using the miniaturized pyrometer (rear surface) and the spectral pyrometer (front surface) were noticed (**Table 1**). The measured rear surface temperature is higher than the front surface temperature.

| **front surface** | **front surface** | **rear surface (VL 70/8)** |
|---|---|---|
| **spectral pyrometer** | **two colour pyrometer** | |
| $T_{s1}$ [°C] | $T_{q1}$ [°C] | $T_{q2}$ [°C] |
| 1176 | 1180 | 1222 |
| 1318 | 1330 | 1360 |
| 1381 | 1395 | 1437 |

**Table 1. Surface temperatures measured on a SiC sample in L2K**

Because of some heat losses from the sample to the fixing SiC-shell the front surface temperature has to be higher than the rear surface temperature. In radiation equilibrium the heat flux to the sample can be described as:

$$\dot{q} = \varepsilon \cdot \sigma \cdot \left(T_s^4 - T_\infty^4\right) + \dot{q}_{loss} . \qquad (29)$$

Here $\sigma\left(= 7.56042 \cdot 10^{-16}\, j/\left(K^4 \cdot m^3\right)\right)$, $T_s$ and $T_\infty$ are the Stephan-Boltzmann constant, the surface temperature and the temperature of the environment, respectively. Especially the ambient temperature in the test chamber is negligible compared to the sample surface temperature in the stagnation point configuration. If we neglect the heat loss the equation (29) takes the form:

$$\dot{q} \approx \varepsilon \cdot \sigma \cdot T_s^4 . \qquad (30)$$

The differentiation of this equation leads to the relation

$$\frac{d\dot{q}}{\dot{q}} \approx 4 \cdot \frac{dT_s}{T_s} . \qquad (31)$$

Equation (31) shows that a temperature change of 1% causes nearly 4% change in the equilibrium heat flux rate. Similarly an error in the temperature measurement causes about a four times higher error in the heat flux determination.

The isolation material behind the sample has high and different temperature levels along its length and causes additional radiation, which can increase the radiance at the entrance of the miniature optics. Therefore a small aperture stop was installed between the lens and the fibre-optics and the inner surface of the optics tube was coated with a black layer, in order to eliminate the influence of the foreign illumination and reflected light on the results. After the new calibration of the pyrometer with miniaturized optics using a black body, additional control measurements were performed in the L2K-facility. A significant improvement was achieved due to this modification (**Table 2**).

| front surface | | rear surface (VL 70/8) |
|---|---|---|
| spectral pyrometer | two colour pyrometer | |
| $T_{s1}$ [°C] | $T_{q1}$ [°C] | $T_{q2}$ [°C] |
| 1059 | 1055 | 1062 |
| 1115 | – | 1113 |
| 1120 | – | 1120 |
| 1225 | – | 1231 |
| 1262 | – | 1263 |
| 1306 | – | 1306 |
| 1295 | 1288 | 1296 |

**Table 2. Surface temperatures measured on a SiC sample in L2K with modified miniaturized optics VL 70/8**

According to theoretical estimations and some experimental results the front surface temperature should be about 30-50°C higher than the rear surface temperature. Further investigations are necessary to achieve higher accuracy of the temperature measurement on the rear surface of the sample using the pyrometer with miniaturized optics.

### 9.3 Tests to investigate the influence of external windows and impurities

Since surface temperature measurements using pyrometry are mostly performed by keeping the pyrometer outside the test chamber via optical windows, the radiance of the model surface is partly weaked due to the window. The type and geometry of the optical glass can vary depending on pyrometer characteristics and test conditions in the test chamber. Therefore it is more convenient to consider the influence of the window during control measurements first after the calibration. It avoids repeated device calibrations in the case of the replacement of the window. **Table 3** shows the influence of a quartz-glass (suprasil) with a thickness of 10 mm on the temperature measurements on a SiC-sample in an oven.

| spectral pyrometer | | two colour pyrometer | |
|---|---|---|---|
| without window | with window | without window | with window |
| $T_s$ [°C] | $T_s$ [°C] | $T_q$ [°C] | $T_q$ [°C] |
| 939 | 932 | 943 | 942 |
| 1016 | 1009 | 1024 | 1023 |

**Table 3. Measured temperatures of a black body using a quartz window**

During the influence of the quartz window on the temperature measured using the two colour pyrometer is negligible, this window causes a temperature decrease of about 0.7% in the temperature determined with a spectral pyrometer.

Impurities on the window could also cause some uncertainties in the temperature measurement. Especially water has strong absorption bands in the infrared spectrum. A water droplet with a diameter of about 5 mm was placed on the quartz tube in the radiation beam range and surface temperature of a SiC-sample heated in an oven was measured with both spectral and two colour pyrometers via this window. The results are listed in the **Table 4**.

| spectral pyrometer | | two colour pyrometer | |
|---|---|---|---|
| dry window | wet window | dry window | wet window |
| $T_s$ [°C] | $T_s$ [°C] | $T_q$ [°C] | $T_q$ [°C] |
| 932 | 926 | 942 | 942 |
| 1009 | 1003 | 1023 | 1023 |

**Table 4. The influence of a water droplet on temperatures measured with spectral and two colour pyrometers via a quartz window**

Because of the two narrow band pass filters of the two colour pyrometer at the wavelengths of 920 nm and 1040 nm and the constance of the low water absorption at these two wavelengths no temperature change was caused due to the water droplet placed on the quartz-window. Same water droplet caused a temperature decrease of about 0.6% in the temperatures measured with a spectral pyrometer. The reason may be the absorption of the radiation due to water in a relatively broader wavelength range of 800-1100 nm of the spectral pyrometer.

### 9.4 Angle dependence of temperature measurements

As mentioned before the geometry of the heater and the test chamber of high enthalpy facilities allow to perform temperature measurements of a model in the stagnation point test configuration of high enthalpy facilities only under some angle between the axis of the sample holder and the pyrometer axis. The measurements in LBK-facilities are performed in an angle range of between 30° and 60°. To investigate the influence of the angle on the temperature measurement a SiC-sample was heated in the DLR solar furnace, which allows pyrometer measurements in a wide angle range. The main components of this 15 kW facility are a plain mirror (heliostat) and a large concave mirror (concentrator) [11]. The concentrated solar radiation is deflected to the test room located off-side. The concentrator consists of various concave reflector elements with different focal lengths. Energy flux densities up to 2500 kW/m² in a homogeneous core with a diameter of 80-120 mm can be achieved in this facility. Measurements at different angles ($\alpha$) between the axis of the sample surface exposed to the sun beam and the pyrometer axis were performed. Measured temperatures with spectral and two colour pyrometers are listed in **Table 5.**

While the temperature $T_s$ measured with the spectral pyrometer showed a weak dependence on the measurement angle, a remarkably high temperature increase was noticed in the temperature $T_q$ measured with the two colour pyrometer at the angle of 67.5°. The reason of different of two pyrometers has not been clarified yet.

| $\alpha$ (°) | $T_s$ (°C) | $T_q$ (°C) |
|---|---|---|
| 22.5 | 1003 | 986 |
| 45.0 | 1003 | 992 |
| 67.5 | 1006 | 1049 |

**Table 5. Surface temperatures measured with pyrometers under different angles in the DLR solar furnace**

### 9.5 Different application of the IR-camera at LBK

As mentioned before IR-thermograpy provides a temperature map of the surface and allows a quick judgement concerning the gas surface interaction.

A detailed post-analysis of the measured data and corrections in terms of the surface emissivity and transmittance of the optical windows or the atmosphere can be done using sophisticated software of these systems. The complementary surface temperature measurement using a spectral pyrometer, a two colour pyrometer and an IR-camera in LBK facilities increase the reliability of the experimental data significantly.

**Figure 15** shows the measured temperature distribution on a flap model with a gap between the plate and flap representing the hinge line area of the X-38 demonstrators in LBK. The hot structure made of C/SiC is integrated in a water cooled metal model holder. In order to avoid heat losses from the model to the holder an insulation material was used at the interfaces of the model to the holder nose and side plates. Because of its lower radiation cooling and higher catalysis the surface temperature of the insulation material is much higher than the model surface. But it should be mentioned that this IR-picture is produced for the emissivity value of the C/SiC material ($\varepsilon = 0.8$). Since the emissivity of the insulation material in the spectral range of the IR-camera (7.5-13 μm) is around 0.95 the real temperature of the front part is about 280 K lower than the temperature shown in the **Fig. 16**. Another important point is the temperature development in the gap, which is heated due to the high enthalpy gap forced by the pressure difference between the upper and lower surface of the model at 30° angle of attack. Since the gap front and rear walls, which make nearly 90% of its complete radiation surface, have a very small radiation angle, the gap behaves like a black body. Therefore the effective emissivity is larger than 0.85, which would mean a lower gap temperature of the gap compared to the value given in the IR-picture. The data of thermocouples integrated in the gap confirmed this result. This IR-image shows clearly that the flow filed around the model is two dimensional, which was a very important criteria for the test campaign. Although the temperature gradients are smeared as a result of the lateral heat conduction inside the C/SiC material, the measured surface temperature increase in the front part of ramp is directly correlated to the convective heating behind the re-attachment shock on the ramp. Comparative measurement of the surface temperature of a spot on the ramp using spectral and two colour pyrometers with a spectral range around 1 μm provided an emissivity of 0.85 for this wavelength. These results were confirmed with the data of the manufacturer.

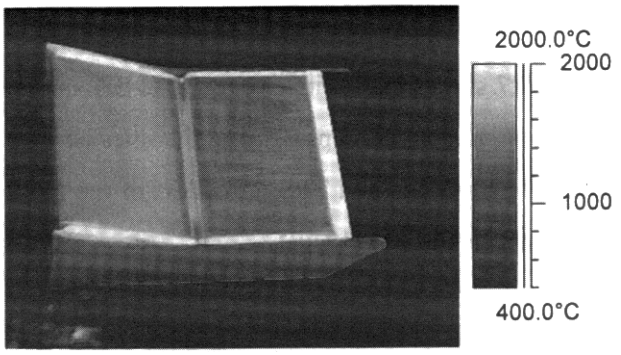


**Figure 15. IR-image of a flap model in LBK (flow from right)**

During qualification tests of the OHB aerothermodynamic measurement system for the first X-38 demonstrator, the IR-image provided a very important result. As it can be seen on the Fig. 16, the heat flux sensor integrated in the centre of the flexible insulation material (FEI) with a protective coating reaches a lower surface temperature than FEI after a testing time of 25 minutes. It is caused

due to the stronger radiative cooling of the sensor and its heat sink effect resulting from a high heat conductivity and large heat capacity of the sub-structure. Again a correct emissivity value of each surface component has to be used, in order to deduce the real surface temperature. Fig. 16 shows the correct temperature of the FEI-material for $\varepsilon = 0.8$.

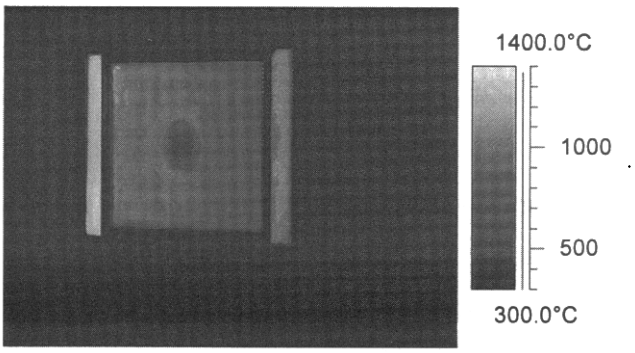


**Figure 16. IR-image of the OHB aerothermodynamic system in the flow field of LBK (flow from left)**

**Figure 17** shows the IR-image of a C/C-SiC model with gap components representing the interface between the nose cap and TPS nose skirt of the X-38 demonstrator in L3K [12,13].

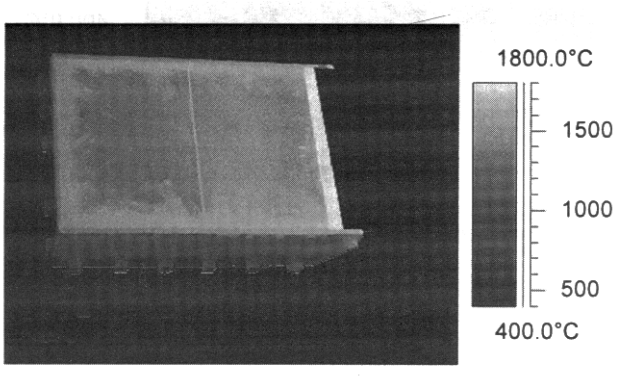


**Figure 17. IR-image of the nose cap and nose skirt interface model in L3K (flow from right)**

Besides its useful information about the temperature development in the gap region, the IR-image confirms the two dimensionality of the flow. The temperature development of a spot about 10 mm upstream of the gap was measured using a spectral pyrometer and a two colour pyrometer (**Fig. 18**).

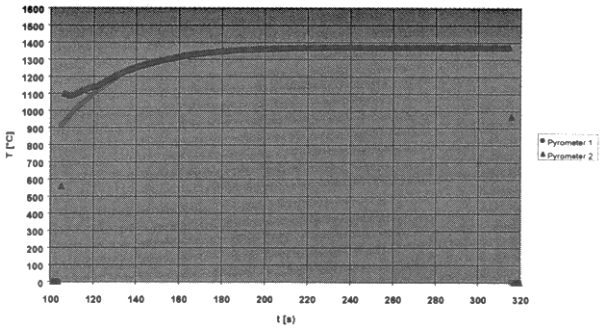


**Figure 18. Surface temperature development measured with a spectral pyrometer and a two colour pyrometer on a C/C-SiC model in L3K**

The analysis of the measured surface temperatures with pyrometers and IR-camera simultaneously indicates a lower emissivity value of 0.8 of the C/C-SiC material at a spectral range of 7.5-13 µm compared to the emittance of 0.85 around 1 µm, which is the spectral range of the pyrometers.

Another IR image of the same model at a different test configuration showed a similar temperature development in the gap region, but indicated an overheating in the edge region of the model holder (**Fig. 19**). The test was performed at an angle of attack of 50°. It seems that even on a two dimensional model at such high angles of attack some three dimensional flow phenomena occur and lead to severe heat loads. The test was interrupted based on the temperature development measured with the IR-camera. Finally an unexpected damage to the

model and model holder was avoided by means of IR-images.

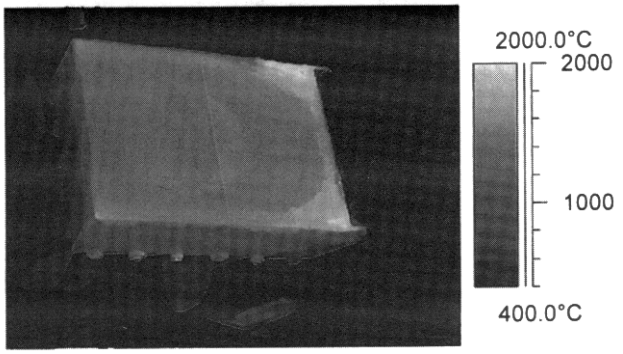


**Figure 19. IR-image of the nose cap and nose skirt interface model in L3K (flow from right)**

## 10. Concluding remarks

Although the accuracy and reliability of the surface temperature measurements using pyrometers and IR-cameras have been improved significantly, further development is necessary for some scientific applications. As mentioned before the very short testing time of few milliseconds of shock tunnels and hot shot facilities requires the use of IR-devices with a very fast response time of some microseconds to measure the surface temperature development of test models in these facilities. Another key issue is the determination of the mostly unknown emissivity of materials and the investigation of its selective behaviour. The two and more colour techniques, which are useful tools for the temperature measurements on grey surfaces, are not sufficient to determine the emissivity of selective materials with high accuracy. Complementary measurement of the thermal radiation and surface reflectance of the model could be an important contribution to the improvement of the accuracy and determination of the emissivity.

## 11. References

[1] Gülhan, A.; *Introduction to pyrometry and comparison of different pyrometer configurations*. VKI Lecture Series on Temperature Measurements, Waterloo, April 22-26, 1996.

[2] Gaussorgues, G.; *Infrared Thermography*. Chapman & Hall, 1995.

[3] TI Technical Journal, Infrared Technology; *Uncooled Infrared Detector Processing*. September-October 1994.

[4] Woerner, B.; *A photoelectric direct current spectral pyrometer with linear characteristics. Temperature, its measurement and control in science and industry*. Volume 5, Editor James F. Schooley. Published by American Institute of Physics.

[5] AGEMA Infrared Systems; *Hintergrundinformationen zu neuen technologischen Entwicklungen auf dem Gebiet der Infrarot-Zustandsüberwachung*. Presseinformation, GE1227P.

[6] Rapp, W.; *Quotientenpyrometer für Temperaturen ab 500°C*. KfK 3371, Kernforschungszentrum Karlsruhe, Juli 1982.

[7] Hunsinger, W.; *Temperaturmessungen mit Strahlungspyrometern*. VDI–Bildungswerk, BW 1456.

[8] Gülhan, A.; *Arc Heated Facility LBK as a Tool to Study High Temperature Phenomena at Re-entry Conditions*. DLR-IB-39113-97A05, 1997.

[9] Gülhan, A.; Esser, B.; *Qualification of TPS-Components in the Arc Heated Facility L3K of DLR.* Proc. of the 3rd European Workshop on Thermal Protection Systems, ESA WPP-141, Noordwijk, pp. 121-130, 1998.

[10] Horstmann, O.; Gülhan, A.; *A pyrometer configuration for measurement of the temperature at the rear side of a TPS-sample.* DLR IB-39113-94A02, 1994.

[11] Becker, M. et al.; *Der Hochflußdichte-Sonnenofen - eine neue Testanlage der DLR.* Einweihung des Sonnenofens am 21. Juni 1994.

[12] Weihs, H.; *Nose Skirt Qualification Test Plan.* TET-DLR-14-TP-3506, 1999.

[13] Gülhan, A.; *Tests on the Feasibility of the Rigid and Flexible Seal Concepts in the Nose Cap Region of X-38.* TET-DLR-21-TN-3514, 1999.

# REPORT DOCUMENTATION PAGE

| 1. Recipient's Reference | 2. Originator's References | 3. Further Reference | 4. Security Classification of Document |
|---|---|---|---|
| | RTO-EN-8<br>AC/323(AVT)TP/23 | ISBN 92-837-1030-4 | UNCLASSIFIED/<br>UNLIMITED |

**5. Originator** Research and Technology Organization
North Atlantic Treaty Organization
BP 25, 7 rue Ancelle, F-92201 Neuilly-sur-Seine Cedex, France

**6. Title**
Measurement Techniques for High Enthalpy and Plasma Flows

**7. Presented at/sponsored by**
the Applied Vehicle Technology Panel (AVT) and held at the von Kármán Institute for Fluid Dynamics (VKI) in Rhode-Saint-Genèse, Belgium, 25-29 October 1999.

| 8. Author(s)/Editor(s) | 9. Date |
|---|---|
| Multiple | April 2000 |
| **10. Author's/Editor's Address** | **11. Pages** |
| Multiple | 400 |

**12. Distribution Statement** There are no restrictions on the distribution of this document. Information about the availability of this and other RTO unclassified publications is given on the back cover.

**13. Keywords/Descriptors**

Enthalpy
Heat measurement
Temperature measuring instruments
Plasmas (physics)
Plasma dynamics
Catalysis
Test facilities
Hypervelocity wind tunnels
Shock tubes
Diagnosis
Reentry vehicles
Hypersonic flow
Temperature measurement
Velocity measurement
Heat transfer
Plasmatrons

**14. Abstract**

The RTO AVT/VKI Special Course on "Measurement Techniques for High Enthalpy and Plasma Flows" gathered specialists in this area from Europe, USA and Russia who combined their efforts to produce this comprehensive set of notes. The following topics were covered:

- review of various high enthalpy and plasma flow facilities,
- intrusive and non intrusive measurement techniques for the characterization of the flows generated in these facilities,
- utilization of the plasma facilities for the evaluation of material catalytic properties.

The material assembled in this report was prepared under the combined sponsorship of the RTO AVT panel, the Consultant and Exchange Program of RTO and the von Kármán Institute (VKI) for Fluid Dynamics.

**NORTH ATLANTIC TREATY ORGANIZATION**

**RESEARCH AND TECHNOLOGY ORGANIZATION**
BP 25 • 7 RUE ANCELLE
F-92201 NEUILLY-SUR-SEINE CEDEX • FRANCE
Télécopie 0(1)55.61.22.99 • E-mail mailbox@rta.nato.int

**DIFFUSION DES PUBLICATIONS**
**RTO NON CLASSIFIEES**

L'Organisation pour la recherche et la technologie de l'OTAN (RTO), détient un stock limité de certaines de ses publications récentes, ainsi que de celles de l'ancien AGARD (Groupe consultatif pour la recherche et les réalisations aérospatiales de l'OTAN). Celles-ci pourront éventuellement être obtenues sous forme de copie papier. Pour de plus amples renseignements concernant l'achat de ces ouvrages, adressez-vous par lettre ou par télécopie à l'adresse indiquée ci-dessus. Veuillez ne pas téléphoner.

Des exemplaires supplémentaires peuvent parfois être obtenus auprès des centres nationaux de distribution indiqués ci-dessous. Si vous souhaitez recevoir toutes les publications de la RTO, ou simplement celles qui concernent certains Panels, vous pouvez demander d'être inclus sur la liste d'envoi de l'un de ces centres.

Les publications de la RTO et de l'AGARD sont en vente auprès des agences de vente indiquées ci-dessous, sous forme de photocopie ou de microfiche. Certains originaux peuvent également être obtenus auprès de CASI.

## CENTRES DE DIFFUSION NATIONAUX

**ALLEMAGNE**
Streitkräfteamt / Abteilung III
Fachinformationszentrum der Bunderswehr, (FIZBw)
Friedrich-Ebert-Allee 34
D-53113 Bonn

**BELGIQUE**
Coordinateur RTO - VSL/RTO
Etat-Major de la Force Aérienne
Quartier Reine Elisabeth
Rue d'Evère, B-1140 Bruxelles

**CANADA**
Directeur - Recherche et développement - Communications et gestion de l'information - DRDCGI 3
Ministère de la Défense nationale
Ottawa, Ontario K1A 0K2

**DANEMARK**
Danish Defence Research Establishment
Ryvangs Allé 1, P.O. Box 2715
DK-2100 Copenhagen Ø

**ESPAGNE**
INTA (RTO/AGARD Publications)
Carretera de Torrejón a Ajalvir, Pk.4
28850 Torrejón de Ardoz - Madrid

**ETATS-UNIS**
NASA Center for AeroSpace Information (CASI)
Parkway Center
7121 Standard Drive
Hanover, MD 21076-1320

**FRANCE**
O.N.E.R.A. (ISP)
29, Avenue de la Division Leclerc
BP 72, 92322 Châtillon Cedex

**GRECE (Correspondant)**
Hellenic Ministry of National Defence
Defence Industry Research & Technology General Directorate
Technological R&D Directorate
D.Soutsou 40, GR-11521, Athens

**HONGRIE**
Department for Scientific Analysis
Institute of Military Technology
Ministry of Defence
H-1525 Budapest P O Box 26

**ISLANDE**
Director of Aviation
c/o Flugrad
Reykjavik

**ITALIE**
Centro documentazione tecnico-scientifica della Difesa
Via Marsala 104
00185 Roma

**LUXEMBOURG**
*Voir* Belgique

**NORVEGE**
Norwegian Defence Research Establishment
Attn: Biblioteket
P.O. Box 25, NO-2007 Kjeller

**PAYS-BAS**
NDRCC
DGM/DWOO
P.O. Box 20701
2500 ES Den Haag

**POLOGNE**
Chief of International Cooperation Division
Research & Development Department
218 Niepodleglosci Av.
00-911 Warsaw

**PORTUGAL**
Estado Maior da Força Aérea
SDFA - Centro de Documentação
Alfragide
P-2720 Amadora

**REPUBLIQUE TCHEQUE**
VTÚL a PVO Praha / Air Force Research Institute Prague
Národní informační středisko obranného výzkumu (NISČR)
Mladoboleslavská ul., 197 06 Praha 9

**ROYAUME-UNI**
Defence Research Information Centre
Kentigern House
65 Brown Street
Glasgow G2 8EX

**TURQUIE**
Millî Savunma Başkanliği (MSB)
ARGE Dairesi Başkanliği (MSB)
06650 Bakanliklar - Ankara

## AGENCES DE VENTE

**NASA Center for AeroSpace Information (CASI)**
Parkway Center
7121 Standard Drive
Hanover, MD 21076-1320
Etats-Unis

**The British Library Document Supply Centre**
Boston Spa, Wetherby
West Yorkshire LS23 7BQ
Royaume-Uni

**Canada Institute for Scientific and Technical Information (CISTI)**
National Research Council
Document Delivery
Montreal Road, Building M-55
Ottawa K1A 0S2, Canada

Les demandes de documents RTO ou AGARD doivent comporter la dénomination "RTO" ou "AGARD" selon le cas, suivie du numéro de série (par exemple AGARD-AG-315). Des informations analogues, telles que le titre et la date de publication sont souhaitables. Des références bibliographiques complètes ainsi que des résumés des publications RTO et AGARD figurent dans les journaux suivants:

**Scientific and Technical Aerospace Reports (STAR)**
STAR peut être consulté en ligne au localisateur de ressources uniformes (URL) suivant:
http://www.sti.nasa.gov/Pubs/star/Star.html
STAR est édité par CASI dans le cadre du programme NASA d'information scientifique et technique (STI)
STI Program Office, MS 157A
NASA Langley Research Center
Hampton, Virginia 23681-0001
Etats-Unis

**Government Reports Announcements & Index (GRA&I)**
publié par le National Technical Information Service
Springfield
Virginia 2216
Etats-Unis
(accessible également en mode interactif dans la base de données bibliographiques en ligne du NTIS, et sur CD-ROM)

*Imprimé par le Groupe Communication Canada Inc.*
*(membre de la Corporation St-Joseph)*
*45, boul. Sacré-Cœur, Hull (Québec), Canada K1A 0S7*

NORTH ATLANTIC TREATY ORGANIZATION

RESEARCH AND TECHNOLOGY ORGANIZATION
BP 25 • 7 RUE ANCELLE
F-92201 NEUILLY-SUR-SEINE CEDEX • FRANCE
Telefax 0(1)55.61.22.99 • E-mail mailbox@rta.nato.int

**DISTRIBUTION OF UNCLASSIFIED RTO PUBLICATIONS**

NATO's Research and Technology Organization (RTO) holds limited quantities of some of its recent publications and those of the former AGARD (Advisory Group for Aerospace Research & Development of NATO), and these may be available for purchase in hard copy form. For more information, write or send a telefax to the address given above. **Please do not telephone**.

Further copies are sometimes available from the National Distribution Centres listed below. If you wish to receive all RTO publications, or just those relating to one or more specific RTO Panels, they may be willing to include you (or your organisation) in their distribution.

RTO and AGARD publications may be purchased from the Sales Agencies listed below, in photocopy or microfiche form. Original copies of some publications may be available from CASI.

## NATIONAL DISTRIBUTION CENTRES

**BELGIUM**
Coordinateur RTO - VSL/RTO
Etat-Major de la Force Aérienne
Quartier Reine Elisabeth
Rue d'Evère, B-1140 Bruxelles

**CANADA**
Director Research & Development
Communications & Information
Management - DRDCIM 3
Dept of National Defence
Ottawa, Ontario K1A 0K2

**CZECH REPUBLIC**
VTÚL a PVO Praha /
Air Force Research Institute Prague
Národní informační středisko
obranného výzkumu (NISČR)
Mladoboleslavská ul., 197 06 Praha 9

**DENMARK**
Danish Defence Research
Establishment
Ryvangs Allé 1, P.O. Box 2715
DK-2100 Copenhagen Ø

**FRANCE**
O.N.E.R.A. (ISP)
29 Avenue de la Division Leclerc
BP 72, 92322 Châtillon Cedex

**GERMANY**
Streitkräfteamt / Abteilung III
Fachinformationszentrum der
Bunderswehr, (FIZBw)
Friedrich-Ebert-Allee 34
D-53113 Bonn

**GREECE (Point of Contact)**
Hellenic Ministry of National
Defence
Defence Industry Research &
Technology General Directorate
Technological R&D Directorate
D.Soutsou 40, GR-11521, Athens

**HUNGARY**
Department for Scientific
Analysis
Institute of Military Technology
Ministry of Defence
H-1525 Budapest P O Box 26

**ICELAND**
Director of Aviation
c/o Flugrad
Reykjavik

**ITALY**
Centro documentazione
tecnico-scientifica della Difesa
Via Marsala 104
00185 Roma

**LUXEMBOURG**
*See* Belgium

**NETHERLANDS**
NDRCC
DGM/DWOO
P.O. Box 20701
2500 ES Den Haag

**NORWAY**
Norwegian Defence Research
Establishment
Attn: Biblioteket
P.O. Box 25, NO-2007 Kjeller

**POLAND**
Chief of International Cooperation
Division
Research & Development
Department
218 Niepodleglosci Av.
00-911 Warsaw

**PORTUGAL**
Estado Maior da Força Aérea
SDFA - Centro de Documentação
Alfragide
P-2720 Amadora

**SPAIN**
INTA (RTO/AGARD Publications)
Carretera de Torrejón a Ajalvir, Pk.4
28850 Torrejón de Ardoz - Madrid

**TURKEY**
Millî Savunma Başkanliği (MSB)
ARGE Dairesi Başkanliği (MSB)
06650 Bakanliklar - Ankara

**UNITED KINGDOM**
Defence Research Information
Centre
Kentigern House
65 Brown Street
Glasgow G2 8EX

**UNITED STATES**
NASA Center for AeroSpace
Information (CASI)
Parkway Center
7121 Standard Drive
Hanover, MD 21076-1320

## SALES AGENCIES

**NASA Center for AeroSpace Information (CASI)**
Parkway Center
7121 Standard Drive
Hanover, MD 21076-1320
United States

**The British Library Document Supply Centre**
Boston Spa, Wetherby
West Yorkshire LS23 7BQ
United Kingdom

**Canada Institute for Scientific and Technical Information (CISTI)**
National Research Council
Document Delivery
Montreal Road, Building M-55
Ottawa K1A 0S2, Canada

Requests for RTO or AGARD documents should include the word 'RTO' or 'AGARD', as appropriate, followed by the serial number (for example AGARD-AG-315). Collateral information such as title and publication date is desirable. Full bibliographical references and abstracts of RTO and AGARD publications are given in the following journals:

**Scientific and Technical Aerospace Reports (STAR)**
STAR is available on-line at the following uniform resource locator:
http://www.sti.nasa.gov/Pubs/star/Star.html
STAR is published by CASI for the NASA Scientific and Technical Information (STI) Program
STI Program Office, MS 157A
NASA Langley Research Center
Hampton, Virginia 23681-0001
United States

**Government Reports Announcements & Index (GRA&I)**
published by the National Technical Information Service
Springfield
Virginia 22161
United States
(also available online in the NTIS Bibliographic Database or on CD-ROM)

*Printed by Canada Communication Group Inc.*
*(A St. Joseph Corporation Company)*
*45 Sacré-Cœur Blvd., Hull (Québec), Canada K1A 0S7*

ISBN 92-837-1030-4